Paul Heitjans
Jörg Kärger
(Editors)

Diffusion in Condensed Matter

Methods, Materials, Models

Springer

Diffusion in Condensed Matter

Paul Heitjans · Jörg Kärger

Diffusion in Condensed Matter

Methods, Materials, Models

With 448 Figures

Springer

Editors

Professor Dr. Paul Heitjans
Universität Hannover
Institut für Physikalische Chemie
und Elektrochemie
Callinstr. 3–3a
D-30167 Hannover, Germany
Email: heitjans@pci.uni-hannover.de

Professor Dr. Jörg Kärger
Universität Leipzig
Institut für Experimentelle Physik I
Linnéstr. 5
D-04103 Leipzig, Germany
Email: kaerger@physik.uni-leipzig.de

Library of Congress Control Number: 2005935206

ISBN-10 3-540-20043-6 Springer Berlin Heidelberg New York
ISBN-13 978-3-540-20043-7 Springer Berlin Heidelberg New York

Springer is a part of Springer Science+Business Media
springeronline.com

Printed in The Netherlands

Typesetting: by the authors and S. Indris using a Springer LaTeX macro package

Cover design: Cover design: *design &production* GmbH, Heidelberg

Printed on acid-free paper SPIN: 10816487 56/3141/jl 5 4 3 2 1 0

To Maria and Birge

Preface

Diffusion as the process of migration and mixing due to irregular movement of particles is one of the basic and ubiquitous phenomena in nature as well as in society. In the latter case the word "particles" may stand for men or ideas, and in the former for atoms or galaxies. In this sense diffusion is a truly universal and transdisciplinary topic.

The present book is confined, of course, to diffusion of atoms and molecules. As this process shows up in all states of matter over very large time and length scales, the subject is still very general involving a large variety of natural sciences such as physics, chemistry, biology, geology and their interfacial disciplines. Besides its scientific interest, diffusion is of enormous practical relevance for industry and life, ranging from steel making to oxide/carbon dioxide exchange in the human lung.

It therefore comes as no surprise that the early history of the subject is marked by scientists from diverse communities, e.g., the botanist R. Brown (1828), the chemist T. Graham (1833), the physiologist A. Fick (1855), the metallurgist W.C. Roberts-Austen (1896) and the physicist A. Einstein (1905). Today, exactly 150 and 100 years after the seminal publications by Fick and Einstein, respectively, the field is flourishing more than ever with about 10.000 scientific papers per year.

From the foregoing it is evident that a single volume book on atomic and molecular diffusion has to be further restricted in its scope. As the title says, the book is confined to diffusion in condensed matter systems, so diffusion in gases is excluded. Furthermore, emphasis is on the fundamental aspects of the experimental observations and theoretical descriptions, whereas practical considerations and technical applications have largely been omitted. The contents are roughly characterized by the headings *Solids*, *Interfaces*, *Liquids*, and *Theoretical Concepts and Models* of the four parts under which the chapters have been grouped.

The book consists of 23 chapters written by leading researchers in their respective fields. Although each chapter is independent and self-contained (using its own notation, listed at the end of the chapter), the editors have taken the liberty of adding many cross-references to other chapters and sections. This has been facilitated by the common classification scheme. Further

help to the reader in this respect is provided by an extended common list of contents, in addition to the contents overview, as well as an extensive subject index.

The book is a greatly enlarged (more than twice) and completely revised edition of a volume first published with Vieweg in 1998. Although the first edition was very well received (and considered as a "must for students and workers in the field"), it was felt that, in addition to the broad coverage of modern methods, materials should also be discussed in greater detail in the new edition. The same applies to theoretical concepts and models. This, in fact, is represented by the new subtitle *Methods, Materials, Models* of *Diffusion in Condensed Matter*.

The experimental *Methods* include radiotracer and mass spectrometry, Mößbauer spectroscopy and nuclear resonant scattering of synchrotron radiation, quasielastic neutron scattering and neutron spin-echo spectroscopy, dynamic light scattering and fluorescence techniques, diffraction and scanning tunneling microscopy in surface diffusion, spin relaxation spectroscopy by nuclear magnetic resonance (NMR) and beta-radiation detected NMR, NMR in a magnetic field gradient, NMR in the presence of an electric field, impedance spectroscopy and other techniques for measuring frequency dependent conductivities.
Materials now dealt with are, among others, metals and alloys, metallic glasses, semiconductors, oxides, proton-, lithium- and other ion-conductors, nanocrystalline materials, micro- and mesoporous systems, inorganic glasses, polymers and colloidal systems, biological membranes, fluids and liquid mixtures. The span from simple monoatomic crystals, with defects in thermal equilibrium enabling elementary jumps, to highly complex systems, exemplarily represented by a biomembrane (cf. Fig. 12.3), is also indicated on the book cover.
Models in the subtitle stands for theoretical descriptions by, e. g., correlation functions, lattice models treated by (approximate) analytical methods, the theory of fractals, percolation models, Monte Carlo simulations, molecular dynamics simulations, phenomenological approaches like the counterion model, the dynamic structure model and the concept of mismatch and relaxation.

Despite the large variety of topics and themes the coverage of diffusion in condensed matter is of course not complete and far from being encyclopedic. Inevitably, it reflects to a certain extent also the editors' main fields of interest. Nevertheless the chapters are believed to present a balanced selection.

The book tries to bridge the transition from the advanced undergraduate to the postgraduate and active research stage. Accordingly, the various chapters are in parts tutorial, but they also lead to the forefront of current research without intending to mimic the topicality of proceedings, which normally have a short expiry date. It is therefore designed as a textbook or refer-

ence work for graduate and undergraduate students as well as a source book for active researchers.

The invaluable technical help of Dr. Sylvio Indris (University of Hannover) in the laborious editing of the chapters, which in some cases included extensive revision, is highly acknowledged. We also thank Jacqueline Lenz and Dr. T. Schneider from Springer-Verlag for accompanying this project. As ever, the editors have to thank their wives, Maria Heitjans and Birge Kärger, for their patience and encouragement.

Hannover, Germany — *Paul Heitjans*
Leipzig, Germany — *Jörg Kärger*
August 2005

Contents – Overview

Contents – In Detail

Part I Solids

Part III Liquids

Part I

Solids

1 Diffusion: Introduction and Case Studies in Metals and Binary Alloys

Helmut Mehrer

1.1 Introduction

Diffusion in solids is an important topic of physical metallurgy and materials science. Diffusion processes play a key role in the kinetics of many microstructural changes that occur during processing of metals, alloys, ceramics, semiconductors, glasses, and polymers. Typical examples are nucleation of new phases, diffusive phase transformations, precipitation and dissolution of a second phase, recrystallization, high-temperature creep, and thermal oxidation. Direct technological applications concern, e.g., diffusion doping during fabrication of microelectronic devices, solid electrolytes for battery and fuel cells, surface hardening of steel through carburization or nitridation, diffusion bonding, and sintering.

The atomic mechanisms of diffusion in crystalline materials are closely connected with defects. Point defects such as vacancies or interstitials are the simplest defects and often mediate diffusion. Dislocations, grain boundaries, phase boundaries, and free surfaces are other types of defects of crystalline solids. They can act as diffusion short circuits, because the mobility of atoms along such defects is usually much higher than in the lattice.

This chapter will concentrate on bulk diffusion in solid metals and alloys. Most of the solid elements are metals. Furthermore, diffusion properties and atomic mechanisms of diffusion have most thoroughly been investigated in metallic solids. On the other hand, many of the physical concepts, which have been developed for metals, apply to diffusion in all crystalline solids. Those effects, which are unique to non-metallic systems such as charge effects in ionic crystals and semiconductors, are treated in Chaps. 4 and 5.

For a comprehensive treatment of diffusion in solid matter the reader is referred to the textbooks of Shewmon [1], Philibert [2], Heumann [3], Allnatt and Lidiard [4], and Glicksman [5]. A critical collection of data for diffusion in metals and alloys was edited in 1990 by Mehrer [6]. Recent developments can be found in the proceedings of a series of international conferences on 'Diffusion in Materials' [7–9]. The field of grain- and interphase-boundary diffusion is described in Chap. 8 and in the book of Kaur, Mishin and Gust [10]. The book of Crank [11] provides an excellent introduction to the mathematics of diffusion.

1.2 Continuum Description of Diffusion

1.2.1 Fick's Laws for Anisotropic Media

The diffusion of atoms through a solid can be described by Fick's equations. The first equation relates the diffusion flux $\boldsymbol{\jmath}$ (number of atoms crossing a unit area per second) to the gradient of the concentration c (number of atoms per unit volume) via

$$\boldsymbol{\jmath} = -\mathcal{D}\nabla c. \tag{1.1}$$

The quantity $\mathcal{D}$ is denoted as diffusion coefficient tensor or as diffusivity tensor. The dimensions of its components are length^2 time^{-1}. Its SI units are [m^{2}s^{-1}]. Equation (1.1) implies that $\mathcal{D}$ varies with direction. In general the diffusion flux and the concentration gradient are not always antiparallel. They are antiparallel for an isotropic medium.

For anisotropic media and non-cubic crystalline solids $\mathcal{D}$ is a symmetric tensor of rank 2 [12]. Each symmetric second rank tensor can be reduced to diagonal form. The diffusion flux is antiparallel to the concentration gradient only for diffusion along the orthogonal principal directions. If x_1, x_2, x_3 denote these directions and j_1, j_2, j_3 the pertaining components of the diffusion flux, (1.1) can be written as

$$j_1 = -D_I \frac{\partial c}{\partial x_1},\; j_2 = -D_{II} \frac{\partial c}{\partial x_2},\; j_3 = -D_{III} \frac{\partial c}{\partial x_3}, \tag{1.2}$$

where D_I, D_{II}, D_{III} denote the three principal diffusivities. The diffusion coefficient for a direction $(\alpha_1, \alpha_2, \alpha_3)$ is obtained from

$$D(\alpha_1, \alpha_2, \alpha_3) \;=\; \alpha_1^2 D_I + \alpha_2^2 D_{II} + \alpha_3^2 D_{III}, \tag{1.3}$$

where α_i denote the direction cosine of the diffusion flux with axis i. Equation (1.3) shows that anisotropic diffusion is completely described by the three principal diffusion coefficients.

For uniaxial (hexagonal, tetragonal, trigonal) crystals and decagonal quasicrystals with the unique axis parallel to the x_3 axis we have $D_I = D_{II} \neq D_{III}$ and (1.3) reduces to

$$D(\Theta) \;=\; D_I \sin^2 \Theta \;+\; D_{III} \cos^2 \Theta, \tag{1.4}$$

where Θ denotes the angle between diffusion direction and crystal axis. For isotropic media such as amorphous metals and inorganic glasses, cubic crystals and icosahedral quasicrystals

$$D_I \;=\; D_{II} \;=\; D_{III} \;\equiv D. \tag{1.5}$$

Then the diffusion coefficient tensor is reduced to a scalar quantity.

Steady state methods for measuring diffusion coefficients, like the permeation method [3], are directly based on Fick's first law. In non-steady state

situations diffusion flux and concentration vary with time t and position x. In addition to Fick's first law a balance equation is necessary. For particles which undergo no reactions (no chemical reaction, no reactions between different types of sites in a crystal, etc.) this is the continuity equation

$$\frac{\partial c}{\partial t} + \nabla \boldsymbol{J} = 0. \tag{1.6}$$

Combining (1.1) and (1.6) leads to Fick's second equation (also called diffusion equation)

$$\frac{\partial c}{\partial t} = \nabla(\mathcal{D}\nabla c). \tag{1.7}$$

1.2.2 Fick's Second Law for Constant Diffusivity

In diffusion studies with trace elements very tiny amounts of the diffusing species can be applied. Then the composition of the sample during the investigation does practically not change (see also Sect. 1.3) and D is independent of the tracer concentration. Also diffusion in ideal solutions is described by a concentration-independent diffusion coefficient. Then for diffusion in a certain direction x (1.7) reduces to

$$\frac{\partial c}{\partial t} = D\frac{\partial^2 c}{\partial x^2}. \tag{1.8}$$

From a mathematical point of view (1.8) is a second order, linear partial differential equation. Initial and boundary conditions are necessary for particular solutions of this equation. Solutions can be found in the book of Crank for a variety of initial and boundary conditions [11]. These solutions permit the determination of D from measurements of the concentration distribution as a function of position and time. We consider two simple examples which, however, are often relevant for the analysis of experiments.

Thin-Film Solution

If a thin layer of the diffusing species (M atoms per unit area) is concentrated at $x = 0$ of a semi-infinite sample, the concentration after time t is described by

$$c(x,t) = \frac{M}{\sqrt{\pi Dt}} \exp\left(-\frac{x^2}{4Dt}\right). \tag{1.9}$$

The quantity $\sqrt{Dt}$, called diffusion length, is a characteristic distance for diffusion problems. The experimental determination of diffusion coefficients by the tracer method discussed in Sect. 1.4 is based on (1.9). It is applicable if $\sqrt{Dt}$ is much larger than the initial layer thickness.

Error Function Solution

Suppose that at $t = 0$ the concentration of the diffusing species is $c(x, 0) = 0$ for $x > 0$. Then, if for $t > 0$ the concentration at $x = 0$ is maintained at $c(0, t) = c_s$, the appropriate solution of (1.8) is

$$c(x,t) \;=\; c_s \mathrm{erfc}\Big(\frac{x}{2\sqrt{Dt}}\Big), \tag{1.10}$$

where the complementary error function is defined by

$$\mathrm{erfc}\, z \;\equiv\; 1 - \mathrm{erf}\, z \tag{1.11}$$

and

$$\mathrm{erf}\, z \equiv \;\frac{2}{\sqrt{\pi}} \int\limits_0^z \exp\left(-u^2\right) \mathrm{d}u \tag{1.12}$$

denotes the error function. Equation (1.10) describes the in-diffusion of a diffuser (or diffusant) into a semi-infinite sample with constant concentration c_s of that species at the surface. It is, e.g., applicable to the in-diffusion of a volatile solute into a non-volatile solvent, to the carburization of a metal in a carbon containing ambient, and to in-diffusion of a solute from an inexhaustible diffusion source into a solvent with solubility c_s.

1.2.3 Fick's Second Law for Concentration-Dependent Diffusivity

Let us consider a case of great practical importance, in which the chemical composition during diffusion varies over a certain concentration range. Diffusing particles will experience different chemical environments and hence different diffusion coefficients. This situation is denoted as interdiffusion or as chemical diffusion. We use the symbol $\tilde{D}$ to indicate that the diffusion coefficient is concentration dependent. $\tilde{D}$ is denoted as interdiffusion coefficient or as chemical diffusion coefficient. Fick's second law (1.7) for diffusion in a certain direction x then reads

$$\frac{\partial c}{\partial t} = \frac{\partial}{\partial x}\left(\tilde{D}(c)\frac{\partial c}{\partial x}\right) = \tilde{D}(c)\frac{\partial^2 c}{\partial x^2} + \frac{\mathrm{d}\tilde{D}(c)}{\mathrm{d}c}\left(\frac{\partial c}{\partial x}\right)^2 . \tag{1.13}$$

Theoretical models which permit the calculation of the composition dependent diffusivity from deeper principles using, e.g., statistical mechanics are nowadays still not broadly available. Then the strategy illustrated in the previous section of calculating the concentration field for certain initial and boundary conditions is not applicable. Instead, it is possible to invert this strategy and to determine the interdiffusion coefficient from a given concentration field by using (1.13). The classical Boltzmann-Matano method for extracting the concentration-dependent diffusivity $\tilde{D}(c)$ from experimental concentration-depth profiles will be considered in Sect. 1.11 of this chapter.

1.3 The Various Diffusion Coefficients

Diffusion in materials is characterized by several diffusion coefficients. In this section we describe various experimental situations which entail different diffusion coefficients. We will, however, concentrate on bulk diffusion in unary and binary systems. Diffusion in ternary systems produces mathematical complexities which are beyond the scope of this chapter. We will focus on bulk diffusion since diffusion along grain boundaries and along surfaces is treated in Chaps. 7 and 8 of this book. In this section we will distinguish the various diffusion coefficients by lower and upper indices. We will drop the indices in the following sections again, whenever it is clear which diffusion coefficient is meant.

1.3.1 Tracer Diffusion Coefficients

In diffusion studies with trace elements (tagged by their radioactivity or by their isotopic mass) tiny amounts of the diffusing species can be used. Although there will be a gradient in the concentration of the trace element, its total concentration can be kept so small that the overall composition of the sample during the investigation does practically not change[1]. In such cases a constant tracer diffusion coefficient is appropriate for the analysis of the experiments.

Self-Diffusion Coefficient

If the diffusion of A-atoms in a solid element A is studied, one speaks of self-diffusion. Studies of self-diffusion utilize a tracer isotope A^* of the same element. A typical initial configuration for a tracer self-diffusion experiment is illustrated in Fig. 1.1a. If the applied tracer layer is very thin as compared to the average diffusion length, the tracer self-diffusion coefficient $D_A^{A^*}$ is obtained from such an experiment.

The connection between the macroscopically defined tracer self-diffusion coefficient and the atomistic picture of diffusion is the famous Einstein-Smoluchowski relation discussed in detail in Sect. 1.6. In simple cases it reads

$$D_A^{A^*} = f D_E \quad \text{with} \quad D_E = \frac{l^2}{6\tau}, \tag{1.14}$$

where l denotes the jump length and τ the mean residence time of an atom on a certain site of the crystal[2]. The quantity f is the correlation factor. For self-diffusion in cubic crystals f is a numeric factor. Its value is characteristic

[1] From an atomistic viewpoint this implies that a tracer atom is not influenced by other tracer atoms.

[2] Equation (1.14) considers only the simplest case: cubic structure, all sites are energetically equivalent, only jumps to nearest neighbours are allowed.

of the lattice geometry and the diffusion mechanism (see Sect. 1.6). In some textbooks the quantity D_{E} is denoted as the Einstein diffusion coefficient[3].

In a homogeneous binary $\mathrm{A}_X\mathrm{B}_{1-X}$ alloy or compound two tracer diffusion coefficients for both, A^* and B^* tracer atoms, can be measured. A typical experimental starting configuration is displayed in Fig. 1.1b. We denote the tracer diffusion coefficients by $D^{\mathrm{A}^*}_{\mathrm{A}_X\mathrm{B}_{1-X}}$ and $D^{\mathrm{B}^*}_{\mathrm{A}_X\mathrm{B}_{1-X}}$. Both tracer diffusion coefficients will in general be different:

$$D^{\mathrm{A}^*}_{\mathrm{A}_X\mathrm{B}_{1-X}} \neq D^{\mathrm{B}^*}_{\mathrm{A}_X\mathrm{B}_{1-X}}. \tag{1.15}$$

This diffusion asymmetry depends on the crystal structure of the material and on the atomic mechanisms which mediate diffusion. Both diffusivities, of course, also depend on temperature and composition of the alloy or compound and for anisotropic media on the direction of diffusion. Self-diffusion in metallic elements will be considered in Sect. 1.8. Self-diffusion in binary intermetallics is the subject of Sect. 1.10.

Impurity Diffusion Coefficient

When the diffusion of a trace solute C^* in a monoatomic solvent A or in a homogeneous binary solvent $\mathrm{A}_X\mathrm{B}_{1-X}$ (Fig. 1.1) is measured, the tracer diffusion coefficients

$$D^{\mathrm{C}^*}_{\mathrm{A}} \text{ and } D^{\mathrm{C}^*}_{\mathrm{A}_X\mathrm{B}_{1-X}}$$

are obtained. These diffusion coefficients are denoted as impurity diffusion coefficients or sometimes also as foreign atom diffusion coefficients.

1.3.2 Chemical Diffusion (or Interdiffusion) Coefficient

So far we have considered in this section cases where the concentration gradient is the only cause for the flow of matter. We have seen that such situations can be studied using tiny amounts of trace elements in an otherwise homogeneous material. However, from a general viewpoint a diffusion flux is proportional to the gradient of the chemical potential.

The chemical potential of a species i in a binary alloy is given by (cf. Chap. 5)

$$\mu_i = \left(\frac{\partial G}{\partial n_i}\right)_{p,T,n_{j\neq i}} \qquad i = \mathrm{A}, \mathrm{B} \tag{1.16}$$

In (1.16) G denotes Gibbs free energy, n_i the number of moles of species i, T the temperature, and p the hydrostatic pressure. The chemical potential

[3] This notation is a bit misleading, since the original Einstein-Smoluchowski relation relates the total macroscopic mean square displacement of atoms to the diffusion coefficient (see Sect. 1.6), in which correlation effects are included.

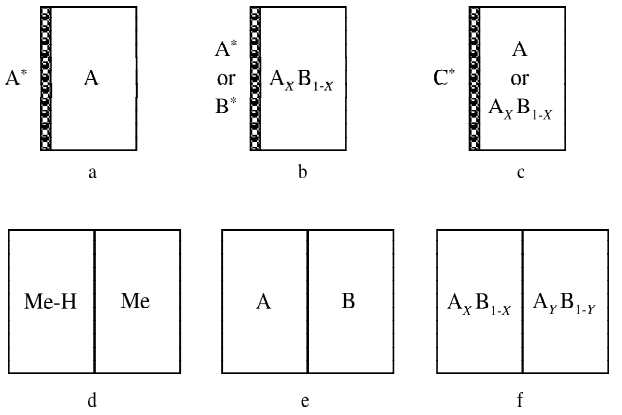

Fig. 1.1. Initial configurations for diffusion experiments:
a) Thin layer of A^* on A: tracer diffusion in pure elements.
b) Thin layer of A^* or B^* on homogeneous alloy: tracer diffusion of alloy components.
c) Thin layer of C^* on element A or homogeneous alloy: Impurity diffusion.
d) Diffusion couple between metal-hydrogen alloy and a pure metal.
e) Diffusion couple between pure end-members.
f) Diffusion couple between two homogeneous alloys.

depends on the alloy composition. For ideal solutions the chemical potentials are

$$\mu_i = \mu_i^0 + RT \ln \frac{n_i}{n_\mathrm{A} + n_\mathrm{B}} \quad , \tag{1.17}$$

where μ_i^0 depend on T and p only. In this case the gradient of the chemical potential is directly proportional to the logarithmic gradient of the concentration. In non-ideal solutions the gradient of the chemical potential gives rise to an 'internal' driving force. As a consequence the interdiffusion diffusion coefficient is concentration-dependent and Fick's equation in the form of (1.13) must be used.

Examples of diffusion couples which entail an interdiffusion coefficient are (see Fig. 1.1):
(i) Pure end-member diffusion couples consisting of two samples of pure elements joined together (e.g. Ni/Pd, Cu/Ag, ...).
(ii) Incremental diffusion couples consisting of two samples of homogenous alloys joined together (e.g. $Ni_{50}Pd_{50}/Ni_{70}Pd_{30}$, $Ni/Ni_{70}Pd_{30}$, ...).
(iii) Diffusion couples which involve solutions of hydrogen in a metal (e.g. Pd-H/Pd, $Ag_{1-X}H_X/Ag_{1-Y}H_Y$, ...). Binary metal-hydrogen systems are often special in the sense that hydrogen is the only mobile component.

Interdiffusion results in a composition gradient in the diffusion zone. Interdiffusion profiles are analysed by the Boltzmann-Matano method or related procedures. This method will be described in Sect. 1.11. It permits to deduce the concentration dependence of the interdiffusion coefficient

$$\tilde{D} = \tilde{D}(c) \tag{1.18}$$

from the experimental diffusion profile.

1.3.3 Intrinsic Diffusion Coefficients

The intrinsic diffusion coefficients (sometimes also component diffusion coefficients) D_{A} and D_{B} of a binary A-B alloy describe diffusion of the components A and B relative to the lattice planes. The diffusion rates of A and B atoms are usually not equal. Therefore, in an interdiffusion experiment a net flux of atoms across any lattice plane exists. The shift of lattice planes with respect to a sample fixed axis is denoted as Kirkendall effect, which is illustrated in Fig. 1.27 in Sect. 1.11. The Kirkendall shift can be observed by incorporating inert markers at the initial interface of a diffusion couple. This shift was for the first time observed for Cu/Cu-Zn diffusion couples by Kirkendall and coworkers [13]. In the following decades work on many different alloy systems and a variety of markers demonstrated that the Kirkendall effect is a widespread phenomenon of interdiffusion.

The intrinsic diffusion coefficients D_{A} and D_{B} of a substitutional binary A-B alloy are related to the interdiffusion coefficient $\tilde{D}$ and the marker velocity v_{K} (Kirkendall velocity). These relations were deduced for the first time by Darken [14] and refined later on by Manning [15]. They will be discussed in Sect. 1.11. If the quantities $\tilde{D}$ and v_{K} are known from experiment the intrinsic diffusion coefficients can be deduced.

We emphasize that the intrinsic diffusion coefficients and the tracer diffusion coefficients are different. D_{A} and D_{B} pertain to diffusion in a composition gradient whereas $D_{\mathrm{AB}}^{\mathrm{A}^*}$ and $D_{\mathrm{AB}}^{\mathrm{B}^*}$ are determined in a homogenous alloy. They are approximately related (see Sect. 1.11 for details) via

$$D_{\mathrm{A}} = D_{\mathrm{AB}}^{\mathrm{A}^*}\Phi \quad \text{and} \quad D_{\mathrm{B}} = D_{\mathrm{AB}}^{\mathrm{B}^*}\Phi, \tag{1.19}$$

where Φ denotes the so-called thermodynamic factor (see Sect. 1.11). In a metal-hydrogen system ususally only the H atoms are mobile. Then the intrinsic diffusion coefficient and the chemical diffusion coefficient of hydrogen are identical.

1.4 Experimental Methods

Methods for the measurement of diffusion coefficients can be grouped into two major categories: Direct methods are based on Fick's laws and the phenomenological definition of the diffusion coefficients given in Sect. 1.3. Indirect methods are not based directly on Fick's laws. Their interpretation requires a microscopic model of the atomic jump processes and then uses the Einstein-Smoluchowski relation to deduce a diffusion coefficient.

1.4.1 Direct Methods

Tracer Method

The tracer method is the most direct and most accurate technique for the determination of diffusion coefficients in solids. Since very tiny amounts of trace isotopes can be applied in tracer experiments, the chemical composition of the sample is practically not influenced by the tracer. In this way self-diffusion and impurity diffusion can be studied in a material which is homogeneous – apart from the tracer gradient.

As indicated schematically in Fig. 1.2 the tracer is usually deposited onto a polished, flat surface of the diffusion sample. Normally a radioactive isotope of the investigated atomic species is used as tracer. Enriched stable isotopes have also been used in a few cases. Evaporation, dripping of a liquid solution, and electrodeposition of the tracer onto the surface are common deposition techniques. Sometimes the tracer is ion-implanted as a thin layer below the sample surface in order to overcome disturbing surface oxide hold-up and solubility problems [16]. The sample is usually encapsulated in quartz ampoules under vacuum or inert (e.g. Ar) atmosphere and an isothermal diffusion anneal is performed at temperature T for some diffusion time t. For temperatures below 1500 K quartz ampoules and resistance furnaces can be used. For higher temperatures more sophisticated heating techniques are necessary.

The best way to determine the resulting concentration-depth profile is serial sectioning of the sample and subsequent determination of the amount of tracer per section.

For average diffusion lengths of at least several ten micrometers mechanical sectioning techniques are applicable (for a review see, e.g., [17]). Lathes and microtomes are appropriate for ductile, grinding devices for brittle samples. For extended diffusion anneals and diffusivities $D > 10^{-15}\,\mathrm{m^2 s^{-1}}$ lathe sectioning is sufficient whereas diffusivities $D > 10^{-17}\,\mathrm{m^2 s^{-1}}$ are accessible by microtome sectioning. In favourable cases, grinder sectioning can be used for diffusivities $D > 10^{-18}\,\mathrm{m^2 s^{-1}}$.

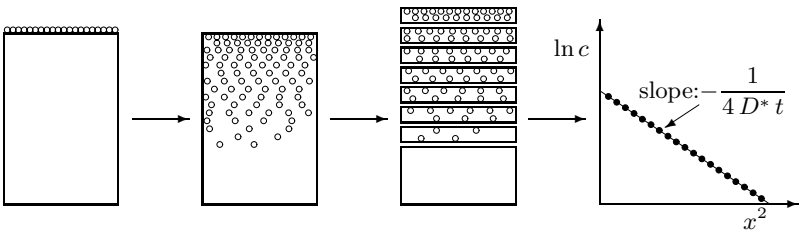

Fig. 1.2. Schematic illustration of the tracer method: The major steps – deposition of the tracer, diffusion anneal, serial sectioning, and evaluation of the penetration profile – are indicated.

Diffusion studies at lower temperatures require measurements of very small diffusivities. Measurements of diffusion profiles with diffusion lengths in the micrometer or nanometer range are possible using sputter sectioning techniques. Devices for serial sectioning of radioactive diffusion samples by ion-beam-sputtering are described in [18, 19]. Such devices permit serial sectioning of shallow diffusion zones, which correspond to average diffusion lengths between several nm and a few μm. This implies that for annealing times of about 10^6 s a diffusivity range between $D \approx 10^{-24}\,\mathrm{m^2 s^{-1}}$ and $D \approx 10^{-16}\,\mathrm{m^2 s^{-1}}$ can be examined.

Provided that the experimental conditions were chosen in such a way that the deposited layer is thin compared with the mean diffusion length, the distribution after the diffusion anneal is described by (1.9). If radioactive tracers are used, the specific activity per section (count rate divided by the section mass) is proportional to the tracer concentration. The count rate is conveniently determined by nuclear counting facilities (γ- or β-counting, depending on the isotope). According to (1.9) a plot of the logarithm of the specific activity versus the penetration distance squared is linear, if bulk diffusion is the dominating diffusion process. Its slope equals $-(4D^*t)^{-1}$. From the slope and the diffusion time the tracer diffusivity D^* is obtained. An obvious advantage of the tracer method is that a determination of the absolute tracer concentration is not necessary.

Fig. 1.3 shows a penetration profile of the radioisotope ^{59}Fe in the intermetallic phase Fe_3Si obtained by grinder sectioning [20]. Gaussian behaviour as stated by (1.9) is observed over several orders of magnitude in concentration. An example for a penetration profile of ^{59}Fe in the intermetallic phase Fe_3Al obtained with the sputtering device described in [18] is displayed in Fig. 1.4 according to [21]. From diffusion profiles of the quality of Figs. 1.3 and 1.4 diffusion coefficients can be determined with an accuracy of a few percent.

Deviations from the Gaussian behaviour in experimentally determined penetration profiles may occur for many reasons. We mention two frequent ones:

- Grain boundaries in a polycrystal often act as diffusion short-circuits with enhanced mobility of atoms. Grain boundaries usually cause a 'grain-boundary tail' in the deeper penetrating part of the profile. In this 'tail' region the concentration of the diffuser is enhanced with respect to mere bulk diffusion.
- Evaporation losses of the tracer itself and/or of the diffusion sample will cause deviations from Gaussian behaviour in the near-surface region.

For a more detailed discussion of implications and pitfalls of the tracer method the reader is referred to [17]. The grain-boundary tails mentioned above can be used for a systematic study of grain-boundary diffusion in bi- or polycrystals as described in Chap. 8 and in [10].

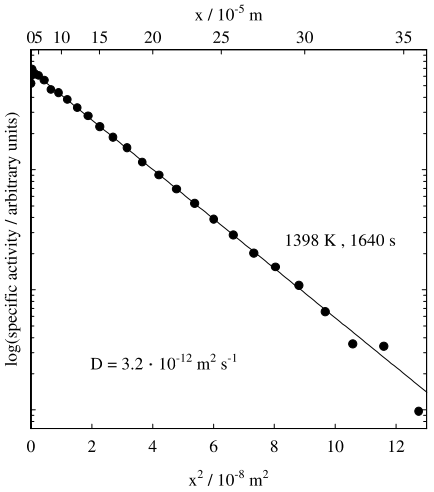

Fig. 1.3. Penetration profile of the radioisotope ^{59}Fe in Fe_3Si obtained by grinder sectioning. The solid line represents a fit of the thin-film solution of Fick's second law to the data points.

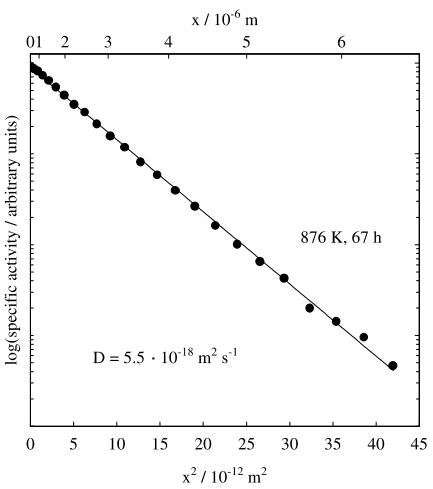

Fig. 1.4. Penetration profile of the radioisotope ^{59}Fe in Fe_3Al obtained by sputter sectioning. The solid line represents a fit of the thin-film solution of Fick's second law to the data points.

In some cases several tracer isotopes of the same element are available. Differences between the isotopic masses lead to isotope effects in diffusion. Isotope effects are interesting phenomena although the differences between diffusivities of two isotopes of the same element are usually a few percent only. An exception is hydrogen with its three isotopes H, D, and T, which have significantly different masses (see Sect. 1.7.2). Isotope effects of self- and solute-diffusion in metals can contribute useful information about the atomic mechanisms of diffusion. For a detailed discussion the reader is referred to [22–24] (see also Chap. 6, Sect. 6.5.3).

Other Profiling and Detection Methods

Several other profiling and detection methods can be used to measure concentration-depth profiles. We mention the more important ones:

1. *Secondary Ion Mass Spectrometry (SIMS)*
   As already mentioned foreign elements or stable isotopes of the matrix can be used as tracers in combination with SIMS for depth profiling. SIMS is mainly appropriate for the diffusion of foreign elements. Contrary to self-diffusion studies by radiotracer experiments, in the case of stable tracers the natural abundance of the stable isotope in the matrix limits the concentration range of the diffusion profile. Highly enriched isotopes should be used. An example of this technique can be found in a recent

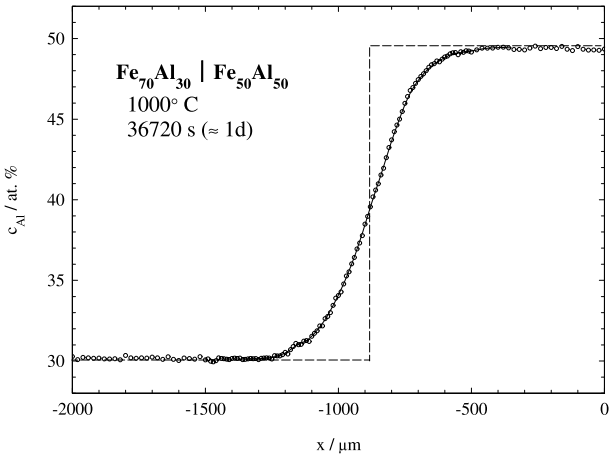

Fig. 1.5. Interdiffusion profile of a $Fe_{70}Al_{30}$–$Fe_{50}Al_{50}$ couple measured by EMPA.

study of Ni self-diffusion in the intermetallic compound Ni_3Al in which the highly enriched stable ^{64}Ni isotope was used [25]. Average diffusion lengths between several nm and several μm are accessible.

2. *Electron Microprobe Analysis (EMPA)*
   In EMPA an electron beam of several tens of keV with a diameter of about one micrometer stimulates X-ray emission in the diffusion zone of the sample. The diffusion profile can be obtained by analysing the intensity of the characteristic radiation of the elements in a line scan along the diffusion direction. The detection limit is about 10^{-3} to 10^{-4} mole fractions depending on the element. Light elements cannot be analysed. Because of the finite size of the excited volume (several μm^3) only fairly large diffusion coefficients $\geq 10^{-15} m^2 s^{-1}$ can be measured. EMPA is mainly appropriate for interdiffusion studies. An example of a single-phase interdiffusion profile resulting from a $Fe_{70}Al_{30}$–$Fe_{50}Al_{50}$ couple is shown in Fig. 1.5 according to [26]. The analysis of interdiffusion profiles is discussed in Sect. 1.11.
3. *Auger Electron Spectroscopy (AES)*
   AES in combination with sputter profiling can be used to measure diffusion profiles in the range of several nm to several μm. It is, however, only applicable to diffusion of foreign atoms since AES only discriminates between different elements.

4. *Rutherford Backscattering Spectrometry (RBS)*
   In RBS experiments a high-energy beam of monoenergetic α-particles is used. These particles are preferentially scattered by heavy nuclei in the sample and the energy spectrum of scattered α-particles can be used to determine the concentration-depth distribution of scattering nuclei. This technique is mainly suitable for detecting heavy elements in a matrix of

substantially lower atomic weight. Due to the energy straggling of the incident beam the profile depth is limited to less than a few μm.

5. *Nuclear Reaction Analysis (NRA)*
   High energy particles can also be used to study diffusion of light elements, if the nuclei undergo a suitable resonant nuclear reaction. An example is diffusion of boron in an alloy. During irradiation with high energy protons α-particles are emitted from the nuclear reaction $^{11}\mathrm{B} + \mathrm{p} \rightarrow {}^{8}\mathrm{B} + \alpha$. The concentration profile of ^{11}B can be determined from the number and energy of emitted α-particles as a function of the incident proton energy. Like in RBS energy straggling limits the depth resolution of NRA.
   RBS and NRA methods need a depth calibration which is based on not always very accurate data for the stopping power in the matrix for those particles emitted by the nuclear reaction. Also the depth resolution is usually inferior to that achievable in careful radiotracer and SIMS profiling studies.

6. *Field Gradient Nuclear Magnetic Resonance (FG NMR, PFG NMR)*
   Nuclear magnetic resonance (NMR) measurements in a magnetic field gradient (FG) or in a pulsed field gradient (PFG, see Chap. 10) provide a direct macroscopic method for diffusion studies. In a magnetic field gradient the Larmor frequency of a nuclear moment depends on its position. FG NMR and PFG NMR utilize the fact that nuclear spins that diffuse in a magnetic field gradient experience an irreversible phase shift, which leads to a decrease in transversal magnetization. This decrease can be observed in so-called spin-echo experiments [27, 28]. A measurement of the diffusion-related part of the spin echo provides the diffusion coefficient without any further hypothesis. In contrast to tracer diffusion, FG NMR and PFG NMR techniques permit diffusion measurements in isotopically pure systems. These techniques are applicable for relatively large diffusion coefficients $D \gtrsim 10^{-13}\,\mathrm{m^2 s^{-1}}$ [29].

1.4.2 Indirect Methods

Indirect methods are based on phenomena which are influenced by the diffusive jumps of atoms. Some of these methods are often sensitive to one or a few atomic jumps only. Quantities like relaxation times, relaxation rates or linewidths are measured. Using a microscopic model of the jump process the mean residence time of the diffusing species is determined and then via the Einstein-Smoluchowski relation (see Sect. 1.6) the diffusivity is deduced. Indirect methods can be grouped into two categories – relaxation methods (mechanical and magnetic) and nuclear methods.

Relaxation Methods (Mechanical and Magnetic)

Mechanical relaxation methods make use of the fact that atomic motion in a material can be induced by external influences such as the application of constant or oscillating mechanical stress. In ferromagnetic materials the interaction between the magnetic moments and local order can give rise to various relaxation phenomena similar to those observed in anelasticity. A great variety of experimental devices have been used for such studies. Their description is, however, beyond the scope of this chapter.

Some of the more important relaxation phenomena related to diffusion are the following [30–32]:

The *Snoek effect* is observed in bcc metals which contain interstitial solutes such as C, N, or O. These solutes occupy octahedral or tetrahedral interstitial sites. These sites have tetragonal symmetry, which is lower than the cubic symmetry of the matrix. Therefore the lattice distortions caused by interstitial solutes give rise to elastic dipoles. Under the influence of external stress these dipoles can reorient (para-elasticity). The reorientation of solutes gives rise to a strain relaxation or an internal friction peak. The relaxation time or the (frequency or temperature) position of the internal friction peak can be used to deduce information about the mean residence time of a solute. A Snoek effect of interstitial solutes in fcc metals cannot be observed, because the interstitial sites have cubic symmetry.

The *Gorski effect* is due to solutes in a solvent which produce a lattice dilatation. In a macroscopic strain gradient solutes redistribute by diffusion. This redistribution gives rise to an anelastic relaxation. The Gorski effect is detectable if the diffusion coefficient of the solute is high enough. Gorski effect measurements have been widely used for studies of hydrogen diffusion in metals [30].

In substitutional A-B alloys the reorientation of solute-solvent pairs under the influence of stress can give rise to an anelastic relaxation called *Zener effect*.

Nuclear Methods

Examples of nuclear methods are NMR, Mößbauer spectroscopy (MBS), and quasielastic neutron scattering (QENS). Since MBS, QENS, NMR and PFG NMR are the subjects of the Chaps. 2, 3, 9 and 10 and QENS also of a recent textbook [33] we confine ourselves here to a few remarks:

The width of the resonance line and the spin-lattice relaxation rate T_1^{-1} in NMR have contributions which are due to the thermally activated jumps of atoms. Measurements of the 'diffusional narrowing' of the linewidth or of T_1^{-1} as a function of temperature permit a determination of the mean residence time τ of the atoms. NMR methods are mainly appropriate for self-diffusion measurements on solid or liquid metals. In favourable cases (e.g. Li and Na) self-diffusion coefficients between 10^{-18} and 10^{-10} m^2s^{-1} are

accessible (see [6]). In the case of foreign atom diffusion, NMR studies suffer from the fact that a signal from nuclear spins of the minority component must be detected. Nevertheless, detailed studies were conducted, e. g., in the case of Li-based Li-Mg and Li-Ag alloys via the spin-lattice relaxation of polarized radioactive ^{8}Li nuclei [34].

The linewidth in MBS and QENS both have a contribution $\Delta\Gamma$ which is due to the diffusion jumps of atoms. This diffusion broadening can be observed only in systems with fairly high diffusivities since $\Delta\Gamma$ must at least be comparable with the natural linewidth in MBS experiments or with the energy resolution of the neutron spectrometer in QENS experiments. Appropriate probes for MBS must be available. The usual working horse in MBS is the isotope ^{57}Fe although there are a few other Mößbauer isotopes available (e.g. ^{119}Sn, ^{115}Eu, ^{161}Dy). MBS has been mainly used to study fast Fe diffusion. QENS experiments are suitable for fast diffusing elements with a sizable incoherent scattering cross section for neutrons. Examples are hydrogen diffusion in metals or hydrides and Na self-diffusion (see Chap. 3).

Neither MBS nor QENS are routine methods for diffusion measurements. The most interesting aspect is that these methods can provide microscopic information about the elementary jump process of atoms. For single crystals $\Delta\Gamma$ depends on the crystal orientation. This orientation dependence can be used to deduce information about the jump direction and about the jump length (see Chaps. 2 and 3), which is not accessible by conventional diffusion studies.

For a more comprehensive discussion of experimental methods for the determination of diffusion coefficients we refer the reader to the already mentioned textbooks on diffusion [1–3] and to Chap. 1 in [6] as well as to a recent article [29] where also an overview of the accessible windows for the mean residence time τ are given.

1.5 Dependence of Diffusion on Thermodynamic Variables

So far we have said nothing about the dependence of diffusion processes upon thermodynamic variables, i.e. upon temperature T and hydrostatic pressure p. In binary systems also variations of the diffusivity with the variable 'composition' are of interest. These variations can range from very slight to striking. They will be not considered in this section since they depend very much on the system. Examples can be found in Sect. 1.10.

1.5.1 Temperature Dependence

It is well known that diffusion coefficients in solids generally depend rather strongly on temperature, being low at low temperatures but appreciable at

high temperatures. Empirically, measurements of diffusion coefficients over a certain temperature range may be often, but by no means always, described by an Arrhenius relation [4]

$$D = D_0 \exp\left(-\frac{\Delta H}{RT}\right). \tag{1.20}$$

In (1.20) D_0 is denoted as pre-exponential factor and ΔH (or Q)[5] as activation enthalpy of diffusion. The pre-exponential factor can be written as

$$D_0 = D_0' \exp \frac{\Delta S}{R}\,, \tag{1.21}$$

where ΔS is the diffusion entropy and D_0' contains geometric factors, the correlation factor, the lattice parameter squared, and an attempt frequency of the order of the Debye frequency.

In an Arrhenius diagram the logarithm of the diffusivity is plotted versus the reciprocal temperature T^{-1}. For a diffusion process with a temperature-independent activation enthalpy ΔH the Arrhenius diagram is a straight line with slope $-\Delta H/R$. From its intercept for $T^{-1} \to 0$ the pre-exponential factor D_0 can be deduced. Such simple Arrhenius behaviour should, however, not be considered to be universal. Departures from it may arise for many reasons, ranging from fundamental aspects of the atomic mechanism, temperature dependent activation parameters[6], effects associated with impurities or microstructural features such as grain boundaries. Nevertheless, (1.20) provides a very useful standard.

1.5.2 Pressure Dependence

The variation of diffusivity with hydrostatic pressure p is far less pronounced than with temperature. Usually the diffusivity decreases as the pressure is

[4] Equation (1.20) is often also written as

$$D = D_0 \exp\left(-\frac{\Delta H}{k_{\mathrm{B}} T}\right).$$

If the first version of the Arrhenius equation is used the unit of ΔH is kJ mol^{-1}. If the second version is used the appropriate unit of ΔH is eV per atom. Note that 1 eV per atom = 96.472 kJ mol^{-1}. The gas constant R and the Boltzmann constant k_{B} are related via $R = N_{\mathrm{A}} k_{\mathrm{B}} = 8.314 \times 10^{-3}$ kJ mol^{-1} K^{-1}, where N_{A} denotes the Avogadro constant.

[5] The symbol Q for the activation enthalpy is also widely used in the literature.

[6] Thermodynamics tells us that a temperature-dependent enthalpy according to

$$\frac{\partial \Delta H}{\partial T} = T \frac{\partial \Delta S}{\partial T} \tag{1.22}$$

automatically entails a temperature-dependent entropy and vice versa. If enthalpy and entropy increase with temperature the Arrhenius diagram will show some upward curvature.

increased. Typical pressure effects range from factors of 2 to 10 for a pressure of 1 GPa (10 kbar). This variation is largely due to the fact that the Gibbs free energy of activation ΔG varies with pressure according to

$$\Delta G \;=\; \Delta H - T\Delta S \;=\; \Delta E - T\Delta S + p\Delta V \tag{1.23}$$

where ΔV denotes the activation volume and ΔE the activation energy of diffusion. Using (1.21) and (1.23) the Arrhenius equation (1.20) can also be written as

$$D \;=\; D_0' \exp\left(-\frac{\Delta G}{RT}\right). \tag{1.24}$$

Thermodynamics tells us that

$$\Delta V = \left(\frac{\partial \Delta G}{\partial p}\right)_T. \tag{1.25}$$

Equation (1.25) can be considered as the definition of the activation volume. Using (1.24) and (1.25) the activation volume can be obtained from measurements of the diffusion coefficient at constant temperature as a function of pressure via

$$\Delta V \;=\; -RT\left(\frac{\partial \ln D}{\partial p}\right)_T + RT \underbrace{\frac{\partial \ln D_0'}{\partial p}}_{\text{correction term}}. \tag{1.26}$$

The term arising from the pressure dependence of D_0' can be estimated from the isothermal compressibility and the Grueneisen constant of the material. It is often negligibly small (a few percent of the molar volume V_m or of the atomic volume $\Omega = V_\mathrm{m}/N_\mathrm{A}$, respectively). Typical values for the activation volume for various metals lie between 0.5 and 0.9 Ω. For a recent review see [35].

We emphasize that a complete characterization of the diffusion process requires knowledge of the three activation parameters $\Delta H = \Delta E + p\,\Delta V$ (valid for $p = \text{const.}$), ΔS and ΔV. For solids the term $p\,\Delta V$ becomes significant only at high pressures. At ambient pressure it is negligible and hence $\Delta H \approx \Delta E$.

1.6 Atomistic Description of Diffusion

1.6.1 Einstein-Smoluchowski Relation and Correlation Factor

Diffusion in crystalline solids takes place by a series of jumps of individual atoms [7]. For interstitial diffusers the 'diffusion lattice' is formed by the interstitial sites of the crystal lattice. Substitutional diffusers perform jumps

[7] Near the melting temperature of fcc metals the self-diffusion coefficient (see Sect. 1.8) has a value of about $10^{-12}\mathrm{m}^2\mathrm{s}^{-1}$. This corresponds to about 10 million jumps of each atom per second.

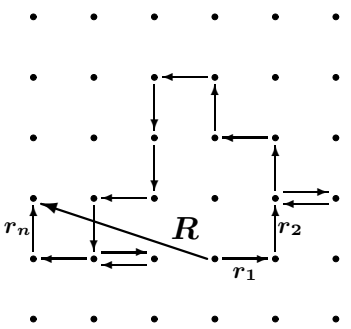

Fig. 1.6. Total displacement $\boldsymbol{R}$ of a particle on a lattice composed of many individual jumps $\boldsymbol{r_i}$.

between sites of the normal lattice. The diffusivity on a lattice can be expressed in terms of physical quantities that describe the elementary jump process. As we shall see below, these quantities are the jump length and the jump rate.

The link between the displacement of particles on a (cubic) lattice and the diffusion coefficient is given by the relation [8]

$$D = \frac{1}{6t}\langle \boldsymbol{R}^2 \rangle \tag{1.27}$$

where $\langle \boldsymbol{R}^2 \rangle$ denotes the mean square displacement of particles (see also Chap. 18). Equation (1.27) is due to Einstein [36] and Smoluchowski [37]. It also includes correlation effects as we shall see below.

Suppose that a particle carries out n jumps during time t. As illustrated in Fig. 1.6 its total displacement

$$\boldsymbol{R} = \sum_{i=1}^{n} \boldsymbol{r}_i \tag{1.28}$$

is composed of n individual jump vectors $\boldsymbol{r}_i$ and hence

$$\boldsymbol{R}^2 = \sum_{i=1}^{n} \boldsymbol{r}_i^2 + 2\sum_{i=1}^{n-1}\sum_{j=i+1}^{n} \boldsymbol{r}_i \boldsymbol{r}_j. \tag{1.29}$$

Taking the average over an ensemble of particles and using the fact that the average of a sum of terms equals the sum of the averages of the terms we get

$$\langle \boldsymbol{R}^2 \rangle = \sum_{i=1}^{n} \langle \boldsymbol{r}_i^2 \rangle + 2\sum_{i=1}^{n-1}\sum_{j=i+1}^{n} \langle \boldsymbol{r}_i \boldsymbol{r}_j \rangle. \tag{1.30}$$

[8] We restrict ourselves for reasons of simplicity to cubic lattices. The extension to non-cubic lattices is straightforward and can be found, e.g., in [2].

Correlation effects are contained in the double sum of (1.30). For a true random walk (index RW) the double sum in (1.30) vanishes as for every pair $\boldsymbol{r}_i\boldsymbol{r}_j$ one can find another pair equal and opposite in sign. Then

$$\left\langle {\boldsymbol{R}_{\mathrm{RW}}}^2 \right\rangle = \sum_{i=1}^{n} \left\langle \boldsymbol{r}_i^2 \right\rangle . \tag{1.31}$$

The degree of randomness in a long sequence of jumps can be expressed by the so-called correlation factor f, which can be written as

$$f = \lim_{n\to\infty} \frac{\left\langle \boldsymbol{R}^2 \right\rangle}{\left\langle \boldsymbol{R}_{\mathrm{RW}}^2 \right\rangle} = 1 + 2 \lim_{n\to\infty} \frac{\sum\limits_{i=1}^{n-1} \sum\limits_{j=i+1}^{n} \left\langle \boldsymbol{r}_i\boldsymbol{r}_j \right\rangle}{\sum\limits_{i=1}^{n} \left\langle \boldsymbol{r}_i^2 \right\rangle}. \tag{1.32}$$

For diffusion on a lattice the jump vectors $\boldsymbol{r}_i$ can take only a few definite values. Let us consider a cubic coordination lattice with coordination number Z and let us suppose that only nearest-neighbour jumps of equal length l occur. Then (1.31) reduces to

$$\left\langle \boldsymbol{R}_{\mathrm{RW}}^2 \right\rangle = \left\langle n \right\rangle l^2 , \tag{1.33}$$

where $\left\langle n \right\rangle$ denotes the average number of jumps. For a true random walk (no correlation) we get from (1.32) $f = 1$. It is convenient to define an average jump rate of atoms *into a certain direction*, Γ, by

$$\Gamma = \frac{\left\langle n \right\rangle}{Zt}. \tag{1.34}$$

The mean residence time τ of an atom on a certain lattice site is related to the jump rate of the atom in a certain direction Γ via

$$\tau = \frac{1}{\Gamma Z} . \tag{1.35}$$

τ^{-1} is the mean atomic jump rate *in any direction* on a lattice. Then (1.27) can be written as

$$D = \frac{1}{6} l^2 Z\Gamma = \frac{l^2}{6\tau}, \tag{1.36}$$

which is identical with (1.14) discussed in Sect. 1.3. Diffusion of interstitial atoms in a dilute interstitial solution can be considered as a true random walk process and hence (1.36) is an appropriate expression for the diffusion coefficient of interstitial diffusers.

Diffusion of self-atoms and of substitutional foreign atoms in metals, metallic alloys, and in non-metallic solids is usually mediated by lattice vacancies. As already noticed by Bardeen and Herring [38] atoms migrating by exchange with vacancies perform a correlated walk. The atom experiences

some 'backward correlation' since immediately after its exchange with the vacancy the latter is still available for a backward hop of the atom. Then the double sum in (1.30) does not vanish. For correlated diffusion on cubic Bravais lattices[9] (1.36) must be replaced by

$$D = \frac{1}{6} f l^2 Z \Gamma. \tag{1.37}$$

In summary we can say that the diffusion coefficient (in cubic crystals) for interstitial diffusers as well as that for diffusers which migrate by exchange with defects (vacancies, divacancies, self-interstitials, etc.) is described by (1.37). For interstitial diffusers (in very dilute interstitial alloys) the correlation factor is unity whereas for defect-mediated diffusion the correlation factor is smaller than unity. Numerical values for the correlation factors of self-diffusion can be found in Sect. 1.8. We emphasize that with increasing degree of correlation the correlation factor decreases.

1.6.2 Atomic Jumps and Diffusion

Due to lattice vibrations atoms in a crystal oscillate around their equilibrium positions with frequencies ν_0 of the order of the Debye frequency (typically 10^{12} to 10^{13} Hz). Usually an atom is confined to a certain site by a potential barrier of height G^{M}, which corresponds to the Gibbs free energy difference between the configuration of the jumping atom at the saddle point and at its equilibrium position. G^{M} is denoted as Gibbs free energy of migration. Diffusion is thermally activated which means that a fluctuation of thermal energy pushes the atom over the energy barrier between two neighbouring sites.

Using statistical thermodynamics Vineyard showed [39] that the jump rate ω, at which an atomic jump into an *empty* neighbouring site occurs, can be written in the form

$$\omega = \nu_0 \exp\left(-\frac{G^{\mathrm{M}}}{RT}\right) = \nu_0 \exp\left(\frac{S^{\mathrm{M}}}{R}\right) \exp\left(-\frac{H^{\mathrm{M}}}{RT}\right). \tag{1.38}$$

On the right-hand side of (1.38) the Gibbs free energy according to

$$G^{\mathrm{M}} = H^{\mathrm{M}} - TS^{\mathrm{M}} \tag{1.39}$$

is decomposed into enthalpy H^{M} and entropy S^{M} of migration (superscript M).

A diffusion jump of a self-atom or of a substitutional solute atom will only occur if a neighbouring lattice site is occupied by a vacancy. If p denotes the vacancy availability factor (the probability that the neighbouring site of the

[9] For an extension to non-cubic lattices see, e.g., [2].

jumping atom is empty) the jump rate of the atom to this particular site is given by

$$\Gamma = \omega p. \tag{1.40}$$

Inserting this expression into (1.37) yields

$$D = \frac{1}{6} f l^2 Z \omega p. \tag{1.41}$$

For interstitial diffusion in a very dilute interstitial alloy we have $f = 1$, $p = 1$, and $\Gamma \equiv \omega$. Then (1.41) reduces to (1.36).

1.6.3 Diffusion Mechanisms

Solid-state physics tells us that atoms in crystals oscillate around their equilibrium positions. Occasionally these oscillations become large enough to allow an atom to change its site. As outlined above these jumps give rise to diffusion in solids. Various atomic mechanisms of diffusion in crystals have been identified and are catalogued in what follows:

Interstitial Mechanism

Solute atoms which are considerably smaller than the solvent (lattice) atoms (e.g. hydrogen, carbon, nitrogen, and oxygen) are usually incorporated in interstitial sites of a metal. In this way an interstitial solid solution is formed. Interstitial solutes usually occupy octahedral or tetrahedral sites of the lattice. Octahedral and tetrahedral interstitial sites in the fcc and bcc lattices are illustrated in Fig. 1.7. Interstitial solutes can diffuse by jumping from one interstitial site to the next as shown in Fig. 1.8. This mechanism is sometimes also denoted as direct interstitial mechanism in order to distinguish it more clearly from the interstitialcy mechanism discussed below.

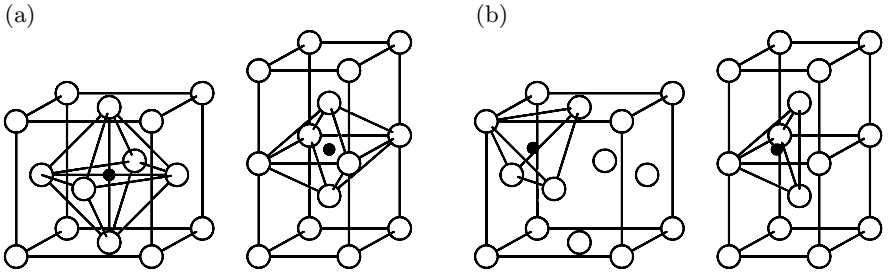

Fig. 1.7. Octahedral (a) and tetrahedral (b) interstitial sites in the fcc (left) and bcc (right) lattice. Lattice atoms (open circles); interstitial sites (full circles).

Vacancy Mechanism

Self-atoms or substitutional solute atoms migrate by jumping into a neighbouring vacant site as illustrated in Fig. 1.9. In thermal equilibrium the atomic fraction of vacancies $C_{\mathrm{V}}^{\mathrm{eq}}$ in a monoatomic crystal is given by

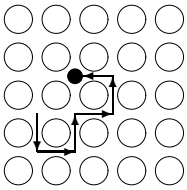

Fig. 1.8. Direct interstitial mechanism of diffusion.

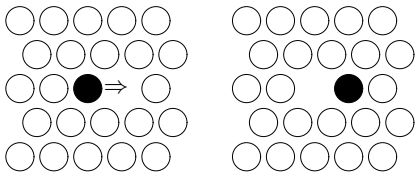

Fig. 1.9. Vacancy mechanism of diffusion.

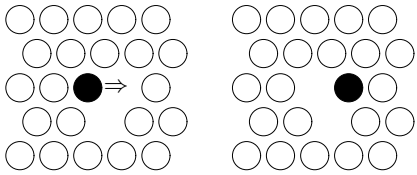

Fig. 1.10. Divacancy mechanism of diffusion.

$$C_{\mathrm{V}}^{\mathrm{eq}} \;=\; \exp\Big(\frac{S^{\mathrm{F}}}{R}\Big)\exp\Big(-\frac{H^{\mathrm{F}}}{RT}\Big), \tag{1.42}$$

where S^{F} and H^{F} denote formation entropy and enthalpy of a vacancy (superscript F). For self-diffusion the vacancy availability factor p in (1.40) equals $C_{\mathrm{V}}^{\mathrm{eq}}$. Typical values for $C_{\mathrm{V}}^{\mathrm{eq}}$ near the melting temperature of metallic elements lie between 10^{-4} and 10^{-3} (in molar fractions) [40]. From (1.38), (1.40), and (1.42) we get for the jump rate of an atom in the case of self-diffusion

$$\Gamma \;=\; \nu_0 \exp\Big(\frac{S^{\mathrm{F}}+S^{\mathrm{M}}}{R}\Big)\exp\Big(-\frac{H^{\mathrm{F}}+H^{\mathrm{M}}}{RT}\Big). \tag{1.43}$$

Self-diffusion in metals and alloys, in many ionic crystals (e.g. alkali halides) and ceramic materials occurs by the vacancy mechanism.

Attractive or repulsive interactions modify the probability to find a vacancy on a nearest-neighbour site of a solute atom. For a very dilute substitutional solution the probability p of finding a vacancy next to the solute atom is given by

$$p \;=\; C_{\mathrm{V}}^{\mathrm{eq}} \exp\Big(\frac{G^{\mathrm{B}}}{RT}\Big), \tag{1.44}$$

where G^{B} denotes the Gibbs free energy of binding between vacancy and solute (superscript B). The quantity $G^{\mathrm{F}} - G^{\mathrm{B}}$ can be considered as the Gibbs free energy for the formation of a vacancy on a nearest neighbour site of the foreign atom. For attractive interaction ($G^{\mathrm{B}} > 0$) p is enhanced and for repulsive interaction ($G^{\mathrm{B}} < 0$) p is reduced compared to the equilibrium site fraction of vacancies $C_{\mathrm{V}}^{\mathrm{eq}}$ in a pure solvent[10].

[10] Note the convention: The binding energy is positive for attractive interaction.

Divacancy Mechanism

Diffusion of self-atoms or substitutional solute atoms can also occur via bound pairs of vacancies (denoted as divacancies or as vacancy pairs) as illustrated in Fig. 1.10. At thermal equilibrium divacancies in an elemental crystal are formed from monovacancies according to the reaction

$$\mathrm{V} + \mathrm{V} \rightleftharpoons 2\mathrm{V} \quad . \tag{1.45}$$

As a consequence of the law of mass action we have for the mole fractions C_{V} and $C_{2\mathrm{V}}$ of mono- and divacancies

$$C_{2\mathrm{V}}^{\mathrm{eq}} = K\,(C_{\mathrm{V}}^{\mathrm{eq}})^2 \quad . \tag{1.46}$$

The quantity K contains the Gibbs free binding energy of the vacancy pair. Since the monovacancy population under equilibrium conditions increases with temperature, the concentration of divacancies $C_{2\mathrm{V}}^{\mathrm{eq}}$ becomes more significant at high temperatures. Divacancies in fcc metals have a higher mobility than monovacancies [40]. Therefore self-diffusion of fcc metals usually has some divacancy contribution in addition to the vacancy mechanism. The latter is, however, the dominating mechanism at temperatures below 2/3 of the melting temperature [22].

Interstitialcy Mechanism

In this case self-interstitials – extra atoms located between lattice sites – act as diffusion vehicles. As illustrated in Fig. 1.11 a self-interstitial replaces an atom on a substitutional site which then replaces again a neighbouring lattice atom. Self-interstitials are responsible for diffusion in the silver sublattice of silver halides. In silicon, the base material of microelectronic devices, the interstitialcy mechanism dominates self-diffusion and plays a prominent role in the diffusion of some solute atoms including important doping elements [41]. This is not surprising since the diamond lattice (coordination number 4) provides sufficient space for interstitial species. For a detailed discussion of the diffusion mechanism in Si see Chap. 4, Sect. 3.

In densely packed metals contributions of this mechanism are negligible for thermal diffusion. Self-interstitials in metals have a fairly high formation enthalpy compared to vacancies [40]. Therefore the concentration of the latter is dominating completely under equilibrium conditions. The interstitialcy

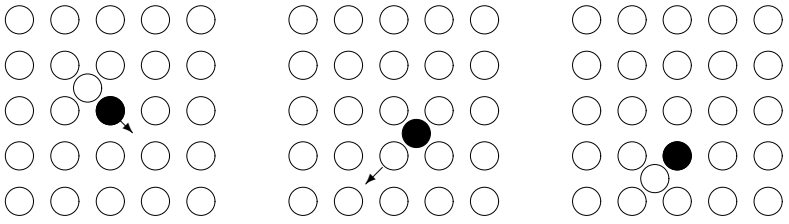

Fig. 1.11. Interstitialcy mechanism of diffusion.

mechanism is, however, important for radiation induced diffusion, since then self-interstitials and vacancies are created in equal numbers by irradiation of a crystal with energetic particles.

Interstitial-Substitutional Exchange Mechanisms

Some solute atoms (B) can be dissolved on interstitial (B_i) and substitutional sites (B_s) of a solvent crystal (A) and diffuse via an interstitial-substitutional exchange mechanism (see Fig. 1.12). For some of these so-called 'hybride solutes' the diffusivity of B_i is much higher than the diffusivity of B_s whereas the opposite is true for the solubilities. Under such conditions the incorporation of B atoms can occur by the fast diffusion of B_i and the subsequent change-over to B_s. Two types of interstitial-substitutional exchange mechanisms can be distinguished:

If the change-over involves vacancies (V) according to

$$B_i + V \rightleftharpoons B_s \tag{1.47}$$

the mechanism is denoted as dissociative mechanism (sometimes also: Frank-Turnbull mechanism or Longini mechanism). The rapid diffusion of Cu in germanium (see Chap. 4, Sect. 4.3) and of some foreign metallic elements in polyvalent metals such as lead, tin, niobium, titanium, and zirconium has been attributed to this mechanism (see Sect. 1.9).

If the change-over involves self-interstitials (A_i) according to

$$B_i \rightleftharpoons B_s + A_i \tag{1.48}$$

the mechanism is denoted as kick-out mechanism. The fast diffusion of Au, Pt and Zn in silicon has been attributed to this mechanism [41,42] (see Chap. 4, Sect. 4.3).

For a description of diffusion processes, which involve interstitial-substitutional exchange reactions, Fick's equations must be supplemented by reaction

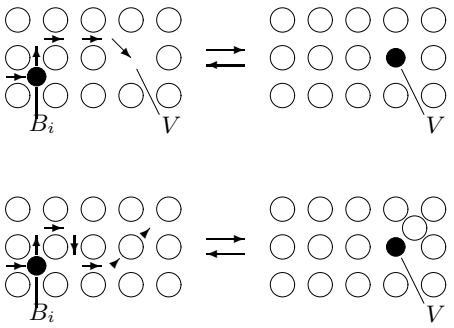

Fig. 1.12. Interstitial-substitutional exchange mechanisms of foreign atom diffusion. Upper part: dissociative mechanism. Lower part: kick-out mechanism.

terms. Since three species are involved, sets of three coupled diffusion-reaction equations result for both mechanisms mentioned above. Solutions of these equations – apart from a few (interesting) special cases – can only be obtained by numerical methods. For details we refer the reader to the literature (e.g. [41, 42]).

In the following four sections we consider examples of normal interstitial diffusion, diffusion of hydrogen, self-diffusion in pure metals, and of impurity diffusion in metals[11]. We shall see below that the Arrhenius parameters of (1.20) can be readily interpreted in terms of properties of atomic defects.

1.7 Interstitial Diffusion in Metals

1.7.1 'Normal' Interstitial Solutes

Carbon, nitrogen, and oxygen often form interstitial solid solutions with metals. Interstitial sites in fcc and bcc lattices are illustrated in Fig. 1.7. Interstitial diffusers have diffusion coefficients that are much larger than those of self- and substitutional solute diffusion. Examples are shown in Fig. 1.13, where diffusion of C, N, and O in niobium is displayed together with niobium self-diffusion. The pertaining activation enthalpies and pre-exponential factors are collected in Table 1.1 (for references see Chap. 8 in [6]).

Table 1.1. Activation parameters of some solutes in niobium (for references see [6]).

Diffuser	C	N	O	Nb
$\Delta H\,[\mathrm{kJmol^{-1}}]$	142	161	107	395
$D_0[\,\mathrm{m^2s^{-1}}]$	1×10^{-6}	6.3×10^{-6}	4.2×10^{-7}	5.2×10^{-5}

For a dilute interstitial alloy the probability p in (1.40) is unity. The magnitude of the activation enthalpy is also small with the result that the diffusion coefficients for interstitial diffusion are many orders of magnitude larger than those for self-diffusion of lattice atoms. Interstitial diffusivities near the melting temperature of the solvent can be as high as diffusivities in liquids.

For interstitial solutes, which migrate by the direct interstitial mechanism, (1.36) can be written as

$$D \;=\; ga^2\nu_0 \exp\Big(\frac{S^{\mathrm{M}}}{R}\Big)\exp\Big(-\frac{H^{\mathrm{M}}}{RT}\Big). \tag{1.49}$$

Here a is the cubic lattice parameter and g a geometric factor, which depends on the lattice geometry and on the type of interstitial sites (octahedral or

[11] For reasons of simplicity we restrict ourselves to cubic crystals.

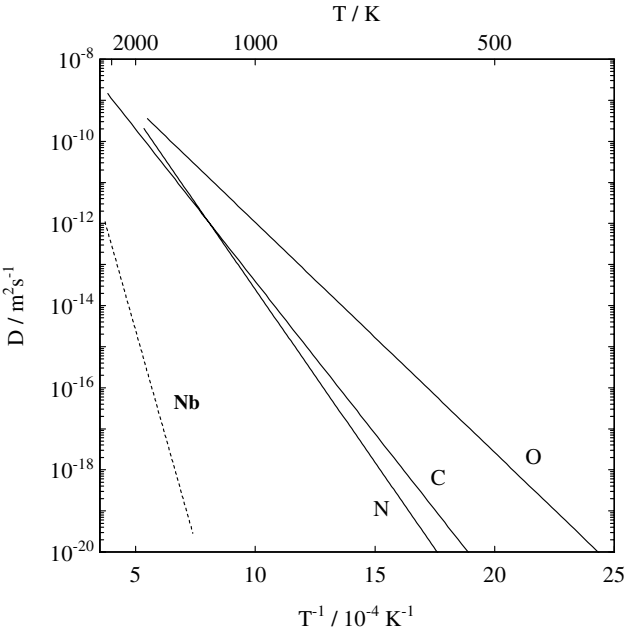

Fig. 1.13. Diffusion of C, N, O and Nb in niobium.

tetrahedral) occupied by the solute. For octahedral sites (Fig. 1.7) we have $g = 1$ for the fcc lattice and $g = 1/6$ for the bcc lattice. For interstitial diffusers the Arrhenius parameters of (1.20) have the following meaning:

$$\Delta H = H^{\mathrm{M}} \tag{1.50}$$

and

$$D_0 = ga^2\nu_0 \exp\Big(\frac{S^{\mathrm{M}}}{R}\Big). \tag{1.51}$$

With reasonable values for the migration entropy (between zero and several R) and the attempt frequency (between 10^{12} and 10^{13} s^{-1}) (1.51) yields the following limits for the pre-exponential factors of interstitial solutes:

$$10^{-7}\mathrm{m}^2\mathrm{s}^{-1} \leq D_0 \leq 10^{-5}\mathrm{m}^2\mathrm{s}^{-1}. \tag{1.52}$$

The experimental values of Table 1.1 confirm this estimate.

The fast diffusion of C, N, and O and the fact that N_2 and O_2 are gases, or, in the case of carbon, readily available in gas or vapour form (CO_2, CH_4,...) have an impact on the choice and availability of methods used to measure their diffusion coefficients. Anelastic relaxation, magnetic relaxation (in the case of ferromagnetic materials), internal friction, steady-state and in- and out-diffusion methods are often applied. For details the reader is referred to textbooks [2, 3].

1.7.2 Hydrogen Diffusion

Hydrogen in metals provides itself an important and fascinating topic of materials science. It has also attracted considerable interest from the viewpoint of applications. For example, the idea of hydrogen storage in metals is based on the high solubility and fast diffusion of hydrogen in some metal-hydrogen systems. Permeation of hydrogen through palladium membranes for hydrogen purification is an old and well-known application based on the very fast diffusion. Nowadays, diffusion of hydrogen plays a key role for fuel cells which use hydrogen or hydrocarbons as fuels.

Hydrogen forms interstitial solid solutions with most metallic elements. Some metals have a negative enthalpy of solution and a high solubility for hydrogen (e.g. group IV transition metals, group V transitions metals, and palladium) and form hydrides at higher hydrogen concentrations. Other metals have a positive enthalpy of solution and a relatively low solubility (e.g. group VI metals, group VII metals, and iron).

From a scientific point of view diffusion of hydrogen is significantly different from diffusion of other interstitial solutes. Fig. 1.14 shows an Arrhenius plot for diffusion of hydrogen and its isotopes deuterium and tritium in the bcc transition metal niobium (for references see Chap. 9 in [6]). We use Fig. 1.14 to illustrate some characteristic features of hydrogen diffusion:

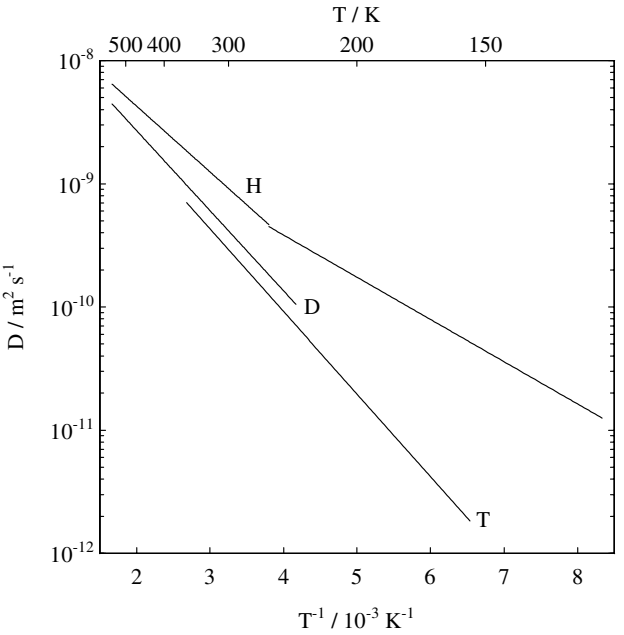

Fig. 1.14. Diffusion of the hydrogen isotopes H, D, and T in niobium.

– Diffusion of hydrogen and its isotopes is extremely rapid: Diffusivities exceed that of heavier interstitials by many orders of magnitude as can be seen from a comparison of Figs. 1.13 and 1.14. From Fig. 1.14 we get $D_{\mathrm{H}} = 8 \times 10^{-9}$ m^{2}s^{-1} near 300 ^{0}C. According to (1.36) the reciprocal mean residence time τ^{-1} of H atoms is about 10^{12} s^{-1}. This extremely high value is of the order of the Debye frequency of niobium.

– Hydrogen has three isotopes (H, D, T): These isotopes differ considerably in their isotopic masses, which offers the possibility to study large isotope effects. Fig. 1.14 shows that normal hydrogen (H) diffuses more rapidly than deuterium (D), and deuterium diffuses more rapidly than tritium (T). In addition the activation enthalpies of hydrogen isotopes are different and obey the inequalities

$$\Delta H_{\mathrm{H}} < \Delta H_{\mathrm{D}} < \Delta H_{\mathrm{T}}. \tag{1.53}$$

In the classical regime the activation enthalpy of a diffuser is exclusively determined by the chemistry of the system and not by the isotopic mass. The latter enters the diffusion coefficient only via the mass dependence of the attempt frequency. If many-body and quantum effects are negligible the attempt frequency ν_0 is related to the mass m of the diffuser simply by

$$\nu_0 \propto \frac{1}{\sqrt{m}}. \tag{1.54}$$

This shows that (1.53) represents a non-classical effect. Similar non-classical effects have been observed for hydrogen diffusion in the metals vanadium and tantalum.

– Hydrogen is the lightest atom. As a consequence, quantum effects in diffusion can be observed which are hardly detectable for heavier diffusers. The deviation of hydrogen diffusivity from an Arrhenius law below room temperature (see Fig. 1.14) has been attributed to incoherent tunneling (e.g. [33]).

– Positive muons can be considered in several respects as light isotopes of hydrogen [43]. The muon mass is by a factor of nine smaller than the proton mass. Like the hydrogen nuclei, the muons may be considered as very heavy compared with the electrons but nevertheless light compared with most metal atoms. A prefered topic studied with positive muons in metals is quantum diffusion (see, e. g., [44]).

The very fast diffusion and the often high solubility of hydrogen have consequences for the experimental techniques used in hydrogen diffusion studies. Concentration-profile methods, permeation methods based on Fick's first law, absorption and desorption methods, electrochemical methods, and relaxation methods (Gorsky effect, magnetic after effect, etc.) are in use. Due to the favourable gyromagnetic ratio of the proton and due its large incoherent scattering cross section for neutrons, NMR and QENS, respectively, (see

Chaps. 2 and 3 and [33]) are well suited for hydrogen diffusion studies. For a more thorough discussion of hydrogen diffusion the reader is referred to textbooks [2,3], to reviews [30,32] and to Chap. 9 of the data collection [6]. Muon diffusion can be studied by the muon spin resonance (μSR) technique [45], which has some similarities with β-NMR (see Chap. 9).

1.8 Self-Diffusion in Metals

Self-diffusion is most conveniently studied by the tracer method described in Sect. 1.4. As an example D values from ^{63}Ni tracer measurements in nickel are displayed in Fig. 1.15 according to [46, 47]. An enormous diffusivity range of about 9 orders of magnitude has been covered by the combination of mechanical sectioning [46] and sputter sectioning [47]. Most of the more important metallic elements have been studied by tracer methods over similarly wide ranges. In some cases the tracer data have been supplemented by additional techniques. For example, NMR proved to be very useful in the cases of aluminium and lithium (cf. Chap. 9) where no radioisotopes appropriate for tracer diffusion studies are available. For a collection of data and information about the method(s) used for each metal the reader is referred to Chap. 2 in [6].

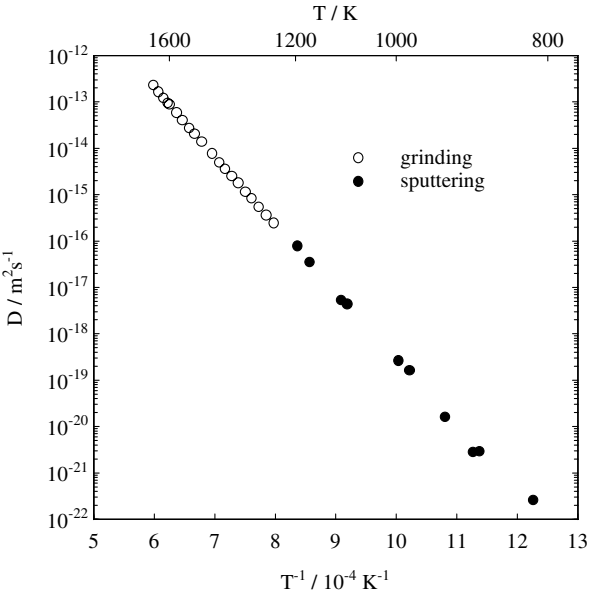

Fig. 1.15. Self-diffusion of ^{63}Ni in nickel. Open circles: data from mechanical sectioning; full circles: data from sputter sectioning.

The dominating mechanism of self-diffusion[12] in metallic elements is the vacancy mechanism illustrated in Fig. 1.9. Using (1.37) and (1.43) the diffusion coefficient of tracer atoms can be written as

$$D = fa^2\omega C_{\mathrm{V}}^{\mathrm{eq}} = fa^2\nu_0 \exp\Big(\frac{S^{\mathrm{F}} + S^{\mathrm{M}}}{R}\Big) \exp\Big(-\frac{H^{\mathrm{F}} + H^{\mathrm{M}}}{RT}\Big). \qquad (1.55)$$

The Arrhenius parameters of (1.20) have the following meaning for vacancy mediated self-diffusion:

$$\Delta H = H^{\mathrm{F}} + H^{\mathrm{M}} \qquad (1.56)$$

and

$$D_0 = fa^2\nu_0 \exp\Big(\frac{S^{\mathrm{F}} + S^{\mathrm{M}}}{R}\Big). \qquad (1.57)$$

As already mentioned in Sect. 1.6 the correlation factor accounts for the fact that for vacancy-mediated diffusion the tracer atom experiences some 'backward correlation' whereas the vacancy itself performs a random walk. For monovacancies in cubic lattices f is a temperature-independent quantity, which is approximately given by

$$f \approx 1 - \frac{2}{Z} \qquad (1.58)$$

where Z is the coordination number. Vacancy jumps into one of the Z directions occur with the probability $1/Z$ and an immediate backward jump effectively 'cancels' two tracer jumps. (1.58) is a 'rule of thumb'. Exact values according to [2] are listed in Table 1.2.

Table 1.2. Correlation factors of vacancy-mediated self-diffusion in cubic lattices.

Structure	fcc	bcc	sc	diamond
f	0.7815	0.727	0.653	0.5

For self-diffusion in non-cubic crystals correlation factors are orientation and temperature dependent. For example, the two correlation factors in hcp crystals depend on the ratio of the jump rates within and oblique to the basal plane (see, e.g., [2]).

1.8.1 Face-Centered Cubic Metals

Self-diffusion coefficients of several face-centered cubic (fcc) metals are shown in the Arrhenius diagram of Fig. 1.16. For each metal the temperature scale is

[12] For fcc metals at temperatures above about 2/3 of the melting temperature an additional contribution of divacancies (see Fig. 1.10) has been proposed (see [22] and the textbooks [2, 3]), which for reasons of simplicity will be not considered here.

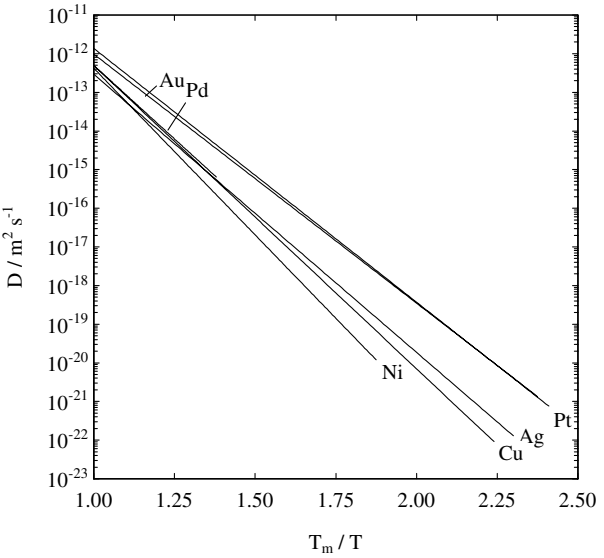

Fig. 1.16. Self-diffusion of several fcc metals versus reciprocal temperature normalized to their melting temperatures T_m.

normalized by its melting temperature T_m (homologous temperature scale). The following empirical rules for fcc metals are evident:

- Diffusivities near the melting temperature are similar for all fcc metals and lie between about 10^{-12} $\mathrm{m^2 s^{-1}}$ and 10^{-13} $\mathrm{m^2 s^{-1}}$.
- The Arrhenius lines on homologous scale have approximately the same slope. Since the slope equals $-\Delta H/RT_\mathrm{m}$ an empirical correlation between the activation enthalpy ΔH and the melting temperature T_m exists. This can be stated as follows:

$$\Delta H \approx (17 \,\mathrm{to}\, 18) R T_\mathrm{m} \quad . \tag{1.59}$$

  Equation (1.59) is sometimes denoted as the rule of van Liempt. The melting temperature in (1.59) is expressed in Kelvin.
- The pre-exponential factors lie typically within the following range:

$$5 \times 10^{-6}\,\mathrm{m^2 s^{-1}} < D_0 < 10^{-3}\,\mathrm{m^2 s^{-1}} \quad . \tag{1.60}$$

For the explanation of the empirical rules the reader is referred to [48]. Activation parameters for self-diffusion of some fcc metals are listed in Table 1.3 (for references see Chap. 2 in [6]). According to (1.57) the pre-exponential factors of Table 1.3 correspond to self-diffusion entropies

Table 1.3. Activation parameters for self-diffusion in some fcc metals.

Metal	Cu	Ag	Au	Ni	Pd	Pt
ΔH [kJ mol^{-1}]	204	170	165	285	266	257
D_0 [10^{-4} m^{2}s^{-1}]	0.35	0.046	0.027	1.77	0.205	0.05

$$\Delta S = S^{\mathrm{F}} + S^{\mathrm{M}} \tag{1.61}$$

of several R. According to (1.56) the activation enthalpy Q equals the sum of formation and migration enthalpies of the vacancy. For fcc metals independent experimental determinations of the formation and migration properties show that

$$\frac{H^{\mathrm{M}}}{H^{\mathrm{F}}} \leq 1 \tag{1.62}$$

is fulfilled. For a review of point defect properties in metals the reader is referred to [40].

1.8.2 Body-Centered Cubic Metals

Self-diffusion coefficients of several body-centered cubic (bcc) metals are shown in the Arrhenius diagram of Fig. 1.17 on a homologous temperature scale. A comparison of Figs. 1.17 and 1.16 reveals the following differences between fcc and bcc metals:

- Diffusivities at homologous temperatures are usually higher for bcc metals than for fcc metals. At the melting temperature T_m the difference is about one order of magnitude. Diffusivities for bcc metals near T_m lie between about $10^{-11}\,\mathrm{m^2s^{-1}}$ and $10^{-12}\,\mathrm{m^2s^{-1}}$.
- The 'spectrum' of self-diffusivities is much wider for bcc metals than for fcc metals. Self-diffusion is slowest for group VI metals and fastest for group IV metals. It is interesting to note that the latter undergo a structural phase transition from a hexagonal close-packed (hcp) low-temperature to a bcc high-temperature phase.
- The Arrhenius diagram of self-diffusion for some bcc high-temperature phases (β-titanium, β-zirconium) shows considerable upward curvature.

A common feature of fcc and bcc metals is that within one group of the periodic table self-diffusion at homologous temperatures is slowest for the lightest and fastest for the heaviest element of the group.

The very fast self-diffusion of bcc high-temperature phases and the wide spectrum of diffusivities of bcc metals has been attributed to special features of the lattice dynamics in bcc structures. A nearest-neighbour jump of a self-atom in the bcc lattice is a jump in [111] direction. For bcc metals the longitudinal phonon branch shows a minimum for 2/3[111] phonons, which is

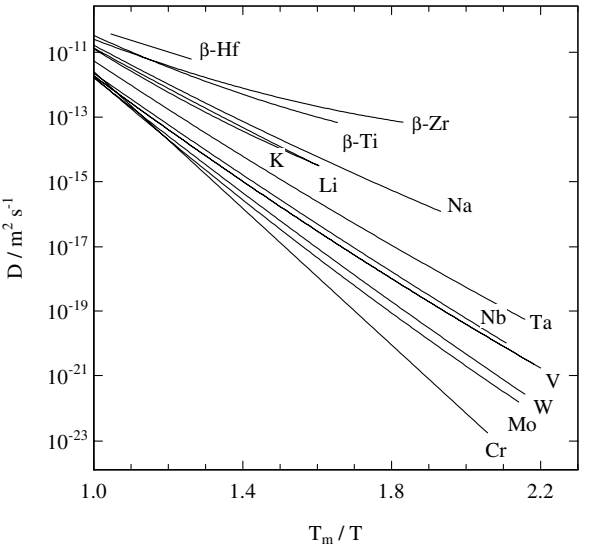

Fig. 1.17. Self-diffusion of several bcc metals versus reciprocal temperature normalized to their melting temperatures.

most pronounced for group IV metals. The associated low-phonon frequencies indicate a small activation barrier for nearest-neighbour exchange jumps between atom and vacancy [49, 50].

1.9 Impurity Diffusion in Metals

Let us now consider a very dilute substitutional binary alloy of metals A and B with the mole fraction of B atoms much smaller than that of A atoms. Then A is denoted as solvent (or matrix) and B is denoted as solute. Diffusion in a dilute alloy has always two aspects: solute diffusion and solvent diffusion. In this section we consider only solute diffusion in very dilute fcc alloys[13]. This is often denoted as impurity diffusion. It implies that the solute is isolated from other solutes in the matrix. In what follows we consider first the 'normal' behaviour of substitutional impurities. There are, however, some remarkable exceptions from 'normal' impurity diffusion, which will be mentioned afterwards.

[13] For solvent diffusion in dilute alloys the reader may consult [2, 3].

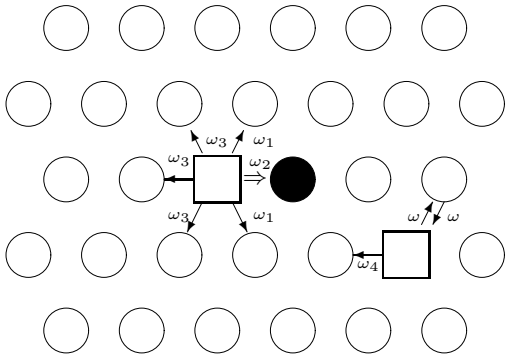

Fig. 1.18. Substitutional impurity diffusion in an fcc lattice: 'five-frequency model' for vacancy jumps in the presence of an impurity atom. Impurity (full circle), solvent atoms (open circles), vacancy (squares).

1.9.1 'Normal' Impurity Diffusion in fcc Metals

From the atomistic expression (1.41) derived in Sect. 1.6.1 and (1.44) we get for the impurity diffusion coefficient $D_{\mathrm{A}}^{\mathrm{B}^*}$ (denoted in the following by D_2) of vacancy-mediated diffusion in cubic Bravais lattices

$$D_2 \;=\; f_2 a^2 \omega_2 C_{\mathrm{V}}^{\mathrm{eq}} \exp\Big(\frac{G^{\mathrm{B}}}{RT}\Big). \tag{1.63}$$

To be specific we consider in the following fcc solvents[14]. If only nearest-neighbour interactions between vacancy and impurity occur, four vacancy jump rates apart from the jump rate ω in the pure solvent must be considered. This so-called five-frequency model introduced by Lidiard [51] is illustrated in Fig. 1.18.[15] The jump rates of the vacancy are denoted as follows:

ω_1: jump rate for rotation of vacancy-solute complex,
ω_2: jump rate of vacancy-solute exchange,
ω_3: dissociation jump rate of vacancy-solute complex,
ω_4: association jump rate of vacancy-solute complex,
ω: vacancy jump rate in the pure solvent.

As shown by Manning [15], the correlation factor of impurity diffusion can be written as

$$f_2 \;=\; \frac{\omega_1 + (7/2)F\omega_3}{\omega_2 + \omega_1 + (7/2)F\omega_3}, \tag{1.64}$$

[14] For impurity diffusion in bcc or hcp solvents see [2,3].
[15] We adopt the name 'five-frequency model' commonly used in the literature. The physical meaning of the quantities ω_i is that of jump rates.

where $F = F(\omega/\omega_4)$ is a function of the rate ratio ω/ω_4 [15]. F approaches unity for small ω_4/ω. $F = 0.7357$ for $\omega_4 = \omega$ and $F = 2/7$ for large ω_4/ω. In the case of self-diffusion all jump rates are equal. Then $f_2 = f = 0.7815$ (see Table 1.2). It is interesting to note that because of the condition of detailed thermal equilibrium the relationship

$$\frac{\omega_4}{\omega_3} = \exp\left(\frac{G^{\mathrm{B}}}{RT}\right) \tag{1.65}$$

must hold. This equation relates the dissociation and association rates of the vacancy-solute complex to its Gibbs free energy of binding G^{B}.

The impurity diffusion coefficient (1.63) can be recast to give

$$D_2 = f_2 a^2 \nu_0 \exp\left(\frac{S^{\mathrm{F}} - S^{\mathrm{B}} + S_2^{\mathrm{M}}}{R}\right) \exp\left(-\frac{H^{\mathrm{F}} - H^{\mathrm{B}} + H_2^{\mathrm{M}}}{RT}\right), \tag{1.66}$$

where H^{B} and S^{B} denote binding enthalpy and entropy of the vacancy-solute complex and H_2^{M} and S_2^{M} enthalpy and entropy of the vacancy-solute exchange jump. The activation enthalpy for impurity diffusion is then given by

$$\Delta H_2 = H^{\mathrm{F}} - H^{\mathrm{B}} + H_2^{\mathrm{M}} - C \tag{1.67}$$

where the correlation term

$$C = R\frac{\partial \ln f_2}{\partial \frac{1}{T}} \tag{1.68}$$

results from the temperature dependence of the impurity diffusion correlation factor.

It is evident from (1.55), (1.63), and (1.65) that the ratio of the diffusion coefficients between impurity- and self-diffusion can be written as

$$\frac{D_2}{D} = \frac{\omega_4}{\omega_3}\frac{\omega_2}{\omega}\frac{f_2}{f}. \tag{1.69}$$

This expression shows that the diffusion coefficient D_2 of a substitutional impurity differs from that for self-diffusion D in the pure solvent for three reasons:

- The factor ω_4/ω_3 shows that the probability to find a vacancy on a nearest-neighbour site of the impurity is different from the equilibrium vacancy concentration in the pure matrix because of vacancy-solute interaction (1.65).
- The factor ω_2/ω arises because the exchange rate between vacancy and impurity and those between vacancy and host atoms are different.
- The factor f_2/f arises because the correlation factor f_2 of impurity diffusion is no longer a geometric factor as in the case of self-diffusion. It depends on various jump rates and hence also on temperature.

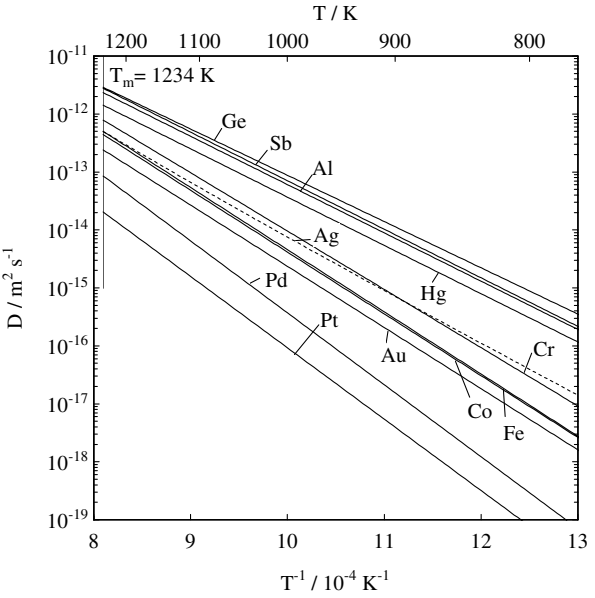

Fig. 1.19. Diffusion of several solutes and self-diffusion (dashed line) in silver.

Fig. 1.19 shows an Arrhenius diagram of various solutes in silver together with silver self-diffusion (for references see Chap. 3 in [6]). It reveals characteristic features of 'normal' diffusion of substitutional solute atoms:

– The D_2 values of solutes lie in a relatively narrow band around self-diffusion according to

$$1/100 \lesssim D_2/D \lesssim 100. \tag{1.70}$$

– The following empirical limits are found for pre-exponential factors

$$0.1 \lesssim \frac{D_0(\text{solute})}{D_0(\text{self})} \lesssim 10 \tag{1.71}$$

and activation enthalpies

$$0.75 \lesssim \frac{\Delta H_2(\text{solute})}{\Delta H(\text{self})} \lesssim 1.25. \tag{1.72}$$

Substitutional solutes in other fcc solvents like Cu, Au, and Ni also confirm these limits (see Chap. 3 in [6] for references).

Since solute and solvent atoms are located on the same lattice and since their diffusion is mediated by vacancies this rather small diffusivity dispersion is not surprising. It reflects the high efficiency of screening of point charges in some metals (e.g. noble metals) which normally limits the vacancy-impurity interaction enthalpy to values between 0.1 and 0.3 eV. Such values

are small relative to the vacancy formation enthalpies, which are in the order of 1 eV [40]. Using $\Delta H = H^{\mathrm{F}} + H^{\mathrm{M}}$ we get for the difference of the activation enthalpies between solute- and self-diffusion

$$\Delta Q = \Delta H_2 - \Delta H = -H^{\mathrm{B}} + (H_2^{\mathrm{M}} - H^{\mathrm{M}}) - C. \tag{1.73}$$

A useful theoretical approach associates ΔQ with the charge difference between solute and vacancy. Positive solutes, generally those of higher nominal valence than the solvent, tend to have a net attraction with the vacancies. Such solutes diffuse more rapidly and with lower activation energies than self-diffusion. Calculations of ΔQ from a theory based on the free electron model using the Thomas-Fermi approximation for the interaction potential have been made, e. g., by LeClaire [52]. Good agreement was found with experiments for solute diffusion in noble metals and zinc. ΔQ is negative and its absolute value increases with the difference in valence between the solvent and the solute. For transition-metal solutes in noble metals and for other solvents such as the alkali metals, divalent magnesium, and trivalent aluminium the calculated values of ΔQ do not agree with the experiment.

1.9.2 Slow Diffusion of Transition-Metal Solutes in Aluminium

Fig. 1.20 shows an Arrhenius diagram of various solutes in aluminium together with aluminium self-diffusion according to [53]. The transition ele-

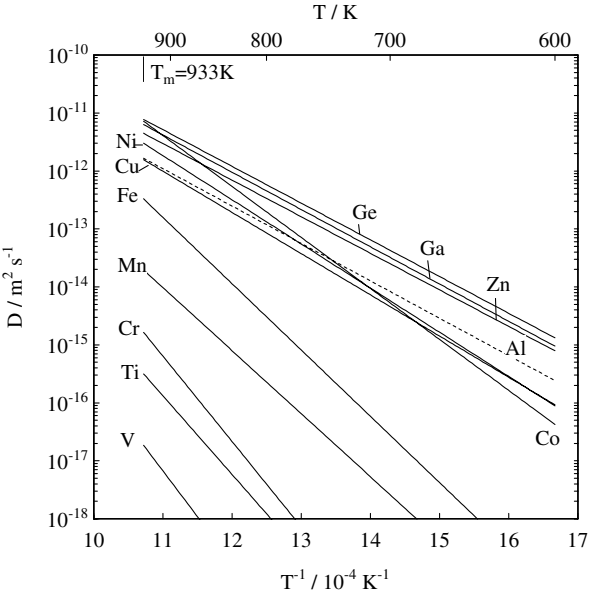

Fig. 1.20. Diffusion of several solutes and self-diffusion (dashed line) in aluminium.

ments are diffusers with high activation energies and high pre-exponential factors. Most of them have extremely low diffusivities as compared to aluminium self-diffusion. In contrast, non-transition elements have diffusion rates similar or slightly higher than self-diffusion and show only small diffusivity dispersion.

The pressure dependence of the solute diffusion coefficients in aluminium has been studied in [35,54]. The activation volumes of non-transition element solute diffusers are close to one atomic volume (Ω) and not much different from the activation volume of self-diffusion. However, the transition elements are diffusers with high activation volumes between 1.67 and 2.7 Ω. These findings can be attributed to differences in vacancy-solute interaction in aluminium between transition and non-transition element solutes [54]. The large ΔH_2 values of transition element solutes according to (1.67) indicate a strong repulsion between solute and vacancy ($H^{\mathrm{B}} < 0$) and/or a large activation enthalpy H_2^{M} for the solute-vacancy exchange jump.

1.9.3 Fast Solute Diffusion in 'Open' Metals

Fast solute diffusion is observed in some polyvalent metals, which are sometimes also denoted as 'open' metals [55]. 'Open' refers to the large ratio between atomic and ionic radius of the solvent. This solvent property leads for solutes with relatively small radii to the occurrence of fast solute diffusion.

As an example, Fig. 1.21 shows an Arrhenius diagram of solutes in lead together with lead self-diffusion (for references see Chap. 3 in [6]). Some solutes (thallium, tin) in lead show 'normal' behaviour. However, noble metals, nickel group solutes, and zinc have diffusivities which are three or more orders of magnitude faster than self-diffusion.

Noble metal solutes are also fast diffusers in the group IVB metal tin and in the group IIIB metals indium and thallium. The late transition elements Fe, Co, and Ni in group IVA metals (α-titanium, α-zirconium, and α-hafnium), and Co in niobium are very fast diffusers as well [55, 56].

Fast solute diffusion in metals has been attributed to the dissociative mechanism (see, e.g., [57]). This mechanism operates for solutes which are incorporated not only on substitutional sites but also to some extend in interstitial sites of the solvent metal (see Sect. 1.6). According to (1.47) the dissociative reaction involves vacancies. Provided that local equilibrium is established, the concentrations of the three involved species must fulfill the law of mass action

$$\frac{C_{\mathrm{i}} C_{\mathrm{V}}}{C_{\mathrm{s}}} = K(T) = \frac{C_{\mathrm{i}}^{\mathrm{eq}} C_{\mathrm{V}}^{\mathrm{eq}}}{C_{\mathrm{s}}^{\mathrm{eq}}}, \tag{1.74}$$

where C_{i}, C_{s}, and C_{V} denote molar fractions of interstitial solute, substitutional solute, and vacancies. $K(T)$ is a constant which depends on temperature and the superscript eq denotes thermal equilibrium.

A metal crystal with a normal density of dislocations has a sufficient abundance of vacancy sources or sinks to keep the vacancies everywhere in

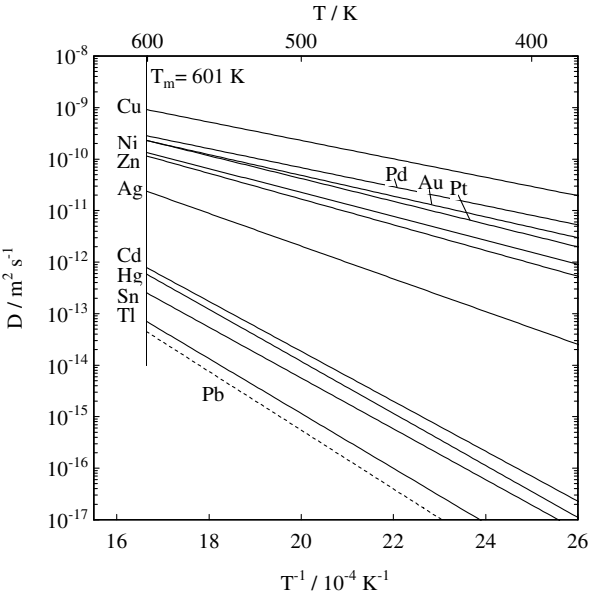

Fig. 1.21. Diffusion of several solutes and self-diffusion (dashed line) in lead.

equilibrium. Then the effective diffusivity of solutes is given by [41, 57]

$$D^{\text{eff}} = \frac{D_{\text{s}} C_{\text{s}}^{\text{eq}}}{C_{\text{i}}^{\text{eq}} + C_{\text{s}}^{\text{eq}}} + \frac{D_{\text{i}} C_{\text{i}}^{\text{eq}}}{C_{\text{i}}^{\text{eq}} + C_{\text{s}}^{\text{eq}}}, \tag{1.75}$$

where D_{i} denotes the diffusivity of the solute in its interstitial state and D_{s} its vacancy-mediated diffusivity on substitutional sites.

For solutes with dominating interstitial solubility and diffusivity ($C_{\text{i}}^{\text{eq}} \gg C_{\text{s}}^{\text{eq}}$ and $D_{\text{i}} \gg D_{\text{s}}$), (1.75) reduces to the trivial case of interstitial diffusion

$$D^{\text{eff}} \approx D_{\text{i}}. \tag{1.76}$$

For so-called hybrid solutes the substitutional solubility dominates ($C_{\text{s}}^{\text{eq}} \gg C_{\text{i}}^{\text{eq}}$) but the interstitial diffusivity is much faster than the substitutional one ($D_{\text{i}} >\!\!> D_{\text{s}}$). Then the effective diffusivity (1.75) approaches

$$D^{\text{eff}} \approx \frac{D_{\text{i}} C_{\text{i}}^{\text{eq}}}{C_{\text{s}}^{\text{eq}}}. \tag{1.77}$$

This relation contains the factor

$$\frac{C_{\text{i}}^{\text{eq}}}{C_{\text{s}}^{\text{eq}}} = \exp\left(-\frac{G_{\text{is}}}{RT}\right), \tag{1.78}$$

where G_{is} denotes the Gibbs free energy difference between the interstitial and substitutional positions of the solute. The rather wide 'diffusivity dispersion' of fast solute diffusers can be largely attributed to this factor.

Fast diffusion of solutes is well known for the semiconducting elements silicon and germanium [41,58,59] (see also Chap. 4). It has been also attributed to interstitial-substitutional exchange mechanisms. The kick-out mechanism is dominating diffusion of Au, Pt, and Zn in silicon [41,42], whereas the dissociative mechanism is operating, e. g., for Cu in germanium [60]. From a chemical viewpoint these similarities are not surprising. Silicon and germanium are group IV elements such as the 'open' metals lead and tin. Fast diffusion is also observed for compound semiconductors (e. g. Zn in GaAs [61]). Actually, the concepts growing out from studies of fast diffusion in semiconductors (see Chap. 4) have strongly influenced the interpretation of fast diffusion in metals.

1.10 Self-Diffusion in Binary Intermetallics

Some intermetallics (intermetallic compounds or ordered alloys) have attracted much attention as technological materials for high-temperature applications. A knowledge of their diffusion behaviour is of interest for the production of these materials and for their use in technological applications. Whereas diffusion in many pure metals and dilute alloys is thoroughly investigated and reasonably well understood, systematic diffusion studies for intermetallics are still relatively scarce although considerable progress has been achieved in recent years [62–67].

An atomistic understanding of diffusion in intermetallics in terms of defect structure and diffusion mechanisms is obviously more complex than for metallic elements:

Intermetallics crystallize in a variety of structures with ordered atom distributions. Examples are the B2-, $D0_3$-, $L1_2$-, $L1_0$-, $D0_{19}$-, B20-, and Laves-phase structures. Some intermetallics are ordered up to the melting temperature, others undergo order-disorder transitions because entropy favours a less ordered or even a random arrangement of atoms at high temperatures. We know intermetallic phases with wide phase fields and others which exist as line compounds. Some intermetallics occur for certain stoichiometric compositions, others are observed for off-stoichiometric compositions only. Some phases compensate off-stoichiometry by vacancies others by antisite atoms.

Let us concentrate on the more common cubic intermetallics. Their structures are the following (see Fig. 1.22):

B2 (or CsCl) Structure: The approximate composition is AB. The B2 structure can be derived from the bcc lattice, if the two primitive cubic sublattices are occupied by different kinds of atoms. Examples are FeAl, CoAl, NiAl, CoGa, PdIn, CuZn, AuZn, and AuCd.

$D0_3$ (or Fe_3Si) Structure: The approximate composition is A_3B. The $D0_3$-structure can also be considered as an ordered structure derived from the bcc lattice. In Fig. 1.22 (middle) A-atoms occupy white and grey sites,

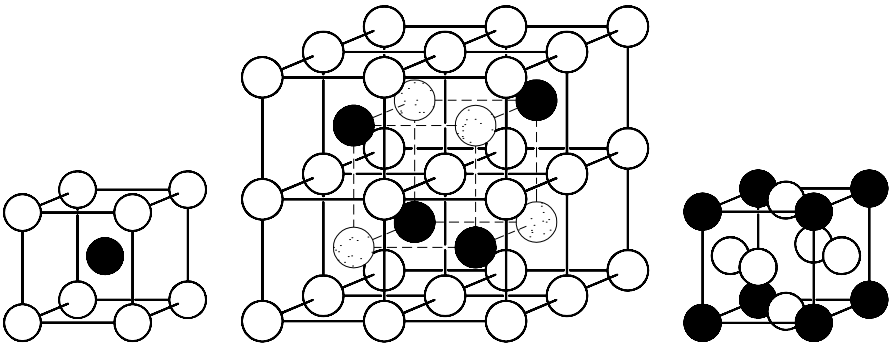

Fig. 1.22. Some frequent structures of intermetallics: B2 (left), $D0_3$ (middle), $L1_2$ (right).

B-atoms occupy black sites. $D0_3$ order is observed for example in Fe_3Si, in Fe_3Al below about 825 K, and for some high-temperature phases.

$L1_2$ (or Cu_3Au) Structure: The approximate composition is A_3B. The $L1_2$-structure is an ordered structure in the fcc lattice. In Fig. 1.22 (right) A-atoms occupy white sites, B-atoms occupy black sites . Examples are the Ni-based compounds Ni_3Al, Ni_3Ga, and Ni_3Ge.

Self-diffusion is the most basic diffusion process also in alloys and compounds. Like in the case of pure metals studies of self-diffusion utilize such tiny amounts of tracer atoms (see Sect. 1.4) of the diffusing species that the chemical composition of the sample does practically not change due to diffusion. In a binary system two tracer self-diffusion coefficients – one for A atoms and another one for B atoms – can be determined.

Table 1.4 compiles those binary intermetallics with B2, $D0_3$, and $L1_2$ structures for which self-diffusion data are available. In some cases self-diffusion of both components has indeed been studied. For NiAl and FeAl impurity diffusion of some solutes has been studied, since no appropriate Al tracer is available. Also interdiffusion studies were used to deduce the Al diffusivity via the Darken-Manning equation (see Sect. 1.11) from the interdiffusion coefficient, the tracer diffusivity of the other alloy constituent, and the thermodynamic factor (see, e. g., [68]). In what follows it may suffice to illustrate some characteristic features of self-diffusion in intermetallics. A comprehensive discussion of all aspects of self-diffusion is beyond the scope of this chapter. For further information the reader is referred to several overviews [62–66, 69].

1.10.1 Influence of Order-Disorder Transition

An order-disorder transition occurs, for example, between the β- and β'-brass phases of the Cu-Zn system. Below the order-disorder transition (at about 741 K) the compound shows B2 order (β' brass). At high temperatures the

Table 1.4. Self-diffusion in B2, $D0_3$, and $L1_2$ structure intermetallics. For the underlined components tracer self-diffusion data or data of suitable substitutional substitutes (in brackets) are available[16].

Structure	Intermetallic
B2	CuZn, AuCd, AuZn, CoGa, PdIn, FeCo, NiAl(Ga), FeAl(Zn,In,Cr,Mn,Ni,Co) AgMg, NiGa
$L1_2$	Ni_3Al, Ni_3Ge, Ni_3Ga, Co_3Ti, Pt_3Mn, Cu_3Au (disordered)
$D0_3$	Fe_3Si(Ge), Cu_3Sn, Cu_3Sb, Ni_3Sb, Fe_3Al

disordered A2 structure (β brass) is formed. The beautiful pioneering work of Kuper et al. [70] on self-diffusion of ^{64}Cu and ^{65}Zn in CuZn is displayed in Fig. 1.23. The influence of the order-disorder transition on the diffusion behaviour of both components is visible as a change in slope of the Arrhenius plot. The activation energies obey the inequality

$$Q_{\mathrm{B2}} > Q_{\mathrm{A2}}. \tag{1.79}$$

The occurrence of order impedes the diffusion of both components in a similar way. Similar effects of the B2-A2 transition have been observed for diffusion in FeCo.

Recently Fe diffusion in Fe_3Al has been studied over a wide temperature range [21]. Fe_3Al undergoes two order-disorder transitions from $D0_3$ order at low temperatures to B2 order at elevated temperatures to the completely disordered A2 structure at high temperatures. At the critical temperatures the slope of the Arrhenius diagram changes and the activation energies obey the following sequence

$$Q_{D0_3} > Q_{\mathrm{B2}} > Q_{\mathrm{A2}}. \tag{1.80}$$

The activation energy is highest for the structure with the highest degree of order and lowest for the disordered structure. The effect is, however, less pronounced in Fe_3Al than in CuZn.

1.10.2 Coupled Diffusion in B2 Intermetallics

Fig. 1.23 reveals another remarkable feature of self-diffusion in B2 intermetallics. We recognize that Zn in β-brass diffuses only slightly faster than Cu and that the ratio $D_{\mathrm{Zn}}/D_{\mathrm{Cu}}$ never exceeds 2.3 [70]. For equiatomic FeCo

[16] For references see [63–65].

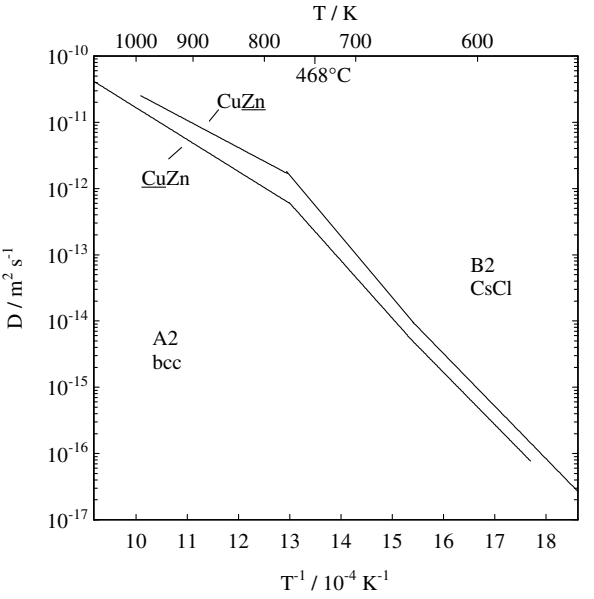

Fig. 1.23. Self-diffusion of ^{64}Cu and ^{65}Zn in CuZn.

the ratio $D_{\mathrm{Fe}}/D_{\mathrm{Co}}$ is always close to unity [71]. This type of 'coupling' between the diffusivities of the components seems to be typical of B2 phases. It can be observed in Fig. 1.24 for practically all B2 compounds, for which both constituents have been investigated. In some cases (e.g. NiGa, CoGa) the bounds for $D^{\mathrm{A}^*}_{\mathrm{AB}}/D^{\mathrm{B}^*}_{\mathrm{AB}}$ are somewhat wider than in the cases of CuZn and FeCo. However, the difference between the diffusivities is less than one order of magnitude. This 'coupling' between the diffusivities of the components indicates that the diffusion of both atomic species is likely mediated by the same defect.

As already mentioned the B2 structure consists of two primitive cubic sublattices. In the completely ordered state of a stoichiometric B2 compound, A atoms occupy one sublattice and B atoms the other. This implies that each A atom is surrounded by 8 B atoms on nearest-neighbour sites and vice versa. If the A and B atoms are distributed at random, a body-centered cubic (bcc) structure (A2 structure) is obtained. When atomic diffusion in a highly B2 ordered compound would take place by a random interchange between vacancies and atoms via nearest-neighbour jumps, migrating vacancies would leave traces of antisite defects ($\mathrm{A_B}$ and $\mathrm{B_A}$) behind. In order to maintain order such disordered regions must either be avoided or compensated during the diffusion process.

If the order energy is high and the degree of order close to unity sublattice diffusion of each component via second nearest-neighbour jumps is conceivable. It is well known that diffusion of the components in ionic crystals and in simple oxides occurs indeed by sublattice diffusion (see Chap. 5 and, e. g., [2]).

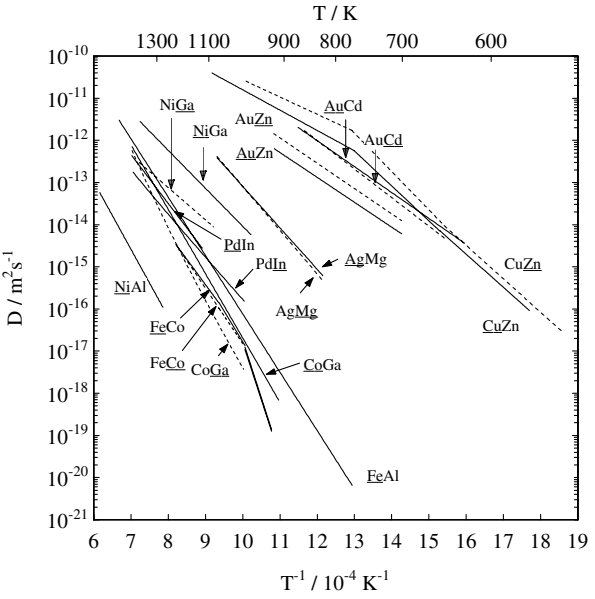

Fig. 1.24. Self-diffusion in B2 structure intermetallics.

However, sublattice diffusion cannot be the dominating mechanism in B2 intermetallics since sublattice diffusion does not lead to a coupled diffusion of the components.

Ingenious order-retaining mechanisms, for which diffusion of both components is coupled, have been proposed for B2 intermetallics:

- **Six-Jump-Cycle Mechanism**: A vacancy trajectory of 6 consecutive nearest-neighbour jumps displaces atoms in such a way that after the cycle is completed the order is re-established [72]. The ratio of the diffusivities for this mechanism for a highly ordered stochiometric compound lies within the following narrow limits [69]: $0.5 < D^{A^*}_{AB}/D^{B^*}_{AB} < 2$.
- **Triple-Defect Mechanism**: In a stoichiometric B2 compound vacancies and antisite defects can associate to form triple defects A_B+2V_A, with V_A denoting a vacancy on the A-sublattice and A_B an A-antite atom on the B-sublattice. Then the ratio of the diffusivities for this mechanism lies within the following limits: $1/13.3 < D^{A^*}_{AB}/D^{B^*}_{AB} < 13.3$ [73]. As the composition deviates from stochiometry antisite atoms widen these limits [74]. Thus, in a less ordered state, values of $D^{A^*}_{AB}/D^{B^*}_{AB}$ beyond these limits can no longer be considered as an indication that the six-jump-cycle mechanism does not operate.
- **Antistructure-Bridge Mechanism**: For an ordered B2 phase with some substitutional disorder antisite defects can act as 'bridges' to establish low-energy sequences for vacancy jumps [75]. Long-range diffusion

via this mechanism requires a sufficient concentration of antisite defects to reach the percolation threshold [76].

– **Vacancy-Pair Mechanism**: A bound pair of vacancies (on both sublattices) can mediate diffusion of both components by successive correlated next-nearest-neighbour jumps. Whereas this mechanism has some relevance for CsCl-type ionic crystals it is unlikely for B2 intermetallics.

A detailed description of these mechanisms can be found in [63, 67]. It seems that in those B2 compounds, which are composed of a group VIIIB metal (Co, Fe, Ni, Pd, etc.) and a group IIIA metal (Al, Ga, In, etc.), the triple defect mechanism is important. By contrast, B2 phases composed of a noble metal (Cu, Ag, Au) and a divalent metal (Mg, Zn, Cd) are considered as candidates for the 6-jump cycle mechanism. Clearly, the antistructure bridge mechanism becomes more important at deviations from stoichiometry.

Perhaps the most thoroughly studied B2 compound is NiAl, where Ni diffusion has been measured for various compositions on both Al- and Ni-rich sides and over wide temperature intervals [77, 78]. While the Ni tracer diffusivity increases notably on the Ni-rich side of the stoichiometric composition it is practically not changed with the composition on the Al-rich side in spite of the large amount of structural Ni-vacancies (several %). Calculations of the atomic mechanism using embedded atom potentials showed that the triple-defect mechanism dominates self-diffusion on the Al-rich side and for stoichiometric NiAl. With increasing Ni-content after reaching the percolation threshold the antistructure-bridge mechanism dominates on the Ni-rich side [77]. These findings for NiAl agree with the pioneering work on the B2 phase CoGa by Stolwijk et al. [79] .

1.10.3 The Cu_3Au Rule

The Cu_3Au rule (see, e.g., [2]) provides a logical tool to fathom the self-diffusion behaviour in non-equiatomic intermetallics. It states that in some compounds of type A_mB_n, where the ratio m/n is equal to or greater than 2, the majority element diffuses faster than the minority element:

$$D_{AB}^{A^*} > D_{AB}^{B^*}. \tag{1.81}$$

Here $D_{AB}^{A^*}$ and $D_{AB}^{B^*}$ denote the tracer diffusion coefficients of the components A and B. For geometric reasons discussed below, A_3B intermetallics with $L1_2$ or $D0_3$ structure are good candidates to test the validity of the 'Cu_3Au' rule[17].

[17] According to [2] it should only be applied to intermetallics in which diffusion occurs via vacancies. Phases such as, e.g., Fe_3C, where one of the two elements is sufficiently small to occupy interstitial sites in a matrix composed of the other element, must be excluded. A nice essay about the Cu_3Au rule can be found in [80].

The A sublattice in $D0_3$ structure compounds is interconnected by nearest-neighbour bonds, whereas this is not the case for the B sublattice (see Fig. 1.22). Thus the A atoms can diffuse within their own sublattice via nearest-neighbour (NN) jumps. If B atoms migrate within their own sublattice, their jump vector corresponds to a third-nearest neighbour jump with respect to the bcc unit cell. An alternative for the diffusion of B atoms are nearest-neighbour jumps which, however, create B antisite defects. Both options are very likely associated with higher activation enthalpies for diffusion of B atoms compared to A atoms. Those $D0_3$ compounds (Fe_3Si, Cu_3Sn, see Table 1.4), for which reliable diffusion data for both constituents are available, indeed fulfill this rule [63]. In $L1_2$ compounds each A atom is surrounded by 8 A atoms and 4 B atoms on nearest-neighbour sites (see Fig. 1.22). In contrast to this situation, a B atom faces only A atoms on surrounding nearest-neighbour sites. This implies that similar to the $D0_3$ structure the sublattice of the majority component A is interconnected by nearest-neighbour bonds, whereas this is not the case for the sublattice of the minority component B. Vacancy motion restricted to the majority sublattice can promote diffusion of A atoms. However, diffusion of B atoms either requires jump lengths larger than the nearest-neighbour distance or the formation of antisite defects, if it is promoted by NN jumps of vacancies.

As can be seen from Fig. 1.25, diffusion of the majority component Ni in Ni_3Ge is indeed significantly faster than that of the minority component Ge. Experiments on Ni_3Ga revealed that the trend is similar to the case of Ni_3Ge, but the difference of the diffusivities is not so large [81].

For the technologically important compound Ni_3Al no unquestioned data of Al diffusion are available [62,63]. There are, however, indications that the ratio of the two diffusion coefficients is not far from unity [64]. It is quite natural that Ni diffusion in $L1_2$ compounds occurs by a sublattice vacancy mechanism. On the other hand, it is not clear how the diffusion of the minority elements occurs in Ni based $L1_2$ compounds. Possible mechanisms have been discussed in [64]. Most likely minority elements diffuse as antisite atoms in the majority sublattice. Thus the Cu_3Au rule should not be considered to be universal. A compound which is a beautiful example for the validity of the rule is $MoSi_2$. Tracer diffusion studies of Si and Mo diffusion revealed a huge asymmetry between the diffusion of the majority and the minority component. Si diffusion is 6 to 7 orders of magnitude faster than Mo diffusion [82]. It is interesting to note that $MoSi_2$ is one of the compounds on which the formulation of the rule was based to interpret silicide formation from thin Mo layers on Si wafers [80].

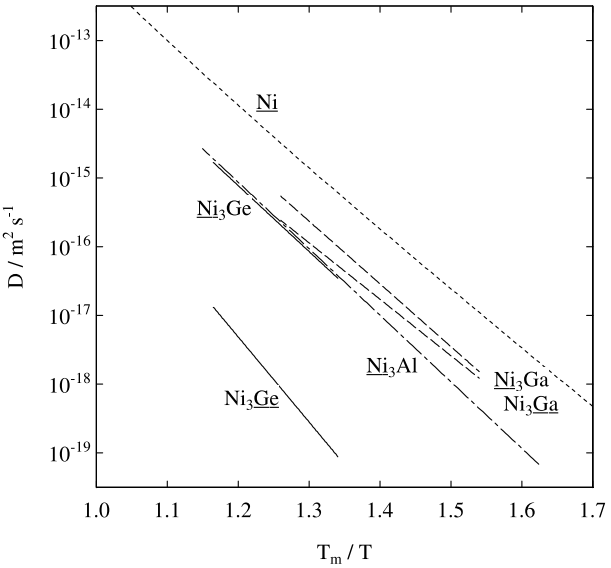

Fig. 1.25. Self-diffusion in three $L1_2$ structure intermetallics (Ni_3Ge, Ni_3Ga, Ni_3Al) and in Ni normalized to the melting temperatures (1405 K, 1383 K, 1635 K, and 1726 K).

1.11 Interdiffusion in Substitutional Binary Alloys

1.11.1 Boltzmann-Matano Method

A diffusion coefficient in a binary alloy measured in a chemical composition gradient is denoted as chemical or interdiffusion coefficient $\tilde{D}$ (see also Sect. 1.3 and Chap. 5). The experimental procedure of an interdiffusion study is schematically illustrated in Fig. 1.26. A diffusion couple consisting of two homogeneous, homo-phase alloys with different compositions (A_XB_{1-X} and A_YB_{1-Y}), but within the same phase field of the phase diagram, is formed. Usually the thicknesses of the couple members are chosen very large as compared to the average diffusion length. Then each couple member can be considered to be semi-infinite. The interdiffusion profile is measured after the diffusion anneal, e.g., by electron microprobe analysis.

Boltzmann-Matano analysis, which is based on Boltzmann's transformation of Fick's second law [83] and a procedure suggested by Matano [84], is employed to evaluate – in general concentration-dependent – interdiffusion coefficients from an experimental profile according to

$$\tilde{D}(c^*) \;=\; \left(2\;t\;\left.\frac{\partial c}{\partial x}\right|_{x^*}\right)^{-1} \quad \int_{c^-}^{c^*} (x_{\mathrm{M}} - x)\;\mathrm{d}c \quad . \tag{1.82}$$

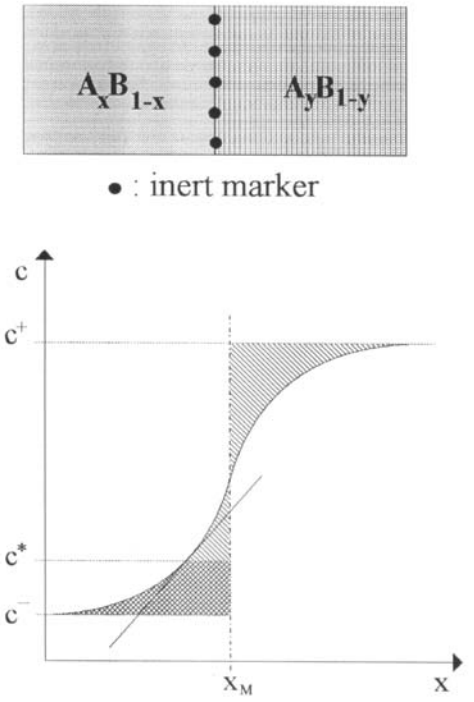

Fig. 1.26. Schematic illustration of a single-phase interdiffusion experiment. The original interface (Kirkendall plane) is marked by inert markers. The position of the Matano plane (x_M) is also indicated.

Here t is the time of the diffusion anneal and x the position. In (1.82) x_{M} denotes the position of the so-called Matano plane, which is defined by

$$\int_{c^-}^{c^+} (x_{\mathrm{M}} - x)\, dc \;=\; 0 \quad . \tag{1.83}$$

c^- and c^+ refer to the initial compositions of the two starting alloys (see Fig. 1.26). To deduce $\tilde{D}$ one determines the Matano plane first. Afterwards, the area corresponding to the integral in (1.82) and the slope of the tangent to the $c(x)$ curve at the concentration c^* must be calculated (see Fig. 1.26). This procedure is repeated for various choices of c^*. In this way $\tilde{D}$ values are obtained for various compositions.

In (1.82) and in the rest of this chapter volume changes have been neglected for reasons of simplicity. There are systems in which the volume will change in the course of interdiffusion. The generalisation of (1.82) for non-constant volume was given by Sauer and Freise [85] and can be found in textbooks [2, 3, 5].

1.11.2 Darken's Equations

As already mentioned in Sect. 1.3 the intrinsic diffusion coefficients D_{A} and D_{B} are related to the interdiffusion coefficient $\tilde{D}$ and to the velocity of the marker movement v_{K} (Kirkendall velocity) in a Kirkendall experiment (see Fig. 1.27). The relations deduced by Darken [14] are as follows:

$$\tilde{D} \;=\; X_{\mathrm{B}} D_{\mathrm{A}} + X_{\mathrm{A}} D_{\mathrm{B}}, \tag{1.84}$$

where X_{A} and X_{B} denote the mole fractions of the elements A and B respectively. The Kirkendall velocity is given by

$$v_{\mathrm{K}} \;=\; (D_{\mathrm{A}} - D_{\mathrm{B}}) \frac{\partial X_{\mathrm{A}}}{\partial x} \tag{1.85}$$

with $\partial X_{\mathrm{A}}/\partial x$ denoting the concentration gradient at the Kirkendall plane. Using (1.84) and (1.85) the intrinsic diffusion coefficients D_{A} and D_{B} can be deduced if the interdiffusion coefficient and the Kirkendall velocity are known from the experiment.

The reason why diffusion occurs is always a decrease in the Gibbs free energy of the system. This implies that the atoms are diffusing from regions where their chemical potential is high to regions where it is low, i.e., the driving force for diffusion is the gradient of the chemical potential (see also Sect. 1.3.2). As a consequence the interdiffusion coefficient $\tilde{D}$ is related to the tracer self-diffusion coefficients of the components in a homogeneous alloy via

$$\tilde{D} \;=\; (X_{\mathrm{A}} D_{\mathrm{AB}}^{\mathrm{B}^*} + X_{\mathrm{B}} D_{\mathrm{AB}}^{\mathrm{A}^*})\, \Phi. \tag{1.86}$$

Here X_{A} and X_{B} denote the mole fractions of the components and Φ is the thermodynamic factor of the alloy. Using a classical result from thermodynamics of binary systems, the thermodynamic factor can be written as [2]

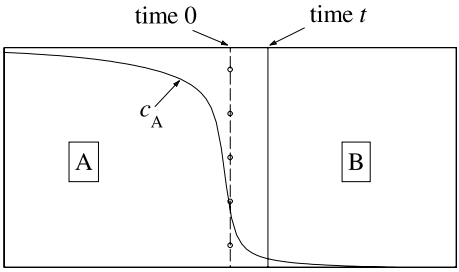

Fig. 1.27. Schematic illustration of the Kirkendall effect in a diffusion couple composed of two pure metals A and B. The circles represent inert markers inserted at the original interface. The line at time t represent the position of the markers after the diffusion anneal. The solid line is a graph of the concentration of A atoms in the couple after diffusion time t. As drawn, the B atoms diffuse into A faster than those of A diffuse into B. As a result the interface moves to the right ($D_{\mathrm{B}} > D_{\mathrm{A}}$).

$$\Phi \;=\; \frac{X_{\rm A}\,X_{\rm B}}{RT}\;\frac{{\rm d}^2G}{{\rm d}X_{\rm A}^2} \;=\; \frac{\partial \ln a_i}{\partial \ln X_i} \;=\; 1+\frac{\partial \ln \gamma_i}{\partial \ln X_i}, \tag{1.87}$$

where G denotes Gibbs free energy, a_i the (chemical) activity, and γ_i the coefficient of activity of species i (= A or B). According to the Gibbs-Duhem relation for binary systems, the thermodynamic factor is identical for both species. Equations (1.84), (1.85), and (1.86) are denoted as the equations of Darken.

The thermodynamic factor is unity for ideal solutions. It is larger than unity for phases with negative deviations from ideality and smaller than unity in the opposite case. Negative deviations are expected for systems with order. Therefore thermodynamic factors of intermetallic compounds are often larger, sometimes even considerably larger than unity due to the attractive interaction between the constituents of the intermetallic phase. As a consequence interdiffusion coefficients are often larger than the bracket term in (1.86). The latter corresponds to a weighted average of the tracer diffusivities. Activation enthalpies of interdiffusion are often smaller than those for tracer diffusion due to the temperature variation of the thermodynamic factor.

1.11.3 Darken-Manning Relations

The Darken relation between tracer diffusivities and the chemical diffusion coefficient (1.86) is widely used in practice. Although it remains a very useful equation it was recognized soon that from a theoretical viewpoint (1.86) is incomplete. Manning [15, 86] developed equations for vacancy-mediated diffusion in a so-called 'random alloy' (vacancies and A and B atoms distributed at random on the same lattice). In general, the results are like those obtained by Darken but with 'vacancy-wind' corrections[18]. The intrinsic diffusion coefficients and the interdiffusion coefficient, respectively, are given by

$$D_{\rm A} \;=\; D_{\rm AB}^{\rm A^*}\Phi\left[1+\frac{1-f}{f}\,\frac{X_{\rm A}(D_{\rm AB}^{\rm A^*}-D_{\rm AB}^{\rm B^*})}{(X_{\rm A}D_{\rm AB}^{\rm A^*}+X_{\rm B}D_{\rm AB}^{\rm B^*})}\right] \tag{1.88}$$

and an analogous equation for $D_{\rm B}$, and

$$\begin{aligned}\tilde{D} \;=\; & (X_{\rm A}D_{\rm AB}^{\rm B^*}+X_{\rm B}D_{\rm AB}^{\rm A^*})\,\Phi \\ & \times\left[1+\frac{1-f}{f}\,\frac{X_{\rm A}X_{\rm B}(D_{\rm AB}^{\rm A^*}-D_{\rm AB}^{\rm B^*})^2}{(X_{\rm A}D_{\rm AB}^{\rm A^*}+X_{\rm B}D_{\rm AB}^{\rm B^*})(X_{\rm A}D_{\rm AB}^{\rm B^*}+X_{\rm B}D_{\rm AB}^{\rm A^*})}\right].\end{aligned} \tag{1.89}$$

The factors in square brackets are Manning's vacancy-wind corrections to Darken's equations. One also finds that the Kirkendall velocity is increased by the addition of a factor f^{-1} to (1.85). As usual f denotes the correlation factor of self-diffusion. In substitutional alloys the Manning corrections,

[18] A transparent derivation can be found in [4].

while significant, will never be very large even when one of the tracer self-diffusivities is much greater than the other. For instance the Kirkendall velocity is increased by about 30 % in an fcc alloy.

It is a debated question whether the Darken-Manning equations can be applied to ordered intermetallics. The answer depends on the structure, the type of disorder, and the diffusion mechanism. For example, according to Belova and Murch [87] (1.89) can be used for B2 compounds with antisite disorder.

1.12 Multiphase Diffusion in Binary Systems

The experimental procedure in a multiphase diffusion experiment is schematically illustrated in the upper part of Fig. 1.28. A diffusion couple is formed from the two elements A and B or from two compounds A_XB_{1-X} and A_YB_{1-Y}. Let us suppose that the phase diagram of the system contains intermetallics. Then interdiffusion will give rise to the formation of intermetallic layers. A hypothetical phase diagram (containing only one intermetallic compound) and a concentration profile resulting from interdiffusion is illustrated in the lower part of Fig. 1.28.

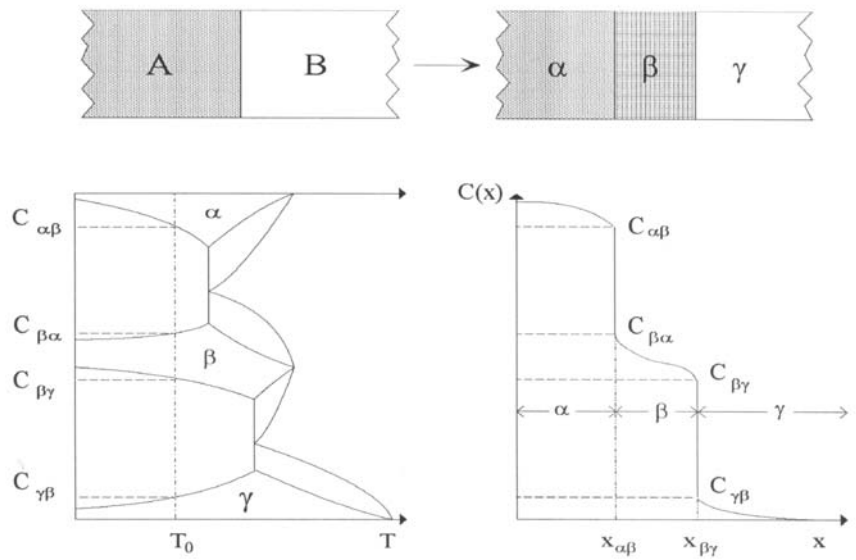

Fig. 1.28. Schematic illustration of a multi-phase diffusion experiment. Upper part: Diffusion couple before and after a diffusion anneal. Lower part: Interrelation between a hypothetical phase diagram and an interdiffusion profile after a diffusion anneal at temperature T_0.

The name multi-phase diffusion emphasizes the diffusional aspect of the whole process. However, there is also the aspect of a chemical reaction between the atomic species at the phase boundaries. The overall kinetics of phase formation and growth can be either governed by diffusion across the growing product phase(s) or by reaction(s) occurring at the interfaces. In the first case the process is denoted to be diffusion controlled; in the second case it is called to be reaction controlled. In general the kinetics of formation and growth of intermetallic layers will be the result of both processes. For this phenomenon the name reaction (reactive) diffusion has been suggested. In very thin layers gradients are very large and diffusion processes proceed very fast. Then the process is in the interface-reaction controlled regime. However, during progress of reaction diffusion the layer thickness increases. Then diffusion of the reacting species needs more and more time. Finally, diffusion processes determine the overall kinetics [88, 89].

When the whole process is diffusion controlled, the growth of the intermetallic layers in a binary system obeys a parabolic growth law

$$\Delta x_\beta^2 \quad = 2\ k_\beta\ t, \tag{1.90}$$

where Δx_β denotes the thickness of the layer. Kidson has shown that growth constants have the following meaning [90]:

$$k_\beta \ = \ 2 \left\{ \left[\frac{\tilde{D}_{\gamma\beta}\, K_{\gamma\beta} - \tilde{D}_{\beta\gamma}\, K_{\beta\gamma}}{C_{\beta\gamma} - C_{\gamma\beta}} \right] - \left[\frac{\tilde{D}_{\beta\alpha}\, K_{\beta\alpha} - \tilde{D}_{\alpha\beta}\, K_{\alpha\beta}}{C_{\alpha\beta} - C_{\beta\alpha}} \right] \right\}^2 . \tag{1.91}$$

$C_{\alpha\beta}$ denotes the equilibrium composition (in atomic fractions) on the α-side of an α/β-interface, $\tilde{D}_{\alpha\beta}$ the interdiffusion coefficient in the α-phase near the α/β -interface, and $K_{\alpha\beta}$ is the composition gradient in the α-phase near the α/β-interface in a diagram of concentration versus $x/\sqrt{t}$. As already mentioned, in the derivation of (1.91) any explicit influence of interface processes like phase nucleation, atomic transfer across the interface, and the creation and/or annihilation of point defects at the interfaces has been disregarded. This is only justified for long diffusion times. Then the growth process is diffusion controlled [91, 92].

We consider as an example multiphase diffusion in the system Ni-Al [93]. Apart from the primary and terminal solid solutions five intermetallic compounds are present in the phase diagram of Ni–Al: Al_3Ni, Al_3Ni_2, AlNi, Al_3Ni_5 and Ni_3Al [94]. Fig. 1.29 shows an optical micrograph of a diffusion couple of pure Al and Ni after a diffusion anneal of 48 h at 823 K. Layers of the Al-rich intermetallic compounds Al_3Ni and Al_3Ni_2 are clearly visible. Their compositions can be identified in the profile across the diffusion zone measured by electron microprobe analysis. The layer thicknesses of Ni-rich compounds – at the relatively low temperature of the diffusion anneal – are too small to be detectable in Fig. 1.29. As can be seen from Fig. 1.30 the

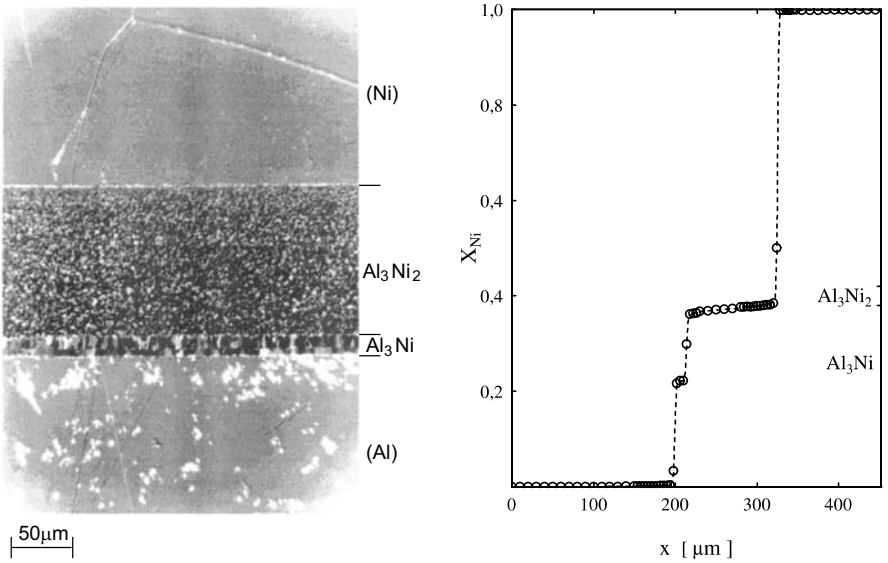

Fig. 1.29. Optical micrograph of Al–Ni diffusion couple after a diffusion anneal of 48 h at 823 K (left). Composition profile obtained by electron microprobe analysis (right).

compound Al_3Ni_2 indeed shows a parabolic growth. The growth constant obtained from these experiments is thermally activated with an enthalpy of $126\,\mathrm{kJ\,mol^{-1}}$.

We emphasize that according to (1.91) growth constants have a complex meaning. They depend on diffusivities in the bordering layers as well as on the diffusivity of the growing phase, on the concentration gradients on both sides of the interfaces, and on the (in general temperature dependent) solubility limits of the phases. If one deduces an activation enthalpy for the growth process it has a complex meaning as well. Its value is usually not identical with the activation enthalpy of interdiffusion in the growing layer. The activation enthalpy assigned to the growth of an intermetallic layer is at most only an average of several more fundamental activation enthalpies. If a linear Arrhenius plot is observed for the growth constant, this is only empirically useful. It indicates either that one of the terms dominates over the others or that the activation enthalpies are similar to each other. In addition, growth constants may be influenced by mass transport along diffusion short circuits like grain boundaries in the growing layer.

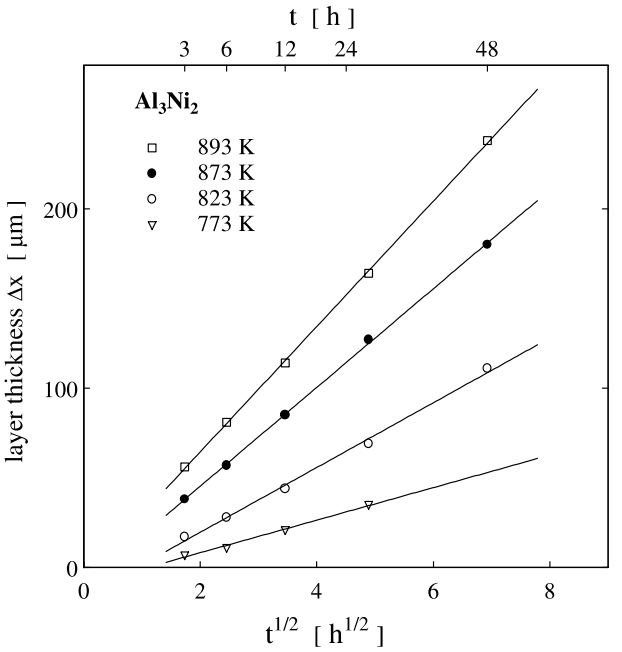

Fig. 1.30. Parabolic growth of the intermetallic compound Al_3Ni_2 in Al–Ni diffusion couples.

1.13 Conclusion

Diffusion is an important topic of materials science since the phenomenon of diffusion is of both practical importance and of fundamental interest. In this chapter we have outlined the continuum description and the basic atomic mechanisms of bulk diffusion in solids. The various diffusion coefficients, which are relevant for diffusion in solid elements and binary alloys, have been introduced: the tracer diffusion coefficient(s) of self-diffusion, tracer diffusion coefficients of foreign elements, the chemical (or interdiffusion) coefficient in a composition gradient, and the intrinsic diffusion coefficients. The most important experimental method for diffusion studies is the tracer technique in combination with mechanical and/or sputter sectioning for depth profiling. Various other techniques for the measurement of diffusion profiles have been also considered. Indirect methods including mechanical and magnetic relaxation and nuclear methods such as nuclear magnetic relaxation, Mößbauer spectroscopy and quasielastic neutron scattering have been mentioned only briefly since they are the main topics of Chaps. 2, 3 and 9.

Self-diffusion is the most basic diffusion process in a solid. It is well studied for most metallic elements. In close-packed metals self-diffusion occurs predominantly by a vacancy mechanism with some small contributions of divacancies at temperatures above 2/3 of the melting temperature. Self-diffusion in bcc metals is also vacancy-mediated. In a homologous temperature scale

it is faster and the range of diffusivities is much wider than for close-packed metals.

Diffusion of small foreign atoms proceeds much faster than self-diffusion of the host metal. Small foreign atoms such as H, C, N, and O are usually incorporated in octahedral or tetrahedral interstitial sites of the host lattice and diffuse via a direct interstitial mechanism. Diffusion of hydrogen is a particularly interesting case for scientific and application-oriented reasons. Its diffusion is extremely rapid, non-classical isotope effects occur, and quantum effects may cause strong deviations from a linear Arrhenius-like temperature dependence of H diffusion.

Diffusion of solutes in substitutional alloys is vacancy-mediated. Solute diffusion in very dilute alloys (impurity diffusion) is normally described by diffusion coefficients which lie in a relatively narrow band around those of self-diffusion of the host (solvent). This rather small diffusivity dispersion is understandable since solute and solvent atoms are located on sites of the same lattice and both use vacancies as diffusion vehicles. It reflects the high efficiency for screening of electrical point charges of some metallic hosts such as the noble metals and zinc. This efficient screening limits the solute-vacancy interaction to relatively small values.

Remarkable exceptions from 'normal' behaviour of solute diffusion are observed for polyvalent metals: Transition-metal solutes in aluminium are extremely slow diffusers with high activation energies, high pre-exponential factors and high activation volumes. Very likely this indicates a strong repulsion between vacancy and solute somewhere on the vacancy-solute exchange path. Fast solute diffusion is observed, e.g., for noble metal solutes in lead and tin and for late-transition-element solutes in group IVA solvents (zirconium, titanium and hafnium). The fast diffusion has been attributed to the dissociative mechanism. The latter operates for solutes which are dissolved on substitutional and interstitial sites. Even when its interstitial fraction is very small it can be responsible for the rapid diffusion. Fast solute diffusion is also observed in the semiconductors silicon and germanium (see Chap. 4).

Systematic studies of diffusion in intermetallics (intermetallic compounds and ordered alloys) have become available only recently. An understanding of diffusion in terms of atomic mechanisms is more complex than for metallic elements. The current knowledge about self-diffusion has been illustrated for binary intermetallics with B2-, $L1_2$-, and $D0_3$-structures. Important factors which influence diffusion such as the crystal structure, the state of order and disorder, the temperature and the composition have been illustrated. In a broad sense diffusion is mediated by vacancy-type defects, which include triple-defects and antistructure-bridge mechanisms. Relevant atomic mechanism must take into account that the degree of order in the material is maintained during diffusion. Despite of the progress made in recent years, diffusion in intermetallics is a field that deserves further attention.

The field of interdiffusion in binary alloys has been only touched in this chapter. The Boltzmann-Matano method (or a related method) is necessary to deduce interdiffusion coefficients from composition profiles. A detailed interpretation of the interdiffusion coefficient requires also measurements of the Kirkendall effect. The analysis given by Darken and its refinement by Manning permits to deduce the intrinsic diffusion coefficients. The latter are related to the tracer diffusion coefficients of the components in homogeneous alloys via the thermodynamic factor of the alloy and the so-called vacancy-wind corrections.

Multiphase diffusion or reaction diffusion occurs in a binary alloy system with one or several intermediate phases. In an appropriate diffusion couple layers of the intermediate phase(s) form and grow. Their growth is often diffusion controlled. Then their growth constants are related to the interdiffusion coefficients.

Notation

a	cubic lattice parameter
a_i	activity (chemical) of species i
c	volume concentration of diffusing species
C_{V} ($C_{\mathrm{V}}^{\mathrm{eq}}$)	mole fraction of vacancies (in thermal equilibrium)
$C_{2\mathrm{V}}$ ($C_{2\mathrm{V}}^{\mathrm{eq}}$)	mole fraction of divacancies (in thermal equilibrium)
C_{i} ($C_{\mathrm{i}}^{\mathrm{eq}}$)	mole fraction of interstitial solutes (in equilibrium)
C_{s} ($C_{\mathrm{s}}^{\mathrm{eq}}$)	mole fraction of substitutional solutes (in equilibrium)
$\mathcal{D}$	diffusion coefficient (second rank tensor)
D_I, D_{II}, D_{III}	diffusion coefficients in principal diffusion directions
D	diffusion coefficient, also self-diffusion coefficient in a cubic crystal
$\tilde{D}$	interdiffusion coefficient (also chemical diffusion coefficient)
D_2	diffusion coefficient of solute (impurity) in dilute alloy (also $D_{\mathrm{A}}^{\mathrm{C}^*}$)
D_{i}	diffusion coefficient of a solute in interstitial sites
$D_{\mathrm{A}}^{\mathrm{A}^*}$,	tracer self-diffusion coefficients of in pure metal A
$D_{\mathrm{AB}}^{\mathrm{A}^*}$, $D_{\mathrm{AB}}^{\mathrm{B}^*}$	tracer diffusion coefficients of component A or B in a binary material
$D_{\mathrm{A}}^{\mathrm{C}^*}$, $D_{\mathrm{AB}}^{\mathrm{C}^*}$,	tracer diffusion coefficients of impurity C in pure metal A or in a binary A-B material
D_0	pre-exponential factor of diffusion (including diffusion entropy)
$D_0^{'}$	pre-exponential factor of diffusion (without diffusion entropy)
f	correlation factor, correlation factor of self-diffusion
f_2	correlation factor of solute diffusion
g	geometry factor

G^{B}	Gibbs free energy of binding for vacancy-solute complex
G^{F}	Gibbs free energy of vacancy formation
G^{M}	Gibbs free energy of vacancy migration
G_{is}	Gibbs free energy of formation of an interstitial solute from a substitutional one
H^{B}	binding enthalpy of vacancy-solute complex
H^{F}	enthalpy of vacancy formation
H^{M}	enthalpy of vacancy migration
H_2^{M}	enthalpy of vacancy-solute exchange
ΔH	activation enthalpy of self-diffusion
ΔH_2	activation enthalpy of substitutional impurity diffusion
ΔH_{H}	activation enthalpy of hydrogen diffusion
ΔH_{D}	activation enthalpy of deuterium diffusion
ΔH_{T}	activation enthalpy of tritium diffusion
$\boldsymbol{J}$	diffusion flux (number of particles per second and unit area)
j_1, j_2, j_3	components of diffusion flux
l	jump length of an atomic jump
ΔQ	$\Delta H_2 - \Delta H$
R	gas constant
$\boldsymbol{r}_i$	jump vector of an atom
$\boldsymbol{R}$	total displacement vector of an atom
$\langle \boldsymbol{R}^2 \rangle$	mean square displacement of atoms
$\langle \boldsymbol{R}_{\mathbf{RW}}{}^2 \rangle$	mean square displacement of atoms for a true random walk
S^{F}	entropy of vacancy formation
S^{M}	entropy of vacancy migration
ΔS	diffusion entropy
t	time
T	temperature
x	position
x_{M}	position of Matano plane
$X_{\mathrm{A}}, X_{\mathrm{B}}$	mole fractions of A and B in a binary A-B alloy
Z	coordination number
α_i	direction cosine of diffusion flux with axis $i = 1, 2, 3$
γ_i	coefficient of activity of species i
Γ	jump rate of an atom in a certain direction
Θ	angle between diffusion flux and crystal axis
μ_i	chemical potential of species i
ν_0	attempt frequency ($\approx$ Debye frequency)
$\tau = 1/\Gamma Z$	mean residence time of an atom in a coordination lattice with coordination number Z
τ^{-1}	mean jump rate of an atom in any direction on a lattice
Φ	thermodynamic factor
ω	jump rate of vacancy in the matrix

ω_1	jump rate for rotation of vacancy-solute complex in a dilute (fcc) alloy
ω_2	jump rate of vacancy-solute exchange
ω_3	dissociation jump rate of vacancy-solute complex
ω_4	association jump rate of vacancy-solute complex

References

1. P. Shewmon: *Diffusion in Solids*, 2nd edn (The Minerals, Metals and Materials Society, Warrendale 1989)
2. J. Philibert: *Atom Movements - Diffusion and Mass Transport in Solids* (Les Editions de Physique, Les Ulis 1991)
3. Th. Heumann: *Diffusion in Metallen* (Springer, Berlin Heidelberg New York 1992)
4. A.R. Allnatt, A.B. Lidiard: *Atomic Transport in Solids* (Cambridge University Press, Cambridge 1993)
5. M.E. Glicksman: *Diffusion in Solids* (Wiley, New York 2000)
6. *Diffusion in Metals and Alloys*, Landolt-Börnstein, Numerical Data and Functional Relationships in Science and Technology, New Series Vol. III/26, ed by H. Mehrer (Springer Verlag, Berlin Heidelberg New York 1990)
7. Proc. Int. Conf. on *Diffusion in Materials* held in Kyoto (Japan) 1992, ed by M. Koiwa, H. Nakajima, K.-I. Hirano, also: Defect and Diffusion Forum **95 – 98** (1993).
8. Proc. Int. Conf. on *Diffusion in Materials* held in Nordkirchen (Germany) 1996, ed by H. Mehrer, Chr. Herzig, N.A. Stolwijk, H. Bracht, also: Defect and Diffusion Forum **143 – 147** (1997).
9. Proc. Int. Conf. on *Diffusion in Materials* held in Paris (France) 2000, ed by Y. Limoge, J.L. Bocquet, also: Defect and Diffusion Forum **194 – 199** (2001).
10. I. Kaur, Y. Mishin, W. Gust: *Fundamentals of Grain and Interphase Boundary Diffusion* (Wiley, New York 1995)
11. J. Crank: *The Mathematics of Diffusion*, 2nd edn (Clarendon, Oxford 1975)
12. L. Onsager: Phys. Rev. **54**, 554 (1938)
13. A. Smigelskas, E. Kirkendall: Trans. AIME **171**, 130 (1947)
14. L.S. Darken: Transactions AIME **175**, 184 (1948)
15. J.R. Manning: *Diffusion Kinetics for Atoms in Crystals* (van Norstrand, Princeton 1968)
16. H. Mehrer: Phys. Stat. Sol. (a) **104**, 247 (1987)
17. S. J. Rothman. In *Diffusion in Crystalline Solids*, ed by G.E. Murch, A.S. Nowick (Academic Press, New York 1964), p 1
18. F. Wenwer, A. Gude, G. Rummel, M. Eggersmann, Th. Zumkley, N.A. Stolwijk, H. Mehrer: Meas. Sci. Technol. **7**, 632 (1996)
19. F. Faupel, P.W. Hüppe, K. Rätzke, R. Willecke, T. Hehenkamp: J. Vac. Sci. Technol. **A 10**, 92 (1992)
20. A. Gude, H. Mehrer: Philos. Mag. **A 76**, 1 (1996)
21. M. Eggersmann, H. Mehrer: Philos. Mag. **A 80**, 1219 (2000)
22. A. Seeger, H. Mehrer. In: *Vacancies and Interstitials in Metals*, ed by A. Seeger, D. Schumacher, J. Diehl, W. Schilling (North-Holland, Amsterdam 1970), p 1

23. N.L. Peterson. In: *Diffusion in Solids – Recent Developments*, ed by A.S. Nowick, J.J Burton, (Academic Press, New York 1975), p 116 and J. Nucl. Mat. **69/70**, 3 (1978)
24. H. Mehrer: J. Nucl. Mat. **69/70**, 38 (1978)
25. S. Frank, U. Södervall, Chr. Herzig: Phys. Stat. Sol. (b) **191**, 45 (1995)
26. M. Salamon, S. Dorfman, D. Fuks, G. Inden, H. Mehrer: Defect and Diffusion Forum **194 - 199**, 553 (2001)
27. E.L. Hahn: Phys. Rev. **80**, 580 (1950)
28. E.O. Stejskal, J.E. Tanner: J. Chem. Phys. **42**, 288 (1965)
29. P. Heitjans, S. Indris, J. Phys.: Condens. Matter **15**, R1257 (2003)
30. J. Völkl, G. Alefeld. In: *Hydrogen in Metals I*, Topics in Applied Physics, vol 28, ed by G. Alefeld, J. Völkl, (Springer, Berlin Heidelberg New York 1978) p 321
31. *Nontraditional Methods in Diffusion*, ed by G.E. Murch, H.K.L. Birnbaum, J.R. Cost (The Metallurgical Society of AIME, 1984)
32. H. Wipf. In: *Hydrogen in Metals III*, Topics in Applied Physics, vol 73, ed by H. Wipf, (Springer, Berlin Heidelberg New York 1995) p 51
33. R. Hempelmann: *Quasielastic Neutron Scattering and Solid State Diffusion* (Oxford Science Publication, 2000)
34. A. Körblein, P. Heitjans, H.-J. Stöckmann, F. Fujara, H. Ackermann, W. Buttler, K. Dörr, H. Grupp: J. Phys. F: Met. Phys. **15**, 561 (1985)
35. H. Mehrer: Defect and Diffusion Forum **129-130**, 57 (1996)
36. A. Einstein: Ann. Phys., Lpz. **17**, 549 (1905)
37. M. v. Smoluchowski: Ann. Phys., Lpz. **21**, 756 (1906)
38. J. Bardeen, C. Herring. In: *Imperfections in nearly Perfect Solids*, ed by W. Shockley (Wiley, New York 1952) p 262
39. G.H. Vineyard: J. Phys. Chem. Sol. **3**, 121 (1957)
40. H.J. Wollenberger. In: *Physical Metallurgy*, part 2, ed by R.W. Cahn, P. Haasen (North Holland, Amsterdam 1996) p 1621
41. W. Frank, U. Gösele, H. Mehrer, A. Seeger. In: *Diffusion in Crystalline Solids*, ed by G.E. Murch, A.S. Nowick, (Academic Press, New York 1984) p 63
42. H. Bracht, N.A. Stolwijk, H. Mehrer: Phys. Rev. B. **52**, 16542 (1995)
43. A. Seeger. In: *Hydrogen in Metals I*, Topics in Applied Physics, vol 28, ed by G. Alefeld, J. Völkl, (Springer, Berlin Heidelberg New York 1978) p 349
44. G.M. Luke, J.H. Brewer, S.R. Kreitzman, D.R. Noakes, M. Celio, R. Kadono, E.J. Ansaldo: Phys. Rev. B **43**, 3284 (1991)
45. A. Schenck: *Muon Spin Spectroscopy: Principles and Applications in Solid State Physics* (Adam Hilger, Bristol 1986)
46. H. Bakker: Phys. Stat. Sol. **28**, 569 (1968)
47. K. Maier, H. Mehrer, E. Lessmann, W. Schüle: Phys. Stat. Sol. (b) **78**, 689 (1976)
48. D.L. Beke, G. Erdelyi, F.J. Kedves: J. Phys. Chem. Solids **42**, 163 (1981)
49. U. Köhler, Chr. Herzig: Philos. Mag. **A58**, 769 (1988)
50. G. Vogl, W. Petry: Physik. Blätter **50**, 925 (1994)
51. A.B. Lidiard: Philos. Mag. **46**, 1218 (1955)
52. A.D. LeClaire: Philos. Mag. **7**, 141 (1962)
53. G. Rummel, Th. Zumkley, M. Eggersmann, K. Freitag, H. Mehrer: Z. Metallkde. **86**, 121 (1995)
54. G. Rummel, Th. Zumkley, M. Eggersmann, K. Freitag, H. Mehrer: Z. Metallkde. **86**, 131 (1995)

55. G.M. Hood: Defect and Diffusion Forum **95 - 98**, 755(1993)
56. F. Wenwer, N.A. Stolwijk, H. Mehrer: Z. Metallkd. **80**, 205 (1989)
57. W.K. Warburton, D. Turnbull. In: *Diffusion in Solids – Recent Developments*, ed by A.S. Nowick, J.J. Burton, (Academic Press, New York 1975) p 171
58. A. Seeger, K.P. Chik: Phys. Stat. Sol. **29**, 455 (1968)
59. N.A. Stolwijk, H. Bracht. In: *Diffusion in Semiconductors and Non-Metallic Solids*, Landolt-Börnstein, Numerical Data and Functional Relationships in Science and Technology, New Series Vol. III/33, ed by D.L. Beke, (Springer, Berlin Heidelberg New York 1998)
60. F.C. Frank, D. Turnbull: Phys. Rev. **104**, 617 (1956)
61. N.A. Stolwijk, G. Bösker, J. Pöpping: Defect and Diffusion Forum **194 -199**, 687 (2001)
62. H. Wever: Defect and Diffusion Forum **83**, 55 (1992)
63. H. Mehrer: Materials Transactions, JIM, **37**, 1259 (1996)
64. M. Koiwa, H. Numakura, S. Ishioka: Defect and Diffusion Forum **143 - 147**, 209 (1997)
65. H. Mehrer, Chr. Herzig. In: *Advances in Science and Technology 29, Mass and Charge Transport in Inorganic Materials: Fundamentals to Devices*, ed by P. Vicenzini, V. Buscaglia, (Techna Srl. 2000) p.187.
66. Chr. Herzig, S.V. Divinski, St. Frank, T. Przeorski: Defect and Diffusion Forum **194 - 199**, 317 (2001)
67. Chr. Herzig, S.V. Divinski. In: *Diffusion Processes in Advanced Technological Materials*, ed by D. Gupta (William Andrew Publishing, Norwich 2005) p 173
68. M. Salomon, H. Mehrer: Z. Metallkd. **96**, 1 (2005)
69. H. Bakker. In: *Diffusion in Crystalline Solids*, ed by G.E. Murch, A.S. Nowick, (Academic Press, New York 1984) p 189
70. A.B. Kuper, D. Lazarus, J.R. Manning, C.T. Tomizuka: Phys. Rev. **104**, 1536 (1956)
71. S.G. Fishman, D. Gupta, D.S. Lieberman: Phys. Rev. **B2**, 1451 (1970)
72. E.W. Elcock, C.W. McCombie: Phys. Rev. **109**, 605 (1958)
73. H. Bakker, N.A. Stolwijk, M.A. Hoetjes-Eijkel: Philos. Mag. A **43**, 251 (1981)
74. I.V. Belova, G.E. Murch: Philos. Mag. A **82**, 269 (2002)
75. C.R. Kao, Y.A. Chang: Intermetallics **1**, 237 (1993)
76. S.V. Divinski, L.N. Larikov: J. Phys.: Condensed Matter **35**, 7377 (1997)
77. S. Frank, S.V. Divinski, U. Södervall, Chr. Herzig: Acta mater. **49**, 1399 (2001)
78. S.V. Divinski, Chr. Herzig: Defect and Diffusion Forum **203-205**, 177 (2002)
79. N.A. Stolwijk, M. van Gend, H. Bakker: Philos. Mag. **A 42**, 783 (1980)
80. F.M. d'Heurle, P. Gas, Ch. Lavoie, J. Philibert: Z. Metallkd. **95**, 852 (2004)
81. K. Nonaka, T. Arayashiki, H. Nakajima, A. Almazouzi, T. Ikeda, K. Tanaka, H. Numakura, M. Koiwa: Defect and Diffusion Forum **143 - 147**, 209 (1997)
82. M. Salamon, A. Strohm, T. Voss, P. Laitinen, I. Riihimäki, S. Divinski, W. Frank, J. Räisäken, H. Mehrer: Philos. Mag. **84**, 737 (2004)
83. L. Boltzmann: Wiedemanns Ann. Physik **53**, 959 (1894)
84. C. Matano: Jap. J. Phys. **8**, 109 (1933)
85. F. Sauer, V. Freise: Z. Elektrochem. **66**, 353 (1962)
86. J.R. Manning: Acta metall. **15**, 817 (1967)
87. I.V. Belova, G.E. Murch: Philos. Mag. **75**, 1715 (1997)
88. F.J.J. van Loo: Prog. Solid St. Chem. **20**, 47 (1990)
89. H. Schmalzried: *Solid State Reactions* (Academic Press, New York 1974)

90. G.V. Kidson: J. Nucl. Mater. **3**, 21 (1961)
91. J. Philibert: Defect and Diffusion Forum **95 - 98**, 493 (1993)
92. U. Gösele. In: *Alloying*, ed by J. Walters (ASM International, 1988) p 489
93. U. Schoo, M. Hirscher, H. Mehrer: Defect and Diffusion Forum **143 - 147**, 631 (1997)
94. *Binary Alloy Phase Diagrams*, vol 2, ed by T.B. Massalski, (American Society for Metals, Ohio 1986)

2 The Elementary Diffusion Step in Metals Studied by the Interference of Gamma-Rays, X-Rays and Neutrons

Gero Vogl and Bogdan Sepiol

2.1 Introduction

The elementary diffusion jump in solids can be traced down with a bundle of methods from solid state physics. In this chapter first the possibilities for studying diffusion with the quasielastic version of Mößbauer spectroscopy and neutron scattering are discussed. Since the first edition of this book two new methods were adopted for studying the elementary diffusion jump. Whereas as quasielastic methods Mößbauer spectroscopy and neutron scattering both work in the energy domain, the new methods work in the time domain. The new methods are nuclear resonance scattering (NRS) of synchrotron radiation, i. e. a daughter of Mößbauer spectroscopy using synchrotron radiation, and neutron spin echo spectroscopy. Nuclear resonance scattering was adopted to diffusion studies in 1996, i.e. shortly before the appearance of the first edition and was shortly mentioned there. Neutron spin echo had not been applied to diffusion in crystalline systems before 2001. The spectrum of systems studied has considerably widened, firstly by the addition of these methods, secondly due to more experiments performed with quasielastic neutron scattering at improved spectrometers. This chapter is therefore considerably renewed compared to the first edition.

Our contribution will report on vacancy-induced diffusion in metals and alloys. The sensitivity of the methods cited in the preceding paragraph to the elementary step of diffusion on a microscopic scale is their outstanding virtue. Together with nuclear magnetic resonance measurements (see Chaps. 9 and 10) they are the representatives of diffusion methods provided by nuclear solid state physics. These methods are "microscopic" in the sense that they directly study jump vectors and jump rates (cf. Fig. 2.1). In addition we can calculate the "macroscopic" diffusion coefficients from these quantities and compare them with literature data obtained by tracer diffusion measurements (Chap. 1 and [1, 2]), but this is not the main virtue of microscopic methods.

Of course there are other mechanisms proposed for diffusion than vacancy mechanisms (see Chap. 1). Some of them will be shortly discussed for the cases of self-diffusion in titanium but – just as it turns out in these examples – the most important process of self-diffusion in metals is the vacancy mechanism [3]. We will only discuss the basic results, more sophisticated ar-

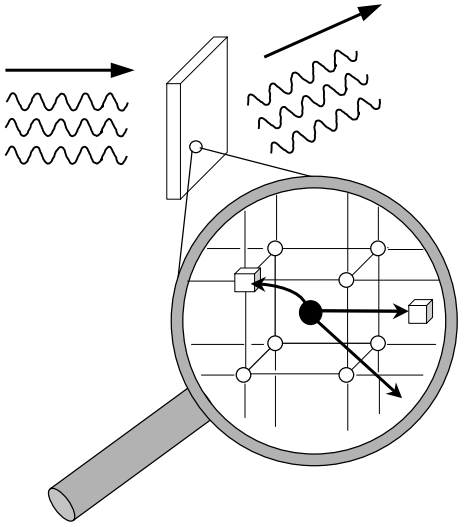

Fig. 2.1. Microscopic methods study the frequency and the displacement vectors of elementary diffusion jumps.

gumentation is found in the cited literature. For a general review on diffusion in solids see, e.g. [4, 5] and Chap. 1 of this book.

Sect. 2.2 introduces to the formalism, which relates jump diffusion of atoms to the experimental methods, starting with diffusion on Bravais lattices and ending with diffusion on the non-Bravais lattices of ordered phases. Sect. 2.3 discusses experimental results, Sect. 2.4 sums up and concludes.

2.2 Self-Correlation Function and Quasielastic Methods

In this chapter we use the "scattering terminology" for all methods. Thus for Mößbauer spectroscopy we use $\boldsymbol{Q}$ instead of $\boldsymbol{k}$ for the wave vector and the scattering function $S(\boldsymbol{Q}, \omega)$ instead of the absorption cross section $\sigma_a(\boldsymbol{k}, \omega)$. The advantage of directly comparable results for all methods outweighs the inconvenience of an unusual terminology for Mößbauer spectroscopy. As the formalism is discussed in detail in Chaps. 3, 18 and, e. g., in [6] we will only give a short introduction to the most important equations.

The simple-minded picture of atoms jumping on the lattice can be precisely formulated applying the Van Hove correlation function [7]. Displacements of atoms in space and time are described by the self-correlation function $G_\mathrm{s}(\boldsymbol{r}, t)$. This is the probability density to find an atom displaced by a vector $\boldsymbol{r}$ within a time interval t, averaged over all possible starting positions[1]. Van Hove [7] introduced the formalism of the self-correlation function for the scattering of thermal neutrons, Chudley and Elliott [8] used it for neutron

[1] Note that here $\boldsymbol{r}$ denotes a displacement (in our case the jump vector) and not a position.

scattering in liquids and Singwi and Sjölander [9] for neutron scattering as well as for the resonant absorption of γ-radiation (Mößbauer spectroscopy). We are interested in the self-correlation function because the incoherent scattering function $S(\boldsymbol{Q},\omega)$ is the double Fourier transform of $G_\mathrm{s}(\boldsymbol{r},t)$ in space and time

$$S(\boldsymbol{Q},\omega) \propto \mathrm{Re}\left\{\int_0^\infty \mathrm{d}t \exp\left(-\left[\frac{\Gamma_0}{2\hbar} + \mathrm{i}\omega\right] t\right) \int \mathrm{d}r \exp(\mathrm{i}\boldsymbol{Q}\cdot\boldsymbol{r}) G_\mathrm{s}(\boldsymbol{r},t)\right\} . \quad (2.1)$$

All prefactors have been omitted since they are different for neutron scattering (see Chap. 3) and Mößbauer spectroscopy (see [10]). For neutron scattering, $\boldsymbol{Q}$ is the scattering vector and $\hbar\omega$ the energy transfer. As $\hbar\omega$ is very small the scattering process is nearly elastic or "quasielastic", that is why the method is called *quasielastic* neutron scattering (QENS). In analogy we speak of *quasielastic* Mößbauer spectroscopy (QEMS) because the method is based on the same theory as QENS, $\hbar\omega$ again being very small. The term $\Gamma_0 t/2\hbar$ has no meaning for QENS, it is specific for QEMS: Γ_0 is the natural width of the nuclear Mößbauer transition. Here $S(\boldsymbol{Q},\omega)$ is the cross section for resonant nuclear absorption of γ radiation. Remember, that in any case the calculated $S(\boldsymbol{Q},\omega)$ has to be convoluted with the resolution of the given experimental set-up.

$G_\mathrm{s}(\boldsymbol{r},t)$ contains both, diffusional motion and motion induced by lattice vibrations. Under certain conditions usually fulfilled in metals these two contributions can be separated. The vibrational part gives the Debye-Waller (Lamb-Mößbauer) factor $\mathrm{f_{DW}}$ which rules the total intensity of scattered (resonantly absorbed) radiation while the diffusional part determines the shape of the spectra.

Another important consequence of (2.1) is that due to the product $\boldsymbol{Q}\cdot\boldsymbol{r}$ the scattering function $S(\boldsymbol{Q},\omega)$ depends on the relative orientation between the scattering vector $\boldsymbol{Q}$ and the jump vector $\boldsymbol{r}$ and hence on the orientation of the crystal lattice. Thus full information is obtained only by series of measurements on single crystals at various orientations[2].

At the first glance it seems possible to measure spectra of interesting materials, then to perform an inverse double Fourier transform and arrive directly at the self-correlation function $G_\mathrm{s}(\boldsymbol{r},t)$. Unfortunately, this is not possible because of the finite experimental resolution. The loss of information due to the finite resolution can not be reversed by an analytical deconvolution of the measured spectra. Thus one has to choose a different way. Starting from a diffusion model we calculate $S(\boldsymbol{Q},\omega)$, perform a convolution with the resolution function and compare the obtained "theoretical" spectra with the measured spectra. At the end of a selection process the most probable diffusion mechanism remains.

[2] In the case of non-crystalline samples (glasses, fluids etc.) there is no such anisotropy.

The next subsection deals with the way from a proposed diffusion mechanism to the spectrum.

2.2.1 Quasielastic Methods: Mößbauer Spectroscopy and Neutron Scattering

Quasielastic neutron scattering is the method promoted in the late fifties by Brockhouse [11] and for diffusion jumps in metals was first applied in 1976 [12,13], whereas quasielastic Mößbauer spectroscopy started in the late sixties [14].

If diffusion in a solid is fast enough (D in the range from 10^{-14} to $10^{-10}\,\mathrm{m^2 s^{-1}}$ for quasielastic Mößbauer spectroscopy and from 10^{-13} to $10^{-7}\,\mathrm{m^2 s^{-1}}$ for quasielastic neutron scattering) this leads to the so-called diffusional broadening of measured Mößbauer or neutron scattering spectra. The Mößbauer effect is the following phenomenon: A γ quantum emitted by a nucleus decaying from an excited to the ground level is resonantly absorbed at the ground level of a second nucleus of the same isotope. Because of the extreme sharpness of nuclear levels, any energy change of the γ quantum beyond tenth of μeV (for the nucleus ^{57}Fe) – i.e. any recoil or even phonon excitation – must be absent or be compensated, otherwise the energy of the γ-quantum would not match and resonance absorption would not occur. For ^{57}Fe, by far the most frequently used isotope in Mößbauer spectroscopy, the energy difference between excited and ground level, i.e. the energy of the γ quantum, is 14.4 keV corresponding to a length of its wave vector $Q = 7.3\,\mathrm{Å^{-1}}$. This can be understood in a roughly simplified picture: If at low temperatures the emitting Mößbauer nuclei stay on their sites during the emission process, the energy width of the emitted radiation is ruled by the mean lifetime τ_0 of the excited Mößbauer level. If at sufficiently high temperatures, however, the mean residence time τ of diffusing atoms between two successive jumps is of the same order of magnitude as or even smaller than the mean lifetime τ_0 of the Mößbauer level, on the average each emitting Mößbauer atom changes its position during the emission process. Thus the wave train emitted by a diffusing atom is "cut" to several shorter wave trains which leads to a larger width (Fig. 2.2). As these wave trains are emitted by one and the same nucleus they are coherent. The interference between wave trains emitted by the same nucleus depends on the relative orientation between the jump vector and the direction of the wave vectors. Therefore, in certain crystal directions the line width is small while in other directions it is very large. In this picture the broadening will be the larger the stronger the fragmentation of the wave train is.

An analogous argumentation is possible for QENS where the wave train of neutrons scattered by a diffusing atom is cut into several wave trains. While QEMS has proved to be an appropriate tool for diffusion studies in iron aluminides and silicides, it can not be applied to other B2 alloys. QENS, on the other hand, can be applied for diffusion investigations in a broader range

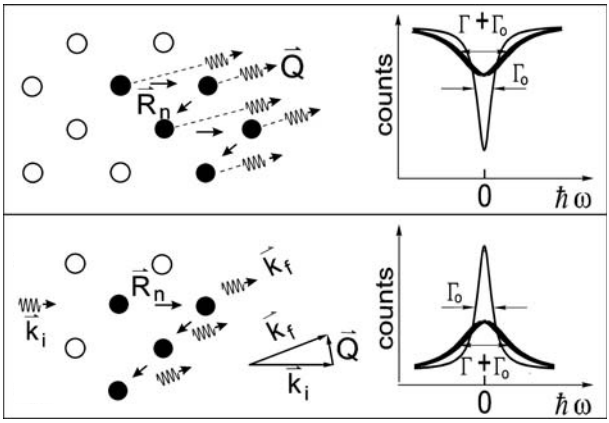

Fig. 2.2. Simplified, semi-classical explanation of the diffusional line broadening for QEMS (top) and QENS (bottom). $\boldsymbol{Q}$: wave vector (QEMS) or scattering vector (QENS), $\boldsymbol{k}_i$, $\boldsymbol{k}_f$: initial and final wave vector.

of alloys, provided the diffusivity is fast enough because of about a factor of hundred lower energy resolution of backscattering spectrometers IN10 or IN16 at the high flux reactor ILL Grenoble.

Below we will treat this phenomenon in a more formalistic way.

Bravais Lattices

For a continuous medium, neglecting the discrete structure of real material, the diffusion of particles must obey Fick's equation (see Chap. 1). The solution of this equation neglects the discontinuous nature of real materials. In a real material and at not too much elevated temperatures, diffusion can be considered as jump diffusion as in the model of Chudley and Elliott [8]. This model, although originally developed for liquids, found more applications in solid state diffusion with the following assumptions [6]:

1. All sites on which diffusion takes place are equivalent, i.e. we have a Bravais lattice.
2. The diffusion is independent of other kinds of motion like vibrations.
3. Only jumps to nearest-neighbour sites are allowed, $\boldsymbol{r}_i$ is an ith vector connecting these sites.
4. The jump time is negligible compared with the residence time τ on the lattice site.
5. Successive jumps are uncorrelated, i.e. the jump direction of the following jump is independent from the preceding one. With other words: the present state of the system is determined only by the past state at a particular time (Markov process).

We restrict the discussion to the simple case of Markov processes. This leads to a Markov master equation (see Chaps. 3 and 18) [15], which is a linear differential equation (rate equation) for the evolution of the probability density $P(\boldsymbol{r},t)$ to find an atom at site $\boldsymbol{r}$ at time t

$$\frac{\partial}{\partial t}P(\boldsymbol{r},t) = \frac{1}{N\tau}\sum_{i=1}^{N}\left\{P(\boldsymbol{r}+\boldsymbol{r}_i,t) - P(\boldsymbol{r},t)\right\} . \tag{2.2}$$

With respect to some boundary conditions the solutions of this equation give the self-correlation function $G_\mathrm{s}(\boldsymbol{r},t)$. The shape of the resulting $S(\boldsymbol{Q},\omega)$ (see (2.1)) is a Lorentzian

$$S(\boldsymbol{Q},\omega) \propto f_\mathrm{DW}\cdot\frac{\Gamma(\boldsymbol{Q})/2}{(\Gamma(\boldsymbol{Q}))/2)^2+(\hbar\omega)^2} \tag{2.3}$$

where $\mathrm{f_{DW}}$ is the above mentioned Debye-Waller factor (lattice vibrations) and $\Gamma(\boldsymbol{Q})$ is the full width at half maximum (in the following denoted as "(diffusional) line broadening") of the Lorentzian. $\Gamma(\boldsymbol{Q})$ depends on $\boldsymbol{Q}\cdot\boldsymbol{r}$ and hence on the relative orientation between radiation and crystal:

$$\begin{aligned}\Gamma(\boldsymbol{Q}) &= \frac{2\hbar}{\tau}\cdot\left[1-\sum_j W_j E_j\right] ,\\ E_j &= \frac{1}{N_j}\sum_{i=1}^{N_j} e^{\mathrm{i}\boldsymbol{Q}\cdot\boldsymbol{r}_i} .\end{aligned} \tag{2.4}$$

Here τ^{-1} is the jump rate (τ is the mean residence time of an atom between two successive jumps), W_j is the probability[3] for a jump to coordination shell j and E_j the corresponding structure factor. N_j denotes the number of sites in coordination shell j and the $\boldsymbol{r}_i$ are the $i = 1\ldots N_j$ jump vectors to sites in shell j.

Non-Bravais Lattices

Some alloys do not form a "simple" solid solution, i.e. a Bravais lattice with sites *statistically* occupied by atoms of the alloy constituents, but exhibit an additional type of order: they form a superlattice made up of different sublattices each of which belongs to one species of atoms. Because in the stoichiometry they are well ordered, a degree of order can be well controlled by temperature, chemical composition and, beyond that, they are of high technological interest [16]. Such lattices contain more than one atom per primitive unit cell depending on the type of superstructure. It is energetically disfavoured to place an atom of a given species at a site on a "wrong"

[3] Note that the W_j are normalized, i.e. the sum over all W_j equals unity.

sublattice (antistructure defects). This complicates the diffusion mechanisms, as e.g. jumps of a given atom species leading to wrong sites may be markedly less probable than jumps to sites on the own sublattice, i.e. there are different jump rates. In this case it is not sufficient to set up only one Markov equation as in Sect. 2.2.1 for Bravais phases. For a superstructure with m sublattices one needs m Markov equations. To solve such a system of m coupled rate equations a matrix formalism is used. The Chudley and Elliott theory [8] was extended by Rowe et al. [17] for hydrogen diffusion on interstitial sites of a non-Bravais lattice. The Rowe theory assumes equal occupation of different sublattices (sites with different "local symmetry" in the unit cell), and attempts to extend the theory for systems with differently occupied sublattices have been undertaken [18, 19]. This problem has been treated in details by Randl et al. [20] for non-Bravais structures.

The jump matrix containing the coefficients of the Markov equation is in general not Hermitian but has always real eigenvalues and thus can be transformed to a Hermitian matrix [18]. Diagonalization of the hermitized jump matrix gives the solutions of the Markov equations. The spectra of an alloy with m sublattices are made up from m Lorentzian lines[4]. The linewidths of the subspectra are calculated from the eigenvalues and the relative contribution (weight) of each subspectrum is determined by the eigenvectors.

The jump rates between nearest neighbour (NN) sites are constrained by the *detailed balance* which demands that the number of atoms jumping in a time unit from one sublattice into another must be equal to the number of reverse jumps

$$\frac{c_i}{n_i \tau_i} = \frac{c_j}{n_j \tau_j} \tag{2.5}$$

where c_i is the probability of occupation of the ith sublattice and $\sum c_i = 1$. $1/\tau_i$ is the jump rate from a site of symmetry i to any of n_i nearest-neighbour sites.

We treat the so-called B2 structure (see Sect. 1.10 in Chap. 1) as an example. This superstructure of two-component alloys AB is of special interest for diffusion studies because in a B2 lattice each atom is surrounded by lattice sites, which belong to the other species. It is based on a bcc unit cell where atoms of one species occupy the edges of the unit cell while the body centred positions belong to atoms of the other species. Thus NN jumps lead always to antistructure sites. If such NN jumps are the only operative diffusion mechanism, we have to set up a 2×2 jump matrix and arrive at spectra which are a sum of two Lorentzians. A useful quantity is the asymmetry parameter $\alpha = \tau_1/\tau_2$ (where τ_1 is the mean residence time of diffusing atoms on their own sublattice 1 and τ_2 analogous for the wrong sublattice 2)[5].

[4] A sum of Lorentzians is – in general – not a Lorentzian.

[5] Note that the same number of A atoms per unit time must jump from sublattice 1 to sublattice 2 and vice versa ("detailed balance"). Thus α is directly connected to the occupation of the sublattices via $\alpha = \tau_1/\tau_2 = c_1/c_2$.

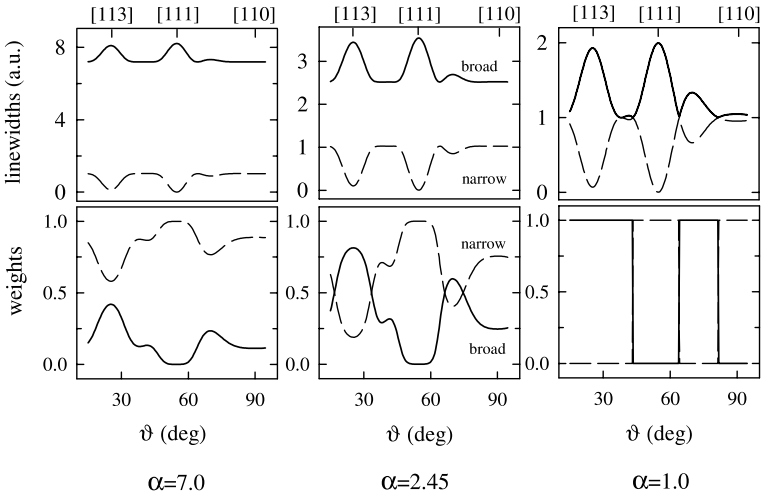

Fig. 2.3. B2 Structure: broadening and relative contributions (weights) of the two quasielastic Mößbauer lines as a function of orientation ϑ for different values of the asymmetry parameter α.

This parameter rules the shape of the spectra because the two residence times τ_1 and τ_2 (or – in turn – the two jump rates τ_1^{-1} and τ_2^{-1}) are "responsible" for the diffusional line broadening of the two subspectra and their respective contribution to the sum spectrum. Figure 2.3 shows the orientation-dependent part of the line broadenings of the two subspectra (upper row) and their contributions (lower row) for three different values of α. For a well ordered B2 alloy AB the mean residence time τ_1 of atoms of species A on their own sublattice 1 is much longer than the mean residence time τ_2 on the "wrong" sublattice 2, which belongs to the other species B (as the total concentration of antistructure defects is low). Therefore α has a large value and for large α one of the two Lorentzians is very broad while the other is rather narrow (upper row in Fig. 2.3). But in turn the contribution of the broad line is small (lower row). This leads to an experimental difficulty: such a broad but weak line can hardly be observed because it vanishes in the background of the measured spectra. The spectra seem to consist of one Lorentzian. This holds even for an alloy, which already contains some excess iron atoms (e.g. $Fe_{55}Al_{45}$ with $\alpha = 7.0$, see Sect. 2.3.2).

The less well-ordered a B2 alloy is, i.e. the more antistructure defects a B2 alloy contains, the more α decreases. For a moderate value of α like, e.g., $\alpha = 2.45$ the broad line is not "too broad" and the relative contribution of the broad line is higher (in some directions even higher than the contribution of the narrow one). In such a case the two lines are easily resolvable, e.g., in [113] direction. If α equals unity – i.e. the two residence times are equal – in any direction one of the two lines vanishes. The resulting line broadening

of the remaining single line is essentially the same as for diffusion in a bcc Bravais lattice.

If the jump mechanism and jump rates are known one can calculate the macroscopic diffusion coefficient, which can be compared with the tracer diffusion coefficient. The diffusion coefficient is in a non-Bravais lattice a sum of partial diffusion coefficients [4], where $1/\tau_{ij}$ is the jump rate from a site of symmetry i to any nearest-neighbour site of symmetry j

$$D = \frac{1}{6} \sum_{i,j} (\boldsymbol{r}_i - \boldsymbol{r}_j)^2 \tau_{ij}^{-1} c_i \,. \tag{2.6}$$

Applying (2.6) to the B2 lattice structure one obtains

$$D = \frac{1}{4} \frac{a^2}{\tau_{12}} \frac{\alpha}{\alpha + 1} \,, \tag{2.7}$$

where a is the lattice constant. QEMS diffusion coefficients [21,22], measured without assuming any correlation effects, coincide well with tracer diffusion values [23–25]. This is an argument against highly correlated diffusion mechanisms in B2 alloys (see Sect. 2.3.2).

2.2.2 Nuclear Resonant Scattering of Synchrotron Radiation

Nuclear resonant scattering of synchrotron radiation (NRS) was applied for diffusion studies in the middle nineties [26]. Immediately after the theoretical paper of Smirnov and Kohn [27] the first feasibility study has been performed at ESRF Grenoble [26].The most important difference between NRS and the quasielastic methods QEMS and QENS is that NRS works in the *time domain* whereas the quasielastic methods work in the *energy domain*. The principal idea of NRS is: the coherence of the synchrotron radiation (SR) in the forward direction, after nuclear resonance absorption in the sample, is destroyed by diffusion, which leads to a faster decay of the scattered intensity in forward direction with respect to an undisturbed process. From this "diffusionally accelerated" decay, details on the diffusion process can be derived.

The mathematical formulation of the problem can be found in [28–30]. Here we give only an outline characterizing differences between NRS and QEMS/QENS.

In QEMS and QENS techniques the experimental spectrum $S(\boldsymbol{Q}, \omega)$ is obtained in the energy domain. In order to be compared with the microscopic diffusion mechanism described by the theory through the self-correlation function $G_\mathrm{s}(\boldsymbol{r}, t)$, it must be double Fourier transformed (see (2.1)) $S(\boldsymbol{Q}, \omega) \leftrightarrow I(\boldsymbol{Q}, t) \leftrightarrow G_\mathrm{s}(\boldsymbol{r}, t)$, where the intermediate scattering function $I(\boldsymbol{Q}, t)$ is the result of the first (space-momentum) Fourier transform. For simple Markovian diffusion on a crystalline Bravais lattice, the intermediate scattering function in forward direction, $I_\mathrm{FS}(\boldsymbol{Q}, t)$ can be calculated analytically yielding the following exponential time-dependent function

$$I_{\mathrm{FS}}(\boldsymbol{Q},t) \approx I_0 \frac{L^2}{4\tau_0} \exp\left[-\frac{t}{\hbar}(\Gamma_0 + \Gamma(\boldsymbol{Q}))\right], \tag{2.8}$$

where L is the effective sample thickness proportional to the Debye-Waller factor, I_0 the scattered intensity at time zero and $\Gamma(\boldsymbol{Q})$ is the linewidth of (2.4). Equation (2.8) shows that the logarithm of the decay rate is proportional to the width of the diffusional broadening $\Gamma(\boldsymbol{Q})$ as measured in classical QEMS. Equation (2.8) is correct only in the thin-sample approximation due to the much more important role of the effective sample thickness in NRS than in QEMS or QENS. The most important isotope, which can be used for diffusion studies by NRS, is once again ^{57}Fe [6]. In Fig. 2.4 the effect of increasing temperature resulting in the faster decay of the scattered intensity in forward direction is clearly visible. At lower temperatures an effect of increased effective sample thickness L results in the curvature of the exponential. If the sample is enriched in ^{57}Fe isotope one can obtain very high count-rates and much shorter measuring times compared to quasielastic methods from Sect. 2.2.1.

2.2.3 Neutron Spin-Echo Spectroscopy

Neutron spin-echo (NSE) spectroscopy [31] has been successfully applied to the study of the dynamics in amorphous systems (proteins, polymers, glassy dynamics etc.) but we have shown that it is also suited for the investigation of diffusion on lattices giving direct access to the jump mechanism [32].

NSE is a Fourier method and is sensitive to the time-dependent correlation function yielding directly the intermediate scattering function $I(\boldsymbol{Q},t)$ (see preceding section). It bridges the gap in time scale between conventional quasielastic neutron scattering and dynamic light scattering. NSE combines the high energy resolution from QENS with the high intensity of a beam which is only moderately monochromatic. In NSE the velocity change of neutrons after scattering by a sample is measured by comparing the Larmor precession in known magnetic fields before and after the scattering. This comparison is made for each neutron individually, thus the resolution of the velocity change can be much better than that corresponding to the width of the incident beam. A detailed explanation of the method can be found in Chap. 13.

To demonstrate the potential of the method to observe directly the jump of atoms, NiGa as a model system was used (see figures in Sect. 2.3.2). An unambiguous decision between two opposed diffusion models can be obtained on the basis of two spectra only, provided the measurement is performed at $\boldsymbol{Q}$ values near reciprocal superlattice points. From the experimental resolution one can conclude, that diffusivities are around $10^{-13}\,\mathrm{m^2 s^{-1}}$.

[6] NRS may be called Mößbauer spectroscopy in the time domain.

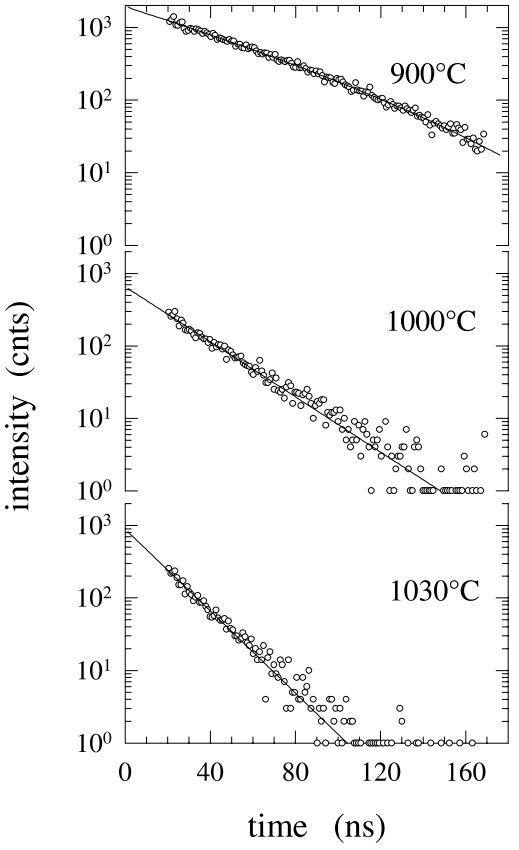

Fig. 2.4. Time dependence of forward scattered intensity at three temperatures with the beam parallel to the crystal direction [110] of a stoichiometric FeAl sample.

2.2.4 Non-Resonant Methods

In the following a very basic approach for the calculation of the structure factor will be presented. Description of atomic movements by the self-correlation function $G_{\mathrm{s}}(\boldsymbol{r},t)$ is actually only a special case of the more general description by the pair correlation function $G(\boldsymbol{r},t)$. An expression for the *coherent* scattering function on Bravais lattices has been given by Ross and Wilson [33] (this problem is also discussed in Chap. 3 and in [34]).

One can split the pair-correlation function into a time-dependent part $G'(\boldsymbol{r},t)$ and a static part: $G(\boldsymbol{r},t) = G'(\boldsymbol{r},t) + c\Sigma\delta(\boldsymbol{r}-\boldsymbol{r}_i)$ [35], where c is the concentration of the scattering atoms on the Bravais lattice, $\boldsymbol{r}_i$ is the ith lattice site and the summation is over all lattice sites. Inserting this equation into (2.2) and solving by Fourier transformation with the boundary condition $G(\boldsymbol{r},0) = (1-c)\delta(\boldsymbol{r}) + c\Sigma\delta(\boldsymbol{r}-\boldsymbol{r}_i)$ the coherent scattering function reads

$$S(\boldsymbol{Q},\omega) = c(1-c)\frac{\frac{1}{2}\Gamma(\boldsymbol{Q})}{\left(\frac{1}{2}\Gamma(\boldsymbol{Q})\right)^2 - (\hbar\omega)^2} + cN\delta(\omega)\delta(\boldsymbol{Q}-\boldsymbol{G})\,. \tag{2.9}$$

Equation (2.9) describes coherent scattering on Bravais lattices [34, 35]. The quasielastic term with Lorentzian lineshape is, apart from a factor $c(1-c)$, identical with the scattering function calculated from the self-correlation function $G_{\mathrm{S}}(\boldsymbol{r}, t)$ for incoherent scattering (2.3). The purely elastic term describes Bragg scattering in directions, where the scattering vector equals the reciprocal lattice vector $\boldsymbol{G}$. The quasielastic term describes isotropic diffuse scattering (note the pre-factor $c(1-c)$ characteristic for the Laue-diffuse scattering [36]). Note, that (2.9) is derived for a lattice occupied by one type of scattering atoms only. Derivation for the case of a non-Bravais lattice with one or more scattering atoms was achieved for the first time by Kaisermayr et al. [35,37]. General conclusions are similar to conclusions in a Bravais lattice; no quasielastic broadening apart from a negligible contribution from diffuse scattering, can be expected in the Bragg reflections, irrespective if they are of fundamental or superstructure type. If the lattice is occupied by more than one scattering element, the different quasielastic parts are obtained by simple summation of all elementary contributions. This prediction was experimentally proven by measuring diffusion in B2 $Co_{60}Ga_{40}$ using time-domain interferometry of synchrotron radiation [37]. For the idea of the method we refer to Baron et al. [38].

From (2.9) and from equivalent derivation for non-Bravais lattices [35,37] the following conclusions can be drawn:

- The coherent scattering function for diffusion in crystal structures is elastic in Bragg reflections of fundamental and superstructure peaks.
- In the regions between the reciprocal lattice points, the quasielastic diffuse scattering can be observed, i.e. scattering due to lattice disorder (Laue-diffuse scattering). The scattering function $S(\boldsymbol{Q}, \omega)$ is calculated in the same way as the scattering function for the incoherent scattering, i.e., is calculated from the self-correlation function (2.1).
- The largest intensity of the quasielastic component is in superstructure lattice directions of the non-Bravais lattice[7]. It is not possible, however, to measure quasielastic broadening at these positions since the diffuse intensity will be completely hidden under the elastic Bragg line.

Observation of the diffuse scattering is difficult due to the very low intensities, thus large detectors are necessary. Higher intensities can be measured by scattering on samples without lattice structure, e.g. on glassy samples. Such a glassy sample was measured by synchrotron radiation in the first time-domain interferometry experiment of Baron et al. [38], or by Rayleigh scattering of Mößbauer γ-quanta [39].

Finally a most interesting development should be mentioned: a new method in diffusion studies is the X-ray photon correlation spectroscopy

[7] For instance in the ordered B2 structure the largest intensity is in the [100] direction.

(XPCS), which is a version of the old laser-speckles spectroscopy, but with X-rays that can be used for the studies of metallic systems [40]. Although in the best current third-generation X-ray sources the degree of coherence is much lower than for lasers in the visible range, it is still sufficient for studies of nanometer-size objects like studies of the dynamics of coarsening processes or the motion of antiphase boundaries.

Preliminary results of time-domain interferometry, Rayleigh scattering of Mößbauer radiation or XPCS, which are all *non-resonant* methods, i.e. not limited to studies of selected isotopes only, are very promising. They predict new possibilities for diffusion studies of atomistic processes. Though brilliance of current synchrotron radiation sources is insufficient for the studies of atomic motion in crystalline solids, future sources like free electron lasers will definitely enable this kind of research.

2.3 Experimental Results

2.3.1 Pure Metals and Dilute Alloys

Self-Diffusion in β-Titanium

Self-diffusion in titanium belongs to the fastest self-diffusion processes in metals. The interesting question of the underlying mechanism was solved by the use of QENS [41] and phonon spectroscopy [42] (see also Chap. 3 of this book).

The driving force for diffusion jumps in metals are phonons. With the help of phonon spectroscopy the reason for the high diffusivity in titanium could be found [42]. At elevated temperatures the phonon spectrum of titanium contains some very soft phonon modes, which influence the diffusion process. Soft phonons correspond to large vibration amplitudes in real space. Parts of the experimentally found atomic periodic displacements are parallel to the direction of NN diffusion jumps while others periodically open and close the configurational "windows" made up from other atoms through which an atom has to pass in order to change the site. Therefore the atoms are "pushed" to vacant NN sites and the migration energy is considerably lowered. This explains the high diffusivity in titanium. Of course – for other metals or alloys – other reasons for fast diffusion are possible. One of these will be discussed for the case of Fe_3Si in Sect. 2.3.2.

Iron Diffusion in Aluminium and Copper

Diffusion of dilute ^{57}Fe in f.c.c Al or Cu single crystals has been investigated by QEMS ([43] and [44]). As this is not self-diffusion but impurity diffusion one needs a somewhat extended theory, which was elaborated by Le Claire [45] and Krivoglaz and Repetskiy [46] (see also Sect. 1.9) and adapted to the

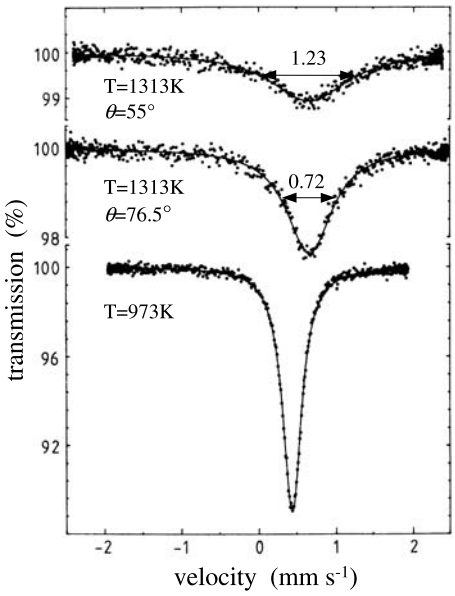

Fig. 2.5. QEMS spectra of dilute ^{57}Fe in copper single crystals. Notice that the linewidth of the spectra measured at 1313 K is different for different directions of observation $\vartheta = 55°$ and $\vartheta = 76.5°$.

current cases in [43] and [44]. This theory accounts for the fact that vacancies are preferentially situated near the impurity atoms.

Figure 2.5 shows, as an example, four spectra measured on iron-doped copper single crystals at 973 K (bottom) and at 1313 K at three different orientations. The fitted single Lorentzian lines at 1313 K are not only broader than at 973 K but also show a variation of the linewidth with orientation ϑ (which is the angle between the Mößbauer wave vector $\boldsymbol{Q}$ and the [001] crystal axis). In both metals the basic impurity diffusion mechanism could be identified as a jump of an impurity atom to a nearest neighbour vacancy. The diffusion coefficients determined for iron in copper at various temperatures agree well with reference data [47] obtained by the tracer diffusion method.

2.3.2 Ordered Alloys

B2 Structure (CsCl Structure)

Iron Diffusion in FeAl

Within a wide homogeneity range on the iron rich side $Fe_{1-x}Al_x$ alloys crystallise in the B2 structure. As pointed out in Sect. 2.2.1, NN jumps in B2 lattices always lead to antistructure sites and should therefore be energetically disfavoured. Of course, this is only valid near equiatomic stoichiometry. In alloys with more than 50 at.% Fe the excess iron atoms are situated on aluminium sites, i.e. they form "built-in" antistructure defects.

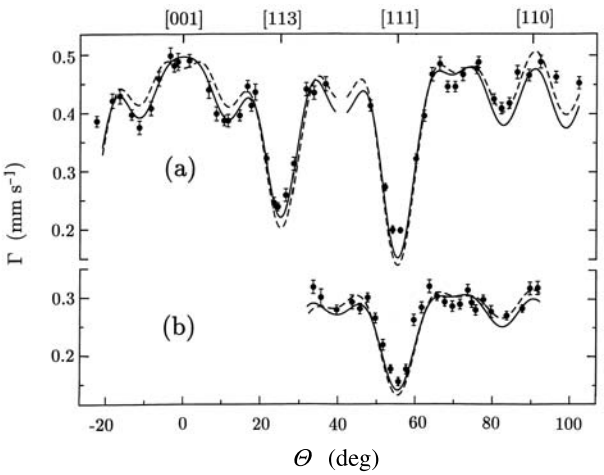

Fig. 2.6. Diffusional line broadening in $Fe_{50.5}Al_{49.5}$ (**a**) at 1065°C for two differently oriented slices (1 and 2) of the same crystal and (**b**) at 1040°C for slice 1.

The most intriguing question for well ordered FeAl is, whether diffusing atoms overcome the ordering energy and jump to NN sites or whether they perform "far" jumps to e.g., second or third neighbour sites, which belong to their own sublattice. Secondly, if a vacancy diffuses *randomly* via NN jumps in a B2 lattice, it leaves a trace of antistructure defects behind. Thus *random* diffusion of vacancies via NN jumps destroys the B2 superstructure. In order to conserve the superstructure, vacancy diffusion via NN jumps requires mechanisms, which restore the order after disordering jumps. Some of the proposed mechanisms, which fulfil this condition, are discussed in Chap. 1.

Measurements on well-ordered $Fe_{50.5}Al_{49.5}$ [21] show, that all spectra are well fitted by single Lorentzian lines. At first glance it follows from this that iron diffusion occurs on a Bravais lattice, i.e. via "far" jumps between sites on the iron sublattice and *not* via NN jumps to aluminium sites. If we plot the line broadening (Γ_0 already subtracted) as a function of orientation we obtain Fig. 2.6. These data can be fitted with a superposition of the functions corresponding to [100]- and [110]-jumps (solid line). A similar good fit is obtained with an additional 10% contribution of [111]-jumps (broken line). Further measurements on the off-stoichiometric alloy $Fe_{55}Al_{45}$ [22] give similar results, but in this case the data can not be fitted without a 20% contribution of [111] jumps. Note that jumps directly to a [111] site, i.e. across the body diagonal of the B2 unit cell, are hardly possible unless the body-centered aluminium site is vacant.

Measurements of nearly-stoichiometric FeAl have been repeated with the NRS method yielding a combination of [100] and [110] jumps in the ratio

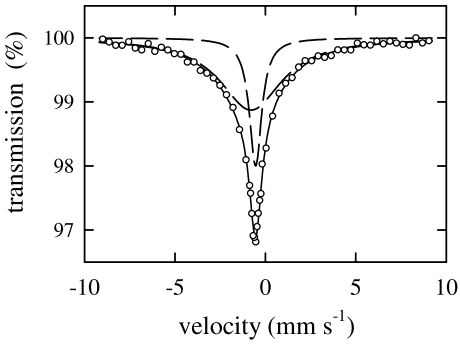

Fig. 2.7. Two-line spectrum of $Fe_{66}Al_{35}$ at 1020°C in [113] direction.

of $(1.9 \pm 0.1) : 1$ [48], which agrees with conventional QEMS [21], but the uncertainty of the NRS measurement is considerably smaller.

As pointed out in Sect. 2.2.1 the spectra of a B2 alloy may seem to consist of one single Lorentzian even though diffusion takes places via NN jumps if the asymmetry parameter α is large. For highly ordered $Fe_{50.5}Al_{49.5}$, α should be high due to the relatively low concentration of antistructure defects and a still large α can be expected for the still well ordered $Fe_{55}Al_{45}$. Therefore, the amount of excess iron atoms was raised further and $Fe_{65}Al_{35}$ was measured, which is still B2 ordered but – due to the composition – exhibits a considerable amount of disorder [22]. The spectra of this alloy clearly consist of two Lorentzians (Fig. 2.7) and the complete set of spectra measured at different orientations can only be fitted under the assumption of NN jumps from the iron to the aluminium sublattice and vice versa.

This leads to a consistent picture of diffusion in $Fe_{1-x}Al_x$ alloys. Starting near the ideal B2 composition FeAl we find that iron atoms diffuse via NN jumps to antistructure sites with a remarkably *short* residence time on the aluminium sublattice (and hence a large α). With increasing iron content the residence time of iron atoms on the aluminium sublattice increases and thus (at comparable temperatures from 1020°C to 1090°C) the asymmetry parameter α decreases from 30 over 7.0 to 2.45 ($Fe_{50.5}Al_{49.5}$, $Fe_{55}Al_{45}$ and $Fe_{65}Al_{35}$, respectively). In "disordered" Fe_3Al iron diffuses on a Bravais lattice, i.e. $\alpha = 1$.

In the interpretation of the diffusion mechanism in near-stoichiometric FeAl another QEMS result is of prime importance. The relative intensity of the Mößbauer spectrum measured as a function of the angle between the [001] axis and the γ-radiation wave vector shows a clear minimum in the [113] direction (Fig. 2.8). There is only one possible interpretation of this result: iron jumps are NN-jumps via short occupation of the Al sublattice. If the short residence time is much smaller than the Mößbauer time window ($\tau_0 = 141\,\mathrm{ns}$), everything that happens within this extremely short time is invisible for Mößbauer spectroscopy and only the start and end positions

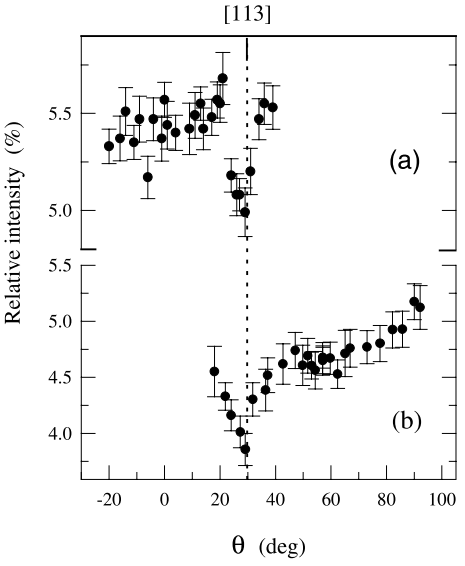

Fig. 2.8. Angular dependence of the Mößbauer line intensity for (**a**) $Fe_{50.5}Al_{49.5}$ and (**b**) $Fe_{55}Al_{45}$.

enter into the Mößbauer spectra. The only effect on the spectrum is the intensity minimum in the direction characteristic for NN jumps.

It should be pointed out that the picture obtained by QEMS and NRS can today be confirmed by independent experimental results. Even theoretical simulations, which contradicted this picture in the past [49], today confirm it. On the basis of [50] and [51], one can exclude the six-jump cycle as a mechanism of iron diffusion due to much too high concentration of vacancies and antistructure atoms at temperatures where microscopic studies have been performed. Neither mechanisms like an antistructure-bridge mechanism and a triple-defect mechanism are operative (e.g. [51, 52]). The energy barrier for direct Fe jumps on its own sublattice have been calculated by Fähnle et al. [53]. The energy barrier for the next-nearest neighbour jump was 2.16 eV, which is only slightly larger than the experimental migration energy, but for the direct third-nearest neighbour jump the calculated energy was 6 eV, which entirely excludes this possibility. Fähnle proposed a modified six-jump cycle where two atoms jump in a correlated manner avoiding in this way the creation of the Al vacancy [48, 53]. Recent defect-structure simulations [54], which take into account the defect vibrational entropies and the effect of magnetism, confirm the hybrid character of stoichiometric B2 FeAl [8] and a considerable amount of Al antistructure atoms. These results confirm the NN jump as the most reasonable elementary diffusion jump in B2 FeAl.

Thus the conclusion for Fe diffusion in Fe_xAl_{1-x} alloys is: at stoichiometry and also far-off stoichiometry the elementary Fe jump is a jump into a

[8] This means that stoichiometric FeAl is neither a pure antistructure type system nor a pure triple defect type system (see [2]).

NN vacancy on an antistructure site. The Fe residence time on this antistructure site is very short close to stoichiometry and becomes longer until being comparable to the residence time at a regular site with increasing deviation from stoichiometry, i.e. the larger is the disorder.

Diffusion of Nickel in NiGa and of Cobalt in CoGa

In order to obtain a consistent picture of the elementary diffusion jump in B2 alloys, neutron scattering was added to the repertoire of methods.

QENS was used by Kaisermayr et al. to study diffusion in two B2 alloys: NiGa [55] and CoGa [56]. NiGa and CoGa are very suitable for QENS because the incoherent neutron scattering cross section [6] of Ga is much smaller than that of Ni or Co. Thus the scattered intensity can be exclusively attributed to neutron scattering at nickel and Co nuclei, respectively. The QENS measurements were performed at ILL on single crystals with 51.2 at.% Ni and on polycrystals with 57 and 62 at.% Ni. Figure 2.9 shows the spectrum measured at 1400 K. From the $\boldsymbol{Q}$-dependence of the quasielastic line broadening the Ni jump mechanism was determined. The very weak concentration dependence of the Ni diffusivity observed by Donaldson and Rawlings [57] was confirmed over a wide concentration range on the Ni-rich side of the B2 phase. However, the next-nearest neighbour jumps of Ni [57] could not be found. On the contrary, the QENS experiment showed that the Ni atoms diffuse via nearest-neighbour jumps. In the near-stoichiometric composition the best fit of the $\boldsymbol{Q}$-dependence was achieved assuming effective jumps of Ni atoms with the preference of [100] over [110] jumps with an admixture of [111] jumps (ratio $4:2:1$, respectively). From the occupation times of both B2 sublattices Kaisermayr et al. [55] derived the antistructure-atoms concentration and, assuming triple defects[9] as a dominant defect structure of NiGa, very high vacancy concentrations in both alloys. These results are in agreement with vacancy concentrations extrapolated from dilatometric measurements (see [55] for more references).

Very recently the jump model of Ni atoms into antistructure-defect sites was confirmed on the same NiGa crystal but with higher accuracy using the neutron spin-echo technique [32]. Figure 2.10 shows fits to the spectra obtained from the single crystal for two wave vectors. For a wave vector $Q = 1.8\,\text{Å}^{-1}$ which coincides with the reciprocal superlattice lattice point the next nearest neighbour (NNN) model (dashed line) gives a very unsatisfactory fit to the experimental data. A perfect agreement with the experiment can be achieved with NN jumps, i.e. jumps to antistructure sites (solid line).

QENS measurements on CoGa [56] were performed at ILL on single crystals with 54 and 64 at.% Co. For both compositions a maximum of the quasielastic line broadening has been observed near a reciprocal lattice point corresponding to a B2 superlattice [100] reflection. This can be explained

[9] A triple defect consists of two A-sublattice vacancies and one antistructure atom on B-sublattice.

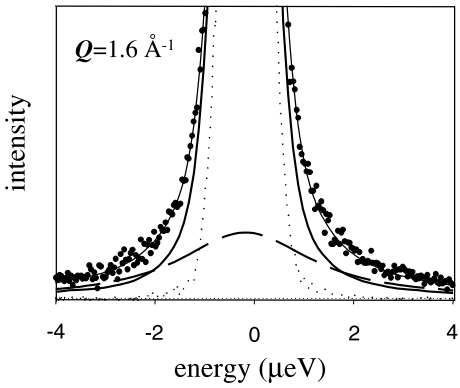

Fig. 2.9. Quasielastic spectrum obtained from a $Ni_{51}Ga_{49}$ single crystal at 1400 K. The thick solid and dashed lines represent two Lorentzians, dotted line the resolution function.

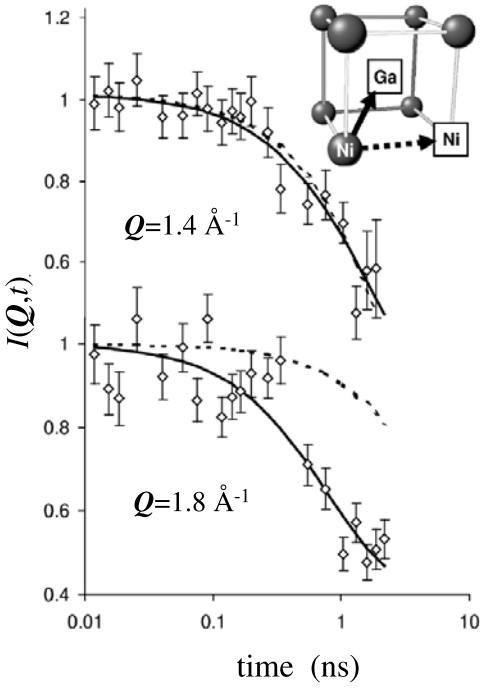

Fig. 2.10. Time correlation function measured on the $Ni_{52.5}Ga_{47.5}$ single crystal at 1130°C. Inset: B2-unit cell with a Ni atom jumping into a NN vacancy on a Ga site (solid arrow) and into a NNN vacancy on the Ni sublattice (dashed arrow).

only by the presence of a second Lorentzian arising from jumps to antistructure sites. The elementary jump of Co in CoGa has therefore been identified as a nearest-neighbour jump between regular and antistructure sites. From the residence times on the antistructure sites high vacancy concentrations were deduced (see e.g. [58]). Moreover, on the basis of the diffusion coefficient resulting from the line broadening at high Q values and from tracer measurements a correlation factor for Co diffusion not smaller than approximately 0.6 was found [56,59]. Hence, Co diffusion in CoGa seems to be, like Fe in FeAl alloys, surprisingly effective. This again suggests that it cannot be described in terms of defined cycles (six-jump, four-jump cycle), percolation-driven diffusion (antistructure-bridge mechanism) or a correlated triple-defect mechanism as proposed by Stolwijk et al. [60]. Note, however, that van Ommen and Miranda [61] suggested that NN Co and Ga atoms alone can explain the experimental results on activation enthalpy in the same manner as the triple-defect mechanism.

Thus the conclusion is again: transition metal (Ni, Co) atoms in NiGa and CoGa jump via antistructure sites. Their residence time on the antistructure sites is the shorter the closer to stoichiometry the alloy is.

Summary of Diffusion of Atoms of Transition Elements in B2 Ordered Alloys

- Diffusion always proceeds via jumps into a vacancy on a nearest-neighbour site.
- This is true for stoichiometric and non-stoichiometric alloys.
- The residence time on the antistructure site increases with deviation from stoichiometry.
- The diffusivity increases with deviation from stoichiometry.

$D0_3$ Alloys (Fe_3Si Structure)

Iron Diffusion in Fe_3Si

The $D0_3$ superstructure of Fe_3Si is more complicated than the B2 superstructure (see Fig. 2.11 inset). The cubic supercell consists of eight bcc cells. It can be divided into four sublattices, i.e. three iron sublattices (α_1, α_2 and γ sublattice) and one silicon (β) sublattice. The lattice constant of these sublattices of the supercell is twice as large as the lattice constant of the small bcc cells. Each iron atom on a γ site has eight iron neighbours. The two iron lattices α_1 and α_2 are energetically identical (and will be referenced below as "the α sublattices"). They both have four silicon and four iron nearest neighbours but the configuration of these neighbours around α_1 is mirrored in comparison to the neighbours surrounding an α_2 site. Silicon atoms on the β sublattice are surrounded by eight iron neighbours. In Fe_3Si the superstructure is stable up to the melting point due to a very high ordering

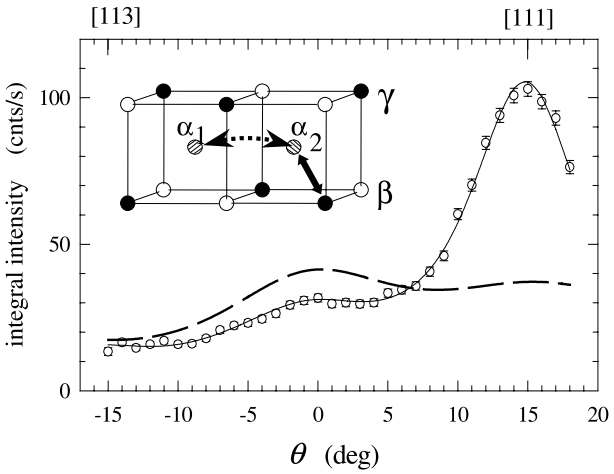

Fig. 2.11. $D0_3$ structure of Fe_3Si (2/8 of elementary cell) with iron NN (solid arrow) and NNN (broken arrow) jumps between regular α and γ lattice sites. Orientation dependence of time-integrated intensity of delayed NRS counts with lines fitted assuming NN (solid line) and NNN (broken line) iron jumps.

energy, while less ordered off-stoichiometric $Fe_{1-x}Si_x$ ($x < 0.25$) undergoes a $D0_3 \leftrightarrow B2$ phase transition before reaching the solidus line (excess iron atoms in off-stoichiometric $Fe_{1-x}Si_x$ are placed on silicon sites).

Mößbauer studies were the first to detect that despite the high degree of order in Fe_3Si, iron diffusion in this compound is very fast [62] (see Arrhenius plots in Chap. 1) and – most surprisingly – becomes *slower* with decreasing order. This was very soon later confirmed by tracer studies [63], and later-on by studies with NRS [26]. These facts lead to two questions: Is a special diffusion mechanism operative in Fe_3Si and what causes the decrease in diffusion coefficient with increasing iron content? Experiments using QEMS and phonon spectroscopy help to solve these problems.

In principle, jumps between all four sublattices are possible, i.e. the spectra of Fe_3Si should consist of four Lorentzians. The spectra measured by QEMS and NRS turn out to be simpler. In contrast to the situation in B2 structures an iron atom in Fe_3Si can diffuse exclusively between iron sublattices via NN jumps without creating antistructure defects. Thus in highly ordered Fe_3Si no antistructure jumps are observed and the jump matrix reduces to a 3×3 matrix, i.e. the number of lines reduces to three Lorentzians. All spectra measured at Fe_3Si are well fitted by use of a model with a 3×3 jump matrix. No jumps directly between α are found. From Fig. 2.11 it is clear that iron jumps only between NN sites and, moreover, the lower limit of NNN-jumps contribution can be fitted. The contribution of NNN-jumps is below 5% of the NN-jump rate, in other words an upper limit for the direct NNN-jump diffusivity is below 5% of the total iron diffusivity.

In off-stoichiometric samples the excess iron atoms already occupy silicon sites and thus diffusion via antistructure sites is less unfavoured than in stoichiometric Fe_3Si. Spectra taken at different orientations on off-stoichiometric samples could only be fitted using a 4×4 jump matrix [62].

In the Fe_3Si system relatively soft phonon modes [64] which give low migration energies are found, but they do not vary with composition. Hence the composition dependency of D cannot be attributed to phonon characteristics. The diffusion mechanism turns out to be a rather conventional one: Diffusion in Fe_3Si is fast due to a very large concentration of vacancies and occurs via NN jumps from γ to α sites and vice versa. Off-stoichiometric $Fe_{1-x}Si_x$ alloys contain much less vacancies [65] and thus diffusion is slow. In contrast to stoichiometric Fe_3Si iron jumps between α and β sites (silicon sublattice) are not only possible in off-stoichiometric alloys but even more frequent than jumps between the regular iron sites α and β [62] which was also confirmed by Monte Carlo simulations [66].

The high vacancy concentration in Fe_3Si may be due to the high ordering energy: introducing a large number of vacancies is the sole possibility to increase entropy upon heating without creating antistructure defects. In off-stoichiometric $Fe_{1-x}Si_x$ where already built-in antistructure defects exist creation of additional defects of this type is less expensive in energy than in Fe_3Si and thus less vacancies are formed and diffusion is slow.

Nickel Diffusion in Ni_3Sb

Again neutron scattering can serve to widen the field of accessible alloys because neutron measurements are not limited to the diffusion of Fe atoms. Another compound with $D0_3$ structure is Ni_3Sb (at the high temperatures mandatory for quasielastic measurements). Nickel diffusion in Ni_3Sb, which contains many vacancies, together with Cu diffusion in Cu_3Sn, is the fastest ever found in an intermetallic alloy[10]. Typical values at 800°C are $D \approx 6 \times 10^{-11}\,\mathrm{m^2 s^{-1}}$. In contrast to the case of Fe_3Si, however, they are asymmetrically distributed among the sublattices: the vacancies are concentrated on the α sublattices [67]. This may lead to a high rate of "far" jumps between α sites. Ni_3Sb is very suitable for QENS because again the incoherent neutron scattering cross section of the metalloid (here Sb) is much smaller for antimony than for the transition element (Ni). Thus the scattered intensity can be exclusively attributed to neutron scattering at nickel nuclei.

At two temperatures the quasielastic line broadening was measured on a $Ni_{72.5}Sb_{27.5}$ crystal at different orientations. Figure 2.12 shows the result for different orientations of the single crystal. The bulk lines are fits according to the model of NN jumps between γ and α sites. The dotted, dashed-dotted and dashed lines are calculated under the assumption of jumps between α sites (see arrows in Fig. 2.11). The corresponding jump lengths in terms of

[10] To the best of our knowledge, it is even the fastest self-diffusion in a pure metallic system on the reduced temperature scale T/T_{melting}.

the bcc lattice constant a for these jumps are a (dotted), $a/\sqrt{2}$ (dashed-dotted, along the face diagonal of the cube formed by the α sites, e.g. from α_1 to α_1) and $a/2$ (dashed, along the edges of the α-site cube, e.g. from α_1 to α_2). Under the assumption that nickel atoms jump between γ and α sites (nearest neighbours) the measured linewidth is well fitted, while other jump models give markedly worse results. Even in this case the elementary steps of diffusion are NN jumps, profiting from the high vacancy concentration on two of the three nickel sublattices. Details can be found, e.g., in [68].

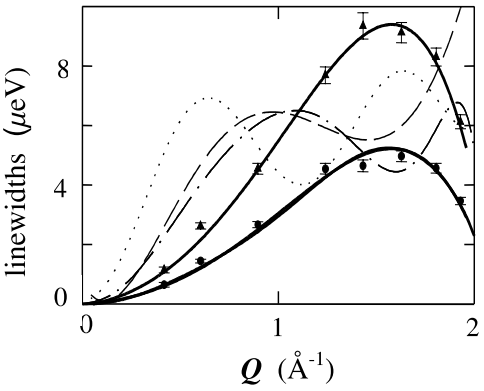

Fig. 2.12. Linewidths measured by QENS on Ni_3Sb at 690°C (dots) and 780°C (triangles) and comparison with different models.

Summary of the Diffusion of Atoms of Transition Elements in $D0_3$ Alloys

Here the picture is not at all as consistent as for B2 alloys, it rather demonstrates considerable differences and contrasts: fastest diffusion of transition element atoms for stoichiometry in Fe_3Si, slowest in Ni_3Sb. This appears to be still a not completely solved problem. First principle density functional calculations for Ni_3Sb [69] completely confirm the experimental results [68], for Fe_3Si work is still underway.

2.4 Conclusion

The central aim of this chapter was to demonstrate the potential of methods working with scattering of X-rays, including Mößbauer gamma rays, and neutrons for determining the elementary diffusion jump. These methods either work in the energy domain or in the time domain.

We have discussed the results of quasielastic Mößbauer spectroscopy (QEMS) and nuclear resonance scattering of synchrotron X-rays (NRS) on the one hand; quasielastic neutron scattering (QENS) and neutron spin echo (NSE) on the other hand, for studying the elementary diffusion jump in

metallic systems. By way of examples we reported on the determination of the elementary diffusion jump in pure metals, of impurities in dilute alloys and in ordered intermetallic alloys. We chose mostly examples from our own work, not aiming at completeness. For the sake of simplicity, which we regarded necessary for an overview, we dwelled exclusively on cubic systems. Thus we did not report on non-cubic lattices as, e.g., the QENS experiments on Ni diffusion in NiSb [70] or QEMS experiments on Fe diffusion in FeSb [71], both hexagonal intermetallic alloys. For more complicated diffusion processes studied by QEMS and QENS we point to our earlier reviews about diffusion studies by Mößbauer spectroscopy [10, 72, 73], neutron scattering [74] and NRS [28]. Reference [10] includes the first atomistic results on diffusion in restricted regions, i.e. cages [75], which recently gained great interest in biological systems; this is the large regime of diffusion in confined regions.

As a conclusion for this report limited to long-range diffusion in cubic metals we could choose: the basic step for these processes is the jump of an atom into a NN vacancy. World appears to be so simple in these simple cases, but this had first to be demonstrated. What is not so simple, is the time scale for occupation of antistructure sites in the particularly interesting class of ordered alloys: the whole zoo of possibilities exists, connected to the degree of order of an alloy and to the way the partners match.

The future appears bright: the highly collimated synchrotron beam will enable studies of surface diffusion, the high coherence of present and more so of future sources of synchrotron radiation will finally enable photon correlation spectroscopy to study much slower diffusion than possible now. In neutron spectroscopy considerable progress will be accomplished with the new spallation sources. Since – and that should not be tacitly omitted because we want to remain modest – until now diffusion has to be rather fast to be unveiled by the scattering methods.

Notation

a	lattice constant (Å)
A2	two component phase $A_{1-x}B_x$; solid solution with b.c.c structure
B2	two component intermetallic phase AB; superstructure basing on a b.c.c cell with edges occupied by atoms of one species while the body centred position belongs to atoms of the other species
$D0_3$	two component intermetallic phase A_3B ; superstructure basing on eight b.c.c cells; can also be described as simple cubic lattice with a base of four atoms
D	diffusion coefficient or diffusivity (m^2s^{-1})
f	correlation factor
f_{DW}	Debye-Waller (Lamb-Mößbauer) factor; relative intensity of scattered (resonantly absorbed) radiation
^{57}Fe	most important Mößbauer isotope; interesting Mößbauer transition with energy 14.4 keV and wave vector $\|\boldsymbol{Q}\| = 7.3\,\text{Å}^{-1}$

$G_s(\boldsymbol{r}, t)$ probability density to find an atom *displaced* by a vector $\boldsymbol{r}$ from its starting position within a time interval t averaged over all possible starting positions
$P(\boldsymbol{r}, t)$ probability density to find an atom on the site $\boldsymbol{r}$ at time t
$\boldsymbol{Q}$ scattering vector (QENS) or Mößbauer radiation wave vector (QEMS)
$S(\boldsymbol{Q}, \omega)$ incoherent scattering function (QENS) or cross section for resonant nuclear absorption (QEMS)
Γ diffusional line broadening
Γ_0 natural line width of the Mößbauer transition ($\Gamma_0 \approx \hbar/\tau_0$)
ϑ angle between $\boldsymbol{Q}$ and the [001] crystal axis
τ_0 mean life time of the excited Mößbauer level
τ_i mean residence time of an atom between jumps from sublattice i (τ^{-1} – jump rate)
τ_{ij} mean residence time between jumps from sublattice i to any nearest-neighbour site of symmetry j

References

1. *Diffusion in Metals and Alloys*, Landolt-Börnstein, Numerical Data and Functional Relationships in Science and Technology, New Series Vol. III/26, ed by H. Mehrer (Springer, Berlin Heidelberg New York 1990)
2. H. Mehrer: Materials Transactions JIM **37**, 1259 (1996)
3. G.E. Murch. In: *Materials Science and Technology*, vol 5, ed by R.W. Cahn, P. Haasen, E.J. Kramer (VCH, Weinheim 1991)
4. J. Philibert: *Atom movements – Diffusion and mass transport in solids*, (Les Éditions de Physique, Les Ulis France 1991)
5. Th. Heumann: *Diffusion in Metallen* (Springer, Berlin Heidelberg New York 1992)
6. R. Hempelmann: *Quasielastic Neutron Scattering and Solid State Diffusion* (Oxford Science Publications, Oxford 2000)
7. L. Van Hove: Phys. Rev. **95**, 249 (1954)
8. C.T. Chudley, R.J. Elliott, Proc. Phys. Soc. London **77**, 353 (1961)
9. K.S. Singwi, A. Sjölander, Phys. Rev. **120**, 1093 (1960)
10. G. Vogl. In: *Mößbauer Spectroscopy Applied to Magnetism and Materials Science* ed by G.J. Long, F. Grandjean (Plenum Press, New York 1996)
11. N. Brockhouse: Phys. Rev. Lett. **2**, 287 (1959)
12. M. Ait-Salem, T. Springer, A. Heidemann, B. Alefeld: Phil. Mag. A **39**, 797 (1979)
13. G. Göltz, A. Heidemann, H. Mehrer, A. Seeger, D. Wolf: Phil. Mag. A **41**, 723 (1980)
14. R.C. Knauer, J.G. Mullen: Phys. Rev. **174**, 711 (1968)
15. J.W. Haus, K.W. Kehr: Physics Reports **150**, 263 (1987)
16. G. Sauthof: *Intermetallics* (VCH, Weinheim 1995)
17. J.W. Rowe, K. Sköld, H.E. Flotow, J.J. Rusch: J. Phys. Chem. Solids **32**, 41 (1971)
18. R. Kutner, I. Sosnowska: J. Phys. Chem. Soc. **38**, 741 (1977)

19. I.S. Anderson, A. Heidemann, J.E. Bonett, D.K. Ross, S.K. Wilson, M. McKergow: J. Less Common Met. **101**, 405 (1984)
20. O.G. Randl, B. Sepiol, G. Vogl, R. Feldwisch, K. Schroeder: Phys. Rev. B **49**, 8768 (1994)
21. G. Vogl, B. Sepiol: Acta Metall. Mater. **42**, 3175 (1994)
22. R. Feldwisch, B. Sepiol, G.Vogl: Acta Metall. Mater. **43**, 2033 (1995)
23. H.M. Eggersmann, B. Sepiol, G. Vogl, H. Mehrer: Defect and Diffusion Forum **143–147**, 339 (1997)
24. M. Eggersmann, H. Mehrer: Phil. Mag. A **80**, 1219 (2000)
25. Zs. Tökei, J. Bernardini, P.Gas, D.L. Beke: Acta Materialia **45**, 541 (1997)
26. B. Sepiol, A. Meyer, G. Vogl, R. Rüffer, A.I. Chumakov, A.Q.R. Baron: Phys. Rev. Lett. **76**, 3220 (1996)
27. G.V. Smirnov, V.G. Kohn: Phys. Rev. B **52**, 3356 (1995)
28. G. Vogl, B. Sepiol. In: *Nuclear Resonant Scattering of Synchrotron Radiation*, ed by G. Langouche, H. de Waard, Hyperfine Interactions **123/124**, (1999) p 595
29. B. Sepiol, A. Meyer, G. Vogl, H. Franz, R. Rüffer: Phys. Rev. B **57**, 10433 (1998)
30. V.G. Kohn, G.V. Smirnov, Phys. Rev. B **57**, 5788 (1998)
31. F. Mezei. In: *Neutron Spin Echo*, ed by F. Mezei (Springer, Berlin Heidelberg New York 1980)
32. M. Kaisermayr, C. Pappas, B. Sepiol, G. Vogl: Phys. Rev. Lett. **87**, 175901 (2001)
33. D.K. Ross, D.L.T. Wilson: *Neutron Inelastic Scattering*, vol 2,(IAEA, Vienna 1978) p 383
34. T. Springer: *Quasielastic Neutron Scattering for the Investigation of Diffusive Motions in Solids and Liquids*, Springer Tract in Modern Physics, vol 64, (Springer, Berlin Heidelberg New York 1972)
35. M. Kaisermayr, B. Sepiol, G. Vogl: Physica B **301**, 115 (2001)
36. B. Schönfeld: Progress in Mat. Science **44**, 435 (1999)
37. M. Kaisermayr, B. Sepiol, H. Thiess, G. Vogl, E.E. Alp, W. Sturhahn: Eur. Phys. J. B **20**, 335 (2001)
38. A.Q.R. Baron, H. Franz, A. Meyer, R. Rüffer, A.I. Chumakov, E. Burkel, W. Petry: Phys. Rev. Lett. **79**, 2823 (1997)
39. D.C. Champeney: Rep. Prog. Phys. **42**, 1017 (1979)
40. S. Brauer, B. Stephenson, M. Sutton, R. Brüning, E. Dufresne, S.G.J. Mochrie, G. Grübel, J. Als-Nielsen, D.L. Abernathy: Phys. Rev. Lett. **74**, 2010 (1995)
41. G. Vogl, W. Petry, Th. Flottmann, A. Heiming: Phys. Rev. B **39**, 5025 (1989)
42. W. Petry, A. Heiming, J. Trampenau, G. Vogl: Defect and Diffusion Forum **66–69**, 157 (1989)
43. S. Mantl, W. Petry, K. Schroeder, G. Vogl: Phys. Rev. B **27**, 5313 (1983)
44. K. H. Steinmetz, G. Vogl, W. Petry, K. Schroeder: Phys. Rev. B **34**, 107 (1986)
45. A.D. Le Claire: J. Nucl.Mater. **69&70**, 70 (1978)
46. M.A. Krivoglaz, S.P. Repetskiy: Fiz. Met. Metalloved. **32**, 899 (1971), (*Phys. Met. Metallogr. (USSR)* **32**, 1 (1971))
47. S.K. Chen, M.B. Dutt, A.K. Barua: Phys. Stat. Sol. A **45**, 657 (1978); containing further references on tracer studies of iron diffusion in copper
48. G. Vogl, B. Sepiol, C. Czichak, R. Rüffer, R. Weinkamer, P. Fratzl, M. Fähnle, M. Meyer: Mat. Res. Soc. Symp. Proc. **527**, 197 (1998)

49. C.L. Fu, Y.Y. Ye, M.H. Yo, K.M. Ho: Phys. Rev. B **48**, 6712 (1993)
50. R. Drautz, M. Fähnle: Acta Mater. **47**, 2437 (1999)
51. S. Divinsky, Chr. Herzig: Intermetallics **8**, 1357 (2000)
52. I.V. Belova, M-E. Ivory, G.E. Murch: Phil. Mag. A **72**, 871 (1995); Phil. Mag. A **80**, 1481 (2000)
53. M. Fähnle, J. Mayer, B. Meyer: Intermetallics **7**, 315 (1999)
54. G. Bester, B. Meyer, M. Fähnle, C.L. Fu: Mater. Science and Engineering A **323**, 478 (2002)
55. M. Kaisermayr, J. Combet, H. Ipser, H. Schicketanz, B. Sepiol, G. Vogl: Phys. Rev. B **61**, 12038 (2000)
56. M. Kaisermayr, J. Combet, H. Ipser, H. Schicketanz, B. Sepiol, G. Vogl: Phys. Rev. B **63**, 054303 (2001)
57. A.T. Donaldson, R.D. Rowlings: Acta Met. **24**, 285 (1976)
58. A.G. Balogh, I. Dezsi, J. Pelloth, R.A. Brand, W. Keune, W. Puff: Mat. Sci. Forum **105–110**, 897 (1992)
59. M. Kaisermayr, J. Combet, B. Sepiol, G. Vogl: Defect and Diffusion Forum **149–199**, 461 (2001)
60. N.A. Stolwijk, M. van Gend, H. Bakker: Phil. Mag. A **42**, 783 (1980)
61. A.H. van Ommen, J. de Miranda: Phil. Mag. A **43**, 387 (1981)
62. B. Sepiol, G. Vogl: Phys. Rev. Lett. **71**, 731 (1993); B. Sepiol, G. Vogl: Hyperfine Interact. **59**, 149 (1995)
63. A. Gude, H. Mehrer: Phil. Mag. A **76**, 1 (1997)
64. O.G. Randl, G. Vogl, W. Petry, B. Hennion, B. Sepiol, K. Nembach: J. Phys.: Condensed Matter **7**, 5983 (1995)
65. E.A. Kümmerle, K. Badura, B. Sepiol, H. Mehrer, H.-E. Schaefer: Phys. Rev. B **52**, R6947 (1995)
66. I.V. Belova, G.E. Murch: J. Phys. Chem. Solids **59**, 1 (1998)
67. O.G. Randl, G. Vogl, W. Bührer, M. Kaisermayr, P. Pannetier, W. Petry: J. Phys.: Condensed Matter **8**, 7689 (1996)
68. G. Vogl, M. Kaisermayr, O.G. Randl: J. Phys.: Condensed Matter **8**, 4727 (1996)
69. G. Bester, B. Meyer, M. Fähnle: Phys. Rev. B **59**, 3274 (1999)
70. G. Vogl, O.G. Randl, W. Petry, J. Hünecke: J. Phys.: Condensed Matter **5**, 7215 (1993)
71. M. Sladecek, M. Miglierini, B. Sepiol, H. Ipser, H. Schicketanz, G. Vogl: Defect and Diffusion Forum **149–199**, 369 (2001)
72. G. Vogl: Hyperfine Interactions **53**, 197 (1990)
73. B. Sepiol: Defect and Diffusion Forum **125–126**, 1 (1995)
74. G. Vogl. In: *Neutron Scattering from Hydrogen in Materials*, ed by A. Furrer (World Scientific, Singapore 1994)
75. G. Vogl, W. Mansel, P.H. Dederich:, Phys. Rev. Lett. **36**, 1497 (1976)

3 Diffusion Studies of Solids by Quasielastic Neutron Scattering

Tasso Springer and Ruep E. Lechner

3.1 Introduction

The diffusion in solids is usually investigated on a macroscopic scale, for instance following the interpenetration of two atomic species across an interface which is related to the chemical diffusion coefficient. On the other hand, the self-diffusion coefficient is measured by labelling atoms with radioactive isotopes. These techniques have been presented in Chap. 1. Labelling can also be achieved by Larmor precession in a magnetic field gradient where the corresponding dephasing depends on the diffusive migration of the precessing particles (Chaps. 10 and 17). In contrast to such "macroscopic" methods the diffusion process can be studied for atomistic time scales by the spin-lattice relaxation in nuclear magnetic resonance spectroscopy (Chap. 9). The method of quasielastic neutron scattering (QENS)[1], which focuses on scattering processes at small energy transfers, penetrates into the region of 10^{-13} to 10^{-8} s. In addition, quasielastic neutron scattering explores the diffusive motion in *space*, for a range comparable with the wavelengths of the neutrons used in spectroscopy. Typical correlation lengths, diffusive paths, jump distances, and vibrational displacements can be evaluated between 10^{-6} and 10^{-9} cm. Inelastic neutron scattering on such diffusive processes leads to a spectrum of energy transfers

$$\hbar\omega = E_1 - E_0 \ , \tag{3.1}$$

in a range from 10^{-3} to 10^{-7} eV, where E_0 and E_1 are the energies before and after scattering, respectively. The corresponding scattering vector in such a process is

$$\boldsymbol{Q} = \boldsymbol{k}_1 - \boldsymbol{k}_0 \ , \tag{3.2}$$

where $\boldsymbol{k}_0$ and $\boldsymbol{k}_1$ are the neutron wave vectors before and after scattering, respectively. The values of $Q = (4\pi/\lambda)\sin(\varphi/2)$ are in the region of typically 0.1 to 5 Å^{-1} (λ = neutron wavelength, φ = scattering angle) such that $1/Q$ corresponds to interatomic distances. The scattered intensity in such a

[1] In the following, we use "QENS" for quasielastic neutron scattering in general, and "QINS", if the quasielastic scattering is purely incoherent, in order to distinguish this case from the coherent one.

process is proportional to the so-called scattering function or dynamic structure factor $S(\boldsymbol{Q},\omega)$, which can be calculated for typical diffusive processes; the calculation and determination of this function is the subject of the following sections. To anticipate briefly what will be explained in detail, the widths of the Lorentzian shaped "quasielastic line" is given by $\Gamma = Q^2 D_\mathrm{s}$ for small values of Q, where D_s is the self-diffusion coefficient. For larger scattering vectors, Γ depends on the details of the jump process. Obviously, for a particle *at rest*, $\Gamma = 0$ and $S(\boldsymbol{Q},\omega)$ is a sharp line $\delta(\omega)$ at $\hbar\omega = 0$. For resonance absorption of gamma rays this corresponds to the well-known Mößbauer line. It results from absorption processes where the gamma quantum transmits momentum $\hbar\boldsymbol{k}$ to the sample *as a whole*, without any measurable energy transfer. Furthermore, for Mößbauer absorption spectroscopy, a diffusing particle produces a corresponding broadening of this line and it is described by the same concepts as used for incoherent neutron scattering (see Chap. 2 for nuclear resonance gamma ray absorption and scattering).

The interpretation of the dynamic structure factor $S(\boldsymbol{Q},\omega)$ in terms of the diffusive process is uncomplicated because

- the diffusion can be described by classical physics; in general, quantum effects can be completely neglected, and
- the scattering is treated in first Born approximation. This allows an evaluation and interpretation of $S(\boldsymbol{Q},\omega)$ by pair correlation functions for the scattering nuclei in space and time.

Within this concept, the following sections deal with different kinds of diffusion. First of all, hydrogen diffusion in metals will be explained. Because of the dominant incoherent scattering of the proton, the interpretation of the results is straightforward. Then we deal with other cases such as vacancy induced diffusion in metals, diffusion in the presence of impurities, ionic diffusion, and, briefly, collective effects as investigated in substances where coherent scattering dominates; this is more complicated, and coherent quasielastic scattering has been exploited to a lesser extent than its incoherent counterpart. It is clear that we cannot cover the whole field. For instance, experiments concerning diffusion in polymers (see Chaps. 13 and 16) are omitted. The methodical aspect, namely high resolution neutron spectroscopy, will be explained to the extent this is needed for the presented experimental studies.

3.2 The Dynamic Structure Factor $S(Q,\omega)$

Atomistic information is obtained by analyzing the intensity of neutrons from a monochromatic beam with a current density I_0 scattered into a solid angle element $\Delta\Omega$ and an energy interval $\Delta\hbar\omega$, on a sample with a volume V and an atomic number density n_0 (see Fig. 3.1). This intensity is given by

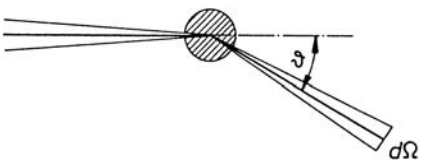

Fig. 3.1. Neutron scattering experiment. The intensity scattered into a solid angle element $\mathrm{d}\Omega$ and an energy element $\mathrm{d}\omega$ is proportional to the double differential scattering cross-section $\mathrm{d}^2\sigma/\mathrm{d}\Omega\mathrm{d}\omega$ in (3.4).

$$\Delta I_\mathrm{s} = I_0 n_0 V \left(\frac{\mathrm{d}^2\sigma}{\mathrm{d}\Omega\,\mathrm{d}\omega}\right) \Delta\Omega\,\Delta\omega, \tag{3.3}$$

where the double differential scattering cross-section is

$$\frac{\mathrm{d}^2\sigma}{\mathrm{d}\Omega\,\mathrm{d}\omega} = \frac{k_1}{k_0}\frac{\sigma}{4\pi} S(\boldsymbol{Q},\omega)\ . \tag{3.4}$$

This cross-section is factorized in three components: i) The ratio of the wave numbers k_1 and k_0 characterizing the scattering process, ii) the cross-section σ for a rigidly bound scattering nucleus (where $\sigma = 4\pi b^2$ and b is the corresponding scattering length of the nucleus), and iii) the dynamic structure factor $S(\boldsymbol{Q},\omega)$. The latter depends on the scattering vector $\boldsymbol{Q}$ and the energy transfer $\hbar\omega$ as defined by (3.2) and (3.1), respectively. The structural and dynamical properties of the scattering sample are described by $S(\boldsymbol{Q},\omega)$ which does not depend on the neutron-nuclear interaction. In the following, we will explain this function. For a detailed derivation and discussion we refer to the corresponding literature [1–3]. To start with, we formulate the well-known static structure factor $S(\boldsymbol{Q})$ for the simplest case of N identical atoms at positions $\boldsymbol{r}_0, \boldsymbol{r}_1 \ldots \boldsymbol{r}_N$. The scattering ("diffraction") intensity is proportional to the square of the amplitude sum, taking into account the mutual phase differences of the outgoing waves for pairs of particles. The structure factor per atom is then

$$I(\boldsymbol{Q}) = N^{-1} \sum_i^N \sum_j^N \mathrm{e}^{-\mathrm{i}\boldsymbol{Q}(\boldsymbol{r}_i - \boldsymbol{r}_j)} = N^{-1} \left| \sum_{i=1}^N \mathrm{e}^{\mathrm{i}\boldsymbol{Q}\boldsymbol{r}_i} \right|^2 \tag{3.5}$$

Instead, for moving nuclei, corresponding to lattice vibrations and diffusion, one gets the so-called intermediate dynamic structure factor (or intermediate scattering function) with time dependent space coordinates $\boldsymbol{r}(t)$

$$I(\boldsymbol{Q},t) = N^{-1} \sum_i^N \sum_j^N \left\langle \mathrm{e}^{-\mathrm{i}\boldsymbol{Q}\boldsymbol{r}_i(0)} \mathrm{e}^{\mathrm{i}\boldsymbol{Q}\boldsymbol{r}_j(t)} \right\rangle\ . \tag{3.6}$$

Actually, $\boldsymbol{r}_i$ are operators, $\langle \cdots \rangle$ is a thermal average of the expectation value for the product enclosed in the brackets. Below we explain that, under the

given conditions, the quantities $\boldsymbol{r}$ are vectors in space and not operators, and $\langle \cdots \rangle$ is just the thermal average. For the following we need mainly the self-terms in (3.6) which leads to

$$I_{\mathrm{s}}(\boldsymbol{Q},t) = \left\langle \mathrm{e}^{-\mathrm{i}\boldsymbol{Q}\boldsymbol{r}(0)} \mathrm{e}^{\mathrm{i}\boldsymbol{Q}\boldsymbol{r}(t)} \right\rangle \ . \tag{3.7}$$

The index i was left out and the sum $\sum$ is replaced by N. From these relations the Van Hove theory [4] derives an elegant formulation of the dynamic structure factor $S(\boldsymbol{Q},\omega)$, namely

$$S(\boldsymbol{Q},\omega) = (2\pi)^{-1} \int I(\boldsymbol{Q},t)\, \mathrm{e}^{-\mathrm{i}\omega t}\, \mathrm{d}t \ , \tag{3.8}$$

and for its self-part, namely the so-called "incoherent" contribution (see below),

$$S_{\mathrm{inc}}(\boldsymbol{Q},\omega) = (2\pi)^{-1} \int I_{\mathrm{s}}(\boldsymbol{Q},t)\, \mathrm{e}^{-\mathrm{i}\omega t}\, \mathrm{d}t \ . \tag{3.9}$$

With these relations, the so-called Van Hove correlation functions can be defined, namely

$$G(\boldsymbol{r},t) = (2\pi)^{-3} \iint \mathrm{e}^{-\mathrm{i}(\boldsymbol{Q}\boldsymbol{r}-\omega t)} S(\boldsymbol{Q},\omega) \mathrm{d}\boldsymbol{Q}\, \mathrm{d}\omega \ , \tag{3.10}$$

and for the self-part

$$G_{\mathrm{s}}(\boldsymbol{r},t) = (2\pi)^{-3} \iint \mathrm{e}^{-\mathrm{i}(\boldsymbol{Q}\boldsymbol{r}-\omega t)} S_{\mathrm{inc}}(\boldsymbol{Q},\omega) \mathrm{d}\boldsymbol{Q}\, \mathrm{d}\omega \ , \tag{3.11}$$

Inversion leads to the dynamic structure factors as a Fourier transform of these correlation functions, namely

$$S(\boldsymbol{Q},\omega) = (2\pi)^{-1} \iint G(\boldsymbol{r},t)\, \mathrm{e}^{\mathrm{i}(\boldsymbol{Q}\boldsymbol{r}-\omega t)} \mathrm{d}\boldsymbol{r}\, \mathrm{d}t \ , \tag{3.12}$$

$$S_{\mathrm{inc}}(\boldsymbol{Q},\omega) = (2\pi)^{-1} \iint G_{\mathrm{s}}(\boldsymbol{r},t)\, \mathrm{e}^{\mathrm{i}(\boldsymbol{Q}\boldsymbol{r}-\omega t)} \mathrm{d}\boldsymbol{r}\, \mathrm{d}t \ . \tag{3.13}$$

In the classical approximation, (3.6) and (3.7) can be interpreted in the following sense. The cross terms with $i \neq j$ in $I(\boldsymbol{Q},t)$ correspond to a superposition of scattered neutron waves originating from *pairs of different particles* at positions $\boldsymbol{r}_i$ and $\boldsymbol{r}_j$ at different times 0 and t. $I_{\mathrm{s}}(\boldsymbol{Q},t)$, however, is obviously caused by scattered waves originating from the *same* nucleus at different positions for different times. Correspondingly, one can show that the Van Hove correlation functions have the following classical meaning (Fig. 3.2): $G(\boldsymbol{r},t)$ is the probability per unit volume to find a particle (nucleus) at a position $\boldsymbol{r}$ for a given time t if this or another particle has been at a position $\boldsymbol{r} = 0$ for a previous time $t = 0$. In the same way, $G_{\mathrm{s}}(\boldsymbol{r},t)$ is the probability of finding

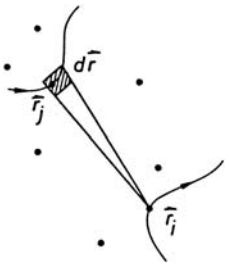

Fig. 3.2. The Van Hove correlation function: $G(\boldsymbol{r}_j - \boldsymbol{r}_i, t)$ is the conditional probability to find an atom at $\boldsymbol{r}_j$for a time t, if this atom or another one was at $\boldsymbol{r}_i$, with a distance vector $\boldsymbol{r} = \boldsymbol{r}_j - \boldsymbol{r}_i$ for $t = 0$. For the self-correlation function $G_\mathrm{s}(\boldsymbol{r}, t)$, $\boldsymbol{r}_j$ and $\boldsymbol{r}_i$ locate the *same* particle.

a particle at $\boldsymbol{r}$ for a time t if the same particle was at the origin $\boldsymbol{r} = 0$ for $t = 0$.

In particular this implies

$$G_\mathrm{s}(\boldsymbol{r}, t = 0) = \delta(\boldsymbol{r}) \quad \text{and} \quad G(\boldsymbol{r}, t = 0) = \delta(\boldsymbol{r}) + g(\boldsymbol{r}) \ , \tag{3.14}$$

where $g(\boldsymbol{r})$ is the usual instantaneous pair correlation function, and one gets

$$S(\boldsymbol{Q}) = \int_{-\infty}^{+\infty} S(\boldsymbol{Q}, \omega)\, \mathrm{d}\omega = 1 + \int g(\boldsymbol{r})\, \mathrm{e}^{\mathrm{i}\boldsymbol{Q}\boldsymbol{r}}\, \mathrm{d}\boldsymbol{r} \ . \tag{3.15}$$

Furthermore, we note that $G_\mathrm{s}(0, t)$ is the probability that a certain nucleus which was at $\boldsymbol{r} = 0$ for $t = 0$, is still (or again) at $\boldsymbol{r} = 0$ for a time t.

For a particle diffusing in a space, which is large as compared to the atomic scale, the self-correlation function $G_\mathrm{s}(\boldsymbol{r}, t)$ vanishes, if t goes to infinity, whereas for a particle *bound to a finite volume* (e. g. as part of a rotating molecule fixed in a crystal), $G_\mathrm{s}(\boldsymbol{r}, t)$ approaches a finite value $G_\mathrm{s}(\boldsymbol{r}, \infty)$ for $\boldsymbol{r}$ varying in the interior of this volume. In fact, following Van Hove [4], Turchin [5] has pointed out that very generally, the self-correlation function can be split into its asymptotic value in the long-time limit and a time-dependent term $G'_\mathrm{s}(\boldsymbol{r}, t)$, according to $G_\mathrm{s}(\boldsymbol{r}, t) = G_\mathrm{s}(\boldsymbol{r}, \infty) + G'_\mathrm{s}(\boldsymbol{r}, t)$. The Fourier transform of this expression reads:

$$S_\mathrm{inc}(\boldsymbol{Q}, \omega) = (2\pi)^{-1} \iint \mathrm{e}^{\mathrm{i}(\boldsymbol{Q}\boldsymbol{r} - \omega t)} [G_\mathrm{s}(\boldsymbol{r}, \infty) + G'_\mathrm{s}(\boldsymbol{r}, t)]\, \mathrm{d}\boldsymbol{r}\, \mathrm{d}t \ . \tag{3.16}$$

which gives

$$S_\mathrm{inc}(\boldsymbol{Q}, \omega) = S^\mathrm{el}_\mathrm{inc}(\boldsymbol{Q})\delta(\omega) + S^\mathrm{in}_\mathrm{inc}(\boldsymbol{Q}, \omega) \tag{3.17}$$

It is seen that the incoherent scattering function is decomposed into a purely elastic line, $S^\mathrm{el}_\mathrm{inc}(\boldsymbol{Q})\delta(\omega)$, with the integrated intensity $S^\mathrm{el}_\mathrm{inc}(\boldsymbol{Q})$, and a nonelastic component, $S^\mathrm{in}_\mathrm{inc}(\boldsymbol{Q}, \omega)$. The elastic line is the result of diffraction of the neutron on the "infinite time" distribution in space of a single nucleus spread over a finite volume by its motion, as already pointed out by Stiller [6]. Therefore we can derive information about the structure in a very direct way from the incoherent scattering [7]. This is clearly a rather important result of the

Van Hove theory. We now turn to its application which will be further discussed later, in the context of practical examples in Sects. 3.4, 3.5, 3.9, 3.10 and 3.12.

In order to exploit the theoretical fact expressed by (3.17) in neutron scattering experiments on orientationally disordered (plastic and liquid) crystals, the concept of the elastic incoherent structure factor (EISF) was formulated by Lechner [8]. First applications of this concept were published, as soon as the progress of instrument development at the Institute Laue-Langevin (ILL) in Grenoble permitted to carry out corresponding experiments [9–13]. First of all, an experimental separation of the elastic component according to (3.17) was required. Novel high-resolution quasielastic spectrometers which could achieve this were built at the start-up of the high-flux reactor of the ILL. Secondly, for the analysis of the data a method was needed that would allow the isolation of the scattering effect of specific motions, such as the stochastic molecular reorientations known to occur in these dynamically disordered crystals. The EISF concept provides such a method. It permits the extraction of structural information on such localized single-particle motions by the determination of the elastic fraction of the measured spectral intensity. The idea is simple: First, by employing sufficiently high energy-resolution, the measured integrals of elastic (I^{el}) and nonelastic (I^{in}) components of the scattering function in (3.17) - after trivial corrections for the factor $\frac{k_1}{k_0}$ (see (3.4)), the sample self-attenuation and the energy-dependent detector efficiency - are determined separately. Then an intensity ratio involving the two integrals can be defined,

$$\mathrm{EISF} = I^{\mathrm{el}}/(I^{\mathrm{el}} + I^{\mathrm{in}}) = AS^{\mathrm{el}}_{\mathrm{inc}}(\boldsymbol{Q})/[A \int S_{\mathrm{inc}}(\boldsymbol{Q}, \omega)\mathrm{d}\omega] \tag{3.18}$$

where A is a normalization factor proportional to experiment parameters such as the incident neutron flux, the sample size, the detector efficiency, the duration of the measurement, etc. Obviously, the difficulty of an absolute intensity calibration is avoided in the determination of the EISF by (3.18): The normalization factor cancels, the integral of the incoherent scattering function is equal to 1, and we simply have $\mathrm{EISF} = S^{\mathrm{el}}_{\mathrm{inc}}(\boldsymbol{Q})$. Here, we have used (3.17) and (3.18) as a starting point for obtaining a definition of the EISF. The coefficient $S^{\mathrm{el}}_{\mathrm{inc}}(\boldsymbol{Q})$ in these two equations is the EISF in its most general form, since it includes all the motions of the scattering atom.

However, the determination of this "global" EISF is generally not the immediate aim of an experiment, for the following reasons. First of all, one is often more interested in specific types of motions than in all of them. Secondly, an unambiguous measurement of a global EISF is not easily achieved in just one single experiment. Every measurement has a well-defined energy resolution connected with an effective energy transfer window (see the corresponding discussion later in this section). Essentially only the dynamics of the specific motions occurring in this energy range are visible, because much slower motions are hidden within the energy resolution function, whereas

much faster motions appear only as a flat background. This can be used to experimentally isolate the effect of a specific motion. It is therefore much more interesting to apply the EISF concept to the elastic component of each specific type of motion, e. g. to molecular rotation, rather than to the combined effect of all atomic motions. The expression to be used for the analysis of such specific motions is formally the same as (3.18). However, we have to replace the nonelastic integral (I^{in}) by the corresponding quasielastic integral (I^{qe}), and keep in mind that the incoherent scattering function, $S_{\mathrm{inc}}(\boldsymbol{Q}, \omega)$, must now be replaced by a partial scattering function consisting merely of an elastic term (measured integral: I^{el}) and a quasielastic term (measured integral: I^{qe}) corresponding to the specific motion under study. The effect of faster motions has been subtracted as a flat "inelastic" background and only appears as an attenuating Debye-Waller factor bound to be cancelled, because it is included in the normalization factor A. The feasibility conditions are that i) the energy resolution is adapted to the time scale of the motion of interest, ii) this motion is sufficiently well separated on the energy-scale from other motions of the same atom, and iii) the assumption of dynamical independence of the different modes from each other, e. g. rotations and vibrations, represents an acceptable approximation (see (3.64), Sect. 3.9). It is this possibility of isolating the EISF of specific modes of motions that has proved to be of most practical importance for the development of the technique. The success of a series of prototype experiments is documented in the original literature [9–13].

The EISF method was developed as a strategy for finding the appropriate differential equations and their boundary conditions for the dynamical mechanisms of localized atomic motions in condensed systems. These early and subsequent experiments have been reviewed extensively [14–16]. In [16] the importance of the dynamic independence approximation for the definition of the EISF of specific motions, the relation between Debye-Waller factor, Lamb-Mößbauer factor and EISF, as well as the observation-time dependence of the latter are discussed in detail. More general discussions of Van Hove's theory and its application can be found in text books; see, e. g. [3,17]. It is interesting to note, that the EISF concept also plays a role in pulsed-field gradient (PFG) NMR studies of diffusion in confined volumes, where at sufficiently large observation time the spin-echo attenuation approaches a time-independent value conveying geometrical information on the spatial restriction (see (10.18) of Chap. 10).

In our explanation we have interpreted the nuclear motion in terms of classical time-dependent coordinates. What does this mean? The average de Broglie wavelength of the scattering nucleus with a mass M is given by

$$\lambda_M = \frac{h}{v_{\mathrm{th}} M} \approx h(2Mk_{\mathrm{B}}T)^{-1/2} \,, \tag{3.19}$$

if this particle moves with the average speed v_{th} within a sample at temperature T. A classical description of the nuclear motion is certainly valid for

times during which the particle has passed a distance which is larger than its de Broglie wavelength: $tv_{\mathrm{th}} > \lambda_M$. For instance, at 300 °C (3.19) yields

$$t \geq \frac{h}{2k_{\mathrm{B}}T} \approx 10^{-13}\ \mathrm{s}\ . \tag{3.20}$$

This holds in all cases to be discussed in the following, i.e. for typical diffusive jump rates $< 10^{12}\ \mathrm{s}^{-1}$ or diffusion coefficients $D_{\mathrm{s}} < 10^{-8}\ \mathrm{m}^2/\mathrm{s}$. On the other hand, the criterium fails for the atomic vibrations in solids with frequencies above $10^{13}\ \mathrm{s}^{-1}$. In this case, the quantum mechanical meaning of the Van Hove correlation functions or the usual matrix element description is preferable.

Let us now turn to the problem of experimental resolution. (3.12) and (3.13) represent a Fourier analysis of the neutron scattering functions $S(\boldsymbol{Q}, \omega)$ and $S_{\mathrm{inc}}(\boldsymbol{Q}, \omega)$, respectively, with the Van Hove correlation functions in space and time as coefficients. We draw the attention to the fact that the scattering functions, i. e. the dynamic structure factors S and S_{inc} defined in (3.4) to (3.13), as well as the corresponding correlation functions G, G_s, and the intermediate scattering functions I, I_s, cannot be determined experimentally in their pure forms: The measured scattering functions are broadened due to convolution with the experimental resolution functions $R(\boldsymbol{Q}, \omega)$ in the four-dimensional $(\boldsymbol{Q}, \omega)$-space. In the case of incoherent scattering, the $\boldsymbol{Q}$-spread of the resolution can often be neglected when the studied functions are only slowly varying with Q. Then it is sufficient to merely deconvolute the measured spectra from the energy resolution function $R(\omega)$. The latter may have a shape close to a Gaussian or a Lorentzian, with an energy width $\Delta(\hbar\omega)$ defined as the half-width at half maximum (HWHM). Note that this width is connected, by the uncertainty relation, with the experimental observation time Δt which is the decay time of the observation function $R^*(t)$ in the Fourier time domain [15–18]:

$$\Delta(\hbar\omega)\Delta t \cong \hbar \tag{3.21}$$

While the resolution function $R(\omega)$ has the effect of broadening the neutron scattering function along the energy transfer coordinate of the experiment, the observation function $R^*(t)$ is a factor, which increasingly attenuates the corresponding correlation function with increasing Fourier time: $R^*(t)$ is the Fourier transform of $R(\omega)$ and is therefore in most practical cases a function essentially decaying with increasing time. The net effect is, that the correlation functions are observed in a Fourier time window, with an upper limit determined by the decay time constant of the observation function. The low-time limit of this window has a different origin: it is a consequence of the (always limited) statistical accuracy of the measurement, because quasielastic intensities typically decrease with increasing energy transfer, and therefore counting statistics become the poorer the larger the energy transfers are as compared to the energy-resolution width.

Let us consider an example, in order to illustrate the implications of experimental resolution in the study of dynamic structure on the basis of the Van Hove formalism (see for instance (3.11), (3.13)). We assume, for simplicity, that the scattering particle carries out a random motion described by a superposition of several components with n different rates, λ_1, λ_2, ..., λ_n. The scattering function will then be a sum of bell-shaped Lorentzians centered at zero energy transfer (see the following sections). If this quasielastic spectrum is studied with an instrument resolution $\Delta(\hbar\omega)$, the resulting resolution-broadened spectrum is again a bell-shaped curve, but with a width larger than $\Delta(\hbar\omega)$. This "quasielastic peak" will be dominated by contributions from those motions which have rates $\lambda_i \sim \Delta(\hbar\omega)$. While much slower motions are hidden within the resolution function, much faster motions will produce only a flat "background" which cannot be easily distinguished from the usual constant background of the experiment. In order to be able to extract information on all relevant motional components, one needs to carry out several measurements with properly chosen resolutions. This procedure may in practice require the application of more than one type of spectrometer. Quasielastic neutron scattering spectra obtained with one single energy resolution only usually furnish incomplete information. The analysis may therefore easily lead to wrong conclusions.

Since $\Delta(\hbar\omega)$ is related in a simple way to the instrumental energy spreads of incident and scattered neutrons, the observation time, Δt, is connected with (although not equal to) the coherence time of the incident neutron wave packet. The principle of experimental observation time, energy and Fourier time windows in quasielastic neutron scattering, and their relevance for the determination of dynamic structure, and especially in problems concerning diffusive atomic and molecular motions in condensed matter, has been discussed more extensively in [16] and [18]. For further detailed literature related to the Van Hove concept and quasielastic neutron scattering we refer to the reviews, monographs and books specially devoted to this topic [3, 14, 15, 17, 19–21].

Finally, we note a complication due to the fact that an atomic species consists of isotopes with different scattering lengths $b_1, b_2 \ldots$ and concentrations $c_1, c_2 \ldots$. Therefore the sum in (3.6) includes terms with different scattering lengths, randomly distributed over the sites $\boldsymbol{r}_i$. This randomness of the amplitudes destroys part of the interference. A similar effect is caused by the spin of the nuclei and of the neutron, because the scattering length depends on their relative orientation. This leads to scattering lengths b_+ and b_- corresponding to parallel and anti-parallel orientation with fractions $c_+ = (I+1)/(2I+1)$ and $c_- = I/(2I+1)$, respectively, where I is the nuclear spin. If nuclei and/or neutron spins are unpolarized, this gives a random distribution of b_+ and b_-. Randomness destroys part of the interference and for ideal disorder the cross section can be separated into a coherent part with interference terms due to pairs of atoms (including the self-terms) and

an incoherent part where interference between waves scattered by different nuclei has completely cancelled out, such that the differential cross-section reads

$$\frac{\mathrm{d}^2\sigma}{\mathrm{d}\Omega\mathrm{d}\omega} = \frac{k_1}{k_0}\left[\frac{\sigma_{\mathrm{coh}}}{4\pi}S_{\mathrm{coh}}(\boldsymbol{Q},\omega) + \frac{\sigma_{\mathrm{inc}}}{4\pi}S_{\mathrm{inc}}(\boldsymbol{Q},\omega)\right] . \tag{3.22}$$

The coherent scattering function, $S_{\mathrm{coh}}(\boldsymbol{Q},\omega)$ in the first term, is due to the atom-atom pair-correlations, whereas the incoherent scattering function, $S_{\mathrm{inc}}(\boldsymbol{Q},\omega)$ in the second term [2], only conveys self-correlations and therefore behaves *as if* not amplitudes but intensities from scattering by different nuclei had to be added.

One can easily show that the total scattering cross sections σ_{coh} and σ_{inc} have the following meaning

$$\sigma_{\mathrm{coh}} = 4\pi\bar{b}^2 \qquad \text{with} \qquad \bar{b} = \sum c_i b_i \ , \tag{3.23}$$

$$\sigma_{\mathrm{inc}} = 4\pi\left(\overline{b^2} - \bar{b}^2\right) \qquad \text{with} \qquad \overline{b^2} = \sum c_i b_i^2 \ . \tag{3.24}$$

In the following section we mainly deal with the incoherent dynamic structure factor. In particular, for hydrogen the incoherent scattering cross section is between 10 and 20 times larger than other scattering cross sections, such that the separation of S_{inc} is especially easy. We point out that the specification "incoherent" is somewhat misleading. In order to calculate the scattered intensities the amplitudes have to be added and the sum has to be squared. Disorder leads to a (partial) cancellation of the cross terms with phase factors. Consequently, the intensities are summed up with reduced interferences. The total coherent and incoherent scattering cross-sections are empirically known and a great number can be found in tables [22](for a review on the fundamental aspects of neutron-nucleus scattering see [23]).

3.3 The Rate Equation and the Self-Correlation Function

A model was originally proposed by Chudley and Elliott [24], to obtain the classical self-correlation function $G_{\mathrm{s}}(\boldsymbol{r},t)$ for an atom diffusing on an assumed quasi-crystalline lattice of a liquid. This so-called CE-model was then widely used for treating atomic diffusion on interstitial lattices in crystals.

We first calculate the probability $P(\boldsymbol{r}_m,t)$ to find the diffusing atom on a site $\boldsymbol{r}_m$ of a Bravais lattice at time t, where it spends a time τ on the average. The time τ_{j} required for the diffusive jump from site to site is neglected. The jumps occur between a given site and its neighbours $\boldsymbol{r}_m + \boldsymbol{d}_\nu$ where $\boldsymbol{d}_\nu$ $(\nu = 1, 2, \ldots s)$ is a set of jump vectors connecting the site with the neighbours. The master equation for $P(\boldsymbol{r}_m,t)$ is then (see Fig. 3.3)

[2] Note that the following notations for the scattering functions (dynamic structure factors) are customary in the literature : $S(\boldsymbol{Q},\omega)$ or $S_{\mathrm{coh}}(\boldsymbol{Q},\omega)$ for coherent, and $S_{\mathrm{s}}(\boldsymbol{Q},\omega)$ or $S_{\mathrm{inc}}(\boldsymbol{Q},\omega)$ for incoherent scattering.

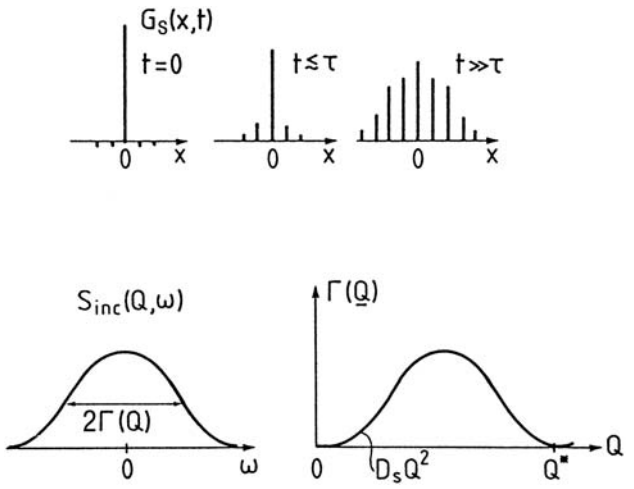

Fig. 3.3. Top: $G_\mathrm{s}(x,t)$ for a regular lattice. The height of the solid lines describes the probability of occupancy per unit cell. Asymptotically, the envelope approaches a Gaussian. τ is the mean rest time at a site.
Bottom: $S_\mathrm{inc}(Q,\omega)$ and quasielastic width Γ vs. scattering vector Q (schematic). Q^* is the reciprocal lattice vector for $\Gamma = 0$ and D_s is the self-diffusion coefficient.

$$\frac{\partial P(\boldsymbol{r}_m,t)}{\partial t} = -\frac{1}{\tau}P(\boldsymbol{r}_m,t) + \frac{1}{s\tau}\sum_{\nu=1}^{s} P(\boldsymbol{r}_m+\boldsymbol{d}_\nu,t)\ . \tag{3.25}$$

The first and second term on the right side are the loss and growth rate due to the jumps to and from adjacent sites, respectively. In order to obtain $G_\mathrm{s}(\boldsymbol{r},t)$ we impose the initial condition

$$P(\boldsymbol{r}_m,0) = \delta(\boldsymbol{r}_m) \tag{3.26}$$

Because in a Bravais lattice all sites are equivalent, we directly obtain the self-correlation function as the solution of the master equation: $G_\mathrm{s}(\boldsymbol{r},t) \equiv P(\boldsymbol{r}_m,t)$. The basic CE-model (represented by (3.25)) has been extended for many special and more complex situations, for instance to include effects due to ion-ion correlations in ionic conductors; see (3.61) to (3.63) in Sect. 3.8. A general theory of the master equation is given in Chap. 18. The approximation $\tau_\mathrm{j} \ll \tau$ holds in most cases. For a H atom at room temperature one gets

$$\tau_\mathrm{j} \cong \frac{d}{v_\mathrm{th}} = d\left(\frac{M}{2k_\mathrm{B}T}\right)^{1/2} \cong 10^{-13}\ \mathrm{s} \tag{3.27}$$

whereas normally $\tau \geq 10^{-12}$ s. Only in certain cases, e.g. for hydrogen in vanadium at high temperatures, τ and τ_j are comparable and the diffusion coefficient D_s has values above 10^{-9} m^2/s, similar to diffusion coefficients in

liquids. Equation (3.25) further assumes that subsequent jumps are uncorrelated. Finally, blocking and mutual interaction effects are neglected which implies a low site occupancy c for the diffusing particles. One could improve the calculation with respect to correlations between different particles, replacing – as a meanfield approximation – τ by $\tau/(1-c)$, where $(1-c)$ is the blocking factor. Correlated jumps are discussed in Sects. 3.8 to 3.10, and in Chaps. 1, 10, 18 and 21. Now we introduce the Fourier transform

$$P(\boldsymbol{r}_m, t) = \int \tilde{P}(\boldsymbol{Q}, t) \mathrm{e}^{-\mathrm{i}\boldsymbol{Q}\boldsymbol{r}_m} \mathrm{d}\boldsymbol{Q}, \tag{3.28}$$

where $\tilde{P}(\boldsymbol{Q}, t) \equiv I_s(\boldsymbol{Q}, t)$ from (3.7).

This leads to a differential equation of 1st order for $\tilde{P}(\boldsymbol{Q}, t)$ whose solution is an exponential decay function

$$\tilde{P}(\boldsymbol{Q}, t) = \mathrm{e}^{-\Gamma(\boldsymbol{Q})t} \ , \tag{3.29}$$

which fulfils the initial condition (3.14). From this one gets

$$\Gamma(\boldsymbol{Q}) = \frac{1}{s\tau} \sum_{\nu=1}^{s} (1 - \mathrm{e}^{-\mathrm{i}\boldsymbol{Q}\boldsymbol{d}_\nu}) \ . \tag{3.30}$$

The resulting dynamic structure factor is the Fourier transform of $\tilde{P}(\boldsymbol{Q}, t) = I_{\mathrm{S}}(\boldsymbol{Q}, t)$, namely a normalized Lorentzian

$$S_{\mathrm{inc}}(\boldsymbol{Q}, \omega) = \frac{\Gamma/\pi}{\omega^2 + \Gamma^2} \ , \tag{3.31}$$

with halfwidth $\Gamma(\boldsymbol{Q})$. For a simple cubic Bravais lattice one gets the expression

$$\Gamma(\boldsymbol{Q}) = \frac{1}{3\tau} \left(3 - \cos(Q_x d) - \cos(Q_y d) - \cos(Q_z d)\right) \ . \tag{3.32}$$

$Q_{x,y,z}$ are the components of $\boldsymbol{Q}$. For $Q \ll 1/d$, where d is the length of the jump vector, one gets the limiting case

$$\Gamma(\boldsymbol{Q}) = \frac{d^2}{6\tau} Q^2 = D_{\mathrm{s}} Q^2 \ . \tag{3.33}$$

This relation holds generally and is independent of the detailed jump geometry, except for "exotic" conditions (e.g. if the diffusion occurs in planes and the jumps between neighbouring planes occur with a very small probability; see Sect. 3.11).

$\Gamma(\boldsymbol{Q})$ is periodic in reciprocal space. It has a maximum at the Brillouin zone boundary and it is zero, if a reciprocal lattice point $\boldsymbol{G}$ is reached, such that $\Gamma(\boldsymbol{Q} = \boldsymbol{G}) = 0$. This "line narrowing" [3] is related to Bragg diffraction of the neutron wave from the probability density of the proton distributed over the sites of the Bravais lattice. Obviously, the zero width at the reciprocal

[3] This effect should not be confused with the coherent line narrowing described in Sect. 3.12.

lattice point is a consequence of the condition under which this theoretical result has been obtained[4], namely the assumption of infinitely high energy and momentum resolution and therefore infinitely large observation time and observation volume. In a real experiment, with finite resolution – just as in coherent Bragg diffraction – the zero width cannot be directly observed. All measured widths are finite, but for sufficiently good resolution, the periodic oscillatory behaviour of the diffusion linewidth due to this diffraction effect is nevertheless qualitatively retained. After correction for the effects of resolution, the theoretical line narrowing is indeed recovered (see below).

Let us consider a practical example. For instance, for a 1 μeV resolution width (e.g. FWHM of a Lorentzian resolution function, corresponding to a single exponential observation function) the observation time is as long as $0.66 \cdot 10^{-9}$ s. During this time a particle diffusing on an interstitial Bravais lattice may thus be spread out over a regular arrangement of about 10^3 sites. Consequently, during the same period the neutron wave packet is diffracted on this extended "crystal-like" single-proton probability density distribution. The time-evolution of the correlation function and the shape of the quasielastic spectrum are shown schematically in Fig. 3.3.

As concerns the Fourier transform in $\boldsymbol{Q}$ the main contribution from the integrand in (3.13) results from a range $\boldsymbol{Q}\boldsymbol{r}_\mathrm{G} < 1$ (contributions for larger $\boldsymbol{Q}$ at fixed $\boldsymbol{r}_\mathrm{G}$ cancel by rapid oscillations of the integrand, if G_s is for instance a Gaussian distribution with "radius" $\boldsymbol{r}_\mathrm{G}$ in space). Consequently, the volume where G_s is "observed" by a scattering experiment is about $1/Q^3$. In particular, measurements on diffusing atoms at small Q image the diffusion over large distances and yield the self-diffusion coefficient only, whereas the results for large Q values predominantly yield information on a single diffusive step or on a few steps. The smallest Q values accessible in experiments are of the order of 0.1 $\mathrm{Å}^{-1}$. This implies that the scattering process "observes" the diffusing ion in a volume of the order of $(10\ \mathrm{Å})^3$. For a diffusive process, about $z \cong (Q\ell)^{-2} \approx 150$ jumps come into play, if a jump length ℓ of 2 Å is assumed. Consequently, the self-diffusion coefficient from the quasielastic width for small Q is a bulk quantity, and grain boundaries (see Chap. 8) will not influence the result, in contrast to macroscopic methods.

There are of course more complicated situations than that described by (3.25), for instance a bcc lattice with 6 non-equivalent interstitial lattices which are interconnected. Here, the dynamic structure factor includes 6 eigenvalues and Lorentzians. For $Q \to 0$ again a single Lorentzian remains with $\Gamma = Q^2 D_\mathrm{s}$ ([25], see Fig. 3.11). The complicated case of a non-cubic lattice with a great number of inequivalent sites was treated for α-$\mathrm{La}^{60}\mathrm{Ni}_5\mathrm{H}_x$. In this case [26], one calculates 9 eigenvalues. Part of them correspond to nearly

[4] Theoretical models for neutron scattering functions are usually derived neglecting experimental resolution; the latter is introduced a posteriori in the analysis of the measured spectra.

localized motions, which means that the corresponding quasielastic width is almost independent of Q.

3.4 High Resolution Neutron Spectroscopy

In neutron scattering spectrometers, the wavelength, velocity or energy of neutrons have to be defined before scattering, and analyzed afterwards. Three methods are being used: Crystal Bragg reflection (XTL), neutron time-of-flight (TOF), or neutron spin-echo (NSE). In the majority of quasielastic neutron scattering experiments the scattering function, $S(\boldsymbol{Q},\omega)$, is measured by TOF spectrometry with resolutions from about 1 μeV to a few 1000 μeV, or by backscattering (BSC) spectroscopy, with resolutions of the order of 0.1 μeV to 1 μeV. This allows to cover, by quasielastic neutron scattering, a range of diffusion coefficients between 10^{-12} m^2/s and 10^{-8} m^2/s, or, correspondingly, of characteristic times from 10^{-9} s to 10^{-13} s. In certain cases, also the NSE method can be used, which permits the direct determination of the intermediate scattering function, $I(\boldsymbol{Q},t)$, instead of $S(\boldsymbol{Q},\omega)$. This technique extends the Fourier time scale up to 10^{-7} s, corresponding to an energy resolution limit in the neV region, where diffusion coefficients of the order of 10^{-13} m^2/s can be measured. For detailed descriptions of the NSE-technique, see [27] and Chap. 13. The TOF and BSC methods will be explained in the following.There are different techniques of neutron time-of-flight spectrometry. XTL-TOF spectrometers [28] use a crystal monochromator to create a continuous monochromatic beam. This is then periodically chopped with a disk or Fermi chopper, before it hits the sample. The energy distribution of the scattered neutrons is obtained by measuring their time-of-flight from the sample to the detectors. The latter should be sufficiently thin, to make their contribution to the flight-time uncertainty negligible. The detectors cover a large range of solid angle and of Q-values. This type of time-of-flight instrument (Fig. 3.4) is characterized essentially by four parameters: The incident neutron wavelength λ_0, its uncertainty $\Delta\lambda_0$, the pulse width $\Delta\tau_\mathrm{p}$, and the pulse repetition rate ν, typically several 100 Hz. While the wavelength uncertainty is due to the divergence of the neutron beam incident on, and reflected from the monochromator, the pulse width is defined by the chopper; typical values are $\Delta\tau_\mathrm{p} = 20$ to 50 μs. In Fig. 3.5 a neutron time-of-flight diagram is shown for a flight path L (of the order of several meters) extending from the sample to the detectors.

The pulse repetition rate is limited by the frame overlap, which means the superposition of the fastest neutrons within a certain cycle and the neutrons scattered with energy loss from the previous one (velocity v_min). This requires

$$\frac{1}{\nu} = \frac{L}{v_\mathrm{min}} \ . \tag{3.34}$$

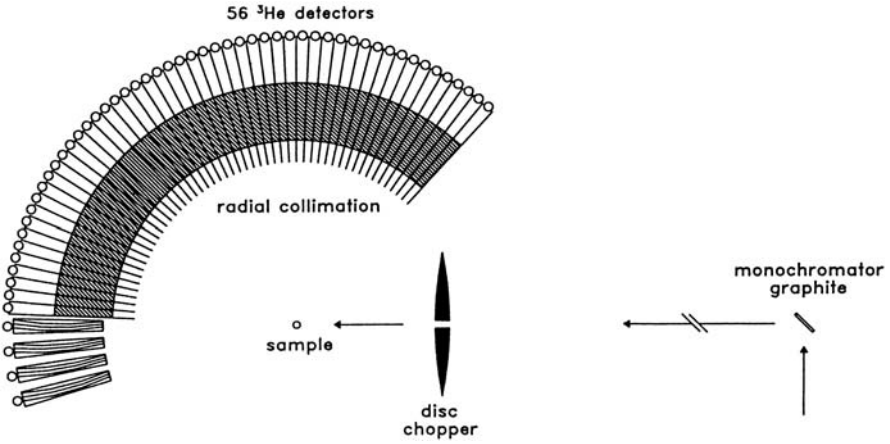

Fig. 3.4. Typical time-of-flight spectrometer with Bragg monochromator at the FRJ-2 reactor. E_0 is selected by a Bragg monochromator crystal, E_1 by measuring the flight time.

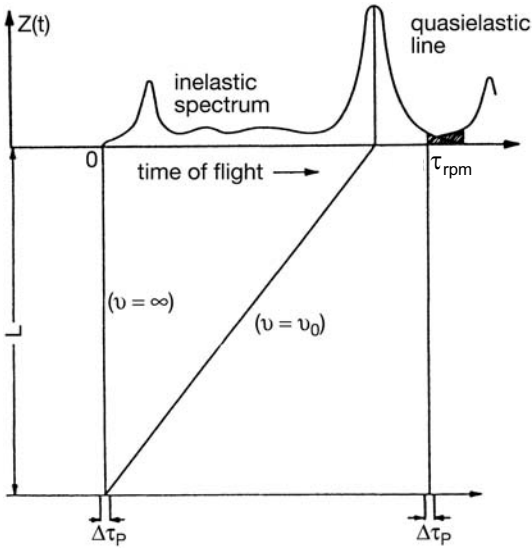

Fig. 3.5. Time schedule for a time-of-flight spectrometer. $\Delta\tau_\mathrm{p}$ = pulse length, L = flight path after scattering, τ_rpm = cycle length. $\nu = 1/\tau_\mathrm{rpm} = v_\mathrm{min}/L$ = repetition rate. Shaded: frame overlap. $v = v_0$ corresponds to zero energy transfer $\hbar\omega = 0$. The incident energy E_0 is selected by Bragg reflection from a monochromator crystal.

The choice of v_min depends on the decay of the quasielastic spectrum on the low-energy side. Obviously, the parameters $\Delta\lambda_0$, ν, *and* $\Delta\tau_\mathrm{p}$ determine the

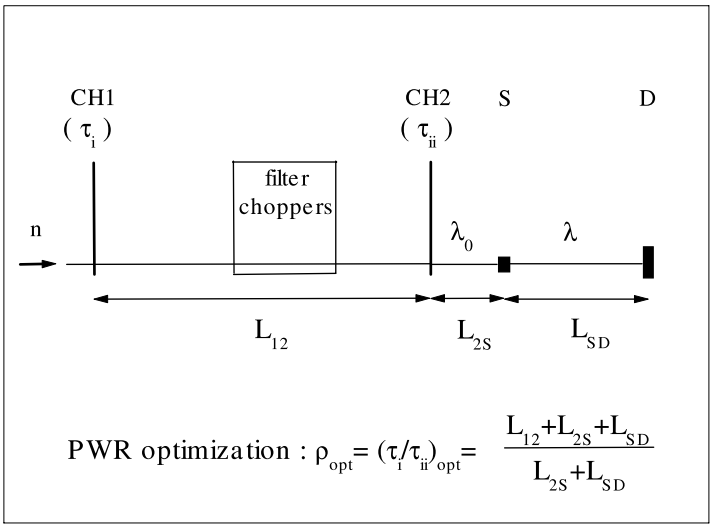

Fig. 3.6. Schematic sketch of a multi-disk chopper time-of-flight (MTOF) spectrometer: CH1 and CH2 are the two principal choppers defining the monochromatic neutron pulse and its wavelength bandwidth; S = sample, D = detectors; L_{12}, L_{2S}, and L_{SD} are the distances between these elements of the instrument; τ_i and τ_{ii} are the widths of the pulses created by CH1 and CH2, λ_0, λ the incident and scattered neutron wavelenths (after [29]). Inset: the pulse-width ratio (PWR) optimization formula for elastic and quasielastic scattering [30]. Typical instruments of this type are IN5 at ILL in Grenoble, MIBEMOL at LLB in Saclay, and NEAT at HMI in Berlin.

average count rate at the detectors, while two of them, $\Delta\lambda_0$ and $\Delta\tau_\mathrm{p}$, govern the energy resolution.

As already mentioned, the incident neutron beam of the XTL-TOF spectrometer is monochromatized by Bragg reflection. It selects a certain wave number $k_0 = mv_0/\hbar$ for a given Bragg angle Θ and reciprocal lattice vector $\boldsymbol{G}$, following the Bragg equation

$$|\boldsymbol{G}| = 2k_0 \sin\Theta \ . \tag{3.35}$$

Alternatively, in the case of a TOF-TOF spectrometer, both v_1 and v_0 are selected by time-of-flight by (at least) two choppers in front of the sample, with a mutual phase shift which determines v_0. Such a multi-disk chopper time-of-flight (MTOF) instrument is illustrated in Fig. 3.6.

The two principal choppers, CH1 and CH2, the sample S and the detectors D are separated by the distances L_{12}, L_{2S}, and L_{SD}, respectively. CH1 and CH2 create neutron pulses with widths τ_i and τ_{ii} and define the incident neutron wavelength λ_0; the scattering processes cause neutron wavelength shifts to smaller or larger values of λ.

For a given incident neutron wavelength, the total intensity at the detectors is essentially governed by the factor $(\tau_i \tau_{ii})$, i.e. by the product of the two chopper opening times [30] (see also: [31]). The latter also control the resolution, and thus intensity and resolution are connected through these parameters. The most important and unique feature of this type of instrument is the capability of varying the energy resolution continuously over several orders of magnitude (see above). The energy resolution width (HWHM) at the detector [30], i.e. the uncertainty in the experimentally determined energy transfer $\hbar\omega$, is given by

$$\Delta(\hbar\omega)\,[\mu\mathrm{eV}] = 647.2(A^2 + B^2 + C^2)^{1/2}/(L_{12} L_{SD} \lambda^3)/2\,, \tag{3.36}$$

where

$$A = 252.78\ \Delta L\ \lambda\ L_{12}\,, \tag{3.37}$$

$$B = \tau_i (L_{2S} + L_{SD}\lambda^3/\lambda_0^3)\,, \tag{3.38}$$

$$C = \tau_{ii} (L_{12} + L_{2S} + L_{SD}\lambda^3/\lambda_0^3)\,. \tag{3.39}$$

ΔL is the uncertainty of the length of the neutron flight path, which is mainly due to beam divergence, sample geometry and detector thickness. The quantities L_{12}, L_{2S}, L_{SD}, ΔL must be given in m, λ_0 and λ in Å and τ_i, τ_{ii} in μs. It follows from these expressions, that the energy dependent resolution, for given λ_0, strongly depends on the scattered neutron wavelength λ, whereas the total intensity, as an integral property of the spectrometer, has no such dependence. Furthermore, high resolution is favoured by short pulse widths and by large values of the distances L_{12} and L_{SD}. If these distances are fixed, and if sample geometry, λ_0 and energy transfer have been chosen, then total intensity and resolution-width only depend on the chopper opening times τ_i and τ_{ii}. Best instrument performance regarding intensity and resolution is achieved not only by selecting suitable values of the individual pulse widths, τ_i and τ_{ii}, but also requires the optimization of their ratio (pulse-width ratio (PWR) optimization [30], [32]). The optimization formula for elastic and quasielastic scattering is shown as an inset in Fig. 3.6.

The μeV-regime is covered by back scattering spectrometry [33–35], which was invented by H. Maier-Leibnitz. BSC-spectrometers are XTL-XTL instruments, i.e. they employ single-crystals as monochromators *and* as analyzers, with Bragg angles close to $\pi/2$ in both cases. For a given incident divergence of the beam, $\Delta\Theta$, the wave number spread produced by reflection from a crystal is given by differentiating (3.35)

$$\frac{\Delta k_{\mathrm{div}}}{k} = \cot\Theta\ \Delta\Theta\ . \tag{3.40}$$

This relation is shown in Fig. 3.7 together with the presentation of the Bragg law in reciprocal space. For typical Bragg angles and $\Delta k_{\mathrm{div}}/k \approx 10^{-2}$ radian one achieves an energy resolution in the percent range. However, for Θ approaching $\pi/2$, Δk_{div} from (3.40) goes to zero and we have to include the curvature of $\sin\Theta$ which leads to a second order contribution (see Fig. 3.7)

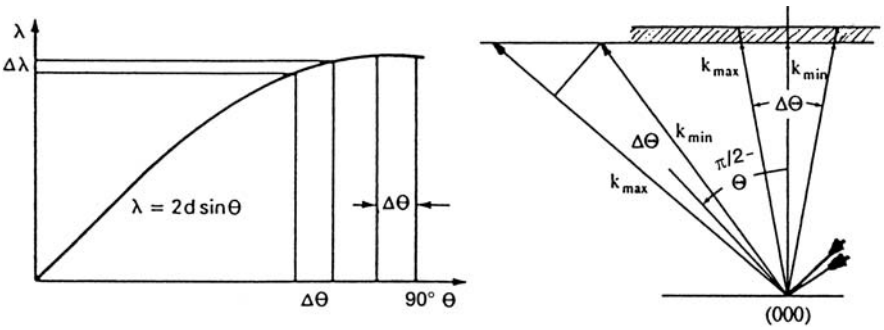

Fig. 3.7. Bragg law and Bragg reflection on a single crystal monochromator in reciprocal space, for Θ_{B} *off* 90°, and for $\Theta_{\mathrm{B}} \approx 90°$ where k depends only in 2nd order on $\Delta\Theta$. Vertical line: $\boldsymbol{G}$ = reciprocal lattice vector. Width of shaded region: Darwin width due to extinction.

$$\frac{\Delta k_{\mathrm{div}}}{k} = \frac{(\Delta\Theta)^2}{8} \quad \text{for} \quad \Theta \to \frac{\pi}{2} \,. \tag{3.41}$$

This situation is called "backscattering" which means that the incident and the Bragg reflected beam are practically antiparallel. The square relation (3.41 replaces the linear relation between Δk_{div} and $\Delta\Theta$: The intensity is proportional to the incident solid angle $(\Delta\Theta)^2$, and we have $(\Delta\Theta)^2 \propto \Delta k_{\mathrm{div}}$ instead of $\Delta\Theta \propto \Delta k_{\mathrm{div}}$, which is valid for Bragg angles other than $\pi/2$. This means that under these conditions resolution and intensity are decoupled in first order.

Actually, the wavevector spread is larger than Δk_{div}. Only a finite number of lattice planes contributes to the Bragg line, which causes a finite width of $\boldsymbol{G}$, the so-called Darwin or extinction width [36], namely

$$\frac{\Delta k_{\mathrm{ex}}}{k} = \frac{16\pi N_{\mathrm{c}} F_G}{G^2} \,, \tag{3.42}$$

where F_G is the structure factor for the Bragg reflection at $\boldsymbol{Q} = \boldsymbol{G}$, N_{c} is the number of lattice cells per unit volume. As an approximation, both contributions can be added such that

$$\frac{\Delta E_0}{E_0} = 2\left[\frac{(\Delta\Theta)^2}{8} + \frac{16\pi N_{\mathrm{c}} F_G}{G^2}\right] \,. \tag{3.43}$$

For neutrons from a Ni neutron guide and reflection on an ideal silicon waver one calculates $\Delta E_0 = (0.24 + 0.08)\,\mu$eV. For the resolution in energy transfer, $\Delta(\hbar\omega)$, of a modern BSC-spectrometer, one obtains values between $0.09\,\mu$eV and $0.43\,\mu$eV (HWHM), depending on the type of crystals used [35]. So far such values have not been reached by any other crystal spectrometer; they will, however, be achieved also by high-resolution TOF-TOF instruments at future spallation sources [29]. The Bragg angle is fixed at 90°, and the energy

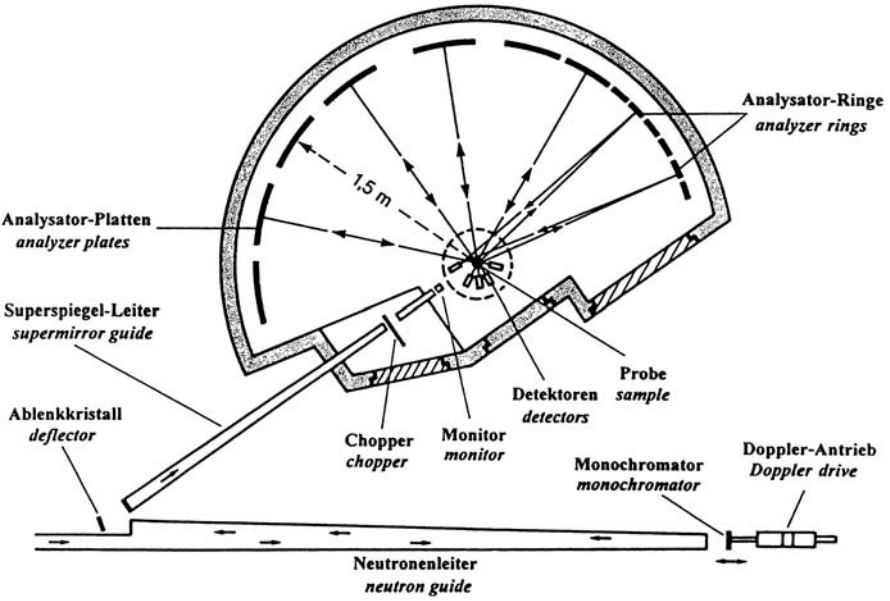

Fig. 3.8. Backscattering spectrometer at the Jülich FRJ-2 reactor. The Bragg angles at the silicon single crystals (before and after scattering of the neutrons by the sample) are close to 90°. Other well-known spectrometers of this type are IN10, IN13 and IN16 at the ILL in Grenoble, and HFBS at NIST in Gaithersburg.

scan is performed by a Doppler drive, moving the monochromator crystal with a speed v_{D}. The resulting energy shift is [37]

$$\frac{\delta E_0}{E_0} = 2\frac{v_{\mathrm{D}}}{v_0} \tag{3.44}$$

which yields an energy window of $\delta E_0 = \pm 15$ μeV for $v_{\mathrm{D}} = 2.5$ m/s and $\lambda_0 = 6.3$ Å.

Fig. 3.8 shows the backscattering spectrometer built at the Jülich FRJ-2 reactor. Cold neutrons are produced in a liquid hydrogen source which moderates the neutrons from the D_2O reflector and transfers the spectrum from an effective temperature close to room temperature to about 20 to 40 K. The resulting intensity gain factor in the desired low-energy spectrum is between 7 and 15. The monochromator crystal (10×10 cm^2) is fixed on a sinusoidally moving Doppler drive. The backscattered neutrons are separated from the incident beam by a (broad band) copper single crystal which reflects the whole energy range of about 30 μeV covered by the Doppler motion. The monochromatic neutrons, falling onto the sample, being scattered, and finally detected, are individually labeled with the corresponding instantaneous speed of the Doppler drive. The neutrons scattered by the sample are backscattered by spherical shells of Si crystals and thus focussed into a set of BF_3 counters.

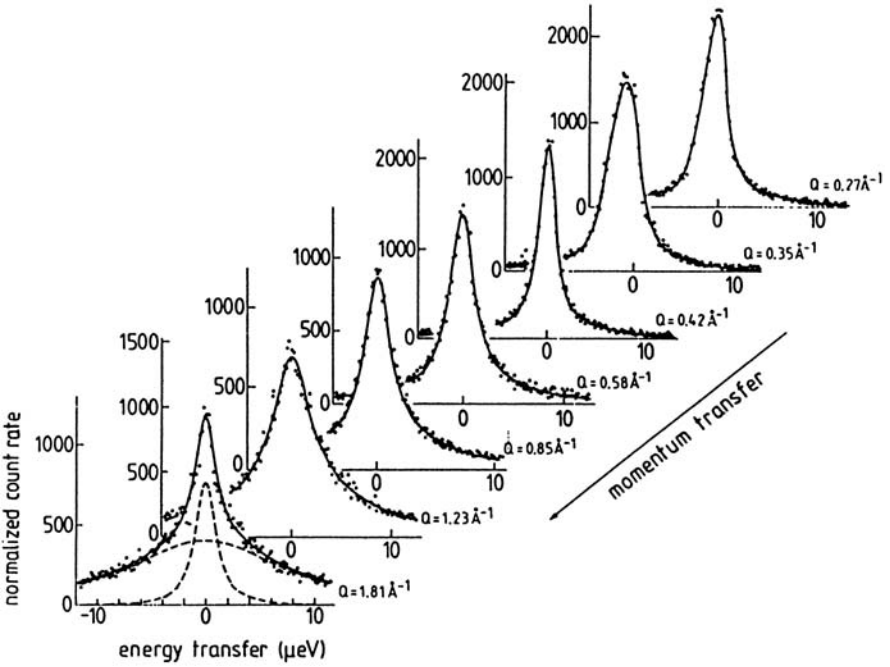

Fig. 3.9. Typical quasielastic spectra measured with backscattering spectrometry in the μeV-region on hydrogen diffusing in ZrV_2 for several scattering vectors Q. Dashed narrow line: Resolution curve of the spectrometer. Dashed broad line: Quasielastic component due to rapid non-diffusive motion at large Q (see Sect. 3.5) [38].

Each counter corresponds to a certain scattering angle or Q-value. To avoid that the scattered neutrons are directly falling onto the counters (before they have been filtered by the Si analyzers), the incident beam is periodically interrupted by a chopper, in phase with the Doppler movement. Only when the beam is closed, the consecutively scattered and analyzed neutrons reach the counters. Fig. 9 presents typical quasielastic spectra for hydrogen diffusing in an alloy, measured with μeV resolution at different Q values.

Very often the energy range is too narrow. The reflected neutron energy can be additionally shifted by heating the monochromator, thus increasing the lattice parameter, and/or using monochromators whose lattice parameter is somewhat smaller or bigger than that of the silicon analyzer [39]. In this way, the range of the spectrometer (and also the resolution) can be adapted to the problems.

Sometimes, backscattering spectrometers are used with the Doppler drive *at rest*. In such a measurement one determines the intensity for the spectrometer set at $\omega = 0$, i.e. the convolution integral $I(\omega = 0) = (S \otimes R)$, where S is the neutron scattering function and R is the energy resolution function. For a Lorentzian-shaped spectrum as in (3.31), $S_{\mathrm{inc}}(Q, \omega) = (\Gamma/\pi)/(\Gamma^2 + \omega^2)$, and assuming a Lorentzian shape for the resolution function as well (approximately valid for the classical BSC spectrometer), with a width (HWHM)

$\Delta(\hbar\omega)$, one obtains for the measured intensity

$$I(Q, \omega = 0, T) = \frac{1}{\pi} \frac{1}{(\Gamma(Q,T) + \Delta(\hbar\omega))} \,. \tag{3.45}$$

Let us now, for the purpose of discussion, assume that in our example a single relaxation process (responsible for the Lorentzian line shape) is active over the whole temperature range considered, and that it shows an Arrhenius type behaviour. Then, for sufficiently small temperatures, the quasielastic line falls entirely into the energy resolution window. Therefore, it does not cause any measurable quasielastic broadening. Then one gets for the "window intensity"

$$I(Q, \omega = 0, T) = 1/(\pi\Delta(\hbar\omega)). \tag{3.46}$$

With increasing temperature, the line width Γ grows, and finally becomes larger than the window $\Delta(\hbar\omega)$; the measured intensity of the window scan then reveals a "stepwise" decrease. Therefore, a simple temperature scan allows one to get a qualitative survey of the diffusion or relaxation processes in the sample as a function of temperature (fixed-window method: first measurements with this method were carried out by Alefeld et al. on $N(CH_3)_4MnCl_3$ [40], tetramethyllead [41], and $(NH_4)_2SnCl_6$ [42]; see also [21] p. 284).

The intensity "step" represents a (purely methodical) transition from non-observability at low T to observability at high T of the relaxation process. From the shape of this step the relaxation time of the single process can easily be determined. Let us consider this problem for the more complex situation of a localized diffusive process, implying an elastic in addition to a quasielastic Lorentzian component. Here the same experimental method can be applied. If the attenuating effect of (harmonic) vibrational motions is described by a classical Debye-Waller factor, the temperature-dependent window-scan intensity, in logarithmic form, is given by [43]

$$\ln(I) = -CTQ^2 + \ln(A(Q)/(\pi\Delta(\hbar\omega)) + (1 - A(Q))/[\pi(2\hbar/\tau_{2S} + \Delta(\hbar\omega))] \,. \tag{3.47}$$

Here CT is the vibrational mean square displacement (with a temperature coefficient C), $A(Q)$ is the EISF, and τ_{2S} is the relaxation time (for a two-site jump model in our example). It is interesting to note that the observability transition described by (3.47) can be used for the determination of the EISF, provided that the mechanism does not change in the T-region of the step.

For this purpose, the measured low-temperature straight line of $\ln(I)$ vs. T is extrapolated to high T and compared with the measured high-temperature line; the latter is obtained, when due to strongly increased line-broadening, the quasielastic contribution to the intensity becomes negligible. A simple division of the intensities yields the EISF according to the equation [43]

$$\ln[A(Q)/(\pi\Delta(\hbar\omega))] = [\ln(I)_{\text{high}\,T}] - [\ln(I)^{\text{extrapol}}_{\text{low}\,T}] \,. \tag{3.48}$$

As an example of such a measurement, Fig. 3.10 shows the result obtained for the solid-state protonic conductor $CsOH \cdot H_2O$ (see Sect. 3.9).

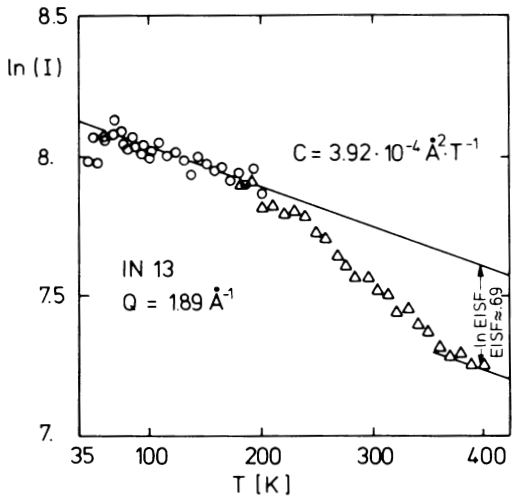

Fig. 3.10. Example of an apparent observability transition exhibited experimentally by the elastic intensity of $CsOH \cdot H_2O$ measured as a function of temperature: Logarithmic plot of the elastic-window intensity obtained with IN13 (ILL Grenoble) at $Q = 1.89\,\text{Å}^{-1}$. The straight lines show the variation of the Debye-Waller factor in the limits of low T and high T, respectively. The logarithm of the EISF is simply the difference between the values of the two lines at a given temperature [43].

Last, but not least, the TOF-XTL technique should be mentioned. This type of hybrid instrument, employing a pulsed polychromatic ("white") incident beam and single-crystals in BSC-geometry as analyzing filters, is represented by IRIS [44] at RAL in Chilton. It is well adapted to the time-structure of spallation neutron sources. The energies of the incident neutrons are measured with time-of-flight techniques, while the energy of scattered neutrons is fixed by the analyzers. Depending on the type of crystals used, several discrete values of energy resolution in the range from about 1 to 16 μeV are achieved. An example of application is given in Sect. 3.11.

Let us finally mention a few technical points concerning the analysis of QENS data. An important problem in the evaluation of quasielastic neutron spectra is the accurate consideration of the experimental resolution. Although straightforward, this is complex, if the spectrum is a sum of several quasielastic components, eventually superimposed by a purely elastic line, either due to the fact that the diffusive motion is localized, or caused by parasitic incoherent scattering on the host material in which the particles diffuse. The measured spectra are convolutions of the dynamic structure factor with the resolution function. Since a direct deconvolution often encounters practical difficulties, in a typical analysis the data are usually not corrected for resolution, but an inverse procedure is employed. It consists in folding the theoretical model with the measured resolution function and comparing the

result to the measured spectra. This procedure, which amounts to an indirect deconvolution, is well-known, and standard software packages are available in the Neutron Scattering Centers.

Another problem is multiple scattering (MSC). In principle, a neutron reaching the detector, may have been scattered in the sample once , twice, or even several times. For a given nominal scattering angle φ or nominal Q value ($Q \cong (4\pi/\lambda)\sin(\varphi/2)$) the convolutions of two or more quasielastic spectra are then superimposed on the single-scattering data. The MSC components should be minimized by using sufficiently thin samples. Nevertheless, a numerical correction is often necessary. Analytical methods [45] directly applied to the theoretical models, and model-independent Monte-Carlo techniques (see for instance [46], [47]) are employed for this purpose.

The third problem is calibration, which means the absolute determination of the scattered intensity, instead of quoting "arbitrary units". Calibration is performed, for instance, by a vanadium scatterer which has the same geometry as the sample itself, and whose incoherent scattering cross-section is well-known (provided that there is no hydrogen contamination).

For many elements coherent and incoherent scattering coexists, and it is difficult to separate the contributions $S_{\mathrm{coh}}(\boldsymbol{Q},\omega)$ and $S_{\mathrm{inc}}(\boldsymbol{Q},\omega)$. Spin incoherent scattering causes $(2/3)[\sigma_{\mathrm{inc}}/(\sigma_{\mathrm{inc}}+\sigma_{\mathrm{coh}})]$ of the neutrons to flip their spin in a polarized neutron beam, whereas coherent scattering occurs without spin flip. The high intensity of polarized beams available at the reactor in the Institut Laue-Langevin in Grenoble allows one to apply this property for a direct separation of the coherent and incoherent contributions, by orienting spin analyzer and polarizer parallel and anti-parallel ([48], see also [49] and Sect. 13.2.2 in Chap. 13).

More information on modern QENS spectrometers can be found in the Instrumentation Booklets of the Neutron Scattering Centers (ILL in Grenoble, LLB in Saclay, BENSC at HMI in Berlin, ISIS at RAL in Chilton, NIST in Gaithersburg, FZ Jülich, IPNS at Argonne).

3.5 Hydrogen Diffusion in Metals and in Metallic Alloys

The first investigations of quasielastic scattering on diffusing atoms were performed by Sköld and Nelin [50] on palladium hydride where the H atoms diffuse over an interstitial lattice. The experiments on powder samples indicate clearly that, for small scattering vectors $\boldsymbol{Q}$, the diffusion coefficient is obtained following (3.33). For larger $\boldsymbol{Q}$, the data are consistent with diffusion on an octahedral lattice (see Fig. 3.11). More recent experiments on palladium single crystals are shown in Fig. 3.12 [51]. The results agree very well with the Chudley-Elliott model. Results from computer simulations by Li and Wahnström [52] are included in the figure, where the hydrogen potential was modelled in the adiabatic Born-Oppenheimer approximation, tested with the help of the known vibrational frequencies of the dissolved hydrogen. These

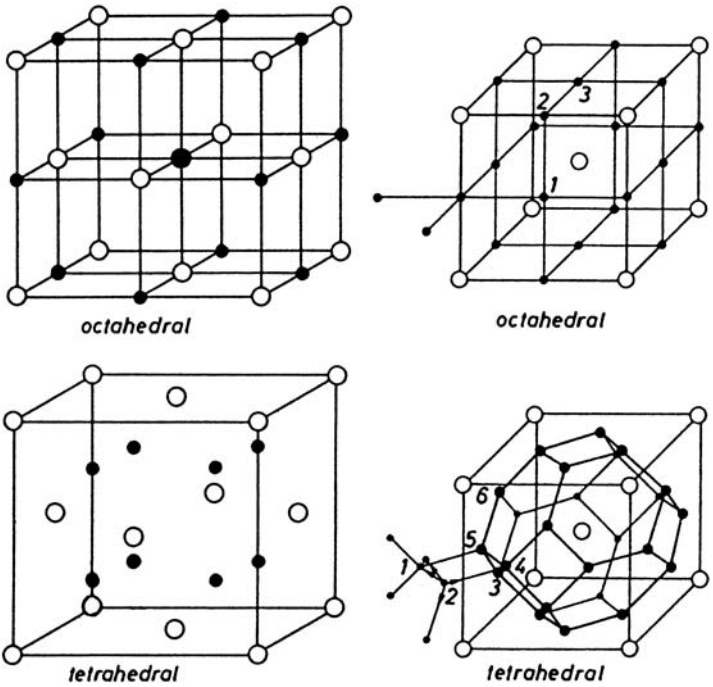

Fig. 3.11. Tetrahedral and octahedral interstitial sites (•) for fcc (left) and bcc (right) host lattices. The sites can be occupied by H atoms. The 6 (3) non-equivalent sublattices in the bcc (fcc) lattice are labeled. The bcc tetrahedral sites are connected by [110] jump vectors.

calculations strongly deviate from the Chudley-Elliott model and from the experiments. Agreement between the computer simulations and the experiments was obtained by introducing a dissipative force which is supposed to follow from the interaction of the protons with the conduction electrons.

The process of diffusive motions of hydrogen in bcc metals, in particular in niobium hydride, is complicated and not yet fully understood, despite the great number of investigations published so far (e.g. [53–55]). Hydrogen atoms occupy tetrahedral sites in the bcc lattice (Fig. 3.11) forming six non-equivalent sublattices. Consequently, the quasielastic line is a superposition of six Lorentzians and it is finally dominated by a single Lorentzian for $Q \to 0$ whose width is $Q^2 D_s$. A comparison between quasielastic scattering experiments and theory is shown in Fig. 3.13. For simplicity, only the half width of the *combined* quasielastic line is used [53]. Obviously, for larger Q the effective width is considerably smaller than expected from the simple Chudley-Elliott model. One speculates that this might be due to an effective jump distance larger than expected from the lattice parameters.

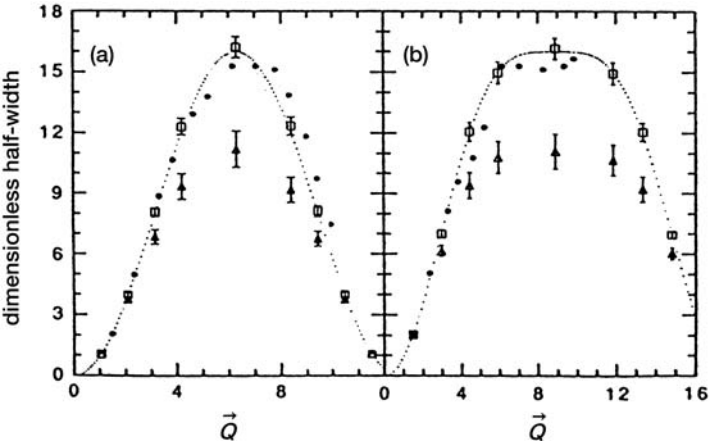

Fig. 3.12. Quasielastic width in units of D_s/a^2 (a = lattice constant) for H diffusion on octahedral sites in fcc Pd. • Quasielastic experiments with $\boldsymbol{Q}$ parallel [100] (a) and [110] (b). Dashed: Chudley-Elliott theory; triangles: computer simulation without friction force due to interaction between protons and conduction electrons; squares: with such a friction force [51, 52].

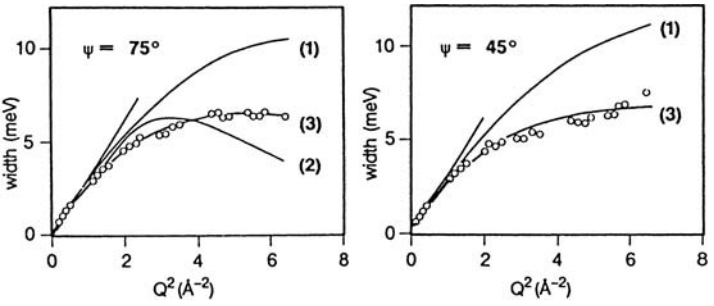

Fig. 3.13. Quasielastic width for cubic α-$NbH_{0.02}$ with $\Gamma(Q)$ determined from the composite spectrum. Ψ = angle between [110] and $\boldsymbol{k}_0$. (1) Chudley-Elliott model (tetrahedral jump vectors, Fig. 3.11). (2) Correlated double jumps. (3) Jump sequences (from [54]).

The following model [54] describes the obtained experimental results. At elevated temperature the hydrogen alternates between a 'state' where it is *localized* by the strong elastic relaxation of the surrounding host lattice, with a rest time τ_0, and a *mobile* state, where it follows a rapid sequence of two, three or more jumps between adjacent tetrahedral sites, with a rate several times larger than $1/\tau_0$. This memory effect follows from the relaxation of the host lattice. The hydrogen ion on a tetrahedral site creates an elastic distortion of *tetragonal* symmetry as in Fig. 3.14 with a certain axis shown in this figure. A jump leading to an adjacent site reorients this axis by 90°, and a finite

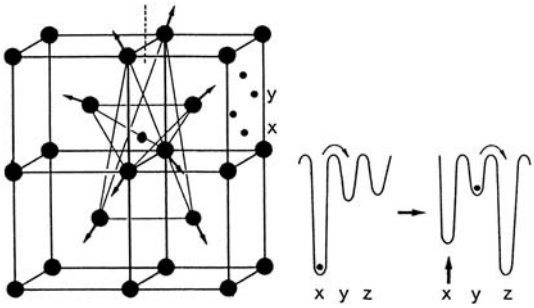

Fig. 3.14. Left: Atomic displacements around a H atom on a tetrahedral site x in the Nb lattice. A nearest neighbour jump (e.g. from site x to y) causes a rotation of the symmetry axis (dashed) by 90° with a relaxation time of the displacement field $\tau_r \cong 10^{-12}$ s. Right: Potential for sequence of correlated jumps with incomplete relaxation of the potential minima (see also Sect. 18.3 in Chap. 18).

time τ_r is required until the new arrangement of the surrounding lattice is entirely restored. Small-polaron theory allows a calculation of this time with $\tau_r \sim 10^{-12}$ s [56]. Consequently, for the first moment (i.e. for $t \ll \tau_r$), the activation barrier opposing a hydrogen ion to leave the site is lower than for a fully relaxed site. Obviously, there is an enhanced probability to leave this shallow site before full relaxation has occurred. This favours correlated jump sequences, as well as back jumps to the original site. Fig. 3.15 shows typical hydrogen trajectories in Nb from molecular dynamics calculations [57].

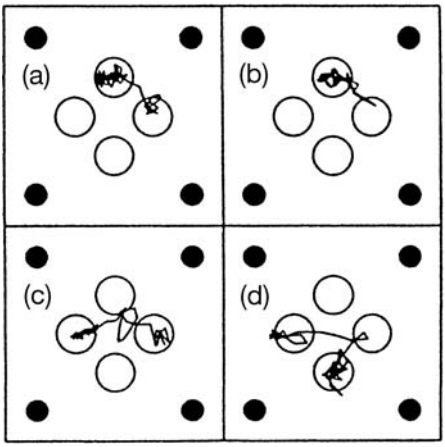

Fig. 3.15. Typical trajectories of hydrogen motion projected in a (100) plane of the Nb lattice from molecular dynamics calculation over a time interval of $5{\cdot}10^{-12}$ s [57]. Correlated "forward" and "backward" jumps can be identified.

Two striking anomalies of the bcc hydrides may be related to the strain field caused by the jumps. (i) Huang scattering (i.e. scattering close to the Bragg lines) probes the symmetry of the long-range strain field due to the dissolved H atoms [58]. X-ray experiments on niobium hydride show that the strain field is practically cubic. (ii) The inelastic Snoek relaxation of the bcc Nb hydride is proportional to the squared difference of the two diagonal components of the Kanzaki double force tensor $(\mathrm{A–B})^2$. Also the Snoek relaxation experiments lead to the conclusion of a nearly cubic strain field [59]. If the time of a jump sequence is comparable to or shorter than the long-range lattice relaxation, the contributions due to the occupancy of an occupied site and of previously occupied sites are superimposed. Since the orientation of the strain fields are mutually orthogonal, the resulting long-range field is supposed to approach a distribution close to cubic symmetry.

A detailed experimental and theoretical analysis by Dosch et al. [55] treats the dynamics of the strain field. For the first time, these authors were able to observe the quasielastic scattering due to the strain field fluctuations originating from hydrogen jumps. From these results the authors conclude the existence of very fast back- and forth-jumps between adjacent sites; also these could be responsible for a reduction of the tetragonal components in the double force tensor and, therefore, of the long-range field. Such fast "local" motions distribute the proton over adjacent sites. If this motion is resolved energetically, it should cause a Q-dependent factor in addition to the Debye-Waller factor, $\exp(-\langle u^2\rangle Q^2)$, where $\langle u^2\rangle$ is the mean square vibrational amplitude. This would amount to a very steep decay of the quasielastic intensity with increasing Q, and would have to be identified with the elastic incoherent structure factor (EISF) as defined in (3.16)-(3.18). The interpretation of Debye-Waller factor and EISF needs special attention. The hydrogen motion in the 10^{-12} s regime can be identified by a fit of a suitable theoretical function $S_{\mathrm{fit}}(Q,\omega)$ to the experimental data, in an experimentally limited window $-\hbar\omega_{\max} \le \hbar\omega \le \hbar\omega_{\max}$. The corresponding quasielastic intensity is then calculated by integration, assuming that S_{fit} also reproduces sufficiently well the contribution of the diffusive motion to the scattered intensity outside of the fitting region:

$$I(Q) = \int_{-\infty}^{\infty} S_{\mathrm{fit}}(Q,\omega)\mathrm{d}\omega\,. \tag{3.49}$$

If there are fast motions not covered by $S_{\mathrm{fit}}(Q,\omega)$, e.g. the rapid back- and forth-jumps as described in [55], in the 10^{-13} to 10^{-14} s region, the quasielastic intensity should read

$$I(Q) = \mathrm{e}^{-\langle u^2\rangle Q^2} F(\boldsymbol{Q})\,. \tag{3.50}$$

The first factor is the usual Debye-Waller factor of the proton due to phonons and localized vibrational modes, and $F(\boldsymbol{Q})$ is the EISF, i.e. the Fourier transform of the proton distribution in space by diffusive motions which are faster than the 10^{-12} s jumps.

Table 3.1. Hydrogen diffusion coefficients in different intermetallic hydrides. For comparison, the values for dilute PdH_x and NbH_x are also included.

Specimen	D_0 (cm^2/s)	$E_{\rm act}$ (meV)	$D_{300\,\rm K}$ (cm^2/s)	Reference
$PdH_{x\to 0}$	$5.3 \cdot 10^{-3}$	236	$5.7 \cdot 10^{-7}$	[60]
$NbH_{x\to 0, T>250K}$	$3.6 \cdot 10^{-4}$	108	$5.5 \cdot 10^{-6}$	[61]
Ti_2NiH_2	$2.0 \cdot 10^{-4}$	345	$3.2 \cdot 10^{-10}$	[62]
TiFeH	$7.2 \cdot 10^{-4}$	500	$2.9 \cdot 10^{-12}$	[63]
TiFeH	$4.2 \cdot 10^{-7}$	330	$1.2 \cdot 10^{-12}$	[64]
$LaNi_5H_6$	$3.2 \cdot 10^{-4}$	249	$2.1 \cdot 10^{-8}$	[65]
$LaNi_5H_6$	$2.1 \cdot 10^{-3}$	275	$5.0 \cdot 10^{-8}$	[66]
$TiCr_{1.8}H_{2.6}$		270		[67]
$Ti_{1.2}Mn_{1.8}H_3$	$5.9 \cdot 10^{-4}$	225	$9.8 \cdot 10^{-8}$	[68]
$Ti_{0.8}Zr_{0.2}CrMnH_3$	$3.1 \cdot 10^{-4}$	220	$6.2 \cdot 10^{-8}$	[69]
$Mg_2NiH_{0.3}$	$6.7 \cdot 10^{-5}$	280	$1.3 \cdot 10^{-9}$	[70]

Numerous quasielastic scattering studies were performed on alloy hydrides which reveal high solubilities and mobilities of the hydrogen atoms. One objective of the investigations was the determination of the bulk self-diffusion coefficient from quasielastic experiments at small Q. Table 3.1 summarizes results from such investigations, namely $D_{\rm s}$ for 300 K and the parameters for an Arrhenius law describing the temperature dependence, namely

$$D_{\rm s}(T) = D_0 {\rm e}^{-E_{\rm act}/k_{\rm B}T} \ . \tag{3.51}$$

With these bulk diffusion coefficients the hydrogen absorption or desorption rate, $K_{\rm r}$, in a storage powder was calculated and compared with experiments. For a grain size R one obtains approximately

$$K_{\rm r} = \pi^2 D_{\rm s}/R^2 \ . \tag{3.52}$$

For $Ti_{0.8}Zr_{1.2}CrMnH_3$ [69] one gets $D_{\rm s} = 6 \cdot 10^{-12}$ m^2/s from quasielastic scattering; the grain size of the storage powder is $R \approx 0.5$ μm. This leads to a reaction rate of $K_{\rm r} = 400$ s^{-1}, provided that absorption and desorption is diffusion controlled. The measured rate, however, is only 0.1 s^{-1}. This implies that the reaction rate is retarded by the surface and not controlled by the fast bulk diffusion. The opposite situation was found for $TiFeH_x$ [63] where the self-diffusion is very slow and the reaction is diffusion controlled. However, if one calculates $K_{\rm r}$, the resulting value is smaller than measured. Using metallographic pictures this was explained by microcracks in the grains which bypass the diffusion path. Obviously, quasielastic neutron scattering

does not "see" this effect since the distance between microcracks is much larger than $1/Q$.

3.6 Diffusion with Traps

In disordered alloys the potential for a diffusing atom fluctuates randomly in space, and the potential depth or binding energy changes from site to site, as well as the barrier connecting adjacent sites. The calculation of the self-correlation function $G_s(r,t)$ is possible by means of Monte Carlo methods and only a simplified case can be treated analytically, namely by the so-called two-state model [71]. We consider a regular lattice doped with impurities at low concentration where the diffusing atom is temporarily bound by the impurities. Under these circumstances, the problem is solved by treating the diffusion as a random sequence of steps, namely an alternation between

- a free "state" where the atom diffuses in an undisturbed lattice, with a self-diffusion coefficient D_1 during an average time interval τ_1 and
- a trapped or immobile state during an average time τ_0 in the vicinity of an impurity atom.

The self-correlation function is then obtained as a series expansion where each term is a multiple convolution of the free and trapped-state self-correlation functions. The "macroscopic" self-diffusion coefficient D_s is then related to D_1 by

$$D_s = D_1 \frac{\tau_1}{\tau_1 + \tau_0} \ , \tag{3.53}$$

and the free diffusion coefficient is

$$D_1 = \frac{\ell^2}{6\tau} \ . \tag{3.54}$$

τ is the mean rest time on the undisturbed lattice sites and ℓ is the corresponding jump distance. The escape rate from the immobile trapped state is $1/\tau_0$; the rate of trapping can be calculated on the basis of a continuum theory, namely

$$\frac{1}{\tau_1} = 4\pi R_{\text{eff}}(T) D_1(T) c_T \ . \tag{3.55}$$

c_T is the concentration of the impurities. R_{eff} is an effective trapping radius. For an attractive potential caused by the impurity, R_{eff} decreases with increasing temperature.

The results are schematically shown in Fig. 3.16. The width for an undoped crystal is presented by the dashed line following the basic Chudley-Elliott result (3.30). For small Q there is only a single Lorentzian whose width approaches $\Gamma = Q^2 D_s$, related to the macroscopic diffusion coefficient. This is only obtained for sufficiently small Q, namely such that the diffusive

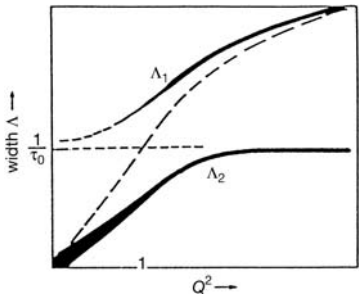

Fig. 3.16. The two eigenvalues $\Lambda_{1,2}$ calculated for the two-state model corresponding to the width of the quasielastic components $\Gamma_{1,2}$ vs. Q^2. The line thickness symbolizes the intensities of the two components. Dashed: Width for undisturbed crystal. $1/\tau_0$ = escape rate from trap. The maximum value of Λ_2 is $1/\tau_0$.

process is observed over a range larger than the average distance between the impurities. At large Q, the *two eigenvalues* are visible in the spectrum. A narrow quasielastic component appears whose width is related to the escape rate of hydrogen from the trapping centres and whose intensity is proportional to the fraction of atoms in the immobile state. In addition, there is a broad component whose width approaches the jump rate in the undisturbed lattice. Details of this model are found in [71] and in Chap. 18.

This behaviour has been observed and successfully interpreted for niobium crystals, doped with 0.4 and 0.7 at % nitrogen and with 0.3 at % dissolved hydrogen. Fig. 3.17 shows the intensity of the line related to the trapped

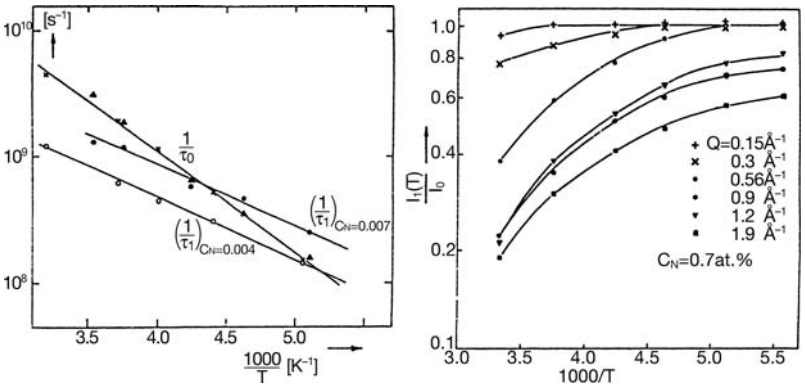

Fig. 3.17. Diffusion of H (0.3 mol %) in Nb doped with c_N = 0.4 and 0.7 mol % N atoms. Left side: τ_1 = average time of free diffusion, $1/\tau_1$ is proportional to c_N; $1/\tau_0$= escape rate, independent of c_N. Right side: Intensity of the narrow component in the quasielastic spectrum corresponding to eigenvalue Λ_2. For small Q: Single line with $I_2/I_0 \simeq 1$; for large Q: Intensity proportional to fraction of trapped protons, increasing with decreasing temperature [71].

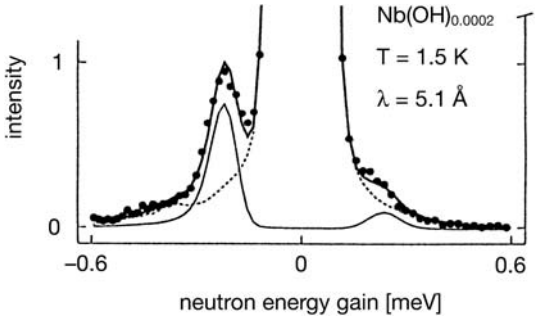

Fig. 3.18. Tunneling spectrum for Nb doped with 0.2 mol % H and 0.2 mol % O. The hydrogen is trapped in a double potential well near the O impurity at 1.5 K. The asymmetry of the spectral doublet is due to the Boltzmann factor. The intensity of the tunneling lines is only 1 % of the central elastic peak [73].

state. Expectedly for large Q the intensity of this narrow line (width $\simeq 1/\tau_0$) decreases with increasing temperature because the H atoms spend a decreasing fraction of their time near the N impurities. As seen from Fig. 3.17, the trapping rate $1/\tau_1$ is proportional to the nitrogen concentration c_{N}, whereas $1/\tau_0$, the escape rate, is independent of c_{N}. Both rates are thermally activated with activation energies which, in a good approximation, can be understood by elastic strain fields caused by the impurities. The model has also been applied to a disordered alloy, namely $Ti_{1.2}Mn_{1.8}H_3$ where the free motion cannot be clearly separated from the trapped state. Nevertheless, the evaluation of the spectra yielded a consistent description of the spectra [68].

An interesting effect is connected with hydrogen or deuterium dissolved in niobium and trapped on impurities [72, 73]. It has been observed that the specific heat for niobium doped with hydrogen or deuterium reveals an anomaly at low temperatures with a strong isotope effect if the sample was loaded with a certain amount of oxygen or nitrogen. Investigations of neutron spectra at low temperatures revealed two lines on the energy gain and loss side. They correspond to transitions between stationary tunneling states of the proton attached to the impurities, with energies of a few 0.1 meV. It has been assumed that the N or O impurity occupies an octahedral site of the bcc Nb lattice (see Fig. 3.11). This leads to two adjacent tetrahedral sites separated by a low potential barrier where the proton wave function is distributed over both sites. For a simple double-well model, with an exchange integral J and an asymmetry ϵ caused by the elastic distortions, one calculates a tunneling splitting of

$$\hbar\omega_T = \left(J^2 + \epsilon^2\right)^{1/2} \quad . \tag{3.56}$$

For hydrogen trapped on oxygen one gets $J = 0.22$ meV, $\epsilon = 0.10$ meV depending on concentration, and for deuterium $J = 0.02$ meV (Fig. 3.18).

3.7 Vacancy Induced Diffusion

In many metals the atoms diffuse in the presence of thermally induced vacancies. These vacancies themselves diffuse rapidly through the lattice, and each jump of a vacancy is connected with a jump of a lattice atom. For dilute vacancies, a selected atom undergoes a jump to a neighbouring site whenever it has an "encounter" with a vacancy, where the time between jumps of the vacancy $\tau_\mathrm{v} \simeq 10^{-12}$ s is short compared to the time between two encounters with different vacancies, $\tau_\mathrm{e} \simeq 10^{-9}$. Normally, one and the same vacancy leads to several correlated jumps of the same atom, such that one encounter comprises a number of jumps where the sequences are still short compared to τ_e (see Chap. 1).

As a consequence, for incoherent scattering by the nuclei in the lattice, the quasielastic spectrum can be calculated in the framework of the Chudley Elliott equation (3.25) where the rapid jump sequence during the encounter is treated as *instantaneous*. One obtains [74]

$$\Gamma = \frac{1}{\tau_\mathrm{e}} \left[1 - \sum_{\text{all } \boldsymbol{r}_m} w(\boldsymbol{r}_m) \cos \boldsymbol{Q}\boldsymbol{r}_m \right] \ . \tag{3.57}$$

$w(\boldsymbol{r}_m)$ denotes the probability that, during the encounter, the atom was originally at $\boldsymbol{r}_m = 0$ and has reached the lattice site $\boldsymbol{r}_m$ by one or several jumps. The sum includes a term $w(\boldsymbol{r}_m = 0)$ where several jumps of the sequence led the atom back to its origin. The probabilities w can be calculated by computer simulation [75]. Detailed theoretical investigations on the encounter model, also including different types of jumps, can be found in the literature [76]. If the encounter consists only of a single jump, in a bcc metal it reaches only the $n = 8$ nearest neighbours with $\boldsymbol{r}_k \equiv \boldsymbol{\ell}_k = \frac{a}{2}\langle 111 \rangle$; one has

$$\Gamma = \frac{1}{n\tau_\mathrm{e}} \sum_{k=1}^{n} \left[1 - \cos \boldsymbol{Q}\boldsymbol{\ell}_k \right] \ . \tag{3.58}$$

It should be emphasized that the rapid jump sequence during the encounter causes an additional quasielastic spectrum. However, the corresponding jump rate $1/\tau_\mathrm{v} \simeq 10^{12}$ s^{-1} is very large compared to $1/\tau_\mathrm{e} \simeq 10^8 \ldots 10^9$ s^{-1}. Consequently, the spectrum is 10^3 to 10^4 times broader than the spectrum related to $\Gamma(\boldsymbol{Q})$ in (3.57); in a high-resolution experiment designed for the study of the encounter rate, $1/\tau_\mathrm{e}$, this is practically an unobservable background. In a lattice with *coherently* scattering nuclei, in principle, one should observe also vacancy diffusion itself, where the missing atoms have the cross-section of the atoms. Quasielastic scattering concerning the diffusion in sodium single crystals has been investigated and the diffusion is dominated by $\frac{a}{2}[111]$ jumps [74,77]. A detailed study has been carried out for the diffusion in bcc titanium single crystals whose results are shown in Fig. 3.19 [78]. The dependence of the quasielastic width in the μeV-region is consistent with jumps of

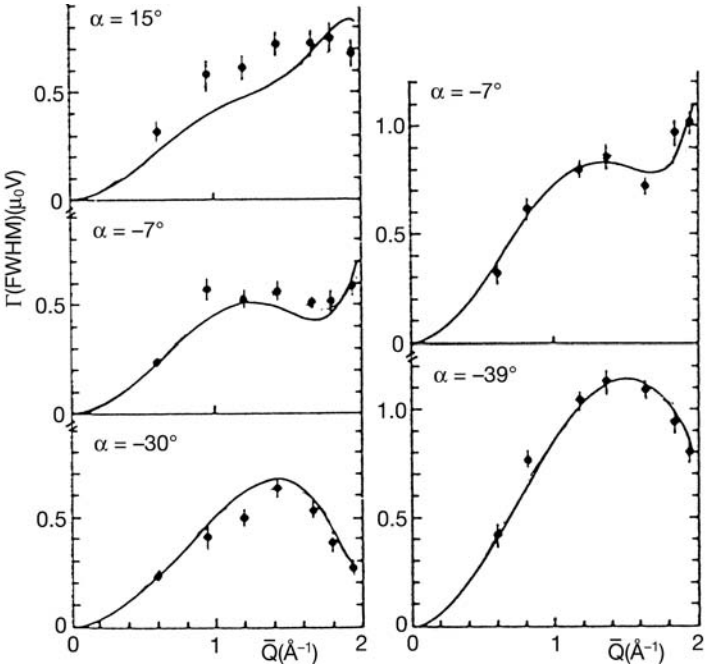

Fig. 3.19. Quasielastic scattering width for vacancy induced diffusion of Ti in a bcc single crystal. $\Gamma(Q)$ is the *full* width at half maximum. Different orientations are indicated ($\alpha = [110] \wedge \boldsymbol{k}_0$). Left: 1460 °C, right: 1530 °C. Full circles: Experiment. Solid line calculated for $\frac{a}{2}[111]$ jumps with correlations during encounter [78].

the $\frac{a}{2}[111]$ type including the contribution of next nearest neighbour $a[100]$ jumps. The high diffusion coefficients of bcc alkali and group IV metals, with relatively low activation energies has stimulated the investigation of phonon dispersion curves of such substances, i.e. the relation between the propagation vector q and the phonon frequency ω. Fig. 3.20 shows such results [79] for a titanium single crystal. A rather low transverse acoustic mode can be recognized, and, in particular, the collapse of a phonon branch near $\frac{2}{3}[111]$ where the phonon line degenerates and becomes a relaxation spectrum centered at energy transfer $\hbar\omega = 0$. It is possible to establish a systematic relation between phonon frequencies ω^* and the activation energy E^* for diffusion, namely

$$\omega^{*2} \propto \frac{E^*}{k_\mathrm{B} T_\mathrm{m}}, \tag{3.59}$$

where T_m is the melting temperature. This relation is plausible since for a cosine potential $\frac{E^*}{2}\cos(\pi x/\ell)$ the curvature is proportional to the activation energy E^*, and the squared frequency ω^{*2} is proportional to the curvature [80].

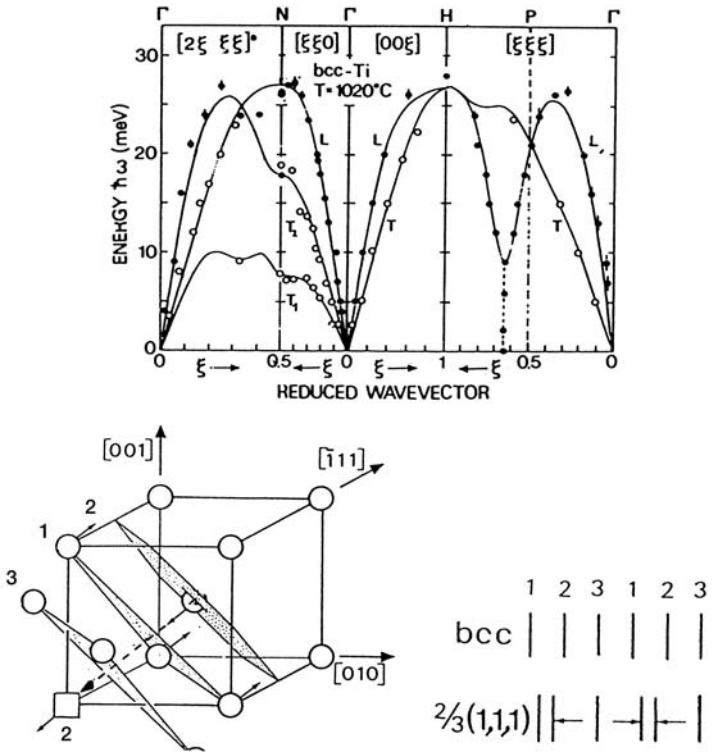

Fig. 3.20. Top: Phonon dispersion curves $\omega(\boldsymbol{q})$ ($\xi = q/q_{\max}$) for a Ti single crystal. Anomalies for the transverse acoustic [211] branch and for $q = \frac{2}{3}[111]$. Bottom: The $\frac{2}{3}[111]$ phonon assists the $\frac{a}{2}[111]$ jump into a vacancy at the cube corner, combined with an opening of the transition through plane 1 by a [110] mode (from [79], see also Sect. 2.3.1 in Chap. 2).

3.8 Ion Diffusion Related to Ionic Conduction

At elevated temperatures many materials, such as high-temperature solid modifications of salts and their melts, certain solid metal hydroxide hydrates, solid acidic salts and hydrates, and concentrated aqueous solutions of acids are ionic conductors with electric conductivities σ of similar orders of magnitude in the solid and in the liquid state. Especially amenable to quasielastic neutron scattering studies are those ionic conductors, where the charge carriers are negatively or positively charged hydrogen atoms (i. e. protons in the latter case).

The connection between ionic diffusion and conductivity is given by the Nernst-Einstein equation, which relates σ with the ionic charge diffusion coefficient D_σ, namely

$$D_\sigma = \sigma(T)\frac{k_\mathrm{B}T}{(n \cdot e)^2 N} \ . \tag{3.60}$$

Here N is the number density of the mobile ions, e the electron charge, $(n \cdot e)$ the module of the charge of the mobile ions ($n = 1$ in the case of hydrogen ions); k_B is the Boltzmann constant, and T the temperature . The relation between the atomic self-diffusion coefficient, D_s, obtained from neutron scattering by the nuclei of the diffusing ions, and the charge diffusion coefficient, D_σ, determined by the measurement of the ionic conductivity, is defined by the Haven ratio, $H_R = D_s/D_\sigma$. The latter quantity, a priori unknown, takes into account correlation effects occurring in ion diffusion, such as deviations from directional and/or temporal randomness of consecutive ion jumps and, perhaps even more important, cooperative phenomena involving the correlated diffusive motion of more than one charge carrier. Because of the Coulomb interaction between neighbouring ions, such effects can be particularly important in ionic conductors. Since correlation effects are practically always present, H_R may have values between slightly smaller or larger than 1, but may also be larger than 1 by an order of magnitude, as in the case of cation diffusion in $LiNaSO_4$ [81], or even larger by several orders of magnitude, as observed with the PFG-NMR technique (see Chap. 10) in the cubic phase of very pure NaOH [82]. The latter observations have been explained as the result of cooperative ring exchange mechanisms with no or minor charge separation. A cation leaving its site induces correlated jumps of neighbouring ions in the opposite direction. While the original cation jump still contributes to self-diffusion, the backward-correlated jumps of neighbouring ions strongly reduce the efficiency of charge transport. Beyond the mere measurement of D_s, and of microscopic quantities, such as residence times and jump distances, QENS can give access to further information on such correlation phenomena [83], as will be discussed below.

At higher temperatures, atomic or ionic jump rates in the crystal lattice may become so large, that they are no longer well separated from the lower part of the phonon frequencies. As a consequence, even at very low concentrations of the mobile particles (high concentration of empty sites) the simple CE model breaks down, memory effects appear, i.e. the diffusing atom "remembers" part of its history, and therefore a step of the diffusional motion will to some extent depend on the previous step(s). This effect is mediated by the lattice during the time of mechanical relaxation from the local distortion caused by the diffusing ion. Thus phonons may assist the diffusion process (see Sect. 3.7) and for instance lead to more than one consecutive nearest-neighbour jump at a time. An example for this case has already been discussed in Sect. 3.5.

If, however, the concentration of diffusing species is high (low concentration of vacancies), it becomes necessary to take account of the correlations between different diffusing ions, because the probability of neighbouring sites being blocked due to the presence of other mobile particles, is finite. Since the theoretical treatment is very difficult, Monte Carlo techniques have been employed. At sufficiently high ion concentration, the problem can be treated

as a random walk of vacancies. One of the useful concepts for this case is the encounter model already mentioned in Sect. 3.7, which has been developed by Wolf [76]. An encounter is defined as the ensemble of diffusional jumps resulting from the interaction of a vacancy with a particular ion. At very low vacancy concentration the duration of the encounter is short, as compared to the average time interval τ_e between two consecutive encounters of the same ion with *different* vacancies. Therefore, different encounters are uncorrelated and the ionic diffusion can be treated as a random series of discrete encounters. Spatial and temporal correlation effects are caused by the fact, that the ion performs, on the average, more than one single jump during an encounter with a particular vacancy. The QENS function, derived in a way analogous to the case of the simple CE model, is a Lorentzian, formally identical with the expression on the right side of (3.31), where however the linewidth Γ is now given by (3.57).

The encounter model has been applied to the "superionic" anion conductor $SrCl_2$ and compared to various versions of the CE model by Dickens et al. [84] and Schnabel et al. [85]. $SrCl_2$ has the fluorite structure which may be described as a simple cubic array of anions, with cations occupying every other cube center. Because of the relatively large incoherent scattering cross-section of the chlorine nucleus, (5.5 barn), the QENS technique is readily applied. In the region of the 'diffuse' transition around $T_c = 1000\,\mathrm{K}$, anionic conductivity and self-diffusion coefficient rise rapidly up to values approaching those of the molten salt. The quasielastic linewidths measured at 1053 K in three different crystallographic directions of a single crystal are shown in Fig. 3.21 [84] as a function of the scattering vector $\boldsymbol{Q}$, together with theoretical width functions of three different models. In particular, the simple CE model (broken line) is compared with two models taking account of correlation effects, namely a CE model with nearest neighbour (nn) and next nearest neighbour (nnn) jumps, i.e. forward correlated double jumps (full line), and the encounter model (chain curve). The latter models are in better agreement with the experimental data than the former. An important result of this work is the proof, that the diffusion mechanism essentially involves only the regular sites of the simple cubic (sc) anion lattice. This is contrary to previous conjectures with respect to interstitial sites, but consistent with the conclusions from tracer and ionic conductivity measurements, at lower temperatures, by Bénière et al. [86]. Another important result is the confirmation of the phenomenon of neutron diffraction by the single particle probability density distribution (PDD) extending over a large region of the lattice of diffusion sites at long times (see discussion in Sect. 3). The curves in Fig. 3.21 clearly show a zero value of the QENS width function in the [001] direction, where the location of the (002) reflection of the $SrCl_2$ fluorite lattice is indicated by an arrow. If the coherent (001) reflection (corresponding to the pair correlation function) of the sc Cl^- sublattice (with half the lattice spacing) were observable, it would be located at the same place. This

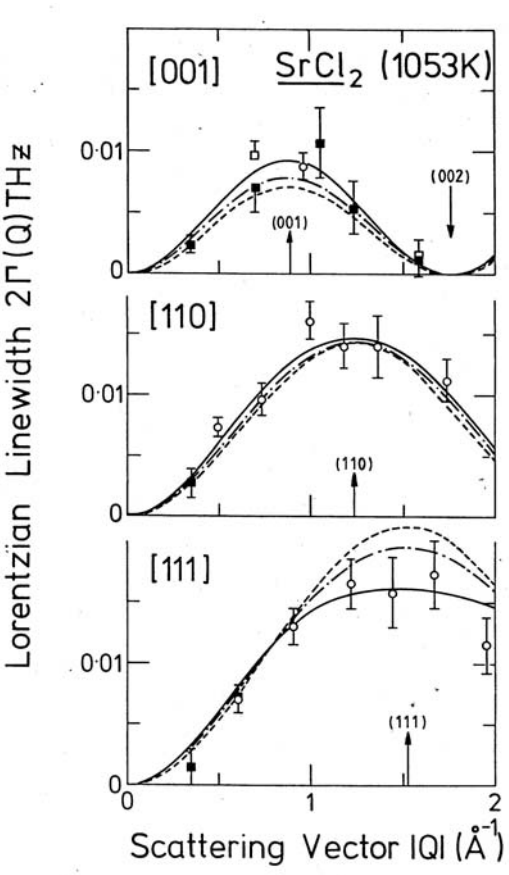

Fig. 3.21. Superionic anion conductor $SrCl_2$: Quasielastic width functions measured at 1053 K (after Fig. 2 of [84]); dashed line: simple CE model with nn jumps only; full line: CE model with nn and nnn jumps, i.e. with forward correlation; chain curve: encounter model implying spatial and temporal correlation.

demonstrates, how incoherent neutron scattering can be employed as a means for determining the structure of the lattice of diffusion sites in a crystal, provided the structure of the latter is known. Such structure determination is in fact implicitly carried out, when lattice diffusion models are fitted to QENS spectra.

Another anion conductor, Ba_2NH, is of special interest. The charge carrier is the H^- ion, the ionic conductivity is extremely high ($1\,S\,cm^{-1}$ near 700 K [87]), and it is essentially two-dimensional. This compound has a layered trigonal structure (space group ($R\bar{3}m$)), with separated H^- and N^{3-} ion layers, these ions being alternately located in the centers of distorted Ba-octahedra. The analysis of quasielastic neutron scattering spectra, using

a planar CE diffusion model, has shown that the H^- diffusion process takes place by uncorrelated jumps between regular hydrogen sites of the trigonal lattice [88]. The scattering function of a two-dimensional diffusion process has a singularity at zero energy transfer, and an analytical expression was not available. Therefore a numerical method of calculating the distribution of Lorentzian linewidths was used for comparison to the measured spectra. According to crystallographic studies, about 15 % of the hydrogen ions are on interstitial sites; therefore, a large amount of vacancies must exist on the regular lattice of the basal plane. As a result, the self-diffusion coefficient is very high: $D_\mathrm{s} = 2.1 \cdot 10^{-5} \mathrm{cm}^2/\mathrm{s}$ at 823 K. The mean residence time of the H^- ion in a regular lattice site was found to be 20 ps at this temperature. However, the authors do not mention the contribution of the 15 % of hydrogen ions on interstitial sites, nor do they discuss their role in the diffusion mechanism. In this example, the question of low-dimensionality has been implicitly addressed by the numerical calculation of the linewidth distribution specific for two dimensions. For further experimental results on low-dimensional diffusion and a discussion of theoretical results concerning 2D-diffusion we refer to Sects. 3.9 to 3.11.

Cationic conductors like AgI or $RbAg_4I_5$ are another family of ionic crystals with very high concentration of charge carriers, where all or most of the mobile metal ions contribute to the electrical conductivity. Again a more sophisticated description is required to take into account ion-ion correlations. For this situation Funke [89] has developed a concept to calculate $S(Q, \omega)$, which has many features in common with the Debye-Hückel theory of ionic liquids (see Chap. 21). We assume that an atomic jump occurs at the time $t = 0$ from an equilibrium lattice site A to another site B. For small times t, the site B is still unrelaxed and Coulomb repulsion has reduced the barrier for a reverse jump, where the particle moves back to A over a barrier lower than in the relaxed state. Now the particle has the choice, either to jump back, or to stay on B, until the surrounding charges have relaxed such that a new equilibrium situation has developed (this situation is similar to the one for the strain field shown in Fig. 3.14). We introduce a probability $W(t)$ that a back jump has not occurred until time t. This implies $W(0) = 1$ and $W(t \to \infty)$ approaches a finite value W_∞ such that the ionic self-diffusion coefficient is $D_\mathrm{s} = W_\infty \ell^2 / 6\tau$. Then the Chudley-Elliott equation can be rewritten, reducing the right side of (3.25) by a "success factor" $W(t)$. Integration of this equation then yields

$$G_\mathrm{s}(\boldsymbol{r}_m, t) = \delta(\boldsymbol{r}_m) + \int_0^t W(t - t') \left[-\frac{1}{\tau} G_\mathrm{s}(\boldsymbol{r}_m, t') + \frac{1}{s\tau} \sum_{v=1}^{s} G_\mathrm{s}(\boldsymbol{r}_m + \boldsymbol{l}_\mathrm{v}, t') \right] \mathrm{d}t' \,. \tag{3.61}$$

After Fourier transformation, $W(t)$ can be related to the complex conductivity $\tilde{\sigma}(\omega)$, and we introduce

$$\Phi(\omega) = \Phi' + \mathrm{i}\Phi'' = 1 + \int_0^\infty \dot{W}(t')\mathrm{e}^{\mathrm{i}\omega t'}\mathrm{d}t' \ . \tag{3.62}$$

With this relation one derives a generalized Nernst-Einstein equation with correlations, where the conductivity σ is replaced by the complex function $\tilde{\sigma}(\omega)/\Phi(\omega)$ [89]. These relations lead to a modified Chudley-Elliott formula which now reads

$$S_{\mathrm{inc}}(Q,\omega) = \frac{\Gamma_{\mathrm{CE}}\Phi'/\pi}{\Gamma_{\mathrm{CE}}^2\Phi'^2 + [\omega + \Gamma_{\mathrm{CE}}\Phi'']^2} \ , \tag{3.63}$$

where Γ_{CE} is the width as defined in (3.30). Obviously, for $\Phi = \Phi' = 1$ and $\Phi'' = 0$ the conventional Chudley-Elliott result is recovered. A very accurate shape analysis of the quasielastic line, taking the complex conductivity $\tilde{\sigma}$ and Φ from impedance spectroscopy, could demonstrate the validity of this concept and may contribute to the understanding of the conductivity in terms of correlated back jumps. Attempts with this goal were published for $RbAg_4I_5$ [90]. The key problem is the accurate shape analysis and also the careful elimination of coherent scattering contributions in such crystals.

3.9 Proton Diffusion in Solid-State Protonic Conductors

The specific dynamical features which generally distinguish protonic from other ionic conductors, are connected with the fact, that hydrogen bonding plays an important role. In particular, it is the process of formation and breaking of H-bonds, which represents an important ingredient of the diffusion mechanisms in these materials. Although the details of such mechanisms may be quite complex, there are four basic types which have been discussed in the literature [91]. They all take account of the fact that the proton is - at least temporarily - bonded to an acceptor atom or molecular subunit.

(i) Grotthuß Mechanism

The original idea of Grotthuß (1806) which had dealt with electrical charge transport along chains of water dipoles in liquid water, has been transformed through extensive work during the 20th century [92–95] to a description valid for proton transfer within extended H-bonding networks [96] in solids. The essential ingredients of this mechanism are alternating translational and rotational steps of the proton motion. In a translational step the proton is exchanged via a hydrogen bridge between different molecular units. Subsequently the proton is transferred into another H-bond by a reorientational motion of the acceptor molecule, whereby the latter remains fixed to its site in the crystal lattice. The repeated occurrence of these alternating processes leads to the uninterrupted trajectory of proton migration inherent in translational diffusion. The Grotthuß mechanism is of importance for instance in certain solid alkali metal hydroxide hydrates, such as

$CsOH \cdot H_2O$ [97] (see below), crystalline framework hydrates [98], solid acidic salts [99], and in many other materials.

(ii) Simple Molecular Diffusion Mechanism

When the proton is part of a stable mobile ion in a liquid, for instance of the $(NH_4)^+$ ion in liquid ammonium salts, it is simply transported through the material by translational diffusion of the ion, whereby this charge carrier is also performing a diffusive rotational motion. But there is no transfer of protons between different carriers. This mechanism appears to be relevant not only in molecular liquids, but also for the high-temperature superionic conducting regimes of the quasi-liquid layers in solid $(NH_4)^+$ and $(H_3O)^+$ β-aluminas [100–103].

(iii) Vehicle Mechanism

This name has been given to the mechanism in systems, where - as in the case of molecular diffusion - the proton is not migrating as the bare hydrogen ion H^+, but in a bound state, attached to a vehicle such as for instance H_2O forming (H_3O^+) or NH_3 forming $(NH_4)^+$. In contrast to simple molecular diffusion, however, the neutral vehicles participate in a cooperative motion together with the charged vehicles, for instance, by changing place with their partners (counter-diffusion). The vehicle mechanism has been proposed, e.g., for concentrated aqueous solutions of acids [104] and for acidic solid hydrates [105, 106].

(iv) Mixed Mechanism

This mechanism combines essential ingredients of the Grotthuß mechanism (orientational rearrangement of neighbouring charged and uncharged units with respect to each other, and proton transfer via H-bonds) with those of the vehicle mechanism (inter-diffusion of charged and uncharged particles). The lifetime of the vehicle-proton complex is finite, as compared to the time constant of translational diffusion. This situation has been found to exist in diluted aqueous solutions of acids and bases [104] and in certain acidic solid hydrates with high water content [107]. Note that the mixed mechanism may be considered as the Grotthuß mechanism of liquids and lattice liquids, since it differs from the mechanism *(i)* mainly by the fact that its vehicles are not fixed to lattice sites.

The interest in comparing Grotthuß, vehicle and mixed mechanisms to the simple molecular diffusion model mentioned above, resides in the fact that the latter allows a very simple theoretical derivation of the incoherent neutron scattering function, $S_{\mathrm{inc}}(\boldsymbol{Q}, \omega)$, which - under certain conditions - is also applicable to the former mechanisms. This will be outlined in the following.

In a molecular liquid or in quasi-liquid two-dimensional systems (e.g. certain liquid crystalline phases or quasi-liquid layers of intercalation compounds) molecules are performing a diffusive rotational motion, while they are migrating through the bulk of the material by some random-walk long-

range translational diffusion process. At any given instant, the molecule is sitting in a (possibly transient) local potential well, where it is taking part in the external and internal molecular vibrations characterizing the system. The calculation is greatly facilitated, if vibrational, rotational and translational motions are assumed to be (dynamically) independent. This convolution approximation allows us to write (see [14, 15])

$$S_{\mathrm{inc}}(\boldsymbol{Q},\omega) = S_{\mathrm{vib}}(\boldsymbol{Q},\omega) \otimes S_{\mathrm{rot}}(\boldsymbol{Q},\omega) \otimes S_{\mathrm{trans}}(\boldsymbol{Q},\omega)\,. \tag{3.64}$$

Here, $S_{\mathrm{vib}}(\boldsymbol{Q},\omega), S_{\mathrm{rot}}(\boldsymbol{Q},\omega), S_{\mathrm{trans}}(\boldsymbol{Q},\omega)$ are the incoherent scattering functions of the three individual types of motions, and the symbol $\otimes$ stands for the convolution in energy transfer $\hbar\omega$. The question, why this convolution approximation can be applied, for instance, to the Grotthuß mechanism, requires some discussion. The vibrational term in this convolution can usually be replaced by a Debye-Waller factor, as long as the study is restricted to the quasielastic region. Strictly speaking, the independence approximation of rotational and translational motions is invalid, since the two motions are not occurring simultaneously and independently of each other, but as a sequence of alternating steps. The validity of the approximation is however recovered, if the rate of rotational steps, H_{rot}, is much higher than the rate of translational steps, H_{trans}, because then it can be argued that the proton is quasi-continuously participating in the rotational motion. This has been the justification for applying the molecular diffusion model for a number of superprotonic conductors exhibiting the Grotthuß mechanism [97, 99, 108]. The vehicle and mixed mechanisms can also be treated with the same method, if differences in the parameters of charged and uncharged vehicles are taken into account.

Now let us consider the application of this approximation to the Grotthuß case. Under the condition that the rates differ by at least one order of magnitude (a situation typical for many protonic conductors), one can study the rotational motion "alone" in a low or medium resolution experiment by choosing an intermediate energy resolution $\Delta(\hbar\omega)$ such that $\hbar H_{\mathrm{trans}} \ll \Delta(\hbar\omega) \leq \hbar H_{\mathrm{rot}}$. This simply means that the experimental observation time Δt (which in practice cannot be made infinite; see the related discussion in Sect. 3.2) is larger than the build-up time of the local PDD (for instance due to a reorientational motion), but much smaller than its time of decay due to long-range diffusion. The EISF of the rotational motion can then be determined from the integral of the only weakly broadened elastic peak, whereas the rotation rate is obtained from the quasielastic line width of the broader spectral component. Vice versa translational diffusion is studied alone in a high-resolution experiment with $\Delta(\hbar\omega) \leq \hbar H_{\mathrm{trans}} \ll \hbar H_{\mathrm{rot}}$, because under this condition the rotational component will contribute only a flat background to the spectrum, whereas the diffusion parameters can be determined from the Q-dependent linewidth of the central component of $S_{\mathrm{inc}}(\boldsymbol{Q},\omega)$.

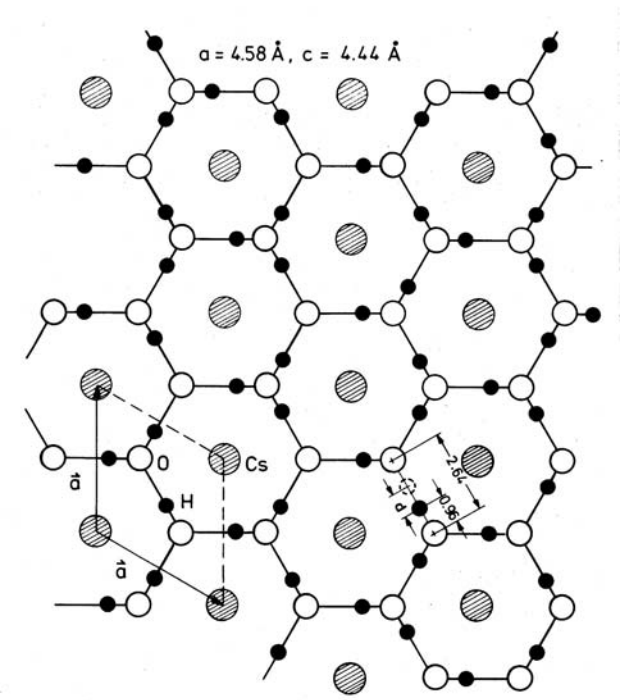

Fig. 3.22. Trigonal modification ($T > 340\,\mathrm{K}$) of the solid-state protonic conductor $CsOH \cdot H_2O$: Projection onto the a-a plane, assuming a random distribution of the hydrogen atoms between the oxygen atoms, with an O-H bond length of 0.96 Å. The Cs atoms are located at the corners of the unit cell, the O atoms are placed at $(\frac{1}{3}, \frac{2}{3}, \frac{1}{2})$ and $(\frac{2}{3}, \frac{1}{3}, \frac{1}{2})$; (after [109]).

This concept has been applied by Lechner et al. [97] to the analysis of quasielastic neutron scattering data of the quasi two-dimensional solid-state protonic conductor $CsOH \cdot H_2O$. The crystal has a trigonal structure consisting of pseudo-hexagonal planar $[H_2O - OH]^-$ networks sandwiched between and alternating with Cs^+-ion layers (Fig. 3.22). Protons are transported through the crystal lattice by a combination of translational motion across the H-bond connecting adjacent H_2O and OH^- groups, and reorientation of the latter. At 402 K, for medium energy resolution, this material exhibits a two-component spectrum. The Q-dependence of the relative elastic intensity (EISF; see Sect. 3.2) was shown to be consistent with the assumption of OH^- reorientations acting as mediators in the much slower translational diffusion process (model E in Fig. 3.23; after [97]). However, this result which concerns the fast localized motions alone, is not unique, because there is a second type of local diffusive motion (model B in Fig. 3.23 : two-site proton jumps in a non-linear H-bond [109]). It agrees equally well with the data.

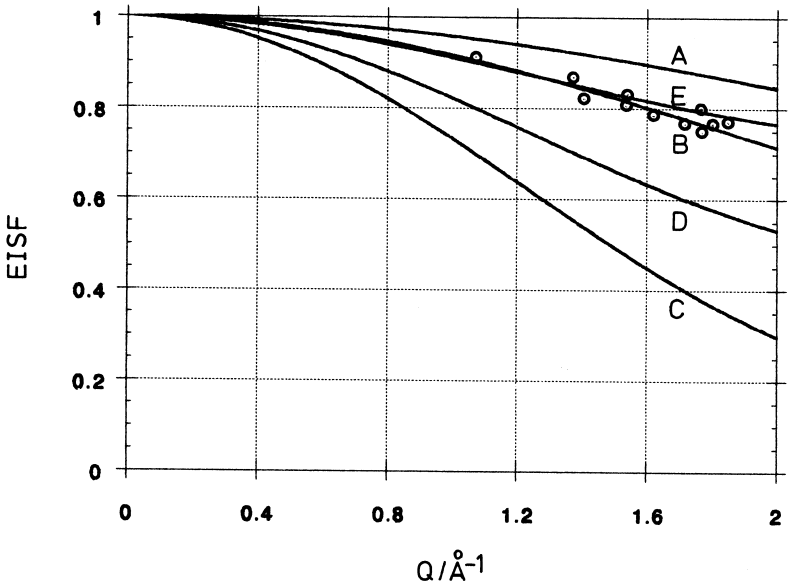

Fig. 3.23. EISF data (circles) of $CsOH \cdot H_2O$, compared to five different models (Fig. 4 in [97] and Fig. 5 in [91]). A) two-site proton jumps in a linear H-bond; B) two- site jumps in a non-linear H-bond; C) three-fold reorientation of OH^- and H_2O groups; D) three-fold reorientation of H_2O molecules alone; E) three-fold reorientation of OH^- groups alone. An ambiguity remains: both models B and E agree with the experimental results; compare Fig. 3.24.

Both types of local motion are apparently required as a combination to result in translational proton diffusion through the crystal lattice. A Q-dependent broadening, due to the latter motion, of the elastic spectral component was observed at much higher resolution. The question, which one of the two local processes determines the rate of translational diffusion, was answered by the study of this Q-dependent linewidth. Fig. 3.24 (following [91, 97]) shows the comparison of models B and E, mentioned above, to the measured line widths (circles) which have been corrected for multiple scattering. Both models imply Grotthuß mechanisms. In model B the intra-H-bond jumps are assumed to have the higher rate; OH^-−reorientations would consequently determine the diffusion rate. In model E, the 120° OH^-−reorientation (corresponding to inter-H-bond jumps) is assumed to be the fast local motion, whereas the proton transfer process within the H-bond represents the rate-determining step of the diffusion mechanism. The figure shows clearly, that only model E agrees with the data.

It should be emphasized, that the self-diffusion coefficient D_s from PFG-NMR measurements was used to fix the slope of the linewidth curve in the low-Q limit (Fig. 3.24). This has been decisive for obtaining this unambiguous

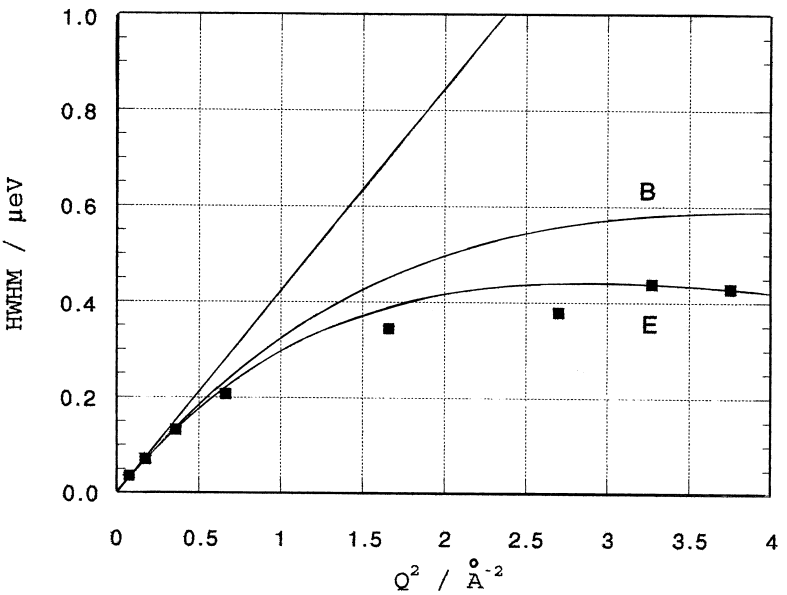

Fig. 3.24. Translational proton jump diffusion in $CsOH \cdot H_2O$ (Fig. 6 in [91]; after [97]): the measured quasielastic diffusion linewidths (squares) are compared to the width functions $\Gamma(Q)$ of models B and E. Only model E agrees with the experimental results. The straight line corresponds to the low-Q limit $\Gamma(Q) = D_s Q^2$ of the width function, where D_s is the proton self-diffusion coefficient obtained from PFG-NMR measurements [97]. The ambiguity mentioned in the legend of Fig. 3.23 has now been resolved.

result from the comparison of the theoretical curves to the measured neutron data, and it is a demonstration of the usefulness of combining $^1H - NMR$ techniques with QINS experiments on protonic conductors. The direct determination of D_s by QINS, which requires low Q, is presently limited to the regime $D_s \geq 10^{-7} cm^2/s$. Since at low Q, the linewidth is equal to $D_s Q^2$, it rapidly approaches the limit of timescale imposed by the best possible energy resolution. Therefore, when the QINS resolution becomes insufficient, it is recommended to resort to the NMR spin-echo technique employing a steady-state or pulsed magnetic field gradient (PFG) for the measurement of the proton self-diffusion coefficient D_s (see Chap. 10). This allows one to reach values down to about $10^{-9} cm^2/s$. They may be used as an input to the analysis of large-Q QINS spectra, permitting to extract the unique geometrical and dynamical information on the microscopic details of the proton motion, contained in them. Note that at large Q the requirements of energy resolution are much less stringent as long as the diffusion coefficient is known.

Another important class of ion conducting substances are doped perovskites of the type $A(BO_3)$. For instance, $Sr(CeO_3)$ is ion conducting if

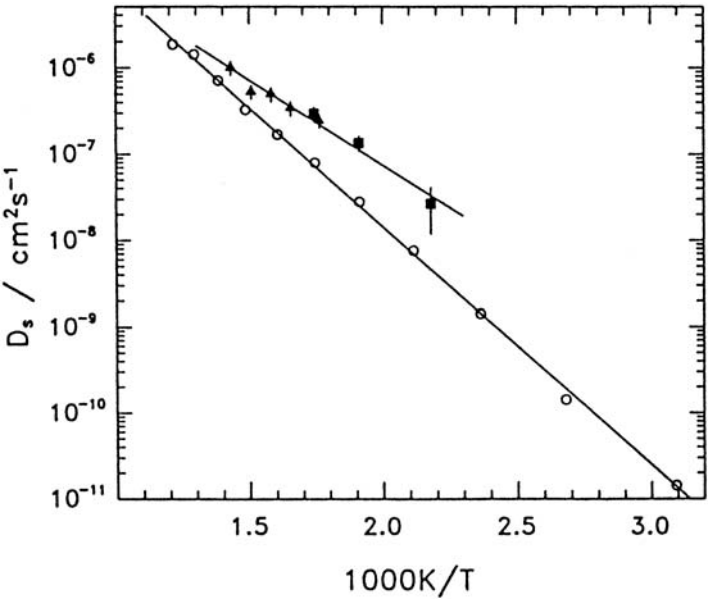

Fig. 3.25. Protonic self-diffusion coefficient for the protonic conduction in a H_2O-vapour doped perovskite:
$Ba[Ca^{2+}_{(1+x)/3}Nb^{5+}_{(2-x)/3}]O^{2-}_{(3-x)/2}H_x$; full squares, full triangles: D_s from quasielastic neutron scattering, $\Gamma = Q^2 D_s$; open circles: D_σ from electrical conductivity $\sigma(T)$ using the Nernst-Einstein equation [108], with H_R set equal to 1.

a few (x) % of the Ce^{4+} ions are substituted by Yb^{3+} thus creating $(x/2)$ oxygen-site vacancies. This leads to oxygen conduction by the mobility of the vacancies. If, in addition, the material is exposed to water vapour, the H_2O molecules disintegrate. All hydrogens are forming OH^- ions and the hydrogen (proton) is highly mobile. Also in these materials, it is assumed that the electrical conductivity of the substance is determined by proton transfer or jumps between the oxygen atoms (OH–O→O–HO) combined with fast rotations of the hydroxyl ions (Grotthuß process) [110]. Proton diffusion in a ceramic strontium cerate was observed for the first time by quasielastic neutron scattering [111], with a value of D_s roughly consistent with the experimental conductivity σ. The hydrogen concentration was obtained by microgravimetry. Similar experiments were carried out by Pionke et al. [108] for a mixed niobate of the type $Ba[Ca_{(1+x)/3}Nb_{(2-x)/3}]O_{(3-x/2)}H_x$, where the vacancies are produced by the mixture of the 2- and 5- valent Ca and Nb ions. Fig. 3.25 compares the D_s values resulting from QENS experiments extrapolated to small Q, and the charge-diffusion coefficient D_σ calculated by the Nernst-Einstein equation from the electrical conductivities. The (unknown) Haven ratio H_R was set equal to 1. The approximate agreement suggests that the conductivity is predominantly protonic, and not due to hole or electron con-

duction. We emphasize that in impedance spectroscopy the bulk conductivity is determined by an extrapolation procedure to eliminate the strong influence of grain boundaries and electrode effects on the electrical measurements. On the other hand, the scattering experiments should not be influenced by grain boundaries.

For large Q values, the quasielastic spectrum shows the superposition of two Lorentzians in the μeV region. They were tentatively explained by two groups of potential wells for the protons, namely shallow and deep ones depending on the charge of the adjacent ions. Further experiments with low resolution ($\sim$ 0.1 meV) yield a very broad spectrum. It is interpreted by rapid OH^- rotations connected with the conduction process [108]. For a proton, rotating in the hydroxyl ion, and jumping from time to time between neighboring O^- ions, one expects an incoherent dynamic structure factor for an isotropic powder sample.

$$S_{\mathrm{inc}}(Q,\omega) = F(Q)\mathrm{e}^{-Q^2\langle u\rangle^2}\left[\sum_i \frac{\Gamma_i/\pi}{\Gamma_i^2+\omega^2}\right] + [1-F(Q)]\mathrm{e}^{-Q^2\langle u^2\rangle}\frac{\Gamma_{\mathrm{R}}/\pi}{\Gamma_{\mathrm{R}}^2+\omega^2}\ . \tag{3.65}$$

This expression is again based on the approximation of dynamical independence already described above. The first term describes the translational diffusion of the hydrogen atoms. The second term results from the OH^- rotation, whereby the small additional broadening of this term due to translational diffusion has been neglected. $F(Q)$ is the elastic incoherent structure factor (EISF; see (3.18)) of the protonic motion on a spherical shell with a radius ρ, namely (see [3])

$$F(Q) = \left(\frac{\sin\rho Q}{\rho Q}\right)^2\ . \tag{3.66}$$

The function $\exp(-Q^2\langle u^2\rangle)$ is the Debye-Waller factor and $\langle u^2\rangle$ is the mean square amplitude of the phonon vibrations. The width of the line Γ_{R} is related to the rotational diffusion coefficient $D_{\mathrm{R}} = 1/\tau_{\mathrm{R}}$, where τ_{R} is the relaxation time for the diffusion on the sphere. The rotational term holds approximately for $Q\rho < 1$. Otherwise, further terms have to be added with widths $\Gamma_{\mathrm{R}} = \ell(1+\ell)D_{\mathrm{R}}$ ($\ell = 1, 2, \ldots$). The experiments lead to a width $\hbar\Gamma_{\mathrm{R}} = 0.70$ meV at 670 K which does not depend on Q and yields $1/\tau_{\mathrm{R}} = 10^{12}$ s^{-1}. The protonic transfer or jump rate is about 100 times smaller. The Q dependence of the intensity for the (resolution broadened) central line corresponding to the first term is shown in Fig. 3.26. It yields $F(Q)$, the EISF, and a value of $\rho = 0.70$ Å. The value of ρ can be compared with the OH-distance in water or ice which is about 1 Å. These results are consistent with the Grotthuß process introduced at the beginning of this section. They bear some striking similarity to those observed in $CsOH\cdot H_2O$ by Lechner et al. [97] (see above).

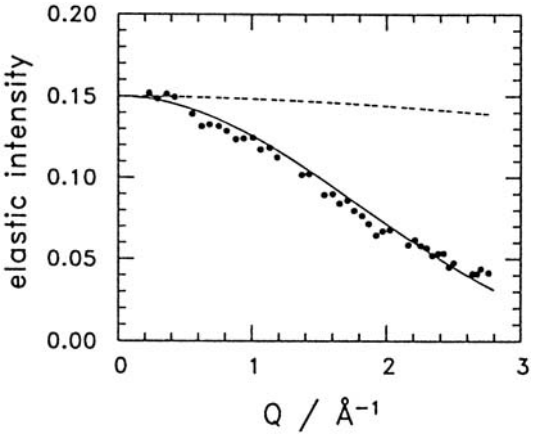

Fig. 3.26. Intensity of the experimental narrow quasielastic line for the mixed perovskite as in Fig. 3.25, vs. Q (black dots): The steep decrease vs. Q, corrected for the Debye-Waller factor (dashed), yields the elastic incoherent structure factor (EISF), calculated for OH^- rotations with an average sphere radius of 0.7 Å (solid line) [108].

3.10 Proton Conduction: Diffusion Mechanism Based on a Chemical Reaction Equilibrium

The Grotthuß type proton diffusion mechanism described in the previous section, for instance in the case of $CsOH \cdot H_2O$, implies a simple chemical reaction equilibrium between proton donor and acceptor molecules, which reads: $H_2O + OH^- \Longleftrightarrow OH^- + H_2O$. An analogous reaction has been studied in more detail in the solid-state protonic conductor $Rb_3H(SeO_4)_2$ [112, 113].

The crystalline compounds with the general formula $M_3H(XO_4)_2$, (M=K, Rb, Cs; X=S, Se), where hydrogen bonding plays an important role, are quasi two-dimensional solid-state protonic conductors (SSPC). They have high-temperature phases with rhombohedral symmetry and extremely high protonic conductivity. The crystallographic phases existing at lower temperatures are monoclinic or triclinic and show lower but still appreciable protonic conductivities in a fairly broad temperature range in the vicinity of the SSPC phase transition [114, 115]. Information on the diffusive proton motion has been obtained from a series of QINS studies on $Rb_3H(SeO_4)_2$ [112]. In the following we will discuss results from a part of these experiments, where medium-resolution QINS has been used. The time-averaged crystal structure of $Rb_3H(SeO_4)_2$ [116–119] can be described as a sequence of $Rb \cdots H[SeO_4]_2$ layers alternating with Rb-coordination polyhedra layers, both perpendicular to the pseudo-hexagonal c-axis. The atoms in the Rb- layers, of type Rb(2), have 9-fold coordination by the oxygen atoms forming the bases (O(1), O(3) and O(4)) of the selenate tetrahedra, which are parallel to the layers. The top

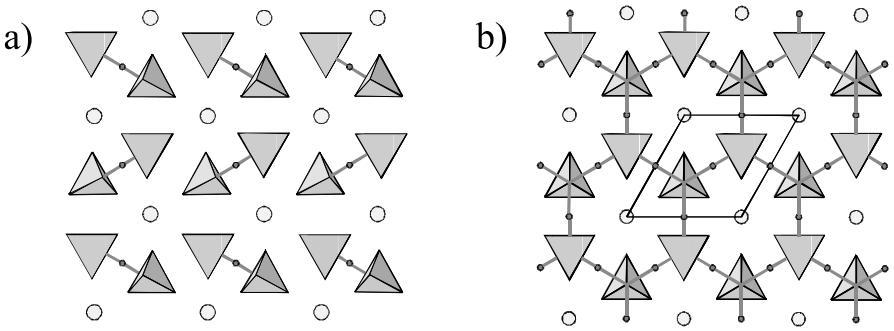

Fig. 3.27. a) Monoclinic $Rb_3H(SeO_4)_2$: "zero-dimensional" H-bond network as seen in a projection along the c-axis. Small circles: protons; large circles: Rb^+ ions; b) Trigonal $Rb_3H(SeO_4)_2$: two-dimensional dynamically disordered H-bond network in plane perpendicular to *c*-axis; after [113].

oxygen atoms (O(2)) of the selenate tetrahedra are inter-connected by hydrogen bonds, forming $H[SeO_4]_2^{3-}$ dimers at low temperatures (see Fig. 3.27 a): "zero-dimensional" H-bond network) and layers of two-dimensional dynamically disordered H-bond networks in the proton conducting high-temperature phase ($T \geq 449\,\mathrm{K}$; Fig. 3.27 b)). The time averaged structure of the latter is trigonal, space group ($R\bar{3}m$). The quasi-planar H-bond networks exhibit a protonic conductivity exceeding, by an order of magnitude, that observed along the c-axis which is perpendicular to these planes [114, 115].

In the QINS measurements, translational proton diffusion occurring on the $10^{-8}s$ time scale was directly observed [120] as well as much faster localized diffusive proton motions (time scales: $10^{-9}\,\mathrm{s}$ to $10^{-11}\,\mathrm{s}$ [121]). Only the latter will be discussed here.

An EISF study [112, 122] suggests that the local proton-density distribution resulting from a limited time-average (from $10^{-11}\,\mathrm{s}$ to $10^{-10}\,\mathrm{s}$;) already has threefold symmetry. It comprises the regions of the three H-bonds connecting a given (selenate top) oxygen to its three neighbouring selenate top oxygens in the same proton conducting plane (Fig. 3.28).

The "trigonal-asymmetric hydrogen bond" (TAHB) model [122] corresponds to this picture: The local proton site arrangement comprises a central site 1, with an average proton residence time τ_1 , connected by the jump vectors $\boldsymbol{R}_{21}$, $\boldsymbol{R}_{31}$ and $\boldsymbol{R}_{41}$ to 3 external sites with identical residence times τ_2. The 3 vectors (of equal lengths) point into the directions of the three H-bonds (Fig. 3.29), with end points located fairly close to the bond centers. The two jump rates, $1/\tau_1$ and $1/\tau_2$, are allowed to be different from each other, implying an asymmetry of the potential in which the proton is moving on the time-scale of this experiment.

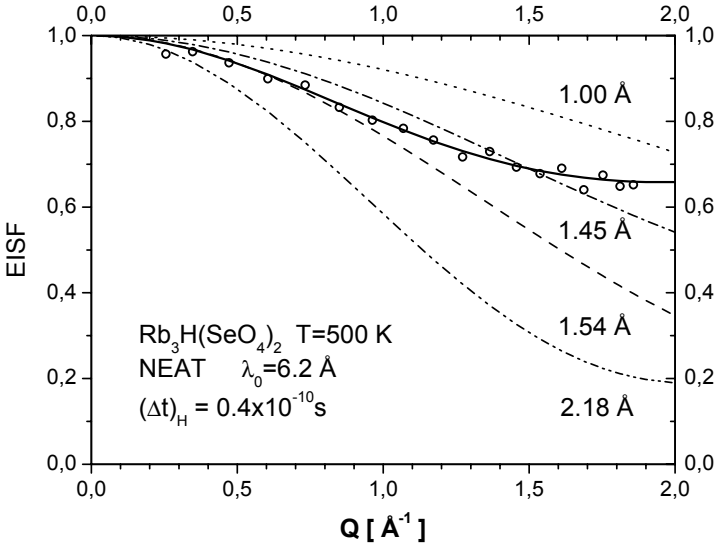

Fig. 3.28. Theoretical EISF curves for several examples of simple two-site and three-site proton jump models (dashed, dotted and dashed-dotted lines) are compared to the "apparent" EISF (open circles) obtained at medium energy resolution with the time-of-flight spectrometer NEAT (after [112]). The simple models are not able to reproduce the experimentally observed data, whereas the successful trigonal-asymmetric hydrogen bond (TAHB) model (solid line; see text) gives good agreement [122].

The time-dependent site occupation probabilities for the 4 sites are denoted by $W_j(t)$. Their time-averages,

$$W_j^{\infty}(t) = \lim_{t\to\infty} W_j(t), \tag{3.67}$$

are used to introduce an order parameter η,

$$\eta = 2W_1^{\infty} - 1, \tag{3.68}$$

where full order ($\eta = 1$) means that there is no proton exchange with the external sites. The incoherent scattering function of the model is given by [122]:

$$S_{\mathrm{inc}}(\boldsymbol{Q},\omega) = \mathrm{EISF}(\boldsymbol{Q}) \cdot \delta(\omega) + \mathrm{QISF}_2(\boldsymbol{Q}) \cdot \mathcal{L}_2(H_2,\omega) + \mathrm{QISF}_3(\boldsymbol{Q}) \cdot \mathcal{L}_3(H_3,\omega) \tag{3.69}$$

Here the elastic and quasielastic incoherent structure factors, EISF and QISF_j, depend on the jump vectors and on η. The two Lorentzians are given by:

$$\mathcal{L}_j(H_j,\omega) = H_j/[(H_j)^2 + \omega^2]/\pi \tag{3.70}$$

$$H_2 = (3/\tau_1 + 1/\tau_2) = 6/(1-\eta)/\tau_1; \tag{3.71}$$

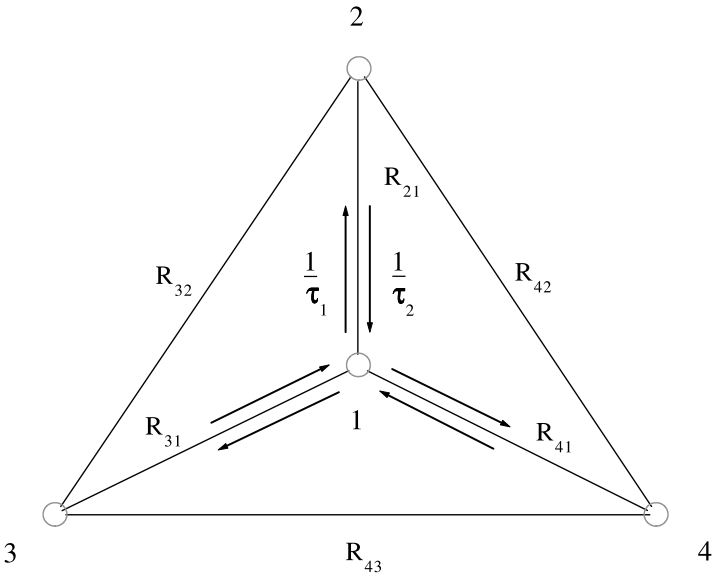

Fig. 3.29. Local site arrangement corresponding to the trigonal-asymmetric hydrogen bond model. This model is compatible with the trigonal symmetry of $Rb_3H(SeO_4)_2$ and with the measured EISF. The central site 1, with the average proton residence time τ_1, is connected to the three external sites, with residence time τ_2, by the jump vectors $\boldsymbol{R}_{21}$, $\boldsymbol{R}_{31}$ and $\boldsymbol{R}_{41}$. The EISF analysis (Fig. 3.28) suggests that most of the proton probability density is located in site 1. This is, because the two proton exchange rates, $1/\tau_1$ and $1/\tau_2$, are different (after [122]).

$$H_3 = 1/\tau_2 = 3(1+\eta)/(1-\eta)/\tau_1. \tag{3.72}$$

A comparison of this model to the QINS spectra obtained at 500 K gave η = 0.746 and R_{21} = 1.785 Å. The asymmetry represented by this value of η is appreciable. Accordingly, the occupancy of site 1 is at least 5 times larger than the sum of the occupation probabilities of the 3 external sites. From this it also follows, that – at the temperature of the experiment – the average lifetime of the dimer is about 20 times shorter than that of the monomers, a consequence of the asymmetry of the potential. The meaning of these observations has been discussed in more detail in [112] and [122]. To summarize, the important aspect of the obtained η-value is the result that the proton essentially remains bonded to the original selenate top oxygen, i.e. to one selenate group, for a period of the order of at least $10^{-10}s$. The value of the jump distance R_{21} may, however, be taken as an indication that the proton is also exploring - on the $10^{-11}s$ to $10^{-10}s$ time scale - a path into the hydrogen bridge, although with rather low probability. These observations have been interpreted as a consequence of the presence of an intracrystalline chemical equilibrium reaction: alternation between the association of the monomers $[HSeO_4]^{1-}$ and $[SeO_4]^{2-}$, resulting in the dimer $[H(SeO_4)_2]^{3-}$ (H-bond for-

mation), and the dissociation of the latter into the two monomers (H-bond breaking) [112]. Reaction rates and potential barriers for association and dissociation processes have been determined, as well as temperature-dependent proton exchange rates between neighbouring selenate ions.

It may be concluded, that the dynamical disorder existing in the high-temperature phase of $Rb_3H(SeO_4)_2$ can be described by the above-mentioned chemical equilibrium reaction. The two distinct transient chemical states play different specific roles in the mechanism of protonic conductivity. While in the monomer state the protonated monomer via reorientation makes the proton available for three different elongated (and therefore weak) hydrogen bonds, the dimer state corresponding to the creation of a strong (but short-lived) H-bond, with the proton close to the center of the bond, provides the opportunity for proton transfer across the hydrogen bridge.

3.11 Two-Dimensional Diffusion

In view of the important role played by low-dimensional ionic conduction and diffusion in solid-state physics, electrochemistry and even in biology, we present several results concerning this problem. These have been obtained, for instance, in studies of layered structures exhibiting quasi two-dimensional proton conduction and diffusion, such as $CsOX \cdot X_2O$, $M_3X(AO_4)_2$, and $Zr(XBO_4)_2 \cdot X_2O$, (where M = NH_4, Rb, Cs; A = S, Se; B = P, As; X = H, D).

Obviously, the concept of low-dimensionality should not be understood in the sense of strictly planar motions, since there will be local deviations from this idealized picture. The essential condition is, that the diffusing protons stay within the conducting layers of the crystal at least during the observation time defined by the energy resolution of the experiment (see Sect. 3.2, (3.21), and the related discussion). This also implies that the mean square displacement parallel to the layer, the proton has acquired during this time, is much larger than perpendicular to it.

In previous paragraphs, we have already mentioned the cases of the layered structures Ba_2NH [88] (see Sect. 3.8), $CsOH \cdot H_2O$ [97] (see Sect. 3.9) and $Rb_3H(SeO_4)_2$ [122] (see Sect. 3.10). All these structures are pseudo-hexagonal or trigonal. The distances between neighbouring (transient) sites of mobile ions found in crystallographic studies are much shorter within the layer planes than in directions parallel to the c-axes being perpendicular to these planes. This leads to the assumption, that ion diffusion and ionic conductivity are likely to be confined to two dimensions. Such assumptions have been made occasionally, in the absence of single crystals which would allow the direct determination of the dimensionality by a QENS experiment. For $CsOH \cdot H_2O$, this assumption has been confirmed by spin-lattice relaxation time (T_1) measurements revealing a logarithmic frequency dependence of the relaxation rate T_1^{-1} [43], typical for two-dimensional diffusion. It is

known from theory [123–125], that the corresponding behaviour of T_1^{-1} as a function of $\ln \nu_0$ is linear, whereas for three-dimensional diffusion T_1^{-1} is independent of the nuclear magnetic resonance frequency ν_0 at high frequencies (for details see Sect. 9.2 in Chap. 9). Spin-lattice relaxation also led to the experimental confirmation of 2D-diffusion of Li ions between graphite layers in Li-graphite intercalation compounds via the observed logarithmic magnetic-field dependence of the diffusion-induced component of T_1^{-1} [126]. The same authors also employed quasielastic neutron scattering in order to determine the mean residence time and the jump distance in the diffusion plane of Li ions from the oscillatory Q-dependent behaviour of the measured quasielastic linewidth. In the case of $Rb_3H(SeO_4)_2$, the two-dimensional character of proton diffusion was revealed by conductivity measurements on single crystals [114, 115]. $Zr(HPO_4)_2$, in its β-phase, is another two-dimensional proton conductor with a proton site lattice similar to that of $Rb_3H(SeO_4)_2$ [127]. The proton diffusion mechanism in this crystal comprises – in addition to the two-dimensional long-range transport – a very fast localized diffusive motion related to librations of protonated phosphate tetrahedra [121].

The incoherent neutron scattering function in the low-Q limit for long-range translational diffusion (TD) was already considered in Sect. 3.3 (see (3.31) to (3.33). Accordingly, in three dimensions, when the diffusive motion is isotropic, with a diffusion coefficient D_{3D}, we have for this function

$$S_{\mathrm{TD}}^{3\mathrm{D}}(\boldsymbol{Q},\omega) = \frac{1}{\pi}\frac{D_{3\mathrm{D}}Q^2}{(D_{3\mathrm{D}}Q^2)^2+\omega^2} \quad , \tag{3.73}$$

Certain analytic results [128] concerning the anisotropic case, where the diffusion process is restricted to the planes of a layered structure, will be discussed in the following. For a single-crystalline sample we have then [129]

$$S_{\mathrm{TD}}^{2\mathrm{D}}(\boldsymbol{Q},\omega) = \frac{1}{\pi}\frac{D_{2\mathrm{D}}(Q\sin\theta)^2}{(D_{2\mathrm{D}}(Q\sin\theta)^2)^2+\omega^2} \quad , \tag{3.74}$$

where D_{2D} is the coefficient of self-diffusion in two dimensions, $Q\sin\theta$ the component of the the scattering vector in the diffusion plane, and θ the angle between $\boldsymbol{Q}$ and the normal to this plane. If single-crystals are not available, one has to resort to polycrystalline samples requiring orientational averaging of the above expression. It is known, that the resulting integral over all orientations exhibits a logarithmic singularity at zero energy transfer [129]. This is caused by the fact that diffusion planes which are perpendicular (or close to perpendicular) to the scattering vector $\boldsymbol{Q}$ contribute elastic (or almost elastic) scattering to the QINS function. Experimentally, such a singularity cannot easily be distinguished from truly elastic scattering, and the numerical convolution with a resolution function is rather tedious. The question is to what extent the characteristic feature of low-dimensionality represented by the above-mentioned singularity can still be exploited when the observed

scattering function is resolution-broadened. Evidently the logarithmic singularity is cancelled by finite resolution. It has been shown that for resolution functions which have the shape of a Lorentzian (with HWHM equal to H) or of a sum of Lorentzians (which is typically the case in BSC experiments) the orientationally averaged resolution-broadened QINS function for 2D-diffusion,

$$\langle S^{\mathrm{2D}}_{\mathrm{TD}}(\boldsymbol{Q},\omega)\rangle^{\mathrm{resol}}_{\mathrm{orient}} = \frac{1}{2\pi}\int_0^{2\pi} \mathrm{d}\Phi\ \frac{1}{2}\int_0^{\pi} \sin\theta \mathrm{d}\theta\ L(\theta,\omega) \tag{3.75}$$

where

$$L(\theta,\omega) = \frac{1}{\pi}\frac{D_{\mathrm{2D}}(Q\sin\theta)^2 + H}{[D_{\mathrm{2D}}(Q\sin\theta)^2 + H]^2 + \omega^2} \tag{3.76}$$

can be written in closed form [128]. The explicit expression is lengthy and will not be given here. Instead, Fig. 3.30 shows the result of numerical calculations of this function for a two-dimensional diffusion coefficient D_{2D} with $D_{\mathrm{2D}}Q^2 = 7.5\,\mu\mathrm{eV}$ and for four different values of the resolution $\Delta(\hbar\omega) = H$. The curves are shown as full lines with circles. For comparison, the Lorentzian- shaped three-dimensional diffusion scattering functions are also shown (simple full lines). Here D_{3D} has been set equal to $2D_{\mathrm{2D}}/3$, because this leads to identical linewidths (and lineshapes) for two- and three-dimensional diffusion in the low-resolution limit. The resolution functions are shown together with the scattering functions, but on a reduced scale. Although a difference between the lineshapes for different dimensionality starts to be visible, when $D_{\mathrm{2D}}Q^2 \sim H$ (see Fig. 3.30b), it is seen that H must be about 10 times smaller than $D_{\mathrm{2D}}Q^2$ in order to permit a clear distinction of 2D- and 3D-diffusion by the shapes of the respective scattering functions. The expression given above is valid only at small Q, where Lorentzian linewidths (for single-crystals) exhibit the $D_{\mathrm{2D}}Q^2$-behaviour and are therefore very small and difficult to be measured. At large Q, i.e. outside of the $D_{\mathrm{2D}}Q^2$-regime, where much larger and correspondingly more easily measurable linewidths are observed, lineshapes very similar to expression (3.75) are expected. But unfortunately, in this Q-region the shape typical for low-dimensionality cannot be observed in its pure form, because of the simultaneous presence of additional quasielastic components due to fast localized diffusive motions usually connected with the diffusion mechanism. These are probably the reasons, why the lineshape predicted for polycrystalline samples by (3.75) has so far not been observed experimentally.

The study of the anisotropy of translational diffusion in single-crystalline material is straight-forward. As an example we discuss the transport of water molecules on the surface of a membrane with a two-dimensional crystalline structure [130, 131]. In biological membranes (cf. Chap 12), proton diffusion connected with conduction of protons provides an important mechanism of energy transduction in living organisms. The purple membrane

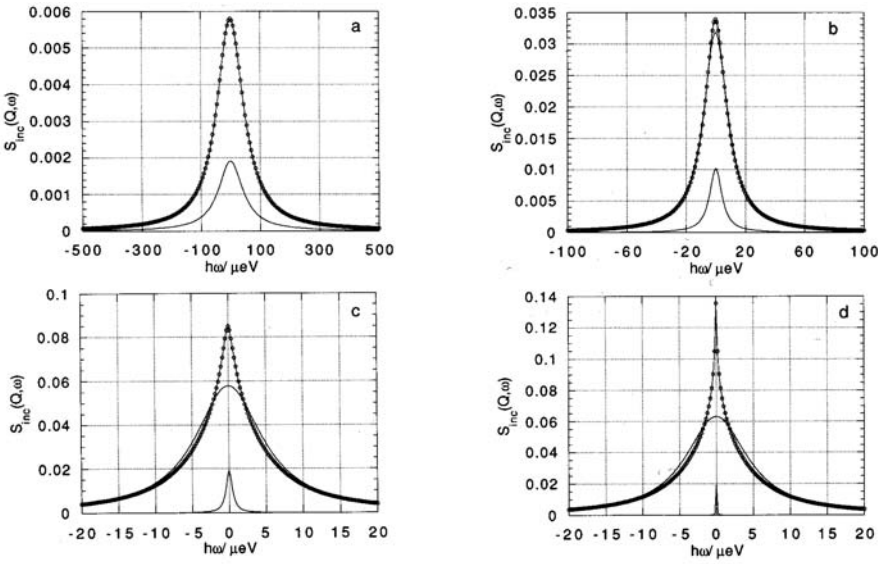

Fig. 3.30. Assuming a two-dimensional diffusion coefficient D_{2D}, with $D_{2D}Q^2 = 7.5\,\mu$eV, the resolution-broadened scattering function (3.75) has been calculated for four different energy resolutions H (HWHM): (a) $50\,\mu$eV; (b) $5\,\mu$eV; (c) $0.5\,\mu$eV; (d) $0.05\,\mu$eV. The corresponding curves are shown as full lines with circles. For comparison the Lorentzian-shaped three-dimensional diffusion scattering functions for the same "effective" diffusion coefficient are also shown (simple full lines). The resolution functions are given on a reduced scale (after [128]).

(PM) of Halobacterium salinarum, for instance, contains the protein bacteriorhodopsin (BR) which becomes a one-dimensional pulsed proton conductor when activated by light. This is a light-driven proton pump generating an electrochemical gradient across the membrane, which is employed by the bacterium as an energy source. After having been pumped from the cell-interior to the membrane surface, the protons are transported by a mechanism of surface conduction towards other proteins located within the same membrane: The light-generated electrochemical potential across the cell membrane is utilised by the halobacteria to furnish the driving force for ATP synthesis by energizing the rotation of the turbine-like machinery in ATP synthase. Water molecules near the surface are known to be relevant for this biological function, since they have been shown to assist the proton conductivity [132]. Hydration water, its interaction with the surface of biological macromolecules and macromolecular complexes, and its diffusion generally play an important role in structure, dynamics and function of biological systems [133, 134]. It is therefore of considerable interest to study the proton diffusion mechanism within and close to the hydration layers of membranes. Similar to the case of bulk water, it is expected that during the diffusion process protons are

exchanged between water molecules acting either as acceptors (forming for instance $(H_3O)^+$) or as donors (producing $(OH)^-$ ions). A "solid-like" Grotthuß feature (see Sect. 3.9) is added to the diffusion in the liquid water phase by the presence of fixed protonation sites on the surface of purple membrane. It is worthwhile to note, that these sites are arranged in space in a perfectly regular manner, since the bacteria use the most efficient packing of BR: trimers of BR molecules embedded in a lipid bilayer matrix are aligned in a two-dimensional hexagonal single-crystalline structure [135]. However, since the pH-value is not very different from 7, the concentration of charged particles is very low. The protons spend most of the time as part of diffusing neutral water molecules with only rare events of exchange between different "vehicles" (see Sect. 3.9). Therefore, for the purpose of analyzing neutron scattering experiments, the whole mechanism of diffusion may to a good approximation be classified as that of molecular diffusion.

The crystalline order of PM has been exploited in QINS [130] and PFG-NMR [131] measurements in a study of the anisotropy of proton diffusion relative to the membrane surface. For this purpose about 20.000 layers of purple membranes were stacked approximately parallel to each other (mosaic spread: about 12° FWHM) at defined relative humidities (r.h.). The membrane stacks had been produced, starting from an aqueous suspension of membrane pieces, by alignment of the membranes through evaporation of water, using aluminium foils as a substrate. At 100 % r.h., with water layer thicknesses of about 10 Å between neighbouring membranes, the protons of water molecules were found to participate in a process of two-dimensional long-range translational diffusion parallel to the membrane plane, with a self-diffusion coefficient $D_s = 4.4 \cdot 10^{-6} cm^2 s^{-1}$ at room temperature, i.e. about five times smaller than the known bulk value of water. At the same time, they are also participating in a fast localized diffusive motion which can - at least partially - be asigned to the rotation of water molecules. This was observed to be about six times slower than in bulk water. These motions are sufficiently fast to produce quasielastic broadenings clearly seen with an elastic energy resolution of 16 μeV FWHM (see Fig. 3.31). Finally, a translational diffusion jump distance of 4.1 Å was derived from the Q-dependent behaviour of the quasielastic linewidth at large scattering angles (see Fig. 3.32). This distance is three times larger than the corresponding quantity of bulk water.

The relative slowness of the diffusion process may partly be due to the restricted space available within the hydration layers. It might also be caused, together with the large value of the jump distance, by the presence of fixed protonation sites on the membrane surface. These might have nearest-neighbour distances similar to those of neighbouring lipid head groups, which are of this order of magnitude. At these protonation sites, hydrogen bonds are expected to be formed, with lifetimes exceeding those of bonds which exist between neighbouring H_2O molecules in bulk water.

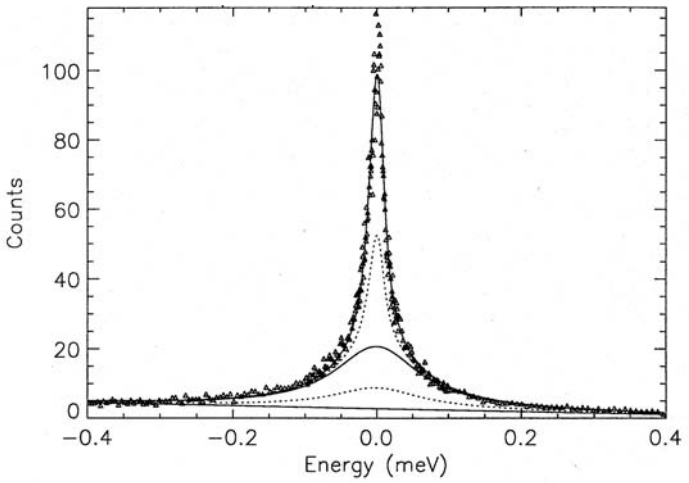

Fig. 3.31. Fit of a model for two-dimensional translational diffusion of water to QINS spectra (data points shown as triangles) of hydrated purple membrane stacks oriented with an angle $\alpha = 135°$ with respect to the incident neutron beam. These data were taken with the inverted time-of- flight technique (IRIS, see Sect. 3.4) at the scattering angle $\varphi = 90.4°$. The spectra were not corrected for multiple scattering (MSC), but MSC was taken into account in the fitted theoretical model: The solid lines represent (from top to bottom) the fit result for the total scattering function including all terms, the sum of all rotation-broadened components of the scattering function (including the backgound B), and B. The dotted lines are the two MSC contributions: a rotation-broadened MSC component sitting on the background line, and a MSC component without rotation broadening on top of the rotation-broadened single-scattering contribution; after [131].

An attempt to relate the measured proton diffusion coefficient D_s to the protonic conductivity σ (see Sect. 3.8) is of interest for elucidating the transport mechanism [91]. The surface conductivity is known from dielectric measurements [136]. By extrapolation to the hydration level of $\mathcal{H} = 0.28$ employed in [130, 131] ($\mathcal{H}$ is given in units of g of water per g of PM), a value of $\sigma = 2.15 \cdot 10^{-8} \Omega^{-1}\mathrm{cm}^{-1}$ was obtained. From this the charge diffusion coefficient D_σ is found in the region $4.4 \cdot 10^{-6}\mathrm{cm}^2\mathrm{s}^{-1} \leq D_\sigma \leq 58 \cdot 10^{-6}\mathrm{cm}^2\mathrm{s}^{-1}$, if the (unknown) concentration of the positive charge carriers is varied from pH = 5.9 to pH = 7.0, where the lower limit would correspond to $D_\sigma = D_\mathrm{s}$. The Haven ratio, $H_\mathrm{R} = D_\mathrm{s}/D_\sigma$, contains information on the proton transport mechanism (see Sect. 3.8 and Chap. 1). Whereas $H_\mathrm{R} = 1$ would correspond to the unrealistic case of a pure vehicle mechanism, the upper limit ($H_\mathrm{R} = 1/13$) probably is equally unrealistic, because the PM surface is known to be negatively charged, which means that pH < 7.0 near the membrane surface. An intermediate ratio D_s/D_σ appears to be the reality. It corresponds to a mixed mechanism, where protons are transported by molecular ion diffusion

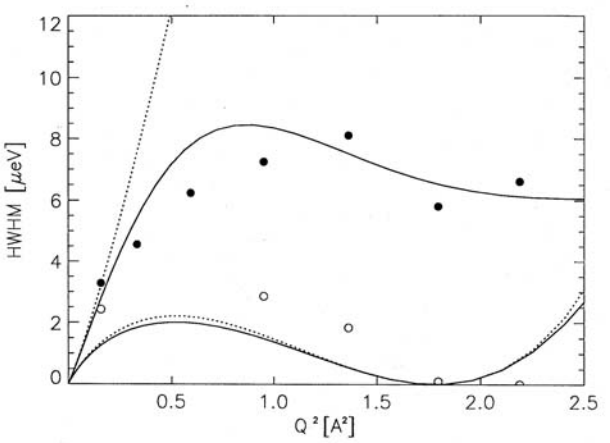

Fig. 3.32. Translational diffusion linewidths (exhibited by spectra as shown in Fig. 3.31) of water on hydrated purple membrane, plotted as a function of Q^2 for two sample orientations: $\alpha = 45°$, open circles; $\alpha = 135°$, full circles. The experimental values are compared with the theoretical width corresponding to an isotropic approximation of the Chudley-Elliott jump-diffusion model in two dimensions. Note that for $\alpha = 135°$, the $\boldsymbol{Q}$ vector is exactly parallel to the membrane plane, when the scattering angle is $\varphi = 90°$, whereas $\boldsymbol{Q}$ is perpendicular to the membrane for the same scattering angle, when $\alpha = 45°$. Therefore the linewidth curve for the latter case approaches zero near $Q^2 = 1.784\,\text{Å}^{-2}$, in agreement with the values observed experimentally. This means that diffusion parallel to the membrane plane has clearly been seen in this experiment, whereas in the direction perpendicular to it the diffusive motion is too slow to be observable with the QINS technique. Dotted lines: behaviour of the width according to the $D_\text{s}Q^2$-law, if this was valid in the whole region of Q^2 shown in the figure (after [131]).

and exchanged from time to time between diffusing particles which encounter each other.

3.12 Coherent Quasielastic Scattering

The diffusion of individual particles treated in the preceding experimental sections is investigated by measuring $S_\text{inc}(Q, \omega)$, i.e. by scattering without the interference of waves that have been scattered by different atoms. Now we deal with aspects of collective motions which reflect correlations between different diffusing particles. Information on these correlations is obtained from the coherent dynamic structure factor $S_\text{coh}(\boldsymbol{Q}, \omega)$. It yields more details on the scattering system; however, the theoretical interpretation is a priori more complex; so far the number of experimental studies on this matter has remained comparatively small.

The theoretical derivation of the coherent scattering function for translational diffusion requires the introduction of the mutual interaction between different particles. A very simple description is the "hard core" or exclusion potential: The particles diffuse over a lattice of cells or sites which are accessible or blocked. This leads to a modified Chudley-Elliott formula [137] and the resulting coherent width is given by

$$\Gamma_{\mathrm{coh}}(c) = \Gamma_{\mathrm{CE}}(\boldsymbol{Q}, c \to 0) \ . \tag{3.77}$$

which we call $\Gamma_0(\boldsymbol{Q})$, and where c is the average site occupancy. In this case the width is equal to the result for incoherent scattering on the dilute system, Γ_{CE}, as derived before (see (3.30)). This coincidence is due to the fact that the thermodynamic coefficient in the chemical diffusion coefficient, $\partial(\mu/k_{\mathrm{B}}T)/\partial \ln c$ (proportional to $1/(1-c)$) just cancels the blocking factor in the single particle diffusion coefficient, $(1-c)$.

Instead of the hard core model, a general potential of the mutual interaction is introduced by the method of linear response in the mean-field approximation [138] which leads to the result

$$S_{\mathrm{coh}}(\boldsymbol{Q}, \omega) = \frac{c(1-c)\Gamma_0(\boldsymbol{Q})/\pi}{\Gamma^2_{\mathrm{coh}}(\boldsymbol{Q}) + \omega^2} \tag{3.78}$$

with

$$\Gamma_{\mathrm{coh}} = \Gamma_0(\boldsymbol{Q}) \left[1 + \frac{c(1-c)V(\boldsymbol{Q})}{kT}\right] \ . \tag{3.79}$$

$\Gamma_0(\boldsymbol{Q})$ is again the value for the dilute case of incoherent scattering, $c \to 0$. $V(\boldsymbol{Q})$ is the Fourier transform in space of the atomic interaction potential. With the Clapp-Moss relation [139] the unknown potential can be directly expressed by the static structure factor for the short-range order of the diffusing particles (corrected for contributions from the host lattice distortion)

$$S_{\mathrm{coh}}(\boldsymbol{Q}) = \frac{c(1-c)}{1 + \frac{c(1-c)V(\boldsymbol{Q})}{kT}} \ . \tag{3.80}$$

This finally leads to

$$S_{\mathrm{coh}}(\boldsymbol{Q}, \omega) = S_{\mathrm{coh}}(\boldsymbol{Q}) \frac{\Gamma_{\mathrm{coh}}/\pi}{\Gamma^2_{\mathrm{coh}} + \omega^2} \tag{3.81}$$

with the coherent line width

$$\Gamma_{\mathrm{coh}}(\boldsymbol{Q}) = \frac{c(1-c)\Gamma_0(\boldsymbol{Q})}{S_{\mathrm{coh}}(\boldsymbol{Q})} \ . \tag{3.82}$$

For very small Q, $S_{\mathrm{coh}}(\boldsymbol{Q})^{-1}$ is proportional to the thermodynamic factor $\partial(\mu/k_{\mathrm{B}}T)/\partial \ln c$, the derivative of the chemical potential with respect to the

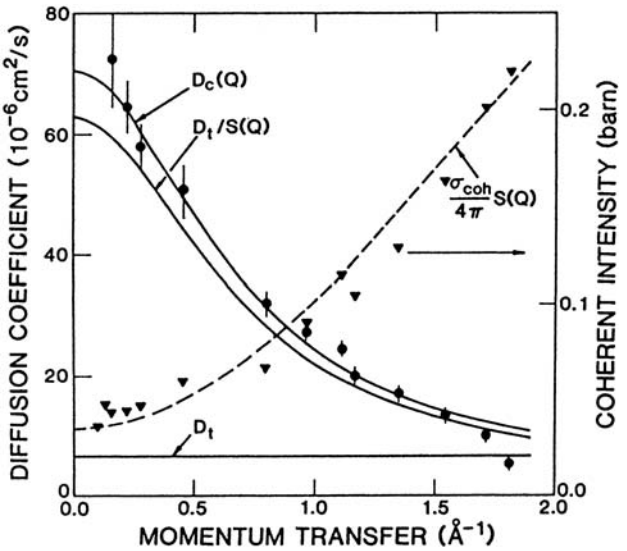

Fig. 3.33. Diffusion of deuterium in Nb: $D_c(Q) = \Gamma_{coh}(Q)/Q^2$ - generalized chemical diffusion coefficient as a function of Q; D_t = tracer or single particle diffusion coefficient obtained from incoherent quasielastic scattering. $S(Q)$ = experimental structure factor for deuterium dissolved in Nb. The ratio $D_t/S(Q)$ is close to $D_c(Q)$ [140].

concentration. This allows one to introduce the chemical diffusion coefficient D_c, namely

$$\Gamma_{coh}(Q \to 0) = \frac{c(1-c)Q^2 D_s(c \to 0)}{S_{coh}(0)} = Q^2 D_c \ . \tag{3.83}$$

Like in diffusion measurements by light scattering (see Chap. 15), the coherent quasielastic width can be intuitively understood by the decay rate of concentration fluctuations with a wave number Q. In (3.82) a maximum of the static structure factor $S(\boldsymbol{Q})$ causes a minimum of the quasielastic width which means: density fluctuations corresponding to strong short-range correlations decay with a very small relaxation rate. For the first time, this "line narrowing" was predicted by De Gennes [141] and observed for liquid argon [142].

In a deuterium loaded bcc niobium crystal the relation between the structure factor $S(\boldsymbol{Q})$ and the coherent width, see (3.82), was investigated (deuterium has a strong coherent scattering contribution). Γ_{coh} and Γ_0 are compared in Fig. 3.33 [140] defining $D_c(\boldsymbol{Q}) = \Gamma_{coh}(\boldsymbol{Q})/Q^2$, whereas the structure factor was calculated with a site blocking model (dashed line) and also experimentally determined, after correction for the strain field contributions from the host lattice.

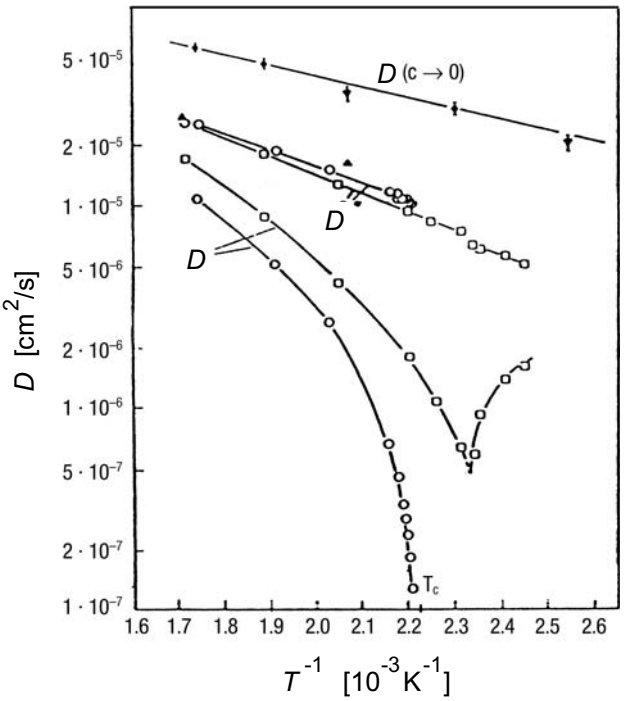

Fig. 3.34. Lower curves: Chemical diffusion coefficient D (called D_c in the text) from mechanical relaxation experiments. Slowing down for $T \to T_c$ near the critical point at the coexistence curve of the NbH_x phase diagram. Open circles: H/Nb = 34.4 at % (critical concentration); open squares: 40.4 at %. D^* = self-diffusion coefficient calculated from the chemical diffusion coefficient using the measured factor $(\partial\mu/\partial \ln c)$. Fair agreement of this quantity is found with D^* from quasielastic scattering with $\Gamma = Q^2 D^*$ for 33 % (full triangle-up) and for 3.2 % H/Nb (full circle and full triangle-down: upper curve). From [143].

Fig. 3.34 compares the diffusion coefficient as obtained from the width Γ_0 of incoherent quasielastic scattering for NbH_x with the chemical diffusion coefficient; this was measured by the long-range mechanical relaxation on such samples (Gorski effect) [59,143]. The results are consistent with (3.83). The "critical slowing down" of the chemical diffusion coefficient D_c is caused by the singularity of the thermodynamic factor $\partial(\mu/k_B T)/\partial \ln c$ near the critical temperature T_c on the top of the miscibility gap in the Nb-H phase diagram. This effect does not show up in the self-diffusion coefficient D_s.

For hydrogen or deuterium atoms the incoherent and the coherent structure factor can be separated in the same scattering experiment, using polarized neutrons and spin analysis after scattering [49].

An entirely different aspect of quasielastic coherent scattering is related to the fluctuations of the host lattice, caused by the diffusing particle [144].

For instance, a hydrogen atom dissolved in niobium is surrounded by atomic displacements. The resulting long-range strain field induces diffuse scattering between the Bragg reflections, which is especially strong close to the Bragg lines, the so-called Huang scattering. The strain field can be described by mutually interpenetrating "distortion clouds", moving along with the protons. Consequently, the coherent diffuse scattering on the host lattice is quasielastic due to these density fluctuations. Neglecting retardation and assuming a linear superposition of the weak distortion fields, the resulting coherent dynamic structure factor can be factorized into two terms: the static structure factor caused by the strain fields of uncorrelated single particles, and the incoherent dynamic structure factor following the Chudley-Elliott formula for the diffusing particles. First quasielastic measurements on the distortion field were performed for hydrogen in niobium [55] (see Sect. 3.5). The coherent quasielastic scattering yields interesting information on the diffusion in the lattice; however, its observation is difficult. Although the distortion scattering is strong close to the Bragg reflections and therefore its integral is easy to observe, the width of the quasielastic spectra is very small in these regions, because it goes as $(\boldsymbol{Q} - \boldsymbol{G})^2$, where $\boldsymbol{G}$ is the reciprocal lattice vector corresponding to the Bragg line. So, in the experiment, a suitable compromise must be found between the intensity of this effect, the resolution, and the closest distance from the reciprocal lattice point, where measurements are feasible with the available energy and momentum resolutions.

A third type of quasielastic coherent scattering concerns the observation of molecular structure factors in the context of translational diffusion. This problem occurs, for instance, in studies of the crystalline high-temperature fast-ion conductor modifications of alkali metal (M) salts, M_2SO_4 and M_3PO_4, of sulfuric and phosphoric acid, respectively. These phases with the polyatomic anions SO_4^{2-} and PO_4^{3-}, are not only cation conductors, but also plastic crystals, since the anions exhibit dynamic rotational disorder. Part of the motivation for quasielastic neutron scattering studies of these compounds [145–147], has arisen from a dispute about a possible cation mobility enhancement by dynamical coupling of cation migration and anion reorientation. Proponents of this coupling model have coined the term "paddle-wheel" mechanism [148–150].

Obviously, the reorientation of the polyatomic tetrahedral sulfate and phosphate ions implies a fast and rigidly coupled motion of the four oxygen atoms bound in each anion, whereas the sulfur and phosphorus atoms may be assumed to stay immobile if coupling between translation and rotation of these ions is neglected. Since oxygen is a purely coherent scatterer, the scattering function $S_{\mathrm{coh}}(\boldsymbol{Q}, \omega)$ is required. If correlations between different rotating ions are neglected, the calculation is straight-forward, employing the same (well-known) models as used for rotational motions in the incoherent scattering case. Details can be found in the literature [145,151,152]. There are

two essential differences between the incoherent and the coherent scattering functions for rotational (localized) motions:

i) In the case of $S_{\rm coh}(\boldsymbol{Q},\omega)$, the elastic scattering of the rotating molecules is entirely concentrated in crystallographic Bragg peaks: the neutron waves scattered from the (infinite-time) probability density distributions in different unit-cells are capable of interference with each other. In other words, there is no EISF that could be measured between the Bragg peaks, and therefore the possibility of the self-consistent normalization based on a well-known integral property[5] of $S_{\rm inc}(\boldsymbol{Q},\omega)$, customary in incoherent scattering, is not available here.

ii) In the absence of elastic and quasielastic *incoherent* structure factors (EISF and QISF), the spatial information concerning the geometry of the rotational motion can only be extracted from the integral of $S_{\rm coh}(\boldsymbol{Q},\omega)$ (excluding Bragg peaks), i.e. from the quasielastic coherent structure factor (QCSF). The normalization problem can be solved, if the compound studied contains an incoherently scattering component. This is the case, e.g. for the sodium salts of sulfuric and phosphoric acid. The incoherent scattering of sodium, determined at small angles, where the intensity of the coherent component is negligible, has been used for normalization [145].

Earlier QENS measurements of Na_3PO_4 taken in the temperature range from 300 K to 973 K have been successfully interpreted in terms of a uniaxial reorientation model with a single time-constant in the 1 to 0.3 ps range (activation energy: 184 meV) for the observed localized diffusive motion [145]. There is, however, a discrepancy between experiment and theory at low Q, up to about $Q = 1.5\,\text{Å}^{-1}$, where the measured QCSFs are larger than the calculated ones (see Figs. 6 and 7 in [145]). In a subsequent paper [147], the discrepancy was explained by a modification of the molecular structure factor. It is caused by a sodium ion attached temporarily at a distance of 2.15 Å from the central atom, above the center of one of the faces of a tetrahedral anion involved in reorientation. Such transient "binding" increases the effective molecular "radius" and, therefore, leads to additional quasielastic intensity for low Q. The same interpretation was also found to be consistent with similar measurements on solid solutions of sodium phosphate and sodium sulfate (Figs. 5 to 7 in [147]). The translational diffusion of sodium ions in Na_3PO_4 was studied with high-resolution backscattering techniques; it was concluded that sodium ion jumps between tetrahedral sites in the cubic high-temperature phase appear to be most important [146]. The diffusion coefficient shows an Arrhenius-type behaviour,
$D_{\rm s}(T) = 1.3 \times 10^{-3}\text{cm}^2\text{s}^{-1} \exp(-630\ \text{meV}/k_B T)$.

This value of the activation energy is considerably higher than that of the reorientational motion, and the time scales of the two types of motion differ by roughly three orders of magnitude: While characteristic times of the an-

[5] The integral of the incoherent scattering function over energy transfer is equal to 1 [3].

ion rotation are in the picosecond range, average residence times of diffusing sodium ions are of the order of nanoseconds. This means that cation transport via a rotational step does not automatically lead to a step of translational diffusion. It should rather be seen as a thermally activated phenomenon related with local potential fluctuations which favour translational diffusion, and which – from time to time – bring a cation into a position favorable for jumping away to a more distant site. These results clearly suggest a certain dynamical correlation between the diffusion of cations and anions in these compounds. But, because of the very different time-scales, a paddle-wheel mechanism in the sense of a synchronous action of rotatory and translatory motions can be excluded for Na_3PO_4.

3.13 Conclusion

Quasielastic scattering of neutrons is an excellent tool to evaluate the elementary steps of diffusion in solids on scales from atomic to mesoscopic dimensions and times. Good examples are the understanding of correlation effects of diffusion in metals with vacancies or of hydrogen diffusion in metals. The latter problem is still exciting regarding, for instance, the elastic displacements and the long-range strain fields produced by rapidly moving protons, as well as the question, to what extent quantum effects related to the protonic motion might exist. So far no such effects were observed, except for the localized modes of a trapped proton. Many questions are still unsolved and need more experiments, for instance quasielastic Huang scattering. Another class of problems deals with diffusion in disordered solids. While the theoretical treatment of systems with highly dilute or extremely concentrated impurities is relatively simple, intermediate concentrations are much more difficult to handle. The behaviour of disordered alloys has not yet been systematically treated.

In the case of ionic crystals, ion diffusion, and especially proton diffusion has been studied in solid-state protonic conductors, e.g. in hydroxide hydrates, hydrogen sulfates and selenates of alkali metals, and in the perovskite structures of acceptor-doped barium or strontium rare earth metal oxides. The specific dynamical features which generally distinguish protonic conductors from other ionic conductors are connected with the fact that, in addition to the ionic character of these crystals, hydrogen bonding plays an important role. In particular, it is the process of formation and breaking of H-bonds, which represents an important ingredient of the proton diffusion mechanisms. The relation between this solid-state chemical reaction and the diffusion of protons has been established. Suitable approximations have been developed which allow a comparatively simple treatment also of systems with intermediate concentrations of mobile ions. When Coulomb interactions, e.g. in silver iodide crystals, play a major role, ion-ion correlations become important and must be taken into account; diffusing ions carry a “correlation cloud” along

with themselves (similar to the Debye-Hückel cloud in ionic solutions). A new theoretical model has been developed along these lines and contributes to the understanding of the relation between ionic diffusion and conductivity in terms of backward-correlated ion jumps. Also non-stoichiometric metallic oxides are interesting with respect to diffusion and electrical conductivity.

An interesting special case are solid rotator phases with ionic conductivity, where the rotating polyatomic anions contribute quasielastic coherent scattering, whereas the translational diffusion of incoherently scattering simple cations is easily isolated if the time-scales are sufficiently different. A certain dynamical correlation between the diffusive cation and anion motions in these compounds has been shown to exist. But, the renowned picture of a "paddle-wheel" mechanism in the sense of a synchronous action of rotatory and translatory motions has so far not been confirmed by QENS experiments.

The interpretation of coherent quasielastic scattering in order to investigate collective effects of diffusion is a new field with a promising future. The high intensities available at modern neutron scattering instruments and especially at the high-power spallation neutron sources now under construction will allow the systematic experimental separation of coherent and incoherent scattering by spin analysis.

In general, future efforts aiming at the synthesis of the results of quasielastic neutron scattering, Mößbauer spectroscopy, nuclear resonance scattering of synchrotron radiation, nuclear magnetic resonance studies, frequency-dependent conductivity spectroscopy using electromagnetic waves from the microwave to the (far) infrared region, and ultrasonic measurements, computer simulation and the development of new analytical approaches will further contribute to a more comprehensive and sophisticated understanding of the diffusion processes in solids.

Notation

a	lattice parameter
b	scattering length
c	site occupancy probability
c_i	isotope concentration of species i
c_t	concentration of traps
$\boldsymbol{d}$	jump vector
D_c	collective or chemical diffusion coefficient
D_1	diffusion coefficient for free diffusion
D_R	rotational diffusion coefficient
D_s	self-diffusion coefficient (usually in 3 dimensions)
D_2D	two-dimensional self-diffusion coefficient
D_3D	three-dimensional self-diffusion coefficient
D_σ	ionic charge or conductivity diffusion coefficient
$E_0,\ E_1$	energy of neutron before and after scattering, respectively

E_{act}	activation energy
$A(Q), F(Q)$	incoherent elastic structure factor (EISF)
$\boldsymbol{G}$	reciprocal lattice vector
$g(\boldsymbol{r})$	pair-correlation function
$G(\boldsymbol{r}, t)$	space and time dependent pair-correlation function
$G_{\mathrm{s}}(\boldsymbol{r}, t)$	space and time dependent self-correlation function
$\mathcal{H}$	hydration level (given in units of g of water per g of biological material)
h	Planck's constant
$\hbar$	Planck's constant / 2π
H_{R}	Haven ratio
$I(\boldsymbol{Q}, t)$	coherent intermediate scattering function
$I_{\mathrm{s}}(\boldsymbol{Q}, t)$	incoherent intermediate scattering function
I_0	incident neutron current density
ΔI_{s}	scattered intensity
$\boldsymbol{k}_0,\ \boldsymbol{k}_1$	wave vector of neutron before and after scattering, respectively
k_0, k_1	wave numbers of neutron before and after scattering, respectively
Δk_{div}	wave number spread caused by divergence
$l,\ d$	jump distances
L_{xy}	distance between elements x and y of a TOF spectrometer
ΔL	uncertainty in the length of the flight path
$\mathcal{L}(H_j, \omega)$	Lorentzian in energy transfer with HWHM = H_j
M	atomic mass
n_0	number density of scattering atoms
N_{c}	number of identical atoms in the scattering specimen
$P(\boldsymbol{r}, t)$	time dependent probability of occupancy
$\tilde{P}(\boldsymbol{Q}, t)$	Fourier transform of P
$\boldsymbol{Q}$	scattering vector
R_{eff}	trapping radius
$S(\boldsymbol{Q}, \omega)$	scattering function, or dynamic structure factor
$S_{\mathrm{inc}}(\boldsymbol{Q}, \omega)$	incoherent scattering function or dynamic structure factor
$S_{\mathrm{coh}}(\boldsymbol{Q}, \omega)$	coherent scattering function or dynamic structure factor
$S^{\mathrm{2D}}_{\mathrm{TD}}(\boldsymbol{Q}, \omega)$	incoherent scattering function for two-dimensional translational diffusion
$S^{\mathrm{3D}}_{\mathrm{TD}}(\boldsymbol{Q}, \omega)$	incoherent scattering function for three-dimensional translational diffusion
Δt	experimental observation time
V	sample volume
v	velocity
v_{th}	thermal velocity
v_0	velocity of incident neutrons
v_1	velocity of scattered neutrons
$V(\boldsymbol{Q})$	Fourier transform of interaction potential
Γ	quasielastic widths

Γ_{R}	quasielastic widths for rotation
$\Gamma_{\mathrm{CE}},\ \Gamma_0$	widths following Chudley-Elliott model
Γ_{coh}	widths of coherent scattering
η	order parameter
θ	polar angle of spherical coordinates
Θ	angle of Bragg reflection
$\Delta\Theta$	beam divergence
λ	neutron wave length
ν	repetition rate of chopper
σ	ionic conductivity
σ_{coh}	coherent bound scattering cross-section
σ_{inc}	incoherent bound scattering cross-section
τ	mean residence (or rest) time a particle spends on a single site, when diffusing on an undisturbed lattice (according to the Chudley-Elliott model)
τ_{j}	time required for diffusive jump
τ_{e}	mean time elapsing between two consecutive encounters, when a particle undergoes diffusion according to the encounter model
τ_{i}	MTOF spectrometer pulse length of pulsing chopper
τ_{ii}	MTOF spectrometer pulse length of monochromating chopper
τ_{r}	relaxation time for the restoration of a displacement field of elastic distortion
τ_{R}	relaxation time of (rotational) diffusion on a spherical surface
τ_{rpm}	duration of the (spectral) period of a TOF spectrometer
τ_{v}	mean residence time of a diffusing vacancy
τ_0	residence (or rest) time of a particle in a trapped state (two-state model of translational diffusion)
τ_1	mean duration of free diffusion in the undisturbed lattice (two-state model of translational diffusion)
τ_1, τ_2	relaxation times of the TAHB model
$\tau_{2\mathrm{S}}$	relaxation time of the two-site jump model
$\Delta\tau_{\mathrm{p}}$	chopper pulse length of XTL-TOF spectrometer
ϕ	scattering angle
Φ	azimuthal angle of spherical coordinates
Ω	solid angle
$\hbar\omega$	energy transfer
$\Delta(\hbar\omega)$	half-width at half maximum (HWHM) of the energy transfer resolution function.
BSC	back scattering
CE	Chudley-Elliott (jump-diffusion model)
CHx	chopper number x
EISF	elastic incoherent structure factor
FWHM	full-width-at-half-maximum
HWHM	half-width-at-half-maximum

MSC	multiple scattering
MTOF	multi-disk chopper time-of-flight
nn	nearest neighbour
nnn	next-nearest neighbour
NSE	neutron spin-echo
PDD	probability density distribution
PWR	pulse-width ratio (optimization method)
QCNS	quasielastic coherent neutron scattering
QCSF	quasielastic coherent structure factor
QENS	quasielastic neutron scattering
QINS	quasielastic incoherent neutron scattering
QISF	quasielastic incoherent structure factor
sc	simple cubic
SSPC	solid-state protonic conductor
TAHB	trigonal-asymmetric hydrogen bond
TD	translational diffusion
TOF	time-of-flight
XTL	(monochromator or analyzer) crystal

References

1. S.W. Lovesey: *Theory of Neutron Scattering from Condensed Matter* (Clarendon Press, Oxford 1984)
2. G.L. Squires: *Introduction to the Theory of Thermal Neutron Scattering* (University Press, Cambridge 1978)
3. M. Bée: *Quasielastic Neutron Scattering: Principles and Applications in Solid State Chemistry, Biology and Materials Science* (Adam Hilger, Bristol 1988)
4. L. Van Hove: Phys. Rev. **95**, 249 (1954)
5. V.F. Turchin: *Slow Neutrons*, Israel program for scientific translations (Sivan Press, Jerusalem, 1965); Russian original: Moscow, 1963
6. H. Stiller. In: *Inelastic Scattering of Neutrons*, vol 2 (IAEA, Vienna 1965) p 179
7. K. Sköld: J. Chem. Phys. **49**, 2443 (1968)
8. R.E. Lechner: *Study of Molecular Rotation by Quasielastic Neutron Scattering*, Lecture presented at the College 4 Meeting, Institut Laue-Langevin Grenoble, Nov. 18, 1971 (unpublished)
9. R.E. Lechner, A. Heidemann: Communications on Physics **1**, 213 (1976)
10. R.E. Lechner. In: *Proceedings of the Conference on Neutron Scattering*, Gatlinburg, Tenn. USA 1976, ed by R.M. Moon (National Techn. Information Service, U.S. Dept. Of Comm., Springfield 1976) pp 310-316
11. H. Hervet, F. Volino, A.J. Dianoux, R.E. Lechner: Phys. Rev. Lett. **34**, 451 (1975)
12. H. Hervet, A.J. Dianoux, R.E. Lechner, F. Volino: J. de Phys. **37**, 587 (1976)
13. R.E. Lechner, J.P. Amoureux, M. Bée, R. Fouret: Communications on Physics **2**, 207 (1977)

14. A.J. Leadbetter, R.E. Lechner. In: *The Plastically Crystalline State*, ed by J.N. Sherwood (Wiley, New York 1979) pp 285-320
15. R.E. Lechner. In: *Mass Transport in Solids*, NATO ASI Series B: Physics, vol 97, ed by F. Benière, C.R.A. Catlow (Plenum Publ. Corp., New York 1983) pp 169-226
16. R.E. Lechner. In: *Quasielastic Neutron Scattering*, Proceedings of the Quasielastic Neutron Scattering Workshop QENS'93, San Sebastián, Spain 1993, ed by J. Colmenero, A. Alegría, F.J. Bermejo (World Scientific, Singapore 1994) pp 62-92
17. T. Springer: *Quasielastic Neutron Scattering for the Investigation of Diffusive Motions in Solids Liquids*, Springer Tracts in Modern Physics, vol 64 (Springer-Verlag, Berlin Heidelberg New York 1972)
18. R.E. Lechner: Physica B **301**, 83 (2001)
19. *Methods of Experimental Physics* vol 23, part B, chap 8-11, ed by D.L. Price, K. Sköld (Academic Press, London 1987)
20. R.E. Lechner, C. Riekel, D. Richter: *Neutron Scattering and Muon Spin Rotation*, Springer Tracts in Modern Physics, vol 101 (Springer, Berlin Heidelberg New York 1983)
21. *Dynamics of Solids and Liquids by Neutron Scattering*, Topics in Current Physics, vol 3, ed by S.W. Lovesey, T. Springer (Springer, Berlin Heidelberg New York 1977)
22. L. Koester, H. Rauch, E. Seymann: Atomic Data and Nuclear Data Tables **49**, 65 (1991)
23. V.F. Sears: Physics Reports **82**, 1 (1982)
24. C.T. Chudley, R.J. Elliott: Proc. Phys. Soc. **77**, 353 (1961)
25. G. Blaesser, J. Perretti, G. Toth: Phys. Rev. **171**, 665 (1968)
26. C. Schönfeld, R. Hempelmann, D. Richter, T. Springer, A.J. Dianoux, J.J. Rush, T.J. Udovic, S.M. Bennington: Phys. Rev. B **50**, 853 (1994)
27. *Neutron Spin Echo*, Lecture Notes in Physics **128**, ed by F. Mezei (Springer, Berlin Heidelberg New York 1980)
28. C.G. Windsor: *Pulsed Neutron Scattering* (Taylor & Francis, London 1981)
29. R.E. Lechner. In: *Proceedings of ICANS-XV Conference, Tsukuba, 2000*, ed by J. Suzuki, S. Itoh (JAERI, Tokai-mura Japan 2001) pp 357-376
30. R.E. Lechner. In: *Neutron Scattering in the 'Nineties* (IAEA, Vienna 1985) pp 401-407
31. R.E. Lechner: Appl. Phys. A **74** [Suppl.], S151 (2002)
32. R.E. Lechner. In: *Proceedings of ICANS-XI*, KEK Report 90-25, ed by M. Misawa, M.Furusaka, H. Ikeda, N. Watanabe (Natl. Lab. for High-Energy Physics, Tsukuba 1991) pp 717-732
33. B. Alefeld, M. Birr, A. Heidemann: Naturwissenschaften **56**, 410 (1969)
34. B. Alefeld, T. Springer, A. Heidemann: Nucl. Sci. Eng. **110**, 84 (1992)
35. B. Frick: Neutron News **13**, 15 (2002)
36. H. Rauch. In: *Topics in Current Physics*, vol 6, ed by H. Dachs (Springer, Berlin Heidelberg New York 1978)
37. C.G. Shull, N.S. Ginrich: J. Appl. Phys. **35**, 678 (1964)
38. C. Schönfeld, R. Schätzler, R. Hempelmann: Ber. Bunsen- Ges. Phys. Chem. **93**, 1326 (1989)
39. A.J. Dianoux: Physica B 182, 389 (1992)
40. B. Alefeld, (unpublished) private communication

41. A. Kollmar, B. Alefeld. In: *Proceedings of the Conference on Neutron Scattering*, Gatlinburg, Tenn. USA 1976, ed by R.M. Moon (National Techn. Information Service, U.S. Dept. Of Comm., Springfield 1976) pp 330-336.
42. M. Prager, W. Press, B. Alefeld, A. Hüller: J. Chem. Phys. **67**, 5126 (1977)
43. R.E. Lechner, H.-J. Bleif, H. Dachs, R. Marx, M. Stahn: Solid State Ionics **46**, 25 (1991)
44. C.J. Carlile, M.A. Adams: Physica B **182**, 431 (1992)
45. V.F. Sears: Adv. Physics **24**, 1 (1975)
46. R.E. Lechner, G. Badurek, A.J. Dianoux, H. Hervet, F. Volino: J. Chem. Phys. **73**, 934 (1980)
47. M. Russina, F. Mezei, R.E. Lechner, S. Longeville, B. Urban: Phys. Rev. Lett. **84**, 3630 (2000)
48. C. Lamers, O. Schärpf, W. Schweika, J. Batoulis, K. Sommer, D. Richter: Physica B **180**&**181**, 515 (1992)
49. J.C. Cook, D. Richter, O. Schärpf, M.J. Benham, D.K. Ross, R. Hempelmann, I.S. Anderson, S.K. Sinha: J. Phys.: Condensed Matter **2**, 79 (1990)
50. K. Sköld, G. Nelin: J. Phys. Chem. Solids **28**, 2369 (1967)
51. J.M. Rowe, J.J. Rush, L.A. de Graaf, G.A. Ferguson, Phys. Rev. Lett. **29**, 1250 (1972)
52. Y. Li, G. Wahnström: Phys. Rev. Lett. **68**, 3444 (1992); Y. Li, G. Wahnström: Phys. Rev. B **46**, 14528 (1992)
53. W. Gissler, G. Alefeld, T. Springer: J. Phys. Chem. Solids **31**, 2361 (1970)
54. V. Lottner, J.W. Haus, A. Heim, K.W. Kehr: J. Phys. Chem. Solids **40**, 557 (1979); V. Lottner, A. Heim, T. Springer: Z. Phys. B **32**, 157 (1979)
55. H. Dosch, F. Schmid, P. Wiethoff, J. Peisl: Phys. Rev. B **46**, 55 (1992)
56. S. Emin: Phys. Rev. B **3**, 1321 (1971)
57. Y. Li, G. Wahnström: Phys. Rev. B **51**, 12233 (1995); see also B. von Sydow, G. Wahnström: Phys. Rev. B **53**, 3171 (1996)
58. H. Metzger, J. Peisl, J. Wanagel: J. Phys. F **6**, 2195 (1976); H. Dosch, J. Peisl: Phys. Rev. Lett. **56**, 1385 (1986)
59. J. Buchholz, J. Völkl, G. Alefeld: Phys. Rev. Lett. **30**, 318 (1973)
60. E. Wicke, H. Brodowsky, H. Züchner: Top. Appl. Phys. **29**, 73 (1978)
61. J. Völkl, G. Alefeld. In: *Diffusion in Solids*, ed by A.S. Nowick, J.J. Burton (Academic Press, London 1975) p 232; Top. Appl. Phys. **28**, 321 (1978)
62. J. Töpler, E. Lebsanft, R. Schätzler: J. Phys. F **8**, L25 (1978)
63. E. Lebsanft, D. Richter, J.M. Töpler: J. Phys. F **9**, 1057 (1979)
64. R.C. Bowman, W.E. Tadlock: Solid State Commun. **32**, 313 (1979)
65. T.K. Halstead, N.A. Abood, K.H.J. Buschow: Solid State Commun. **19**, 425 (1976)
66. D. Richter, R. Hempelmann, L.A. Vinhas: J. Less-Common Met. **88**, 353 (1982)
67. R.C. Bowman, J.R. Johnson: J. Less-Common Met. **73**, 254 (1980)
68. R. Hempelmann, D. Richter, A. Heidemann: J. Less-Common Met. **88**, 343 (1982)
69. R. Hempelmann, D. Richter, R. Pugliesi, L.A. Vinhas: J.Phys. F **13**, 59 (1983)
70. J. Töpler, H. Buchner, H. Säufferer, K. Knorr, I. J. Prandl: J. Less-Common Met. **88**, 397 (1982)
71. D. Richter, T. Springer: Phys. Rev. B **18**, 126 (1978)
72. H. Grabert, H. Wipf: Festkörperprobleme **30**, 1 (1990)

73. D. Steinbinder, H. Wipf, A.-J. Dianoux, A. Magerl, K. Neumaier, D. Richter, R. Hempelmann: Europhys. Lett. **16**, 211 (1991)
74. G. Göltz, A. Heidemann, H. Mehrer, A. Seeger, D. Wolf, Philos. Mag. A **41**, 723 (1980)
75. D. Wolf: Phys. Rev. B **15**, 37 (1977)
76. D. Wolf: Solid State Commun. **23**, 853 (1977)
77. M. Ait-Salem, T. Springer, A. Heidemann, B. Alefeld, Philos. Mag. A **39**, 797 (1979)
78. G. Vogl, W. Petry, Th. Flottmann, A. Heiming: Phys. Rev. B **39**, 5025 (1989)
79. W. Petry: Phase Transitions **31**, 119 (1991); W. Petry, A. Heiming, C. Herzig, J. Trampenau: Defect and Diffusion Forum **75**, 211 (1991)
80. H. R. Schober, W. Petry, J. Trampenau: J. Phys.: Condens. Matter **4**, 9321 (1992)
81. H. Feldmann, R. E. Lechner, D. Wilmer, Mat. Res. Soc. Symp. Proc. **756**, EE2.4.1 (2003)
82. M. Spaeth, K. D. Kreuer, J. Maier, C. Cramer: J. Solid State Chem. **148**, 169 (1999)
83. R. E. Lechner: Solid State Ionics **61**, 3 (1993)
84. M. H. Dickens, W. Hayes, P. Schnabel, M. T. Hutchings, R. E. Lechner, B. Renker: J.Phys. C **16**, L1 (1983)
85. P. Schnabel, W. Hayes, M. T. Hutchings, R. E. Lechner, B. Renker: Radiation Effects **75**, 73 (1983)
86. M. Bénière, M. Chemla, F. Bénière: J. Phys. Chem. Solids **40**, 729 (1979)
87. B. Wegener, R. Essmann, J. Bock, H. Jacobs, P. Fischer: Eur. J. Solid State Inorg. Chem. **29**, 1217 (1992)
88. F. Altorfer, W. Bührer, B. Winkler, G. Coddens, R. Essmann, H. Jacobs: Solid State Ionics **70/71**, 272 (1994)
89. K. Funke: Prog. Solid St. Chem. **22**, 111 (1993); K. Funke, Z. Phys. Chem. **188**, 243 (1995)
90. K. Funke, T. Kloidt, D. Wilmer, C.J. Carlile: Solid State Ionics **53–56**, 947 (1992)
91. R.E. Lechner: Ferroelectrics **167**, 83 (1995)
92. E. Hückel: Z. Elektrochem. **34**, 546 (1928)
93. J.D. Bernal, R. H. Fowler: J. Chem. Phys. **1**, 515 (1933)
94. H.G. Hertz: Z. Phys. Chem. Neue Folge **135**, 89 (1983)
95. H.G. Hertz, B.M. Braun, K.J. Müller, R. Maurer: J. Chem. Educ. **64**, 777 (1987)
96. K. D. Kreuer. In: *Proton Conductors, Chemistry of Solid State Materials 2*, ed by Ph. Colomban (Cambridge University Press, Cambridge 1992)
97. R.E. Lechner, Th. Dippel, R. Marx, I. Lamprecht: Solid State Ionics **61**, 47 (1993)
98. H. Arribart, Y. Piffard: Solid State Commun. **45**, 571 (1983)
99. A. V. Belushkin, C. J. Carlile, L. A. Shuvalov: J. Phys.: Condens. Matter **4**, 389 (1992)
100. Ph. Colomban, G. Lucazeau, R. Mercier, A. Novak: J. Chem. Phys. **67**, 5244 (1977)
101. J.D. Axe, L.M. Corliss, J.M. Hastings, W.L. Roth, O. Muller: J. Phys. Chem. Solids **39**, 155 (1978)
102. J.C. Lassègues, M. Fouassier, N. Baffier, Ph. Colomban, A.J. Dianoux: J. Physique **41**, 273 (1980)

103. N. Baffier, J.C. Badot, Ph. Colomban: Solid State Ionics **2**, 107 (1980)
104. Th. Dippel, K. D. Kreuer: Solid State Ionics **46**, 3 (1991)
105. A.T. Howe, M.G. Shilton: J. Solid State Chem. **34**, 149 (1980)
106. K.D. Kreuer, A. Rabenau, R. Messer: Appl. Phys. A **32**, 45 (1983)
107. K.D. Kreuer, M. Hampele, K. Dolde, A. Rabenau: Solid State Ionics **28-30**, 589 (1988)
108. M. Pionke, T. Mono, W. Schweika, T. Springer, H. Schober: Solid State Ionics **97**, 497 (1997)
109. M. Stahn, R.E. Lechner, H. Dachs, H.E. Jacobs: J. Phys. C **16**, 5073 (1983)
110. K.-D. Kreuer: Chem. Mater. **8**, 610 (1996); C. Herzig: *Diffusion in Metals and Alloys*, ed by F.J. Kedves, D.L. Beke (Trans. Tech. Publ., Switzerland 1983)
111. Ch. Karmonik, R. Hempelmann, Th. Matzke, T. Springer: Z. Naturf. **50a**, 539 (1995)
112. R.E. Lechner, G. Schuck, K. Langer: J. Phys. Soc. Jpn. **70**, 274 (2001) Suppl.
113. G. Schuck, R.E. Lechner, K. Langer: Applied Physics A **74** [Suppl.], S1098 (2002)
114. A.I. Baranov, I.P. Makarova, L.A. Muradyan, A.V. Tregubchenko, L.A. Shuvalov, V.I. Simonov: Sov. Phys. Crystallogr. **32**, 400 (1987, AIP:1988)
115. A. Pawlowski, Cz. Pawlaczyk: Ferroelectrics **81**, 201 (1988)
116. I.P. Makarova, I.A. Verin, N.M. Shchagina: Sov. Phys. Crystallogr. **31**, 105 (1986)
117. A. Bohn, R. Melzer, R. Sonntag, R.E. Lechner, G. Schuck, K. Langer: Solid State Ionics **77**, 111 (1995)
118. R. Melzer, R. Sonntag, K.S. Knight: Acta Cryst. C **52**, 1061 (1996)
119. R. Melzer, T. Wessels, M. Reehuis: Solid State Ionics **92**, 119 (1996)
120. R.E. Lechner, G. Schuck, K. Langer, Th. Dippel, W. Renz, M. Casciola: Solid State Ionics (2003) to be published
121. R.E. Lechner, R. Melzer, J. Fitter: Physica B **226**, 86 (1996)
122. R.E. Lechner: Solid State Ionics **145**, 167 (2001)
123. A. Avogadro, M. Villa: J. Chem. Phys. **66**, 2359 (1977)
124. C.A. Sholl: J. Phys. C **14**, 447 (1980)
125. P.H. Fries: Mol. Phys. **48**, 503 (1983)
126. A. Schirmer, P. Heitjans: Z. Naturforsch. **50a**, 643 (1995)
127. G. Schuck, R. Melzer, R. Sonntag, R.E. Lechner, A. Bohn, K. Langer, M. Casciola: Solid State Ionics **77**, 55 (1995)
128. R.E. Lechner: Solid State Ionics **77**, 280 (1995)
129. A.J. Dianoux, F. Volino, H. Hervet: Mol. Phys. **30**, 1181 (1975)
130. R.E. Lechner, N.A. Dencher, J. Fitter, G. Büldt, A.V. Belushkin: Biophys. Chem. **49**, 91 (1994)
131. R.E. Lechner, J. Fitter, Th. Dippel, N.A. Dencher: Solid State Ionics **70/71**, 296 (1994)
132. G. Careri, M. Geraci, A. Giansanti, J.A. Rupley: Proc. Natl. Acad. Sci. USA **82**, 5342 (1985)
133. N.A. Dencher, J. Fitter, R.E. Lechner. In: *Hydration Processes in Biology*, ed by M.-C. Bellissent-Funel (IOS Press 1999) p 195
134. J. Fitter, R.E. Lechner, N.A. Dencher: J. Phys. Chem. B **103**, 8036 (1999)
135. R. Henderson, P.N.T. Unwin: Nature **257**, 28 (1975)
136. J.A. Rupley, L. Siemankowski, G. Careri, F. Bruni: Proc. Natl. Acad. Sci. USA **85**, 9022 (1988)

137. R. Kutner: Phys. Lett. **81A**, 239 (1981); see also K.W. Kehr, R. Kutner, K. Binder: Phys. Rev. B **23**, 4931 (1981)
138. S.K. Sinha, D.K. Ross: Physica B **149**, 51 (1988)
139. P.C. Clapp, S.C. Moss: Phys. Rev. **171**, 754 (1968); ibid. Phys. Rev. **171** 764 (1968)
140. R. Hempelmann, D. Richter, D.A. Faux, D.K. Ross: Z. Phys. Chem. Neue Folge **159**, 175 (1988)
141. P.G. De Gennes: Physica **25**, 825 (1959)
142. B.A. Dasannacharia, K.R. Rao: Phys. Rev. **137**, 417 (1965)
143. J. Völkl, Ber. Bunsen-Ges. Phys. Chem. **76**, 797 (1972)
144. M.J. Gillan, D. Wolf: Phys. Rev. Lett. **55**, 1299 (1985)
145. D. Wilmer, K. Funke, M. Witschas, R.D. Banhatti, M. Jansen, G. Korus, J. Fitter, R.E. Lechner: Physica B **266**, 60 (1999)
146. D. Wilmer, H. Feldmann, J. Combet, R.E. Lechner: Physica B **301**, 99 (2001)
147. D. Wilmer, H. Feldmann, R.E. Lechner: Phys. Chem. Chem. Phys. **4**, 3260 (2002)
148. A. Kvist, A. Bengtzelius. In: *Fast Ion Transport in Solids*, ed by W. van Gool (North-Holland, Amsterdam 1973) p 193
149. A. Lundén: Solid State Ionics **28-30**, 163 (1988)
150. A. Lundén: Solid State Ionics **68**, 77 (1994)
151. V.F. Sears, Can. J. Phys. **45**, 237 (1967)
152. D.A. Neumann, J.R.D. Copley, R.L. Cappelletti, W.A. Kamitakahara, R.M. Lindstrom, K.M. Kreegan, D.M. Cox, W.J. Romanow, N. Coustel, J.P. McCauley Jr, N.C. Maliszewskyj, J.E. Fischer, A.B. Smith III: Phys. Rev. Lett. **67**, 3808 (1991)

4 Diffusion in Semiconductors

Teh Yu Tan and Ulrich Gösele

4.1 Introduction

This chapter discusses diffusion phenomena in the semiconductors Si, Ge, and GaAs. Silicon and GaAs are the two main materials used in fabricating electronic and optoelectronic devices. Diffusion in Ge will also be mentioned for the reason that it is the simplest case among semiconductors. Diffusion processes are used in doping a semiconductor with n-type and p-type dopant atoms to produce pn-junctions for device operations. The n- and p-type dopants are specific kinds of substitutional impurity species producing the electric carriers electrons (e) and holes (h), respectively, in a semiconductor. Diffusion processes are also involved in the removal of detrimental metallic impurities, in silicide formation and in thermal SiO_2 growth in fabricating devices using Si.

4.2 Diffusion Mechanisms and Point Defects in Semiconductors

Impurity atoms may dissolve in a semiconductor by occupying interstitial (i) or substitutional (s) sites, or both. As in metals (see Chap. 1), atoms of i species in semiconductors migrate directly between the appropriate interstitial sites, which is described well by Fick's second law

$$\frac{\partial C}{\partial t} = D\frac{\partial^2 C}{\partial x^2}\,, \tag{4.1}$$

where D is the diffusivity and C is the concentration. The diffusivity of an i species is characterized by a single activation enthalpy.

The semiconductor crystal host atom self-diffusion and the diffusion of s impurity species utilize native point defects. While the dominant native point defect species in metals are vacancies (V), both V and self-interstitials (I) contribute in semiconductors. To diffuse, an impurity s atom may directly *exchange* or migrate as a *pair or complex* with an I or a V, but only the exchange mechanism is operative for the host crystal atom self-diffusion, which is slower than that of a s species utilizing the same point defect species as diffusion

vehicles via the pairing mechanism. Furthermore, in a semiconductor both V and I can be in several different charge states with their concentrations dependent upon the semiconductor doping level and temperature. These factors lead to complications in the Fick's second law description of self-diffusion and diffusion of substitutional impurities in that the diffusivity shall consist of the contributions of all the involved point defect species which may not be a constant at a given temperature, and may also not reveal a single activation enthalpy over a temperature range. Furthermore, some impurity species are interstitial-substitutional (i-s) species which dissolve predominantly on substitutional sites but their diffusion is actually due to the rapid migration of those occupying interstitial sites and the interchange between atoms occupying the two different types of sites. The diffusivity in the Fick's second law description of the diffusion process of the i-s species is an *effective* diffusivity D^{eff} which may exhibit a strong dependence on its own concentration. These aspects will be examined with the diffusion phenomena of the specific semiconductor.

4.3 Diffusion in Silicon

Because of its use in fabricating integrated circuits, Si is the most important electronic material presently used and is likely to keep that position in the future. Diffusion processes are essential in the electronic device fabrication processes. Figure 4.1 shows the diffusivities of the most important impurities and that of Si self-diffusion. Borrowing the knowledge from metals, diffusion in Si had been first thought to be dominated by V-related mechanisms. In 1968 Seeger and Chik [1] suggested that in Si both V and I contribute to self- and dopant diffusion processes. The problem of the dominant point defect species in Si constituted a controversy for more than 20 years. Finally, during the 1980s [2], it was generally accepted that both I and V have to be taken into account, so as to consistently interpret the results of a large number of different experiments. The main indications for the involvement of I came from experiments performed under non-equilibrium native point defect conditions, such as the influence of surface oxidation or nitridation on dopant diffusion. In this regard, diffusion of the i-s species such as Au or Pt was also crucial. What is still uncertain is the diffusivity and the thermal equilibrium concentration values of I and V, to be mentioned later.

4.3.1 Silicon Self-Diffusion

Because I and V both contribute, the transport of Si self-atoms under thermal equilibrium conditions is governed by the uncorrelated self-diffusion coefficient

$$D_{\text{SD}} = D_I c_I^{\text{eq}} + D_V c_V^{\text{eq}} , \tag{4.2}$$

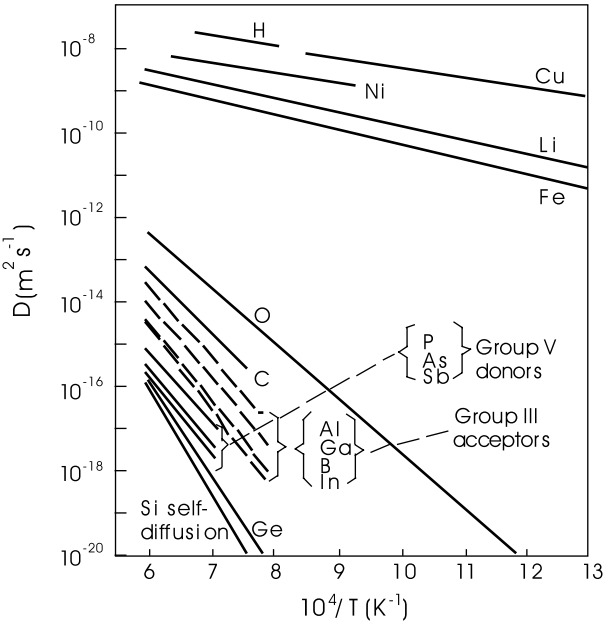

Fig. 4.1. A survey of diffusivity values of the most important impurities in Si and of Si self-diffusion.

where D_I and D_V are respectively the diffusivities of I and V, and $c_I^{\rm eq}$ and $c_V^{\rm eq}$ are respectively the I and V thermal equilibrium concentrations normalized by the appropriate site densities into atomic fractions. As has been mentioned, native point defects may exist in several charge states. The observed doping dependence of group-III and V dopant diffusion (Sect. 4.3.3) indicates the contributions of neutral, positively charged, negatively and doubly negatively charged native point defects, but it is not known whether all these charge states occur for both I and V. Taking all observed charge states into account we may write $D_I c_I^{\rm eq}$ as

$$D_I c_I^{\rm eq} = D_{I^o} c_{I^o}^{\rm eq} + D_{I^+} c_{I^+}^{\rm eq} + D_{I^-} c_{I^-}^{\rm eq} + D_{I^{2-}} c_{I^{2-}}^{\rm eq} \,, \tag{4.3}$$

and an analogous expression for V. The quantity $D_I c_I^{\rm eq}$ comprises the sum of the concentrations of self-interstitials in the various charge states according to

$$c_I^{\rm eq} = c_{I^o}^{\rm eq} + c_{I^+}^{\rm eq} + c_{I^-}^{\rm eq} + c_{I^{2-}}^{\rm eq} \,. \tag{4.4}$$

Therefore, the diffusivity D_I is actually an effective diffusion coefficient consisting of an weighted average of the diffusivities in the different charge states. The same holds analogously for $c_V^{\rm eq}$ and D_V.

Self-diffusion in Si is studied by measuring the diffusion of Si isotope tracer atoms $D_{\rm T}$ which differs slightly from $D_{\rm SD}$ of (4.1), since it contains the correlation factors f_I and f_V in the expression $D_{\rm T} = f_I D_I c_I^{\rm eq} + f_V D_V c_V^{\rm eq}$ (see Chap. 1 for details). In the diamond cubic lattice, $f_V = 0.5$, and $f_I \leq 1$

(depends on the unknown self-interstitial configuration). Measured results for D_{T} are usually fitted to the expression $D_{\mathrm{T}} = D_o \exp(-Q/k_{\mathrm{B}}T)$, where D_o is a pre-exponential factor, Q is the activation enthalpy, k_{B} is Boltzmann's constant and T is absolute temperature. A summary of these results is shown in Fig. 4.2 and elsewhere [3]. Tracer measurements do not allow to separate I and V contributions to self-diffusion. Such a separation became possible by investigating the diffusion of Au, Pt and Zn in Si, described in some detail in Sect. 4.3.2. These experiments allowed a fairly accurate determination of $D_I c_I^{\mathrm{eq}}$ but only a crude estimate of $D_V c_V^{\mathrm{eq}}$ derived from a combination of different types of experiments [2, 3]. The results are

$$D_I c_I^{\mathrm{eq}} = 9.4 \times 10^{-2} \exp(-4.84\,\mathrm{eV}/k_{\mathrm{B}}T)\,\mathrm{m^2 s^{-1}}\,, \tag{4.5}$$

$$D_V c_V^{\mathrm{eq}} = 6 \times 10^{-5} \exp(-4.03\,\mathrm{eV}/k_{\mathrm{B}}T)\,\mathrm{m^2 s^{-1}}\,. \tag{4.6}$$

The values of (4.5) and (4.6) are within the experimental range of the measured Si tracer diffusion coefficient D_{T}. The doping dependence of Si self-diffusion [4] allows to conclude that neutral as well as positively and negatively charged point defects are involved in self-diffusion, but the data are not accurate enough to determine the individual terms of (4.3) or the analogous expression for vacancies. Since D_{T} as well as $D_I c_I^{\mathrm{eq}}$ and $D_V c_V^{\mathrm{eq}}$ each consist of various terms, their representation in terms of an expression of the type of (4.5) and (4.6) can only be an approximation holding over a limited temperature range. In Sect. 4.3.5 we will discuss what is known about the individual factors D_I, c_I^{eq}, D_V and c_V^{eq}.

4.3.2 Interstitial-Substitutional Diffusion: Au, Pt and Zn in Si

Both Au and Pt can reduce minority carrier lifetimes in Si because their energy levels are close to the middle of the band gap. They are used in power devices to improve the device frequency behavior. In contrast, Au and to a lesser extent Pt are undesirable contaminants in integrated circuits and hence have to be avoided or removed. For these reasons, the behavior of Au and Pt has been investigated extensively. Zinc is not a technologically important impurity in Si, but scientifically it served as an example with diffusion behavior in between substitutional dopants and Au and Pt in Si.

These impurities are i-s species dissolved mainly on substitutional sites ($\mathrm{A_s}$) but accomplish diffusion by switching over to an interstitial configuration ($\mathrm{A_i}$) in which their diffusivity $\mathrm{D_i}$ is extremely high. The change-over from i-site to s-site and vice versa involves native point defects. For uncharged species the two basic forms of the i-s change-over processes are the kick-out (KO) mechanism involving I [4, 5]

$$\mathrm{A_i} \Leftrightarrow \mathrm{A_s} + I\,, \tag{4.7}$$

and the much earlier proposed dissociative mechanism or Frank-Turnbull (FT) mechanism involving V [6]

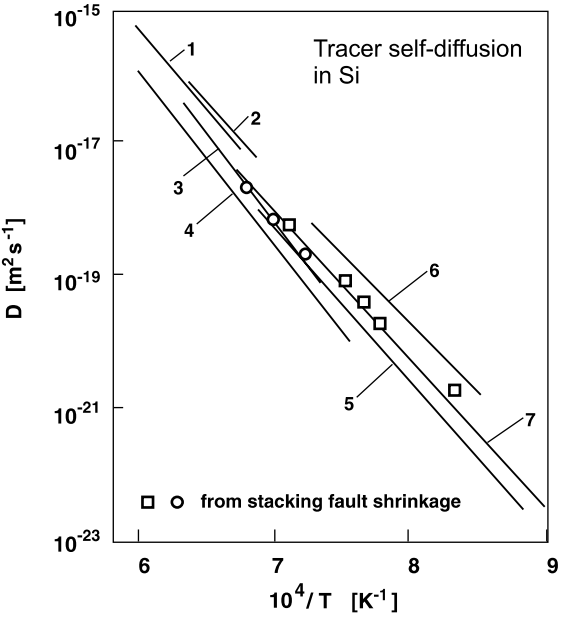

Fig. 4.2. Tracer self-diffusion coefficients of silicon as a function of reciprocal temperature. Partly from [4].

1. R.F. Peart: Phys. Stat. Sol. **15**, K119 (1966)
2. R.N. Ghostagore: Phys. Rev. Lett. **16**, 890 (1966)
3. J.M. Fairfield, B.J. Masters: J. Appl. Phys. **38**, 3148 (1967)
4. J.J. Mayer, H. Mehrer, K. Maier: Inst. Phys. Conf. Ser. **31**, 186K (1977)
5. L. Kalinowski, R. Seguin: Appl. Phys. Lett. **35**, 171 (1980)
6. J. Hirvonen, A. Antilla: Appl. Phys. Lett. **35**, 703 (1979)
7. F.J. Demond, S. Kalbitzer, H. Mannsperger, H. Damjantschitsch: Phys. Lett. **93A**, 503 (1983)

$$A_i + V \Leftrightarrow A_s \,. \tag{4.8}$$

Both mechanisms are schematically shown in Fig. 4.3. The KO mechanism is closely related to the interstitialcy mechanism. The main difference is that the foreign atom, once in an interstitial position, remains there for only one step in the interstitialcy mechanism and for many steps in the KO mechanism. In contrast, the FT mechanism and the vacancy exchange mechanism are qualitatively different. For the vacancy exchange mechanism an increase in V concentration enhances the diffusivity, whereas for the FT mechanism an increase in V concentration rather decreases the diffusivity of the substitutional species.

For a detailed description of i-s atoms diffusing via the KO or FT mechanism, it requires to solve a coupled system of three partial differential equations describing diffusion and reaction of A_i, A_s and the native point defect

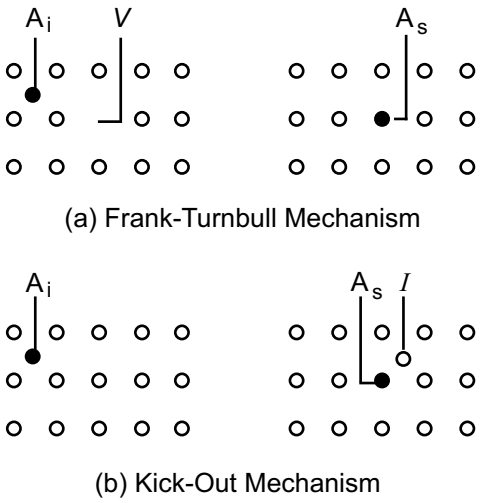

Fig. 4.3. Schematic representation of the Frank-Turnbull mechanism (a) and the kick-out mechanism (b).

involved, V or I [4]. But for cases of in-diffusion from the surface the profile shapes are described well by an *effective* diffusivity D^{eff} obtained for use in the Fick's second law representation, (4.1), of the A_s diffusion process. This requires to assume that the local equilibrium conditions in accordance with reactions (4.7) and (4.8) are

$$C_s C_I / C_i = C_s^{eq} C_I^{eq} / C_i^{eq} , \tag{4.9}$$

$$C_i C_V / C_s = C_i^{eq} C_V^{eq} / C_s^{eq} , \tag{4.10}$$

where C_s and C_i are respectively the concentrations of the s and i atoms of the i-s species, holds for the KO and FT mechanisms, respectively. For the KO mechanism, if the in-diffusion of A_i is slow enough to allow the Is generated to migrate out to the surface to keep their thermal equilibrium concentration (i.e., $D_i C_i^{eq} \ll D_I C_I^{eq}$ holds), then the effective diffusivity of A_s is given by

$$D_{(i)}^{\text{eff}} = D_i C_i / C_s^{eq} , \tag{4.11}$$

provided $C_s^{eq} \gg C_i^{eq}$ holds, which is generally the case. Here the lower index in bracket indicates the rate limiting species. If on the other hand the in-diffusion of A_i is so fast that the generated I cannot escape quickly enough to the surface (i.e., $D_i C_i^{eq} \gg D_I C_I^{eq}$ holds) a supersaturation of I will develop and further incorporation of A_s is limited by the out-diffusion of the generated Is to the surface. This leads to an effective A_s diffusivity $D_{(I)}^{\text{eff}}$ given by

$$D_{(I)}^{\text{eff}} = \left(D_I D_I^{eq} / C_s^{eq}\right) \left(C_s^{eq} / C_s\right)^2 . \tag{4.12}$$

For the FT mechanism, sufficiently slow in-diffusion $D_i C_i^{eq} \ll D_V C_V^{eq}$ leads to the same $D_{(i)}^{\text{eff}}$ as given by (4.11). An effective A_s diffusivity $D_{(V)}^{\text{eff}}$ controlled

by the in-diffusion of V from the surface results, if $D_{\rm i}C_{\rm i}^{\rm eq} \gg D_V C_V^{\rm eq}$ holds, which reads

$$D_{(V)}^{\rm eff} = D_V C_V^{\rm eq}/C_{\rm s}^{\rm eq}\,. \tag{4.13}$$

The strongly concentration-dependent effective diffusivity $D_{(i)}^{\rm eff}$ of (4.12) leads to an A_s concentration profile so strongly deviated away from the erfc-type that it is actually concave upward in $\log C_{\rm s}$ plotted as a function of $1/T$. These profiles can easily be distinguished from the erfc-type profiles which are associated with $D_{(V)}^{\rm eff}$. This macroscopic difference allows one not only to decide between different atomistic diffusion mechanisms of the specific foreign atom involved but also to obtain information on the mechanism of self-diffusion. The effective diffusivities given by (4.12) and (4.13) have been derived under the assumption of dislocation-free crystals. The presence of a high density of dislocations in an elemental crystal maintains the equilibrium concentration of intrinsic point defects and thus an erfc-type profile characterized by the constant diffusivity $D_{\rm (i)}^{\rm eff}$ of (4.11) will result even if $D_{\rm i}C_{\rm i}^{\rm eff} \gg D_I C_I^{\rm eq}$ holds. For compound semiconductors this statement does not hold in general, since the presence of dislocations does not necessarily guarantee native point defects to attain their thermal equilibrium concentrations. If I and V co-exist, such as in the case of Si, the effective A_s diffusion coefficient in dislocation-free material for $D_{\rm i}C_{\rm i}^{\rm eq} \gg (D_I C_I^{\rm eq} + D_V C_V^{\rm eq})$ is given by

$$D_{(I,V)}^{\rm eff} = D_{(I)}^{\rm eff} + D_{(V)}^{\rm eff}\,. \tag{4.14}$$

The in-diffusion profiles of both Au and Pt in dislocation-free Si show the concave profile shape typical for the KO mechanism [4, 7, 8]. Examples are shown in Figs. 4.4 and 4.5 respectively for Au and for Pt. From profiles like these and from the measured solubility $C_{\rm s}^{\rm eq}$ of Au_s and Pt_s in Si, the values of $D_I c_I^{\rm eq}$ given by (4.5) have been determined. Diffusion of Au into thin Si wafers leads to characteristic U-shaped profiles even if the Au has been deposited on one side only. The increase of the Au concentration in the center of the wafer has also been used to determine $D_I c_I^{\rm eq}$ [6].

In heavily dislocated Si the dislocations act as efficient sinks for I to keep C_I close to $C_I^{\rm eq}$ so that the constant effective diffusivity $D_{\rm (i)}^{\rm eff}$ of (4.11) governs the A_s profile, which is erfc-shaped. This has been observed by Stolwijk et al. for Au [9]. Analysis of the resulting erfc-profiles yielded

$$D_{\rm i}c_{\rm i}^{\rm eq} \approx 6.4 \times 10^{-3} \exp\left(-3.93\,{\rm eV}/k_{\rm B}T\right)\ {\rm m^2 s^{-1}}\,. \tag{4.15}$$

This $D_{\rm i}c_{\rm i}^{\rm eq}$ value turns out to be much larger than $D_I c_I^{\rm eq}$ given by (4.5), which is consistent with the observation that Au_s concentration profiles are governed by $D_{(I)}^{\rm eff}$ in dislocation-free Si.

Zinc diffusion in Si has also been investigated [10]. In highly dislocated material, an erfc-profile develops as expected. In dislocation-free material only the profile part close to the surface shows the concave shape typical for the kickout diffusion mechanism. For lower Zn concentrations, a constant

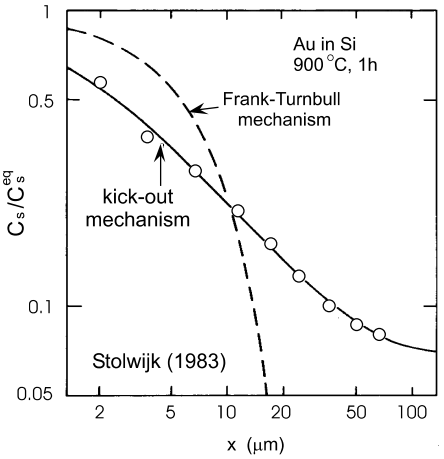

Fig. 4.4. Experimental Au concentration profile in dislocation-free Si (circles) compared with predictions of the Frank-Turnbull and the kick-out mechanism. From [7].

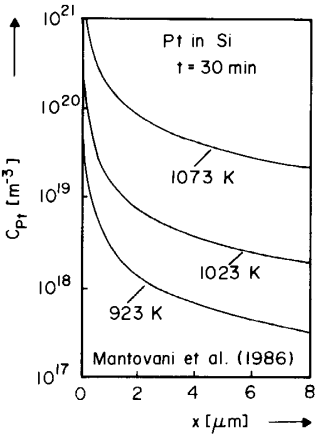

Fig. 4.5. Platinum concentration profiles in dislocation-free Si. From [8].

diffusivity takes over. The reason for this change-over from one profile type to another is as follows. In contrast to the case of Au, the $D_i c_i^{eq}$ value determined for Zn is not much higher than $D_I c_I^{eq}$ so that even in dislocation-free Si only the profile close to the surface is governed by $D_{(I)}^{eff}$ of (4.12) which strongly increases with depth. For sufficiently large penetration depths $D_{(I)}^{eff}$ finally exceeds $D_{(i)}^{eff}$ and a constant effective diffusivity begins to determine the concentration profile. A detailed analysis of this situation can be found elsewhere [3]. The change-over from a concave to an erfc-type profile has also been observed for the diffusion of Au either into very thick Si samples [11] or for short-time diffusion [12] into normal silicon wafers 300–800 μm in thickness.

4.3.3 Dopant Diffusion

Fermi Level Effect

Dopant diffusion has been studied extensively because of its importance in device fabrication. A detailed quantitative understanding of dopant diffusion is also a pre-requisite for accurate and meaningful modeling in numerical process simulation programs. It is not our intention to compile all available data on dopant diffusion in silicon, which may conveniently be found elsewhere (see [3] for a list of references). We will instead concentrate on the diffusion mechanisms and native point defects involved in dopant diffusion,

the effect of the Fermi level on dopant diffusion and on non-equilibrium point defect phenomena induced by high-concentration in-diffusion of dopants.

The diffusivities D_s of all dopants in Si depend on the Fermi level. The experimentally observed doping dependencies may be described in terms of the expression

$$D_s(n) = D_s^0 + D_s^+(n_i/n) + D_s^-(n/n_i) + D_s^{2-}(n/n_i)^2 \,, \tag{4.16}$$

which reduces to

$$D_s(n_i) = D_s^0 + D_s^+ + D_s^- + D_s^{-2} \tag{4.17}$$

for intrinsic conditions $n = n_i$. Depending on the specific dopant, some of the quantities in (4.17) may be negligibly small. $D_s(n_i)$ is an exponential function of inverse temperature as shown in Fig. 4.1. Values of these quantities in terms of pre-exponential factors and activation enthalpies are given in Table 4.1. Conflicting results exist on the doping dependence of Sb.

Table 4.1. Diffusion data of various dopants fitted to (4.17). Each term fitted to $D_0 \exp(-Q/k_B T)$; D_0 values in $10^{-4}\,m^2 s^{-1}$ and Q values in eV

element	D_0^0	Q^0	D_0^+	Q^+	D_0^-	Q^-	D_0^{2-}	Q^{2-}
B	0.037	3.46	0.72	3.46	–	–	–	–
P	3.85	3.66	–	–	4.44	4.00	44.20	4.37
As	0.066	3.44	–	–	12.0	4.05	–	–
Sb	0.214	3.65	–	–	15.0	4.08	–	–

The higher diffusivities of all dopants as compared to self-diffusion requires faster moving complexes formed by the dopants and native point defects. The doping dependence of $D_s(n)$ is generally explained in terms of the various charge states of the native point defects carrying dopant diffusion. Since both I and V can be involved in dopant diffusion each of the terms in (4.17) in general consists of an I and a V related contribution, e.g.,

$$D_s^+ = D_s^{I^+} + D_s^{V^+} \,. \tag{4.18}$$

$D_s(n)$ may also be written in terms of I- and V-related contributions as

$$D_s(n) = D_s^I(n) + D_s^V(n) \tag{4.19}$$

with

$$D_s^I(n) = D_s^{I^o} + D_s^{I^+}(n_i/n) + D_s^{I^-}(n/n_i) + D_s^{I^{2-}}(n/n_i)^2 \tag{4.20}$$

and an analogous expression for $D_s^V(n)$.

Contrary to a common opinion, the observed doping dependence expressed in (4.16) just shows that charged point defects are involved in the

diffusion process, but nothing can be learned on the relative contributions of I and V in the various charge states. Strictly speaking, in contrast to the case of self-diffusion, the doping dependence of dopant diffusion does not necessarily prove the presence of charged native point defects but rather the presence of charged point-defect/dopant complexes. In Sect. 4.3.3 we will describe a way to determine the relative contribution of I and V to dopant diffusion by measuring the effect of non-equilibrium concentrations of native point defects on dopant diffusion.

Influence of Surface Reactions

Thermal oxidation is a standard process for forming field and gate oxides, or oxides protecting certain device regions from ion implantation in Si device fabrications. The oxidation process leads to the injection of I which can enhance the diffusivity of dopants using mainly I as diffusion vehicles or retard diffusion of dopants which diffuse mainly via a V mechanism. Oxidation-enhanced diffusion (OED) has been observed for the dopants B, Al, Ga, P and As, and oxidation-retarded diffusion (ORD) was observed for Sb [2–4]. OED is explained by the I supersaturation and that the dopants diffuse via mainly the interstitialcy mechanism. On the other hand, ORD of Sb is explained in terms of the I-V recombination reaction $I + V \Leftrightarrow \phi$, where ϕ is a lattice atom, which leads to

$$C_I C_V = C_I^{\mathrm{eq}} C_V^{\mathrm{eq}} , \tag{4.21}$$

and that Sb diffuses mainly via the vacancy mechanism. The presence of an I supersaturation leads to a V undersaturation as described by (4.21). The oxidation-induced I may also nucleate and form I-type dislocation loops on (111) planes containing a stacking fault and are therefore termed oxidation-induced stacking faults (OSF).

The physical reason for the I injection during surface oxidation is as follows [2]. Oxidation occurs by the diffusion of oxygen through the oxide layer to react with the Si crystal atoms at the SiO_2/Si interface. The oxidation reaction is associated with a volume expansion of about a factor of two which is mostly accommodated by viscoelastic flow of the oxide but partly also by the injection of Si interstitials into the Si crystal matrix which leads to an I supersaturation. Oxidation can also cause V injection provided the oxidation occurs at sufficiently high temperatures (typically 1150°C or higher) and the oxide is thick enough. Under these circumstances, Si, probably in the form of SiO [13, 14], diffuses from the interface and reacts with oxygen in the oxide away from the interface. The resulting supersaturation of V associated with an undersaturation of I gives rise to ORD of B and P diffusion [15] and OED of Sb [16]. Thermal nitridation of Si surfaces also causes a supersaturation of V coupled with an undersaturation of I, whereas oxynitridation (nitridation of oxides) behaves more like normal oxidation. Silicidation reactions have

also been found to inject native point defects and to cause enhanced dopant diffusion [17, 18].

A simple quantitative formulation of oxidation- and nitridation-influenced diffusion is based on (4.19), which changes with perturbed native point-defect concentrations C_I and C_V approximately to

$$D_{\mathrm{s}}^{\mathrm{per}}(n) = D_{\mathrm{s}}^{I}(n)\,[C_I/C_I^{\mathrm{eq}}(n)] + D_{\mathrm{s}}^{V}(n)\,[C_V/C_V^{\mathrm{eq}}(n)]\ . \tag{4.22}$$

For long enough times and sufficiently high temperatures (e.g., one hour at 1100°C) local dynamical equilibrium between V and I according to (4.21) is established and (4.22) may be reformulated in terms of C_I/C_I^{eq}. Defining the normalized diffusivity enhancement as $\Delta_{\mathrm{s}}^{\mathrm{per}} = [D_{\mathrm{s}}^{\mathrm{per}}(n) - D_{\mathrm{s}}(n)]/D_{\mathrm{s}}(n)$, the fractional interstitialcy diffusion component as $\Phi_I(n) = D_{\mathrm{s}}^{i}(n)/D_{\mathrm{s}}(n)$, and the I supersaturation ratio as $s_I(n) = [C_I - C_I^{\mathrm{eq}}(n)]/C_I^{\mathrm{eq}}(n)$, (4.22) may be rewritten as [2, 13]

$$\Delta_{\mathrm{s}}^{\mathrm{per}}(n) = \left[2\Phi_I(n) + S_I\Phi_I(n) - 1\right]/(1 + s_I) \tag{4.23}$$

with (4.21) holding. Usually (4.23) is given for intrinsic conditions and the dependence of Φ_I on n is not indicated. Equation (4.23) is plotted in Fig. 4.6 for Φ_I values of 0.85, 0.5 and 0.2.

The left-hand side of Fig. 4.6, where $s_I < 0$ (associated with a V supersaturation) has been realized by high-temperature oxidation and thermal nitridation of silicon surfaces, as mentioned above. Another possibility to generate a vacancy supersaturation is the oxidation in an HCl containing atmosphere at sufficiently high temperatures and for sufficiently large HCl contents [2]. As expected, $s_I < 0$ results in enhanced Sb diffusion and retarded diffusion of P and B. Arsenic diffusion is enhanced as in the case of oxidation, which indicates that arsenic has appreciable components via both V and I ($\Phi_I \sim 0.5$).

Several different procedures have been used to evaluate Φ_I for the different dopants, resulting in a wide range of conflicting published Φ_I values. With the availability of oxidation for generating a self-interstitial supersaturation ($s_I > 0$) and of thermal nitridation for generating a vacancy supersaturation ($s_I < 0$), the most accurate procedure to determine Φ_I appears to be the following: check for the diffusion changes under oxidation and under nitridation conditions. If for $s_I > 0$ the diffusion is enhanced and for $s_I < 0$ it is retarded (as for P and B) then $\Phi_I > 0.5$ holds. Based on the largest observed retardation $\Delta_{\mathrm{s}}^{\mathrm{per}}(\mathrm{min})$, which has a negative value, a lower limit of Φ_I may be estimated according to

$$\Phi_I > 0.5 + 0.5\left[1 - \left(1 + \Delta_{\mathrm{s}}^{\mathrm{per}}(\mathrm{min})^2\right)\right]^{1/2} \tag{4.24}$$

Analogously, an upper limit for Φ_I may be estimated for the case when retarded diffusion occurs for $s_I > 0$ and enhanced diffusion for $s_I < 0$, as in the case of Sb. A different procedure is required for elements with Φ_I values close to 0.5, such as As.

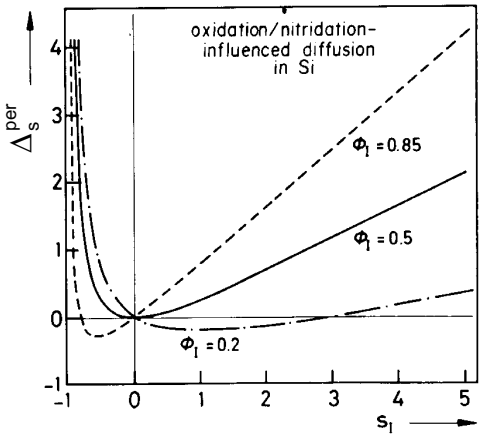

Fig. 4.6. Normalized diffusion enhancement Δ_s^{per} versus self-interstitial supersaturation $s_I = (C_I - C_I^{eq})/C_I^{eq}$ for different values of Φ_I. From [2, 13].

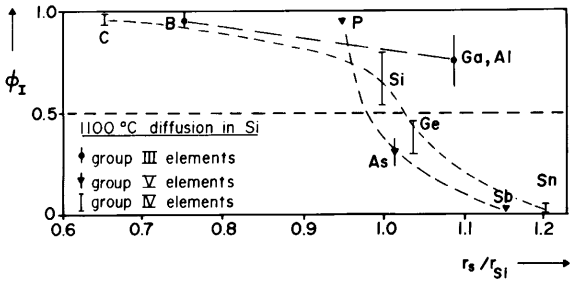

Fig. 4.7. Interstitial-related fractional diffusion component ϕ_I for group III, IV and V elements versus their atomic radius in units of the atomic radius r_{Si} of silicon. The values for carbon and tin are expected from theoretical considerations and limited experimental results. From [3].

In Fig. 4.7 values of Φ_I at 1100°C are shown as a function of the atomic radius r_s of the various dopants for intrinsic doping conditions. Both the charge state (group III or V dopants) and the atomic size influence Φ_I. Φ_I has a tendency to increase with increasing temperature. Oxidation and nitridation experiments and extrinsic conditions indicate a decreasing value of Φ_I for P with increasing n-doping, but both P and B still remain dominated by I ($\Phi_I(n) > 0.5$).

Dopant-Diffusion-Induced Non-Equilibrium Effects

Non-equilibrium concentrations of native point defects may be induced not only by various surface reactions, but also by the in-diffusion of some dopants starting from a high surface concentration. These non-equilibrium effects are most pronounced for high-concentration P diffusion, but also present for other dopants such as B and to a lesser extend for Al and Ga. Phosphorus in-diffusion profiles (Fig. 4.8) show a tail in which the P diffusivity is much

higher (up to a factor of 100 at 900°C) than expected from isoconcentration studies. In n-p-n transistor structures in which high-concentration P is used for the emitter diffusion, the diffusion of the base dopant B below the P diffused region is similarly enhanced, the so-called 'emitter-push effect'. The diffusion of B, P, or Ga in buried layers many microns away from the P diffused region is also greatly enhanced. In contrast, the diffusion of Sb in buried layers is retarded under the same conditions. The enhanced and retarded diffusion phenomena are analogous to those occurring during surface oxidation. As has also been confirmed by dislocation-climb experiments [19], all these phenomena are due to a supersaturation of I, associated with an undersaturation of V, induced by high-concentration in-diffusion of P. The basic features of high-concentration P diffusion are schematically shown in Fig. 4.9, which also indicates the presence of electrically neutral precipitates at P concentrations exceeding the solubility limit at the diffusion temperature. A much less pronounced supersaturation of I is generated by B starting from a high surface concentration as can be concluded from the B profiles and from the growth of interstitial-type stacking faults induced by B diffusion [20, 21].

Many models have been proposed to explain the phenomena associated with high-concentration P diffusion. The earlier models are vacancy based and predict a P-induced V supersaturation which contradict the experimental results obtained in the meantime. In 1986, Morehead and Lever [21] presented a mathematical treatment of high-concentration dopant diffusion which is primarily based on the point-defect species dominating the diffusion of the dopant, e.g., I for P and B and V for Sb. The concentration of the other native point-defect type is assumed to be determined by the dominating point defect via the local equilibrium condition, (4.21). The dopant-induced self-interstitial supersaturation s_I may be estimated by the influx of dopants which release part of the I involved in their diffusion process. These self-interstitials will diffuse to the surface where it is assumed that $C_I = C_I^{\mathrm{eq}}$ holds, and also into the Si bulk. Finally, a quasi-steady-state supersaturation of self-interstitials will develop for which the dopant-induced flux of injected I just cancels the flux of I to the surface. Figure 4.9 shows schematically the situation.

4.3.4 Diffusion of Carbon and Other Group IV Elements

The group IV elements carbon C, Ge and Sn dissolve in Si substitutionally, but knowledge on their diffusion mechanisms is incomplete. Ge and Sn diffusion are similarly slow as Si self-diffusion, whereas C diffusion is much faster (Fig. 4.1).

Germanium atoms are slightly larger than Si atoms. Oxidation and nitridation experiments show a Φ_I value of Ge around 0.4 at 1100°C [24] which is slightly lower than that derived for Si self-diffusion. Diffusion of the much larger Sn atoms in Si is expected to be almost entirely due to the vacancy

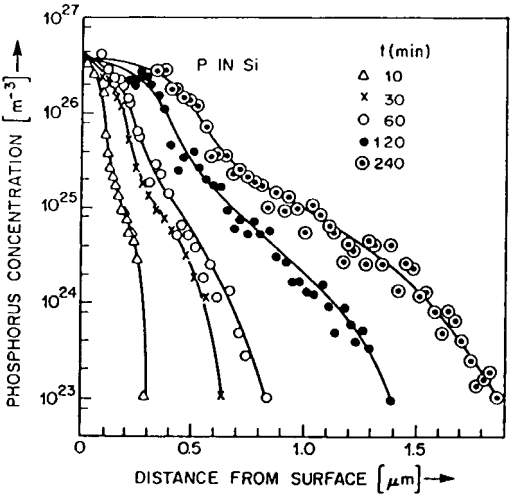

Fig. 4.8. Concentration profiles of P diffused into Si at 900°C for the times t indicated. From [22].

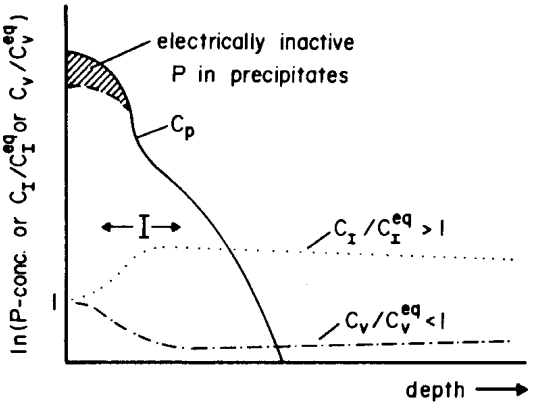

Fig. 4.9. A schematic P concentration profile (C_P) and the normalized native point-defect concentrations C_I/C_I^{eq} and C_V/C_V^{eq}. From [23].

exchange mechanism, similar as for the group V dopant Sb. Consistent with this expectation, a nitridation-induced supersaturation of V increases Sn diffusion [25]), but no quantitative determination of Φ_I is available for Sn.

In-diffusion C profiles in Si are error function-shaped. Considering the atomic volume, it can be expected that the diffusion of C atoms, which are much smaller than Si, involves mainly Si interstitials. Based on EPR measurements, Watkins and Brower [26] proposed 29 years ago that C diffusion is accomplished by a highly mobile CI complex according to $C_s + I \Leftrightarrow CI$, where C_s denotes substitutional C. This is consistent with the experimental observation that I injected by oxidation or high-concentration P in-diffusion enhance C diffusion [27]. Equivalently, we may regard C as an i-s impurity, just as Au. That is, to regard the diffusion of C according to [28, 29]

$$C_s + I \Leftrightarrow C_i \tag{4.25}$$

where C_i denotes an interstitial carbon atom. Since whether C_s diffusion is actually carried by CI complexes or by C_i atoms have not yet been distinguished on a physical basis, and the mathematical descriptions for both cases are identical in form, we can regard C_s diffusion as being carried by C_i atoms in accordance with the KO mechanism of the i-s impurities. Under this assumption, diffusion of C into Si for which the substitutional C concentration is at or below the solubility of the substitutional carbon atoms, C_s^{eq}, the substitutional C diffusivity D_s^{eff} is given by the effective diffusivity $D_i C_i^{eq}/C_s^{eq}$ where D_i is the diffusivity of the fast diffusing C_i atoms and C_i^{eq} is the solubilities of the C_i atoms. Error function type C_s in-diffusion profiles obtain under in-diffusion conditions, because

$$D_s^{eff} C_s^{eq} = D_i C_i^{eq} < D_I C_I^{eq} \tag{4.26}$$

holds. Under this condition, C in-diffusion induced Si interstitials migrated rapidly out to the Si surface and hence the C_I^{eq} condition is basically maintained, in agreement with experimental observations [30,31].

From the C in-diffusion data, the solubility of C_s is given by [30,31]

$$C_s^{eq} = 4 \times 10^{30} \exp(-2.3\,\mathrm{eV}/k_B T)\,\mathrm{m}^{-3} \tag{4.27}$$

and the diffusion coefficient of C_s is given by

$$D_s = 1.9 \times 10^{-4} \exp(-3.1\,\mathrm{eV}/k_B T)\,\mathrm{m}^2\mathrm{s}^{-1}\,. \tag{4.28}$$

Interpreted in accordance with the i-s nature of C, we obtain

$$C_i^{eq} = 2 \times 10^{31} \exp(-4.52\,\mathrm{eV}/k_B T)\,\mathrm{m}^{-3}\,, \tag{4.29}$$

$$D_i = 4.4 \times 10^{4} \exp(-0.88\,\mathrm{eV}/k_B T)\,\mathrm{m}^2\mathrm{s}^{-1}\,. \tag{4.30}$$

For out-diffusion of C_s pre-introduced to high concentrations, however, the situation is very different. For cases for which the C_s concentration significantly exceeded its solubility, as pointed out by Scholz et al. [32],

$$D_i C_i^{eq} > D_I C_I^{eq} \tag{4.31}$$

may be satisfied, leading to a severe undersaturation of I in the high C_s concentration region which significantly retard the out-diffusion of C_s atoms from the region. Indeed, such phenomena have been observed by Rücker et al. [33] and by Werner et al. [34]. These experiments were performed using molecular beam epitaxy (MBE) grown Si layers containing regions with C_s concentrations in the 10^{25} to $10^{26}\,\mathrm{m}^{-3}$ range, and hence tremendously exceeded the C_s solubility of the experimental temperature. A similar retardation of the diffusion of other impurity species diffusing via primarily I, e.g., B, in the same region is also expected. This is indeed the case of the experimental results of Rücker et al. [33], see Fig. 4.10. In order to highly satisfactorily fit both the C_s profile as well as all the B spike-region profiles, Scholz et al. [32]

found that additionally the contribution of Si V must also be included. Vacancy contributes a component to C_s diffusion via the dissociative or FT mechanism as given by reaction (4.8) and a component to B diffusion via the vacancy-pairing mechanism. The V contribution to C_s diffusion is important in regions outside the initial C_s high-concentration region and to B diffusion in all regions.

Using similarly grown samples containing C_s and B spikes, ion implantation induced Si interstitials were found to be substantially attenuated in the C_s spike regions so that the diffusion of B buried beneath the C_s spikes were severely retarded when compared to cases of having no C_s spikes [35]. The phenomenon was interpreted by the authors as due to the reaction $C_s + I \Leftrightarrow CI$ but with the so formed CI complexes assumed to be *immobile*, which is in contrast to the suggestion of Watkins and Brower [26]. The assumption that immobile CI complexes are responsible for the retarded boron diffusion is not needed in the analysis of Scholz et al. [32]. It is expected that ion implantation or oxidation induced Si I supersaturation will enhance the diffusion of C and B with C in concentrations to a moderate level, e.g., in the range of $10^{23}\,\mathrm{m}^{-3}$.

4.3.5 Diffusion of Si Self-Interstitials and Vacancies

For Si, although the product $D_I C_I^{\mathrm{eq}}$ is known and estimates of $D_V C_V^{\mathrm{eq}}$ are available, our knowledge of the individual factors D_I, D_V, C_I^{eq} and C_V^{eq} is limited in spite of immense experimental efforts to determine these quantities. These individual quantities enter most numerical programs for simulating device processing and their elusiveness hinders progress in this area [36].

The most direct way of measuring D_I is the injection of I (e.g., via surface oxidation) at one location of the Si crystal and the observation of its effect on dopant diffusion or on growth or shrinkage of stacking faults at another location as a function of time and of distance between the two locations. That is, the two locations may be the front- and the backside of a Si wafer. Extensive experiments on the spread of oxidation-induced I through wafers by Mizuo and Higuchi [37] have shown that a supersaturation of I arrives at about the same time as a corresponding undersaturation of V. Therefore, these kind of experiments at 1100°C just give information on an effective diffusivity of a perturbation in the I and V concentrations. This effective diffusivity may be expressed approximately by [2]

$$D_{(I,V)}^{\mathrm{eff}} \approx \left(D_I C_I^{\mathrm{eq}} + D_V C_V^{\mathrm{eq}}\right) / \left(C_I^{\mathrm{eq}} + C_V^{\mathrm{eq}}\right) \tag{4.32}$$

and probably corresponds to the diffusivity values of about $3 \times 10^{-13}\,\mathrm{m}^2\,\mathrm{s}^{-1}$ in the experiments of Mizuo and Higuchi at 1100°C [37]. Much efforts had been expended on this approach in the past but the results are inconsistent.

In most experiments aimed at determining D_I it has not been taken into account that I may react with V according to the reaction $I + V \Leftrightarrow \phi$ which

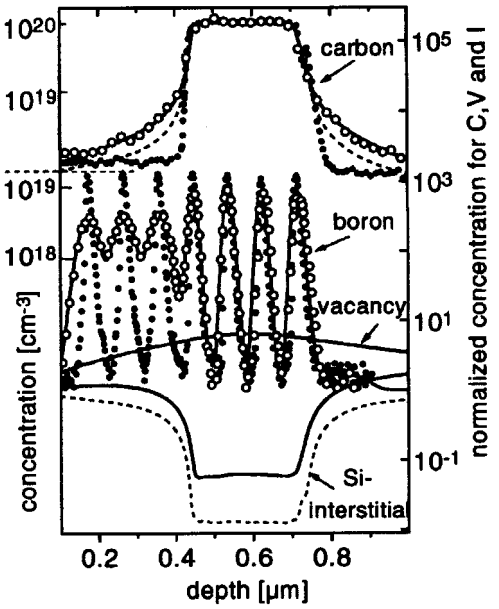

Fig. 4.10. SIMS profiles of a 300 nm thick carbon layer with seven boron spikes [33]. Filled and open circles are respectively data of as-grown and annealed (900°C/45 min) cases. Dashed fitting lines are those with only the kick-out model, and solid lines are those with the dissociative mechanism also included. From [32].

establishes local dynamical equilibrium condition given by (4.21). Based on experiments on oxidation-retarded diffusion of antimony [18, 38] it has been estimated that an astonishingly long time, about one hour, is required to establish local dynamical equilibrium at 1100°C. This long recombination time indicates the presence of an energy or entropy barrier slowing down the recombination reaction. At lower temperatures much longer recombination times can be expected. These long recombination times hold for lightly doped material. There are indications that dopants or other foreign elements may act as recombination centers which can considerably speed up the recombination reaction, but no reliable data are available in this area. The D_I values so determined (and therefore indirectly also of C_I^{eq} via the known product $D_I C_I^{\mathrm{eq}}$) were found to diverge over many orders of magnitude [3, 39] and with I formation enthalpies from ~ 1 to 4 eV. This is clearly an unsatisfactory situation. The problem is further complicated by the observation that the measured effective diffusivity $D_{(I,V)}^{\mathrm{eff}}$ depends on the type of Si material used. In the experiments of Fahey et al. [18] the transport of oxidation-induced Si interstitials through epitaxially-grown Si layers was much faster than through equally thick layers of as grown float-zone (FZ) or Czochralski (CZ) Si. This difference has been attributed to the presence of vacancy-type agglomerates left from the crystal growth process which might not be present in epitaxial Si layers. These vacancy agglomerates would have to be consumed by the injected I before further spread of interstitials can occur.

Nonetheless, considering the recent development involving several different categories of studies, we can now tentatively conclude that the migration enthalpies of vacancies and self-interstitials in silicon, h_V^{m} and h_I^{m} respectively, are relatively small while their formation enthalpies, h_V^{f} and h_I^{f} respectively, are large. This means that the V and I are moving fairly fast while their thermal equilibrium concentrations are fairly small. The most probable value of h_V^{m} is ~ 0.5–$1\,\mathrm{eV}$ while that of h_I^{m} is $\sim 1\,\mathrm{eV}$, and the corresponding most probable values of h_V^{f} is $\sim$ 3.5–3 eV while that of h_I^{f} is $\sim 4\,\mathrm{eV}$. Sinno et al. [40] used values of 0.457 and 0.937 eV respectively for h_V^{m} and h_I^{m} to satisfactorily model the formation of swirl defects (interstitial-type dislocation loops and vacancy-type clusters) in FZ Si, including the defect location, density, size, and their dependence on the crystal growth rate and the thermal gradient. Plekhanov et al. [41] used a h_V^{f} value of $\sim$ 3–3.4 eV to satisfactorily model the formation of voids in large diameter CZ Si. Moreover, in fitting the C and B diffusion results of Rücker et al. [33], as shown in Fig. 4.10, Scholz et al. [32] also needed to use h_I^{m} and h_V^{m} values smaller than 1 eV. This knowledge is consistent with recent quantum mechanical calculations which yielded fairly high h_I^{f} and h_V^{f} values and correspondingly low h_V^{m} and h_I^{m} values [42–46]. With the present estimates, it becomes also possible to connect in a reasonable and consistent way the fairly high diffusivities of native point defects found after low temperature electron irradiation [47] with the much lower apparent diffusivities which appear to be required to explain high-temperature diffusion experiments.

4.3.6 Oxygen and Hydrogen Diffusion

Oxygen is the most important electrically inactive impurity element in Si. In CZ Si, O is incorporated from the quartz crucible and usually present in concentrations in the order $10^{24}\,\mathrm{m}^{-3}$. An O atom in Si occupies the bond-centered interstitial position of two Si atoms and forms covalent bonds with the two Si atoms. Hence, its diffusion requires the breaking of bonds. The diffusivity of interstitial oxygen, $\mathrm{O_i}$, has been measured between about 300°C and the melting point of Si and is in good approximation described by

$$D_{\mathrm{i}} = 0.07 \exp(-2.44\,\mathrm{eV}/k_{\mathrm{B}}T)\,\mathrm{m}^2\mathrm{s}^{-1}\,. \tag{4.33}$$

The solubility $C_{\mathrm{i}}^{\mathrm{eq}}$ of interstitial O has been determined to be

$$C_{\mathrm{i}}^{\mathrm{eq}} = 1.53 \times 10^{27} \exp(-1.03\,\mathrm{eV}/k_{\mathrm{B}}T)\,\mathrm{m}^{-3}\,. \tag{4.34}$$

Since in most CZ Si crystals the grown-in $\mathrm{O_i}$ concentration exceeds $C_{\mathrm{i}}^{\mathrm{eq}}$ at typical processing temperatures, $\mathrm{O_i}$ precipitation will occur in the interior but not the surface regions (because of Oi out-diffusion) of CZ Si. This leads to the important technological application of intrinsic gettering [48] for improving the junction leakage and MOS capacitor charge holding time characteristics

of integrated circuit devices fabricated using CZ Si, which is not available to FZ Si.

Around 450°C O_i forms electrically active agglomerates, called thermal donors [49]. The formation kinetics of these agglomerates appears to require a fast diffusing species, for which both Si I [50] and molecular oxygen have been suggested [51]. The question of molecular oxygen in Si has not yet been settled.

Hydrogen plays an increasingly important role in silicon device technology because of its capability to passivate electrically active defects. The passivation of dislocations and grain boundaries is especially important for inexpensive multicrystalline Si used for solar cells. Both acceptors and donors can be passivated by H which is usually supplied to Si from a plasma. H in Si is assumed to diffuse as unbounded i atom in either a neutral or a positively charged form. The diffusivity of H in Si has been measured by Van Wieringen and Warmoltz [52] between 970 and 1200°C, see Fig. 4.1. Between room temperature and 600°C H diffusivities much lower than those extrapolated from the high-temperature data have been measured. Corbett and co-workers [53] rationalized this observation by suggesting that atomic H may form interstitially dissolved, essentially immobile H_2 molecules. Apparently, these molecules can then form plate-like precipitates [54]. As in the case of oxygen, the existence of H molecules has not been proven experimentally.

4.4 Diffusion in Germanium

Germanium has lost its leading role for electronic devices about four decades ago and is now mainly used as a detector material or in Si/Ge superlattices. Therefore, basically no papers have recently been published on diffusion in Ge. Another reason might be that diffusion in Ge can be consistently explained in terms of V-related mechanisms and no I contribution has to be invoked.

Figure 4.11 shows the diffusivities of group III and V dopants and of Ge in Ge as a function of inverse absolute temperature under intrinsic conditions. The doping dependence of dopant diffusion can be explained by one kind of acceptor-type native point defect. These native point defects have been assumed to be V since the earliest studies of diffusion in Ge [1], but a convincing experimental proof has only been given in 1985 by Stolwijk et al. based on the diffusion behavior of Cu in Ge [55].

Copper diffuses in Ge via an i-s mechanism [6]. In analogy to the case of Au and Pt in Si, its diffusion behavior may be used to check diffusion profiles for any indication of an I contribution via the KO mechanism. A concentration profile of Cu diffusion into a germanium wafer is shown in Fig. 4.12 [55]. The dashed U-shaped profile which is typical for the kickout mechanism obviously does not fit the experimental data. In contrast, the experimental profiles may

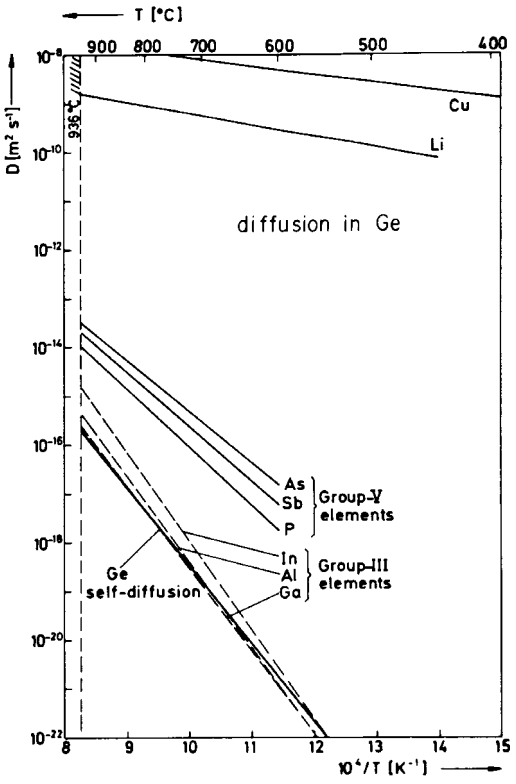

Fig. 4.11. Diffusivities of various elements (including Ge) in Ge as a function of inverse absolute temperature [4].

be well described by the constant diffusivity $D^{\text{eff}}_{(I,V)}$ given by (4.13). Values of the vacancy contribution to Ge self-diffusion

$$D_V C_V^{\text{eq}} = 21.3 \times 10^{-4} \exp(-3.11\,\text{eV}/k_\text{B}T)\,\text{m}^2\text{s}^{-1}\,, \tag{4.35}$$

as determined from Cu diffusion profiles, agree well with those measured from tracer self-diffusion in Ge [3,55]. The kind of excellent agreement shows that any Ge I contribution to the Ge self-diffusion process is negligible and hence Ge self-diffusion appears to be entirely governed by V. It is unclear why I play such an important role in diffusion processes in Si but no noticeable effect in Ge.

4.5 Diffusion in Gallium Arsenide

Gallium arsenide is the most important base material used for optoelectronic applications with diffusion processes essential in fabricating the devices. Self-diffusion and diffusion of dopant and other important impurity species in GaAs (and in other compound semiconductors) are governed by native point

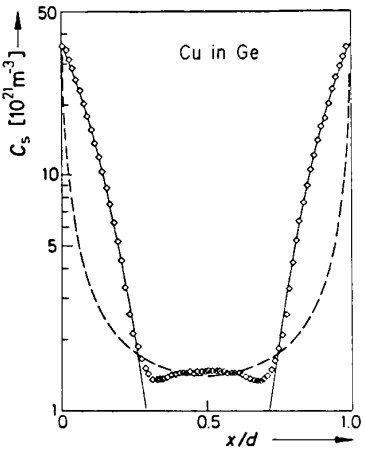

Fig. 4.12. Concentration profiles of Cu into a dislocation-free Ge wafer after diffusion for 15 minutes at 878°C. The solid line holds for the Frank-Turnbull and the dashed line for the kickout mechanism. From [55].

defects. Compared to that in Si, diffusion in GaAs exhibits a much more prominent dependence on the Fermi-level effect, and it also shows a dependence on the pressure of an As vapor phase. Moreover, the number of participating point defect species is more than that in Si. Vacancy, interstitialcy, as well as i-s diffusion mechanisms are involved. Detailed reviews can be found elsewhere [3, 56, 57].

4.5.1 Native Point Defects and General Aspects

The compound semiconductor GaAs has a thermodynamically allowed equilibrium composition range around the $Ga_{0.5}As_{0.5}$ composition. In thermal equilibrium coexistence with a GaAs crystal, there are four vapor phase species: Ga_1, As_1, As_2, and As_4. In the crystal, there are six single point defect species: vacancies of the Ga and As sublattices (V_{Ga} and V_{As}), self-interstitials of Ga and As (I_{Ga} and I_{As}), and antisite defects of a Ga atom on an As sublattice site (GaAs) and of an As atom on a Ga sublattice site (As_{Ga}). Any two single point defect species can form a paired species. There is no convincing evidence of the involvement of paired point defects in diffusion processes in GaAs, and the role of paired point defect species will not be considered here. The sum of the thermal equilibrium concentrations of the point defects constitutes the allowed GaAs crystal composition variation within its thermodynamically allowed range. For instance, considering the contributions of only the single point defects, the excess As concentration (δC_{As}) is given by

$$\delta C_{As} = \left[C^{eq}_{I_{As}} + C^{eq}_{As_{Ga}} - C^{eq}_{V_{As}}\right] - \left[C^{eq}_{I_{As}} + C^{eq}_{Ga_{As}} - C^{eq}_{V_{Ga}}\right] , \qquad (4.36)$$

while $\delta C_{Ga} = -\delta C_{As}$ is the excess Ga concentration, which is responsible for the compound crystal composition deviation from the $Ga_{0.5}As_{0.5}$ stoichiometry. In (4.36), the C are the various thermal equilibrium concentrations of

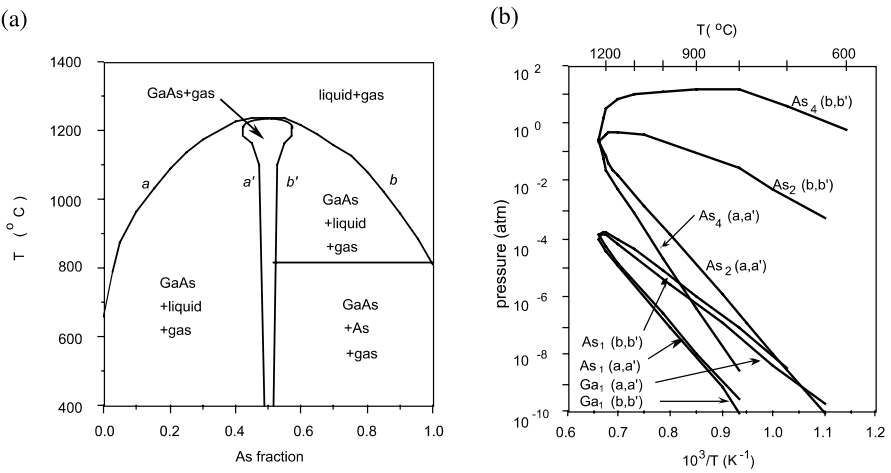

Fig. 4.13. (**a**) The schematic phase diagram of GaAs, with the thermodynamically allowed GaAs crystal composition range greatly exaggerated. (**b**) Partial pressures of the Ga and As vapor phases in equilibrium with the most gallium rich GaAs (a,a′) or the most arsenic rich GaAs (b,b′) [58].

the appropriate point defect species. Here the concentration of a point defect species includes those in all charge states.

Clearly, the following three categories of quantities form a mutual dependence, each of which may be regarded as the cause for the other two: (i) the vapor phase pressures; (ii) the GaAs crystal composition; and (iii) the point defect concentrations of the crystal.

To analyze experiments, it is convenient to regard the vapor phase pressure as the cause and the other quantities as consequences. For III-V compounds, the group V element vapor phase pressure are large, e.g., P_{As_4} and/or P_{As_2}, and can be readily measured. Figure 4.13a shows the GaAs phase diagram and Fig. 4.13b shows the vapor phase pressures [58]. Thus, for GaAs, according to the pressure effect,

$$C^{\mathrm{eq}}_{I^0_{\mathrm{As}}} \propto 1/C^{\mathrm{eq}}_{V^0_{\mathrm{As}}} \propto C^{\mathrm{eq}}_{V^0_{\mathrm{Ga}}} \propto 1/C^{\mathrm{eq}}_{I^0_{\mathrm{Ga}}} \propto (P_{\mathrm{As}_4})^{1/4} \tag{4.37}$$

holds for the four mobile point defect species in the neutral state. For GaAs, explicit expressions for the thermal equilibrium concentrations of all neutral single point defects have been obtained [59]. Such expressions should also be applicable to other III-V semiconductors.

Diffusion of many elements in GaAs have been investigated, with most of the studies focused on p-type dopants Zn and Be, on n-type dopants Si and Se, and on Cr which is used for producing semi-insulating GaAs. Since Zn, Be, Cr and a number of other elements diffuse via an i-s mechanism, this type of diffusion mechanism has historically received much more attention in GaAs than in Si and Ge. Similarly as for Si and Ge, it had been assumed for

a long time that only vacancies need to be taken into account to understand diffusion processes in GaAs, see the book of Tuck [60].

The compilation of earlier diffusion data in GaAs may be found elsewhere [60]. Only a few studies of self-diffusion in GaAs are available, but with advances in growing GaAs/AlAs-type superlattices using molecular beam epitaxy (MBE) or metalorganic chemical vapor deposition (MOCVD) methods, Al has served as an important foreign tracer element for elucidating Ga self-diffusion mechanisms. The observation that high-concentration Zn diffusion into a $GaAs/Al_xGa_{1-x}As$ superlattice leads to a dramatic increase in the Al-Ga interdiffusion coefficient [61] opened up the possibility to fabricate laterally structured optoelectronic devices by locally disordering superlattices. This dopant-enhanced superlattice disordering is a general phenomena occuring for other p-type dopants, e.g., Mg, and for n-type dopants, e.g., Si, Se and Te [57, 58]. The dopant-enhanced superlattice disordering also has helped to unravel the contributions of I and V to self- and dopants diffusion processes in GaAs. These superlattices with their typical period of about 10 nm allow one to measure Al-Ga interdiffusion coefficients, which turned out to be close to the Ga self-diffusion coefficient, down to much lower values than had been previously possible for Ga self-diffusion in bulk GaAs using radioactive Ga tracer atoms. The dependence of diffusion processes on the As vapor pressure has helped in establishing the role of self-interstitials versus vacancies.

The diffusivity of a substitutional species in GaAs generally shows a dependence on P_{As_4}, because the concentration of the responsible point defect species is dependent upon P_{As_4}, (4.37). The diffusivity will also exhibit a dependence on doping because of the involvement of charged point defects whose concentration is influenced via the Fermi-level effect. Furthermore, non-equilibrium concentrations of native point defects may be induced by the in-diffusion of dopants such as Zn starting from a high surface concentration. Much less is known on the diffusion processes of atoms dissolved on the As sublattice, but recent experiments indicate the dominance of As I on the diffusion of the isoelectronic group V element N [62], P and Sb [63–65], and the group VI n-type dopant S [66]. These results imply also the dominance of As I on As self-diffusion, which is in contrast to the earlier As self-diffusion results of Palfrey et al. [67] favoring the dominance of As V.

4.5.2 Gallium Self-Diffusion and Superlattice Disordering

Intrinsic Gallium Arsenide

The self-diffusion coefficient $D_{Ga}(n_i)$ of Ga in intrinsic GaAs has been measured by Goldstein [68] and Palfrey et al. [69] using radioactive Ga tracer atoms. This method allows measurements of $D_{Ga}(n_i)$ down to about $10^{-19}\,m^2/s$. Measurements of the interdiffusion of Ga and Al in $GaAs/Al_xGa_{1-x}As$ superlattices extended the range to much lower values [70–74].

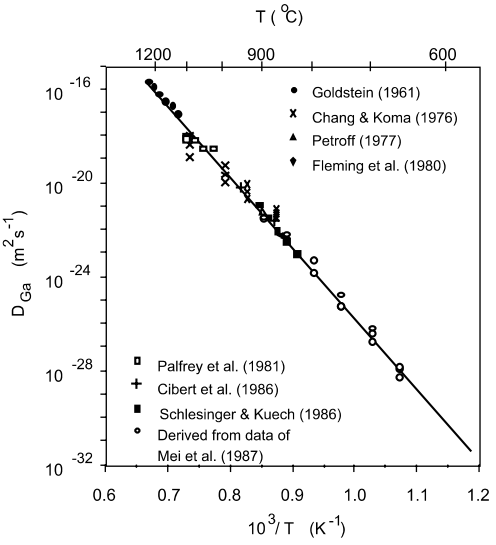

Fig. 4.14. Plot of available data on Ga self-diffusion in GaAs and data on Ga/Al interdiffusion in GaAs/AlGaAs superlattices under intrinsic conditions together with D_{Ga} derived [75] from the data of Mei et al. [87].

The various data points have been approximately fitted by Tan and Gösele [75, 76] to the expression

$$D^{V}_{\mathrm{Ga}}(n_{\mathrm{i}}, 1\,\mathrm{atm}) \approx 2.9 \times 10^{4} \exp(-6\,\mathrm{eV}/k_{\mathrm{B}}T)\,\mathrm{m^{2}s^{-1}}\,, \tag{4.38}$$

see Fig. 4.14. Equation (4.38) is valid for the As_4 pressure of 1 atm or for GaAs crystals with compositions at the As-rich boundary shown in Fig. 4.13a, and the superscript V in the quantity D^{V}_{Ga} specifies that the quantity is due to the Ga sublattice V contribution to Ga self-diffusion. This is because, at ~ 1 atm, the disordering rate of the GaAs/$Al_xGa_{1-x}As$ superlattices increases as the ambient As_4 pressure is increased [77, 78]. The corresponding D^{V}_{Ga} values for GaAs crystals at the Ga-rich boundary is then

$$D^{V}_{\mathrm{Ga}}(n_{\mathrm{i}}, \text{Ga-rich}) \approx 3.93 \times 10^{8} \exp(-7.34\,\mathrm{eV}/k_{\mathrm{B}}T)\,\mathrm{m^{2}s^{-1}}\,. \tag{4.39}$$

For (4.38) and (4.39), it turned out that the responsible vacancy species is the triply-negatively-charged Ga vacancies V^{3-}_{Ga}, to be discussed in the next paragraph. However, the Al-Ga interdiffusion coefficient also increases for very low arsenic vapor pressures [77, 78], indicating that D_{Ga} is governed by Ga I for sufficiently low As vapor pressures [57]. The role of Ga V and I will become clearer when Ga diffusion in doped GaAs/$Al_xGa_{1-x}As$ superlattices is considered and when diffusion of the p-type dopant Zn and Be is considered. Combining the Al-Ga interdiffusion data of Hsieh et al. [79] obtained under Ga-rich ambient conditions, and the deduced Ga self-diffusion coefficients from analyzing Zn diffusion [80] and Cr diffusion [81], Tan et al. [82] summarized that

$$D^{I}_{\mathrm{Ga}}(n_{\mathrm{i}}, \text{Ga-rich}) \approx 4.46 \times 10^{-8} \exp(-3.37\,\mathrm{eV}/k_{\mathrm{B}}T)\,\mathrm{m^{2}s^{-1}} \tag{4.40}$$

holds for the Ga I contribution to Ga self-diffusion in GaAs crystals with composition at the Ga-rich boundary shown in Fig. 4.13a. The corresponding values for GaAs crystals with composition at the As-rich boundary shown in Fig. 4.13a is then

$$D^I_{\mathrm{Ga}}(n_{\mathrm{i}}, 1\,\mathrm{atm}) \approx 6.05 \times 10^{-4} \exp(-4.71\,\mathrm{eV}/k_{\mathrm{B}}T)\,\mathrm{m^2 s^{-1}}\,. \tag{4.41}$$

For (4.40) and (4.41), it turned out that the responsible point defect species is the doubly-positively-charged Ga self-interstitials I^{2+}_{Ga}, as will be discussed in Sect. 4.5.2.

However, as has been first noticed by Tan et al. [83], under intrinsic conditions, for a number of Al-Ga interdiffusion studies [70, 84, 85] and two recent Ga self-diffusion studies using stable Ga isotopes [83,86], the results are fitted better by

$$D_{\mathrm{Ga}}(n_{\mathrm{i}}, 1\,\mathrm{atm}) \approx 4.3 \times 10^{-3} \exp(-4.24\,\mathrm{eV}/k_{\mathrm{B}}T)\,\mathrm{m^2 s^{-1}} \tag{4.42}$$

instead of by (4.38). Figure 4.15 shows the values per (4.38) and (4.42) and the associated data. There has yet to be a satisfactory explanation of the discrepancy between these expressions. On the one hand, (4.42) does offer a better fit to the more recent data, but on the other, it does not seem to be consistent with the Al-Ga data of Mei et al. [87] under Si doping which are associated with a 4 eV activation enthalpy. In accordance with the Fermi-level effect, the Ga diffusion activation enthalpy decreases by about 2 eV in n-doped materials [57], which would mean that (4.38) is more reasonable. A number of reasons, however, could affect the accuracy of the experimental results. These will include accidental contamination by n-type dopants in the nominal intrinsic materials, band off-sets in the case of Al-Ga interdiffusion, and the fact that the materials did not have the As-rich composition to start with and the experimental temperature-time was not sufficient to change the materials into As-rich for most part of the experimental time.

Doped Gallium Arsenide

No studies of Ga self-diffusion in doped bulk GaAs have been reported, but a wealth of data on Al-Ga interdiffusion in both n-type and p-type doped GaAs/$\mathrm{Al_xGa_{1-x}As}$ superlattices is available. These interdiffusion experiments were triggered by the observation of Zn in-diffusion enhanced superlattice disordering due to Laidig et al. [61]. A number of disordering mechanisms have been proposed [61, 88–90] for a particular dopant, but none is general enough to account for the occurrence of an enhanced Al-Ga interdiffusion rate for also other dopants. The observed dopant enhanced interdiffusion appears to be due to two main effects [75, 76]: (i). The thermal equilibrium concentration of appropriately charged point defects is enhanced by doping, i.e., the Fermi-level effect. In the case of the n-type dopant Si, mainly the *presence* of the dopant is of importance, but not its movement. Compensation

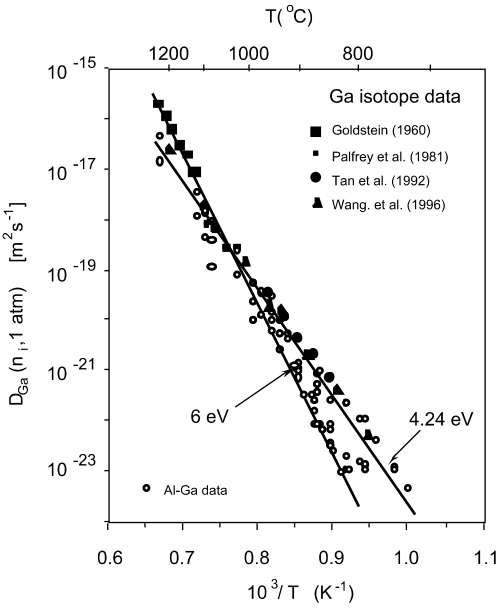

Fig. 4.15. Data and fitting lines for the intrinsic Ga or Al-Ga diffusivity under 1 atm of As_4 pressure. The 6 eV line is that given by (4.38) and the 4.24 eV line that given by (4.42). All Ga data are directly measured ones using norminaly intrinsic GaAs. The Al-Ga data include directly measured ones using norminaly intrinsic $GaAs/Al_xGa_{1-x}As$ superlattices as well as those deduced [75] from the Mei et al. data [87] obtained using Si doped $GaAs/Al_xGa_{1-x}As$ superlattices.

doping, e.g. with Si and Be, should not lead to enhanced Al-Ga interdiffusion, in agreement with experimental results [91, 92]. (ii) For a dopant with high diffusivity and solubility, *non-equilibrium native point defects* are generated.

Depending on whether a supersaturation or an undersaturation of point defects develops, the enhanced disordering rate due to the Fermi level effect may be further increased or decreased. Irrespective of the starting material composition, such non-equilibrium native point defects drive the dopant diffused region crystal composition first toward an appropriate allowed GaAs crystal composition limit shown in Fig. 4.13a. When the super- or undersaturation of point defects becomes so large that the crystal local region exceeded the allowed composition limit, extended defects form to bring the composition of the region back to that composition limit. Afterwards, this permits the diffusion processes to be described by an equilibrium point defect process appropriate for the crystal local region which is at an appropriate allowed composition limit. The crystal is in a non-equilibrium state because of the spatially changing composition. The diffusion of high-concentration Zn and Be in GaAs [80, 93] and their effects on $GaAs/Al_xGa_{1-x}As$ superlattices [94] appear to be such cases. Interdiffusion of Al-Ga in *n-type* GaAs/AlAs su-

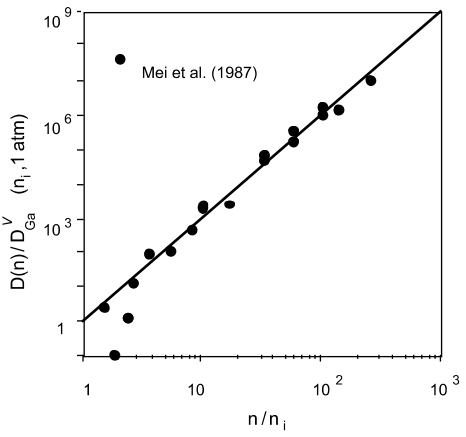

Fig. 4.16. The $(n/n_\mathrm{i})^3$ dependence of the Al-Ga interdiffusion data of Mei et al. [87], with $D^V_\mathrm{Ga}(n_\mathrm{i}, 1\,\mathrm{atm})$ given by (4.38). The data cannot be analyzed to a similar degree of satisfaction via the use of (4.42) to a power law dependence on n/n_i. Redrawn from [75].

perlattices will be first discussed. This concerns with the case of Si-doped GaAs which allows to identify the type and the charge state of the native point defect dominating Ga self-diffusion in n-type GaAs. In Fig. 4.16, the enhanced Al-Ga interdiffusion coefficients under Si-doping are plotted in a normalized form as a function of n/n_i of the appropriate temperature. These data, obtained by Mei et al. [87], show a clear doping dependence [75, 76]

$$D_{\mathrm{Al-Ga}}(n, 1\,\mathrm{atm}) = D_\mathrm{Ga}(n_\mathrm{i}, 1\,\mathrm{atm})[n/n_\mathrm{i}]^3 \tag{4.43}$$

with $D^V_\mathrm{Ga}(n_\mathrm{i}, 1\,\mathrm{atm})$ given by (4.38). Equation (4.43) indicates the involvement of a triply-negatively-charged native point defect species. Based on the pressure dependence of the interdiffusion coefficient of n-doped superlattices [56, 78] this defect has to be the gallium vacancy V^{-3}_Ga, as predicted by Baraff and Schlüter [95]. Values of $D^V_\mathrm{Ga}(n_\mathrm{i}, 1\,\mathrm{atm})$ calculated from the Mei et al. data and shown in Fig. 4.14 are in good agreement with values extrapolated from higher temperatures. Thus, including the As vapor pressure dependence, we may write the Ga self-diffusion coefficient in n-type GaAs as

$$D_\mathrm{Ga}(n, P_{\mathrm{As_4}}) = D^V_\mathrm{Ga}(n_\mathrm{i}, 1\,\mathrm{atm})[n/n_\mathrm{i}]^3[P_{\mathrm{As_4}}]^{1/4} \tag{4.44}$$

where $D^V_\mathrm{Ga}(n_\mathrm{i}, 1\,\mathrm{atm})$ is given by (4.38). The much later claim that these Si-doping induced Al-Ga interdiffusion data show a quadratic dependence on n [96] is erroneous, because of the use of the room temperature n_i value as that for high temperature ones by the authors. Furthermore, the statement that there is no Fermi-level effect [97] bears little credence, for it is based on Al-Ga interdiffusion results with extremely low Si doping, which are threshold phenomena that may be influenced by many other uncontrolled factors. Tellurium-doped GaAs based superlattices show a weaker dependence of the Al-Ga interdiffusion coefficient on the Te concentration than expected from (4.44) [98], especially at very high concentrations. The probable cause is that,

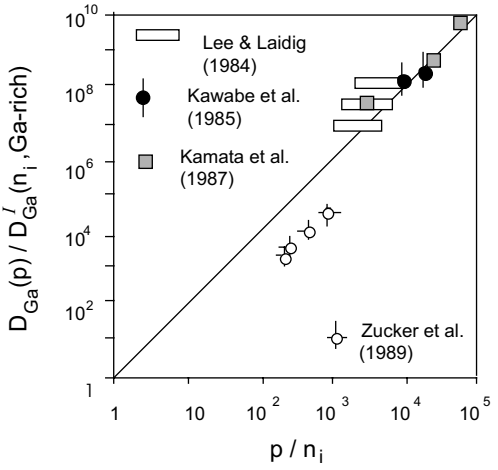

Fig. 4.17. Fits of some of the available p-dopant enhanced Al-Ga interdiffusion data, with $D^I_{\rm Ga}(n_{\rm i}, \text{Ga-rich})$ given by (4.40). The data exhibit an approximately quadratic dependence on $p/n_{\rm i}$, indicating that the dominant native point defect is $I^{2+}_{\rm Ga}$. From [94].

due to clustering, not all Te atoms are electrically active to contribute to the electron concentration [99].

The available Al-Ga interdiffusion data in *p-type* GaAs based superlattices [61, 91, 100–104] had been first thought to be not analyzable in a manner analogous to that done for the n-doping effect [75, 76]. As shown in Fig. 4.17, however, some of these data has been later approximately fitted by [94]

$$D_{\rm Al-Ga}(p, \text{Ga-rich}) = D^I_{\rm Ga}(n_{\rm i}, \text{Ga-rich})[p/n_{\rm i}]^2 \tag{4.45}$$

where $D^I_{\rm Ga}(n_{\rm i}, \text{Ga-rich})$ is given by (4.40). Equation (4.45) shows that the dominant native point defects under p-doping to a sufficient concentration are $I_{\rm Ga}$ species, and the p^2 dependence of $D_{\rm Al-Ga}(p, \text{Ga-rich})$ shows that the $I_{\rm Ga}$ are doubly-positively-charged. The data shown in Fig. 4.17 [91, 100, 103, 104] are those under the dopant *in-diffusion* conditions, while the rest are those under the dopant *out-diffusion* conditions involving grown-in dopants without an outside dopant source. Under out-diffusion conditions, the dopant diffusivity values are too small to be reliably measured. The fit shown in Fig. 4.17 is seemingly satisfactory but nowhere near that for the Si-doping case (Fig. 4.16). Even if the fit were perfect, the essential native point defect equilibrium situation implied by Fig. 4.17 is only an apparent phenomenon, for it applies only to the p-dopant diffusion front region while the whole crystal is having a spatially varying composition. This point is most obvious in the data of Lee and Laidig [100] which were obtained in a high As_4 vapor pressure ambient.

The grossly different results for in- and out-diffusion conditions is due to non-equilibrium concentrations of native point defects induced by high-concentration diffusion of Zn or Be. Both Zn and Be diffuse via an i-s mechanism as will be discussed in more detail in the subsequent section. Historically, most authors [60] considered that diffusion of p-type dopants is governed by

the Longini mechanism [105] involving Ga vacancies

$$A_i^+ + V_{Ga}^0 \Leftrightarrow A_s^- + 2h\,, \tag{4.46}$$

where h is a hole and the interstitial species of the dopant is assumed to be positively charged, A_i^+. The Longini mechanism is the same as the FT mechanism, except it deals with charged species. The superlattice disordering results indicate that for these dopants, the KO mechanism [106] involving Ga self-interstitials

$$A_i^+ \Leftrightarrow A_s^- + I_{Ga}^{2+} \tag{4.47}$$

is operating instead. This also indicates that Ga self-diffusion is governed by Ga I under p-doping conditions. Within the framework of the kickout mechanism the dopant in-diffusion generates a supersaturation of I_{Ga} with a corresponding increase of dopant diffusion and the Ga self-diffusion component involving Ga I. Because of the I_{Ga} supersaturation, the dopant diffused region tends toward the Ga-rich composition. In the case of Zn in-diffusion to very high concentrations, it will be discussed in detail that the I_{Ga} supersaturation is so large that in a small fraction of the diffusion time extended defects form [93, 107], resulting in that the Zn diffused region composition is at the thermodynamically allowed Ga-rich composition limit, and is associated with the appropriate thermal equilibrium point defect concentrations. This is the reason for the satisfactory fit shown in Fig. 4.17.

In the case of grown-in dopants without an outside source the KO mechanism involves the consumption of I_{Ga} which leads to an I_{Ga} undersaturation with a corresponding decrease in dopant diffusion [108–111] and the Ga self-diffusion component involving I_{Ga}. The results of the superlattice disordering experiments are consistent with the expectations based on the KO mechanism. In contrast, the Longini mechanism predicts an undersaturation of V for in-diffusion conditions and a supersaturation for out-diffusion conditions with a corresponding decrease and increase of a V dominated Ga self-diffusion component, respectively. Since the predictions based on the Longini mechanism are just opposite to the observed superlattice disordering results, it can be concluded that: (i) Zn diffusion occurs via the KO mechanism, and (ii) Ga self-diffusion in p-type GaAs is governed by I_{Ga}.

In contrast to the group II acceptors Zn and Be, the group IV acceptor carbon (C) occupying the As sublattice sites diffuses slowly. This allows the native point defects to be maintained at their thermal equilibrium values. The effect of C on the disordering of GaAs/$Al_xGa_{1-x}As$ superlattices [112] is described well by

$$D_{Al-Ga}^{eq} = D_{Ga}^{I}(n_i)[p/n_i]^2\,, \tag{4.48}$$

where $D_{Ga}^{I}(n_i)$ is given by (4.40) and (4.41) respectively for data obtained under Ga-rich and As-rich ambient conditions.

The pressure dependence of disordering of p-doped superlattices confirms the predominance of Ga I in Ga self-diffusion [56]. The magnitude of the

enhancement effect, its restriction to the dopant-diffused region and the implantation results of Zucker et al. [104] indicate that a Fermi level effect has to be considered in addition to non-equilibrium point defects.

Combining the results for the p-type and the n-type dopant induced disordering including an I supersaturation s_I defined as $s_I = C_I(n(p))/C_i^{\mathrm{eq}}(n(p))$, and an analogous V supersaturation s_V defined as $s_V = C_V(n(p))/C_V^{\mathrm{eq}}(n(p))$, where $(n(p))$ indicates doping conditions, we may express the Ga self-diffusion coefficient approximately as

$$D_{\mathrm{Ga}}\,(n(p), P_{\mathrm{As_4}}) = D^I_{\mathrm{Ga}}(n_{\mathrm{i}}, 1\,\mathrm{atm})[p/n_{\mathrm{i}}]^2 P^{-1/4}_{\mathrm{As_4}} s_I + D^V_{\mathrm{Ga}}(n_{\mathrm{i}}, 1\,\mathrm{atm})[n/n_{\mathrm{i}}]^3 P^{1/4}_{\mathrm{As_4}} s_V\,. \tag{4.49}$$

In (4.49) the quantities $D^V_{\mathrm{Ga}}(n_{\mathrm{i}}, 1\,\mathrm{atm})$ and $D^I_{\mathrm{Ga}}(n_{\mathrm{i}}, 1\,\mathrm{atm})$ are given respectively by (4.38) and (4.41). In writing down (4.49), the As-rich GaAs, designated by $P_{\mathrm{As_4}} = 1\,\mathrm{atm}$, is chosen as the reference material state, and with GaAs crystals of all other compositions represented by an appropriate $P_{\mathrm{As_4}}$ value. Equation (4.49) describes all presently known essential effects on $\mathrm{GaAs/Al_xGa_{1-x}As}$ superlattice disordering. In the case of non-equilibrium Ga V injected by a Si/As cap [113], $s_V > 0$ holds. In the case of ion-implantation, both $s_I > 0$ and $s_V > 0$ may hold and both quantities will be time dependent. In the case of diffusion-induced non-equilibrium point defects the presence of dislocations will allow local equilibrium between intrinsic point defects to establish in the two sublattices. In this way a large supersaturation of I_{Ga} in the Ga sublattice may lead to an undersaturation of I_{As} or a supersaturation of V_{As} in the As sublattice.

4.5.3 Arsenic Self-Diffusion and Superlattice Disordering

Since there is only one stable As isotope, ^{75}As, As self-diffusion in GaAs cannot be studied using stable As isotopes. In intrinsic GaAs, however, three arsenic self-diffusion studies have been conducted using radioactive tracers [62, 63, 67]. In the experiment of Palfrey et al. [67], the $\mathrm{As_4}$ pressure dependence of As self-diffusion indicated that V_{As} may be the responsible native point-defect species. This is, however, in qualitative contradiction to the conclusion reached recently from a large number of studies involving As atoms and other group V and VI elements that the responsible native point-defect species should be I_{As}. The latter studies include: (i) As-Sb and As-P interdiffusion in intrinsic $\mathrm{GaAs/GaSb}_x\mathrm{As}_{1-x}$ and $\mathrm{GaAs/GaP}_x\mathrm{As}_{1-x}$ type superlattices for which x is small so as to avoid a large lattice mismatch [63–65]; (ii) P and Sb in-diffusion into GaAs under appropriate P and As pressures so as to avoid extended defect formation which leads to complications [63–65]; (iii) an extensive analysis of the S in-diffusion data in GaAs [66]; (iv) out-diffusion of N from GaAs [62]. A plot of the relevant data is shown in Fig. 4.18, from which the lower limit of the As self-diffusion coefficient, assigned to be due to the As self-interstitial contribution, is determined to be

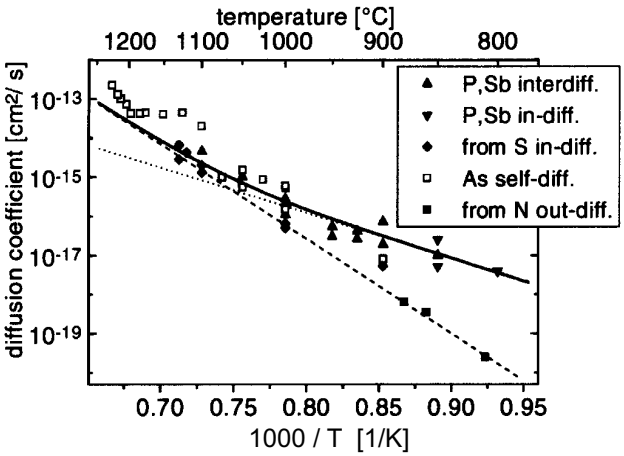

Fig. 4.18. Data on As self-diffusion coefficient, obtained using radioactive As tracers (open squares), the group V elements N, P, and Sb and the group VI donor S (filled symbols). The dashed fitting line is given by (4.50), and the solid line is a better overall fitting. From [64].

$$D^I_{\mathrm{As}}(n_{\mathrm{i}}, 1\,\mathrm{atm}) \approx 6 \times 10^{-2} \exp(-4.8\,\mathrm{eV}/k_{\mathrm{B}}T)\,\mathrm{m^2 s^{-1}}\,. \tag{4.50}$$

For P-As and Sb-As interdiffusion as well as P and Sb in-diffusion cases [63–65], the profiles are error function shaped. With P and Sb assumed to be i-s elements, such diffusion profiles are described by an effective diffusivity of the type

$$D^{\mathrm{eff}}_{\mathrm{s}} = D_{\mathrm{i}} C^{\mathrm{eq}}_{\mathrm{i}} / C^{\mathrm{eq}}_{\mathrm{s}} \tag{4.51}$$

under native point defect equilibrium conditions, which is satisfied by either the KO mechanism involving I_{As} or the Longini (or FT) mechanism involving V_{As}. The conclusion that I_{As} is the responsible species is reached for this group of experiments because the diffusion rate increases upon increasing the ambient As vapor pressure. I_{As} should be the responsible species in the N out-diffusion experiments [62] because the N profile is typical of that due to the KO reaction (4.47) under the condition of an I_{As} undersaturation, which is qualitatively different from those obtainable from the dissociative reaction (4.46). I_{As} should also be the responsible species in the S in-diffusion experiments because the S profile [66] is typical of that due to the KO mechanism reaction $\mathrm{S}^+_{\mathrm{i}} \Leftrightarrow \mathrm{S}^+_{\mathrm{s}} + I^0$ under the condition of an I_{As} supersaturation, which is also qualitatively different from those obtained from any possible reactions of the FT or Longini mechanisms. It is seen from Fig. 4.18 that the available As self-diffusion data lie close to those deduced from the P, Sb, N, and S studies, and it may thus be inferred that As self-diffusion has a component contributed by I_{As}.

There are yet no doping dependence studies using the isoelectronic group V elements N, P, and Sb, and hence the charge nature of the involved I_{As} has not yet been determined. However, S is a group VI donor occupying the As sublattice sites. In analyzing S in-diffusion [66], it was necessary to assume that neutral I_{As} species were involved, which is therefore a most likely species responsible for As self-diffusion.

There is also a study on the disordering of GaAs/$\mathrm{Al_xGa_{1-x}As}$ superlattices by the group IV acceptor species C [112] which occupy the As sublattice sites. While there is no information obtained from this study on As self-diffusivity, satisfactory descriptions of the C diffusion profiles themselves were obtained also with the use of a kickout reaction involving neutral As self-interstitials, discussed later. This lends further support to the interpretation that neutral As self-interstitials are responsible for As self-diffusion.

4.5.4 Impurity Diffusion in Gallium Arsenide

Silicon

For GaAs the main n-type dopant is Si. It is an amphoteric dopant mainly dissolved on the Ga sublattice but shows a high degree of self-compensation at high concentrations due to an increased solubility on the As sublattice.

The Si diffusivity shows a strong dependence on its own concentration, which had been modeled by a variety of mechanisms [113–115]. Apparently, Si diffusion is dominated by negatively charged V_{Ga} and that its apparent concentration dependence is actually a Fermi level effect. Results on Si diffusion into n-type (Sn-doped) GaAs confirm the Fermi level effect [115] and contradict the other models, e.g., the $\mathrm{Si_{Ga}}$-$\mathrm{Si_{As}}$ pair-diffusion model of Greiner-Gibbons [114]. In the Fermi-level effect model, Yu et al. [115] used mainly V_{Ga}^{3-} to fit the Si in-diffusion profiles, and more recently Chen et al. [116] found *only* V_{Ga}^{-3} is needed to fit these profiles. This is in consistency with the fact that V_{Ga}^{3-} dominating GaAs/AlAs superlattice disordering under n-doping conditions. In the work of Chen et al. [116] the Si source material and the GaAs crystal are regarded as forming a heterostructure so that electrical effects due to the heterojunction are also accounted for. In these analyses [115, 116], the diffusivity of the Si donor species $\mathrm{Si_{Ga}^{+}}$ satisfies

$$D_{\mathrm{Si}}(n) = D_{\mathrm{Si}}(n_{\mathrm{i}})(n/n_{\mathrm{i}})^3\,, \tag{4.52}$$

which indicates that V_{Ga}^{3-} governs the diffusion of $\mathrm{Si_{Ga}^{+}}$. Satisfactory fits of the experimental data of Greiner and Gibbons [114] and of Kavanagh et at. [113] were obtained using (4.51) with

$$D_{\mathrm{Si}}(n_{\mathrm{i}}) = 5.2\exp(-4.98\,\mathrm{eV}/k_{\mathrm{B}}T)\,\mathrm{m^2 s^{-1}} \tag{4.53}$$

in the work of Yu et al. [115], while $D_{\mathrm{Si}}(n_{\mathrm{i}})$ values 10 times larger than that given by (4.53) were needed in the analysis of Chen et al. [116].

In a set of Si out-diffusion experiments, You et al. [117] found that the Si profiles also satisfy (4.52) but the needed $D_{\mathrm{Si}}(n_{\mathrm{i}})$ values are

$$D_{\mathrm{Si}}(n_{\mathrm{i}}, 1\,\mathrm{atm}) = 6.67 \exp(-3.91\,\mathrm{eV}/k_{\mathrm{B}}T)\,\mathrm{m^2 s^{-1}}\,, \tag{4.54}$$

$$D_{\mathrm{Si}}(n_{\mathrm{i}}, \text{Ga-rich}) = 9.18 \times 10^4 \exp(-5.25\,\mathrm{eV}/k_{\mathrm{B}}T)\,\mathrm{m^2 s^{-1}}\,, \tag{4.55}$$

respectively, for experiments conducted under As-rich and Ga-rich ambient conditions.

The $D_{\mathrm{Si}}(n_{\mathrm{i}})$ expressed by (4.54) and (4.55) are larger than those of (4.53) by several orders of magnitude at temperatures above $\sim 800°\mathrm{C}$, which indicates the presence of an undersaturation and a supersaturation of V_{Ga}^{3-}, respectively, under the Si in- and out-diffusion conditions [117]. For the in-diffusion case, the starting GaAs crystal contains V_{Ga}^{3-} and the neutral Ga vacancies V_{Ga}^{0} to the thermal equilibrium concentrations of those of the intrinsic material. Upon in-diffusion of Si atoms, V_{Ga}^{3-} (and hence also V_{Ga}^{0}) become undersaturated relative to the thermal equilibrium V_{Ga}^{3-} concentration values appropriate for the n-doping conditions, which can only be alleviated via inflow of V_{Ga}^{3-} from the interface of the Si source material and the GaAs crystal. The reverse analogy holds for the Si out-diffusion case. Since V_{Ga}^{3-} diffusion should be much faster than that of the $\mathrm{Si}_{\mathrm{Ga}}^{+}$ atoms, in either case there shall be no substantial spatial variations in the distribution of the V_{Ga}^{0} species while the spatial distribution of V_{Ga}^{3-} follows the local n^3 value.

Diffusion of Interstitial-Substitutional Species

Carbon

The group IV element carbon (C) occupies the As sublattice sites in GaAs and is a shallow acceptor, designated as $\mathrm{C_s^-}$ to emphasize that it is most likely an i-s species. By in-situ doping during MBE crystal growth, $\mathrm{C_s^-}$ reaches high solubilities [118] and diffuses slowly [119], which are attractive features when compared to the main p-type dopants Zn and Be in GaAs. The measured $\mathrm{C_s^-}$ diffusivity values of a few groups obtained under As-rich annealing conditions [112, 118–122] are fitted well by the expression

$$D_{\mathrm{s}}(1\,\mathrm{atm}) = 4.79 \times \exp(-3.13\,\mathrm{eV}/k_{\mathrm{B}}T)\,\mathrm{m^2 s^{-1}}\,. \tag{4.56}$$

The corresponding Ds values under Ga-rich conditions should therefore be

$$D_{\mathrm{s}}(\text{Ga-rich}) = 6.5 \times \exp(-4.47\,\mathrm{eV}/k_{\mathrm{B}}T)\,\mathrm{m^2 s^{-1}}\,. \tag{4.57}$$

These fits are shown in Fig. 4.19. In the work of You et al. [112] the $\mathrm{C_s^-}$ diffusivity data were obtained by the individual fittings of $\mathrm{C_s^-}$ profiles which are not quite error function shaped. In order to fit these profiles well, together with a carbon precipitation process, it was also necessary to use the kickout reaction

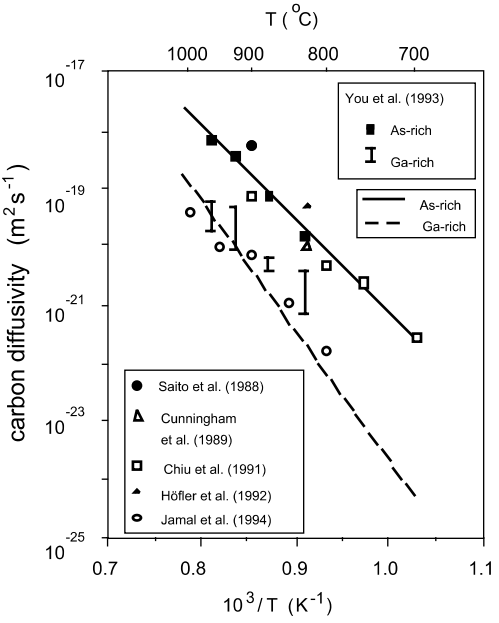

Fig. 4.19. Available carbon diffusivity data and fittings in GaAs. From [112].

$$C_s^- + I_{As}^0 \Leftrightarrow C_i^- , \tag{4.58}$$

where C_i^- is an interstitial C atom which is also assumed to be an acceptor, and I_{As}^0 is a neutral As self-interstitial. Later, Moll et al. [123] identified the nature of the precipitation process as that of graphite formation. The As self-interstitials are maintained at their thermal equilibrium values during C diffusion, because of the low diffusivity value of C.

Zinc and Beryllium

The main p-type dopants in GaAs based devices, Zn and Be, diffuse via an i-s mechanism in GaAs as well as in many other III-V compounds. In most works Zn and Be diffusion have been discussed in terms of the much earlier suggested FT or Longini mechanism [60], but only the KO mechanism involving I_{Ga} is quantitatively consistent with the superlattice disordering results as well as with Zn diffusion results [80, 93].

Isoconcentration diffusion of Zn isotopes in GaAs predoped by Zn showed error function profiles [124, 125] with the substitutional Zn diffusivity values of

$$D_s(p, 1\,\text{atm}) = D_s(n_i, 1\,\text{atm})(C_s/n_i)^2 \tag{4.59}$$

for As-rich GaAs and an analogous expression for Ga-rich GaAs. At sufficiently high Zn concentrations, since the GaAs hole concentration p equals approximately the Zn_s concentration ($p \sim C_s$), (4.59) shows that the responsible native point defect species can only be the doubly-positively-charged

Ga self-interstitials or vacancies, I_{Ga}^{2+} or V_{Ga}^{2+}. Under high-concentration Zn in-diffusion conditions, the GaAs/$Al_xGa_{1-x}As$ superlattices disordering rates are tremendously high, indicating the presence of a high supersaturation of the responsible point defects. Thus, the native point-defect species responsible for Zn diffusion, and also for Ga self-diffusion and Al-Ga interdiffusion under p-doping conditions, is I_{Ga}^{2+} according to reaction (4.47), and not V_{Ga}^{2+} according to reaction (4.46). In the latter case only an undersaturation of V_{Ga}^{2+} can be incurred by Zn in-diffusion which should then retard Al-Ga interdiffusion rates in superlattices, in contradiction with experimental results. In the Zn isoconcentration diffusion experiments, a non-equilibrium I_{Ga}^{2+} concentration is not involved. Similarly, for Zn diffusion to low concentrations below the n_i value, a non-equilibrium concentration of I_{Ga}^{2+} is also not present, and the Zn diffusivity values may be represented by that under the intrinsic conditions, $D_s(n_i)$. As analyzed by Yu et al. [80], Zn isoconcentration experiments and Zn in-diffusion experiments at high concentrations yielded the value range of

$$D_s(n_i, 1\,\text{atm}) = 1.6 \times 10^{-6} \exp(-2.98\,\text{eV}/k_BT)\,\text{m}^2\text{s}^{-1}\,, \tag{4.60a}$$

$$D_s(n_i, 1\,\text{atm}) = 9.68 \times 10^{-3} \exp(-4.07\,\text{eV}/k_BT)\,\text{m}^2\text{s}^{-1}\,. \tag{4.60b}$$

The two analogous expressions for Ga-rich materials are respectively

$$D_s(n_i, \text{Ga-rich}) = 1.18 \times 10^{-10} \exp(-1.64\,\text{eV}/k_BT)\,\text{m}^2\text{s}^{-1}\,, \tag{4.61a}$$

$$D_s(n_i, \text{Ga-rich}) = 7.14 \times 10^{-7} \exp(-2.73\,\text{eV}/k_BT)\,\text{m}^2\text{s}^{-1}\,. \tag{4.61b}$$

The values of (4.60ab) and (4.61ab) and the associated data are plotted in Fig. 4.20.

The correspondingly deduced I_{Ga}^{2+} contribution to Ga self-diffusion has been included in (4.38) and (4.39). Because of the lack of a proper Be source for in-diffusion studies, and in Be out-diffusion studies with Be incorporated using MBE or MOCVD methods the Be diffusivity is too small, there are no reliable Be diffusivity data.

Out-diffusion of Zn or Be in GaAs doped to fairly high concentrations during crystal is associated with a high I_{Ga}^{2+} undersaturation, leading to Zn or Be out-diffusion rates orders of magnitude smaller than those under in-diffusion conditions [109,110,126]. In-diffusion of high concentration Zn into GaAs induces an extremely large I_{Ga}^{2+} supersaturation, because the condition

$$D_i C_i^{eq} \gg D_{Ga}^{SD}(p) \tag{4.62}$$

holds. As first noted by Winteler [107], this I_{Ga}^{2+} supersaturation leads to the formation of extended defects. In recent works three kinds of extended defects have been characterized and their formation process analyzed [57,93,127]: (i) interstitial-type dislocation loops, which degenerate into dislocation tangles in time; (ii) voids; and (iii) Ga precipitates co-existing with neighboring voids. For diffusing Zn into GaAs in a Ga-rich ambient, a Zn diffused GaAs crystal

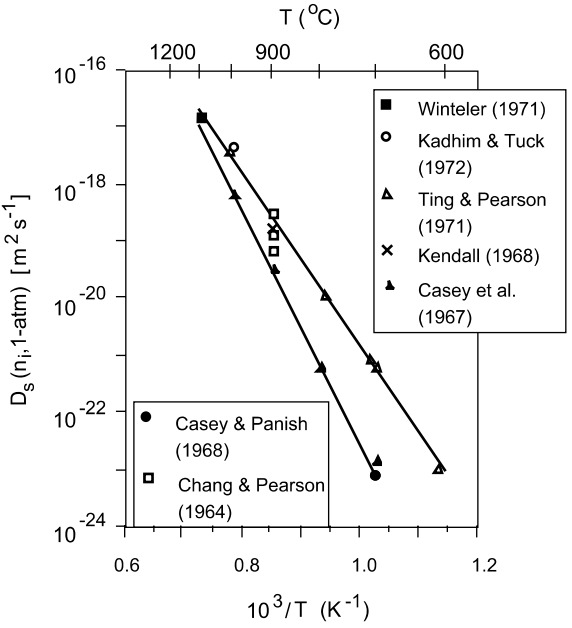

Fig. 4.20. The substitutional Zn diffusivity values under intrinsic and 1-atm As_4 pressure conditions. From [80].

region with compositions at the allowed Ga-rich boundary shown in Fig. 4.13a is obtained, irrespective of the GaAs starting composition. The fact that the Zn diffused region is indeed rich in Ga is evidenced by the presence of Ga precipitates in the voids [93]. Formation of these defects ensures the Zn in-diffusion profile to be governed by the thermal equilibrium concentrations of native point defects of the Ga-rich GaAs crystal, and the profile is box-shaped which reveals the p^2 (or C_s^2) dependence of the substitutional Zn diffusivity D_s. Such a profile is shown in Fig. 4.21 together with an illustration of the involved extended defects. It is, however, noted that the crystal is in a highly non-equilibrium state, for two reasons. First, extended defects are generated. Second, the starting material may not be rich in Ga and hence the crystal will now contain regions with different compositions which is of course a highly non-equilibrium crystal.

For diffusing Zn into GaAs in an As-rich ambient, the situation is more complicated. After a sufficient elapse of diffusion time, the crystal surface region becomes As-rich because of the presence of a high ambient As_4 pressure. But, since

$$D_i C_i^{eq} \gg D_{As}^{SD}(p) \tag{4.63}$$

holds in the Zn diffusion front region, it is Ga-rich. Thus, the high-concentration Zn in-diffusion profiles are of a kink-and-tail type resembling those of high concentration P in-diffusion profiles in Si, see Fig. 4.22. The kink-and-tail profile develops because the Zn_s solubility value in the As-rich and Ga-rich GaAs materials are different [93]. In the high Zn concentration region the

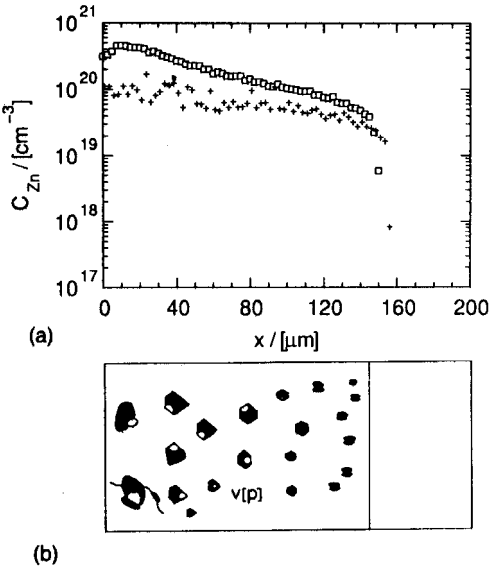

Fig. 4.21. (a) Zn in-diffusion profiles obtained at 900°C under Ga-rich ambient conditions. Squares are the total Zn concentration and crosses are the hole or Zn_s concentration. The higher total Zn concentration indicates formation of Zn containing precipitates caused by the use of a non-equilibrium Zn source material which diffused Zn into GaAs exceeding its solubility at 900°C. (b) A schematic diagram indicating the morphologies and distributions of voids (open) and Ga precipitates (filled), indicated by also v[p]. The presence of dislocations is not shown. From [93].

$D_s(n_i)$ values are those given by (4.60a) and (4.60b), while in the tail or Zn diffusion front region the $D_s(n_i)$ values are those given by (4.61a) and (4.61b). These profiles cannot be modelled with a high degree of self-consistency, because the extended defect formation process cannot be modelled without the use of some phenomenological parameters [80]. The evolution of the extended defects, as suggested by Tan et al. [57] and Luysberg et al. [127], are as follows: (i) to reduce I_{Ga}^{2+} supersaturation, they form interstitial type dislocation loops containing extra GaAs molecules, with the needed As atoms taken from the surrounding As sites which generates a V_{As} supersaturation; (ii) the supersaturated V_{As} collapses to form voids, each of an initial volume about that of a neighboring Ga precipitate formed from Ga atoms lost the neighboring As atoms to the formation of the dislocation loops. The voids will be rapidly filled by subsequently generated Ga self-interstitials due to further Zn in-diffusion. For cases of diffusing Zn into GaAs in a Ga-rich ambient, the voids contain Ga precipitates throughout the Zn in-diffused region, but for cases of diffusing Zn into GaAs in an As-rich ambient, the surface region voids are empty.

Chromium

Chromium is a deep acceptor occupying Ga sites and is used for fabricating semi-insulating GaAs. In undoped GaAs, diffusion of Cr involves no charge effects. In-diffusion profiles of Cr are characterized by a kickout type profile from the crystal surface to a substantial depth and an erfc-type profile deeper in the material near the diffusion front [60, 128]. Out-diffusion profiles are

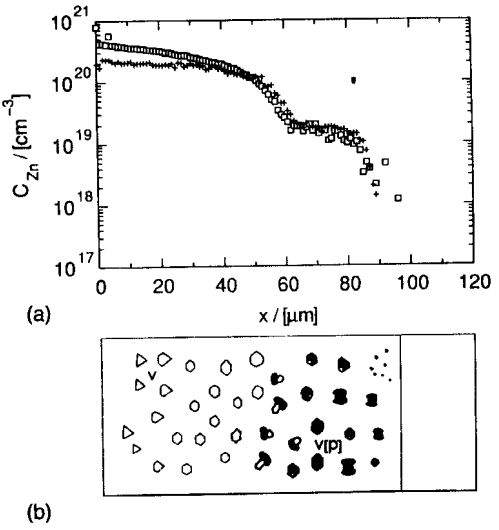

Fig. 4.22. (a) Zn in-diffusion profiles obtained at 900°C under As-rich ambient conditions. Squares are the total Zn concentration and crosses are the hole or Zn_s concentration. The higher total Zn concentration indicates formation of Zn containing precipitates caused by the use of a non-equilibrium Zn source material which diffused Zn into GaAs exceeding its solubility at 900°C. (b) A schematic diagram indicating the morphologies and distributions of voids (open) and Ga precipitates (filled). The presence of dislocations is not shown. From [93].

characterized by a constant diffusivity which is much lower than that for in-diffusion. The existence of the two types of profiles needs the description of the i-s diffusion mechanism in terms of the KO mechanism $Cr_i \Leftrightarrow C_s + I_{Ga}^{2+} + 2e$ and/or the Longini mechanism $Cr_i + V_{Ga}^{3-} \Leftrightarrow C_s + 3e$, where e denotes an electron.

Tuck [60] and Deal and Stevenson [128] have discussed Cr diffusion in terms of the Longini mechanism. The satisfactory treatment of the diffusion behavior of Cr in intrinsic GaAs [81], however, includes the co-existence of V_{Ga} and I_{Ga}, the dependence of C_s^{eq} and C_i^{eq} on the outside Cr vapor pressure, and a dynamical equilibrium between the native point defects in the Ga and the As sublattice at the crystal surface region. In-diffusion of Cr turned out to be governed by the effective diffusivity $D_{surf}^{eff} = (D_I C_I^{eq}/C_s^{eq})(C_s^{eq}/C_s)$ in the surface region, which is concentration dependent, and by the much faster constant diffusivity $D_{tail}^{eff} = D_i C_i^{eq}/C_s^{eq}$ in the tail region. The deduced $D_I C_I^{eq}$ value from Cr in-diffusion profiles [81] were included in (4.40).

In the case of out-diffusion the Cr vapor pressure is so low that, similarly to the case of out-diffusion of Zn, a much lower diffusivity prevails. This slower out-diffusion turned out to be dominated either by the constant V-dominated diffusivity $D_s^{eff} = D_V C_V^{eq}/C_s^{eq}$ or the constant S_i dominated diffusivity $D_s^{eff} = D_i C_i^{eq}/C_s^{eq}$, whichever is larger for low outside chromium vapor pressure.

Sulfur

The group VI donor S occupies As sites. With lower surface concentrations, the S in-diffusion profiles [66,129,130] resemble the erfc-function, but a concave shape develops in the surface region for higher concentration cases. The latter cases are indicative of the operation of the KO mechanism for an i-s

impurity. The available S in-diffusion profiles have been quantitatively explained [66] using the KO mechanism assuming the involvement of the neutral As self-interstitials, I^0_{As}. The deduced $D^I_{As}(n_i, 1\,\text{atm})$ values were included in (4.50).

4.5.5 Diffusion in Other III-V Compounds

Gallium arsenide is certainly the one III-V compound in which self and impurity diffusion processes have been studied most extensively. The available results on self-diffusion in III-V compounds have been summarized by Willoughby [131]. The Group III and the Group V diffusivities appear to be so close in some compounds that a common defect mechanism involving multiple native point defects appears to be the case, although no definite conclusion has been reached. There are hardly any experimental results available which would allow one to draw conclusions on the type and charge states of the native point defects involved in self-diffusion processes. Zinc is an important p-type dopant also for other III-V compounds and its diffusion behavior appears to be governed by an i-s mechanism as well. No information is available on whether the FT mechanism or the KO mechanism is operating. It can be expected that dopant diffusion induced superlattice disordering may rapidly advance the understanding of diffusion mechanisms in other III-V compounds similarly as has been accomplished in GaAs.

4.6 Conclusion

Diffusion phenomena in semiconductors are now understood to a high degree of consistency, mainly due to progresses during the last 20 years or so. In semiconductors, the lattice vacancies and self-interstitials both contribute to the crystal host atom self-diffusion and to the diffusion of substitutional impurity atoms. Often the point defects are charged which leads the diffusivity of the diffusing species to be dependent upon the crystal Fermi-level. In compound semiconductors, the diffusivity of the diffusing species will further depend on the ambient pressure of an appropriate vapor phase. The i-s diffusion mechanism appears to govern the diffusion processes of many impurities.

Notation

A_i	interstitialy dissolved atom of species A
As_{Ga}	the antisite defect of an As atom occupying a Ga-sublattice site
A_s	substitutionally dissolved atom of species A
C	carbon

C	concentration
$C_{\mathrm{x}}^{\mathrm{eq}}$ or $c_{\mathrm{x}}^{\mathrm{eq}}$	actual or normalized thermal equilibrium concentration of species x
D or D_{y}	diffusivity (diffusion coefficient) or diffusivity of species y
D^{eff}	effective diffusivity
$D_{(j)}^{\mathrm{eff}}$	effective diffusivity of a species controlled diffusion of species j
D_{s}	diffusivity of species s
D_{SD}	self-diffusion coefficient
D_{SD}^{I} or D_{SD}^{V}	I or V contribution to the self-diffusion coefficient
D_{T}	tracer self-diffusion coefficient
D_0	pre-exponential factor of D_{T} or D_{SD}
$D_{\mathrm{s}}^{\mathrm{per}}$ or $\Delta_{\mathrm{s}}^{\mathrm{per}}$	actual or normalized s diffusivity perturbed by non-equilibrium point defect concentrations
e	the electrical carrier electrons
f_I or f_V	tracer diffusion correlation factors or interstitialcy or vacancy mechanism
$\mathrm{Ga}_{\mathrm{As}}$	the antisite defect of a Ga atom occupying an As-sublattice site
h	the electrical carrier holes
h_I^{f} or h_V^{f}	formation enthalpy of I or V
h_I^{m} or h_V^{m}	migration enthalpy of I or V
i	interstitialy dissolved impurity
i-s	interstitial-substitutional impurity
I	self-interstitials
I_{Ga} or I_{As}	Ga or As self-interstitials
I_{Ga}^{2+}	doubly-positively-charged Ga self-interstitials
I^0, I^+, I^-, etc.	neutral, singly-positively-charged, singly-negatively charged I, etc.
k_{B}	Boltzmann's constant
n	donor doped or electron concentration of a semiconductor
n_{i}	intrinsic carrier concentration
p	acceptor doped or hole concentration of a semiconductor
P	pressure
Q	activation enthalpy
s	substitutionally dissolved impurity
s_I or s_V	self-interstitial or vacancy supersaturation ratio
T	absolute temperature
V	vacancies
V_{Ga} or V_{As}	Ga- or As-sublattice vacancies
V_{Ga}^{3+}	triply-negatively-charged Ga-sublattice vacancies
V^0, V^+, V^-, etc.	neutral, singly-positively-charged, singly-negatively charged V, etc.
Φ_I	interstitialcy fraction of the Si self-diffusion coefficient

References

1. A. Seeger, C.P. Chik: Phys Stat. Sol. **29**, 455 (1968)
2. T.Y. Tan, U. Gösele: Appl. Phys. A **37**, 1 (1985)
3. T.Y. Tan, U. Gösele. In: *Handbook of Semiconductor Technology, vol 1: Electronic Structure and Properties of Semiconductors*, ed by K.A. Jackson, W. Schröter (Wiley-VCH, New York 2000) pp 231–290
4. W. Frank, U. Gösele, H. Mehrer, A. Seeger. In: *Diffusion in Crystalline Solids*, ed by G.E. Murch, A. Nowick (New York: Academic Press 1984) pp 31–142
5. U. Gösele, W. Frank, A. Seeger: Appl. Phys. **23**, 361 (1980)
6. F.C. Frank, D. Turnbull: Phys. Rev. **104**, 617 (1956)
7. N.A. Stolwijk, B. Schuster, J. Hölzl, H. Mehrer, W. Frank: Physica B+C **116**, 335 (1983)
8. S. Mantovani, F. Nava, C. Nobili, G. Ottaviani: Phys. Rev. B **33**, 5536 (1986)
9. N.A. Stolwijk, M. Perret, H. Mehrer: Defect and Diffusion Forum **59**, 79 (1988)
10. M. Perret, N.A. Stolwijk, L. Cohausz: J. Phys.: Condens. Mater. **1**, 6347 (1989)
11. F.A. Huntley, A.F.W. Willoughby: Phil. Mag. **28**, 1319 (1973)
12. C. Boit, F. Lay, R. Sittig: Appl. Phys. A **50**, 197 (1990)
13. T.Y. Tan, U. Gösele: Appl. Phys. Lett. **40**, 616 (1982)
14. G.K. Celler, L.E. Trimble: Appl. Phys. Lett. **53**, 2492 (1988)
15. R. Francis, P.S. Dobson: J. Appl. Phys. **50**, 280 (1979)
16. T.Y. Tan, B.J. Ginsberg: Appl. Phys. Lett. **42**, 448 (1983)
17. S.M. Hu: Appl. Phys. Lett. **51**, 308 (1987)
18. P. Fahey, P.B. Griffin, J.D. Plummer: Rev. Mod. Phys. **61**, 289 (1989)
19. H. Strunk, U. Gösele, B.O. Kolbesen: Appl. Phys. Lett. **34**, 530 (1979)
20. C.L. Claeys, G.J. DeClerck, P.J. van Overstraeten: Rév. Phys. Appliqueé **13**, 797 (1978)
21. F.F. Morehead, R.F. Lever: Appl. Phys. Lett. **48**, 151 (1986)
22. M. Yoshida, E. Arai, H. Nakamura, Y. Terunuma: J. Appl. Phys. **45**, 1498 (1974)
23. U. Gösele. In: *Microelectronic Materials and Processes*, ed by R.A. Levy (Kluwer Academic, Dordrecht 1989) pp 588–634
24. P. Fahey, S.S. Iyer, G.J. Scilla: Appl. Phys. Lett. **54**, 843 (1989)
25. B.P.R. Marioton, U. Gösele: Jpn. J. Appl. Phys. **28**, 1274 (1989)
26. G.C. Watkins, K.L. Brower: Phys. Rev. Lett. **36**, 1329 (1976)
27. L.A. Ladd, J.P. Kalejs. In: *Oxygen, Carbon, Hydrogen and Nitrogen in Crystalline Silicon*, ed by J.C. Mikkelsen Jr, S.J. Pearton, J.W. Corbett, S.J. Pennycook (Proc. 59, Mat. Res. Soc., Pittsburgh 1986) pp 445–450
28. U. Gösele, A. Plössl, T.Y. Tan. In: *Electrochem. Soc. Proc. 96–4*, (Electcochem. Soc., Pennington 1996) pp 309–323
29. R. Scholz, U. Gösele, J.-Y. Huh, T.Y. Tan: Appl. Phys. Lett. **72**, 200 (1998)
30. R. C. Newman, J. Wakefield: J. Phys. Chem. Solids **19**, 230 (1961)
31. F. Rollert, N.A. Stolwijk, H. Mehrer: Mater. Sci. Forum **38–41**, 753 (1989)
32. R.F. Scholz, P. Werner, U. Gösele, T.Y. Tan: Appl. Phys. Lett. **74**, 392 (1999)
33. H. Rücker, B. Heinemann, W. Röpke, D. Krüger, G. Lipert, H. J. Osten: Appl. Phys. Lett. **73**, 2682 (1998)
34. P. Werner, H-J. Gossmann, D.C. Jacobson, U. Gösele: Appl. Phys. Lett. **73**, 2465 (1998)

35. P.A. Stolk, H-J. Gossmann, D.J. Eaglesham, D.C. Jacobson, C.S. Raferty, G.H. Gilmer, M. Jaraiz, J.M. Poate: J. Appl. Phys. **81**, 6031 (1997)
36. M.R. Kump, R. Dutton: IEEE Trans. CAD **7**, 191 (1988)
37. S. Mizuo, H. Higuchi: J. Electrochem. Soc. **130**, 1942 (1983)
38. D.A. Antoniadis, I. Moskowitz: J. Appl. Phys. **53**, 6788 (1982)
39. W. Taylor, B.P.R. Marioton, T.Y. Tan, U. Gösele: Rad. Eff. and Defects in Solids **111 & 112**, 131 (1989)
40. T. Sinno, R.A. Brown, W. von Ammon, E. Dornberger: J. Electrochem. Soc. **145**, 302 (1998)
41. P.S. Plekhanov, U.M. Gösele, T.Y. Tan: J. Appl. Phys. **84**, 718 (1998)
42. L. Goodwin, A.J. Skinner, D.G. Pittfor: Europhys. Lett. **9**, 701 (1989)
43. C. Nichols, C.G. Van de Walle, S.T. Pantelides: Phys. Rev. Lett. **62**, 1049 (1989)
44. C.Z. Wang, C.T. Chan, K.M. Ho: Phys. Rev. Lett. **66**, 189 (1991)
45. J. Zhu, D. de la Rubia, L.H. Yang, C. Mailhiot, G.H. Gilmer: Phys. Rev. B **54**, 4741 (1996)
46. M. Tang, L. Colombo, J. Zhu, D. de la Rubia: Phys. Rev. B **55**, 14279 (1997)
47. G. Watkins. In: *Lattice Defects in Semiconductors 1974*, ed by I.A. Huntley (Inst. Phys. Conf. Ser. 23, London 1975) pp 1–22
48. T.Y. Tan, E.E. Gardner, W.K. Tice: Appl. Phys. Lett. **30**, 175 (1977)
49. W. Kaiser, H.L. Frisch, H. Reiss: Phys. Rev. **112**, 1546 (1958)
50. R.C. Newman: J. Phys. C **18**, L967 (1985)
51. U. Gösele, T.Y. Tan: Appl. Phys. A **28**, 79 (1982)
52. A. Van Wieringen, N. Warmoltz: Physica **22**, 849 (1956)
53. S.J. Pearton, J.W. Corbett, T.S. Shi: Appl. Phys. A **43**, 153 (1987)
54. N.M. Johnson, F.A. Ponce, R.A. Street, R.J. Nemanich: Phys. Rev. B **35**, 4166 (1987)
55. N.A. Stolwijk, W. Frank, J. Hölzl, S.J. Pearton, E.E. Haller: J. Appl. Phys. **57**, 5211 (1985)
56. D.G. Deppe, N. Holonyak Jr: J. Appl. Phys. **64**, R93 (1988)
57. T.Y. Tan, U. Gösele, S. Yu: Cri. Rev. Solids Mater. Sci. **17**, 47 (1991)
58. J. R. Arthur: J. Phys. Chem. Solids **28**, 2257 (1967)
59. T.Y. Tan: Mater. Sci. Eng. **B10**, 227 (1991)
60. B. Tuck: *Atomic Diffusion in III-V Semiconductors* (Adam Hilger, Bristol 1988)
61. W.D. Laidig, N. Holonyak Jr, M.D. Camras, K. Hess, J.J. Coleman, P.D. Dapkus, J. Bardeen: Appl. Phys. Lett. **38**, 776 (1981)
62. G. Bösker, N.A. Stolwijk, H. Mahrer, U. Södervall, J.V. Thordson, T.G. Anderson, A. Buchard. In: *Diffusion Mechanisms in Crystalline Materials*, ed by Y. Mishin, G. Vogl, N. Cowern, R. Catlow, D. Farkas (Materials Research Soc., Pittsburgh 1998) pp 347–356
63. U. Egger, M. Schultz, P. Werner, O. Breitenstein, T.Y. Tan, U. Gösele U, R. Franzheld, M. Uetmatsu, H. Ito: J. Appl. Phys. **81**, 6056 (1997)
64. R. Scholz, U. Gösele U, O. Breitenstein, U. Egger, T.Y. Tan: Diffusion and Defect Data B **63–64**, 183 (1998)
65. M. Schultz, U. Egger, R. Scholz, O. Breitenstein, U. Gösele, T.Y. Tan: J. Appl. Phys. **83**, 5295 (1998)
66. M. Uematsu, P. Werner, M. Schultz, T.Y. Tan, U. Gösele: Appl. Phys. Lett. **67**, 2863 (1995)

67. H. Palfrey, M. Brown, A. Willoughby: J. Electr. Mater. **12**, 863 (1983)
68. B. Goldstein: Phys. Rev. **121**, 1305 (1961)
69. H.D. Palfrey, M. Brown, A.F.W. Willoughby: J. Electrochem. Soc. **128**, 2224 (1981)
70. L.L. Chang, A. Koma: Appl. Phys. Lett. **29**, 138 (1976)
71. P.M. Petroff: J. Vac. Sci. Technol. **14**, 973 (1977)
72. R.M. Fleming, D.B. McWhan, A.C. Gossard, W. Weigmann, R.A. Logan: J. Appl. Phys. **51**, 357 (1980)
73. J. Cibert, P.M. Petroff, D.J. Werder, S.J. Pearton, A.C. Gossard, J.H. English: Appl. Phys. Lett. **49**, 223 (1986)
74. T.E. Schlesinger, T. Kuech: Appl. Phys. Lett. **49**, 519 (1986)
75. T.Y. Tan, U. Gösele: Appl. Phys. Lett. **52**, 1240 (1988)
76. T.Y. Tan, U. Gösele: Mat. Science and Eng. **B1**, 47 (1988)
77. A. Furuya, O. Wada, A. Takamori, H. Hashimoto: Jpn. J. Appl. Phys. **26**, L926 (1987)
78. L.J. Guido, N. Holonyak Jr, K.C. Hsieh, R.W. Kalisiki, W.E. Plano, P.D. Burtham, R.L. Thornton, J.E. Epler, T.L. Paoli: J. Appl. Phys. **61**, 1372 (1987)
79. K.Y. Hsieh, Y.C. Lo, J.H. Lee, R.M. Kolbas: Inst. Phys. Ser. **96**, 393 (1988)
80. S. Yu, T.Y. Tan, U. Gösele: J. Appl. Phys. **69**, 3547 (1991)
81. S. Yu, T.Y. Tan, U. Gösele: J. Appl. Phys. **70**, 4827 (1991)
82. T.Y. Tan, S. Yu, U. Gösele: J. Appl. Phys. **70**, 4823 (1991)
83. T.Y. Tan, H.M. You, S. Yu, U. Gösele, W. Jäger, D.W. Boeringer, F. Zypman, R. Tsu, S.-T. Lee: J. Appl. Phys. **72**, 5206 (1992)
84. J.-C. Lee, T.E. Schlesinger, T.F. Kuech: J. Vac. Sci. Technol. **B5**, 1187 (1987)
85. H. Bracht, E.E. Haller, K. Eberl, M. Cardona, R. Clark-Phelps. In: *Diffusion Mechanisms in Crystalline Materials*, ed by Y. Mishin, G. Vogl, N. Cowern, R. Catlow, D. Farkas (Materials Research Society, Pittsburgh 1998) pp 335–346
86. L. Wang, L. Hsu, E.E. Haller, J.W. Erickson, A. Fischer, K. Eberl, M. Cardona: Phys. Rev. Lett. **76**, 2342 (1996)
87. P. Mei, H.W. Yoon, T. Venkatesan, S.A. Schwarz, J.B. Harbison: Appl. Phys. Lett. **50**, 1823 (1987)
88. J.A. Van Vechten: J. Appl. Phys. **53**, 7082 (1982)
89. J.A. Van Vechten: J. Vac. Sci. Technol. **B2**, 569 (1984)
90. S.R. Tatti, S. Mitra, J.P. Stark: J. Appl. Phys. **65**, 2547 (1989)
91. M. Kawabe, N. Shimizu, F. Hasegawa, Y. Nannidi: Appl. Phys. Lett. **46**, 849 (1985)
92. J. Kobayashi, M. Nakajima, T. Fukunagon, T. Takamori, K. Shida, H. Nakashima, K. Ishida: Jpn. J. Appl. Phy. **25**, L 736 (1986)
93. W. Jäger, A. Rucki, K. Urban, H.-G. Hettwer, N.A. Stolwijk, H. Mehrer, T.Y. Tan: J. Appl. Phys. **74**, 4409 (1993)
94. T.Y. Tan, U. Gösele: Mater. Chem. Phys. **44**, 45 (1995)
95. G.A. Baraff, M. Schlüter: Phys. Rev. Lett. **55**, 1327 (1985)
96. W.M. Li, R.M. Cohen, D.S. Simons, P.H. Chi: Appl. Phys. Lett. **70**, 3392 (1997)
97. Z.H. Jafri, W.P. Gillin: J. Appl. Phys. **81**, 2179 (1997)
98. P. Mei, S.A. Schwartz, T. Venkatesan, C.L. Schwartz, E. Colas: J. Appl. Phys. **65**, 2165 (1989)

99. T.Y. Tan, U. Gösele. In: *Advances in Materials, Processing and Devices in III-V Compound Semiconductors*, ed by D.K. Sadana, L. Eastman, R. Dupuis, Proc. 144 (Materials Research Society, Pittsburgh 1989) pp 221–232
100. J.W. Lee, W.D. Laidig: J. Electron. Mater. **13**, 147 (1984)
101. Y. Hirayama, Y. Susuki, H. Okamoto: Jpn. J. Appl. Phys. **24**, 1498 (1985)
102. J. Ralston, G.W. Wicks, L.F. Eastman, B.C. Deooman, C.B. Carter: J. Appl. Phys. **59**, 120 (1986)
103. N. Kamata, K. Koboyashi, K. Endo, T. Sasudi, A. Misu: Jpn. J. Appl. Phys. **26**, 1092 (1987)
104. E.P. Zucker, A. Hasimoto, T. Fukunaga, N. Watanabe: Appl. Phys. Lett. **54**, 564 (1989)
105. R.L. Longini: Solid-State Electronics **5**, 127 (1962)
106. U. Gösele, F. Morehead: J. Appl. Phys. **54**, 4617 (1981)
107. H.R. Winteler: Helvetca Physica Acta **44**, 451 (1971)
108. K. Masu, M. Konagai, V. Takahoshi: Appl. Phys. Lett. **37**, 182 (1980)
109. B. Tuck, A.J.N. Houghton: J. Phys. **D14**, 2147 (1981)
110. P. Enquis, G.W. Wicks, L.F. Eastman, C. Hitzman: J. Appl. Phys. **58**, 4130 (1985)
111. P. Enquist, J.H. Hutchby, T.J. de Lyon: J. Appl. Phys. **63**, 4485 (1988)
112. H.M. You, T.Y. Tan, U. M. Gösele, S.-T. Lee, G.E. Höfler, K.C. Hsieh, N. Holonyak Jr, J. Appl. Phys. **74**, 2450 (1993)
113. K.L. Kavanagh, C.W. Magee, J. Sheets, J.W. Mayer: J. Appl. Phys. **64**, 1845 (1988)
114. M.E. Greiner, J.F. Gibbons: J. Appl. Phys. **57**, 5181 (1985)
115. S. Yu, U. Gösele, T.Y. Tan: J. Appl. Phys. **66**, 2952 (1989)
116. C.H. Chen, U.M. Gösele, T.Y. Tan: Appl. Phys. **A69**, 313 (1999)
117. H.-M. You, U.M. Gösele, T.Y. Tan: J. Appl. Phys. **73**, 7207 (1993)
118. M. Konagai, T. Yamada, T. Akatsuka, K. Saito, E. Tokumitsu: J. Cryst. Growth **98**, 167 (1989)
119. B.T. Cunningham, L.J. Guido, J.E. Baker, J.S. Major Jr, N. Holonyak Jr, G.E. Stillman: Appl. Phys. Lett. **55**, 687 (1989)
120. T.H. Chiu, J.E. Cunningham, J.A. Ditzenberger, W.Y. Jan, S.N.G. Chu: J. Crys. Growth **111**, 274 (1991)
121. G.E. Höfler, H.J. Höfler, N. Holonyak Jr, K.C. Hsieh: J. Appl. Phys. **72**, 5318 (1992)
122. Z. Jamal, P.J. Goodhew. In: *Chemical Perspectives of Microelectronic Materials III*, ed by C.R. Abernathy, C.W. Bates Jr, D.A. Bohling, W.S. Hobson (Proc. 282, Materials Research Society, Pittsburgh 1993) p 145
123. A.J. Moll, E.E. Haller, J.W. Ager III, W. Walukiewicz: Appl. Phys. Lett. **65**, 1145 (1994)
124. C.H. Ting, G.L. Pearson: J. Appl. Phys. **42**, 2247 (1971)
125. M.A.H. Kadhim, B. Tuck: J. Mater. Sci. **7**, 68 (1972)
126. D.L. Kendall. In: *Semiconductors and Semimetals*, vol 4, ed by R.K. Willardson, A.C. Beer (Academic Press, New York 1968) pp 163–259
127. M. Luysberg, W. Jäger, K. Urban, M. Schänzer, N. Stolwijk, H. Mehrer: Mat. Sci. Eng. **B13**, 137 (1992)
128. M.D. Deal, D.A. Stevenson: J. Appl. Phys. **59**, 2398 (1986)
129. A.B.Y. Young, G.L. Pearson: J. Phys. Chem. Solids **31**, 517 (1970)
130. B. Tuck, R.G. Powell: J. Phys. **D14**, 1317 (1981)
131. A.F.W. Willoughby. In: *Defects in Semiconductors II*, ed by S. Mahajan, J.W. Corbett (North-Holland, New York 1983) pp 237–252

5 Diffusion in Oxides

Manfred Martin

5.1 Introduction

Diffusion processes in crystalline oxides are governed by the same mechanisms as in crystalline metals, i.e. they proceed by means of point defects, and the two basic mechanisms are vacancy diffusion and interstitial diffusion. Both mechanisms have been described in detail in Chap. 1 of this book. There are, however, some important differences in the defect structures of oxides and metals, with severe implications for diffusion processes in oxides:

- Most oxides are ionic compounds, i.e. they consist of cations and anions with well defined, opposite charges.
- Crystalline oxides consist of at least two sublattices, a metal and an oxygen sublattice, or a cation and an anion sublattice. Due to the opposite charges of cations and anions diffusion proceeds always in the corresponding sublattice.
- The concentrations of point defects, vacancies as well as interstitials, which are necessary for diffusion depend not only on the intensive thermodynamic variables pressure, p, and temperature, T, but also on the chemical potential of the component oxygen, $\mu_{O_2} = \mu^0_{O_2} + RT \ln a_{O_2}$. The oxygen activity, $a_{O_2} = p_{O_2}/\mathrm{bar}$, can be established easily by means of gas mixtures with different oxygen partial pressures, p_{O_2}, and can be varied over many orders of magnitude.
- Oxides cover a wide range of materials, such as insulators, pure ionic conductors, semiconductors, mixed electronic and ionic conductors and also metallic oxides. The latter will not be considered in this chapter.
- The crystal structure of the oxide influences the defect structure. In structures with cubic close packing of the oxygen ions, such as the NaCl- or the spinel-structure, defects in the oxygen sublattice have much higher formation enthalpies and therefore much lower concentrations than defects in the cation sublattice(s). Consequently, oxygen diffusion is much slower than cation diffusion. In oxides with more open oxygen sublattices, such as the perovskite structure or the fluorite structure, oxygen defects are

formed more easily than cation defects. Therefore, these oxides show very often high oxygen diffusivities and are good oxygen ion conductors.

These introductory remarks show that diffusion in oxides depends largely on the defect structure of the oxide. The important dependence of the defect structure on the thermodynamic variables p, T and p_{O_2} (so-called defect chemistry) will be discussed in detail in Sect. 5.2, where at first transition metal oxides with dominating cation disorder and then doped perovskites and fluorites with dominating disorder in the oxygen sublattice will be treated. In the subsequent sections self- and impurity diffusion, chemical diffusion and diffusion in external forces will be considered.

For a comprehensive treatment of defect chemistry and diffusion processes in oxides the reader is referred to the books of Schmalzried [1,2], Philibert [3], Kofstad [4], Allnatt and Lidiard [5], and Laskar et al. [6].

5.2 Defect Chemistry of Oxides

In this section the dependence of the defect fractions on the thermodynamic variables, p, T and oxygen partial pressure, p_{O_2}, will be calculated for binary oxides. A binary oxide can be written as A_mO_n, where m and n are integers. To consider deviations from the ideal stoichiometry, the so-called non-stoichiometry, δ, is introduced. Then the correct formula for the non-stoichiometric oxide is $A_{n-\delta}O_m$ (or $A_mO_{n+\delta}$). For the sake of simplicity, in the subsequent discussion only monoxides with $m = n = 1$ will be considered. The generalization of the results obtained for $A_{1-\delta}O$ to $A_{m-\delta}O_n$ is straightforward and results will be given if necessary.

In the exactly stoichiometric oxide AO, i.e. $\delta = 0$, we have only thermal disorder, and the concentrations of point defects are determined by intrinsic defect equilibria such as the Schottky equilibrium, the Frenkel equilibrium and the anti-Frenkel equilibrium [7,8]. The corresponding defect formation processes are depicted in Fig. 5.1. For a quantitative description we use quasi-chemical reactions and the corresponding chemical equilibria:

$$\text{Schottky equilibrium:} \quad \text{nil} \rightleftharpoons V''_A + V^{\bullet\bullet}_O \qquad K_S = [V''_A] \cdot [V^{\bullet\bullet}_O] \tag{5.1}$$

$$\text{Frenkel equilibrium:} \quad A^x_A + V^x_i \rightleftharpoons V''_A + A^{\bullet\bullet}_i \qquad K_{F_A} = [V''_A] \cdot [A^{\bullet\bullet}_i] \tag{5.2}$$

$$\text{anti-Frenkel equilibrium:} \quad O^x_O + V^x_i \rightleftharpoons V^{\bullet\bullet}_O + O''_i \qquad K_{F_O} = [V^{\bullet\bullet}_O] \cdot [O''_i] \tag{5.3}$$

Here we have used the so-called Kröger-Vink notation [9] for the structure element S^q_p. S stands for an ion (cation A or anion O) or a vacancy (V) and p for the sublattice (A, O or interstitial). An excess charge, q, of -1, 0 or $+1$ of the structure element relative to the ideal crystal is denoted by the symbols $'$, x or $^\bullet$. These quasi-chemical reactions describe the defect formation processes shown in Fig. 5.1. K_S, K_{F_A} and K_{F_O} are the chemical equilibrium

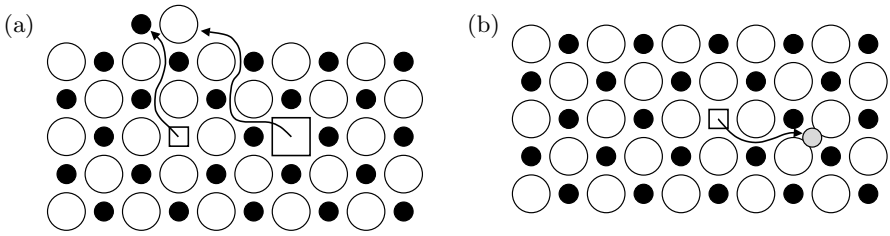

Fig. 5.1. Formation of Schottky defects (a) and Frenkel defects (b) in an oxide AO (• = cation, ◯ = anion).

constants for the three equilibria, depending on temperature[1]. In the mass action laws in (5.1)–(5.3) we have assumed that the site fractions of vacancies and interstitials (defects), denoted by brackets, are small compared to the site fractions of regular cations and anions, and that the structure elements in each sublattice form an ideal mixture.

Incorporation of oxygen from the surrounding atmosphere into the crystal or removal of oxygen from the crystal results in the formation of a non-stoichiometric oxide with oxygen excess or oxygen deficit. It can also be described by a quasi-chemical reaction:

$$\tfrac{1}{2}\mathrm{O_2(g)} + \mathrm{V_O^{\bullet\bullet}} \rightleftharpoons \mathrm{O_O^x} + 2\mathrm{h^\bullet} \qquad K_\mathrm{O} = \frac{[\mathrm{h^\bullet}]^2}{(p_{\mathrm{O_2}})^{1/2} \cdot [\mathrm{V_O^{\bullet\bullet}}]}\,. \tag{5.4}$$

Oxygen from the gas phase, $\frac{1}{2}\mathrm{O_2(g)}$, occupies an oxygen vacancy, $\mathrm{V_O^{\bullet\bullet}}$, and for charge compensation electron holes, $\mathrm{h^\bullet}$, are produced (see also Fig. 5.2). Finally, the electronic equilibrium, resulting in the formation of electrons, $\mathrm{e'}$, and electron holes, $\mathrm{h^\bullet}$, has to be considered:

$$\mathrm{nil} \rightleftharpoons \mathrm{e'} + \mathrm{h^\bullet} \qquad K_\mathrm{e} = [\mathrm{e'}] \cdot [\mathrm{h^\bullet}]\,. \tag{5.5}$$

The fractions of all charged structure elements are coupled by the condition of local electrical neutrality:

$$2[\mathrm{V_A''}] + 2[\mathrm{O_i''}] + [\mathrm{e'}] = 2[\mathrm{V_O^{\bullet\bullet}}] + 2[\mathrm{A_i^{\bullet\bullet}}] + [\mathrm{h^\bullet}]\,. \tag{5.6}$$

The set of equations is completed by the site balances for each sublattice, e.g. $[\mathrm{A_A^x}] + [\mathrm{V_A''}] = 1$. Provided the equilibrium constants are known, all defect fractions and the non-stoichiometry

$$\delta = [\mathrm{V_A''}] + [\mathrm{O_i''}] - [\mathrm{V_O^{\bullet\bullet}}] - [\mathrm{A_i^{\bullet\bullet}}] \tag{5.7}$$

can be calculated as a function of the thermodynamic variables, p, T and $p_{\mathrm{O_2}}$.

[1] The temperature dependence of the equilibrium constants is given by $K = \exp(-\Delta G^0/RT) = \exp(\Delta S^0/R) \cdot \exp(-\Delta H^0/RT)$, where ΔG^0, ΔS^0 and ΔH^0 are the standard Gibbs energy, entropy and enthalpy of the corresponding quasi-chemical reaction.

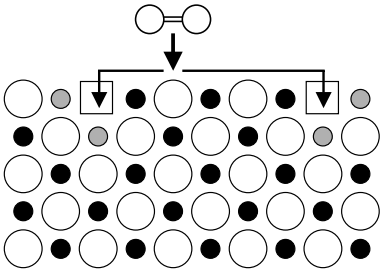

Fig. 5.2. Incorporation of an oxygen molecule (◯=◯) from the gas phase into an oxide AO with dominating oxygen vacancies (see (5.4)). For each oxygen atom two electron holes are produced. For the sake of simplicity they are localized on cations (●).

5.2.1 Dominating Cation Disorder

Oxygen Activity Dependent Disorder

In oxides with a fcc oxygen sublattice, i.e. cubic close packing of the oxygen ions, as in most transition metal oxides, the formation of oxygen vacancies and oxygen interstitials is energetically unfavourable in comparison with the formation of cation defects. Thus, we may regard the oxygen sublattice as perfect compared to the cation sublattice. This means that in the exactly stoichiometric oxide with $\delta = 0$ the Frenkel equilibrium dominates[2] and (5.2) and (5.6) simplify to $[\mathrm{V}''_\mathrm{A}] = [\mathrm{A}_\mathrm{i}^{\bullet\bullet}] = (K_\mathrm{F})^{1/2}$. At fixed temperature, T, and pressure, p, the so-called stoichiometric point, $\delta = 0$, corresponds to a well defined oxygen partial pressure, $p^*_{\mathrm{O}_2}$. If we increase the oxygen partial pressure relative to $p^*_{\mathrm{O}_2}$, oxygen is incorporated into the crystal. Since oxygen defects are only minority defects it is more convenient to formulate the incorporation of oxygen from the ambient atmosphere in terms of cation defects which is possible by 'adding' (5.4) and (5.1):

$$\tfrac{1}{2}\mathrm{O}_2(\mathrm{g}) \rightleftharpoons \mathrm{O}^\mathrm{x}_\mathrm{O} + \mathrm{V}''_\mathrm{A} + 2\mathrm{h}^\bullet \quad , \qquad K_\mathrm{A} = \frac{[\mathrm{V}''_\mathrm{A}] \cdot [\mathrm{h}^\bullet]^2}{(p_{\mathrm{O}_2})^{1/2}} \quad . \tag{5.8}$$

Oxidation of the oxide results in the formation of new lattice sites in both the oxygen and the cation sublattices, i.e. now the crystal grows, in contrast to the incorporation of oxygen described in (5.4). While the new oxygen sublattice sites are occupied by oxygen ions the new cation lattice sites are empty, i.e. cation vacancies are formed (see Fig. 5.3). They are electrically compensated by the formation of electron holes.

Thus, for oxygen partial pressures that are sufficiently large compared to $p^*_{\mathrm{O}_2}$ cation vacancies and electron holes will be the majority defects, which results in a simplified condition of electrical neutrality, $2[\mathrm{V}''_\mathrm{A}] = [\mathrm{h}^\bullet]$. Using this relation, the p_{O_2}-dependence of the majority type of defects can be calculated from (5.8):

[2] Here we have assumed that the fractions of the electronic defects are small compared to the fractions of the Frenkel defects. The opposite case, dominating electronic disorder, will not be considered.

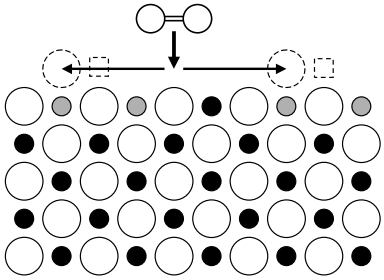

Fig. 5.3. Incorporation of an oxygen molecule (◯=◯) from the gas phase into an oxide AO with dominating cation vacancies. For each oxygen atom a new occupied anion lattice site (◯), a new unoccupied cation lattice site (□) and two electron holes (•) are produced. For the sake of simplicity the electron holes are localized on cations.

$$[\mathrm{V}_\mathrm{A}''] = \tfrac{1}{2}[\mathrm{h}^\bullet] = \left(\frac{K_\mathrm{A}}{4}\right)^{1/3} \cdot (p_{\mathrm{O}_2})^{1/6} \quad . \tag{5.9}$$

On the other hand, cation interstitials, $\mathrm{A}_\mathrm{i}^{\bullet\bullet}$, and electrons, e', are only minority defects, and their fractions decrease with increasing p_{O_2} (see (5.2) and (5.5)) according to

$$\begin{aligned} [\mathrm{A}_\mathrm{i}^{\bullet\bullet}] &= K_{\mathrm{F_A}} \cdot \left(\frac{K_\mathrm{A}}{4}\right)^{-1/3} \cdot (p_{\mathrm{O}_2})^{-1/6} \quad , \\ [\mathrm{e}'] &= K_\mathrm{e} \cdot (2K_\mathrm{A})^{-1/3} \cdot (p_{\mathrm{O}_2})^{-1/6} \quad . \end{aligned} \tag{5.10}$$

For oxygen partial pressures that are sufficiently small compared to $p^*_{\mathrm{O}_2}$, cation interstitials and electrons will be the majority defects, which results in a simplified condition of electrical neutrality $[\mathrm{e}'] = 2[\mathrm{A}_\mathrm{i}^{\bullet\bullet}]$. With this relation, the p_{O_2}-dependence of the majority type of defects can be calculated from (5.8) and (5.2) by

$$[\mathrm{A}_\mathrm{i}^{\bullet\bullet}] = \tfrac{1}{2}[\mathrm{e}'] = \left(\frac{K_{\mathrm{F_A}} \cdot K_\mathrm{e}}{4K_\mathrm{A}}\right)^{1/3} \cdot (p_{\mathrm{O}_2})^{-1/6} \quad . \tag{5.11}$$

In this regime, cation vacancies, V_A'', and electron holes, $\mathrm{h}^\bullet$, are the minority defects and their fractions decrease with decreasing p_{O_2}:

$$\begin{aligned} [\mathrm{V}_\mathrm{A}''] &= \left(\frac{4K_\mathrm{A} \cdot K_{\mathrm{F_A}}^2}{K_\mathrm{e}^2}\right)^{1/3} \cdot (p_{\mathrm{O}_2})^{+1/6} \quad , \\ [\mathrm{h}^\bullet] &= \left(\frac{K_\mathrm{A} \cdot K_\mathrm{e}}{2K_{\mathrm{F_A}}}\right)^{1/3} \cdot (p_{\mathrm{O}_2})^{+1/6} \quad . \end{aligned} \tag{5.12}$$

Equations (5.9) to (5.12) show that all defect fractions follow a power law dependence on p_{O_2} with typical exponents $1/6$ and $-1/6$ for oxygen partial pressures which are sufficiently larger or smaller than $p^*_{\mathrm{O}_2}$. In the close vicinity of $p^*_{\mathrm{O}_2}$ the fractions of the Frenkel defects do not depend on p_{O_2}, $[\mathrm{V}_\mathrm{A}''] = [\mathrm{A}_\mathrm{i}^{\bullet\bullet}] = (K_\mathrm{F})^{1/2}$. In contrast, the fractions of the minority defects, e' and $\mathrm{h}^\bullet$, exhibit p_{O_2}-dependencies with exponents $-1/4$ and $1/4$, respectively

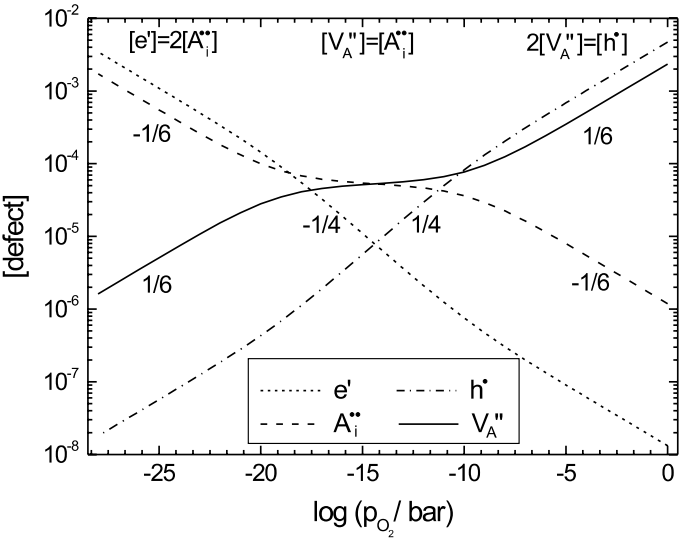

Fig. 5.4. Dependence of the defect fractions on the oxygen partial pressure p_{O_2} (Kröger-Vink-diagram) in an oxide AO with dominating Frenkel disorder at the stoichiometric point (see (5.9)–(5.12)).

(see (5.5) and (5.8)). In a double-logarithmic plot (Kröger-Vink diagram) we therefore obtain straight lines (see Fig. 5.4) and three typical regions corresponding to $\delta < 0$, $\delta \approx 0$ and $\delta > 0$.

Without going into further details we note that other exponents are also possible, mainly for two reasons:

i) Defects might form associates, e.g. a vacancy might trap an electron hole resulting in a singly ionised vacancy:

$$\mathrm{V}''_\mathrm{A} + \mathrm{h}^\bullet \rightleftharpoons \mathrm{V}'_\mathrm{A} \quad . \tag{5.13}$$

If these vacancies become the majority defects they show a dependence $[\mathrm{V}'_\mathrm{A}] \propto (p_{O_2})^{1/4}$. Similarly, cation interstitials might trap an electron, $\mathrm{A}_\mathrm{i}^{\bullet\bullet} + \mathrm{e}' \rightleftharpoons \mathrm{A}_\mathrm{i}^{\bullet}$, resulting in a dependence $[\mathrm{A}_\mathrm{i}^{\bullet}] \propto (p_{O_2})^{-1/4}$.

ii) Often, there are also oxides of different stoichiometry, i.e. A_3O_4, A_2O_3 or A_2O. For the oxide of a monovalent metal, e. g. Cu_2O, we obtain typical exponents $1/4$ and $-1/4$, and in the mixed-valent oxide Fe_3O_4 the exponents are $2/3$ and $-2/3$.

Doping

Doping an oxide $A_{1-\delta}O$ with dominant cation disorder with an oxide of a higher valent metal B, e.g. B_2O_3 can be described by

$$B_2O_3 \rightarrow 2B_A^{\bullet} + V_A'' + 3O_O^{x} \tag{5.14}$$

where we have assumed that the dopant B occupies regular cation lattice sites. To conserve the lattice structure of the host oxide AO the incorporation of two dopant cations, $B_A^{\bullet}$, and three oxygen ions, O_O^{x}, demands the formation of one cation vacancy, V_A''. Since the dopant is charged it must be considered in the condition of electrical neutrality in (5.6), and the defect structure of the doped oxide will be changed:

$$2[V_A''] + [e'] = 2[A_i^{\bullet\bullet}] + [h^{\bullet}] + [B_A^{\bullet}] \quad . \tag{5.15}$$

i) For strong doping, the fraction of cation vacancies is directly given by the dopant fraction, (see (5.14)), and is independent of the thermodynamic variables p, T and p_{O_2}, i.e. the exponent of the p_{O_2}-dependence is zero.

ii) For small dopant fractions, however, the disorder of the host oxide cannot be neglected, and the defect structure depends on the thermodynamic variables p, T, p_{O_2} and the dopant fraction as well.

iii) Coulombic interaction between the dopant ions, $B_A^{\bullet}$, and differently charged cation vacancies, V_A'' and V_A', may lead to the formation of solute-vacancy pairs:

$$B_A^{\bullet} + V_A' \rightleftharpoons \left\{B_A^{\bullet}, V_A'\right\}^{x} \quad , \qquad K_{P_1} = \frac{[P_1]}{[B_A^{\bullet}] \cdot [V_A']} \quad , \tag{5.16}$$

$$B_A^{\bullet} + V_A'' \rightleftharpoons \left\{B_A^{\bullet}, V_A''\right\}' \quad , \qquad K_{P_2} = \frac{[P_2]}{[B_A^{\bullet}] \cdot [V_A'']} \quad . \tag{5.17}$$

Here we have denoted the solute-vacancy pairs containing singly and doubly ionised vacancies by P_1 and P_2.

5.2.2 Dominating Oxygen Disorder

In oxides where the oxygen ions do not form a cubic close packing but a more open substructure, for example, in the perovskites or fluorites, oxygen defects may be the dominating defects while cation defects are only minority defects. As before, the defect fractions are determined by (5.1)–(5.7), and typical exponents are obtained for the different disorder types. To increase the fraction of oxygen vacancies, these oxides are often doped with oxides of lower valent metals. Then, the condition of electrical neutrality in (5.6) simplifies to

$$[B_A'] = 2[V_O^{\bullet\bullet}] \quad . \tag{5.18}$$

Thus, the negative excess charge of the dopant cation, B_A', is compensated by oxygen vacancies, and these oxides are good oxygen ion conductors. Some well know examples are

- yttria-stabilized zirconia, $(Zr_{1-x}Y_x)O_{2-x/2}$ (YSZ). Here, doping with Y_2O_3 increases the fraction of oxygen vacancies, $[Y'_{Zr}] = 2[V_O^{\bullet\bullet}]$, and stabilizes the cubic fluorite structure. YSZ is a pure oxygen ion conductor over many orders of magnitude in p_{O_2} and is used as such in oxygen sensors and solid oxygen fuel cells (SOFC).
- Sr- and Mg-doped lanthanum gallate, $(La_{1-x}Sr_x)(Ga_{1-y}Mg_y)O_{3-(x+y)/2}$ (LSGM), which belongs to the class of perovskites ABO_3. In LSGM oxygen vacancies are produced by co-doping in both cation sublattices, $[Sr'_{La}] + [Mg'_{Ga}] = 2[V_O^{\bullet\bullet}]$, resulting also in a good oxygen ion conductor.

However, at very low or very high oxygen partial pressures the electronic disorder can no longer be neglected and the oxide becomes a mixed ionic and electronic conductor. Examples are

- YSZ and LSGM, both of which become mixed conductors ($V_O^{\bullet\bullet}$ and e') at low oxygen partial pressures.
- strontium-doped lanthanum-chromate, $(La_{1-x}Sr_x)CrO_{3-\delta}$, which is a good semiconductor at high oxygen partial pressures and becomes a mixed conductor at low oxygen partial pressures.

5.3 Self- and Impurity Diffusion in Oxides

For the definition of diffusion coefficients and flux equations the reader is referred to Sects. 1.1 to 1.3 of Chap. 1.

5.3.1 Diffusion in Oxides with Dominating Cation Disorder

Since cations are mobile in the cation sublattice by means of cation vacancies and in the interstitial sublattice as cation interstitials, the cation self-diffusion coefficient, D_A, can be written as

$$D_A = D_{V_A} \cdot [V_A] + D_{A_i} \cdot [A_i] \quad . \tag{5.19}$$

Here D_{V_A} and D_{A_i} are the self-diffusion coefficients of cation vacancies and cation interstitials, and $[V_A]$ and $[A_i]$ are the corresponding site fractions. If the self-diffusion coefficients of vacancies and interstitials do not depend on the oxygen partial pressure, the p_{O_2}-dependence of the cation diffusion coefficient is solely determined by the p_{O_2}-dependence of the defect fractions which has been calculated in the previous section. Then, the p_{O_2}-dependence of the diffusion coefficient can be used to identify the disorder type of the oxide under investigation. At high p_{O_2} cation vacancies dominate while at low p_{O_2} cation interstitials are the dominating defects (see Fig. 5.4). We therefore obtain a minimum of the cation self-diffusion coefficient as a function of p_{O_2} and typical exponents in the p_{O_2}-dependence left and right of the minimum. Since D_{V_A} and D_{A_i} are usually different from each other, the minimum in the diffusion coefficient is shifted relative to the stoichiometric point ($\delta = 0$).

Cation Self- and Impurity Diffusion in Spinels $A_{3-\delta}O_4$

The best-known oxide where the transition from a vacancy to an interstitial regime was found experimentally is magnetite, $Fe_{3-\delta}O_4$ [10]. It crystallizes in the spinel structure where the oxygen ions form a cubic close packing while the cations occupy well defined octahedral and tetrahedral sites. The observed exponents of the iron diffusion coefficients are 2/3 at high p_{O_2} and $-2/3$ at low p_{O_2}, as expected for dominating cation vacancies and cation interstitials, respectively (see Sect. 5.2.1). This typical behaviour of the cation diffusion coefficients remains the same if the spinel consists of several cations, e.g. $(Co,Fe,Mn)_3O_4$ [11, 12]. Another example is manganese-zinc-ferrite, $Mn_{1-x}Zn_xFe_2O_4$, where part of the Fe-ions in magnetite has been replaced by Mn- and Zn-ions. Cation tracer diffusion coefficients have been measured with radioactive isotopes in the thin-film geometry, using both the sectioning method (described already in Sect. 1.4.1 in Chap. 1) and the residual activity method [13]. In the sectioning method a thin layer of the sample is ground off and its activity, A_{sect}, is counted, while in the residual activity method the residual activity, A_{res}, of the sample after grinding off a thin layer is counted. In the first case the activity profile is a Gaussian curve, $A_{\text{sect}} \propto \exp(-x^2/4D^*t)$, while in the second case an error function is obtained, $A_{\text{res}} \propto (1-\text{erf}(x/\sqrt{4D^*t}))$. Typical profiles from both methods are shown in Fig. 5.5 for diffusion of the radioisotope ^{54}Mn in manganese-ferrite. The diffusion coefficients obtained from both methods agree well. Figure 5.6 shows in a double-logarithmic plot results for the tracer diffusion coefficients of Mn, Fe and Zn and the impurity diffusion coefficient of Co as a function of the oxygen partial pressure [13]. All diffusion coefficients show a minimum as a function of p_{O_2}. The slopes $+2/3$ and $-2/3$ at high and low p_{O_2} indicate that diffusion proceeds via cation vacancies and cation interstitials, respectively. While all diffusion coefficients are nearly the same in the vacancy regime, the diffusion coefficient of zinc is higher in the interstitial regime, resulting in a minimum of the Zn-diffusion coefficient which is shifted to higher oxygen partial pressures compared to the other cations. A more detailed analysis, considering that the cation sublattice in the spinel structure consists of two sublattices with octahedral and tetrahedral sites and that iron, manganese and cobalt cations exist in two charge states, +2 and +3, can be found in [13].

Cation Self- and Impurity Diffusion in Monoxides $A_{1-\delta}O$

In most transition metal monoxides, such as $Co_{1-\delta}O$, $Ni_{1-\delta}O$ or $Mn_{1-\delta}O$, the oxide is reduced to the metal before the stoichiometric point, $\delta = 0$, is reached. Thus, only a vacancy regime for cation diffusion is observed [14–16]. However, as mentioned before, the typical exponent in the p_{O_2}-dependence of the cation diffusion coefficient quite often differs from the value 1/6 that is expected if cation vacancies V''_A would dominate. Subsequently, two examples will be discussed, pure cobalt oxide and gallium-doped cobalt oxide.

(a)

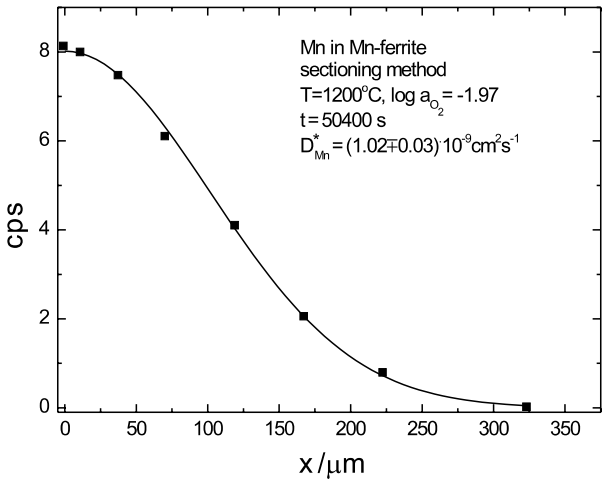

(b)

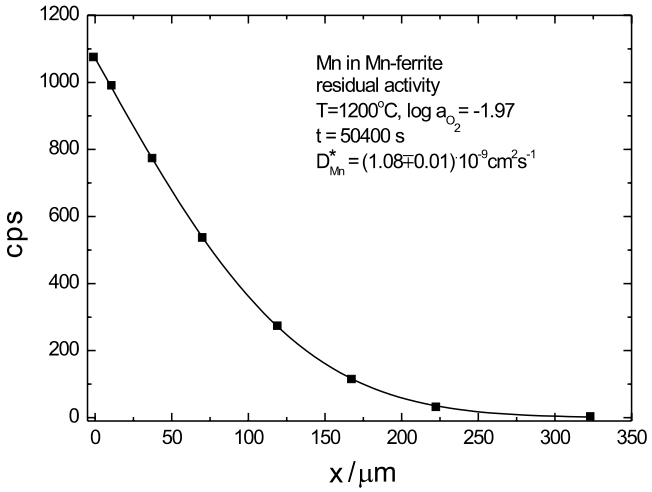

Fig. 5.5. Tracer sectioning profile (a) and residual activity profile (b) of ^{54}Mn in manganese ferrite [13] and corresponding fits with a Gaussian (a) and an error-function (b).

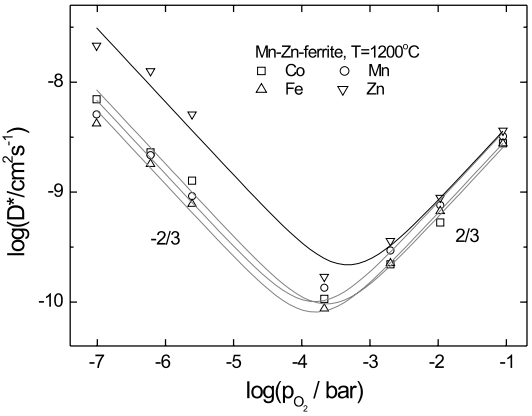

Fig. 5.6. Tracer diffusion coefficients of ^{54}Mn, ^{59}Fe, ^{65}Zn, and ^{57}Co in $Mn_{0.54}Zn_{0.35}Fe_{2.11}O_4$ as a function of the oxygen activity at $T = 1200°C$ (symbols) and fits (solid lines) [13].

Cobalt Monoxide, $Co_{1-\delta}O$

Cobalt monoxide, $Co_{1-\delta}O$, exists only with a cation deficit and is a p-type semiconductor. As shown by Dieckmann [17], the p_{O_2}-dependence of three defect-dependent quantities, the non-stoichiometry, δ, the cation tracer diffusion coefficient, D^*_{Co}, and the electrical conductivity, σ, can be explained by a defect structure, where differently charged cation vacancies, V''_{Co} and V'_{Co}, and electron holes, $h^\bullet$, are the dominating defects (see (5.13)). At intermediate oxygen partial pressures singly ionised cation vacancies V'_{Co} dominate, and all three quantities, $\delta = [V'_{Co}]$ (see (5.7)), σ, which is proportional to $[h^\bullet]$, as well as the cation tracer diffusion coefficient[3], $D^*_{Co} = f_0 \cdot D_V \cdot [V'_A]$, show the same dependence on p_{O_2} with a typical exponent 1/4. Results for the tracer diffusion coefficient of cobalt, D^*_{Co}, measured with the radiotracer method [18] and demonstrating this p_{O_2}-dependence are shown in Fig. 5.7 together with results for impurity diffusion of Fe in CoO. The smaller slope can be explained by impurity-vacancy binding between iron ions and cation vacancies (see (5.16) and (5.17)). In the exact analysis one must consider that the charge states of both the iron ions and the cation vacancies change with decreasing p_{O_2} [19, 20].

Ga-Doped Cobalt Monoxide, $(Co_{1-x}Ga_x)_{1-\delta}O$

In $Co_{1-\delta}O$ doped with Ga_2O_3, resulting in $(Co_{1-x}Ga_x)_{1-\delta}O$, both cation tracer diffusion coefficients, D^*_{Co} and D^*_{Ga}, have been measured as a function

[3] f_0 is the geometrical correlation factor appearing in tracer diffusion (see Sect. 1.3.1 in Chap. 1).

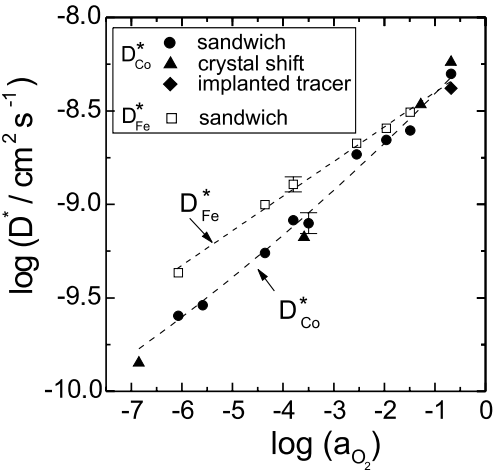

Fig. 5.7. Tracer diffusion coefficients of ^{57}Co and ^{59}Fe in $Co_{1-\delta}O$ as function of the oxygen activity at 1100°C. Dashed lines are guides to the eyes. For the different experimental techniques see [18].

of the oxygen partial pressure, p_{O_2}, and the dopant fraction, x, using radioisotopes [21]. The results depicted in Fig. 5.8 for a temperature of 1350°C show two typical features: (i) The dependence of both diffusion coefficients on the dopant fraction, x, is non-linear. (ii) At high oxygen partial pressures Co is the faster moving species while at low oxygen partial pressures Ga is faster than Co. To explain this behaviour we have to consider that the solute, Ga, and the solvent, Co, move by means of different diffusion mechanisms.

– In the dilute system, $x \ll 1$, the Ga ions are distinguishable, as tracer ions in tracer self-diffusion. Therefore, Ga is only mobile via solute-vacancy pairs, P_1 and P_2 (see (5.16) and (5.17)), and the solute diffusion coefficient, D^*_{Ga}, is proportional to the association degrees $p_1 = [P_1]/[Ga]$ and $p_2 = [P_2]/[Ga]$ of solute ions bound in these pairs [22].

$$D^*_{Ga} = D_{Ga,1} \cdot p_1 + D_{Ga,2} \cdot p_2 \tag{5.20}$$

The diffusion coefficients per defect, $D_{Ga,1}$ and $D_{Ga,2}$, depend only on temperature and include the mobilities of the defects and all physical correlation effects arising in solute tracer diffusion [22] (see also Sect. 1.9.1 in Chap. 1). The dependence of D^*_{Ga} on the defect concentrations, and hence on x, T and p_{O_2} is given by the association degrees p_1 and p_2.

– In contrast, the solvent ion Co is mobile by means of free, i.e. unbound vacancies, V''_A and V'_A, and conceivably by vacancies bound in pairs. Since Co is the majority component, its tracer diffusion coefficient is proportional to the appropriate defect fractions (and not to the association degrees, as for the solute):

$$D^*_{Co} = D_{Co,1} \cdot [V'_{Co}] + D_{Co,2} \cdot [V''_O] + D_{Co,P_1} \cdot [P_1] + D_{Co,P_2} \cdot [P_2] \quad . \tag{5.21}$$

Here we have permitted different mobilities for the vacancies V''_A and V'_A.

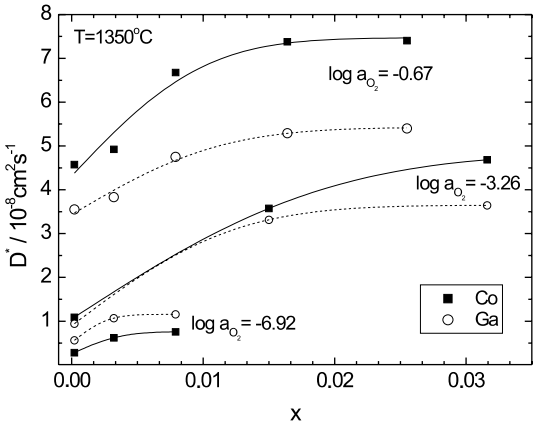

Fig. 5.8. Tracer diffusion coefficients of ^{58}Co and ^{67}Ga in $(Co_{1-x}Ga_x)_{1-\delta}O$ as a function of the dopant fraction, x, at $T = 1350°C$ and different oxygen activities [21].

The modelling of both measured diffusion coefficients, D^*_{Co} and D^*_{Ga}, as a function of the oxygen partial pressure, p_{O_2}, and the dopant fraction, x, yields the equilibrium constants K_{P_1} and K_{P_2} (see (5.16) and (5.17)) and the diffusion coefficients $D_{Co,i}$ and $D_{Ga,i}$ $(i = 1, 2)$ [21]. The results show that there is essentially no binding between the dopant, $Ga^{\bullet}_{Co}$, and singly ionised vacancies, V'_{Co}, while there is strong binding between $Ga^{\bullet}_{Co}$ and V''_{Co}. As a consequence, $D_{Co,1}$ and D_{Co,P_1} are identical. D_{Co,P_2} is two orders of magnitude smaller than $D_{Co,1}$ and $D_{Co,2}$ and can therefore be neglected. In summary, Ga is mobile by means of strongly bound pairs, $\{Ga^{\bullet}_{Co}, V''_{Co}\}'$, and weakly bound pairs, $\{Ga^{\bullet}_{Co}, V'_{Co}\}$. Co is mobile by means of free vacancies, V''_{Co} and V'_{Co}, and also by exchange with vacancies which are strongly bound in pairs $\{Ga^{\bullet}_{Co}, V''_{Co}\}$. In the latter mechanism the vacancy performs jumps around the Ga ion, thereby moving the Co ion but without dissociating the pair.

The binding energy E_{P_2} determined from the equilibrium constant $K_{P_2} = z \cdot \exp(E_{P_2}/RT)$ turns out to depend slightly on temperature. Assuming nearest-neighbour pairs ($z = 12$) we obtain a binding energy of about 40 kJ/mol, while we obtain values of about 50 kJ/mol if we assume next-nearest neighbour pairs ($z = 6$). The corresponding Coulomb energies (assuming point charges) are 72 kJ/mol ($z = 12$) and 50 kJ/mol ($z = 6$) which might be an indication for the next-nearest neighbour pairs, as proposed by theoretical calculations [23].

A detailed analysis of the diffusion coefficients, $D_{Ga,i}$ and $D_{Co,i}$, obtained from the fitting in terms of defect mobilities and correlation factors is impossible because the (physical) correlation factors are not known. However, we can draw some general conclusions.

– The diffusion coefficients $D_{Co,1}$ and $D_{Co,2}$ describe the motion of the solvent Co via free vacancies V'_{Co} and V''_{Co}, and can both be written

as a product of a vacancy diffusion coefficient and a correlation factor. If we assume that these correlation factors are identical to the geometric correlation factor in an fcc lattice, $f_0 = 0.781$, we obtain different vacancy diffusion coefficients, $D_{V'}$ and $D_{V''}$ in Ga-doped CoO. This result is in agreement with measurements of the charge of transport[4] in pure CoO [24], and the modelling of these data in terms of the Onsager-Fuoss-theory of liquid electrolytes shows also that the average mobility of the vacancies changes with the oxygen activity.

– The diffusion coefficients $D_{Ga,1}$ and $D_{Ga,2}$ describe the motion of the solute Ga by means of pairs P_1 and P_2, and both can be written in the form $D_{Ga,i} = (1/6) \cdot s^2 \cdot f_{B,i} \cdot \omega_{B,i}$ $(i = 1, 2)$, where s is the jump distance, $f_{B,i}$ the correlation factor and $\omega_{B,i}$ the impurity-vacancy exchange rate. The experimentally obtained ratio $D_{Ga,1}/D_{Ga,2}$ is about ten. If we assume that the exchange rates $\omega_{Ga,1}$ and $\omega_{Ga,2}$ are about the same for both mechanisms we can conclude that the correlation factor $f_{Ga,2}$ must be much smaller than $f_{Ga,1}$. This is in qualitative agreement with strong binding between $Ga^{\bullet}_{Co}$ and V''_{Co}, compared to weak binding between $Ga^{\bullet}_{Co}$ and V'_{Co}.

5.3.2 Diffusion in Oxides with Dominating Oxygen Disorder

Oxygen defects are now the majority defects, while cation defects are only minority defects. Thus, oxygen diffusion will be much faster than cation diffusion.

Oxygen Self-Diffusion

The determination of the self-diffusion coefficient of oxygen is accomplished by using one of the two stable oxygen isotopes, ^{17}O or ^{18}O. The sample is annealed in an isotope-enriched atmosphere and the diffusion profile is generally determined by secondary ion mass spectrometry (SIMS) [25] (see Chap. 1, Sect. 1.4.1). Mathematically the experimental setup corresponds to the well-known infinite source solution [26]. However, if exchange of the oxygen isotope between the atmosphere and the oxide is not sufficiently fast there will be no equilibrium for the isotope at the surface. Most often, the rate of isotope exchange at the oxide surface is assumed to be proportional to the isotope concentrations in the gas and the solid, c_g and c_s, resulting in

$$-D^*_O \cdot \left.\frac{\partial c}{\partial x}\right|_{x=0} = k \cdot (c_s - c_g) \tag{5.22}$$

where D^*_O is the oxygen tracer diffusion coefficient and k the surface exchange coefficient. The solution of the diffusion equation for a semi-infinite

[4] The charge of transport will be discussed in more detail in Sect. 5.5.2

medium subject to the boundary condition in (5.22) and having an initial concentration c_0 is [26]

$$c(x,t) = c_0 + (c_g - c_0) \cdot \left\{ \operatorname{erfc}\left(\frac{x}{\sqrt{4D^*t}}\right) - \exp\left(\frac{kx}{D^*} + \frac{k^2 t}{D^*}\right) \cdot \operatorname{erfc}\left(\frac{x}{\sqrt{4D^*t}} + k\sqrt{\frac{t}{D^*}}\right)\right\} \quad . \tag{5.23}$$

The parameters D^*_O and k are then obtained by fitting (5.23) to the experimental profile. A detailed analysis of the conditions where D^*_O and k can be determined unambiguously can be found in [27].

Two typical examples of oxygen diffusion in oxides of the ABO_3 perovskite structure are shown in Fig. 5.9 [28]. Both examples belong to samples in the solid solution series between Sr-doped lanthanum cobaltate, $La_{0.8}Sr_{0.2}CoO_{3-\delta}$, and Sr-doped lanthanum manganate, $La_{0.8}Sr_{0.2}MnO_{3-\delta}$. The oxides are doped with SrO to increase the fraction of oxygen vacancies (see (5.18)). In the manganese-rich sample, $La_{0.8}Sr_{0.2}Mn_{0.8}Co_{0.2}O_{3-\delta}$, the oxygen diffusion profile extends over a few microns and can be determined by SIMS depth profiling (Fig. 5.9a). In Sr-doped lanthanum cobaltate, $La_{0.8}Sr_{0.2}CoO_{3-\delta}$, however, oxygen diffusion is much faster and the penetration depth is about two orders of magnitude larger (Fig. 5.9b). For such large penetration depths the SIMS depth profiling technique is no longer applicable; the SIMS line-scanning technique [25] is used instead. Here the SIMS analysis is performed on a section perpendicular to the sample surface. By fitting (5.23) to the profiles, the oxygen diffusion coefficient and the surface exchange coefficient in both materials were determined. It turns out that in $La_{0.8}Sr_{0.2}CoO_{3-\delta}$ the oxygen diffusion coefficient is about five orders of magnitude larger than in $La_{0.8}Sr_{0.2}Mn_{0.8}Co_{0.2}O_{3-\delta}$, while the surface exchange coefficient is about 2 orders of magnitude larger in the former oxide than in the latter.

In general, oxygen diffusion can proceed in the same way as described for cation diffusion in (5.19), namely by means of oxygen vacancies and oxygen interstitials. As discussed in [28] there is, however, no evidence for oxygen interstitials in ABO_3 perovskite oxides, mainly for geometrical reasons. Thus the oxygen tracer diffusion coefficient is simply given by

$$D^*_O = f_0 \cdot D_V \cdot [V^{\bullet\bullet}_O] \tag{5.24}$$

where $f_0 = 0.69$ is the geometrical correlation factor for oxygen tracer diffusion in the oxygen sublattice of the ABO_3 structure [29] and D_V the self-diffusion coefficient of oxygen vacancies. In several other perovskites the combination of oxygen diffusion coefficients and measured vacancy fractions shows that the self-diffusion coefficient of oxygen vacancies, D_V, exhibits only small variations between different perovskites [29]. Thus, the

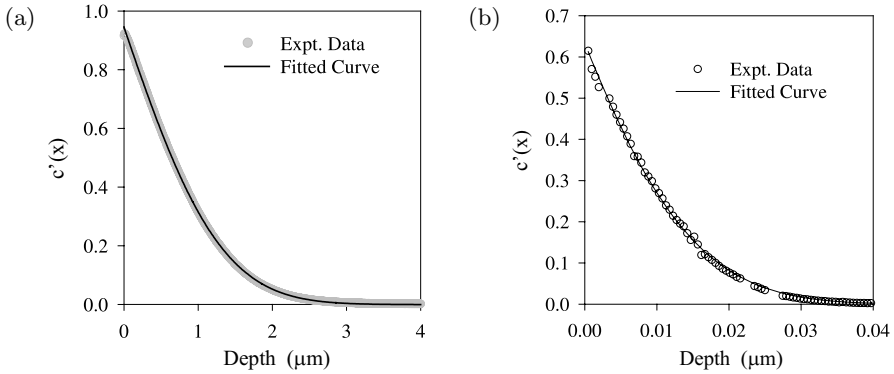

Fig. 5.9. Typical ^{18}O diffusion profiles, showing the normalized isotope fraction, $c'(x) = (c(x) - c_0)/(c_g - c_0)$, against depth, together with the fitted curves according to (5.23) [28]. (a) determined by SIMS depth profiling of a $La_{0.8}Sr_{0.2}Mn_{0.8}Co_{0.2}O_{3-\delta}$ sample (^{18}O anneal at 1000°C for 3840 s). (b) determined by SIMS linescanning of a $La_{0.8}Sr_{0.2}CoO_{3-\delta}$ sample (^{18}O anneal at 1000°C for 1675 s).

large difference of the observed oxygen diffusion coefficients is predominantly due to the difference in the oxygen vacancy concentrations between $La_{0.8}Sr_{0.2}Mn_{0.8}Co_{0.2}O_{3-\delta}$ and $La_{0.8}Sr_{0.2}CoO_{3-\delta}$.

Cation Diffusion

In oxides with dominating oxygen disorder cation defects are only minority defects and consequently cation diffusion is much slower than oxygen diffusion. Cation diffusion is nevertheless important since the slowest moving species determine many fundamental processes, such as sintering [30], creep [31] or internal friction [32].

An important example is yttria-stabilized zirconia, $(Zr_{1-x}Y_x)O_{2-x/2}$ (YSZ), which exhibits very high oxygen ion conductivity and is therefore used as electrolyte material in high-temperature applications [33]. While there is a considerable amount of data available on the oxygen transport (e.g. [34,35]), only little is known about the cation transport in YSZ [36,37]. Figure 5.10 shows recent results for the diffusion coefficients of Y and Zr in single crystalline YSZ [38]. The diffusion coefficient of yttrium was measured using the radioactive isotope ^{88}Y, while the diffusion coefficient of Zr was obtained by implanting the stable isotope ^{96}Zr, annealing at elevated temperatures and subsequent SIMS analysis.

From Fig. 5.10 it can be seen that Zr diffusion becomes slower with increasing Y-content. This is due to the fact that the dopant yttrium determines the fraction of oxygen vacancies, $[Y'_{Zr}] = 2[V_O^{\bullet\bullet}]$, which again determines via the Schottky equilibrium (see (5.1)) the fraction of cation vacancies. Thus cation diffusion should be slower the higher the dopant fraction, as

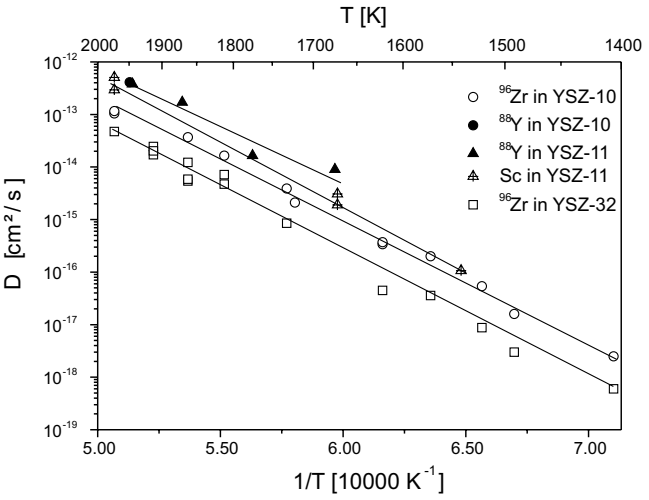

Fig. 5.10. Temperature dependence of the tracer diffusion coefficients of Zr, Y and Sc in yttria-doped zirconia, YSZ, containing 10, 11 and 32 mol% Y_2O_3 [38].

observed. As expected, comparison of the self-diffusion coefficients of oxygen and cations in YSZ shows that D_O is about 5 orders of magnitude larger than D_{cation}.

Similar results were found for doped lanthanum gallate, $La_{1-x}Sr_xGa_{1-y}Mg_yO_{3-(x+y)/2}$ (LSGM), which has a higher oxygen ion conductivity than YSZ and is therefore a candidate for solid oxide fuel cells working at intermediate temperatures [39]. Here oxygen diffusion coefficients [40] and cation self- and impurity diffusion coefficients [41, 42] have been measured. In contrast to YSZ there are two cation sublattices in the ABO_3-perovskite LSGM, an A- and a B-sublattice. In the perovskite structure (see Fig. 5.11), a direct jump of A-cations within the A-sublattice is possible, while a direct jump of B-cations within the B-sublattice is impossible due to the oxygen ion located between two nearest neighbour B-sites. Thus, for diffusion of B-cations curved diffusion pathways or jumps to next-nearest neighbour sites must be considered. Atomistic simulations of migration energies in lanthanum gallate [43] yield much higher migration energies for diffusion of B-cations than for diffusion of A-cations. The measured tracer diffusion coefficients of La, Sr and Mg [41] and the impurity diffusion coefficients for Fe, Cr and Y [41] are, however, very similar and show identical activation energies, although Mg, Fe and Cr should occupy B-sites while La, Sr and Y occupy A-sites. These observations may be an indication for antisite disorder in the perovskite LSGM, i.e. a small fraction of B-cations may occupy A-sites. This would be sufficient to enable diffusion of B-cations with similar diffusion coefficients as A-cations. A more detailled diffusion model

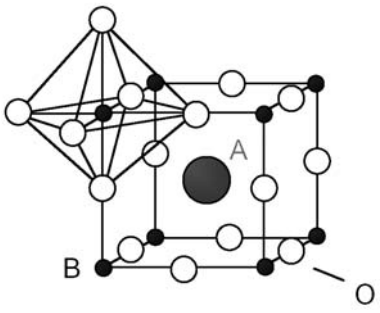

Fig. 5.11. Structure of the perovskite ABO_3.

considers a defect cluster consisting of an A-site vacancy, a B-site vacancy and at least one oxygen vacancy [41]. This cluster is mobile as an entity, i.e. without dissociation by means of four, correlated jumps of A- and B-cations and oxygen ions. As a result, A- and B-cations have identical diffusivities.

5.4 Chemical Diffusion

So far we have considered self- and impurity diffusion processes in chemically homogeneous oxides without any concentration gradients. We will now consider diffusion in concentration gradients, which is called chemical diffusion. It is well known, from irreversible thermodynamics, that the real driving force for isothermal mass transport of a component i is not its concentration gradient but the gradient of its electrochemical potential, $\eta_i = \mu_i + z_i \cdot F \cdot \Phi$, where μ_i is the chemical potential and Φ the electric potential [44] (z_i is the charge number and F, Faraday's constant)[5]. The resulting flux equation for component i is

$$j_i = -L_{ii} \cdot \nabla(\mu_i + z_i \cdot F \cdot \Phi) \tag{5.25}$$

where L_{ii} is the so-called Onsager transport coefficient[6]. For the sake of simplicity, we will consider only a binary oxide AO with dominating cation disorder. The results can easily be transferred to oxides with dominating oxygen disorder. We start with an oxide which is equilibrated at elevated temperatures and at a certain oxygen partial pressure, $p_{O_2}^{(1)}$. If the partial pressure of the surrounding atmosphere is increased to $p_{O_2}^{(2)}$ an oxidation process takes place. Oxygen is incorporated into the crystal by adding new lattice sites to the crystal and producing cation vacancies and electron holes (see (5.8)). In the case of reduction, lattice planes are annihilated and oxygen is released

[5] For neutral particles ($z_i = 0$) the driving force for mass transport is the gradient of the chemical potential, as already discussed for metals in Sect. 1.3.2 of Chap. 1.

[6] Cross coefficients L_{ij} are neglected in this section but will be considered in Sect. 5.5.

to the atmosphere. To preserve local electrical neutrality during the resulting transport processes of cations and electronic defects their fluxes must be coupled:

$$2j_{\mathrm{A}^{2+}} + j_{\mathrm{h}^{\bullet}} = 0 \quad . \tag{5.26}$$

From (5.26) we can calculate the internal electrical potential gradient, $\nabla\Phi$ (the so-called Nernst field), and insert the resulting expression into the flux equation for the cations in (5.25). With the equilibrium $\mathrm{A} + 2\mathrm{h}^{\bullet} \rightleftharpoons \mathrm{A}^{2+}$ between metal, A, cations, A^{2+}, and electron holes, $\mathrm{h}^{\bullet}$, the flux of cations can be written as

$$j_{\mathrm{A}^{2+}} = -L_{\mathrm{AA}} \cdot t_{\mathrm{el}} \cdot \nabla\mu_{\mathrm{A}} \tag{5.27}$$

where $t_{\mathrm{el}} = L_{\mathrm{hh}}/(4L_{\mathrm{AA}} + L_{\mathrm{hh}})$ is the electronic transference number. Equation (5.27) is the so-called Wagner formula for chemical or ambipolar diffusion [45]. If the thermodynamic driving force, $\nabla\mu_{\mathrm{A}}$, is written in terms of the concentration gradient, $\nabla\mu_{\mathrm{A}} = (\partial\mu_{\mathrm{A}}/\partial c_{\mathrm{A}}) \cdot \nabla c_{\mathrm{A}}$, we obtain

$$j_{\mathrm{A}^{2+}} = -L_{\mathrm{AA}} \cdot t_{\mathrm{el}} \cdot (\partial\mu_{\mathrm{A}}/\partial c_{\mathrm{A}}) \cdot \nabla c_{\mathrm{A}} = -\tilde{D} \cdot \nabla c_{\mathrm{A}} \tag{5.28}$$

which defines the chemical diffusion coefficient, $\tilde{D}$. Due to the flux coupling, $j_{\mathrm{A}^{2+}} + j_{\mathrm{V}} = 0$, the vacancy flux can also be written in terms of the chemical diffusion coefficient:

$$j_{\mathrm{V}} = -\tilde{D} \cdot \nabla c_{\mathrm{V}} \quad . \tag{5.29}$$

Finally, we write L_{AA} in terms of the diffusion coefficient D_{A} and the concentration c_{A}, $L_{\mathrm{AA}} = D_{\mathrm{A}} \cdot c_{\mathrm{A}}/RT$ (Einstein relation) and make use of $\mu_{\mathrm{A}} = \mu_{\mathrm{A}}^{0} + RT \ln a_{\mathrm{A}}$, where a_{A} is the activity of A. The result for $\tilde{D}$ is

$$\tilde{D} = D_{\mathrm{A}} \cdot t_{\mathrm{el}} \cdot \frac{\partial \ln a_{\mathrm{A}}}{\partial \ln x_{\mathrm{A}}} \quad . \tag{5.30}$$

Thus, the chemical diffusion coefficient, $\tilde{D}$, is the product of the cation self-diffusion coefficient, D_{A}, the electronic transference number, t_{el}, and the thermodynamic factor, $\partial \ln a_{\mathrm{A}}/\partial \ln x_{\mathrm{A}}$. Equation (5.30) applies also to oxides with dominating oxygen disorder if D_{A}, a_{A} and x_{A} are substituted by D_{O}, a_{O} and x_{O}.

The chemical diffusion coefficient, $\tilde{D}$, of an oxide $\mathrm{A}_{1-\delta}\mathrm{O}$ determines the equilibration kinetics of δ after a change of the external oxygen partial pressure. It can be determined by measuring δ directly, e.g. via thermogravimetry or by measuring a quantity which is proportional to δ, such as the electronic conductivity. These so-called relaxation experiments have been used to measure $\tilde{D}$ in various oxides such as CoO with dominating cation disorder [46], or $(\mathrm{La,Mn})\mathrm{CoO}_3$ [47] and $(\mathrm{La,Sr})\mathrm{CrO}_3$ [48] with dominating oxygen disorder.

If the oxide is a good semiconductor ($t_{\mathrm{el}} = 1$) and the majority defects are cation vacancies, $\mathrm{V}_{\mathrm{A}}^{\alpha'}$ (with negative excess charge $\alpha = 2, 1, 0$), and electron holes, $\mathrm{h}^{\bullet}$, (or oxygen vacancies, $\mathrm{V}_{\mathrm{O}}^{\alpha\bullet}$, and electrons, e') the formula for $\tilde{D}$ in (5.30) simplifies to (see appendix)

$$\tilde{D} = D_{\mathrm{V}} \cdot (1 + \alpha) \quad . \tag{5.31}$$

Thus, from the measured chemical diffusion coefficient, $\tilde{D}$, the self-diffusion coefficient, D_{V}, of the dominating vacancies can be calculated, if their excess charge is known. This is the normal procedure, e.g. mostly adopted in oxides with oxygen disorder where vacancies $\mathrm{V}_{\mathrm{O}}^{\bullet\bullet}$ ($\alpha = 2$) dominate. If, on the other hand, the vacancy self-diffusion coefficient is known the excess charge of the vacancies can be calculated. As will be shown in Sect. 5.5.1, both the vacancy self-diffusion coefficient, D_{V}, and the chemical diffusion coefficient, $\tilde{D}$, can be obtained simultaneously by performing tracer self-diffusion experiments during chemical diffusion. Then, from both diffusion coefficients the excess charge α can be obtained via (5.31).

In the general case of a mixed conductor, $t_{\mathrm{el}} \neq 1$, the chemical diffusion coefficient may show a strong dependence on the oxygen partial pressure for two reasons: (i) the electronic transference number, t_{el}, depends on the oxygen partial pressure. (ii) if the stability field of the oxide contains the stoichiometric point, $\delta(p^*_{\mathrm{O}_2}) = 0$, the thermodynamic factor and also the chemical diffusion coefficient exhibit a maximum at this oxygen partial pressure. This case is found, e.g., in $BaTiO_3$ [49].

Another technique that has been used recently for the measurement of chemical diffusion coefficients in Fe-doped $SrTiO_3$, which is a mixed conductor, uses the optical absorption of the sample [50]. In this way, time- and position-resolved concentration profiles of oxygen can be determined from which the chemical diffusion coefficient is evaluated.

5.5 Diffusion in Oxides Exposed to External Forces

If an oxide is exposed to external thermodynamic forces, e.g. an oxygen potential gradient or an electric potential gradient, defect fluxes are induced which again cause fluxes of the chemical components. As before, it is reasonable to distinguish between dominating oxygen disorder and dominating cation disorder.

In oxides where the oxygen ions are much more mobile than the cations, essentially only oxygen is driven through the oxide[7]. For pure oxygen ion conductors this situation corresponds to an electrolyte in a solid oxide fuel cell (applied oxygen potential gradient) or an electrochemical oxygen pump (applied electric potential gradient). For mixed conductors this situation corresponds to oxygen permeation cells. A detailed analysis of these cases is, however, beyond the scope of this chapter and can be found, e.g., in [51].

[7] The (driven) motion of the slower cations is, however, a possible origin of long-term degradation processes, such as creep or kinetic demixing (see also Sect. 5.5.1).

In oxides with dominating cation disorder external forces act on the mobile cations. The implications will be considered in more detail in the following sections.

5.5.1 Diffusion in an Oxygen Potential Gradient

Chemical Diffusion in an Oxygen Potential Gradient

If an oxide $A_{1-\delta}O$ of thickness Δz is exposed to an oxygen potential gradient, established, e.g., by different gas mixtures on both sides of the disc, different concentrations of cation vacancies, $c_V^{(1)}$ and $c_V^{(2)}$, are established on both sides of the disc (according to (5.9)). As a consequence, a vacancy flux, $j_V = -\tilde{D} \cdot \nabla c_V$ (see (5.29)), occurs from the high- to the low-oxygen potential side. Due to the flux coupling, $j_{A^{2+}} + j_V = 0$, cations are driven in the opposite direction. When vacancies and cations arrive at the oxide surfaces, reduction and oxidation of the oxide occur at the low- and high-oxygen potential side, respectively:

$$V''_A + 2h^\bullet + AO \underset{\text{oxidation}}{\overset{\text{reduction}}{\rightleftharpoons}} A_A^x + \tfrac{1}{2}O_2(g) \quad . \tag{5.32}$$

Thus, lattice planes are removed from the low oxygen potential side and added to the high oxygen potential side. As a result, the crystal surfaces move relatively to the immobile oxygen sublattice to the side of the higher oxygen activity. The crystal displacement and the vacancy concentration profile can be calculated by solving the diffusion equation [52]. After a short transient period the crystal moves with a constant velocity. A steady-state solution can be calculated by transforming from the laboratory reference frame[8] to a moving coordinate system (coordinate z) which is fixed at one surface. The steady-state vacancy fraction profile in the moving system, $x_V(z)$, is linear in position, z, to a very good approximation, and the steady state velocity, v, is given by

$$x_V = a + b \cdot z \quad , \qquad v = \tilde{D} \cdot b \tag{5.33}$$

with

$$a = x_V^{(1)} \quad , \qquad b = \frac{x_V^{(2)} - x_V^{(1)}}{\Delta z} \quad . \tag{5.34}$$

Experiments with the model system CoO exposed to an oxygen potential gradient confirm the shift of the crystal surfaces relatively to the immobile oxygen sublattice [52].

[8] Since oxygen is essentially immobile, the laboratory reference frame is identical to the lattice reference frame.

Tracer Diffusion in an Oxygen Potential Gradient

The motion of cation tracers (being chemically identical to the cation A or being an impurity) in an oxide which is exposed to an oxygen potential gradient is influenced by the directed vacancy flux in (5.29) in two respects: Firstly, the tracer diffusion coefficient is proportional to the vacancy fraction which varies linearly with position. Thus, tracer diffusion takes place with a linearly position dependent tracer diffusion coefficient. Secondly, the tracer ions are moved by the drifting vacancies. This drift flux of the tracer particles, which is over and above their normal Brownian motion, reflects the interaction of the tracer ions with the vacancies. In summary, the tracer flux consists of two parts: the first part, $j^{\mathrm{diff}}_{\mathrm{tracer}}$, describes Brownian motion, as in the case of a homogeneous crystal, but with the difference that the diffusion coefficient is position dependent. The second part is a drift term, $j^{\mathrm{drift}}_{\mathrm{tracer}}$, which is proportional to the vacancy flux, as will be shown below.

Tracer Self-Diffusion in an Oxygen Potential Gradient

In this case the tracer ions A^* are chemically identical to the normal cations A, but in contrast to them they are distinguishable. Thus, the tracer diffusion coefficient, $D_{\mathrm{A}^*} = f_0 \cdot D_{\mathrm{V}} \cdot x_{\mathrm{V}}$, contains the geometrical tracer correlation factor, f_0, and the first part of the flux of the tracer particles has the form

$$j^{\mathrm{diff}}_{\mathrm{A}^*} = -f_0 \cdot D_{\mathrm{V}} \cdot x_{\mathrm{V}} \cdot \nabla c_{\mathrm{A}^*} \quad . \tag{5.35}$$

Since the tracer particles are chemically identical to the normal cations they are moved by the directed vacancy flux in the same way as the normal cations. However, only a fraction x_{A^*} of the total amount of A exists as tracer. Therefore the drift flux of the tracer has the form:

$$j^{\mathrm{drift}}_{\mathrm{A}^*} = -x_{\mathrm{A}^*} \cdot j_{\mathrm{V}} \quad . \tag{5.36}$$

The source solution for this diffusion problem is given by [53]

$$c_{\mathrm{A}^*}(z,t) = \frac{M}{D_{\mathrm{V}} \cdot b \cdot t} \cdot \exp\left(-\frac{2a + b \cdot (z + z_0)}{D_{\mathrm{V}} \cdot f_0 \cdot b^2 \cdot t}\right) \cdot I_0\left(\frac{(a + bz)^{1/2} \cdot (a + bz_0)^{1/2}}{D_{\mathrm{V}} \cdot f_0 \cdot b^2 \cdot t}\right) \tag{5.37}$$

where M is the total amount of tracer per unit area, z_0 the initial position of the tracer source, and I_0 a Bessel function of order zero. In contrast to the source solution for a constant diffusion coefficient (Gaussian) the maximum of the curve shifts with increasing time to the side of higher oxygen potential, and the profile becomes more and more asymmetric. The initial tracer source position can be marked by inert markers. Its position in the moving system is $z_{\mathrm{marker}} = z_0 + v \cdot t$. The position of the maximum, $z_{\max}(t)$, relative to the marker position is then given by

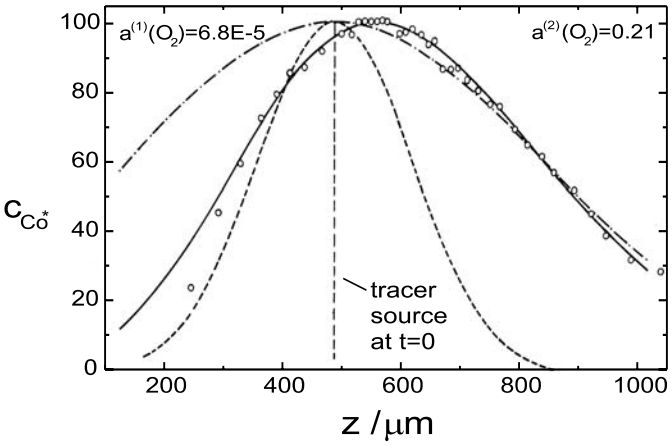

Fig. 5.12. Normalised tracer concentration profile of ^{60}Co in CoO in an oxygen potential gradient ($T = 1210°C$, $a^{(1)}_{O_2} = 6.8 \cdot 10^{-5}$, $a^{(2)}_{O_2} = 0.21$, $\Delta z = 1184\,\mu m$, $t = 15\,h$) [20]. ∘ experimental concentrations; — best fit using (5.37); – – – Gaussian profile for a homogeneous crystal at $a^{(1)}_{O_2}$; –·– Gaussian profile for a homogeneous crystal at $a^{(2)}_{O_2}$.

$$z_{max}(t) - z_{marker} = \left(\tilde{D} - \tfrac{1}{2} \cdot f_0 \cdot D_V\right) \cdot b \cdot t \quad . \tag{5.38}$$

Figure 5.12 shows a typical tracer concentration profile of ^{60}Co in $Co_{1-\delta}O$ in an oxygen potential gradient. By fitting of (5.37) the vacancy diffusion coefficient, D_V, and the chemical diffusion coefficient, $\tilde{D}$, can be determined simultaneously. Using (5.31) the average excess charge of the cation vacancies was found to be $\alpha = 0.86$ [20]. This value is in reasonable agreement with values calculated on the basis of equilibrium constants (see Sect. 5.2.1). For comparison, the Gaussian profiles which one would obtain in a homogeneous crystal equilibrated at oxygen activities $a^{(1)}_{O_2}$ and $a^{(2)}_{O_2}$ are also shown in Fig. 5.12. The actual profile lies between the two Gaussian profiles.

Similar experiments have been performed for tracer diffusion of Fe in magnetite, Fe_3O_4, which was exposed to an oxygen potential gradient [54]. Due to the high electronic disorder in magnetite (Fe^{2+} and Fe^{3+} ions are regular structure elements) the chemical diffusion coefficient, $\tilde{D}$, is identical to the vacancy diffusion coefficient, D_V, in the vacancy regime, and identical to the interstitial diffusion coefficient, D_I, in the interstitial regime [20]. This means, that the two parameters which can be determined simultaneously are the self-diffusion coefficient of the dominating defect and the correlation factor for tracer diffusion via this defect. In contrast to oxides with the NaCl-structure, e.g. CoO, the effective correlation factor for a jump sequence in the spinel Fe_3O_4 cannot be specified a priori since several vacancy and interstitial or interstitialcy mechanisms are possible in magnetite. This is due to the fact

that in the spinel structure two regular cation sites exist, an octahedrally and a tetrahedrally coordinated site. Likewise, several interstitial positions are possible.

In the vacancy regime, three basic vacancy mechanisms are discussed. They are characterised by jumps only within the octahedral sublattice, only within the tetetrahedral sublattice [55], or jumps between these two sublattices [56]. The geometrical correlation factors for these mechanisms are $f_V = 0.50$, $f_V = 0.56$, and $f_V = 0.73$, respectively. The correlation factor obtained from tracer experiments in an oxygen potential gradient is $f_V = 0.56 \pm 0.07$ [54] indicating preferred diffusion of Fe within the octahedral sublattice, in agreement with results of in situ Mößbauer spectroscopy [56].

In the interstitial regime, the correlation factor obtained from tracer experiments in an oxygen potential gradient is $f_I = 0.43 \pm 0.1$. Only a direct interstitial mechanism ($f_I = 1$) can be excluded. The experimental accuracy is, however, too small to distinguish between different interstitial or interstitialcy mechanisms for which the theoretical correlation factors, f_I, are between 0 and 1 [55].

Impurity Diffusion in an Oxygen Potential Gradient

The flux of impurity ions, B, in an oxide which is exposed to an oxygen potential gradient consists also of two parts: a pure, diffusion term, which is characterized by the impurity diffusion coefficient, D_B, and which describes Brownian motion of the impurity ions, and a second part which is again a drift term caused by the directed flux of vacancies which drift through the oxide. However, in contrast to self-diffusion, where the drift flux was always opposite to the vacancy flux and directly proportional to the fraction of tracers, now the magnitude and direction of the drift flux have to be calculated with the aid of linear transport theory. This means that transport coefficients L_{ij} $(i, j = A, B)$ have to be used which describe the coupled transport of A and B under the influence of an applied oxygen potential gradient. The impurity drift flux was calculated in detail in [20] and can be written as

$$j_B^{drift} = -j_V \cdot x_B \cdot \frac{D_B}{D_A} \cdot \beta \quad . \tag{5.39}$$

As expected, the impurity drift flux is proportional to the vacancy flux, j_V, and the fraction of impurities, x_B. In addition it is proportional to the ratio of the diffusion coefficients of the impurity, D_B, and the solvent, D_A. This ratio reflects the fact that impurities and solvent ions exchange with different rates with vacancies. As a result they are moved differently by the vacancies. In contrast to these first terms, which are model independent, the last factor, β, depends on the microscopic model used. It describes essentially the interaction of the impurity with its neighbours which can be small (as is expected for homovalent impurities) or stronger (for aliovalent impurities). Particularly for higher valent impurities which possess a positive excess

charge there can be strong interaction with the negatively charged vacancies. Now the two possible limiting cases will be discussed: First, the situation where the interaction is small. This means that impurities and vacancies should drift in opposite directions, as in the case of self-diffusion. Second, the case of attractive interaction between impurities and vacancies. Then impurities and vacancies form bound pairs and the impurities should drift in the same direction as the vacancies. This qualitative picture is confirmed by the theoretical results for the constant β in (5.39) which was calculated in [57] within the five-frequency model. Within this model the transport coefficients L_{ij} $(i, j = \mathrm{A}, \mathrm{B})$ are known exactly [22]. The five-frequency model (Fig. 1.18, note also footnote 15 in Chap. 1) is a nearest-neighbour model and uses five exchange rates of vacancies and ions: ω_0 and ω_1 for exchange of vacancies with solvent ions in the pure crystal (i.e. far away from the impurity) and in the next neighbourhood of the impurity; ω_3 for vacancy jumps, which dissociate an impurity-vacancy pair; ω_4 which creates a new pair; and ω_2 for exchange of a vacancy and an impurity. For strong binding the parameter β is negative, yielding an impurity drift flux in the same direction as the vacancies, while for weak binding β is positive, and the drift flux is opposite to the vacancies. Thus, an impurity drift experiment in an oxygen potential gradient performed in the same way as described for tracer self-diffusion shows first by the direction in which the profile moves whether strong or weak impurity-vacancy binding prevails, and second allows the determination of ratios of the exchange jump rates ω_i $(i = 0, 1, 2, 3, 4)$.

An example is impurity diffusion of Fe in CoO in an oxygen potential gradient. It was found, that the drift direction of the Fe-tracer profile depends on the oxygen potential region [19]. In region I ($\log a_{\mathrm{O}_2} \approx -2$) the profile drifts to the high oxygen potential side, i.e. opposite to the vacancies, while in region II ($\log a_{\mathrm{O}_2} \approx -8$) the profile shifts to the low oxygen potential side, i.e. in the same direction as the vacancies. The impurity diffusion coefficient, D^*_{Fe}, and the constant β in (5.39) can be obtained from the profiles. To calculate from these data the vacancy exchange rates ω_i in the five-frequency model, or at least ratios of them, two additional experimental parameters are needed. These are: (i) the impurity correlation factor which was obtained from the isotope effect [58] and which changes from 0.78 in region I to 0.87 in region II. (ii) the impurity-vacancy binding energy, Δg_{pair}, which was obtained from the p_{O_2}-dependence of the Fe-tracer diffusion coefficient. It is small compared to the thermal energy in region I and about 0.7 eV in region II [19]. All four quantities are known exactly as functions of the five rates ω_i $(i = 0, 1, 2, 3, 4)$ within the five-frequency model [22] [9]. As a result four ratios of exchange rates can be calculated in regions I and II, respectively:

[9] The dependence of the impurity diffusion coefficient and the impurity correlation factor on the exchange ratees ω_i can be found in Sect. 1.9.1 in Chap. 1, the expression for β in [19], and the relation for the impurity-vacancy binding energy is given by $\omega_4/\omega_3 = \exp(-\Delta g_{\mathrm{pair}}/k_{\mathrm{B}}T)$.

region I: $\omega_3/\omega_1 = 0.29$, $\omega_2/\omega_1 = 0.52$, $\omega_4/\omega_0 = 0.53$, $\omega_4/\omega_3 \cong 1$
region II: $\omega_3/\omega_1 = 0.02$, $\omega_2/\omega_1 = 0.14$, $\omega_4/\omega_0 = 0.60$, $\omega_4/\omega_3 \cong 300$

While the ratios ω_2/ω_1 and ω_4/ω_0 remain nearly unchanged in passing from region I to region II, ω_4/ω_3 increases drastically and ω_3/ω_1 decreases. This is mainly due to the fact that the escape rate, ω_3, decreases in passing from region I to region II indicating the transition from weak to strong binding between Fe and vacancies. If the binding is mainly due to Coulombic interaction between oppositely charged structure elements, one cause for the change in Δg_{pair} could be the change in the relative concentrations of the differently charged cation vacancies. At high oxygen activities (region I) vacancies V'_{Co} dominate, whereas vacancies V''_{Co} become more important at lower oxygen activities (region II). As a result, there is stronger Coulombic interaction with trivalent iron at lower oxygen activities. On the other hand, iron exists as Fe^{2+} and Fe^{3+}, and the fraction of trivalent iron decreases with decreasing oxygen activity, which results in a smaller degree of association. Another possible cause for the increase of Δg_{pair} goes back to the different sizes of di- and trivalent iron ions. The larger ionic radius of Fe^{2+} would result in displacements of neighbouring ions which may be compensated by association of a vacancy.

Demixing in an Oxygen Potential Gradient

If, instead of a pure oxide, a mixed oxide, $(A_{1-x}B_x)O$, in which oxygen is immobile, is exposed to a stationary oxygen potential gradient, again different cation vacancy fractions are established at the high and low oxygen potential sides. However, the resulting cation vacancy flux from the high to the low oxygen potential side causes fluxes of both cations, A and B. In general, they have different mobilities and the oxide will become enriched in the more mobile cation at the high oxygen potential side, while it will become enriched in the less mobile cation at the low oxygen potential side (see Fig. 5.13). This kinetic demixing process was studied first by Schmalzried et al. [59,60] considering steady-state demixing and homovalent solid solutions, e.g. (Co,Mg)O, where Co is the faster cation and becomes enriched at the high oxygen potential side of the oxide. The formal solution of the transient demixing problem with moving boundaries and time-dependent boundary values can be found in [61].

However, kinetic demixing may also be important in doped oxides $(A_{1-x}B_x)O$, where the kinetic segregation of impurities is of interest, e.g. during sintering or alloy corrosion [62]. The basis for the subsequent analysis is given by the general transport equations [44]

$$j_i = -\sum_j L_{ij} \cdot \nabla \eta_j \tag{5.40}$$

where L_{ij} are the transport coefficients and η_j is the electrochemical potential (see Sect. 5.4). As shown in [63], in a dilute oxide, $A_{1-x}B_xO$ ($x \ll 1$)), the

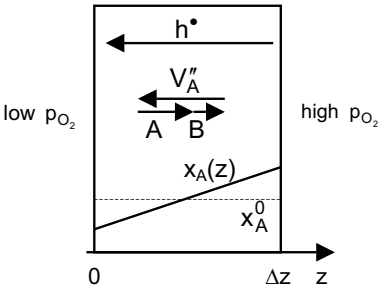

Fig. 5.13. Schematic representation of the fluxes of electron holes, cation vacancies and cations A and B, and the initial and steady state concentration profile of A in a mixed oxide (A,B)O exposed to an oxygen potential gradient for the case that component A is faster than B.

flux of the dopant, B, can be written as

$$j_{\mathrm{B}} = -D_{\mathrm{B}} \cdot \nabla c_{\mathrm{B}} - j_{\mathrm{V}} \cdot \frac{L_{\mathrm{BB}}}{L_{\mathrm{AA}}} \cdot \left(\gamma + \frac{L_{\mathrm{BA}}}{L_{\mathrm{BB}}} \right) \quad . \tag{5.41}$$

The dimensionless quantity γ contains all physical correlation effects and is of the order of unity. Equation (5.41) shows that the dopant flux consists of two terms, a pure diffusion term, $-D_{\mathrm{B}} \nabla c_{\mathrm{B}}$, characterized by the dopant diffusion coefficient, D_{B} ($= L_{\mathrm{BB}} RT/c_{\mathrm{B}}$), and a drift term, which is proportional to the vacancy flux, j_{V}. The direction of the drift term, which determines at which side of the sample the dopant becomes enriched, depends crucially on the sign and magnitude of the non-diagonal element L_{BA}. Particularly in trivalent doped oxides, $\mathrm{AO}(+\mathrm{B_2O_3})$, solute-vacancy interactions might result in a non-vanishing cross term L_{AB}. Thus the demixing behaviour or the kinetic segregation of the dopant B strongly depends on the strength of the solute-vacancy binding energy.

Demixing experiments with $\mathrm{Ga_2O_3}$-doped CoO [64] clearly show demixing of Co and Ga with enrichment of Ga at the low oxygen potential side (see Fig. 5.14). Since the tracer diffusion coefficients of Co and Ga are also known (see Sect. 5.3.1), the ratio $L_{\mathrm{GaCo}}/L_{\mathrm{GaGa}}$ can be obtained from the demixing profile using (5.41). The result is $L_{\mathrm{CoGa}}/L_{\mathrm{GaGa}} = -1.7$, leading to the following interpretation. Due to the strong binding between the dopant Ga and the vacancies the drift flux of the dopant is directed to the side of lower oxygen potential (i.e. in the same direction as the vacancy flux), where the dopant Ga therefore becomes enriched. As shown in detail in [64] the result $L_{\mathrm{CoGa}}/L_{\mathrm{GaGa}} = -1.7$ can be explained adequately in terms of the five-frequency model of impurity diffusion [22] and strong impurity-vacancy binding, which was found independently in the tracer diffusion studies of this system [21].

Finally it should be mentioned that demixing in an oxygen potential gradient might be important also in oxygen ion conductors, such as yttria-doped zirconia (YSZ) or doped lanthanum gallate (LSGM). When these oxides are used as electrolytes, e.g. in solid oxide fuel cells (SOFCs), oxygen ions are driven through the electrolyte and simultaneously electrons are flowing through the external circuit. As soon as the cations, e.g. $\mathrm{Zr^{4+}}$ and $\mathrm{Y^{3+}}$ in

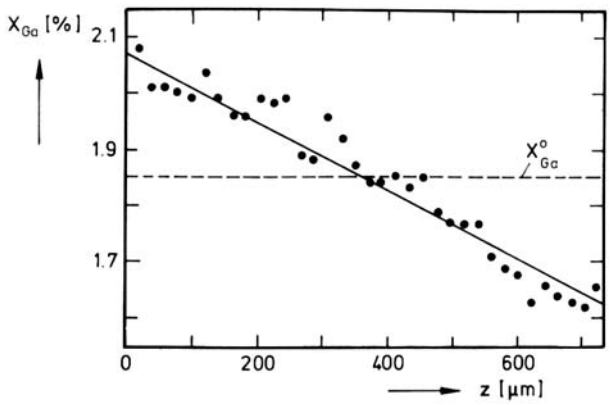

Fig. 5.14. Demixing profile of Ga in $(Co_{1-x}Ga_x)O$ exposed to an oxygen potential gradient ($T = 1250°C$, $a_{O_2}^{(1)} = 10^{-6}$ (left), $a_{O_2}^{(2)} = 10^{-5}$ (right), $\Delta z = 725\,\mu m$, $x_{Ga}^0 = 1.85\%$, $t = 38.5\,h$) [64].

YSZ, have different diffusion coefficients (see Sect. 5.3.2) there will be demixing of the electrolyte. However, since cation diffusion is very slow, steady-state demixing will be reached only after rather long times. If, for example, the slowest diffusion coefficient is taken as $D = 10^{-18}\,m^2s^{-1}$, one obtains 15 000 years for an electrolyte thickness of 1mm. However, for a thickness of 10 µm the time to reach the steady state is only 1.5 years which is comparable to the desired operating times of SOFCs.

5.5.2 Diffusion in an Electric Potential Gradient

In this section, electro-transport in oxides, i.e. the motion of ions due to an external electric potential gradient, $\nabla\Phi$, will be discussed. As in the previous section, where diffusion in an applied oxygen potential gradient was analyzed, the fluxes of the mobile components i (ions and electronic defects) can be written as a sum of a diffusion and a drift flux, $j_i = j_i^{diff} + j_i^{drift}$. In a chemically homogeneous oxide without any gradients in chemical potentials, the diffusion fluxes vanish, and the drift flux can be written as

$$j_i^{drift} = -L_{ii}\left(\sum_k z_k \cdot \frac{L_{ik}}{L_{ii}}\right) \cdot F \cdot \nabla\Phi \quad . \tag{5.42}$$

The sum in parentheses is usually denoted as effective charge, $z_{i,eff}$. It is identical to the formal charge, z_i, only if the cross coefficients L_{ik} $(i \neq k)$ are zero and, consequently, the fluxes are independent of each other[10].

[10] In metals, the effective charge is frequently denoted by the symbol z_i^*.

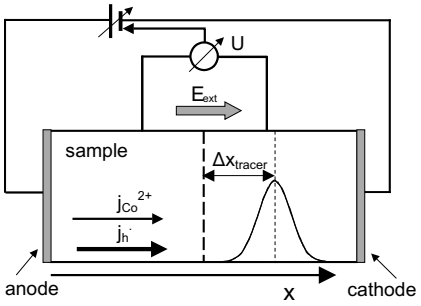

Fig. 5.15. Schematic experimental setup for the measurement of the effective charge in a constant electric potential gradient (sandwich experiment). The Gaussian curve shows the broadening and shift of a tracer concentration profile which has developed from a point source located originally in the middle of the crystal.

The effective charges are thus a measure of the cross coefficients which are again indicating defect-defect interactions. In homogeneous oxides exposed to an electric field, (radioactive) tracers can be used to measure the drift velocities of ions from which their effective charges can be calculated (Sect. 5.5.2). During demixing experiments, however, the oxide becomes chemically inhomogeneous resulting in drift and diffusion fluxes as well. This situation will be discussed in Sect. 5.5.2.

Tracer Diffusion in an Electric Potential Gradient

Figure 5.15 shows the typical experimental setup which can be used to measure the effective charges, $z_{i,\mathrm{eff}}$, of the host cation A or of impurity cations B in an oxide AO using radioactive tracers, A^* and B^*. The tracer source is located between two single crystals of the oxide in a sandwich arrangement, and the electric potential gradient is applied by two reversible electrodes. Diffusional broadening of the tracer source results in a Gaussian profile from which the tracer diffusion coefficient can be obtained. Superimposed is a drift of the tracer concentration profile due to the applied electric field. As shown in detail in [18], the drift velocity of the tracer concentration profile, $v_{\mathrm{A}^*}^{\mathrm{drift}}$ or $v_{\mathrm{B}^*}^{\mathrm{drift}}$, allows the determination of the effective charges of the corresponding cations, A or B. For self-diffusion, i.e. tracers A^*, we obtain

$$v_{\mathrm{A}^*}^{\mathrm{drift}} = \frac{D_{\mathrm{A}}}{RT} \cdot z_{\mathrm{A,eff}} \cdot F \cdot \nabla \Phi, \qquad z_{\mathrm{A,eff}} = z_{\mathrm{A}} + \frac{L_{\mathrm{Ah}}}{L_{\mathrm{AA}}} \quad . \tag{5.43}$$

The effective charge of cation A, $z_{\mathrm{A,eff}}$, contains the cross coefficient, L_{Ah}, which indicates the flux coupling between cations and electron holes. $z_{\mathrm{A,eff}}$ is often called 'charge of transport'. For impurity tracer cations, B^*, the result is

$$v_{\mathrm{B}^*}^{\mathrm{drift}} = \frac{D_{\mathrm{B}}}{RT} \cdot z_{\mathrm{B,eff}} \cdot F \cdot \nabla \Phi, \qquad z_{\mathrm{B,eff}} = z_{\mathrm{B}} + \frac{L_{\mathrm{Bh}}}{L_{\mathrm{BB}}} + \frac{L_{\mathrm{BA}}}{L_{\mathrm{BB}}} \quad . \tag{5.44}$$

The effective charge of B, $z_{\mathrm{B,eff}}$, now contains two cross coefficients, L_{Bh} and L_{BA}, which indicate flux coupling between B and h and between B and A.

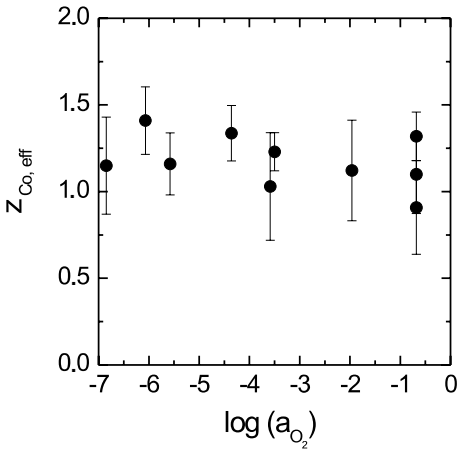

Fig. 5.16. Effective charge of cobalt in $Co_{1-\delta}O$ as a function of the oxygen activity at 1100°C [18].

Figure 5.16 shows results for the charge of transport of Co in CoO as a function of the oxygen partial pressure [18]. $z_{\mathrm{Co,eff}}$ has a value close to +1. Since the formal charge of Co in CoO is $z_{\mathrm{Co}} = 2$ this result demonstrates clearly that the cross coefficient $L_{\mathrm{Co\,h}}$ is by no means negligible. The cross effect may be understood in terms of vacancy-electron hole associates, $V''_{\mathrm{Co}} + h^{\bullet} \rightleftharpoons V'_{\mathrm{Co}}$, and long-range Coulomb interactions between the oppositely charged vacancies and electron holes. Application of the Onsager-Fuoss theory to this system [65] has shown that long-range interactions are of minor significance compared to association reactions. If the lifetime of the associate, V'_{Co}, is long enough to move as an entity, a simple interpretation of the effective charge can be given: in an electric field, Co^{2+} ions move towards the cathode via lattice site exchange with vacancies. If the vacancy is associated with an electron hole, two positive charges (fixed on the cobalt ion) move towards the cathode and, at the same time, one positive charge (the hole associated with the vacancy) moves in the opposite direction during the exchange step. Thus, the net charge which is moved towards the cathode and which is the only quantity that can be measured is +1. Additional evidence for vacancy-electron hole associates stems from measurements of the electrical conductivity [66]. The data were modelled by two different electronic conductivity processes, by means of free electron holes and by means of electron holes bound by vacancies. The lifetime of a vacancy-electron hole associate was found to be 20 times larger than the residence time of a free electron hole on a cation site.

The effective charges of the impurities indium and iron are shown in Fig. 5.17. Whereas $z_{\mathrm{Fe,eff}}$ remains nearly constant with changing oxygen activity with a value of about +1, $z_{\mathrm{In,eff}}$ decreases drastically with changing $a_{\mathrm{O_2}}$ and becomes even negative at $a_{\mathrm{O_2}} < 10^{-4}$. This is equivalent to a reversal of the migration direction in the electric field. In the range of high

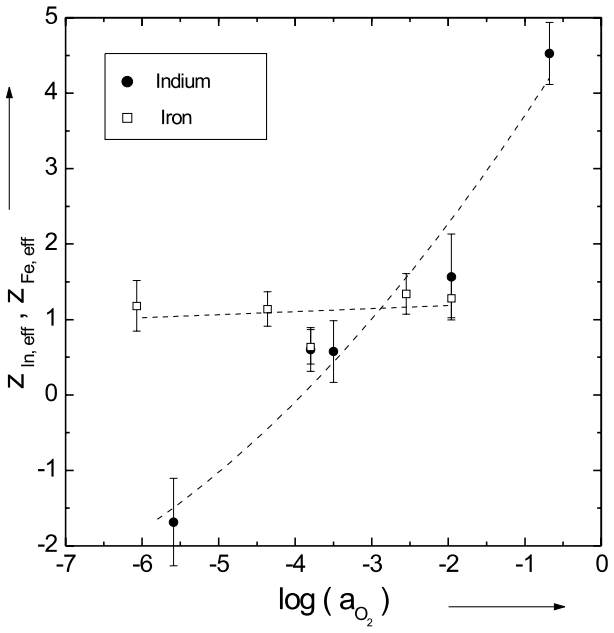

Fig. 5.17. Effective charges of indium and iron in $Co_{1-\delta}O$ as a function of the oxygen activity at 1100°C [18].

oxygen activities, the indium tracer moves towards the cathode, at low activities it moves towards the anode, and therefore virtually behaves like an anion. If we try to explain the observed behavior in the same way as for the Co ions and assume that the impurity ions move via vacancy-electron hole associates, V'_{Co} (majority defects), we expect $z_{In,eff} = +2$ (with the formal charge $z_{In} = +3$) and $z_{Fe,eff} = +2$ or $+1$ (with $z_{Fe} = +3$ or $+2$, respectively). It is obvious from Fig. 5.17 that the strong decrease of $z_{In,eff}$ and the appearance of negative values at low oxygen activities cannot be interpreted in this manner. Furthermore, the experimentally obtained value of $z_{Fe,eff} \approx +1$ at high oxygen activities is unexpected, because iron should have a formal charge of about $+3$ in this region. This means that in (5.44) the second ratio including the cross coefficient L_{BA} is also important. It is well known that this cross coefficient is due to the formation of impurity-vacancy pairs [22]. If the pair binding energy is strong enough to make the lifetime of the pair much longer than the time required for an individual jump of the impurity ion, the pair moves as an entity and the vacancy drags the impurity cation towards the anode. As a result, we find a negative effective charge, as observed experimentally. A more detailed formal analysis can be found in [67] and [68].

Demixing in an Electric Potential Gradient

The external electric field can also cause demixing of an initially homogeneous oxide solid solution, e.g. $(A_{1-x}B_x)O$, if the cations have different mobilities. In semiconducting oxides demixing due to an electric field was found by several authors [69–72]. Demixing processes have important practical implications. Local composition changes can severely alter the physical, chemical and electrical properties and are therefore a source of high temperature degradation of materials in electric fields.

We consider a semiconducting, ternary oxide, $(A_{1-x}B_x)_{1-\delta}O$, with an immobile oxygen sublattice, where the cations are mobile via a vacancy mechanism. As in the previous section, the external electric field (see Fig. 5.18) causes fluxes of the homovalent cations, A^{2+} and B^{2+}, and electron holes, $h^{\bullet}$, which are given by (5.40).

At the reversible electrodes the cations are involved in chemical reactions, e.g. at the cathode:

$$\begin{aligned} &A^{2+} + 2e^-(Pt) + \tfrac{1}{2}O_2(g) \rightarrow AO, \\ &B^{2+} + 2e^- + \tfrac{1}{2}O_2(g) \rightarrow BO \end{aligned} \tag{5.45}$$

This means that the oxide grows at the cathode. At the anode the opposite reactions take place, i.e. here the oxide dissociates into cations, electrons and oxygen molecules. Thus, both oxide surfaces move to the cathode side. In the steady state both surfaces and also both cations move with the same velocity, v:

$$v = \frac{j_{A^{2+}}}{c_A} = \frac{j_{B^{2+}}}{c_B}\,. \tag{5.46}$$

Integration of (5.46) over the sample thickness yields

$$\frac{x_A^{(1)}}{x_A^{(2)}} \cdot \frac{1 - x_A^{(2)}}{1 - x_A^{(1)}} = \exp\left(\frac{2FU}{RT} \cdot \frac{\gamma - 1}{\gamma}\right) \tag{5.47}$$

where $x_A^{(1)}$ and $x_A^{(2)}$ are the unknown molar fractions of A at the oxide surfaces and U is the applied voltage. $\gamma = D_A/D_B$ is a constant, since both

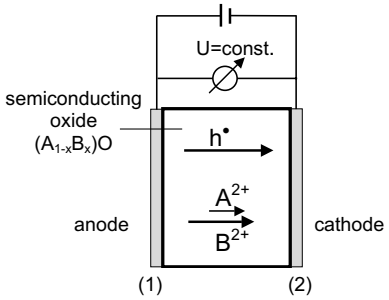

Fig. 5.18. Schematic representation of the fluxes in a mixed oxide (A,B)O exposed to an electric potential gradient established by Pt-electodes.

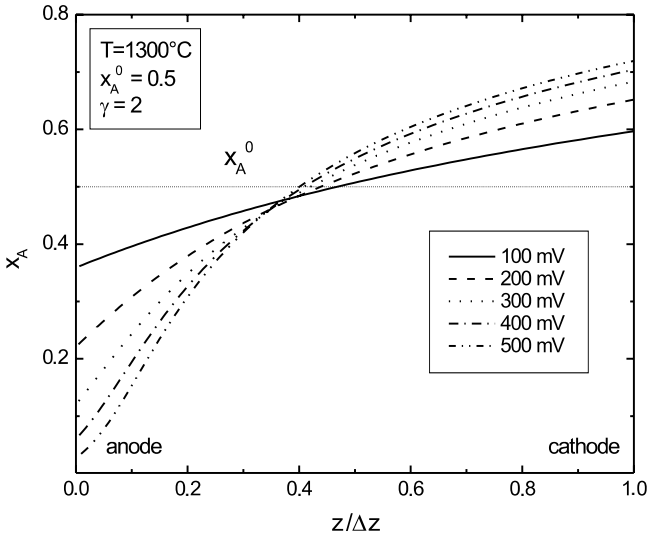

Fig. 5.19. Calculated steady state demixing profiles of component A in a mixed oxide (A,B)O as a function of the applied voltage U ($T = 1300°\mathrm{C}$, $x_\mathrm{A}^0 = 0.5$, $\gamma = D_\mathrm{A}/D_\mathrm{B} = 2$) [70].

diffusion coefficients are proportional to the cation vacancy fraction, x_V. The concentration profile of A (and B, $x_\mathrm{A} + x_\mathrm{B} = 1$) can be obtained by integration of (5.46) and the overall mass balance for A. Details can be found in [70]. Figure 5.19 shows steady-state demixing profiles calculated in this way for different values of the applied voltage U. With increasing voltage the anode-side of the oxide is more and more depleted by the faster component A.

A typical result of a steady-state demixing experiment for $(\mathrm{Co}_{1-x}\mathrm{Ni}_x)\mathrm{O}$ is shown in Fig 5.20. Enrichment of Co near the cathode side of the oxide is found [73], as expected qualitatively due to the higher diffusivity of Co compared to Ni [74]. For a quantitative modelling of the demixing (solid line in Fig. 5.20) one also has to consider the cross terms in the transport coefficient matrix L_{ij} ($i, j = \mathrm{A}, \mathrm{B}, \mathrm{h}^\bullet$). In particular the cross terms L_Ah and L_Bh are important, as shown in the previous sections. Finally it should be emphasized that the electric current during demixing is mainly conducted by electron holes, because $t_\mathrm{h} \cong 1$ and $t_\mathrm{cation} \approx 10^{-4}$. Nevertheless, there is a demixing process for the cations as long as they have different mobilities.

Demixing in a heterovalently doped oxide, $(\mathrm{A}_{1-x}\mathrm{B}_x)\mathrm{O}$, is more complicated. Due to Coulomb interactions between the defects (impurity-vacancy pairs) the cross term L_AB can no longer be neglected and might even determine the complete demixing behavior. An example is Ga-doped CoO, $(\mathrm{Co}_{1-x}\mathrm{Ga}_x)\mathrm{O}$, in which $\mathrm{Ga}_\mathrm{Co}^\bullet$ and V_A'' form impurity-vacancy pairs, $\{\mathrm{Ga}_\mathrm{Co}^\bullet, \mathrm{V}_\mathrm{Co}''\}'$ [21]. These pairs have a negative excess charge and move to-

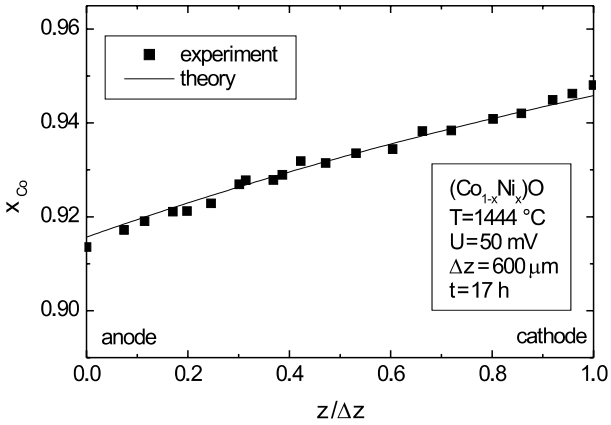

Fig. 5.20. Steady state demixing profile of Co in $(Ni_{1-x}Co_x)O$ ($T = 1444°C$, $x_A^0 = 0.932$, $\Delta z = 600\,\mu m$, $t = 17\,h$); ■ experiment; — theory.

wards the anode. Thus Ga is enriched at the anode side, independent of the ratio of the diffusion coefficients of Co and Ga [71].

5.6 Conclusion

In this chapter we have outlined the basics of diffusion processes in oxides. We have started in Sect. 5.2 with the so-called defect chemistry which describes all defect formation processes by quasi-chemical reactions and the corresponding equilibria. In this way, a quantitative calculation of the defect fractions in an oxide as a function of the intensive thermodynamic variables temperature, T, and oxygen partial pressure, p_{O_2}, is possible. The most important reaction is the incorporation of oxygen into the oxide which results in the formation of a non-stoichiometric oxide, either with oxygen excess or oxygen deficit. In the most simple cases, we obtain typical regimes in the p_{O_2}-dependence of the defect fractions. In each regime only two oppositely charged defects dominate which exhibit a power-law dependence on p_{O_2} with a typical exponent (Kröger-Vink-diagram, see Fig. 5.4).

In Sect. 5.3, the basic diffusion processes in oxides, vacancy diffusion and interstitial diffusion, have been considered. Self-diffusion and impurity diffusion were discussed for oxides with dominating cation disorder and for oxides with dominating oxygen disorder. Special emphasis was put on the role of defect-defect interactions, such as the formation of impurity–vacancy pairs. Chemical diffusion was treated in Sect. 5.4, and in Sect. 5.5 diffusion in oxides exposed to external forces was analysed. In particular the latter section shows that – apart from a fundamental interest – diffusion in oxides is of great practical importance, e.g. for long-term degradation processes of oxides in technical applications, such as fuel cells, sensors etc..

Finally it should be mentioned that several important topics concerning diffusion in oxides could not be discussed in detail in this chapter. Some of them are:

Creep of oxides: Mass transport in oxides due to mechanical forces is determined by the slowest moving species, which are the oxygen ions in oxides with cation disorder and the cations in oxides with oxygen disorder. Thus, measurements of the creep rate as a function of stress provide not only data on the mechanical strength of an oxide but they yield also information on the diffusivities of the minority defects (see e.g. [31]).

Solid state reactions between oxides: The formation of ternary oxides, for example the spinel formation $MgO + Al_2O_3 \rightarrow MgAl_2O_4$, proceeds by counter-diffusion of Mg^{2+} and Al^{3+} through the spinel $MgAl_2O_4$ resulting in parabolic growth laws for the thickness of the spinel layer, $\Delta x(t) = (2k_p t)^{1/2}$. The parabolic rate constant, k_p, is a function of the diffusion coefficients of both cations [75].

Oxidation of metals: Diffusion controlled growth of an oxide layer on a metal is determined by ambipolar diffusion of cations and/or oxygen anions and electronic defects through the oxide. As shown by Wagner [45], the growth rate of the oxide layer is also determined by a parabolic rate law, where the parabolic rate constant, k_p, is given as a function of the diffusion coefficients of cations and anions and the electronic transference number. If the oxide is anisotropic the parabolic rate constant depends on the orientation of the oxide relative to the metal substrate. This case was found in a recent investigation on the oxidation of the intermetallic, ordered compound CoGa [76, 77] where only Ga is oxidised and β-Ga_2O_3 is formed.

5.7 Appendix

We consider a binary oxide $A_{1-\delta}O$ with cation disorder. Using $x_A + x_V = 1$, the thermodynamic factor $\partial \ln a_A / \partial \ln x_A$ can be rewritten as:

$$\frac{\partial \ln a_A}{\partial \ln x_A} = -x_A \cdot \frac{\partial \ln a_A}{\partial x_V}$$

Considering the equilibrium for the reaction $A + \frac{1}{2}O_2 \rightleftharpoons AO$, $K = 1/(a_A \cdot a_{O_2}^{1/2})$, the activity a_A can be expressed in terms of a_{O_2}:

$$\frac{\partial \ln a_A}{\partial \ln x_A} = \frac{1}{2} \cdot \frac{x_A}{x_V} \cdot \frac{\partial \ln a_{O_2}}{\partial \ln x_V}$$

As shown in Sect. 5.2.1, the vacancy fraction shows a simple power law dependence on a_{O_2}, $x_V = \text{const} \cdot (a_{O_2})^{1/m}$, where m is the typical exponent for the dominating disorder type. For differently charged cation vacancies, $V_A^{\alpha'}$, m is given by $m = 2 + 2\alpha$, resulting in

$$\frac{\partial \ln a_\mathrm{A}}{\partial \ln x_\mathrm{A}} = \frac{1}{2} \cdot \frac{x_\mathrm{A}}{x_\mathrm{V}} \cdot (2 + 2\alpha) \quad .$$

With this expression for the thermodynamic factor, the chemical diffusion coefficient $\tilde{D}$ in (5.30) can be written as

$$\tilde{D} = \frac{D_\mathrm{A} \cdot x_\mathrm{A}}{x_\mathrm{V}} \cdot t_\mathrm{el} \cdot (1 + \alpha) \quad .$$

Finally, we use the jump balance, $D_\mathrm{A} x_\mathrm{A} = D_\mathrm{V} x_\mathrm{V}$, and obtain

$$\tilde{D} = D_\mathrm{V} \cdot (1 + \alpha) \cdot t_\mathrm{el} \quad .$$

If $t_\mathrm{el} = 1$ this expression simplifies to (5.31).

Notation

a_i	chemical activity of component i
a_{O_2}	chemical activity of oxygen
A	metal A in the binary oxide AO or the ternary oxide (A,B)O
A_res	residual activity
A_sect	activity during sectioning
B	metal B in the ternary oxide (A,B)O
c_i	concentration of species i
D_i	diffusion coefficient of species i
D_A	self-diffusion coefficient of A
$D_{\mathrm{A_i}}$	interstitial self-diffusion coefficient
D_V	vacancy self-diffusion coefficient
$\tilde{D}$	chemical diffusion coefficient
e'	electron
f_0	geometrical correlation factor
f_B	impurity correlation factor
F	Faraday constant
$\mathrm{h}^\bullet$	electron hole
j_i	diffusion flux of species i
k	surface exchange coefficient
k_B	Boltzmann constant
K	equilibrium constant
L_{ij}	transport coefficient
p	pressure
p_{O_2}	oxygen partial pressure
$p^*_{\mathrm{O}_2}$	oxygen partial pressure at the stoichiometric point ($\delta = 0$)
R	universal gas constant
S^q_p	structure element with excess charge q in sublattice p
t	time
T	temperature

t_{el}	electronic transference number
V_{m}	molar volume
x	position
x_i	molar fraction of species i (identical to $[i]$)
z	position in the moving reference frame
z_i	formal charge of species i
$z_{i,\mathrm{eff}}$	effective charge of species i
δ	non-stoichiometry of the oxide $\mathrm{A}_{1-\delta}\mathrm{O}$
η_i	electrochemical potential of species i
μ_i	chemical potential of species i
μ_{O_2}	chemical potential of oxygen
σ	electrical conductivity
Φ	electrical potential
ω_i	jump rate of a vacancy in jump of type i

References

1. H. Schmalzried: *Solid State Reactions* (VCH, Weinheim 1981)
2. H. Schmalzried: *Chemical Kinetics of Solids* (VCH, Weinheim 1995)
3. J. Philibert: *Atom Movements – Diffusion and Mass Transport in Solids* (Les Editions de Physique, Les Ulis 1991)
4. P. Kofstad: *Nonstoichiometry, Diffusion and Electrical Conductivity in Binary Oxides* (Wiley, New York 1972)
5. A.R. Allnatt, A.B. Lidiard: *Atomic Transport in Solids* (Cambridge University Press, Cambridge 1993)
6. *Diffusion in Materials*, ed by A.L. Laskar, J.L. Bocquet, G. Brebec, C. Monty (Kluwer Academic Publishers, Dordrecht 1990)
7. C. Wagner, W. Schottky: Z. Phys. Chem. **B11**, 163 (1930)
8. J. Frenkel: Z. Physik **53**, 652 (1926)
9. F.A. Kröger: *Chemistry of Imperfect Crystals* (North-Holland, Amsterdam 1964)
10. R. Dieckmann, H. Schmalzried: Ber. Bunsenges. Phys. Chem. **81**, 344 (1977)
11. R. Subramanian, S. Tinkler, R. Dieckmann: J. Phys. Chem. Solids **5**, 69 (1994)
12. F.-H. Lu, S. Tinkler, R. Dieckmann: Solid State Ionics **62**, 39 (1993)
13. J.-H. Lee, M. Martin, H.-I. Yoo: J. Phys. Chem. Solids **61**, 1597 (2000)
14. M.L. Volpe, J. Reddy: J. Chem. Phys. **53**, 1117 (1970)
15. R.A. Perkins, R.A. Rapp: Metall. Transact. **4**, 193 (1973)
16. H. Boussetta, C. Monty: J. Phys. Chem. Solids **49**, 369 (1988)
17. R. Dieckmann: Z. Phys. Chem. NF **107**, 189 (1977)
18. M. Schroeder, M. Martin: Z. Phys. Chem. **207**, 1 (1998)
19. M. Martin, S. Dorris: Ber. Bunsenges. Phys. Chem. **91**, 779 (1987)
20. M. Martin: Mat. Sci. Rep. **7**, 1 (1991)
21. R. Schmackpfeffer, M. Martin: Phil. Mag. A **68**, 747 (1993)
22. A.R. Allnatt, A.B. Lidiard: Rep. Prog. Phys. **50**, 373 (1987)
23. R.W. Grimes, S.P. Chen: J. Phys. Chem. Solids **61**, 1263 (2000)
24. J. Janek, M. Martin, H.-I. Yoo: Ber. Bunsenges. Phys. Chem. **98**, 655 (1994)

25. *Secondary Ion Mass Spectrometry: Principles and Applications*, ed by J.C. Vickerman, A. Brown, N.M. Reed (Clarendon Press, Oxford 1989)
26. J. Crank: *The Mathematics of Diffusion* (Oxford University Press, Oxford 1975)
27. P. Fielitz, G. Borchardt: Solid State Ionics **144**, 71 (2001)
28. R.A. De Souza, J.A. Kilner: Solid State Ionics **106**, 175 (1998)
29. T. Ishigaki, S. Yamaushi, K. Kishio, J. Mizusaki, K. Fueki: J. Solid State Chem. **73**, 179 (1988)
30. Yet-Ming Chiang, Dunbar Bernie III, W.D. Kingery: *Physical Ceramics*, Chap. 5 (Wiley, New York 1977)
31. J.L. Routbort, K.C. Goretta, R.E. Cook, J. Wolfenstine: Solid State Ionics **129**, 53 (2000)
32. M. Weller: Z. Metallk. **84**, 381 (1993)
33. A. Hammou, J. Guindet. In: *The CRC Handbook of Solid State Electrochemistry*, ed by P.J. Gellings, H.J.M. Bouwmeester (CRC Press, Boca Raton 1996) p 407
34. S.P.S. Badwal: Solid State Ionics **52**, 23 (1992)
35. P.S. Manning, J.D. Sirman, R.A. De Souza, J.A. Kilner: Solid State Ionics **100**, 107 (1997)
36. H. Solmon, J. Chaumont, C. Dolin, C. Monty: Ceram. Trans. **24**, 175 (1991)
37. M. Kilo, G. Borchardt, S. Weber, S. Scherrer, K. Tinschert: Ber. Bunsenges. Phys. Chem. **101**, 1361 (1997)
38. M. Kilo, G. Borchardt, B. Lesage, S. Weber, S. Scherrer, M. Martin, M. Schroeder. In: *SOFC-VII*, PV 2001-16, ed by H. Yokokawa, S.C. Singhal (The Electrochemical Society Proceedings Series, Pennington NJ 2001) p 275
39. B.C.H. Steele: J. Materials Sci. **36**, 1053 (2001)
40. T. Ishihara, J.A. Kilner, M. Honda: Solid State Ionics **113-115**, 593 (1998)
41. O. Schulz, M. Martin, C. Argirusis, G. Borchardt: Phys. Chem. Chem. Phys. **5**, 2308 (2003)
42. O. Schulz, S. Flege, M. Martin. In: *SOFC-VIII*, PV 2003-07, ed by S.C. Singhal, M. Dokiya (The Electrochemical Society Proceedings Series, Pennington NJ 2003) p 304
43. R.A. De Souza, J. Maier: Phys. Chem. Chem. Phys. **5**, 740 (2003)
44. S.R. de Groot, P. Mazur: *Non-Equilibrium Thermodynamics* (North-Holland, Amsterdam 1962)
45. C. Wagner: Z. Phys. Chem. B **21**, 25 (1933)
46. F. Morin, R. Dieckmann: J. Phys. Chem. Solids **51**, 283 (1990)
47. A. Belzner, T.M. Gür, R.A. Huggins: Solid State Ionics **57**, 327 (1992)
48. I. Yasuda, M. Hishinuma: Solid State Ionics **80**, 141 (1995)
49. C.-R. Song, H.-I. Yoo: Solid State Ionics **124**, 289 (1999)
50. I. Denk, U. Traub, F. Noll, J. Maier: Ber. Bunsenges. Phys. Chem. **99**, 798 (1995)
51. *The CRC Handbook of Solid State Electrochemistry*, ed by P.J. Gellings, H.J.M. Bouwmeester (CRC Press, Boca Raton 1996)
52. M. Martin, H. Schmalzried: Ber. Bunsenges. Phys. Chem. **89**, 124 (1985)
53. M. Martin: Z. Physik. Chem. NF **162**, 245 (1989)
54. S. Dorris, M. Martin: Ber. Bunsenges. Phys. Chem. **94**, 721 (1990)
55. N.L. Peterson, W.K. Chen, D. Wolf: J. Phys. Chem. Solids **41**, 709 (1980)
56. K.D. Becker, V. von Wurmb: Z. Phys. Chem. NF **149**, 77 (1986)
57. M. Martin: Ber. Bunsenges. Phys. Chem. **91**, 772 (1987)

58. K. Hoshino, N. Peterson: J. Phys. Chem. Solids **46**, 229 (1987)
59. H. Schmalzried, W. Laqua, P.L. Lin: Z. Naturforsch. **34a**, 192 (1979)
60. H. Schmalzried, W. Laqua: Oxid. Met. **15**, 339 (1981)
61. J.-O. Hong, O. Teller, M. Martin, H.-I. Yoo: Solid State Ionics **123**, 75 (1999)
62. G. Petot-Ervas, C.J. Petot: J. Phys. Chem. Solids **51**, 9016 (1990)
63. M. Martin: Ceramic Transactions **24**, 91 (1991)
64. M. Martin, R. Schmackpfeffer: Solid State Ionics **72**, 67 (1994)
65. J. Janek, M. Martin: Ber. Bunsenges. Phys. Chem. **98**, 665 (1994)
66. F. Lange, M. Martin: Ber. Bunsenges. Phys. Chem. **101**, 1 (1997)
67. M. Schroeder, M. Martin: Defect and Diffusion Forum **143–147**, 1683 (1997)
68. M. Schoeder, J.-H. Lee, M. Martin: Solid State Ionics **101–103**, 403 (1997)
69. D. Monceau. M. Filal, M. Tebtoub, C. Petot, G. Petot-Ervas: Solid State Ionics **73**, 21 (1994)
70. O. Teller, M. Martin: Solid State Ionics **101–103**, 475 (1997)
71. O. Teller, M. Martin: Ber. Bunsenges. Phys. Chem. **101**, 1377 (1997)
72. J.-O. Hong, H.-I. Yoo: Solid State Ionics **113–115**, 265 (1998)
73. M. Martin: Solid State Ionics **136–137**, 331 (2000)
74. W.K. Chen, N.L. Peterson: J. Phys. Chem. Solids **34**, 1093 (1973)
75. C. Wagner: Z. Anorg. Allg. Chem. **236**, 320 (1938)
76. U. Koops, D. Hesse, M. Martin: J. Mater. Res. **17**, 2489 (2002)
77. U. Koops, M. Martin: Z. Anorg. Allg. Chem. **629**, 1688 (2003)

6 Diffusion in Metallic Glasses and Supercooled Melts

Franz Faupel and Klaus Rätzke

6.1 Introduction

A wide variety of materials ranging from oxide glasses to polymers can solidify as glasses rather than crystals. While diffusion plays an important role in all media at elevated temperatures, diffusion in glasses is of particular interest. The metastability of these materials makes them prone to various rearrangement processes such as structural relaxation, phase separation and crystallization. In the supercooled liquid state diffusion is very important in connection with the glass transition, which appears to be a kinetic phenomenon [1]. With the recent discovery of novel bulk-glass-forming alloys, exhibiting high stability against crystallization in the supercooled state [2,3], the dynamics of the glass transition could also be studied in metallic systems, which are the paradigm of dense random packing. Stimulated by the development of bulk metallic glasses and advances in computer simulation, recent progress in the understanding of the diffusion mechanisms in metallic glasses and supercooled melts has been considerable. For recent reviews the reader is referred to [4,5]

In this chapter, after discussing some general aspects of diffusion in non-crystalline matter, which are not related to a particular class of materials, we focus on metallic glass-forming systems. Metallic glasses are so-called 'fragile glasses'. Unlike silica and other strong inorganic glasses fragile glasses exhibit a glass transition in a narrow temperature range, where marked changes in physical properties can be observed. Emphasis is placed on results from radiotracer measurements. Moreover, we frequently refer to results from computer simulations which provide valuable insight into the atomic dynamics. The following section briefly recalls important characteristics of diffusion in crystalline solids. Normal liquids well above the melting point are treated in Sect. 6.3. In this context, the free-volume model and the Stokes-Einstein relation are introduced. The transition from liquid-like continuous small motion to thermally activated hopping is the subject of Sect. 6.4. In this connection the mode-coupling theory and a recent extension to medium-assisted hopping in the glassy state are discussed. The concept of medium-assisted hopping implies strongly collective diffusion and is applied to the interpretation of isotope effect measurements in metallic glasses in Sect. 6.5. Relaxation phenomena that are pertinent to the understanding of diffusion near the glass

transition temperature are examined in Sect. 6.4, too. Furthermore, consequences of a distribution of activation energies are considered. In Sect. 6.5 atomic transport in conventional metallic glasses is critically reviewed, and measurements of the pressure and mass dependence of diffusion are presented. These measurements point to highly cooperative hopping processes in fully relaxed metastable glasses. The effect of excess volume, quenched in from the liquid state, is also addressed. Sect. 6.6 covers diffusion in supercooled melts of the novel bulk-glass-forming alloys. Of particular interest are the changes in the atomic dynamics concomitant with the liquid-to-glass transition. It will be shown that from the microscopic point of view diffusion in the deeply supercooled liquid state is solid-like, taking place by thermally activated collective processes. Microscopic viscous flow via atomic collisions is observed to set in well above the caloric glass transition temperature in full accord with the mode coupling scenario. In this section we also discuss very recent diffusion and isotope effect data in the equilibrium melt of a particularly stable metallic glass-forming alloy. Diffusion measurements from the glassy to the equilibrium liquid state have not been possible so far. It is demonstrated that even in the equilibrium melt the atomic dynamics are highly collective and still depart strongly from the hydrodynamic regime of uncorrelated binary collisions. A summary is given in Sect. 6.7.

6.2 Characteristics of Diffusion in Crystals

Unlike diffusion in amorphous matter, transport in crystalline solids is well understood, at least as far as self-diffusion and diffusion of trace impurities are concerned (see Chap. 1). Small solute atoms occupy interstitial sites and perform thermally activated jumps between equilibrium positions (Chap. 1, Fig. 1.8). The temperature dependence of interstitial diffusion obeys the well known Arrhenius law (Chap. 1). Diffusion coefficients for interstitials approach values in liquids near the melting point ($\tilde{=}10^{-10}\,\mathrm{m}^2/\mathrm{s}$). A representative value for the pre-exponential factor D_0 in metals is $10^{-6}\,\mathrm{m}^2/\mathrm{s}$.

Large impurities substitute for solvent atoms in the lattice. It is now well established that diffusion of these substitutional solutes and self-diffusion in most crystalline solids generally proceeds via vacancies (Chap. 1). For a vacancy mechanism (Chap. 1, Fig. 1.9) one again ends up with an Arrhenius law. It has to be pointed out, however, that the activation enthalpy now contains the additional contribution for the formation of a vacancy, which is of the same order of magnitude as the migration enthalpy (Chap. 1, (1.56)). Consequently, substitutional diffusion is many orders of magnitude slower than interstitial diffusion. Moreover, an additional term arising from the formation entropy enters into D_0 (Chap. 1, (1.57)). D_0 is typically of the order of $10^{-4}\,\mathrm{m}^2/\mathrm{s}$. As discussed in Chap. 1, a correlation factor f comes into play for indirect diffusion of tracer atoms via vacancies. If there is no interaction between tracer atoms and vacancies, specifically if the tracer is a self isotope

of the host, f is an additional geometry constant in D_0 which can be estimated as $f \cong 1 - 2/Z$ (Chap. 1, (1.58)). We note that f is of the order of unity in close packed crystals. Impurity-vacancy binding can significantly lower the correlation factor for impurities provided these are strongly diluted [6].

In view of the great success of the vacancy model for diffusion in crystals, many investigators also invoked vacancy-like defects to explain diffusion in glasses and even in liquids. While there is general agreement now that solid-like vacancies do not exist in liquids (Sect. 6.3), their role in metallic glasses is still a controversial issue in literature (Sect. 6.5.2).

6.3 Diffusion in Simple Liquids

We have seen in the preceding section that diffusion in crystals occurs by very infrequent large jumps from one lattice point to a neighboring site. The other extreme is a dilute gas, where all molecules fly freely between frequent binary collisions. According to the kinetic theory of gases in the Chapman-Enskog formulation [7], the diffusivity is determined by the mean free path λ and the collision frequency ν or the mean velocity $\overline{v}$ according to

$$D = \frac{1}{3}\nu\lambda^2 = \frac{1}{3}\overline{v}\lambda \quad . \tag{6.1}$$

In air at standard temperature and pressure ($\overline{v}$ = speed of sound, $\lambda = 300$ molecular diameters) (6.1) yields $D \cong 10^{-5}\,\mathrm{m}^2/\mathrm{s}$ for an average molecule.

The properties of liquids are somewhere in between those of crystalline solids and gases. Liquids are almost as compact as solids and they exhibit a pronounced short-range order, which is reflected in the pair correlation function $g(r)$ (see Fig. 6.1). The latter describes the probability of finding an atom at a distance $(r, r + \mathrm{d}r)$ from a given atom. $ng(r)\mathrm{d}V$ is the average number of atoms in the volume $\mathrm{d}V$ at a distance r, where n is the number density. The Fourier transform of $g(r)$, the structure factor $S(q)$, can be measured with x-rays and neutrons (see Chap. 3). If the atoms move, the correlation between two given atoms decays. The so-called Van Hove space-time correlation function $G(r,t) = G_\mathrm{s}(r,t) + G_\mathrm{d}(r,t)$ is related by Fourier transformation to the dynamical structure factor, which is accessible to neutron scattering. The self and distinct parts G_s and G_d represent the probability that a given particle or some other atoms, respectively, will be at (r,t) when the given atom is at $r = 0$ at $t = 0$.

Diffusion in liquids [8] is much faster than in solids because of the more open structure. A typical melting-point value of D is $10^{-9}\,\mathrm{m}^2/\mathrm{s}$. Unlike in solids, the temperature dependence of D is weak. The early experimental findings that diffusion rates in liquids could be fitted to an exponential dependence on $1/T$ over short temperature ranges and the compact structure of liquids led to an identification of the mechanism with that of vacancy diffusion in solids. However, there is evidence now from various experimental

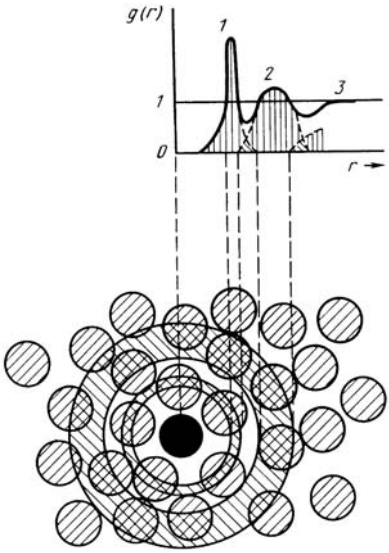

Fig. 6.1. Scheme of a monoatomic liquid and the corresponding pair correlation function $g(r)$. Note the pronounced peak at the nearest-neighbor distance r_1.

methods [8], including neutron and x-ray techniques, Mößbauer spectroscopy, and nuclear magnetic resonance, as well as from molecular dynamics calculations [9], that jumps of the size of lattice constants do not take place in simple liquids. Diffusion rather proceeds continuously by frequent small motions. The atoms create their macroscopic displacement from a very large number of collisions on a time scale of 10^{-12} s, and the mean free path for diffusion is at least one order of magnitude smaller than the atomic spacing. Moreover, the pressure dependence of diffusion in liquids is much smaller than predicted for a vacancy-like mechanism [7,10]. We shall see in Sect. 6.5.4 that the pressure dependence of diffusion in some metallic glasses is not consistent with a vacancy-like mechanism, either.

Apparently, transport in simple liquids such as metallic and van der Waals liquids is much more gas-like than solid-like. Kinetic theories of self-diffusion that are based upon the classical gas equation (6.1), Dulong Petit's rule, and geometrical arguments for the mean free path predict

$$D \propto \frac{1}{\sqrt{m}} T^{3/2} \quad . \tag{6.2}$$

Equation (6.2) reproduces the approximate temperature and pressure dependence of D quite successfully in many simple liquids [7].

Molecular dynamics simulations [11] have confirmed a temperature dependence $D \propto T^n$ where n was found to be between 1.7 and 2.3. Such simulations also allow one to investigate the time dependence of the mean square displacement $\langle r^2(t) \rangle$ on a microscopic level. A transition from gas-like 'free flight' for very short times ($t < 10^{-13}$ s) to Brownian displacement $\langle r^2(t) \rangle = 6Dt$ for

long times has been observed, which was also found experimentally, e.g., by neutron scattering [12]. In the transition interval many-body interactions and memory effects play a role, and the motion of a given atom is correlated with the motion of its neighbors. This collective behavior is the subject of mode-coupling theories and becomes more pronounced in supercooled liquids, where a dynamical glass transition is predicted at a critical temperature T_c (see below).

High precision isotope-effect measurements of self diffusion in liquid Sn under microgravity conditions [13] clearly show that cooperative effects substantially influence the diffusive motion of single atoms even at temperatures well above the melting point (232°C for Sn). At 800°C an isotope effect of $E \equiv (D_\alpha/D_\beta - 1)/(\sqrt{m_\beta/m_\alpha} - 1) = 0.7$ was found. It indicates only relatively small deviations from ideal single-particle motion, which is characterized by $D \propto m^{-1/2}$ (see (6.2)) and $E = 1$. At 250°C however, E drops to a value of 0.3, reflecting a high degree of collectivity. Here the mass effect is strongly reduced by correlated motion of the tracer atom and surrounding particles. The departure from gas-like uncorrelated binary collisions at low temperatures is to be expected in view of the decrease of free volume. It is shown in Sect. 6.5.3 that diffusion in structurally relaxed metallic glasses requires an even higher degree of cooperativity, causing a very small isotope effect.

The concept of free volume results from a crude but physically plausible approach. It has provided a deeper understanding of transport phenomena and the liquid-to-glass transition. Free-volume models [14] have affinities with kinetic theories and attribute most of the change in the diffusivity to thermal expansion. But unlike simple kinetic theories diffusion is visualized as a cooperative process. The basic assumption is that each molecule resides within a 'cage' that is stable for times much longer than the vibration times. A molecule is regarded as being able to move out of the 'cage' as soon as random molecular movements produce a void, larger than some critical size v^*, into which it can move, there being no energy barrier to the movement.

From this notion it is easy to show that the diffusion coefficient has the form

$$D = D_0 \exp\left(-\frac{\gamma v^*}{v_f}\right) \tag{6.3}$$

where the exponential term represents the probability that the redistribution of free volume leads to fluctuations greater than v^*. v_f is the mean free volume per molecule, and γ is an overlap factor, typically between 0.5 and 1. It considers that the same free volume is available to more than one molecule. The temperature dependence of D is determined by $v_f(T)$, whereas the pre-exponential factor D_0 is a much weaker function of T. Cohen and Turnbull [14] assumed that v_f may be expressed approximately as

$$v_f = \alpha \overline{V}(T - T_0) \quad . \tag{6.4}$$

In this simple approach T_0 is the temperature at which the free volume disappears, α and $\overline{V}$ are the mean values of the coefficient of thermal expansion

and the molecular volume over the temperature range of interest, respectively. Although it is a weak point of the model that T_0 is found to be well above absolute zero, (6.3) and (6.4) give a relatively good account of the temperature dependence of D and of the viscosity (cf. Sect. 6.4) in many liquids. An even better description has been obtained in a later development of the theory by Cohen and Grest [15]. However, additional parameters were introduced to describe $v_\mathrm{f}(T)$.

Free-volume models have also been applied extensively to transport in polymers and also in metallic glasses (see Sect. 6.5).

In liquids the viscosity η is closely related to the diffusivity. Usually at high temperatures the generalized Stokes-Einstein equation

$$D = \frac{k_\mathrm{B}T}{a\eta} \tag{6.5}$$

is obeyed, where the parameter a is almost independent of T. The hydrodynamic theory in the elementary Stokes-Einstein form, combining the theory of Brownian motion ($\Lambda_0 = D/k_\mathrm{B}T$) with Stokes law for the mobility Λ_0 of a big spherical particle of diameter d in a continuous viscous fluid ($\Lambda_0 = 1/(3\pi d\eta)$), yields $a = 3\pi d$. Various hydrodynamic theories are concerned with relationships between η and D for more complicated cases, including non-spherical molecules and concentrated solutions, where correlation effects, which are not accounted for in Einstein's expression of Λ_0, come into play [8].

At high viscosities, for instance in supercooled liquids near the glass transition temperature, diffusion is eventually governed by activated hopping mechanisms (Sect. 6.4). In this regime, as in crystalline solids, diffusion and viscous flow are decoupled.

Several other theories have been developed for diffusion in ordinary liquids, the discussion of which is beyond the scope of this chapter. The reader is referred to reviews by Nachtrieb [16], Tyrell and Harris [8], Shimoji and Itami [11], and DeBenedetti [17].

6.4 General Aspects of Mass Transport and Relaxation in Supercooled Liquids and Glasses

In the foregoing section we have been concerned with molecular transport in normal liquids at high temperatures under conditions of complete ergodicity. Upon supercooling the viscosity increases markedly until at the so-called glass-transition temperature macroscopic flow freezes in. Glasses exhibiting this behavior are called 'fragile'. By contrast, in some glasses termed 'strong' all physical properties change so gradually during cooling that no particular temperature can be marked as border between the undercooled liquid and the glass. Typical representatives of strong glasses are oxide glasses [18]. Fragile behavior is observed in organic glasses and conventional metallic glasses. The

new bulk metallic glasses are significantly stronger than the conventionally ones [1].

Every class of material can be transformed into an amorphous solid (without crystallinity) if the experimental parameters are adjusted to the dynamics of the system. While, e.g., quenching rates well above 10^{10} K/s are required for systems consisting of spherical molecules such as rare gases, many polymers undergo always a glass transition on cooling. Generally, glasses are not in a well defined metastable state after quenching, but exhibit irreversible relaxation processes, also referred to as 'physical aging' in polymers, which are accompanied by annealing out of excess volume and changes in the chemical short-range order.

T_g is often somewhat arbitrarily defined as the temperature where $\eta = 10^{12}$ Pa s. This value corresponds to solid-like behavior on ordinary time scales and results in T_g values close to the caloric glass transition temperature which is determined by the additional degrees of freedom above the glass transition [19]. In the glassy state the temperature dependence of η follows an Arrhenius law. Fragile glasses, particularly polymers and amorphous metals generally obey the Vogel-Fulcher equation

$$\eta = \eta_0 \exp\left(\frac{B_0}{T - T_\mathrm{VF}}\right) \tag{6.6}$$

in a certain temperature range near T_g. η_0, B_0 and the Vogel-Fulcher temperature T_VF are constant parameters. T_g depends on the sample history, for instance on the quenching rate. Equation (6.6) can be derived analogously to (6.3). Within the free-volume concept, T_VF is identical with the temperature T_0 (see (6.4)) where v_f vanishes. The functional form of the Vogel-Fulcher law can also be shown to be a direct consequence of cooperativity in the movement of the molecules [20] and can also be derived from the more advanced mode coupling concept discussed below.

The glass-to-liquid transition is closely related to the relaxation of shear stress and dielectric properties, for example. The corresponding relaxation function $\Phi(t)$ for this so-called α relaxation can be described by an universal empirical expression

$$\Phi(t) = \exp\left[-(t/\tau)^\beta\right] \quad . \tag{6.7}$$

Here β is usually in the range between 0.3 and 0.7 depending on the material. This 'stretched exponential' or Kohlrausch behavior [19] departs markedly from simple Debye relaxation ($\beta = 1$), which is characterized by a thermally activated process with a single activation energy. $\Phi(t)$ drops much faster for short times and has a pronounced long time tail typical of transport processes in disordered media (see below). The relaxation function $\Phi(t)$ obeys a time-temperature scaling principle [21], i.e. relaxation functions measured at different temperatures fall on a single 'master curve' $\Phi(t/\tau(T))$.

In addition to the slow α relaxation, which involves long range atomic transport, there is a second fast process in amorphous media referred to as β

relaxation. It can be associated with local rearrangements of molecules. The time-temperature scaling obeys an Arrhenius law through the glass transition. At high temperatures the α relaxation becomes increasingly faster until at a certain temperature above T_g α and β relaxation coincide, i.e. β relaxation becomes part of the flow process. In polymers β relaxation has been attributed to well defined local mechanisms like movements of chain segments or side chain rotations [22], but β relaxation has also been observed in metallic glasses (see Sect. 6.5.1).

So far we have discussed theoretical descriptions of the glass transition and the dynamics around T_g that are related to a critical temperature below T_g, for example to T_{VF}, and to a true thermodynamical transition. On the other hand, recent mode coupling theories [23,24] predict a dynamical phase transition at a critical temperature T_c, well, typically 30–150 K, above T_g. They are based on the hydrodynamic theory of liquids. The classical theory is linear, however, and is only valid exactly in the limit of long times and wavelengths, whereas the glass transition is characterized by a freezing-in of density fluctuations with finite wavelengths due to strong interactions between the atoms or molecules in a liquid. Therefore, non-linear coupling between density-density correlations, the relevant modes of the theory, are introduced, and memory effects are taken into account.

Upon cooling a dense liquid the aforementioned (Sect. 6.3) cage effect, viz. the trapping of molecules by surrounding particles, which induces time dependent potential barriers, becomes more and more effective and may eventually, at a critical temperature T_c, lead to a partial localization of molecules or clusters of molecules in a metastable state. If activated hopping between metastable states (jump diffusion) can be neglected, a sharp transition from an ergodic to a non-ergodic state occurs. This transition is reflected in an algebraic divergence of the viscosity at T_c. Below T_c only local rearrangement of molecules but no transport over macroscopic distances is possible. Real systems are always expected to return to ergodicity at sufficiently long times as a consequence of hopping diffusion, not included in the original mode-coupling theory.

The predictions of mode coupling theory have been tested in numerous systems resulting in a qualitative and sometimes even quantitative agreement of microscopic dynamics with the theory. For a review we refer to [24].

Recently, thermally activated hopping processes have been incorporated into mode-coupling theories [25]. It has been shown [23] that the viscosity may exhibit a Vogel-Fulcher-like dependence in a certain temperature range below T_c. In particular, the cross-over to an Arrhenius behavior that is experimentally observed at $T \cong T_g$ has been predicted for sufficiently strong coupling [25]. In these terms the Arrhenius law $\eta \propto \exp(H/k_B T)$ results from the dynamics of the β process. As mentioned earlier the β process reflects the decay of local density fluctuations and does not freeze in below T_c. Local displacements, i.e. short wavelength clusters, induce a disturbance in the sur-

rounding medium that may give rise to rearrangements of long wavelengths in a macroscopic volume and induce a feedback effect on the original cluster. This may lead to a medium-assisted hopping process, caused by the nonlinear coupling between longitudinal currents of quite different wavelengths but identical time dependence, being governed by the dynamics of β relaxation in the initial stage of the diffusion process. In this extended mode coupling theory, transport in the glassy state is a highly cooperative process on all length scales. We shall see in Sect. 6.5.3 that isotope effect measurements of diffusion in a structurally relaxed metallic glass strongly support this view.

While atomic transport in glasses obviously proceeds via jump diffusion, the disordered nature of these materials gives rise to further peculiarities that are absent in crystalline solids. Apart from the difficulty in defining defects like vacancies or interstitials, which are directly related to the existence of a lattice and govern diffusion in crystals, activation barriers, site energies, and jump distances exhibit a certain distribution around their average values. Modeling of these phenomena in three dimensions requires drastic simplifications (see Chap. 18 and [26]). On the other hand, the salient features are already revealed by a separate study of the different types of disorder and under the assumption of a Gaussian distribution function.

Disorder in the jump distance only affects the pre-exponential factor D_0 (see Chap. 1) and usually does not induce a significant perturbation unless the spectrum is very broad [27]. The effect of a random distribution of site energies is illustrated in Fig. 6.2a. The diffusivity D is smaller than that for a sharp site energy, and the apparent activation energy is larger because trapping in the deep wells cannot be avoided. Conversely, randomness in the barrier heights (Fig. 6.2b) enhances diffusion in three dimensions, where the high barriers can be by-passed. Here D becomes time dependent. For short times or high frequencies, i.e. short-range diffusion, the small activation enthalpies essentially govern the diffusion behavior. Long-range diffusion, however, is mainly controlled by the high barriers and, thus, proceeds slower.

In real glasses a combination of site and saddle point disorder is expected (Fig. 6.2c). At high frequencies both effects cancel out, but for long times the deep traps dominate. The deviations from crystal-like linear Arrhenius behavior without frequency dependence go to zero for $T \to \infty$ and are most pronounced at low temperatures.

The time dependence of D causes anomalous diffusion on a certain time or frequency scale where the mean square distance walked by the diffusing particle increases sublinearly instead of linearly with time (see Chaps. 10, 18, 19). Disorder related anomalous diffusion is well known from ionic conduction in glasses (see Chaps. 20 and 21 and [28]) and has also been observed for hydrogen in metallic glasses. At room temperature the range of strong frequency dependence of the hydrogen mobility proved to be between 10^7 and $10^{11}\,\mathrm{s}^{-1}$ [29].

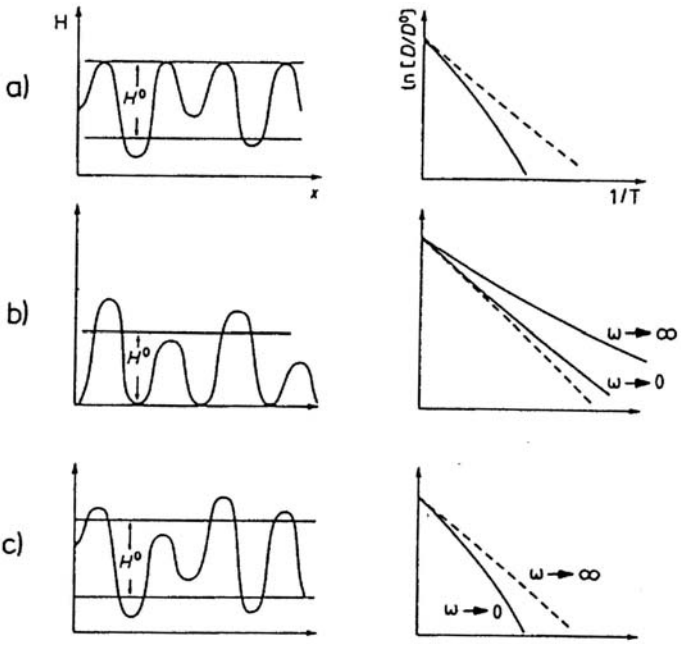

Fig. 6.2. Effect of (**a**) site and (**b**) barrier height disorder and (**c**) of their combination on diffusion in three dimensions (schematically). The straight dashed lines in the Arrhenius plots represent the average activation energy H^0. D^0 is the high-temperature limit of the diffusivity D. The behavior at low and high frequencies, ω, corresponding to long and short times, respectively, is indicated (after Kronmüller et al. [30]).

Transport in disordered media with a Gaussian activation-energy distribution around H^0 with variance σ leads to a characteristic temperature law for the zero-frequency diffusion coefficient (long-time limit)

$$D(T, \omega = 0) = D_0 \exp\left(-\frac{H^0}{k_\mathrm{B}T}\right) \exp\left[-\left(\frac{T_0}{T}\right)^2\right] \quad . \tag{6.8}$$

Here $k_\mathrm{B}T_0 = \sigma/\sqrt{2}$ (see e.g. Kronmüller and Frank [30]). For low temperatures and/or large widths of the energy distribution one obtains an $\exp[-(T_0/T)^2]$ variation with temperature. Equation (6.8) has been confirmed by Monte-Carlo simulations [31]. Moreover, Bässler [32], reanalyzing viscosity data of various supercooled liquids, has shown that $\eta(T)$ is proportional to $\exp[(T_0/T)^2]$ over ten decades in η and extending to the glass transition. As expected, the concept fails at high temperatures where the barriers can no longer be regarded as quasi-static.

In summary, there is ample evidence from experiment, theory, and computer simulation that liquid-like diffusion has come to rest in glasses and

that transport is clearly of the jump type. The details of the diffusion mechanisms, in particular the role of defects and the number of atoms or molecules involved certainly depend on the material under consideration.

6.5 Diffusion in Metallic Glasses

6.5.1 Structure and Properties of Metallic Glasses

Metallic glasses of practical importance are always alloys of at least two components because of the ease of crystallization of monoatomic systems (Sect. 6.4). They can essentially be subdivided into two groups [33]: those of the metal-metalloid type and those of the metal-metal type. In the first group transition metals like Fe, Co, Ni, and Pd are alloyed with typically 15–20% of metalloids, such as B, C, P, Si, and Ge. The second group often consists of an early transition metal, e.g. Zr and Nb and a late one, for instance Co, Ni, and Pd. Frequently, especially for technological applications, these elements are used in multicomponent systems.

The structure of amorphous alloys, in particular the absence of extended defects and the inherent free volume, gives rise to a variety of desirable properties and unique property combinations [34]. Metallic glasses can be very ductile, for example, and still exhibit a high flow stress and fracture toughness. The electrical resistivity is large and almost independent of temperature. Magnetic glassy metals are generally characterized by excellent soft magnetic properties. The new bulk metallic glasses can be produced at relatively low cooling rates similar to processing of oxide glasses and hence offer additional applications [35] such as the fabrication of very precise microcomponents, for instance [36].

Various methods have been developed for the preparation of conventional amorphous metals [37]. They can be quenched from the liquid state, e.g., by melt spinning or splat quenching, and can be produced by vapor condensation and sputter deposition. Moreover, it is possible to transform crystalline solids into the amorphous state by solid-state reaction, ion implantation, neutron irradiation, ball milling, high-pressure application, and other techniques [38].

As one would expect, there are close similarities between the structure of glassy and liquid metals, which are also reflected in the pair-correlation function $g(r)$ (Fig. 6.1). The maxima and minima are somewhat more pronounced in amorphous metals and the second peak is split into two subpeaks. Since $g(r)$ is a one-dimensional representation of the unknown three dimensional structure, further modelling is required to reveal the atom arrangement [39]. One approach is based on the dense random packing of hard spheres introduced by Bernal [40]. Here the structure consists of a number of different kinds of polyhedra, the majority of which are tetrahedra and octahedra. This simple model already explains the main features in $g(r)$ for metallic glasses. The subpeaks of the second peak are attributed to atoms occupying

the vertices of two tetrahedra having a common base and to three collinear atoms, respectively. Major improvements have been attained by taking into account chemical short-range order and by sequential computer relaxation of soft spheres [39]. Recent molecular dynamics simulations are based on realistic interatomic potentials and benefit strongly from progress in computer processing speed [41–43].

Chemical short-range order is a common characteristic of amorphous alloys. Partial pair correlation functions indicate that close contact between metalloid atoms is very unlikely in metal-metalloid glasses [44]. In metal-metal glasses atoms of the same kind are nearest neighbors, but nearest neighborhoods between different components are more likely [44].

The pronounced chemical short-range order of most metallic glasses is due to the fact that these systems tend to form strong compounds upon crystallization. Therefore, Gaskell [45] modelled the amorphous structure as a random network of unit cells of the nearest, in composition, crystalline compounds.

Amorphous alloys have also been described in terms of icosahedral packing [46, 47]. In icosahedra, which consist of twenty slightly distorted tetrahedra, twelve atoms are grouped around a central atom. Their local fivefold symmetry is broken up by a disordered entangled array of $+72°$ and $-72°$ disclination lines. The disclinations are associated with sixfold and fourfold symmetries, respectively. They are forced in by 'frustration', viz. the incompatibility of flat space with a space-filling icosahedral crystal.

Most glass forming alloy systems are able to form glasses over an extended composition range. In some cases discontinuities in physical properties are observed, which have been related to structural changes [37]. For instance, a transition from dense random packing to the formation of random networks was proposed for $Fe_{1-x}B_x$ at $x = 0.18$. The above mentioned molecular dynamics simulations have revealed more complex structural transitions in metal-metal glasses [48].

Upon heat treatment amorphous alloys undergo rearrangement processes. Structural relaxation and sometimes also phase separation, which are generally accompanied by drastic and detrimental changes in properties [49], may occur already at temperatures well below T_g. Phase separation, giving rise to inhomogeneities on a scale of some 10 nm, appears to be closely related to the changes in the glassy structure with composition, mentioned above [50, 51].

Structural relaxation affects to a greater or lesser extent all physical properties, specifically structure sensitive quantities such as the viscosity and the diffusion coefficient. Irreversible relaxation takes place when as-prepared samples are heated for the first time at elevated temperatures. On the time scale of this process, there occur also much faster reversible relaxation processes, which are superimposed on the irreversible background. The degree of irreversible relaxation appears to depend strongly on the rate of cooling during preparation of the glass and is higher, e.g., for splat quenched than for melt

spun samples [52]. Irreversible relaxation is accompanied by an increase in density of the order of 0.1% and a narrowing of the first peak in the pair correlation function $g(r)$. These effects have been interpreted as resulting from an elimination of extremely short and long atom distances in the nearest-neighbor shell of a given atom [53].

After extended isothermal structural relaxation metallic glasses are in a metastable non-equilibrium state that can be described in terms of thermodynamics of metastable systems [54]. This is also reflected in the course of η and D as function of time. η was found to increase linearly with t during relaxation. Consequently, the relative increase $\mathrm{d}\ln\eta/\mathrm{d}t$ decreases continuously, and the system has often been described to approach a so-called isoconfigurational state after sufficiently long times [55]. The diffusion coefficient drops initially and reaches a plateau value which is reproducible and constant within experimental error as long as annealing is not performed at very long times close to T_g [56–58] (see also Fig. 6.6). Such conditions are excluded in conventional metallic glasses due to the onset of crystallization. Recent investigations on bulk metallic glasses have shown that the 'plateau value' is not constant and that complete relaxation from the frozen-in glassy non-equilibrium state to the metastable equilibrium supercooled liquid state can be achieved upon long-time relaxation [59, 60].

The mechanisms of structural relaxation are still discussed controversially, though there is general agreement that the increase in density ρ and the changes in $g(r)$ involve the annealing of quenched-in excess volume. According to Egami [61], the large effect in η and the relatively small change in ρ can be attributed to the mutual annihilation of regions of high positive and negative atomic level stress. The movement of these 'p and n defects' involves collective rearrangements of atoms. Within this concept the small increase in ρ is caused by a second order effect that arises from the anharmonicity of the interatomic potentials. Spaepen [62] has explained the increase in η during structural relaxation within the free-volume model as resulting from the bimolecular annihilation of frozen in free-volume fluctuations. There are similarities between both models, in particular with regard to the internal annihilation of frozen-in defects. Horváth et al. [56] have studied the relaxation behavior of D. The time and temperature dependence could be described by a single activation enthalpy. These authors came to the conclusion that relaxation takes place by annihilation of quenched-in 'quasi-vacancies' mainly through migration to the outer surface. The quasi-vacancies are envisioned as localized defects that are stable on the time scale of several atomic jumps. We will come back to the mechanisms of structural relaxation in Sect. 6.5.5.

The role of defects, especially of thermal quasi-vacancies, in diffusion will be discussed in the following sections. Unfortunately, positron annihilation, which has been so successful in monitoring vacancies in crystals, does not allow to identify unequivocally vacancy-like defects in metallic glasses because of saturation trapping of the positrons at large interstices [63]. Computer

simulations of the dense random packing of soft spheres of single component glasses [64] indicate the existence of a high concentration of relatively large octahedral and a portion of even larger interstices similar in size to a relaxed vacancy in crystals. In multicomponent glasses the large voids may be filled by the smaller atoms. Brandt [65] has demonstrated the stability of vacancies at 0 K in computer simulations of a one-component system. However, this result does not allow one to draw conclusions on the stability of vacancies at high temperatures. Bennet et al. [66] have shown vacancies to be unstable in a Lennard-Jones computer glass at elevated temperatures, whereas a Keating potential was found to stabilize a point defect. More recent simulations based in realistic metallic interatomic potentials have shown vacancy-like defects to be stable on the limited time scale below 1 ns [67].

So far we have focussed on irreversible structural relaxations. These can be associated with long-range atomic transport. The aforementioned fast reversible relaxation phenomena are most pronounced in multicomponent glasses and have been attributed to local rearrangements of atoms within of the general framework of β relaxation (Sect. 6.4, [68]). Anelastic cooperative changes in the local structure, which may lead to a different chemical short-range order, seem to be involved [69, 70].

In addition to fast reversible relaxation, slow reversible changes are expected to occur for many properties near the glass transition temperature T_g [62]. As mentioned above the rapid crystallization of almost all conventional glasses near T_g, however, made it difficult to study this behavior. Gerling et al. [71] utilizing an up-quenching technique and neutron irradiation [72] have demonstrated the occurrence of reversible changes in ductility and density in several amorphous alloys. In the new bulk glasses, of course, reversibility of properties can always be achieved by annealing above T_g and subsequent cooling [59].

6.5.2 Possible Diffusion Mechanisms

We have seen that metallic glasses are prone to structural relaxation, phase separation, and crystallization. Diffusion plays a mayor role in these processes and is also important for solid-state amorphization alluded to in Sect. 6.5.1. Nevertheless, despite of a considerable amount of research effort during the last decades [4, 5, 45, 56, 73–76], the knowledge of diffusion in amorphous alloys has long been rather limited. Even after the discovery of the new bulk metallic glasses with their stimulating effect on research several issues remain controversial. As for conventional metallic glasses, this is partly due to experimental difficulties, such as the onset of crystallization, which restricts the maximum annealing temperature and time to values corresponding to a typical diffusion length of some ten nm. In order to circumvent the problems concomitant with recording diffusion profiles on this length scale, conclusions were often drawn from results of indirect methods like measurements of the crystallization kinetics, viscosity, resistivity, magnetic anisotropy, and from

x-ray and Mößbauer techniques. Often, however, an unequivocal relationship between the measured quantity and the diffusion coefficient in the amorphous phase could not be established. Moreover, despite employing direct techniques based on high-resolution ion-beam depth profiling in combination with a radiotracer method, mass spectrometry, or Auger analysis, many investigators, particularly in the early measurements, did not properly take into account structural relaxation. We have seen in Sect. 6.5.1 that the diffusivity is very sensitive to relaxation, and that reproducible results can only be obtained in well relaxed samples.

While, in view of the disordered nature of amorphous alloys, one would expect a temperature-dependent effective activation energy (Sect. 6.4), it is now well established that Arrhenius plots for diffusion in the relaxed metastable amorphous state are linear, i.e. they exhibit a constant activation energy H. This has often been interpreted as being indicative of a diffusion mechanism similar to that in crystals, where vacancy-like defects in thermal equilibrium are the carriers of diffusion, even though resulting D_0 values were sometimes many orders of magnitude different from those typical of a vacancy mechanism. Moreover, numerous observations, e.g., the occurrence of anomalous hydrogen diffusion [29] (cf. Sect. 6.4) and the difference in the activation energies for self-diffusion and magnetic relaxation, Kronmüller and Frank [27] point to a broad spectrum of activation energies. Apparently, only a narrow range of this spectrum is probed during long-range diffusion experiments in the small accessible temperature interval. Furthermore, it has been shown that compensation of side and saddle point disorder (see Fig. 6.2) may also lead to a almost linear Arrhenius plot [26, 77]. An additional explanation of the linear Arrhenius plots can be given in terms of a highly cooperative diffusion mechanism, discussed below, which averages over local differences in the barrier heights.

There are several experimental results that lend support to the idea of defect-mediated diffusion in metallic glasses. For example, diffusion can be enhanced by irradiation, which in crystalline materials produces additional point defects. The annealing behavior of the radiation-induced excess volume also resembles that of crystals [78, 79]. Moreover, the crystallization kinetics of amorphous $(FeNi)_8(PB)_2$ were studied under hydrostatic pressure [76]. The resulting activation volume of the order of one atomic volume was taken as evidence of diffusion via point-defectlike entities in thermal equilibrium. It should be noted, however, that the evaluation of diffusion coefficients from measurements of the crystallization kinetics is a rather indirect approach which has often been criticized [73, 80]. Direct measurements of the pressure dependence of diffusion will be discussed in detail in Sect. 6.5.4.

Tu and Chou [81] studied interdiffusion in electron-beam evaporated amorphous NiZr trilayer films. Void formation was observed when both Ni and Zr diffused. Since the voids formed on the side with the higher concentration of the slower species this was termed ‘opposite Kirkendall effect’.

No voids were seen when Ni was the dominant diffusing species. The authors concluded that self diffusion in the glass can be mediated by localized vacancy-like defects, which may agglomerate like vacancies in crystals if their concentration is out of equilibrium, as well as by non-localized 'free-volume defects'. A free-volume model of diffusion in metallic glasses has been proposed by Spaepen [55]. The original theory for liquids (Sect. 6.3) was modified by introduction of an activation barrier for a diffusive jump into an evolving hole. The free volume concept was corroborated by Chason and Mizoguchi [82] who evaluated diffusion coefficients from the shift in position of the modulated diffraction peak in compositionally modulated amorphous Fe-Ti films as function of densification. The expected exponential dependence of D on the free volume was indeed observed. Hahn and coworkers [83] measured the dependence of tracer diffusion on atomic size and alloy composition in amorphous Ni-Zr. From similarities to α-zirconium they drew the conclusion that small atoms, including Ni, diffuse by an interstitial-like mechanism, using the interstices of the amorphous structure as jump positions. Such an interstitial model of diffusion has been proposed by Ahmadzadeh and Cantor [84]. For larger atoms like Zr diffusion was explained in terms of the coordinated motion of many atoms creating a localized free volume defect.

Cooperative diffusion mechanisms in metallic glasses have also been proposed by others, [55, 73, 85–87], mostly in view of the extreme variety of D_0 values alluded to above, which reflects a corresponding variability of the entropy of diffusion (Chap. 1). Furthermore, the $\ln D_0$-vs-H relationship deviates strongly from that for single-jump diffusion in crystals. The envisioned atomistic picture is often reminiscent of or directly related to the free-volume approach. Highly collective thermally activated processes, such as chain-like displacements of many atoms have been observed in computer simulations, which will be discussed in more detail below [41, 88, 89].

The new bulk metallic glasses have offered the opportunity to measure diffusion in the supercooled liquid state and to investigate changes in the transport mechanism concomitant with the glass transition and even in the equilibrium melt. Several groups have carried out diffusion measurements in bulk glasses during the last years by means of the radiotracer technique [90,91] or secondary ion mass spectrometry [92] (see Chap. 1 for experimental techniques). One generally observes a kink in the Arrhenius plot near the caloric glass transition temperature as measured, e.g., by differential scanning calorimetry (DSC). In accord with the expected time scale dependence of the caloric glass transition temperature the kink is shifted to lower temperatures for slower diffusing elements, and for Al no kink is observed in the investigated temperature range, for instance. The kink in the Arrhenius plot has often been interpreted as being due to a change in the diffusion mechanism [92, 93]. In particular, a transition from single-atom hopping to liquid-like viscous flow has been proposed at the caloric glass transition temperature T_g [94, 95].

The notion of a change in the mechanism of atomic transport at T_g is in conflict with predictions of the mode coupling theory (MCT) [96] discussed in Sect. 6.4. According to MCT, a gradual transition in the atomic transport mechanism from solid-like thermally activated local hopping – envisioned as a highly collective process involving many atoms [25] – to liquid-like motion occurs well above T_g at a microscopic glass transition temperature T_c. T_c does not depend on the time scale of the experiment and is the temperature where, upon cooling, due to the concomitant increase of density, the cage formed by the neighboring atoms of a given atom is frozen in and can only be overcome by hopping processes.

In the present light we are left with the following questions:

1. Is diffusion in fully relaxed metallic glasses generally mediated by thermal equilibrium defects similar to vacancies in crystals as often suggested (see review articles [18, 97])?
2. If thermal defects do not mediate diffusion, is diffusion in relaxed amorphous alloys a highly cooperative process as one would infer from computer simulations and the concept of 'medium assisted hopping' discussed in Sect. 6.4?
3. Which role do non-equilibrium defects play?
4. Do we have to consider different mechanisms for diffusion in relaxed and as-quenched samples, in other words: how does quenched-in excess volume affect diffusion?
5. Is there a change in the diffusion mechanism at the caloric glass transition temperature or does the change occur above the critical temperature Tc where, according to the mode coupling theory liquid-like atomic motion sets in?

In the next sections we shall see that these questions can be answered satisfactorily by critical experiments. Investigations of the isotope-mass dependence of diffusion in relaxed samples (Sect. 6.5.3) are pertinent to the second question. In Sect. 6.5.4 measurements of the pressure dependence of diffusion will be discussed, which are related to the role of equilibrium defects. The role of excess volume will be addressed in Sect. 6.5.5 mainly based on measurements of the isotope effect during structural relaxation. Section 6.6 will be devoted to the 5th question. Here we will also discuss very recent diffusion and isotope measurements in the equilibrium liquid.

6.5.3 Isotope Effect

A salient feature of diffusion in metallic glasses is the extremely small isotope effect. The isotope effect E for diffusion of two isotopes with diffusivities D_i and masses m_i is defined as ([98], see also Chap. 1, Sect. 1.7.2)

$$E = (D_\alpha/D_\beta - 1) \Big/ \left(\sqrt{m_\beta/m_\alpha} - 1\right). \tag{6.9}$$

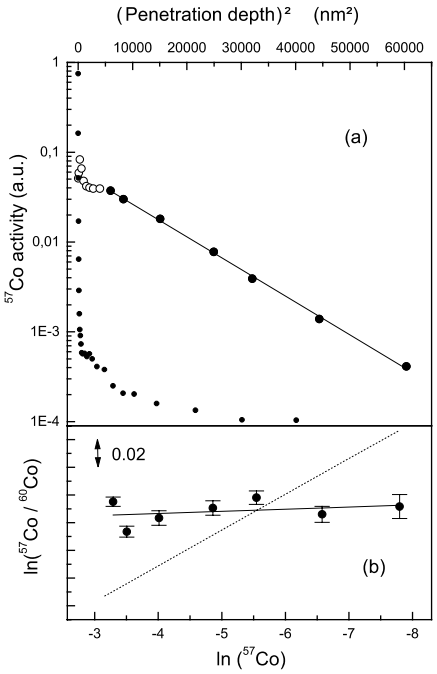

Fig. 6.3. (a) Typical penetration profile of ^{57}Co diffusion in $Pd_{40}Cu_{30}Ni_{10}P_{20}$ at 603 K and 1 h annealing time. The activity is plotted vs. the square of penetration depth. (The very first data points (*open symbols*) are affected by surface effects and were not taken in to account.) The resolution function of the depth profiling technique, obtained from a thin tracer layer without annealing, is shown in black. (b) Corresponding isotope effect profile. The activity ratio of ^{57}Co and ^{60}Co is plotted vs. the ^{57}Co activity on a logarithmic scale. The dotted line indicates an isotope effect of $E = 1$ and is shown for comparison (from [60]).

For single jump diffusion in densely packed lattices E is generally of the order of unity because of the $m^{-1/2}$ dependence of the attempt frequency [98], although correlation effects may give rise to a significant reduction of E, particularly in case of diffusion of diluted impurities due to impurity-vacancy binding (Chap. 1) [99]. E can also be strongly reduced by relaxation of the surrounding [100] and a broad distribution of activation energies [101].

Almost vanishing isotope effects have been observed for Co diffusion in various metallic glasses [102–106]. E was determined by measuring the simultaneous diffusion of the radiotracers ^{57}Co and ^{60}Co employing the serial sectioning technique in conjunction with ion-beam sputtering. For illustration of the technique, which is described in Chap. 1, Fig. 6.3 depicts a typical radiotracer profile on a semilogarithmic scale. According to the thin film solution of Fick's 2nd law (Chap. 1, (1.9)) a straight line fitted to the profile has the slope $1/(4Dt)$ and thus yields the tracer diffusivity D if the annealing time t is known. In order to obtain the isotope effect one can easily derive the following equation based on the thin film solution

$$\ln[c_\alpha(x,t)/c_\beta(x,t)] = \text{const.} - (D_\beta/D_\alpha - 1) \cdot \ln[c_\beta(x,t)] \quad . \tag{6.10}$$

Equation (6.10) shows that the slope of a straight line fitted to the data in Fig. 6.3b is given by $D_\alpha/D_\beta - 1$. The isotope effect E then follows from (6.9) and the isotope masses. Representative isotope effects for Co-Zr glasses are shown in Fig. 6.4.

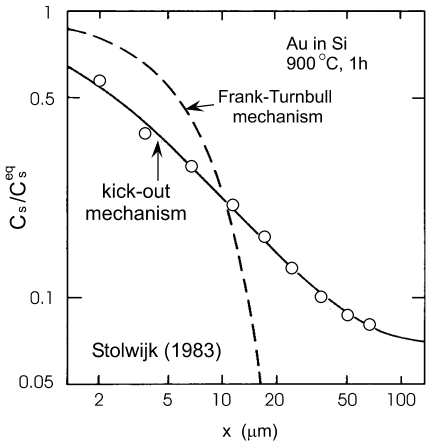

Fig. 6.4. Isotope effect in Co_xZr_{1-x} glasses for $0.31 < x < 0.86$. One notes that the isotope effect is very close to zero in the whole concentration range [105].

The essentially vanishing isotope effects measured in metallic glasses were taken as strong evidence of a highly collective hopping mechanism, as suggested by the notion of highly cooperative medium assisted hopping (see Sect. 6.4) and molecular dynamics (MD) simulations [107–109]. In these terms the extremely small isotope effects are attributed to a strong dilution of the mass dependence of diffusion due to the participation of a large number of atoms in collective hopping processes.

In MD simulations mainly chain-like displacements have been observed [88]. Both the computer simulations as well as the isotope effect measurements suggest the number of atoms participating in a cooperative hopping process to be very high, typically well above ten [109, 110].

Computer simulations also indicate a connection between the low-frequency excitations in glasses and long-range diffusion [88]. These low-frequency excitations appear to be characteristic of topologically disordered solids [111–114]. They give rise to extra specific heat at low temperatures and to additional contributions to the low-frequency part of the vibrational density of states as obtained by Raman and inelastic scattering. Close to absolute zero temperature the excitations can be attributed to tunneling (two-level) systems and at somewhat higher temperatures to quasi-localized vibrational states [113]. In addition to the periodic low frequency excitations aperiodic thermally activated relaxations have been observed [115]. Fits of an extended soft-potential model to experimental data resulted in effective masses of 20 to 100 atomic masses for the entities moving in the effective soft potentials. In a soft-sphere glass, which is a first approximation of a metallic glass, the local relaxations turned out to be collective jumps of groups of atoms, predominantly chains (sometimes with side-branches) along dense directions [115]. The effective mass and the total jump length of the atoms were found to increase with increasing temperature, and the possibility of fusion of isolated

relaxations at high temperatures was demonstrated. It is not unlikely that such processes lead to long-range diffusion. We emphasize, however, that our isotope effect measurements do not rule out other cooperative mechanisms, e.g., those involving smeared out defects.

6.5.4 Pressure Dependence

Information on the role of thermal defects have been obtained from measurements of the pressure dependence of diffusion. For a single-jump-type vacancy mechanism in crystalline close packed metals the activation volume, given by

$$V_{\mathrm{act}} \approx -k_{\mathrm{B}}T \left(\frac{\partial \ln D}{\partial p} \right)_T , \tag{6.11}$$

is of the order of the size of the relaxed vacancy, i.e., somewhat smaller than one atomic volume [98]. In (6.11) D, p, T, and k_{B} are diffusivity, pressure, absolute temperature, and Boltzmann constant, respectively. For interstitial diffusion, i.e. a direct mechanism without thermally generated defects, the activation volume proved to be nearly vanishing [98]. Both observations suggest the activation volume to be essentially given by the formation volume of the defect and the migration volume for a single-jump mechanism to be very small.

Several measurements, carried out by our group [116–118] and the Münster group [119], have revealed an almost vanishing pressure dependence for Co diffusion in the metallic glasses $Co_{76.7}Fe_2Nb_{14,3}B_7$, $Fe_{40}Ni_{40}B_{20}$, and $Co_{81}Zr_{19}$. A recent example is shown in Fig. 6.5 [118]. This in conjunction with the very small isotope effects, measured in these systems, led us to the conclusion that the migration volume can be close to zero even for a cooperative hopping process involving many atoms. Consequently, diffusion was interpreted in terms of direct cooperative hopping process as observed in the above mentioned MD simulations.

On the other hand, a pronounced pressure dependence, corresponding to activation volumes between one half and two atomic volumes, expressed in terms of the average atomic volume of the alloy, was reported for Au diffusion in amorphous $Pd_{40}Ni_{40}P_{20}$ [120], Ni diffusion in Ni_xZr_{100-x} ($42 < x < 62$) [121] and $Co_{42}Zr_{58}$ glasses [122], Hf diffusion in $Ni_{54}Zr_{46}$ [123], and Zr diffusion in $Co_{91}Zr_9$ [124]. Based on our aforementioned conclusion on the possibility of very small migration volumes even for cooperative hopping processes we tend to attribute the observed significant activation volumes to formation of thermal defects, which, however, may not necessarily be localized like a vacancy in a crystal but are expected to be spread out. On the other hand, recent results from MD simulations indicate that collective hopping processes may have a significant migration volume [109].

Of particular interest is the case of Co-rich Co-Zr glasses. Here Co seems to diffuse by a cooperative hopping process without assistance of thermal

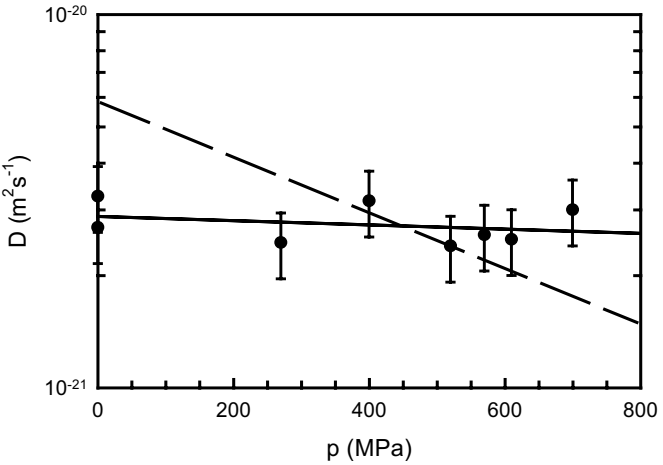

Fig. 6.5. Isothermal pressure dependence of ^{57}Co diffusion in structurally relaxed amorphous $Co_{81}Zr_{19}$ at 563 K [118]. The dashed line corresponds to an activation volume of one atomic volume.

defects, judging from a vanishing isotope effect [104] and an almost vanishing pressure dependence [118]. Diffusion of Zr, in contrast, is characterize by a large activation volume of the order of an atomic volume, which we attributed to diffusion via thermal defects [124]. This points to the existence of an opposite Kirkendall effect in interdiffusion in amorphous Co-Zr or Ni-Zr alloys which should behave similarly. An opposite Kirkendall effect, evidenced by void formation on the side with a higher concentration of the slower component, was indeed reported under conditions where both Ni and Zr were mobile in interdiffusion experiments involving amorphous Ni-Zr couples of different composition. As expected no such effect was seen when only Ni was mobile (see Sect. 6.5.1) [81]. These experiments lend support to the existence of thermal defects that mediate diffusion.

Mechanisms based on delocalized thermal defect have been proposed before [55, 97, 125, 126]. A well known example is the spread out free volume within the free-volume approach modified for glasses (see Sect. 6.5.2) [55, 94, 127].

6.5.5 Effect of Excess Volume on Diffusion

So far, we have discussed diffusion in structurally relaxed metallic glasses. Only in these systems the structure is stable during a diffusion experiment, and reproducible diffusion measurements can be made, if the diffusion temperature does not significantly exceed the relaxation temperature and the diffusion time in not too long. On the other hand, conventional metallic glasses, and to some extend also bulk glasses [128, 129], contain excess vol-

ume quenched in from the liquid state. This excess volume affects nearly all properties [130] and enhances diffusion [131,132]. Therefore, we have investigated the influence of excess volume on the diffusion mechanism by measuring both the diffusivity and the isotope effect during structural relaxation of as quenched glasses. First measurements were carried out for Co diffusion in a Co-rich metal-metalloid glass [133]. The isotope effect was found to be as high as 0.5 in the as-quenched state and to drop to a very low value of 0.1 in the relaxed state evidenced by a plateau region of the diffusivity. The high isotope effects in an as quenched state corroborates the notion of quenched-in quasi-vacancies, which migrate to the outer sample surface during structural relaxation [56].

On the other hand, our recent isotope effect measurements in thin amorphous Co-Zr films do not show any change in the diffusion mechanism during structural relaxation and point to a collective hopping mechanism in the relaxed and in the as-quenched state [132,134]. As shown in Fig. 6.6a the diffusivity drops substantially during relaxation and finally reaches the expected plateau value. The course of $D(t)$ is well described by the Kohlrausch law given in (6.7). The isotope effect in very low in the whole range (Fig. 6.6b) reflecting highly collective diffusion. Similar behavior was observed in thin $Co_{81}Zr_{19}$ films. Apparently, in the thin Co-Zr films excess volume appears to annihilate intrinsically, e.g., by recombination of regions of higher and lower density on the nanoscopic scale as first suggested by Egami et al. [130].

6.6 Diffusion in Supercooled and Equilibrium Melts

Most diffusion studies in the new bulk-glass formers where performed in the amorphous 'Johnson alloy' $Zr_{47}Ti_8Cu_{7.5}Ni_{10}Be_{27.5}$ also termed Vitrelloy 4. An Arrhenius plot summarizing the results for the is shown in Fig. 6.7, for example. One notes the aforementioned kinks shifting to lower temperatures for slower diffusing species, which have often been interpreted as a change in the diffusion mechanism at the caloric glass transition temperature. The diffusivities follow the expected size dependence (for a detailed discussion see, e. g., Chap. 5 in [5]) in both the glassy and the supercooled liquid state except for the Be data reported by Geyer et al. (dashed line in Fig. 6.7). The intersection of the Be diffusivity with those of substantially larger elements is quite unusual and contradicts expectations on the size dependence of diffusion as well as more general concepts of the convergence of the diffusivities at higher temperatures (above T_c) as predicted by the Stokes-Einstein equation. While Geyer at al. performed chemical diffusion experiments, which are influenced by the thermodynamic factor [99] recent radiotracer experiments of our group in cooperation with the group of Geyer demonstrated that the behavior of Be is by no means exceptional. As shown in Fig. 6.7, the radiotracer data of Rehmet et al. [135] (solid line) nicely fit in with the overall picture. The differences between the tracer and the chemical diffusion data

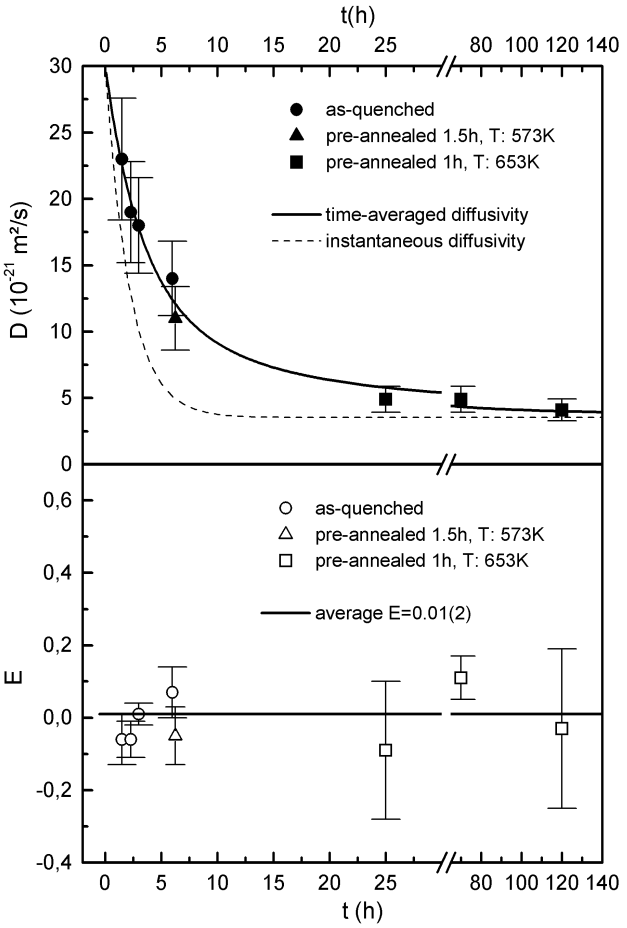

Fig. 6.6. (*top*) Time dependence of ^{57}Co diffusion in $Co_{51}Zr_{49}$ during structural relaxation at $T = 300^{\circ}$C. The squares indicate samples that have been preannealed at $T = 380^{\circ}$C for 1 h. Circles indicate specimens that have not been preannealed before diffusion treatment while the specimen described by a triangle was annealed for 1.5 h and again for 4.75 h. The straight line represents the time-averaged diffusivity, the dashed line shows the instantaneous diffusivity (for details see 132). (*bottom*) Isotope effect E in $Co_{51}Zr_{49}$ during structural relaxation. The squares indicate the preannealed samples while circles display the specimens which have not been preannealed before diffusion annealing. The specimen represented by a triangle was annealed for 1.5 h and again for 4.75 h.

are not yet understood. They cannot be attributed to the thermodynamic factor, which goes to unity at high temperatures.

Recently, we have also carried out isotope effect measurements involving the isotopes ^{57}Co and ^{60}Co by means of the radiotracer technique in the

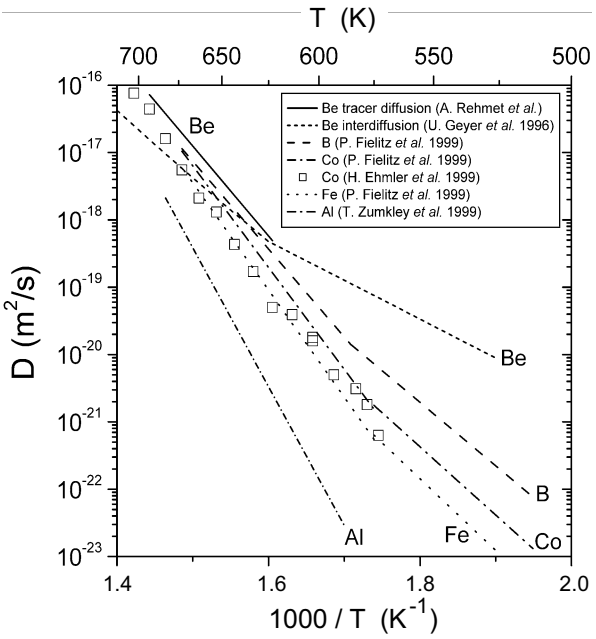

Fig. 6.7. Arrhenius plot summarizing the diffusivities of various tracers in amorphous $Zr_{47}Ti_8Cu_{7.5}Ni_{10}Be_{27.5}$. The data were taken from the following references: Be [143], B, Co, Fe, Al [92], Co [90]. The sequence of the curves is as in the legend. Data for Ni [91], being close to those of Co, are omitted for sake of clarity.

deeply supercooled liquid state of metallic bulk-glass-forming alloys. Results for Vitrelloy 4 and a well known 'Inoue glass' are displayed in Fig. 6.8. For experimental details the reader is referred to [90, 136].

One notes that the isotope effect is very small in the whole temperature range and exhibits no temperature dependence. The magnitude of the isotope effect is similar to the isotope effects found in the glassy state of conventional metallic glasses [103–105,116]. This support the view that the diffusion mechanism does not change at the caloric glass transition temperature and that the highly collective hopping processes occurring in the glassy state still determine long-range diffusion in the deeply supercooled melt. Collective hopping of many atoms has recently also been observed in deeply supercooled melts in MD simulations [137]. The order of magnitude of 10 atoms participating in the hopping processes is in agreement with the measured E values [90, 136].

Recently, we measured the isotope effect in a $Pd_{40}Cu_{30}Ni_{10}P_{20}$ alloy at one and the same temperature in the glassy state and after long-time relaxation in the supercooled liquid state [60]. Although the diffusivity dropped by about an order of magnitude, the isotope effect did not change and was close to zero in both states (Fig. 6.9). This provides further evidence of the absence of a change in the diffusion mechanism at the caloric glass transition temperature.

Since this macroscopic glass transition is a transition from a metastable equilibrium state above T_g to a non-equilibrium state below T_g there is an obvious explanation of the kinks in Arrhenius plots. In the glassy state diffusion

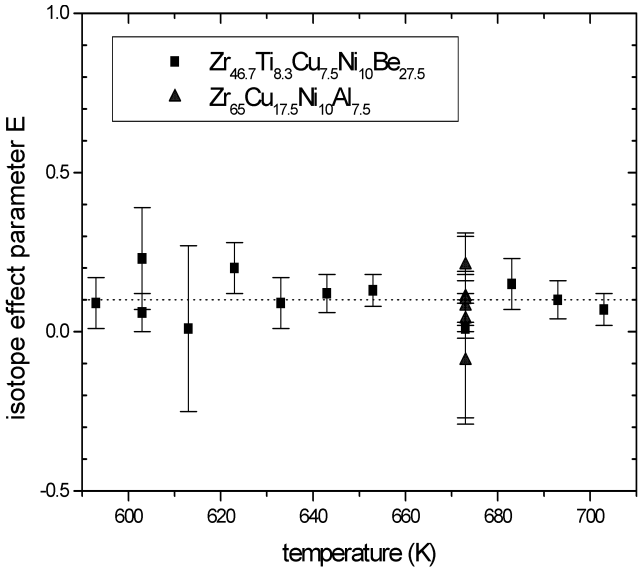

Fig. 6.8. Isotope effect as function of temperature for Co diffusion in bulk metallic glasses. The data are taken from [90]. The diffusivities in the Be-containing "Johnson glass" are displayed as squares.

takes place in a frozen-in structure which does not change with temperature (except for irreversible structural relaxation [59, 131, 138]). Above T_g, however, any increase in temperature gives rise to structural changes, e.g., an increase in free volume which is certainly expected to enhance diffusion. In these terms the increase in slope in the Arrhenius plots near the calorimetric glass transition temperature (see Fig. 6.7) is simply due to temperature dependent structural changes. Therefore, the slope $-k_B \partial \ln D / \partial T^{-1}$ above T_g can no longer be regarded as an activation energy and should be termed apparent or effective activation energy.

Using a novel $Pd_{43}Cu_{27}Ni_{10}P_{20}$ alloy, which exhibits exceptional stability against crystallization, we were recently able to study for the first time long-range diffusion at and above T_c in a metallic system [139]. The results are shown in Fig. 6.9. Below T_c one notes Arrhenius behavior in conjunction with a very low isotope effect as observed before (see Figs. 6.7 and 6.8, and the data for $Pd_{40}Cu_{30}Ni_{10}P_{20}$ in Fig. 6.9). This was attributed to thermally activated highly collective hopping in the preceding chapter. Above T_c, however, our data provide clear evidence of a change in the atomic dynamics. The effective activation energy $-k_B \partial \ln D / \partial T^{-1}$ (slope in Fig. 6.9) drops gradually as expected from the onset of viscous flow in the mode coupling scenario. Due to the increasing influence of liquid-like motion the nearest neighbor barriers should gradually decay as the temperature is increased above T_c. Our diffusion data are even in good quantitative agreement with a fit of the idealized

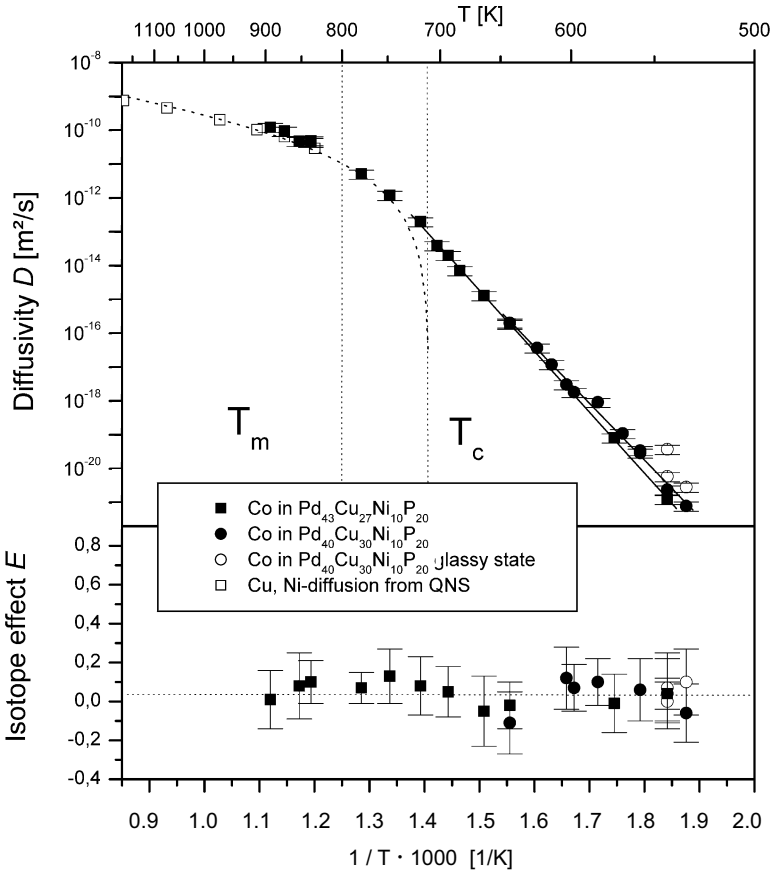

Fig. 6.9. Temperature dependence of (*top*) Co diffusivity and (bottom) isotope effect in $Pd_{40}Cu_{30}Ni_{10}P_{20}$ and $Pd_{43}Cu_{27}Ni_{10}P_{20}$. The diffusivity is plotted on a semi-logarithmic scale vs. $1/T$. Open squares show data for Ni and Cu diffusion from quasielastic neutron scattering (QENS) in $Pd_{43}Cu_{27}Ni_{10}P_{20}$. The dashed line is a fit of the idealized mode coupling theory to the QENS data (see text). The melting temperature T_m (more precisely, the quasi-eutectic melting temperature) and T_c, determined from the fit to the QENS, data are displayed. Below T_c the tracer diffusivity data were fitted by an Arrhenius law. Open circles represent samples in the glassy state at different stages of structural relaxation.

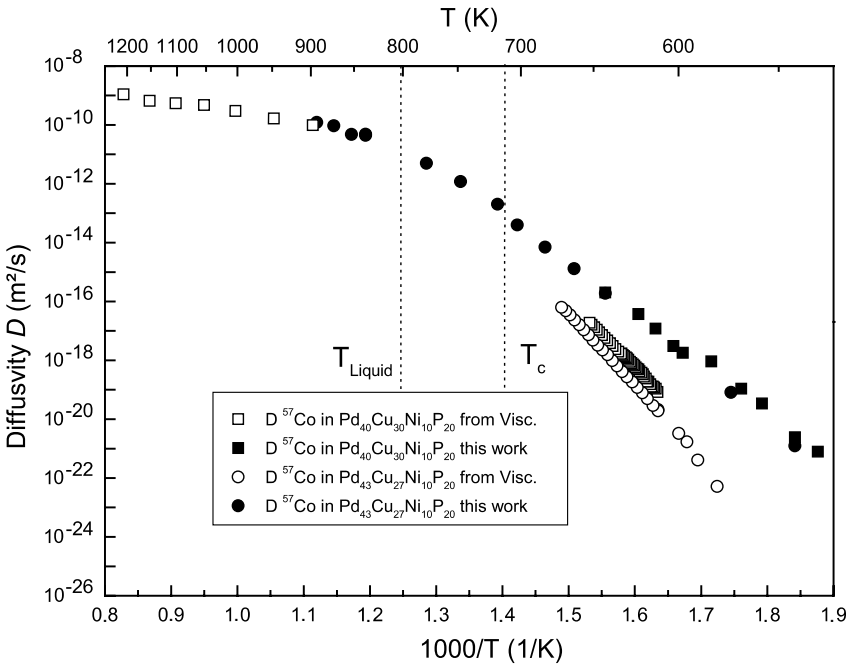

Fig. 6.10. Comparison of measured tracer diffusivities with diffusivities calculated from the Stokes-Einstein relation [141, 144].

mode coupling theory to quasielastic neutron scattering data [140] above T_{m}. The idealised MCT neglects hopping processes and predicts a $[(T - T_{\mathrm{c}})/T_{\mathrm{c}}]^{\gamma}$ dependence, as shown in Fig. 6.9 (dashed line). Thus, the present results strongly support the mode coupling approach for metallic glass formers.

The transition from solid-like hopping below T_{c} to liquid-like atomic motion above T_{c} is also reflected in the behavior of the viscosity. Above T_{c} diffusivities calculated from the Stokes-Einstein relation (see (6.5)) agree well with the tracer diffusion data (Fig. 6.10). Below T_{c}, however, Co diffusion and viscous flow are clearly decoupled.

We point out that the excellent agreement between our long-range diffusion data and the diffusivities from quasielastic neutron scattering, which measures short-range diffusion, allows convection effects to be ruled out. The absence of convection effects, which are a severe problem in diffusion measurements in ordinary liquids and melts under gravity conditions, is in accord with the about two orders of magnitude higher viscosity of the present melt, compared to ordinary melts, at the liquidus temperature [141].

The high viscosity of the $Pd_{43}Cu_{27}Ni_{10}P_{20}$ melt is reflected in a remarkably low isotope effect close to zero even in the equilibrium melt. This shows that the present Pd-Cu-Ni-P melt is still far away from the hydrodynamic regime of uncorrelated binary collisions as much as 200 K above T_{c}. For the

hydrodynamic regime kinetic theories predict [7, 16] predict a $m^{-1/2}$ mass dependence and hence an isotope effect close to unity (see (6.2)

The behavior of the excellent glass-forming alloy contrasts sharply with that of simple melts such as liquid Sn, which exhibits an isotope effect of the expected order of unity [13]. Molecular dynamics simulations [142] indicate a strong correlation of isotope effect and density of the liquid and suggest the present very low E value to be due to the small density difference between glassy and liquid state of only about 3%. The strongly coordinated atomic motion up to the equilibrium liquid, evidenced by the very low isotope effect, appears to be the key to exceptional glass forming ability of the present alloy.

6.7 Conclusion

Amorphous metallic alloys, also termed metallic glasses, are the paradigm of dense random packing. Conventional metallic glasses are very prone to crystallization and do not lend themselves for diffusion studies above the glass transition temperature. With the discovery of novel bulk-glass-forming alloys diffusion in metallic systems can now be investigated from the glassy state up to the equilibrium melt. This is of considerable interest not only from the technological point of view but also in terms of fundamental science, particularly in connection with the glass transition. According to the mode coupling theory the glass transition is a kinetic phenomenon characterized by the arrest of viscous flow at a critical temperature T_c well above the calorimetric glass transition temperature T_g. Below T_c an extension of the original theory predicts cooperative hopping processes.

In this chapter we focus on results from radiotracer measurements of diffusion and frequently refer to molecular dynamics simulations, which have provided much insight into the underlying diffusion mechanisms. The tracer diffusivity is not affected by thermodynamic effects and is hence directly related to the atomic dynamics. In particular, we present results from isotope effect measurements which indeed confirm the highly collective nature of diffusion in structurally relaxed metallic glasses. The highly cooperative hopping processes seem to be closely related to the universal low-frequency excitations.

We also address the role of defects based on measurements of the isothermal pressure dependence which can be interpreted in terms of the activation volume of diffusion. The corresponding results do not reflect a uniform picture. Depending on the structure of the glass, essentially vanishing activation volumes and those of the order of an atomic volume have been observed. The vanishing activation volumes found in several conventional metallic glasses clearly allow diffusion via thermal defects to be ruled out. Large activation volumes in conjunction with a very small isotope effect have mainly been interpreted as being indicative of cooperative hopping that takes place by assistance of thermally generated defects. This interpretation is not unique,

judging from recent molecular dynamics simulations which reveal a significant migration volume for a direct collective hopping process. In line with the possibility of defect-mediated diffusion we provide evidence of the existence of an opposite Kirkendall effect in interdiffusion between certain amorphous alloys that combine slow diffusion via thermal defects and fast direct diffusion.

We also address the role of quenched-in excess volume in metallic glasses. On the one hand, isotope effect measurements during structural relaxation in melt-spun ribbons support the notion of quenched-in vacancy-like defect that enhance diffusion and anneal out during irreversible structural relaxation by migration to the outer surface. On the other hand, similar measurements in thin metal-metal glasses clearly point to highly cooperative diffusion even in the as-quenched glassy state and to internal annihilation of excess volume.

In accord with the mode coupling scenario cooperative hopping processes are also observed in the supercooled liquid state up to T_c. Kinks in Arrhenius plots are shown to be related to structural changes above T_g but not to a change in the diffusion mechanism. Above T_c the effective activation energy drops gradually as expected from the decay of barriers, induced by the onset of liquid-like atomic motion. Isotope effect measurements in Pd-based alloys show atomic transport up to the equilibrium melt to be far away from the hydrodynamic regime of uncorrelated binary collisions. This appears to be a prerequisite of excellent glass forming abilities.

Notation

a	atomic radius (in Stokes-Einstein eq.)
D	diffusion coefficient
D_0	prefactor of Arrhenius law
D^0	diffusion coefficient at zero frequency
E	isotope effect parameter
f	correlation factor
$g(r)$	pair correlation function
H	activation enthalpy of diffusion
H^0	activation enthalpy distribution
k_B	Boltzmann's constant
m_i	mass of isotope i
$m + M$	effective mass
p	(hydrostatic) pressure
$S(q)$	structure factor
T	absolute temperature
T_c	critical temperature of mode coupling theory
T_g	caloric glass transition temperature
T_m	quasi-eutectic melting temperature
T_{VF}	Vogel-Fulcher temperature
T_0	reference temperature for free volume theory

V_{act}	activation volume
$\bar{v}$	mean velocity
v_{f}	mean free volume per molecule
β	parameter of Kohlrausch law
η	viscosity
λ	mean free path
τ	relaxation time
ν_0	attempt frequency
$\Phi(t)$	relaxation function
Ω	atomic volume
ω	frequency

References

1. C.A. Angell, K.L. Ngai, G.B. McKenna, P.F. McMillanand, S.W. Martin: J. Appl. Phys. **88** , 3113 (2000)
2. T. Zhang, A. Inoue, T. Masumoto: Mater. Trans. Japan. Inst. Metals **32**, 1005 (1991)
3. A. Peker, W.L. Johnson: Appl. Phys. Lett. **63**, 2342 (1993)
4. H. Kronmüller. In: *Springer Series in Materials Sciences*, vol 29, ed by M.A. Otooni (Springer, Berlin Heidelberg New York 1998) p 93
5. F. Faupel, W. Frank, M.P. Macht, H. Mehrer, V. Naundorf, K. Rätzke, H.R. Schober, S.K. Sharma, H. Teichler: Rev. Mod. Phys. **75**, 237 (2003)
6. J. Philibert: *Diffusion and Mass Transport in Solids* (Les Editions de Physique, Les Ulis 1991)
7. J.S. Kirkaldy, D.J. Young: *Diffusion in the Condensed State* (The Institute of Metals, London 1987)
8. H.J. Tyrell, K.R. Harris: *Diffusion in Liquids* (Butterworth, London 1984)
9. M. Allen, D. Tildesley: *Computer Simulations of Liquids* (Oxford University Press, Oxford 1987)
10. N.H. Nachtrieb: *Liquid Metals and Solidification*, vol 49 (ASM, Cleveland 1958)
11. M. Shimoji, T. Itami: *Diffusion and Defect Data, Atomic Transport in Liquids and Metals* (Trans Tech Publ., Aedermannsdorf 1986)
12. W. Gläser. In: *Amorphous and Liquid Materials*, ed by E. Lüscher, G. Frisch, G. Jaccuci (Martinus Nijhoff Publisher, Dordrecht 1987) p 34
13. G. Frohberg, K.H. Kraatz, H. Wever: Materials Science Forum **15–18**, 529 (1987)
14. M.H. Cohen, D. Turnbull: J. Chem. Phys. **31**, 1164 (1959)
15. M.H. Cohen, G.S. Grest: J. Non-Cryst. Solids **61/62**, 749 (1984)
16. N.H. Nachtrieb: Ber. Bunsenges. Phys. Chem. **80**, 678 (1976)
17. P.G. Debenedetti: *Metastable Liquids-Concepts and Principles* (Princeton University Press, New Jersey 1996)
18. Y. Limoge. In: *Diffusion in Materials*, NATO ASI Series E, vol 179, ed by A.L. Laskar, J.L. Bocquet, G. Brebec, C. Monty (Kluwer Academic Publishers, Dordrecht 1990) p 601

19. J. Jäckle: Rep. Prog. Phys. **49**, 171 (1986)
20. S.F. Edwards, T.A. Vilgis. In: *Time Dependent Effects in Disordered Materials*, NATO ASI Series B, vol 167, ed by R. Pynn, T. Reste (Plenum Press, New York 1987) p 279
21. J.D. Ferry: *Viscoelastic Properties of Polymers*, 3rd edn (Wiley, New York 1980)
22. G.P. Johari. In: *Molecular Dynamics and Relaxation Phenomena in Glasses*, Lecture Notes in Physics, vol 277, ed by Th. Dorfmüller, G. Williams (Springer, Berlin Heidelberg New York 1987) p 90
23. W. Götze, L. Sögren: J. Phys.: Condensed Matter **1**, 4183 (1989); ibid. 4203 (1989)
24. W. Götze: J. Phys.: Cond. Matt. **11**, A1 (1999)
25. L. Sjögren: J. Phys. B **79**, 5 (1991)
26. J.W. Haus, K.W. Kehr: Phys. Rep. **150**, 263 (1987)
27. H. Kronmüller, W. Frank, A. Hörner: Mater. Sci. Eng. A **133**, 410 (1991)
28. A.K. Jonscher: Nature (London) **267**, 673 (1979)
29. W. Schirmacher, M. Prem, J.-B. Suck, A. Heidemann: Europhys. Lett. **13**, 523 (1990)
30. H. Kronmüller, W. Frank: Radiation Effects and Defects in Solids **108**, 81 (1989)
31. G. Schönherr, H. Bässler, M. Silver: Phil. Mag. B **44**, 369 (1981)
32. H. Bässler: Phys. Rev. Lett. **58**, 767 (1987)
33. G. S. Cargill: Sol. St. Phys. **30**, 227 (1975)
34. H. Warlimont: Z. Metallkde. **75**, 679 (1984)
35. S. Ashley: Mech. Engineering **6**, 72 (1998)
36. N. Nishiyama, A. Inoue: Mat. Trans. JIM **40**, 64 (1999)
37. R.W. Cahn. In: *Physical Metallurgy*, ed by R.W. Cahn, P. Haasen (Elsevier, Amsterdam 1983) p 1779
38. K. Samwer: Physics Reports **161**, 1 (1988)
39. J.L. Finney. In: *Amorphous Metallic Alloys*, ed by F.E. Luborsky (Butterworth, London 1983) p 42
40. J.D. Bernal: Proc. Roy. Soc. A **284**, 299 (1964)
41. H. Teichler: Phys. Rev. B **59**, 8473 (1999)
42. H.R. Schober: Sol. State Comm. **119**, 73 (2001)
43. C. Donati, J.F. Douglas, W. Kob, S.J. Plimpton, P.H. Poole, S.C. Glotzer: Phys. Rev. Lett. **80**, 2338 (1998)
44. P. Lamparter. In: *Atomic Transport and Defects in Metals by Neutron Scattering*, Proceedings in Physics, vol 10, ed by C. Janot, W. Petry, D. Richter, T. Springer (Springer, Berlin Heidelberg New York 1986) p 49
45. P.H. Gaskell: J. Phys. C **12**, 4337 (1979)
46. D.R. Nelson, S. Sachdev. In: *Amorphous Metals and Semiconductors*, ed by P. Haasen, R.I. Jaffee (Pergamon Press, Oxford New York Frankfurt 1986) p 28
47. C. Park, M. Saito, Y. Waseda, N. Nishijama, A. Inoue: Mater. Trans. JIM **40**, 491 (1999)
48. U.K. Rößler, H. Teichler: Phys. Rev. E **61**, 394 (2000)
49. R. Gerling, F.P. Schimansky, R. Wagner: Mater. Sci. Eng. **97**, 515 (1988)
50. P. Haasen. In: *Amorphous Metals and Semiconductors*, ed by P. Haasen, R.I. Jaffee (Pergamon Press, Oxford New York Frankfurt 1986) p 45

51. F. Gärtner, C. Michaelsen, R. Bormann: Phil. Mag. B **76**, 511 (1997)
52. B. Cantor. In: *Amorphous Metals and Semiconductors*, ed by P. Haasen, R. I. Jaffee (Pergamon Press, Oxford New York Frankfurt 1986) p 108
53. J.B. Suck. In: *Dynamics of Disordered Materials*, Proceedings in Physics, vol 37, ed by D. Richter, A.J. Dianoux, W. Petry, (Springer, Berlin Heidelberg New Yorl 1989) p 182
54. R. Bormann. Habilitation thesis, University of Göttingen (1988)
55. F. Spaepen. In: *Physics of Defects Les Houches Lectures XXXV*, ed by R. Balian, M. Kléman, J.P. Poirer (North Holland, Amsterdam 1981) p 133
56. J. Horváth, K. Pfahler, W. Ulfert, W. Frank, H. Mehrer: J. Phys. C **8**, 645 (1985)
57. A.K. Tyagi, M.-P. Macht, V. Naundorf: Scripta Metall. Mater. **24**, 2369 (1990)
58. P. Scharwaechter, W. Frank, H. Kronmueller: Z. Metallkd. **87**, 885 (1996); P. Scharwaechter, W. Frank, H. Kronmueller: Z. Metallkd. **87**, 892 (1996)
59. Th. Zumkley, V. Naundorf, M.-P. Macht, G. Frohberg: Scripta Mater. **45**, 471 (2001)
60. V. Zöllmer, K. Rätzke, F. Faupel, A. Rehmet, U. Geyer: Phys. Rev. B **65**, 220201 (2002)
61. T. Egami: Annals of the New York Academy of Science **371**, 238 (1981)
62. F. Spaepen: Mater. Sci. Eng **97**, 403 (1988)
63. W. Triftshäuser, G. Kögel. In: *Amorphous and Liquid Materials*, NATO ASI Series E, vol 118, ed by E. Lüscher, G. Fritsch, G. Jacucci (Martinus Nijhoff Publ., Dordrecht 1987)
64. J.L. Finney, J. Wallace: J. Non-Cryst. Solids **43**, 165 (1981)
65. E.H. Brandt: J. Phys. F **14**, 2485 (1984)
66. C.H. Bennet, P. Chaudhari, V. Moruzzi, P. Steinhardt: Phil. Mag. A **40**, 485 (1979)
67. H. Teichler: Def. Diff. Forum **143–147**, 717 (1997)
68. H.S. Chen. In: *Amorphous Metallic Alloys*, ed by F.E. Luborsky (Butterworth, London 1983) p 169
69. T. Egami. In: *Amorphous Metals and Semiconductors*, ed by P. Haasen, R.I. Jaffee (Pergamon Press, Oxford New York Frankfurt 1986) p 222
70. B. Porscha, H. Neuhäuser: Scripta Metallurgica et Materialia **32**, 931 (1995)
71. R. Gerling, F.P. Schimansky, R. Wagner: Scripta Metall. **22**, 1291 (1988)
72. R. Gerling, F.P. Schimansky, R. Wagner: Acta Metall. **35**, 1001 (1986)
73. H. Mehrer: Defect Diffus. Forum **129-130**, 57 (1996)
74. R.S. Averback, H.J. Höfler: Defect Diffus. Forum, **95**, 1131 (1993)
75. B. Cantor. In: *Proc. 5th Int. Conf. Rapidly Quenched Metals*, ed by S. Steeb, H. Warlimont (North-Holland: Amsterdam 1985) p 595; and references therein
76. Y. Limoge: Materials Science Forum **15–18**, 517 (1987)
77. Y. Limoge, J.L. Bocquet: Phys. Rev. Lett. **65**, 60 (1990)
78. R.S. Averback, H. Hahn: Phys. Rev. B **37**, 10383 (1988)
79. A.K. Tyagi, M.-P. Macht, V. Naundorf: J. Nucl. Mat. **179–181**, 1026 (1991)
80. H. Mehrer, W. Dörner: Defect Diffus. Forum **66–69**, 189 (1989)
81. K.N. Tu, T.C. Chou, Phys. Rev. Lett. **61**, 1863 (1988)
82. E. Chason, T. Mizoguchi: Z. Phys. Chem. **156/157**, (1987)
83. H. Hahn, R.S. Averback, H.M. Shyu: J. Less Common Metals **140**, 345 (1988)
84. M. Ahmadzadeh, B. Cantor: J. Non Cryst. Solids **43**, 189 (1981)
85. W. Frank, J. Horváth, H. Kronmüller: Mater Sci. Eng. **97**, 415 (1988)

86. E. Stelter, D. Lazarus: Phys. Rev. B **36**, 9545 (1987)
87. D. Lazarus. In: *Phase Transition in Condensed Systems*, ed by C.G. Cargill, F. Spaepen, K. Tu (MRS Symposia Proceedings Vol. 57, 1987) p 297
88. H.R. Schober, C. Oligschleger, B.B. Laird: J. Non-Cryst. Solids **156–158**, 965 (1993)
89. W. Frank, U. Hamlescher, H. Kronmüller, P. Scharwaechter, T. Schuler: Physica Scripta T **66**, 201 (1996)
90. H. Ehmler, A. Heesemann, K. Rätzke, F. Faupel, U. Geyer: Phys. Rev. Lett. **80**, 4919 (1998); H. Ehmler. PhD Thesis, University of Kiel (1999)
91. K. Knorr, M.P. Macht, K. Freitag, H. Mehrer: J. Non-Cryst. Solids **250**, 669 (1999); K. Knorr. PhD Thesis, University of Münster (1999)
92. P. Fielitz, M.P. Macht, V. Naundorf, G. Frohberg, J. Non-Cryst. Solids **250**, 674 (1999)
93. U. Geyer, S. Schneider, W.L. Johnson, Y. Qiu, T.A. Tombrello, M.P. Macht: Phys. Rev. Lett. **75**, 2364 (1995)
94. X.P. Tang, U. Geyer, R. Busch, W.L. Johnson, Y. Wu: Nature **402**, 160 (1999)
95. A.L. Greer: Nature **402**, 132 (1999)
96. W. Götze, L. Sjögren: J. Non-Cryst. Solids **131–133**, 161 (1991)
97. R. S. Averback: MRS Bulletin **XVI**, 47 (1991)
98. H.Mehrer. In: *Landolt Börnstein, Diffusion in Solid Metals and Alloys*, New Series, Group III, vol 26 (Springer, Berlin Heidelberg New York 1991)
99. J. Philibert: *Diffusion and Mass Transport in Solids*, Chap. 4 (Les Editions de Physique, Les Ulis 1991)
100. S. Ishioka, H. Nakajima, M. Koiwa: Phil. Mag. A **55**, 359 (1987)
101. N.P. Lazarev, A.S. Bakai, C. Abromeit, V. Naundorf: Phys. Rev. Lett. **88**(4), 045502 (2002)
102. P.-W. Hüppe, F. Faupel: Phys. Rev. B **46**, 120 (1992)
103. K. Rätzke, A. Heesemann, F. Faupel: J. Phys.: Condens. Matter **7**, 7633 (1995)
104. A. Heesemann, K. Rätzke, F. Faupel, J. Hoffmann, K. Heinemann: Europhys. Lett. **29**, 221 (1995)
105. A. Heesemann, V. Zöllmer, K. Rätzke, F. Faupel: Phys. Rev. Lett. **84**, 1467 (2000)
106. K. Rätzke, P. Klugkist, F. Faupel: Defect Diffus. Forum. **165–166**, 43 (1999)
107. U.K. Rößler, H. Teichler: Phys. Rev. E **61**, 394 (2000)
108. M. Kluge, H. Schober: Defect Diffus. Forum **194–199**, 849 (2001)
109. H. Teichler, J. Non-Cryst. Solids **293**, 339 (2001)
110. C. Gaukel, H.R. Schober: Solid State Comm. **107**, 1 (1998)
111. J.-B. Suck, H. Rudin. In: *Glassy Metals II*, Topics in Applied Physics, vol 53, ed by H. Beck, H.-J. Güntherodt (Springer, Berlin Heidelberg New York 1983) p 217
112. U. Buchenau, M.Prager, N. Nücker, A.J. Dianoux, N. Ahmad, W.A. Phillips: Phys. Rev. B **34**, 5665 (1986)
113. U. Buchenau, H.M. Zhou, N. Nücker, K.S. Gilroy, W.A. Philips: Phys. Rev. Lett. **60**, 1368 (1988)
114. K. Inoue.,T. Kanaya, S. Ikeda, D. Kaji, K. Shibata, M. Misawa,Y. Kiyanagi: J. Chem. Phys. **95**, 5332 (1991)
115. H.R. Schober: Physica A **201**, 14 (1993)
116. F. Faupel, P.W. Hüppe, K. Rätzke: Phys. Rev. Lett. **65**, 1219 (1990)
117. K. Rätzke, A. Heesemann, F. Faupel: J. Phys.: Condens. Matter **7**, 7633 (1995)

118. P. Klugkist, K. Rätzke, S. Rehders, P. Troche, F. Faupel: Phys. Rev. Lett. **80**, 3288 (1998)
119. G. Rummel, H. Mehrer: Phys. Stat. Sol. (a) **185**, 327 (1994)
120. P.A. Duine, S.K. Wonnell, J. Sietsma: Mater. Sci. Eng. A **179/180**, 270 (1994)
121. H.J. Höfler, R.S. Averback, G. Rummel, H. Mehrer: Phil. Mag. Lett. **66**, 301 (1992)
122. P. Klugkist, K. Rätzke, F. Faupel, P. Troche, P. Fielitz, V. Naundorf: Phil. Mag. Lett. **79**, 827 (1999)
123. Y. Loirat, J.L. Bocquet, Y. Limoge, J. Non-Cryst. Solids **265**, 252 (2000)
124. P. Klugkist, K. Rätzke, F. Faupel: Phys. Rev. Lett. **81**, 614 (1998)
125. E. Stelter, D. Lazarus: Phys. Rev. B **36**, 9545 (1987)
126. A. van den Beukel: Key Eng. Mat. **81–83**, 3 (1993)
127. X.P. Tang, R. Busch, W.L. Johnson, Y. Wu: Phys. Rev. Lett. **81**, 5358 (1998)
128. C. Nagel, K. Rätzke, E. Schmidtke, J. Wolff, U. Geyer, F. Faupel, Phys. Rev. B. **57**, 10224 (1998)
129. C. Nagel, K. Rätzke, E. Schmidtke, F. Faupel, W. Ulfert: Phys. Rev. B **60**, 9212 (1999)
130. T. Egami: Ann. New York Acad. Sci. **371**, 238 (1981)
131. J. Horváth, K.Pfahler, W. Ulfert, W. Frank H. Kronmüller: Mat. Sci. Eng. **15**, 523 (1987)
132. V. Zöllmer, H. Ehmler, K. Rätzke, P. Troche, F. Faupel: Europhys. Lett. **51**, 75 (2000)
133. K. Rätzke, P.W. Hüppe, F. Faupel: Phys. Rev. Lett. **68**, 2347 (1992)
134. A. Heesemann, K. Rätzke, V. Zöllmer, F. Faupel, New J. Phys. **3**, 6.1 (2001)
135. A.Rehmet, K. Rätzke, F. Faupel, P.D. Eversheim, K. Freitag, U. Geyer, S. Schneider: Applied Phys. Lett. **79**, 2892 (2001)
136. H. Ehmler, K. Rätzke, F. Faupel: J. Non-Cryst. Solids **250**, 684 (1999)
137. H.R. Schober, C. Gaukel, C. Oligschleger: Prog. Theor. Phys. **126**, 67 (1997)
138. T. Zumkley, V. Naundorf, M.-P. Macht, G. Frohberg: Scripta Met. Mater. **45**, 471 (2001)
139. V. Zöllmer, A. Meyer, K. Rätzke, F. Faupel: Phys. Rev. Lett. **92**, 195502 (2003)
140. A. Meyer: Phys. Rev. B **66**, 134206 (2002)
141. H. Haumesser, J. Bancillon, M. Daniel, J.P. Garandet, J.C. Barbé, N. Kernevez: Int. J. Thermophysics **23**, 1217 (2002)
142. M. Kluge, H.R. Schober: Phys. Rev. E **62**, 597 (2000)
143. U. Geyer, W.L. Johnson, S. Schneider, Y. Qiu, T.A. Tombrello, M.P. Macht: Appl. Phys. Lett. **69**, 17 (1996)
144. V. Zöllmer, K. Rätzke, F. Faupel: J. Mat. Res. **18**, 2688 (2003)

Part II

Interfaces

7 Fluctuations and Growth Phenomena in Surface Diffusion

Michael C. Tringides and Myron Hupalo

7.1 Introduction

The development of new and innovative techniques over the last 40 years to study in a controlled way the adsorption of atoms on surfaces has led to increased interest in the problem of surface diffusion and to explosive publication growth in the field [1, 2]. The interest in the problem is driven both by questions of fundamental science and by the role of surface diffusion in controlling the growth of atomic scale structures, which can have potential technological applications. Atoms adsorbed on surfaces (at least in the submonolayer regime) provide a true realization of two-dimensional (2D) systems, so it is possible to test many theoretical predictions of dynamic phenomena in 2D statistical mechanics. At the same time, surface diffusion is the key process that controls the formation of nanostructures which can be used as building blocks in electronic nanodevices (i.e. lasers, switches, transistors etc.) of increasing speed and storage capacity. However within the limited space of this chapter it is not possible to give justice to the wide-range activity in the field and only selected topics covering different aspects of the problem will be presented. Still we hope even this limited view of surface diffusion will convey the tremendous progress and excitement in the field.

The chapter is organized as follows. In Sect. 7.2 a broad overview of surface diffusion is presented, with a short discussion of measurement methods and unique features of the diffusion problem related to properties of surfaces (i. e. geometry of surfaces, adatom interactions, equilibrium vs non-equilibrium methods). Next, four experiments are discussed in detail in order to illustrate the general issues presented in the overview. Section 7.3.1 describes equilibrium diffusion measurements in reciprocal space on stepped Si(100) from diffraction fluctuations. Section 7.3.2 describes equilibrium diffusion measurements in real space on H/Si(111) with scanning tunnelling microscopy (STM) current fluctuations. Next, non-equilibrium methods are discussed, viz in Sect. 7.4.1 non-equilibrium growth studies on Pb/Si(111) at low temperatures and the observation of self-organized uniform height islands as a result of quantum size effects (QSE). Section 7.4.2 presents measurements and theoretical analysis of interlayer diffusion in Ag/Ag(111) which is responsible for the 3D growth observed at all temperatures. Section 7.5 lists some general remarks about equilibrium vs non-equilibrium diffusion.

Hopefully the reader can appreciate the wide-ranging concepts and diversity in the field of surface diffusion despite the subjective and limited choice of experiments discussed.

7.2 Surface Diffusion Beyond a Random Walk

7.2.1 The Role of Structure and Geometry of the Substrate

The traditional paradigm used to describe surface diffusion is the random walk of an atom diffusing on a rigid 2D lattice. The atom jumps to nearest neighbour sites with constant probability and its mean square displacement $\langle (R_t - R_0)^2 \rangle = 4D_t t$ grows linearly vs time with the constant D_t, the so-called tracer diffusion coefficient. The lattice is described in an abstract way, as a periodic arrangement of mathematical points which is far from the structure and geometry of a real surface. Surface atoms have finite size and varying coordination with their neighbors depending on the symmetry of the underlying lattice and the atom position on the lattice. Surface atoms are connected with their neighbours and the diffusing atom with finite forces. As a result of the motion of the diffusing atom, they can move out of their initial equilibrium to new relaxed positions to minimize the total energy of the system. The substrate is therefore not passive and rigid, as in the picture of a mathematical random walk, but actively participates in determining the optimal pathway of the lowest barrier. Although the relaxation of the surface atoms affects the jumping probability to the nearest site and the energetic barrier, it does not change the basic stochastic nature of the process as a random walk.

Figure 7.1 illustrates the complexities related to the structure of real surfaces by using the ball model for an fcc(111) surface with two exposed levels separated by a step [3]. Different types of atoms are seen with increasing bonding coordination: adatom detached from the step to the terrace, kink atoms, step atoms and terrace atoms. Depending on the specific structure and the growth conditions used, different diffusion processes can be the controlling factors of the observed structures. In general, terrace diffusion of adatoms controls mass transport across the surface. Step shape, whether regular or ramified, is controlled by 1D diffusion of the kink atoms at the island edges. Even this 1D diffusion has additional complexity as seen from the difference in the structure of the two steps shown, denoted by A- (Fig. 7.1(a)) or B-type (Fig. 7.1(b)), dictated by the stacking sequence of the fcc(111) lattice. Atoms at A-type edges form square (100)-type unit cells with the row of substrate atoms below; while atoms at B-type steps occupy the in-between sites of the row of atoms below and form triangular (111)-type unit cells. (If the islands were of multiple heights, A-type steps develop into (100) and B-type steps develop into (111) facets).

We have briefly described one major aspect of the surface diffusion problem, the role of the energetic barriers and kinetic pathways on the formation

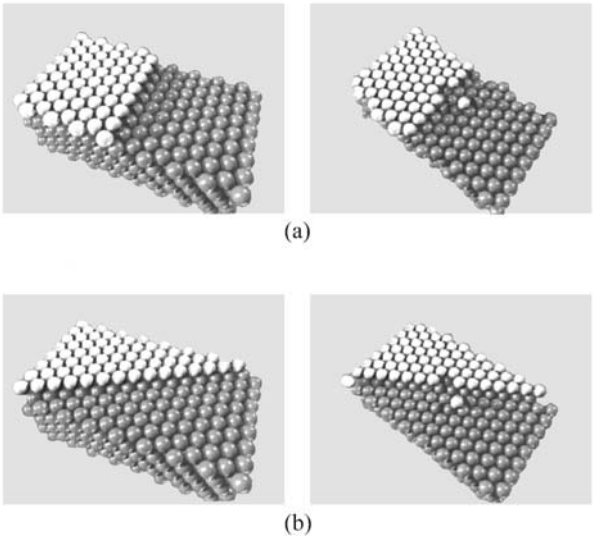

Fig. 7.1. Ball models for the two types of fcc(111) steps: A- (at the top) and B-type (at the bottom). In each case a straight step and a step with kinks is shown.

of the different atomic scale structures. This is a major research area within the surface diffusion community, driven by close interaction between theory and experiment: the potential energy surfaces can be reliably mapped out with an arsenal of theoretical techniques and directly compared to experiments to identify the corresponding kinetic pathways. The theoretical methods range from ab initio methods [4] (i.e. the force fields of the adsorbed atom to the substrate are calculated from Quantum Mechanics) and approximate methods [5] (where the adatom-substrate interactions are parametrized with effective classical potentials and the time evolution of the system follows Newton's equations of motion). Correspondingly the atomic pathways in real systems are inferred by comparing initial to final state images obtained with atom resolving techniques (i.e. scanning tunneling microscopy (STM), field ion microscopy (FIM)). Although this aspect of the problem is a very active research area in surface diffusion, it will not be covered in this article and interested readers can consult the literature [1, 2].

However, even after the pathway of individual atoms is fully determined, it is still an open question to show how this atomistic information can be used to account for the results of finite coverage experiments, when many atoms cooperate to form complicated configurations . As will be seen in this chapter, which emphasizes the many-body aspect and cooperativity in the problem of surface diffusion, this is another active research area within the community. The cooperativity is particularly important under equilibrium conditions when thermal averaging over all the microscopic processes is required.

However, atomistic information can be sufficient under non-equilibrium conditions. A single microscopic process can fully determine the outcome of the experiment if this process has a time constant comparable to the duration of the experiment and all other processes "freeze out" because they have larger time constants. In epitaxy, for example, single atom terrace diffusion can fully determine the nucleated island density during irreversible growth at sufficiently low temperatures [6].

7.2.2 The Role of Adsorbate-Adsorbate Interactions

The second complexity of the problem of surface diffusion, stated in the previous section, is related to the cooperativity and interactions between the diffusing atoms at finite coverage [7]. As seen from the formation of ordered phases of different symmetry formed at low temperatures, the atoms experience strong mutual interactions to generate the ordering. When interactions are present diffusion is not a simple random walk, because the jumping probability to the nearest neighbor sites depends on the local environment of the diffusing atom rather than being constant. For example, in a simple model with nearest-neighbour repulsive interaction J the jumping probability $\mathrm{e}^{zJ/k_\mathrm{B}T}$ depends on the number of nearest neighbours z of the diffusing atom, as implemented in Monte Carlo algorithms.

At high temperatures no single microscopic process of barrier E_i (i.e. terrace diffusion, edge diffusion, dimer diffusion, atom detachment from islands etc.) controls the dynamics of the system because all rates ($\sim \mathrm{e}^{E_i/k_\mathrm{B}T}$) of the different microscopic processes become comparable and an averaging over all the processes is necessary (cf. Chap. 18).

The magnitude of the interactions between the adatoms depends on the strength of the bonding to the substrate. For example, in chemisorbed systems the bonding to the substrate is strong and the adatom interactions larger than about 0.1 eV, because they involve charge transfer or are mediated via the conducting electrons of the substrate [8]. Physisorbed atoms (e. g. noble gases) are weakly bound to the substrate, with van der Waals type interactions between the adatoms that are less than about 0.1 eV, i. e. comparable to the potential corrugation of the substrate. In some systems, strong long-range adatom interactions mediated through the anisotropy of the intrinsic substrate stress can be present (i. e. stepped Si(100), Au($23 \times \sqrt{3}$). They result in the spontaneous formation of periodically arranged domains of large size determined by the competition between the energy increase (because of missing bonds at the domain boundary) and the energy decrease due to the long-range stress mediated interactions [9].

Adatom interactions modify the energy minima at the binding site of the adsorbed atom and the corresponding diffusion barrier. Qualitatively, the effect of the interactions on diffusion is summarized as: repulsive interactions lower the diffusion barrier while attractive interactions raise it. It is not a priori clear how competing interactions will affect the barrier. Since the number

of atoms within the local environment of the diffusing atom increases with coverage, one expects the diffusion coefficient to be coverage dependent. This in turn changes the linear diffusion equation into a non-linear one

$$\frac{\partial\theta}{\partial t} = \nabla D_{\mathrm{c}}(\theta)\nabla\theta \tag{7.1}$$

where $\theta(r,t)$ is the coverage at position r and time t and D_{c} the collective diffusion coefficient. The coverage is defined as the ratio $\theta = c(r,t)/c_0$ with $c(r,t)$ the concentration at r, t and c_0 the saturation concentration, i. e. when all binding sites on the surface are filled. However, as will be discussed later, for systems truly at equilibrium the coverage dependence is not a severe problem and the diffusion equation can be still treated as linear if the variation of θ is small (a few % from its average value $\overline{\theta}$), which justifies the assumption that $D_{\mathrm{c}}(\theta)$ is constant.

Extensive theoretical work has already been carried out to answer quantitatively the question how adsorbate-adsorbate interactions affect diffusion [1, 2]. Commonly a lattice gas model is used, with an effective Hamiltonian which includes the adatom interactions, to deduce the concentration and temperature dependence of the diffusion coefficient $D(\theta,T)$ (where D refers to either D_{t} and D_{c}). The Hamiltonian is written in the form

$$H = \sum_{\langle n_i n_j\rangle} J_{ij} n_i n_j + \sum_{\langle n_i n_j n_k\rangle} J_{ijk} n_i n_j n_k + \ldots \tag{7.2}$$

where $n_i = 1$, 0 denotes the occupation of site i, J_{ij} denotes the pairwise interaction energy between sites i and j, J_{ijk} a trio interaction between a triplet of sites, etc.. In principle, the Hamiltonian can include more complex interactions than the pairwise and trio interactions shown above, but (7.2) can account for the majority of the ordered phases observed experimentally. The calculation of $D(\theta,T)$ for a given Hamiltonian and set of interaction energies $\{J\text{'s}\}$ is carried out either analytically (i.e. mean field theory of various levels of sophistication, renormalization group techniques), numerically (series expansion methods), or, far more commonly, with Monte Carlo simulations. The family of calculated curves $D(\theta,T)$ from (7.2) are compared to the corresponding measured curves to obtain the best agreement with the experimental results. Since the temperature dependence of the diffusion coefficient is commonly parametrized in Arrhenius form $D = D_0(\theta)\exp -(E(\theta)/k_{\mathrm{B}}T)$, in practice, the extracted parameters from the data (i.e. the prefactor $D_0(\theta)$ vs θ and activation energy $E(\theta)$ vs θ) are compared to the calculated ones. It would have been far more efficient if it were possible to do the analysis inversely i. e. to start from the experimental quantities $D_0(\theta)$ and $E(\theta)$ and deduce the appropriate Hamiltonian (7.2) and the interaction parameters $\{J\text{'s}\}$. In practice, the Hamiltonian is based on information obtained independently in other experiments (for example low energy electron diffraction (LEED) measurements of I vs θ or I vs T to determine the different ordered regions of the system and to map out the phase diagram [10]). But

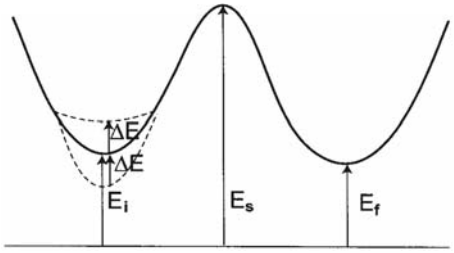

Fig. 7.2. Schematic energy diagram of hopping from an initial energy state E_i to a final state E_f, through the saddle point of energy E_s. ΔE denotes the energy change because of adatom interactions.

even if such inversion in the data analysis were possible, there would still be the question whether the Arrhenius pametrization of $D(\theta, T)$ over the whole temperature range is justified or whether non-Arrhenius behaviour should be expected. Arrhenius expressions are empirically used by experimentalists over limited temperature range ($\sim 100\,\mathrm{K}$) but it is not clear what is the full theoretical justification of this practice.

In a simple-minded way the Arrhenius expression is explained in terms of the 1D energy diagram of Fig. 7.2. At temperature T and in the harmonic approximation the adsorbed adatom oscillates at the well minimum because of its thermal energy. It can overcome the energy barrier with a temperature-dependent probability which leads to the Arrhenius-like expression $D = D_0(\theta)\exp(-E(\theta)/k_\mathrm{B}T)$. In the $\theta \to 0$ limit $E(\theta)$ is the energy difference between the minimum and the saddle point in the potential energy surface of a single adatom and the prefactor is simply $D_0(\theta \to 0) = 1/4a^2\nu$ where a is the lattice constant and ν the typical adatom vibrational frequency. Such expressions are better justified at low temperatures or for strong barriers, when the typical residence time of the adatom in the potential well is much longer than the vibrational time of the substrate phonons, so the picture of an adatom adsorbed at the minima of a rigid potential energy surface as shown in Fig. 7.2 is better justified.

In addition to the coverage and temperature dependence of the diffusion coefficient, important questions related to how sensitive $D(\theta, T)$ is to the phase boundaries separating different ordered regions and whether critical effects resulting from phase transitions can be observed in the θ or T dependence of D, have been actively pursued and will be discussed later.

7.2.3 Diffusion in Equilibrium and Non-Equilibrium Concentration Gradients

Fluctuation Measurements

Diffusion is a result of the presence of non-zero concentration gradients in the system. These gradients exist either because they are imposed as initial conditions, i.e. at $t = 0$ the coverage $\theta(r, t)$ has an externally imposed value $\theta_0(r, 0)$ (different from its average equilibrium value $\overline{\theta}$) or they are generated

because chemical potential gradients $\nabla\mu(r)$ exist in the system. Such chemical potential gradients are present even at equilibrium (i.e. when the average coverage $\overline{\theta}$ is constant both in time and space) because the energy cost of adsorption at a site depends on the type of site occupied. It is more general to write the diffusion equation in terms of the chemical potential gradient (cf., e. g., Chap. 5)

$$J = -L\nabla\mu \tag{7.3}$$

where J is the adatom flux generated by the gradient $\nabla\mu$ and L a phenomenological transport coefficient. Using the continuity equation

$$c_0 \frac{\partial\theta}{\partial t} + \nabla J = 0 \tag{7.4}$$

we derive (7.1) with D_c related to L by the expression $D_\mathrm{c} = (\partial\mu/\partial\theta)L$. When the system is at equilibrium, the derivative $\partial\mu/\partial\theta$ is determined thermodynamically from the $\mu_\mathrm{eq}(\theta)$ isotherm of the system, otherwise the chemical potential $\mu(\theta)$ under non-equilibrium conditions depends on the specific condition $\theta_0(r,0)$ applied initially. For example, in non-equilibrium step profile experiments when the coverage has a value θ_1 for $r < 0$ and a different value θ_2 for $r > 0$, as will be discussed below, $\mu(\theta)$ if different from $\mu_\mathrm{eq}(\theta)$ and the extracted D_c depends explicitly on $\partial\theta/\partial r$.

It is more relevant to discuss differences between equilibrium vs non-equilibrium configurations in systems when ordered phases are present, i. e. in interactive systems at sufficiently low temperatures. As an illustration assume the ordered state is $c(2\times2)$. At equilibrium, atoms can diffuse into neighboring sites even when there is no externally imposed gradient, because within the ordered domains neighboring sites are vacant or at the domain walls the sites are energetically costly, i. e. they have different chemical potentials. If one monitors the coverage at position r and time t, $\theta(r,t)$, its occupation will fluctuate in time around its average value $\overline{\theta}$. As a result of diffusion in or out of position r, a random initial fluctuation $\delta\theta(r,0) = (\theta(r,0) - \overline{\theta})$ will spread out. At distance r' away and at later time t, we expect to see the "remnant" fluctuation $\delta\theta(r',t) = (\theta(r',t) - \overline{\theta})$ if the time of the fluctuation at r to diffuse to site r' is larger than t. Information about the diffusion coefficient is obtained from the time dependence of the autocorrelation function $S(r'-r,t) = \langle\delta\theta(r,0)\delta\theta(r',t)\rangle$ where the bracket average includes an average over all sites in the system, since at equilibrium all sites are equivalent. Since the diffusion equation (7.1) is linear for systems at equilibrium (even when $D_\mathrm{c}(\theta)$ is coverage dependent) it is also obeyed by $S(r'-r,t)$. Truly equilibrium systems have low amplitude concentration fluctuations (when compared to the average concentration $\overline{\theta}$) $|\langle\delta\theta^2(0,0)\rangle^{1/2}|/\overline{\theta} \ll 1$ and as discussed earlier a constant diffusion coefficient can be assumed. Since $S(r'-r,t)$ depends on the difference $(r'-r)$ it can be simplified to $S(r,t)$ and is given by

$$S(r,t) = S_0\left(\exp -(r^2/(4D_\mathrm{c}t))\right) \tag{7.5}$$

with $S_0 = \langle \delta\theta^2(0,0)\rangle$. As will be discussed in Sect. 7.3.2, more commonly the initial fluctuation is probed within an area with several sites in order to increase the measurable signal. The expression for $S(r,t)$ can be written equivalently in terms of its Fourier transforms for the conjugate variables of r and t, i.e. wavevector k and frequency ω. The Fourier components $S(k,t)$ follow exponential decay with k-dependent initial amplitudes. For the $k \to 0$ component the decay is given by

$$S(k,t) = \left(S_0/a^2\right) \cdot \exp(-D_c k^2 t) \tag{7.6}$$

where a^2 is the unit cell area and $S(k,\omega)$ has a Lorentzian dependence on ω

$$S(k,\omega) = 2S_0 k^2 D_c / \left(a^2(\omega^2 + (k^2 D_c)^2)\right) \ . \tag{7.7}$$

For the measurement of the diffusion coefficient D_c different experimental methods based on the three equivalent expressions (7.5), (7.6), (7.7) have been developed.

The extraction of D_c from (7.5) requires the measurement of time correlations between fluctuations at two sites separated by distance $r' - r$. Such measurements are difficult because (i) precise control of the separation $(r'-r)$ is necessary and (ii) the measurable signal is low if the correlation between only two single sites is probed. However, it is not necessary to restrict the experiment to the correlation of single sites [11]. The signal can be increased considerably if instead fluctuations within a finite area, which includes several sites, are monitored in time. For example for a circular area A of radius r_0, shown schematically in the upper part of Fig. 7.3, it can be easily shown that the autocorrelation function is given by the integral

$$\langle \Delta N(0)\Delta N(t)\rangle = \int c_0^2 \, \mathrm{d}^2 r \, \mathrm{d}^2 r' \langle \delta\theta(r,0)\delta\theta(r',t)\rangle = \int c_0^2 \, \mathrm{d}^2 r' \, \mathrm{d}^2 r S(r'-r,t) \tag{7.8}$$

where $N(t)$ is the number of adatoms within the area A at time t and c_0 the saturation concentration. The magnitude of the initial fluctuation at $t = 0$ is given by $\langle \Delta N^2(0)\rangle = A c_0^2 S(k=0,0)$. Since the signal increases linearly with the probe area A, it is easier to be detected in the experiment. D_c depends on the time constant τ of the decay of the correlation function and the probe area A via $D_c = A/(4\tau)$.

Equation (7.6) has been implemented in simulations where a periodic long-wavelength ($\lambda = 2\pi/k$) modulation of the coverage is generated by imposing at $t = 0$ a small-amplitude variation of the chemical potential $\mu(r) = \mu_0 + \delta\mu \cos(kr)$ whith $\delta\mu/\mu_0 \ll 1$. The system is still close to equilibrium but the coverage differs in a sinusoidal fashion from the average value $\overline{\theta}$ (determined from $\mu_0 = \mu_{\mathrm{eq}}(\overline{\theta})$ by a small amount $\delta\theta$ proportional to $\delta\mu$). For times $t > 0$ the variation $\delta\mu\cos(kr)$ is removed and the system relaxes back to equilibrium. This is shown schematically in the lower part of Fig. 7.3 where the amplitude of the coverage modulation decays with times t_1, t_2, t_3.

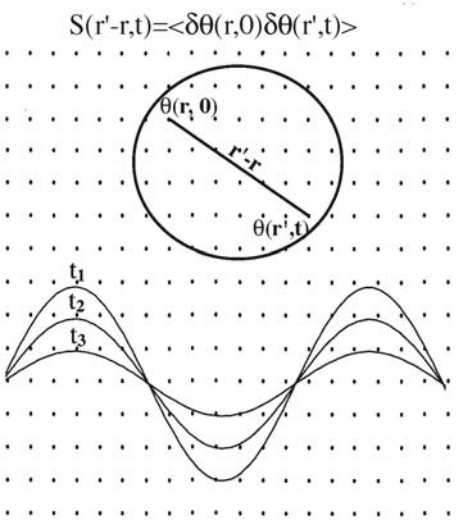

Fig. 7.3. Schematic presentation of the diffusion experiment to measure the decay of coverage fluctuations within a probe area (upper part). Presentation of the grating experiment when an initial sinusoidal coverage profile decays exponentially in time (lower part).

Since only one spatial Fourier component of wavevector k is present, both $S(k,t)$ and the amplitude of the coverage variation $\delta\theta(t)$ decay exponentially according to (7.6). The time constant τ of the decay can be used to deduce the value of the diffusion coefficient $D_c = (2\pi/k)^2/\tau$. Experimentally a method based on (7.6) has been implemented by forming a 1D grating from the interference of two laser beams incident on the same surface spot [13]. Atoms within the illuminated region desorb according to the local laser power which varies sinusoidally because of the interference of the two waves. So within the grating the coverage is lower than the average $\overline{\theta}$. Diffusion of atoms from the surrounding area refills the grating and returns the coverage back to its average value $\overline{\theta}$. The refilling is measured in time by using a third low power laser which monitors the decaying second harmonic generation (SHG) or the first order diffraction signal, as the grating refills in time. Although the coverage within the 1D grating is always below $\overline{\theta}$ (while in the case of the oscillatory chemical potential the coverage oscillates around $\overline{\theta}$) its refilling follows a similar time dependence as (7.6).

Equation (7.7) can be implemented in the frequency domain with a spectroscopic technique to measure $S(k,\omega)$. This technique is a well-developed method to measure diffusion coefficients in 3D systems with the use of quasielastic neutron scattering (see Chap. 3). The equivalent technique in two dimensions is quasielastic He-scattering which fulfills the necessary requirements to have both wavevector and energy resolution [14]. A monochromatic beam of He-atoms scatters from the surface with momentum transfer wavevector k and the scattered atoms are energy resolved to obtain the spectrum $S(k,\omega)$ (of (7.7)). The energy loss of the atom beam at fixed wavevector k is measured from the full width at half maximum (FWHM) of the quasi-

elastic spectra $\Delta E = \hbar\Delta\omega$ (extracted after fitting the experimental spectra to Lorentzian lineshapes). The inverse $\Delta\omega^{-1}$ corresponds to the time $\Delta t = (D_c k^2)^{-1}$ for the diffusing atom to reach a distance of about $\lambda = 2\pi/k$. For "hydrodynamic" (i.e. long wavelength) diffusion measurements, (especially at high coverage for systems with interactions when D_c can differ from the one deduced at smaller length or time scales) it is necessary to perform the measurements at sufficiently small wavevectors k and long scattering times $\Delta\omega^{-1}$ being larger than the time for a time to the nearest neighbor site. This imposes strong requirements on the wavevector and energy resolution of the technique.

Diffusion in Externally Imposed Concentration Gradients

Other methods to measure surface diffusion are carried out under conditions when the coverage gradient $\partial\theta/\partial r$ is externally imposed. For example, in 1D step profile evolution experiments along a line r the coverage has one value θ_1 in region $r < 0$ and a different value θ_2 in region $r > 0$. With time, atoms will move from the region of higher to the region of lower coverage (shown schematically in Fig. 7.4) until a uniform concentration is established. If there are no adatom interactions (except site exclusion) the profile is described by

$$\theta(r,t) = \frac{(\theta_1 - \theta_2)}{2}\left(1 - \mathrm{erf}\left(r^2/\sqrt{2D_c t}\right)\right) . \tag{7.9}$$

Such profile experiments result in coverage independent D_c values in agreement with equilibrium methods.

In systems with interactions the coverage dependence $D_c(\theta)$ is obtained from the Boltzmann-Matano (BM) analysis (see Chap. 1, Sect. 1.11.1) of the profile shape. However, before applying the method to the experimental or simulation results, it is essential to show first that the profiles scale (i.e. they can be written in the form $\theta(r,t) = \theta(r/t^{0.5})$). It is not possible to satisfy the scaling condition in the case of an initial 2D patch geometry [15]. If the scaling condition is met, $D_c(\theta_0)$ is obtained for a range of coverages θ_0 ($\theta_2 < \theta_0 < \theta_1$) by

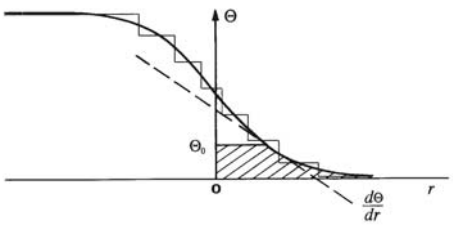

Fig. 7.4. Schematic representation of a step-profile evolution experiment and the geometric parameters (shaded integrated area and local slope) needed to evaluate the Boltzmann-Matano integral (7.10). Each flat segment of constant coverage can approximately be thought to be at equilibrium.

$$D_{\mathrm{c}}(\theta_0) = \frac{1}{2t\left(\dfrac{\mathrm{d}\theta}{\mathrm{d}r}\right)_{\theta_0}} \int_{\theta_2}^{\theta_0} r\,\mathrm{d}\theta\,. \tag{7.10}$$

If the scaling condition is not fulfilled, a time-dependent diffusion coefficient will be extracted from (7.10) where the value obtained at the earliest times deviates the most from the equilibrium value. At longer times the profile smoothes out, the gradient $\partial\theta/\partial r$ is reduced, the coverage differences are smaller and the scaling condition is met more easily.

We can consider limits in the steepness of the gradient $\partial\theta/\partial r$, so $D_{\mathrm{c}}(\theta)$ extracted from profile evolution experiments agrees with $D_{\mathrm{c}}(\theta)$ obtained at equilibrium [16]. For a given system the gradient $\partial\theta/\partial r$ must not exceed a certain maximum value to ensure that the externally imposed fluctuations (from the initial steepness of the profile) do not exceed the thermodynamically generated fluctuations. The profile can be approximated as a staircase of flat segments of length L, (with $L \approx 5L_{\mathrm{res}}$, i. e. equal to several times the optimal spatial resolution limit $L_{\mathrm{res}} \approx 0.1\,\mu\mathrm{m}$) for reliable differentiation. It is necessary that the externally imposed gradient $(\Delta\theta/\Delta r)_{\mathrm{exp}}$ is smaller than the coverage gradient due to mean square fluctuations within a system of size L. The coverage variation $(\Delta\theta)_{\mathrm{therm}}$ is simply given by the ratio of the mean square fluctuations $\langle\delta N^2(0)\rangle^{0.5}$ and the number of sites (L/a_0) (with a_0 the lattice constant). This ratio, in turn, is simply the normalized compressibility of the system. We thus have

$$(\Delta\theta)_{\mathrm{therm}} = \langle\delta N^2(0)\rangle^{0.5}/(L/a_0) = (\partial\theta/\partial(\mu/k_{\mathrm{B}}T))^{0.5}\,. \tag{7.11}$$

It follows that the condition

$$(\Delta\theta/\Delta r)_{\mathrm{exp}} < (\Delta\theta/\Delta r)_{\mathrm{therm}} = (\partial\theta/\partial(\mu/k_{\mathrm{B}}T))^{0.5}/L \tag{7.12}$$

between the experimental and the thermodynamically generated gradient should hold for the extracted $D_{\mathrm{c}}(\theta)$ to be the same as the equilibrium one. Equation (7.12) most probably will not be satisfied at early times when $(\Delta\theta/\Delta r)_{\mathrm{exp}}$ has its largest value of about θ/L (in practise larger than $10^4\theta/\mathrm{cm}$). This value is comparable to the right-hand side of (7.12), at least for the case of the Langmuir gas (i. e. site exclusion interaction) when $\partial\theta/\partial(\mu/k_{\mathrm{B}}T) = \theta(1-\theta) < 1$. Even at later times (7.12) can be violated close to the ideal coverage of an ordered phase (i.e. at $\theta = 0.5\,\mathrm{ML}$ for the $p(2\times1)$ phase and for $T < T_{\mathrm{c}}$ the phase is least compressible, which means $\partial\theta/\partial(\mu/k_{\mathrm{B}}T) \to 0$).

This discussion explains a recent Monte Carlo study of O/W(110) with the $p(2\times1)$ the ordered phase from step profile evolution with the BM method [17]. In these simulations the larger deviation between the D_{c} extracted from BM and equilibrium methods was observed at early times and for a coverage close to $\theta = 0.5\,\mathrm{ML}$.

The BM step profile method should fail to follow critical fluctuations as $T \to T_{\mathrm{c}}$ and $\partial\theta/\partial(\mu/k_{\mathrm{B}}T) \to \infty$, since finite size effects become important,

especially at early times when the constant coverage segments in Fig. 7.4 are the smallest. Smaller "subsystems" cannot measure correctly thermodynamic singularities of the free energy or its derivatives.

One of the major predictions in the variation of $D_c(\theta, T)$ is the critical slowing down close to a second-order phase transition [18]. This is easily seen from a widely used mean field expression for the diffusion coefficient, namely $D_c = \Gamma a_0^2/(\partial \ln\theta/\partial(\mu/k_B T))$ with Γ denoting the average jump rate. This expression is referred to also as the Darken equation when Γa_0^2 is identified with the tracer diffusion coefficient D_t (cf., e. g., Chap. 1, Sect. 1.11.2). Close to a second-order phase transition, critical fluctuations generated thermodynamically are so large ($\partial\mu/\partial\theta \to \infty$ as $T \to T_c$) that no diffusion currents can eliminate them. This effectively means that $D_c(T)$ goes to 0 as $T \to T_c$. Strictly speaking this is true for systems where the order parameter is the coverage θ, since only then the compressibility $\partial\mu/\partial\theta$ is singular at T_c. However, for systems which have order parameters different from θ (e. g. an Ising model with repulsive interactions and the order parameter being the "staggered magnetization") a weaker singularity is expected for $(\partial\theta/\partial\mu)^{-1}$ at the phase transition. Critical slowing down effects both in equilibrium and profile evolution methods should be smeared out, since only the "staggered" compressibility (i.e. the inverse derivative of the order parameter with respect to μ) is truly singular. However, D_c is still reduced close to T_c as a result of the less singular behavior of $\partial\mu/\partial\theta$ (as will be seen later in Sect. 7.3.2 in connection with Fig. 7.9). In addition to the temperature dependence of D_c close to a phase transition, the coverage dependence D_c vs θ (for fixed temperature $T < T_c$) can show maxima as the ideal coverage of the ordered phase $\theta \to \theta_c$ is approached, since at θ_c the perfect defect-free phase is least compressible. The reason is that large energy is needed to generate deviations from this ideal phase, i.e. $\partial\theta/\partial\mu \to 0$ as $\theta \to \theta_c$. For the Ising model with repulsive interactions at $\theta_c = 0.5$ (the coverage of the $c(2 \times 2)$ phase) D_c shows a maximum both in equilibrium and profile evolution methods [19,20]. Clearly the behaviour of D_c, whether it shows maxima or minima, depends on the interaction Hamiltonian (i. e. the nature of the order parameter) and the control parameters, i. e. temperature and coverage. Step profile evolution methods have been used in [21] to study phase transitions.

In addition to the interest in profile evolution measurements of surface diffusion, non-equilibrium methods based in the time evolution of a system from a disordered to an ordered phase after a deep quench have been reviewed in [22] and will not be covered here. Instead we will discuss the role of surface diffusion in epitaxial growth because it has more technological significance. Since epitaxial growth is commonly carried out at far-from-equilibrium conditions (i.e. low temperatures or high deposition rates) the observed structures are metastable [1]. These epitaxially grown structures can have technological importance when they are regular in size, shape and separation. In general, many different microscopic processes with different activation barriers can

operate during the growth. As discussed earlier, at low temperatures the process with the lowest barrier is the controlling one.

We present below specific examples for equilibrium and non-equilibrium experiments to illustrate the previous general discussion. The equilibrium experiments are based on measuring coverage fluctuations with high resolution low energy electron diffraction (HLEED) on stepped Si(100) and with STM. As for non-equilibrium experiments, we discuss the formation of Pb islands of uniform height, flat tops and steep edges on Si(111) and measurements of interlayer diffusion on Ag/Ag(111).

7.3 Equilibrium Measurements of Surface Diffusion

7.3.1 Equilibrium Diffusion Measurements from Diffraction Intensity Fluctuations

Are Diffraction Intensity Fluctuations Possible?

Experiments measuring diffusion at equilibrium are based on coverage fluctuations which have a low amplitude for systems truly at equilibrium. If the fluctuations are large, as discussed for step profile evolution experiments, they introduce a non-thermodynamic driving force in the diffusion current and the extracted parameters cannot always be compared to the ones from equilibrium experiments. However, fluctuations of low amplitude imply that the measurable signal is small and it is necessary for the experimental technique to have sufficient amplification. Such a fluctuation method has been implemented with great success by exploiting the high magnification ($\approx 10^6$) of the field emission microscope [11, 16] to monitor the time dependence of coverage fluctuations within a probe area, as discussed in connection with (7.8). Since it is reviewed elsewhere it will not be discussed further in this chapter. An STM based probe area method [22, 23] will be described in Sect. 7.3.2. The electron emission process requires high electric fields (typically $0.5\,\mathrm{V/\AA}$) which can potentially introduce bias to the random walk with atoms preferentially diffusing towards the tip.

Despite the success of these methods, there are reasons to develop a reciprocal-space method (i.e., surface diffraction) to measure equilibrium fluctuations. In addition to the disadvantages associated with the presence of an electric field, real space methods have to integrate over the atoms occupying the probe area (cf (7.8)) and therefore are not sensitive to the state of the overlayer, i. e. are unable to decide whether it is an ordered or disordered phase. On the other hand, diffraction-based methods are wavevector selective and therefore sensitive to the fluctuations within a specific phase, when the overlayer supports the formation of different phases. By "tuning" the wavevector to the phase of interest the sensitivity of the technique is enhanced. In such methods fluctuations of the diffracted intensity defined by

$$I(k,t) = \frac{1}{(N\theta)^2} \int \theta(r,t)\theta(r'+r,t) \exp(-kr)\, \mathrm{d}^2 r'\, \mathrm{d}^2 r \qquad (7.13)$$

are measured which are more intimately related to theoretical quantities like, e. g., $S(k,t)$ (cf. (7.6)). The autocorrelation function of $I(k,t)$ is defined in terms of fluctuations $\delta I(k,t) = I(k,t) - \langle I(k,t)\rangle$ from the average value $\langle I(k,t)\rangle$ at time t. Although it involves 4-point correlation functions, as shown in [24], it can be expressed in terms of the structure factor $S(k,t)$

$$G(k,t) = \langle \delta I(k,0)\delta I(k,t)\rangle = cS^2(k,t) \qquad (7.14)$$

with c representing a constant which depends on the details of the system under investigation. Measurements of the autocorrelation function of $I(k,t)$ provide a new method of measuring $S(k,t)$ [25–28].

The idea of the diffraction experiment is straightforward but it has not been implemented earlier because several demanding experimental conditions should be met [25, 26]: (i) coherence in the diffraction experiments extends up to a finite distance ζ, so that the intensity fluctuations are correlated only up to this distance. Since the beam size d is larger than ζ it includes $(d/\zeta)^2$ incoherent scattering regions and the fluctuation signal is reduced since temporal correlations between different regions are lost. To minimize this effect it is necessary to employ high-resolution diffractometers (i.e Δk better than 0.1% of the Brillouin Zone) or small d. The high resolution has the additional advantage of prohibiting the integration of the measured time constant $\tau(k)$ over a wider wavevector range. (ii) it is also essential to have high acquisition speed to take full advantage of the high resolution, otherwise a larger time constant than the true one will be extracted, a severe problem at high temperatures.

As shown recently [25, 26] condition (i) depends on the brightness of the incident beam (i.e. number of electrons per solid angle per time). It is met with specialized electron guns of high current densities. The use of such guns and modern high-gain channeltron-based detectors has shown the feasibility of the technique, as discussed below in diffraction experiments on stepped surfaces.

Fluctuation measurements have been also pursued in "speckle" X-ray experiments [29] where the incident beam size is reduced to size comparable to the coherence length $d \sim \zeta$ with the use of μm size geometric apertures. Such a stringent condition is necessary for "speckle" measurements (i. e. when the relative scattering phase of all the atoms within the illuminated region is preserved). Features of the static structure factor $S(k)$ (i. e. interference fringes) have a one-to-one correspondence with the exact location of the atoms within the illuminated area, which effectively enables the technique to function like a real space "microscope". However, such reduction of beam size is not necessarily beneficial for time-dependent fluctuation measurements, if the brightness of the source (i. e. number of photons per area per second) remains the same after the aperture is introduced. Because of the reduced beam size, the

incident photon flux will be correspondingly reduced which also lowers the measurable signal.

Thermal Fluctuations at Steps

What kind of dynamic processes can be studied from diffraction intensity fluctuations? As the simplest example we can think of point defects or adatoms diffusing on the surface, with atomic scattering factors different from the one of the substrate atoms $f_{\mathrm{D}} \neq f_{\mathrm{s}}$. As the adatoms diffuse their position and scattering phase is time-dependent ($f_{\mathrm{D}}(r,t)$), which will cause fluctuations in the diffracted intensity $I(k,t) = |\sum f_j \exp(\mathrm{i}kr)|^2$. The autocorrelation function of the intensity fluctuations will decay with time constant $\tau(k) = (2\pi/k)^2/4D_{\mathrm{c}}$ where D_{c} is the adatom diffusion coefficient. Such low coverage experiments can be best performed with He-scattering since the adatom scattering factor can differ substantially from the substrate scattering factor [30] thus maximizing the measured signal. In a different experiment, fluctuation measurements can be used to study the dynamics close to phase transitions. This is an area where practically no experimental work has been done so far in 2D systems. Close to a second-order phase transition, large fluctuations of the order parameter (i.e. superstructure intensity) at the ordering wavevector are expected. Changes in the functional form of the time-dependent correlation function, critical slowing down and dynamical critical exponents can be measured from the superstructure spot fluctuations. Another example are physisorbed systems (i.e. inert gases adsorbed at low temperatures) with fluctuations in the intensity of integer order spots, originating either from adatom diffusion or adsorption-desorption from or to the gas phase. As shown in [24], the form of the autocorrelation function changes as the relative contribution of the two processes, diffusion and desorption, is varied with temperature. In such experiments the autocorrelation function measured at different temperatures can be used to deduce the barriers of the two processes, i.e. the desorption energy, the corrugation of the potential energy surface in the limit $\theta \to 0$ and the adatom interactions.

In general, for any microscopic process monitored with diffraction fluctuations of $I(k,t)$, the first theoretical priority is to work out the form of the autocorrelation function to check if it agrees with the measured one. Such comparison can be used to deduce the details of the microscopic mechanism controlling the dynamic process and to measure in real time the relevant time constants. Both pieces of information are difficult to obtain with other methods.

A full comparison between theoretical and experimental results has been carried out in the dynamics of thermally induced step fluctuations [27, 28]. When steps are heated to higher temperatures they deviate from their straight positions because a fluctuating step leads to a gain in entropy. Elementary excitations such as kinks, vacancies etc. are created which are highly mobile and cause the fluctuations. Dynamic measurements of the fluctuations

can be used to determine the type of microscopic process generating them and the relevant energetic barriers.

Step fluctuations result from several competing processes described in [31]. Step mobility $\Gamma(T)$ is responsible for generating thermal excitations at temperature T. This is opposed by the restoring force acting to return the step back to its straight position. The restoring force consists of two terms. First, the step stiffness $\overline{\beta}$ describes the energy cost to generate a kink on a straight step, since a kink atom has lower coordination than an atom at a straight step. Second, long-range step-step interactions described in terms of an effective potential $U(x)$ (where x is the separation between two steps) constraints the step to maintain the initial terrace length L. Excursions of the step separation from L will increase the potential energy $U(x)$ and as a result the elastic forces between the steps act to restore the step back to its straight position. This second component of the restoring force is parametrized by the "force constant" of the potential $c = \partial^2 U/\partial x^2|_L$ evaluated at the initial average terrace size L. The two parameters of the restoring force $\overline{\beta}$ and c determine the step average equilibrium properties: the mean square displacement $w_\infty^2 = \sum_i (x_i - \overline{x})^2$ (where $(x_i - \overline{x})$ is the deviation of the ith atom from its average position), the correlation length ξ along the step (defined by the correlation function $C(y) \sim \exp(-|y|/\xi)$ between two atoms separated by distance y) and $\overline{\beta}$ the step-stiffness

$$w_\infty^2 = k_\mathrm{B} T \left(\frac{1}{8c\overline{\beta}}\right)^{1/2}, \quad \xi(T) = \left(\frac{\overline{\beta}}{2c}\right)^{1/2} . \tag{7.15}$$

The Cartesian coordinate system is chosen in such a way that z is normal to the terrace and x, y lie on the terrace, with x normal to the step and y along the step. Both w_∞ and ξ can be extracted from fits of the static intensity profile $I(k_x, k_y)$ at the out-of-phase condition $k_z = (\mathrm{odd})\ \pi/d = (2l+1)\pi/d$, where d is the step height and l an integer. At the out-of-phase condition, neighboring terraces scatter destructively because the phase difference of the scattered wave normal to the terrace is an odd multiple of π and therefore $I(\boldsymbol{k}, t)$ is maximally sensitive to step fluctuations. The static diffraction profile of an integer order beam normal to the step $I(k_x)$ is split with the separation between the two split spots (located at $k_x = \pm\pi/L$) proportional to the inverse of the average terrace length. The FWHM of each split spot in the x direction can be used to extract w_∞. On the other hand the static profile along the step $I(k_y)$ is sensitive to correlations in the atom positions and in the step fluctuations up to the correlation length $\xi(T)$ [28]. The inverse of the FWHM of spot profile along the spot for fixed out-of-phase values of $k_x = \pm\pi/L$ (at the two maxima of the split spot) can be used to deduce the correlation length $\xi(T)$ along the step.

Temporal step fluctuations are measured by monitoring the peak of the diffracted intensity at the maxima of the out-of-phase split spot $I(k_x = \pm\pi/L,\ k_y = 0)$. At in-phase-conditions, $k_z = (\mathrm{even})\pi = 2l\pi/d$, no fluctua-

tions (and no splitting of the profile $I(k_x)$) are expected because neighboring terraces scatter constructively. This difference between the temporal signal measured at in-phase vs out-of-phase conditions, is the first experimental evidence that the experiment has sufficient sensitivity to step fluctuations and incoherent scattering has not washed out the fluctuation signal.

The relative magnitude of the expected diffraction fluctuations $\langle \delta I^2(0) \rangle / \langle I \rangle$ for average intensity $\langle I \rangle$ with M incoherent domains (for a beam of size d and coherence length ζ, $M \approx (d/\zeta)^2$ domains) can be expressed in terms of the relative fluctuation $\langle \delta^2 I_\mathrm{p}(0) \rangle / \langle I_\mathrm{p} \rangle$ within a single coherent domain [26,28] by

$$\frac{\langle \delta I^2(0) \rangle}{\langle I \rangle} = 1 + \frac{\langle I \rangle}{M} \frac{\langle \delta I_\mathrm{p}^2(0) \rangle}{\langle I_\mathrm{p} \rangle} \quad . \tag{7.16}$$

The unity term in the right hand side is simply the known result for statistical uncorrelated noise $\langle \delta^2 I_\mathrm{s}(0) \rangle / \langle I \rangle = 1$, expected for any measurement with average signal $\langle I \rangle$. It can be shown [28] that for the case of step fluctuations the term $\langle \delta^2 I_\mathrm{p}(0) \rangle / \langle I_\mathrm{p} \rangle$ can be expressed as

$$\frac{\langle \delta^2 I_\mathrm{p}(0) \rangle}{I_\mathrm{p}} = \frac{2}{N_x(\zeta/\xi)} (k_x w_\infty)^4 (1 - \exp(-(\zeta/\xi))) \tag{7.17}$$

with all other symbols defined earlier. Equations (7.16) and (7.17) indicate the optimal conditions for the step fluctuation signal to be observed. First, although the decrease of the beam size reduces the number of incoherent domains M and suppresses the incoherent summation, this is not necessarily an advantage, as seen in (7.16), if the current density $\langle I \rangle / M$ remains constant. Second, experiments on surfaces with higher vicinality (i.e. lower L for the same w_∞, ζ, ξ) will have larger signal in the temporal measurement since $k_x^4 / N_x \sim L^{-3}$. Such experiments demonstrating the feasibility of temporal fluctuation experiments with high resolution LEED [26], have been first carried out on high-index stepped W(430) surfaces in the range $T = 700$–$900\,\mathrm{K}$ by taking advantage of the improved brightness of the electron source, the high resolving power of the instrument ($\Delta k = 0.005\,\mathrm{nm}^{-1}$ or $\zeta = 1/\Delta k = 200\,\mathrm{nm}$) and the high vicinality of the surface ($L = 7a_0$, i. e. 7 lattice units). Fluctuations $\langle \delta^2 I_\mathrm{p}(0) \rangle / \langle I_\mathrm{p} \rangle$ which increase with temperature as high as up to 5 times the statistical fluctuations were observed at an out-of-phase condition $k_z = 5\pi/d$, while smaller fluctuations, consistent with statistical fluctuations, were observed at the adjacent in-phase-condition.

Microscopic Mechanisms for Step Fluctuations

The usefulness of diffraction fluctuation experiments can be assessed further from the time dependence of the correlation function and the extraction of diffusion barriers from the corresponding Arrhenius plots. For step fluctuations, the measured diffraction signal (which originates from phase differences

between neighboring steps) is a collective result of the contribution of single atom hopping events. Information about the nature of these atomistic processes can still be extracted from the fluctuation signal, because the form of the correlation function and the measured time constants are sensitive to the atomistic processes operating.

Three atomistic processes have been proposed in the literature to explain how collective step fluctuations are generated [31]. Each process is described by a characteristic quantity: the step mobility Γ, the 1D diffusivity along the step edge D_s and $\theta_0 D_\mathrm{t}$ (the product of the equilibrium adatom concentration θ_0 and the tracer diffusion coefficient D_t since in the third process atom detachment from the step is balanced by diffusion away on the terrace). Depending on which of these three rates is the controlling one, the analysis of step fluctuations results in different functional forms for the correlation function. By testing which form is in agreement with the experimental data the controlling process can be identified. In the evaporation and condensation mechanism (EC), atom transport to other steps is controlled by Γ. It is valid whenever Γ is sufficiently small. Step diffusion (SD) applies in the opposite limit when the detachment of atoms from the steps is fast and diffusion along steps is faster than terrace transport ($D_\mathrm{s} \gg \theta_0 D_\mathrm{t}$). Terrace diffusion (TD) applies when Γ is very large and terrace transport is faster than step edge diffusion ($D_\mathrm{s} \ll \theta_0 D_\mathrm{t}$). These limits are deduced from the general expression for the effective time constant $\tau(k)$ (of a step fluctuation of wavevector k with Σ the area of an elementary hop of the diffusing entity) when all three atomistic processes have comparable contributions [32]

$$\tau(k) = \frac{2k_\mathrm{B}T(\Gamma + 2\theta_0 D_\mathrm{t}\Sigma^2 k + \Sigma^{3/2} D_\mathrm{s} k^2)}{\Gamma\theta_0\overline{\beta}k^2(2\theta_0 D_\mathrm{t}\Sigma^2 k + \Sigma^{3/2} D_\mathrm{s} k^2)} \quad . \tag{7.18}$$

When one of the three limits dominates, the measurement can be analyzed as if only one of the three processes operates; otherwise in crossover regimes more than one process should be taken into account.

Next we outline briefly the methodology of deriving the form of the correlation functions for the different atomistic processes. In general, the step fluctuation correlation function $G_\mathrm{p}(t)$ originating from a single coherent domain can be written [28] in terms of the time-dependent correlation along the step $C(y,t)$

$$\frac{G_\mathrm{p}(t)}{\langle I_\mathrm{p}\rangle^2} = \frac{4}{N_x(\varsigma/a_\parallel)} \sum_{-\varsigma/2a}^{\varsigma/2a} \left\{\cosh((k_\parallel w)^2 C(y,t) - 1\right\} \quad . \tag{7.19}$$

Equation (7.19) has been derived from the summation of the amplitude of N_x independently fluctuating steps in the x-direction within the coherence length of the instrument ζ and the summation along the step in the y-direction still present in (7.19). Fluctuations along the step are correlated up to $\xi(T)$, i.e. essentially the distance over which $C(y,t)$ is non-zero. $\xi(T)$ is

temperature dependent and is determined by the thermodynamics of the step interactions (cf (7.15)) while ζ as a parameter of the instrument is independent of temperature. The step can be thought of as divided into ζ/ξ separate regions and each region contributes independently to the total fluctuation signal. The expression (7.19) is evaluated at the wavevector of maximum sensitivity at the split spot $k_x = \pm\pi/L$.

The different atomistic models differ as to the functional form of the correlation function $C(y,t)$ or equivalently the form of its Fourier components $C_k(t)$

$$C(y,t) = \exp(-|y|/\xi a_{\parallel}) - \frac{1Na_{\parallel}}{\pi 4w^2}\int_{-\infty}^{\infty} C_k(t)\cos(kya_{\parallel})\,\mathrm{d}k \quad . \tag{7.20}$$

Expressions for $C_k(t)$ have been derived from the solution of differential equations describing the local fluctuating step amplitude $\Delta(y,t)$ for the different atomistic mechanisms. We have

$$\frac{\partial\Delta}{\partial t} = \frac{\Gamma\overline{\beta}}{k_{\mathrm{B}}T}\frac{\partial^4\Delta}{\partial y^4} - \frac{2\Gamma\theta_0}{k_{\mathrm{B}}T}\frac{\partial^2\Delta}{\partial y^2} + \frac{\eta(y,t)}{a} \tag{7.21}$$

where $\eta(y,t)$ is uncorrelated thermal noise. As an illustration, we give the result for the SD model. Full derivations for the other models can be found in [28]. The solution for the Fourier coefficients of the correlation function $C(y,t)$ is

$$C_k(t) = \xi\frac{4w^2}{Na}\frac{(1-\exp(-(t/\tau_{\mathrm{s}})(a/\xi)^2\{(\xi k)^2 + (\xi k)^4\}))}{(\xi k)^2+1} \quad . \tag{7.22}$$

All symbols in (7.22) have been defined before except τ_{s}, which is the characteristic time for the rate controlling atomic event, i. e. the time for the diffusing entity (i. e. atom, dimer, etc.) to hop a distance $\Sigma^{0.5}$ along the step edge i. e. $\tau_{\mathrm{s}} \approx \Sigma/2D_{\mathrm{s}}$.

From (7.22) one can derive the correlation function $C(y,t)$ by means of (7.20), the expected expression $G_{\mathrm{p}}(t)$ for the single-domain (7.19) at an out-of-phase condition $k_z = (2l+1)\pi/d$, and finally the expression for the measured correlation function (7.16) which includes the effect of the incoherent summation over the beam size.

It has been shown in [28] that the expression for $G_{\mathrm{p}}(t)$ at times $t > \tau_{1/2}$ (where $\tau_{1/2}$ is the time for the correlation function to drop to half its initial value, $G_{\mathrm{p}}(\tau_{1/2}) = G_{\mathrm{p}}(0)/2)$) can be written in the general form

$$G_{\mathrm{p}}(t) = G_{\mathrm{p}}(0)\exp\left[-A(n)(t/\tau_n)^{1/n}\right] \tag{7.23}$$

with the exponent n different for the three atomistic models, $n = 1$ for EC, $n = 3$ for TD and $n = 4$ for SD kinetics. Equally important is the determination of the energetic barriers of the atomistic process, from the temperature

dependence of the time constant $\tau_{1/2}(T)$ of the correlation function. The connection between $\tau_{1/2}(T)$ and the microscopic time τ_n of the individual atomistic event is different for each of the three cases and is made through the model-dependent parameter $A(n)$ via

$$\tau_n = \left(\frac{A(n)}{0.693}\right)^n \tau_{1/2} \quad . \tag{7.24}$$

For example, for the specific SD model already discussed in (7.21) and (7.22) we have

$$A(n=4) = (0.74)\left(\frac{a}{\xi}\right)^2 (2\theta_0 \Omega^{3/2})/k_{\mathrm{B}}T \quad . \tag{7.25}$$

Thermal Fluctuations on Stepped Si(100) with High Resolution LEED

These theoretical predictions have been tested in high resolution LEED experiments [27] on vicinal Si(100) crystals of misorientation $\sim 1^\circ$ (i.e. the average terrace is $L = 6.5\,\mathrm{nm}$). 200 independent samples were averaged to minimize statistical noise. The experiment was performed in the range $950\,\mathrm{K} < T < 1130\,\mathrm{K}$. Fitting the static profiles along the step $I(k_y)$ was used to deduce the correlation length $\xi(T)$ and to extract the step stiffness $\overline{\beta}$ from (7.15) ($\overline{\beta}$ in turn can be used to deduce the kink and corner step energies within the terrace-step-kink TSK model [27]) and the step-step interaction "force constant" $c = \partial^2 U/\partial x^2|_L$. It is possible to deduce two independent parameters, $\overline{\beta}(T)$ and c, from a single measured one ($\xi(T)$), because $\xi(T)$ can be uniquely written as the sum of a term varying strongly with temperature and another term practically temperature independent. As seen from (7.15) these components correspond to $\overline{\beta}$ and c, respectively.

Time-dependent correlation functions are shown in Fig. 7.5(a) for the two extreme temperatures 948 K and 1123 K. Both $G(0)$ and $\tau_{1/2}(T)$ follow the expected temperature dependence described earlier: $G(0)$ being proportional to w_∞^4 (where w_∞ is the mean square deviation of the step) increases with T, and $\tau_{1/2}(T)$, the time constant of the fluctuations, decreases with T. The value of $G(0)/\langle I\rangle = \langle \delta^2 I(0)\rangle/\langle I\rangle$ is equal to 4×10^{-3} and still small with respect to the value 1 of statistical noise at $t = 0$. However, averaging over 200 independent samples reduces statistical noise for finite times $t > 0$ so that the correlation function is observed above the noise. Figure 7.5(b) shows a fit of the time dependence of the form of the correlation function according to (7.23). Exponential decay (i.e. $n = 1$) is ruled out by the fit so EC is not the operating mechanism. The data are compatible with $n = 4$ (SD mechanism) and with $n = 3$ (TD). The test of the functional form of $G(t)$ is therefore not sufficient to distinguish between these two possibilities. Energetic considerations of the extracted diffusion barriers, to be discussed next, favor $n = 4$.

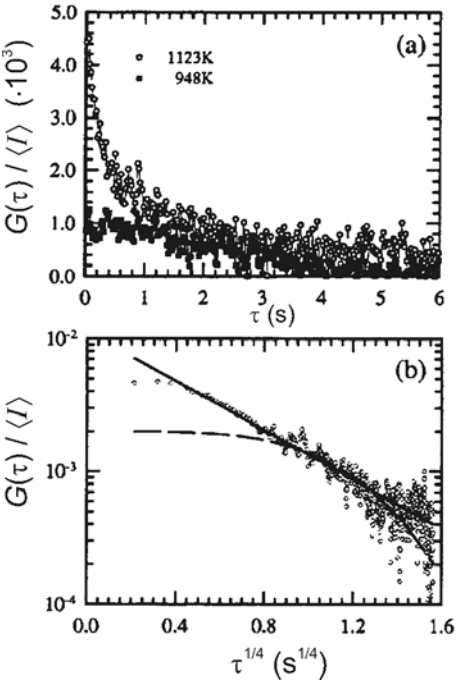

Fig. 7.5. (a) High-resolution LEED correlation function on stepped Si(100) at two temperatures. (b) The fits of the time dependence of the correlation function exclude exponential decay and therefore rule out the EC model for step fluctuations.

From the temperature dependent data the decay times $\tau_{1/2}(T)$ are extracted for each correlation function with the two compatible fits ($n = 3$ or 4). The $\tau_{1/2}$ values clearly do not depend on n, however the atomistic times τ_n which correspond to the single atomistic events generating the fluctuations (and therefore the microscopic barriers) do, through (7.24), (7.25). For SD kinetics we measure the step edge diffusion barrier $E_s = 0.8 \pm 0.2\,\text{eV}$ and the prefactor $\nu_s = 10^{10\pm2}\,\text{s}^{-1}$, while for the TD case we measure $E_t = 1 \pm 0.2\,\text{eV}$ and $\nu_t = 3 \times 10^{8\pm2}\,\text{s}^{-1}$. In TD kinetics two activated barriers are involved additively in the final activation energy, i.e. the barrier controlling the equilibrium coverage θ_0 of the detached entity (i.e. the dimer formation energy E_F for Si(100)) and the terrace diffusion barrier E_D. The extracted activation energy from the fluctuation experiments should be the sum $E_t = E_D + E_F$. As discussed in [27], from other experiments $E_D = 0.67\,\text{eV}$ is known and theoretical estimates give $E_F = 1.6\,\text{eV}$, so the measured activation energy of 1 eV (if $n = 3$ is assumed) is too low to be consistent with these independently known energies. The data suggest that SD and $n = 4$ is the most probable microscopic mechanism.

Step fluctuations of Si(100) have been studied before with low energy electron microscopy (LEEM), both at equilibrium [31] (by analyzing real-space LEEM images of fluctuating steps with video acquisition speed and at length scales ≈ 10 times the LEED coherence length ζ) and during non-

equilibrium ripening experiments [35] (by monitoring after Si deposition, how the nucleated islands grow in time). Because the LEEM experiments follow the evolution of the system over larger length scales higher temperatures were used ($T > 1090\,\mathrm{K}$) than in the diffraction experiments. From the LEEM studies it was deduced that the microscopic mechanism responsible for the step fluctuations is not SD, as in the diffraction experiment, but EC. This conclusion was based on the wavevector dependence of the time constants ($\tau(k) \sim k^2$) deduced from the relaxation of the Fourier components $C_k(t)$ of the correlation function calculated from time-dependent LEEM images. It was further supported from the linear dependence of the growing island area ($A \sim t$) in the non-equilibrium ripening experiments [35]. This raises the interesting question why the diffraction experiments indicate that SD is most probably the microscopic mechanism operating and not EC kinetics.

As mentioned before in discussing (7.18) all atomistic mechanisms operate simultaneously and one can identify a single mechanism responsible for the fluctuations only when the inequalities between the atomistic rates Γ, $\theta_0 D_\mathrm{t}$, D_s described in Sect. 7.3.1 (p. 302) are strictly obeyed. However, as seen in (7.18), the limiting values, where a single atomistic process is the dominant one, are strong functions of the temperature and the length scale of the experiment (i.e. the inverse of the probing wavevector of the technique k^{-1}). From (7.18) it is seen that the various limits between Γ, $\theta_0 D_\mathrm{t}$, D_s depend both on T (since in principle different activation energies and prefactors describe the different rates) and the wavevector k. Since in LEEM both the temperature range is higher (by approximately 300 K) and the probing wavevector is smaller by a factor of 10 than in the diffraction experiment, the EC process is weighted more, but at lower temperatures or larger k the SD process is favored. The main conclusion from this comparison is that although it is not appropriate to assign a single atomistic process, the comparison of different experiments is legitimate, in terms of the Arrhenius parameters (i.e. activation energies and prefactors). The Arrhenius parameters are independent of which atomistic process operates in a given temperature range.

7.3.2 STM Tunneling Current Fluctuations

Correlation Functions in Probe Area STM Experiments

The use of STM to study finite coverage diffusion and the role of interactions has been demonstrated in [33, 34] by measuring the mean residence time of an adatom as a function of adatom separation. Such FIM-like experiments require a large number of statistics. No time-dependent correlation functions were measured. As shown by (7.8), equilibrium diffusion measurements can be carried out by analysing the decay of the autocorrelation of concentration fluctuations within a probe area A. In such experiments the possibility of measuring fluctuations at selective wavevectors is lost, since the measured signal integrates the total number of adatoms within A. An area is naturally

defined in the STM geometry because the tunneling current depends exponentially on the tip-surface separation and most of the current is confined within a narrow cone with its apex at the tip.

If the surface coverage θ is constant, the number of adatoms in A, $N(t)$, will fluctuate around its average value $\overline{N} = A\theta$ as adatoms diffuse in and out of the area. The tunneling current $i(t)$ depends on the tip-surface separation z and the electronic structure within A (i. e. the local "workfunction" $\Delta\varphi$) which is determined by the number of adatoms within A. $I(t)$ is uniquely determined by $N(t)$ at a given time, since both z and $\Delta\varphi$ are functions of $N(t)$. As $N(t)$ changes, its fluctuations $\delta N(t) = N(t) - \overline{N}$ will produce fluctuations in the tunneling current $\Delta i(t) = i(t) - \overline{i}$ with $\overline{i}$ denoting the average tunneling current. The time dependence of the current fluctuations $\Delta i(t)$ will follow the time dependence of $\Delta N(t)$ and hence the fluctuations due to the adatom diffusion in and out of A. Equation (7.8) can be measured from the tunneling current autocorrelation function for sufficiently small $\Delta N/\overline{N} \ll 1$,

$$\langle \Delta N(t)\Delta N(0)\rangle = \gamma^2 \langle \Delta i(t)\Delta(0)\rangle = \gamma^2 \sum_{k=1}^{k=N} \left(i(t_k + t) - \overline{i}\right)\left(i(t_k) - \overline{i}\right) \quad (7.26)$$

where γ is a proportionality constant relating $\Delta i(t)$ to $\Delta N(t)$. For systems with no interactions and for any size A (even as small as one unit cell) it has been shown by Monte Carlo simulations [36] that the functional form of (7.8) is given by

$$\langle \Delta N(t)\Delta N(0)\rangle = \langle \delta N^2(0)\rangle \int_A \frac{e^{-r^2/4Dt}}{4\pi D_c t}\, \mathrm{d}^2 r \quad (7.27)$$

which is simply the probability for an initial fluctuation of strength $\langle \delta N^2(0)\rangle$ to remain within A after time t. Equivalently, if the power spectrum $W(\omega)$ is measured, instead of the correlation function, it is given by the Fourier transform of (7.27),

$$W(\omega) = \int \langle \Delta N(t)\Delta N(0)\rangle e^{i\omega t}\, \mathrm{d}t \quad . \quad (7.28)$$

The experimental situation is shown schematically in Fig. 7.6. The decay of the correlation function in the short-time limit is approximately exponential (equivalently (7.28) follows the Lorentzian ω^{-2} dependence in frequency). In the long-time or zero-frequency limit, the correlation function has the characteristic $1/D_c t$ tail, typical of diffusion in two dimensions. Equivalently, $W(\omega)$ has the form

$$W(\omega) = \frac{\langle \delta N^2(0)\rangle A \ln \omega}{4\pi D_c} \quad \text{for} \quad \omega \to 0 \quad . \quad (7.29)$$

Preliminary experiments [23] on O/Si(111) have shown that such STM fluctuation measurements are possible. The evidence was based on the much

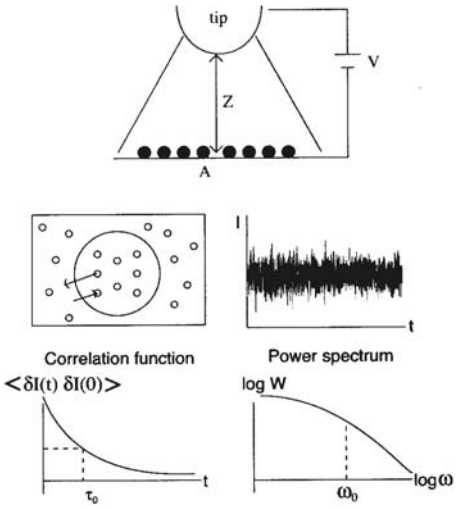

Fig. 7.6. Schematic presentation of the STM fluctuation experiment where either the time dependent correlation (left) or, equivalently, the power spectrum (right) of the tunneling current I vs time t can be used to measure the diffusion coefficient.

higher fluctuation level $\langle \Delta i^2(0)\rangle^{0.5}/\bar{i}$ for the adsorbate covered vs clean surface, on fitting the measured spectra to the characteristic $\ln\omega$ dependence on ω as in (7.29) and to the Arrhenius dependence of the time constants $\tau(T)$ vs $1/T$ in the range $T = 400$–$550\,\mathrm{K}$ to extract an activation energy of diffusion $E = 1\,\mathrm{eV}$. However, the O/Si(111) system is highly complex with adsorbed oxygen in different bonding configurations [37], so it is difficult to interpret the extracted value of E in terms of the energetic barrier of a single diffusing species.

Figure 7.7 presents power spectra obtained for the H/Si(111) system at saturation coverage, $\theta \to 1$, in the range $T = 500$–$730\,\mathrm{K}$. The tunneling conditions are $\bar{i} = 1\,\mathrm{nA}$ and $V = -15\,\mathrm{V}$ (tunneling from the sample to the tip) which corresponds to a tip-surface separation of $\approx 3\,\mathrm{nm}$. The separation is measured experimentally by modulating the position of the z-piezo Δz and detecting the corresponding current component ΔI with a lock-in amplifier.

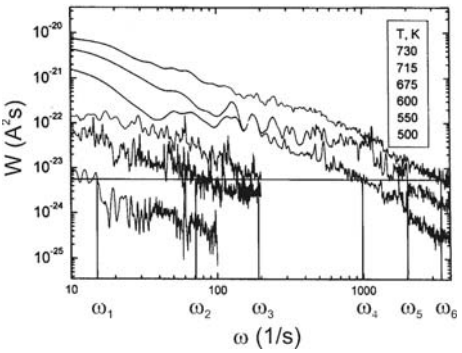

Fig. 7.7. Power spectra for H/Si(111) close to saturation ($\theta \to 1$) as a function of temperature ($T = 500$–$730\,\mathrm{K}$) showing that the mean square fluctuations $\langle \delta N^2(0)\rangle$ increase while the spectral content shifts to higher frequencies with increasing temperature.

$\Delta \log I/\Delta z$ corresponds to the tunneling barrier. The point where the barrier "collapses" is identified as the contact point between tip and surface. Once this point is identified, the tip-surface separation is determined by the difference in the z-piezo voltages between the "contact" voltage and the voltage of interest.

The spectra include higher frequencies outside the low frequency limit of (7.29), so the fitting requires the full expression (7.28). The spectra are consistent with H diffusion as seen from the increase of the integrated area under the curves (which is a measure of $\langle \Delta N^2(0) \rangle$) and the shift of the spectral content to higher frequencies with increasing temperature. The time constants $\tau(T)$ are obtained by fitting the spectra to (7.27), (7.28) and, when plotted in Arrhenius form, an activation energy $E = 1.3\,\mathrm{eV}$ is extracted, in good agreement with earlier optical grating measurements on H/Si(111) [38] over mesoscopic length scales.

For measuring only the diffusion activation energy, it is sufficient to obtain the ratios of the time constants at different temperatures $\tau(T_1)/\tau(T_2)$. However, full information about surface diffusion requires two additional issues to be addressed. First, it is important to deduce the absolute value of D_c (i.e. in addition to E) to be able to extract the diffusion prefactor. Second, it is not clear whether the form of the correlation function (cf (7.27)) is true in systems with interactions (i. e. it is an open question whether in the limit $t \to \infty$ the correlation function follows the $1/D_c t$ dependence), especially at low temperatures when ordered phases are present. Although changes in the form of the correlation function do not affect the extracted value of E, they can indicate different cooperative dynamics (i.e. critical slowing down close to a second-order phase transition).

Tunneling Area Determination from STM Fluctuations

We can answer the first question if the size of the tunneling area A can be measured. In principle, the area can be estimated from a solution of the Schroedinger equation to match the measured tunneling current $i(V)$ at a given voltage V. The accuracy of the estimate depends on the sophistication of the model of the tunneling process and unknown experimental parameters like tip shape and sharpness. Because of these caveats, we suggest an experimental method to measure the tunneling area which is based on only measurable quantities.

The tunneling area is expected to increase monotonically with the tip-surface separation z. The tunneling current $i(z, N)$ for a fixed voltage V is a function also of N where N is the number of adatoms within the tunneling area since the local "workfunction" $\Delta\varphi$ is determined by N. For a change ΔN (and fixed z), we can write the corresponding tunneling current change as a result of an equivalent change of z

$$\Delta i = \frac{\Delta i}{\Delta z} \cdot \frac{\Delta z}{\Delta N} \cdot \Delta N \tag{7.30}$$

or for the relative current change

$$\frac{\Delta i}{\overline{i}} = \frac{\Delta \log i}{\Delta z} \cdot \frac{\Delta z}{\Delta N} \cdot \Delta N \quad . \tag{7.31}$$

This assumption is justified since $\Delta \log i/\Delta z$ is the effective barrier in the tunneling process with $\overline{N}$ adatoms in A. $\Delta \log i/\Delta z$ is uniquely defined because $\overline{N}$ is approximately constant (when $\Delta N/\overline{N} \ll 1$ is satisfied) and the geometry of the two electrodes (i.e. "conically"-shaped tip and planar surface) remains unchanged.

In the limit of $\theta \to 1$ diffusion is caused by the motion of a small number of vacancies ($\theta_v \approx (1-\theta)$), so the problem can be analyzed by considering a dilute gas of N_v vacancies. When $N_v \to 0$, the relative fluctuation (using the compressibility of a Langmuir gas) can be approximated as $\Delta N_v/\overline{N}_v = (N_{\max}(1-\theta)^2\theta)^{0.5}/N_{\max}(1-\theta) \cong N_{\max}^{-1/2}$, i. e. it is the inverse of the square root of the number of sites in the tunneling area.

The N_v vacancies are generated in the adatom layer of thickness z_0 (where z_0 is the apparent height of a single adatom). The rate of change $\Delta z/\Delta N$ for N close to $N_{\max}$ can be written as $z_0/N_{\max}$ since the motion of one atom into or out of A causes on the average only $1/N_{\max}$ fractional change of z_0, (i.e. z_0 is the change of the tip-surface separation when all atoms are removed).

We can rewrite (7.31) in terms of the unknown quantity $N_{\max}$, which is the number of sites within A,

$$N_{\max} = \left((\Delta \log i/\Delta z) z_0/\Delta i/\overline{i}\right)^2 \quad . \tag{7.32}$$

All three quantities on the right hand side of (7.32) can be measured experimentally: $\Delta i/\overline{i}$ is the ratio of the mean square fluctuation to the average current (or, equivalently, the area under the power spectrum $W(\omega)$) to $\overline{i}$), $\Delta \log i/\Delta z$ is the effective barrier height, measured with the lock-in technique described before and z_0 (= 0.1 nm) is obtained from the apparent atom height in STM images.

Figure 7.8 shows such power spectra at three tip-surface separations on H/Si(111) at $\theta \to 1$ in the frequency range 0–200 Hz and $T = 600$ K [22].

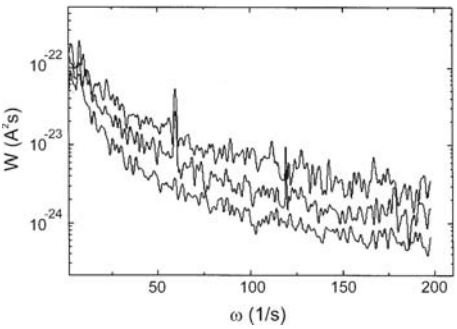

Fig. 7.8. Power spectra for H/Si(111) close to $\theta \to 1$ as a function of the tip surface separation z showing that the lower spectrum ($V = -15$ V and larger tip-surface separation $z \approx 3$ nm) has spectral content shifted to lower frequencies because of the larger tunneling area.

In the spectra of Fig. 7.8 the tunneling current is fixed ($I = 1\,\mathrm{nA}$) and the tip-surface separation is varied from 0.4 nm to 3 nm by varying V (z is measured from the point of "collapse" of the barrier $\Delta \log I/\Delta z \approx 0$ and the change of the voltage on the z-piezo). The spectra for the larger voltage $V = -15\,\mathrm{V}$ (i.e. larger tip-surface separation $z = 3\,\mathrm{nm}$) have more spectral weight to lower frequencies, as expected for larger tunneling area. By using the measured values $V = -15\,\mathrm{V}$, $\Delta \log I/\Delta z = 2.5\,\mathrm{nm}^{-1}$, $\Delta i/\overline{i} = 0.038$, $z_0 = 0.1\,\mathrm{nm}$ we obtain $N_{\max} = 43$ hydrogen binding sites. If we assume that each site corresponds to a Si(1 × 1) unit cell this amounts to an area $A = 4.5\,\mathrm{nm}^2$ which is used to deduce a prefactor $D_0 = 1.5 \times 10^{-7}\,\mathrm{m}^2/\mathrm{s}$ in the experiments of Fig. 7.7.

Correlation Functions in Interactive Systems

We return to the second question raised previously, viz what is the shape of the correlation function $\langle \Delta N(t) \Delta N(0) \rangle$ if there are interactions between the adatoms. Such questions have been addressed with mean field theory [39] and Monte Carlo simulations in model systems [36], with the results of the two methods being in good agreement with each other.

An Ising model with repulsive interactions was used for illustration. At low temperatures the ordered $c(2 \times 2)$ phase forms. The most demanding condition for determining whether $\langle \Delta N(t) \Delta N(0) \rangle$ follows the non-interactive (i. e. site exclusion) expression (7.27) is for the smallest probe area A because in this case the most pronounced deviations from the long-wavelength "hydrodynamic" regime are present. For this reason, in [36] the single-site correlation function (i.e. the probe area side is one lattice constant) was used. As stated before for the case of site-exclusion, even for such small areas $\langle \Delta N(t) \Delta N(0) \rangle$ obeys (7.27) and has the characteristic $1/D_c t$ tail. This is not surprising since the evolution of the step concentration profile for site exclusion (which also includes short-wavelength components) follows (7.9). i. e. the solution for non-interactive systems.

Figure 7.9 shows results for the single-site correlation function obtained in [36] as a function of T/T_c. The results are plotted in terms of the scaled variable $t/\tau_{1/2}$ (where $\tau_{1/2}$ is the time for the correlation function to drop to 1/2 of its initial value) to check for deviations from the non-interactive form obtained for $T/T_c \to \infty$. Deviations are seen at lower temperatures and the characteristic $1/D_c t$ tail is not observed for intensity levels as low as 10^{-3} of the initial value of the correlation function at $t = 0$. It is not known whether the tail will be seen for lower values of the correlation function, although such values are below the detectability limit of current fluctuation experiments. Deviations of the correlation function from the non-interactive form (cf (7.27)), are also expected for larger probe areas, but the degree of deviation should be less. It is an open question to determine these deviations in other lattice gas models with different types of interactions.

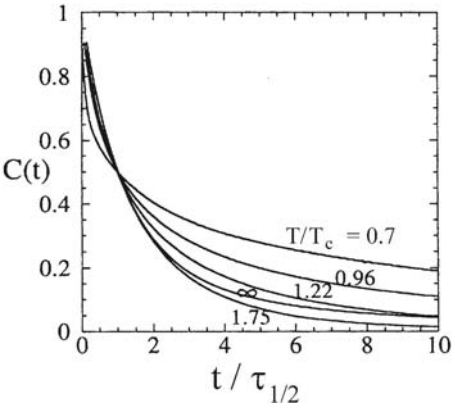

Fig. 7.9. Single-site (i.e. probe area is 1×1 cell) correlation functions as a function of the scaled variable $t/\tau_{1/2}$ in an Ising model with repulsive interaction $\theta = 0.5$ calculated with Monte Carlo simulations. The results show that for temperatures within the ordered region ($T/T_c < 1$) there are deviations from the non-interactive ($T/T_c = \infty$) form of the correlation function.

The high electric field $E(r)$ present in STM experiments raises the question whether the field can affect the measurements by changing diffusion, from purely random to a biased random walk [40]. The magnitude of the effect will depend on the type of the adsorbed atom. Larger effects should be expected for adatoms which have non-zero dipole moments. For adatoms with zero dipole moments the effect should be smaller and should depend on the adatom polarizability. We examine this latter case in detail because it is applicable to the two fluctuation experiments described earlier, i. e. H/Si(111) and O/Si(111). The electrostatic energy between an adatom with polarizibility α in an electric field $E(r)$ is given by $U_0(r) = \frac{1}{2}\alpha E^2(r)$. Since the energy does not depend on the sign of the electric field, similar effects should be expected independent of the voltage polarity. The energy U_0 will be lower where $E(r)$ is strongest (i. e. underneath the tip), so the diffusing atoms will move towards the tunneling area. The ratio of the probability to diffuse towards ($P_\uparrow$) over the probability to diffuse away ($P_\downarrow$) from the tunneling area is given by

$$\frac{P_\uparrow}{P_\downarrow} = \mathrm{e}^{2U_0(r)/k_\mathrm{B}T} \quad . \tag{7.33}$$

Since the electric field falls with the distance r from the tunneling area with a power law dependence, this biased diffusion will extend over long distances. The role of the field on diffusion is based on two effects. First, diffusion in this "tilted" potential energy surface will have the effect of rearranging the atom distribution (if initially the atoms are deposited randomly on the surface) to one with maximum coverage within the tunneling area underneath the tip. This effect has been observed in the H-on-Si(111) system, when after randomly depositing $\theta < 0.05$ ML, a circular region of higher coverage ($\theta \approx 0.25$ ML, i. e. five times the initial θ) is seen underneath the tip if the tunneling voltage 6 V is kept on for 1/2 hour [22]. Second, the shape of the correlation function can deviate from the non-interactive shape (cf (7.27))

and the calculated time constant $\tau_{1/2}$ can be smaller than the expected one for zero field ($\tau = A/4D_c$).

Biased diffusion in the presence of an electric field was modeled with Monte Carlo simulations and simple site-exclusion interaction [40]. The correlation function was calculated for different starting times t_0 (starting from $t_0 = 0$ when there is a random distribution of atoms on the surface) as atoms diffuse towards the tunneling area. For shorter times t_0, strong deviations from the expected form (7.27) are observed, as a result of both the coverage rearrangement and the biased character of diffusion. For long enough times t_0 the shape of the correlation function becomes identical to (7.27) for the non-biased potential energy surface, although the value of the time constant is half the expected one ($A/4D_c$), i.e. an initial fluctuation decays faster on the "tilted" than on the flat surface. It is left to further studies to justify these results analytically.

7.4 Non-Equilibrium Experiments

Two growth experiments shall be described where diffusion controls the final outcome. Because such experiments are non-equilibrium ones (i.e. carried out at low temperatures or high flux rates so that equilibrium cannot be established), a single microscopic process is sufficient to account for the observations. There is no need for averaging over the different microscopic processes, as in fluctuation experiments.

7.4.1 Uniform-Height Pb Islands on Si(111)

Growth of Uniform-Height Islands in Pb/Si(111) at Low Temperatures

Epitaxial growth is widely used to fabricate custom-made structures with nano-scale dimensions that do not exist in nature. Because the confinement of the electrons in these small structures leads to sharp quantization of their energy levels, these structures can have important technological applications as lasing devices, sensors, ultrafast switches, etc. The spacing of these energy levels (and thus the electronic properties of the nano-scale devices) can be adjusted if the size of the growing structure can be controlled.

Since epitaxial growth is commonly carried out far from equilibrium the grown structures are metastable. The key controlling processes for the growth in a specific system are the ones with time constants smaller than the duration of the experiment. Because it is not clear which microscopic process is the controlling one, it is important to check the full space of growth parameters (i. e. coverage, temperature, flux rate, kinetic pathway, etc.) in order to determine the types of structures which form, especially whether it is possible, to observe structures which are self-organized and regular.

A lot of effort in growth experiments is necessary to produce smooth (i. e. layer-by-layer) films where a layer is completed before a new one starts to grow. This type of growth results in films of minimal roughness and well-defined electronic states. On the other hand, if growth is rough (i.e. three-dimensional) the electronic levels are smeared out which degrades their potential technological applications. Great efforts have been made to understand the factors that determine the type of growth mode and, in case it is 3D, to find ways to modify it to layer-by-layer growth. One way to accomplish this is with the use of surfactants [41] i. e. by involving a small amount of impurities that modify the kinetic barriers and enhance interlayer diffusion.

It is far more challenging to fabricate regular structures where confinement is in more than the normal direction as in an ultrathin film. Sharper electronic levels are expected. For example, islands of sufficiently small lateral size, the so-called quantum dots, confine the electrons in all three dimensions. By adjusting the geometrical dimensions, energy selectivity and improved monochromaticity of the emitted radiation during electronic transitions become possible.

Strain can play an important role in fabricating quantum dots, like in Ge-Si alloys [42]. Islands, already buried within a Si-capped layer, generate a strain field propagating through the capped layer producing deep energy minima at specific locations on the surface. These minima "stir" the nucleation of new islands deposited on the capped layer to positions highly correlated to the buried islands below and can lead to highly uniform island size/separation distributions, if several consecutive cycles of deposition/capping are used.

Next we describe a different method to produce uniform-height metallic quantum dots on semiconductor substrates observed during low-temperature growth. Such uniformity has been observed in the Pb/Si(111)-(7×7) [43, 44] system and is not driven by stress, since a wetting layer of one ML forms initially to relieve the stress and to allow perfect Pb(111) crystallites to grow on top of it.

In these experiments two complementary techniques are used, STM and high resolution electron diffraction (SPA-LEED) to determine the growth mode, as a function of coverage and temperature. With SPA-LEED at 185 K intensity oscillations are observed as a function of perpendicular momentum transfer k_z of the scattered wave, for different deposited Pb amounts as shown in Fig. 7.10. Oscillations are produced as the scattering condition changes from in-phase (i. e. $Hk_z = 2\pi$(integer), when the scattered intensity has maxima, with H denoting the island height) to out-of-phase (i. e. $Hk_z = \pi$(odd), when the scattered intensity has minima) as discussed in Sect. 7.3.1. The island height H can be found from the oscillation period Δk_z, $H = 2\pi/\Delta k_z$. If single steps were present ($H = d$) the maxima would correspond to integer values of $k_z/(2\pi/d) = 3, 4$ (the variable on the abscissa) shown schematically at the bottom of Fig. 7.10. Since the observed period Δk_z is 1/7 of the oscillation for single steps, it implies that $H = 7d$. More

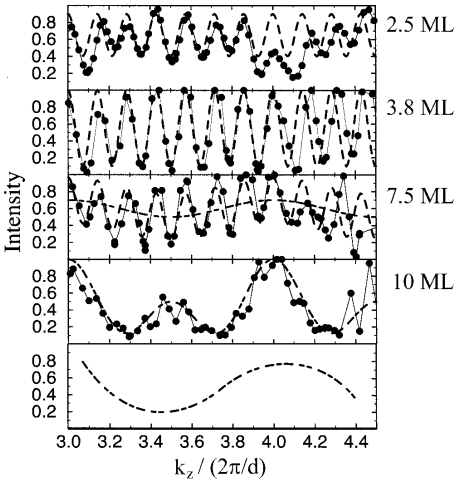

Fig. 7.10. 7-fold diffraction oscillations of the (00) intensity vs normal-component momentum transfer $k_z/(2\pi/d)$ indicating 7-step islands for Pb/Si(111)-(7 × 7) grown at $T = 185\,\mathrm{K}$ for coverage $\theta \leq 7.5\,\mathrm{ML}$. The bottom curve indicates the expected 1-fold oscillation, if single steps were present.

detailed analysis of the amplitude of the oscillations, to extract all Fourier components, suggests that the islands have flat tops and steep edges. In fact, the width of the facets regions at the sides of the island turns out to be smaller than 10% of the island size.

These diffraction results have been confirmed with variable temperature STM. Figure 7.11 shows an STM 200 nm × 200 nm image for $\theta = 3.3\,\mathrm{ML}$ Pb deposited on Si(111)-(7 × 7) at $T = 190\,\mathrm{K}$ [44]. This unusual growth has been also reproduced with STM in [45]. One sees directly the regular Pb islands with striking flat tops and steep edges in excellent agreement with the diffraction results. A histogram of the island heights is shown at the bottom of Fig. 7.11. The main peak in the histogram corresponds to islands with 6.7-single-step and a smaller peak is present at 3.8-single-step islands. The non-integer height values are related to the difficulty in defining the origin of the layer between the islands with STM, since in STM one measures the electron density contours and not the atomic centers. The presence of a sharper height distribution in diffraction is because of the vastly superior statistical average (10^6 islands are included in collecting the data of Fig. 7.10 while only 40 islands are considered for the histogram of Fig. 7.11). At 190 K, from Fig. 7.11 the average island diameter is found to be 10 nm (consistent with the inverse of the FWHM of the Pb(10) spot) and the average island separation is 30 nm (consistent with the satellite spots close to the (00) spot expected for a spatially correlated island separation). The island size and separation increase by approximately a factor of 3 as the temperature changes from 130 K to 240 K.

Extensive studies on Pb/Si(111)-(7 × 7) were carried out by varying the growth temperature, coverage, annealing temperature and annealing time to measure how the selected island height depends on the growth conditions. Although for a given T and θ only one island height is the preferred one

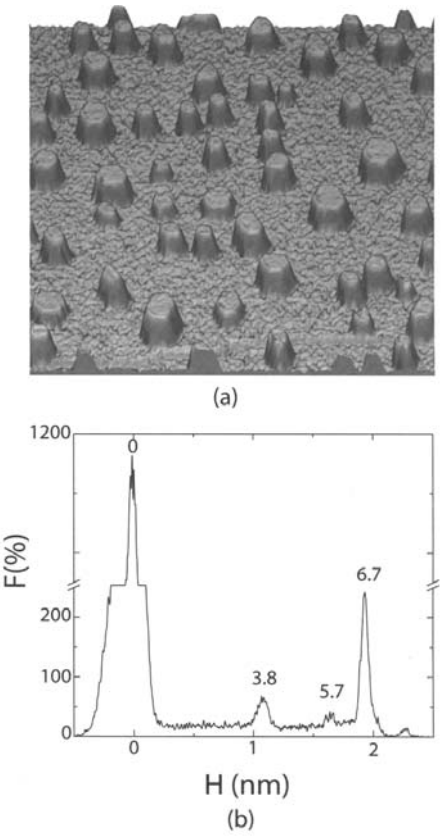

Fig. 7.11. (a) 200 nm × 200 nm STM image and (b) height histogram of Pb/Si(111)-(7 × 7) at 190 K and $\theta = 3.3$ ML confirming the diffraction data of Fig. 7.10 that the islands grow in preferred 7-step heights.

(for example at $T = 185$ K 7-step is the preferred height) the selected height changes with growth conditions by bilayer $2d = 0.58$ nm height increments ($d = 0.29$ nm is the single-step height of Pb(111)). 5-step oscillations are observed at the lower temperatures 130–160 K, followed by 7-step islands, followed by 9-step islands for $T > 210$ K etc.. From these studies a $T - \theta$ kinetic phase diagram shown in Fig. 7.12 [44] was constructed and by choosing the appropriate $T - \theta$ range a given height can be selected in the experiment.

The growth experiments were performed by direct deposition of a fixed amount or by stepwise deposition of small increments. No difference in the island dimensions was found which indicates that diffusion in the system is extremely fast, since these islands are completed within the deposition time (i.e. 4 minutes to deposit 4 ML). Annealing experiments were also performed with the surface heated from the initial lower temperature T_{i} to a higher final temperature T_{f}. Although the same island height is selected in annealing and growth experiments (for the same T_{f}), islands larger in size form after annealing than after growth experiments. However, once a final temperature

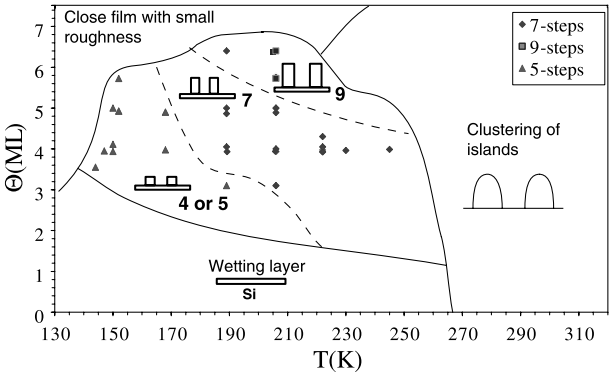

Fig. 7.12. θ-vs-T kinetic phase diagram for growth on Pb/Si(111)-(7 × 7) showing that preferred island heights 4, 7, 9 ... can be selected for different growth conditions.

is reached no further increase in island height and minor increase in size is observed despite prolonged ($\approx$ 1/2 hour) heating at constant T_{f}, which indicates the extraordinary mobility of $\sim 10^4$ deposited Pb atoms to diffuse and build the islands within $\sim$ 4 minutes and, most likely, some type of non-thermal diffusion.

Quantum Size Effects (QSE) and Charge Transfer in Pb/Si(111) Growth

What is the driving force for the formation of the uniform-height islands? An explanation was proposed in terms of quantum size effects (QSE), i. e. the dependence of the energy of the confined electrons occupying discrete energy levels on island thickness [46, 47]. The boundary conditions on the electron wavefunction imposed by the two interfaces (metal-semiconductor and metal-vacuum) is matched for preferred film thickness $nd = s\lambda_{\mathrm{F}}/2$ (with n and s integers), $d = 0.29\,\mathrm{nm}$ and Fermi wavelength $\lambda_{\mathrm{F}} = 0.393\,\mathrm{nm}$ [48] with approximately $n = 5, 7, 9 \ldots$. Because of the special relation between λ_{F} and d (i. e., $d \approx 3/4\lambda_{\mathrm{F}}$) the bilayer height increments provide evidence of QSE. Since bilayer height increments add approximately three nodes to the electron wavefunction, $2d \approx 3\lambda_{\mathrm{F}}/2$, they are favored. These simple estimates have been fully supported by first-principle calculations [49].

Other experiments using He-scattering on Pb/Cu(111) [50], X-ray scattering on Pb/Si(111) [51] and in-situ conductivity on Pb/Si(111) at $T = 90\,\mathrm{K}$ [48], show bilayer intensity oscillations consistent with bilayer height increments. He-scattering studies of Pb/Ge(001) [52] growth show that the interlayer spacing adjusts in a way that the film height is always close to an integer multiple of $\lambda_{\mathrm{F}}/2$. Ni on hydrogen-terminated C(111) surfaces at

$T = 800\,\mathrm{K}$ show the formation of multiple-height islands with flat tops [53]. Other low-temperature studies on Ag/GaAs(100) [54] of films which normally grow three-dimensionally, show "magic" thickness effects after annealing to room temperature. Depending on the deposited amount the film separates into regions of "magic" 7-layer thickness and empty "pits" indicating that the electronic energy of the film dictates its structure, a novel growth mode labeled "electronic growth" [55].

A test whether the confinement energy of the electrons in the Pb islands is sufficient to explain the height selection or whether other factors (i.e. charge transfer at the metal/semiconductor interface) are needed, is to grow on a different reconstructed surface the Si(111)-Pb$\sqrt{3} \times \sqrt{3}$ phase [56, 57]. The electronic structures on the (7×7) and $\sqrt{3}$ phases are known from angle-resolved photoemission [58]. They show that the Fermi level is 0.19 eV above the valence band on the $\sqrt{3} \times \sqrt{3}$ phase vs 0.42 eV on the (7×7) phase. This implies that initially there is a larger difference ΔE_{F} between the Fermi levels on the metal and the semiconductor side for the $\sqrt{3} \times \sqrt{3}$ than for the (7×7) interface. The charge transfer energy ΔU, to a first approximation, can be estimated as the energy stored in a capacitor of capacitance C and potential difference $(\Delta E_{\mathrm{F}}/e)$ so $\Delta U = (1/2)C(\Delta E_{\mathrm{F}}/e)^2$.

Experiments on the $\sqrt{3} \times \sqrt{3}$ phase show that for the same growth conditions ($\theta = 4\,\mathrm{ML}$, $T = 190\,\mathrm{K}$) 5-step islands are those of the preferred height, while for growth on the (7×7) phase it is 7-steps. Since the Fermi level is lower on the $\sqrt{3} \times \sqrt{3}$ phase than on the (7×7) phase, the charge transfer contribution is larger for growth on the $\sqrt{3} \times \sqrt{3}$ interface, with larger energy gain at 5-step compared to the 7-step thickness [56]. This confirms that charge transfer (and different initial reconstructions on the substrate) play a role in island height selection.

Low-Temperature Mobility

While QSE provide energetic reasons that Pb islands with preferred height are formed, it is still not clear what are the key kinetic processes that lead to the unusual self-organization. Although QSE explain why at preferred island heights the energy have minima, it leaves wide open the question of how mass transport gives rise to the ordering. Specifically, how do the deposited Pb atoms move from initially random positions where they land on the surface to well-defined positions in specific island layers, within the relatively short time of the deposition rate ($\sim$ minutes) and at such low temperatures?

Other growth experiments at low temperatures have shown that regular structures can form, as evidenced from diffraction oscillations during growth [59]. Such oscillations were observed for Pb/Si(111) [60] even at 16 K. STM and FIM studies in other systems have shown that impinging atoms at low temperatures can have finite mobility. A review of low-temperature growth and the presence of finite mobility is given in [59]. Despite numerous studies suggesting some type of mobility at low temperatures its origin is still

unclear. One explanation is based on the efficiency of the energy transfer from the incoming adatom to the substrate. Depending on the desorption energy, this additional energy can amount to a few eV. While it is difficult to observe the accommodation process experimentally because it is ultrafast (i. e. with time constants of some picoseconds), Molecular Dynamics simulations of the landing process have been performed [61]. The simulations give mixed results since the evidence for non-thermal mobility depends on the interatomic potential used to describe the interactions between the adatom and substrate atoms. Depending on the softness of the potential, the energy transfer can be completed within the first landing or if the adatom retains some of its energy after the impact, it can come to rest after several hops. Such mechanism was invoked to explain the diffraction oscillations in Pb/Si(111) [51]. It is still an open question whether the necessary mass transport for the buildup of the uniform-height Pb islands can be accounted for only by thermal diffusion or whether some type of non-thermal mobility is necessary.

The buildup of the Pb uniform-height islands is the outcome of the balanced interplay between several kinetic processes: thermal and possibly non-thermal mobility on the terrace, hopping on the island side planes (facets) from lower to higher levels, and atom retainment at preferred heights. Normally, atoms are retained on top of islands because a barrier is present at step edges (to be discussed more extensively for Ag/Ag(111) in 4.2). Experiments with SPA-LEED (similar to the Ag/Ag(111) experiments) were carried out to identify which of these barriers is the controlling one. An initial predominantly 5-step island height distribution is prepared followed by an additional deposition of $\Delta\theta = 0.5\,\mathrm{ML}$ Pb at different growth temperatures T_g to determine the transition temperature when 2-step islands nucleate on top of the 5-step islands. It is found that the transition is at $T_g \approx 175\,\mathrm{K}$, which indicates that the transfer of atoms from the surrounding region to the island top is the rate limiting step. Terrace diffusion is faster than transfer to the top, since growth and stepwise growth (by depositing small coverage increments) give identical results. Diffusion at the island facets is also faster than transfer over the edges, otherwise a decrease in the facet slope would be observed as the atoms accumulate on the facets.

The metastable phases in the kinetic phase diagram of Fig. 7.12 are the kinetically stabilized phases from the interplay of energy gain at the potential energy minima and kinetics with incoming atoms overcoming the island edge barrier. It was also shown that with oxygen the island height and size can be stabilized over a wider temperature range (up to room temperature) because oxygen increases the step edge barrier and limits the Pb transfer to the top [62].

7.4.2 Measurements of Interlayer Diffusion on Ag/Ag(111)

Second-Layer Nucleation Experiments to Measure Interlayer Probability on Ag/Ag(111)

The growth mode (2D or 3D) observed in a system depends on the so-called interlayer probability of an atom encountering a step, i. e. the probability to hop from a higher to a lower level [1, 2]. Usually the interlayer probability is described by an Arrhenius expression $p = (\nu_s/\nu_t)e^{-(\Delta E_s/k_B T)}$ where ν_s is the prefactor at the step edge, ν_t the prefactor on the terrace and ΔE_s is the step edge barrier. For Ag/Ag(111) the growth was found to be three-dimensional for all temperatures studied [63–65]. This has been attributed to the presence of a strong step edge barrier and therefore a low interlayer probability.

Several methods have been applied with different experimental techniques (STM, Diffraction) and over different temperature ranges to measure the step edge barrier and to separate the two contributions to p, i.e. the ratio ν_s/ν_t and the step edge barrier ΔE_s.

Although the simple Arrhenius expression for the interlayer probability has been widely used in the analysis of experiments, several factors have been considered which can complicate the picture of hopping over a single step edge barrier and can result in a more complex dependence of p on temperature. The step edge barrier can be lower at a kink than at a straight step [66]. Furthermore, different step edge barriers can be present at different step types (i. e. A- or B-types on fcc(111) substrates). Such complications can lead to a non-Arrhenius temperature dependence since the step morphology, the relative population of A- or B-type steps or the number of atoms at kink sites etc. can change with temperature.

Experiments to measure the interlayer probability for Ag/Ag(111) with different methods and over different temperature ranges have resulted in the same high barrier $\Delta E_s = 0.13$–$0.15\,\mathrm{eV}$ but in different prefactor ratios ν_s/ν_t [67]. Low-temperature ($T < 150\,\mathrm{K}$) experiments under growth conditions indicate $\nu_s/\nu_t > 1$ while quasi-equilibrium experiments carried out close to room temperature show $\nu_s/\nu_t \sim 1$. In this section we review the different experiments and examine possible reasons for the difference in ν_s/ν_t.

The low-temperature experiments [68, 69] were carried out under growth conditions, with a constant flux of atoms incident on the surface. In one experiment, performed with STM [68], an initial island distribution is prepared by annealing the surface to different temperatures T_{anne} so the average island size $R(T_{anne})$ can be varied. After a second deposition with a smaller amount $\Delta\theta = 0.1\,\mathrm{ML}$ at a lower temperature T_{gr} the fraction of islands with second-layer occupation on top $f(T_{gr}, R)$ is measured as a function of temperature T_{gr} and R. Figure 7.13(a) shows STM results for two growth temperatures $T = 70\,\mathrm{K}$, $130\,\mathrm{K}$ [68]. At $70\,\mathrm{K}$ practically all islands have second-layer occupation ($f = 1$), while at $T = 130\,\mathrm{K}$ only a fraction of the islands is occupied, despite the islands being larger in size. This behavior of $f(T_{gr}, R)$ is the one

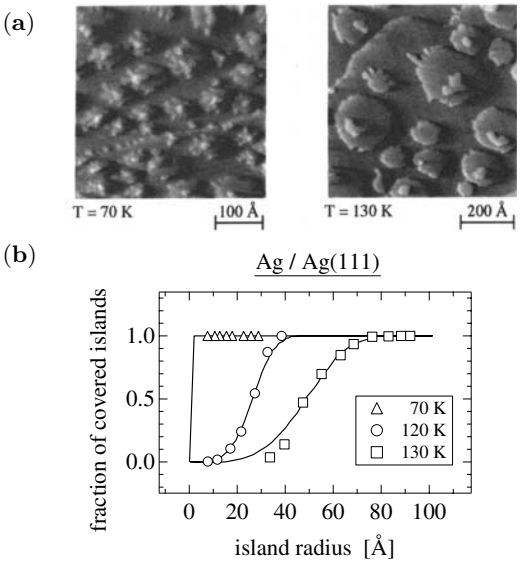

Fig. 7.13. (**a**) STM images of second-layer nucleation experiments on Ag/Ag(111) at $T = 70\,\mathrm{K}$, 130 K showing how interlayer diffusion increases with temperature. (**b**) Fractional occupation of first-layer islands vs island size at fixed temperatures (70 K, 120 K, 130 K).

expected from the temperature dependence of the interlayer probability p. At 70 K, p is very low, so practically no atoms overcome the step edge barrier, even for small size islands. At 130 K, however, p increases, so many atoms can hop to the lower level. The $f(T_{\mathrm{gr}}, R)$-vs-R function for fixed T_{gr} is expected to have a step-like shape, with no second-layer occupation ($f = 0$) for small R, complete occupation ($f = 1$) for large R and a transition region defined by a characteristic critical size R_c where the function shows a sudden jump. At lower T_{gr} the transition becomes steeper and R_c moves to smaller sizes. The data for Ag/Ag(111) are shown in Fig. 7.13(b). By measuring the $f(T_{\mathrm{gr}}, R)$ curves at least at two temperatures, it is possible to separate the two contributions to p, the prefactor ratio $\nu_{\mathrm{s}}/\nu_{\mathrm{t}}$ and the barrier ΔE_{s}. Qualitatively one expects that the larger the difference in the two occupation curves $f(T_{\mathrm{gr}}, R)$, measured for the same two temperatures, the larger the barrier ΔE_{s} will be; while the absolute value of R_c determines the prefactor ratio $\nu_{\mathrm{s}}/\nu_{\mathrm{t}}$. Larger values of R_c imply larger values of $\nu_{\mathrm{s}}/\nu_{\mathrm{t}}$ since the atoms must have larger interlayer probability to compensate for the reduced probability to reach the island edge.

Theoretical Analysis of Second-Layer Nucleation Experiments

The form of the function $f(R,T)$ depends on the theory used for the analysis. Initially a mean field theory was proposed [70] to relate the rate of second-layer nucleation (Ω, i. e. number of nucleated islands/time), on top of an island of size R, to p. It is assumed that on top of the island there is a distance-dependent monomer density $c(r)$ (where r is the distance from the center of the island) as a result of the incident flux. Because of the absorptive boundary conditions at $r = R$, $c(r)$ drops off with r; but as p becomes smaller (i.e. an atom has higher probability to be reflected at the island edge), the difference between the density at $r = 0$ and $r = R$ is reduced according to

$$c(r) = \frac{FR^2}{4D}(1 + 2a/pR) - \frac{Fr^2}{4D} \quad . \tag{7.34}$$

Following nucleation theory [71] monomers diffusing in the presence of the density $c(r)$ on top of an island of size R will irreversibly aggregate into second-layer islands with the rate

$$\Omega(R) = \frac{\kappa D_\mathrm{t}}{a^2} \int_0^R \frac{2\pi r \,\mathrm{d}r}{a^2} [c(r)a^2]^{i+1} \tag{7.35}$$

where D_t denotes the terrace diffusion coefficient. Integrating this expression over the island area, it simplifies in the limit of a strong step edge barrier ($p \ll 1$) to

$$\Omega(R) = \frac{\alpha_g F^2 R^4}{4D_\mathrm{t} p^2} \tag{7.36}$$

with α_g being a geometric factor related to the shape of the islands. The fractional occupation of the islands, shown in Fig. 7.13b, can be obtained by integrating the rate of change $\mathrm{d}f/\mathrm{d}t = \Omega(1 - f)$ over the time of the second deposition, since only islands free of second-layer nucleation can increase f.

In [70] as a main assumption of the mean field theory it is supposed that the monomer density $c(r)$ on top of the first layer island and monomer diffusion determines the second layer nucleation rate Ω. This assumption has been questioned in [72]. Instead, the nucleation of a second-layer island has been analyzed in terms of the probability of two atoms (deposited successively on top of the island) to diffuse and encounter each other. This analysis leads to different form of f(R,T) than the mean field theory. $\Omega(R)$ is given by the rate of monomer deposition on top of the island of area A, FA, (with F the flux rate) times the probability for two of the deposited monomers to encounter each other. In the limit of very fast terrace diffusion (e. g. about 10^7 hops/s at 130 K for Ag(111)) it can be shown that this probability is given by the ratio of the residence time of the first atom τ_r to the time between depositions $\tau = (FA)^{-1}$, namely

$$\Omega = FA\tau_{\mathrm{r}}/\tau = (FA)^2\tau_{\mathrm{r}} \quad . \tag{7.37}$$

Since an atom diffusing very fast can explore all the sites on the island top with the same probability, the residence time τ_{r} is the inverse of the escape probability to the lower layer. Thus the escape probability is simply the product of $2\pi Ra/\pi R^2$ (the probability to reach the island edge) times the probability to hop over the barrier $D_{\mathrm{t}}p$ (which is the product of terrace diffusion coefficient times the interlayer probability). Equation (7.37) becomes

$$\Omega(R) = \alpha_g F^2 R^5/D_{\mathrm{t}}p \quad . \tag{7.38}$$

The two expressions for the rate $\Omega(R)$ are very different in the two theories. For fixed Ω, (7.36) shows that the interlayer probability depends less strongly on R ($p \sim R^2$) than predicted by the result of the revised theory (cf (7.38), $p \sim R^5$). This implies that if the same second-layer nucleation data are analyzed by the two theories, a lower probability (and therefore a higher barrier) will be deduced in the revised theory than in the mean field theory. Because the mean field theory assumes a monomer density $c(r)$ to be present, it is easier for second-layer nucleation to occur. Ω is overestimated and therefore a higher p is sufficient to match the experimental $f(T, R)$ curve.

Anomalous Prefactors in Interlayer Diffusion of Ag/Ag(111)

In principle, for a given $f(T, R)$, p can be used as a fitting parameter to obtain the best agreement with the data, but such fits have large uncertainty. A direct method was proposed in [73] by using at least two temperatures, to deduce uniquely the two contributions to p, $\nu_{\mathrm{s}}/\nu_{\mathrm{t}}$ and ΔE_{s}. From the theoretical expression of the nucleation rate $\Omega(R)$ (either (7.36) or (7.38)) the limiting values $\Omega_{\min}$ (when only one island has a second-layer island on top) and $\Omega_{\max}$ (when all the islands have second-layer islands on top) the corresponding values $R_{\min}$, (the largest island size with no second layer occupation) and $R_{\max}$ (the smallest island size with all islands having second layer occupation) are plotted vs p in Fig. 7.14 (for (7.38)). From the measured values of ($R_{\min}$, $R_{\max}$) in Fig. 7.13b: (2 nm, 4 nm at $T = 120$ K and 3 nm, 7.5 nm at $T = 130$ K) these values are best matched on the two values of $\ln p$ at -9.2 and -6.6 shown by the vertical lines. From these two values of p the parameters $\nu_{\mathrm{s}}/\nu_{\mathrm{t}} = 10^9$, and $\Delta E_{\mathrm{s}} = 0.32$ eV are uniquely extracted for the revised theory [72]. If the mean field expression (7.36) for $\Omega(R)$ is used the corresponding parameters are $\nu_{\mathrm{s}}/\nu_{\mathrm{t}} = 10^3$ and $\Delta E_{\mathrm{s}} = 0.13$ eV because the mean field theory overestimates $\Omega(R)$ and underestimates the barrier. Although the exact form of the function $f(T, R)$ depends on the theory, the result $\nu_{\mathrm{s}}/\nu_{\mathrm{t}} > 1$ is independent of the theory and follows from visual inspection of the raw data of [68], because a dramatic change of the measured function $f(T, R)$ is seen even within a 10 K temperature change (from 120 K to 130 K).

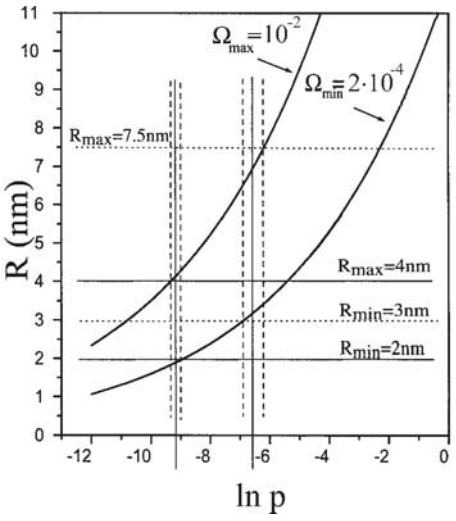

Fig. 7.14. Plots of the minimum island size ($R_{\max}$) with all islands occupied (top curve) and maximum island size ($R_{\min}$) when none of the islands is occupied (bottom curve) vs $\ln p$ (where $p = \nu_s/\nu_t e^{-\Delta E/k_B T}$) for the theory of [72]. The experimentally determined sizes $R_{\min}$ and $R_{\max}$ at two temperatures 120 K and 130 K are used to determine the corresponding values of p (shown by vertical lines) and to extract ν_s/ν_t and ΔE_s.

Since the interlayer parameters can depend on the step morphology (i.e. whether straight or kinked, whether A- or B-type are present etc.) experiments on macroscopic crystals measure an effective barrier averaged over different length scales and step morphologies, with techniques which sample a larger area and different step types. During growth of Ag on Ag(111) over a wide temperature range ($T = 90$–600 K) and with different scattering techniques (X-ray, He-scattering, reflection high energy electron diffraction (RHEED) [63–65]) monotonic intensity decay is observed (instead of diffraction oscillations), which confirms 3D growth and, hence, the small values of p. Such diffraction experiments can be also used to measure the step edge barrier at the edges of the finite terraces on the clean surface. Terraces are present in all crystals, even under the best preparation conditions.

RHEED experiments were carried out to measure the step edge barrier at the edge of Ag(111) crystals with small average terraces of 50 nm diameter [69]. Since the diffracted intensity is summed over more than 10^4 terraces, the experiment averages over different step configurations and local barriers. The temperature of the experiment is chosen to be in the "1-island regime". In this regime, because diffusion is so fast, the deposited atoms will attach to existing islands and only few (1 or 2) islands nucleate on the terrace. After a fixed deposition $\Delta\theta = 0.1$ ML, the deposited atoms end either at ascending or descending steps at the terrace edges or at the few nucleated islands. At ascending steps the arriving atoms stick irreversibly. At descending steps, atoms have only a finite probability p to descend and attach to the step below. As the temperature is increased more atoms at descending steps overcome the barrier at the expense of the atoms which attach to the nucleated islands. The size of the nucleated island determines the magnitude of the RHEED intensity drop. By comparing the RHEED intensity drop both at in-phase and

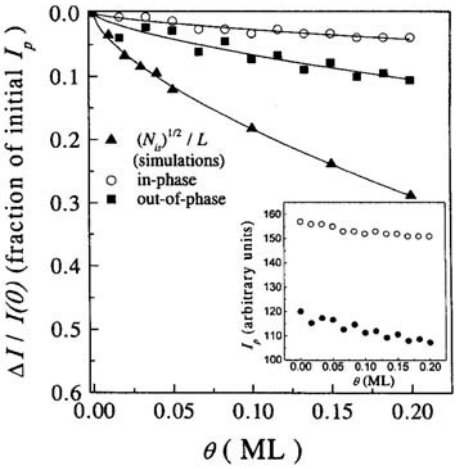

Fig. 7.15. RHEED intensity decay after deposition in Ag/Ag(111) for in-phase and out-of-phase conditions (top two sets of data also shown in the inset). The lower curve is the result of Monte Carlo simulations. The difference between the experimental and simulation data implies higher interlayer probability p and therefore $\nu_\mathrm{s}/\nu_\mathrm{t} = 100$.

out-of-phase condition (see the discussion in Sect. 7.3.1) it is deduced that at in-phase ($k_z d = (\mathrm{even})\pi$) the intensity drop is not determined kinematically, but is related to the change of the step density on the surface. Quantitative information about the step edge barrier at the terrace edges can be extracted from the difference between the measured and the simulated step density. The experimental intensity drop is essentially determined by the increase in the step density at the nucleated island (since the step density increase at the terrace perimeter is much smaller than at the island perimeter).

The process was modeled with Monte Carlo simulations with parameter $D_\mathrm{t}/F \approx 10^{11}$ (i. e. with terrace diffusion to flux rate ratios at $T \approx 150\,\mathrm{K}$ typical of the "1-island" regime for 200×200 lattice or 50 nm Ag(111) terrace [69]). The additional amount $\Delta\theta = 0.1\,\mathrm{ML}$ deposited on the lattice is divided between ascending steps, descending steps and the nucleated island. By monitoring the increase of the nucleated island perimeter $N_\mathrm{isl}^{1/2}/L$, with N denoting the number of atoms in the island and L the system size (i.e. increase in the step density and therefore the intensity drop $\Delta I/I$) the simulation result is compared to the experimental result in Fig. 7.15. The top curves are for in-phase and out-of-phase conditions and the bottom curve shows the result of the simulations. From the comparison one can deduce the temperature dependence of the interlayer probability $p(T)$ and extract the Arrhenius parameters $\nu_\mathrm{s}/\nu_\mathrm{t} \sim 100$ and $\Delta E_\mathrm{s} = 0.13\,\mathrm{eV}$, in good agreement with the second-layer nucleation experiments [68]. The reason for the larger prefactor ratio can be directly seen from Fig. 7.15. $\Delta I/I$ both at in-phase and out-of-phase conditions is less than the simulation result $N_\mathrm{isl}^{1/2}/L$ for $\nu_\mathrm{s}/\nu_\mathrm{t} \sim 1$ and $\Delta E_\mathrm{s} = 0.13\,\mathrm{eV}$ (at $T = 150\,\mathrm{K}$ p is so low that only one out of 10^5 atoms encountering a step will descend). For such high-step edge barriers many atoms will be reflected at descending steps, the reflected atoms will attach to the nucleated island, resulting in larger perimeter and larger

intensity drop. Since the experimental drop is well above the expected one, p is larger than 10^{-5} as the fitting result $\nu_s/\nu_t = 100$ suggests.

It is not clear what is the physical reason for the prefactor at steps to be larger than the terrace prefactor. As discussed in Sect. 7.2.2, the "normal" value of the prefactor is $D_0 = 1/4a^2\nu \sim 10^{-8}\,\mathrm{m}^2/\mathrm{s}$ where a is the lattice constant and ν the typical vibrational frequency. Numerous diffusion experiments have measured prefactor values different from this "normal" result. Several heuristic reasons have been suggested to explain these "anomalous" values, but there is still no clear understanding of the underlying physics. First, as stated in Sect. 7.2.2, even for single-atom diffusion non-Arrhenius behavior (and "anomalous" prefactors) can result when the residence time of an atom in the potential well becomes comparable to the phonon vibrational time of the substrate atoms, which invalidates the assumption of a rigid potential energy surface. Second, finite coverage experiments on interactive systems can lead to a coverage-dependent activation energy $E(\theta)$, non-Arrhenius temperature dependence and "anomalous" prefactors. An almost complete understanding of such effects has been attained for O/W(110) where prefactor changes from $10^{-11}\,\mathrm{m}^2/\mathrm{s}$ to $10^{-8}\ \mathrm{m}^2/\mathrm{s}$ and activation energy increase from 0.6 eV to 1 eV have been observed with increasing θ. These increases have been correlated to a phase transition from a disordered phase at low θ to an ordered $p(2\times 1)$ phase at higher θ [74]. "Anomalous" prefactors have been also related to the presence of impurities, to long-range interactions and to concerted collective cluster motion, mediated through substrate elastic interactions [2]. However, a better understanding of diffusion prefactors and reasons why prefactors can vary so widely is one of the major open questions in the field.

Adatom vs Vacancy Island Decay Experiments to Measure Interlayer Diffusion on Ag/Ag(111)

Experiments to measure the interlayer parameters for Ag/Ag(111) were also carried out at higher temperatures ($T \approx 300\,\mathrm{K}$) under assumed quasi-equilibrium conditions during the decay of adatom and vacancy islands of radius r inside larger vacancy islands of radius R [75]. The geometry of the vacancy island decay experiment is shown schematically in Fig. 7.16. Adatom islands decay because the atom detachment rate exceeds the rate at which atoms attach to the island from the terrace; vacancy islands decay because the refilling rate by atoms hopping over its edge exceeds the detachment rate from its boundary. Vacancy islands decay over longer times than adatom islands because in the analysis of [75] incoming atoms experience the step edge barrier and hop into the island with probability $p < 1$. In [75] the decay rates for an $r = 7\,\mathrm{nm}$ adatom (and vacancy) island located at the center of an $R = 70\,\mathrm{nm}$ vacancy island were studied as a function of temperature ($T = 280$–$360\,\mathrm{K}$). For example, at 300 K the decay rate for the adatom island is 25 times faster than the decay rate of the vacancy island.

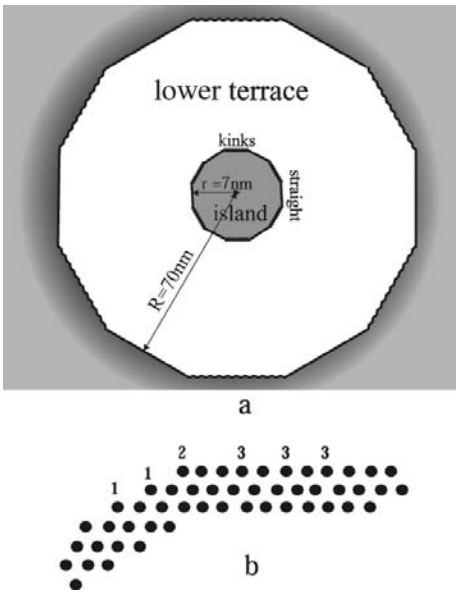

Fig. 7.16. Schematic presentation of the experiment of [75] for adatom-island decay of radius $r = 7\,\mathrm{nm}$ in the middle of a larger vacancy island $R = 70\,\mathrm{nm}$. Dark areas are at the same height and the region between them is one step lower. The bottom curve shows the atom arrangement at the island corner: #1 denotes kink atoms, #2 corner atoms and #3 straight segment atoms. If the independent detachment model is used the prefactor ratio $\nu_\mathrm{s}/\nu_\mathrm{t} \gg 25$ is deduced at $T = 300\,\mathrm{K}$ (in agreement with the low-temperature experiments of [68, 69]).

The experiment was analyzed under the assumption of steady state. For the adatom island this means that the 2D atom flux (i.e. number of atoms per unit length per time) at r is equal to the flux diffusing away from r and also equal to the atom flux incorporated at R. Similar steady-state condition holds for the vacancy-island decay. The steady-state condition implies that the concentration $c(r')$ (within the annular disc $R \geq r' \geq r$) is described by the same functional form at all times, which is a solution of the diffusion equation in cylindrical coordinates. Atoms are evaporated from the island perimeter because of differences between the real monomer density outside the island from the expected equilibrium monomer density $c_\mathrm{eq}(r)$ which is given by the Gibbs Thomson relation $c_\mathrm{eq}(r) = c_\infty \exp(\gamma/k_\mathrm{B}Tnr)$ where γ is the 1D "surface" tension, $n = 13.6\,\mathrm{atoms/nm}^2$ the two-dimensional Ag(111) density and c_∞ the monomer density in front of a straight step. The decay of the adatom island of radius r obeys the relation

$$\frac{\mathrm{d}(\pi r^2)}{\mathrm{d}t} = -\kappa \left[\frac{a}{r} + \ln(R/r) + a/R\right]^{-1} \times [\exp(\gamma/k_\mathrm{B}Tnr) - \exp(-\gamma/k_\mathrm{B}TnR)] \tag{7.39}$$

which is derived from the steady-state condition with $\kappa = 2\pi D_\mathrm{t} c_\infty/n$ denoting the effective detachment rate. The three terms in the first bracket of the right hand side represent the contribution of the three microscopic processes which are needed to transport atoms from r to R, i. e. evaporation at r because $c(r) < c_\mathrm{eq}(r)$, diffusion in the annular region $R \geq r' \geq r$, and incorporation at R because $c(R) > c_\mathrm{eq}(R)$. A similar equation holds for the

decay of the vacancy island except in this case the curvature in the Gibss Thomson relation is negative, because it is easier to evaporate atoms from the boundary of a larger than a smaller vacancy island. In addition, the first term (a/r) in the first bracket in the right hand side is replaced by (pa/r) since the incorporation of atoms at r has probability p because of the step edge barrier, which leads to

$$\frac{\mathrm{d}(\pi r^2)}{\mathrm{d}t} = \kappa \left[\frac{pa}{r} + \ln(R/r) + a/R\right]^{-1} \times [\exp(-\gamma/k_\mathrm{B}Tnr) - \exp(-\gamma/k_\mathrm{B}TnR)] \quad . \tag{7.40}$$

Depending on which of the three processes dominates, (7.39) and (7.40) can be simplified. Different regimes are defined for the vacancy-island decay (i.e. diffusion limited when $\ln(R/r) \gg pa/r$ or interface limited when $pa/r \gg \ln(R/r)$), while for adatom-island decay the decay is always diffusion limited (since $\ln(R/r) > a/r$, a/R)). For each adatom-island decay curve at a given temperature T two parameters γ and $\kappa(T)$ and for the vacancy-island decay, in addition to these two, the interlayer probability $p(T)$ are extracted by fitting the decreasing island area vs time according to (7.39) and (7.40). From this analysis the step edge barrier parameters $\Delta E_\mathrm{s} = 0.13\,\mathrm{eV}$, $\nu_\mathrm{s}/\nu_\mathrm{t} \approx 1$, the "surface" tension $\gamma = 0.22\,\mathrm{eV/atom}$ and the detachment activation energy $\kappa = 0.71\,\mathrm{eV}$ were extracted.

It is puzzling why the prefactor ratio deduced in this experiment ($\nu_\mathrm{s}/\nu_\mathrm{t} \approx 1$) is lower than the one deduced in the growth experiments [68, 69], which implies different interlayer probability p. However, a single Arrhenius form might fail over a temperature range of 150 K between the two experiments. In addition, if the step edge barrier depends on site type (i.e. whether it is kink vs straight step site, A- or B-step site type, etc.) the measured step edge barrier will be an effective average over the distribution of different sites. The quasi-equilibrium experiments were carried out on well-equilibrated islands with a larger fraction of straight steps, while the low temperature experiments were carried out on partially equilibrated island shapes, with a larger fraction of kink sites. The interlayer probability p should be lower in the high- than in the low-temperature experiments, because interlayer diffusion is higher at kink than straight step sites. However, it is not clear why the extracted barrier ΔE_s is the same in the two experiments and only the prefactor is different.

Independent Atom Detachment Model for Island Decay Experiments

As another possible explanation for the difference in the prefactor ratios the assumption of steady-state conditions might not be applicable to Ag/Ag(111) at 300 K. The validity of this assumption depends on the time scales of the different microscopic processes in the system [76]. If $\tau(= \kappa^{-1})$ is the average detachment time and t_d the time for an atom to diffuse across the

region $R \geq r' \geq r$, then $t_{\rm d}$ must be larger than a minimum value (which depends on τ). Otherwise, for very fast diffusion, the detached atoms are transferred "instantaneously" to the boundaries, the concentration on the terrace falls to zero and steady-state conditions cannot be established. For Ag(111), terrace diffusion measured in a different experiment is extremely high ($2\times10^{11}{\rm e}^{-0.1{\rm eV}/k_{\rm B}T}$ hops/s [68]). At 300 K, using the measured value of κ (obtained in [75]) and $D_{\rm t}$ corresponding to $\sim 10^9$ hops/s, the equilibrium density in front of a straight step is $c_\infty = (\kappa n/2\pi D_{\rm t}) = 0.25 \times 10^{-9}\,{\rm atoms/nm^2}$ (with $n = 13.8\,{\rm atoms/nm^2}$ as the Ag(111) density). At 300 K, for the measured "surface" energy $\gamma = 0.22\,{\rm eV/atom}$ and $r = 7\,{\rm nm}$, $R = 70\,{\rm nm}$ we obtain $c_{\rm eq}(r) = 0.33\times10^{-9}\,{\rm atoms/nm^2}$ and $c_{\rm eq}(R) = 0.24\times10^{-9}\,{\rm atoms/nm^2}$, respectively. This implies differences $c_{\rm eq}(r) - c_{\rm eq}(R)$ of less than $10^{-9}\,{\rm atoms/nm^2}$, indicating that steady-state condition might be violated.

An alternative way to view the island decay is to assume that it is a result of independent atom detachment, followed by single-atom random walk until the atom is adsorbed at the island boundaries. In this analysis the steady-state condition is not satisfied [76].

One way to decide which analysis is applicable in a given experiment, is to relate the detachment rates for adatom and vacancy islands to the expected rates from the experimentally determined island shapes [77]. As found in [77] the island shape consists of two types of segments: six straight segments connected with six kinked segments, shown schematically in Fig. 7.16 for the small adatom island in the middle of the large vacancy island. Straight and kinked segments have comparable free energies at $T \sim 300\,{\rm K}$; so the ratio of their lengths is ~ 1. Atoms can detach easier from kinked than straight segments simply because they have lower coordination (i. e. 3 vs 4 neighbors). We can determine the average detachment rate $E(r)$ for an adatom island of radius r and $E(-R)$ for a vacancy island of radius R based on their shapes, if we use a simple bond counting estimate of the corresponding energy barriers. These simple estimates of the barriers have been also confirmed with more sophisticated calculations [66].

For the adatom island we assume that all the atoms at the kinked segments evaporate first within $\tau_{\rm k}$ since they have lower number (3) of bonds. Since the corner atoms also have 3 bonds they detach next, followed by the "unzipping" of the atoms at the straight segment in time $(n_{\rm s}/2)\tau_{\rm k}$ (where $n_{\rm s}$ is the number of atoms on the straight segment). There are two corner atoms to initiate the "unzipping" which accounts for the factor of 2. For the adatom island of [75] with $r = 7\,{\rm nm}$ we have $n_{\rm s} = 12$ and $n_{\rm k} = 7$, so the average detachment time is $\tau_a = (1 + n_{\rm s}/2)\tau_{\rm k} = 7\tau_{\rm k}$.

The time for an atom to detach from the vacancy island of radius R determines the decay of the smaller vacancy island, since these detached atoms diffuse "instantaneously" to r and refill the small vacancy island. As argued before, first the atoms at the kinked segments detach within time $\tau_{\rm k}$. However, a major difference between the convex adatom vs the concave

vacancy island is that once the atoms in the kinked segment are evaporated, the corner atom has 5 bonds (instead of 3 for the adatom island) so it does not detach next. Atoms need to detach from the straight segment (where an atom has 4 bonds) to generate kink atoms (with 3 bonds). The time for a kink atom to be generated on a straight step of the vacancy island will be by a factor e^{ε/k_BT} longer (with ε denoting the nearest neighbor attractive energy), followed by the "unzipping" process as before. The kink atom can be generated anywhere on the straight segment, so averaging over this position we find the average time to "unzip" $(3/4n'_s)\tau_k$. Since these processes are sequential, the total time is $\tau_V = \tau_k + e^{\varepsilon/k_BT}\tau_k + (3/4n'_s\tau_k)$ corresponding respectively to detachment from kink segment, straight segment and "unzipping" of the straight segment. For $R = 70\,\text{nm}$ one has $n'_s = 120$, which results in $\tau_V = 5053\tau_k$ using $\varepsilon = 0.22\,\text{eV/atom}$ [75]. Since $E(r)$ and $E(-R)$ are rates per detached atom and the number of atoms that can detach is proportional to the island perimeter, the ratio of detachment rates is $E(r)/E(-R) = (\tau_V/\tau_a)(2\pi r/2\pi R) = 72.1$. This ratio is much larger than the ratio $E(r)/E(-R) = D_t c(r)/D_t c(-R)$ expected for the steady-state analysis, since using the Gibbs Thompson expression one has $c(r)/c(-R) = \exp(\gamma/k_BT(1/r+1/R)) \approx 1.4$. Such a low ratio is not compatible with the difference in the island shape discussed before, i. e. convex for the adatom vs concave for the vacancy island.

The decay rates for the adatom and vacancy islands can now be estimated in an independent atom model. For the adatom island

$$dA_a/dt = (2\pi r)aE(r)P_r/n \tag{7.41}$$

where P_r is the probability of an atom detached from the island at r, to reach the boundary at R. The other possible outcome for the atom is to return back to r with probability $(1 - P_r)$. The contribution of the atoms detached from the boundary of the vacancy island at R is neglected because $E(-R) \ll E(r)$. P_r has been shown to be $a/r\ln(R/r)$ [75].

Similarly, the vacancy island decay rate is given by

$$dA_V/dt = (2\pi R)aE(-R)P_{Rs}/n \tag{7.42}$$

where P_{Rs} is the probability for an atom detached at R to be adsorbed at r after overcoming the step edge barrier. The probability P_R for the atom detached at R to be adsorbed at r, if there was no reflecting boundary at r (i.e. $p = 1$), is $P_R = a/R\ln(R/r)$. P_{Rs} is easily found to be $P_R\,p/(1-(1-p)(1-P_r))$ by summing the probabilities $p(1-P_r)^n(1-p)^nP_R$ of all possible paths to reach the small vacancy island before the atom overcomes the barrier. n denotes number of reflections at r.

We can express the ratio of adatom- vs vacancy-island decay rates in terms of the detachment rates, $(dA_a/dt)/(dA_V/dt) = (r)(P_rE(r))/(RP_{Rs}E(-R)) = E(r)(1-(1-p)(1-P_r))/E(-R)$. Using the data for island vs vacancy decay of Ag/Ag(111) at $T = 300\,\text{K}$ [$r = 7\,\text{nm}$, $R = 70\,\text{nm}$, $E_s = 0.13\,\text{eV}$ (for

$p = \nu_s/\nu_t \exp(-\Delta E_s/k_B T)$), $E(r)/E(-R) = 72.1$, $(dA_a/dt)/(dA_V/dt) = 25$] we obtain a ratio $\nu_s/\nu_t \gg 25$. We have a strong inequality in ν_s/ν_t (instead of an exact value) because from the measured ratio of the decay rates it follows that $p > P_R$, which implies that p is sufficiently large so that it does not control the atom attachment to the small vacancy island at r. Any value of $p > P_R$ is allowed and therefore (for a fixed value $\Delta E_s = 0.13\,\mathrm{eV}$ of the barrier) the experiment is consistent with any ratio $\nu_s/\nu_t \gg 25$.

The re-examination of the island decay experiments in terms of the independent atom model brings the value of ν_s/ν_t in good agreement with the low-temperature experiments. It is also consistent with the fact that the ratio of atom-detachment rates $E(r)/E(-R)$, expected from the experimentally known island shapes and the contribution of the different segments (kink vs straight), is larger than the ratio found under the steady-state assumption.

7.5 Conclusion

We have reviewed recent developments in the fast growing field of surface diffusion by presenting results from four different experiments to illustrate different techniques and objectives in the field, especially the important distinction between equilibrium and non-equilibrium experiments. We would like to stress again that the issues and problems discussed in this chapter can only be a small subset of the wide-ranging activities in the field, focused on the authors' expertise. Despite this limitation, the reader is expected to gain a good idea about the breadth and diversity of the field.

The basic dichotomy in the field, i. e. equilibrium vs non-equilibrium methods, is characteristic of surface diffusion. Work in the first area is more intimately related to topics covered in other chapters of this volume. Non-equilibrium diffusion especially in the context of epitaxy, growth and in developing the ability to control nanostructures, as discussed in Sects. 7.4.1 and 7.4.2, is unique to surface diffusion with no clear analogue to bulk diffusion.

After recognizing this essential fact, which defines two subcommunities in surface diffusion, it is worth commenting on pragmatic limitations in the relation between theory and experiment in each subcommunity. Equilibrium surface diffusion is highly developed theoretically with mature methods of high sophistication to deduce the coverage and temperature dependence of the diffusion coefficient $D(\theta, T)$ and its relation to phase transitions and thermodynamic parameters, for a given set of adatom interactions. This connection is universally amenable to general and global predictions. Unfortunately, this area is difficult to implement experimentally because the measurable signal is small, originating from few percent concentration fluctuations. The methods presented in Sects. 7.3.1 and 7.3.2, based on fluctuation measurements in reciprocal and real space, have shown that such methods are now possible, but further tests are necessary, to carry fluctuation experiments to other systems and compare them with the results from other techniques.

On the other hand, non-equilibrium experiments such as profile evolution methods, island growth in epitaxy, second layer nucleation, island decay etc. are easier to implement experimentally because the measurable signal is large and easy to detect. However, such methods are either less developed theoretically or they easily lead to ambiguities in their interpretation. The implicit expectation, i. e. to apply the results universally to other physical phenomena, is not easily achieved in non-equilibrium experiments, since the questions posed are specific to the situation at hand, and the controlling factors in non-equilibrium experiments are different microscopic processes. The main issue is the identification of the kinetically limiting key processes which control the evolution of the system. This was clear both in the uniform-height island in Pb/Si(111) and in the different interpretations of the interlayer diffusion experiments on Ag/Ag(111). However, the ultimate justification of non-equilibrium experiments is the potential to fabricate well-controlled atomic-scale structures which are technologically useful. Success even in one system may therefore have a larger payoff than finding, if possible, a universal description of all non-equilibrium phenomena.

Notation

a	lattice constant
$c(r,t)$	local concentration at r, t
d	single step height
D_{s}	step edge diffusion coefficient
D_{c}	collective Diffusion coefficient
D_{t}	tracer Diffusion coefficient
$E(r)$	detachment rate from island of radius r
ΔE_{s}	step edge barrier
F	flux rate
f	atomic scattering factor
I	diffraction Intensity
k	wavevector
k_{B}	Boltzmann constant
L	terrace length of stepped surfaces
n	Ag(111) atom density in atom/nm^2
p	interlayer probability
P_r	probability to diffuse from r to R
P_R	probability to diffuse from R to r
$P_{R\mathrm{s}}$	probability to diffuse from R to r in the presence of a step edge barrier at r
$S(k,t)$	structure factor
t	time
T	temperature
T_{c}	critical temperature

w	fluctuating step width
z	tip-surface separation
α	atom polarizability
$\overline{\beta}$	step stiffness
Γ	step mobility
γ	1D "surface" tension
Δ	amplitude of step fluctuations
ζ	instrumental correlation length
θ	coverage
κ	atom detachment rate in the steady state model
λ_{F}	Fermi wavevector
μ	chemical potential
ν_{s}	prefactor at step edge
ν_{t}	prefactor at terraces
ξ	step correlation length
Σ	area of elementary hops along step
EC	evaporation and condensation mechanism
FIM	field ion microscopy
LEED	low energy electron diffraction
LEEM	low energy electron microscopy
ML	monolayer
QSE	quantum size effects
RHEED	reflection high energy electron diffraction
STM	scanning tunneling microscopy
SD	step diffusion
TD	terrace diffusion

References

1. *Surface Diffusion: Atomistic and Collective Processes*, ed by M.C. Tringides (Plenum, New York 1997)
2. *Collective Diffusion on Surfaces: Correlation Effects and Adatom Interactions*, ed by M.C. Tringides, Z. Chvoj (Kluwer, Dordrecht 2001)
3. W.N. Unertl. In: *Handbook of Surface Science Vol. 1, Physical Structure*, ed by W.N. Unertl (Elsevier, Amsterdam 1996)
4. C. Ratsch, P. Ruggerone, M. Scheffler. In: *Surface Diffusion: Atomistic and Collective Processes*, ed by M.C. Tringides (Plenum, New York 1997)
5. Gun-Do Lee, C.Z. Wang, Z.Y. Lu, K.M. Ho: Surf. Sci. **426**, L427 (1999)
6. H. Brune: Surf. Sci. Rep. **31**, 121 (1998)
7. M.C. Tringides, R. Gomer: Surf. Sci. **265**, 283 (1992)
8. T.L. Einstein. In: *Handbook of Surface Science Vol. 1, Physical Structure*, ed by W.N. Unertl (Elsevier, Amsterdam 1996)
9. D. Meade, D. Vanderbilt: Phys. Rev. Lett. **63**, 1404 (1989)
10. *Ordering in Two Dimensions*, ed by S.K. Sinha (North Holland, New York 1980)

11. R. Gomer: Surf. Sci. **38**, 373 (1973)
12. A. Sadiq, K. Binder: Surf. Sci. **35**, 617 (1984)
13. X. Xiao, X.D. Zhu, W. Daum, Y.R. Shen: Phys. Rev. Lett. **61**, 2883 (1988)
14. J.W. Frenken, B.J. Hinch, J.P. Toennies, Ch. Wöll: Phys. Rev. B **41**, 938 (1990)
15. J.R. Sanchez, D. Quinn, M.C. Tringides: Surf. Sci. **391**, 101 (1997)
16. R. Gomer: Rep. Prog. Phys. **53**, 917 (1990)
17. P. Nikunen, I. Vattulainen, T. Ala-Nissila: Surf. Sci. **447**, L162 (2000)
18. D. Foster: *Hydrodynamic Fluctuations, Broken Symmetry and Correlation Functions* (Addison Wesley, Reading MA 1990)
19. C. Uebing. In: *Surface Diffusion: Atomistic and Collective Processes*, ed by M.C. Tringides (Plenum, New York 1997)
20. M.R. Dudek, M.C. Tringides. In: *Collective Diffusion on Surfaces: Correlation Effects and Adatom Interactions*, ed by M.C. Tringides, Z. Chvoj (Kluwer, Dordrecht 2001)
21. A.T. Loburets, A.G. Naumovets, Y.S. Vedula. In: *Surface Diffusion: Atomistic and Collective Processes*, ed by M. Tringides (Plenum Press, New York 1997) pp 509–528
22. M.C. Tringides, M. Gupalo, Q. Li, X. Wang. In: *Proceedings of XI Max Born Symposium*, ed by R. Kutner, A. Pelkalski, K. Sznajd-Weron (Springer, Berlin Heidelberg New York 1999)
23. M.L. Lozano, M.C. Tringides: Europhys. Lett. **30**, 537 (1995)
24. Z. Chvoj, E.H. Conrad, M.C. Tringides: Phys. Rev. B **62**, 4672 (2000)
25. M.C. Tringides, M.I. Larson, H. Pfnuer, H. Frischart, K. Budde, M. Henzler: J. Appl. Phys. **82**, 1507 (1997)
26. E.H. Conrad, A. Menzel, S. Kiriukhin, M.C. Tringides: Phys. Rev. Lett. **81**, 3175 (1998)
27. M. Kammler, M. Horn von Hoegen, N. Voss, M.C. Tringides, A. Menzel, E.H. Conrad: Phys Rev. B **65**, 075312 (2002)
28. A. Menzel, K. Wiesenfeld, E.H. Conrad, M.C. Tringides: Phys. Rev. B **61**, 2997 (2000)
29. S. Brauer, G. B. Stephenson, M. Sutton, R. Bruning, E. Dufresne, S.G.J. Mochrie, G. Grubel, J. Als-Nilesen, D.L. Abernathy: Phys. Rev. Lett. **74**, 2010 (1995)
30. B. Poelsema, G. Comsa: *Scattering of Thermal Energy Atoms from Disordered Surfaces* (Springer, Berlin Heidelberg New York 1989)
31. N.C. Bartelt, R.M. Tromp: Phys. Rev B **54**, 11731 (1996)
32. H.P. Bonzel, W.W. Mullins: Surf. Sci. **350**, 285 (1996)
33. T. Zambelli, J. Trost, J. Wintterlin, G. Ertl: Phys. Rev. Lett. **76**, 795 (1996)
34. S. Renisch, R. Schuster, J. Wintterlin, G. Ertl: Phys. Rev. Lett. **82**, 3839 (1999)
35. N.C. Bartelt, W. Theis, R.M. Tromp: Phys. Rev. B **54** 11741 (1996)
36. Q. Li, M.C. Tringides: Surf. Sci. **365**, 495 (1996)
37. F. Bozso, I.W. Lyo, P. Avouris: J. Vac. Sci. Techn. B **9**, 428 (1991)
38. U. Hofer, T.F. Heinz: Phys. Rev. Lett. **66**, 1994 (1991)
39. A. Memsouk, Y. Boughaleb, R. Nassif, K.Saadouni: Phys. Lett. A **248** (2001)
40. X. Wang, Q. Li, M.C. Tringides: Phys. Rev. B **57**, 7275 (1998)
41. M. Horn von Hoegen, F.K. LeGoues, M. Copel, M.C. Reuter, R.M. Tromp: Phys. Rev Lett. **67**, 1130 (1991)
42. J. Tersoff, C. Teichert, M.G. Lagally: Phys. Rev. Lett. **76**, 1675 (1996)
43. K. Budde, E. Abram, V. Yeh, M.C. Tringides: Phys. Rev. B **61**, 10602 (2000)

44. M. Hupalo, S. Kremmer, V. Yeh, L. Berbil-Bautista, E. Abram, M.C. Tringides: Surf. Sci. **493**, 526 (2001)
45. W.B. Su, S.H. Chang, W.B. Jian, C.S. Chang, L.J. Chen, T.T. Tsong: Phys. Rev. Lett. **64**, 1589 (2001)
46. F.K. Schulte: Surf. Sci. **55**, 427 (1976)
47. N. Trivedi, N. Ashcroft: Phys. Rev. B **38**, 12298 (1988)
48. M. Jalochowski, E. Bauer: Phys. Rev. B **38**, 5272 (1988)
49. C.M. Wei, M.Y. Chou: Phys. Rev. B **66**, 233408 (2002)
50. B.J. Hinch, C. Koziol, J.P. Toennies, G. Zhang: Europhys. Lett. **10**(4), 341 (1989)
51. D. Schmicker, T. Hibna, K.A. Edwards, P.B. Howest, J.E. MacDonald, M.A. James, M. Breeman, G.T. Barkema: J. Phys.: Cond. Matt. **9**, 969 (1997)
52. A. Grottini, D. Cvetko, L. Floreano, R. Gotter, A. Morgante, F. Tommasini: Phys. Rev. Lett. **79**, 1527 (1997)
53. J. Braun, J.P. Toennies, Ch. Wöll: Phys. Rev. B **60**, 11707 (1999)
54. A.R. Smith, K.J. Chao, Q. Niu, C.K. Shih: Science **273**, 226 (1996)
55. Z.Y. Zhang, Q. Niu, C.K. Shih: Phys. Rev. Lett. **80**, 5381 (1998)
56. V. Yeh, L. Berbil-Bautista, C.Z. Wang, K.M. Ho, M.C. Tringides: Phys. Rev. Lett. **85**, 5158 (2000)
57. M. Hupalo, V. Yeh, L. Berbil-Bautista, S. Kremmer, E. Abram, M.C. Tringides: Phys Rev. B **64**, 155307 (2001)
58. H.H. Weitering, A.R.H.F. Ettema, T. Hibma: Phys. Rev. B **45**, 9126 (1992)
59. M.C. Tringides. In: *Morphological Organizations in Epitaxial Growth and Renewal*, ed by Z. Zhang, M.G. Lagally (Word Scientific, Singapore 1998)
60. M. Jalochowski, M. Hoffmann, E. Bauer: Phys. Rev. B **51**, 7231 (1995)
61. R. Biswas, K. Roos, M.C. Tringides: Phys. Rev. B **50**, 10932 (1994)
62. S. Stepanovskyy, V. Yeh, M. Hupalo, M.C. Tringides: Surf. Sci. **515**, 187 (2002)
63. G. Rosenfeld, R. Servanty, C. Teichert, B. Polsema, G. Comsa: Phys. Rev. Lett. **72**, 895 (1993)
64. J. Vrijmoeth, H.A. van der Vegt, J.A. Meyer, E. Vlieg, R.J. Behm: Phys. Rev. Lett. **72**, 383 (1994)
65. M. Stanley, C. Papageorgopolos, K.R. Roos, M.C. Tringides: Surf. Sci. **355**, L264 (1996)
66. Z. Chvoj, C. Ghosh, T.S. Rahman, M.C. Tringides: J. Phys. C **15**, 5223 (2003)
67. K.R. Roos, M.C. Tringides: Phys. Rev. Lett. **87** 149604 (2001)
68. K. Bromann, H. Brune, H. Roder, K. Kern: Phys. Rev. Lett. **75**, 677 (1995)
69. K.R. Roos, M.C. Tringides: Phys. Rev. Lett. **85**, 1480 (2000)
70. J. Tersoff, A.W. Denier van Der Gon, R.M. Tromp: Phys. Rev. Lett. **72**, 266 (1994)
71. J.A. Venables, G.D.T. Spiller, M. Hanbucken: Rep. Prog. Phys. **47**, 399 (1984)
72. J. Krug, P. Politi, T. Michely: Phys. Rev. B **61**, 14037 (2000)
73. K.R. Roos, M.C. Tringides: Surf. Sci. Rev. and Lett. **5**, 3 (1998)
74. M.C. Tringides, R. Gomer: Surf. Sci. **145**, 1212 (1984)
75. K. Morgenstern, G. Rosenfeld, Laegsgaard, F. Besenbacher, G. Comsa: Phys. Rev. Lett. **80**, 556 (1998)
76. Z. Chvoj, M.C. Tringides: Phys. Rev. B **66**, 035418 (2002)
77. M. Giesen, C. Steimer, H. Ibach: Surf. Sci. **471**, 80 (2001)

8 Grain Boundary Diffusion in Metals

Christian Herzig and Yuri Mishin

8.1 Introduction

Grain boundary (GB) diffusion plays an important role in many processes taking place in engineering materials at elevated temperatures. Such processes include Coble creep, sintering, diffusion-induced grain boundary migration, discontinuous reactions (such as discontinuous precipitation, discontinuous coarsening, etc.), recrystallization, and grain growth. GB diffusion is important not only at high temperatures but sometimes also at relatively low, even ambient temperatures. In particular, the service life of many microelectronic elements and devices is limited by room temperature diffusion or electromigration of detrimental impurities along GBs resulting in the degradation of service characteristics.

The fact that GBs provide high diffusivity ("short circuit") paths in metals has been known since a few decades. First indications of enhanced atomic mobility at GBs were obtained as early as in the 1920–1930s, for example from grain size dependence of creep and sintering rates in polycrystalline materials. However, the first direct proof of GB diffusion was obtained in the early 1950s using autoradiography [1]: the additional blackening of autoradiographic images along GBs indicated that the radiotracer atoms penetrated into GBs much faster than in the regular lattice [2]. These observations were immediately followed by two important events: the appearance of the nowadays classic Fisher model of boundary diffusion [3], on one hand, and the development and extensive use of the radiotracer serial sectioning technique, on the other hand. It was largely due to these events that GB diffusion studies were put on a quantitative basis and GB diffusion measurements became the subject of many investigations and publications. Over the five decades that followed, the experimental techniques for GB diffusion measurements have been drastically improved and extended to a wide range of temperatures and a broad spectrum of metallic, semiconductor, and ceramic materials. On the theoretical side, the Fisher model, being still the footing stone of GB diffusion theory, has been subject to careful mathematical analysis and extended to various situations encountered in diffusion experiments and technological processes. For an overview of both fundamentals and recent achievements in this area see the book of Kaur et al. [4] and review articles [5–7]. A com-

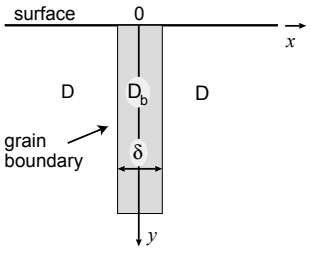

Fig. 8.1. Schematic geometry of the Fisher model of grain boundary diffusion.

plete collection of experimental data published before the end of 1980s can be found in the handbook of Kaur et al. [8].

This chapter presents a brief review of fundamental aspects of GB diffusion with emphasis on metals and metallic alloys. In Sects. 8.2 and 8.3 we introduce classifications of GB diffusion kinetics and mathematical models applied for the analysis of experimental concentration profiles. We also give a brief summary of the current knowledge of GB diffusion in metals. In Sect. 8.4 we discuss in more detail the problem of GB diffusion accompanied by GB segregation and discuss the recent progress in this area. In Sect. 8.5 we summarize. The idea which we wish to emphasize in this review is that many problems in this area could only be solved by combining new theoretical models with precise measurements using novel experimental techniques.

8.2 Fundamentals of Grain Boundary Diffusion

8.2.1 Basic Equations of Grain Boundary Diffusion

Most mathematical treatments of GB diffusion are based on the Fisher model [3] describing diffusion along a single GB. In the Fisher model, a GB is represented as a high-diffusivity uniform and isotropic slab embedded in a low-diffusivity isotropic crystal perpendicular to its surface (Fig. 8.1). The GB is thus described by two physical parameters: the GB width δ and the GB diffusion coefficient D_b such that $D_\mathrm{b} \gg D$, D being the volume diffusion coefficient. In a typical diffusion experiment, a layer of foreign atoms or tracer atoms of the same material is created at the surface and the specimen is annealed at a constant temperature T for a time t. During the anneal the atoms diffuse from the surface into the specimen in two ways: directly into the grains and, much faster, along the GB. In turn, the atoms which diffuse along the GB eventually leave it and continue to diffuse in the lattice regions adjacent to the GB, thus giving rise to a volume diffusion field around the GB.

Mathematically, the diffusion process is described by two coupled equations:

$$\frac{\partial c}{\partial t} = D\left(\frac{\partial^2 c}{\partial x^2} + \frac{\partial^2 c}{\partial y^2}\right), \qquad \text{where } |x| > \delta/2, \tag{8.1}$$

$$\frac{\partial c_\mathrm{b}}{\partial t} = D_\mathrm{b}\frac{\partial^2 c_\mathrm{b}}{\partial y^2} + \frac{2D}{\delta}\left(\frac{\partial c}{\partial x}\right)_{x=\delta/2}. \tag{8.2}$$

These equations represent diffusion in the volume and along the GB, respectively. $c(x, y, t)$ is the volume concentration of the diffusing atoms and $c_\mathrm{b}(y, t)$ is their concentration in the GB. The second term in the right-hand side of (8.2) takes into account the leakage of the diffusing atoms from the GB to the volume. Any solution of (8.1) and (8.2) should meet the surface condition, which can be different in different experiments (see below), as well as the natural initial and boundary conditions at $x \to \pm\infty$ and $y \to \infty$. The joining condition between functions $c(x, y, t)$ and $c_\mathrm{b}(y, t)$ depends on whether we study self-diffusion or impurity diffusion. For self-diffusion, the joining condition simply reflects the continuity of the concentration across the GB,

$$c_\mathrm{b}(y, t) = c(\pm\delta/2, y, t). \tag{8.3}$$

For impurity diffusion, the joining condition involves the equilibrium segregation factor s and reads

$$c_\mathrm{b}(y, t) = sc(\pm\delta/2, y, t). \tag{8.4}$$

The physical meaning of this relation will be discussed later.

8.2.2 Surface Conditions

Fisher [3] postulated a constant source condition at the surface,

$$c(x, 0, t) = c_0 = \text{const}. \tag{8.5}$$

This condition is also called a thick-layer condition because it can be established by depositing a thick layer of diffusant, $h \gg (Dt)^{1/2}$. The constant source condition also applies when diffusion takes place from a gas phase.

Later Suzouka [9, 10] introduced an instantaneous source, or thin-layer condition,

$$c(x, y, 0) = M\delta(y), \qquad (\partial c/\partial y)_{y=0} = 0, \tag{8.6}$$

where M is the amount of diffusant deposited per unit area of the surface. This surface condition assumes that the initial layer is completely consumed by the specimen during the diffusion experiment, i.e. $h \ll (Dt)^{1/2}$. Note that (8.6) unrealistically assumes that the rate of surface diffusion is the same as the rate of volume diffusion, which contradicts existing experimental data.

A more realistic thin-layer condition, called fast surface diffusion condition, was proposed in [4, 11]. That condition postulates that surface diffusion is much faster than volume and even GB diffusion, which results in a uniform

surface concentration near the GB-surface intersect. The respective surface condition is

$$c(x, y, 0) = M\delta(y), \qquad c(x, 0, t) = M/(\pi Dt)^{1/2}. \tag{8.7}$$

This condition also assumes that $h \ll (Dt)^{1/2}$.

In modern experiments thin-layer conditions are established more often than the constant source condition. This is due to the use of extremely thin radiotracer layers which do not disturb the structural or chemical state of GBs in the course of the diffusion experiment.

8.2.3 Methods of Profile Analysis

The basic equations of the Fisher model, (8.1) and (8.2), can be solved analytically. The integral representations of the exact solutions for the constant and instantaneous sources were derived by Whipple [12] and Suzuoka [9, 10], respectively. Using the same Fourier-Laplace transformation method, the exact analytical solution was also obtained for the fast surface diffusion condition, (8.7) [4]. Unfortunately, the practical significance of exact solutions is very limited because of their very complicated mathematical form. In practical terms, any mathematical solution is only useful if it offers a way to process the experimental concentration profile and determine GB diffusion characteristics.

GB diffusion measurements typically employ the radiotracer serial sectioning method. After the diffusion anneal, thin-layers of the material parallel to the source surface are removed from the specimen (either mechanically or by ion beam sputtering) and the radioactivity of each section is measured with a crystalline γ-detector or a liquid scintillation counter. Experimental details of this method can be found in the literature [13, 14], see also Chap. 1. The quantity measured by this method is the average layered concentration of the diffusant, $\overline{c}$, as a function of the penetration depth y. This function, called a concentration (or penetration) profile, bears information about GB diffusion parameters and is therefore subject to a mathematical treatment with the purpose of extracting that information. Much work has been devoted to the development of approximate analytical solutions of the Fisher model and simple recipes of profile analysis.

Fisher [3] derived the following approximate solution for self-diffusion from a constant source:

$$\overline{c} \propto c_0 \exp(-\pi^{-1/4} w), \tag{8.8}$$

where the precise value of the proportionality constant is not important. Here w is the reduced penetration depth defined by

$$w = \frac{y}{(\delta D_{\mathrm{b}})^{1/2}} \left(\frac{4D}{t}\right)^{1/4}. \tag{8.9}$$

Equation (8.8) suggests that the penetration profile $\overline{c}(y)$ plotted in the coordinates $\log \overline{c}$ versus y should yield a straight line. Then, knowing the slope $\partial \ln \overline{c}/\partial y$ of that line we can determine the product δD_{b}:

$$\delta D_{\mathrm{b}} = 1.128(D/t)^{1/2}(-\partial \ln \overline{c}/\partial y)^{-2}. \tag{8.10}$$

The volume diffusion coefficient D is assumed to be known from independent measurements.

Fisher's exponential solution, (8.8), is not very accurate. If a profile calculated using Whipple's [12] exact analytical solution is plotted in the coordinates $\log \overline{c}$ versus y^n with various powers n, the best straight line is obtained with the power of $n = 6/5$ [15, 16]. Moreover, the linear part of the profile scales with the reduced depth w defined by (8.9) with a constant slope of about -0.78:

$$\frac{\partial \ln \overline{c}}{\partial w^{6/5}} \approx -0.78. \tag{8.11}$$

It immediately follows that, knowing the slope of the experimental profile in the coordinates $\log \overline{c}$ versus $y^{6/5}$, we can calculate the product δD_{b}:

$$\delta D_{\mathrm{b}} = 1.322(D/t)^{1/2}\left(-\partial \ln \overline{c}/\partial y^{6/5}\right)^{-5/3}. \tag{8.12}$$

Equations (8.11) and (8.12) are only valid under two conditions:

- The so-called LeClaire's parameter β defined by
$$\beta = \frac{\delta D_{\mathrm{b}}}{2D(Dt)^{1/2}} \tag{8.13}$$
must be large enough, in practical conditions $\beta > 10$.
- Parameter
$$\alpha = \frac{\delta}{2(Dt)^{1/2}} \tag{8.14}$$
must be small enough, in practical conditions $\alpha < 0.1$.

Similarly, for diffusion from an instantaneous source it was found that

$$\frac{\partial \ln \overline{c}}{\partial w^{6/5}} \approx -0.775 \tag{8.15}$$

provided that α is small enough and $\beta > 10^4$ [9, 10]. Therefore, the product δD_{b} can be determined from the linear part of the profile $\log \overline{c}$ versus $y^{6/5}$:

$$\delta D_{\mathrm{b}} = 1.308(D/t)^{1/2}\left(-\partial \ln \overline{c}/\partial y^{6/5}\right)^{-5/3}. \tag{8.16}$$

If $\beta < 10^4$, the right-hand side of (8.15) is no longer constant; instead, it becomes a function of β (and thus time). Then, (8.16) should be slightly modified to become

$$\delta D_{\mathrm{b}} = 1.206(D^{0.585}/t^{0.605})^{1/1.19}\left(-\partial \ln \overline{c}/\partial y^{6/5}\right)^{-5/2.975} \tag{8.17}$$

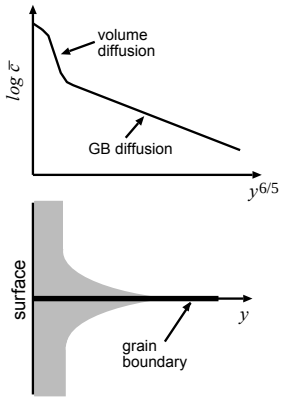

Fig. 8.2. Schematic shape of a typical penetration profile of grain boundary diffusion. If $\alpha \ll 1$ and $\beta \gg 1$, where α and β are defined by (8.13) and (8.14), then the tail of the profile is a straight line in the coordinates $\log \overline{c}$ versus $y^{6/5}$.

for $10^2 < \beta < 10^4$, and

$$\delta D_{\mathrm{b}} = 1.084 (D^{0.91}/t^{1.03})^{1/1.94} \left(-\partial \ln \overline{c}/\partial y^{6/5}\right)^{-5/2.91} \tag{8.18}$$

for $10 < \beta < 10^2$.

The preceding relations describe only one part of the profile, namely, the part which is dominated by GB diffusion. The overall penetration profile typically consists of two parts as shown schematically in Fig. 8.2:

- A near-surface region caused by direct volume diffusion from the surface. The concentration in this region follows a Gaussian function or an error function, depending on the surface condition. If measured accurately, this part can be used to determine the volume diffusion coefficient.
- A long-penetration tail caused by the simultaneous GB diffusion and lateral volume diffusion from the GB to the adjacent grains. It is this tail that should become a straight line when plotted as $\log \overline{c}$ versus $y^{6/5}$. The slope of this line is used to determine the GB diffusivity.

It should be pointed out that the power $n = 6/5$ has no physical meaning and cannot be derived analytically. It simply provides a good numerical approximation of the exact profile in a convenient concentration range and is therefore widely used for the analysis of experimental profiles. A slightly more accurate value of n can be obtained for each particular surface condition or GB geometry in the sample [17]. The obtained values range from 1.1 to 1.2, i.e. are rather close to 6/5. Given the scatter of data points on experimental profiles, the use of one universal power $n = 6/5$ and thus (8.12), (8.16)-(8.18) is a well-justified procedure for all practical purposes. Carefully measured experimental profiles do follow the $y^{6/5}$-rule in a wide concentration range, see examples in Fig. 8.3. Moreover, the linearity of $\log \overline{c}$ versus $y^{6/5}$ is often used as a proof of predominant GB diffusion in the sample and a measure of the profile quality.

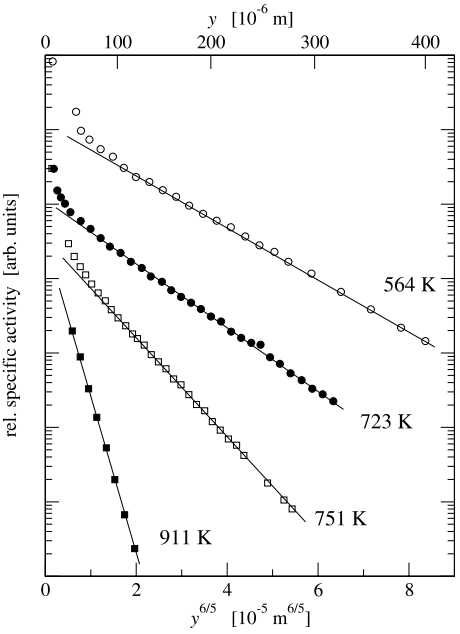

Fig. 8.3. Penetration profiles for self-diffusion in polycrystalline silver [23]. This diagram demonstrates that the GB-related tail of high quality profiles becomes a straight line when plotted as $\log \overline{c}$ versus $y^{6/5}$.

Equations (8.12), (8.16)-(8.18) are only valid for self-diffusion in metals. The case of impurity diffusion was first analyzed by Bokshtein et al. [18] and Gibbs [19] and later revisited by other authors (see [4] for references). It has been shown that, provided the segregation factor s is a constant, all solutions of the Fisher model remain the same as for self-diffusion except that δ should be replaced by the product $s\delta$. In particular, (8.12), (8.16)-(8.18) should be modified by replacing their left-hand side by $s\delta D_{\mathrm{b}}$. After this modification they can be applied for the determination of the triple product $s\delta D_{\mathrm{b}}$ of impurity diffusion.

8.2.4 What Do We Know About Grain Boundary Diffusion?

It is not our intention to give a complete answer to this question, especially because many topics in this area are still the subject of debates in the literature. We will focus on facts that appear to be well established and will restrict our discussion to self-diffusion in metals.

The Grain Boundary Width

In the case of self-diffusion we can only determine the product δD_{b}. We thus need to know δ if we want to determine the GB diffusion coefficient D_{b}. The assumption $\delta = 0.5$ nm introduced by Fisher [3] seems to be a good approximation. This value of δ is well-consistent with evaluations of GB width

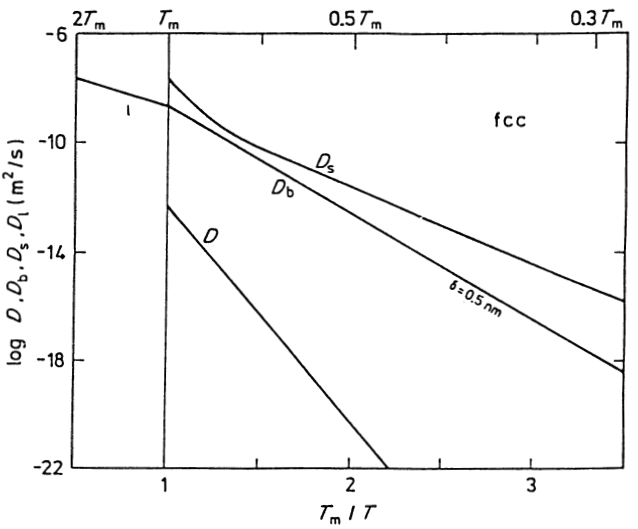

Fig. 8.4. Arrhenius lines for self-diffusion in fcc metals in the lattice (D) [31], along grain boundaries (D_b) [32], on the surface (D_s) [30] and in the liquid phase [30].

by high-resolution transmission electron microscopy, field ion microscopy, and other techniques [4, 20–22]. Furthermore, recent combined B-regime and C-regime measurements (see definitions of these regimes below) of self-diffusion in silver indicate that $\delta = 0.5$ nm is a very good estimate of δ in metals [23,24]. Atomistic computer simulations also confirm that the enhanced diffusivity at GBs is confined to the GB core of around 0.5 nm in thickness [25–29].

Empirical Rules

Like lattice diffusion, GB diffusion normally follows the Arrhenius temperature dependence, $D_\mathrm{b} = D_{\mathrm{b}0} \exp(-Q_\mathrm{b}/RT)$, R being the gas constant. The activation energy Q_b of GB diffusion is about a factor of two smaller than the activation energy Q of lattice diffusion; more exactly, in most metals $Q_\mathrm{b}/Q \approx 0.4$ to 0.6. Typically, GB diffusion is 4 to 8 orders of magnitude

Table 8.1. Empirical correlation between grain boundary self-diffusion and the melting temperature for three classes of metals. T_m is the melting temperature.

	Brown and Ashby [31]		Gust et. al. [32]	
structure	$\delta D_{\mathrm{b}0}$ (m^3/s)	Q_b (J/mol)	$\delta D_{\mathrm{b}0}$ (m^3/s)	Q_b (J/mol)
fcc	9.44×10^{-15}	83.0 T_m	9.7×10^{-15}	75.4 T_m
bcc	3.35×10^{-13}	97.6 T_m	9.2×10^{-15}	86.7 T_m
hcp	2.74×10^{-14}	89.8 T_m	1.5×10^{-14}	85.4 T_m

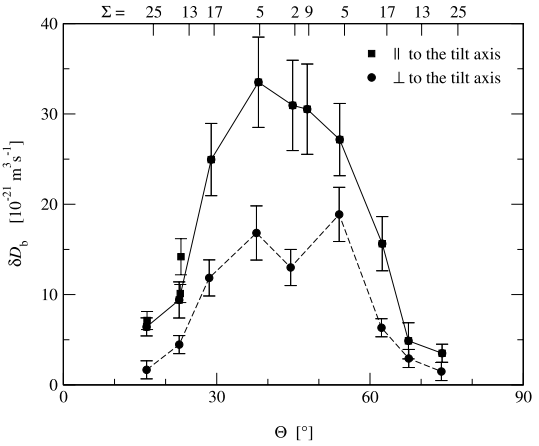

Fig. 8.5. Orientation dependence of self-diffusion in [001] symmetrical tilt grain boundaries in silver at $T = 771\,\mathrm{K}$ [34].

faster than volume diffusion depending on the temperature (Fig. 8.4). This tremendous difference in the diffusion coefficients is mainly due to the difference in the activation energies while the respective pre-exponential factors are close to one another. For all metals, D_b approaches a common value of about 10^{-9} to 3×10^{-9} $\mathrm{m^2 s^{-1}}$ at the melting temperature T_m [30]. Even near the melting point, D_b remains significantly higher than D and approaches the diffusion coefficient in the liquid phase (Fig. 8.4). In Table 8.1 we summarize empirical correlations between GB diffusion data and T_m for three classes of metals (fcc, bcc and hcp) derived by Brown and Ashby [31] and Gust et al. [32]. These correlations offer a good base for the systematics of available GB diffusion data and the evaluation of new data.

Anisotropy of Grain Boundary Diffusion

If diffusion is measured in two mutually perpendicular directions in the same GB, the obtained diffusion coefficients are generally different. The first measurements of this type were performed by Hoffman [33] for self-diffusion along [001] tilt GBs in Ag. He diffused a silver radiotracer into a single GB in silver bicrystals, i.e., samples prepared by the diffusion bonding of two properly oriented single crystals. For small-angle misorientations between the grains the anisotropy was especially strong, with diffusion parallel to the tilt axis ($D_\mathrm{b}^{\parallel}$) being a factor of 15 faster than diffusion perpendicular to the tilt axis ($D_\mathrm{b}^{\perp}$). These observations were explained in terms of the dislocation model of small-angle GBs. However, some anisotropy $D_\mathrm{b}^{\parallel}/D_\mathrm{b}^{\perp} \approx 2$ still remained even when the tilt angle θ became as large as 45°. Since the dislocation model is not valid at large misorientations, the measurements of Hoffman suggest that even large-angle GBs are not amorphous but instead have a well-ordered anisotropic structure. Figure 8.5 shows more recent results of diffusion anisotropy measurements, also in bicrystals with a [001] symmet-

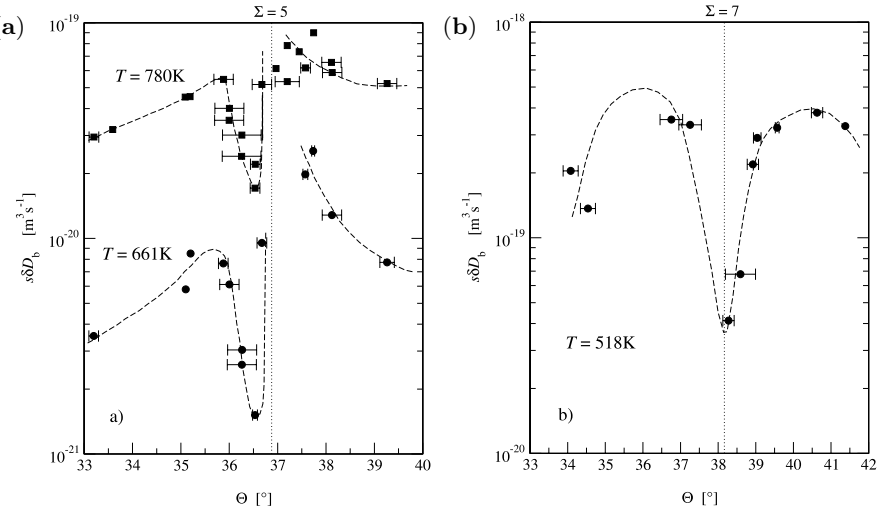

Fig. 8.6. (a) Orientation dependence of ^{195}Au diffusion in [001] symmetrical tilt grain boundaries in Cu measured on oriented bicrystals around the $\Sigma = 5$ (310)[111] orientation [36]. The grain boundary diffusivity $P = s\delta D_{\mathrm{b}}$ is plotted as a function of the tilt angle θ. (b) orientation dependence of Ge diffusion in Al bicrystals around the $\Sigma = 7$ (321)[111] orientation [38].

rical tilt GB in Ag, in the range of high-angle misorientations [34]. Similar results were obtained in other metallic systems [4]. Atomistic computer simulations also predict a significant anisotropy of GB diffusion in metals [26,27].

Orientation Dependence of Grain Boundary Diffusion

If the lattice misorientation between two grains changes continuously and GB diffusion is measured along a fixed direction in the GB plane (e.g., parallel to the tilt axis), will the diffusion characteristics change monotonically or will they show maxima or minima at some special orientations? The first attempt to answer this question was made in the pioneering work of Turnbull and Hoffman [35], again on bicrystals with a [001] symmetrical tilt GB in Ag. They studied only small-angle GBs and found a monotonic increase in the diffusivity with the misorientation angle. Later measurements on large-angle GBs revealed sharp minima at some misorientations with low values of Σ (reciprocal density of coincident sites). For example, Budke et al. [36,37] have studied tracer self-diffusion and Au impurity diffusion in a series of well-characterized Cu GBs in a narrow range ($\Delta\theta = 6°$) of tilt angles around the $\Sigma 5$ (310)[001] symmetrical tilt misorientation. The diffusivity showed a minimum and the activation energy a maximum very close to the perfect $\theta = 36.9°$ misorientation (Fig. 8.6(a)). Similar minima of GB diffusivity were observed for Ge tracer diffusion along the $\Sigma 7$ (321)[111] GB in Al [38] (Fig. 8.6(b)), as well

as for Zn chemical diffusion along the $\Sigma 5$ (310)[001], $\Sigma 9$ (122)[011], and $\Sigma 7$ (321)[111] symmetrical tilt GBs in Al [39]. At first sight, these observations stand in contrast with the continuous orientation dependencies found earlier on [001] symmetrical tilt GBs in Ni [40] and Ag [34, 41] (cf. Fig. 8.5). However, if the minima of D_{b} are confined to narrow ranges around some special misorientations, as was observed in [36–38], they could have been overlooked in the previous studies [34, 40, 41] where the measurements were taken in every 5–7°.

Atomistic Mechanisms of Grain Boundary Diffusion

There is experimental evidence suggesting that GB diffusion in metals and metallic systems takes place by the vacancy mechanism [4, 20, 42]. However, alternative mechanisms cannot be excluded, especially the interstitial mechanism. Recent atomistic computer simulations [25–27, 43] suggest that the full description of GB diffusion should include both the vacancy and interstitial-related mechanisms. Simulations also reveal that vacancies can move by "long jumps" involving a simultaneous displacement of two or more atoms [26, 27]. Interstitials move by the interstitialcy mechanism in which two or more atoms jump in a concerted manner. On some (although rare) occasions even the ring mechanism was found to operate in certain GBs [26]. Which mechanism dominates the overall atomic transport depends on the particular GB structure. Atomistic modeling also suggests that at high temperatures GBs can develop a significantly disordered, "liquid-like" structure [28, 29]. Diffusion in such GBs is believed to occur by mechanisms similar to those in liquids.

8.3 Classification of Diffusion Kinetics

GB diffusion is a complex process involving several elementary processes, such as direct volume diffusion from the surface, diffusion along the GBs, partial leakage of the diffusant from the GBs to the volume, and the subsequent volume diffusion around the GBs. In a polycrystalline material, diffusion transport between individual GBs can also play an important role. Depending on the relative importance of these elementary processes, essentially different diffusion regimes, or kinetics, can occur. In each particular regime one or two elementary processes control the overall rate of diffusion, whereas other processes are unimportant. Each regime dominates in a certain domain of anneal temperatures, times, grain sizes, and other relevant parameters. The knowledge of all regimes that can occur is important for both planning diffusion experiments and the interpretation of their results. The shape of the experimental concentration profile depends on the kinetic regime. Furthermore, the diffusion characteristics that can be extracted from the penetration profile also depend on the kinetic regime and should be identified *a priori*.

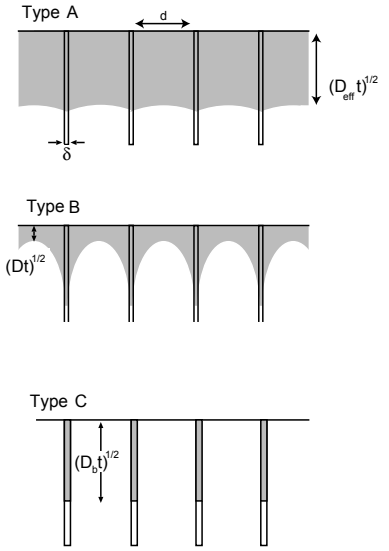

Fig. 8.7. Schematic illustration of type A, B and C diffusion regimes in Harrison's classification.

In this section we consider Harrison's [44] A-B-C classification for a polycrystal containing parallel GBs (Sect. 8.3.1). Some other classifications are discussed in Sect. 8.3.2.

8.3.1 Harrison's Classification

Harrison [44] proposed the first and still the most widely used classification of diffusion kinetics in a polycrystal with parallel GBs. His classification introduces three regimes called type A, type B, and type C (Fig. 8.7).

Type A Kinetics

The A regime is observed at high temperatures, or/and after very long anneals, or/and when the grain size is small. In this regime, the volume diffusion length $(Dt)^{1/2}$ is larger than the spacing d between the GBs, so that volume diffusion fields of neighboring GBs overlap very extensively. Thus, the condition of the A regime is

$$(Dt)^{1/2} \gg d. \tag{8.19}$$

Under this condition an average tracer atom visits many grains and GBs during the anneal time t, which results in planar front diffusion with the penetration depth proportional to $t^{1/2}$. On the macroscopic scale, the polycrystal obeys Fick's law with an effective diffusion coefficient D_{eff}. The latter represents an average of D and D_{b} weighted in the ratio of the number of atomic sites in the grains and in GBs [45],

$$D_{\text{eff}} = fD_{\text{b}} + (1 - f)D \tag{8.20}$$

(Hart's formula). Here f is the volume fraction of GBs in the polycrystal, i.e., $f = q\delta/d$, q being a numerical factor depending on the grain shape ($q = 1$ for parallel GBs). Thus, the experimental penetration profile should follow a Gaussian or an error function solution (depending on the surface condition) with the diffusion coefficient D_{eff}. Since $D_{\text{b}} \gg D$, D_{eff} is generally larger than D, which explains why diffusion coefficients measured on polycrystals are typically higher than the true value of D. If the grain size is large enough, then $f \to 0$ and D_{eff} approaches D. In the other extreme, when d is very small, D_{eff} is dominated by the first term and $D_{\text{eff}} \approx q\delta D_{\text{b}}/d$. Then, knowing the grain size and measuring D_{eff}, we can determine the product δD_{b}.

Type B Kinetics

If the temperature is lower, or/and the diffusion anneal time is shorter, or/and the grain size is larger than in the previous case, then diffusion takes place in the B regime in which

$$\delta \ll (Dt)^{1/2} \ll d. \tag{8.21}$$

As before, GB diffusion is accompanied by volume diffusion around GBs, but volume diffusion fields of neighboring GBs do not overlap (Fig. 8.7). Individual GBs are effectively isolated and mathematical solutions obtained for a single GB (Sect. 8.2) are also valid for a polycrystal. The relation (8.21) also implies that $\alpha \ll 1$. When analyzing the B regime, it is additionally assumed that also $\beta \gg 1$. Under these conditions the penetration profile has a two-step shape (Fig. 8.2) and (8.12), (8.16)-(8.18) can be applied for the profile analysis. The product δD_{b} (for impurity diffusion, $s\delta D_{\text{b}}$) is the only quantity that can be determined in the B regime. This regime comprises the widest and the most convenient temperature range of diffusion measurements in comparison with other regimes.

Type C Kinetics

If, starting from the B regime, we go towards lower temperatures or/and shorter anneal times, we eventually arrive at a situation when volume diffusion is almost "frozen out" and diffusion takes place only along GBs without any leakage to the volume (Fig. 8.7). In this regime, called type C, we have

$$(Dt)^{1/2} \ll \delta, \tag{8.22}$$

and thus $\alpha \gg 1$. The concentration profile is either a Gaussian function

$$\overline{c} \propto \exp\left(-\frac{y^2}{4D_{\text{b}}t}\right) \tag{8.23}$$

(instantaneous source) or an error function

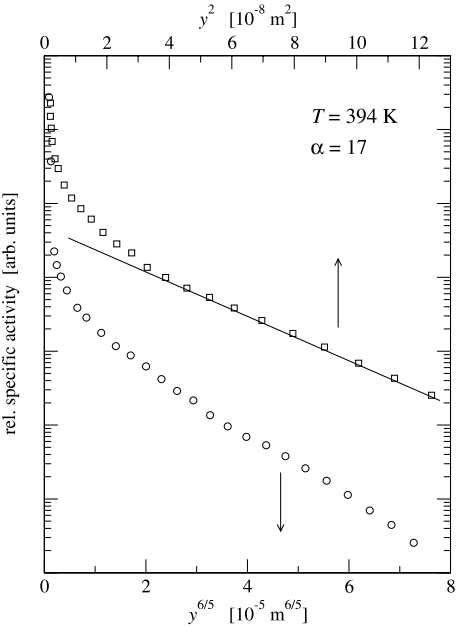

Fig. 8.8. Penetration profile of GB self-diffusion in polycrystalline Ag measured in the C regime ($\alpha = 17$) [23]. In order to measure this profile in a wide concentration range, carrier-free ^{105}Ag radiotracer was implanted at the ISOLDE/CERN facility. After a microtome sectioning, the radioactivities of the sections were determined with a well-type intrinsic Ge γ-detector. The tail of the profile shows a downward curvature when plotted as $\log \overline{c}$ vs $y^{6/5}$ (B-regime format, lower scale) but becomes a straight line when plotted as $\log \overline{c}$ vs y^2 (C-regime format, upper scale).

$$\overline{c} \propto \operatorname{erfc}\left[\frac{y}{2(D_{\mathrm{b}}t)^{1/2}}\right] \tag{8.24}$$

(constant source). If the profile has been measured experimentally (which is extremely difficult to do because the amount of tracer penetrated into the sample is very small), then we can determine D_{b} separately from δ. If the profile has been measured over a wide concentration range, we can distinguish between the B and C regimes already from its shape and not only from the value of α. This fact is illustrated in Fig. 8.8 in which a C-regime profile of GB self-diffusion in Ag is plotted in two different formats [23]. The linearity of the plot $\log \overline{c}$ versus y^2 confirms the C regime.

It is important to know the physical meaning of the parameters α and β used in this classification [4,5]. Parameter α determines the relation between diffusion along the GBs and the leakage of the diffusant from the GBs to the volume. When $\alpha \gg 1$, which is the case in the C regime, then diffusion along the GBs takes place without any leakage to the volume. Then the leakage term in (8.2) can be neglected and this equation is easily solved to give (8.23) and (8.24). If $\alpha \ll 1$ (B regime), the leakage of the diffusant from the GBs is the rate-controlling step while GB diffusion itself is quasi-steady. The latter means that the derivative $\partial c_{\mathrm{b}}/\partial t$ in (8.2) can be neglected, which simplifies this equation and makes the concentration a function of the reduced depth w only.

Parameter β determines the relation between the x and y components of volume diffusion near the GBs. When $\beta \gg 1$ (C and B regimes), volume

diffusion takes place predominantly in the x direction and the term $\partial^2 c/\partial y^2$ in (8.1) can be neglected. This approximation does not apply to the zone of direct volume diffusion near the surface, which is dominated by the term $\partial^2 c/\partial y^2$. However, as long as $\beta \gg 1$, the depth of the direct volume diffusion zone is much smaller than the penetration depth along the GBs. Because β decreases with temperature and time, at high temperatures or after long anneals β becomes small and we arrive at the A regime in which most of the penetration profile lies in the zone of direct volume diffusion.

If the grain size is small, the volume diffusion fields around GBs come to overlap while β is still large. In that case the onset of the A regime is determined by the condition $\Lambda \equiv d/\sqrt{Dt} \ll 1$. Murch and Belova [46] have recently performed kinetic Monte Carlo simulations of GB diffusion across the A and B regimes and established a more practical criterion of the A-B kinetic transition. Namely, the A regime dominates at $\Lambda \leq 0.4$–0.7 (depending on the surface conditions), whereas lower limit of the B regime is $\Lambda \approx 2.0$. The range $0.5 \leq \Lambda \leq 2$ therefore corresponds to the A-B transition kinetics.

Another transient kinetics, namely between the B and C regimes, in which $\alpha \approx 1$, is particularly interesting. It has even been argued that this transition deserves to be treated as separate kinetic regime [4, 11]. In this regime, the diffusion profile depends on both w and α, which opens a possibility to determine both δD_b and δ from the profile shape. Although the respective mathematical treatments have been developed and experimental profiles measured in this transient regime are available in the literature, attempts to determine D_b and δ in such conditions have not been very successful so far [4].

8.3.2 Other Classifications

So far we have only considered a polycrystal with parallel GBs. More realistic models of a polycrystal have been proposed, such as the cubic grain model of Suzuoka [9], the spherical grain model of Bokshtein et al. [18], and the general model of diffusion in isotropic polycrystals by Levine and MacCallum [15]. The spherical grain model has been particularly useful due to its ability to treat diffusion in fine-grained polycrystals. The model was analyzed in several publications and applied to diffusion in fine-grained oxides [47] and growing oxide films [48, 49]. Along with standard regimes that fit into Harrison's classification, both Bokshtein et al. [18] and Levine and MacCallum [15] identified a new regime in which

$$\delta \ll \sqrt{Dt} \ll d \ll L_\mathrm{b}, \tag{8.25}$$

where L_b is the penetration depth along GBs. In this regime the diffusing atoms penetrate to a large depth $L_\mathrm{b} \gg d$ along the GB network but volume diffusion fields around individual GBs still do not overlap. It has been shown [4] that the penetration profile has the same shape as in Harrison's B regime

and that (8.12), (8.16)-(8.18) are still valid, but δ should be replaced by an "effective" GB width $q\delta$, where q is a geometric factor of order unity depending on the grain shape.

A general classification of diffusion kinetics in isotropic polycrystalline materials has been developed in [4, 50]. If the grain size d is allowed to vary over a wide range, a number of new regimes can occur, each defined by a certain relation between the four characteristic lengths involved in the problem: δ, d, $(Dt)^{1/2}$, and L_{b}. In particular, the kinetics defined by (8.25) is one of such regimes. Each regime is characterized by a certain time dependence of the penetration length, a certain shape of the concentration profile, and certain diffusion characteristics that can be determined from the profile. The analysis also shows that all isotropic polycrystals can be divided into three classes called "coarse-grained", "fine-grained", and "ultrafine-grained" polycrystals according to their grain size. Polycrystals of each class exhibit their own set of diffusion regimes. GB segregation has a strong effect on both the concentration profiles and the critical grain sizes separating the three classes of polycrystals. The interested reader is referred to Sect. 2.4.13 of [4] for more details.

Other generalizations of Harrison's classification include the analysis of diffusion in structurally non-uniform GBs [51, 52] and GB diffusion in conditions when the grains are non-uniform [52, 53]. In particular, Klinger and Rabkin [53] proposed an extension of Harrison's classification which recognizes that lattice dislocations, subgrain boundaries, and other extended defects present in the bulk can alter the GB diffusion kinetics. They have identified a new ("type D") regime in which the effective rate of GB diffusion is controlled by short circuit diffusion inside the grains. These and other generalizations are very important as they reach out to more realistic conditions of diffusion experiments and diffusion-controlled processes in materials.

The following example demonstrates the practical usefullness of the analyses of kinetic regimes in polycrystals. Ni GB diffusion in a two-scale material was investigated in [54, 55]. The nanocrystalline γ-Fe–40 wt.%Ni alloy consisted of nanometer-scale grains arranged in micrometer-scale clusters, or agglomerates (cf. Fig. 9.22 in Chap. 9). For the analysis of the complex penetration profiles in this material with two types of short-circuit diffusion paths (the nanocrystalline GBs and the inter-agglomerate interfaces) a further extention of the Harrison classification was suggested [54], which resembles the one introduced in [53]. Diffusion profiles were observed which corresponded to three concurrent processes: (i) Harrison's type B regime of GB diffusion along the nanocrystalline GBs, (ii) type B regime of short-circuit diffusion along the inter-agglomerate boundaries with subsequent outdiffusion into the adjacent nanocrystaline GBs, and finally (iii) volume diffusion (B-B regime). At higher temperatures, when the bulk diffusion fluxes from individual nanocrystalline GBs overlapped, the diffusion process proceeded in the type A regime along the nanocrystalline GBs and in the type B regime along the inter-agglomerate

boundaries with subsequent outdiffusion via combined nanocrystalline GB and bulk diffusion (A-B regime). Mathematical methods for analysing the obtained penetration profiles were also proposed in [54].

8.4 Grain Boundary Diffusion and Segregation

8.4.1 Determination of the Segregation Factor from Grain Boundary Diffusion Data

As mentioned above, GB diffusion experiments are typically performed in the B regime and the measured penetration profiles are analyzed using the $y^{6/5}$-method, see (8.12), (8.16)-(8.18). If we study impurity diffusion, this method gives only the triple product $s\delta D_{\mathrm{b}}$, the only quantity that can be determined in the B regime. While the GB width δ can be considered as a known constant, $\delta = 0.5$ nm (Sect. 8.2.4), the GB segregation factor s and the GB diffusion coefficient D_{b} are still to be determined. Because both quantities are essentially temperature dependent and can vary by orders of magnitude, knowing only their product means knowing almost nothing about each of them individually.

In some cases the equilibrium segregation factor s can be determined by independent direct measurements. In direct measurements, the impurity is introduced into the host material and the sample is annealed at a chosen temperature T to let the impurity form an equilibrium GB segregation. The sample is then fractured *in situ* along GBs and the chemical composition of the fracture surface is analyzed using Auger electron spectroscopy or some other surface analytic technique [20–22]. Combining the obtained GB segregation factor with the product $s\delta D_{\mathrm{b}}$ measured at the same temperature, we can calculate the GB diffusion coefficient D_{b}. Unfortunately, direct measurements of s are only possible in intrinsically brittle materials, such as ceramics and some intermetallic compounds, and are practically impossible in most of pure metals.

Another way to separate s and D_{b} is to perform GB diffusion measurements in a wide temperature range covering both B and C regimes. By C regime measurements we can directly determine D_{b} (Sect. 8.3.1). By combining the obtained D_{b} values with $s\delta D_{\mathrm{b}}$ values extrapolated from B regime measurements at high temperatures, we find $s\delta = s\delta D_{\mathrm{b}}/D_{\mathrm{b}}$ and thus s assuming $\delta = 0.5$ nm. This approach offers a key to solving two important problems at the same time. Firstly, the GB diffusion coefficients are determined separately. By making systematic measurements of volume and GB diffusion in binary systems, insights can be obtained into mechanisms of GB diffusion and segregation. Secondly, we determine the GB segregation factor and thus the GB segregation energy. That way, diffusion measurements can be used as a tool to study equilibrium GB segregation. This capability

is especially important for non-brittle materials in which direct segregation measurements are not possible.

It should be pointed out that the separate determination of s and D_b from diffusion measurements is based on the following assumptions:

- Local thermodynamic equilibrium is constantly maintained between GBs and the adjacent lattice regions at any depth within the diffusion zone.
- Both volume and GB concentrations of the impurity are small enough to be coupled by the linear equation (8.4) with a constant s. In other words, the GB segregation follows a linear, or Henry-type, isotherm.

A major problem of this approach is that diffusion measurements in the C regime are very difficult. Strong GB segregation favours such measurements by extending the temperature range of the C regime towards higher temperatures. Indeed, since $\alpha = s\delta/2(Dt)^{1/2}$, large s values increase α and allow us to meet the condition $\alpha \gg 1$ at temperatures higher than for self-diffusion. Nevertheless, due to the experimental challenges C regime measurements have practically not been performed until recently even for impurity diffusion. It is only since a few years that reliable and systematic C regime measurements have become possible, mainly due to the use of carrier-free radioisotopes and extremely sensitive γ-detectors with a large counting efficiency and low background. To date, combined B and C regime measurements have been performed in a few systems [56–60]. We will discuss the results for two systems, Te in Ag [56] and Au in Cu [57], which represent the extreme cases of very strong and very weak segregation, respectively.

GB diffusion of Te in Ag was studied in the temperature range 378 to 970 K using the radiotracers ^{123}Te (deposited by vacuum evaporation) and ^{121}Te (carrier-free, implanted at the ISOLDE/CERN facility). Each penetration profile was analyzed in two ways: assuming the B and the C regimes. The actual regime that dominated the experiment was established from the profile shape (whether it became linear in the respective coordinates), and by comparing the α and β values with those required by the B and C regimes. It was found that the B regime prevailed in the temperature range > 600 K (Fig. 8.9). At these temperatures, the $s\delta D_b$ values determined from $\log \overline{c}$ versus $y^{6/5}$ plots followed the Arrhenius relation

$$s\delta D_b = 2.34 \times 10^{-15} \exp\left(-\frac{43.47 \text{ kJ/mol}}{RT}\right) \text{ m}^3/\text{s}. \tag{8.26}$$

It was also established that the measurements below 500 K were dominated by the C regime. At these temperatures the GB diffusion coefficients were determined by fitting the profiles to the Gaussian function. The diffusion coefficients were found to follow the Arrhenius relation

$$D_b = 1.01 \times 10^{-4} \exp\left(-\frac{86.75 \text{ kJ/mol}}{RT}\right) \text{ m}^2/\text{s}. \tag{8.27}$$

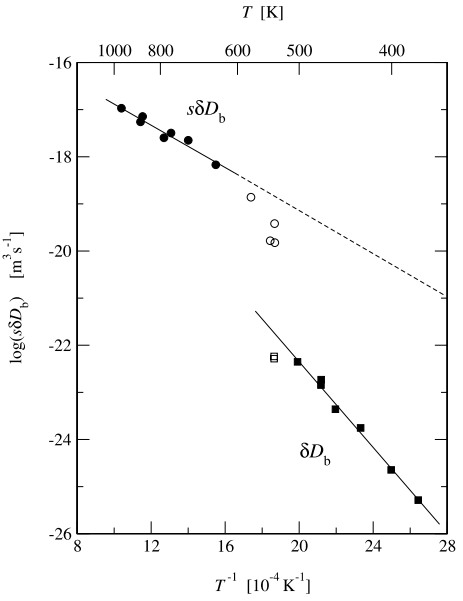

Fig. 8.9. The Arrhenius plot of $s\delta D_\mathrm{b}$ (circles) and δD_b (squares) ($\delta = 0.5$ nm) for Te impurity diffusion along GBs in Ag [56]. The B and C regimes dominate above 600 K and below 500 K, respectively. In the range 500 to 600 K the apparent values of both $s\delta D_\mathrm{b}$ and δD_b are significantly underestimated. The difference between the two Arrhenius lines is due to GB segregation of Te.

In the transition temperature range 500-600 K, the $s\delta D_\mathrm{b}$ and D_b values showed significant downward deviations from the respective Arrhenius lines (Fig. 8.9). This behavior is perfectly consistent with the theoretical analysis [4, 61] and is typical of the transient regime between B and C.

In Fig. 8.9, the δD_b values measured in the C regime are plotted together with $s\delta D_\mathrm{b}$ values extrapolated from the B regime measurements at $T > 600$ K. The difference between the two lines gives the segregation factor s. The high values of s (10^3 to 10^5) are well-consistent with the very small solubility of Te in Ag. The segregation energy determined from the Arrhenius plot of s (Fig. 8.10) equals $E_\mathrm{s} = -43.3$ kJ/mol.

In contrast to the previous case, Au in Cu is a system with complete mutual solubility of the components, so that the GB segregation should be weak. The results of combined B and C regime measurements for this system [57], using the carrier-free radiotracer ^{195}Au, are shown in Fig. 8.11. The Arrhenius relations obtained in the B and C regimes are

$$s\delta D_\mathrm{b} = 2.11 \times 10^{-15} \exp\left(-\frac{81.24 \ \mathrm{kJ/mol}}{RT}\right) \ \mathrm{m^3/s} \tag{8.28}$$

and

$$D_\mathrm{b} = 4.87 \times 10^{-6} \exp\left(-\frac{91.03 \ \mathrm{kJ/mol}}{RT}\right) \ \mathrm{m^2/s}, \tag{8.29}$$

respectively. The segregation factors s deduced from the diffusion data are shown in Fig. 8.10. As expected, the obtained values of s (8 to 11) and the segregation energy $E_\mathrm{s} = -9.7$ kJ/mol are relatively small. The segregation

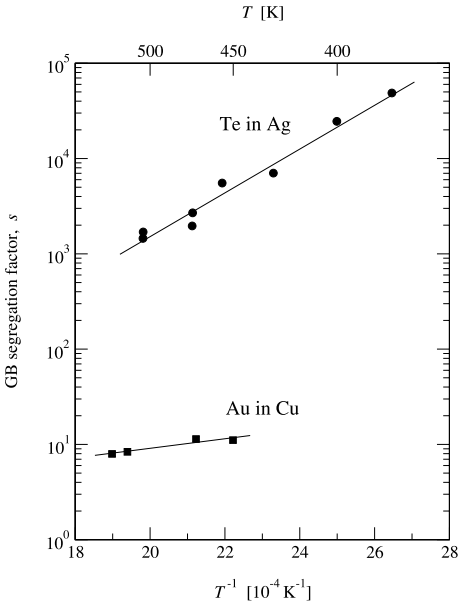

Fig. 8.10. Temperature dependence of the GB segregation factor s of Te in Ag [56] and Au in Cu [57] determined from combined B and C regime measurements.

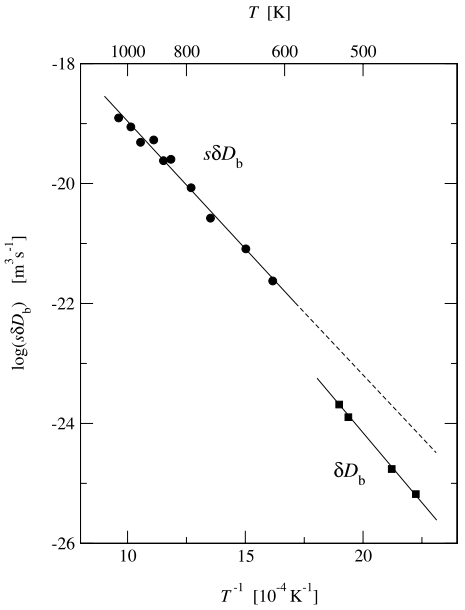

Fig. 8.11. The Arrhenius plot of $s\delta D_\mathrm{b}$ (circles) and δD_b (squares) ($\delta = 0.5$ nm) for Au impurity diffusion along GBs in Cu [57]. The B and C regimes prevail above 618 K and below 526 K, respectively. The difference between the two Arrhenius lines is due to GB segregation of Au.

energy has a reasonably lower absolute value than $E_\mathrm{s} = -13.0$ kJ/mol obtained earlier for Au segregation at the surface of a Cu-7.5at.%Au alloy [62].

These two examples demonstrate that separate measurements of s and D_b are now possible for both strongly and weakly segregating impurities. As

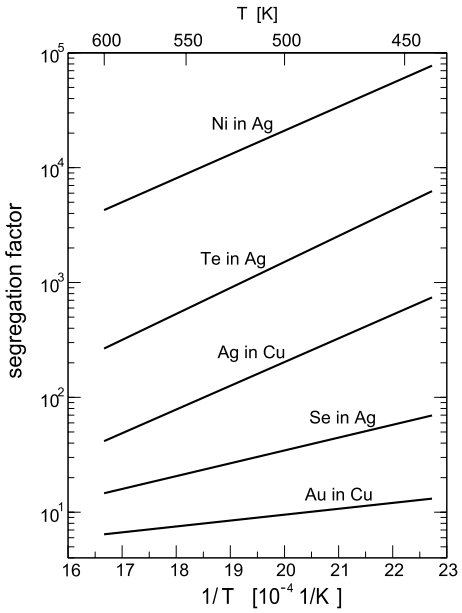

Fig. 8.12. GB segregation factors obtained by combined B and C regime measurements: Te in Ag [56], Au in Cu [57], Se in Ag [58, 59], Ni in Ag [59], and Ag in Cu [60].

mentioned before, such measurements offer the only way to study GB segregation in materials in which direct segregation measurements are hampered by their ductility or tendency to transgranular fracture. Figure 8.12 presents a summary of GB segregation data in other systems obtained by diffusion measurements. We see again that segregation factors can be determined over a wide range spanning almost five orders of magnitude. In all cases studied, GB segregation tends to reduce the GB diffusion rate of the impurity. In particular, impurities which are slow diffusers in the lattice diffuse even slower in GBs, as exemplified by Ni in Ag [59]. Furthermore, a fast diffuser in the lattice may be a slow diffuser in GBs if the segregation level is high enough, e.g. Te in Ag [56]. An atomistic theory explaining this "retardation effect" is yet to come.

8.4.2 Beyond the Linear Segregation

Until this point we assumed that the GB segregation followed a Henry-type isotherm, i.e., that the segregation factor s in (8.4) was a function of temperature only. This approximation is only valid when both the volume concentration $c_{\mathrm{v}}(y,t) = c(\pm\delta/2, y, t)$ and the GB concentration $c_{\mathrm{b}}(y,t)$ of the impurity, expressed in mole fractions with respect to the host element, are small. This condition in turn can only be met when the segregation is not very strong. In systems with a high level of segregation, especially at low temperatures, the GB concentration c_{b} can be relatively large. Then, the GBs can show a tendency to a saturation with the impurity and thus to a non-linear de-

pendence between c_v and c_b. A non-linear dependence means that the ratio $c_\mathrm{b}/c_\mathrm{v}$ in the joining condition (8.4) is no longer constant. Instead, it depends on the volume concentration c_v, and since c_v changes with depth y, the ratio $c_\mathrm{b}/c_\mathrm{v}$ also changes along the penetration profile. The depth dependence of $c_\mathrm{b}/c_\mathrm{v}$ can affect the shape of the penetration profile and should be taken into account in the profile analysis.

This problem was first analyzed by Martin and Perraillon [63] and more recently by Bokshtein et al. [64] and the present authors [65]. All these analyses included the non-linearity of GB segregation by using McLean's isotherm instead of the Henry isotherm. McLean's isotherm of GB segregation has the form

$$c_\mathrm{b} = \frac{sc_\mathrm{v}}{1 + (s-1)c_\mathrm{v}}, \tag{8.30}$$

where s depends only on temperature, $s = s_0 \exp(-E_\mathrm{s}/RT)$. If the volume concentration is small, $c_\mathrm{v} \to 0$, then (8.30) reduces to the Henry isotherm, $c_\mathrm{b} = sc_\mathrm{v}$. If c_v is large, (8.30) gives $c_\mathrm{b} \to 1$, meaning that the GB is saturated with the impurity.

Using the approximations introduced by Fisher [3], the basic equations of the model can be solved analytically. For a constant source, we obtain the following expression for c_b as a function of the reduced depth w:

$$w = \pi^{1/4} \int_{\sigma c_\mathrm{b}}^{\sigma c_0} \frac{\mathrm{d}c}{[-2\ln(1-c) - 2c]^{1/2}}. \tag{8.31}$$

Here $\sigma \equiv (s-1)/s$ and c_0 is the surface concentration. The average concentration measured in sectioning experiments equals

$$\overline{c} = 2\int_0^\infty c(x,y,t)\mathrm{d}x = 4\left(\frac{Dt}{\pi}\right)^{1/2} \cdot c_\mathrm{v} = 4\left(\frac{Dt}{\pi}\right)^{1/2} \cdot \frac{c_\mathrm{b}}{s-(s-1)c_\mathrm{b}}. \tag{8.32}$$

We thus have two functions, $w = w(c_\mathrm{b})$ given by (8.31) and $\overline{c} = \overline{c}(c_\mathrm{b})$ given by (8.32), which define the penetration profile $\overline{c}(w)$ parametrically.

Typical penetration profiles $\log \overline{c}/\overline{c}_0$ versus w calculated from (8.31) and (8.32) are shown in Fig. 8.13, $\overline{c}_0$ being the surface value of the average concentration $\overline{c}$. The profiles consist of two parts:

1. The GB saturation region ($w < 1$) in which $\overline{c}$ rapidly decreases and the profile has a strong upward curvature. In this region the GB concentration remains almost constant, $c_\mathrm{b} \approx 1$, while the volume concentration c_v drops rapidly.

2. The linear-segregation region ($w > 1$) in which the profile is consistent with Fisher's exponential solution, (8.8). In this region both c_v and c_b are small and the linear segregation isotherm is a good approximation. It is this part of the profile that can be used for the determination of $s\delta D_\mathrm{b}$ using standard methods of profile analysis.

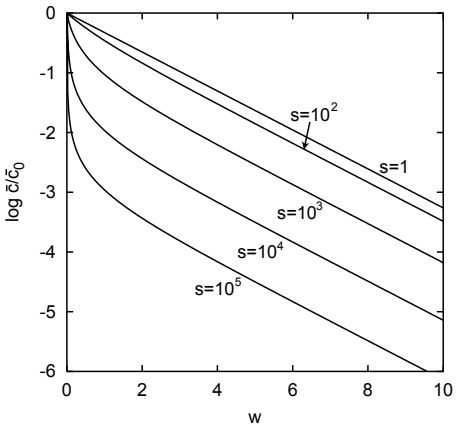

Fig. 8.13. Typical GB penetration profiles calculated with McLean's isotherm [65].

The profile shape shown in Fig. 8.13 is rather general and could be obtained by using more accurate mathematical solutions of the model or other forms of the non-linear isotherm of segregation. With more accurate solutions, the linear-segregation part of the profile has a slight downward curvature according to the $w^{6/5}$-approximation.

Examples of experimental profiles measured for a strongly segregating impurity and containing two steps are available in the literature. Although it seems tempting to immediately explain the near-surface part of such profiles by the solute-saturation effect, one should bear in mind that the near-surface region of the profiles can be affected by many other factors, such as direct volume diffusion from the surface, diffusion along dislocations, GB motion, etc.

In order to avoid such complications, GB diffusion measurements in well-oriented bicrystals offer a convenient way of studying the effect of non-linear segregation. This has been demonstrated in a recent investigation of Ag GB diffusion in Cu bicrystals near the $\Sigma = 5(310)[001]$ orientation [66]. A curved penetration profile similar to those presented in Fig. 8.13 has been measured for Ag GB diffusion (Fig. 8.14, circles), whereas a perfectly linear, type-B profile has been measured for Au GB diffusion in the same bicrystal (squares). Because Au diffusion closely represents Cu self-diffusion (very low segregation, cf. Fig. 8.12), the difference in the shape of the profiles can be directly attributed to the strong GB segregation of Ag in Cu and the associated effect of GB saturation near the surface. Further details of this study can be found in [66].

8.5 Conclusion

Diffusion along GBs is a phenomenon of both practical importance and significant fundamental interest. Modern GB diffusion studies employ novel ex-

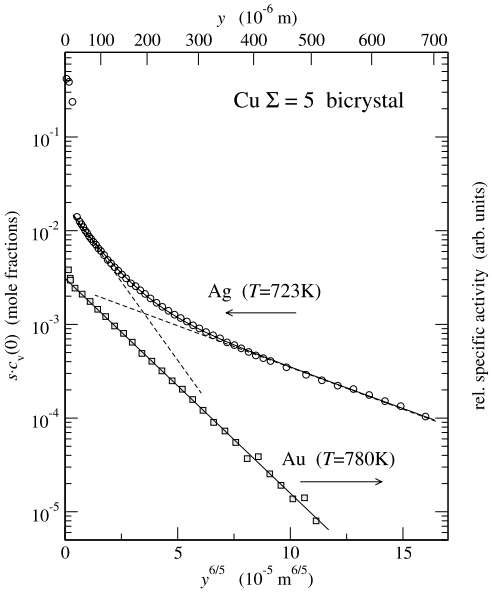

Fig. 8.14. Experimental demonstration of non-linear segregation of Ag in Cu. The concentration profiles have been measured for Ag (circles, left axis) [66] and Au (squares, right axis) [37] GB diffusion in a Cu bicrystal near the $\Sigma = 5(310)[001]$ orientation. The measured specific radioactivity of the ^{110m}Ag tracer has been recalculated to the absolute concentration of Ag (in mole fractions). $c_v(0)$ is the Ag bulk concentration in lattice regions adjacent to the GB and s is the GB segregation factor measured under dilute limit conditions in [60].

perimental techniques for precise radiotracer measurements combined with elaborate mathematical treatments of the experimental profiles. The large volume of experimental data accumulated to date follows clear systematics and provides a reasonably good understanding of GB diffusion, at least on a phenomenological level. One of the most impressive achievements in this area is the implementation of GB diffusion measurements at relatively low temperatures in the C-regime. Such measurements, combined with traditional measurements in the B regime, open the long awaited possibility of separate determination of the GB diffusion coefficient D_b and the impurity segregation factor s.

GB diffusion measurements can be used as a tool to study other properties of GBs, such as their structure, migration, impurity segregation, etc. Since GB diffusion is sensitive to GB structure and chemistry and because radiotracer experiments do not practically disturb the initial state of GBs, diffusion measurements provide useful information on the structural and chemical state of GBs. The importance of this capability is emphasized by the fact that, in contrast to an open surface, GBs are buried interfaces, which makes their studies more difficult. Cleavage of a material along GBs may strongly disturb the initial state of the GBs and in addition is not feasible for many materials. High-resolution transmission electron microscopy is probably the most effective technique for GB studies, but it involves some other problems which will not be discussed here. In this situation, GB diffusion measurements can serve as a useful complimentary technique to study GB properties averaged over a 10^{-4} m length scale (typical penetration length along GBs).

In what follows we will briefly discuss a few other interesting topics that have not been addressed here in detail.

Grain boundary diffusion and segregation in solid solutions: GB diffusion in a binary solution A-B depends on tracer diffusion coefficients of both components in the volume and in GBs, as well as the respective GB segregation factors. In contrast to impurity diffusion, all these quantities generally depend on the bulk composition. There are systems in which both components have suitable radiotracers and their diffusion characteristics can thus be established as functions of the bulk composition. However, there is only one system, Fe-Sn [67], in which both GB diffusion coefficients and segregation factors were determined by independent measurements. In all other systems (e.g. Ag-Sn [68], Ag-Ni [69]) only the products $(s\delta D_\mathrm{b})_\mathrm{A}$ and $(s\delta D_\mathrm{b})_\mathrm{B}$ were determined, and not s_A and s_B separately, which makes the interpretation of the results very difficult. Now that a separate determination of D_b and s is possible, it seems timely to revisit some of those systems and determine the composition dependencies of both diffusion and segregation characteristics of A and B over a range of temperatures and compositions.

Grain boundary diffusion in intermetallic compounds: GB diffusion data in ordered intermetallics are scarce. Meanwhile, the need for such data is rapidly growing, especially for transition metal aluminides in view of their potential applications as high temperature structural materials. Intermetallics are also suitable model systems to study the effect of bulk ordering and non-stoichiometry on GB diffusion. The compounds in which GB diffusion has been measured include Ni_3Al [70–72], NiAl [73, 74], Ti_3Al [73, 74], TiAl [73, 74], Fe_3Al [75], FeCo [75], Ni_2Si [77], Ni_2Si_5 [78], $CoSi_2$ [78], and NiSb [79]. While Al and Si diffusion measurements are hampered by the lack of suitable isotopes, diffusion of the transition element does not present a particular problem. In most Ni and Ti aluminides and in FeCo, the ratio Q_b/Q lies within the same range 0.4–0.6 as in pure metals, whereas in silicides Q_b/Q is anomalously high, 0.7–0.9. Ti diffusion in Ti_3Al also shows unusually high Q_b/Q values varying between 0.68 (which is a borderline value) for the stoichiometric composition and 0.88 for the 35 at.%Al alloy.

Tôkei et al. [75] have studied the effect of a bulk phase transition on GB diffusion of Fe in Fe_3Al and Fe and Co in FeCo. In FeCo, GB diffusion shows a discontinuity near the temperature of the bulk order-disorder transition. In contrast, in Fe_3Al GB diffusion does respond to the order-disorder transition. This difference was tentatively explained by a partial atomic order around GBs in Fe_3Al pertaining even above the bulk transition temperature, but this interesting hypothesis requires an atomic level verification.

The effect of non-stoichiometry on GB diffusion has been studied in Ni and Ti aluminides [70, 71, 73, 74]. In Ni_3Al [70, 71], Ni GB diffusion has a minimum at the ideal stoichiometry and increases with deviations from the stoichiometry on either side. In Ti_3Al [73, 74], the measurements have only been performed on the Al-rich side, and Ti GB diffusion has been found to

decrease with the bulk Al concentration. Interestingly, in both compounds bulk diffusion of Ni and Ti almost does not depend on the composition, suggesting that the observed composition dependence of GB diffusion is due to local effects such as GB segregation and/or disorder. On the other hand, the data available for the equiatomic compounds NiAl and TiAl do not indicate any composition dependence of GB diffusion [73, 74]. It appears that more measurements and theoretical work need to be done in this area before any understanding can be reached.

Diffusion in moving grain boundaries: Under real conditions GBs often move as a result of recrystallization, grain growth, and other processes. Moreover, GB diffusion itself is capable of making otherwise stationary GBs move in a random manner. The diffusion induced GB migration (DIGM) is only observed during interdiffusion, i.e., when a substantial amount of foreign atoms is diffused into the sample [80]. Although the nature of DIGM is still not well-understood, many GB diffusion experiments have probably been affected by DIGM. Even during a radiotracer self-diffusion experiment in a well-annealed polycrystalline sample some GBs can still move due to the continued grain growth and/or the trend to establish equilibrium inclination angles between GBs and the surface. GB migration can have a noticeable effect on the shape of the measured concentration profiles and should be taken into account in their analysis. It has been shown that GB motion only modifies a near-surface part of the profile whereas the tail of the profile is not affected. Thus, from the shape of the entire profile measured in the B regime we can determine not only the product $s\delta D_{\mathrm{b}}$ for stationary GBs but also the average velocity v of moving GBs [81]. Again, diffusion measurements can be used as a tool to study the kinetics of GB migration [82]. The first experimental study of this type was performed for self-diffusion in α-Hf [83] and was followed by similar studies of Co and Ni impurity diffusion in Nb [84–86]. An interesting observation in [83] is that the activation energy of GB migration, 195 ± 18 kJ/mol, evaluated from the temperature dependence of v, is close to the measured activation energy of self-diffusion along stationary GBs, 212 ± 9 kJ/mol. This result can be interpreted as evidence that the activation barrier for atomic transport *across* GBs during their migration is essentially the same as the barrier of the atomic transport *along* GBs.

Atomistic theory of grain boundary diffusion: Much progress has been recently achieved in the atomistic interpretation of GB diffusion through computer modeling. The atomistic computer simulations have employed many-body interatomic potentials and a variety of simulation methods, see e.g. [25–29]. It has been recognized that, in contrast to lattice diffusion, GB diffusion is accompanied by strong and temperature dependent correlations between successive atomic jumps [87]. Analysis of jump correlation effects is thus a prerequisite for the understanding of the diffusion-structure relationship in GBs. It has also been established that GBs support both vacancies and interstitials, but these defects can show interesting structural effects such

as vacancy delocalization, vacancy instability at certain cites in the GB core, etc. [26, 27]. Vacancies can move in GBs by single-atom exchanges, like in a regular lattice, but can also make collective jumps involving several atoms. Interstitial formation energies in GBs are close to vacancy formation energies, which makes both defects equally important for diffusion. Interstitials can be either localized or form split dumbbell configurations. They move predominantly by the interstitialcy mechanism involving 2-4 atoms. A challenging problem in this area is to calculate GB diffusion characteristics as functions of misorientation between the two grains, particularly around a low-Σ orientation for which experimental data are available or can be measured.

Notation

bcc	body-centered cubic
c	diffusant concentration in the volume
c_b	diffusant concentration in the grain boundary
c_0	constant course concentration
$\overline{c}$	average concentration of the diffusant measured by the serial sectioning technique
D	volume diffusion coefficient
D_b	grain boundary diffusion coefficient
D_b0	pre-exponential factor of grain boundary diffusion
D_eff	effective diffusion coefficient in a polycrystalline material
d	spacing between grain boundaries in a polycrystalline material
DIGM	diffusion induced grain boundary migration
E_s	segregation energy
fcc	face-centered cubic
f	volume fraction of grain boundaries in a polycrystalline material
h	thickness of the initial layer of diffusant
hcp	hexagonal close-packed
ISOLDE	isotope separator on-line detector
L	diffusion penetration depth in the volume
L_b	diffusion penetration depth along grain boundaries
ln	natural logarithm (on base e)
log	common logarithm (on base 10)
M	amount of diffusant deposited per unit area of the surface
Q	activation energy of volume diffusion
Q_b	activation energy of grain boundary diffusion
R	gas constant
s	segregation factor
T	absolute temperature
T_m	melting temperature
t	diffusion anneal time
v	grain boundary migration velocity

w	reduced coordinate along the diffusion direction
α	diffusion parameter
β	diffusion parameter
δ	grain boundary width
θ	tilt angle
Λ	kinetic parameter of the A regime
Σ	reciprocal density of coincident site in the grain boundary

References

1. R.S. Barnes: Nature **166**, 1032 (1950)
2. A.D. Le Claire: Phil. Mag. **42**, 468 (1951)
3. J.C. Fisher: J. Appl. Phys. **22**, 74 (1951)
4. I. Kaur, Y. Mishin, W. Gust: *Fundamentals of Grain and Interphase Boundary Diffusion* (Wiley, Chichester West Sussex 1995)
5. Y. Mishin, Chr. Herzig, J. Bernardini, W. Gust: Intern. Mater. Reviews **42**, 155 (1997)
6. Y. Mishin, Chr. Herzig: Mater. Sci. Eng. A **260**, 55 (1999)
7. Y. Mishin: Defect Diffus. Forum **194-199**, 1113 (2001)
8. I. Kaur, W. Gust, L. Kozma: *Handbook of Grain and Interphase Boundary Diffusion Data* (Ziegler, Stuttgart 1989)
9. T. Suzuoka: Trans. Jap. Inst. Metals **2**, 25 (1961)
10. T. Suzuoka: J. Phys. Soc. Japan **19**, 839 (1964)
11. Y.M. Mishin, I.M. Razumovskii: Acta Metall. Mater. **40**, 597 (1992)
12. R.T.P. Whipple: Phil. Mag. **45**, 1225 (1954)
13. S.J. Rothman: The measurement of tracer diffusion coefficients in solids. In: *Diffusion in Crystalline Solids*, ed by G.E. Murch, A.S. Nowick (Academic Press, New York 1984) p 1
14. J. Philibert: *Atom Movements – Diffusion and Mass Transport in Solids* (Les Éditions de Physique, Les Ulis 1991)
15. H.S. Levine, C.J. MacCallum: J. Appl. Phys. **31**, 595 (1960)
16. A.D. Le Claire: Brit. J. Appl. Phys. **14**, 351 (1963)
17. Y.M. Mishin: Phys. Stat. Solidi (a) **133**, 259 (1992)
18. B.S. Bokshtein, I.A. Magidson, I.L. Svetlov: Phys. Met. Metallogr. **6**, 81 (1958)
19. G.B. Gibbs: Phys. Status Solidi **16**, K 27 (1966)
20. A.P. Sutton, R.W. Balluffi: *Interfaces in Crystalline Materials* (Clarendon Press, Oxford 1995)
21. *Materials Interfaces. Atomic-Level Structure and Properties*, ed by D. Wolf, S. Yip (Chapman & Hall, London 1992)
22. J.M. Howe: *Interfaces in Materials* (Wiley, New York 1997)
23. J. Sommer, Chr. Herzig: J. Appl. Phys. **72**, 2758 (1992)
24. P. Gas, D.L. Beke, J. Bernardini: Phil. Mag. Lett. **65**, 133 (1992)
25. Y. Mishin: Defect Diffus. Forum **143–147**, 1357 (1997)
26. M.R. Sørensen, Y. Mishin, A.F. Voter: Phys. Rev. B **62**, 3658 (2000)
27. A. Suzuki, Y. Mishin: Interface Sci. **11**, 131 (2003)
28. P. Keblinski, D. Wolf, S.R. Phillpot, H. Gleiter: Phil. Mag. A **79**, 2735 (1999)
29. P. Keblinski, V. Yamakov: Interface Sci. **11**, 111 (2003)

30. N.A. Gjostein. In: *Diffusion* (Amer. Soc. Metals, Metals Park OH 1974) p 241
31. A.M. Brown, M.F. Ashby: Acta Metall. **28**, 1085 (1980)
32. W. Gust, S. Mayer, A. Bögel, B. Predel: J. de Physique **46**, 537 (1985)
33. R.E. Hoffman: Acta Metall. **4**, 56 (1956)
34. J. Sommer, Chr. Herzig, S. Mayer, W. Gust: Defect Diffus. Forum **66–69**, 843 (1989)
35. D. Turnbull, R.E. Hoffman: Acta Metall. **2**, 419 (1954)
36. E. Budke, Chr. Herzig, S. Prokofjev, L.S. Shvindlerman: Mater. Sci. Forum **207–209**, 465 (1996)
37. E. Budke, T. Surholt, S. Prokofjev, L.S. Shvindlerman, Chr. Herzig: Acta Mater. **47**, 385 (1999)
38. T. Surholt, D. Molodov, Chr. Herzig: Acta Mater. **46**, 5345 (1998)
39. P. Klugkist, A.N. Aleshin, W. Lojkowski, L.S. Shvindlerman, W. Gust, E.J. Mittemeijer: Acta Mater. **49**, 2941 (2001)
40. W.R. Upthegrove, M.J. Sinnot: Trans. ASM **50**, 1031 (1958)
41. Quing Ma, R.W. Balluffi: Acta Metall. Mater. **41**, 133 (1993)
42. R.W. Balluffi: Mechanisms of grain boundary diffusion. In: *Diffusion in Crystalline Solids*, ed by G.E. Murch, A.S. Nowick (Academic Press, New York 1984) p 319
43. Quing Ma, C.L. Liu, J.B. Adams, R.W. Balluffi: Acta Metall. Mater. **41**, 143 (1993)
44. L.G. Harrison: Trans. Faraday Soc. **57**, 1191 (1961)
45. E.W. Hart: Acta Metall. **5**, 597 (1957)
46. I.V. Belova, G.E. Murch: Phil. Mag. A **81**, 2447 (2001)
47. Y. Oishi, H. Ichimura: J. Chem. Phys. **71**, 5134 (1979)
48. N.S. Basu, J.W. Halloran: Oxid. Metals **27**, 143 (1987)
49. W. Wegener, G. Borchardt: Oxid. Metals **36**, 339 (1991)
50. Y. Mishin, Chr. Herzig: Nanostruct. Mater. **6**, 859 (1995)
51. Y. Mishin, I.V. Yurovitskii: Phil. Mag. A **64**, 1239 (1991)
52. V.V. Kondratev, I.S. Trachtenberg: Phys. Status Solidi (b) **171**, 303 (1992)
53. L. Klinger, E. Rabkin: Acta Mater. **47**, 725 (1999)
54. S.V. Divinski, Y.-S. Kang, J.-S. Lee, F. Hisker, Chr. Herzig: Interface Sci. **11**, 67 (2003)
55. Y.-S. Kang, J.-S. Lee, S.V. Divinski, Chr. Herzig: Z. Metallkd. **95**, 76 (2004)
56. Chr. Herzig, J. Geise, Y. Mishin: Acta Metall. Mater. **41**, 1683 (1993)
57. T. Surholt, Y. Mishin, Chr. Herzig: Phys. Rev. **B50**, 3577 (1994)
58. T. Surholt, Chr. Herzig: Mater. Sci. Forum. **207–209**, 481 (1996)
59. T. Surholt, C. Minkwitz, Chr. Herzig: Acta Mater **46**, 1849 (1998)
60. S.V. Divinski, M. Lohman, Chr. Herzig: Defect Diffus. Forum, **194-199**, 1127 (2001)
61. A. Atkinson, R.I. Taylor: Phil Mag. A **43**, 979
62. W. Losch, J. Kirschner: J. Vac. Sci. Technol. **15**, 1541 (1978)
63. G. Martin, B. Perraillon: Measurements of Grain Boundary Diffusion. In: *Grain Boundary Structure and Kinetics*, ed by R. W. Balluffi (Amer. Soc. Metals, Metals Park OH 1980) p 239
64. B.S. Bokshtein, V.E. Fradkov, D.L. Beke: Phil. Mag. A **65**, 277 (1992)
65. Y. Mishin, Chr. Herzig: J. Appl. Phys. **73**, 8206 (1993)
66. S.V. Divinski, M. Lohman, Chr. Herzig: Interface Sci. **11**, 21 (2003)
67. J. Bernardini, P. Gas, E.D. Hondros, M.P. Sea: Proc. Royal Soc. Lond. **A379**, 159 (1982)

68. P. Gas, J. Bernardini: Surf. Sci. **72**, 365 (1978)
69. P. Gas, J. Bernardini. In: *Proc. 18th Int. Congr. Vacuum Technology and Vacuum Metallurgy*, vol 2 (Cannes 1980) p 501
70. S. Frank, J. Rüsing, Chr. Herzig: Intermetallics **4**, 601 (1996)
71. S. Frank, Chr. Herzig: Mater. Sci. Eng. **239-240**, 882 (1997)
72. J. Čermak, I. Stloukal, J. Ruvzikova: Intermetallics **8**, 21 (1998)
73. Chr. Herzig, S.V. Divinski, S. Frank, T. Przeorski: Defect Diffus. Forum **194-199**, 317 (2001)
74. Chr. Herzig, T. Wilger, T. Przeorski, F. Hisker, S.V. Divinski: Intermetallics **9**, 431 (2001)
75. Z. Tôkei, J. Bernardini, D.L. Beke: Acta Mater. **47**, 1371 (1999)
76. J. Bernardini, P. Gas: Defect Diffus. Forum **143-147**, 1343 (1997)
77. J.C. Ciccarriello, S. Poize, P. Gas: J. Appl. Phys. **67**, 3315 (1990)
78. T. Barge, P. Gas, F.M. d'Heurle: J. Mater. Res. **10**, 1134 (1995)
79. R. Hahnel, W. Miekeley, H. Wever: Phys. Status Solidi (a) **97**, 181 (1986)
80. A.H. King: Intern. Metals Reviews **32**, 173 (1987)
81. Y.M. Mishin, I.M. Razumovskii: Acta Metall. Mater. **40**, 839 (1992)
82. Y. Mishin, M. Köppers, Chr. Herzig: Solid State Phenom. **41**, 79 (1995)
83. F. Güthoff, Y. Mishin, Chr. Herzig: Z. Metallkd. **84**, 584 (1993)
84. M. Köppers, Y. Mishin, Chr. Herzig: Acta Metall. Mater. **42**, 2859 (1994)
85. M. Köppers, Y. Mishin, Chr. Herzig: Scr. Metall. Mater. **32**, 1113 (1995)
86. I.M. Razumovskii, Y. Mishin, Chr. Herzig: Mater. Sci. Eng. A **212**, 45 (1996)
87. Y. Mishin: Phil. Mag. A **72**, 1589 (1995)

9 NMR and β-NMR Studies of Diffusion in Interface-Dominated and Disordered Solids

Paul Heitjans, Andreas Schirmer, and Sylvio Indris

9.1 Introduction

The topic of this chapter concerns diffusion studies via nuclear magnetic relaxation in solids with deviations from three-dimensional (3D) long-range order. These include, on the one hand, well-defined layer-crystalline materials with very large planar internal interfaces and, on the other hand, systems with highly complex internal interfaces as well as 3D amorphous solids where the structural disorder is of interest.

In layer-crystalline materials a strong anisotropy of the atomic or intermolecular coupling prevails. It often leads to the formation of atomic or molecular layers being weakly bonded in the direction perpendicular to the planes. As examples graphite and transition metal dichalcogenides will be considered. Between the layers of these materials, regarded as 'hosts', other atomic or molecular species may be built in as weakly bonded 'guests' which often are quite mobile. The corresponding process is called intercalation, its result is an intercalation compound [1–3]. These are quasi-2D solids with large internal interfaces. On the one hand, they are of technical interest; e. g., intercalation and deintercalation may in the case of an ionic guest be used as a charging and decharging cycle of a secondary battery component. On the other hand, intercalation materials show a large variety of structural and dynamical properties and may thus be used as model systems to study many phenomena in reduced dimensionality. Even with in-plane disorder, intercalation compounds show long-range ordered stacking of the layers with a fixed periodicity which is governed by the host material.

Another class of interface-dominated materials, which however are highly complex, are nanocrystalline materials [4,5]. They consist of crystalline grains of a diameter of typically 10 nm which is about three orders of magnitude below the respective value for normal poly-, i. e. microcrystalline materials. The nanometer-sized grains are surrounded by grain boundary regions with high defect concentration. These regions may form a network and share up to 50 % of the volume of the material. The mass density of the interfacial regions can be reduced to 80 % of the crystalline bulk. Nanocrystalline solids may thus be regarded as materials with inhomogeneously distributed free volume; they exhibit heterogeneous disorder. The density of interfaces is of the order of $10^9\,\mathrm{m}^2/\mathrm{m}^3$, similar to that of the planar interfaces in the intercalation

compounds. The nanocrystalline materials dealt with in this chapter are oxide and non-oxide ceramics. Nanocrystalline metals are briefly addressed in Chap. 8.

A third class of solid state systems considered here are amorphous materials, in particular ion conducting oxide glasses [6–8]. Contrary to nanocrystalline materials, these are homogeneously disordered with no internal interfaces. In this case free volume is homogeneously distributed. In general the density is reduced only by a few percent with respect to the ordered phase.

In order to disentangle the influences of disorder and low-dimensionality on the diffusional properties, the respective 3D ordered modifications should be studied in parallel as reference materials. In fact, besides the quasi-2D layered crystals the respective 3D modification, besides the nanocrystalline the normal coarse-grained material and besides the glass the respective crystal with identical chemical composition were investigated whenever possible.

As explained in Chap. 1, diffusion has aspects of both macroscopic material transport and microscopic jump processes. Correspondingly, macroscopic and microscopic experimental methods may be distinguished [9]. Nuclear magnetic resonance (NMR) techniques measuring spin relaxation, including beta-radiation detected NMR (β-NMR), which are dealt with in this chapter, belong to the latter. Macroscopic and microscopic techniques may further be classified as nuclear [10] and non-nuclear methods, respectively (cf. [9, 11]). Microscopic nuclear methods other than NMR relaxation spectroscopy are quasielastic neutron scattering (Chaps. 3 and 13) and Mößbauer spectroscopy (Chap. 2). They are capable to explore the jump geometry in addition to the jump rates. However, their dynamical ranges are more restricted [9]. An example for a microscopic non-nuclear technique is the measurement of the frequency-dependent ionic conductivity (Chap. 21).

An NMR technique probing macroscopic transport is field gradient NMR, which is treated in Chap. 10. Classical macroscopic nuclear and non-nuclear techniques are, respectively, the radiotracer technique (Chap. 1) and measurements of the d.c. ionic conductivity [12].

In the following we first recall the basic features of the influence of diffusion on NMR longitudinal relaxation (spin-lattice relaxation) and transverse relaxation (spin-spin relaxation), the latter being closely related to the NMR linewidth. We start from the ordinary case of 3D media and point out the deviations expected for two-dimensional and disordered systems (Sect. 9.2). Some principles of NMR techniques for measuring spin relaxation times of stable (Sect. 9.3) and β-radioactive probe nuclei (Sect. 9.4) are then presented. Finally experimental examples obtained by these methods in intercalation compounds (Sect. 9.5), nanocrystalline materials (Sect. 9.6) and glasses (Sect. 9.7) are reviewed.

9.2 Influence of Diffusion on NMR Spin-Lattice Relaxation and Linewidth

Diffusion can be probed by spin-lattice relaxation (SLR) caused by the temporal fluctuations of local fields due to the motion of particles carrying a nuclear spin. The principle can be understood from the simple picture of a probe spin precessing in an external magnetic field $\boldsymbol{B}_0$ with a Larmor precession frequency ω_L given by $\omega_\mathrm{L} = \gamma B_0$, where the magnetogyric ratio γ connects nuclear magnetic moment and angular momentum. The nuclear spin will be reversed, i. e. the transition probability will be maximum, when ω_L is in resonance with the frequency of a transverse alternating field $\boldsymbol{B}_1$. This may be an external radio-frequency field or the internal fluctuating field due to the motion of the atoms. In the following the latter case will be regarded more closely.

The fluctuating field which may be dipolar magnetic from neighbouring nuclei as well as quadrupolar electric from local electric field gradients can be described by the correlation function $G(t)$ which contains the temporal information on the atomic diffusion process [13–15]. The correlation time τ_c characterizing $G(t)$ is within a factor of the order of unity equal to the mean residence time τ between successive atomic jumps. Relevant for SLR is the spectral density function $J(\omega)$ of the fluctuating local field which is the Fourier transform of the correlation function $G(t)$ and extends up to frequencies of the order of τ_c^{-1}. Transitions between the energy levels of the spin system will be induced, i. e. spin-lattice relaxation becomes effective, when $J(\omega)$ has components at the transition frequencies. The spin-lattice relaxation rate T_1^{-1}, being a measure of the transition probability, is roughly given by

$$T_1^{-1} \propto J(\omega_\mathrm{L}) \quad . \tag{9.1}$$

Full expressions describing the relaxation due to dipolar interaction between like and unlike spins are given in (9.27) and (9.31), respectively, in the Appendix (Sect. 9.9)). The basic characteristics of T_1^{-1} in a 3D system with random jump diffusion can be derived from the simple exponential correlation function

$$G(t) = G(0) \cdot \exp(-|t|/\tau_\mathrm{c}) \tag{9.2}$$

assumed by Bloembergen, Purcell and Pound (BPP) [16]. The corresponding Lorentzian shaped spectral density function is given by

$$J(\omega) = G(0) \cdot \frac{2\tau_\mathrm{c}}{1 + (\omega\tau_\mathrm{c})^2} \quad . \tag{9.3}$$

The correlation time τ_c, like the mean residence time τ, will generally depend on temperature T according to the Arrhenius relation

$$\tau_\mathrm{c} = \tau_{\mathrm{c}0} \cdot \exp(E_\mathrm{A}/k_\mathrm{B}T) \quad , \tag{9.4}$$

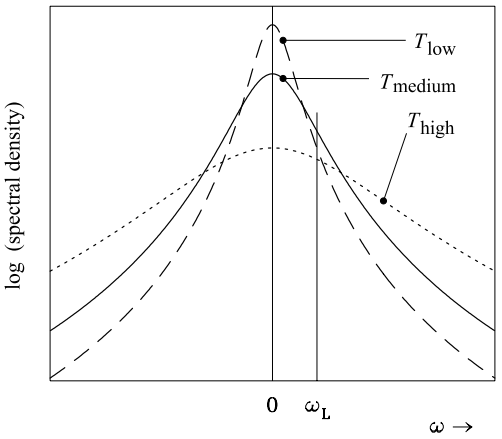

Fig. 9.1. Lorentzian spectral density function for different temperatures T. For a chosen value of the Larmor frequency ω_L the spectral density will be maximum for the medium T value where $\omega_L \tau_c \simeq 1$.

where E_A is the activation energy of the diffusion process. Fig. 9.1 shows $J(\omega)$ as an even function for three different temperatures taking into account that $\int J(\omega) d\omega$ is constant. It illustrates that $T_1^{-1}(T)$, measured at a certain Larmor frequency ω_L, passes through a maximum at a specific temperature which is determined by the condition $\omega_L \tau_c \approx 1$.

Quantitatively, the standard behaviour of T_1^{-1} in a 3D system is shown in Fig. 9.2 for the experimental example of self-diffusion in lithium [17] which was studied by β-NMR (Sect. 9.4). In the usual representation of $\log T_1^{-1}$ vs. $1/T$ the peak for each Larmor frequency (magnetic field) is symmetric. At temperatures above and below the maximum, which correspond to the limiting cases $\omega_L \tau_c \ll 1$ and $\omega_L \tau_c \gg 1$, respectively, the slopes yield the activation energy E_A. The SLR rate shows no ω_L dependence in the high-T limit and follows the power law $T_1^{-1} \propto \omega_L^{-2}$ in the low-T limit.

While Fig. 9.2 apparently reflects the main features of the BPP model predictions, the accuracy of the data enabled a comparison with a more refined model, namely the encounter model of correlated self-diffusion (cf. Chap. 3, Sect. 3.7) which, in fact, is represented by the continuous lines. There it has been taken into account that in the present case of β-NMR the ^{8}Li nuclei interact with unlike nuclei only (cf. (9.31) in the Appendix (Sect. 9.9)). From the fit τ_c values have been extracted over almost seven decades. Li has in fact been used as a test case for further diffusion-related NMR work and seems to be the best studied 3D ordered system concerning relaxation [18–23].

Much more pronounced deviations from the BPP model than in the case of the 3D encounter model are to be expected for low-dimensional and disordered systems being of interest here. The quantities bearing information spe-

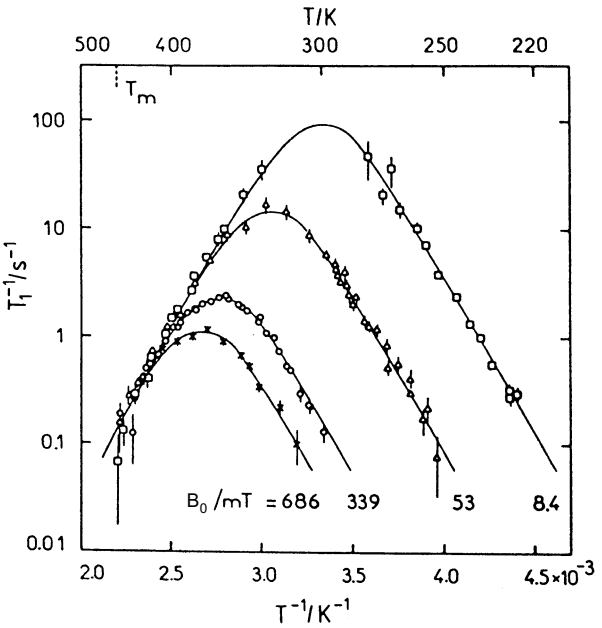

Fig. 9.2. Demonstration of the characteristic temperature and frequency dependence of the diffusion-induced SLR rate in 3D systems exemplified by ^{8}Li in polycrystalline Li. The B_0 values correspond to $\omega_L/2\pi = 4.32$ MHz, 2.14 MHz, 334 kHz and 53 kHz [17].

cific for the jump diffusion mechanism are the slopes of the high-T and low-T flanks of the $\log T_1^{-1}$ vs. $1/T$ plot. In Table 9.1 the corresponding predictions from simple models for low-dimensional diffusion [24, 25] are compared with the standard 3D behaviour. It is noted that dimensionality effects show up only in the high-T region where several jumps occur before one precession of the probe spin is completed ($\tau_c \ll \omega_L^{-1}$). The functional dependences are valid not only in the case of discrete jump vectors pertaining to ordered solids but also in the case of continuous diffusion. In the low-T region, however, the $\tau_c^{-1}\omega_L^{-2}$ dependence (cf. Fig. 9.2), which applies to the 1D through 3D cases, is true only for jump diffusion. In the case of continuum diffusion a $\tau_c^{-1/2}\omega_L^{-3/2}$ dependence is predicted, which is thus weaker in both variables than for jump diffusion.

SLR in disordered systems is not explicitly included in Table 9.1. However, continuum diffusion is discussed as bearing resemblance to diffusion in disordered solids due to varying distances of atomic sites. Indeed, the SLR rate in amorphous and defective crystalline materials has often been found to show an asymmetric $\log T_1^{-1}$ vs. $1/T$ peak with a smaller (absolute) slope on the low-T side and an ω_L dependence characterized by

Table 9.1. Asymptotic behaviour of $T_1^{-1}(\tau_c, \omega_L)$ for diffusion processes with different dimensionalities

	$\omega_L\tau_c \ll 1$ (high T)	$\omega_L\tau_c \gg 1$ (low T)	
		jump diffusion	continuum diffusion
3D	$\propto \tau_c$	$\propto \tau_c^{-1}\omega_L^{-2}$	$\propto \tau_c^{-1/2}\omega_L^{-3/2}$
2D	$\propto \tau_c \ln(1/\omega_L\tau_c)$		
1D	$\propto \tau_c(\omega_L\tau_c)^{-1/2}$		

$$T_1^{-1} \propto \omega_L^{-\alpha} \tag{9.5}$$

with $\alpha \leq 2$.

There are models for SLR in disordered ion conductors such as the assumption of distribution functions of jump correlation times [26], the counterion model [27], the coupling concept [28] and the jump relaxation model [29]. In Chaps. 20 and 21 up-to-date versions of the latter ones are presented mainly with respect to conductivity measurements. These models predict

$$T_1^{-1} \propto \omega_L^{-\alpha} \cdot \exp\left(-\frac{E_{NMR}^{lT}}{k_B T}\right) \tag{9.6}$$

with $1 < \alpha \leq 2$ on the low-T side. The corresponding activation energy E_{NMR}^{lT} should be related to E_{NMR}^{hT}, characterizing the slope on the high-T side, by

$$E_{NMR}^{lT} = (\alpha - 1) \cdot E_{NMR}^{hT} \quad . \tag{9.7}$$

Thus, in the frame of these models, the parameter α links the frequency dependence of T_1^{-1} to the asymmetry of the peak.

Monte Carlo simulation studies of the correlation functions in disordered ionic conductors ([30], see also Chap. 20) agree with these findings and show that the deviations from the BPP behaviour are the consequence of the combined effect of structural disorder and Coulomb interactions of the moving particles. Structural disorder is modelled in these simulations by using a percolation approach.

By means of the parameter α, SLR data may be related to data from other spectroscopic methods investigating, e. g., the dynamic conductivity or incoherent neutron scattering (cf. Chap. 20). Figs. 9.3 and 9.4 summarize the expected behaviour of the diffusion-induced SLR rate as a function of correlation time and frequency, respectively, for diffusion in an (ordered) 2D system and a (3D) disordered system in comparison with the BPP case.

If spin-lattice relaxation is not probed with reference to the static external field $\boldsymbol{B}_0$ but in a resonant alternating field $\boldsymbol{B}_1$ (see Sect. 9.3), the SLR rate in the rotating frame, $T_{1\rho}^{-1}$, is measured. It approximately obeys the relation

$$T_{1\rho}^{-1} \propto J(2\omega_1) \tag{9.8}$$

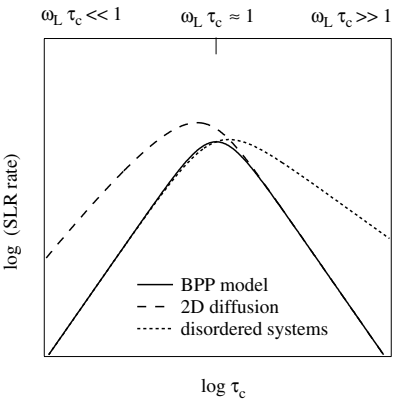

Fig. 9.3. Schematic representation of log (SLR rate) vs. log (correlation time) (corresponding to reciprocal temperature) for diffusion in the BPP case and the expected deviations for 2D systems and disordered systems.

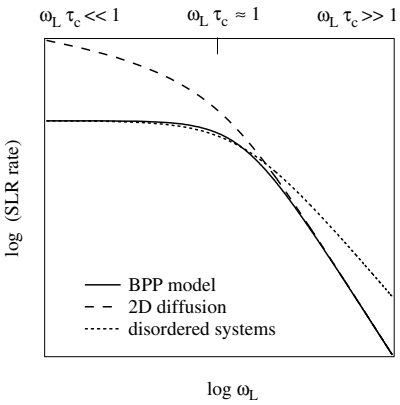

Fig. 9.4. Schematic representation of log (SLR rate) vs. log (Larmor frequency) (or magnetic field) for the BPP case and the expected deviations for 2D systems and disordered systems.

where $\omega_1 = \gamma B_1$. The full expression for the case of 3D diffusion is given in (9.30) in the Appendix (Sect. 9.9). Since $B_1 \ll B_0$, the condition $\omega_1 \tau_c \approx 0.5$ for the maximum of $T_{1\rho}^{-1}(T)$ entails that considerably longer correlation times are probed than by T_1^{-1} measurements.

Besides SLR measurements of T_1^{-1} and $T_{1\rho}^{-1}$ also measurements of the NMR linewidth, which is related to the spin-spin relaxation time T_2, can give information about microscopic parameters of diffusion. In general, nuclear spins in an external magnetic field B_0 experiencing dipolar interaction in a homogeneous solid at low temperatures show one broad static NMR line without substructure. This is because the nuclei under investigation are located at sites with different spin environments resulting in different local magnetic fields superimposed on the external magnetic field B_0. In this way many contributions with different resonance frequencies form a broad NMR line with a width of some kHz. This is the rigid lattice linewidth $\Delta\nu_{\mathrm{R}}$ which corresponds to the spin-spin relaxation rate T_2^{-1} at low temperatures. When the sample is heated the ions start moving through the solid. The temperature dependence of the jump rate τ^{-1} is given by an Arrhenius relation analogous to that of the correlation rate τ_{c}^{-1} (cf. (9.4)).

At higher temperatures the hopping of the ions becomes so fast that they are experiencing the same average local field. This sets in when the correlation rate becomes larger than the width of the rigid lattice line, i. e.

$$\tau_{\mathrm{c}}^{-1} \gtrsim 2\pi \cdot \Delta\nu_{\mathrm{R}} \quad . \tag{9.9}$$

Then all nuclei have the same resonance frequency and a narrowed NMR line is observed. This phenomenon is called motional narrowing. In this temperature regime the spin-spin relaxation rate is approximately given by

$$T_2^{-1} \propto J(0) \propto \tau_c \quad . \tag{9.10}$$

The functional dependence of the linewidth on temperature allows one to determine τ_{c0} and E_A.

The situation when at even higher temperatures the correlation rate exceeds the Larmor frequency,

$$\tau_c^{-1} > \omega_L \quad , \tag{9.11}$$

is called extreme motional narrowing. The full expression for the spin-spin relaxation rate in the motional narrowing and the extreme motional narrowing regime for 3D diffusion is given in (9.28) in the Appendix (Sect. 9.9). Then the spin-spin relaxation rate T_2^{-1} and the spin-lattice relaxation rates T_1^{-1} and $T_{1\rho}^{-1}$ should all have the same value, and the residual NMR linewidth is determined by the inhomogeneity of the magnetic field.

Additional contributions to the lineshape can occur for nuclei with spin $I \geq 1$. These have a quadrupolar moment which interacts with electric field gradients, when present due to low crystal symmetry at the site of the nuclei.

The general features of the relaxation rates T_1^{-1}, $T_{1\rho}^{-1}$ and T_2^{-1} in the standard case of 3D diffusion via random jumps are summarized in Fig. 9.5. The rates are plotted here as a function of $\omega_L \tau_c$ so that it can readily be seen that the T_1^{-1} maximum occurs for $\omega_L \tau_c \approx 1$. As mentioned above, the maximum of $T_{1\rho}^{-1}$ shows up for $\omega_1 \tau_c \approx 0.5$ and the constant value for T_2^{-1} is reached when $2\pi\,\Delta\nu_R \approx 1$. In the plot we used $\omega_L : \omega_1 : 2\pi\,\Delta\nu_R = 10^4 : 20 : 1$.

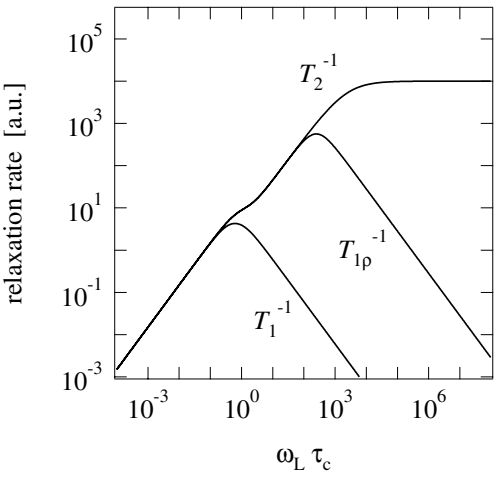

Fig. 9.5. Schematic representation of the relaxation rates T_1^{-1}, $T_{1\rho}^{-1}$ and T_2^{-1} vs. $\omega_L \tau_c$ for 3D diffusion via random jumps.

$\Delta\nu_{\mathrm{R}}$ is typically some tens kHz. The shoulder in the curves of $T_{1\rho}^{-1}$ and T_2^{-1} is due to contributions by the spectral densities at ω_{L} and $2\omega_{\mathrm{L}}$ in addition to those at $2\omega_1$ and $\omega = 0$, respectively (see (9.30) and (9.28)).

Concluding this section, we note that besides the description of diffusion induced NMR relaxation in the perturbation approach by spectral density functions, sketched here in a qualitative way, there are stochastic models. These yield a more general access to spin relaxation being not confined to the motional narrowing regimes (see, e. g., [31, 32] and references therein).

9.3 Basics of NMR Relaxation Techniques

Solid-state NMR, being based on the Boltzmann polarization of stable nuclei, is a very broad field and for a comprehensive treatment the reader is referred to various monographs [13, 14, 33–35]. Furthermore, detailed descriptions of NMR relaxation techniques are available (e. g. [36, 37]), and corresponding pulse programs are nowadays implemented in standard NMR spectrometers. We here confine ourselves to a brief outline of the basic principles of the measurements of longitudinal and transverse, i. e. spin-lattice and spin-spin relaxation times, respectively. A T_1 or T_2 measurement proceeds in two steps in the time domain:
(i) tilting the nuclear magnetization

$$\boldsymbol{M}_0 = N \cdot \frac{\gamma^2 \hbar^2 I(I+1)}{3k_{\mathrm{B}}T} \cdot \boldsymbol{B}_0 \tag{9.12}$$

of an ensemble of nuclei (number density N, spin I) at equilibrium in a static magnetic field $\boldsymbol{B}_0$ at temperature T by a pulsed alternating field.
(ii) detection of the magnetization $\boldsymbol{M}(t)$ as it relaxes back to $\boldsymbol{M}_0$.

The experimental set-up consists of the sample placed in a strong magnetic field $\boldsymbol{B}_0$ (of the order of some Tesla) in the z-direction and a coil wound around the sample for application of a perpendicular alternating field $\boldsymbol{B}_1(t)$ with frequency $\omega/2\pi$ in the radio-frequency (rf) regime. In this arrangement an equilibrium magnetization $\boldsymbol{M}_0$ is built up in the z-direction due to the Boltzmann population of the Zeeman energy levels (Fig. 9.6), which is given by (9.12).

The effect of simple rf-pulse sequences is discussed in the classical picture of a magnetization $\boldsymbol{M}$ moving in an external magnetic field. The equation of motion is [14]

$$\frac{\mathrm{d}\boldsymbol{M}}{\mathrm{d}t} = \boldsymbol{M} \times \gamma \left[\boldsymbol{B}_0 + \boldsymbol{B}_1(t)\right] \quad . \tag{9.13}$$

For discussion of the motion in an alternating magnetic field applied in the x-direction ($\boldsymbol{B}_1(t) = B_{x0}\cos(\omega t)\boldsymbol{e}_x$), time dependences are eliminated by using a coordinate system rotating about the $\boldsymbol{B}_0$ direction with angular velocity ω. Its axes are denoted in the following with x', y' and z', see Fig. 9.7. In such

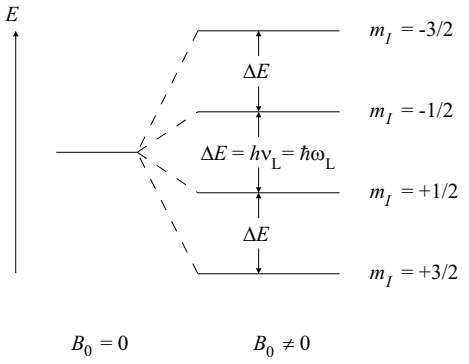

Fig. 9.6. Zeeman splitting of the nuclear energy level due to interaction of the nuclear spins with a static external field $\boldsymbol{B}_0$, here shown exemplarily for spin $I = 3/2$, $\gamma > 0$.

a system the effective magnetic field $\boldsymbol{B}_{\text{eff}}$ is composed of the static field $\boldsymbol{B}_0$, the alternating field $\boldsymbol{B}_1$ and a term $\boldsymbol{\omega}/\gamma$ which results from the transition to an accelerated reference frame (see Fig 9.8 (a)). When the x'-axis is chosen along $\boldsymbol{B}_1$ the equation of motion can be rewritten as

$$\frac{\mathrm{d}\boldsymbol{M}}{\mathrm{d}t} = \boldsymbol{M} \times \gamma \left[\left(B_0 - \frac{\omega}{\gamma} \right) \boldsymbol{e}_{z'} + B_1 \boldsymbol{e}_{x'} \right] = \boldsymbol{M} \times \gamma \boldsymbol{B}_{\text{eff}} \tag{9.14}$$

which means that the magnetization behaves as if it experienced a stationary magnetic field $\boldsymbol{B}_{\text{eff}}$. If the resonance condition $\omega = \omega_{\text{L}} = \gamma B_0$ is fulfilled for the alternating $\boldsymbol{B}_1$ field, the z' component of $\boldsymbol{B}_{\text{eff}}$ vanishes and the effective field is $B_1 \boldsymbol{e}_{x'}$ and $\boldsymbol{M}$ will rotate in the $z'-y'$ plane with a frequency $\omega_1 = \gamma B_1$ (see Fig. 9.8). The application of an alternating $\boldsymbol{B}_1$ with the duration t_{p} will result in a flipping of $\boldsymbol{M}$ to the angle $\theta_{\text{p}} = \gamma B_1 t_{\text{p}}$. In the laboratory reference frame this results in a nutational motion as shown in Fig. 9.9. By proper choice of t_{p}, $\boldsymbol{M}$ can be inverted ($\theta_{\text{p}} = \pi$) or tilted into the $x - y$ plane ($\theta_{\text{p}} = \pi/2$), where it will precess (in the laboratory reference frame) and induce an observable voltage in the coil. This is the free induction decay (FID).

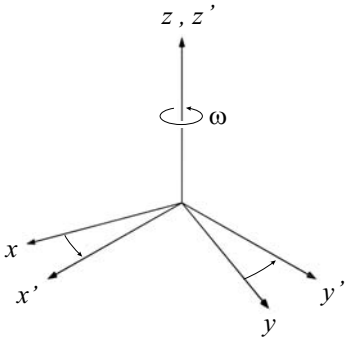

Fig. 9.7. The rotating reference frame rotating about the direction of the external magnetic field (z axis) with angular velocity ω.

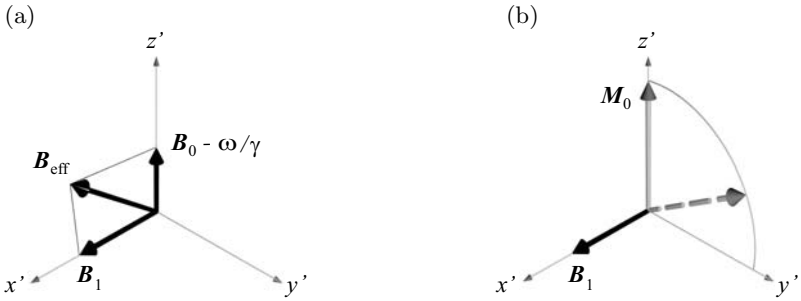

Fig. 9.8. (a) The effective magnetic field in the rotating reference frame. (b) The motion of the magnetization in the rotating reference frame for $\omega = \omega_{\mathrm{L}}$.

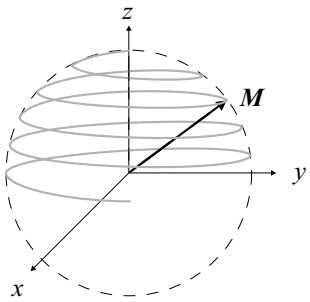

Fig. 9.9. Nutational motion of the magnetization in the laboratory reference frame due to an alternating magnetic field perpendicular to the static external field which is applied along the z axis.

After the π or $\pi/2$ pulse $\boldsymbol{M}$ will relax towards its equilibrium value M_0 along the $+z$-direction in the laboratory reference frame. The instantaneous M_z value may be described by

$$\frac{\mathrm{d}M_z}{\mathrm{d}t} = \frac{M_0 - M_z}{T_1} \tag{9.15}$$

with T_1 being the longitudinal or spin-lattice relaxation time. Equation (9.15) yields

$$M_z(t) = M_0[1 - A_{\mathrm{p}} \exp(-t/T_1)] \tag{9.16}$$

with $A_{\mathrm{p}} = 2$ (1) for an initial π pulse ($\pi/2$ pulse). $M_z(t)$ is monitored by the amplitude of the FID after a $\pi/2$ reading pulse at the evolution time τ_{e} which is varied.

In case that the magnetization $\boldsymbol{M}$ is not aligned parallel to the external magnetic field $\boldsymbol{B}_0$ the magnetization will precess around the magnetic field. Furthermore, the transverse components $M_{x'}$ and $M_{y'}$ will decay due to a dephasing of the nuclear spins which are in phase only directly after the rf pulse. The equilibrium values of $M_{x'}$ and $M_{y'}$ are zero. The magnitudes of $M_{x'}$ and $M_{y'}$ obey the equations

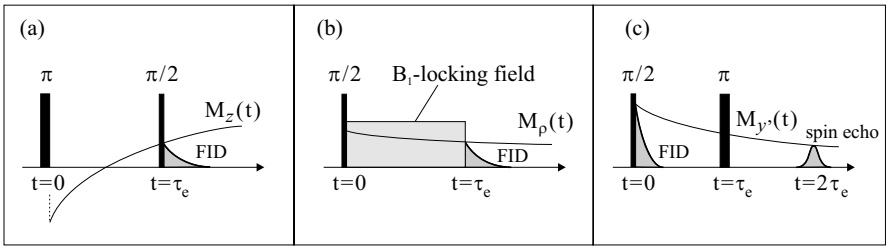

Fig. 9.10. (a) Principle of a T_1 measurement with the inversion-recovery pulse sequence $(\pi - \tau_e - \pi/2)$: After inversion and evolution time τ_e the magnetization $M(\tau_e)$ is probed with the $\pi/2$ pulse. (b) Principle of a $T_{1\rho}$ measurement: After a $\pi/2$ pulse $M_\rho(t)$ is locked by a $\pi/2$ phase shifted B_1-locking field and decays according to $M_\rho(t) = M_\rho(0)\exp(-t/T_{1\rho})$ which is probed at $t = \tau_e$ after switching off the locking field. (c) Principle of a T_2 measurement with a spin echo pulse sequence $(\pi/2 - \tau_e - \pi)$: After a $\pi/2$ pulse has turned the magnetization to the plane perpendicular to the external magnetic field it starts precessing around this field and its transverse component decays due to dephasing of the nuclear spins according to $M_{y'}(t) = M_0\exp(-t/T_2)$. The π pulse at time τ_e causes a refocussing of the spins at time $2\tau_e$ resulting in a spin echo signal. Its amplitude can be used to probe the magnetization $M_{y'}(2\tau_e)$.

$$\frac{\mathrm{d}M_{x'}}{\mathrm{d}t} = -\frac{M_{x'}}{T_2}$$
$$\frac{\mathrm{d}M_{y'}}{\mathrm{d}t} = -\frac{M_{y'}}{T_2} \tag{9.17}$$

with T_2 being the transverse or spin-spin relaxation time. After an initial $\pi/2$ pulse has turned the magnetization to the y direction, (9.17) yields

$$M_{y'}(t) = M_0\exp(-t/T_2) \quad . \tag{9.18}$$

In NMR spectrometers the coil around the sample is used for both steps of the experiment, irradiation of the rf pulse and detection of the signal response, i. e. the voltage induced by the precessing magnetization. Modern NMR spectrometers further supply rf pulses which are coherent with the possibility to control and switch the phase of different pulses. A widely used pulse sequence for measurements of the longitudinal relaxation time is illustrated in Fig. 9.10 (a). It should be noted that for T_1 measurements longer and more complex pulse sequences may be tailored to overcome limitations of the simple sequences. The latter suffer, e. g., from the dead time of the detection system after the strong rf pulse; in this case echo sequences may be used to shift the FID away from the rf pulse.

As an example of how phase and power switching with modern NMR spectrometers are used to extend the effective magnetic field range for spin-lattice relaxation measurements, the pulse sequence for spin locking and longitudinal relaxation in the rotating frame is shown in Fig. 9.10 (b). With a $\pi/2$

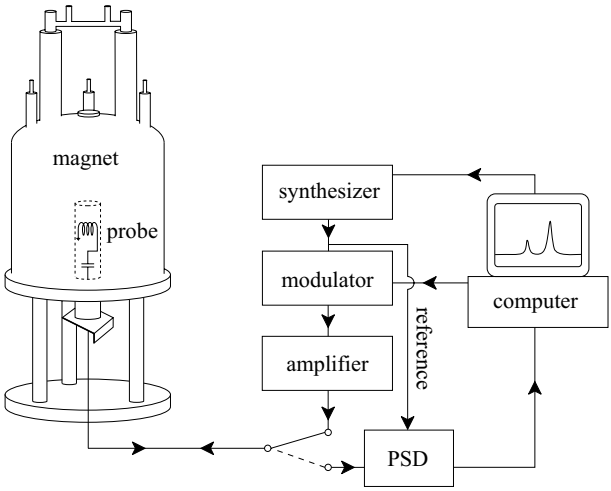

Fig. 9.11. Typical setup of an NMR spectrometer.

pulse the magnetization M_z is turned into the $x-y$ plane and locked parallel to $\boldsymbol{B}_1$ in a frame rotating about $\boldsymbol{B}_0$ with $\omega_\mathrm{L} = \gamma B_0$. During application of the $\boldsymbol{B}_1$ locking field the magnetization M_ρ in the rotating frame relaxes and $M_\rho(\tau_\mathrm{e})$ can be measured by monitoring the FID at the end of the pulse. Thus the relaxation time $T_{1\rho}$ is obtained. It reflects the spin relaxation in the locking field being typically some 10^{-4} T. Variation of the locking field amplitude gives access to studies of the field dependence of $T_{1\rho}$. Corresponding to the change in frequencies from the MHz to the kHz regime when SLR times in the rotating instead of the laboratory frame are measured, considerably longer motional correlation times can be studied. We note, that a technique to measure SLR times also in the laboratory frame at frequencies down to the kHz regime is field-cycling relaxometry [38], which, however, will not be discussed here.

Fig. 9.10 (c) shows a spin echo pulse sequence which can be used to probe the decay of the transverse magnetization component $M_{y'}$ and thus to measure the transverse relaxation time T_2. A $\pi/2$ pulse turns the magnetization to the plane perpendicular to the external magnetic field where it starts precessing around this field. Its transverse component which is built by the sum of the nuclear spins starts to decay because of a dephasing of the spins. The π pulse at time τ_e causes a refocussing of the spin system resulting in a so-called spin echo signal at time $2\tau_\mathrm{e}$. Its height is proportional to the magnetization $M_{y'}(2\tau_\mathrm{e})$ which is measured for different evolution times τ_e between the two pulses. According to (9.18) measurements with different delay times τ_e allow one to probe the decay of the transverse components and thus to determine T_2.

It is obvious from the discussion above that the basis of modern NMR techniques is data acquisition after pulsed excitation and subsequent Fourier transformation. The main components of a Fourier-NMR spectrometer are shown in Fig. 9.11. The sample is located in the coil of a rf resonant circuit which is part of the probe. This is located in the center of a superconductive magnet. The nuclei in the sample are excited by rf pulses which are generated, starting from a highly precise synthesizer, with a rf modulator and a high-power amplifier. The response signal of the sample nuclei, being weaker by many orders of magnitude, is directed via a rf switch to a phase sensitive detector (PSD), whose reference signal is provided by the synthesizer. The whole procedure which may include not only single pulses but complex pulse sequences, as described above, is controlled by a computer.

9.4 Method of β-Radiation Detected NMR Relaxation

Technical improvements have made NMR relaxation techniques described in Sect. 9.3 a tool of steadily increasing versatility. On the one hand, higher magnetic fields have improved the signal-to-noise ratio by increasing the Boltzmann factor. On the other hand, by using more sensitive amplifiers and digitized signal recorders weaker signals can be measured and less sample material or smaller samples under extreme conditions (e. g. high-pressure cells) can be used. An alternative approach is to replace the steps of the NMR relaxation experiments by unconventional ones which avoid certain limitations. In this section concepts of such a method, known as β-radiation detected NMR (β-NMR [39]) relaxation, will be introduced and discussed.

The principle of β-NMR relaxation is the use of the β-decay radiation asymmetry of polarized, short-lived β-emitters embedded in the solid in order to monitor the nuclear polarization and its decrease due to longitudinal, i. e. spin-lattice relaxation [11]. The two steps of the classical NMR relaxation experiment (Sect. 9.3) are replaced by (i) on-line production of the short-lived polarized probe nuclei with lifetimes τ_β ranging from some 10 ms to some 100 s, and (ii) in-situ measurement of the β-asymmetry during a subsequent time interval of a few lifetimes. The signal amplitude resulting from step (i) is determined by the angular distribution of the emission probability $W(\theta)$ of β-particles from an ensemble of polarized β-active nuclei into a solid angle element at angle θ between polarization and emission direction

$$W(\theta) = 1 + f \cdot \frac{v}{c} \cdot A \cdot \cos\theta \quad . \tag{9.19}$$

f is the dipolar polarization characterized by a linearly varying population of the nuclear Zeeman levels, v is the electron velocity, c the velocity of light and A is a constant for the specific β-decay. The β-decay radiation asymmetry a_β is given by the 0°-180°-difference of $W(\theta)$ and is a direct measure of

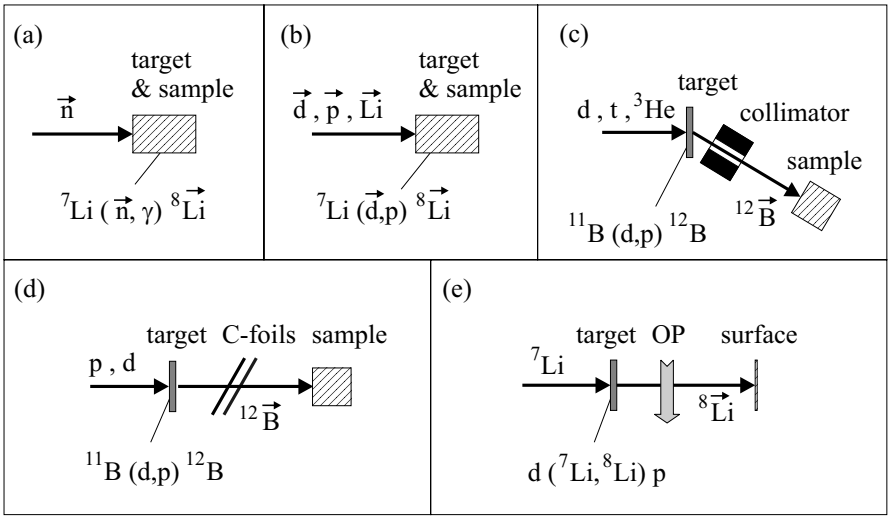

Fig. 9.12. Different techniques to produce polarized β-active nuclei in condensed matter: (a) capture of polarized neutrons, (b) nuclear reaction with polarized accelerated particles, (c) particle reaction with selected recoil angle, (d) nuclear reaction with beam-foil polarization, (e) particle reaction and polarization by optical pumping (OP). In each case an exemplary nuclear reaction is given.

$P = f\frac{v}{c}A$, the experimentally accessible polarization. It reflects the dipolar polarization f and any changes of it.

Variants of the β-NMR method can be classified according to the way the short-lived β-emitters embedded in the sample are generated and polarized, which may be done in one or two steps. The polarized β-emitters can be produced on-line in nuclear reactions with polarized reactor neutrons or with accelerator ions [39, 40]. Schemes of various production routes are shown in Fig. 9.12. The generation and polarization by capture of polarized thermal or cold neutrons (Fig. 9.12 (a)) will be dealt with in some detail below. With accelerators different techniques may be applied (Fig. 9.12 (b)-(e)). First, polarized incident particles may be used again (Fig. 9.12 (b)). In this case one can profit from a sufficiently high polarization transfer to the short-lived β-emitters in reactions of the type ^{7}Li($\vec{d}$,p)$^{8}\vec{Li}$ or ^{16}O($\vec{d}$,n)$^{17}\vec{F}$ [39]. The accelerator ions have typically to have energies above 1 MeV. The β-emitters, which can be β^{+} as well as β^{-}-emitters, have kinetic recoil energies in the range of several keV and are stopped in the sample.

With unpolarized accelerator ions (Fig. 9.12 (c)-(e)) the short-lived β-emitters emerging as recoil nuclei from the target foil have to be polarized prior to implantation into the sample. This can be achieved either by a proper selection of the recoil angle, into which the β-emitters escape from the reaction (Fig. 9.12 (c)), or by polarizing the short-lived β-emitters after the reac-

tion (Figs. 9.12 (d) and (e)). In the former case, the recoil angle selection of the short-lived β-emitters corresponds to an angular momentum selection with a polarization perpendicular to the reaction plane which is given by the trajectories of the accelerator ion and the recoil nuclei [39,41]. Another technique to obtain polarized β-emitters with unpolarized accelerator ions hitting the target is the use of hyperfine effects by passage of the β-emitters through carbon foils which are tilted with respect to the beam direction [42,43] (Fig. 9.12 (d)). A more established technique to polarize the recoil nuclei is optical pumping which in combination with mass-separator extraction offers access to a large variety of probe nuclei [44, 45] (Fig. 9.12 (e)).

In all these nuclear techniques the polarization P, which in the classical NMR experiments is determined by a Boltzmann factor and which gives rise to a macroscopic magnetization M_0 (cf. (9.12)), is larger by many orders of magnitude than a usual Boltzmann polarization and reaches some per cent.

Among the various β-NMR techniques sketched above, diffusion studies have essentially been performed with β-NMR after capture of polarized neutrons (Fig. 9.12 (a)) and after a particle reaction with selected recoil angle (Fig. 9.12 (c)). In the latter case the investigations were confined to bulk metals and semiconductors [46–50] which is beyond the scope of this chapter. Only very few diffusion studies were done using the optical pumping technique (Fig. 9.12 (e)), e. g. ^{8}Li surface diffusion on Ru(001) [51] and on Si(111) [52].

In the following the β-NMR technique after capture of polarized neutrons will be further outlined [53]. The sample abundantly containing the nuclei for the production reaction is placed in the field $\boldsymbol{B}_0$ of an electromagnet and irradiated with polarized cold neutrons. For example, in the case of the probe nucleus ^{8}Li the reaction is

$$\overrightarrow{\mathrm{n}} + {}^7\mathrm{Li} \longrightarrow {}^8\overrightarrow{\mathrm{Li}}^{*} \xrightarrow{\gamma's} {}^8\overrightarrow{\mathrm{Li}} \xrightarrow{\beta^-} 2\alpha\,.$$

Established probe nuclei available with the neutron capture technique are: ^{8}Li (τ_β = 1.2 s), ^{12}B (29 ms), ^{20}F (16 s), ^{23}Ne (57 s), ^{28}Al (3.2 min), ^{108}Ag (3.5 min), ^{110}Ag (35 s), ^{116}In (20 s).

Special features of the β-NMR method with respect to relaxation measurements are as follows. As outlined above, the polarization P is high and independent of a Boltzmann factor. Thus low values of the magnetic field (which provides the quantization axis) and high temperatures are accessible. The magnetic field has to be stronger than parasitic internal and external fields. The concentration of the probe nuclei is extremely small (typically 1 in 10^{18} other nuclei) and as a consequence spin diffusion, i. e. the polarization transfer by resonant mutual spin flips of like nuclei, is suppressed due to their large distance. Thus SLR by distant paramagnetic impurities, generally effective via spin diffusion in classical NMR relaxation measurements, does not contribute to β-NMR relaxation. The highly diluted probe nuclei

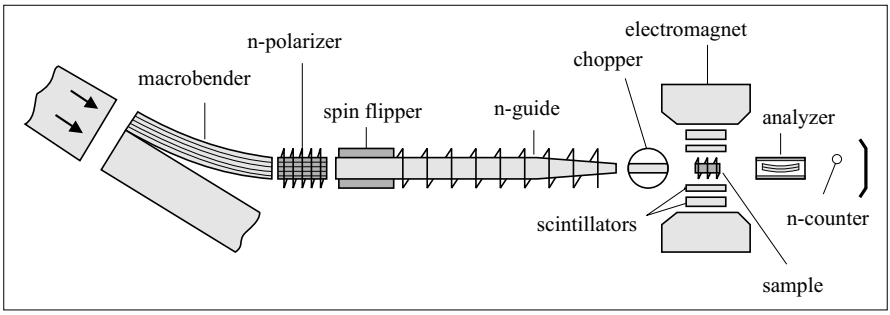

Fig. 9.13. Experimental set-up of the β-NMR spectrometer at the reactor FRJ-2 of the Forschungszentrum Jülich.

relax individually and the β-asymmetry signal stems from an inhomogeneous polarization average of the probe nuclei.

A technical advantage of β-radiation detected SLR is that no rf irradiation is required. The field B_0, correspondingly the Larmor frequency of the measurement, is easily variable and skin effect problems do not arise. Bulk metallic samples and/or metallic sample containers can be used. The latter is often desirable when corrosive materials are to be studied. The measurement of SLR times T_1 is restricted to a time window of at most $0.01\tau_\beta < T_1 < 100\tau_\beta$.

Fig. 9.13 shows the scheme of the β-NMR spectrometer at the research reactor of the Forschungszentrum Jülich [53]. The set-up consists of a neutron beam section with macrobender, neutron-polarizer and spin-flipper for branching-off, polarizing and polarization switching of cold neutrons with a broad wavelength distribution. The polarization switching is used in order to cancel instrumental asymmetries of the NMR apparatus. Its main components are chopper, collimator, sample in oven or cryostat, β-scintillator telescope detectors and electromagnet. The chopper is used for the separation of the production and the relaxation measurement periods of the short-lived nuclei. The β-scintillator telescopes are mounted on the pole faces 'North' and 'South' and register the counting rates Z_N and Z_S at $\theta = 0°$ and 180°, respectively, which yield the experimental β-asymmetry

$$a_\beta = \frac{Z_\mathrm{N} - Z_\mathrm{S}}{Z_\mathrm{N} + Z_\mathrm{S}} \quad . \tag{9.20}$$

As pointed out above, a_β is proportional to the nuclear polarization P. β-NMR relaxation measurements are performed by monitoring transients $a_\beta(t)$ after neutron activation pulses produced by the chopper. In simple cases monoexponential transients

$$a_\beta(t) = a_{\beta 0} \cdot \exp(-t/T_1) \tag{9.21}$$

with the SLR time T_1 are observed.

The NMR apparatus is further equipped with an rf source and a coil around the sample for recording resonance signals. In this mode the β-asymmetry is monitored under quasi-continuous neutron-activation conditions while an rf field, scanning a frequency range in the vicinity of the Larmor frequency, is irradiated on the sample. Neutron flux and polarization can be controlled with a counter and an analyser.

9.5 Intercalation Compounds

In the introduction to this chapter (Sect. 9.1) the role of a prototype 2D material for understanding both, diffusion mechanisms and material modifications, has been mentioned. Due to its simple structure and amphoteric character, graphite as host material for intercalation has attracted much interest for structural [2] and dynamic [3] studies. Graphite can be intercalated with electron donors like alkali metals or with electron acceptors like Br or more complex molecules (as for example HNO_3, AsF_5). Other prototype host materials with 2D internal interfaces are transition metal dichalcogenides [54]. Similar to the case of graphite, Li-intercalated TiS_2 as a model system for translational diffusion was investigated.

9.5.1 Lithium Graphite Intercalation Compounds

Lithium can easily be intercalated into graphite to form the stage-1 compound LiC_6, i. e. to attain a stacking of alternating C and Li layers. The number of subsequent host layers of an intercalation compound, here the graphite sheets, denotes the stage of the compound. The Li layers in LiC_6 form a commensurate $(\sqrt{3} \times \sqrt{3})\ R30°$ superstructure as shown in Fig. 9.14. The stage-2 compound LiC_{12} has the same structure of the Li planes, which are separated by two C layers.

SLR of ^{8}Li in both stages was investigated with the β-NMR method. The samples were made from highly oriented pyrolytic graphite (HOPG). The

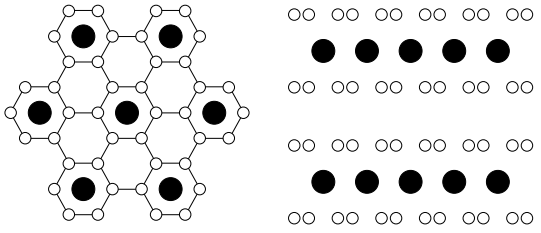

Fig. 9.14. Structure of Li graphite intercalation compounds. Left: View upon the in-plane structure of LiC_6 and LiC_{12}. Li atoms (full circles) are located above the hexagons of C atoms (open circles). Right: View upon a plane containing the $\boldsymbol{c}$ axis of LiC_{12}

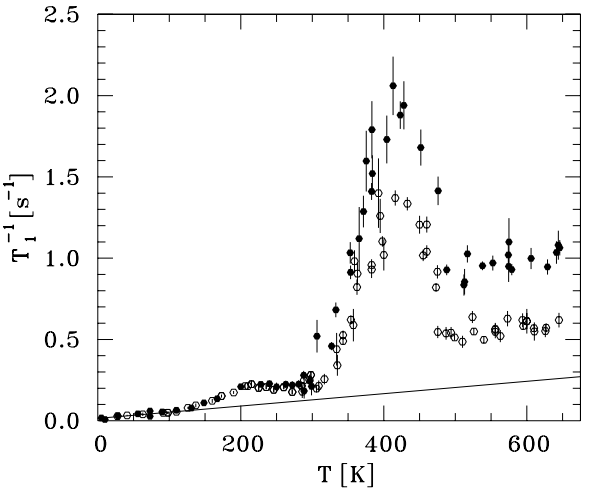

Fig. 9.15. T dependence of the SLR rate of ^{8}Li in the stage-2 graphite intercalation compound LiC_{12} for $B_0 = 37\,\mathrm{mT}$ and two orientations of $\boldsymbol{B}_0$ with respect to the $\boldsymbol{c}$ axis ($\boldsymbol{B}_0 \parallel \boldsymbol{c}$: open dots, $\boldsymbol{B}_0 \perp \boldsymbol{c}$: full dots). The straight line represents the SLR rate contribution due to coupling to conduction electrons [59].

graphite sheets in HOPG are stacked in a single-crystalline manner in the $\boldsymbol{c}$ direction. In the crystallographic $(\boldsymbol{a}, \boldsymbol{b})$ plane the C layers are oriented at random.

Fig. 9.15 gives an overview of T_1^{-1} measured as a function of T at a constant value of B_0 for the orientations $\boldsymbol{B}_0 \parallel \boldsymbol{c}$ and $\boldsymbol{B}_0 \perp \boldsymbol{c}$. As another important parameter, the value of B_0 was varied between 10 mT and 400 mT. This corresponds to an $\omega_\mathrm{L}/2\pi$ range from 0.06 MHz to 2.5 MHz which is hardly accessible with conventional NMR techniques. The temperature dependence of T_1^{-1} shows different regions. Here we only touch upon the temperature region below 100 K and concentrate on the range between 300 K and 500 K, where a pronounced T_1^{-1} peak shows up.

For $T < 100\,\mathrm{K}$, T_1^{-1} increases linearly with T and does neither depend on orientation nor on magnitude of $\boldsymbol{B}_0$. This is a feature of SLR due to coupling to conduction electrons. A detailed representation of the data and a discussion of the implications on the electronic properties of LiC_{12} is given in [55]. This SLR mechanism persists also at higher temperatures and contributes as a background to the experimental T_1^{-1} values.

Between 300 K and 500 K, SLR is dominated by long-range Li motion [56] and the rate $T_{1\mathrm{d}}^{-1}$, obtained by subtracting the contribution due to conduction electrons from T_1^{-1}, exhibits a temperature dependence qualitatively similar to that depicted in Fig. 9.2. However, B_0 dependences of $T_{1\mathrm{d}}^{-1}$ were found on the low-T and high-T flanks of the diffusion-induced peak which can be characterized by

$$T_{1\mathrm{d}}^{-1} \propto B_0^{-\alpha} \text{ with } \begin{cases} \alpha \simeq 1.2 & \text{for low } T \ (\omega_\mathrm{L}\tau_\mathrm{c} \gg 1) \\ \alpha \simeq 0.4 \ldots 0.7 & \text{for high } T \ (\omega_\mathrm{L}\tau_\mathrm{c} \ll 1) \ . \end{cases}$$

On the low-T side, the value for α is smaller than expected for jump diffusion in ordered systems ($\alpha = 2$; cf. Table 9.1). It is close to that for continuum diffusion ($\alpha = 1.5$) and compatible with B_0 dependences observed in disordered systems with highly correlated ionic motion. On the high-T side, the observation of a B_0 dependence ($\alpha \neq 0$) indicates that SLR is governed by a low-D diffusion process. For a direct comparison with the asymptotic laws for 1D and 2D diffusion given in Table 1, however, one has to take into account that above 500 K T_1^{-1} does not reduce to the conduction electron contribution. This implies an additional contribution to T_1^{-1} which is weakly T dependent (partly reflected by the above spread of α values). After correction for this contribution the SLR data are compatible with a logarithmic B_0 dependence as predicted for 2D diffusion.

From the slope of the $\log T_{1\mathrm{d}}^{-1}$ vs. $1/T$ on the low-T side of the peak an activation energy of about 1 eV was estimated [56].

Analogous measurements on the stage-1 compound LiC_6 [57], where similar conclusions from the B_0 dependence of the SLR rate were drawn, yielded an activation energy of about 0.6 eV. Thus an additional C sheet between the Li layers seems to slow down the Li diffusion. This trend was also found in a lattice simulation calculation [58].

It is noted that the dependence of the SLR rate on orientation of the layer stacking $\boldsymbol{c}$ axis with respect to $\boldsymbol{B}_0$, not further discussed here, gives information on the type of interaction dominating SLR [57]. For a comparison of the β-NMR results with those from quasielastic neutron scattering on the same samples we refer to [59] and to Chap. 3, Sect. 3.11.

9.5.2 Lithium Titanium Disulfide – Hexagonal Versus Cubic

In the previous subsection diffusion-induced SLR in quasi-2D Li graphite intercalation compounds of different compositions (stages) with identical in-plane structures were studied. We now compare a layered (2D) Li dichalcogenide with a cubic 3D one having the same chemical composition.

The host material TiS_2, in its hexagonal modification (h-TiS_2), consists of two hexagonal closed packed S layers between which the Ti atoms occupy octahedral sites. h-TiS_2 may be regarded as a layer structure of these interconnected octahedra as illustrated in the top part of Fig. 9.16. In the van der Waals gap between the TiS_2 layers (ABA sequence) Li may easily be intercalated at any concentration x to form a stage-1 compound h-Li_xTiS_2 ($0 < x \leq 1$). The intercalated Li atoms are at rest at octahedral sites [54]. The cubic polymorph c-TiS_2 can be obtained [60,61] from h-TiS_2 by moving one quarter of the Ti atoms to the van der Waals gap as indicated in the lower part of Fig. 9.16. The ABA stacking is then shifted to a stacking of the type ABCA. Li insertion is possible again in the whole concentration range

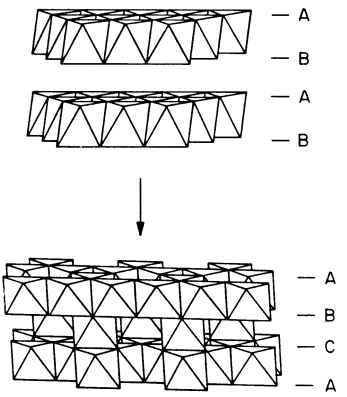

Fig. 9.16. Structure of h-TiS_2 (top), the 2D modification, and of c-TiS_2 (bottom), the cubic modification of the host material. The latter may be derived from h-TiS_2 by shifting the layers from hexagonal closed packed to cubic closed packed anion packing and moving one quarter of the Ti to interlayer octahedra [60].

yielding c-Li_xTiS_2 ($0 < x \leq 1$) and leads to the occupation of the empty octahedra. It is noted that c-TiS_2 irreversibly transforms to h-TiS_2 above 700 K.

SLR was investigated by ^{7}Li-NMR on polycrystalline samples of both modifications at Li concentrations between $x = 0.35$ and $x = 1$ [62]. By use of a Bruker MSL100 spectrometer and a tunable (0 – 7 T) cryomagnet spin-lattice relaxation times both in the laboratory frame (T_1) and in the rotating frame ($T_{1\rho}$) were measured at various fields B_0 and B_1, respectively, (cf. Sect. 9.3). The temperatures of the hexagonal and the cubic samples were varied up to 950 K and 700 K, respectively.

Figs. 9.17 and 9.18 show examples of the T dependence of T_1^{-1} at two frequencies for different Li concentrations. In both modifications diffusion-induced T_1^{-1} peaks are observed.

On the high-T side, T_1^{-1} does not depend on frequency in the case of the cubic modification, which verifies that diffusion is 3D (cf. Sect. 9.2). For the hexagonal polymorph a distinct frequency dependence is found which indicates low-D diffusion. Figure 9.19 explicitly shows data for T_1^{-1} as a function of B_0 at constant T on the high-T side following the logarithmic frequency dependence expected for 2D diffusion. The characteristics showing up in the frequency and temperature dependence of T_1^{-1} are clearly reflected also by the $T_{1\rho}^{-1}$ result, i. e. at lower frequencies and correspondingly lower temperatures. As an example, Fig. 9.20 shows the B_1 dependence of $T_{1\rho}^{-1}$ at a temperature on the high-T side of the $T_{1\rho}^{-1}$ peak. Again a logarithmic frequency dependence is verified over nearly two orders of magnitude. Taken together, the T_1^{-1} and $T_{1\rho}^{-1}$ results on the frequency dependence at high T confirm the logarithmic law in different frequency regimes, which span a total range of five orders of magnitude, and unambiguously show that diffusion is 2D in h-Li_xTiS_2 and 3D in c-Li_xTiS_2.

On the low-T side, T_1^{-1} shows a frequency dependence for both modifications which can be described by a power law according to (9.5), with the

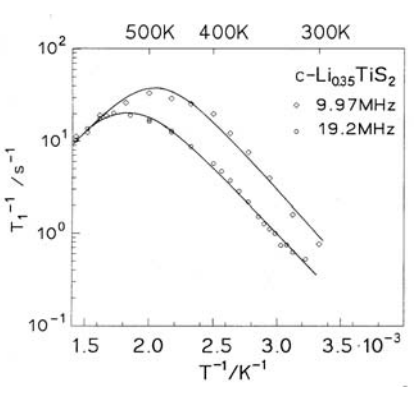

Fig. 9.17. T dependence of the diffusion-induced SLR rate T_1^{-1} in the laboratory frame of ^{7}Li in c-$Li_{0.35}TiS_2$ for two frequencies $\omega_L/2\pi$. The lines are to guide the eye [62].

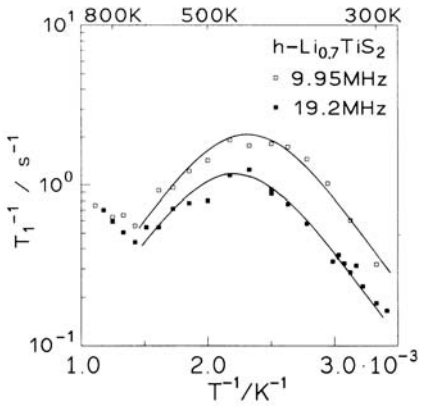

Fig. 9.18. T dependence of the diffusion-induced SLR rate T_1^{-1} in the laboratory frame of ^{7}Li in h-$Li_{0.7}TiS_2$ at two frequencies $\omega_L/2\pi$. The lines are to guide the eye and represent symmetrical curves with respect to the rate maximum [62].

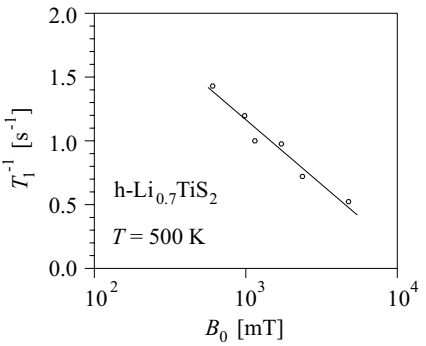

Fig. 9.19. B_0 dependence of the SLR rate in the laboratory frame of ^{7}Li in h-$Li_{0.7}TiS_2$ on the high-T side of the diffusion-induced peak. The solid line represents a logarithmic frequency dependence according to a 2D diffusional process.

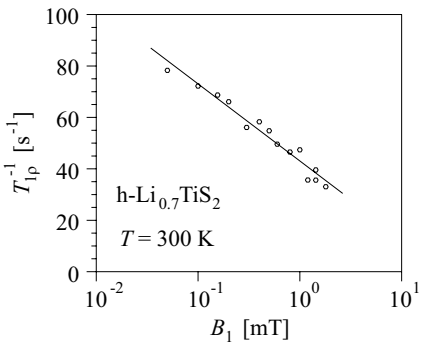

Fig. 9.20. B_1 dependence of the SLR rate in the rotating frame of ^{7}Li in h-$Li_{0.7}TiS_2$ on the high-T side of the diffusion-induced peak. The solid line represents a logarithmic frequency dependence according to a 2D diffusional process [62].

exponent $\alpha \approx 1.3$ both for h-$Li_{0.7}TiS_2$ and c-$Li_{0.6}TiS_2$. This value is significantly smaller than $\alpha = 2$, expected regardless of dimensionality. Similar to the case of the Li graphite intercalation compounds this is in accordance with various theoretical approaches [28–30] where the weak frequency dependence is ascribed to highly correlated diffusion. According to (9.7) and the

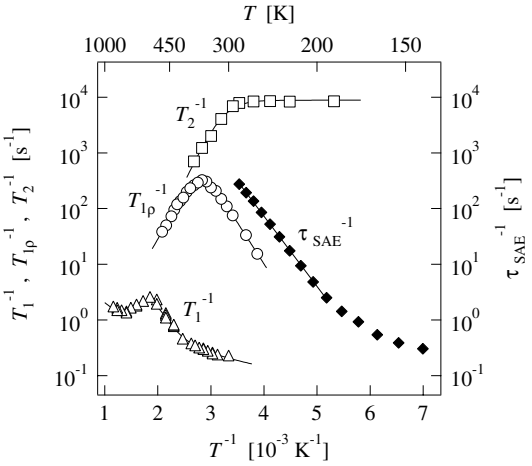

Fig. 9.21. Temperature dependence of the relaxation rates T_1^{-1}, $T_{1\rho}^{-1}$, T_2^{-1} (left-hand ordinate) and of the correlation rate τ_{SAE}^{-1} (right-hand ordinate) obtained from spin-alignment echo (SAE) measurements, for ^{7}Li in h-$Li_{1.0}TiS_2$. T_1^{-1} and $T_{1\rho}^{-1}$ were measured at 10 MHz and 20 kHz, respectively. For the spin-lattice relaxation rate T_1^{-1} a background is visible on which the diffusion-induced peak is superimposed (after [66]).

schematic representation in Fig. 9.3 an exponent $\alpha < 2$ also leads to a smaller (absolute) slope of $\log T_1^{-1}$ vs. $1/T$ on the low-T side. On the other hand, for 2D diffusion the slope of the high-T side will be reduced as compared to the BPP case (cf. Fig. 9.3). If the effects of correlated and 2D diffusion come together, experimentally a pseudo-symmetric peak may be found which, indeed, is the case for h-$Li_{0.7}TiS_2$ (Fig. 9.18, for the corresponding $T_{1\rho}^{-1}$ data see Fig. 3 in [62]). Apparent activation energies $E_{\mathrm{NMR}}^{\mathrm{lT}}$ obtained from the slope of the low-T side are around 0.3 eV for the various samples. This agrees with an early result for h-Li_xTiS_2 obtained by $T_{1\rho}^{-1}$ measurements [63]. From the condition for $T_1^{-1}(T)$ and $T_{1\rho}^{-1}(T)$ maxima ($\omega_{\mathrm{L}}\tau_{\mathrm{c}} \approx 1$ and $\omega_1\tau_{\mathrm{c}} \approx 0.5$, respectively; see Sect. 9.2) and the temperature values where they occur for the various measuring frequencies the important conclusion was drawn that at comparable Li content in the two modifications the jump rate in the interfacial planes of h-Li_xTiS_2 is higher than in the 3D pathways of the cubic polymorph [62].

The large range of frequencies and correlation (or jump) rates probed by T_1^{-1} and $T_{1\rho}^{-1}$ studies[1] can be further extended by T_2^{-1} measurements. An example is shown in a joint representation for h-$Li_{1.0}TiS_2$ in Fig. 9.21 [66].

[1] The gap between the frequency and correlation rate regimes covered by T_1^{-1} and $T_{1\rho}^{-1}$ studies is bridged in certain cases by β-NMR T_1^{-1} measurements [17] as well as by field cycling NMR relaxometry [38].

Though it reflects the main features shown in Fig. 9.5 it has to be kept in mind that in the case of 2D diffusion present here there are deviations from the 3D case. Additionally the figure shows on the right-hand ordinate correlation rates determined by the spin-alignment echo (SAE) technique which is sensitive to ultraslow motions with correlation rates of the order of $1\,s^{-1}$ [64–66]. These correlation rates can be attributed to local jumps between inequivalent sites being characterized by different electric field gradients. These may be identified with two sites in the van der Waals gap, namely the octahedral one, normally occupied by Li, and the tetrahedral one [66]. According to quantum chemical calculations the field gradient at the tetrahedral site differs from that at the octahedral site by a factor of three [67]. Altogether, correlation rates have been covered over nine decades which, as far as NMR studies of Li ion conductors are concerned, seems to have been exceeded up to now only in a β-NMR investigation of Li_3N [11, 68].

Concluding this section, we recall the importance of frequency variation in NMR relaxation measurements to disentangle effects of dimensionality and correlation.

9.6 Nanocrystalline Materials

Another class of interface-dominated systems is represented by nanocrystalline materials [4, 5, 9]. They have been the topic of broad research activity aiming both at a better understanding of the fundamental aspects and at new applications. In contrast to intercalation compounds where an ordered stacking sequence of host and guest layers prevails, nanocrystalline materials consist of an assembly of randomly oriented nanometer-sized crystal grains and of interfacial regions. From an atomistic point of view two types of sites occur, those in the nearly perfect crystallites and those in the highly defective grain boundary regions characterized by a distribution of interatomic distances. This is illustrated in a very simplified way in the left part of Fig. 9.22 where the full and open circles denote chemically identical atomic species. An alternative approach is to regard nanocrystalline materials as consisting of a crystalline phase and an interfacial phase with pores as depicted in the middle part of Fig. 9.22. There is presently no generally accepted model representing all aspects of nanocrystalline materials. A high-resolution transmission electron micrograph of nanocrystalline CaF_2 with an average crystallite size of 9 nm [9, 69] is shown in the right part of Fig. 9.22.

From the broad range of preparation techniques [4] here only two will be regarded. Nanocrystalline materials can be built up from their atomic or molecular constituents or, starting from the other extreme, they are obtained by milling the polycrystalline educt. An example of the former is the inert gas condensation technique. The material is evaporated in an inert gas atmosphere where it thermalizes and precipitates on a cold finger. Then it is gathered and compacted under high pressure (up to 5 GPa). An example of

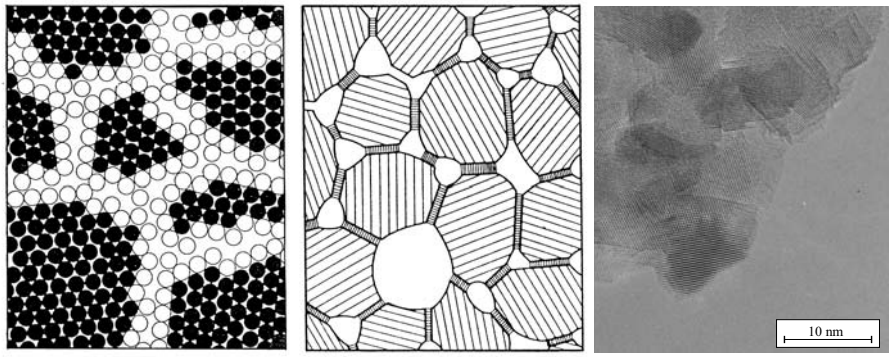

Fig. 9.22. Schematic representations and transmission electron micrograph of nanocrystalline materials. Left: Atoms in crystalline regions (full circles) and in grain boundary regions (open circles) [4]. Middle: Nanocrystalline material consisting of a crystalline phase, the interfacial phase and pores [70]. Right: High-resolution transmission electron micrograph of nanocrystalline CaF_2 with an average grain size of about 9 nm [9].

the alternative route is high-energy ball milling, where the grain size of the microcrystalline starting material is reduced by mechanical attrition [71–73]. The size of the grains is controlled by the duration of the milling process. The excess energy is stored in the grain boundary regions by a highly disordered atomic arrangement.

Here investigations on nanocrystalline CaF_2 (n-CaF_2), prepared by the inert gas condensation technique, and on nanocrystalline $LiNbO_3$, $Li_{0.7}TiS_2$ and $(1-x)Li_2O{:}xB_2O_3$ composites, prepared by high-energy ball milling, will be discussed.

9.6.1 Nanocrystalline Calcium Fluoride

The average grain diameter of the n-CaF_2 material obtained with the inert gas condensation technique was about 9 nm according to X-ray diffraction line broadening and transmission electron microscopy (TEM), see right part of Fig. 9.22. After compaction the density was 96 % of that of single crystalline CaF_2.

Single- or polycrystalline CaF_2 is a F^--ion conductor and the dominant self-diffusion mechanism at elevated temperatures consists of F^--jumps via thermally activated vacancies in the anion sublattice. Fig. 9.23 shows the diffusion-induced peak of T_1^{-1} of ^{19}F in a CaF_2 single crystal (s-CaF_2) [74] including a temperature-independent background, which becomes apparent at low temperatures, in comparison with the SLR rate in n-CaF_2 [75]. For the latter several temperature runs were made, which will be discussed below.

Though measured at a higher Larmor frequency, the SLR rate in n-CaF_2 rises to a peak at considerably lower temperatures than in s-CaF_2. The ac-

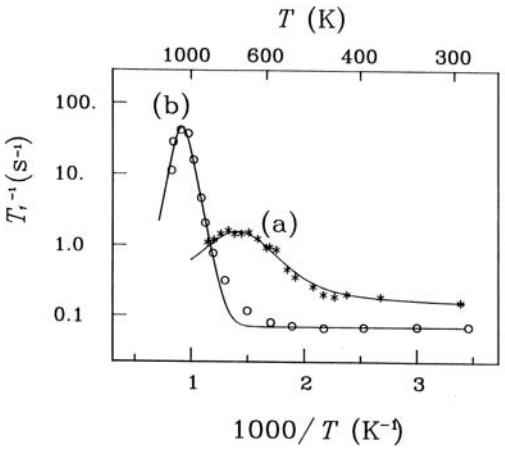

Fig. 9.23. Temperature dependence of the spin-lattice relaxation rate T_1^{-1} of ^{19}F in (a) nanocrystalline CaF_2 ($\omega_L/2\pi = 47\,MHz$, second temperature run) [75] and (b) single-crystalline CaF_2 ($\omega_L/2\pi = 15\,MHz$, data points from [74]). The solid lines are fits of a simple spectral density function as guide to the eye.

tivation energy estimated from the slope of the peak is found to be reduced to typically 0.4 eV compared to 1.6 eV in s-CaF_2. These findings indicate a drastically enhanced F^--diffusivity which is ascribed to the influence of the interfacial regions. A realistic estimate of the enhancement at, e. g., 500 K where the diffusion coefficient in s-CaF_2 itself is increased due to the presence of extrinsic vacancies in addition to the thermal ones (cf. the deviation of the SLR data from the fit curve (b) in Fig. 9.23) can be obtained from a comparison of the corresponding conductivities of n-CaF_2 and s-CaF_2 [76]. The ratio amounts to about 10^4.

Up to temperatures $T \leq 500\,K$, measured values of the SLR rate in n-CaF_2 are reproducible in different $T_1^{-1}(T)$ runs. For higher T, the SLR rate reduces upon thermal cycling and approaches that of s-CaF_2 due to substantial grain growth. A similar observation of thermal metastability and instability, respectively, was made in $T_{1\rho}$ measurements on ^{63}Cu in n-Cu [77]. The activation energies observed in n-CaF_2 in successive temperature runs increase towards the value for s-CaF_2. TEM of the n-CaF_2 material after three $T_1^{-1}(T)$ runs up to 870 K showed growth of the average grain diameter to about 50 nm [69].

Further information on the fast interfacial diffusion was obtained from temperature-dependent lineshape measurements as shown in Fig. 9.24 [75]. At room temperature the ^{19}F resonance can be described by a broad Gaussian line (Fig. 9.24a[2]). This corresponds to the rigid lattice. As the temperature

[2] The small dip in the line centre is due to a dead time effect at the start of the FID recording.

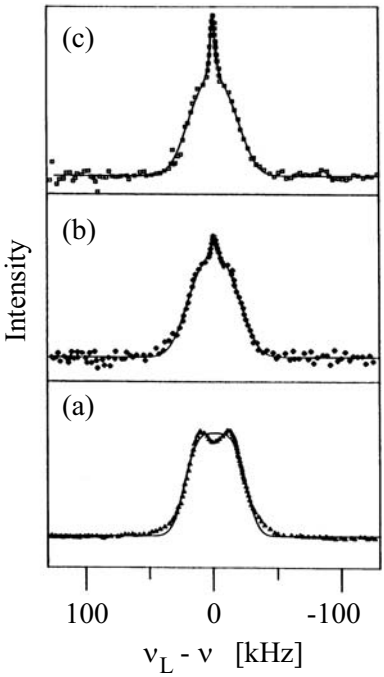

Fig. 9.24. NMR lineshapes of ^{19}F in an as-prepared nanocrystalline CaF_2 sample at 298 K (a), 400 K (b), and 440 K (c) at $\omega_L/2\pi = 24$ MHz. The lines through the data represent fits by a Lorentzian and/or a Gaussian.

of the virgin sample is raised up to 440 K the width of the broad line remains essentially constant and a superimposed motionally narrowed line shows up

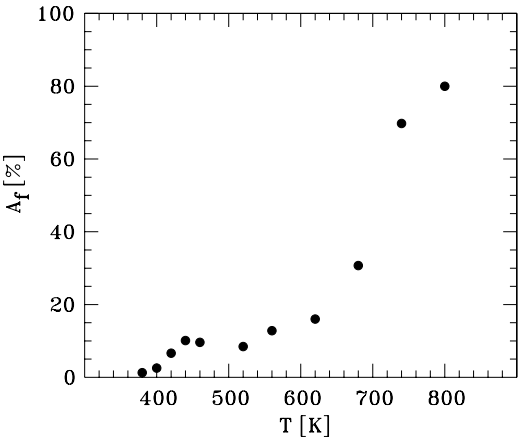

Fig. 9.25. Fraction A_f of the motionally narrowed ^{19}F signal with respect to the total signal intensity in n-CaF_2 as a function of temperature. Between about 440 K and 600 K a T independent fraction of mobile ions corresponding to the mass fraction of the interfacial regions is observed.

which can be described by a Lorentzian (Fig. 9.24b,c). The two components whose centres of gravity coincide are attributed to the stationary fluorine ions in the grains and the highly mobile ones in the interfacial regions.

Fig. 9.25 shows the fraction A_f of the area under the Lorentzian line with respect to the total lineshape area. A_f corresponds to the fraction of mobile F^-. At 440 K the narrowed line has attained about 10 % of the signal intensity and remains constant up to about 600 K where the onset of line narrowing also in the grains is observed. The plateau value of A_f should reflect the mass fraction of the interfacial regions. Taking their reduced mass density into account (cf. Sect. 9.1) the volume fraction is somewhat higher than 10 % but still smaller than the value of 25 % which may be estimated [5] using the XRD result for the average grain diameter. The difference may be attributed to different weighting of interfacial and crystal regions in the dynamic and static measurements, respectively.

First measurements on the analogous system n-BaF_2 [78], which, however, was not prepared by inert-gas condensation but by high-energy ball milling, show SLR results which are consistent with those on n-CaF_2 presented above.

9.6.2 Nanocrystalline, Microcrystalline and Amorphous Lithium Niobate

In spite of the extensive research work performed on $LiNbO_3$ mainly because of its technical relevance, e. g. in electro-optic applications, NMR investigations of the Li ion dynamics have been rather scarce. Thus for comparison reasons not only nanocrystalline $LiNbO_3$, prepared by high-energy ball milling, but also the coarse-grained polycrystalline source material (i.e. microcrystalline $LiNbO_3$, m-$LiNbO_3$) and amorphous $LiNbO_3$ (a-$LiNbO_3$) were studied in detail [79–81]. Fig. 9.26 shows results of ^{7}Li $T_1^{-1}(T)$ measurements at various frequencies in the MHz regime on n-$LiNbO_3$ with an average grain diameter of 23 nm and on m-$LiNbO_3$ (average grain size of some μm) at one of the above frequencies for comparison. For both modifications only the low-T sides of the diffusion-induced $T_1^{-1}(T)$ peaks, being superimposed on background relaxation rates, were observable in the accessible temperature ranges up to 1400 K and 500 K, respectively. From the shift of the flank to lower T it can be concluded that in n-$LiNbO_3$ the effective correlation time τ_c is by orders of magnitude smaller, i. e. diffusion is much faster. The slopes indicate that the activation energy is reduced from 0.75 eV for m-$LiNbO_3$ to about one third of this value.

Figure 9.27 shows an Arrhenius plot of the SLR rate in the rotating reference frame at various frequencies in the kHz regime for m-$LiNbO_3$. Instead of conventional $T_{1\rho}^{-1}$ (cf. Sect. 9.3) the SLR rate T_{1e}^{-1} in the pulsed rotating frame, being a time saving alternative [82], was measured. In this case also the maxima of the curves and parts of their high-temperature sides were detectable. From the T_{1e}^{-1} maximum for a given frequency an absolute value for τ_c in m-$LiNbO_3$ can be estimated which amounts at, e. g., 890 K to

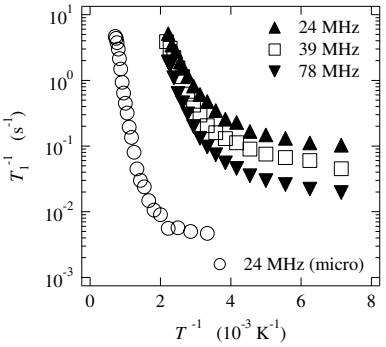

Fig. 9.26. ^{7}Li SLR rate versus inverse temperature in n-$LiNbO_3$ at three frequencies measured in the laboratory reference frame. For comparison the T_1^{-1} results from m-$LiNbO_3$ at $\omega_L/2\pi = 24\,\mathrm{MHz}$ are displayed, too [79, 80].

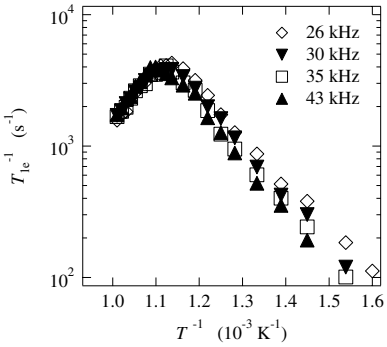

Fig. 9.27. ^{7}Li SLR rate versus inverse temperature in m-$LiNbO_3$ at four frequencies measured in the pulsed rotating frame [79, 80].

$3 \cdot 10^{-6}\,\mathrm{s}$. For uncorrelated jumps this corresponds to a diffusion coefficient $D = 8 \cdot 10^{-15}\ \mathrm{m^2\,s^{-1}}$ as obtained from the Einstein-Smoluchowski equation (see (1.36) in Chap. 1). For the mean square displacement the Li-Li distance of about 0.38 nm in the crystal structure of $LiNbO_3$ was adopted and the dimensionality of the jump process is taken to be three because the SLR rate on the high-T side is independent of frequency (Fig. 9.27, cf. Table 9.1). The activation energy of 0.88 eV obtained from the high-T side, which applies to long-range diffusion, is greater than the value 0.75 eV from the low-T side which agrees with that from the T_1^{-1} measurements and reflects short-range motion. The asymmetry of the $T_{1e}^{-1}(T)$ peak corresponds qualitatively to a frequency dependence on the low-T side described by $\alpha < 2$; this is also found for the SLR rate in the laboratory frame both for microcrystalline and nanocrystalline $LiNbO_3$. Quantitatively, however, (9.7) is not fulfilled.

In additon to the SLR measurements also lineshape measurements were done [80, 81, 83]. Fig. 9.28 shows the lineshape obtained in n-$LiNbO_3$ in comparison with m-$LiNbO_3$ and a-$LiNbO_3$. We focus on the central line of the spectrum of ^{7}Li ($I = 3/2$). The figure shows the motional narrowing for all three samples. Similar to the ^{19}F spectrum in n-CaF_2 (Fig. 9.24), the central line of ^{7}Li in n-$LiNbO_3$ reveals a superposition of two distinct contributions already at moderate temperatures (Fig. 9.28, middle row). The narrow component is caused by Li ions mobile at 450 K in the interfacial regions whereas the broad line can be attributed to Li ions within the grains being still immobile at that temperature. In contrast, the spectra of m-$LiNbO_3$ (Fig. 9.28, bottom row) do not show a comparable structuring at any temperature indi-

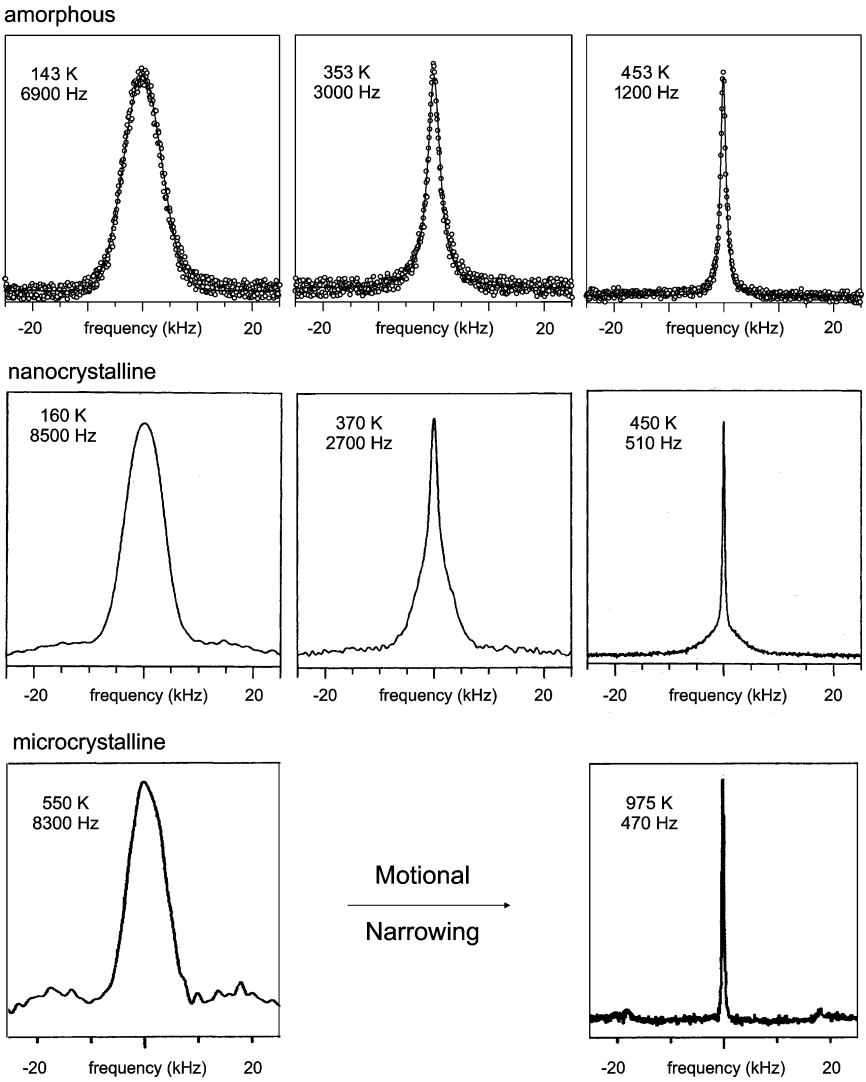

Fig. 9.28. Shape of the central line of the ^{7}Li-NMR spectrum. Top row: signal of a-$LiNbO_3$ at 143 K, 353 K and 453 K. Middle row: signal of n-$LiNbO_3$ at 160 K, 370 K and 450 K. Bottom row: signal of m-$LiNbO_3$ at 550 K and 975 K. The frequencies denote the linewidths (FWHM) [81].

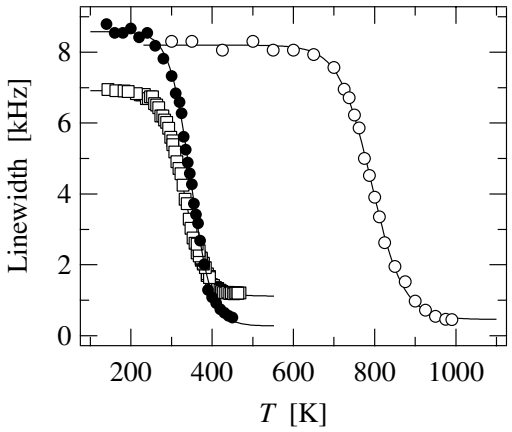

Fig. 9.29. Temperature dependence of the ^{7}Li linewidth in n-$LiNbO_3$ (full circles), m-$LiNbO_3$ (open circles) and amorphous $LiNbO_3$ (squares). The lines show fits yielding activation energies [81].

cating equivalent sites, i. e. a line contribution from bulk material only. For comparison Fig. 9.28 (top row) also shows the motional narrowing in the amorphous material. It starts at temperatures similar to those in n-$LiNbO_3$, but the lineshape has no comparable structure. This indicates that, as expected, the amorphous material is homogeneously disordered in contrast to n-$LiNbO_3$ where heterogeneous disorder is found. Fig. 9.29 displays the effective linewidth of the n- , m- and a-material as a function of temperature. Motional narrowing for Li ions in the interfacial regions of the nanocrystalline material starts at a temperature some 400 K below that in the undisturbed crystal and very similar to that in the amorphous material. The T dependence of the linewidth, analyzed with a phenomenological equation [84], yields an activation energy of 0.39 eV for n-$LiNbO_3$, 1.25 eV for p-$LiNbO_3$ and 0.35 eV for a-$LiNbO_3$. These values are in reasonable agreement with those obtained by SLR measurements on the same samples and suggest that the fast diffusion pathways in the interfacial regions of nanocrystalline $LiNbO_3$ being prepared by ball milling are similar to those in the amorphous material.

A further source of information not discussed here are the quadrupole satellites in the ^{7}Li spectra.

9.6.3 Nanocrystalline Lithium Titanium Disulfide

In Sect. 9.5.2 ^{7}Li spin-lattice relaxation results on microcrystalline hexagonal $Li_{0.7}TiS_2$ were presented in comparison with those on the corresponding cubic modification. We now turn to a study of nanocrystalline hexagonal $Li_{0.7}TiS_2$ and compare it with the above microcrystalline reference material from which it was produced by ball milling. Furthermore nanocrystalline

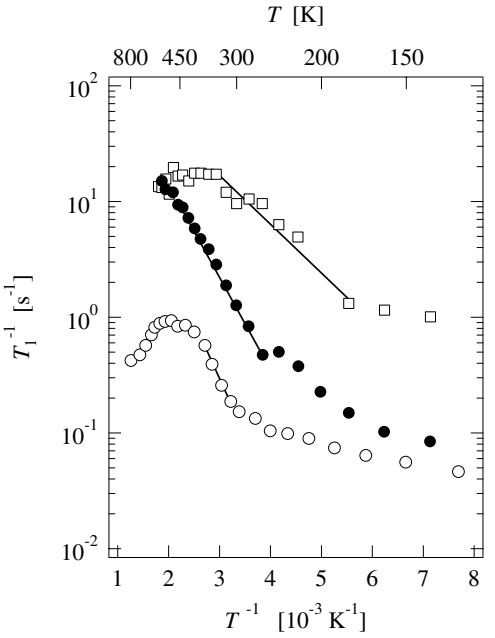

Fig. 9.30. Relaxation rates T_1^{-1} of microcrystalline (open circles), nanocrystalline (full circles) and amorphous (squares) Li_xTiS_2 at $\omega_L/2\pi = 24.5\,MHz$ [85].

$Li_{0.7}TiS_2$ is compared with amorphous $Li_{0.7}TiS_2$ [85]. An Arrhenius plot of T_1^{-1} for all three forms is shown in Fig. 9.30. Contrary to the case of $LiNbO_3$ (Sect. 9.6.2), the activation energy in nanocrystalline $Li_{0.7}TiS_2$, estimated from the slope of the low-temperature flank to be about 0.2 eV, is not considerably smaller than that in the microcrystalline material and larger than that in the amorphous one (about 0.1 eV). This indicates that the diffusion pathways in the two crystalline forms are similar and determined by the layer structure of the grains, even if the interfacial regions are essentially amorphous, while in the bulk amorphous phase the less dense packing may be responsible for the reduction of the activation energy. The spin-lattice relaxation rate measured after annealing a freshly prepared nanocrystalline Li_xTiS_2 sample at various temperatures was also used to study the kinetics of the Li intercalation process [85].

Concerning the frequency dependence of T_1^{-1} in the regime of the low-temperature flank of the diffusion-induced peaks for the nanocrystalline and the amorphous forms, the exponent α (cf. (9.5)) was found to be smaller than 1 (approximately 0.6). This result for the two disordered forms contrasts with that for microcrystalline h-$Li_{0.7}TiS_2$ where α was larger than one (approximately 1.3, see Sect. 9.5.2). Sublinear frequency dependencies have also been observed in ionic glasses by NMR (e. g. [86–88]) as well as β-NMR [56, 89, 90] (cf. Sect. 9.7). In [86] $\alpha < 1$ was interpreted in the frame

of the coupling concept [28] as being due to spin-lattice relaxation by localized ion motion involving two-level systems, typical of disordered systems. A sublinear frequency dependence of the motion-induced relaxation rate corresponds to a superlinear frequency dependence of the ionic conductivity (see Chap. 20) which has also been observed in disordered systems (e. g. [92]). Such a behaviour has also been treated in terms of the concept of mismatch and relaxation treated in Chap. 21 (cf. [29]).

9.6.4 Nanocrystalline Composites of Lithium Oxide and Boron Oxide

Besides single-phase nanocrystalline materials also composite systems of an ionic conductor and an insulator have been studied. Such systems are called dispersed ionic conductors and can show surprising effects in the overall conductivity [93–96] (see also Sect. 22.9.2 of Chap. 22). Fig. 9.31 shows a sketch of such a composite material consisting of two different types of grains which are shown as light grey and dark grey hatched areas for the ionic conductor and the insulator, respectively. There are now three different types of interfaces. These are interfaces between ionic conductor grains (dotted lines), interfaces between insulator grains (dashed lines) and interfaces between an ionic conductor and an insulator grain (solid lines). The latter ones seem to play a crucial role for the overall conductivity in many dispersed ionic conductors [97–102]. The composition and the grain sizes of such composites can easily be varied which gives the possibility to modify the network of the different interfaces which in turn might lead to materials with tailored macroscopic properties.

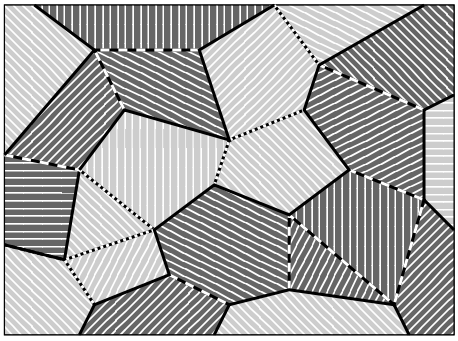

Fig. 9.31. Sketch of a composite material of ionic conductor grains (light grey areas) and insulator grains (dark grey areas). The network of interfaces consists of interfaces between ionic conductor grains (dotted lines), interfaces between insulator grains (dashed lines) and interfaces between ionic conductor and insulator grains (solid lines).

In order to study the dynamics of Li ions in such composites, among others ^{7}Li NMR lineshape measurements on nanocrystalline $(1-x)Li_2O{:}xB_2O_3$ at, e. g., $x = 0.5$ and a temperature of 433 K were performed [103]. The central line shows two contributions similar to the results found for nanocrystalline CaF_2 (Sect. 9.6.1) and nanocrystalline $LiNbO_3$ (Sect. 9.6.2) which again can be attributed to fast and slow Li ions in the interfaces and the bulk of the grains, respectively. The microcrystalline counterparts again show only one broad line.

This is consistent with the time dependence of the free induction decay (FID) found for this composite material at 433 K (Fig. 9.32). The microcrystalline material (Fig. 9.32(a)) shows only one fast decaying part in the time regime below 50 μs which can be described by $\exp(-a_1 t^2)\sin(a_2 t)/a_2 t$ (cf. [13]), with a_1 and a_2 being fit parameters. For the nanocrystalline material (Fig. 9.32(b)) this component is also present, but now there is an additional slowly decaying component (marked by an arrow), which becomes apparent for times larger than 100 μs and can be described by a simple exponential function. Of course, the NMR lineshapes are the Fourier transforms of these FIDs and one can easily show that the fast decaying component in the FID belongs to a broad component in the NMR lineshape and the slowly decaying component in the FID belongs to a motionally narrowed component. These are attributed to the slow ions in the grains and the fast ones in the interfacial regions, respectively. For the microcrystalline sample only Li ions in the grains can be detected because the number fraction of Li ions in the interfacial regions is too small. The fact that for the nanocrystalline composite material the two different Li species can be discriminated by their different time dependences in the FID is due to their different T_2 values.

Another way to discriminate the two Li species is via their different T_1 values. Fig. 9.33 shows the magnetization transients of the micro- and the nanocrystalline composites. Whereas for the microcrystalline material the magnetization transients $M(t)$ can be described by a monoexponential function, the nanocrystalline composite shows significant deviation from monoexponential behaviour and has to be described by a sum of two exponential functions reflecting the fact that the fast and slow Li species have different T_1 values. This also reveals that in the present case spin diffusion between the two Li reservoirs is not fast enough for a homogeneous averaging to set in which would result in a monoexponential magnetization behaviour (cf. Sect. 9.7.1). Spin diffusion becomes apparent only in the fact that the relaxation time of the slow Li ions in the nanocrystalline composite is slightly reduced in comparison with the corresponding microcrystalline composite (see values given in Fig. 9.33).

Fig. 9.34 shows the temperature dependence of the spin-lattice relaxation rates of the fast and the slow Li ions of nanocrystalline $(1-x)Li_2O{:}xB_2O_3$, $x = 0.5$. The slope of the Arrhenius fits which represent the low-temperature flanks of the corresponding diffusion-induced peaks yield the activation bar-

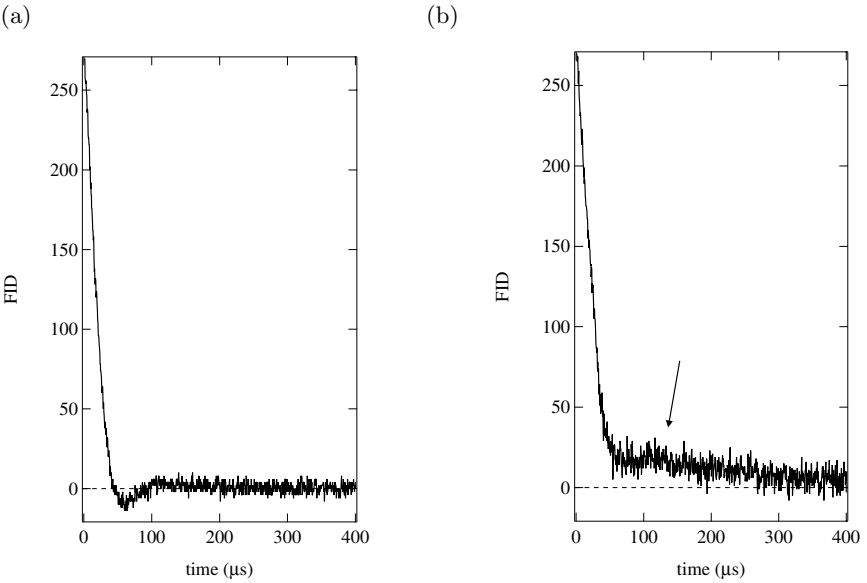

Fig. 9.32. Free induction decay of ^{7}Li in (a) microcrystalline and (b) nanocrystalline $(1-x)Li_2O{:}xB_2O_3$, $x = 0.5$, at 58 MHz and 433 K. The arrow indicates a slowly decaying component in the case of the nanocrystalline material which is not present for the microcrystalline sample.

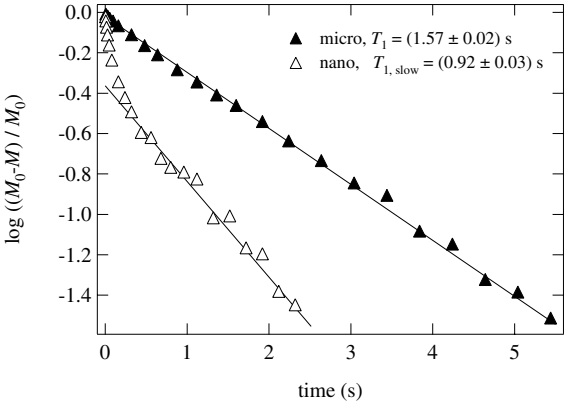

Fig. 9.33. Magnetization transients of ^{7}Li in microcrystalline and nanocrystalline $(1-x)Li_2O{:}xB_2O_3$, $x = 0.5$, at 58 MHz and 433 K. The lines represent a monoexponential fit in the case of the microcrystalline material and the slow component of a biexponential fit in the case of the nanocrystalline material.

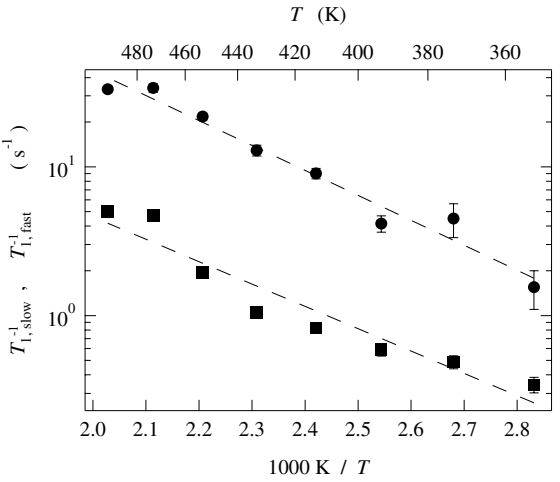

Fig. 9.34. Discriminated fast and slow relaxation rates T_1^{-1} of ^{7}Li in nanocrystalline $(1-x)Li_2O{:}xB_2O_3$, $x = 0.5$, at 58 MHz. The dashed lines represent Arrhenius fits.

riers for single ion jumps. Within the experimental errors they are the same for the slow and the fast Li ions. Therefore the different diffusivities of the two species of Li ions are not caused by an enhanced mobility but by an enhanced concentration of defects in the neighbourhood of the interfaces.

In summary, the different diffusivities of the two Li species in the nanocrystalline composites become apparent in three different results: (i) two contributions to the NMR lineshape, (ii) two contributions to the FID and (iii) two components in the magnetization transients. In all cases the microcrystalline composites show only one species of Li ions.

The effects described in this section for the composites of Li_2O and B_2O_3 can be also found in pure nanocrystalline Li_2O but they are much weaker there. This shows that an interface between unlike crystallites generates a larger number of Li ions than an interface between Li_2O grains.

It is remarkable that results for the analogous system $(1-x)Li_2O{:}xAl_2O_3$ are very similar to those presented in this section [104]. This suggests that it is not important which specific insulator is added to Li_2O and that the results reveal a generic behaviour of such composites.

9.7 Glasses

In the previous section on nanocrystalline materials, systems with heterogeneous disorder were studied. We now turn to materials with homogeneous disorder. First the question how local disorder influences the decay behaviour of the nuclear polarization of the probe nuclei in β-NMR relaxation is

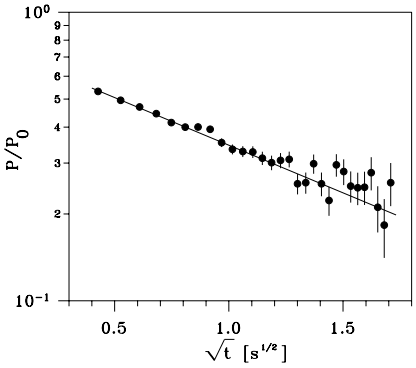

Fig. 9.35. Time dependence of the polarization of ^{8}Li in $Li_2O \cdot 3\,B_2O_3$ glass at $T = 120\,K$, $B_0 = 37\,mT$. The solid line represents a fit with $P/P_0 = \exp(-\sqrt{t/T_{1inh}})$.

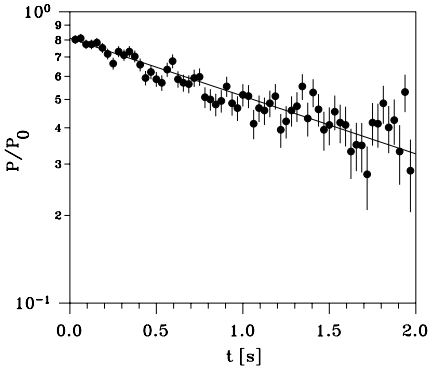

Fig. 9.36. Time dependence of the ^{8}Li polarization in the glassy electrolyte solution $LiCl \cdot 4\,D_2O$ at $T = 10\,K$, $B_0 = 300\,mT$. The solid line represents a fit with $P/P_0 = \exp(-t/T_{1hom})$.

addressed. The answer will be exemplified by experimental results on glasses with different short-range order. In the next subsection direct comparison of homogeneously disordered systems with their ordered counterparts will be made using, as example, lithium aluminosilicates where compounds with identical compositions in the glassy and the crystalline state can easily be prepared. The comparison will be based on ^{7}Li-NMR and ^{8}Li-β-NMR relaxation studies.

9.7.1 Inhomogeneous Spin-Lattice Relaxation in Glasses with Different Short-Range Order

In the study of SLR in materials with structural disorder – whether homogeneous or heterogeneous – the question arises if the relaxation behaviour of nuclei on inequivalent sites can be discriminated. This was possible, e. g., in the case of the ^{7}Li-NMR T_1 measurements on nanocrystalline Li_2O:B_2O_3 composites reported in Sect. 9.6.4 where spin diffusion did not play an important role. Often, however, in conventional NMR measurements on homogeneous systems polarization transfer among neighbouring nuclei by resonant mutual spin flips, i. e. spin diffusion, will hamper such a discrimination. In β-NMR the highly diluted probe nuclei differ in their magnetogyric ratio γ from the surrounding stable nuclei and thus relax independently without resonant polarization transfer (cf. Sect. 9.4).

Two classes of glassy systems were investigated with the β-NMR method. These are on the one hand oxide glasses represented here by the borate glass $Li_2O \cdot 3\,B_2O_3$ and on the other hand electrolyte glasses exemplified by the solution $LiCl \cdot n\,D_2O$ ($n = 4$ and 7).

As shown in Fig. 9.35 the polarization $P(t)$ of ^{8}Li in the borate glass decays non-exponentially and can well be represented by

$$P(t) = P_0 \cdot \exp\left[-\sqrt{t/T_{1\mathrm{inh}}}\right] \quad , \tag{9.22}$$

where $T_{1\mathrm{inh}}$ is the so-called inhomogeneous relaxation time to be addressed in the following. Contrary to such a single transient, the bulk of data also allows one to determine the parameter β in the stretched exponential

$$P(t) = P_0 \cdot \exp\left[-(t/T_{1\mathrm{inh}})^{\beta}\right] \quad . \tag{9.23}$$

Taking together, for example, the data on ^{8}Li in $Li_2O \cdot 3\,B_2O_3$ in the temperature range 5 K - 200 K the value $\beta = 0.52(1)$ was found [90]. Furthermore, transients of the polarization of the β-NMR probe ^{12}B in the same glass and again of ^{8}Li in other oxide glasses ($Li_2O \cdot 2\,SiO_2$, $Li_2O \cdot Na_2O \cdot 4\,SiO_2$ and $Li_2O \cdot Al_2O_3 \cdot 4\,SiO_2$) showed a behaviour according to (9.22) [90, 91, 105].

Essential in the explanation of the $\exp(-\sqrt{t/T_{1\mathrm{inh}}})$ law is the fact that an observed transient results from inhomogeneous polarization averaging [106]. The β-NMR probes are isolated and relax independently with different rates

$$1/T_1^{(k)} = \sum_i a(r_{ik})\ J(\omega_\mathrm{L}, \tau_i) \tag{9.24}$$

where $a(r_{ik}) = a_0(r_0/r_{ik})^m$ is the coupling constant of the probe nucleus k to a relaxation centre ('defect') i at distance r_{ik} and $J(\omega, \tau_i)$ is the spectral density function of the field fluctuations attributed to this centre.

Inhomogeneous polarization averaging over all probe nuclei yields

$$P_{\mathrm{inh}}(t) = \left\langle P_0 \exp\left[-t/T_1^{(k)}\right]\right\rangle_k = P_0 \cdot \exp\left[-\left(\frac{t}{T_{1\mathrm{inh}}}\right)^{3/m}\right] \quad . \tag{9.25}$$

For $m = 6$ which applies to dipolar and quadrupolar coupling, the observed $\exp(-\sqrt{t/T_{1\mathrm{inh}}})$ law is obtained. It is noted that homogeneous averaging, which in general is performed in classical NMR relaxation where rapid polarization transfer due to high probe concentration is possible, results in a single exponential

$$P_{\mathrm{hom}}(t) = P_0 \cdot \exp\left[-t/\langle T_1^{(k)}\rangle_k\right] = P_0 \cdot \exp[-t/T_{1\mathrm{hom}}] \quad . \tag{9.26}$$

Contrary to the oxide glasses, β-NMR relaxation in the electrolyte glass $LiCl{\cdot}nD_2O$ ($n = 4$; 7) was found to be monoexponential as illustrated in Fig. 9.36 [53, 107]. The bulk of $P(t)$ data obtained in the glassy state clearly shows that here β is near unity and not 1/2. $LiCl{\cdot}nD_2O$ has a disordered structure consisting of Cl^- ions and $Li^+(4D_2O)$ complexes as basic units. For $n = 7$ the excess water is interstitially incorporated between $Li^+(4D_2O)Cl^-$

clusters. In each case the Li^+ ions are tetrahedrally surrounded by D_2O molecules. Thus, despite the overall amorphous structure, the near neighbourhood of each Li ion is largely equivalent[3]. This contrasts with the oxide glasses, where Li as network modifier (or B as network constituent) occupies many inequivalent sites. This difference in local structure near the probe is the reason for the different transient behaviour of the polarization found in the two classes of glassy systems.

In conclusion, β-NMR relaxation is inherently sensitive to local order and a deviation from monoexponential polarization decay is a fingerprint of the disorder near the probe.

9.7.2 Glassy and Crystalline Lithium Aluminosilicates

Lithium aluminosilicates are of interest for the design of materials with negligible thermal expansion which is possible due to opposite signs of the expansion coefficients in the crystalline and the glassy state [108]. Another point of interest, relevant here, is the lithium conductivity and diffusivity.

In the system Li_2O - Al_2O_3 - $n SiO_2$, Li motions were studied in glasses with $n = 2$; 4; 8, and in their crystalline counterparts β-$LiAlSiO_4$ (β-eucryptite), β-$LiAlSi_2O_6$ (β-spodumene) and $LiAlSi_4O_{10}$ (petalite composition). The ratio of Li_2O to Al_2O_3 is always one, i. e. the charge of each Li^+ is compensated by AlO_4^-. Non-bridging oxygen atoms which interrupt the silicate network in binary oxide glasses with high alkali content are not present in these ternary glasses and their silicate network is fully polymerised. In the following, the discussion is mainly confined to glassy and polycrystalline samples with the spodumene composition ($n = 4$). In the crystal structure of β-spodumene there are four pairs of closely neighboured Li sites per unit cell. Their distance is 0.13 nm and only one site is occupied at a time. The distance between different pairs of Li sites is about 0.45 nm. This suggests two types of possible Li jumps, long-range jumps between different pairs and a localized motion by hops between the sites of a pair.

In Fig. 9.37, ^{7}Li $T_1^{-1}(T)$ data for the glassy and the crystalline sample at one frequency are compared [87]. For both modifications a pronounced diffusion-induced peak shows up which in the case of the glass occurs at roughly 700 K, i. e. some 250 K below the glass transition temperature, and in the case of the crystal at about 820 K. These peaks are due to the long-range Li jumps. The temperature values of the T_1^{-1} maxima and the slopes of the low-T flanks show that the jump rate of Li^+ is faster and the activation energy is smaller in the glass than in the crystal. Similar behaviour was found in the other Li aluminosilicates [88]. The activation energies $E_{\mathrm{NMR}}^{\mathrm{lT}}$ obtained from the slopes of the low-T side of the T_1^{-1} peak, corrected for a

[3] To some extend this type of glass may also be regarded as heterogeneously disordered.

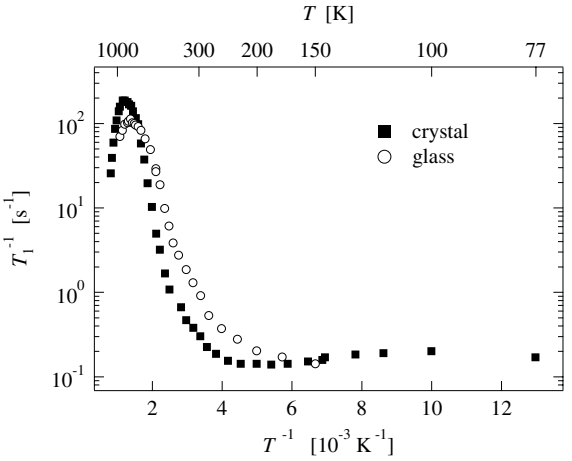

Fig. 9.37. Temperature dependence of T_1^{-1} of ^{7}Li in glassy and polycrystalline $LiAlSi_2O_6$ (β-spodumene) at $\omega_L/2\pi = 38.9$ MHz [87].

small background contribution to T_1^{-1}, are summarized in Table 9.2, neglecting a possible slight frequency dependence. There is no obvious trend with Li concentration. Provided that the diffusion mechanism does not change, a logarithmic decrease of the activation energy with increasing mobile-ion concentration is predicted by various model calculations of diffusion in disordered systems [109–111] (see also Chap. 20).

Inspection of Fig. 9.37 further shows that a peak asymmetry, expected according to Sect. 9.2 for the glass, is also found for the crystal. For crystalline $Li_2O \cdot Al_2O_3 \cdot 4\,SiO_2$ the value $E_{NMR}^{hT} = 0.86(3)$ eV is obtained from the slope of the high-T side [87]. Comparison with the corresponding E_{NMR}^{lT} value in Table 9.2 yields $\alpha = 1.6$ for the parameter in (9.7). For the glass the high-T flank and thus E_{NMR}^{hT} was not accessible. However, as verified for crystalline $Li_2O \cdot Al_2O_3 \cdot 4\,SiO_2$ [112] and generally predicted (e. g. [29]) E_{NMR}^{hT} is essentially equal to the activation energy E_σ^{dc} from dc conductivity measurements

Table 9.2. Activation energies E_{NMR}^{lT} [eV] obtained from the low-T slopes of ^{7}Li SLR rate peaks in glassy and crystalline lithium aluminosilicates with various mineral compositions. The error in E_{NMR}^{lT} is typically 2 in the last digit.

	glass	crystal
$Li_2O \cdot Al_2O_3 \cdot 2\,SiO_2$ (eucryptite)	0.30	0.40
$Li_2O \cdot Al_2O_3 \cdot 4\,SiO_2$ (spodumene)	0.34	0.50
$Li_2O \cdot Al_2O_3 \cdot 8\,SiO_2$ (petalite)	0.22	0.47

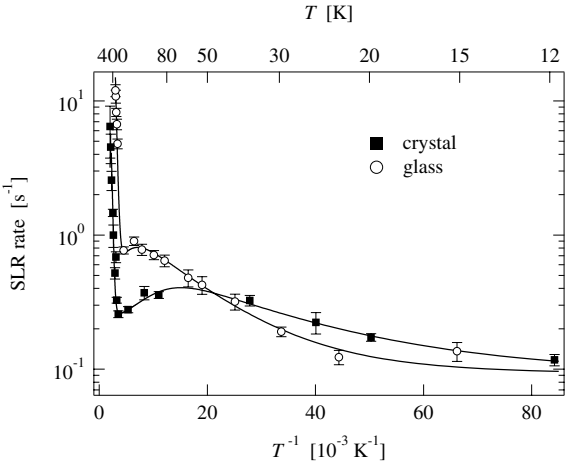

Fig. 9.38. Temperature dependence of the spin-lattice relaxation rate of ^{8}Li in glassy (○) and polycrystalline (■) $LiAlSi_2O_6$ (β-spodumene) at a magnetic field corresponding to $\omega_L/2\pi = 3\,\mathrm{MHz}$. The lines are drawn to guide the eye.

(for a small difference between the two see [113] and Chap. 20). In the case of the glass $E_\sigma^{\mathrm{dc}} = 0.66\,\mathrm{eV}$ was found [112]. Using (9.7), this results in $\alpha = 1.5$. The deviation from standard SLR behaviour [16] is also reflected by a sub-quadratic frequency dependence of T_1^{-1} found on the low-T flank of the peak for both modifications [87]. The experimental power law (cf. (9.5)) is even weaker than that expected on account of the asymmetry of the rate peak (cf. (9.6)) and can be described by $\alpha = 0.9(2)$ and $\alpha = 0.8(1)$ for crystalline and glassy $Li_2O \cdot Al_2O_3 \cdot 4\,SiO_2$, respectively [87]. Thus, in this regard the apparently ordered ion conductor shows nearly the same 'anomalies' as the disordered one. The sublinear frequency dependence being indicated in the glass shows up also in other glasses [86, 88–91] as well as in nanocrystalline ion conductors, e. g. $Li_{0.7}TiS_2$, as mentioned in Sect. 9.6.3.

Besides the main peak at about 820 K, in Fig. 9.37 a second, broad maximum can be seen for the crystalline sample around roughly 100 K. This can be attributed to the short-range hopping of the Li ions between the pair sites mentioned above. Fig. 9.38 shows the corresponding data obtained by β-NMR on ^{8}Li at 3 MHz [114] covering the temperature range from about 500 K down to 10 K. Whereas in the case of polycrystalline $LiAlSi_2O_6$ transients $P(t)$ of the ^{8}Li polarization could be fitted by a single exponential, in the glass $P(t)$ followed the expected $\exp(-\sqrt{t/T_{1\mathrm{inh}}})$ behaviour (9.22). The resulting values of the inhomogeneous relaxation rate $T_{1\mathrm{inh}}^{-1}$ are displayed in Fig. 9.38. For temperatures above 200 K the low-temperature flank of the long-range diffusion induced peak is visible again. The maximum of the relaxation rate due to the localized jumps in crystalline $LiAlSi_2O_6$ occurs at about 70 K. For the glassy material this maximum appears only as a slight

shoulder. Using the temperature of the SLR rate maximum of ^{7}Li together with that of ^{8}Li (Figs. 9.37 and 9.38) one can estimate the activation energy for the jumps between the pair sites in the crystalline material to be roughly 50 meV. This result is also consistent with ^{7}Li-T_1 data obtained at different frequencies [115].

In summary, glassy and crystalline aluminosilicates, besides being interesting for applications, provide a playground for the study of the influence of disorder on ion transport properties by complementary techniques, as exemplified here for the spodumene system.

9.8 Conclusion

In this chapter the use of stable and β-radioactive NMR nuclei for probing diffusive motion was reviewed. After having shown how microscopic information on the diffusive motion can be obtained from the SLR rate, the corresponding NMR and β-NMR techniques were outlined.

The materials discussed in this chapter were Li intercalation compounds as examples of layer-crystalline systems with simple internal interfaces, nanocrystalline ceramics as examples of materials with complex internal interfaces and, finally, oxide glasses representing homogeneously disordered systems. In all three classes the 3D ordered modifications were also examined for comparison.

Emphasis in the SLR investigations was put on the variation of frequency besides temperature. In the case of the intercalation compounds this allowed one to study the high-temperature (low-frequency) limit and to trace in-plane 2D diffusion processes. In all materials of interest here and contrary to the 'ideal' case of Li metal, the frequency dependence of the SLR rate in the low-temperature limit was found to be weaker than that predicted by the standard (BPP) model which was ascribed to the influence of disorder and/or Coulomb interaction. In the nanocrystalline ceramics, in addition to NMR relaxation studies, lineshape measurements helped to elucidate the heterogeneous structure where the interfacial regions provide a network of pathways for fast diffusion. The heterogeneous structure results in heterogeneous dynamics of the mobile ions with fast ions in the interfacial regions and slower ones in the bulk of the grains.

Finally in glassy materials the potential of the β-NMR relaxation technique to probe the local disorder was demonstrated. A systematic comparison of glassy and crystalline modifications of ion conductors covered lithium aluminosilicates where higher diffusion jump rates showed up in the glasses.

9.9 Appendix

In the following we list the full expressions for the dependence of the different NMR relaxation rates on the spectral densities described in Sect. 9.2 in a more qualitative way. A quantitative description includes a linear combination of spectral density functions $J^{(q)}$ which result in transitions of spin pairs, where the combined angular momentum changes by $q\hbar$, and thus involve contributions at ω_L and $2\omega_\mathrm{L}$. For pure dipolar interaction one gets for the spin-lattice relaxation rate [13]

$$\frac{1}{T_1} = \frac{3}{2}\gamma^4\hbar^2 I(I+1)\left[J^{(1)}(\omega_\mathrm{L}) + J^{(2)}(2\omega_\mathrm{L})\right] \tag{9.27}$$

and for the spin-spin relaxation rate

$$\frac{1}{T_2} = \frac{3}{8}\gamma^4\hbar^2 I(I+1)\left[J^{(0)}(0) + 10\,J^{(1)}(\omega_\mathrm{L}) + J^{(2)}(2\omega_\mathrm{L})\right] \quad . \tag{9.28}$$

The different contributions $J^{(0)}(\omega)$, $J^{(1)}(\omega)$ and $J^{(2)}(\omega)$ to the spectral density stem from the partitioning of the Hamiltonian to contributions which do not change the overall magnetization and those which cause a single or twofold spin flip. The spectral densities $J^{(q)}(\omega)$ $(q = 0, 1, 2)$ are calculated from the corresponding correlation functions $G^{(q)}(t)$ via a Fourier transform

$$J^{(q)}(\omega) = \int_{-\infty}^{\infty} G^{(q)}(t)\,\mathrm{e}^{\mathrm{i}\omega t}\,\mathrm{d}t \quad . \tag{9.29}$$

For powder samples the relation $J^{(0)}(\omega) : J^{(1)}(\omega) : J^{(2)}(\omega) = 6 : 1 : 4$ holds.

For the spin-lattice relaxation rate in the rotating reference frame the full expression is [15]

$$\frac{1}{T_{1\rho}} = \frac{3}{8}\gamma^4\hbar^2 I(I+1)\left[J^{(0)}(2\omega_1) + 10\,J^{(1)}(\omega_\mathrm{L}) + J^{(2)}(2\omega_\mathrm{L})\right] \tag{9.30}$$

where ω_1 denotes the Larmor frequency in the locking field B_1.

For β-NMR measurements we have to treat the case of highly diluted spins I interacting with a reservoir of spins S. For the longitudinal relaxation time one gets [13, 17]

$$\frac{1}{T_1} = \gamma_I^2\gamma_S^2\hbar^2 S(S+1)\left[\frac{1}{12}J^{(0)}(\omega_I - \omega_S) + \frac{3}{2}J^{(1)}(\omega_I) + \frac{3}{4}J^{(2)}(\omega_I + \omega_S)\right] \tag{9.31}$$

where ω_I and ω_S are the Larmor frequency of the spin I and S, respectively (see also Sect. 9.7.1). In case of quadrupolar interaction analogous results are obtained for NMR and β-NMR relaxation [13, 15, 39, 116].

Notation

a	unit cell dimension in x-direction
$a(r_{ik})$	coupling constant
a_β	β-asymmetry
A	asymmetry coefficient of a β-decay
A_f	fraction of motionally narrowed signal
A_p	pulse sequence parameter
b	unit cell dimension in y-direction
B_0	static magnetic induction ('field')
B_1	alternating magnetic induction ('field')
B_eff	effective magnetic induction ('field') in the rotating frame
c	unit cell dimension in z-direction
E_A	activation energy
$E_\mathrm{NMR}^\mathrm{lT}$, $E_\mathrm{NMR}^\mathrm{hT}$	activation energy from low-T, high-T side of T_1^{-1} peak
f	dipolar polarization
G	correlation function
$\hbar$	Planck constant divided by 2π
I	nuclear spin
J, $J^{(q)}$	spectral density function (angular momentum change $q\hbar$)
k_B	Boltzmann constant
m	power of distance dependence of coupling constant
M, M_0	magnetization (equilibrium value)
M_x, M_y, M_z	magnetization components in the laboratory frame
$M_{x'}$, $M_{y'}$, $M_{z'}$	magnetization components in the rotating frame
M_ρ	magnetization in the rotating frame
N	number density
P	nuclear polarization
P_hom, P_inh	homogeneously, inhomogeneously averaged nuclear polarization
r	distance
t	time
t_p	duration of a pulse
T	temperature
T_1	spin-lattice relaxation time in the laboratory frame
$T_{1\rho}$	spin-lattice relaxation time in the rotating frame
$T_{1\rho}$	spin-lattice relaxation time in the pulsed rotating frame
T_1inh, T_1hom	inhomogeneous, homogeneous spin-lattice relaxation time
T_2	spin-spin relaxation time
v/c	velocity of β-particle in units of light velocity
W	emission probability of β-particles
Z_N, Z_S	counting rates in counter 'North','South'
α	exponent for frequency dependence
β	exponent in stretched exponential
γ	magnetogyric ratio

$\Delta\nu_{\mathrm{R}}$	NMR linewidth of the rigid lattice
θ	angle between β-emission and nuclear polarization direction
θ_{p}	tilt angle of magnetization
τ	mean residence time between successive jumps
τ_{e}	time interval in magnetization recovery experiment
τ_{SAE}	correlation time obtained from spin-alignment echo NMR measurements
τ_β	mean lifetime of β-radioactive nuclide
τ_{c}	correlation time
ω	angular frequency
$\omega_{\mathrm{L}} = 2\pi\nu_{\mathrm{L}}$	Larmor frequency

References

1. *Materials Interfaces - Atomic-Level Structure and Properties*, ed by D. Wolf, S. Yip (Chapman & Hall, London 1992)
2. *Graphite Intercalation Compounds I, Structure and Dynamics*, Springer Series in Materials Science, vol 14, ed by H. Zabel, S.A. Solin (Springer, Berlin Heidelberg New York 1990)
3. *Graphite Intercalation Compounds II, Transport and Electronic Properties*, Springer Series in Materials Science, 14, ed by H. Zabel, S.A. Solin (Springer, Berlin Heidelberg New York 1992)
4. H. Gleiter: Progress in Materials Science **33**, 223 (1989)
5. R.W. Siegel: Nanophase Materials. In: *Encyclopedia of Applied Physics*, vol 11, ed by G.L. Trigg, E.H. Immergut, E.S. Vera, W. Greulich (VCH, New York 1994) pp 173–200
6. A. Feltz: *Amorphous Inorganic Materials and Glasses* (VCH, Weinheim 1993)
7. R. Zallen: *The Physics of Amorphous Solids* (Wiley, New York 1983)
8. M.D. Ingram: Phys. Chem. Glasses **28**, 215 (1987)
9. P. Heitjans, S. Indris: J. Phys.: Condens. Matter **15**, R1257 (2003)
10. G. Schatz, A. Weidinger: *Nuclear Condensed Matter Physics: Nuclear Methods and Applications* (Wiley, Chicester 1996)
11. P. Heitjans: Solid State Ionics **18/19**, 50 (1986)
12. H. Rickert: *Electrochemistry of Solids - An Introduction* (Springer, Berlin 1982)
13. A. Abragam: *The Principles of Nuclear Magnetism* (Clarendon, Oxford 1961)
14. C.P. Slichter: *Principles of Magnetic Resonance* (Springer, Berlin Heidelberg New York 1989)
15. A.R. Allnatt, A.B. Lidiard: *Atomic Transport in Solids* (Cambridge Univ. Press, Cambridge 1993)
16. N. Bloembergen, E.M. Purcell, R.V. Pound: Phys. Rev. **73**, 679 (1948)
17. P. Heitjans, A. Körblein, H. Ackermann, D. Dubbers, F. Fujara, H.-J. Stöckmann: J. Phys. F: Met. Phys. **15**, 41 (1985)
18. R. Messer, A. Seeger, K. Zick: Z. Metallkunde **80**, 299 (1989)
19. A. Schirmer, P. Heitjans. In: *XXVIIIth Congress Ampere on Magnetic Resonance and Related Phenomena*, ed by M.E. Smith, J.H. Strange (University of Kent, Canterbury 1996) p 416

20. A. Schirmer, P. Heitjans, G. Majer, A. Seeger: Defect Diffus. Forum **143-147**, 1317 (1997)
21. M. Mali, J. Roos, M. Sonderegger, D. Brinkmann, P. Heitjans: J. Phys. F: Met. Phys. **18**, 403 (1988)
22. R. Bertani, M. Mali, J. Roos, D. Brinkmann: J. Phys.: Condens. Matter **2**, 7911 (1990)
23. D.M. Fischer, P. Duwe, S. Indris, P. Heitjans: Solid State Nucl. Magn. Reson. **26**, 74 (2004)
24. C.A. Sholl: J. Phys. C: Solid State Phys. **14**, 447 (1981)
25. J.L. Bjorkstam, M. Villa: Magn. Res. Rev. **6**, 1 (1980)
26. E. Goebel, W. Müller-Warmuth, H. Olyschläger, H. Dutz: J. Magn. Reson. **36** 371 (1979)
27. D. Knödler, P. Pendzig, W. Dieterich: Solid State Ionics **86–88**, 29 (1996)
28. K.L. Ngai, O. Kanert: Solid State Ionics **53-56**, 936 (1992)
29. K. Funke: Progr. Solid State Chem. **22**, 111 (1993)
30. M. Meyer, P. Maass, A. Bunde: Phys. Rev. Lett. **71**, 573 (1993)
31. H.-J. Stöckmann: J. Phys.: Condens. Matter **1**, 5101 (1989)
32. P. Borgs, K.W. Kehr, P. Heitjans: Phys. Rev. B **52**, 6668 (1995)
33. R.R. Ernst, G. Bodenhausen, A. Wokaun: *Principles of Nuclear Magnetic Resonance in One and Two Dimensions* (Clarendon Press, Oxford 1987)
34. M. Mehring: *High Resolution NMR Spectroscopy in Solids* (Springer, Berlin Heidelberg New York 1983)
35. *Solid State NMR I, III, IV*, ed by B. Blümich. In: *NMR Basic Principles and Progress* vol 30, 32, 33, ed by P. Diehl, E. Fluck, H. Günther, R. Kosfeld, J. Seelig (Springer, Berlin Heidelberg New York 1994)
36. E. Fukushima, R. Roeder: *Experimental Pulse NMR* (Addison Wesley, London 1981)
37. B.C. Gerstein, C.R. Dybowski: *Transient Techniques in NMR of Solids* (Academic, New York 1985)
38. R. Kimmich, E. Anoardo: Prog. Nucl. Magn. Reson. Spectrosc. **44**, 257 (2004)
39. H. Ackermann, P. Heitjans, H.-J. Stöckmann: β Emitters and Isomeric Nuclei as Probes in Condensed Matter. In: *Hyperfine Interactions of Radioactive Nuclei*, Topics in Current Physics, vol 31, ed by J. Christiansen (Springer, Berlin Heidelberg New York 1983) pp 291–361
40. H. Ackermann, N.T. Bagraev, R.T. Harley, J. Schneider. In: *Hyperfine Interaction of Defects in Semiconductors*, ed by G. Langouche (Elsevier, Amsterdam 1992) p 323
41. K. Sugimoto, A. Mizobuchi, K. Nakai, K. Matuda: J. Phys. Soc. Jpn. **21**, 213 (1966)
42. Y. Nojiri, B.I. Deutch: Phys. Rev. Lett. **51**, 180 (1983)
43. W. Faber, E. Jäger, B. Ittermann, H. Ackermann, P. Heitjans, H.-J. Stöckmann: Nucl. Instrum. Methods Phys. Res. B **16**, 439 (1986)
44. B. Ittermann, M. Füllgrabe, M. Heemeier, F. Kroll, F. Mai, K. Marbach, P. Meier, D. Peters, G. Welker, W. Geithner, S. Kappertz, S. Wilbert, P. Neugart, P. Lievens, U. Georg, M. Keim, and the ISOLDE Collaboration: Hyperfine Interact. **129**, 423 (2000)
45. R.F. Kiefl, W.A. MacFarlane, G.D. Morris, P. Amaudruz, D. Arsenau, H. Azumi, R. Baartman, T.R. Beals, J. Behr, C. Bommas, J.H. Brewer, K.H. Chow, E. Dumont, S.R. Dunsiger, S. Daviel, L. Greene, A. Hatakeyama

R.H. Heffner, Y. Hirayama, B. Hitti, S.R. Kreitzmann, C.D.P. Levy, R.I. Miller, M. Olivio, R. Poutissou: Physica B **326**, 189 (2003)
46. T.K. McNab, J.D. Perez, R.E. McDonald: Phys. Rev. B **18**, 92 (1978)
47. J.D. Perez, R.E. McDonald, T.K. McNab: Phys. Rev. B **19**, 163 (1979)
48. B. Ittermann, H. Ackermann, H.-J. Stöckmann, K.-H. Ergezinger, M. Heemeier, F. Kroll, F. Mai, K. Marbach, D. Peters, G. Sulzer: Phys. Rev. Lett. **77**, 4784 (1996)
49. M. Füllgrabe, B. Ittermann, H.-J. Stöckmann, F. Kroll, D. Peters, H. Ackermann: Phys. Rev. B **64**, 224302 (2001)
50. B. Ittermann, D. Peters, M. Füllgrabe, F. Kroll, H. Ackermann, H.-J. Stöckmann: Physica B **308–310**, 236 (2001)
51. H.D. Ebinger, H. Arnolds, C. Polenz, B. Polivka, W. Preyß, R. Veith, D. Fick, H.J. Jänsch: Surf. Sci. **412/413**, 586 (1998)
52. C. Bromberger, H.J. Jänsch, O. Kühlert, R. Schillinger, D. Fick: Phys. Rev. B **69**, 245424 (2004).
53. P. Heitjans, W. Faber, A. Schirmer: J. Non-Cryst. Solids **131-133**, 1053 (1991)
54. M.S. Wittingham: Prog. Solid State Chem. **12**, 41 (1978)
55. A. Schirmer, P. Heitjans, W. Faber, J.E. Fischer: Synth. Met. **34**, 589 (1989)
56. A. Schirmer, P. Heitjans, W. Faber, J.E. Fischer: Mater. Sci. Forum **91-93**, 589 (1992)
57. P. Freiländer, P. Heitjans, H. Ackermann, B. Bader, G. Kiese, A. Schirmer, H.-J. Stöckmann, C. Van der Marel, A. Magerl, H. Zabel: Z. Phys. Chem. N. F. **151**, 93 (1987)
58. J. Corish, F. Jugie, D.A. Morton-Blake, M. Leslie, F. Bénière: Phys. Rev. B **41**, 10870 (1990)
59. A. Schirmer, P. Heitjans: Z. Naturforsch. **50a**, 643 (1995)
60. S. Sinha, D. W. Murphy: Solid State Ionics **20**, 81 (1986)
61. R. Schöllhorn, A. Payer: Angew. Chem. **97**, 57 (1985)
62. W. Küchler, P. Heitjans, A. Payer, R. Schöllhorn: Solid State Ionics **70/71**, 434 (1994)
63. R.L. Kleinberg, B.G. Silbernagel: Solid State Comm. **36**, 345 (1980)
64. H.W. Spiess: J. Chem. Phys. **72**, 6755 (1980)
65. R. Böhmer: J. Magn. Reson. **147**, 78 (2000)
66. M. Wilkening, P. Heitjans: Defect Diffus. Forum **237-240**, 1182 (2005)
67. T. Bredow, P. Heitjans, M. Wilkening: Phys. Rev. B **70**, 115111 (2004)
68. B. Bader, P. Heitjans, H.-J. Stöckmann, H. Ackermann, W. Buttler, P. Freiländer, G. Kiese, C. van der Marel, A. Schirmer: J. Phys.: Condens. Matter **4**, 4779 (1992)
69. W. Puin, S. Rodewald, R. Ramlau, P. Heitjans, J. Maier: Solid State Ionics **131**, 159 (2000)
70. R.S. Averbach, H. Hahn, H.J. Höfler, J.L. Logas, T.C. Shen: Mat. Res. Soc. Symp. Proc. **153**, 3 (1989)
71. S. Indris, P. Heitjans: Mater. Sci. Forum **343-346**, 417 (2000)
72. S. Indris, D. Bork, P. Heitjans: J. Mater. Synth. Process. **8**, 245 (2000)
73. P. Heitjans, S. Indris. In: *Synthesis, Functional Properties and Applications of Nanostructures*, MRS symposium proceedings, vol 676, ed by H.W. Hahn, D.L. Feldheim, C.P. Kubiak, R. Tannenbaum, R.W. Siegel (Materials Research Society, Pittsburgh 2002) pp 6.6.1–6.6.10
74. R. Van Steenwinkel: Z. Naturforsch. **29a**, 278 (1974)

75. W. Puin, P. Heitjans, W. Dickenscheidt, H. Gleiter. In: *Defects in Insulating Materials*, ed by O. Kanert, J.M. Spaeth (World Scientific, Singapore 1993) pp 137–139
76. W. Puin, P. Heitjans: Nanostructured Materials **6**, 885 (1995)
77. W. Dickenscheid, R. Birringer, R. Strauß, H. Gleiter, O. Kanert, B. Michel, B. Günther: Solid State Comm. **79**, 683 (1991)
78. P. Heitjans, S. Indris: J. Mater. Sci. **39**, 5091 (2004)
79. D. Bork, P. Heitjans: J. Phys. Chem. B **102**, 7303 (1998)
80. D. Bork, P. Heitjans: J. Phys. Chem. B **105**, 9162 (2001)
81. M. Wilkening, D. Bork, S. Indris, P. Heitjans: Phys. Chem. Chem. Phys. **4**, 3246 (2002)
82. W.-K. Rhim, D.P. Burum, D.D. Ellemann: J. Chem. Phys. **68**, 692 (1978)
83. D. Bork, P. Heitjans. In: *XXVIIIth Congress Ampere on Magnetic Resonance and Related Phenomena*, ed by M.E. Smith, J.H. Strange (University of Kent, Canterbury 1996) p 418
84. J.R. Hendrickson, P.J. Bray: J. Magn. Reson. **9**, 341 (1973)
85. R. Winter, P. Heitjans: J. Phys. Chem. B **105**, 6108 (2001)
86. G. Balzer-Jöllenbeck, O. Kanert, H. Jain, K.L. Ngai: Phys. Rev. B **39**, 6071 (1989)
87. W. Franke, P. Heitjans: Ber. Bunsenges. Phys. Chem. **96**, 1674 (1992)
88. R. Winter, K. Siegmund, P. Heitjans: J. Non-Cryst. Solids **212**, 215 (1997)
89. A. Schirmer, P. Heitjans, H. Ackermann, B. Bader, P. Freiländer, H.-J. Stöckmann: Solid State Ionics **28–30**, 717 (1988)
90. A. Schirmer, P. Heitjans, B. Bader, P. Freiländer, H.-J. Stöckmann, H. Ackermann: J. Phys.: Condens. Matter **3**, 4323 (1991)
91. A. Schirmer, P. Heitjans. In: *The Physics of Non-Crystalline Solids*, ed by D. Pye, W.C. LaCourse, H.J. Stevens (Taylor & Francis, London 1992) p 59
92. A. Pradel, G. Taillades, C. Cramer, M. Ribes: Solid State Ionics **105**, 139 (1998)
93. S. Indris, P. Heitjans, H. E. Roman, A. Bunde: Phys. Rev. Lett. **84**, 2889 (2000)
94. S. Indris, P. Heitjans, H. E. Roman, A. Bunde: Defect Diffus. Forum **194-199**, 935 (2001)
95. M. Ulrich, A. Bunde, S. Indris, P. Heitjans: Phys. Chem. Chem. Phys. **6**, 3680 (2004)
96. S. Indris, P. Heitjans, M. Ulrich, A. Bunde: Z. Phys. Chem. **219**, 89 (2005)
97. N.J. Dudney: Ann. Rev. Mater. Sci. **19**, 113 (1989)
98. J. Maier: Prog. Solid St. Chem. **23**, 171 (1995)
99. J. Maier: Solid State Ionics **154-155**, 291 (2002); *ibid.* **157**, 327 (2003)
100. J. Maier: *Physical Chemistry of Materials: Ions and Electrons in Solids* (Wiley, Chichester 2004)
101. J.-M. Debierre, P. Knauth, G. Albinet: Appl. Phys. Lett. **71**, 1335 (1997)
102. A. Bunde, W. Dieterich, H.E. Roman: Phys. Rev. Lett. **55**, 5 (1985)
103. S. Indris, P. Heitjans: J. Non-Cryst. Solids **307–310**, 555 (2002)
104. M. Wilkening, S. Indris, P. Heitjans: Phys. Chem. Chem. Phys. **5**, 2225 (2003)
105. P. Heitjans, B. Bader, H.-J. Stöckmann, K. Dörr, G. Kiese, H. Ackermann, P. Freiländer, W. Müller-Warmuth, K. Meise-Gresch: Hyperfine Interact. **15/16**, 597 (1983)
106. H.-J. Stöckmann, P. Heitjans: J. Non-Cyst. Solids **66**, 501 (1984)

107. W. Faber, P. Heitjans, A. Schirmer. In: *Dynamics of Disordered Materials*, Springer Proceedings in Physics, vol 37, ed by D. Richter, A.J. Dianoux, W. Petry, J. Teixeira (Springer, Berlin Heidelberg New York 1989) p 69
108. W. Pannhorst, R. Haug, E. Rodek, K. Stetter: J. Non-Cryst. Solids **131-133**, 488 (1991)
109. P. Maass, A. Bunde, M.D. Ingram: Phys. Rev. Lett. **68**, 3064 (1992)
110. W. Dieterich, D. Knödler, P. Pendzig: J. Non-Cryst. Solids **172-174**, 1237 (1994)
111. T. Wichmann, K.G. Wang, K.W. Kehr: J. Phys. A: Math. Gen. **27**, L263 (1994)
112. B. Munro, M. Schrader, P. Heitjans: Ber. Bunsenges. Phys. Chem. **96**, 1718 (1992)
113. K. Ngai: J. Chem. Phys. **98**, 6424 (1993)
114. R. Goldstein: Diploma Thesis, Universität Hannover (2001)
115. F. Qi, C. Rier, R. Böhmer, W. Franke, P. Heitjans: Phys. Rev. B **72**, 104301 (2005)
116. A. Körblein, P. Heitjans, H.-J. Stöckmann, F. Fujara, H. Ackermann, W. Buttler, K. Dörr, H. Grupp: J. Phys. F: Met. Phys. **15**, 561 (1985)

10 PFG NMR Studies of Anomalous Diffusion

Jörg Kärger and Frank Stallmach

10.1 Introduction

Depending on the system under study, particle diffusivities cover a huge range of values from $\sim 10^{-20}$ m^2s^{-1} for solids (see Chaps. 1-9) up to ~ 1 m^2s^{-1} for dilute gases. However, the nature of a system does not only affect the *rate* of particle propagation, it is also the *pattern of its time dependence*, which may be a function of the system. In general, the mean square displacement of the migrating particles increases in proportion to the observation time. This is the case of normal diffusion, which is commonly described by Fick's laws. The fundamental relations of normal diffusion are summarized in Chap. 1 of this textbook, and most of the other chapters are also devoted to this case. However, under the influence of internal structures, particle propagation may deviate from this pattern. Owing to the intimate relation between structure and mobility, in the last few years the study of "anomalous diffusion" has become a most attractive subject of both fundamental and applied research. Since the time exponent of the mean square displacement is generally found to be smaller than 1, anomalous diffusion is often referred to as *subdiffusion*. Chapters 13, 16 - 19, 21 and 22 deal with experimental and theoretical aspects of this case. The present chapter is devoted to the influence of interfaces on molecular propagation. It is based on the corresponding chapter of the first edition, which one of us has co-authored with G. Fleischer and U. Roland. With great regret we have to announce that Gerald Fleischer has passed away in 1999. His oeuvre as one of the pioneers in applying PFG NMR to diffusion in macromolecular systems remains of lasting value.

In the present chapter, the term interface is meant in a rather broad sense. It refers to fluid/solid interaction in microporous zeolitic adsorbate-adsorbent systems (Sect. 10.4) and in meso- and macroporous amorphous materials (Sect. 10.5) as well as to fluid/fluid interaction in internally structured macromolecular melts and solutions (Sect. 10.6). In all these cases, deviations from ordinary diffusion occur, and the method of pulsed field gradient (PFG) NMR (Sect. 10.3) turns out to be a most helpful technique for their investigation.

10.2 The Origin of Anomalous Diffusion

The diffusion path of a particle consists of numerous displacements caused by the stochastically changing interaction between the particle and its surroundings. In many cases, in particular in homogeneous systems and for sufficiently large observation times, it is possible to divide the diffusion time into intervals, which are large enough so that the displacements in any of these time intervals are independent of each other. In this case, the mean square displacement $\langle r^2(t)\rangle$ of the particles may be shown to depend in a simple way on the observation time t. For this purpose we consider the vector sum of the displacements $\Delta \boldsymbol{r}_i$ during the individual time intervals, which for simplicity are assumed to be of equal duration Δt. It holds

$$\begin{aligned}\langle r^2(t)\rangle &= \left\langle \left(\sum \Delta \boldsymbol{r}_i\right)^2 \right\rangle \\ &= \left\langle \sum_i (\Delta \boldsymbol{r}_i)^2 \right\rangle + \left\langle \sum_{i\neq j} \Delta \boldsymbol{r}_i \Delta \boldsymbol{r}_j \right\rangle = \left\langle (\Delta \boldsymbol{r})^2 \right\rangle \cdot t/\Delta t \end{aligned} \tag{10.1}$$

where the last equality results as a consequence of the missing correlation between subsequent displacements $\Delta \boldsymbol{r}_i$. With $\left\langle (\Delta \boldsymbol{r})^2 \right\rangle$ as the mean square value of the displacement during the considered time interval Δt, (10.1) reflects the expected proportionality between the mean square displacement $\langle r^2(t)\rangle$ and the observation time t in the case of ordinary diffusion. The absence of correlation between the displacements during different time intervals, i.e. the disappearance of the cross term in (10.1), turns out to be a necessary and sufficient condition for normal diffusion. This statement does clearly not imply that under the condition of normal diffusion any correlation between subsequent displacements is excluded. A famous example is the correlation effect of solid state diffusion (see Sect. 1.6.1 in Chap. 1 and Sect. 18.4.3 in Chap. 18), where subsequent displacements are preferentially directed into opposite directions. However, summing the times for the individual steps to longer time intervals with correspondingly larger displacements (being the vector sum of the individual displacements), these larger displacements are soon found to be independent of each other. Hence, the correlation effect in solid state diffusion is found to affect the absolute value of the diffusivity (by the "correlation factor" f – see Sect. 1.6.1 and Sect. 18.4.3) without leading to deviations from normal diffusion. Anomalous diffusion can only be observed if the correlation between the displacements is preserved over the total duration of the experiment. It is therefore one of the crucial questions to be answered in the following sections, what is the mechanism, which ensures the correlation between the displacements over the whole observation time.

Deviations from normal diffusion may follow various patterns. Using the conception of a fractal structure (see Chap. 19), the correlation between the mean square displacement and the observation time may be represented in a quite general way. For deriving this correlation we have only to imply the

self-similarity of the system. Owing to the stochastic nature of diffusion, it is sufficient to imply the self-similarity of the system in a statistical sense. The effect of this self-similarity of the structure on molecular propagation is assumed to be reflected by a scaling law, which implies that by enhancing the elementary structure length from l to μl the corresponding time step has to be enhanced from t to νt. The actual values of the scaling parameters μ and ν depend on the system under study. The efforts to be exerted on their determination (see Chap. 19 and [1, 2]) are generally not negligibly small. However, when these parameters are known, the relation between the mean square displacement and the observation time t may be deduced very easily: As a consequence of the scaling law one may note the correspondence

$$\langle r^2 \rangle = f(t) \leftrightarrow \left\langle (\mu r)^2 \right\rangle = f(\nu t), \tag{10.2}$$

where $f(t)$ is an (at first) unknown function representing the time dependence of the mean square displacement. The right-hand side of this correspondence may be rearranged leading to the equation

$$\langle r^2 \rangle = f(t) = \frac{1}{\mu^2} f(\nu t) \tag{10.3}$$

The second equality is obviously obeyed by

$$\langle r^2(t) \rangle = f(t) \propto t^{\kappa} \tag{10.4}$$

with

$$\kappa = 2 \frac{\log \mu}{\log \nu}. \tag{10.5}$$

The mean square displacement is thus quite generally found to obey a power-law time-dependence (cf. (10.4)) where exponent κ is given by (10.5). In the case of ordinary diffusion due to one-dimensional random walk with constant step size, e.g., μ and ν are found to be 2 and 4, respectively ([3], p. 61). This leads to the familiar result of proportionality between $\langle r^2 \rangle$ and t, which has been verified, already, by means of (10.1). In the case of anomalous diffusion, independent of the considered time interval, subsequent displacements are more likely directed into opposite directions, making the cross term $\sum_{i \neq j} \Delta \boldsymbol{r}_i \Delta \boldsymbol{r}_j$ in (10.1) negative. The mean square displacement is thus expected to increase less than linearly with the observation time. One has therefore to expect that $\kappa \leq 1$, with $\kappa = 1$ characterizing the case of normal diffusion.

In several places of this book (Chaps. 2, 3, 18, 19 and 23), the phenomenon of diffusion is considered on the basis of the so-called propagator or (as generally referred to in neutron scattering and Mößbauer spectroscopy) Van Hove self-correlation function (with the notation $G_{\mathrm{s}}(r, t)$). It represents the probability density of particle propagation and contains the maximum information accessible about the diffusion properties of the system. Like in the

case of quasielastic neutron scattering (QENS, see chapters 2, 3 and 13), the propagator is directly related to the experimental data of pulsed field gradient (PFG) NMR, which shall be explicitly shown in the subsequent section. In contrast to QENS, which traces molecular motion over not more than a few tens of nanometers maximum, typical displacements monitored by PFG NMR are of the order of micrometers. Therefore, the propagator generally results as the superposition of many individual displacements. If – as in the case of normal diffusion – these displacements are independent of each other, on the basis of the central limit theorem [4] the resulting probability distribution may be shown to be a Gaussian ([3], pp. 63–67). In PFG NMR one is able to monitor molecular displacements in the direction of the magnetic field gradient, which is commonly assumed to coincide with the z-direction. In the case of normal diffusion the propagator thus results to be

$$P(z,t) = \frac{1}{\sqrt{2\pi\langle z^2(t)\rangle}} \exp\left(\frac{-z^2}{2\langle z^2(t)\rangle}\right) , \tag{10.6}$$

where $P(z,t)\mathrm{d}z$ denotes the probability that during a time interval t the z coordinate of a particle is shifted by a value between z and $z + \mathrm{d}z$. Equation(10.6) may be interpreted as an immediate consequence of the central limit theorem. However, it also follows by applying Fick's second law (see, e.g., (1.8) of Chap. 1) with the initial condition

$$P(z,0) = \delta(z) \tag{10.7}$$

to the propagator. Moreover, in doing so, the mean square displacement is found to be

$$\langle z^2(t)\rangle = 2Dt \tag{10.8}$$

in complete agreement with (10.1) and with the requirement of the central limit theorem that the square width of the distribution increases in proportion with the number of elements (time intervals) considered for the total distribution. Equation (10.8) is commonly referred to as Einstein's relation with D denoting the coefficient of self-diffusion (tracer diffusion) as appearing in Fick's first law for labelled particles.

Even under the conditions of anomalous diffusion, the propagator is often found to be satisfactorily well approached by a Gaussian (cf. (10.6)). In some cases, e.g. in the long-time limit of single-file diffusion (see Sect. 10.4.5), (10.6) holds even strictly. It is therefore common practice in PFG NMR to analyse diffusion phenomena exclusively on the basis of an effective diffusivity

$$D_{\mathrm{eff}}(t) \equiv \frac{\langle z^2(t)\rangle}{2t}, \tag{10.9}$$

which results by inverting (10.8). In the case of normal diffusion, D_{eff} is clearly independent of the observation time and coincides with the self-diffusivity.

Under the conditions of anomalous diffusion, D_{eff} becomes time dependent. If (10.4) is valid, the time dependence of D_{eff} becomes

$$D_{\mathrm{eff}}(t) \propto t^{\kappa-1}. \tag{10.10}$$

Since $\kappa \leq 1$, the effective diffusivity is found to decrease with increasing observation time. Anomalous diffusion is therefore (like in the cases considered in Chaps. 12, 13, 16 and 19) often referred to as sublinear diffusion or even subdiffusion. In the case of completely restricted diffusion, e.g. diffusion in a space confined by impenetrable barriers, $\langle z^2 \rangle$ remains constant for sufficiently long observation times, and we have $D_{\mathrm{eff}} \propto t^{-1}$ for $t \to \infty$.

10.3 Fundamentals of PFG NMR

10.3.1 The Measuring Principle

As in the case of NMR tomography [5], the application of NMR for studying molecular transport is based on the Larmor condition

$$\omega = \gamma B \tag{10.11}$$

between the magnetic field and the resonance frequency (multiplied by 2π) for transitions between the Zeeman levels of the nuclear spins in the magnetic field. The magnetogyric ratio γ is a characteristic quantity of the nucleus under study (e.g. $2.67 \cdot 10^8$ $\mathrm{T}^{-1}\mathrm{s}^{-1}$ for ^{1}H). The Larmor frequency ω may be intuitively understood as the precessional frequency of the nuclear spins (and hence of the nuclear magnetization) about the direction of the magnetic field. Superimposing the constant magnetic field B_0 by an inhomogeneous field $B_{\mathrm{add}} = gz$ (the "field gradient"), the Larmor frequency becomes space dependent:

$$\omega = \omega(z) = \gamma(B_0 + gz) = \omega_0 + \gamma g z \ , \tag{10.12}$$

where the z-coordinate is assumed to be aligned along the direction of the applied field gradient. In the PFG NMR technique (see, e.g., [3, 6–10]), the inhomogeneous field is applied over two short time intervals of duration δ separated by the "observation time" Δ. These two field gradient pulses are applied either with opposite signs (i.e. the amplitudes $+g$ and $-g$) or with a radiofrequency (rf) pulse of suitable duration (a "π-pulse") in between. In both cases, the effect of the second field gradient pulse has to be subtracted from that of the first one. The phase shift φ of a nuclear spin, which during the observation time Δ has been displaced over a distance $(z_2 - z_1)$ in z-direction, in comparison with a spin, which has remained at the same position, is therefore

$$\varphi = \gamma g \delta (z_2 - z_1) \ . \tag{10.13}$$

The quantity monitored in PFG NMR is the amplitude of the "spin echo" as generated, e.g., in the $\frac{\pi}{2} - \tau - \pi - \tau -$ echo sequence (see also Sect. 9.3

in Chap. 9 (Fig. 9.10), Sect. 13.2.1 in Chap. 13, Sect. 17.2.2 in Chap. 17 (Fig. 17.1)). Instead of PFG NMR, therefore, sometimes also the term PGSE (pulsed gradient spin-echo) NMR is used. The amplitude of this spin echo is proportional to the total magnetization, i.e., to the vector sum of the contributions of the individual spins. The application of field gradient pulses thus leads to a signal (spin-echo) attenuation

$$\begin{aligned} \Psi &= \iint p(z_1)P(z_2, z_1, \Delta) \cos\left(\gamma g \delta (z_2 - z_1)\right) \mathrm{d}z_2 \mathrm{d}z_1 \\ &= \int P(z, \Delta) \cos(\gamma g \delta z) \mathrm{d}z, \end{aligned} \tag{10.14}$$

with

$$P(z, \Delta) = \int p(z_1) P(z_1 + z, z_1, \Delta)\ \mathrm{d}z_1. \tag{10.15}$$

$p(z_1)$ is the *a priori* probability (density) to find a spin at position z_1 for $t = 0$ and $P(z_2, z_1, \Delta)$ the probability (density) that the spin has moved from z_1 to position z_2 in the time interval $t = \Delta$. $P(z, \Delta)$ is the so-called mean propagator, i.e., the propagator averaged over all starting positions z_1. It is the probability density that an arbitrarily selected particle in the sample is shifted over a distance z in z-direction (which is the direction of the magnetic field gradient) during the time interval between the two field gradient pulses. Since in a heterogeneous sample the probability function of molecular displacement may depend on the starting point, in this case the propagator as used in (10.15) is understood as a mean value over the sample.

10.3.2 The Mean Propagator

By Fourier inversion of (10.14) the mean propagator may be directly deduced from the primary data of the PFG NMR experiment, yielding

$$P(z, \Delta) = \frac{1}{2\pi} \int \Psi(\delta g, \Delta)\ \cos(\gamma \delta g z)\, \mathrm{d}(\gamma \delta g)\ . \tag{10.16}$$

As an example, Fig. 10.1 displays the first application of this possibility showing the propagation patterns of ethane in beds of zeolite NaCaA with two different crystallite sizes [11]. Zeolite NaCaA consists of microporous crystallites whose diffusion properties are discussed in more detail in Sect. 10.4 and in Sect. 23.4 of Chap. 23 [12–14]. Being symmetric in z, for simplicity the propagator is only represented for $z \geq 0$. For the lowest temperature (153 K), the distribution widths of molecular displacement during the considered time intervals ($5 \ldots 45$ ms) are found to be small in comparison with the mean radius of the larger crystallites ($8\,\mu$m). In this case, the observed mean square displacement increases in proportion with the observation time as required for normal diffusion so that PFG NMR is able to monitor genuine

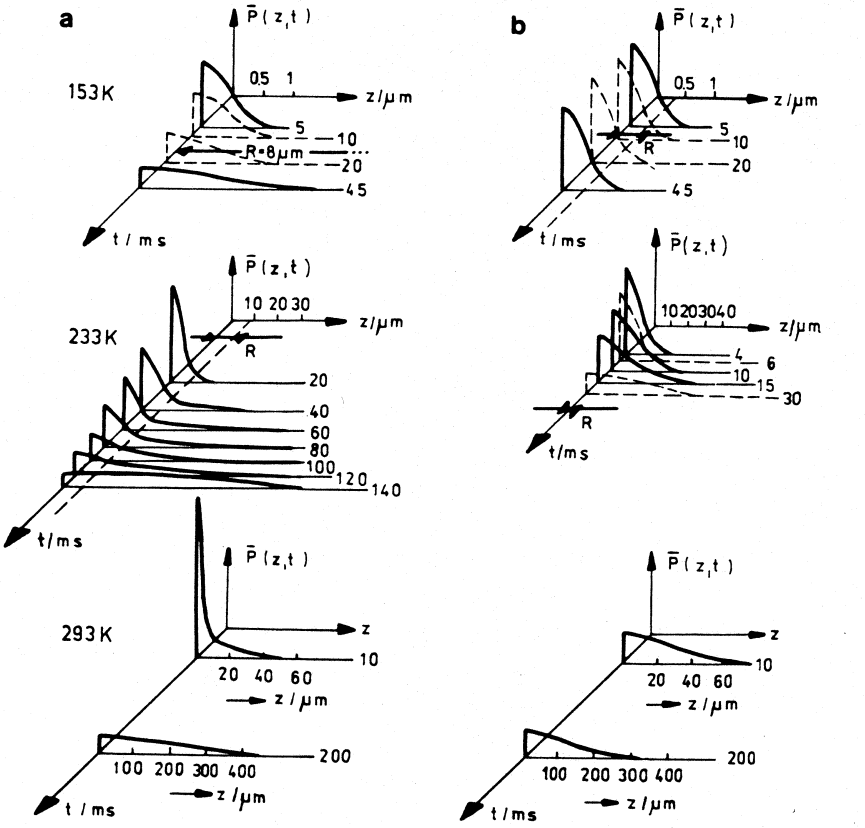

Fig. 10.1. Propagator representation of the self-diffusion of ethane in NaCaA zeolite: (a) loading 40 mg/g, mean crystallite radius $R = 8\,\mu$m; (b) 58 mg/g, $R = 0.4\,\mu$m [11].

intracrystalline self-diffusion. In the smaller crystallites, obviously, molecular propagation is terminated by the surface of the crystallites so that PFG NMR provides information on the size of the crystallites rather than the intrinsic mobility. This way of tracing the extension of microscopic regions has become popular under the name "dynamic imaging" [7, 15]. With increasing temperature, however, the thermal energy of the diffusing molecules becomes large enough so that a substantial fraction of the ethane molecules are able to surpass the step in the potential energy from the intracrystalline space into the surrounding gas phase (intercrystalline space). Consequently, distribution widths of molecular propagation much larger than the crystallite radii become possible. Eventually, the conditions for the application of the central limit theorem are again obeyed and molecular propagation is described by a Gaussian with an effective diffusivity D_{lr}. D_{lr} may be shown to be the prod-

uct of the diffusivity of the molecules in the intercrystalline space and their relative amount [16].

10.3.3 PFG NMR as a Generalized Scattering Experiment

Using complex notation and introducing the magnetic field gradient vector $\boldsymbol{g}$, (10.14) may be written in the form

$$\Psi(\gamma\delta\boldsymbol{g}, \Delta) = \int P(\boldsymbol{r}, \Delta)\, \exp(\mathrm{i}\gamma\delta\boldsymbol{g}\boldsymbol{r})\, \mathrm{d}\boldsymbol{r}\ . \tag{10.17}$$

The structure of this relation coincides with that of the self-term of the intermediate dynamical structure factor $I_\mathrm{s}(Q,t)$ of QENS as introduced by (3.7) in Sect. 3.2 of Chap. 3 and as $S(Q,t)$ in Sect. 13.2 of Chap. 13. Similar relations occur in Mößbauer spectroscopy (Chap. 2) and dynamic light scattering (Chaps. 15 and 16). They may be derived by Fourier transformation of (2.1) in Chap. 2 and of (15.3) together with (15.1) in Chap. 15, respectively, from frequency to time domain. PFG NMR may therefore be considered as a scattering experiment with a generalized scattering vector $\boldsymbol{q} = \gamma\delta\boldsymbol{g}$ [17–20]. With typical maximum values of g (50 T/m) and δ (2 ms; cf., e.g., [21–25]), for protons the generalized scattering vector is found to be of the order of $3 \cdot 10^7\ \mathrm{m}^{-1}$. This corresponds to minimum displacements observable by PFG NMR of $10 \ldots 100\,\mathrm{nm}$.

Inserting (10.6) and (10.8) into (10.14) (or the equivalent three-dimensional expressions into (10.17)), the spin-echo attenuation is found to be a simple exponential

$$\Psi = \exp(-\gamma^2\delta^2 g^2 D\Delta)\ . \tag{10.18}$$

Identifying $\gamma\delta g$ as the generalized scattering vector, (10.18) coincides with the intermediate scattering function in the so-called diffusion limit in QENS and light scattering. Obviously, in this case the self-diffusivity (and via (10.8) the mean square displacement) results in a straightforward way from the slope of the spin-echo attenuation in a semilogarithmic representation versus $\gamma^2\delta^2 g^2$. As long as the propagator is a Gaussian, (10.18) is rigorously correct and implies the cases of normal and anomalous diffusion, if D is understood in the more general sense as an effective diffusivity as defined by (10.9).

If molecular diffusion is confined to a certain range, for sufficiently large observation times the propagator approaches a time-independent function $P_\infty(\boldsymbol{r})$, which is determined by the distribution of the molecules under study in the confining volume. Therefore, the spin-echo attenuation attains a time-independent value

$$\begin{aligned}\Psi_\infty(\gamma\delta\boldsymbol{g}) &\equiv \lim_{\Delta\to\infty} \Psi(\gamma\delta\boldsymbol{g}, \Delta) \\ &= \iint p(z_1)\, P(z_2, z_1, \infty) \exp\left(\mathrm{i}\gamma g\delta(z_2 - z_1)\right)\, \mathrm{d}z_2\, \mathrm{d}z_1 \\ &= \left| \int p(z)\, \exp(\mathrm{i}\gamma g\delta z)\, \mathrm{d}z \right|^2 = |F(q)|^2\ ,\end{aligned} \tag{10.19}$$

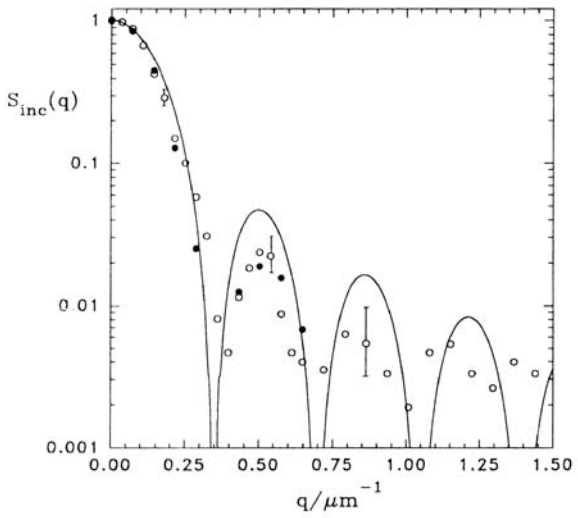

Fig. 10.2. Spin-echo attenuation of n-heptane diffusing in the space between parallel glass plates with the normal parallel to the direction of the field gradient. The curve is the diffraction pattern of a single slit of 18 μm width [26].

where we have used $P(z_2, z_1, \infty) = p(z_2)$. Equation (10.19) corresponds to the elastic incoherent structure factor (EISF) of QENS ((3.18) of Chap. 3). $F(q)$ is the Fourier transform of the confining geometry $p(z)$. The expression in the last line of (10.19) is known as the form factor in scattering theory. It describes the diffraction pattern of the scattering geometry $p(z)$. This analogy of PFG NMR with a scattering experiment was nicely demonstrated in [26], cf. Fig. 10.2, where the echo attenuation of n-heptane diffusing in the space between parallel glass plates was compared with the diffraction pattern of the slit.

10.3.4 Experimental Conditions

The measurement of the spin-echo attenuation Ψ as a function of the field gradient pulse programme clearly implies the existence of a measurable NMR signal. Therefore, the molecules under study must contain "NMR active" atoms, i.e. nuclei with a non-vanishing magnetogyric ratio, which have to occur with a sufficiently large density. For hydrogen, e.g., which offers the best measuring conditions with respect to both the minimum number of diffusants and minimum displacements, typical minimum concentrations are of the order of one hydrogen nucleus per 10 nm^3 which corresponds to about 0.1 moles per litre. Hence, PFG NMR is not very appropriate for studying the diffusivities of species, which are only present in minor concentration. In prin-

ciple, clearly, with a sufficiently large number of acquisitions, even at much smaller concentrations NMR signals may be generated. For the measurement of small diffusivities, however, such a procedure is far more subjected to the risk that signal attenuation is due to a mismatch between the field gradient pulses or mechanical instabilities rather than to diffusion. Diffusivity data determined under such conditions may dramatically exceed the real values. We shall return to this point at the end of this section.

The measuring conditions are furthermore determined by the nuclear magnetic relaxation times (cf. Sect. 9.3 in Chap. 9). In the above introduced primary or Hahn-echo experiment ($\frac{\pi}{2} - \tau - \pi - \tau -$ echo), the observation time is essentially limited by the transverse relaxation time T_2. If the longitudinal relaxation time T_1 is notably larger than T_2, the observation time may be further enhanced by applying the stimulated echo ($\frac{\pi}{2} - \tau_1 - \frac{\pi}{2} - \tau_2 - \frac{\pi}{2} - \tau_1 -$ echo) where the field gradient pulses are applied during the two time intervals of duration τ_1. As in the case of the primary echo, signal attenuation during these two time intervals occurs with the time constant T_2, while during the time interval τ_2 signal attenuation is governed by T_1. Typical values of T_2 and T_1 and hence of the observation times in diffusion studies by PFG NMR are of the order of milliseconds to seconds.

In deriving (10.14, 10.15) and (10.18) we have presumed that during the field gradient pulses the spins assume well-defined positions. Such an assumption is clearly only acceptable if molecular displacements during the field gradient pulses are negligibly small in comparison with those between the pulses. In the case of normal diffusion it may be shown [6–9] that these relations may be maintained also for field gradient pulses of finite duration by simply replacing the quantitiy Δ by an "effective" observation time $\Delta - \frac{\delta}{3}$.

The PFG NMR method works under the supposition that the values of δg for the first and second field gradient pulses are identical. Any difference has the same effect as translational motion of the molecules under study, leading to a signal attenuation. The correct application of PFG NMR therefore necessitates extremely stable gradient currents, which generate the field gradient pulses within suitably structured field gradient coils [5–8]. Likewise high mechanical stability of both the field gradient coils and the sample must be ensured, since any movement of the sample with respect to the coils would also lead to differences in the local field at the instants of the first and second field gradient pulses and to an additional attenuation of the spin echo.

Intrinsic differences in the magnetic susceptibility of heterogeneous samples give rise to internal field gradients, which are superimposed upon the externally applied ones. While under the influence of the modest external magnetic fields produced by iron magnets, for a number of important adsorbate-adsorbent systems such as zeolites these superpositions could be shown to be of no disturbing influence if only sufficiently large pulse gradient intensities are applied [27], in PFG NMR diffusion measurements with superconducting magnets such disturbing influences have to be considered. As a most effec-

tive possibility to circumvent such difficulties, the application of pairs of field gradient pulses with alternating signs ($\pm g$) separated by appropriate rf (viz. π) pulses has been suggested [28, 29].

Methodical development in PFG NMR is focussed on the generation of extremely large field gradient pulses [21–25]. The difficulties due to the requirement of perfect matching between the two field gradient pulses may be circumvented by applying the stimulated spin echo under the influence of a strong constant field gradient [8, 30–32], which is provided by the stray field of the superconducting magnet ("stray field gradient" (SFG) NMR). The intensity of the stimulated echo is influenced by the field gradient only during the two time intervals of duration τ_1. These are exactly those time intervals during which – as we have seen above – also the pulsed field gradients are applied. Therefore, signal attenuation is described by the same equations as in the case of PFG NMR with the pulse width δ replaced by τ_1 and the observation time Δ being equal to $\tau_1 + \tau_2$. By this technique, presently the largest field gradient "amplitudes" (up to 185 T/m) may be achieved [33]. In comparison with PFG NMR, however, the signal-to-noise ratio is dramatically reduced since only a slice of the sample of thickness of the order of 0.1 mm is at resonance, so that much larger acquisition times are inevitable. These are, however, much easier to be accomplished since the requirement of identical field gradient "pulses" is automatically fulfilled in this technique. A severe disadvantage of SFG NMR is the fact that the large constant magnetic field gradient excludes the possibility of Fourier transform PFG NMR for multicomponent diffusion studies [34, 35]. SFG NMR measurements are additionally complicated by the fact that by varying the "width" of the field gradient "pulses" the signal is affected by both diffusion and transverse nuclear magnetic relaxation.

10.4 PFG NMR Diffusion Studies in Regular Pore Networks

At a first glance, regular pore networks do not seem to be a suitable system for studying anomalous diffusion. There are, however, a number of reasons, which justify the inclusion of this section in the present chapter. Regular pore networks of rather diverse nature are provided by the zeolites [3, 36, 37]. Originally, zeolites have only been known as minerals. They are microporous, crystalline aluminosilicates. Starting in the fifties of the last century, however, also artificial zeolites have been synthesized. As an example, Fig. 23.5 of Chap. 23 shows the structure of a zeolite of type LTA – in short – an A-type zeolite. The last few years have been characterized by an explosion of new zeolite structure types [37]. Most of them have no natural counterpart. The great interest in zeolites results from their potential as selective adsorbents, catalysts and cation exchangers, leading to profits of the order of hundreds of billions of dollars worldwide attained per year by their production and

application. However, zeolites have also become an attractive object of fundamental research. Owing to their well-defined structure and the diversity of their nature, zeolites have proved to be ideal model systems, in particular for studying the interaction of molecules with solid surfaces as exemplified in Pfeifer's classical survey [38]. Thus, zeolites have also become a most attractive host system for studying molecular diffusion [3]. They have in particular turned out to be an ideal system for demonstrating the versatility of PFG NMR. This possibility and the numerous correlations with Chap. 23 motivated us to include this section into a chapter about anomalous diffusion. Moreover, we shall also learn that under certain conditions even a regular zeolite pore system may give rise to anomalous diffusion.

10.4.1 The Different Regimes of Diffusion Measurement

As an example, Fig. 10.3 shows an Arrhenius plot of the effective diffusivity (cf. (10.9)) as determined by PFG NMR for n-hexane in a sample of NaX zeolite crystallites of mean diameter 4 μm for an observation time of 4 ms. One may clearly distinguish between three different regimes. For temperatures below about 220 K, the diffusion paths are sufficiently small in comparison with the crystallite diameters, so that the effective diffusivity is exclusively

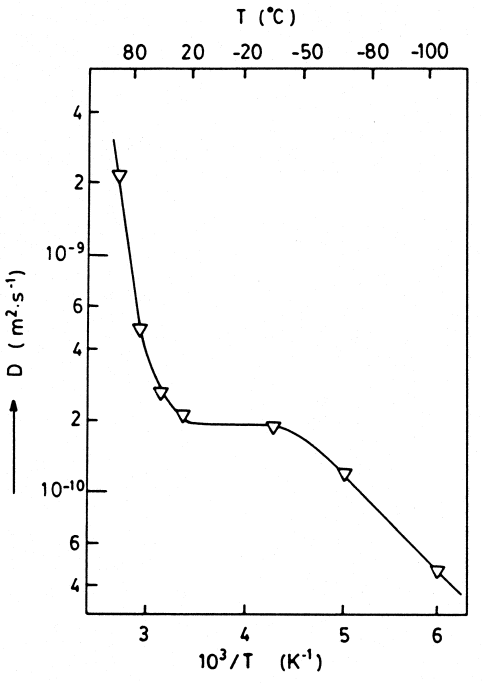

Fig. 10.3. Temperature dependence of the effective self-diffusivity for n-hexane in a sample of NaX zeolite crystals of mean diameter 4 μm at a sorbate concentration of 20 mg/g and observation time 4 ms [3].

determined by intracrystalline diffusion. The situation is the same as in the propagator representation of Fig. 10.1 (a) at 153 K. This is the regime of PFG NMR measurements which shall be exclusively considered in the subsequent Sects. 10.4.2 to 10.4.5. In the subsequent temperature range up to about 290 K, the diffusion paths are limited by the extensions of the crystallites (situation as in Fig. 10.1 (b) at 153 K). Under the assumption that (i) the confinement is perfect and that (ii) the observation time is much larger than the mean diffusion time over a distance of the order of the crystallite radius, the signal attenuation obeys (10.19), being the equivalent of the EISF of QENS. By assuming that the crystallites may be approximated by spheres with mean square radius R^2, (10.19) approaches [6–9]

$$\Psi_\infty(\gamma\delta g) = \exp\left(-\frac{\gamma^2\delta^2 g^2 R^2}{5}\right) \tag{10.20}$$

corresponding to an effective diffusivity

$$D_{\text{eff}} = \frac{R^2}{5\Delta} \,. \tag{10.21}$$

The root mean square radius obtained via (10.21) with the experimental value of D_{eff} ($2 \cdot 10^{-10}$ m^{2}s^{-1}) does in fact coincide with the microscopically determined mean crystallite radius of 2 μm. Finally, for temperatures above 290 K, the thermal energy of the molecules is high enough so that a sufficiently large number of molecules is able to leave the individual crystallites during the observation time. Molecular transport is now determined by long-range diffusion (situation in Fig. 10.1 (b) at 223 K and 293 K).

Deviations from normal diffusion become immediately visible by representing the mean square displacement as a function of the observation time. As an example, Fig. 10.4 shows the mean square displacement of n-butane in a bed of zeolite crystallites of type NaX with a mean diameter of 16 μm. As expected, for displacements either much smaller or much larger than the crystallite diameter, the mean square displacement is found to increase in proportion with the observation time. This corresponds to the limiting cases of intracrystalline and long-range diffusion. The trend of the deviations from straight lines for displacements in the vicinity of the crystallite diameters may be easily rationalized on the basis of (10.1). In contrast to normal diffusion, the cross terms are not negligible anymore. At low temperatures, molecules encountering the crystallite surface are more likely reversed in the direction of propagation. This leads to negative cross terms and hence to deviations of the mean square displacement to lower values. At high temperatures, molecules encountering the surface may easily escape into the intercrystalline space and profit by the high intercrystalline mobility. Subsequent steps are therefore more likely to be oriented into the same direction, leading to an enhancement in the mean square displacements in comparison with linearity in time.

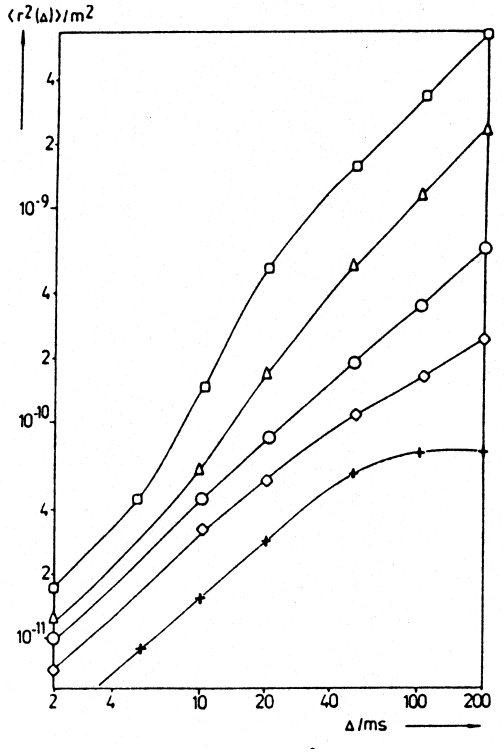

Fig. 10.4. Mean square displacements $\langle r^2(\Delta)\rangle$ of n-butane on zeolite NaX with a mean crystallite diameter of 16 μm at a sorbate concentration of 80 mg/g at 183 K(+), 223 K($\diamond$), 243 K ($\bigcirc$), 258 K($\triangle$), and 273 K($\square$), respectively, in dependence on the observation time Δ [39].

10.4.2 Intracrystalline Self-Diffusion

The MD simulations presented in this textbook (Chap. 23, Sect. 23.4) are exclusively devoted to the regime of intracrystalline zeolitic diffusion. A survey of the different patterns of concentration dependence so far obtained experimentally is displayed in Fig. 10.5. Depending on the nature of the system under study, the self-diffusivity may vary with varying concentration in quite different ways. A decrease of molecular mobility with increasing concentration (patterns 1 and 2) may intuitively be understood by the increasing mutual hindrance of the molecules, while any other dependence indicates the dominating influence of the interaction between the diffusants and the zeolite pore network. This tendency is demonstrated quantitatively in Sect. 23.4 of Chap. 23 (Fig. 23.11, right), where the diffusivity is found to decrease with increasing loading for large diameters of the "windows" between adjacent

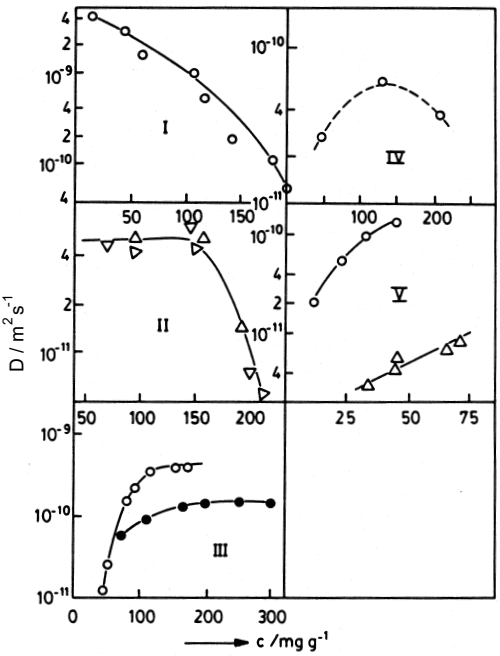

Fig. 10.5. Patterns of concentration dependence of intracrystalline self-diffusivities as determined from PFG NMR measurements. (I) n-hexane in NaX at 358 K; (II) ortho (△), meta (▷) and para (▽) xylenes in NaX at 293 K; (III) ammonia (○) and water (●) in NaX at 298 K; (IV) acetonitrile in NaX at 393 K; (V) ethane (○) at 173 K and propane (▽) at 413 K in NaCaA [3].

pores (dominating interaction between the diffusants) while it increases for small windows (dominating influence of the pore system) [12].

10.4.3 Correlated Diffusion Anisotropy

The fact that zeolitic diffusion has to proceed in a well-defined network of pores and channels gives rise to a special type of correlation in the path of molecular propagation. While the correlation effect in solids (see Sects. 1.6.1 in Chap. 1 and 18.4.3 in Chap. 18) refers to the orientation of subsequent steps, correlation in zeolitic diffusion effects that propagation in different directions may not be independent from each other. As an example, Fig. 10.6 schematically represents the channel network of zeolite ZSM-5 by showing the axes of the so-called straight channels (in y-direction) and of the sinusoidal ones (in x-direction). Obviously, molecular propagation in z-direction implies alternating displacements in x- and y-directions, so that the diffusivities in these three directions (the principal elements of the diffusion tensor – see (1.2) of Chap. 1) are correlated with each other. Under the assumption that

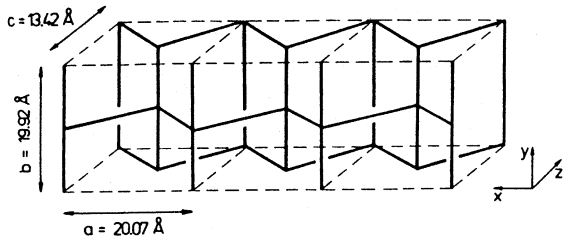

Fig. 10.6. Outline of the channel network of ZSM-5 type zeolites over three adjacent unit cells. The straight and zig-zag channels are oriented along the y and x directions, respectively.

molecular displacements between the intersections of the channel network are independent from each other, the correlation rule of zeolitic diffusion in ZSM-5 may be shown to read [40]

$$\frac{c^2}{D_z} = \frac{a^2}{D_x} + \frac{b^2}{D_y}, \tag{10.22}$$

where a, b and c denote the dimensions of the unit cell as indicated in Fig. 10.6. It has been confirmed by MD simulations [41] that (10.22) provides an excellent first-order estimate of diffusion anisotropy in zeolites ZSM-5 and silicalite-1, and may thus serve as a reasonable starting point for PFG NMR measurements of diffusion anisotropy in ZSM-5 by PFG NMR [42].

Deviations from (10.22) have been quantitatively accounted for in [43] by introducing a memory parameter β via the equation

$$\beta = \frac{\frac{c^2}{D_z}}{\frac{a^2}{D_x} + \frac{b^2}{D_y}} \tag{10.23}$$

Comparison with (10.22) yields $\beta = 1$ for the no-memory case. Since molecular propagation in z-direction can only occur in consequence of particle exchange between different types of channel segments, $\beta > 1$ (i.e. a diminished value of D_z) indicates that molecular propagation tends to proceed within one and the same type of channel, while $\beta < 1$ refers to enhanced exchange rates. These differences may be easily taken account of by allowing for a particle memory, which permits the particles to choose their further migration path depending on the channel segment along which they have got to a given channel intersection [44, 45] .

10.4.4 Transport Diffusion Versus Self-Diffusion

From a practical point of view, molecular transport under the influence of concentration gradients is of much greater relevance than self-diffusion, since

transport diffusion may be the rate limiting step for a number of applications. The coefficients of transport diffusion (D_t, in the terminology of QENS – see Sect. 3.11 in Chap. 3 – generally referred to as the coefficient of chemical or collective diffusion) is usually related to the self-diffusivity by the Darken relation (see Chap. 14, Sect. 14.3 and [3], p. 13)

$$D_{\mathrm{t}} = D\frac{c}{kT}\frac{\mathrm{d}\mu}{\mathrm{d}c} = D\frac{\mathrm{d}\ln p}{\mathrm{d}\ln c}, \tag{10.24}$$

where μ is the chemical potential of the diffusing species and p denotes the equilibrium pressure necessary to maintain the sorbate at concentration c. The "thermodynamic factor" $\mathrm{d}\ln p/\mathrm{d}\ln c$ may be easily determined from the adsorption isotherm $c(p)$. The notation of (10.24) is correct under the assumption of an ideal gas phase. Otherwise, the thermodynamic factor has to be used in the more rigorous form $\frac{1}{kT}\mathrm{d}\mu/\mathrm{d}\ln c$. This is the notation used, e.g., in Sect. 3.12 of Chap. 3. Equation (10.24) implies in particular the quite general result that in the limit of small concentrations (i.e. for $c \propto p$) the coefficients of transport diffusion and self-diffusion coincide. Exactly the same message is provided by diffusion studies with liquid mixtures, where at trace concentration of a component the self-diffusion coefficient of this component approaches the mutual diffusion coefficient (Chap. 14, Sect. 14.3).

In contrast to these theoretical predictions, the comparison between the transport diffusivities deduced from uptake experiments and the PFG NMR self-diffusivity data yielded remarkable discrepancies [38, 46]. A critical reconsideration of the uptake experiments has revealed that in many cases molecular uptake was controlled by processes different from intracrystalline diffusion. The message of PFG NMR about diffusion in zeolites has thus revolutionized the up to this time generally accepted picture, leading to substantially larger diffusivities [3]. However, even now the data on transport diffusion and self-diffusion are not entirely compatible. It is interesting to note that systems showing satisfactory agreement follow the concentration patterns (iii) to (v) of self-diffusion (see Fig. 10.5) while in the case of concentration patterns (i) and (ii) the self-diffusivities are often found to be up to two orders of magnitude larger than expected on the basis of the transport diffusivities resulting from uptake experiments. In complete agreement with this finding, MD simulations with methane in zeolite NaCaA (pattern (v)) reveal satisfactory agreement between the transport and self-diffusivities (see Fig. 23.20 right, of Chap. 23). As a possible explanation of this finding one should have in mind that (10.24) is not strictly correct. On the basis of the linear response theory (see Sects. 14.5 and 14.6 in Chap. 14 and 23.2.2 in Chap. 23) the self-diffusivity (cf. (14.28) in Chap. 14 and (23.15) in Chap. 23) is found to be

$$D = \frac{1}{3N}\sum_i \int_0^\infty \langle \boldsymbol{v}_i(0)\boldsymbol{v}_i(t)\rangle \mathrm{d}t \tag{10.25}$$

and the transport diffusivity (cf. (14.32) in Chap. 14)

$$D_{\mathrm{T}} = \frac{1}{3N} \sum_{i,j} \int_0^\infty \langle \boldsymbol{v}_i(0) \boldsymbol{v}_j(t) \rangle \mathrm{d}t \cdot \mathrm{d} \ln p / \mathrm{d} \ln c \tag{10.26}$$

with N and $\boldsymbol{v}_i(t)$ denoting the number of diffusants and the velocity of the i-th diffusant at time t, respectively. Obviously, the Darken relation (10.24) is an immediate consequence of (10.25) and (10.26) for negligible cross terms $\langle \boldsymbol{v}_i(0) \boldsymbol{v}_j(t) \rangle$ between the velocities of different particles. One may speculate that such a situation can in particular occur for dominating interaction between the diffusants and the zeolite lattice. From this point of view, the agreement of transport and self-diffusivity data with (10.24) for systems following the concentration patterns (iii) to (v) is not unexpected. Similarly, the mutual interaction between the diffusants for concentration patterns (i) and (ii) should lead to deviations from (10.24). Since, however, the largest discrepancies are observed for the smallest concentrations, where the mutual interaction must be expected to vanish, the proposed explanation is still far from exhaustive [47].

10.4.5 Single-File Diffusion

Molecular motion in one-dimensional channels is subject to a special pattern of propagation if mutual passages of the molecules are excluded. This is the famous case of single-file diffusion considered in detail in Chap. 18, Sect. 18.4.4. As a consequence of the confinement by the other diffusants, the propagation of an arbitrarily selected molecule, albeit proceeding in a completely regular pore network, is subjected to anomalous diffusion. Any displacement in a certain direction is only possible if the molecules in front of the diffusant under study are shifted into the same direction. This would lead to an enhanced particle concentration just in front and to a smaller concentration behind the diffusant under consideration. Subsequent displacements are therefore more likely to proceed into the opposite direction, tending to equilibrate concentration. In contrast to diffusion in solids (Chap. 1, Sect. 1.6.1 and Chap. 18, Sect. 18.4.3), the significance of this correlation increases with increasing displacements. The larger the displacements in one direction are, the larger is the probability that they are followed by displacements in the opposite direction. As a consequence, the cross term in (10.1) becomes increasingly important, leading to an exponent κ smaller than one in the time law for the mean square displacement. As the rigorous result ((18.107) of Chap. 18) one obtains

$$\langle z^2(t) \rangle = 2F\sqrt{t} \tag{10.27}$$

with

$$F = \lambda^2 \frac{1-\theta}{\theta} \frac{1}{\sqrt{2\pi\tau}} \ , \tag{10.28}$$

where in analogy to the Einstein relation (cf. (10.8)) the mobility factor F has been introduced [48]. Equations (10.27) and (10.28) are derived under

the assumption that molecular diffusion proceeds by stochastic jumps between adjacent adsorption sites of separation λ with a mean time τ between subsequent jump attempts. Jump attempts are only successful if the sites where the jumps are directed to are unoccupied. The occupation probability is denoted by θ. It could be shown by MD simulations [49] that the validity of (10.27) and (10.28) is not confined to the case of activated jumps but holds quite generally if the quantity θ is understood as a suitably defined pore-filling factor. Moreover, it could be shown [50] that as in the case of normal diffusion the propagator is given by a Gaussian, albeit with a mean square displacement increasing in proportion to the square root of the observation time (cf. (10.27)) rather than with the observation time itself (cf. (10.8)).

By use of the PFG NMR technique, zeolites with one-dimensional channels served as the first model systems where the validity of (10.27) could be demonstrated experimentally [51–54]. As an example, Fig. 10.7 shows the molecular mean square displacement of CF_4 in $AlPO_4$-5 at 180 K as a function of the observation time for different concentrations. At least for the larger concentrations, the validity of (10.27) could be confirmed over up to two orders of magnitude of the observation time. The displacement $z(t)$ of a molecule in a single-file system may be shown to be correlated to the displacement $s(t)$ of the same molecule without any neighbours (i.e. of an isolated molecule) by the equation [55, 56]

$$\langle z^2(t)\rangle = l\,\langle |s(t)|\rangle \ , \tag{10.29}$$

where l denotes the mean free distance (clearance) between adjacent molecules in the single-file system.

Table 10.1 summarizes the values for F taken from Fig. 10.7, together with the values for the mean free distance l calculated from the sorbate

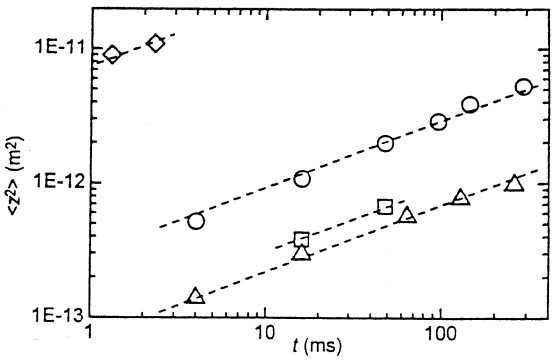

Fig. 10.7. Molecular mean square displacement of CF_4 in $AlPO_4$-5 at 180 K as a function of the observation time at sorbate concentrations of 0.005 (◇), 0.05 (○), 0.2 (□), and 0.4 (△) molecules per unit cell, respectively [54].

Table 10.1. Results of the PFG NMR self-diffusion studies with CF_4 adsorbed in $AlPO_4$-5 at 180 K, represented in terms of the single-file mobility factor F and the limiting diffusivity. The errors of the experimental values are about 50%.

c (mol./unit cell)	l (nm)	F ($m^2s^{-1/2}$)	D (m^2s^{-1})
0.4	1.63	$0.7 \cdot 10^{-12}$	$0.6 \cdot 10^{-6}$
0.2	3.73	$1.5 \cdot 10^{-12}$	$0.5 \cdot 10^{-6}$
0.05	16.3	$4.5 \cdot 10^{-12}$	$0.3 \cdot 10^{-6}$
0.005	167	$1.0 \cdot 10^{-10}$	$1.1 \cdot 10^{-6}$

concentration c and the diffusivities D, which an isolated molecule in the channel would have. The latter quantity follows from (10.29) by using the expression

$$\langle |s(t)| \rangle = \sqrt{\frac{4D}{\pi}} \sqrt{t}, \tag{10.30}$$

which may be easily derived from the propagator for normal diffusion (cf. (10.6) and (10.8)). The estimated single-particle diffusivities are found to be by two orders of magnitude larger than the largest diffusivities so far observed in zeolitic adsorbate-adsorbent systems [3]. In contrast to the three-dimensional pore network of "ordinary" zeolites, in one-dimensional channels the molecular momentum is preserved over much longer time intervals, so that the large values for the single-particle diffusivities are not unexpected. The direct measurement of such diffusivities by PFG NMR is excluded due to the extremely low concentration, which the diffusants should have in such experiments.

For practical applications, one has to take account of the finite size of the zeolite crystallites of single-file type. While under non-equilibrium conditions – i.e. during molecular adsorption or desorption – finite single-file systems do not exhibit any peculiarities in comparison with the case of ordinary diffusion [48,57,58], tracer exchange and chemical reactions are found to be controlled by the single-file confinement. Since any arbitrarily chosen pair of molecules in single-file systems cannot be completely uncorrelated in its movement the boundary conditions relevant for finite single-file systems affect the transport behaviour of all individual diffusants in the single-file system. The influence of the boundary conditions on single-file diffusion is far from being solved, and recent theoretical studies [59–63] try to handle the difficulties arising from these complications.

As a consequence of the finite extension of real single-file systems, particle displacements within the file are subjected to a second mechanism, which is caused by the particle exchange between the marginal sites and the sur-

rounding atmosphere. Since subsequent events of molecular adsorption and desorption on the marginal sites may occur independently from each other, the associated shifts of the particles in the file are also independent from each other. The corresponding molecular displacements are therefore subject to normal rather than to anomalous diffusion. As a consequence, with increasing observation time molecular displacements are very soon dominated by this second mechanism. The ratio between the corresponding diffusivity and the diffusivity of a sole (i.e. isolated) molecule in the file is of the order of the reciprocal value of the site number [60, 64]. Molecular exchange between single-file systems and the surrounding atmosphere is therefore dramatically slowed down in comparison with adsorbents undergoing normal diffusion.

In [65] this mechanism has been identified as the key process for ensuring reactivity enhancement by "molecular traffic control" [66]. Reactivity enhancement by "molecular traffic control" has been postulated to occur if the reactant and product molecules enter and leave pore networks along different diffusion paths. The possibility of substantial differences in the accessibility of different ranges of the intracrystalline pore system by the different components in multi-component adsorbate-adsorbent systems has been recently demonstrated by MD simulations [67]. If the involved molecules are accommodated by different channels, reactant molecules will enter and product molecules will leave the catalysts along separated channels, i.e. without being inhibited by the presence of the other component. Microscopically, this situation appears in the existence of overall concentration gradients along both channel types, viz. into the catalyst particle for the reactant and out of the catalyst particle for the product molecules. From the above considerations it is well known that under such conditions, i.e. under the existence of macroscopic concentration gradients, there is no additional transport inhibition due to the single-file effects. In the conventional case, i.e. for coinciding accommodation probabilities of the two components, however, the overall concentration is constant over the total channel network, so that molecular displacements within the system are subject to the additional transport inhibition of single-file confinement [68]. Obviously, reactivity enhancement by molecular traffic control is based on the suppression of this inhibition mechanism by caring for different accommodation probabilities of the reactant and product molecules in the two channel systems [69, 70].

10.4.6 Diffusion in Ordered Mesoporous Materials

The propagation rate of guest molecules in porous materials depends strongly on the pore structure of the host system. As a consequence, measurement of intraparticle diffusion is able to provide information about structural features, which are not easily accessible by conventional techniques of structural analysis such as scattering and diffraction methods. This is in particular true for structural effects such as pore blockages and leakages in pore walls. As an example, investigations of this type have substantially contributed to an

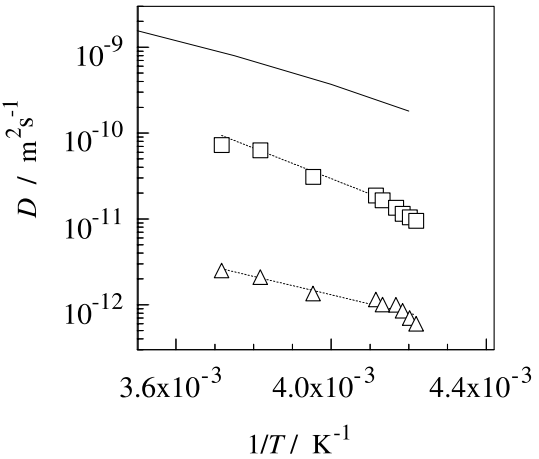

Fig. 10.8. Dependence of the parallel (□) and perpendicular (△) components of the axisymmetrical self-diffusion tensor on the inverse temperature for water in MCM-41 as measured at 10 ms observation time with PFG NMR. The dotted lines may be used as a guide for the eyes. For comparison, the full line represents the self-diffusion coefficients of super-cooled bulk liquid water [74].

improvement of the understanding of the real structure of mesoporous materials of the MCM-41 type. In comparison with zeolites, diffusion measurements with this type of material are complicated by the polydispersity of the sample. As a consequence of the irregular shape of the adsorbent particles, which is quite common for mesoporous materials, analysis of transient adsorption/desorption measurements is not free from some ambiguity. Being sensitive to molecular shifts within the individual adsorbent particles, PFG NMR (like QENS, cf. Chaps. 3 and 13) offers better possibilities for the measurement of intraparticle diffusivities. Some of these measurements, however, have been complicated by the fact that during the observation time of the PFG NMR experiment a substantial fraction of the adsorbate molecules leaves the individual adsorbent particles [71–73].

In [74] this complication has been circumvented by monitoring the water diffusivity in MCM-41 samples overloaded with water at temperatures below 0 °C. In this way it is possible to find experimental conditions under which the phase of intraparticle water is still mobile, while the ice formed in the space between the particles definitely excludes any exchange of water molecules between different adsorbent particles. The signal attenuation observed in PFG NMR is found to be in excellent agreement with the theoretical fit based on the assumption that intraparticle diffusion is described by an axisymmetrical diffusion tensor. Fig. 10.8 shows the main elements of the diffusion tensor in comparison with the diffusivities of free water. The larger component, which represents the diffusivity in the direction of the axis of symmetry, has obviously to be attributed to diffusion in the direction of the

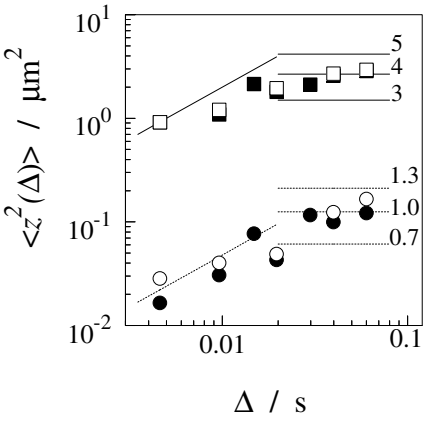

Fig. 10.9. Dependence of the parallel (□, ■) and perpendicular (○, ●) components of the mean square displacement on the observation time for water in two MCM-41 samples at 263 K. The mean square displacements were calculated via (10.8) from the components of the axisymmetrical self-diffusion tensor. The horizontal lines indicate the limiting values for the axial (full lines) and radial (dotted lines) components of the mean square displacements for restricted diffusion in cylindrical rods. The lengths l and diameters d of the rods are written in micrometers on the lines. The oblique lines, which are plotted for short observation times only, represent the calculated time dependences of the mean square displacements for unrestricted (free) diffusion with $D_{\mathrm{par}} = 1.0 \times 10^{-10}\,\mathrm{m^2 s^{-1}}$ (full line) and $D_{\mathrm{perp}} = 2.0 \times 10^{-12}\,\mathrm{m^2 s^{-1}}$ (dotted line), respectively [74].

channels of the MCM-41 structure. Fig. 10.8 allows the following conclusions: (i) Diffusion along the channels is slower than in the free liquid by about one order of magnitude, it is obviously inhibited by partial channel blockages. (ii) Though being much smaller than the diffusivity in axis direction, there is also a finite probability of molecular propagation perpendicular to the channel axes. As the most obvious explanation, the channel walls should therefore be considered as being somewhat permeable to the water molecules.

In the PFG NMR studies, molecular confinement within the intraparticle space was used as an independent check of the data compatibility (Fig. 10.9). With increasing observation times the diffusion path lengths along the main axes of the diffusion tensor were found to be in satisfactory agreement with the particle dimensions.

10.5 Anomalous Diffusion by External Confinement

It has been explained in Sect. 10.2 that anomalous diffusion following the time dependence of (10.4) with a time exponent $\kappa < 1$ is most likely to

be observed under the confinement by self-similar structures, where the displacements must be in the space interval between the lower and upper cut-off of self-similarity. In the regular pore-network of zeolites, anomalous diffusion due to this type of confinement can be excluded if the pore network is not additionally structurized, e.g. by coke depositions [39]. Good prospects for the observation of anomalous diffusion should be provided, however, by amorphous porous materials. While in first detailed PFG NMR studies with amorphous carbonaceous adsorbents molecular displacements were found to follow ordinary diffusion over orders of magnitude [39], polymeric matrices turned out to be most effective host systems for anomalous diffusion. Two examples of molecular diffusion in such systems will be considered. In the third subsection, the benefit of restrictions for elucidating structural details of the samples under study shall be illustrated.

10.5.1 Restricted Diffusion in Polystyrene Matrices

Polystyrene (PS) matrices with inclusions of polydimethylsiloxane (PDMS) droplets turned out to be a useful material for the production of self-lubricating components [75]. PFG NMR measurements with these systems may serve as a model for dynamic imaging. As an example, Fig. 10.10 shows the spin-echo attenuation of the PDMS as a function of the observation time, with the gradient intensity (in terms of the generalized scattering vector $q = \gamma\delta g$) as a parameter. It turns out that with increasing observation time the spin-echo attenuation approaches a finite value Ψ_∞, corresponding to the EISF of QENS (cf. (10.19)). From the q-dependence of the spin-echo attenuation for each individual observation time, via (10.18) and (10.9), one may deduce both the effective diffusivity and the mean square displacement. Fig. 10.11 shows the resulting time dependence of the effective diffusivity. It turns out that for sufficiently small observation times the effective diffusivity approaches the value of the free PDMS (average molecular weight 28 000 g/mol), while with increasing observation time the effective diffusivities approach the reciprocal proportionality required by (10.21). The situation is now the same as for the small crystallites at the lowest temperature considered in Fig. 10.1 where molecular propagation as observed by PFG NMR was controlled by the crystal size as well as for water diffusion in MCM-41 (cf. Sect. 10.4.6), where in Fig. 10.9 for the largest observation times molecular displacements were controlled by the geometrical shape of the adsorbent particles rather than by their intrinsic diffusivity. The mean droplet radii obtained in this way were found to be in excellent agreement with the microscopic measurements [76]. In contrast to these measurements, however, PFG NMR permits a non-destructive determination of the droplet sizes where the external conditions such as pressure and/or temperature may easily be varied. The described experiments revealed that PDMS diffuses out of the cavities into the PS matrix at elevated temperatures (the cavity radius decreases). This process was entirely reversible.

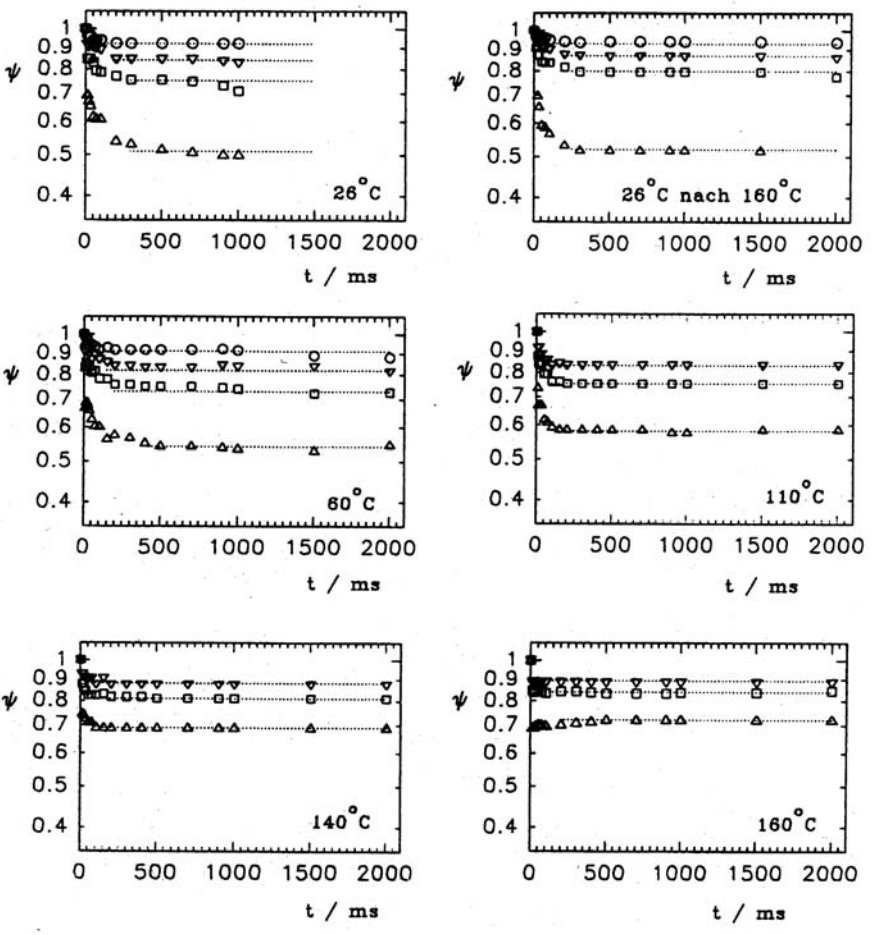

Fig. 10.10. Spin-echo attenuation of PDMS confined to cavities of mean diameter 1.1 μm in a polystyrene matrix in dependence on the observation time [76]. $q/\mathrm{m}^{-1} = 1.13 \cdot 10^6$ (○), $1.71 \cdot 10^6$ (▽), $2.27 \cdot 10^6$ (□) and $3.41 \cdot 10^6$ (△).

10.5.2 Diffusion in Porous Polypropylene Membranes

The total confinement of molecular propagation considered in Sect. 10.5.1 clearly excludes the possibility of anomalous diffusion. For this purpose, molecular propagation has to proceed in a network of interconnected pores, with small pores being the replica of larger ones. Commercially available polypropylene membranes of type "Accurel" [77, 78] proved to be an excellent host matrix for such studies. As an example, Fig. 10.12 shows the time dependence of the effective diffusivities of PDMS (22.5 kg/mol) in this matrix. In contrast to Fig. 10.11, the time regime exhibiting a constant diffusivity is

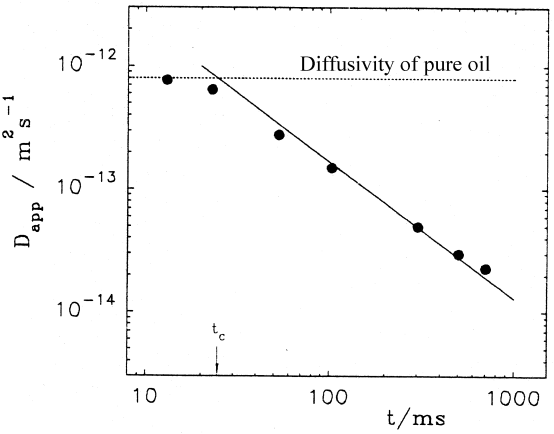

Fig. 10.11. D_{eff} in dependence on the observation time t for PDMS confined to cavities with a mean diameter of 0.6 μm. The diffusivity of the bulk PDMS is indicated as the dashed line [76].

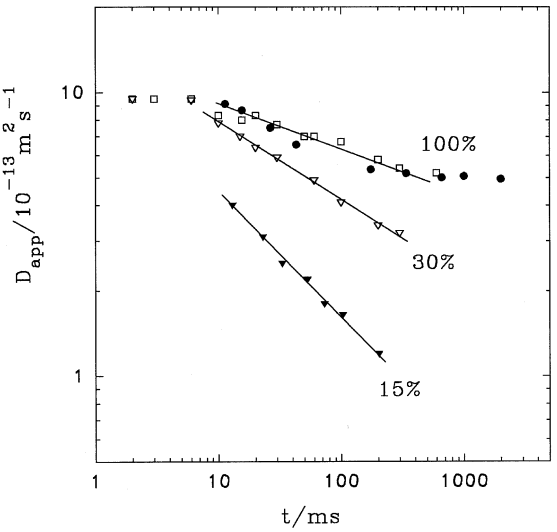

Fig. 10.12. Effective diffusivities of PDMS (22.5 kg/mol) in a polypropylene host matrix at pore filling factors as indicated [78].

now followed by a less pronounced decay, indicating that molecular propagation – though being progressively hindered with increasing observation time – is not completely restricted. It is interesting to note that the slope of the representation, i.e. the effectiveness of the hindrance with increasing observation time, increases with decreasing pore-filling factors. This corre-

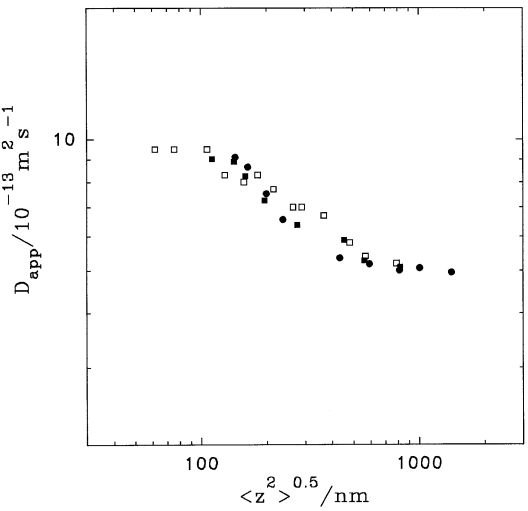

Fig. 10.13. Effective diffusivity of PDMS (22.5 kg/mol) in a polypropylene host matrix at a pore filling factor of 100 % at 293 K as a function of the root mean square displacement of PDMS during the NMR experiment. The filled circles refer to effective diffusivities extrapolated from measurements at 343 K to room temperature by applying the well-established temperature-time shift principle of polymer dynamics [78].

sponds to the fact that the influence of the matrix on molecular propagation is the more pronounced, the larger the relative amount of molecules that are in immediate contact with the matrix. On the basis of (10.4) and (10.9) or (10.10), from the representation of Fig. 10.12 the time exponents κ are found to be $\kappa = 0.83$, 0.72 and 0.55 in the sequence of decreasing pore-filling factors. From the representation of the effective diffusivities as a function of the displacement (Fig. 10.13), it becomes obvious that anomalous diffusion as reflected by a dependence of the diffusivity on the diffusion time and hence on the diffusion path length occurs for displacements between about 100 and 600 nm. It is interesting to note that these lower and upper cut-offs are of the order of the diameters of the smallest and largest pores of the host matrix which has a nominal pore width of 200 nm [77]. The reader will easily find that transfering Fig. 10.13 into a $\langle r^2(t) \rangle$ – vs. – t plot leads to the pattern of Fig. 16.6 in Chap. 16, with the slopes for short and large times given by the large and small diffusivities (i.e. the "short-range" and "long-range" diffusivities) of Fig. 10.13. In the present context, the ratio between these diffusivities is an exclusive function of the architecture of the pore space. It is referred to as the tortuosity factor (cf. Sect. 17.5.1 of Chap. 17).

10.5.3 Tracing Surface-to-Volume Ratios

As an example, Fig. 10.4 has illustrated the different patterns of time dependence of the molecular mean square displacements in zeolitic adsorbate-adsorbent systems, which result as a function of the considered space scales and temperature ranges. For the smallest temperatures, the adsorbate molecules were found to be essentially confined to the intracrystalline space. This can be attributed to the fact that the thermal energy of the molecules is far too small to permit molecular escape into the intercrystalline space with its correspondingly higher potential energy. Molecular propagation in the vicinity of the surface clearly bears features of anomalous diffusion since subsequent displacements are predominantly oriented in opposite directions. Since under the given conditions molecular passage through the surface is essentially excluded, displacements towards the surface are most likely followed by reversed displacements. The resulting confinement in molecular displacements clearly affects their mean values and is therefore reflected in the PFG NMR diffusivities as their direct measure. Fitting the PFG NMR spin echo attenuation under these conditions to (10.18) yields an effective, time-dependent diffusivity $D(\Delta)$. In the limiting case of sufficiently small observation times Δ, $D(\Delta)$ may be expanded as [79, 80]

$$\frac{D(\Delta)}{D_0} = 1 - \frac{4}{9\sqrt{\pi}} S_v \sqrt{D_0 \Delta} + R(\sqrt{D_0 \Delta}). \tag{10.31}$$

where D_0 denotes the unperturbed diffusivity and $S_v = S/V_p$ stands for the surface-to-volume ratio of the confining pore geometry, i.e., the ratio between the surface area (S) of the confining wall and the total (pore) volume (V_p) in which the diffusants are contained. The value $R(\sqrt{D_0 \Delta})$ accounts for higher-order terms in $\sqrt{D_0 \Delta}$, which become increasingly important with increasing observation time. (10.31) may be rationalized by conceiving that the fraction of diffusants, which are subjected to confinement effects, is proportional to the ratio between the total surface area of confinement multiplied by the mean diffusion path during the observation time ($S\sqrt{D_0 \Delta}$) and the total volume occupied by the diffusants (V_p), where it is assumed that the diffusant density over this volume is constant. This dependence is reflected by the second term on the right-hand side of (10.31), which represents the first-order influence of the confinement on the effective diffusivity $D(\Delta)$ with respect to the unperturbed value D_0. It has to be kept in mind that this first-order correction is only justified over a rather modest range of effective diffusivities ($D_0 \geq D(\Delta) \geq 0.85 D_0$). In this range, the plot of $D(\Delta)/D_0$ versus $\sqrt{D_0 \Delta}$ yields a straight line with a slope determined by the S/V_p ratio (cf. (10.31)). With further increasing observation times (viz. as soon as the root mean square displacements in the unconfined space get into the order of the curvature radii of the confining areas), the influence of the higher-order term in $\sqrt{D_0 \Delta}$ on the right-hand side becomes dominating and there is no

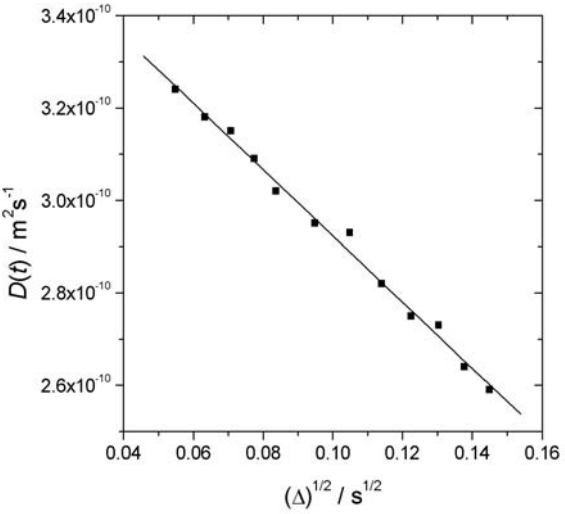

Fig. 10.14. Effective diffusivity of n-hexane in zeolite NaX at 293 K and a loading of 2 molecules per supercage plotted as a function of the observation time [81].

way anymore for simply deducing the surface-to-volume ratios from the time dependence of the effective diffusivity.

As an example, Fig. 10.14 displays the time dependence of the effective diffusivity of n-hexane adsorbed by a bed of zeolite crystallites of type NaX [81]. At the measuring temperature of 293 K the gas phase concentration corresponding to the given loading of two molecules per supercage turns out to be so small that the long-range diffusivity (i.e. the rate of molecular propagation through the bed of crystallites, cf. Sect. 10.4.1) is much smaller than the intracrystalline diffusivity. As a consequence, the diffusants are essentially confined to the space of each individual crystallite with the crystal surface acting as an impenetrable boundary. Hence, in complete agreement with the predictions of (10.31), the effective diffusivity is found to decrease linearly with increasing values of $\sqrt{D_0\Delta}$. Extrapolating to $\sqrt{D_0\Delta} = 0$, the genuine intracrystalline diffusivity is found to be equal to $3.6 \times 10^{-10}\,\mathrm{m^2 s^{-1}}$. From the slope of the representation, S/V_p is found to be $4 \times 10^5\,\mathrm{m^{-1}}$. Approaching the crystallite shapes by spheres, the resulting mean radius is of the order of $8\,\mu$m, which is in satisfactory agreement with the value of $11\,\mu$m determined by scanning electron microscopy.

It is noteworthy that in some way the situation referred to in Fig. 10.14 is opposite to the situation met in PFG NMR experiments with water in the (macro)pores formed by monosized sphere packs [80], which provided first experimental evidence of the validity of (10.31). In [80], the external surface of the spherical particles represents the restricting surface (S) and the volume

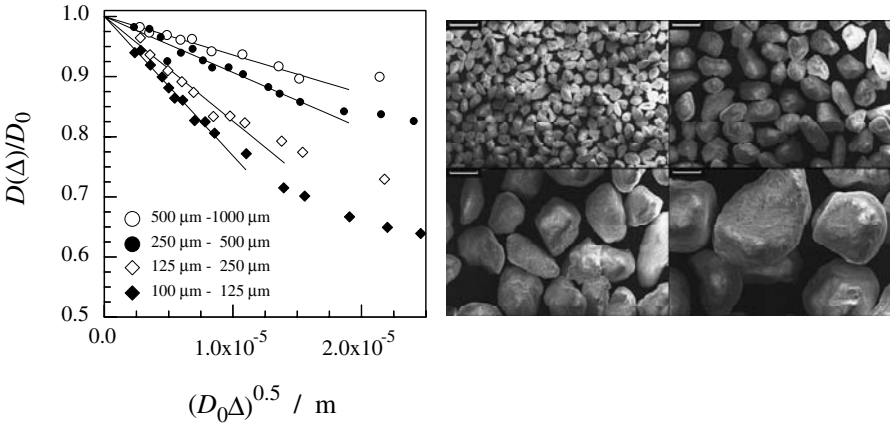

Fig. 10.15. (a, left): Relative effective self-diffusion coefficients $D(\Delta)/D_0$ as a function of $(D_0\Delta)^{0.5}$ for water in the four grain size fractions of the sand. The solid lines represent the results of the fits of (10.31) to the early time dependence of these data [82]. (b, right): SEMs of the four grain size fractions of the sand. The screen intervals used for sieving analysis are given in the legend of Fig. 10.15 (a). The bars represent a length of 300 μm [82].

(V_p) occupied by the diffusants is the space between the particles rather than the intra-particle space as in the case of the zeolites.

A similar situation applies for PFG NMR diffusion studies of natural porous sediments where the pore fluids such as water or oil surround the solid (impermeable) pore matrix. As an example, Fig. 10.15 (a) displays the effective diffusivities of water in the pore volume formed between the grains of a natural quartz sand originating from a glacial sand deposit in Central Germany. Four different size fractions of these grains, which were obtained by sieving the original sediment and which are displayed in Fig. 10.15 (b), were studied [82, 83]. Via (10.31), the distinct increase in the initial slopes of the $D_0/D(\Delta)$ representations (Fig. 10.15 (a)) with decreasing grain diameters may easily be attributed to the corresponding increase in the surface-to-volume ratio. With the known bed density, the resulting surface-to-volume ratios may be transferred into the specific surface areas ($S_m = S/m_g$, surface area per mass of the grains m_g) of the different grain size fractions. Their representation in Fig. 10.16 versus the averaged diameters (d_g) of the grain size fractions reveals an interesting feature of these natural sand grains: Their specific surface area decreases less than linearly with increasing averaged grain diameter [82, 83].

Following the concept of Avnir et al. [84], who proposed an approach to determine the fractal dimension (D_s) of the surface area of granulated porous media by analyzing the scaling behaviour of the measured specific surface in dependence on the grain diameter [82, 84]

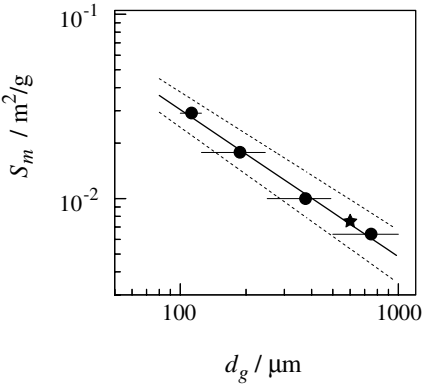

Fig. 10.16. Specific surface areas S_m as function of the averaged grain diameters d_g of the grain size fractions (•) and the original sand (⋆). The full and dotted lines represent the $\log S_m - vs. - \log d_\mathrm{g}$ fit and its confidence interval (slope -0.80 ± 0.05), respectively. The horizontal error bars show the width of the screen intervals used for sieving analysis [82].

$$S_m \equiv \frac{S}{m_g} \propto \frac{d_\mathrm{g}^{D_\mathrm{s}}}{d_\mathrm{g}^3} = d_\mathrm{g}^{D_\mathrm{s}-3}, \tag{10.32}$$

the deviation in the slope of the log-log plot from -1 in Fig. 10.16 may be attributed to a fractal geometry of the grain surfaces. The $\log S_m - vs. - \log d_\mathrm{g}$ fit yields a slope of -0.80 ± 0.05 clearly deviating from -1. According to (10.32), it refers to a fractal dimension of the surface area of the sand grains of $D_\mathrm{s} = 2.20 \pm 0.05$.

Thus, even in samples with irregular pore space geometries such as natural sand grains, PFG NMR self-diffusion studies of the confined pore fluids are suitable to reveal geometric properties of the pore walls. However, for the validity of a fractal analysis of the measured surface areas as performed above one has to keep in mind that a hierarchy of length scales determines its applicability (see Fig. 10.17 and [83, 85]). The length scale of the observed diffusion process ($r \approx \sqrt{D_0 \Delta}$), which is generally on the order of a few μm, determines the lower limit for surface curvature radii (R_s), which contribute to the measured surface-to-volume ratio. Possible smaller features on the surface, which may be explored by adsorption studies, where the radius of the adsorbate molecule (R_m) determines the resolution of the surface area measurements, are averaged over the diffusion length. On the other hand, the surface curvature radii cannot significantly exceed the radii of the grains, which in the present case are on the order of $0.1 \cdots 1\,\mathrm{mm}$. This situation is illustrated in Fig. 10.17.

10.6 Anomalous Diffusion due to Internal Confinement

The existence of hierarchical *external* structures affecting molecular propagation is not the only possibility leading to deviations from normal diffusion. In the following, we shall speak about two possibilities of how the very nature

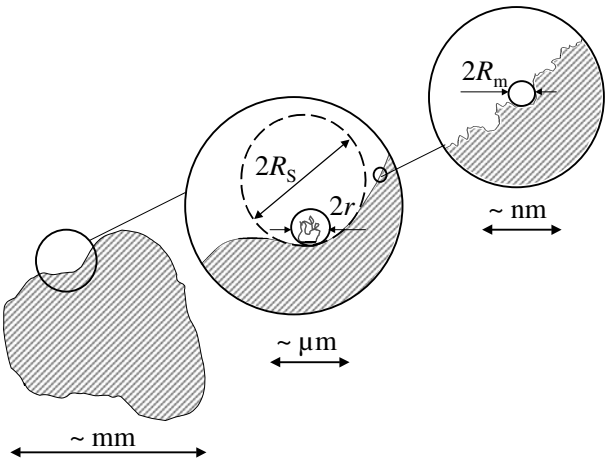

Fig. 10.17. Hierarchy of length scales involved in surface area measurements by PFG NMR self-diffusion studies in granulated porous media.

of the diffusants may compellingly lead to features of anomalous diffusion. The first example (Sect. 10.6.1) refers to the peculiarities of the time dependence of the displacements of the individual segments of a polymer chain (which are in fact the subjects of investigation in PFG NMR) if these displacements are comparable or even smaller than the mean extensions of the macromolecules. These studies are complementary to the QENS investigations of polymer segment mobility presented in Chap. 13 on, however, much shorter time and space scales. The subsequent two sections are devoted to structure-related diffusion phenomena in macromolecular systems with block-copolymers: Sect. 10.6.2 presents data on self-diffusion of a micell-forming triblock copolymer in aqueous solution where deviations from ordinary diffusion are observed for displacements even much larger than the root mean square end-to-end distance R_F of the polymer chains. The occurrence of anomalous diffusion must therefore be explained by the formation of substructures reflecting a process of self-organization within the sample. As an illustration of the technological potentials of block-copolymers, Sect. 10.6.3 communicates diffusion studies in a ternary macromolecular system. It consists of two polymers, which owing to the presence of their diblock copolymer attains completely new structural features, which are also reflected in the internal dynamics.

10.6.1 Anomalous Segment Diffusion in Entangled Polymer Melts

The general characteristics of segmental and chain dynamics in linear polymers are outlined in Chap. 13, Sect. 13.1. The time dependence of the dis-

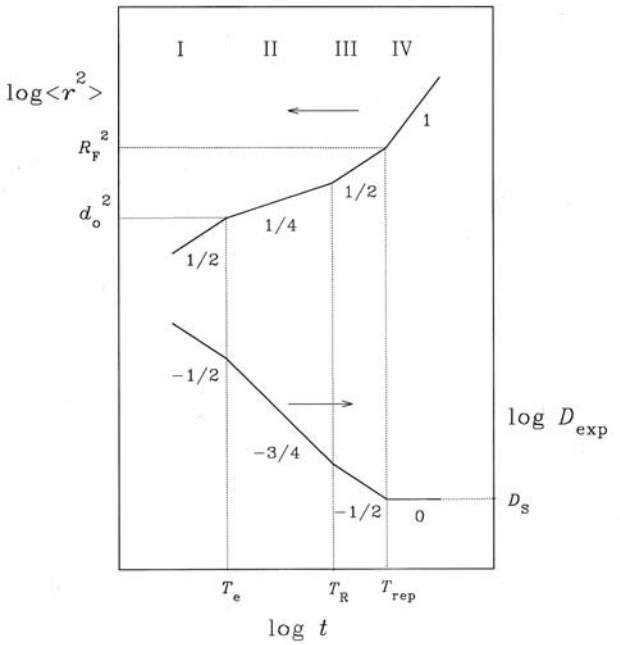

Fig. 10.18. Log-log-plot of the segment mean square displacement and the effective self-diffusivity D_{eff} vs. the observation time t after the tube picture of Doi-Edwards [86]. The cross-overs between the different dynamic regimes occur at T_{e}, where the segments reach the tube wall, at T_{R}, the equilibration time of Rouse dynamics along the tube and T_{rep}, the reptation time, where the initial tube conformation has relaxed.

placement of a polymer segment of a linear chain long enough to be entangled depends on the chosen time interval of observation. Fig. 10.18 shows the different regimes of time dependence to be expected on the basis of the model by Doi and Edwards [86]. For the shortest observation times, a particular segment is subjected to the confinement by the existence of the neighbouring segments, so that $\langle r^2 \rangle$ increases only in proportion to $t^{1/2}$. With further increasing observation time, the propagation of the segment is additionally retarded by the curvature of the diffusion path of the segments since they have to follow the course of the tube. The absolute displacement of a segment therefore increases only in proportion to the square root of the displacement if it is measured along its curvilinear diffusion path. As a result, the overall displacement increases in proportion to $t^{1/4}$. As soon as diffusion of the whole chain along the curvilinear diffusion path becomes predominant (correlated motion) in comparison with the displacements of the individual segments, the mean square displacement again increases with $t^{1/2}$ (though due to a completely different reason than under time regime I). Finally, for diffusion

paths larger than the end-to-end distance of the polymer, segment diffusion coincides with the normal diffusion of the centre of gravity of the molecule. The process of snake-like propagation along the curvilinear diffusion path has become well-known by the term "reptation". It is interesting to note that under the conditions of time-regime II, segment diffusion in polymers may be understood in a way, which is also very helpful for the analytical treatment of single-file diffusion. In the polymer chain, the elementary step of propagation of a segment may be interpreted as the effect of a loop passing the segment under consideration [87], while in a single-file system a particle changes its position, if a "vacancy" is travelling across this particle from one to the other side [50]. The benefit of this interpretation is due to the fact that instead of elements subjected to correlated movements (chain segments and particles in a single-file systems) one has to do with independent elements (loops or vacancies). It is not too complicated, therefore, to obtain in this way the $\sqrt{t}$-dependence for the movement of the mutually dependent elements analytically. In the case of the macromolecules, clearly, another square root has to be applied as a consequence of the curvilinear diffusion path. The space and time scales of transition between the individual regimes in Fig. 10.18 are characterized by characteristic quantities, which are explained in the legend. From the values typical for the different quantities (tube diameter $d_0 = 4$ nm and $R_F = 100$ nm; cf. Chap. 13, Sects. 13.1 and 13.6) one may deduce that – coming from large observation times – PFG NMR is only sensitive to the transition between regimes IV to III, while – coming from short observation times – QENS is only appropriately applied to study regimes I and II. Such investigations shall be presented in much more detail in Chap. 13.

Fig. 10.19 shows the results of time-dependent SFG NMR measurements, with PDMS exhibiting a clear transition between the case of normal diffusion (regime IV) and anomalous, restricted segment diffusion along the tube (regime III) [88]. The cross-over times are found to increase with increasing molecular weights. This trend is an obvious consequence of the increasing molecular extensions and decreasing mobilities. Similar results, though not yet with this accuracy and wealth of data have been obtained by the PFG NMR technique for polymer solutions [18, 89].

10.6.2 Diffusion Under the Influence of Hyperstructures in Polymer Solutions

Recent achievements in polymer chemistry have enabled the production of macromolecules containing groups with quite different chemical properties [90]. Under appropriately chosen conditions, the thus achieved internal structure of the macromolecule favours certain patterns of molecular aggregation, which in turn give rise to the formation of supramolecular hyperstructures. In the following, we visualize the consequences of such molecular aggregations on the diffusion properties of the constituting molecules by presenting the results of PFG NMR studies with aqueous solutions of triblock-copolymers [91, 92].

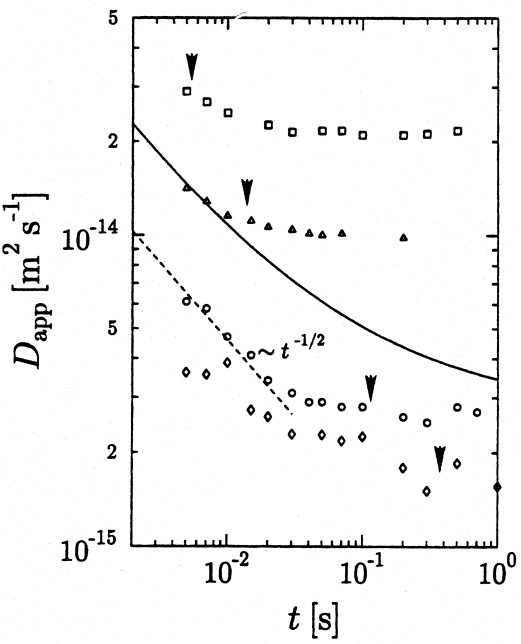

Fig. 10.19. Time-dependent self-diffusion coefficients in PDMS with various molecular weights of M_w = 118 kg/mol (□), 160 kg/mol (△), 344 kg/mol (○) and 716 kg/mol (◇) at T = 305 K. The dashed straight line indicates the proportionality $D_{app} \propto t^{1/2}$ in regime III, cf. Fig. 10.18. The full line is calculated with the Doi-Edwards tube model, the arrows indicate T_{rep} [88].

The triblock-copolymers under study are linear chains with a middle part of poly(propylene oxide) (PPO), containing about 39 C_3H_6O-units, followed on either side by "tails" of poly(ethylene oxide) (PEO), containing about 96 C_2H_4O-units. Since the additional CH_3 group of poly(propylene oxide) reduces the hydrophilicy of the medium part with respect to the tails, in aqueous solutions the central parts of the triblock-copolymers tend to aggregate forming micelles with a core of densely packed poly(propylene oxide) and a corona of poly(ethylene oxide) tails. It turns out that the tendency to form such micelles increases with increasing temperature [93]. Fig. 10.20 shows the results of PFG NMR measurements of the self-diffusion of this PEO-PPO-PEO-triblock-copolymer in an aqueous solution at a concentration of 20 wt.-%. Using deuterated water, the observed ^{1}H NMR signal is exclusively due to the dissolved triblock-copolymers. For low temperatures, Fig. 10.20 displays the astonishing result, that the measured diffusivity decreases with increasing temperature. This rather unusual finding, however, may be explained by the formation of micelles with increasing temperatures. Obviously, at sufficiently low temperatures most of the PEO-PPO-PEO mole-

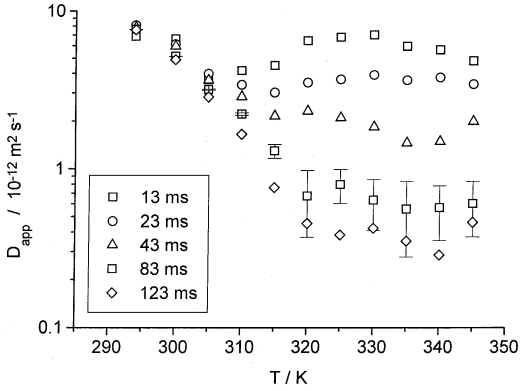

Fig. 10.20. Temperature dependence of the experimental self-diffusion coefficient D_{app} of a 20 % aqueous solution of the triblock copolymer F88 for five different observation times as indicated in the inset [91].

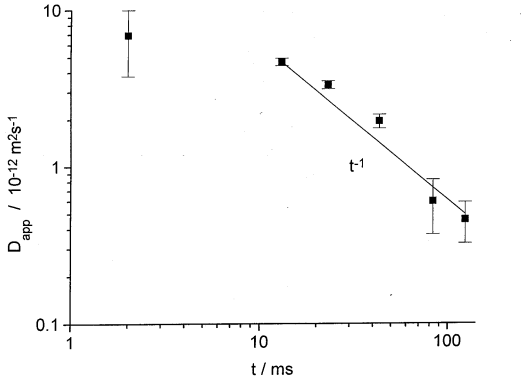

Fig. 10.21. Experimental self-diffusion coefficient in dependence on the observation time t for the triblock copolymer F88 in a 20% aqueous solution at 345 K. Note the cross-over to completely restricted diffusion at about $t = 10$ ms [91].

cules migrate separately from each other as "unimers", while with increasing temperature an increasing percentage of molecules is contained in micelles, which – according to the well-known Stokes-Einstein relation (see, e.g., Sect. 6.3 of Chap. 6 and (15.31) in Chap. 15) – diffuse at a considerably lower rate. It turns out that the molecular exchange between these two states of propagation, viz. as a unimer or in a micelle, is much faster than the shortest observation time of $\Delta = 13$ ms [94]. Otherwise, the PFG NMR spin-echo attenuation should consist of two constituents with vastly differing decay constants. Therefore, it is only possible to determine the mean diffusivity as the weighted average of the diffusivities of the unimers and the micelles.

Starting from temperatures above about 300 K, the diffusivities appear to be time-dependent. For a temperature of 345 K, this dependency is explicitly shown in Fig. 10.21. Over the considered time interval the effective diffusivity obeys the relation $D_{\mathrm{eff}} \propto t^{-1}$. According to (10.21), this proportionality suggests that – at least during the observation time – the molecules are confined within ranges, whose mean radii result to be of the order of 500 nm. This value is much larger than the typical dimensions of the micelles which are of the order of 10 nm. PFG NMR diffusivity data suggest, therefore, the existence of a hyperstructure, being caused, e.g., by the existence of different crystalline domains. The formation of a polycrystalline structure in PEO-PPO-PEO triblock copolymers was confirmed by SANS [95]. Such domains could in fact be observed by static light scattering experiments, which indicate the existence of aggregates with radii of the same order [91, 92]. Moreover, the dimensions of the confining regions were found to depend significantly on the time programme of temperature variation. Such a dependence is most likely if the confining regions are identified with domains of ordered molecular and/or micellar arrangement.

10.6.3 Diffusion Under the Influence of Hyperstructures in Polymer Melts

Two-component systems are well known to tend to disintegrate into two separate phases, if the association of like molecules is favoured over the association of unlike molecules. In two-component polymer systems, such a tendency may be counteracted by involving diblock copolymers of the two constituents as a third component. PFG NMR may serve as a valuable tool for the elucidation of internal dynamics of such systems, which are found to be dramatically affected by the presence of the diblock copolymer. As an example, Fig. 10.22 shows the results of extensive PFG NMR self-diffusion measurements with a ternary blend containing equal molar volumes of the homopolymers poly(dimethylsiloxane) (PDMS) and poly(ethylethylene) (PEE), and the nearly symmetric PDMS-PEE diblock copolymer [96,97]. The copolymer represents about 10 % of the total volume. The blend is known to form a bicontinuous microemulsion below $\approx$ 356 K, while it is in the disordered state at higher temperatures [98]. In addition, Fig. 10.22 also displays the diffusivity data determined separately for the pure components of the blend.

In the ternary blend, two constituents with different diffusivities may be identified. Owing to their prevailing contribution to the molecular volume, they are most likely to be attributed to the homopolymers PDMS and PEE of the blend. This assumption has been confirmed by considering the influence of the nuclear magnetic relaxation times on the relative contributions of the respective constituents [96, 97]. As a remarkable result, the diffusivity in the fast process (which has thus been attributed to PDMS in the blend) is found to be smaller than the diffusivity in the pure PDMS phase, while the diffusivity in the slow process (i.e. the PEE diffusivity in the blend) is larger

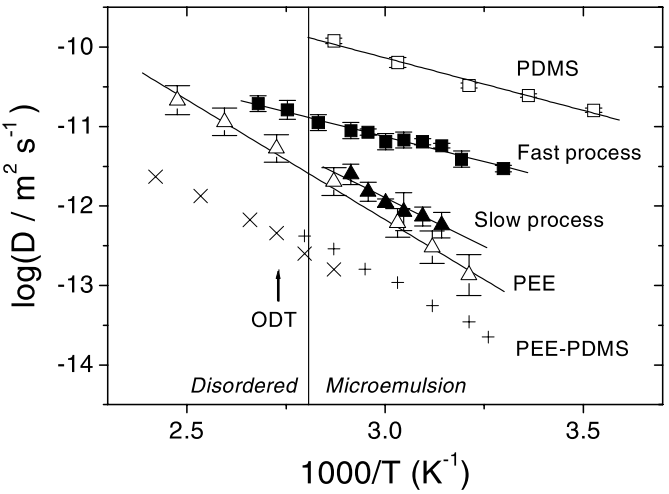

Fig. 10.22. Arrhenius diagram of the PFG NMR diffusivities in the disordered state (•) as well as for the fast (full □) and slow processes (full △) in the ternary blend and comparison with the mean diffusivities of the pure PDMS (□) and PEE (△) homopolymers as well as of the PEE-PDMS diblock copolymer following two different averaging procedures (×, +). The vertical line denotes the phase transition between the microemulsion and the disordered state as identified using dynamic light scattering [98]. The arrow indicates the order-disorder transition in the PEE-PDMS diblock copolymer melt [96, 97].

than the diffusivity in the pure PEE phase. The explanation of this behaviour may be based on the different translational mobility in the pure PDMS and PEE phases due to the differences in their viscosity [99]. There are in fact two mechanisms, which may explain the observed behaviour and which are most likely acting in parallel: Though there is an internal separation of the blent into two phases, there is no perfect disintegration into the two constituents. As a consequence, the contribution of PEE to the PDMS-enriched phase tends to decrease the internal mobility with respect to the pure PDMS phase, while, vice versa, the contribution of PDMS to the PEE-enriched phase is supposed to lead to an enhanced mobility. Further on, molecular propagation has to be influenced by the internal structure. This means that as a consequence of the tortuosity of the two phases, the diffusivity of PDMS will be additionally reduced in comparison with the extended phase. In the case of PEE, however, the existence of different phases may be expected to lead to an additional enhancement of its mobility, since during their residence in the PDMS-enriched phases the PEE molecules will experience an enhanced translational mobility.

In contrast to the studies presented in Sect. 10.6.2, varying the observation time did not show any essential influence on the measured diffusivities. This shows that any internal transport resistances are many times overcome during

the observation time. In fact, an estimate of the domain size of the separated phases by small angle neutron scattering yields values of about 75 nm [98, 100], which are notably exceeded by the diffusion path lengths during the observation times. Studying such effects of molecular restrictions by choosing experimental conditions, where the observed molecular displacements may be of the order of the phase extensions, are among the most challenging tasks of future research.

10.7 Conclusion

PFG NMR has been introduced as a sensitive technique for studying the time dependence of molecular propagation. In homogeneous systems the probability distribution of molecular displacements (the "propagator") is described by a Gaussian, which is completely determined by its mean square width (which is most appropriately visualized by the "mean square displacement"). In homogeneous systems, the mean square displacement increases in proportion to the observation time, with the self-diffusivity being the factor of proportionality. Deviations from homogeneity may lead to characteristic deviations from this proportionality as well as from the Gaussian shape of the propagator. Such deviations are most likely to be encountered for molecules in contact with interfaces. We have highlighted a wide spectrum of possibilities for deviations from homogeneity including micro- and mesoporous adsorbate-adsorbent systems, fluid-saturated natural sediments as well as the case of self-structurization in macromolecular systems. PFG NMR could be shown to provide unique information about both structural and dynamical properties, thus complementing the information from other techniques about these systems.

Notation

a	unit cell dimension in x-direction
b	unit cell dimension in y-direction
B	magnetic flux density
c	sorbate concentration; unit cell dimension in z-direction
d_{g}	grain (particle) diameter
D	coefficient of self-diffusion (self-diffusivity)
D_{lr}	coefficient of long-range diffusion
D_{t}	coefficient of transport diffusion
$D_{\mathrm{par/perp}}$	main components of axisymetrical diffusion tensor
D_{s}	fractal dimension of the grain surface
F	mobility factor of single-file diffusion
g	magnetic field gradient
l	elementary length; mean free distance between adjacent molecules

N	number of diffusants
p	pressure
$P(z,t)$	(mean) propagator in z-direction
$\boldsymbol{q}$	generalized scattering vector
$\boldsymbol{r}$	vector of displacement or position
$\Delta\boldsymbol{r}$	displacement during time interval Δt
R	radius of crystallites
R_F	root mean square end-to-end distance of polymer chains
S_m, S_v	specific surface area, surface-to-volume ratio
t	time, time step
Δt	time interval
T_1	longitudinal nuclear magnetic relaxation time
T_2	transverse nuclear magnetic relaxation time
$\boldsymbol{v}_i(t)$	velocity of particle i at time t
z	coordinate
γ	magnetogyric ratio
δ	duration (width) of the field gradient pulses
Δ	separation of the field gradient pulses ("observation time")
θ	occupation probability
κ	time exponent of anomalous diffusion
λ	jump distance
μ	scaling parameter; chemical potential
ν	scaling parameter
τ	distance between the $\pi/2$- and π-pulse in the spin-echo experiment; mean residence time between subsequent jumps
τ_1, τ_2	distances between the first and second $\pi/2$-pulse, and the second and third $\pi/2$-pulse in the stimulated echo sequence, respectively
φ	phase shift in the precessional motion
Ψ	attenuation of the NMR signal (spin echo) in PFG NMR experiments
ω	Larmor frequency

References

1. S. Havlin, D. Ben-Avraham: Adv. Phys. **36**, 695 (1987)
2. *Fractals in Science*, ed by A. Bunde, S. Havlin (Springer, Berlin Heidelberg New York 1994)
3. J. Kärger, D.M. Ruthven: *Diffusion in Zeolites and Other Microporous Solids* (Wiley, New York, 1992)
4. W. Feller: *An Introduction to Probability Theory* (Wiley, New York 1970)
5. K.H. Hausser, H.R. Kalbitzer: *NMR in Medicine and Biology* (Springer, Berlin Heidelberg New York 1989)
6. E.O. Stejskal, J.E. Tanner: J. Chem. Phys. **42**, 288 (1965)
7. P.T. Callaghan: *Principles of Nuclear Magnetic Resonance Microscopy* (Clarendon Press, Oxford 1991)

8. R. Kimmich: *NMR Tomography, Diffusometry, Relaxometry* (Springer, Berlin Heidelberg New York 1997)
9. J. Kärger, H. Pfeifer, W. Heink: Advances in Magn. Reson. **12**, 2 (1988)
10. F. Stallmach, J. Kärger: Adsorption **5**, 117 (1999)
11. J. Kärger, W. Heink: J. Magn. Reson. **51**, 1 (1983)
12. S. Fritzsche, R. Haberlandt, G. Hofmann, J. Kärger, K. Heinzinger, M. Wolfsberg: Chem. Phys. Lett. **265**, 253 (1997)
13. S. Fritzsche, M. Gaub, R. Haberlandt, G. Hofmann, J. Kärger, M. Wolfsberg. In: *Progress in Zeolite and Microporous Materials*, ed by H. Chon, S.-K. Ihm, Y.S. Uh (Elsevier, Amsterdam 1997); Stud. Surf. Sci. Catal. **105**, 1859 (1997)
14. S. Fritzsche, M. Gaub, R. Haberlandt, G. Hofmann: J. Mol. Model. **2**, 286 (1996)
15. P.T. Callaghan, D. MacGowan, K.J. Packer, F.V. Zelaya: J. Magn. Res. **90**, 177 (1990)
16. J. Kärger, M. Kocirik, A. Zikanova: J. Coll. Interf. Sci. **84**, 240 (1981)
17. H.G. Hertz. In: *Molecular Motion in Liquids*, ed by J. Lascombe (Reidel, Dordrecht 1974,) p 337
18. P.T. Callaghan, A. Coy: Phys. Rev. Lett. **68**, 3176 (1992)
19. A.I. Maklakov, V.D. Skirda, N.F. Fatkullin: *Self-Diffusion in Polymer Solutions and Melts* (in Russian), chap 4.1 (Kazan University Press, Kazan, 1987)
20. G. Fleischer, F. Fujara: NMR - Basic Principles and Progress **30**, 159 (1994)
21. P.T. Callaghan: J. Magn. Res. **88**, 493 (1990)
22. J. Kärger, N.-K. Bär, W. Heink, H. Pfeifer, G. Seiffert: Z. Naturforschung **50**, 186 (1995)
23. W. Heink, J. Kärger, G. Seiffert, G. Fleischer, J. Rauchfuß: J. Magn. Res. A **114**, 101 (1995)
24. V.D. Skirda, I.Yu.Aslanyan, Kazan State University, personal comm.
25. P. Galvosas, F. Stallmach, G. Seiffert, J. Kärger, U. Kaess, G. Majer: J. Magn. Reson. **151**, 260 (2001)
26. M. Appel, G. Fleischer, D. Geschke, J. Kärger, M. Winkler: J. Magn. Res. A **122**, 248 (1996)
27. J. Kärger, H. Pfeifer, S. Rudtsch: J. Magn. Reson. **85**, 381 (1989)
28. R.M. Cotts, M.J.R. Hoch, T. Sun, J.T. Markert: J. Magn. Reson. **83**, 252 (1989)
29. P. Galvosas, F. Stallmach, J. Kärger: J. Magn. Reson. **166**, 164 (2004)
30. R. Kimmich, W. Unrath, G. Schnur, E. Rommel: J. Magn. Res. **91**, 136 (1991)
31. F. Fujara, B. Geil, H. Sillescu, G. Fleischer: Z. Phys. B **88**, 195 (1992)
32. D.M. Fischer, P. Duwe, S. Indris, P. Heitjans: Solid State Nucl. Magn. Reson. **26**, 74 (2004)
33. I. Chang, F. Fujara, B. Geil, G. Hinze, H. Sillescu, A. Tölle: J. Non-Cryst. Solids **172–174**, 674 (1994)
34. U. Hong, J. Kärger, H. Pfeifer: J. Am. Chem. Soc. **113**, 4812 (1991)
35. H.B. Schwarz, S. Ernst, J. Kärger, B. Knorr, G. Seiffert, R.Q. Snurr, B. Staudte, J. Weitkamp: J. Catal. **167**, 248 (1997)
36. S. Fritzsche, R. Haberlandt, J. Kärger, H. Pfeifer, M. Waldherr-Teschner. In: *Zeolites and Related Microporous Materials: State of the Art 1994*, ed by J. Weitkamp, H.G. Karge, H. Pfeifer, W. Hölderich (Elsevier, Amsterdam 1994); Stud. Surf. Sci. Catal. **84**, 2139 (1994)
37. C. Baerlocher, W.M. Meier, D.H. Olson: *Atlas of Zeolite Structure Types* (Elsevier, Amsterdam 2001)

38. H. Pfeifer: Phys. Rep. **26**, 293 (1976)
39. J. Kärger, H. Spindler: J. Am. Chem. Soc. **113**, 7573 (1991)
40. (a) J. Kärger: J. Phys. Chem. **95**, 5558 (1991); (b) J. Kärger, H. Pfeifer: Zeolites **12**, 872 (1992); (c) D. Fenzke, J. Kärger: Z. Phys. D **25**, 345 (1993)
41. S. Jost, N.-K. Bär, S. Fritzsche, R. Haberlandt, J. Kärger: J. Phys. Chem. B **102**, 6375 (1998)
42. U. Hong, J. Kärger, H. Pfeifer, U. Müller, K.K. Unger: Z. Phys. Chem. **173**, 225 (1991)
43. E.J. Maginn, A.T. Bell, D.N. Theodorou: J. Phys. Chem. **100**, 7155 (1996)
44. S. Fritzsche, J. Kärger: J. Phys. Chem. B **107**, 3515 (2003)
45. A. Schüring, S. Fritzsche, R. Haberlandt, S. Vasenkov, J. Kärger: Phys. Chem. Chem. Phys. **6**, 3676 (2004)
46. J. Kärger, J. Caro: J. Chem. Soc., Faraday Trans. I **73**, 1363 (1977)
47. J. Kärger, D.M. Ruthven. In:*Progress in Zeolite and Microporous Materials*, ed by H. Chon, S.-K. Ihm, Y.S. Uh (Elsevier, Amsterdam 1997); Stud. Surf. Sci. Catal. **105**, 1843 (1997)
48. (a) J. Kärger, M. Petzold, H. Pfeifer, S. Ernst, J. Weitkamp: J. Catal. **136**, 283 (1992); (b) C. Rödenbeck, J. Kärger, K. Hahn: J. Catal. **157**, 656 (1995)
49. K. Hahn, J. Kärger: J. Phys. Chem. **100**, 316 (1996)
50. (a) J. Kärger: Phys. Rev. A **45**, 4173 (1992); (b) J. Kärger: Phys. Rev. E **47**, 1427 (1993)
51. V. Gupka, S.S. Nivarthi, A.V. McCormick, H.T. Davis: Chem. Phys. Lett. **247**, 596 (1995)
52. D. Keffer, A.V. McCormick, H.T. Davis: Mol. Phys. **87**, 367 (1996)
53. (a) V. Kukla, K. Hahn, J. Kärger, J. Kornatowski, H. Pfeifer: *Proc. 2nd Polish-German Zeolite Coll.*, (Nicolas Copernicus Univ. Press, Torun 1995) p 110; (b) V. Kukla, J. Kornatowski, D. Demuth, I. Girnus, H. Pfeifer, L.V.C. Rees, S. Schunk, K.K. Unger, J. Kärger: Science **272**, 702 (1996)
54. K. Hahn, J. Kärger, V. Kukla: Phys. Rev. Lett. **76**, 2762 (1996)
55. K. Hahn, J. Kärger: J. Phys. A **28**, 3061 (1995)
56. J.L. Lebowitz, J.K. Percus: Phys. Rev. **155**, 122 (1967)
57. R. Kutner: Phys. Lett. **81A**, 239 (1981)
58. H. van Bejeren, K.W. Kehr, R. Kutner: Phys. Rev. B **28**, 5711 (1983)
59. C. Rödenbeck, J. Kärger, K. Hahn, Phys. Rev. E **55**, 5697 (1997); ibid. Phys. Rev. E **57**, 4382 (1998)
60. P.H. Nelson, S.M. Auerbach: J. Chem. Phys. **110**, 9235 (1999)
61. P.H. Nelson, S.M. Auerbach: Chem. Engin. J. **74**, 43 (1999)
62. S. Vasenkov, J. Kärger: Phys. Rev. E **66** 052601 (2002)
63. J. Kärger, R. Valiullin, S. Vasenkov: New Journal of Physics **7**, 1 (2005)
64. C. Rödenbeck, J. Kärger: J. Chem. Phys. **110**, 3970 (1999)
65. N. Neugebauer, P. Bräuer, J. Kärger: J. Catal. **194**, 1 (2000)
66. E.G. Derouane, Z. Gabelica: J. Catal. **65**, 486 (1980)
67. L.A. Clark, G.T. Ye, R.Q. Snurr: Phys. Rev. Lett. **84**, 2893 (2000)
68. P. Bräuer, J. Kärger, N. Neugebauer: Europhys. Letts. **53**, 8 (2001)
69. P. Bräuer, A. Brzank, J. Kärger: J. Phys. Chem. B **107**, 1821 (2003)
70. A. Brzank, G.M. Schütz, P. Bräuer, J. Kärger: Phys. Rev. E **69** 031101 (2004)
71. E.W. Hansen, F. Courivaut, A. Karlsson, S. Kolboe, M. Stöcker: Microporous Mesoporous Mater. **22**, 309 (1998)

72. F. Courivaut, E.W. Hansen, A. Karlsson, S. Kolboe, M. Stöcker: Microporous Mesopororous Mater. **35/36**, 327 (2000)
73. F.P. Matthae, W.D. Basler, H. Lechert. In *Mesoporous Molecular Sieves*, ed by L. Bounneviot, F. Béland, C. Danumah, S. Giasson, S. Kaliaguine (Elsevier, Amsterdam 1998) pp 301-308
74. F. Stallmach, J. Kärger, C. Krause, M. Jeschke, U. Oberhagemann: J. Am. Chem. Soc. **122**, 9237 (2000)
75. A.C. Dieng, L. Lavielle, G. Riess: New Polymeric Mater. **5**, 13 (1996)
76. M. Appel, G. Fleischer, J. Kärger, A.C. Dieng, G. Riess: Macromolecules **28**, 2345 (1995)
77. Accurel® PP, Akzo Nobel, Wuppertal, Germany
78. M. Appel, G. Fleischer, J. Kärger, F. Fujara, S. Siegel: Europhys. Lett. **34**, 483 (1996)
79. P.P. Mitra, P.N. Sen, L.M. Schwartz: Phys. Rev. B **47**, 8565 (1993)
80. L.L. Latour, P.P. Mitra, R.L. Kleinberg, C.H. Sotak: J. Magn. Reson. A **101**, 342 (1993)
81. O. Geier, R.Q. Snurr, F. Stallmach, J. Kärger: J. Chem. Phys. **120**, 367 (2004)
82. F. Stallmach, C. Vogt, J. Kärger, K. Helbig, F. Jacobs: Phys. Rev. Lett. **88**, 105505 (2002)
83. F. Stallmach, J. Kärger: Phys. Rev. Lett. **90** 039602 (2003)
84. D. Avnir, D. Farin, P. Pfeifer: J. Colloid Interface S. **103**, 112 (1985)
85. D. Candela, P.-Z. Wong: Phys. Rev. Lett. **90**, 039601 (2003)
86. M. Doi, S.F. Edwards: *The Theory of Polymer Dynamics* (Clarendon Press, Oxford 1986)
87. P.G. deGennes: J. Chem. Phys. **55**, 572 (1971)
88. S. Pahl, G. Fleischer, F. Fujara, B. Geil: Macromolecules **30**, 1414 (1997)
89. G. Fleischer, F. Fujara: Macromolecules **25**, 4210 (1992)
90. F.S. Bates, G.H. Fredrickson: Ann. Rev. Phys. Chem. **41**, 525 (1990)
91. H. Scheller, G. Fleischer, J. Kärger: Coll. Polym. Sci. **275**, 730 (1997)
92. H. Scheller. PhD Thesis, Universität Leipzig (1997)
93. K. Mortensen, W. Brown: Macromolecules **26**, 4128 (1993)
94. G. Fleischer: J. Phys. Chem. **97**, 517 (1993)
95. K. Mortensen: J. Phys.: Condens. Matter **8**, A103 (1996)
96. S. Gröger, F. Rittig, F. Stallmach, K. Almdal, P. Stepanek, C.M. Papadakis: J. Chem. Phys. **117**, 396 (2002)
97. S. Gröger, D. Geschke, J. Kärger, F. Stallmach, C. Konak: Macromol. Rapid Commun. **25**, 1015 (2004)
98. T.L. Morkved, B.R. Chapman, F.S. Bates, T.P. Lodge, P. Stepanek, K. Almdal: Faraday Discuss. **112**, 335 (1999)
99. *Polymer Handbook*, ed by J. Brandrup, E.H. Immergut, E.A. Grulke (Wiley, New York 1999)
100. T.L. Morkved, P. Stepanek, K. Krishman, F.S. Bates, T.P. Lodge: J. Chem. Phys. **114**, 7247 (2001)

11 Diffusion Measurements by Ultrasonics

Roger Biel, Martin Schubert, Karl Ullrich Würz, and Wolfgang Grill

11.1 Introduction

The velocity of acoustic waves depends on the elastic properties and the density of the transport medium. The variation of these properties can therefore be observed with ultrasonic waves. The velocity of sound can sensitively be detected by observation of the phases of transit signals. Resolutions of 1 part in 10^8 with respect to changes of the velocity of ultrasound can be achieved for ultrasonic waves in the frequency regime of typically 10 to 100 MHz. Spatial resolution can be obtained with narrow beams of plane waves or with focused ultrasonic waves.

Ultrasonic beams generated and detected by planar transducers are routinely used to observe the temperature dependence of the velocity of sound in liquid or solid materials. Variations of the temperature lead to changes of the elastic properties as well as to thermal expansion. The temperature dependence of the velocity of acoustic waves is often used to observe phase transitions or to gain information on other thermodynamic properties of the samples. The observation of the velocity of sound can also be used as an extremely sensitive thermometer, capable to resolve temperature changes even below 1 mK. It is therefore almost surprising that only little effort has been paid so far to observe thermal diffusion processes or other transport processes by diffusion with ultrasonic detection schemes. An exception are somewhat related photoacoustic excitation schemes including the so-called thermal wave methods which have even been applied with microscopic resolution.

To demonstrate the feasibility of ultrasonic detection schemes with phase resolution, applications are presented for the observation of the diffusion of hydrogen in single-crystalline tantalum and the diffusion of heavy water in gels and living cells. Acoustic interferometric detection schemes and acoustic imaging techniques have so far only been used in these applications. They are demonstrated here to inform about these novel developments and to supply the information needed to decide if such methods can be used advantageously for measurements which cannot easily be performed by established techniques.

11.2 Diffusion of Hydrogen in Single-Crystalline Tantalum

The transport properties of hydrogen in metals have an obvious technical relevance for hydrogen storage devices where metals are employed, capable to store large amounts of hydrogen dissolved in the metal matrix. Single-crystalline samples are normally used to study the basic physical properties under idealized conditions.

A two-beam interferometric setup has been employed (Fig. 11.1) to observe the temperature dependence of the transport properties of hydrogen in metals [1]. The ultrasonic interferometric device is comparable to an optical Mach-Zehnder interferometer. Acoustic waves travel along two paths at different positions in the sample, monitoring integrally the hydrogen concentration along the paths. Piezoelectric transducers (quartz) mounted on the sample convert electric signals into acoustic signals and vice versa. Different to the optical equivalent the remaining part of the interferometer involves only electrical signals. This is possible since ultrasonic transducers are linear devices converting the amplitudes and not simply the power of the respective electric or acoustic signals.

The dependence of the velocity of transverse polarized ultrasonic waves v_t on the hydrogen content c with respect to a small variation of this content Δc is given by [2]:

$$v_\mathrm{t} = \sqrt{\frac{c_{44}^0 + (\Delta c_{44}/\Delta c)c}{\rho + (\Delta\rho/\Delta c)c}}, \tag{11.1}$$

where ρ is the density and c_{ii} the element i, i of the tensor of the elastic stiffness constants of tantalum. The relative change of c_{44} per variation of the hydrogen content of one atomic percent is $1.4 \cdot 10^{-3}$ [2]. The respective value for c_{11} is only $8.9 \cdot 10^{-5}$ [2]. Therefore transverse polarized acoustic waves, travelling along the [100] direction of the tantalum crystal, are employed for

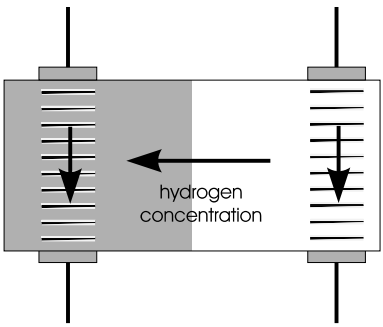

Fig. 11.1. Tantalum sample with gradient in the hydrogen distribution and four transducers for generation and detection of ultrasonic waves travelling along two separated paths.

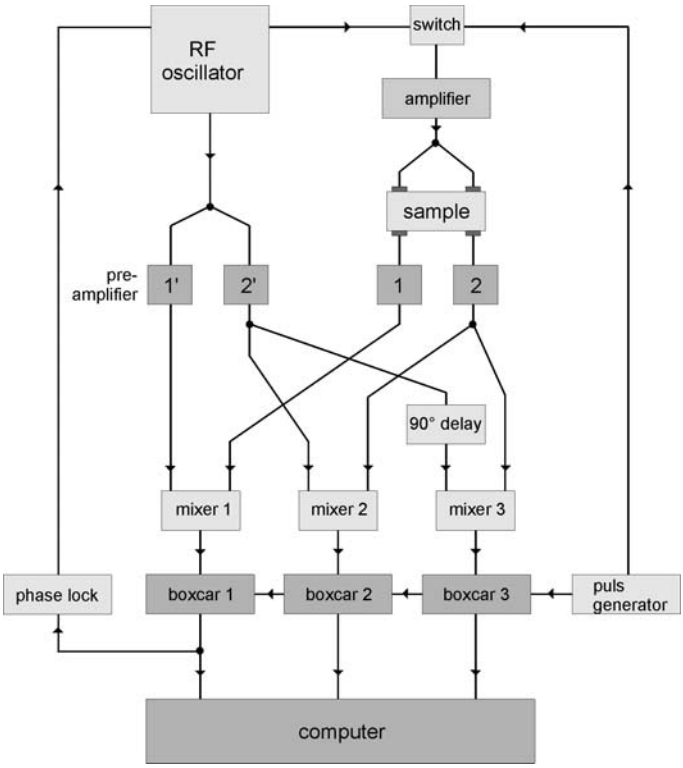

Fig. 11.2. Schematic of the ultrasonic two-path interferometer with vector phase detection. Channel 1 is used for phase-locking of the oscillator. Channels 2 and 3 detect relative changes of the phase of the ultrasonic signal with respect to channel 1. Changes in the velocity in path 1 can be determined from the frequency variation of the locked RF-oscillator.

optimum sensitivity to the hydrogen content which is about 16 times higher than for longitudinal waves.

In the experimental setup phase detection is achieved by multiplicative mixing techniques (Fig. 11.2). The frequency used for excitation is varied in such a way, that the phase observed in one of the paths with respect to an electronic reference derived from the oscillator used for excitation remains at a constant value. The amplitude is stabilized to achieve optimum resolution. The phase observed for the other path is monitored with respect to the same electronic reference by vector detection schemes. Pulses are used to discriminate echoes in the acoustic paths. Some of these features are introduced to achieve optimum sensitivity and long-term stability. This is necessary since rather slow changes have to be observed. Equilibration times for samples of typical sizes of 1 cm can reach several days or even months, depending on the temperature of the sample.

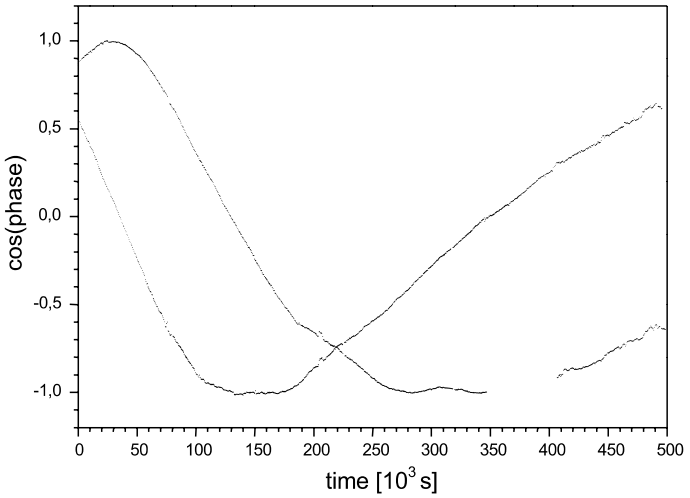

Fig. 11.3. Time dependence of the phase signals (channels 2 and 3 in Fig. 11.2) referenced with a shift of 0° and 90° with respect to the oscillator signal during the equilibration of the graded hydrogen distribution in tantalum by diffusion at a temperature of 273 K (frequency of the ultrasound: 10.6 MHz).

The data are collected and stored with a computer, controlling also the temperature of the sample.

The hydrogen distribution in the tantalum sample is varied by applying unidirectional electric currents at temperatures of about 400 K. This creates a gradient in the hydrogen content across the sample. Subsequently the crystals are cooled to the temperature where the transport processes are studied. The equilibration of the hydrogen distribution is observed with one path of the acoustic interferometer in the region of elevated hydrogen content and the other path in the region where the content has been reduced.

The data collected over time spans up to several days (Fig. 11.3) may be used to determine the diffusion coefficient D taking into account that the relaxation of the hydrogen distribution is determined by a quasi-one dimensional diffusion process following Fick's second law (see, e.g., (1.8) in Chap. 1):

$$\frac{\partial c}{\partial t} = D\frac{\partial^2 c}{\partial x^2} \ . \tag{11.2}$$

The diffusivities obtained for different temperatures are presented in Fig. 11.4. The temperature dependence of the diffusion coefficient is found to follow an Arrhenius relation

$$D = D_0 \mathrm{e}^{-\frac{E_\mathrm{a}}{k_\mathrm{B}\cdot T}} \tag{11.3}$$

with $E_\mathrm{a} = 0.14$ eV, where D_0 is the diffusivity at temperature $T \to \infty$.

Results presented in the literature [3] which have been obtained by conventional methods show errors of up to almost 100%, even for data from the

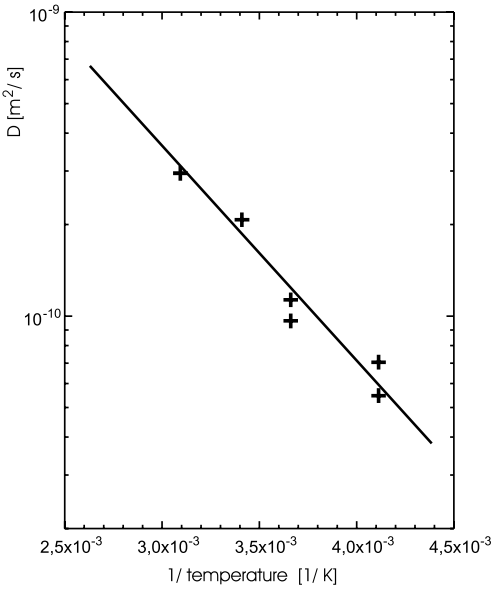

Fig. 11.4. Arrhenius plot of the diffusion coefficient D derived from measurements as represented in Fig. 11.3 (crosses) at different temperatures and line fitted to the data.

same author. The results obtained here show deviations of only up to 23% from the expected linear behaviour. The extrapolation to the value of the diffusion coefficient for $T \to \infty$ leads to $D_0 = 4.5 \cdot 10^{-8}$ m^2/s, which compares well with the value of $D_0 = 4.4 \cdot 10^{-8}$ m^2/s obtained by Völkl and Alefeld [3].

The ultrasonic detection scheme has the advantage, that surface effects play a negligible role, since the hydrogen content is monitored along a path in the volume of the sample. Even extremely slow processes can be studied. As unwillingly demonstrated in the data (Fig. 11.3), the measurement can be continued in the case of temporal failure of the electronics, caused here by a failure of the current supply. Such events are otherwise disastrous for long-time observations. Furthermore the rather low power level of the acoustic signals does not influence the observed hydrogen distribution in the sample.

The method presented here can be used for any sample with two plane parallel surfaces. Due to the integrated detection along the paths of the ultrasonic waves, transport properties can be studied for a direction normal to these surfaces. Lateral resolution is restricted by the fact that planar acoustic waves are employed. Resolutions down to typically 2 mm are feasible with available transducers. Temporal resolution is determined by the repetition rate at which the ultrasonic pulses are generated. The maximum repetition rate depends on the absorption in the sample, since ultrasonic echoes must reach a negligible level prior to the following excitation. Repetition rates of

at least 1 kHz can usually be obtained, leading to a temporal resolution of at least 1 ms. More than two paths can be used with the aid of electronic switches.

11.3 Observation of Diffusion of Heavy Water in Gels and Living Cells by Scanning Acoustic Microscopy with Phase Contrast

Scanning acoustic microscopy (SAM) [4] in the reflection mode is a confocal version of microscopy similar to confocal laser microscopy but based on acoustic waves. In commercially available equipments frequencies up to 2 GHz are used. With water as a coupling fluid a lateral resolution down to 0.6 μm can be achieved.

Recently, high resolution phase contrast has been developed for this version of scanning microscopy [5]. For demonstration of a typical image obtainable by scanning acoustic microscopy with phase contrast (PSAM), Fig. 11.5 shows an image of a cell.

The phase contrast can be employed to detect local changes of the transport properties of ultrasound induced by diffusion processes [6]. To establish this method droplets of gel deposited on a glass substrate have been used. The gel is manufactured from household gelatin dissolved in ordinary water. Heavy water (D_2O) is used in exchange for ordinary water as a coupling fluid. This leads to time-dependent changes in the phase images. A set of images

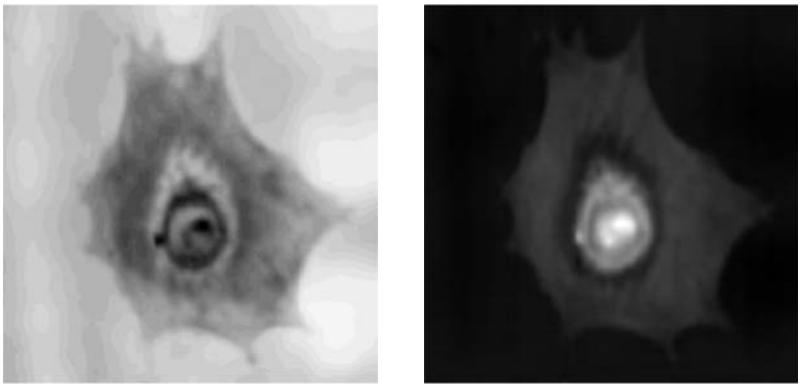

Amplitude contrast Phase contrast

Fig. 11.5. Images of an XTH2-cell on glass. The grey scale in the image in phase contrast is proportional to the phase of the reflected ultrasonic waves. The width of the images is about 100 μm. The images were obtained at a frequency of 1 GHz with water as a coupling fluid. The maximum thickness of the cell somewhat below the center of the images is about 2 μm.

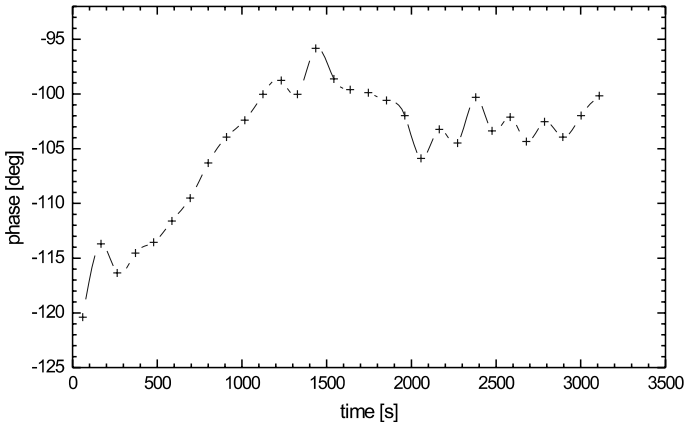

Fig. 11.6. Time dependence of the phase of the reflected ultrasonic waves (1.2 GHz) observed with an ultrasonic microscope for a position on a sample of gelatin deposited on glass. The coupling fluid has been changed from normal water to heavy water at time equal zero.

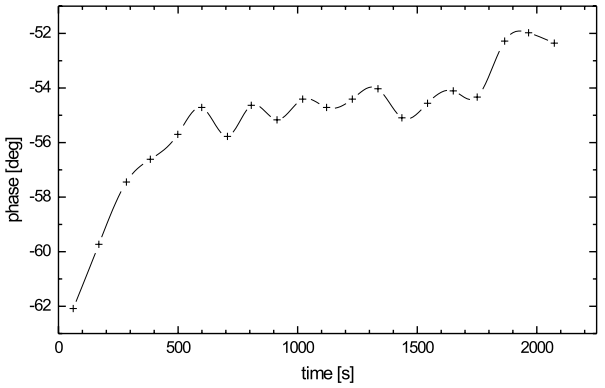

Fig. 11.7. Time dependence of the phase of the reflected ultrasonic waves (1.2 GHz) observed with an ultrasonic microscope for a fixed position on a living cell on glass. The coupling fluid has been changed from normal water to heavy water at time equal zero.

was taken at constant time intervals. A reference area close to the deposited droplet is used as a reference to detect changes of the phases in the image of the droplet. Figure 11.6 shows the result for a fixed position in the image of a droplet. The area at this position is only limited by the lateral resolution of the acoustic microscope of about 1 μm. The temporal dependence of the phase signal exhibits a distinct change following the contact to heavy water over a time span of about 100 s. This change is attributed to the exchange

of normal water by heavy water in the gel by diffusion. Variations at later times are in part caused by solution processes of the deposited material.

Fig. 11.7 shows the response of a living cell under similar conditions. A relaxation time of about 200 s can be derived from the early part of the response. The distinct change at time 1800 s represents the exitus of the cell due to an overdose of heavy water.

These observations represent only a first step to demonstrate the possibility to observe transport processes including diffusion with acoustic microscopy. We restrain therefore from a quantitative analysis of the data. The transport properties in the cell are expected to be dominated by diffusion through the cell membrane. The observation is at least sufficient to determine the typical time scales for transport processes even in living objects.

For determining quantitatively the diffusivities, the thickness of the objects is needed. The technique is therefore especially suitable for coatings of constant thickness. For irregularly shaped objects of limited size on planar substrates (as employed here), the thickness can be monitored by atomic force microscopy (AFM), available in the developed microscope [5]. Homogeneous materials can also be characterized by phase sensitive scanning acoustic microscopy (PSAM) and model calculations fitted to the data [7].

In addition to the techniques demonstrated here microscopic holographic detection schemes have been developed [5, 8], which can be employed for the spatially resolved detection of the variation of the elastic properties in extended objects.

11.4 Conclusion

The novel detection schemes based on ultrasonic interferometers can be used to determine the diffusion coefficient following a non-equilibrium distribution of the diffusing species – in the demonstrated application the diffusing hydrogen. The rather high sensitivity allows the observation of slow processes, respectively small deviations from equilibrated distributions. Scanning acoustic microscopy with phase contrast representing also an interferometric method can be used in a similar way to observe relaxation processes with spatial resolution down to about 1 μm (lateral). Due to the rather short interaction length in the observed objects which is typically in the range of the lateral resolution or below, the sensitivity is significantly reduced with respect to interferometric detection schemes employed in macroscopic objects.

Notation

c	hydrogen concentration in atomic percent
c_{11} , c_{44}	stiffness constants
D	diffusion coefficient

D_0	diffusion coefficient at $T \to \infty$
E_a	activation energy
k_B	Boltzmann constant
t	time
T	temperature
v_t	velocity of transverse ultrasonic waves
x	position
ρ	density

References

1. K.U. Würz: *Ein Ultraschall-Zweistrahlinterferometer zur Messung des Diffusionskoeffizienten von H in Ta.* Diploma thesis, Frankfurt am Main (1987)
2. A. Magerl, B. Berre, G. Alefeld: Phys. Stat. Sol. (a) **36**, 161 (1976)
3. J. Völkl, G. Alefeld: Diffusion of Hydrogen in Metals. In: *Hydrogen in Metals I* (Springer, Berlin Heidelberg New York 1978) p 332
4. R.A. Lemons, C.F. Quate: Appl. Phys. Lett. **24**, 163 (1974)
5. W. Grill, K. Hillmann, K.U. Würz, J. Wesner: Scanning Ultrasonic Microscopy with Phase Contrast. In: *Advances in Acoustic Microscopy*, vol 2, ed by A. Briggs, W. Arnold (Plenum Press, New York 1996)
6. K. Hillmann, W. Grill, J. Bereiter-Hahn: J. of Alloys and Compounds **211/212**, 625 (1994)
7. R. Biel: Ultraschallrastermikroskopie mit Phasenkontrast. Diploma thesis, Frankfurt am Main (1995)
8. K.U. Würz, J. Wesner, K. Hillmann, W. Grill: Z. Phys. B **97** (1995)

12 Diffusion in Membranes

Ilpo Vattulainen and Ole G. Mouritsen

12.1 Introduction

Nature is always in motion. As simple as it is, this statement is true in the sense that numerous phenomena in living systems are characterized by non-equilibrium. Our muscles are in constant need of energy provided by the metabolic pathway, the blood flows in our veins as long as the heart keeps going, and yet old cells are constantly being replaced by fresh ones as a typical life time of a cell is on the order of one day. The state of living beings can therefore only rarely be described by equilibrium. However, even if a true equilibrium were possible in living systems, we would find spontaneous thermal fluctuations to occur around the equilibrium state, again implying that the matter were moving in time.

This book is devoted to the idea of particles moving in condensed matter systems. Our aim in this chapter is to discuss the role of diffusion in soft biological interfaces known as membranes.

In biological systems, diffusion is one of the most intriguing processes that arise from the dynamics of biological molecules. It may sound surprising but many of the diffusion processes in living systems are based on a very simple idea – *a random walk*. Microtubules – long filaments of proteins that search for other molecules inside cells and serve as highways for transporting them inside the cell – grow and shrink in a manner that reminds us of a random walk [1]. Small bacteria, in turn, swim in a fashion involving a long ballistic movement followed by a period during which the particle "tumbles" in a highly erratic manner, thus choosing a new direction for its motion, again followed by another long jump [2]. Interestingly, this joint motion of rushing and tumbling allows the bacterium to move efficiently around its environment as it searches for the best food markets. Then, if we look at the motion of molecules in cell membranes that act as a permeable barrier between the inside and the outside of the cell, we again may notice that the motion of molecules in the plane of the membrane can essentially be described as a random walk [3].

All these examples are kind of confusing since one might expect that Nature works in a manner that is more orderly and deterministic and less random than finance or lottery, in which the random walk plays a major role [4]. Yet we have plenty of evidence that the diffusion in living systems

is often governed by this simple principle. To the best of our knowledge, the first (reported) observations of the random walk were made in 1828 by the botanist Robert Brown [5], who studied the pollen of different plants and observed that, when placed in water, the pollen particles were in uninterrupted and irregular "swarming" motion. Today, we understand that the Brownian motion (as it is called to honor the person who discovered it) concerns the motion of a colloidal particle in a liquid and results from *random* molecular collisions with the liquid molecules, leading to motion, which can be described in terms of the random walk picture. In biological systems, in turn, we are dealing with molecules or clusters of molecules whose size is far greater than the size of surrounding solvent particles. Therefore there is an analogy from colloidal particles to biological molecules, thus providing us with some grounds to use the random walk concept to describe diffusion in living systems.

Random diffusion is a non-specific process, which invariably leads to disorder in a system. Although random diffusion over time may provide for essential reaction pathways in living matter, it is too disordered and disorganized to be relied on in delicate life processes. Therefore, in order to take advantage of the omnipresence and robustness of random diffusion, Nature has over evolutionary time scales developed strategies to compartmentalize and structure living matter on scales from nanometers to the size of whole cells and organisms. Within these structures, macromolecules, macromolecular assemblies, as well as sub-cellular entities perform random as well as directed diffusion. The compartmentalization and structure are provided by biological soft interfaces, so-called membranes, as well as a host of fibers and scaffolding structures. It is noteworthy that the typical length scales of these structures are in the $1-1000\,\mathrm{nm}$ range, i.e. on a scale where diffusional processes can be effective on the time scales that are relevant in biology. Due to the structuring, one can anticipate that the various diffusional processes take place in highly heterogeneous matter and that deviations from normal diffusion under isotropic conditions are likely to occur.

An understanding of the nature of diffusional processes in living matter, and in particular on the level of the individual cell and its various sub-cellular components, is one of the grand challenges in the so-called post-genomic era. Within the last few years, the complete genome of whole organisms, ranging from bacteria, yeast, worms, insects, to that of man, has been mapped out. The genome provides the information about which macromolecules (e.g. proteins) the organism can produce. However, the genome contains seemingly no information on how these macromolecules are organized in space and time and which molecular mechanisms are controlling the organization. Physical principles are here called for. At almost every stage of these controlling mechanisms, elements of diffusional processes are involved: in the molecular self-assembly of fibers and membranes, in the transport and trafficking of RNA, DNA, sugars, fats, and metabolites, in biochemical signaling

cascades as well as intra- and inter-cellular communication, in cell growth, and ultimately in cell death.

In this short review, our aim is to illustrate some of the charming aspects of diffusion in model membranes. We feel that the topic is of a fundamental nature as it is related to the dynamics of cellular functioning. Many present-day medical applications such as drug delivery and gene therapy [6] are essentially dynamic processes that involve the transport of molecules through membranes. Diffusive transport in membranes furthermore plays an important role in processes such as membrane fusion [7], charge transfer [8], and intracellular signaling [9]. It is rather surprising, though, how little is known about the microscopic mechanisms of these dynamic processes in membrane systems. Thus we hope that you will enjoy this little journey, and especially we wish that you will find this topic exciting and let the spirit guide your way to work on these problems. To ease your way on this road, we would like to direct your attention to a number of comprehensive review articles about the overall properties of membrane systems [9–16] as well as about the dynamic processes in membranes and other biological systems [2, 15–17]. It is not an easy road, but it is worth it.

12.2 Short Overview of Biological Membranes

Nature is full of examples of surfaces or interfaces that separate one phase from another and have some important function. For instance, our skin protects our body from hazardous chemicals of the environment and from drying out, and soap bubbles are fragile fluctuating interfaces [18] that are both charming to wonder about and important as an example of the behavior of the detergents we use in our daily life. Further, soap bubbles remind us of biological membranes that surround our cells and serve as an example of soft condensed matter surfaces whose properties can be tuned by weak interactions on the order of thermal energy. Yet there is no doubt that the complexity and biological relevance of membranes are far greater than those of soap bubbles.

Biological membranes are an intriguing example of Nature's talent to make complex systems with a huge number of degrees of freedom but with a well-defined function. The complexity, however, makes our study difficult as we try to understand how membranes work under a variety of physiologically relevant conditions. To ease this burden, one often starts from simple descriptions of such complex systems, and then, after having understood how they work, it is natural to proceed to a higher level of complexity.

Using this idea, we may first think of cell membranes as thin elastic sheets, whose total thickness is typically about 5 nm and depends only weakly on thermodynamic conditions such as the temperature of the system. The membrane is comprised of two monolayers, each of which is made up of lipid mole-

Fig. 12.1. Representation of a typical phosphatidylcholine (PC) lipid molecule on an atomic level (on the left). Additionally, as physicists, we feel obliged to present a simplified description of a lipid (in the middle), where the aim is to grasp the essential features of both the hydrophilic and hydrophobic nature of lipid molecules. In some cases, this structure can be coarse grained even further to obtain a minimal description of a lipid in terms of a two-dimensional disk (shown on the right).

cules. The lipids[1] (see Fig. 12.1) can be thought of as surfactants with some biologically relevant function, and they typically include two non-polar and hydrophobic (water hating) acyl chains connected close to the head group, which in turn is usually polar and hydrophilic (water loving) and therefore capable of forming hydrogen bonds with neighboring water molecules. This "schizophrenic" nature of lipid molecules is the underlying reason why they self-assemble as closed objects such as micelles and liposomes, such that the head groups face water molecules while the acyl chains are as far from the water phase as possible. More precisely speaking, the question is about minimizing the free energy, which contains a substantial entropic component as in most other strongly fluctuating soft matter systems [19]. Often the hydrogen bonds play the most important role for the balance between energy and entropy since hydrogen bonds are significantly stronger than many other non-bonded interactions, such as van der Waals interactions in soft matter systems. Consequently, the lipids form phases of various kinds [19, 20] depending on, e.g., the effective shape of the lipid molecules, their interactions with other molecules in a system, and the relative concentrations of lipids and the solvent. As a simple way of understanding the structure of membranes, we may consider the single-component lipid bilayer shown in Fig. 12.2. Although this example is a highly simplified description of an actual biological membrane, it readily demonstrates the basic structure of membranes. As a matter of fact, due to its "simplicity", this model is often used as a starting point when one aims to understand the complicated properties of biological membranes.

[1] We use the following short-hand notation for di-acyl glycero phospholipids: PC, phosphatidylcholine; PLPC, palmitoyl-laureoyl PC; DMPC, dimyristoyl PC; DPPC, dipalmitoyl PC; DSPC, distearoyl PC; POPC, palmitoyl-oleoyl PC.

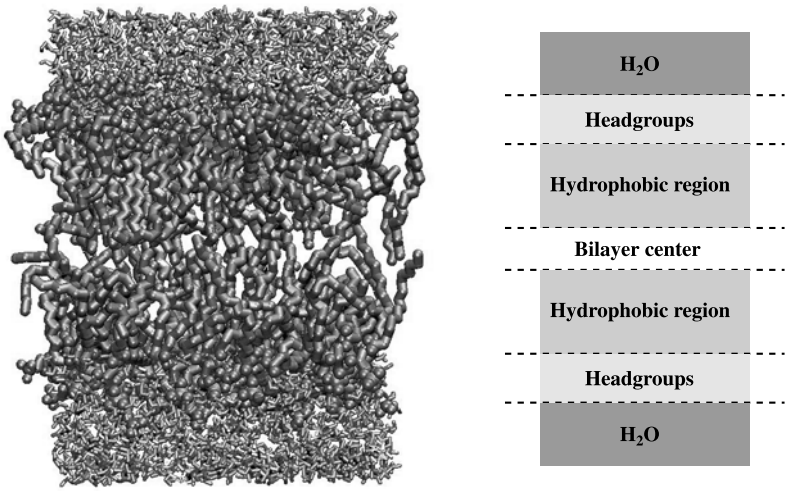

Fig. 12.2. A PLPC lipid bilayer based on molecular dynamics simulations [21] as a representation of the basic model for biological membranes. Water molecules appear at the top and bottom of the picture. Illustration by Marja Hyvönen. A schematic view of the bilayer is shown on the right.

Turning to native biological membranes [9, 11] (see Fig. 12.3) found in living systems, they contain a bilayer of lipids as discussed above. Yet this is just a small part of the story, since biological membranes are not like single-component lipid bilayers but rather they are mixtures of various types

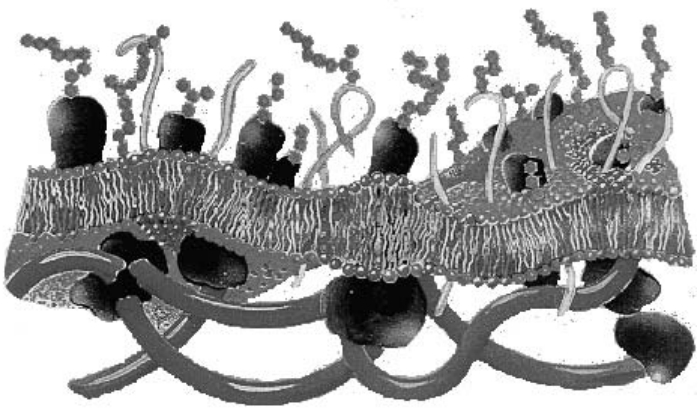

Fig. 12.3. A cartoon of an actual biological membrane including the lipid bilayer, integral proteins, the cytoskeleton (below the bilayer), and glycocalyx carbohydrates (above the bilayer). Illustration by Ove Broo Sørensen.)

of lipids that differ in a number of ways such as with respect to the size, the chemical composition in the polar head group region, and the rigidity of the molecular core [11]. Fats, oils, and certain vitamins and hormones are all lipids. It is fascinating that there are typically more than a hundred different lipid species in a given type of biological membrane, all assumed to have some particular purpose, and many of them are unsaturated or polyunsaturated, increasing the complexity of their nature even further. The lipid bilayer is then complemented by numerous kinds of integral and peripheral proteins that are embedded or attached peripherally to the membrane. The proteins are also related to a dynamic rubber-like network known as the cytoskeleton [11], which is attached to the inner surface of the membrane. The cytoskeleton moves the cell, gives further rigidity to the membrane, and also allows the membrane to adjust its shape to varying non-spherical shapes as is the case, e.g., when red blood cells travel through narrow capillaries. Finally, to make things even more difficult, Nature has chosen that the outer leaflet of the membrane is also covered by a network, which in this case is made of glycocalyx carbohydrates. It has been suggested that this network serves the purpose of cell-cell recognition and adhesion to other cells.

As biological membranes are highly complex objects, the overall picture of their structural and dynamic properties has been rather shady for quite some time. Some 30 years ago, membranes were thought of as fluid-like mattresses of lipid molecules whose main purpose was to provide an environment in which membrane proteins were able to function. This "fluid mosaic model of membranes" [22] has had an enormous impact on the manner in which membranes have been investigated, and it has served its purpose as a good starting point for further work as the picture of membranes and their role have been refined. Thanks to significant activities on the field based on novel experimental techniques and theoretical modeling, a detailed understanding of membranes and their biological relevance has emerged. Rather than being static, membranes are nowadays known to be highly dynamic in nature [23, 24]. Both in-plane and out-of-plane fluctuations are playing a role, although their relative magnitudes are very different. While membranes can be twisted and bent rather easily [12, 24, 25], they cannot be stretched by more than about $2-5\,\%$ of their average area without rupturing [12]. Thus, although there is a danger of misunderstanding here, one can roughly describe membranes as sheets of thin and flexible polymer networks. Further characteristics of membranes include their fluid-like nature in the sense that lipid molecules are able to pass one another relatively easily, their heterogeneity [26] in the sense that there are distinct different small-scale phases and internal structures in membranes, and their mode of compartmentalization in the sense that cells are divided in compartments with specialized functions and membranes thus act as permeable barriers for molecules that are trying to diffuse from the outside to the inside of the cell (or vice versa).

The fluid-like nature of membranes is the key to their various dynamic properties. Out-of-plane fluctuations such as undulations [24] are more like a rule than exception, since their activation energy is of the order of few $k_{\mathrm{B}}T$'s. Fluid-like lipid bilayers have no resistance to shear, unless the cytoskeleton is attached to the membrane. As the molecules are able to pass one another, the lateral diffusion coefficients of individual lipid molecules are relatively high, typically of the order of $10^{-10} - 10^{-12}\,\mathrm{m}^2/\mathrm{s}$. Then, as the lipids and proteins are complex chain-like molecules, they have various internal degrees of freedom, and thus rotational diffusion characterizing their rotation rates around the symmetry axes is also important. The decay of density fluctuations, in turn, gives rise to the so-called collective diffusion (related to area fluctuations of the bilayer), while the diffusive transport of lipids across membranes yields another interesting transport process known as the flip-flop.

The lipid-bilayer component of membranes displays a number of different phases separated by phase transitions. In the present context the most important transition is the so-called *main transition*, which takes the bilayer from a low-temperature solid phase to a high-temperature liquid (fluid) phase. The solid phase has a two-dimensional crystalline character and in addition the lipid acyl chains are conformationally ordered. This phase is therefore usually referred to as the solid-ordered phase. In the fluid phase, the crystalline structure is lost and at the same time the acyl chains display a substantial degree of conformational disorder. This phase is consequently termed the liquid-disordered phase. The diffusional characteristics of the membrane molecules are very different in the two phases.

Our aim in the next few sections is to provide the reader with some flavor of the various diffusion processes taking place in membranes. Rather than presenting an exhaustive description of the topic, we prefer a down-to-earth approach on an introductory level, combined with instructive examples and highlights of a few recent studies that we consider interesting.

12.3 Lateral Diffusion of Single Molecules

Here we discuss the motion of *individual* molecules in membranes as the particles diffuse laterally in the bilayer.

12.3.1 Lateral Tracer Diffusion Coefficient

Let us consider a membrane comprised of two lipid monolayers (see Fig. 12.2). Additionally, we may imagine that there are proteins embedded in the membrane, and all these molecules are allowed to move in the plane of the membrane. For simplicity's sake the membrane is assumed to be flat (zero curva-

ture).[2] Furthermore, we can safely assume that the number of lipid molecules in both monolayers remains constant, since the time scale of lipids exchanging their positions from one monolayer to another (flip-flop) is of the order of several seconds or even hours, while the lateral diffusion of lipids usually takes place on much smaller time scales, typically nanoseconds.

A measure of how fast individual molecules move around is given by the lateral tracer diffusion coefficient [27,28] (cf., e. g., also Chap. 10, (10.8) and Chap. 18, (18.21))

$$D_{\mathrm{T}} = \lim_{t\to\infty} \frac{1}{2dt} \langle |\boldsymbol{r}(t) - \boldsymbol{r}(0)|^2 \rangle, \tag{12.1}$$

where $\boldsymbol{r}(t)$ is the position of the *tagged* particle (or its center of mass) at time t, and $d = 2$ is the dimensionality of a surface.[3] This definition is identical to the original one by Einstein for the motion of Brownian particles in a solvent [27].

We note that D_{T} is essentially defined as a *long-time* limit of $\langle |\boldsymbol{r}(t)|^2 \rangle$, which is the mean square displacement of a given particle. The tracer diffusion coefficient, however, arises from correlations between consecutive displacements of the particle at *small* times, as is demonstrated by the Green-Kubo equation [28] (cf. Chap. 23, (23.15))

$$D_{\mathrm{T}} = \frac{1}{d} \int_0^\infty \mathrm{d}t\, \phi(t), \tag{12.2}$$

where $\phi(t) \equiv \langle \boldsymbol{v}(t) \cdot \boldsymbol{v}(0) \rangle$ is the velocity correlation function of the tagged particle (or its center of mass) in terms of its velocity $\boldsymbol{v}(t)$ at time t.

It can be shown that (12.1) and (12.2) are identical and yield the same diffusion coefficient [28]. However, they probe slightly different properties of the dynamics of the particle and therefore complement each other. While the approach based on the mean square displacement assumes that one has found the long-time limit (the diffusive regime) in which $\langle |\boldsymbol{r}(t)|^2 \rangle \sim t$, the Green-Kubo equation concentrates on the short-time regime and integrates over velocity correlations prior to the long-time regime. At long times, beyond some characteristic time scale τ_{c}, the velocity correlation function $\phi(t) = 0$ for $t > \tau_{\mathrm{c}}$. It is obvious that τ_{c} is closely related to the onset of the diffusive regime in which $\langle |\boldsymbol{r}(t)|^2 \rangle \sim t$ (cf, e. g., Chap. 21, Fig. 21.7).

In practice, the velocity correlation function provides a useful quantity for examining the short-time dynamics through molecular dynamics simulations, thus yielding valuable information of the microscopic details of the diffusion process. Einstein equation, on the other hand, is probably more useful as a means to determine the actual value of the diffusion coefficient D_{T}. Besides this, the mean square displacement provides one with a reliable

[2] In the case of liposomes, the calculation for the diffusion coefficient has to be determined in a spherical geometry. A further complication arises when the bilayer is so soft that the diffusional motion changes the local curvature.

[3] In the following discussion we assume that $\boldsymbol{r}(0) = 0$.

way to find the diffusive regime as well as to obtain information of effects leading to anomalous diffusion (cf. Chap. 10). To illustrate these points, let us argue that $\langle|\boldsymbol{r}(t)|^2\rangle \sim t^x$, where x is some time-dependent exponent. For normal diffusion, $x \to 1$ at long times, which allows one to find the regime in which the Einstein equation is valid. However, there are also cases where the heterogeneity of the membrane or large obstacles such as proteins hinder or bias the diffusion process in such a fashion that $x < 1$ even at very long times [29]. Then the diffusion process is said to be subdiffusive (see Sect. 12.3.3). The concept of anomalous diffusion is generally related to the so-called Levy processes, which are discussed in more detail in [30, 31].

The diffusion of lipids and proteins in a bilayer is essentially a two-dimensional process, and since we are dealing with a hydrodynamic medium in which interparticle interactions are mediated by the solvent, it is worthwhile to point out the well-known problem of diffusion in two spatial dimensions. Under hydrodynamic conditions, $\phi(t)$ decays at long times as $\phi(t) \sim t^{-d/2}$ [32, 33], and therefore for a truly two-dimensional system $\phi(t) \sim t^{-1}$. This seems to imply that (12.2) does not converge and thus the diffusion coefficient is not well defined. However, one should keep in mind that we are looking at the motion of lipids in a bilayer which is interacting with the neighboring environment. These interactions imply that the momentum and the energy of the *bilayer* are not conserved. Thus, the motion of lipids in a bilayer is a dissipative process, and the theoretical result above does not apply in the present case. In brief, as long as anomalous diffusion is not expected, one should find $\langle|\boldsymbol{r}(t)|^2\rangle \sim t$ at long times with a constant slope.

The two approaches mentioned above [(12.1) and (12.2)] are not unique, although they provide the grounds since they can be considered as definitions of the tracer diffusion coefficient. Of the other approaches suggested recently, let us mention the method by which the calculation of D_{T} can be optimized by a so-called "memory expansion" of particle displacements [34]. Finally, once D_{T} has been found, one can use it to estimate the diffusion length $\ell_D \equiv \sqrt{D\tau}$, which the particle undergoes during a time interval of τ.

12.3.2 Methods to Examine Lateral Tracer Diffusion

To start with, we would like to emphasize the special nature of tracer diffusion that should be accounted for in any study of diffusion. The tracer diffusion process refers to a case where one follows the motion of some *tagged individual particle*.

This is relatively easy in computer simulations of model systems, where one can keep track of the positions and velocities of all particles one by one. In experiments the situation is not as simple, however. Many techniques are based on labeling lipid molecules by attaching rather bulky molecules such as pyrene to their acyl chains or a colloidal particle to the head group. The attached molecule has typically some property that allows one to follow

its position, fluorescent labeling being probably the most commonly used technique. In some cases the fluorescence signal from a single lipid molecule or lipid analogue yields a signal large enough to be detected on the background of the noise. Most often one labels a certain fraction (such as 1/1000) of all lipids, however. This leads to two possible problems. First, since the size of the functional group attached to a parent molecule can be quite substantial, and its diffusion characteristics may be very different from those of non-labeled parent molecules, there is an obvious difficulty in interpreting experimental diffusion data. Second, the fact that there are numerous labeled molecules in a bilayer makes it possible that the trajectories of individual lipid molecules cannot be followed any further. Consequently, one cannot use the Einstein equation either. Nevertheless, as discussed later in this chapter, there are certain ways to avoid this problem.

Computational Approaches

For studies of soft matter systems, the first-principles approach including electronic degrees of freedom feels like a method of choice. However, its computational costs are harsh and imply that it is limited to very small systems over short time scales, and is therefore not applicable to membrane systems as such. Current approaches of combining the first-principles techniques with classical molecular dynamics (MD) may provide some relief to this problem [35, 36].

The classical MD approach ([37, 38], see also Chap. 23), however, has developed in recent years to a versatile method for studies of lipid and protein dynamics in lipid bilayers [39–44]. In this approach, all atoms are treated classically, their interactions are well defined, and the time evolution of particle positions is determined by solving Newton's equations of motion. This approach provides one with a classical but detailed description of the system, and can yield plenty of relevant information of the structure and dynamics of membranes at the atomic level. Nevertheless, the price one has to pay is the computational cost. At present, state-of-the-art MD simulations are for about 1000 lipid molecules in a bilayer plus a few thousand water molecules, which allows one to study the system over a time scale of about 100 ns [45]. However, is this enough for studies of lateral lipid diffusion? To address this question, let us first approximate the onset of the diffusive regime τ_c using a rule of thumb $\tau_c \approx R_L^2/D_T$, where R_L^2 is the area per lipid in the plane of the membrane and D_T is its tracer diffusion coefficient. Using typical values of $R_L = 8\,\text{Å}$ and $D_T = 3 \times 10^{-11}\,\text{m}^2/\text{s}$ for a single-component lipid bilayer of DPPC molecules in a liquid-disordered phase [3], we obtain $\tau_c \approx 20 \times 10^{-9}\,\text{s}$. Thus we have to look at times larger than about 20 ns to make sure that an individual lipid molecule in a pure bilayer moves over a distance that is equal to its own size. This time scale should be considered as the lower limit, since displacements of this size can only barely be regarded as macroscopic ones.

In particular in multicomponent systems often characterized by domain formation, the time scale should be far larger since then R_L needs to be replaced by the characteristic size of the domains, which is typically $10-1000$ Å [26].

We can conclude that detailed MD simulations are not the most feasible approach of studying lateral diffusion. Consequently, less detailed approaches have been suggested. The underlying idea is to simplify the model by replacing an atomistic description with a coarse grained one that retains only some of the most essential molecular features (see Fig. 12.1). In practice, this means that the "fast" variables in a system are replaced with stochastic noise and the interactions are chosen to represent those between coarse grained particles rather than actual atoms. Recent progress on the field is encouraging since some of the structural [46, 47] as well as dynamic [48, 49] properties of the membrane have been successfully explored using this idea. However, one can coarse grain the molecular description even further and describe the system in terms of a minimal model, in which lipids and proteins are described in a very simplified fashion in terms of disks or cylinders, for example. This approach allows studies of very large time and length scales and may be highly useful for investigations of processes that are too complicated to be studied by models including molecular information. Studies have shown [50–52] that the approach of using minimal models works fine in a number of cases.

Experimental Techniques

The number of techniques which probe lateral tracer diffusion directly is limited. One popular technique is single-particle tracking [53, 54] in which one attaches a colloidal particle (typically 40 nm in diameter) to the lipid or protein molecules by proper anti-body functionalization. Then, one follows the trajectories of individual labeled molecules in bilayers by computer-enhanced video microscopy, and statistical analysis of a large number of traces allows one to determine the lateral tracer diffusion coefficient in terms of (12.1). In recent years single-molecule fluorescence labeling assays have been developed which by ultra-sensitive fluorescence microscopy or fluorescence correlation spectroscopy have permitted traces of single-molecule diffusion to be observed [55–59]. An example of such observations is given in Fig. 12.4 which shows the motion of an individual fluorescence-labeled molecule in a phospholipid bilayer and the recording of a part of a diffusion trace. The time resolution of such experiments is in the range of 5 ms and the positional accuracy is around 50 nm [58].

In principle, all other approaches we are aware of are based on following some collective property of the whole system, such as the decay rate of density fluctuations. As we will see in Sect. 12.5, this may lead to studies of the collective aspects of diffusion rather than tracer diffusion. Nevertheless, a number of techniques such as fluorescence recovery after photobleaching (FRAP) [60, 61] (cf. also Chap. 16), nuclear magnetic resonance (NMR) [62] (cf. also Chap. 10), (incoherent) quasi-elastic neutron scattering

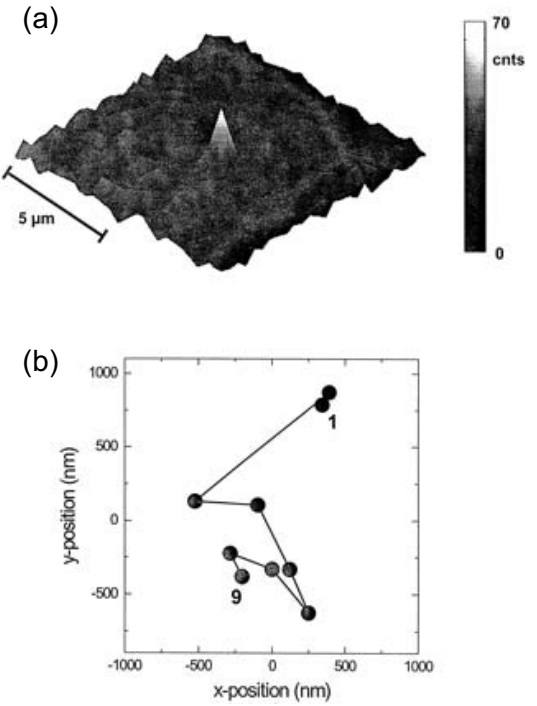

Fig. 12.4. (a) Fluorescent image of a single fluorescence-labeled lipid molecule in a phospholipid bilayer, and (b) the recording of a part of a diffusion trace of a single lipid molecule. From [58].

(QENS) [63–66] (cf. also Chap. 13), and electron spin resonance (ESR) [67] have been used to obtain information of single-molecule motion in membranes. The time and length scales probed by these techniques differ substantially, for which reason they are often characterized as either microscopic or macroscopic methods (see also Chaps. 1, 9 and, e. g., [68]). We will come back to this topic in Sect. 12.5, where some of these techniques are described in more detail.

12.3.3 Lateral Diffusion of Lipids and Proteins

Characteristic Diffusion Coefficients

One of the compelling findings in membranes is the great variety of lateral diffusion coefficients, which range from essentially zero to a value of about $10^{-10}\,\mathrm{m}^2/\mathrm{s}$. To gain some insight into the scales on a practical level, one may consider a molecule diffusing for a period of 10 s at a rate of $10^{-11}\,\mathrm{m}^2/\mathrm{s}$. Then the diffusion length is about $10\,\mu\mathrm{m}$, which is roughly the diameter of an animal cell.

Diffusion in membranes is strongly dependent on phase behavior. As a practical example one may think of diffusion in a single-component bilayer in the vicinity of the main phase transition temperature T_{M} separating the solid-ordered phase from the liquid-disordered phase. As the temperature is changed by a few degrees from $T < T_{\mathrm{M}}$ to $T > T_{\mathrm{M}}$, the system goes through a sudden change from a "frozen and ordered" to a liquid-like bilayer, and similarly the diffusion coefficient changes abruptly from 10^{-20} – $10^{-14}\,\mathrm{m}^2/\mathrm{s}$ [23, 69] to about $10^{-12} - 10^{-10}\,\mathrm{m}^2/\mathrm{s}$ [3, 23, 69]. The wide range of diffusion coefficients in the liquid-disordered phase has been obtained by a number of different experimental techniques, and even though this may seem surprising, the diffusion coefficient actually depends on the technique used for the measurement. Furthermore, the diffusion coefficient depends on whether the bilayer is free as in a liposome or supported on a solid substrate [58] which has in some cases been found to decrease the diffusion coefficient by a factor of $4-5$.

This observation is essentially due to the different time and length scales probed by different techniques. Techniques such as QENS follow the dynamics of molecules in a bilayer over short time scales (less than, say, 1 ns). Thus they examine the "short-time" behavior often denoted as "rattling in a cage", which corresponds to local molecular motion of a lipid within the cage of its nearest neighbors, over a distance smaller than the size of the molecule. Rigorously speaking, the motion of molecules over such short time and length scales is not related to the lateral tracer diffusion coefficient, since the actual diffusion coefficient is defined in the hydrodynamic long-time limit only. However, one may extract a "time-dependent diffusion coefficient" by, e.g., looking at the time-dependence of the slope of the mean square displacement. MD simulation studies using this approach have led to short-time diffusion coefficients (cf., e.g., (10.9) of Chap. 10) on the order of $10^{-11} - 10^{-10}\,\mathrm{m}^2/\mathrm{s}$ [3, 40, 70].

Rather generally, the diffusion coefficients get smaller at larger time scales measured by techniques such as FRAP. This observation is often interpreted as evidence of domain formation. Then one expects that $\langle |\boldsymbol{r}(t)|^2 \rangle \sim t$ over a relatively wide time window (say, from 1 ns to 100 ns), yielding an intermediate-time diffusion coefficient, which describes the diffusion coefficient within the domain. Only at very long times, however, when the diffusion extends over domain boundaries and protein networks that tend to slow down the diffusion coefficient, one eventually finds the hydrodynamic diffusion behavior. The time scales that differentiate these time regimes obviously depend on a system under study, but the point is that macroscopic techniques (over time scales of microseconds and length scales of micrometers or more) may yield diffusion coefficients that are significantly smaller than the short-time values.

As an example of this scale-dependent diffusion behavior, Table 12.1 lists a few recent results for the lateral diffusion of lipids in a DPPC bilayer. This is one of the most extensively studied single-component lipid systems at present.

Table 12.1. Examples of lateral diffusion coefficients of lipids in single-component DPPC (dipalmitoylphosphatidylcholine) bilayers. The time scale over which the diffusion coefficient was determined is also given in some cases. Then "local" refers to short times while "long range" is over a larger scale.

Technique	Time scale	T	Diffusion coefficient	Reference
MD	$< 10\,\mathrm{ps}$	50°C	$20 \times 10^{-11}\ \mathrm{m^2/s}$	[71]
MD	$0.3 - 0.5\,\mathrm{ns}$	60°C	$3 \times 10^{-11}\ \mathrm{m^2/s}$	[3]
QENS		63°C	$40 \times 10^{-11}\ \mathrm{m^2/s}$	[72]
QENS	"local (max)"	60°C	$60 \times 10^{-11}\ \mathrm{m^2/s}$	[64]
QENS	"local (min)"	60°C	$1.5 \times 10^{-11}\ \mathrm{m^2/s}$	[64]
QENS	"long range"	60°C	$1 \times 10^{-11}\ \mathrm{m^2/s}$	[64]
NMR		57°C	$1 \times 10^{-11}\ \mathrm{m^2/s}$	[73]

It is clear that the diffusion coefficients are reduced at long times, as the ideas above suggest, although the effects due to domain formation expected at large scales in many-component lipid bilayers are not included here. Further trends of lipid diffusion have also been discussed in the literature. It has been found that the diffusion coefficient is only weakly dependent on the chain length, while the number of double bonds (unsaturation) has a pronounced effect on diffusion.

Another remarkable feature associated with membranes is the role of fluidity for the diffusion of individual molecules. It has been found that in the liquid-disordered phase the size of the hydrophobic part of the molecule does not have noticeable effect on the diffusion coefficient but it is mostly determined by the properties of the head group [71, 74, 75]. The recent work by Pampel et al. is particularly illustrating, as the pulsed field gradient NMR studies of DOPC diffusion at 37°C yielded a lateral diffusion coefficient of $1.1 \times 10^{-11}\ \mathrm{m^2/s}$. This is in full agreement with the results in Table 12.1 despite the differences in acyl chain length and saturation between DPPC and DOPC. This finding may have major general implications. First of all, it proposes that labeling does not influence the diffusion coefficients of the molecules significantly, but the labeled molecules move laterally essentially at the same rate as non-labeled ones. Recent experiments and model calculations support this view [51, 54, 74]. The same line of thought suggests that molecules inside lipid bilayers move essentially at the same rate as the lipid molecules in a bilayer. Again, a number of works are consistent with this idea. They have shown that molecules close to the headgroups diffuse laterally approximately at the same rate as the lipids, while molecules near the center of the membrane diffuse 3 – 4 times faster than lipid molecules [8,76,77] (see discussion below). Further, if the hydrophobic interior of the molecule and its size are not very important, then one might expect that the lateral diffusion coefficient of integral proteins is roughly as large as the diffusion co-

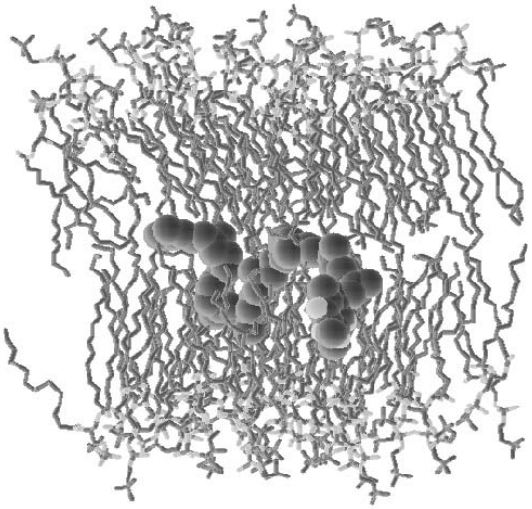

Fig. 12.5. Snapshot of an MD simulation [8] of ubiquinone (UQ-10) inside a DPPC bilayer (water not shown). Here the ubiquinone molecule is "swimming" close to the center of the bilayer, where the density is substantially lower compared to other parts in a membrane. Illustration by J. Arvid Söderhäll and Aatto Laaksonen.

efficient of lipid molecules. It turns out that this idea is supported by various experiments [11].

It is indeed intriguing that the lateral diffusion coefficients of proteins are typically from $10^{-14}\,\mathrm{m}^2/\mathrm{s}$ to $10^{-11}\,\mathrm{m}^2/\mathrm{s}$ [11, 78]. These are slower than the diffusion coefficients of lipids, but only by a factor of ten or so. Yet the size and mass of integral proteins are far larger than those of lipids. Equally remarkable is the finding that the diffusion of proteins is only weakly dependent on the physical dimensions of the protein. This is demonstrated in the classical work by Saffman and Delbrück [79], who described proteins as cylinders with radius $\mathcal{R}$, and found that their diffusion coefficient can be described as [79]

$$D_\ell = \frac{k_\mathrm{B}T}{4\pi\mu h}\left(\log\frac{\mu h}{\mu'\mathcal{R}} - \gamma\right), \tag{12.3}$$

where h is the height of the membrane in which the protein is embedded, μ and μ' are the viscosities of the bilayer and the surrounding fluid, respectively, and γ is the Euler constant. This expression is based on a number of assumptions (including $\mu \gg \mu'$), which are discussed in detail in [78].

Finally, let us briefly discuss the diffusion coefficients of molecules inside lipid bilayers. Söderhäll and Laaksonen studied the diffusion of ubiquinone inside a DPPC bilayer in the liquid-disordered phase through MD simulations [8] (see Fig. 12.5). Ubiquinone acts as a charge carrier inside lipid bilayers from one protein to another, and thus the diffusion properties are of

crucial importance in understanding the charge transfer process. Söderhäll and Laaksonen found that ubiquinone with a short tail (UQ-et) preferred a location close to the headgroups of lipid molecules, which is probably due to the partially hydrophilic nature of UQ-et. The diffusion of UQ-et was found to occur with a rate being essentially the same as the diffusion of DPPC molecules. The diffusion coefficient of ubiquinone with a long tail (UQ-10), in turn, was found to depend on the location of the molecule in a bilayer. Close to the membrane surface, UQ-10 and lipids diffused with similar rates, while in the center of the membrane the diffusion of UQ-10 was found to be almost four times faster compared to the diffusion coefficient of lipids. This finding is consistent with earlier studies of benzene diffusion inside a DMPC bilayer [76, 77]. Thus it seems likely that the diffusion coefficient of molecules inside lipid bilayers depends on the size and density of voids, which are greatest in the bilayer center, and that this is somehow related to the conformational ordering of acyl chains in a membrane.

Above we have discussed the diffusion in the liquid-disordered phase. It is worthwhile pointing out that the picture is likely to be rather different in the solid-ordered phase, where the ordered nature of the membrane comes into play. In the solid-ordered phase, the diffusion of molecules in the center of the bilayer will be relatively rapid, while the diffusion close to the headgroups will slow down due to the "frozen" nature of the bilayer.

Diffusion Mechanisms and Theoretical Frameworks

Despite the significant progress in the field, the knowledge of the microscopic mechanisms of how molecules diffuse in membranes is scarce. It has been proposed [65, 80] that the motion of lipids in bilayers consists of two parts: first of local diffusion of a lipid molecule at its site, and secondly of jumps between adjacent sites. This suggestion has been tested by a number of studies but the overall picture is still cloudy. Essmann and Berkowitz [3] found no evidence in MD simulations for the two regimes expected in this mechanism, while Moore et al. found [70] that the two-step mechanism might be valid. The MD study by Moore et al. dealt with a pure DMPC bilayer, and during a time scale of 10 ns they found two jump events in which a lipid molecule moved relatively rapidly over a distance of its size in the plane of the membrane. Most lipids, however, diffused uniformly like molecules in a fluid. This suggests that the long-range diffusion of lipid molecules in pure bilayers (in the liquid-disordered phase) is a mixture of jumps and uniform motion.

The idea of lateral diffusion as a series of jumps from one site to another is interesting also from a theoretical point of view, since the so-called free-volume theory [23,78,81] is based on this idea. Originally Cohen and Turnbull [81] derived the free-volume theory to describe diffusion of hard spheres, but later it has been applied to a number of systems including the diffusion of lipids in a bilayer. In this approach, one assumes that lipids spend long periods of time at their sites, and long-range diffusion takes place only if there is a

hole (void) nearby to which the lipid can move. The hole may arise from a vacancy left behind by another lipid molecule, or from collective density fluctuations in a bilayer.

In the case of a two-dimensional system, the free-volume theory assumes that the single-particle diffusion coefficient can be written as [81]

$$D = \int_{a^*}^{\infty} \mathrm{d}a\, D(a)\, p(a), \tag{12.4}$$

where $D(a)$ is the diffusion coefficient inside a free area a, and a^* is the critical free area defined as the minimum value of a that allows a jump from one site to another ($D(a) = 0$ for $a < a^*$). The $p(a)$ is the probability of finding a free area of size a, and is written as

$$p(a) = \frac{\Gamma}{a_t - a^*} \exp\left(-\frac{\Gamma a}{a_t - a^*}\right), \tag{12.5}$$

where Γ is a geometric factor and a_t is the average area per molecule. Thus $a_t - a^*$ is the average *free area* per molecule. For constant $D(a)$, one obtains

$$D = D(a^*) \exp\left(-\frac{\Gamma a^*}{a_t - a^*}\right). \tag{12.6}$$

This expression has later been extended to cases where energy fluctuations are important [23, 78].

Although both experiments [23, 64, 82, 83] and simplified model systems [51, 84] have provided support for the free-volume theory, one should bear in mind that the critical free area a^* is assumed constant in this description, while in practice the size and the shape of molecules in membranes fluctuate in time (thus a^* depends on a_t). Further, it has been proposed that the free-volume theory is valid only at high densities over a relatively narrow range of areas per molecule [66, 84]. Nevertheless, the free-volume approach has been shown to describe diffusion specifically in the liquid-disordered phase of single-component lipid bilayers [23].

It is worthwhile pointing out that the microscopic verification of the free-volume theory is still missing. One way to clarify this issue and to provide more insight into the diffusion mechanism is to look at the displacement Δr made by a tagged lipid during a time interval Δt. If the idea of a two-stage diffusion process were true, then the corresponding probability distribution $P(\Delta r, \Delta t)$ would have a relatively narrow peak around $\Delta r \approx R_{\mathrm{L}}$. This kind of experiment would be straightforward to carry out by MD simulations, and has been employed in the case of benzene molecules diffusing inside a lipid bilayer [76, 77]. For lipids in a bilayer, however, this idea is probably out of reach at present due to the high computational cost. Perhaps forthcoming model studies by MD and coarse-grained approaches (of the kind presented in [46–49]) will clarify this issue.

Besides the free-volume theory, there are several theoretical descriptions that have been suggested to describe lateral diffusion under different conditions and in a variety of different systems. These descriptions are discussed in a comprehensive manner, e.g., in [23, 78].

Anomalous diffusion

Lateral diffusion is often assumed to take place in an unrestricted environment such that the mean square displacement is linear in time. In membranes this assumption cannot be taken for granted, however. This idea is supported by a number of experiments [57, 85–87] that have revealed how labeled molecules may be temporally confined to some domain or compartment, or how the mean square displacement may show anomalous behavior [88–90] as characterized by $\langle |\boldsymbol{r}(t)|^2 \rangle \sim t^x$ with $x \neq 1$.

Anomalous diffusion may be due to a number of reasons (cf. also Chap. 10). It has been suggested that proteins embedded in membranes may act as obstacles [91] or binding sites [92] and therefore hinder the diffusion of molecules in a bilayer. In this case the diffusion may look anomalous at small times. At large times, though, one expects normal diffusion unless the motion of lipids is bounded. The diffusion may look anomalous also in a situation where the membrane is locally highly curved or characterized by strong out-of-plane fluctuations. Then, if the diffusion of molecules is interpreted by looking at their trajectories projected onto the average plane of the membrane, it may resemble anomalous diffusion at short times. Also in this case, however, the diffusion is expected to be normal at long times. Another possible scenario giving rise to anomalous diffusion is the heterogeneity of the bilayer. Perhaps the simplest example in this respect is a binary mixture of two lipids at a temperature, where one of the lipids is in the fluid (liquid-disordered) and the other in the solid-ordered phase. A DMPC-DSPC mixture is an example of this situation [23]. Then in coexistence of the two phases there are both liquid-disordered-rich and solid-ordered-rich domains, and the lateral diffusion in the fluid phase is very rapid compared to the solid-ordered phase. Thus, if the relative concentration of lipids in the solid-ordered phase exceeds some critical value, one expects the solid-ordered phase to percolate through the system, implying that long-range diffusion is no longer possible. In biological membranes including the cytoskeleton network the situation is even more subtle, as the membrane-associated network may lead to domains in which the molecules are trapped for a certain (and usually long) period. The transient confinement associated with this situation reminds one of anomalous diffusion at small times, while at (very) long times the molecules are eventually expected to diffuse from one domain to another.

We may conclude that anomalous diffusion is relatively common in membranes. However, one should keep in mind that in many cases the diffusion properties depend on the time scale studied. The true tracer diffusion coefficient characterizing the lateral motion of individual molecules is found only

from the long-time limit through (12.1). Thus, if the technique used looks at times prior to the long-time regime, it provides information of the dynamics over a given time scale instead of the actual hydrodynamic limit.

Lateral Tracer Diffusion in a Lipid-Cholesterol Mixture

Cholesterol is a major component of the plasma membrane of animal eukaryotic cells, comprising up to 50 mol % of the total lipid content [93]. A significant understanding of the role that cholesterol plays in the cell membrane has been obtained from numerous experimental studies of lipid-cholesterol model membranes [94]. These studies have demonstrated that cholesterol has a variety of notable effects on the physical properties of lipid bilayers, including an increase in the bulk bending modulus of bilayers containing cholesterol [95], and changes in the orientational ordering of phospholipid hydrocarbon chains [12]. Cholesterol also has a strong effect on the dynamical properties of lipid bilayers, as is exemplified by numerous experimental studies [62, 83, 96, 97] which have shown how cholesterol affects the rate of lateral diffusion.

We shall here describe some observations for lateral tracer diffusion in lipid bilayers containing cholesterol in order to illustrate how the diffusion coefficient depends both on the phase state and the degree of conformational order of long-chain lipid molecules. Off-lattice Monte Carlo simulations have been used to study lateral diffusion [51] in lipid-cholesterol bilayers using a two-dimensional minimal, strongly coarse grained model system [98,99]. This study was motivated by two important ideas. First, the model predicted a phase diagram in full qualitative agreement with the experimental phase diagram of a lipid-cholesterol system. Second, since the model retains only the key properties, which are expected to govern the behavior of interest thereby omitting details of the molecular description which are not relevant for phase behavior, one obtains an enormous reduction in the computational cost of the simulations. This makes it possible to study much larger systems for longer times, a feature which is necessary in order to be able to investigate diffusion behavior over large time scales.

The phase diagram for the lipid-cholesterol model system [99,100] is shown in Fig. 12.6. Figure 12.7 shows results for the lateral tracer diffusion coefficient D_{T} of a lipid chain as a function of cholesterol concentration X_{chol} for temperatures $T/T_{\mathrm{M}} = 0.99$, 1.0, 1.01, 1.02, and 1.03, where T_{M} denotes the temperature of the main phase transition.

It was found that for $T \geq T_{\mathrm{M}}$, D_{T} generally decreases as X_{chol} is increased from 0 to 0.45. For these temperatures, there is initially a slow decrease in D_{T} for $X_{\mathrm{chol}} < 0.1$, followed by a more rapid decrease up to about $X_{\mathrm{chol}} = 0.3$, after which the curves tend to level off. An interesting observation is that for $T/T_{\mathrm{M}} = 1.0$, D_{T} increases slightly with increasing X_{chol}. At the lowest temperature of $T/T_{\mathrm{M}} = 0.99$, D_{T} increases monotonically with X_{chol}. Finally, for any value of X_{chol}, D_{T} always increases with increasing temperature.

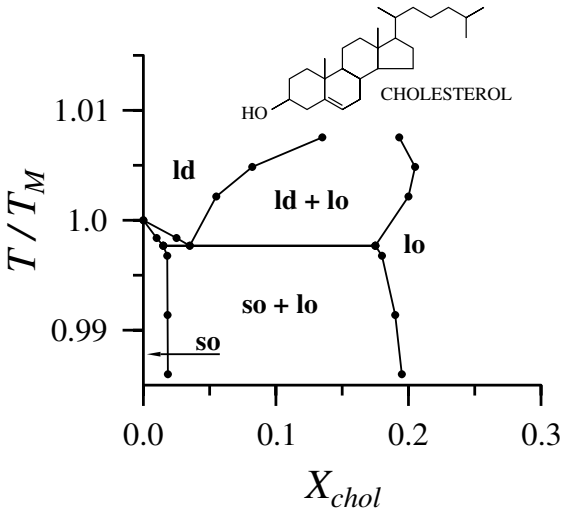

Fig. 12.6. The phase diagram for a model of a lipid-cholesterol mixture as a function of temperature T and cholesterol concentration $X_{\rm chol}$. $T_{\rm M}$ corresponds to the temperature of the main phase transition. Shown here are the solid-ordered (**so**), the liquid-disordered (**ld**), and the liquid-ordered (**lo**) phases. Coexistence phases at intermediate cholesterol concentrations are also illustrated. The molecular structure of cholesterol is shown in the inset.

Generally it was observed in the simulation studies that increasing the cholesterol concentration suppresses $D_{\rm T}$ due to an increased conformational ordering of lipid chains. However, it seems likely that this effect competes with an increase in the average free area per lipid, which favours an increase in $D_{\rm T}$. The interplay of these two effects leads to the diffusion behavior shown in Fig. 12.7, which in turn is in excellent qualitative agreement with available experimental results for lipid-cholesterol mixtures. In these systems the lateral diffusion coefficient decreases by a factor of $2-3$ for increasing the cholesterol concentration from 0 mol %, when the system is in the liquid-disordered (**ld**) phase for $T > T_{\rm M}$, to 50 mol %, for which the system is in the liquid-ordered (**lo**) phase [51, 83]. Furthermore for $T < T_{\rm M}$, experimental observations are in agreement with our results in the sense that increasing the cholesterol concentration increases $D_{\rm T}$, with a rather abrupt change close to the phase boundary between solid-ordered and liquid-ordered phases (**so-lo**) [69, 101]. In addition, the *increase* in $D_{\rm T}$ with $X_{\rm chol}$ at sufficiently low T in the **lo** phase ($T \approx T_{\rm M}$) observed in our simulations was also observed by Almeida et al. [83] in their FRAP study of lateral diffusion of DMPC-cholesterol bilayers. Overall, the model results are in good qualitative agreement with experiments and furthermore provide support for the free-volume theory [51].

Given the simplicity of the model, the results for phase behavior and lipid diffusion in the cholesterol mixtures are in remarkably good qualitative agree-

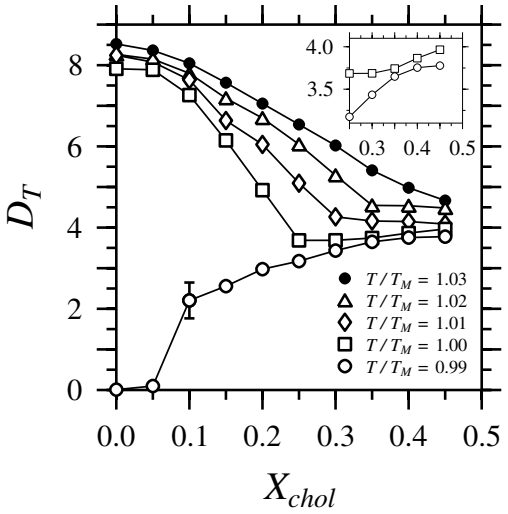

Fig. 12.7. Results for the lateral tracer diffusion coefficient of lipids in the model of a lipid-cholesterol mixture as a function of cholesterol concentration X_{chol}. The curves correspond to different temperatures as described by T/T_{M}. The results for D_{T} are given in units of $\sigma^2 \,/\, t_{\mathrm{MC}}$, where σ is the length scale related to the hard-core size of a molecule (see [98] for details), and t_{MC} is the time in Monte Carlo units. The inset shows details in the data in order to highlight the non-monotonous behavior at T_{M}.

ment with experiment. This demonstrates first of all that microscopic details are in many cases irrelevant for the large-scale properties of complex systems such as lipid membranes. Further, the good agreement between experiments and the model system serves as an instructive example of how statistical physics can contribute to studies of membrane systems. The key idea is to use the concepts and methods of statistical mechanics to simplify complex systems. In this manner, one can obtain models, which grasp the essential features of the system with minimal effort. In the present case, we conclude that the minimal model described in [51, 98–100] is sufficiently well designed to describe a wide range of physical behavior of lipid-sterol systems.

12.4 Rotational Diffusion of Single Molecules

The rotational motion of lipids and proteins is characterized by the rotational diffusion coefficient D_{R}. To this end, let us use (12.1) and replace $\boldsymbol{r}$ with θ. The angle θ is chosen to represent the desired degree of freedom such as the rotation of the vector $\boldsymbol{\ell}_{12}$ from one of the lipid acyl chains to another (i.e., the vector from the center-of-mass of the *sn*-1 chain to the center-of-mass of *sn*-2) around an axis perpendicular to the bilayer plane. Then Einstein

equation yields

$$D_{\mathrm{R}} = \lim_{t\to\infty} \frac{1}{2t} \langle |\theta(t) - \theta(0)|^2 \rangle, \tag{12.7}$$

where $\theta(t) - \theta(0)$ is the overall change in the angle during a time period t (thus θ is *not* bounded by $-\pi$ and π). This definition is very suitable for computational purposes, while in experiments it is less useful. The usual way to circumvent this problem is to look at the decay of time correlation functions that are written in terms of the Wigner rotation matrices [3, 39]. This approach is used in experiments such as NMR relaxation, and it is closely related to the measurement of the lipid conformational order parameter [12], which is one of the key quantities when the structure of lipid membranes is being investigated.

As a specific example, one may consider the correlation function

$$C_2(t) = \langle P_2(\boldsymbol{u}(t) \cdot \boldsymbol{u}(0)) \rangle, \tag{12.8}$$

where $\boldsymbol{u}(t)$ is some unit vector at time t, and $P_2(x) = \frac{3}{2}x^2 - \frac{1}{2}$ is the second Legendre polynomial. The unit vector $\boldsymbol{u}(t)$ can be chosen in various ways, depending on the motion one wishes to examine. One commonly made choice is to look at the time dependence of the CH unit vector of some methylene group in an acyl chain. Then $C_2(t)$ essentially measures the rate of rotational motion of this vector.

Once $C_R(t)$ has been measured, one has to fit the results to a decaying exponential, whose decay rate yields a rotational relaxation rate, which is proportional to D_{R}. Alternatively, one can estimate rotational diffusion coefficients by models such as the one developed by Saffman and Delbrück [79], who treated a lipid molecule (or a protein) as a cylinder. Within this development, the lateral and rotational diffusion coefficients are coupled by the membrane viscosity. However, as Moore et al. pointed out [70], these approaches are marred by the fact that molecules in membranes change their shape in time and therefore they are not modeled well by a cylinder of some fixed shape and size. Nevertheless, both approaches [(12.7) and (12.8)] have been used with success to provide valuable information of rotational diffusion in membranes.

As examples of recent studies on rotational diffusion, we discuss a theoretical and an experimental approach focused on single-molecule imaging. Firstly, let us consider the MD work by Moore et al. for lipids in a DMPC bilayer [70]. They found that the rotational motion of individual components in a lipid span three orders of magnitude from about $25\,\mathrm{rad}^2/\mathrm{ns}$ to $0.04\,\mathrm{rad}^2/\mathrm{ns}$. The fastest component corresponded to the rotation of the *sn*-1 and *sn*-2 chains (for a vector from the first to the last carbon of each chain), while the rotation of interchain vectors such as $\boldsymbol{\ell}_{12}$ were found to be the slowest modes in this system. Moore et al. also concluded that for most of the components, the translational and rotational diffusion are over different time scales and therefore uncoupled.

Secondly, we consider a novel method, called single-molecule anisotropy imaging, that permits a simultaneous measurement of lateral and rotational diffusion on fluorescence-labeled lipids in a bilayer [59]. In contrast to large bead labels, a single fluorophore has a well-defined transition dipole moment with respect to its structure. In the case of the head-group label rhodamine, its dipole is oriented within the plane of the membrane. Under proper conditions of excitation lifetime, rotational time scale, and observation time, the rotational diffusion can be imaged directly and the rotational diffusion coefficient be derived. Harms et al. [59] found for supported bilayers of POPC $D_{\mathrm{R}} = 0.07\,\mathrm{rad}^2/\mathrm{ns}$ in the liquid-disordered phase and $D_{\mathrm{R}} = 1.2 \times 10^{-9}\,\mathrm{rad}^2/\mathrm{ns}$ in the solid-ordered phase.

12.5 Lateral Collective Diffusion of Molecules in Membranes

Like many complex soft-matter systems, membranes are characterized by collective fluctuations that are essentially driven by thermal excitations. Out-of-plane fluctuations such as undulations affect the shape and stability of the membrane as is exemplified by the creation (budding) of liposomes [24] when a part of the membrane separates from the parent membrane, or when a liposome breaks into two. The in-plane fluctuations, in turn, describe density fluctuations in the plane of the membrane, and are related to area fluctuations that may be one of the mechanisms, which lead to pore formation, thus allowing passive diffusion of particles through membranes. Despite its importance, it is rather surprising that the collective motions in membranes are not well understood at the moment [102].

Here we deal with a collective aspect of motion related to density fluctuations in membranes. The density fluctuations are characterized by the motion of particles as local excess density is spread through *collective* diffusion. It may sound surprising but in many cases it is the collective diffusion rather than tracer diffusion that is measured in actual experiments.

12.5.1 Fick's Laws

So far we have considered diffusion in terms of the Einstein equation that is related to Brownian motion. However, the way how diffusion is described in many textbooks is rather different (cf., e.g., (1.1) to (1.8) of Chap. 1). This is probably due to the historical background since the so-called Fick's laws were likely the first attempt to grasp the essential ideas of mass transport. They were formulated already in 1855 [103] by direct analogy with the equations of heat conduction derived some years earlier by Fourier [104].

The starting point is a postulate that some of the quantities in a system are conserved variables. In the case of diffusion, the conserved quantity is the

particle density $\rho(\boldsymbol{r}, t)$. The second necessary ingredient for a hydrodynamical description that one is looking for concerns the explicit form for the driving force in diffusion. The general assumption in this respect is that, for systems close to their equilibrium state, mass transport across a certain unit area is proportional to the *gradient* of the particle density normal to the unit area. These two ideas are described by the continuity equation

$$\frac{\partial \rho}{\partial t} + \nabla \cdot \boldsymbol{j} = 0, \tag{12.9}$$

and the phenomenological Fick's first law for the particle current density

$$\boldsymbol{j}(\boldsymbol{r}, t) = -D(\rho) \nabla \rho(\boldsymbol{r}, t), \tag{12.10}$$

where the hydrodynamic assumption of large length scales and long time scales is already implicitly included. When these two expressions are combined, one obtains

$$\frac{\partial \rho}{\partial t} = \nabla \cdot D(\rho) \nabla \rho(\boldsymbol{r}, t). \tag{12.11}$$

The emerging expression is a non-linear partial differential equation, which unfortunately is not often analytically soluble. For this reason, one usually makes an additional assumption that $D(\rho)$ does not depend on the density of the diffusing particles, or that this dependence is weak. Then we get a linear partial differential equation

$$\frac{\partial \rho}{\partial t} = D \nabla^2 \rho(\boldsymbol{r}, t), \tag{12.12}$$

which is nothing but the usual diffusion equation, which can be often solved exactly to yield the diffusion coefficient D.

Based on Fick's second law, (12.12), D describes the decay rate of a (small) density gradient. Evidently this process does not characterize the same thing as Einstein's relation (12.1), and therefore one makes a clear distinction between the two diffusion coefficients. The diffusion coefficient corresponding to single-particle motion is the tracer diffusion coefficient D_{T}, while the collective motion of the whole many-particle system is denoted as the collective diffusion coefficient D_{C}. Depending on the physical situation, D_{T} may be equal to the self-diffusion coefficient (see, e. g., Chaps. 1 and 10) and D_{C} is sometimes also called the coefficient of chemical diffusion (cf., e. g., Chaps. 3 and 18) or transport diffusion coefficient (Chaps. 10, 18 and 23).

12.5.2 Decay of Density Fluctuations

To gain some further insight into the physical meaning of D_{C}, let us begin with $\rho(\boldsymbol{r}, t)$, which describes the density of the lipid bilayer at position $\boldsymbol{r}$ at time t. As the density of the system fluctuates in time, and we expect the

system to be in equilibrium (or close to it), the relevant quantity here is the density fluctuation $\delta\rho(\boldsymbol{r},t) = \rho(\boldsymbol{r},t) - \langle\,\rho\,\rangle$, where $\langle\,\rho\,\rangle$ is the average density in a membrane. Then we define the density-fluctuation autocorrelation function

$$S(\boldsymbol{r},\boldsymbol{r}\,',t) = \langle \delta\rho(\boldsymbol{r},t)\,\delta\rho(\boldsymbol{r}\,',0)\rangle. \tag{12.13}$$

Now we can write Fick's second law [see (12.12)] for the fluctuation $\delta\rho(\boldsymbol{r},t)$ and assume translational invariance without loss of generality. Consequently we get Fick's second law for the density autocorrelation function:

$$\frac{\partial S(\boldsymbol{r},t)}{\partial t} = D_{\mathrm{C}}\,\nabla^2 S(\boldsymbol{r},t). \tag{12.14}$$

In the hydrodynamic regime (small wave-vector $\boldsymbol{k}$ and large times), and assuming for simplicity the system to be isotropic, the corresponding Fourier transform decays as

$$S(\boldsymbol{k},t) = S(\boldsymbol{k},0)\,\exp(-k^2\,t\,D_{\mathrm{C}}). \tag{12.15}$$

Thus $S(\boldsymbol{k},t)$ provides an interpretation of D_{C} in terms of the decay rate of density fluctuations. With a suitable small value of $\boldsymbol{k}$, the collective diffusion coefficient D_{C} can then be extracted from the long-time tail of (12.15).

As a concrete example, one may think of some region in a membrane in which the local density is obviously larger than the average density in equilibrium. Then the density gradient drives the system towards equilibrium. However, since the excess density at this region cannot spread locally, it must spread over large length scales (small k) in the course of long times, thus giving rise to a hydrodynamic collective diffusion process.

12.5.3 Relation Between Tracer and Collective Diffusion

Under general conditions, there is no simple relationship between the two diffusion coefficients D_{T} and D_{C}. This is noticed by considering the motion of N (identical) labeled molecules in a membrane. Then the Green-Kubo equation for tracer diffusion is given by

$$D_{\mathrm{T}} = \frac{1}{dN}\sum_{i=1}^{N}\int_0^\infty \mathrm{d}t\,\langle \boldsymbol{v}_i(t)\cdot\boldsymbol{v}_i(0)\rangle, \tag{12.16}$$

and the corresponding Green-Kubo equation for collective diffusion is

$$D_{\mathrm{C}} = \frac{1}{d\,k_{\mathrm{B}}T\rho N\kappa_T}\int_0^\infty \mathrm{d}t\;\langle \boldsymbol{J}(t)\cdot\boldsymbol{J}(0)\rangle\,, \tag{12.17}$$

which for simplicity's sake is here given for an isotropic system. The time correlation function of the total particle flux $\boldsymbol{J}(t) = \sum_{i=1}^{N}\boldsymbol{v}_i(t)$ is described in terms of velocities of the particles, the quantity ρ denotes the density of

particles studied in this case, and κ_T is the corresponding compressibility. The corresponding relations for nanoporous host-guest systems are (10.24) and (10.25) of Chap. 10 (mind the difference in the notations for tracer (self-) and collective (transport) diffusion in the respective communities).

Combining (12.16) and (12.17) yields

$$D_{\mathrm{C}} = D_{\mathrm{T}} \frac{1}{k_{\mathrm{B}} T \rho \kappa_T} \left[1 + \frac{\sum_{i \neq j} \int_0^\infty \mathrm{d}t \, \langle \boldsymbol{v}_i(t) \cdot \boldsymbol{v}_j(0) \rangle}{\sum_{i=1}^N \int_0^\infty \mathrm{d}t \, \langle \boldsymbol{v}_i(t) \cdot \boldsymbol{v}_i(0) \rangle} \right]. \tag{12.18}$$

We see that the cross-correlations $\langle \boldsymbol{v}_i(t) \cdot \boldsymbol{v}_j(0) \rangle$ determine whether a simple expression between D_{C} and D_{T} can be established. Such an expression emerges if the velocities (displacements) of different particles are not correlated *at all*. Then we get

$$D_{\mathrm{C}} = D_{\mathrm{T}} \frac{1}{k_{\mathrm{B}} T \rho \kappa_T}. \tag{12.19}$$

This situation is expected to be reasonable at very low concentrations, since then interparticle interactions are not important and (12.19) works well. Further, since the thermodynamic factor approaches a constant value in this limit, $\lim_{\rho \to 0} k_{\mathrm{B}} T \rho \kappa_T = 1$ [105], one obtains $D_{\mathrm{C}} \approx D_{\mathrm{T}}$ at low concentrations.

We can conclude that D_{T} and D_{C} are approximately equal provided that interaction effects between the labeled particles are weak. In practice this implies that one should look at the dilute regime at which the concentration of labeled particles is small. Fortunately this is often the case in experiments such as FRAP measurements where only a tiny fraction of lipid molecules are labeled. However, several interesting issues remain unclear. For example, what is the concentration at which the tracer diffusion begins to deviate significantly from the collective diffusion, and how does the compressibility come into play in collective diffusion. The latter question is particularly important since the isothermal compressibility

$$\kappa_T = \frac{1}{k_{\mathrm{B}} T \rho} \frac{\langle N^2 \rangle - \langle N \rangle^2}{\langle N \rangle} \tag{12.20}$$

is related to particle number fluctuations in the plane of a bilayer. These fluctuations, in turn, are expected to show anomalous behavior in the vicinity of phase transition lines. Thus we can expect that D_{C} may provide one with information of phase transitions and the locations of boundaries between different phases. Further, the compressibility underlines a marked difference between the two diffusion coefficients, and it is therefore justified to expect very different behavior of D_{T} and D_{C} under certain conditions. To address these questions, we will discuss some model results in Sect. 12.5.5.

12.5.4 Methods to Examine Lateral Collective Diffusion

Computational Approaches

Having established a model, which can be studied through computer simulations, one can determine D_{C} from density fluctuations by (12.15) with small k (for a system of size L^3, one obtains $k = 2\pi/L$). Then the slope of $\ln S(\boldsymbol{k}, t)$ at large times yields D_{C}. This approach is particularly suitable in the case of discrete models such as those studied through Monte Carlo simulations, in which velocities are not well defined. In systems with continuous interaction potentials such as those studied in MD simulations, one can use the Green-Kubo approach in (12.17).

The computational cost of calculating D_{C} is nevertheless large compared to tracer diffusion. This is mainly due to the fact that, contrary to tracer diffusion, all (labeled) molecules in a system are needed to provide one sample for the evaluation of D_{C}. In other respects, the discussion presented in Sect. 12.3.2 holds here as well.

Experimental Techniques

The Fourier transform of $S(\boldsymbol{k}, t)$ (in time),

$$S(\boldsymbol{k}, \omega) = \frac{S(\boldsymbol{k}, 0)}{\pi} \frac{D_{\mathrm{C}}\, k^2}{\omega^2 + (D_{\mathrm{C}}\, k^2)^2}, \tag{12.21}$$

is very useful for practical cases, since it can be measured through (quasi-elastic) neutron scattering experiments, for example (cf. Chaps 2, 3 and 13). It yields

$$D_{\mathrm{C}} = \frac{\pi}{S(0,0)} \lim_{\omega \to 0} \omega^2 \lim_{k \to 0} \frac{1}{k^2} S(k, \omega), \tag{12.22}$$

when the direction in $\boldsymbol{k}$-space is fixed.

Another widespread technique used to study lateral diffusion is the fluorescence recovery after photobleaching (FRAP) [60, 61], which has proved to be a popular means to assess the structure and dynamics of membranes. In this technique, a certain fraction of lipids in a membrane is labeled by a fluorescently active probe. A light source is then focused onto a small region of the membrane to determine the background level of fluorescence, after which the fluorescently active molecules within the region of interest are photobleached by a high-intensity laser. Consequently the intensity coming from the blackened area drops down, but recovers in time as the fluorescently labeled molecules in the surrounding area diffuse into the region under study. By measuring the rate of recovery of fluorescence, one is able to determine the diffusion coefficient [29]. Further, the extent of recovery provides information of how many molecules are able to move in a membrane, and therefore FRAP can provide valuable information of regions where the motion of lipids or proteins is confined.

There are reasons to comment on a few subtle issues regarding this approach, however. First, the spatial resolution of FRAP is typically about 100 nm, the time resolution about 100 ns, and thus FRAP is not able to detect the short-time dynamics of diffusing molecules. Second, the experiments are done over hundreds or thousands of labeled molecules, and therefore they do not provide a true description of single-particle motion. Rather, they describe the rate of how fast a large number of interacting molecules fills the region of interest.

It is worthwhile pointing out that the FRAP technique is very similar to the laser-induced thermal desorption method [106] used in surface science for studies of collective diffusion (cf Chap. 7). Another technique closely related to the FRAP experiment is the Boltzmann-Matano (BM) method [104] (cf. Sect. 1.11.1 of Chap. 1), which also is commonly used in studies of collective diffusion of particles migrating on solid surfaces ([106,107], see also Chap. 7). In the BM method, one considers a step-like density gradient which starts to spread at $t = 0$, and the concentration profile in time yields the collective diffusion coefficient. In membranes, the same technique could be applied by labeling a major fraction of lipids and then photobleaching the lipids beyond some regime (say, $x > 0$). By following the concentration profile of fluorescently active molecules as a function of x-coordinate in time, one could extract the collective diffusion coefficient of the photobleached molecules. Although this idea seems worthwhile, it has not, to the best of our knowledge, been carried out yet.

Finally, a number of other techniques are often used in studies of lateral diffusion. NMR T_1 relaxation [62] measures diffusion over short distances, although the results are interpreted in terms of Fick's laws. QENS techniques [63–66] are also microscopic as they extend over short times and distances, and are comparable to current MD simulations. Larger scale properties of diffusion are measured by NMR-spin echo [62] and ESR [67], among others.

12.5.5 Lateral Collective Diffusion in Model Membranes

Collective Diffusion in Lipid-Cholesterol Mixtures

We have emphasized in the discussion above that tracer and collective diffusion characterize different aspects of mass transfer. Let us here illustrate by an example how this difference is manifested in practice.

We use the same minimal model as in the study of lateral tracer diffusion of lipid molecules in Sect. 12.3.3. Our objective is to examine a situation where a certain number of labeled molecules are diffusing in a bilayer comprised mainly of non-labeled lipids. The concentration of labeled molecules is varied such that the total number of molecules in a bilayer remains constant. In the present model system, this setup is accomplished by considering cholesterol molecules as labeled ones, while the lipid molecules form the environment in which the cholesterol molecules diffuse.

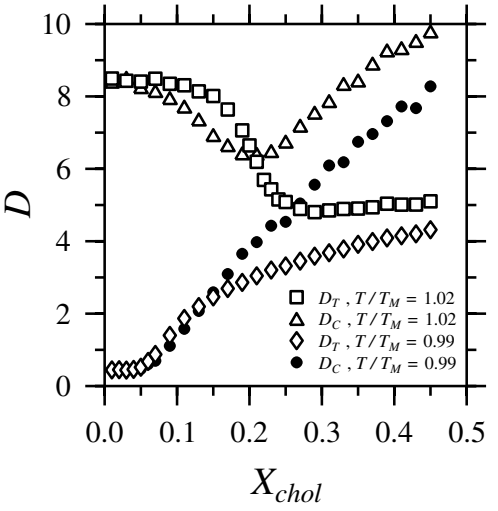

Fig. 12.8. Results for the lateral tracer and collective diffusion coefficients of cholesterol molecules in the model of a lipid-cholesterol mixture as a function of cholesterol concentration $X_{\rm chol}$. The results for $D_{\rm T}$ are given in units of $\sigma^2 \,/\, t_{\rm MC}$, where σ is the length scale related to the hard-core size of a molecule (see [98] for details), and $t_{\rm MC}$ is the time in Monte Carlo units. Results are given at two temperatures as described by $T/T_{\rm M}$, where $T_{\rm M}$ is the temperature of the main phase transition. Tracer diffusion results are shown by squares ($T/T_{\rm M} = 1.02$) and diamonds ($T/T_{\rm M} = 0.99$), while results for collective diffusion are illustrated by triangles ($T/T_{\rm M} = 1.02$) and circles ($T/T_{\rm M} = 0.99$).

In Fig. 12.8 we show data for the tracer and collective diffusion coefficients of cholesterol molecules as a function of cholesterol concentration $X_{\rm chol}$. We find that $D_{\rm T} \approx D_{\rm C}$ at small concentrations, as expected, but at larger concentrations of cholesterol molecules the deviation between $D_{\rm T}$ and $D_{\rm C}$ becomes more and more apparent. In the high-temperature phases at $T > T_{\rm M}$, the crossover from $D_{\rm T} \approx D_{\rm C}$ to $D_{\rm T} \neq D_{\rm C}$ takes place around $X_{\rm chol} = 5\,\%$, after which the two diffusion coefficients have little in common. In the low-temperature phase at $T < T_{\rm M}$, the deviation between $D_{\rm T}$ and $D_{\rm C}$ becomes clear around $X_{\rm chol} = 5-7\,\%$, where one crosses the boundary between **so** and **so-lo** phases. Perhaps surprisingly, the quantitative difference between $D_{\rm T}$ and $D_{\rm C}$ is not prominent. Instead, the difference in both cases is most pronounced in the qualitative features and is somehow related to the phase behavior of the system.

The purpose of this example is not to provide quantitative understanding of how large concentrations of labeled molecules one can safely use in studies of lateral tracer diffusion. However, these results show that $D_{\rm T}$ and $D_{\rm C}$ are distinctly different, and this difference becomes clear even at relatively small concentrations. In practice, the crossover concentration is likely to depend

on the strength and extent of intermolecular interactions, and is obviously system dependent.

12.6 Diffusive Transport Through Membranes

So far we have been concerned with diffusional processes that take place within and along the plane of the membrane sheet. Since membranes serve their main purpose as barriers for diffusion across the membrane in order to maintain various gradients needed for biological activity, it is of major interest to understand what determines these barrier properties and how they may be modulated. The importance of these questions becomes clear when considering that the main reason for cell death is membrane leakage, and that the most efficient way to kill bacteria and microbes is to damage their membranes by lowering their membrane permeability barrier by poking holes in the membrane by certain peptides. The most important barriers for live processes in vertebrates include the blood-brain barrier and the skin, which both are barriers mediated by membranes. One of the most challenging questions is to figure out how new and potent drugs can cross these barriers.

Crossing the lipid-bilayer membrane is a complex process since it involves traversing a stratified and highly structured interface of both hydrophilic and hydrophobic nature [108]. If we first consider membrane proteins, these do not diffuse randomly across the membrane without being facilitated by certain enzymes and transporter molecules. In contrast, the lipid molecules, being amphiphilic, undergo so-called flip-flop diffusion that takes the molecule from one leaflet of the bilayer to the other. However, since this process involves transfer of a hydrophilic head group through the hydrophobic interior, it is exceedingly slow and characterized by time scales in the range from minutes to days. The flip-flop processes that are needed to maintain the membrane in its functional asymmetric state are controlled by specific transmembrane proteins ('flippases'). Spontaneous flip-flop processes can however be enhanced by various solutes that change the trans-membrane profile.

The passive trans-membrane diffusion of various molecular species is referred to as passive permeability. Lipid bilayer membranes are fairly permeable to water, gaseous substances like CO_2 and O_2, and small hydrophobic molecules like benzene, whereas ions and larger molecular species such as glucose and amino acids as well as peptides pass only very slowly.

The permeation of molecular species across lipid bilayers [109, 110] depends on both the diffusion coefficient and the solubility of the permeant in the membrane. The permeability therefore intimately reflects the inhomogeneous nature of the membrane, both transversely and laterally. The detailed motion of permeants in lipid bilayers is difficult to monitor experimentally, and new insight into the mechanism of permeation therefore mostly stems from molecular dynamics calculations [40].

It has appeared from such studies, in accordance with interpretation of experiments [111], that the main barrier to trans-bilayer permeation of small molecules is the region that contains the carbonyl groups which are in between the head-group region and the hydrophobic region in Fig. 12.2. In this region diffusion is hampered by the low free volume. Furthermore, the highly ordered lipid acyl-chain segments underneath the carbonyl groups tend to orient anisotropic permeants. The rate of permeation is strongly dependent on the molecular size and polarity of the permeant. Deeper into the hydrophobic region, small molecules like benzene take advantage of the available free volume and diffuse by a non-Brownian jump mechanism such that the diffusion coefficient turns out to be about the same throughout the hydrophobic bilayer core. In contrast, larger molecules, e.g. the drug analogue molecule nifedipine [112], undergo simple Brownian diffusion and the diffusion coefficient is therefore dependent on the position in the bilayer. The properties of the head-group region, which is about 8 Å wide and has maximum density, are important for the penetration of ionic species into the bilayer. In this region the water density gets very small and all water molecules present are involved in the hydration of the lipid polar head groups. This is the boundary zone where impinging ions will have to change their hydration level and look for water fingers in order to get into the hydrophobic interior of the bilayer. The central core of the hydrophobic region is the region of lowest density because of the disordered chain segments. This hydrophobic region easily dissolves permeating hydrophobic species and can accommodate large and bulky (drug) molecules.

Turning now to the effect on permeation of the lateral structure of the lipid bilayer it is obvious that the considerations for trans-bilayer permeation presented above have to be modified in order to account for the possibility that the actual bilayer profile, which a given permeant sees, can vary laterally across the bilayer [113]. This is particularly important under those conditions where the bilayer undergoes large fluctuations in local density or composition due to the proximity to phase transitions and phase-separation phenomena. In those cases, small-scale structural heterogeneity and lipid-domain structure as illustrated in Fig. 12.9 are expected to prevail [114, 115]. The small-scale structure implies the presence of domain boundaries with less favorable molecular packing conditions. At these boundaries, which act effectively as defect lines, more free volume is available which in general will enhance permeation under the conditions that produce such heterogeneity. This effect is illustrated in Fig. 12.10(a) [116], which shows that at the main transition, the lipid bilayer displays an anomalous permeability behavior in the case of Na^+ permeation through DPPC bilayers. This permeability anomaly is in fact a fairly generic phenomenon, which is not only found for small cations but also for a number of other small and larger molecular compounds.

When several different lipid species are present in a bilayer membrane, a more complex phase behavior arises due to phase coexistence as described

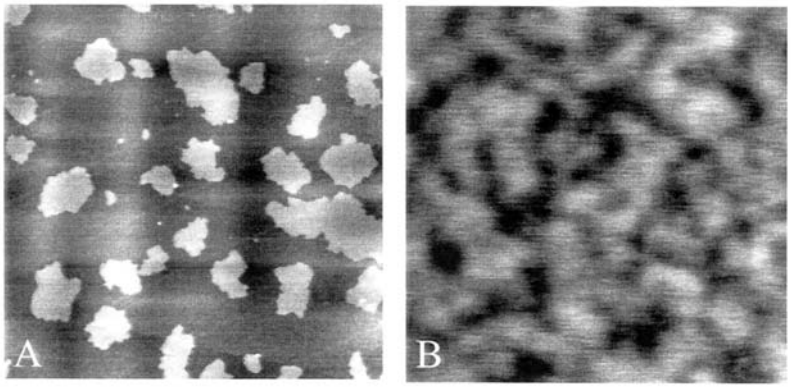

Fig. 12.9. Lateral structure of lipid monolayers transferred to a solid support and subsequently imaged by atomic force microscopy. The lateral structure in these monolayers are similar to that in bilayers. The different grey tones reflect height differences. (a) Lipid monolayer of DMPC in the fluid phase near the phase transition. Image size is $5\,\mu\text{m} \times 5\,\mu\text{m}$. Maximum height difference is about 5 Å. (b) Lipid monolayer of a binary mixture of DMPC-DSPC near the coexistence region. Image size is $250\,\text{nm} \times 250\,\text{nm}$. Maximum height difference is about 2 Å.

by the thermodynamic phase diagram. This has some dramatic consequences for the permeability of the bilayer. Figure 12.10(b) shows the permeability of a small negative ion (dithionite, $S_2O_4^{2-}$) [117] through 1:1 DMPC-DSPC bilayers. It is observed that the permeability displays two peaks corresponding to the liquidus and solidus phase boundaries. This implies that the binary bilayers become leaky at the borders of the coexistence region. Furthermore it is interesting to note that the level of the permeability in the coexistence region is considerably higher than in either of the two phases. This suggests that the mixture is not fully separated and therefore possibly not in thermal equilibrium.

It is possible to take advantage of these special mixing properties of lipid bilayers to design bilayer systems, e.g. in the form of liposomes to be used for drug-delivery purposes, with particularly strong enhancer effects in relation to permeation. An example is a mixture involving short-chain lipids like $DC_{10}PC$ [117]. The short-chain lipid molecules enhance fluctuations and hence the lateral heterogeneity of the liposomal membranes leading to dramatic leakage.

This enhancement of trans-bilayer permeation due to small-scale bilayer structural heterogeneity is expected to be a generic effect and qualitatively independent of the permeating species and the lipid material. Of course, the magnitude of the enhancement and the range of parameter values (temperature, composition, pH, etc.) over which it occurs depends on details, such as the size, charge, and hydrophobicity, of the permeant, as well as the materials

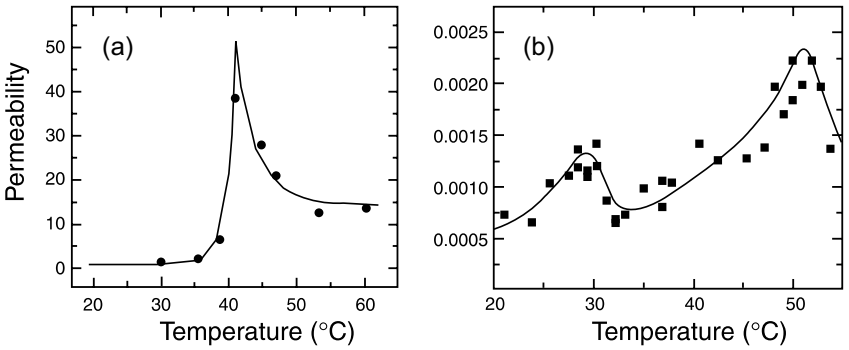

Fig. 12.10. (a) Relationship between passive permeability of Na^+-ions (•) measured by radioactive tracer experiments and computer simulation of lipid-bilayer heterogeneity (—). (b) Thermal scan across the phase diagram of a 1:1 lipid-bilayer mixture of DMPC-DSPC showing the variation of the trans-bilayer permeability of dithionite ions ($S_2O_4^{2-}$) measured by fluorescence quenching techniques.

characteristics of the lipid bilayer (thermodynamic phase, polar head groups, degree of acyl-chain unsaturation, etc.).

Once having established the relationship between small-scale lipid-bilayer structure and trans-bilayer diffusion, it becomes of interest to explore how one can use this relationship to modify permeation of certain substances, such as drugs, by manipulating the microstructure [117]. The effect of cholesterol is a particularly interesting example [118]. In fluid lipid bilayers, cholesterol in amounts larger than about five molar percent effectively acts as an acyl-chain rigidifier hence lowering the free volume in hydrophobic region of the bilayer. This leads to a suppression of the permeation and therefore a sealing effect of bilayer. It is interesting to note that cholesterol (or similar sterols) is universally present in large amounts (about 30 – 50 %) in the plasma membranes of all eucaryotes.

12.7 Conclusion

Diffusion of lipids and other molecules in membranes is an example of the dynamic nature of soft fluctuating interfaces. This feature is characteristic for various soft-matter systems that are governed by interactions on the order of thermal energy. Consequently, understanding the dynamics of membranes is highly challenging, since one needs to work on a bridge between truly solid and fluid phases, and since one has to deal with the time-dependent nature of diffusion as well as the wide range of time and length scales associated with diffusion processes.

In the present chapter, we have tried to illustrate some of the key features of diffusion in membranes. Hopefully we have managed to open the door a

little and guide your way to work on the topic. It is fascinating that despite all work done so far, there are major gaps in our understanding of diffusion, ranging from the microscopic molecular limit of diffusion mechanisms up to the large-scale properties of diffusion in lateral heterogeneous environments of large topological complexity, to name just a few examples. The topic is genuinely interesting, and we wish to encourage all to reveal its secrets.

Notation

a	free area in a bilayer
a^*	critical free area in a bilayer
a_t	average free area per molecule
$C_2(t)$	time autocorrelation function
d	dimensionality
D	diffusion coefficient
$D(a)$	diffusion coefficient inside a free area a
D_{C}	collective diffusion coefficient
D_{T}	tracer diffusion coefficient
D_{R}	rotational diffusion coefficient
D_ℓ	diffusion coefficient of proteins
h	height of the membrane
$\boldsymbol{J}(t)$	total particle flux
$\boldsymbol{j}(\boldsymbol{r}, t)$	particle current density
$\boldsymbol{k}$	wave vector
k_{B}	Boltzmann constant
ℓ_D	diffusion length
ℓ_{12}	vector from site "1" to site "2"
N	number of molecules
$p(a)$	probability of finding a free area of a
$P(\Delta r, \Delta t)$	probability to find a displacement of Δr over a time interval of Δt
P_2	2nd Legendre polynomial
$\boldsymbol{r}(t)$	position at time t
R_{L}^2	area per lipid
$\mathcal{R}$	radius
$S(\boldsymbol{r}, \boldsymbol{r}', t)$	density autocorrelation function
t	time
T	temperature
T_{M}	main phase transition temperature of the lipid bilayer
$\boldsymbol{u}(t)$	unit vector at time t
$\boldsymbol{v}(t)$	velocity at time t
$\boldsymbol{v}_i(t)$	velocity of particle i at time t
x	exponent
X_{chol}	cholesterol concentration

Γ	geometric factor
Δr	particle displacement
Δt	time interval
$\Theta(t)$	angle in time t
κ_T	isothermal compressibility
μ	viscosity of the bilayer
μ'	viscosity of the surrounding fluid
$\langle\rho\rangle$	average density
$\rho(\boldsymbol{r},t)$	local particle density at $\boldsymbol{r}$ at time t
τ_{c}	characteristic time scale
$\phi(t)$	velocity autocorrelation function
ω	frequency
BM	Boltzmann-Matano
DNA	deoxyribonucleic acid
DMPC	dimyristoyl phosphatidylcholine
DPPC	dipalmitoyl phosphatidylcholine
DSPC	distearoyl phosphatidylcholine
ESR	electron spin resonance
FRAP	fluorescence recovery after photobleaching
MD	molecular dynamics
NMR	nuclear magnetic resonance
PC	phosphatidylcholine
PLPC	palmitoyl-laureoyl phosphatidylcholine
POPC	palmitoyl-oleoyl phosphatidylcholine
QENS	quasi-elastic neutron scattering
RNA	ribonucleic acid
UQ	ubiquinone

References

1. H. Flyvbjerg, T. E. Holy, S. Leibler: Phys. Rev. E **54**, 5538 (1996)
2. H.C. Berg: *Random Walks in Biology*, expanded edn (Princeton University Press, Princeton 1993)
3. U. Essmann, M.L. Berkowitz: Biophys. J. **76**, 2081 (1999)
4. G.W. Weiss, R.J. Rubin, Eds.: J. Stat. Phys. **30**, 2 (1983)
5. A. Einstein: *Investigations on the Theory of the Brownian Movement*, edited with notes by R. Fürth and translated by A.D. Cowper (Dover 1956)
6. D. Needham: MRS Bulletin **24**, 32 (1999)
7. S. Ohta-Iino, M. Pasenkiewicz-Gierula, Y. Takaoka, H. Miyagawa, K. Kitamura, A. Kusumi: Biophys. J. **81**, 217 (2001)
8. J.A. Söderhäll, A. Laaksonen: J. Phys. Chem. B **105**, 9308 (2001)
9. D. Voet, J.G. Voet: *Biochemistry*, 2nd edn (Wiley, New York 1995)
10. G. Cevc, D. Marsh: *Phospholipid Bilayers: Physical Principles and Models* (Wiley, New York 1987)

11. R.B. Gennis: *Biomembranes: Molecular Structure and Function* (Springer, Berlin Heidelberg New York 1989)
12. M. Bloom, E. Evans, O.G. Mouritsen: Q. Rev. Biophys. **24**, 293 (1991)
13. J F. Nagle, S. Tristram-Nagle: Biochim. Biophys. Acta **1469**, 159 (2000)
14. *Lipid Bilayers: Structure and Interactions*. ed by J. Katsaras, T. Gutberlet (Springer, Berlin Heidelberg New York 2001)
15. *Structure and Dynamics of Membranes: From Cells to Vesicles*, ed by R. Lipowsky, E. Sackmann (Elsevier, Amsterdam 1995)
16. *Biological Membranes. A Molecular Perspective from Computation and Experiment*, ed by K.M. Merz Jr, B. Roux (Birkhäuser, Boston 1996)
17. *Fluctuations and Scaling in Biology*, ed by T. Vicsek (Oxford University Press, Oxford 2001)
18. C. Isenberg: *The Science of Soap Films and Soap Bubbles* (Dover, New York 1992)
19. D.F. Evans, H. Wennerström: *The Colloidal Domain: Where Physics, Chemistry, Biology, and Technology Meet*, 2nd edn (Wiley-VCH, New York 1999)
20. S. Hyde, S. Andersson, K. Larsson, Z. Blum, T. Landh, S. Lidin, B.W. Ninham: *The Language of Shape. The Role of Curvature in Condensed Matter: Physics, Chemistry and Biology* (Elsevier, Amsterdam 1997)
21. M. Hyvönen, K. Öörni, P.T. Kovanen, M. Ala-Korpela: Biophys. J. **80**, 565 (2001)
22. S.J. Singer, G.L. Nicholson: Science **175**, 720 (1972)
23. P.F.F. Almeida, W.L.C. Vaz: Lateral Diffusion in Membranes. In: *Structure and Dynamics of Membranes: From Cells to Vesicles*, ed by R. Lipowsky, E. Sackmann (Elsevier, Amsterdam 1995) pp 305–357
24. U. Seifert: Curr. Opin. Colloid Interface Sci. **1**, 350 (1996)
25. H.G. Döbereiner: Curr. Opin. Colloid Interface Sci. **5**, 256 (2000)
26. O.G. Mouritsen, K. Jørgensen, J.H. Ipsen, M.M. Sperotto: Domains and Patterns in Biological Membranes. In: *Modelling the Dynamics of Biological Systems. Non-linear Phenomena and Pattern Formation*, ed by E. Mosekilde, O.G. Mouritsen (Springer-Verlag, Berlin Heidelberg New York 1995) pp 77–100
27. A. Einstein: Ann. Phys. **17**, 549 (1905)
28. J.-P. Hansen, I.R. McDonald: *Theory of Simple Liquids*, 2nd edn (Academic Press, San Diego 2000)
29. M.J. Saxton: Biophys. J. **81**, 2226 (2001)
30. J.-P. Bouchaud, A. Georges: Phys. Rep. **195**, 127 (1990)
31. J.W. Haus, K.W. Kehr: Phys. Rep. **150**, 263 (1987)
32. B.J. Alder, T.E. Wainwright: Phys. Rev. Lett. **18**, 988 (1967)
33. B.J. Alder, T.E. Wainwright: Phys. Rev. A **1**, 18 (1970)
34. S.C. Ying, I. Vattulainen, J. Merikoski, T. Hjelt, T. Ala-Nissila: Phys. Rev. B **58**, 2170 (1998)
35. M. Eichinger, P. Tavan, J. Hutter, P. Parrinello: J. Chem. Phys. **110**, 10452 (1999)
36. W. Andreoni, A. Curioni, T. Mordasini: IBM J. Res. & Dev. **45**, 397 (2001)
37. M.P. Allen, D.J. Tildesley: *Computer Simulation of Liquids* (Oxford University Press, Oxford 1993)
38. D. Frenkel, B. Smit: *Understanding Molecular Simulation*, 2nd edn (Academic Press, San Diego 2002)

39. R.W. Pastor, S.E. Feller: Time Scales of Lipid Dynamics and Molecular Dynamics. In: *Biological Membranes: A Molecular Perspective from Computation and Experiment*, ed by K.M. Merz Jr, B. Roux (Birkhäuser, Boston 1996) pp 3–29
40. D.P. Tieleman, S.J. Marrink, H.J.C. Berendsen: Biochim. Biophys. Acta **1331**, 235 (1997)
41. D.J. Tobias, K. Tu, M.L. Klein: Curr. Opin. Colloid Interface Sci. **2**, 15 (1997)
42. S.E. Feller: Curr. Opin. Colloid Interface Sci. **5**, 217 (2000)
43. E. Falck, M. Patra, M. Karttunen, M.T. Hyvonen, I. Vattulainen: Biophys J. **89**, 745 (2005)
44. E. Falck, M. Patra, M. Karttunen, M.T. Hyvonen, I. Vattulainen: Biophys. J. **87**, 1076 (2004)
45. S.A. Pandit, E. Jakobsson, H.L. Scott: Biophys. J. **87**, 3312 (2004); P. Niemelä, M. T. Hyvönen, M. Karttunen, I. Vattulainen: unpublished
46. R.D. Groot, K.L. Rabone: Biophys. J. **81**, 725 (2001)
47. J.C. Shelley, M.Y. Shelley, R.C. Reeder, S. Bandyopadhyay, M.L. Klein: J. Phys. Chem. B **105**, 4464 (2001)
48. R. Goetz, R. Lipowsky: J. Chem. Phys. **108**, 7397 (1998)
49. R. Goetz, G. Gompper, R. Lipowsky: Phys. Rev. Lett. **82**, 221 (1999)
50. M.C. Sabra, O.G. Mouritsen: Monte Carlo Simulations of Lateral Membrane Organization. In: *Methods in Enzymology*, vol 321, ed by M.L. Johnson, L. Brand. (Academic Press, New York, 2000) pp 263–278
51. J.M. Polson, I. Vattulainen, H. Zhu, M.J. Zuckermann: Eur. Phys. J. E **5**, 485 (2001)
52. P. Høyrup, K. Jørgensen, O.G. Mouritsen: Europhys. Lett. **57**, 464 (2002)
53. M.J. Saxton, K. Jacobsen: Annu. Rev. Biophys. Biomol. Struct. **26**, 373 (1997)
54. M.B. Forstner, J. Käs, D. Martin: Langmuir **17**, 567 (2001)
55. T. Schmidt, G. J. Schütz, W. Baumgartner, H.J. Gruber, H. Schindler: J. Phys. Chem. **99**, 17662 (1995)
56. T. Schmidt, G.J. Schütz, W. Baumgartner, H.J. Gruber, H. Schindler: Proc. Natl. Acad. Sci. U.S.A. **93**, 2926 (1996)
57. P. Schwille, J. Korlach, W.W. Webb: Cytometry **36**, 176 (1999)
58. A. Sonnleitner, G.J. Schütz, T. Schmidt: Biophys. J. **77**, 2638 (1999)
59. G.S. Harms, M. Sonnleitner, G.J. Schütz, H.J. Gruber, T. Schmidt: Biophys. J. **77**, 2864 (1999)
60. D. Axelrod, D.E. Koppel, J. Schlessinger, E. Elson, W.W. Webb: Biophys J. **16**, 1055 (1976)
61. D.M. Soumpasis: Biophys. J. **41**, 95 (1983)
62. G. Lindblom, G. Orädd: Prog. NMR Spec. **26**, 483 (1994)
63. W. Pfeiffer, Th. Henkel, E. Sackmann, W. Knoll, D. Richter: Europhys. Lett. **8**, 201 (1989)
64. S. König, W. Pfeiffer, T. Bayerl, D. Richter, E. Sackmann: J. Phys. II **2**, 1589 (1992)
65. E. Sackmann: Physical Basis of Self-Organization and Function of Membranes: Physics of Vesicles. In: *Structure and Dynamics of Membranes: From Cells to Vesicles*, ed by R. Lipowsky, E. Sackmann (Elsevier, Amsterdam 1995) pp 213–304
66. S. König, E. Sackmann: Curr. Opin. Colloid Interface Sci. **1**, 78 (1996)
67. J.H. Freed: Annu. Rev. Biophys. Biomol. Struct. **23**, 1 (1994)

68. P. Heitjans, S. Indris: J. Phys.: Condens. Matter **15**, R1257 (2003)
69. F.T. Presti: The Role of Cholesterol in Regulating Membrane Fluidity. In: *Membrane Fluidity in Biology*, vol 4, ed by R.C. Aloia, J.M. Boggs (Academic Press, Orlando 1985) pp 97–145
70. P.B. Moore, C.F. Lopez, M.L. Klein: Biophys. J. **81**, 2484 (2001)
71. R.M. Venable, Y. Zhang, B.J. Hardy, R.W. Pastor: Science **262**, 223 (1993)
72. J. Tabony, B. Perly: Biochim. Biophys. Acta **1063**, 67 (1990)
73. A.L. Kuo, C.G. Wade: Biochemistry **18**, 2300 (1979)
74. B.J. Balcom, N.O. Petersen: Biophys. J. **65**, 630 (1993)
75. A. Pampel, J. Kärger, D. Michel: Chem. Phys. Lett. **379**, 555 (2003)
76. T.R. Stouch, D. Bassolino: Movement of Small Molecules in Lipid Bilayers: Molecular Dynamics Simulation Studies. In: *Biological Membranes. A Molecular Perspective from Computation and Experiment*, ed by K.M. Merz Jr, B. Roux (Birkhäuser, Boston 1996) pp 255–279
77. D. Bassolino-Klimas, H.E. Alper, T.R. Stouch: Biochemistry **32**, 12624 (1993)
78. R.M. Clegg, W.L.C. Vaz: Translational Diffusion of Proteins and Lipids in Artificial Lipid Bilayer Membranes. A Comparison of Experiment with Theory. In: *Progress in Protein-Lipid Interactions*, ed by A. Watts, J.J.H.H.M. De Pont (Elsevier, Amsterdam 1985) pp 173–229
79. P.G. Saffman, M. Delbrück: Proc. Natl. Acad. Sci. U.S.A. **72**, 3111 (1975)
80. S. König, T.M. Bayerl, G. Coddens, D. Richter, E. Sackmann: Biophys. J. **68**, 1871 (1995)
81. M.H. Cohen, D. Turnbull: J. Chem. Phys. **31**, 1164 (1959)
82. C. Gliss, O. Randel, H. Casalta, E. Sackmann, R. Zom, T. Bayerl: Biophys. J. **77**, 331 (1999)
83. P.F.F. Almeida, W.L.C. Vaz, T.E. Thompson: Biochemistry **31**, 6739 (1992)
84. T. Sintes, A. Baumgärtner, Y.K. Levine: J. Mol. Liq. **84**, 77 (2000)
85. Y. Sako, A. Kusumi: J. Cell. Biol. **125**, 1251 (1994)
86. R. Simson, E.D. Sheets, K. Jacobson: Biophys. J. **69**, 989 (1995)
87. C. Dietrich, B. Yang, T. Fujiwara, A. Kusumi, K. Jacobson: Biophys. J. **82**, 274 (2002)
88. E.D. Sheets, G.M. Lee, R. Simson, K. Jacobson: Biochemistry **36**, 12449 (1997)
89. R. Simson, B. Yang, S.E. Moore, P. Doherty, F.S. Walsh, K.A. Jacobson: Biophys. J. **74**, 297 (1998)
90. P.R. Smith, I.E.G. Morrison, K.M. Wilson, N. Fernández, R.J. Cherry: Biophys. J. **76**, 3331 (1999)
91. M.J. Saxton: Biophys. J. **66**, 394 (1994)
92. M.J. Saxton: Biophys. J. **70**, 1250 (1996)
93. K. Bloch: Cholesterol: evolution of structure and function. In: *Biochemistry of lipids, lipoproteins and membranes*, ed by D.E. Vance, J.E. Vance (Elsevier, Amsterdam 1991) pp 363–381
94. L. Finegold: *Cholesterol in Model Membranes* (CRC Press, Boca Raton Florida 1993)
95. D. Needham, T.J. MacIntosh, E. Evans: Biochemistry **27**, 4668 (1988)
96. W.L.C. Vaz: Comments Mol. Cell. Biophysics **8**, 17 (1992)
97. J.-F. Tocanne, L. Dupou-Cézanne, A. Lopez: Prog. Lipid Res. **33**, 203 (1994)
98. M. Nielsen, L. Miao, J.H. Ipsen, M.J. Zuckermann, O.G. Mouritsen: Phys. Rev. E **59**, 5790 (1999)

99. M. Nielsen, L. Miao, J.H. Ipsen, O.G. Mouritsen, M.J. Zuckermann: Phys. Rev. E **54**, 6889 (1996)
100. M. Nielsen, L. Miao, J.H. Ipsen, O.G. Mouritsen, M.J. Zuckermann, J. Thewalt, M. Bloom: Europhys. Lett. **52**, 368 (2000)
101. J.L.R. Rubenstein, B.A. Smith, H.M. McConnell: Proc. Natl. Acad. Sci. U.S.A. **76**, 15 (1979)
102. T.M. Bayerl: Curr. Opin. Colloid Interface Sci. **5**, 232 (2000)
103. A. Fick: Ann. Phys. **170**, 59 (1855)
104. J. Crank: *The Mathematics of Diffusion*. (Oxford University Press, Oxford 1995)
105. N.H. March, M.P. Tosi: *Atomic Dynamics in Liquids* (Dover Publications, New York 1976)
106. R. Gomer: Rep. Prog. Phys. **53**, 917 (1990)
107. *Collective Diffusion on Surfaces: Correlation Effects and Adatom Interactions*. ed by M.C. Tringides, Z. Chvoj (Kluwer, Dordrecht 2001)
108. S.H. White, M.C. Wiener: The liquid-crystallographic structure of fluid lipid bilayer membranes. In: *Biological Membranes. A Molecular Perspective from Computation and Experiment*, ed by K.M. Merz Jr, B. Roux (Birkhäuser, Boston 1996) pp 127–144
109. *Permeability and Stability of Lipid Bilayers*, ed by E.A. Disalvo, S.A. Simon (CRC Press, Boca Raton 1995)
110. O.G. Mouritsen: Physical properties of lipid-bilayer membranes. In: *Peptide and Protein Drug Delivery, Alfred Benzon Symposium 43*, ed by S. Frøkjær, L. Christrup, P. Krogsgaard-Larsen (Munksgaard, Copenhagen 1998) pp 17–32
111. T.X. Xiang, B.D. Anderson: J. Memb. Biol. **140**, 111 (1994)
112. H.E. Alper, T.R. Stouch: J. Phys. Chem. **99**, 5724 (1995)
113. O.G. Mouritsen, K. Jørgensen, T. Hønger: Permeability of lipid bilayer near the phase transition. In: *Permeability and Stability of Lipid Bilayers*, ed by E.A. Disalvo, S.A. Simon (CRC Press, Boca Raton 1995) pp 89–112
114. L.K. Nielsen, T. Bjørnholm, O.G. Mouritsen: Nature **404**, 352 (2000)
115. L.K. Nielsen, A. Vishnyakov, K. Jørgensen, T. Bjørnholm, O.G. Mouritsen: J. Phys.: Condens. Matter **12**, 309 (2000)
116. D. Papahadjopoulos, K. Jacobsen, S. Nir, T. Isac: Biochim. Biophys. Acta **311**, 330 (1973)
117. O.G. Mouritsen, H.K. Andersen, J.S. Andersen, J. Davidsen, L.K. Nielsen, K. Jørgensen: Structure of liposomal membranes in relation to permeation. In: *Pharmacokinetic Optimization in Drug Research: Biological, Physicochemical and Computational Strategies*, ed by B. Testa, H. van de Waterbeemd, G. Folkers, R. Guy (Wiley-Verlag Helvetica Chemica Acta, Zürich 2000) pp 33–49
118. T.H. Haines: Prog. Lip. Res. **40**, 299 (2001)

Part III

Liquids

13 Viscoelasticity and Microscopic Motion in Dense Polymer Systems

Dieter Richter

13.1 Introduction

The mechanical properties of condensed matter are generally divided into two classes: solids, such as metals or glasses, behave elastically; for small deformations the stress is proportional to the strain – Hooke's law is valid. Liquids display viscous behavior; in this case the stress is proportional to the change in strain, Newton's law persists. In contrast, the mechanical dynamical properties of polymers are extraordinarily versatile. Depending on the temperature or load time, the same polymer may display vitreous, rubberlike or fluid behaviour. This wide range of behaviour is known as viscoelastic.

In particular, the dynamic modulus of long-chain linear polymers displays a plateau regime which expands with growing chain length [1]. In this plateau region, the stress is proportional to strain – although a liquid, the polymer melt behaves elastically. For long times the material yields and viscous behavior takes over. This behaviour reminds us of the rubber elasticity of chemically cross-linked polymers. The elastic modulus of rubbers is proportional to the temperature and inversely proportional to the mesh size of the network. The proportionality to temperature is caused by entropic forces resulting from the conformational entropy of the coiled chains between the network points. If chain pieces are stretched, an entropic force originating from the reduction of free energy acts with the aim of restoring the more probable coiled state for these stretched segments.

Based on this analogy to rubber elasticity it is natural to assume that the elastic behaviour of polymer melts is caused by network-like entanglements of the polymer chains, so that the melt becomes a temporary network. The role of the network points is taken over by entanglements. The plateau modulus is ascribed to the rubber elastic modulus of this temporary network. On this assumption it is possible to estimate the mean distance between the hypothetical entanglement points in the melt from the value of the plateau modulus. The resultant entanglement distances d are typically of the order of $d = 40 - 100\,\text{Å}$. Compared with the two characteristic length scales of a polymer, the monomer length $\ell \sim 5\,\text{Å}$ and the coil end-to-end distance $R_\text{E} \sim 1000\,\text{Å}$, the entanglement distance defines an intermediate length scale of a dynamic nature.

If a solid is subjected to a mechanical strain, then the individual atoms or molecules move in their local potential and take on a new equilibrium position. A macroscopic deformation at a polymer, in contrast, causes complex molecular rearrangements, starting from individual bonds up to and including the molecular dimensions. On the scale of the individual bond, these rearrangements proceed at a speed similar to that in a normal solid. This local bond dynamics is governed by the local potentials and occurs on length scales of a few Ångstrøms and times from several picoseconds upwards and is of particular interest in connection with glass transition phenomena. For intermediate times corresponding to spatial distances shorter than the entanglement distance we expect motional mechanisms which are driven by entropic forces. These motions are described by the so-called Rouse model [2]. As the spatial extension of motion increases and reaches dimensions of the entanglement distance, the freedom of motion of the chain is greatly restricted. The temporary network leads to a localization of the chain, which dominantly moves like a snake along its own profile due to the network, which restricts lateral motions. For very long times, the chain leaves its original topological restrictions behind – the plateau modulus relaxes [3]. This concept is essentially contained in the reptation model of de Gennes. All associated movements, starting from lengths of about 1 Å and times in the order of magnitude of 10^{-11} s up to the size of a molecule of typically 1000 Å, determine the viscoelastic properties of a polymer system.

Applying quasielastic neutron scattering (QENS) the aim of the studies presented here was a space-time analysis of the above-described motions [4–23], in order to achieve molecular understanding of the mechanical properties of polymer melts. After a short introduction to the neutron spin-echo technique, which complements the presentation of quasielastic scattering given in Chaps. 2 and 3, five topics will be dealt with. First of all, experiments on the local bond dynamics and segmental motion giving rise to the α- and β-relaxation in polymer systems will be reported. Thereafter, the entropically driven Rouse motion will be discussed. Subsequently, on long chains this chapter presents direct experimental observation of the reptation process. At the end we address the transition regions: First we report data from the cross over from universal entropic Rouse dynamics to local dynamics. Then we examine the entanglement transition and display how topological restrictions manifest themselves if the polymer chain length increases.

13.2 The Neutron Scattering Method

Scattering methods play a prominent role if spatial structures are to be explored on the atomic and molecular scale. The two most important probes are photons in the X-ray region and neutrons. While photons with appropriate wavelength possess energies of the order of keV, neutrons with de Broglie

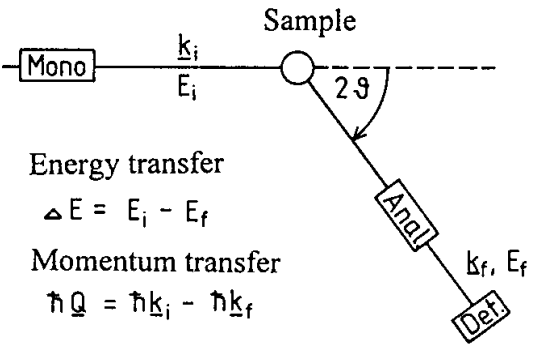

Fig. 13.1. Schematic representation of a neutron scattering experiment; Mono: monochromator; Anal: analyzer; Det: detector; E_i, E_f, incident and scattered neutron energies; k_i, k_f: corresponding wave vectors; ΔE: energy transfer; $\hbar Q$: momentum transfer; 2ϑ: scattering angle.

wavelengths in the Å region have thermal or subthermal energies. The neutron probe thus permits a simultaneous space and time analysis of the thermal motion in condensed matter [24] (see also Chaps. 2 and 3). Whereas the X-ray photon provides information about the molecule location, the neutron reveals the location of an atom and its direction, type and rate of motion. Unlike photons, neutrons are scattered on the atomic nucleus. This provides the possibility of selective atomic labelling by isotope exchange. Especially the scattering properties of protons and deuterons, described by their scattering lengths ($b_\mathrm{H} = -0.34 \cdot 10^{-12}\,\mathrm{m}$, $b_\mathrm{D} = 0.66 \cdot 10^{-12}\,\mathrm{m}$), are particularly different. As a unique feature therefore neutrons provide the opportunity to study synthetic and biological macromolecules among their equals if labelled by deuteration. For example, the coil conformation of the polymer in the melt and in the amorphous state was only confirmed experimentally in this way.

Figure 13.1 shows the schematic setup of a neutron scattering experiment. A monochromator is used to select neutrons with a defined energy, E_i, and a wave vector, $\boldsymbol{k}_\mathrm{i}$, from the neutron spectrum of a neutron source. These neutrons are scattered on a specimen and analysed under the scattering angle 2ϑ. The analyser chooses neutrons with a wave vector $\boldsymbol{k}_\mathrm{f}$ and an end-point energy E_f. These neutrons are identified in a detector. Momentum transfer $\hbar\boldsymbol{Q} = \hbar(\boldsymbol{k}_\mathrm{i} - \boldsymbol{k}_\mathrm{f})$ and energy transfer $\Delta E = E_\mathrm{i} - E_\mathrm{f}$ correspond to distances $r \mathrel{\tilde{=}} 2\pi/Q$ and to times $t \mathrel{\tilde{=}} h/\Delta E$.

A neutron scattering experiment generally measures the space-time Fourier transform of the pair-correlation function $S(Q,\omega)$ or, in specific cases, only the spatial Fourier transform $S(Q,t)$ ($\hbar\omega = \Delta E$) (cf. Sect. 3.2 in Chap. 3). In classical approximation, the pair-correlation function means the conditional probability of finding an atom j at location r and time t, if another atom i was at location $r = 0$ at time $t = 0$. For $i = j$ the self-correlation function is obtained, which measures the time-dependent thermally averaged mean square

displacement $\langle (r_i(0) - r_i(t))^2 \rangle$. For the time-dependent scattering function in the so-called Gaussian approximation we have

$$S(Q,t) = \frac{1}{N} \sum_{ij}^{N} \exp\left(-Q^2 \langle (\boldsymbol{r}_i(0) - \boldsymbol{r}_j(t))^2 \rangle\right) \quad . \tag{13.1}$$

In the case of a labelled polymer, $\boldsymbol{r}_i$ and $\boldsymbol{r}_j$ denote the spatial monomer coordinates and N is the number of monomers in a chain. The sum extends over all monomers in a chain.

13.2.1 The Neutron Spin-Echo Technique Versus Conventional Scattering

The unique property of the neutron spin-echo (NSE) technique [25, 26] is its ability to directly measure energy changes of the neutron during scattering. This distinguishes NSE from conventional scattering techniques which, as explained above, proceed in two steps: first monochromatization of the incident beam and then analysis of the scattered beam. Energy and momentum changes during scattering are determined by taking differences between two measurements. In order to achieve high energy resolutions with these conventional techniques, a very narrow energy interval must be selected from the relatively low-intensity neutron spectrum of the source. Conventional high-resolution techniques therefore always have difficulties with low intensity.

Unlike these conventional techniques, NSE measures the neutron velocities of the incident and scattered neutrons using the Larmor precession of the neutron spin in an external magnetic field. The neutron spin vector acts like the hand of an internal clock, which is linked to each neutron and stores the result of the velocity measurement at the neutron itself. The velocity measurement is thus performed individually for each neutron. For this reason, the velocities prior to and after scattering on one and the same neutron can be directly compared and a measurement of the velocity difference during scattering becomes possible. The energy resolution is thus decoupled from the monochromatization of the incident beam. Energy resolutions of the order of 10^{-5} may be achieved with an incident neutron spectrum of 20% bandwidth.

13.2.2 Neutron Spin Manipulations with Magnetic Fields

The motion of neutron polarization – it is the quantum mechanical expectation value of neutron spin – is described by the Bloch equation

$$\frac{\mathrm{d}}{\mathrm{d}t}\boldsymbol{P} = \frac{|g|\mu_\mathrm{N}}{\hbar}[\boldsymbol{B} \times \boldsymbol{P}] \tag{13.2}$$

where g is the g-factor of the neutron ($g = -3.82$), μ_N the nuclear magneton and $\boldsymbol{B}$ the flux density of the magnetic field $\boldsymbol{H}$. The factor $g\mu_\mathrm{N}/\hbar$ is

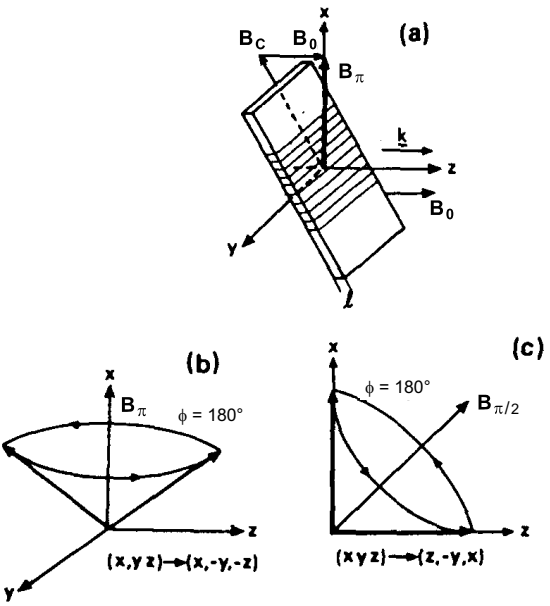

Fig. 13.2. Spin angular operations in neutron spin-echo technique; a) arrangement of a Mezei coil for a rotation of the neutron spin by the angle π; b) motion of neutron polarization during π angular operation; c) motion of neutron polarization during a $\pi/2$ rotation, after [25].

equal to the magnetogyric ratio γ commonly used in NMR (see Chaps. 9, 10 and 17; for the neutron $\gamma = -1.83 \cdot 10^8\,\mathrm{T^{-1}s^{-1}}$). Equation (13.2) is the basis for manipulation of the neutron polarization by external fields. Let us discuss two simple spin angular operations. We consider a neutron beam, which propagates with a polarization parallel to the direction of propagation in the z-direction. A magnetic guide field parallel to z stabilizes the polarization. First of all, we will explain the so-called π-coil, which reverses two components of the neutron spin. Its principle is shown in Figs. 13.2a and b.

A flat, long, rectangular coil, a so-called Mezei coil, is slightly tilted with respect to the x,y plane. A magnetic flux $\boldsymbol{B}_c$ is generated so that the resultant flux $\boldsymbol{B}_\pi = \boldsymbol{B}_o + \boldsymbol{B}_c$ points to the x-direction. A neutron spin entering this field begins to rotate about the x-axis. During a time $t = d/v$, d being the coil thickness and v the neutron velocity, a phase angle $\phi = \omega_\mathrm{L} t$ is passed. With the Larmor frequency $\omega_\mathrm{L} = g(\mu_\mathrm{N}/\hbar)B_\pi$ and $v = h/(\lambda m)$ we find

$$\phi = \left(\frac{2\pi|g|\mu_\mathrm{N} m}{h^2}\right)\lambda B_\pi d \tag{13.3}$$

where m is the neutron mass and λ the neutron wavelength. ϕ is thus given by the line integral $\int B\mathrm{d}s$ and is proportional to the wavelength. If we take, for example, a coil thickness of $d = 1\,\mathrm{cm}$ and a neutron wavelength of $\lambda = 8\,\text{Å}$,

a field B_π of 0.85 mT is needed to rotate the neutron spin by 180°. Such a spin rotation operation is shown schematically in Fig. 13.2b. Thereby, the components of polarization x,y,z are transferred to x,$-y$,$-z$.

The second important spin angular operation is the 90° rotation where the polarization is transformed from the z- to the x-direction or vice versa. A Mezei coil in the x,y-plane is adjusted such that the resultant field points exactly to the direction of the bisectrix of the angle between x and z. A 180° rotation about this axis transforms the z-component of polarization to the x-direction. At the same time, the sign of the y-component is inverted (Fig. 13.2c).

13.2.3 The Spin-Echo Principle

The basic experimental setup of a neutron spin-echo spectrometer is shown in Fig. 13.3. A velocity selector in the primary neutron beam selects a wavelength interval of about 10%–20% width. The spectrometer offers a primary and a secondary neutron flight path passing through the precession fields B and B'. Prior to beginning the first flight path, the neutron beam is polarized in the forward direction with the aid of a supermirror polarizer. A first $\pi/2$ coil rotates the polarization to the x-direction perpendicular to the direction of propagation. Beginning with this well-defined initial condition, the neutrons precess in the precession fields. Without the effect of the π-coil each neutron would go through a phase angle $\phi \propto \int B\mathrm{d}s$ (see (13.3)). Since the wavelengths of the neutrons are distributed over a wide range, the phase angle for each neutron would be different in front of the second $\pi/2$ coil and the beam would be depolarized on a disk perpendicular to z. The π-coil, which is exactly positioned at the value of half the field integral, prevents this effect. Let the neutron spin pass through the phase angle $\Omega_1 = 2\pi n + \Delta\phi_1$ on its way to the π-coil. The effect of the π-coil transforms the angle $\Delta\phi_1$ to $-\Delta\phi_1$. In a symmetric arrangement (both field integrals in front of and behind the π-coil are identical) the neutron spin passes through a second phase angle $\phi_2 = \phi_1 = 2n\pi + \Delta\phi_1$. The spin transformation at the π-coil thus just compensates the angles $\Delta\phi_1$, and in front of the second $\pi/2$ coil the neutron spin points again to the x-direction irrespective of the velocity. This effect is called spin focusing or spin echo and is also the basis of various NMR techniques to study diffusion (see Chap. 9, Sect. 9.3; Chap 10, Sect. 10.3; Chap. 17, Sect 17.2).

The second $\pi/2$ coil projects the x-component of polarization onto the z-direction. It is then determined by a subsequent supermirror analyser and detector. In a spin-echo experiment, the specimen is positioned near the π-coil. With the exception of losses due to field inhomogeneities, the polarization is maintained in the case of elastic scattering. If, however, the neutron energy is changed due to inelastic scattering processes in the specimen, then the neutron wavelength is modified from λ to $\lambda' = \lambda + \delta\lambda$. In this case, the phase angles ϕ_1 and ϕ_2 are not compensated anymore. The second $\pi/2$

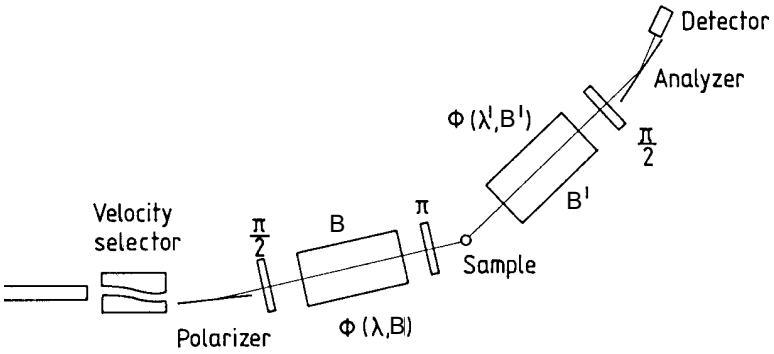

Fig. 13.3. Schematic representation of a neutron spin-echo spectrometer.

coil now only projects the x-component of polarization from a general direction into the z-direction. This part of the polarization is then identified by the analyser. Apart from resolution corrections, the final polarization P_f is obtained from the initial polarization P_i as

$$P_\mathrm{f} = P_\mathrm{i} \int_{-\infty}^{+\infty} \mathrm{d}\omega S(Q,\omega) \cos \omega t \quad . \tag{13.4}$$

The polarization P_f is proportional to the Fourier transform of the scattering function $S(Q,\omega)$. The transformation from $\delta\lambda$ to ω gives the relation between Fourier time, wavelength and magnetic field as $t \propto \lambda^3 B$. NSE is a Fourier technique, which measures the real part of the intermediate scattering function $S(Q,t)$. The time variation in a spin-echo experiment is performed by changing the magnetic field.

Figure 13.4 shows a technical realization of the spin-echo spectrometer at the Jülich FRJ-2 research reactor. Particularly striking are the Larmor precession coils in front of and behind the specimen. Furthermore, some of the coils for the spin angular operations can be recognized.

13.3 Local Chain Dynamics and the Glass Transition

The local chain motion under the influence of freezing processes is characterized by a very broad range of time scales. Figure 13.5 displays a relaxation map for (1–4) polybutadiene (PB) sketching the major dynamical features of a glass-forming polymer. The shown data points are taken from dielectric studies [27], from measurements of the dynamical modulus [28] and from neutron scattering [4, 7, 29].

We distinguish three different dynamical regimes:

(i) the freezing process is controlled by the structural α-relaxation exhibiting a pronounced non-Arrhenius temperature dependence. Phenomeno-

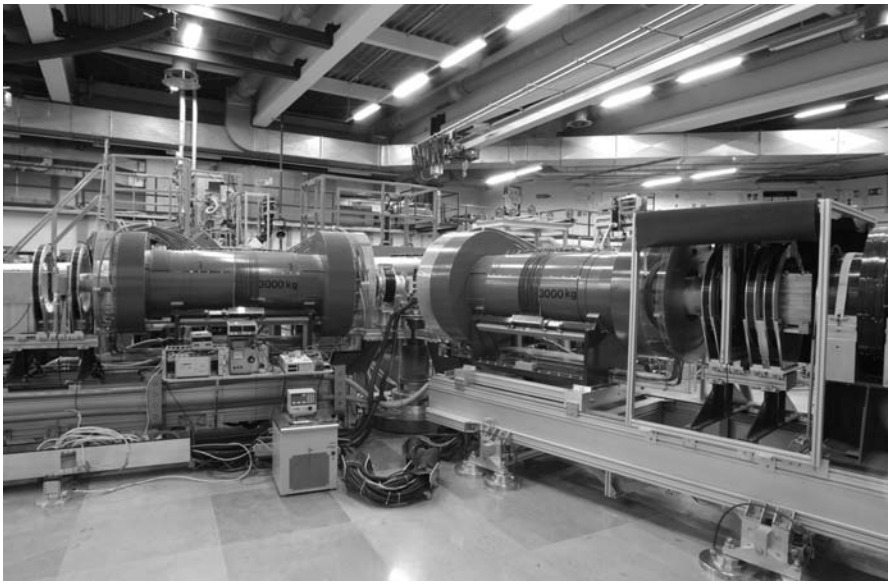

Fig. 13.4. The neutron spin-echo spectrometer in the ELLA laboratory at the FRJ-2 of FZ Jülich. The two large coils producing the precession fields are clearly visible. The smaller Helmholtz coils are used for the spin angular operations.

logically it is well described by a Vogel-Fulcher temperature dependence: $\tau^{-1} \propto \exp(-B/(T - T_0))$.

(ii) At a temperature about 20% above T_g a secondary relaxation process, the β_{slow} relaxation, splits from the α-process. Other than the primary α-relaxation β_{slow} follows an Arrhenius law and is not affected by the glass transition.

(iii) At high frequencies, in the picosecond range, characteristic low frequency excitations – the Boson peak and the associated fast relaxation process called β_{fast} are indicated [30]. Following Fig. 13.5 the relevant time scales for the glass process from the Boson peak and the fast relaxations to the freezing α-relaxation span 14–15 orders of magnitude.

Though the relaxation dynamics of polymers has been investigated by relaxational methods at least for five decades, still little is known about the underlying molecular motions. In principle, varying the momentum transfer Q, quasielastic and inelastic neutron scattering is capable of providing the space-time resolution in order to access the relaxations on a molecular level. In this section we discuss results from coherent quasielastic neutron scattering on the relaxational dynamics in the α/β_{slow} merging region [9, 14, 15] and relate them to some recent incoherent (QENS) results on the self motion [18, 31].

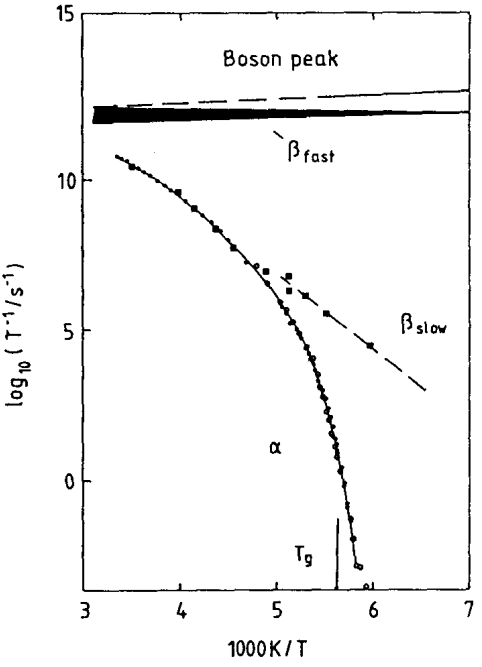

Fig. 13.5. Relaxation map for (1–4) polybutadiene covering the prevailing dynamical features around the glass transition. The frequency range for the Boson peak and the associated fast relaxation-like dynamics (β_{fast}) are indicated schematically. The full and open circle along the α-relaxation trace represent dielectric [27] and mechanical [28] results, respectively. The full squares display characteristic rates obtained from neutron spin echo spectroscopy [4,9]. The time scale of the α-process has been shifted to match that of the microscopic data. The dashed line represents the temperature dependence of the β_{slow} process observed by dielectric spectroscopy [15].

13.3.1 Dynamic Structure Factor

We begin by displaying the qualitative behavior of the dynamic structure factor and then turn to a quantitative evaluation. Figure 13.6 shows the intermediate dynamic structure factor as measured by NSE (cf. (13.1)) at a Q-value close to the first minimum of the static structure factor $S(Q)$ [9]. According to the time-temperature superposition principle the time dependence of $S(Q,t)$ was rescaled with the time scale of the α-relaxation as obtained from dynamic mechanical measurements [32]. Above the merging temperature of the α and β_{slow} relaxation $T_{\text{m}} \approx 220\,\text{K}$ (see Fig. 13.5) the different spectra collapse to a single master curve following a Kohlrausch-William-Watts (KWW) time dependence: $\tau_{\text{KWW}}^{-1} \propto \exp\left(-(t/\tau_0)^{\beta}\right)$ with $\beta = 0.41$. Below 220 K severe deviations from scaling are observed which are accompanied by an increase of the amplitude of the relaxation function. As we shall see this deviation from scaling is a signature of the β_{slow} process.

We now inspect the Q-dependence of the dynamic structure factor in more detail. Figure 13.7 displays NSE spectra taken at the position of the first and second peak of $S(Q)$ – the first peak or amorphous halo thereby relates mainly to interchain correlations while the second peak stems from intrachain distances. The data were rescaled with the time scale τ_η set by the viscosity relaxation. At the first peak all data collapse on a single master curve, which can be described by a stretched exponential using the dielectric

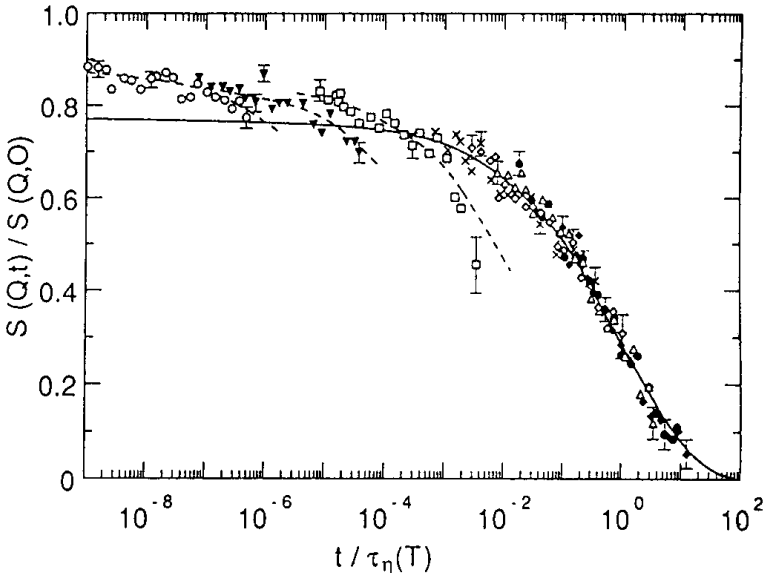

Fig. 13.6. Selected neutron spin echo spectra obtained at $Q = 1.88\,\text{Å}^{-1}$ from polybutadiene [14]. The time was rescaled to the viscosity scale. (⧫ 280 K, • 260 K, △ 250 K, ◇ 240 K, + 230 K, □ 205 K, ▽ 190 K, ○ 180 K) The solid line represents the master curve obtained from the spectra at temperatures higher than 220 K. The dashed lines represent individual fits to the low temperature data.

stretching exponent $\beta_{\text{diel}} = 0.41$. In contrast, at the second peak the spectra do not follow the time-temperature superposition principle determined by τ_η and strong deviations from a single master curve are obvious.

Extracting characteristic times from both sets of spectra, those from the interchain peak follow, as already signified by the master plot, the Vogel-Fulcher temperature dependence of the α relaxation, while those from the second peak obey an Arrhenius law with an activation energy identical to that of the dielectric β relaxation [14]. Thus, at the two first structure factor peaks qualitatively different aspects of the chain dynamics are observed; at the interchain peak the diffusive structural relaxation stands out, while at the intrachain peak the more local β_{slow} relaxation dominates the density fluctuations.

In the range of pure β_{slow} relaxation below the merging temperature T_{m} the main features of the dynamic structure factor can be understood in terms of a simple model based on local jump processes with jump rates determined by a Gaussian distribution of energy barriers as derived from dielectric relaxation. The β_{slow} relaxation is assumed to be a spatially localized process. The simplest picture of an elemental motion is a jump of an atom between two equivalent sites separated by a distance d with a characteristic time $\tau = \tau_0 \exp(E_{\text{A}}/k_{\text{B}}T)$ where E_{A} is the activation energy and k_{B} the Boltzmann

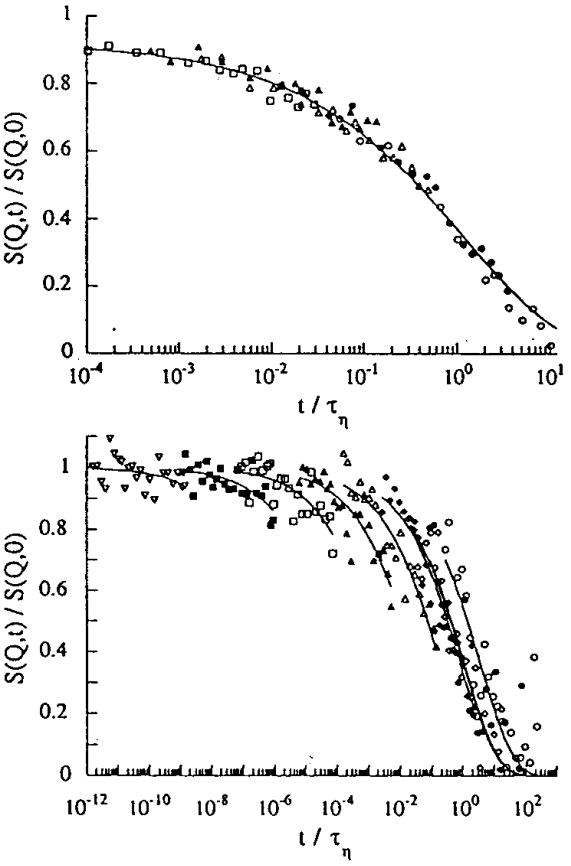

Fig. 13.7. Scaling representation of neutron spin echo data from polybutadiene at $Q = 1.48\,\text{Å}^{-1}$ (○ 280 K, ● 260 K, △ 240 K, △ 230 K, □ 220 K (upper figure) and at $Q = 2.71\,\text{Å}^{-1}$ (○ 300 K, ● 280 K, ◊ 260 K, ♦ 240 K, △ 220 K, △ 205 K, □ 190K, | 180 K, ▽ 170 K). The solid lines correspond to KWW functions (see text) [15].

constant. For such hopping processes the incoherent intermediate scattering function is given by

$$S_{\text{inc}}^{\text{hop}}(Q,t) = 1 - \frac{1}{2}\left(1 - \frac{\sin Qd}{Qd}\right) + \frac{1}{2}\left(1 - \frac{\sin Qd}{Qd}\right) e^{-2t/\tau}$$
$$= 1 - A^{\text{hop}}(Q,d) + f^{\text{hop}}(Q,d,\tau,t) \quad . \tag{13.5}$$

Coherent and incoherent scattering differ with respect to the presence of interference terms in the coherent scattering. Let us consider the jump motion of a pair of atoms. If such atomic jumps are uncorrelated, dynamic constructive interferences are absent and it follows naturally that the dynamic quasielastic part assumes the form of the incoherent part. Note, however, that

interference terms from the average atom distribution remain giving rise to $S(Q)$. If the motions are correlated it can be shown that interference effects are small as long as the jump distances are smaller than the distances between atom pairs. Under this assumption the coherent inelastic part can be approximated by the incoherent inelastic part, and the normalized coherent scattering function can be written as

$$\frac{S^{\beta}_{\mathrm{coh}}(Q,t)}{S(Q)} = 1 - \frac{A^{\mathrm{hop}}(Q,d)}{S(Q)} + \frac{f^{\mathrm{hop}}(Q,d,\tau,t)}{S(Q)} \quad . \tag{13.6}$$

Figure 13.8 displays the result of the fit with this model to the Q and T dependent spectra. Implying for the jump distance the slight barrier energy dependence of the soft potential model $d \propto E_{\mathrm{A}}^{1/4}$ a most probable jump distance of $d = 0.15\,\mathrm{nm}$ evolves. Furthermore, the experiment reveals the very astonishing result that the density fluctuations, which are directly observed by the neutrons, decay two orders of magnitude faster than the dipole reorientations seen by dielectric spectroscopy (see also [33]).

The total scattering function for the β_{slow} process then follows from an averaging over the different relaxation times with the energy barrier distribution from dielectric spectroscopy.

Figure 13.9 shows the relative quasielastic contribution of the β_{slow} process to the structure factor as calculated on the basis of the parameters obtained by the fitting procedure. The result explains immediately the qualitatively different behavior of $S(Q,t)$ at the first two maxima of $S(Q)$. Due to the renormalization of the quasielastic part in (13.6) with $S(Q)$ the contribution of the β_{slow} process at the first maximum of $S(Q)$ is minute, while it becomes very strong close to the second maximum explaining the Arrhenius behavior of the characteristic times at high Q. Further evaluation considering explicitly the coherent form factor of the moving rigid building blocks of the chain (cis and trans units involving the double bond) essentially confirms the outcome of the analysis within the simple hopping model [15].

At temperatures around the merging temperature T_{m} and above, the time scales of α- and β-relaxations become similar and consequently the dynamic structure factor has to be generalized in order to include the structural α-relaxation or so-called segmental diffusion. When this segmental diffusion reaches the timescale of the local relaxation, the atoms and molecular groups will noticeably participate simultaneously in both motional mechanisms: the intrachain β-relaxation and the interchain α-relaxation. We assume that to first order both mechanisms are statistically independent from each other. We shall see that on the basis of this hypothesis the Q- and temperature-dependent dynamic structure factors in the merging regime and above can be consistently accounted for.

Being a conditional probability, the self-correlation function corresponding to an atom undergoing two different statistically independent motions, α and β, can be written as a convolution product of the corresponding self-

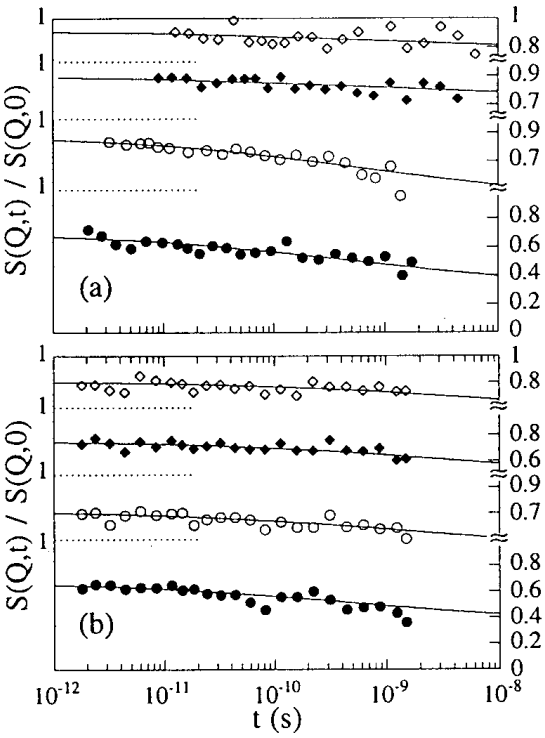

Fig. 13.8. Neutron spin echo spectra from polybutadiene a) at $T = 205\,\mathrm{K}$ and for different Q-values ◊ $1.4\,\mathrm{Å}^{-1}$, ♦ $1.56\,\mathrm{Å}^{-1}$, ○ $1.88\,\mathrm{Å}^{-1}$, • $2.55\,\mathrm{Å}^{-1}$; and b) at $Q = 2.71\,\mathrm{Å}^{-1}$ for various temperatures ◊ 170 K, ♦ 180 K, ○ 190 K, • 205 K. The ordinates corresponding to each spectrum are given on the left and right side, respectively. Solid lines correspond to the fit with the hopping model for the β-relaxation [14].

correlation functions:

$$G_{\mathrm{S}}^{\alpha\beta}(\boldsymbol{r},t) = \int G_{\mathrm{S}}^{\beta}(\boldsymbol{r},t) G_{\mathrm{S}}^{\alpha}(\boldsymbol{r}-\boldsymbol{r}',t)\,\mathrm{d}\boldsymbol{r} \quad . \tag{13.7}$$

This implies that the incoherent structure factor obtained by Fourier transformation of $G_{\mathrm{S}}^{\alpha\beta}(\boldsymbol{r},t)$ becomes a product of the structure factors corresponding to the two processes:

$$S_S^{\alpha\beta}(\boldsymbol{Q},t) = S_S^{\alpha}(\boldsymbol{Q},t) S_S^{\beta}(\boldsymbol{Q},t) \quad . \tag{13.8}$$

In the coherent case the derivation of a similar expression is not straightforward because the correlations between all the pairs of scatterers (j,i) have to be taken into account. It can be shown that a relation similar to (13.8) holds if for the segmental diffusion the incoherent approximation is made.

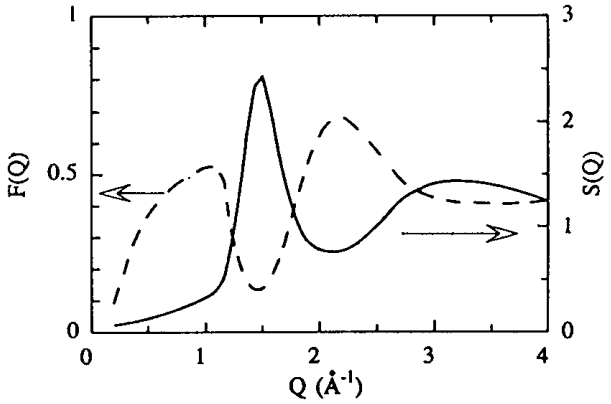

Fig. 13.9. Amplitude of the relative quasielastic contribution of the β_{slow} process to the coherent scattering function obtained from the hopping model as a function of Q. The static structure factor $S(Q)$ at 160 K is shown for comparison (solid line) [14].

This assumption corresponds to the so-called Vineyard approximation [34], in which $S^{\beta}_{\text{coh}}(Q,t)$ takes the role of $S(Q)$.

In incoherent approximation the relaxation function for the α-process φ^{α} can be described by a KWW function

$$\varphi^{\alpha}(Q,t) = \exp\left[-\left[\frac{t}{\tau_{\text{KWW}}(Q,t)}\right]^{\beta}\right] \tag{13.9}$$

with $\beta = 0.41$ from the shape of the dielectric spectra. $\tau_{\text{KWW}}(Q,t)$ is the characteristic Q- and temperature-dependent relaxation time. With the structure factor for the β-process evaluated at low temperature (see above) we obtain similar to (13.8)

$$\frac{S^{\alpha\beta}(Q,t)}{S(Q)} = \varphi^{\alpha}(Q,t) S^{\beta}_{\text{coh}}(Q,t)/S(Q) \quad . \tag{13.10}$$

All parameters involved in the coherent structure factor of the β-relaxation are known from the evaluation at low T and are extrapolated to the higher temperatures. Figure 13.10 shows the comparison between theory and experiment for several temperatures at the first maximum, minimum and second maximum of $S(Q)$ (Fig. 13.10a) and for 260 K at different Q-values (Fig. 13.10b). The excellent agreement between the scattering function (cf. (13.10)) and the experiment strongly supports the hypothesis that the α- and β-relaxation occur independently of each other.

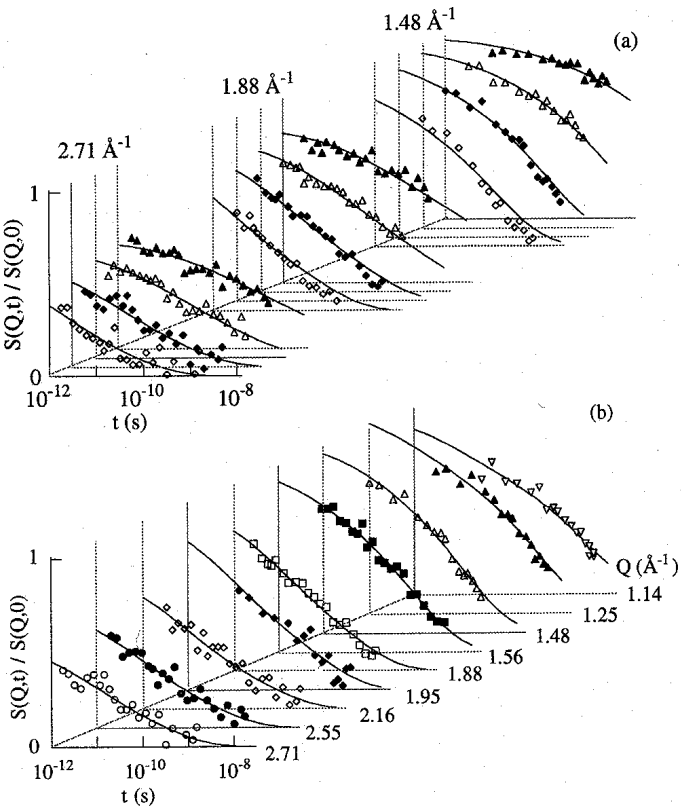

Fig. 13.10. Data from polybutadiene: (**a**) NSE-spectra for the Q-values indicated at 220 K (△); 240 K (△); 260 K (▲) and 280 K (◊). (**b**) at 260 K for the Q-values indicated. The solid lines display the model predictions.

13.3.2 Self-Correlation Function

In Gaussian approximation [20] the self-correlation function for a diffusive process is directly related to the mean square displacement $\langle r^2(t)\rangle$ by

$$S_\alpha^{\text{self}}(Q,t) = \exp\left\{-\frac{Q^2}{6}\langle r^2(t)\rangle\right\} \quad . \tag{13.11}$$

It is measured by analyzing the incoherent scattering from protonated samples. For the α-process the scattering functions are well described by stretched exponentials (see (13.9)). It is worthwhile to note that (13.11) is completely equivalent to the expression for spin-echo attenuation ((10.18) of Chap. 10 with the product $D\Delta$ expressed by the mean square displacement) of pulsed field gradient NMR, whence in the latter technique the quantity $\gamma\delta g$ assuming the position of Q is sometimes referred to as a generalized scattering vector.

If the system is homogenous, i.e. all particles undergo the same fate on the time scale of observation, then a combination of (13.11) and (13.9) implies

$$\langle r^2(t)\rangle = \tilde{D}t^{\beta} \quad \text{and} \quad \tau_{\mathrm{KWW}}(Q) \sim Q^{-2/\beta} \tag{13.12}$$

invoking sublinear diffusion of the polymer segments as the underlying reason for the stretched exponential dependence. Its signature is a power-law dependence of the Kohlrausch-Williams-Watts relaxation times τ_{KWW} with an exponent $2/\beta$.

Figure 13.11 displays the τ_{KWW} values obtained by backscattering spectroscopy (see Chap. 3) for four different polymers, polyvinylether (PVE) at 340 K, polyisobutylene (PIB) at 365 K, polybutadiene (PB) at 280 K and polyisoprene (PI) at 340 K for different momentum transfers [20]. To test (13.12), the relaxation times have been exponentiated with the exponent β obtained from the stretching of the relaxation functions in these polymers by dielectric spectroscopy. According to (13.12) $\tau_{\mathrm{KWW}}^{\beta}$ should be proportional to Q^{-2}. The solid lines in Fig. 13.11 display this power law relation. As may be seen, in all cases the predicted power law within experimental error is followed by the experimental relaxation times. Recent data on PIB and PI confirm these results with high accuracy [35,36]. Thus, the experimental evidence supports a sublinear diffusion process as underlying the α-relaxation. We remark that this result is in disagreement with assertions [19,37], that the stretched exponential relaxation function of the α-process originates from heterogeneous motional processes, where polymer segments in different parts of the sample would relax at different relaxation rates.

In the temperature range, where the α-relaxation is too slow to be observed by neutron scattering, the β-process can be measured. The corresponding spectra are a superposition of elastic and inelastic components indicative of a localized motion.

Figure 13.12 displays this elastic part of the intensity, observed for PIB as a function of Q [31]. The data were corrected for multiple scattering and fitted with the elastic incoherent structure factor (EISF) for a jump process between two sites. The EISF is the Fourier transform of the self-correlation function in the limit of infinite times and reveals the asymptotic proton distribution (see also (3.18), Chap. 3). The fit reveals the jump distance $d = 0.27$ nm. For comparison the solid line displays the prediction for methyl group rotation, which was invoked earlier on the basis of NMR experiments [38]. Within a factor of two the time scale obtained from the neutron results agrees with that from dielectric spectroscopy. Since the underlying process has an amplitude of 0.27 nm and is also dielectrically active, it cannot be understood as due to a methylgroup rotation alone. A possible interpretation is a combined backbone and methyl motion, which is also supported by simulation results [39].

Let us draw a first conclusion: Exploiting the Q-dependence of the coherent dynamic structure factor, which is accessed by NSE, at temperatures below the merging temperature T_{m} spatial information on the chain motions

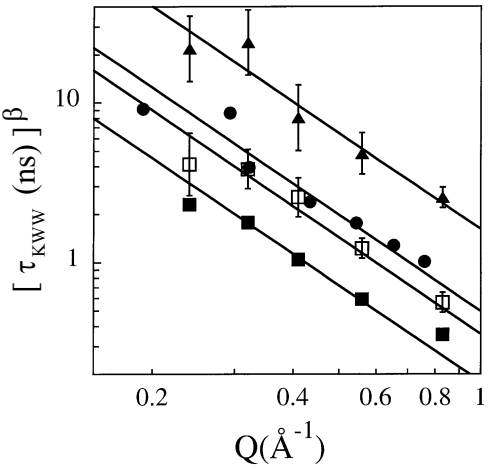

Fig. 13.11. Momentum transfer dependence of the characteristic time of the α-relaxation for the polymers investigated: PVE at 340 K (▲), PIB at 365 K (●), PB at 280 K (□) and PI at 340 K (■): $(\tau_{\mathrm{KWW}})^{\beta}$ as a function of Q in a double logarithmic plot. Solid lines represent the Q-dependence expected in the homogenous scenario $[\tau_{\mathrm{KWW}}]^{\beta} \sim Q^2$.

behind the β-relaxation was obtained. The results suggest intrachain motions like rotations of the chain building blocks (cis and trans units) within one chain. At temperatures around and above T_{m} the NSE results qualified the α-relaxation as being mainly related to interchain motions. The dynamic structure factor, thereby, can consistently be described assuming that α- and β-relaxations in 1,4 PB are statistically independent processes.

The self-correlation function measured on protonated samples reveals the mean squared displacement of the moving hydrogens. The Q-dependence of the characteristic relaxation time shows that motions underlying the α-relaxation at least on a time scale larger than that of the dielectric α-relaxation (corresponding to typically τ_{KWW} $(1\,\mathrm{Å}^{-1})$) are following a Gaussian process and are homogenous in nature.

13.4 Entropic Forces – The Rouse Model

We now turn to longer length scales, where motions resulting from local chain potentials have already taken place, assume that the chains do not interfere with each other in their motion and consider a Gaussian chain in a heat bath as the simplest model for chain relaxation. The elements of such a Gaussian chain are the so-called Kuhn segments, which consist of a few monomers, so that their end-to-end distance follows a Gaussian distribution. Their conformations are described by vectors a_n along the chain. The chain

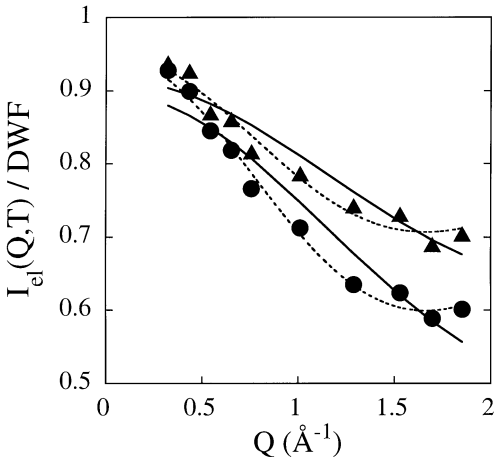

Fig. 13.12. Elastic incoherent intensities from PIB at 260 K (▲) and 280 K (●). The solid lines represent the prediction for methyl group rotation $I_{\rm el} = \frac{3}{4}\left[\frac{1}{3}\left(1+2\frac{\sin Qr_{\rm HH}}{Qr_{\rm HH}}\right)+A\frac{2}{3}\left(1-\frac{\sin Qr_{\rm HH}}{Qr_{\rm HH}}\right)\right]+\frac{1}{4}$ with $r_{\rm HH} = 0.178\,{\rm nm}$ and A relates to the jump time distribution function (see [4]). The dashed line gives the fit result for a two-site jump model with $d = 0.27\,{\rm nm}$.

is then described by a sequence of freely connected segments of length ℓ. We are interested in the motion of these segments on a length scale $\ell < r < R_{\rm E}$.

This motion is described by a Langevin equation

$$\zeta_0 \dot{\boldsymbol{a}}_n + \nabla_n \cdot F\{\boldsymbol{a}_i\} = f_n(t) \tag{13.13}$$

where ζ_o is the friction coefficient, f_n the stochastic force acting on the segment n of extension $\boldsymbol{a}_n$ and F the free energy. For segment motion, the force $\nabla_n F\{\boldsymbol{a}_i\}$ is dominated by the entropic part of the free energy ($S = k\ln {\rm Prob}\{\boldsymbol{a}_i\}$), where

$${\rm Prob}\{\boldsymbol{a}_i\} \sim \prod_{i=1}^{N} \exp\left(-\frac{3\boldsymbol{a}_i^2}{2\ell^2}\right) \tag{13.14}$$

is the probability of a chain conformation $\{\boldsymbol{a}_i\}$. We ascertain that the resultant entropic force is a special property of macromolecular systems with a large number of internal degrees of freedom. This conformational entropy generates the force stabilizing the most probable conformation. As already mentioned above, it is also the basis for rubber elasticity.

The Rouse equation of motion (cf. (13.13)) is solved by a spectrum of normal modes. These solutions are similar to the transverse vibrational modes of a linear chain except that relaxations are involved instead of periodic vibrations. We obtain for the relaxation rates

$$\frac{1}{\tau_p} = \frac{3\pi^2 k_\mathrm{B} T}{\zeta_0 N^2 \ell^2} p^2 \tag{13.15}$$

where N denotes the chain length. The mode index p counts the number of nodes along the chain. The relaxation rate is proportional to the number of nodes to the second power. On the basis of these normal modes we can calculate the dynamic structure factor $S(Q,t)$. This will be done later on. Here, an asymptotic solution for long chains will be briefly dealt with. It was formulated by de Gennes [40], who finds for the characteristic relaxation rate Ω

$$\Omega = \frac{1}{12} \frac{k_\mathrm{B} T}{\zeta_0} \ell^2 Q^4 \quad . \tag{13.16}$$

Unlike diffusion, where the characteristic relaxation rate is proportional to the momentum transfer Q^2, the fourth power is found here. Another characteristic quantity of diffusive motions is the mean square displacement of a segment. For Rouse motion follows

$$\langle (\boldsymbol{r}(0) - \boldsymbol{r}(t))^2 \rangle \sim t^{1/2} \tag{13.17}$$

which, again, is in clear contrast to normal diffusion where a linear time law holds. In Fig. 10.19 of Chap. 10 patterns of PFG NMR results for polymer diffusion are presented which follow the dependence of (13.17), though they do not relate to Rouse motion. The Rouse equation (13.13) applies to a length domain which is greater than the segment length and which is limited upwards by the entanglement distance. In this domain, no further length scale appears. The dynamic structure factor therefore assumes a scaling form linking length and time scales.

$$S(Q,t) = f(Q^2 \ell^2 \sqrt{Wt}) \tag{13.18}$$

with the Rouse rate $W = 3k_\mathrm{B}T/(\zeta_0/l^2)$.

13.4.1 Neutron Spin-Echo Results in PDMS Melts

In order to study the Rouse dynamics, a polymer with a low plateau modulus is needed, i.e. few entanglements and high flexibility and mobility. Polydimethylsiloxane (PDMS) fulfils these conditions. Neutron spin-echo experiments were carried out for both the self-correlation function and the pair-correlation function in PDMS melts.

Neutron measurements of the self-correlation function are normally performed on protonated materials since then the incoherent scattering is strongly dominating. Due to spin flip scattering, which leads to a loss of polarization, this approach is difficult for the NSE method. In order to avoid this obstacle, high-molecular-weight deuterated PDMS containing short protonated labels at random positions was synthesized. Each of these protonated sequences contained eight monomers. In such a specimen, scattering is mainly

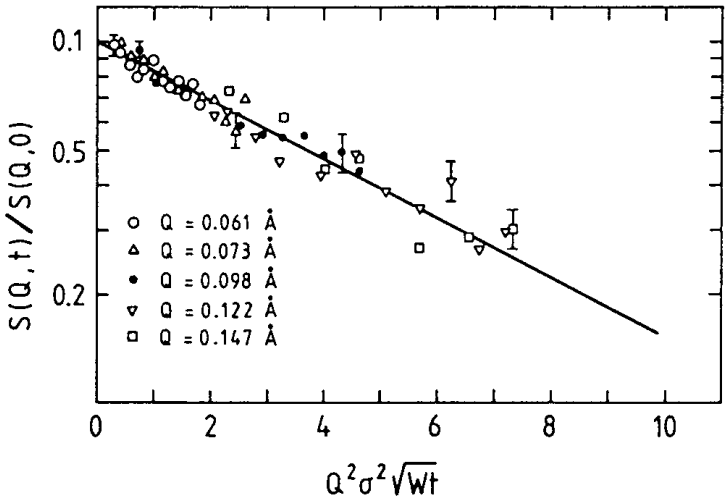

Fig. 13.13. NSE spectra for the self-correlation function measured in a randomly labelled PDMS melt at 100°C. The data are scaled with the Rouse variable ($\sigma^2 \equiv l^2$). The solid line is the result of a fit with the Rouse self-correlation function.

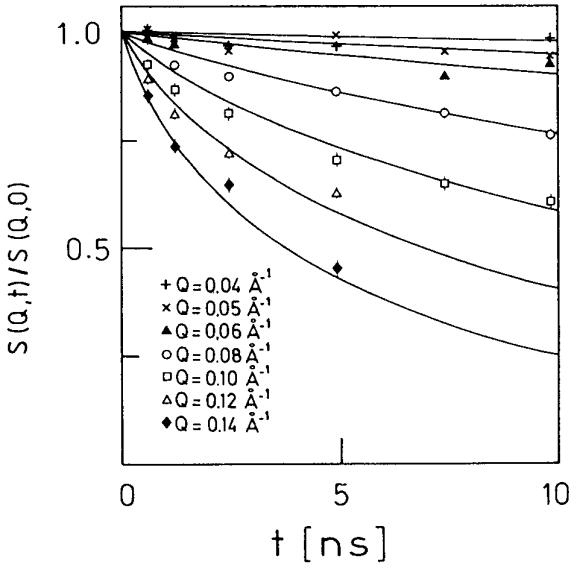

Fig. 13.14. NSE spectra for the pair-correlation function in PDMS melts at 200°C. The solid lines are the result of a fit with the coherent structure factor calculated by de Gennes (see text).

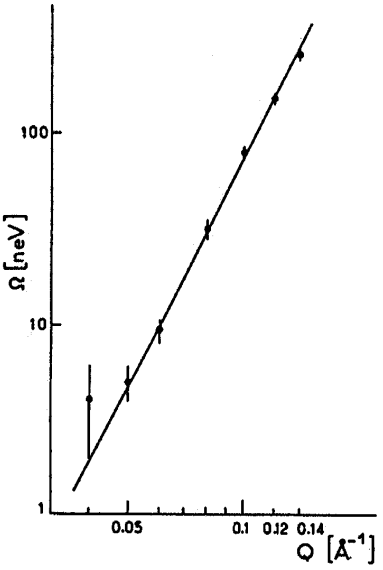

Fig. 13.15. Dependence of the characteristic relaxation rate Ω as a function of the momentum transfer Q resulting from an analysis of the spectra shown in Fig. 13.14. The solid lines denotes the predicted $\Omega \sim Q^4$ dependence.

caused by the contrast between the protonated sequence and the deuterated environment and is therefore coherent. On the other hand, the sequences are randomly distributed, so that there is no constructive interference of partial waves from different sequences. The scattering experiment measures the self-correlation function under these conditions [5].

In Fig. 13.13 the scattering data are plotted versus the scaling variable of the Rouse model (cf. (13.18)). The results for different momentum transfers follow a common straight line. For the case of the self-correlation function, the scattering function directly measures the mean square displacement which, according to (13.17), follows a square root law in time. This behaviour can be directly read from Fig. 13.13 (For data from polyethylene propylene (PEP) see also [41]).

The pair-correlation function for segment dynamics of a chain is observed if some protonated chains are dissolved in a deuterated matrix. The scattering experiment then observes the result of the interfering partial waves originating from such a chain (cf. (13.1)). Figure 13.14 presents the dynamic structure factor of a deuterated melt with 5% protonated chains. The solid lines represent a fit with (13.18) [12]. Obviously, the structure factor calculated by de Gennes satisfactorily describes the neutron data (the only fit parameter $W\ell^4 = 3k_{\mathrm{B}}T\ell^2/\zeta_0$). Figure 13.15 presents the characteristic relaxation rate Ω as a function of momentum transfer Q. The data are in very good agreement with the predicted Q^4 law.

The microscopic Rouse relaxation rate W also determines the viscosity of the non-entangled melt

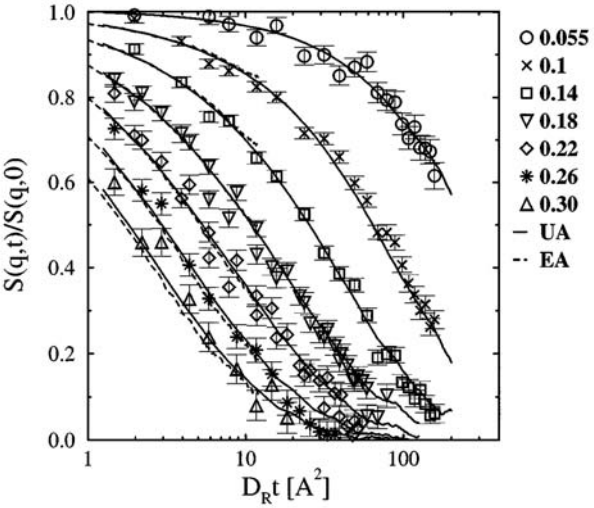

Fig. 13.16. NSE data from PE melts vs. computer simulations using the EA and UA models for different $Q(\equiv q)$ values/Å^{-1}.

$$\eta = \frac{\rho N_\text{A}}{N M_0} \frac{k_\text{B} T}{2} \sum_p \tau_p = \frac{\rho N_\text{A}}{M_0} \frac{k_\text{B} T}{12} \frac{N}{W} \tag{13.19}$$

where ρ is the polymer density and N_A the Avogadro constant. Measured viscosities and calculated viscosities using the microscopically determined rate W are in agreement within 20%.

13.4.2 Computer Simulations

In order to learn about the limits of the Rouse model, recently a detailed quantitative comparison of molecular dynamics (MD, cf. also Chap. 23) computer simulations on a 100 C-atom polyethylene chain (PE) with NSE experiments on PE chains of similar molecular weight has been performed [17]. Both the experiment and the simulation were carried out at $T = 509\,\text{K}$. Simulations were undertaken for an explicit (EA) as well as for a united (UA) atom model. In the latter the H atoms are not explicitly taken into account but reinserted when calculating the dynamic structure factor. The potential parameters for the MD simulation were either based on quantum chemical calculations or taken from literature. No adjusting parameter was introduced. Figure 13.16 compares the results from the MD-simulation (solid and broken lines) with the NSE spectra. In order to correct for the slightly different overall time scales of experiment and simulation, the time axis is scaled with the center-of-mass diffusion coefficient. From Fig. 13.16 quantitative agreement between both results is evident.

Figure 13.17 compares the same experimental data, which agreed quantitatively with the simulations, with a best fit to the Rouse model (see [17]). Here a good description is observed for small Q-values ($Q \leq 0.14\,\text{Å}^{-1}$), while

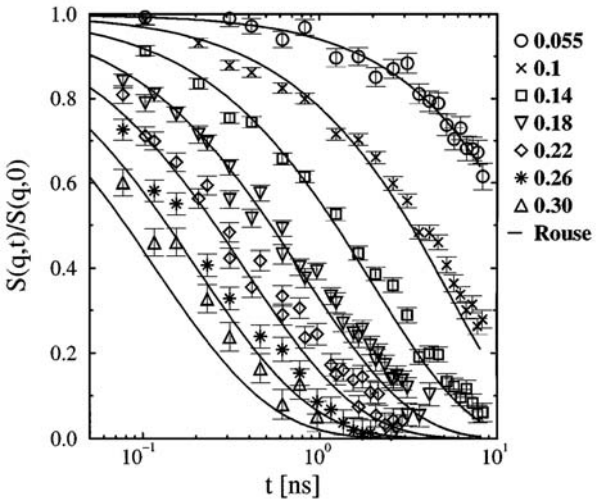

Fig. 13.17. NSE data from PE melts in comparison to a best fit with the Rouse model for different $Q(\equiv q)$ values/Å^{-1}.

at higher Q important deviations appear. Similarly also the simulations cannot be fit in detail with a Rouse structure factor.

Having obtained very good agreement between experiment and simulation, the simulations which contain complete information about the atomic trajectories may be further exploited, in order to rationalize the origin for the discrepancies with the Rouse model. A number of deviations evolve.

1. According to the Rouse model the mode correlators should decay in a single-exponential fashion. A direct evaluation from the atomic trajectories shows that the 3 contributing Rouse modes decay with stretched exponentials displaying stretching exponents β of (0.96 (mode 1) and 0.86 (modes 2 and 3)).
2. A detailed scrutiny of the *Gaussian* assumption reveals that for $t < \tau_R$ deviations occur.
3. While the Rouse model predicts a linear time evolution of the mean squared centre of mass coordinate, within the time window of the simulation ($t < 9\,\text{ns}$) a sublinear diffusion in form of a stretched exponential with a stretching exponent of $\beta = 0.83$ is found. A detailed inspection of the time-dependent mean squared amplitudes reveals that the sublinear diffusion mainly originates from motions at short times $t < \tau_R = 2\,\text{ns}$.

The prediction of a time-dependent center-of-mass diffusion coefficient has recently been corroborated by NSE-experiments on short-chain polybutadienes [42]. Figure 13.18 displays the mean squared center-of-mass displacement from simulation compared to the same quantity obtained from the dynamic structure factor at various Q-values. Both the simulation and the experimen-

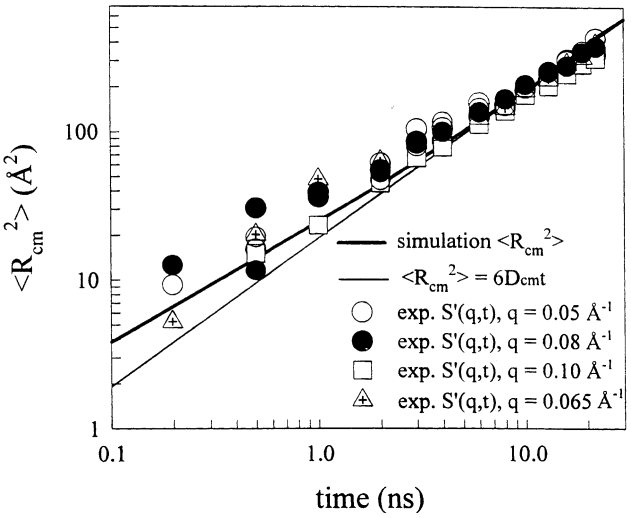

Fig. 13.18. Mean square center-of-mass displacement for PB chains in the melt obtained from $\langle r^2(t)\rangle = -\frac{6}{Q^2} n\ell S(Q,t)$. Solid line: simulation result; thin line $\langle r^2(t)\rangle = D_{\mathrm{R}} t$.

tal data consistently lead to a weaker than linear time dependence of the center-of-mass displacement.

The overall picture emerging from this combined simulational and experimental effort is, that for chains, which should be ideal Rouse chains, the model is capable of quantitatively describing the behaviour only on time scales of the order of the Rouse time or larger and therefore on length scales of the order of the radius of gyration of the chains or larger and in the regime, where the chains actually show Fickian diffusion. The self-diffusion behaviour for times smaller than the Rouse time and the relaxation of the internal modes of the chains show small but systematic deviations from the Rouse prediction. The origin of these discrepancies are traced to interchain interactions. On the other hand, we will see that deviations observed at higher Q relate to intrachain potentials.

Let us draw a second conclusion: The chain dynamics for times, where entanglement effects do not yet play a role, is excellently described by Langevin dynamics with entropic restoring forces. The Rouse model nearly quantitatively describes (i) the Q-dependence of the characteristic relaxation rate, (ii) the spectral form of both the self- and the pair-correlation function and (iii) establishes the correct relation to macroscopic viscosity. (iv) Finally, detailed comparisons with MD-simulation reveal small deviations originating from interchain interactions.

13.5 Long-Chains Reptation

13.5.1 Theoretical Concepts

The reptation model of de Gennes [43], Doi and Edwards [44] proceeds on the intuitive assumption that the motions of a chain in a melt are significantly impeded by the surrounding chains in directions lateral to its own profile. The dominant diffusive motion, therefore, proceeds along the coarse-grained chain profile. A chain meanders through a melt like a snake. The lateral restrictions are modelled by a tube running parallel to the coarse-grained chain profile. Its diameter is correlated with the plateau modulus of the melt, as discussed in the introduction. The restriction of motion by other chains is not effective on the monomer scale, but permits lateral motions on intermediary length scales ($d_\mathrm{t} \cong 50 \ldots 100\,\text{Å}$). In this simple intuitive model, the experimental observations for viscosity and diffusion can be readily made comprehensible.

According to (13.19) the viscosity is determined by the longest relaxation time – here the abandonment of an initial configuration. Assuming that the chain is subject to a Rouse diffusion within its tube, $D_\mathrm{R} \propto 1/N$ holds for the tube diffusion. The chain has left an initial configuration when it is diffused over a contour length $L = \ell N$. This gives

$$\tau_\eta \propto \frac{L^2}{D} \propto N^3 \propto \eta \quad . \tag{13.20}$$

In space, the contour of the chain follows a Gaussian random path, i.e. the chain diffuses over a spatial distance during the time τ_η, which corresponds to its end-to-end distance ($R_\mathrm{E} \propto N^{1/2}$). The reptation diffusion coefficient then reads

$$D_\mathrm{rep} \propto \frac{R_\mathrm{E}^2}{\tau_\eta} \propto \frac{1}{N^2} \quad . \tag{13.21}$$

Whereas the experimentally observed viscosity generally depends on the molecular weight with an exponent slightly greater than 3 – there is reason to suppose that an N^3 law is fulfilled for very long chain lengths – the predicted chain length dependence of the diffusion coefficient is directly confirmed experimentally.

What are the consequences of the localization tube for the dynamic structure factor? For short times during which the mean squared segment displacement is smaller than the tube limitation, the chain motion should proceed without being affected by the tube restriction. In this case, the Rouse law should apply, especially its scaling property of momentum transfer and time (cf. (13.18)). For medium times, density fluctuations transversely to the tube have already equilibrated. Pair correlations along the tube are stabilized by the localization tube and are only decomposed when the chain leaves the tube. We thus expect that the dynamic structure factor tends to a constant dependent on Q. A further decomposition of $S(Q,t)$ only occurs for times

of the order of τ_η. The value of the Q-dependent plateau results from the Fourier transform of the localization tube. The essential new feature in the dynamic structure factor of the reptating chain is the appearance of a length scale d, which invalidates the scaling property of the Rouse model.

Quantification requires analytical models, which can be compared with the data. We would like to briefly discuss three different model categories without explaining them in detail. (i) In so-called generalized Rouse models [45, 46] the effect of the topological constraints is described by a memory function. In the limiting case of long chains, in the time domain of the NSE experiment the dynamic structure factor can be explicitly calculated in such models. (ii) Neglecting the initial Rouse motion for small values of the Rouse scaling variable in his local reptation model de Gennes explicitly calculated the collective chain motion in the localization tube [47]. For the dynamic structure factor in the limit of long times, this gives

$$S(Q,t)\big|_{t\to\infty} = S(Qd_\mathrm{t}; Q^2 t^{1/2})\big|_{t\to\infty} = 1 - \frac{Q^2 d_\mathrm{t}^2}{36} \quad . \tag{13.22}$$

(iii) Des Cloizeaux finally formulated a rubber-like model for the chain motion for intermediate times [48]. He assumed that for intermediate times the entanglement points of the chains are fixed in space and that the chains perform Rouse motions under the boundary condition of fixed entanglement points. This rubber-like model is closest to the concept of a temporary network.

13.5.2 Experimental Observations of Chain Confinement

Figure 13.19 compares the dynamic structure factors from polyethylene melts, both taken at 509 K for two different molecular weights [7, 8, 16, 23]. Figure 13.19a displays the structure factor for a short-chain melt (M_w = 2000 g/mol). The solid lines display a fit with the Rouse dynamic structure factor. Very good agreement is achieved. Figure 13.19b displays similar results from a PE melt with a molecular weight of M_w = 12400 g/mol. The solid lines present the predictions of the Rouse model. While for the short-chain melts this model describes well the experimental observations, for the longer chains the model fails completely. Only in the short-time regime the initial decay of the dynamic structure factor is depicted, while for longer times the relaxation behaviour is strongly retarded signifying confinement effects. In Fig. 13.20 the data from a M_w = 36000 PE-melt at 509 K are plotted as a function of the scaling variable of the Rouse model (see (13.18)). In contrast to Fig. 13.13 the scaled data do not follow a common curve, but after an initial common course they rather split into Q-dependent branches. This splitting is a consequence of a dynamic length scale present in the melt, which invalidates the Rouse scaling properties. We note, that this length is of purely dynamical character and cannot be observed in static experiments.

Figure 13.21 presents recent experimental results on a polyethylene melt (M_w = 190000), which were carried over a time regime of 170 ns [23]. The data

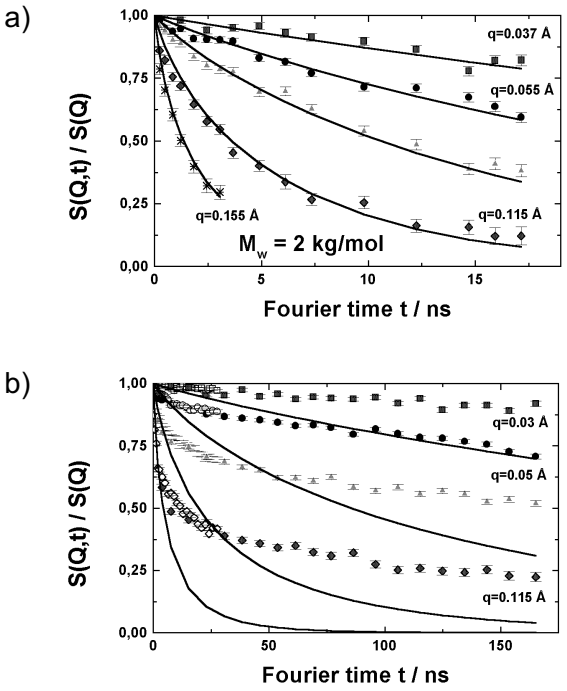

Fig. 13.19. Dynamic structure factors from PE-melts at 509K (a) $M_\mathrm{w} = 2000$; (b) $M_\mathrm{w} = 12400$. The solid lines display the predictions of the Rouse model.

are compared with the dynamic structure factor of the reptation model [47] and are very well described. We note, that the fits were performed varying only one single parameter, namely the tube diameter d, while the Rouse rate was determined from earlier NSE data taken at short times. With this one parameter it is possible to achieve quantitative agreement with respect to both the Q and the time dependence of the dynamic structure factor. We further note, that the dynamic structure factors predicted by the other confinement models discussed above are not able to fit the data [16].

It is illustrative to visualize the large spread of the time regimes relevant for the dynamics of the $M_\mathrm{w} = 190000$ molecule. The elementary Rouse time amounts to 2.5 ps. The cross over time to local reptation $\tau_e = 5\,\mathrm{ns}$. The Rouse time of the chain $\tau_R = 45\,\mu\mathrm{s}$ and finally the disentanglement time $\tau_d = 11.7\,\mathrm{ms}$. Thus, the relevant time scales spread over a range of more than nine orders of magnitude. The corresponding length scales are much closer together. The segment length $\ell = \ell_0\sqrt{C_\infty}$, where C_∞ is the characteristic ratio, is 4 Å, the tube diameter $d = 46\,\text{Å}$ and the chain end-to-end distance $R_\mathrm{E} = 418\,\text{Å}$.

We are now drawing a third conclusion. NSE experiments on long-chain polymer melts have verified the molecular existence of an entanglement length

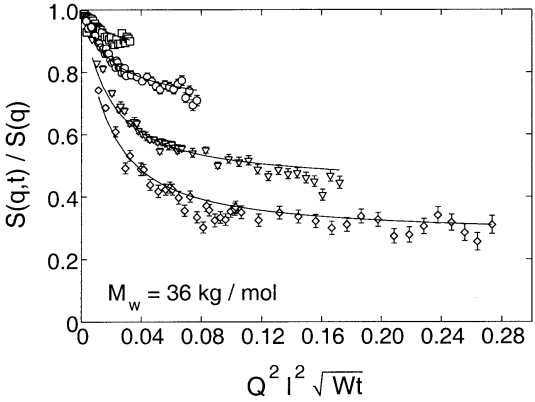

Fig. 13.20. Scaling presentation of the dynamic structure factor from a M_w = 36000 PE-melt at 509 K as a function of the Rouse scaling variable. The solid lines are a fit with the reptation model [47]. The Q-values ($Q \equiv q$) are (from above) $Q = 0.05$, 0.077, 0.115, 0.154 Å^{-1}.

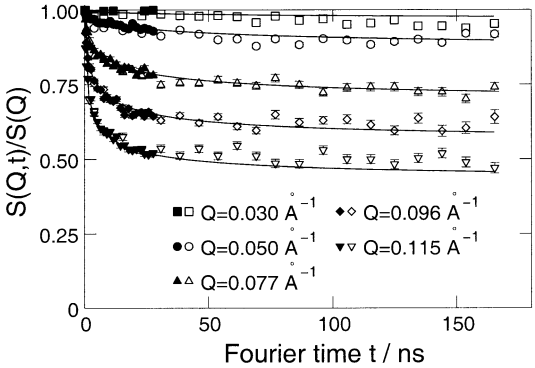

Fig. 13.21. Dynamic structure factor from a long-chain PE-melt (M_w = 190000) at 509 K. The solid lines represent a fit with the reptation model [47].

which, being of dynamic nature, under equilibrium only reveals itself in dynamic experiments. Moreover, the detailed Q-dependent dynamic structure factor validates the idea of chain motion in a confining tube and corroborates quantitatively the celebrated reptation model of de Gennes.

13.6 Intermediate Scale Dynamics

A precondition for the validity of the entropy-driven Rouse model is the requirement that only chain connectivity enters into the equation of motion and any influence from local stiffness or rotational barriers etc. are negligible. In

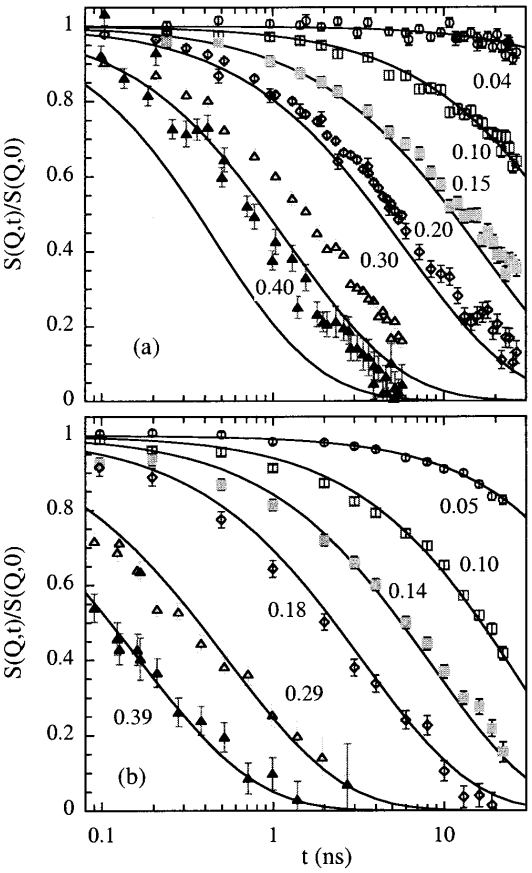

Fig. 13.22. Dynamic structure factor of (**a**) a PIB melt ($M_w = 3870$, $M_w/M_n = 1.06$, radius of gyration $R_g = 19.2$ Å) at 470 K and (**b**) a PDMS melt ($M_w = 6460$, $M_w/M_n = 1.10$, $R_g = 21.3$ Å) at 373 K. The Q-values (in Å^{-1}) are noted in the figures. The solid lines are the respective predictions of the Rouse model.

going to shorter length scales this condition must break down. Measurements of the dynamic structure factor at smaller scales or higher Q-values offer the opportunity to learn about the limitation of the Rouse model towards local scales and to understand the leading processes. Both local chain stiffness as well as rotational potentials may play a role [49–51].

Recently, the relevant factors, which limit the universal Rouse dynamics towards small scales, were studied in comparing the dynamic structure factors $S(Q,t)$ of polyisobutylene (PIB) and polydimethylsiloxane (PDMS) of similar size in the melt and in dilute solution [21,22]. Both polymers show similar static flexibility (the characteristic ratios are very close), but strongly different rotational barriers (PDMS: $E_{rot} \tilde{=} 0.4$ kJ/mol; PIB: $E_{rot} = 12.6$ kJ/mol).

Figure 13.22a presents the dynamic structure factor from a PIB melt at 470 K including a fit with the prediction of the Rouse model. Figure 13.22b displays comparable data from a PDMS melt at 373 K.

While for Q-values above $Q = 0.15\,\text{Å}^{-1}$ increasing deviations between the experimental results from PIB and the Rouse prediction are evident, the PDMS results are described well over the entire Q-range (up to $Q = 0.4\,\text{Å}^{-1}$). Since both polymers exhibit the same static flexibility, we may immediately conclude, that chain stiffness is not the leading mechanism limiting the Rouse dynamics for flexible polymers as proposed earlier [51]. A thorough study of the stiffness effects on the dynamics of this polymer was carried out in [21] applying the approaches of the all-rotational-state model and a bending force model. Stiffness effects were found to be almost negligible.

After the failure of stiffness models, the source for the slowing down of the PIB chain dynamics at intermediate scales must be related to dissipation effects not present in PDMS. Allegra's intrachain viscosity model [49,50] provides a simple access to such an effect. He describes the intrachain dissipation degrees of freedom by a local relaxation mode characterized by a relaxation time τ_0.

In order to access this process without disturbances experiments on solutions were crucial, where interchain friction effects are weak [22]. Figures 13.23a,b compare experimental results on PIB and PDMS in toluene at room temperature and 378 K. While at low Q both data sets agree – both polymers undergo the same translational diffusion – at larger Q a systematic retardation of the dynamic response of PIB compared to PDMS is visible.

The application of the intrachain viscosity model to the PIB solution data on the basis of the PDMS reference led to a very good description of the NSE results for all Q values and temperatures (Fig. 13.24). The activation energy of 13 kJ/mol for the intrachain relaxation time τ_0 agrees very well with the rotational barrier for this hydrocarbon [52].

An application of the model to the melt data allows a quantitative description of the Q-dependent spectra. The activation energy for τ_0 resulted to be about 40 kJ/mol, i.e. more than 3 times as high as in solution. Obviously, chain relaxation occurs via correlated motions over several barriers or interchain effects come in additionally and the activation energy cannot easily be compared with rotational potentials, see also [35].

Drawing a fourth conclusion, we note that Allegra's intrachain viscosity model accounts properly for the deviations from universal dynamics towards shorter time and length scales. In solution, the corresponding relaxation time directly relates to jumps across rotational potentials. Also in the melt, intrachain friction effects limit the Rouse dynamics. The relaxation time, however, is not directly related to crossings of single barriers.

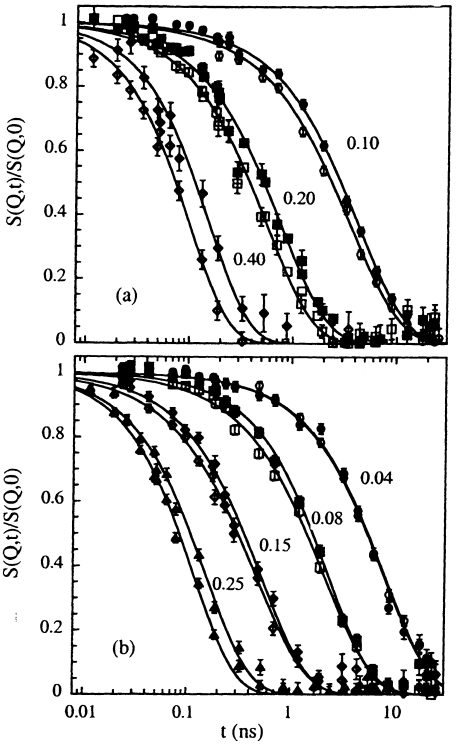

Fig. 13.23. Chain-dynamic structure factor of PDMS (empty symbols) and PIB (full symbols – in each case the upper curve) in toluene solution at 300 K (a) and 378 K (b). The corresponding Q (in Å^{-1}) values are indicated. Lines through the points are guides to the eye.

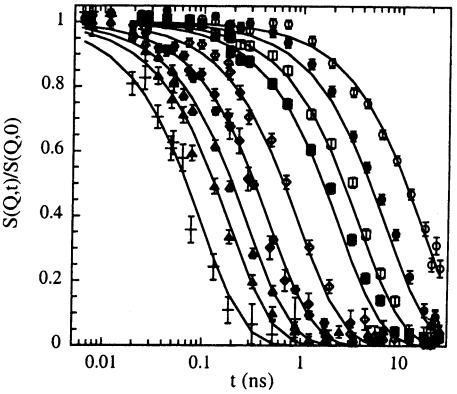

Fig. 13.24. Chain-dynamic structure factor of PIB in toluene solution at 327 K at the Q values: 0.04 Å^{-1} (○); 0.06 Å^{-1} (●); 0.08 Å^{-1} (□); 0.10 Å^{-1} (■); 0.15 Å^{-1} (◇); 0.20 Å^{-1} (◆); 0.25 Å^{-1} (△); 0.30 Å^{-1} (▲); 0.40 Å^{-1} (+). Solid lines correspond to fitting curves with the Rouse-Zimm model including intrachain viscosity.

13.7 The Crossover from Rouse to Reptation Dynamics

Chains of small molecular weight are not able to build entanglements and their dynamics is supposed to be fully compatible with the Rouse model. Increasing the chain length beyond a threshold length, topological hindrance shows itself in (i) reducing the self-diffusion coefficient below the Rouse law

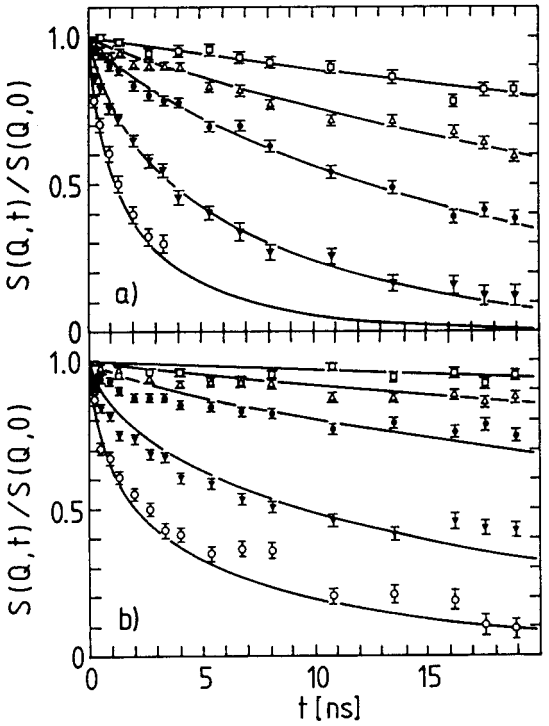

Fig. 13.25. Dynamic structure factor for two polyethylene melts of different molecular weight; a) $M_w = 2 \times 10^3$ b) $M_w = 4.8 \times 10^3$. The momentum transfers Q are $Q = 0.037$; 0.055; 0.077; 0.115 and 0.155 $Å^{-1}$ from top to bottom. The solid lines show the result of mode analysis.

$D_R \sim 1/N$ and (ii) increasing the Rouse linear relationship between viscosity and chain length to a power law $\eta \sim N^{3.4}$.

In order to find out how beginning entanglement effects influence the intrachain motions, we discuss neutron-spin echo experiments on a number of polyethylene melts with molecular weights in the transition range (M_w = 2000, 3600, 4800, 6500) [11, 13]. The monodisperse deuterated melts were mixed with 10% protonated chains of the same length. Figure 13.25 shows experimental spectra obtained on specimens with the molecular weights 2000 and 4800. A comparison of the spectra shows that the relaxation is obviously much less advanced for the longer chain compared to the shorter chain. Let us take the spectrum at the momentum transfer $Q = 0.12\,Å^{-1}$ as an example. While the dynamic structure factor for the shorter chain has already decreased to about 0.1 after 20 nanoseconds, the longer chain only relaxes to about 0.4 for the same Q and the same time.

In the following analysis of these data we want to find out how the individual normal modes of the relaxing chain are influenced by the appearance

of topological hindrance. The starting point for this analysis is the fact that the spatial structure of the eigenmodes of Gaussian chains is given by the Rouse form

$$x_p(t) = \frac{1}{N} \sum_n x_n(t) \cos\left(\frac{p\pi n}{N}\right) \quad . \tag{13.23}$$

The time dependence can have an arbitrary form. Within the framework of this mode structure, the dynamic structure factor can be formulated in a general form [53].

$$\begin{aligned} S(Q,t) = \frac{1}{N} \exp\left(-\frac{Q^2}{6}\left\langle (x_0(t) - x_0(0))^2 \right\rangle\right) \\ \times \left\{ \sum_{mn} \exp\left\{ -\frac{1}{6} Q^2 \ell^2 |m-n| - \frac{2}{3} \frac{R_{\mathrm{E}}^2}{\pi^2} Q^2 \sum_p \frac{1}{p^2} \right. \right. \\ \left. \left. \times \left[\cos\left(\frac{p\pi m}{N}\right) \cos\left(\frac{p\pi n}{N}\right) (1 - \langle x_p(t) x_p(0) \rangle) \right] \right\} \right\} \end{aligned} \tag{13.24}$$

where x_0 denotes the center of mass coordinates and the pointed brackets denote the thermal average. The correlation function $\langle (x_0(t) - x_0(0))^2 \rangle$ describes the diffusive motion of the molecular center of gravity. The relaxation dynamics of the internal modes is hidden in the exact time dependence of the correlators $\langle x_p(t) x_p(0) \rangle$. They describe the time-dependent development of the motion of a normal mode "p". In the case of the entropy-determined Rouse motion, the correlators have the form

$$\begin{aligned} \langle x_p(t) x_p(0) \rangle &\simeq e^{-t/\tau_p} \quad , \\ \frac{1}{6} \left\langle [x_0(t) - x_p(0)]^2 \right\rangle &= \frac{k_{\mathrm{B}} T}{N \zeta_0} t = D_{\mathrm{R}} t \end{aligned} \tag{13.25}$$

where D_{R} is the Rouse diffusion coefficient. The beginning spatial restrictions should lead to a more complicated time dependence.

How can we hope to extract the contributions of the different normal modes from the relaxation behaviour of the dynamic structure factor? The capability of neutron scattering for directly observing molecular motions on their natural time and length scale enables the determination of the mode contributions to the relaxation of $S(Q,t)$. Different relaxation modes influence the scattering function in different Q ranges. Since the dynamic structure factor is not simply decomposed into a sum or a product of mode contributions, this Q-dependence is not easy to represent. In order to make the effects more transparent, we consider the maximum possible contribution of a given mode "p" to the relaxation of the dynamic structure factor. This maximum contribution is reached when the correlator $\langle x_p(t) x_p(0) \rangle$ in (13.24) has fallen to zero. In order to keep the picture simple, we retain all the other relaxation modes: $\langle x_s(t) x_s(0) \rangle = 1$ for $s \neq p$.

Under these conditions, (13.24) indicates the maximum extend to which a particular mode p can reduce $S(Q,t)$ as a function of the momentum transfer

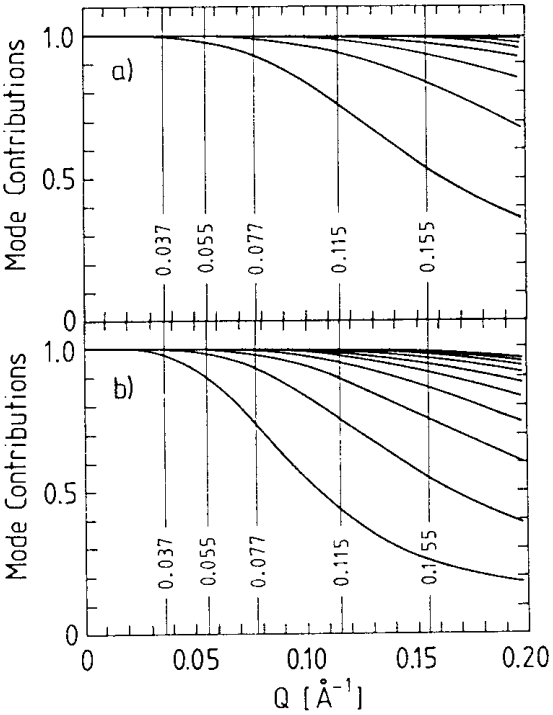

Fig. 13.26. Contributions of the different relaxation modes to the relaxation of the dynamic structure factor $S(Q,t)/S(Q,0)$ for a) $M_\mathrm{w} = 2.0 \times 10^3$ and b) $M_\mathrm{w} = 4.8 \times 10^3$. The experimental Q-values (in $\mathrm{\AA}^{-1}$) are indicated by vertical lines; curves correspond to mode numbers increasing from bottom to top.

Q. Figure 13.26 presents the Q-dependence of the mode contributions for the $M_\mathrm{w} = 2000$ and $M_\mathrm{w} = 4800$ samples. Vertical lines mark the experimentally examined momentum transfers. Let us begin with the short chain. For the smallest Q the internal modes do not influence the dynamic structure factor. There, only the translation diffusion is observed. With increasing Q, first of all, the first mode begins to play a role. If Q is further increased, higher relaxation modes above $Q = 0.1\,\mathrm{\AA}^{-1}$ also begin to influence the dynamic structure factor. If the chain length is enlarged, the influence of the different internal relaxation modes shifts to smaller momentum transfers.

This Q-dependent contribution of different relaxation modes to $S(Q,t)$ permits a separation of their influence on the dynamic structure factor. In order to be able to evaluate the data with a reasonable number of parameters, as a first approximation we assume that the exponential correlation of the correlators (cf. (13.25)) is maintained. For further treatment reference is made to [13].

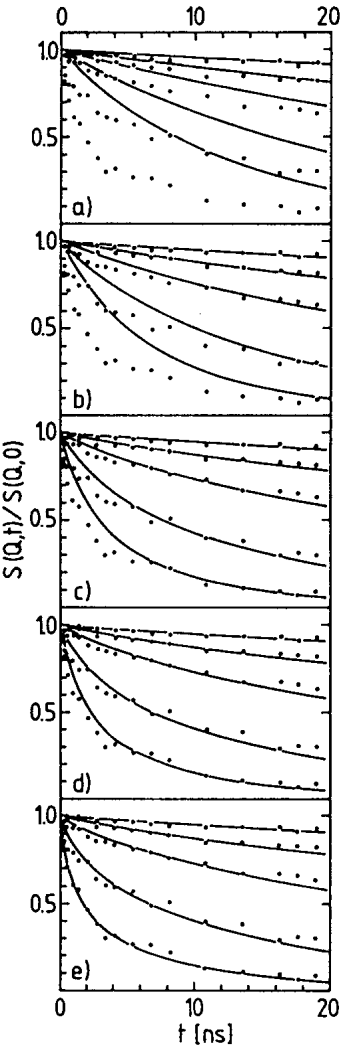

Fig. 13.27. Result of the mode analysis for the $M_w = 3600$ sample. The diagrams show the result of a calculation of the spectra retaining a successively rising number of modes in comparison to the experimental result; a) translation diffusion only, b) translation diffusion and first mode, c) translation diffusion and the first two modes, d) translation diffusion and the first three modes, e) translation diffusion and all modes.

The relaxation rates $1/\tau_p$ may depend in a general form on the mode index p according to

$$1/\tau_p = \frac{\pi^2 p^2}{N^2} W_p \quad . \tag{13.26}$$

The mode-dependent rate W_p is the parameter of analysis.

Figure 13.27 demonstrates the contribution of different modes to the dynamic structure factor for the specimen with the molecular weight 3600. Based on the parameters obtained in a common fit using (13.24) we calculated $S(Q,t)$ including an increasing number of mode contributions. Figures 13.27a show the contribution of translation diffusion. The translation

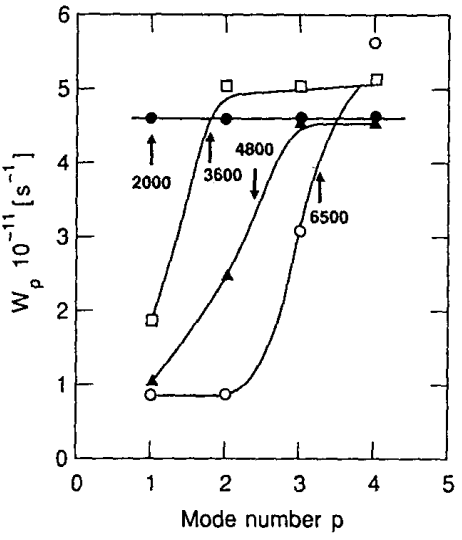

Fig. 13.28. Relaxation rates W_p for the first four relaxation modes of chains of different molecular weight as a function of the mode number p. The arrow indicates the condition $p = N/N_e$ for each molecular weight.

diffusion describes the experimental data for the smallest momentum transfer $Q = 0.037\,\text{Å}^{-1}$. Figure 13.27b presents $S(Q,t)$ retaining the first mode. Obviously, the long-time behaviour of the structure factor is now already adequately represented, whereas at shorter times the chain apparently relaxes much faster than calculated. Figure 13.27c–e shows how the agreement between experimental data and calculated structure factor improves if more and more relaxation modes are included. In Fig. 13.27e, finally, very good agreement between theory and experiment can be noted.

Figure 13.28 shows the results for W_p, the mode-dependent relaxation rate, for the different molecular weights as a function of the mode index "p". For the smallest molecular weight $M_w = 2000$ relaxation rates W_p are obtained which are independent of p. This chain obviously follows the Rouse law. The modes relax at a rate proportional to p^2 (cf. (13.15)). If the molecular weight is increased, the relaxation rates are successively reduced for the low-index modes in comparison to the Rouse relaxation, whereas the higher modes remain uninfluenced within experimental error.

How can we understand this behaviour? From the long-chain results of the last section we know that for polyethylene at the measuring temperature of 509 K the molecular weight between the points of entanglement is about $M_e = 2000$ or the number of monomers between the entanglement points is $N_e = M_e/M_o \approx 140$ (M_o: monomer weight). Let us assume that the characteristic length for a relaxation mode L_p is given by the distance between two nodes ($L_p = \ell N/p$). We then may define a critical mode index $p_{cr} = N/N_e$ below which the characteristic extension of a mode becomes greater than the distance between entanglements in the long-chain melt. These critical mode indices for the different molecular weights are plotted as arrows in Fig. 13.28.

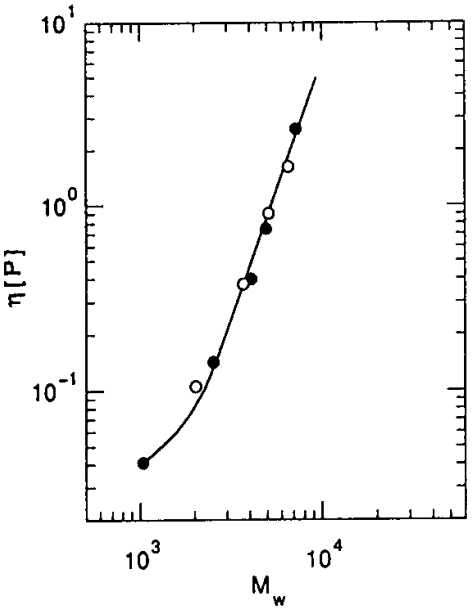

Fig. 13.29. Comparison of measured viscosities and viscosities calculated from the neutron spin-echo results for polyethylene melts at 509 K as a function of molecular weight (•: experimental result; ○ viscosities calculated on the basis of mode analysis).

It is evident that relaxation modes show deviations from Rouse behaviour when their extension is greater than the entanglement distance in the long-chain melt. We thus come to an interpretation of the mode analysis results. Obviously, topological interactions block, or at least very much reduce, the relaxation rate for those modes whose characteristic length becomes greater than the entanglement distance formed in long-chain melts.

We are now going to compare the result of the mode analysis with measurements of the viscosity on polyethylene melts. With the aid of (13.19), which links the viscosity with the relaxation times, we can predict the viscosity using the results of spin-echo measurements and compare it with the measurement [54]. This is done in Fig. 13.29, where the viscosity is shown as a function of molecular weight. The open circles represent the predictions of the NSE result, whereas the filled circles represent the viscosity measurement. Both data sets are in excellent agreement and demonstrate the consistency of evaluation.

Let us draw a fifth conclusion: The Q-dependence of the mode contributions to the dynamic structure factor opens direct access to the individual relaxation modes of a chain. This follows from the fact that neutrons permit motions to be observed on their natural length and time scales. We find that large-scale modes with characteristic lengths greater than the entanglement distance or with a mode index $p < N/N_e$ are significantly slowed down. A quantitative agreement with viscosity measurements is achieved with the aid of the extracted relaxation rates.

13.8 Conclusion

The viscoelasticity of polymer melts is determined by the relaxations of the individual chains. Their space-time analysis is possible with the aid of neutron spin-echo spectroscopy. The experiments described in this chapter allow one to draw the following conclusions:

(i) On the scale of molecular bonds the local relaxations depend on the specific local potentials. In (1–4) PB the two prevailing relaxation processes, the α- and β-relaxation, can be understood as interchain diffusion and intrachain motion, whereby the β-process relates to rotational motions of the chain building blocks. Above the merging temperature of the α- and β-relaxation, both processes persist independently from each other.

(ii) For intermediate time and length scales the segment dynamics of polymer melts follows the entropy-determined dynamics of the Rouse model. The predictions of this model were confirmed in all facets. Detailed comparison with simulation show deviations in detail, which relate to remaining interchain interactions – they are neglected in the Rouse model.

(iii) For long polymer chains the entanglement distance in polymer melts was directly observed using NSE. Moreover, the NSE experiments led to a quantitative validation of the dynamic structure factor for tube-confined reptation. The predictions of all other models put forward so far could be falsified.

(iv) The length- and time-scale regime in between universal Rouse relaxation and local relaxation is dominated by intrachain dissipation effects. NSE experiments on polymers with high (PIB) and low rotational barriers (PDMS) but similar stiffness unambiguously identified the presence of intrachain dissipation. In solution its activation energy coincides with the height of the rotation barrier.

(v) If the chain length in a polymer melt is prolonged beyond the entanglement distance, the relaxation modes of this melt are slowed down, provided that the characteristic length of the mode concerned is larger than the entanglement arc length. This result was obtained by a mode analysis of the dynamic structure factor; the microscopic mode relaxation rates lead to a quantitative agreement with macroscopic viscosity measurements.

Notation

A^{hop}	elastic incoherent structure factor for local hopping
$\boldsymbol{a}_n$	segment vector
$\boldsymbol{B}$	magnetic flux density
D, D_{R}	diffusion coefficients
d	jump distance

d_{t}	tube diameter
$E, \Delta E$	neutron energy, energy transfer
f^{hop}	quasielastic scattering contribution from two site jump processes
G_{S}	self correlation function
g	g-factor of the neutron
h	Planck constant
$\hbar$	$\hbar = h/2\pi$
H	magnetic field
$k, \boldsymbol{k}$	neutron wave vector
k_{B}	Boltzmann constant
ℓ	segment length
L	chain contour length
m	neutron mass
M	polymer molecular weight
M_0	monomer weight
M_{e}	entanglement molecular weight
N	degree of polymerization
N_{A}	Avogadro constant
N_{e}	number of monomers between entanglements
Prob	probability function for chain conformation
P	neutron polarization
Q	momentum transfer
R_{E}	end-to-end vector
$\boldsymbol{r}$	monomer coordinates
$S(Q,t)$, $S(Q,\omega)$	dynamic structure factor
$S(Q)$	static structure factor
t	time variable
$T_{\mathrm{m}}, T_{\mathrm{g}}$	merging, glass transition temperature
W	Rouse rate
x_s, x_p	Rouse normal coordinates
α	structural relaxation
β_{diel}	stretching exponents in the KWW function
$\beta_{\mathrm{slow/fast}}$	secondary relaxations
γ	magnetogyric ratio
ζ_0	monomeric friction coefficient
η	viscosity
$\lambda, \delta\lambda$	neutron wavelength, wavelength change
μ_{N}	nuclear magneton
ρ	density
τ, τ_η	characteristic relaxation time; for viscosity relaxation
ϕ	phase angle of neutron spin
φ^α	relaxation function for α relaxation
Ω	characteristic relaxation rate
ω	energy transfer during scattering

References

1. J.D. Ferry: *Viscoelastic Properties of Polymers* (Wiley, New York 1980)
2. P.E. Rouse: J. Chem. Phys. **21**, 1273 (1953)
3. P.G. de Gennes: *Scaling Concepts in Polymer Physics* (Cornell University Press, New York 1979)
4. D. Richter, B. Frick, B. Farago: Phys. Rev. Lett. **61**, 2465 (1988)
5. D. Richter, B. Ewen, B. Farago, T. Wagner: Phys. Rev. Lett. **62**, 2640 (1989)
6. B. Frick, B. Farago, D. Richter: Phys. Rev. Lett. **64**, 2921 (1990)
7. D. Richter, B. Farago, L.J. Fetters, J.S. Huang, B. Ewen, C. Lartigue: Phys. Rev. Lett. **64**, 1389 (1990)
8. R. Butera, L.J. Fetters, J.S. Huang, D. Richter, W. Pyckhout-Hintzen, A. Zirkel, B. Farago, B. Ewen: Phys. Rev. Lett. **66**, 2088 (1991)
9. D. Richter, R. Zorn, B. Farago, B. Frick, L.J. Fetters: Phys. Rev. Lett. **68**, 71 (1992)
10. D. Richter, R. Butera, L.J. Fetters, J.S. Huang, B. Farago, B. Ewen: Macromolecules **25**, 6156 (1992)
11. D. Richter, L. Willner, A. Zirkel, B. Farago, L.J. Fetters, J.S. Huang: Phys. Rev. Lett. **71**, 4158 (1993)
12. D. Richter, B. Farago, R. Butera, L.J. Fetters, J.S. Huang, B. Ewen: Macromolecules **26**, 795 (1993)
13. D. Richter, L. Willner, A. Zirkel, B. Farago, L.J. Fetters, J.S. Huang: Macromolecules **27**, 7437 (1994)
14. A. Arbe, U. Buchenau, L. Willner, D. Richter, B. Farago, J. Colmenero: Phys. Rev. Lett. **76**, 1872 (1996)
15. A. Arbe, D. Richter, J. Colmenero, B. Farago: Phys. Rev. E **54**, 3853 (1996)
16. P. Schleger, B. Farago, A. Kollmar, C. Lartigue, D. Richter: Phys. Rev. Lett. **81**, 124 (1998)
17. W. Paul, G.D. Smith, D.Y. Yoon, B. Farago, S. Rathgeber, A. Zirkel, L. Willner, D. Richter: Phys. Rev. Lett. **80**, 2346 (1998)
18. A. Arbe, J. Colmenero, M. Monkenbusch, D. Richter: Phys. Rev. Lett. **81**, 590 (1998)
19. A. Heuer, H.W. Spiess: Phys. Rev. Lett. **82**, 1335 (1999)
20. A. Arbe, J. Colmenero, M. Monkenbusch, D. Richter: Phys. Rev. Lett **82**, 1336 (1999)
21. D. Richter, M. Monkenbusch, J. Allgaier, A. Arbe, J. Colmenero, B. Farago, Y. Cheol, R. Faust: J. Chem. Phys. **111**, 6107 (1999)
22. A. Arbe, M. Monkenbusch, J. Stellbrink, D. Richter, B. Farago, K. Almdal, R. Faust: Macromolecules **34**, 1281 (2001)
23. A. Wischnewski, M. Monkenbusch, L. Willner, D. Richer, A. Likthman, T. McLeish: Phys. Rev. Lett. **88**, 058301 (2002)
24. W. Marshall, S.W. Lovesey: *Theory of Thermal Neutron Scattering* (Clarendon, Oxford 1971)
25. *Neutron Spin Echo*, Lecture Notes in Physics, vol 128, ed by F. Mezei (Springer, Berlin Heidelberg New York 1980)
26. *Neutron Spin Echo Spectroscopy: Basics, Trends and Applications*, Lecture Notes in Physics, vol 601, ed by F. Mezei (Springer, Berlin Heidelberg New York 2003)

27. R. Zorn, F.I. Mopsik, G.B. McKenna, L. Willner, D. Richter: J. Chem. Phys. **107**, 3645 (1997)
28. R. Zorn, G.B. McKenna, L. Willner, D. Richter: Macromolecules **28**, 8552 (1995)
29. B. Frick, D. Richter, W. Petry, U. Buchenau: Z. Phys. **B70**, 73 (1988)
30. R. Zorn, A. Arbe, J. Colmenero, B. Frick, D. Richter, U. Buchenau: Phys. Rev. E **52**, 782 (1995)
31. A. Arbe, J. Colmenero, B. Frick, M. Monkenbusch, D. Richter: Macromolecules **31**, (1998) 4926
32. G.B. Berry, T.G. Fox: Adv. Polym. Sci. **5**, 261 (1968)
33. J. Colmenero, A. Arbe, F. Alvarez, A. Narros, M. Monkenbusch, D. Richter: Europhys. Lett., in press (2005)
34. G. Vineyard: Phys. Rev. **110**, 999 (1959)
35. B. Farago, A. Arbe, J. Colmenero, R. Faust, U. Buchenau, D. Richter: Phys. Rev. E **65**, 051803 (2002)
36. A. Arbe, J. Colmenero, F. Alvarez, M. Monkenbusch, D. Richter, B. Farago, B. Frick: Phys. Rev. Lett. **89**, 245701 (2002)
37. A. Arbe, J. Colmenero, M. Monkenbusch, D. Richter: Phys. Rev. Lett. **82**, 1336 (1999)
38. W.P. Slichter: J. Polym. Sci. Part C **14**, 33 (1966)
39. K. Karatasos, J.-P. Ryckaert: Macromolecules **34**, 7323 (2001)
40. P.G. de Gennes: Physics (Long Island City, N.Y.) **3**, 37 (1967)
41. A. Wischneswki, M. Monkenbusch, L. Willner, D. Richter, B. Farago, G. Kali: Phys. Rev. Lett. **90**, 058302 (2003)
42. G. Smith, W. Paul, M. Monkenbusch, D. Richter: J. Chem. Phys. **261**, 61 (2000)
43. P.G. de Gennes: J. Chem. Phys. **55**, 572 (1971)
44. M. Doi, S.F. Edwards: J. Chem. Soc. Faraday. Trans. **2**, 74, 1789 (1978); **74**, 1802 (1978); **75**, 38 (1978)
45. G.J. Ronca: J. Chem. Phys. **79**, 79 (1988)
46. W. Hess: Macromolecules **21**, 2620 (1988)
47. P.G. de Gennes: J. Phys. (Paris) **42**, 735 (1981)
48. J. des Cloizeaux: Macromolecules **23**, 2753 (1990)
49. G. Allegra, F. Ganazzoli Macromolecules **14**, 1110 (1981)
50. G. Allegra, F. Ganazzoli: Advances in Chemical Physics **75**, 265 (1989)
51. L. Harnau, R.G. Winkler, P.J. Reinicker: J. Chem. Phys. **102**, 7750 (1995); **104**, 6355 (1996)
52. R. Dejean de la Batie, F. Lauprêtre, L. Monnerie: Macromolecules **22**, 2617 (1989); A.A. Jones, R.P. Lubianez, M.A. Hanson, S.L.J. Shostak: Polym. Sci., Polym. Phys. Ed. **16**, 1685 (1978); Y. Inoue, A. Nishioka, R. Chûjô: J. Polym. Sci., Polym. Phys. Ed. **11**, 2237 (1973)
53. M. Doi, S.F. Edwards: *The Theory of Polymer Dynamics* (Clarendon, Oxford UK 1986)
54. D.S. Pearsson, L.J. Fetters, W.W. Graessley, G. Verstrate, E.V. Merwall: Macromolecules **27**, 711 (1994)

14 The Molecular Description of Mutual Diffusion Processes in Liquid Mixtures

Hermann Weingärtner

14.1 Introduction

In a liquid, the constituent particles are in rapid translational motion due to thermal agitation. The molecular displacements are characterized by the self-diffusion coefficient D, which in three-dimensional space is related to the mean square displacement after time t via the Einstein relation [1]

$$D = \lim_{t\to\infty} \frac{1}{6t} \langle |\boldsymbol{r}_\alpha(t) - \boldsymbol{r}_\alpha(0)|^2 \rangle. \tag{14.1}$$

Here $\boldsymbol{r}_\alpha(t)$ describes the location of a particle numbered α at time t. The brackets $\langle \cdots \rangle$ denote the ensemble average. In a liquid mixture of r components, self-diffusion coefficients D_a can be assigned to any of the components $a = 1, 2 \ldots r$.

The limiting process in (14.1) implies that the displacements of molecules are observed over a much longer time than the time scale set up by the underlying molecular motions. This situation is often called normal diffusion. In liquids of low or moderate viscosity the relevant molecular time scale is typically of the order of some picoseconds. On the other hand, depending on the experimental method, conventional diffusion experiments observe diffusion over some milliseconds to hours or days. Clearly, the condition for normal diffusion is fulfilled, e.g., in these cases. It may not be fulfilled for supercooled liquids, glasses or polymer systems, where molecular relaxation times reach the experimental observation time. Such cases of anomalous diffusion, dealt with in Chaps. 10 and 13, will not be considered in the present chapter.

Following the general trend of looking for a molecular description of the properties of matter, self-diffusion in liquids has become a key quantity for interpreting and modelling transport in liquids, because among all transport coefficients the self-diffusion coefficient is certainly the most simple to interpret [1]. For example, the extraction of self-diffusion coefficients from molecular dynamics simulations of liquids is straightforward by evaluation of the mean square displacement from the simulated trajectories of the particles [2] (see also Chap. 23).

If, as an external perturbation, a concentration inhomogeneity is set up for one of the components, the liquid responds with another diffusion process, because a concentration gradient of any component results in mass fluxes of

all other components. In this case the species diffuse cooperatively, so as to smear out the concentration inhomogeneity. In work on fluid mixtures the term mutual diffusion has become common for this process [1], in other fields the terms interdiffusion, mass diffusion, chemical diffusion or transport diffusion are also in use. The cooperativity of the mass flows distinguishes mutual diffusion from the stochastic motion of individual molecules reflected by the self-diffusion process. For example, the mass flows of the two components in binary systems are coupled, and a single quantity, called mutual-diffusion coefficient D_{12}, is sufficient to characterize the diffusion process, regardless of which of the mass flows is observed [1].

From the applications' point of view, mutual diffusion is by far more important than self-diffusion, and plays a major role in many physical and chemical processes. Hence, the necessity of predicting mutual-diffusion coefficients often arises, and many efforts have been made to understand and predict mutual-diffusion data [1]. Again, there is much interest in a microscopic description of mutual diffusion processes, which is firmly based on statistical mechanics and liquid-state theory. In particular, it is desirable to put the description of mutual diffusion on a basis, which is analogous to that used for interpreting self-diffusion data. Owing to its cooperative nature, a theoretical description of mutual diffusion, however, is expected to be more complex than that of self-diffusion. This chapter aims at discussing the basic foundations of such a molecular-based description of mutual diffusion in relation to that of self-diffusion.

Actually, attempts to understand mutual diffusion processes at a microscopic level are very closely related to the understanding of self-diffusion – mutual-diffusion relationships. Many diffusion models in quite different fields such as chemistry, metallurgy, chemical engineering or geochemistry give relations between self-diffusion and mutual-diffusion coefficients. As an example, we mention the use of self-diffusion coefficients measured by NMR techniques as input data in modelling multi-component mass transport in industrial processes [3] or in oil recovery and oil technology [4, 5].

From the theoretical point of view, this problem is intriguing, because it tackles our fundamental understanding of the interrelation between single-particle and cooperative motions in liquids [6]. This problem is not only present in translational dynamics, but is also a long-standing problem in the interpretation of rotational dynamics in liquids, where some experiments such as nuclear magnetic relaxation monitor single-particle motions, while other techniques such as dielectric relaxation [7, 8] or depolarized light scattering [9] monitor cooperative processes. Moreover, the electrical conductance in molten salts and in electrolyte solutions is a cooperative process as well, which is closely related to the diffusive motions considered here [6].

Finally, the use of nuclear magnetic resonance spin-echo experiments [10] provides an elegant and convenient method for monitoring self-diffusion in liquids [11, 12]. Furthermore, by applying Fourier transform techniques in NMR

spectroscopy, self-diffusion coefficients can be determined simultaneously for many components [10, 13]. From this experimental perspective, theoretical relations, which interconnect mutual-diffusion coefficients with self-diffusion coefficients, are of considerable interest as well.

In fact, the interrelation between mutual and self-diffusion in liquid mixtures has been under debate since a long time. The simplest self-diffusion – mutual-diffusion relationship for binary systems is the Darken relation [14], sometimes called Hartley-Crank relation [15]

$$D_{12} = x_2 D_1 + x_1 D_2 \,. \tag{14.2}$$

Here, the x_i are the mole fractions of the components. Equation (14.2) and other closely related versions of this equation are well suited for estimating diffusion coefficients in thermodynamically near-ideal systems such as mixtures of hydrocarbons [4, 16, 17]. It will be shown below under which approximations this well-known relation evolves from rigorous theory.

On the other hand, (14.2) and many analogues reported in the literature rapidly loose their validity in thermodynamically non-ideal systems [1,18,19], because the effect of intermolecular interactions cannot easily be taken into account theoretically. Thus, diffusion theory faces similar difficulties as the calculation of equilibrium thermodynamic properties. Of course, the intermolecular interactions, which determine equilibrium properties, also govern the transport processes. Therefore, it is often useful to take the thermodynamic properties as a guide for interpreting diffusion data. On the other hand, this sensitivity of diffusion coefficients to molecular aggregation provides useful information on molecular interactions in liquid mixtures [18,19]. The present chapter will discuss a conceptual framework for such interpretations.

The chapter is organized as follows: After a brief review of experimental aspects in Sect. 14.2, the basic quantities for describing diffusion on a phenomenological level will be introduced in Sect. 14.3. In Sect. 14.4 we will reformulate these relations within the framework of the thermodynamics of irreversible processes. In Sect. 14.5 time correlation functions will be introduced for describing transport processes on a microscopic level. In Sect. 14.6 this formalism is applied to mutual diffusion. As a result, the experimental diffusion coefficients can be rewritten in terms of generalized interaction coefficients. These interaction coefficients, denoted as distinct-diffusion coefficients, describe the coupling of the diffusive motions of the particles in the mixture. Their basic properties will be outlined in Sect. 14.7. Finally, in Sect. 14.8 some predictive equations based on this approach are discussed and illustrated in application by some examples for diffusion in liquid mixtures of non-electrolytes and electrolytes with specific interactions between the components.

14.2 Experimental Background

Before considering theoretical aspects, it seems helpful to throw a glance at the basic experimental situation. In the past, many sophisticated techniques for measuring self-diffusion and mutual-diffusion coefficients have been developed [1, 20] . When assessing and comparing their benefits, the recent literature has, however, seen a considerable change in accentuation.

Mutual diffusion causes local changes in composition and can therefore be studied by any physical and chemical method that is sufficiently sensitive to the composition of the mixture. The most precise measurements in two- and three-component liquid systems have been the Gouy and Rayleigh optical techniques [21]. In both methods fringe patterns are generated by passing monochromatic light through a diffusion boundary. The basic principles of these methods have been described almost five decades ago, and detailed reviews can be found in the literature [1,21]. If equipped with suitable computer control and electronic data recording, such techniques still today are methods of choice, when requiring highly accurate mutual-diffusion data [22, 23].

More simple methods monitor diffusion through diaphragms or diffusion out of capillaries by appropriate chemical or physical methods of concentration analysis [1, 20]. A more modern and faster technique uses dynamic light scattering [24] which is described in Chaps. 15 and 16 of this book. Finally, there is the Taylor dispersion method in which the diffusing component is injected into the flowing solvent, and its dispersion in the flowing liquid is subsequently measured at a detector [1, 20]. In recent years, Taylor diffusion has become a convenient and economic method for collecting diffusion data over wide ranges of state with fair accuracy, including, for example, the highly fluid or supercritical regime [25].

In view of these powerful experimental techniques for studying mutual diffusion, there rises the question, why to go a long way round by developing theories to estimate mutual-diffusion data from self-diffusion data. The answer is that NMR spin-echo methods possess some major experimental advantages [10] resulting, for example, from fast experiments, small sample volumes, and easy applications over wide ranges of temperature and pressure. Moreover, most techniques for determining mutual-diffusion coefficients apply non-equilibrium conditions. When working away from room temperature and ambient pressure, it is often difficult to stabilize the resulting concentration gradients against thermal or mechanical perturbations. In contrast, self-diffusion measurements by NMR techniques are performed at equilibrium. (Other experimental methods for determining self-diffusion coefficients based on isotopic tracer techniques, still extensively used in the 1970s and 1980s [1] have almost completely disappeared from the scene.)

The major advantage of NMR methods is however encountered, when dealing with multi-component systems. In nature as well as in industrial practice, systems are usually composed of three or more components. As discussed later in detail, a system composed of r components is characterized

by an $r \times r$ matrix of diffusion coefficients with $r(r-1)/2$ independent elements [1]. Except for the interferometric techniques, where the very high accuracy of the data allows the determination of the matrix at least in the ternary systems [1,21,22], the extraction of multi-component diffusion coefficients from measured concentration distributions is exceedingly difficult. The possibility of measuring simultaneously the self-diffusion coefficients of many constituents in multi-component mixtures by Fourier transform techniques is one of the powerful features [10,12] that make NMR experiments uniquely suited for studying multi-component diffusion.

14.3 Phenomenological Description of Mutual Diffusion

At isothermal conditions mutual diffusion is described by Fick's law. If, for simplicity, we confine the discussion to binary mixtures, Fick's law relates the concentration gradients of the components $a = 1, 2$ to their flux densities $\boldsymbol{j}_a$. These flux densities depend on the reference frame in the experiment. Usually, one observes diffusion in a laboratory-fixed frame, defined by some plane in the diffusion cell perpendicular to the flux [1]. Then Fick's law reads for component 1

$$-\boldsymbol{j}_1 = D_{12} \operatorname{grad} c_1. \tag{14.3}$$

If component 2 rather than component 1 is observed, one has

$$-\boldsymbol{j}_2 = D_{21} \operatorname{grad} c_2. \tag{14.4}$$

Experimentally one finds the same value for D_{12} and D_{21}.

From the theoretical point of view, it is more adequate to define the fluxes with respect to internal coordinate systems, for example, based on a reference frame, which assumes the local center of volume to be at rest [1]. In principle, flows in the laboratory-fixed and volume-fixed frames of reference are not the same, because there may be diffusion-induced bulk volume flows. In isothermal-isobaric liquid systems these flows can only result from volume change on mixing. For small concentration gradients such volume changes are negligible, so that in most experimental situations the equality of both reference frames is assumed.

In passing we note that other reference frames can be chosen. For example, when considering diffusion of a mobile phase into a comparatively immobile phase, such as a gas into a solid, it is convenient to relate the flow of the mobile phase to a coordinate system set up by the immobile phase, which is assumed to be at rest. As an example, Chaps. 10 and 23 consider in detail the diffusion properties of molecules in zeolites. The analogue in liquid systems is the so-called solvent-fixed reference system, where the flux of one or more solutes is considered relative to the solvent at rest [1]. In binary liquid mixtures this reference frame is of comparatively little use. It may however be the

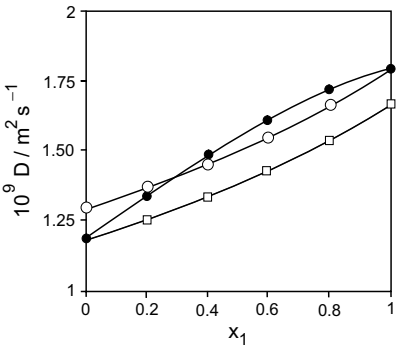

Fig. 14.1. Composition dependence of diffusion coefficients in the system mesithylene (1) + carbon tetrachloride (2) at 298.15 K: D_1 (open circles), D_2 (squares), D_{12} (filled circles).

frame of choice for ternary and multi-component systems in the presence of a large excess of one of the components. Moreover, when describing diffusion in electrolyte solutions, it is also quite natural to express mass flows in aqueous electrolyte solutions relative to the solvent water at rest (see Chap. 17).

Presuming that experimental fluxes are indeed measured in the volume-fixed frame, one can show that the two mass flows are not independent. The special choice of the coordinate system imposes the condition [1]

$$J_1\overline{V}_1 + J_2\overline{V}_2 = 0. \tag{14.5}$$

The $\overline{V}_1$ are the partial specific volumes of the components $a = 1, 2$. Using the thermodynamic definition of the partial specific volumes, $\overline{V}_a = (\partial V/\partial m_i)_{p,T}$, where m_a is the mass of component a in the total volume V, and their interconnection via the Gibbs-Duhem equation, one can rigorously show that

$$D_{12} = D_{21}. \tag{14.6}$$

Thus, the mutual-diffusion coefficient is one and the same value, regardless of which of the components is monitored in the diffusion experiment.

Fig. 14.1 shows as an example the composition dependence of the mutual-diffusion coefficient in the system mesithylene + carbon tetrachloride, which is a standard example for systems with specific interactions between dislike components [26]. This interaction between mesithylene and carbon tetrachloride is well established from thermodynamic data. The figure also contains the self-diffusion coefficients of both components. It is seen that the concentration dependence of D_{12} differs markedly in shape from those of D_1 and D_2. It is also not correlated with the concentration dependence of other transport coefficients such as the viscosity.

One may however note that at both ends of the concentration range self- and mutual-diffusion coefficients approach one another. In fact, at trace concentration of a component the self-diffusion coefficient of this component

approaches the mutual-diffusion coefficient. This limiting behavior evolves from rigorous theory, and is well established experimentally.

One attempt to bring some order into this confusing behavior is related to a more detailed analysis of the driving force of diffusion. From the point of view of thermodynamics, as described later in Sect. 14.4, the correct driving force of diffusion is the gradient of the chemical potential rather than the concentration gradient. Noting that

$$\operatorname{grad} c_a = \left(\frac{\partial c_a}{\partial \mu_a}\right) \operatorname{grad} \mu_a, \tag{14.7}$$

and rewriting the concentration in terms of mole fractions leads to a transformation factor of the form

$$Q = \frac{\mathrm{d} \ln a_1}{\mathrm{d} \ln x_1} = \frac{\mathrm{d} \ln a_2}{\mathrm{d} \ln x_2}, \tag{14.8}$$

where a_i is the activity of component i. Q is denoted as thermodynamic factor. Therefore, one often considers the experimental diffusion coefficient D_{12} to consist of a product of a thermodynamic diffusion coefficient D_{12}^* which refers to the correct driving force and the correction term Q, i.e.

$$D_{12} = D_{12}^* Q. \tag{14.9}$$

From this line of arguing it is more convenient to compare and interpret data for the quotient D_{12}/Q rather than D_{12} itself . In practice, the concentration dependence of Q is often stronger than that of D_{12}^*, and the superposition of the two terms often leads to quite complex concentration dependencies of D_{12} [1]. It is shown below that such a correction, often introduced by qualitative reasoning, has indeed a theoretical basis.

Depending on the system, the magnitude of such corrections may be largely different. Fig. 14.2 illustrates the behavior of Q for systems exhibiting different thermodynamic situations. Thermodynamic ideality may be defined by Raoult's law, which implies that $Q = 1$. Examples for this type are binary mixtures of rare gases, or hydrocarbons. Fig. 14.2 shows data for n-hexane + n-dodecane mixtures, where Q is indeed very close to unity. Model calculations show that, to a first approximation, binary mixtures of Lennard-Jones fluids are ideal as well [6] . Thus, for ideal mixtures the correction does not play a role at all. The same is true for sufficiently dilute solutions, because for $x_1 \to 0$ and $x_2 \to 0$ we have by definition $Q \to 1$.

Systems with aggregation between dislike components show negative deviations from Raoult's law and one finds $Q > 1$. This behavior is illustrated in Fig. 14.2 for mesithylene + carbon tetrachloride. In contrast, self-aggregation of the components reflects itself by positive deviations and $0 < Q < 1$. Examples are solutions of alcohols or carboxylic acids in comparatively inert solvents such as carbon tetrachloride. Fig. 14.2 shows, as an example, data for methanol + carbon tetrachloride, where in parts of the concentration

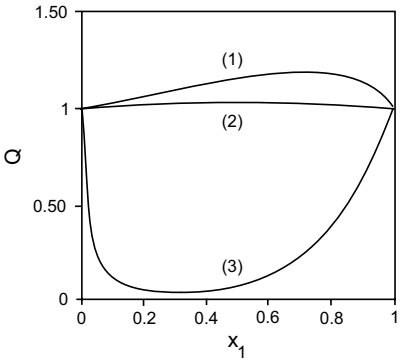

Fig. 14.2. Composition dependence of the thermodynamic factor Q in the systems mesithylene + carbon tetrachloride (1), n-hexane + n-dodecane (2), and methanol + CCl_4 (3) at 298.15 K. The first-mentioned components are denoted as component 1.

range Q differs by more than an order of magnitude from unity. Thus, thermodynamic non-ideality enhances diffusion in the case of negative deviations of Raoult's law and slows down diffusion for positive deviations of Raoult's law.

In view of these reasonings one often reformulates the Darken relation (2) by

$$D_{12} = (x_2 D_1 + x_1 D_2)\, Q \quad . \tag{14.10}$$

In the case of thermodynamically non-ideal systems, an incorporation of the thermodynamic factor often leads to an improved estimate of D_{12} in comparison with Darken's original relation (14.2). In fact, in most cases the Darken relation is applied in the form of (14.10) rather than (14.2). We show in

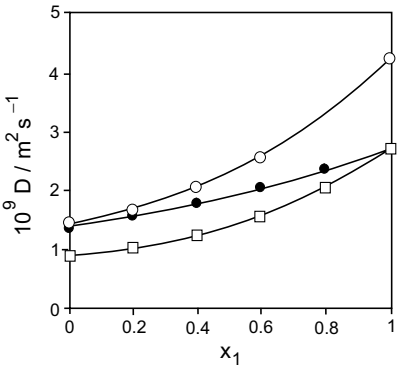

Fig. 14.3. Composition dependence of diffusion coefficients in the system n-hexane (1) + n-dodecane (2) at 298.15 K: D_1 (open circles), D_2 (squares), D_{12} (filled circles). n-hexane is component 1.

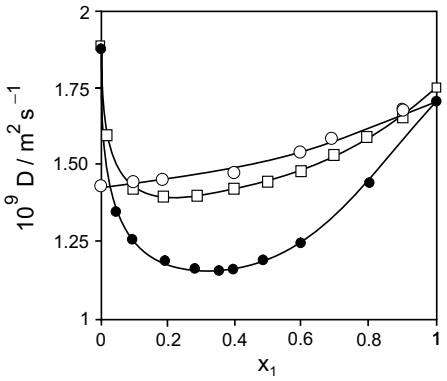

Fig. 14.4. Composition dependence of diffusion coefficients in the system methanol (1) + carbon tetrachloride (2) at 298.15 K: D_1 (squares), D_2 (open circles), D_{12} (filled circles).

Fig. 14.3 diffusion data for the near-ideal system n-hexane + n-dodecane [4]. Equation (14.10) represents the experimental data for D_{12} practically within the limits of experimental uncertainty.

However, even in this improved form, the Darken equation is of little use for predicting diffusion data for systems with comparatively strong specific interactions between the components. We show in Fig. 14.4 experimental data for methanol + carbon tetrachloride [27] with strong self-aggregation of methanol molecules. Fig. 14.5 shows that (14.2) overestimates D_{12} by more than a factor of two in parts of the concentration range. If (14.10) is used instead, D_{12} is largely underestimated. Near the minimum of D_{12} experimental and predicted data differ by an order of magnitude.

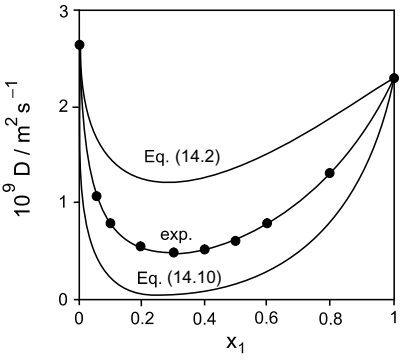

Fig. 14.5. Estimate of mutual-diffusion coefficients in the system methanol + carbon tetrachloride by (14.2) and (14.20), respectively. Methanol is component 1.

Finally, we note that in thermodynamics (14.8) is just a measure for the thermodynamic stability of mixtures, because the thermodynamic stability condition for mixtures can be rewritten in terms of Q, leading to $Q > 0$. In other words, the spinodal line for liquid-liquid phase separation is defined by $Q = 0$. This stability criterion is therefore often denoted as condition for diffusional stability. As a consequence, when approaching the spinodal line, mutual diffusion slows down, because the driving force vanishes. Very slow diffusion in systems of comparatively low viscosity may therefore imply that one is close to phase separation or to a critical point. This observation is well established experimentally for systems with liquid-liquid phase separations like triethylamine + water [28] or n-hexane + nitrobenzene (see Fig. 15.14 of Chap. 15).

14.4 Thermodynamics of Mutual Diffusion

By using the thermodynamics of irreversible processes, transport phenomena can be described in a unified formalism [1, 29, 30]. This type of approach is particularly adequate, when seeking for a starting point for a microscopic description of transport phenomena. Again, it is necessary to define a reference frame to which the fluxes are referred to. Although, in principle, the equations of the thermodynamics of irreversible processes can be set up in any of these frames, the desired interconnection with statistical mechanics suggests to do this analysis in the barycentric frame with the center-of-mass at rest.

To transform Fick's law to the barycentric frame we first introduce the partial mass densities of the components as $\varrho_i = m_i/V$. Moreover, we consider specific chemical potentials defined by the mass derivative of the Gibbs free energy, μ_1^*, rather than chemical potentials defined as partial molar quantities. Then, Fick's law may be formulated as

$$-\boldsymbol{J}_1^m = D_{12}^m \operatorname{grad} \varrho_1$$

and

$$-\boldsymbol{J}_2^m = D_{21}^m \operatorname{grad} \varrho_2. \tag{14.11}$$

Superscript m indicates quantities defined in the barycentric frame. Procedures for reference-frame transformation are extensively discussed in the literature [1, 29, 30]. Detailed analysis shows that the diffusion coefficients D_{12}^m and D_{21}^m are not equal, but interrelated by

$$D_{12}^m \overline{V}_2 = D_{21}^m \overline{V}_1. \tag{14.12}$$

However, within the framework of thermodynamics of irreversible processes, the gradient of the partial mass density is not a suitable driving force. To derive the correct force we consider linear equations between fluxes $\boldsymbol{J}_i$ and forces $\boldsymbol{X}_i$ of the form

$$\begin{array}{l} -\boldsymbol{J}_1 = L_{11}\boldsymbol{X}_1 + L_{12}\boldsymbol{X}_2 + L_{13}\boldsymbol{X}_3 + \cdots \\ -\boldsymbol{J}_2 = L_{21}\boldsymbol{X}_1 + L_{22}\boldsymbol{X}_2 + L_{23}\boldsymbol{X}_3 + \cdots \\ -\boldsymbol{J}_3 = L_{31}\boldsymbol{X}_1 + L_{32}\boldsymbol{X}_2 + L_{33}\boldsymbol{X}_3 + \cdots \\ \quad\vdots \qquad\quad \vdots \qquad\quad \vdots \qquad\quad \vdots \qquad \ddots \end{array} \tag{14.13}$$

Thermodynamics of irreversible processes says that the fluxes and forces have to be chosen in such a way that their product is equal to the entropy production $T\sigma$ of the system. In the latter case the coefficients L_{ij} in (14.13) are called phenomenological coefficients. One can show that in the barycentric system the entropy production is given by [1, 29, 30]

$$T\sigma = -\boldsymbol{J}_1^{\boldsymbol{m}} \operatorname{grad}(\mu_1^* - \mu_2^*) \tag{14.14}$$

or an analogous expression for the flow of component 2. Thus, the correct driving force is the gradient of the specific chemical potential. In a binary system the phenomenological equations are then given by

$$\begin{aligned} -\boldsymbol{J}_1^m &= L_{11} \operatorname{grad}\mu_1^* + L_{12} \operatorname{grad}\mu_2^*, \\ -\boldsymbol{J}_2^m &= L_{21} \operatorname{grad}\mu_1^* + L_{22} \operatorname{grad}\mu_2^*. \end{aligned} \tag{14.15}$$

There are, however, two restrictions among the fluxes and forces. First, the fluxes are not independent. If the local center-of-mass is at rest we have

$$\boldsymbol{J}_1^m + \boldsymbol{J}_2^m = 0 \tag{14.16}$$

which represents the analogue to (14.5). Furthermore, the Gibbs-Duhem equation interrelates the specific chemical potentials through

$$\varrho_1 \operatorname{grad}\mu_1^* + \varrho_2 \operatorname{grad}\mu_2^* = 0. \tag{14.17}$$

It can be shown [1, 29, 30] that these restrictions lead to the condition

$$L_{12} = L_{21} = -L_{11} = -L_{22}. \tag{14.18}$$

Thus, information on the mutual-diffusion coefficient is sufficient to determine all four phenomenological coefficients. This simplicity is, however, lost in systems composed of more than two components. In detail, one finds

$$D_{12} = -\frac{(x_1M_1 + x_2M_2)^2}{x_1x_2M_1M_2} \left(\frac{\mathrm{d}\ln a_1}{\mathrm{d}\ln x_1}\right) L_{12}. \tag{14.19}$$

M_i is the molecular mass of component i.

Let us briefly consider this situation from a more general point of view. In a system of r components there are r forces and r fluxes described by the phenomenological relations (14.13). Accordingly, one obtains a matrix of phenomenological coefficients

$$\begin{pmatrix} L_{11} & L_{12} & \cdots & L_{1r} \\ L_{21} & L_{22} & \cdots & L_{2r} \\ \vdots & \vdots & \ddots & \vdots \\ L_{r1} & L_{r2} & \cdots & L_{rr} \end{pmatrix}. \tag{14.20}$$

The coefficients of this matrix are not independent, because the gradients of the chemical potentials are interrelated by the Gibbs-Duhem relation and the sum of the fluxes has to be zero. For a binary system these restrictions lead directly to (14.18). For ternary and higher-order systems these conditions are not sufficient to determine the matrix. There is, however, an additional postulate, saying that the matrix of the coefficients has to be symmetric, i.e.

$$L_{ij} = L_{ji}. \tag{14.21}$$

This is Onsager's well-known reciprocity relation which, in a molecular picture, reflects microscopic reversibility. Thus, in general, in a system of r components there are only $r \cdot (r-1)/2$ independent coefficients.

Now, for a binary system with $r = 2$ we are back to a single diffusion coefficient. However, for a ternary system, presuming the reciprocity relation, we have already three independent diffusion coefficients. If, however, one aims at proving the Onsager relation rather than implementing this relation in data analysis, one has to extract four coefficients from the experimental concentration distribution [1, 20].

One of the pressing questions is of course, whether the cross terms of the matrix with $i \neq j$ are sufficiently different from zero to be of importance in data analysis. Otherwise, the analysis is largely simplified. In fact, in many models for diffusion in complex systems, approximations are made which implicitly imply that the cross terms are negligible. However, in this regard the answer by accurate experiments is desillusioning: The cross terms may be even larger in magnitude than the main terms [22, 23].

Finally, we consider briefly systems with charged species such as electrolyte solutions or molten salt mixtures. Thermodynamically, an electrolyte solution consisting of the salt (s) and water (w) is a binary system with a single mutual-diffusion coefficient D_{sw}, because diffusion arises from the gradients of the neutral salt and water. There cannot be gradients of single ions, because the concentrations of the ions are not independent variables, but are interrelated by the constraint of overall charge neutrality. Then, with regard to mutual diffusion there is a set of four Onsager coefficients, which according to (14.18) are interrelated by

$$L_{\mathrm{sw}} = L_{\mathrm{ws}} = -L_{\mathrm{ss}} = -L_{\mathrm{ww}} \tag{14.22}$$

However, one can also try to apply the formalism of the thermodynamics of irreversible processes to a ternary system consisting of the cation (c), anion (a) and the solvent water (w). (Note that the three self-diffusion coefficients of the ionic constituents can indeed be measured separately.) Such

a formalism yields a 3×3 matrix of Onsager coefficients. We denote these coefficients by l_{ij} $(i, j = \text{c,a,w})$. It is an intriguing problem to relate the l_{ij} of the ternary model system to the L_{ij} of the salt-water system obtained by direct thermodynamical analysis.

By symmetry, only three of the nine l_{ij} of the 3×3 matrix are independent. Obviously, in addition to the mutual-diffusion coefficient, two other experimental quantities are needed for determining the l_{ij}. The solution of this problem is given by the fact, that thermodynamics of irreversible processes relates two other transport coefficients to the l_{ij} [29, 30], namely the ionic mobilities of the cations and anions in the electric field. These can be determined directly, for example, by the new technique of electrophoretic NMR discussed in Chap. 17. Traditionally, one measures, however, the electrical conductance of the solution and the transference numbers that allow to separate the conductance into single-ion contributions. The resulting formalism to determine the Onsager coefficients l_{ij} has been worked out in detail long time ago by Miller [31].

14.5 Linear Response Theory and Time Correlation Functions

In statistical mechanics the time dependence of the dynamical variables of N-particle systems are described by Hamilton's equations of motion. These can, for example, be solved for some hundreds or thousands of particles by numerical solution in molecular dynamics simulations ([2] and Chap. 23). Self-diffusion coefficients can then be derived from the simulated trajectories, e.g. via (14.1).

For an analytical description it is only possible to consider certain time and ensemble averages. For this purpose one considers the time dependence of the N-particle correlation function ([6, 32], see also Chap. 23)

$$F_N(\boldsymbol{r}^N, \boldsymbol{p}^N),$$

where $\boldsymbol{r}^N$ and $\boldsymbol{p}^N$ stand symbolically for the generalized position and momentum vectors of the N-particle system. At equilibrium, this correlation function is given by

$$F_N^0 = \text{const} \cdot \exp(-H_0/kT), \tag{14.23}$$

where H_0 is the classical Hamiltonian of the N-particle system. If there is a weak perturbation due to an external force, the Hamiltonian contains an additional contribution H_{ext}, i.e. H_0 is replaced by

$$H = H_0 + H_{\text{ext}}. \tag{14.24}$$

In this case, the time dependence of the correlation function is given by Liouville's equation

$$\frac{\partial F_N}{\partial t} = i\mathrm{L}F_N, \tag{14.25}$$

where

$$\mathrm{L} = i\sum_k^N \left\{ \left(\frac{\partial H}{\partial \boldsymbol{p}_k}\right)\left(\frac{\partial}{\partial \boldsymbol{r}_k}\right) - \left(\frac{\partial H}{\partial \boldsymbol{r}_k}\right)\left(\frac{\partial}{\partial \boldsymbol{p}_k}\right) \right\} \tag{14.26}$$

is the Liouville-Operator. If H_{ext} is known, one can calculate expectation values of the dynamical variables due to this perturbation. In the case of diffusion the perturbation is related to a local gradient in the specific chemical potential.

In the regime of linear response due to sufficiently weak perturbations, the application of this formalism shows that any transport coefficient A can be written as an integral over a time correlation function of the form [6, 32]

$$A \propto \int_0^\infty \langle \boldsymbol{J}_A(0) \cdot \boldsymbol{J}_A(t)\rangle \mathrm{d}t, \tag{14.27}$$

where $\boldsymbol{J}_A(\tau)$ is the flux associated with A at time $\tau = 0$ and t, respectively. Expressions of this type are denoted as Green-Kubo relations.

Probably the most well-known and most simple example of a Green-Kubo relation is the expression for the self-diffusion coefficient D_i in terms of the velocity auto-correlation function

$$D_a = \frac{1}{3}\int_0^\infty \langle \boldsymbol{v}_{a,\alpha}(0) \cdot \boldsymbol{v}_{a,\alpha}(t)\rangle \mathrm{d}t, \tag{14.28}$$

where the velocity of a particle α of component a at time $t = 0$ is correlated with that of the *same* particle at time t. These velocities refer to the barycentric reference frame. Because self-diffusion does not lead to macroscopic gradients in the system, the barycentric frame coincides with the volume- and laboratory-fixed frames. In other words, the self-diffusion coefficient is independent of the reference frame.

By using the proper relation between position vectors and velocities one can show that (14.28) is fully equivalent to the relation for the self-diffusion coefficient in terms of the mean square displacement, (14.1). For example, when determining the self-diffusion coefficient in molecular dynamics simulations it is only a technical problem, whether the self-diffusion coefficient is extracted via (14.1) or (14.28) [2] (see also Chap. 23).

Moreover, another equivalent expression may be mentioned which is particularly suitable when monitoring diffusion processes in neutron scattering experiments (see Chaps. 2, 3, and 13). In this case, the quantity of interest is the Van Hove dynamic structure factor $S(\kappa, \omega)$, where κ and ω refer to the momentum and energy transfer in the scattering experiment. If one rewrites (14.1) in terms of $S(\kappa, \omega)$ one finds the self-diffusion coefficient to be

related to the hydrodynamic ($\kappa \to 0,\ \omega \to 0$) limit of the self-part of the dynamical structure factor $S^{\mathrm{S}}(\kappa, \omega)$ which is available by incoherent scattering experiments [6]

$$D_a = \pi \lim_{\omega \to 0} \lim_{\kappa \to 0} \frac{\omega^2}{\kappa^2} S_a^{\mathrm{S}}(\kappa, \omega)\,. \tag{14.29}$$

In fact, it is well-known that in the hydrodynamic limit incoherent neutron scattering leads to a Lorentzian spectrum with a half-width determined by the self-diffusion coefficient [6] (see also Chap. 3).

14.6 The Time Correlation Function for Mutual Diffusion

In order to obtain the equivalents to (14.1), (14.28), and (14.29) for mutual diffusion, the Green-Kubo theory has to be applied to the phenomenological coefficients L_{ab}. The result is [32]

$$L_{ab} = (3kTV)^{-1} \int_0^\infty \langle \boldsymbol{J}_a(0) \cdot \boldsymbol{J}_b(t) \rangle \mathrm{d}t, \tag{14.30}$$

where $\boldsymbol{J}_i$ is the microscopic mass flow of species $i = a$ or b in the barycentric frame. This mass flow has to be summed up over the velocities of all particles of component i:

$$\boldsymbol{J}_i(t) = \sum_{k=1}^{N_i} \left(\frac{m_i}{V} \right) \boldsymbol{v}_{i,k}(t); \qquad i = a, b. \tag{14.31}$$

We consider first the expression for L_{12} in the case of which $a = 1$ and $b = 2$. Then, according to (14.30) the velocities of the species of component 1 are coupled to those of the species of component 2. If (14.31) is inserted into (14.30) one obtains an expression involving velocity cross-correlations for particles of different components, in contrast to the velocity auto-correlation function entering into the expression for the self-diffusion coefficient.

Alternatively, we may consider the coefficient L_{11} (or, by interchange of indices, L_{22}), instead of L_{12}. Then, the situation turns out to be different. After inserting (14.31) into (14.30) and expanding the sums, we can sort out two different types of terms: In the first type, the velocity of a particle α of component 1 (or 2) at time zero is correlated with that of the *same* particle α at time t. However, there are also contributions, which correlate the velocity of a particle α of component 1 (or 2) with that of a *distinct* particle β of the same component. This suggests to split up L_{11} (and L_{22}) into a contribution from a velocity auto-correlation function plus a contribution from velocity cross-correlations of distinct particles of the same component. We note that

these cross-correlation functions depend on the reference frame. As defined here, they depend on the barycentric frame.

To formulate this observation quantitatively, we define now a distinct-diffusion coefficient for the a–b interaction by [18, 33–36]

$$D_{ab}^{d} = \frac{1}{3} N \int_{0}^{\infty} \langle \boldsymbol{v}_{a,\alpha}(0) \cdot \boldsymbol{v}_{b,\beta} \rangle \mathrm{d}t, \tag{14.32}$$

where the superscripts α and β indicate that the velocities belong to distinct particles even if $a = b$. N is the total number of particles in the system. Note that, originally, Mills and Hertz [34], adapting an older approach by McCall and Douglass [37], have used so-called velocity cross-correlation coefficients f_{ab} related to the coefficents used here by

$$f_{ab}/x_b = D_{ab}^{d}. \tag{14.33}$$

In a binary system of components 1 and 2 the definition used here leads to four coefficients for 1–1, 2–2, 1–2 and 2–1 interactions, which by symmetry satisfy the relation

$$D_{12}^{d} = D_{21}^{d}\,. \tag{14.34}$$

This symmetry is not shown by the f_{ij}. Using (14.32), we see that one can formally split the L_{ab} into self- and distinct contributions according to [18,36]

$$L_{ab} = \begin{cases} L_{ab}^{d} & \text{for } a \neq b \\ L_{ab}^{d} + L_{ab}^{s} & \text{for } a = b \end{cases} \tag{14.35}$$

with the definitions

$$L_{ab}^{d} = \left(\frac{N}{V}\right) \frac{M_a M_b}{kT} x_a x_b D_{ab}^{d} \tag{14.36}$$

and

$$L_{aa}^{s} = \left(\frac{N}{V}\right) \frac{M_a^2}{kT} x_a D_a. \tag{14.37}$$

If these expressions are combined with (14.19), one obtains a set of equations which allows to determine the three distinct-diffusion coefficients D_{11}^{d}, D_{22}^{d} and $D_{12}^{d} = D_{21}^{d}$ from the three experimental quantities D_1, D_2 and D_{12}:

$$D_{12} = -\frac{(x_1 M_1 + x_2 M_2)^2}{M_1 M_2}\, Q D_{12}^{d}\,, \tag{14.38}$$

$$D_1 = -x_1 D_{11}^{d} - x_2 \left(\frac{M_2}{M_1}\right) D_{12}^{d}\,, \tag{14.39}$$

$$D_2 = -x_1 \left(\frac{M_2}{M_1}\right) D_{12}^{d} - x_2 D_{22}^{d}\,. \tag{14.40}$$

Finally, these equations may be combined to a single one for the mutual-diffusion coefficient

$$D_{12}Q^{-1} = x_2 D_1 + x_1 D_2 + x_1 x_2 (D_{11}^d + D_{22}^d - 2D_{12}^d), \tag{14.41}$$

but now not all coefficients on the right hand site of this equation are independent.

It may be noted that it is straightforward, albeit tedious, to extend this type of analysis to multi-component systems and to electrolyte solutions. We omit a detailed discussion of the multi-component case here, and refer to a paper of Zhou and Miller [38] for a comprehensive and mathematically compact survey of the resulting expressions.

Of greater interest in the present context is the application of the concept of distinct-diffusion coefficients (or, in Hertz's notation, velocity correlation coefficients) to transport processes in electrolyte solutions. This type of work has been initiated in 1978 by Hertz [39]. Later, the interconnection with the Onsager coefficients has been worked out in a particularly lucid way by Miller [40]. Again, the mathematical formalism is quite tedious, and it serves no purpose to give here details.

The basic procedure is to define distinct-diffusion coefficients for the pairwise interactions of cations, anions and water and to relate these to the ionic l_{ij}. Just as in the binary non-electrolyte case the l_{ij} are then separated into self- and distinct contributions. The self-contributions are experimentally available, because the self-diffusion coefficients can be measured for cations, anions and water. The l_{ij} are obtained from conductance, transference and diffusion data, as described earlier. Eventually, one ends up with six distinct-diffusion coefficients. Three coefficients, D_{ac}^d, D_{aa}^d and D_{cc}^d, reflect pairwise interionic interactions between like and dislike ions, respectively. Two further coefficients, D_{aw}^d and D_{cw}^d, characterize cation–water and anion–water interactions, thus reflecting hydration properties. Finally, there is a further coefficient D_{ww}^d characterizing water–water interactions. This type of approach is quite fascinating, because modern electrolyte theory allows to model these coefficients, not only in dilute solutions, where the famous Debye-Hückel laws apply [40, 41], but also for concentrated solutions [41].

14.7 Properties of Distinct-Diffusion Coefficients

It is seen that mutual diffusion is related to velocity cross-correlations between different particles in the same way as self-diffusion is related to velocity auto-correlations. This reflects the collective nature of the mutual diffusion process. Moreover, one can reformulate the definition of the distinct-diffusion coefficients by replacing velocities by displacements of particles. If this is done correctly, one obtains

$$D_{ab}^d = N \lim_{t\to\infty} \frac{1}{6t} \langle [\boldsymbol{r}_{a,\alpha}(t) - \boldsymbol{r}_{a,\alpha}(0)] \cdot [\boldsymbol{r}_{b,\beta}(t) - \boldsymbol{r}_{b,\beta}(0)] \rangle \tag{14.42}$$

which is the direct equivalent to the Einstein relation (14.1) for self-diffusion. This relation or the equivalent relation (14.32) form the recipe to extract information on mutual diffusion processes from molecular dynamics simulations. In fact, the recent literature has seen some attempts to study along these lines velocity cross correlations in simple model systems such as mixtures of Lennard-Jones particles. We quote for example the work of Padro and coworkers [42–44]). First attempts of such studies in adsorbate-adsorbent systems are described in Chap. 23.

Moreover, the application of basic scattering theory yields [35]

$$D_{ab}^{d} = N\pi \lim_{\kappa \to 0} \lim_{\omega \to 0} \frac{\omega^2}{\kappa^2} S_{ab}^{d}(\kappa, \omega), \tag{14.43}$$

where $S_{ab}^{d}(\kappa, \omega)$ is the so-called distinct part of the partial dynamic structure factor, which is responsible for coherent neutron scattering [6] (see also Chap. 3). Thus, the distinct-diffusion coefficient is related to the distinct part of the partial dynamic structure factor in the same way as the self-diffusion coefficient is related to the self-part, which justifies the name 'distinct-diffusion coefficient'.

What are the major features of these coefficients? Experiments show that, in contrast to self-diffusion coefficients, the distinct-diffusion coefficients can be negative. This is most obvious for the coefficient D_{12}^{d} which reflects correlations between dislike molecules. Here, the minus sign in (14.38) implies that D_{12}^{d} is negative by definition, because all other quantities in this equation are positively defined. On the other hand, it depends on the relative weight of the self- and distinct terms in (14.39) and (14.40), whether the coefficients for interactions between like molecules, D_{11}^{d} and D_{22}^{d}, are positive or negative.

Finally, it should be emphasized again that distinct-diffusion coefficients depend on the chosen reference frame, and the approach used here and in most other studies of non-electrolyte systems adopts the mass-fixed frame. However, formulations in other reference frames are now available. A comparative analysis of results formulated in different frames has been given by Mills et al. [16]. One may argue that, to some extent, the choice of the reference frame is a matter of taste. Actually, the comparison with results of statistical-mechanical calculations suggests, however, the mass-fixed frame to be the most convenient choice. With electrolyte solutions, the situation is somewhat different. While in the early work the mass-fixed frame has been in use, it seems that the description of interionic correlations is best performed in a frame with the solvent being at rest [41].

An interesting idea is, of course, to look for reformulations and combination of the coefficients, which are independent of the reference frame. In fact, Trullas and Padro [43] have introduced a set of time correlation functions based on relative mean molecular velocities that satisfy this requirement.

14.8 Information on Intermolecular Interactions Deduced from Diffusion Data

To illustrate the formalism, we first discuss diffusion in ideal systems. To sharpen the interpretation of diffusion data, it is suitable to assess the data for real systems relative to what is expected for ideal systems where specific chemical interactions are absent. This procedure corresponds clearly to that in equilibrium thermodynamics, where phenomenological laws for ideal mixtures are used for interpreting data for real mixtures.

In fact, many attempts have been made for predicting ideal diffusion behavior [1]. From these, Darken's relation has already been mentioned. This relation is usually considered to represent a simple empirical mixing rule. The formalism introduced above allows to examine under which approximations this relation evolves from rigorous theory. It immediately follows from (14.41) that in this case

$$D_{11}^d + D_{22}^d - 2D_{12}^d = 0. \tag{14.44}$$

Thus, the Darken relation implies that the cross-correlations between molecules of different type, 1–2, just compensate the cross-correlations between molecules of the same type, 1–1 and 2–2. This situation is conceptually analogous to that in equilibrium thermodynamics, where Raoult's law implies that effects of 1–2 interactions just compensate those of 1–1 and 2–2 interactions. Zhou and Miller [38] have discussed the role of some other simple relations and their extension to multi-component fluids.

To interpret diffusion in real systems we re-emphasize that the distinct-diffusion coefficients are measures for the correlation of the velocities of distinct particles. If we turn on an attractive interaction between these particles, they will tend to stick together and move in the same direction, so that their velocities are positively correlated over a long time. In the latter case one expects positive distinct-diffusion coefficients or at least values that are more positive than expected for ideal systems. In contrast, repulsive interactions may cause the distinct-diffusion coefficients to become more negative than found for ideal systems. This scheme, introduced here by intuitive arguments, is supported by some more elaborate theories, which indeed predict the distinct-diffusion coefficients to be negative for ideal systems and to become positive in the case of specific attractive interactions [19,33]. Such arguments apply to both non-electrolyte and electrolyte systems.

We postpone a discussion of electrolytes and consider first some studies of binary non-electrolyte mixtures. From the line of arguments given above one can deduce a simple prediction for direction of the deviations from Darken's relation: If molecules of the same species have more tendency to diffuse together than those of differing species, we expect $D_{11}^d + D_{22}^d > 2D_{12}^d$, leading to positive deviations from Darken's relation. The reverse is true for systems with specific interactions between differing species.

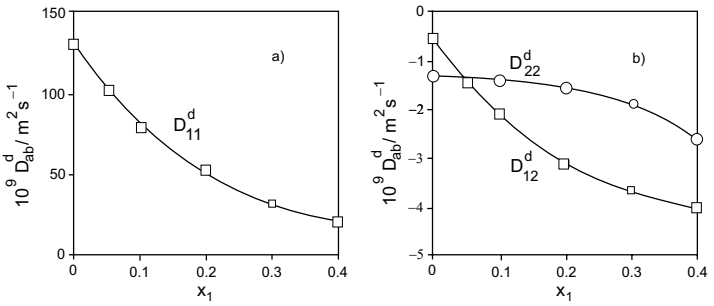

Fig. 14.6. Distinct-diffusion coefficients in the system methanol + carbon tetrachloride at 298.15 K. Methanol is component 1.

We illustrate this idea by considering in Fig. 14.6a and Fig. 14.6b some data for solutions of methanol in carbon tetrachloride [27]. D^d_{12} and D^d_{22} are negative, while D^d_{11} is large and positive. If Darken's relation is built into the system of (14.38), (14.39), and (14.40), D^d_{11} turns out to be negative. It is obviously the strong methanol-methanol self-association in this system which causes the velocities of methanol molecules to be correlated over long times. Thus, strong methanol-methanol correlations are responsible for the peculiar diffusion behavior in this system [27].

Meanwhile, a lot of similar investigations may be found in the literature, and only some selected examples can be quoted here. With regard to comparatively simple systems, mixtures of hydrocarbons [4,16,17] have been considered. Already when going to mixtures of hydrocarbons with fluorocarbons, quite complex behavior is observed, in accordance with known thermodynamic peculiarities of these mixtures [17]. Much attention has been given to aqueous solutions of hydrophobic molecules [45–47], where hydrophobic effects give rise to very subtle behavior of the distinct-diffusion coefficients. Pronounced temperature effects are notable in these systems [16]. Recently attempts have also been made to extend this sort of analysis to polymer–solvent systems [48].

Turning to electrolyte solutions, aqueous solutions of simple alkali halides or alkaline earth halides have been investigated some time ago [49], indicating the behavior of highly dissociated salts. More interesting is certainly the application to systems with strong interionic interactions. For example, there are special problems in modelling the thermodynamic and transport coefficients in solutions of some salts containing two-valent ions such as $ZnSO_4$ or Na_2SO_4, where one expects significant electrostatic ion pairing. However, little is known on the fate of these ion pairs in concentrated solutions. Comprehensive studies of transport properties and their analysis in terms of distinct-diffusion coefficients have given much insight into the details of interionic interactions in such systems, where at high salt concentrations there is

strong evidence for attractive like-ion interactions, predicted by statistical-mechanical model calculations [50, 51].

While all these studies have provided a quite coherent picture of the effect of attractive and repulsive interactions on distinct-diffusion coefficients, there is, of course, the pressing question, whether predictive theories can be developed. For electrolyte solutions this is a current problem of modern electrolyte theory, and there is indeed some obvious success in applying theories to the problems of interest [41]. With regard to non-electrolytes, molecular transport theories for systems involving strong intermolecular interactions are less well established. One promising approach has come from hydrodynamic theory. Friedman and Mills [33] showed by hydrodynamic arguments that the distinct-diffusion coefficients D_{ab}^d are proportional to an integral over the pair correlation function g_{ab} that describes the structure of the solution

$$D_{ab}^d = \frac{2kT}{3\eta} \int_0^\infty [g_{ab}(r) - 1]\, r \, \mathrm{d}r \,, \tag{14.45}$$

where η is the shear viscosity, and all other symbols have their usual meanings. This simple relation predicts already some crucial features of the experimental behavior of distinct-diffusion coefficients, namely negative contributions due to excluded volume effects at short distances and positive contributions from large peaks in $g_{ab}(r)$. Also, the factor r in the integrand tends to increase the contributions at larger separations so that correlations over comparatively large distances may affect diffusion behavior.

This type of analysis appears to be particularly apt, when noting that the well-known Kirkwood-Buff theory of equilibrium thermodynamics enables the determination of interaction coefficients

$$G_{ab} = \int_0^\infty [g_{ab}(r) - 1]\, 4\pi r^2 \, \mathrm{d}r \,, \tag{14.46}$$

denoted as Kirkwood-Buff coefficients. This integral is sufficiently similar to the integral appearing in the hydrodynamic expression (14.45) for the distinct-diffusion coefficient that one may try simple models for the distribution function $g_{ab}(r)$ to interrelate the two integrals. This type of approach, discussed in some detail by Bender and Pecora [19], seems particularly promising for predictive purposes. It allows to tune the parameters of a model distribution function $g_{ab}(r)$ to reproduce thermodynamic properties. Subsequently, these parameters are then used to predict diffusion coefficients. In fact, it was noted [18] that there is a close connection between Kirkwood-Buff integrals and distinct-diffusion coefficients even in the case of methanol-CCl_4 mixtures, where particularly strong interactions are present.

On a somewhat more empirical level, one could adopt another well-known approach from the thermodynamics of mixtures. If intermolecular interactions are strong, it is often profitable to presume in a chemical model the

formation of distinct aggregates. For example, a binary system of components A and B with strong A-B interactions is modelled as ternary mixture of A, B and the complex AB, subject to a mass action equilibrium A + B $\rightleftharpoons$ AB. By treating the ternary model system as a thermodynamically ideal system, the deviations from ideality in the real system can be accounted for by an equilibrium constant. The possibility to extend such chemical models for dealing with transport properties is evident. In fact, this is a common approach in the analysis of conductance data for systems exhibiting ion pairing. Comparatively simple approaches have been made to treat diffusion in non-electrolyte mixtures along such lines as well [1, 52], but such ideas still await a more rigorous analysis, firmly based in statistical mechanics.

14.9 Conclusion

The mutual diffusion process is strongly influenced by cooperative motions between distinct particles. Linear response theory allows to develop a formalism in which these cooperative motions are described by a set of coefficients for the various pairwise interactions in the mixture. As a result, the experimental diffusion coefficients D_{12}, D_1 and D_2 can be rewritten in terms of these interaction coefficients, denoted as distinct-diffusion coefficients. It is the specificity of the distinct-diffusion coefficients to the various interactions which makes them particularly useful for analyzing diffusion data. It is now obvious that diffusion theories on the molecular level should be formulated in terms of the distinct-diffusion coefficients. In the future, predictive equations may result from the incorporation of hydrodynamic theories into the formalism. Some promising attempts in this direction are already available from modern electrolyte theory.

Notation

a_i	activity of component i
c_i	volume concentration of component i
D	self-diffusion coefficient of pure liquid
D_i	self-diffusion coefficient of component i in a mixture
D_{12}	mutual-diffusion coefficient in the laboratory-fixed and volume-fixed reference frame
D_{12}^m	mutual-diffusion coefficient in the mass-fixed reference frame
D_{ab}^d	distinct-diffusion coefficient for a–b interaction
D_{12}^*	thermodynamic diffusion coefficient
f_{ab}	velocity cross-correlation coefficient for a–b interaction
$F_N(\boldsymbol{r}^N, \boldsymbol{p}^N)$	N-particle correlation function
H_0	classical Hamiltonian of the N-particle
H_{ext}	perturbation part of the Hamiltonian

$\boldsymbol{j}_i$	flux density of component i in the cell-fixed frame
$\boldsymbol{J}_i$	flow of component i
$\boldsymbol{J}_i^m$	flow of component i in the mass-fixed frame
L	Liouville-Operator
L_{ij}	phenomenological coefficient of the linear transport equations
m_i	mass of particle of type i
M_i	molecular mass of component i
N	total number of particles
Q	thermodynamic factor
$\boldsymbol{r}_{i,\alpha}(t)$	location of particle α of component i at time t
$S_{ij}^d(\kappa,\omega)$	distinct part of the partial dynamic structure factor
$S_{ij}^S(\kappa,\omega)$	self-part of the partial dynamic structure factor
t	time
T	temperature
$\boldsymbol{v}_{i,\alpha}(t)$	velocity of particle α of component i at time t
$\overline{V_i}$	partial molal volume of component i
x_i	mole fraction of component i
$\boldsymbol{X}_i$	thermodynamic driving force
μ_i	chemical potential for component i
μ_i^*	specific chemical potential of component i
ρ_i	partial mass density of component i

References

1. H.J.V. Tyrrell, K.R. Harris: *Diffusion in Liquids* (Butterworths, London 1984)
2. R. Haberlandt, S. Fritzsche, G. Peinel, K. Heinzinger: *Molekulardynamik. Grundlagen und Anwendungen*, (with a chapter *MC-Methods* by H.L.Vörtler) (Vieweg, Wiesbaden 1995)
3. J.F. Zielinski, B.F. Hanley: J. Amer. Inst. Eng. **45**, 1 (1999)
4. W. Marbach, H. Weingärtner, H.G. Hertz: Z. Phys. Chem. **189**, 63 (1995)
5. M. Helbaek, B. Hafskøld, D.H. Dyste, G.H. Sorland: J. Chem. Eng. Data, **41**, 598 (1996)
6. J.P. Hansen, I.R. McDonald: *Theory of Simple Liquids* (Academic Press, New York 1986)
7. A. Volmari, H. Weingärtner: J. Mol. Liq. **98/99**, 293 (2002)
8. P.A. Madden, D. Kivelson: Adv. Chem. Phys. **56**, 467 (1984)
9. H. Langer, H. Versmold: Ber. Bunsenges. Phys. Chem. **82**, 451 (1978)
10. For a pertinent review of concepts and experimental techniques of NMR self-diffusion measurements see for example: W.S. Price: Concepts Magn. Reson. **9**, 299 (1997); **19**, 197 (1998); see also Chap. 10 of this textbook.
11. H. Weingärtner. In: *Annual Rep. Prog. Chem.*, Ser. C (The Royal Society of Chemistry, Cambridge 2002)
12. H. Weingärtner, In: *Annual Rep. Prog. Chem.*, Ser. C (The Royal Society of Chemistry, Cambridge 1994)
13. P. Stilbs: Progr. NMR Spectrosc. **19**, 1 (1986)

14. L.S. Darken: Trans. Am. Inst. Min. Metal. Pet. Eng. **175**, 184 (1948)
15. G.S. Hartley, J. Crank: Trans. Faraday Soc. **45**, 801 (1949)
16. R. Mills, R. Malhotra, L.A. Woolf, D.G. Miller: J. Phys. Chem. **98**, 5565 (1994)
17. B.M. Braun, H. Weingärtner: Ber. Bunsenges. Phys. Chem. **89** 906 (1985)
18. H. Weingärtner: Ber. Bunsenges. Phys. Chem. **94**, 361 (1990)
19. T.M. Bender, R. Pecora: J. Phys. Chem. **93**, 2614 (1989)
20. *Measurement of the Transport Properties of Fluids*, IUPAC Chemical Data Series No. 37, ed by W.A. Wakeham, A. Nagashima, J.V. Sengers (Blackwell Scientific Publications, Oxford 1991)
21. D.G. Miller, J.G. Albright. In Ref. [20], p 272
22. J.A. Rard, J.G. Albright, D.G. Miller, M.E. Zeidler: J. Chem. Soc. Faraday Trans **92**, 4187 (1996)
23. L. Paduano, O. Annunziata, A.J. Pearlstein, D.G. Miller, J.G. Albright: J. Cryst. Growth **232**, 273 (2001)
24. J.N. Shaumeyer, R.W. Gammon, J.V. Sengers. In Ref. [20], p 197
25. J.M.H. Levelt Sengers, U.K. Deiters, U. Klask, P. Swiderski, G.M. Schneider: Int. J. Thermophys. **14**, 893 (1993)
26. H. Weingärtner, unpublished data
27. S. Prabhakar, H. Weingärtner: Z. Phys. Chem. Neue Folge **137**,1 (1983)
28. G.J. Dudley, H.J.V. Tyrrell: J. Chem. Soc. Faraday **1**, 69, (1973)
29. S.R. de Groot, P. Mazur: *Thermodynamics of Irreversible Processes* (North Holland, Amsterdam 196)
30. D.D. Fitts: *Non-Equilibrium Thermodynamics* (McGraw-Hill, New York 1962)
31. D.G. Miller: J. Phys. Chem. **70**, 2639 (1966)
32. W.A. Steele. In: *Transport Phenomena in Fluids*, ed by H.J.M. Hanley (Marcel Dekker, New York 1969)
33. H.L. Friedman, R. Mills: J. Solution Chem. **15**, 69 (1986)
34. R. Mills, H.G. Hertz: J. Phys. Chem. **84**, 220 (1980)
35. H. Bertagnolli, H. Weingärtner: Ber. Bunsenges. Phys. Chem. **90**, 1167 (1986)
36. H.L. Friedman, R. Mills: J. Solution Chem. **10**, 395 (1981)
37. D.W. McCall, D.C. Douglass: J. Phys. Chem. **71**, 987 (1967)
38. Y. Zhou, G.H. Miller: J. Phys. Chem. **100**, 5516 (1996)
39. G.H. Hertz: Ber. Bunsenges. Phys. Chem. **81**, 656 (1977)
40. D.G. Miller: J. Phys. Chem. **85**, 1137 (1981)
41. E.C. Zhong, H.L. Friedman: J. Phys. Chem. **92** 1685 (1988)
42. J. Trullas, J.A. Padro: J. Chem. Phys. **99**, 3983 (1993)
43. A. Verdaguer, J.A. Padro, J. Trullas: J. Mol. Liq. **85**, 23 (2000)
44. A. Verdaguer, J.A. Padro: J. Chem. Phys. **114**, 2738 (2001)
45. H.G. Hertz, H. Leiter: Z. Phys. Chem. Neue Folge **133**, 45 (1982)
46. T. Kato: J. Phys. Chem. **89**, 5750 (1985)
47. L. Constantino, G. D'Errico, O. Ortona, V. Vitagliano: J. Mol. Liq. **84**, 179 (2000)
48. A. Vergara, L. Paduano, R. Sartorio: J. Polymer Sci. B **40**, 43 (2002)
49. L.A. Woolf, K.R. Harris: J. Chem. Soc. Faraday Trans. 1 **74**, 933 (1978)
50. W.E. Price, H. Weingärtner: J. Phys. Chem. **95**, 8933 (1991)
51. H. Weingärtner, W.E. Price, A.V.J. Edge, R. Mills: J. Phys. Chem. **99**, 6289 (1993)
52. H. Schönert: Z. Phys. Chem. Neue Folge **119**, 53 (1979)

15 Diffusion Measurements in Fluids by Dynamic Light Scattering

Alfred Leipertz and Andreas P. Fröba

15.1 Introduction

Diffusion measurements in condensed matter mainly stand for the accurate determination of transport properties, e. g., of fluids. Due to different diffusion processes, these properties are the thermal diffusivity a (often also denoted D_T), the mutual diffusion coefficient D_{12}, the sound attenuation D_S and the particle diffusion coefficient D_P which is directly related to the dynamic viscosity η. Conventional measurement techniques make use of macroscopic gradients of temperature, concentration, pressure, or fluid velocity which must be large enough to give rise to a measurable effect but small enough to cause only very little perturbation in the system under investigation. This difficulty is strongly enhanced in the vicinity of critical points where induced gradients may make any reasonable measurement impossible. However, information collected in these regions is of great importance both for a fundamental understanding of critical phenomena and for setting up correlations for the individual properties of a substance.

A very successful approach to overcome these limitations is the application of light scattering techniques [1–4]. A fundamental advantage of these methods is given by the fact that these may be used in or – in some instances – close to thermodynamic equilibrium. They make use of microscopic statistical fluctuations of the local electric susceptibility χ_e which may be related to various diffusive processes and thus to the transport properties to be measured. The basic justification for this relation is Onsager's regression hypothesis [5], which states that, on a statistical average, microscopic fluctuations are governed by the very same macroscopic transport equations and which has been confirmed also by light scattering investigations.

Here, an introduction is given to dynamic light scattering (DLS) as a valuable tool for the measurement of diffusion processes. Additionally, various applications are presented, which especially are related to the determination of transport and other thermophysical properties in liquids. The subsequent Chap. 16 shall be devoted to the application of this technique to colloidal and polymeric systems. In dynamic light scattering (often also denoted as quasielastic light scattering or light beating spectroscopy) the temporal behavior of light is analysed. This chapter focuses on "classical" photon correlation spectroscopy (PCS), using correlation techniques in the

temporal analysis of scattered light, and gives additionally some information on related techniques, namely surface light scattering (SLS), where light scattered from liquid/vapour interfaces is analysed, and forced Rayleigh scattering (FRS), where an additional thermal grating is employed. It is a revised and significantly extended version of the chapter published in the first edition of this textbook [6].

15.2 Basic Principles

15.2.1 Spectrum of Scattered Light

When coherent light in form of a plane wave $\boldsymbol{E}_\mathrm{I} = \boldsymbol{E}_0 \exp[\mathrm{i}(\boldsymbol{k}_\mathrm{I}\boldsymbol{r} - \omega_\mathrm{I} t)]$ with electric field amplitude $\boldsymbol{E}_0$, wave vector $\boldsymbol{k}_\mathrm{I}$, and frequency ω_I impinges on an isotropic fluid sample with permittivity ϵ, the scattered field at a sufficiently large distance R from the scattering volume V with electric susceptibility fluctuations $\Delta\chi_\mathrm{e}$ is found to be (for details, see, e.g., Chap. 16 and [7,8])

$$\begin{aligned}\boldsymbol{E}_\mathrm{S}(\boldsymbol{R},t) = \boldsymbol{k}_\mathrm{S} \times (\boldsymbol{k}_\mathrm{S} \times \boldsymbol{E}_0)\left(\frac{\epsilon}{\epsilon_0}\right) \frac{\exp\left[\mathrm{i}(k_\mathrm{S}R - \omega_\mathrm{I} t)\right]}{4\pi R} \\ \times \int_V \Delta\chi_\mathrm{e}(\boldsymbol{r}',t) \exp\left[\mathrm{i}(\boldsymbol{k}_\mathrm{I} - \boldsymbol{k}_\mathrm{S})\boldsymbol{r}\,'\right] \mathrm{d}\boldsymbol{r}'.\end{aligned} \tag{15.1}$$

Here, ϵ_0 denotes the permittivity in vacuo, and $\boldsymbol{k}_\mathrm{S}$ the wave vector of the scattered light. By the difference between the wave vector of the incident light and that one of the scattered light the scattering vector $\boldsymbol{q} = \boldsymbol{k}_\mathrm{I} - \boldsymbol{k}_\mathrm{S}$ is defined. For a quasielastic scattering process, i. e. for $k_\mathrm{I} \cong k_\mathrm{S}$, the modulus of the scattering vector directly follows from the geometry, see Fig. 15.1,

$$q = |\boldsymbol{k}_\mathrm{I} - \boldsymbol{k}_\mathrm{S}| \cong 2k_\mathrm{I} \sin(\Theta_\mathrm{S}/2) = \frac{4\pi n}{\lambda_0} \sin\Theta_\mathrm{S}/2, \tag{15.2}$$

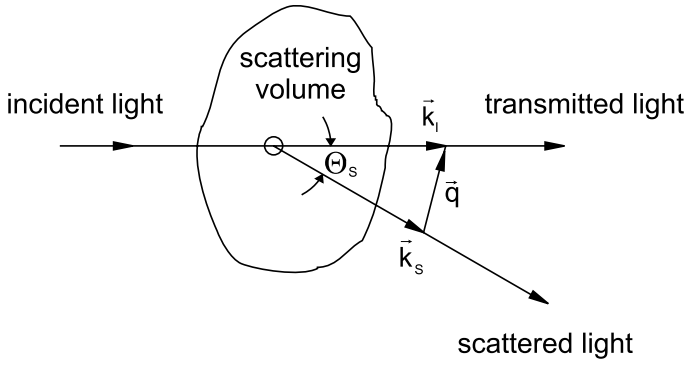

Fig. 15.1. Scattering geometry.

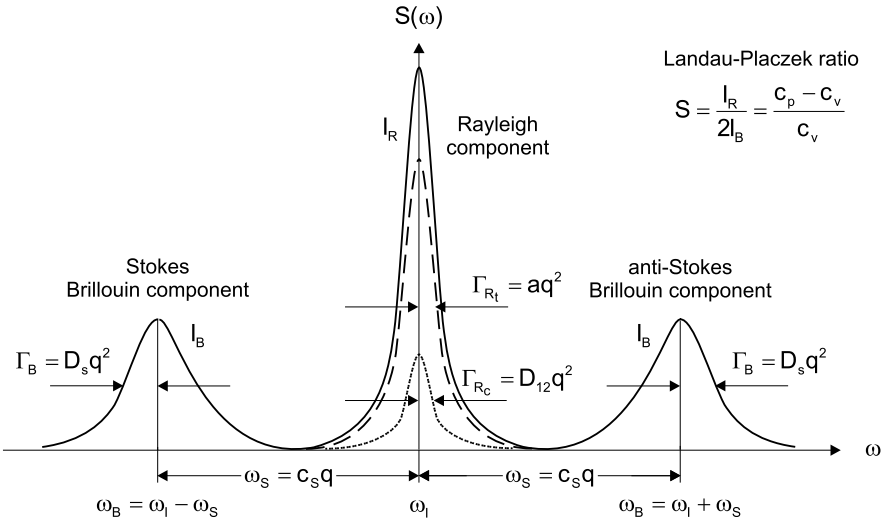

Fig. 15.2. Schematic representation of the spectrum of scattered light for a binary fluid mixture.

where n is the refractive index of the fluid, λ_0 is the wavelength of the light in vacuo, and Θ_S is the scattering angle.

It is the key feature of the DLS technique to analyse the fluctuations in the electric susceptibility $\Delta\chi_e$. In a fluid in macroscopic thermodynamic equilibrium, the local statistical fluctuations in the electric susceptibility are caused by microscopic fluctuations of temperature (or entropy), of pressure, and of species concentration in mixtures. The relaxations of these statistical fluctuations follow the same rules which are valid for the relaxation of macroscopic systems. Thus, the decay of temperature fluctuations is governed by the thermal diffusivity a. Pressure fluctuations in fluids are moving with sound speed c_S and their decay is governed by the sound attenuation D_S. In a binary fluid mixture the decay of concentration fluctuations is governed by the mutual diffusion coefficient. Altogether, these fluctuations result in a characteristic spectrum of the scattered light [7] which is shown schematically in Fig. 15.2.

The temperature and/or concentration fluctuations contribute to the central or frequency-unshifted Rayleigh component of the spectrum of the scattered light. The pressure fluctuations cause the Brillouin lines which are shifted by ω_S relative to the frequency ω_I of the incident light. The widths of these three lines, which in good approximation all exhibit a Lorentzian form, yield information on the relaxation of the fluctuations in the fluid and thus on the transport properties. In particular, the widths of the Brillouin lines are governed by the attenuation of sound D_S, the width of the Rayleigh line is determined by the thermal diffusivity a, and, in case of a binary fluid mixture, also by the mutual diffusion coefficient D_{12}. Additionally, the fre-

quency spacing ω_S between the Rayleigh and Brillouin lines is proportional to the speed of sound c_S, and the ratio of the intensities of the Rayleigh and the Brillouin lines results in the Landau-Placzek ratio $S = I_R/(2I_B)$, which contains information on the specific heats, c_p and c_v, at constant pressure and constant volume, respectively. When adding spherical particles to the fluid, the width of the Rayleigh line is governed by the particle diffusion coefficient D_P, which is related to the particle diameter and the dynamic viscosity. Thus, several different thermophysical properties of interest can be determined nearly simultaneously by analysing the spectrum of the scattered light.

15.2.2 Correlation Technique

The use of classical interference spectroscopy (Fabry-Perot spectroscopy) seems to be the straightforward way to analyse the Rayleigh-Brillouin triplet. This filtering scheme is, however, only possible under special conditions, for instance in the transition region from the kinetic to the hydrodynamic regime where the Rayleigh line is relatively broad [9, 10]. Usually, the width of the Rayleigh lines of order MHz or below for most cases of practical interest is such small that it is far beyond the resolving power of Fabry-Perot interferometers. This is the reason for analysing the spectrum of the scattered light in a post-detection filtering scheme where the total intensity is first detected and the detector signal is later filtered and processed. In this type of detection one measures optionally the second-order power spectrum of the scattered light or, as is described in some detail in the following, the time-dependent intensity correlation function which also is named second-order correlation function

$$G^{(2)}(\tau) \equiv \langle I(0)I(\tau)\rangle = \lim_{T\to\infty} \frac{1}{2T} \int_{-T}^{T} I(t)I(t+\tau)\mathrm{d}t\,. \tag{15.3}$$

The brackets indicate the time average of the product $I(t)I(t+\tau)$. The spectral range has an upper limit of about 20 MHz corresponding to the time resolution of the correlator instrument.

In general, the time correlation function gives information on the degree to which two dynamical properties are correlated over a considered period of time. In the following we first discuss some of the basic properties of these functions which are relevant to our understanding of light-scattering spectroscopy. The time-dependence of the intensity $I(t)$ will generally resemble a noise pattern. The noise signal in Fig. 15.3 shows that the intensity at the two times t and $t+\tau$ can in general have different values. However, when τ is very small compared to the period of the fluctuations in the intensity, $I(t+\tau)$ will be very close to $I(t)$ and thus both values are correlated. If τ increases, $I(t+\tau)$ and $I(t)$ become more and more different. The correlation between both values is lost if τ becomes large compared to times typifying the fluctuations in the intensity. A measure of this correlation is the

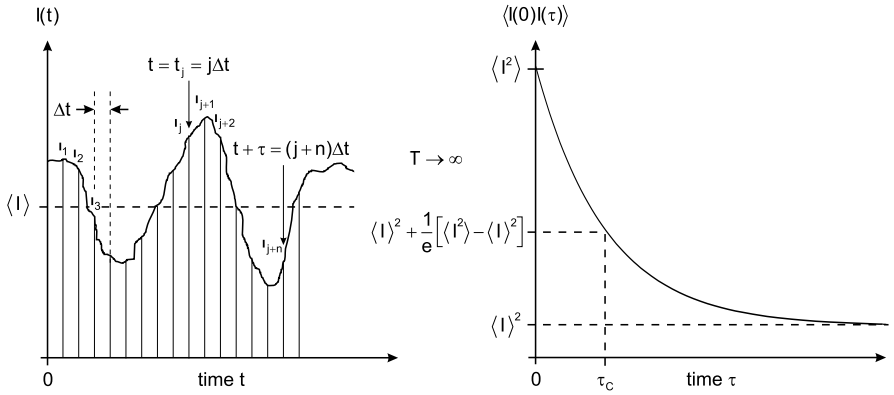

Fig. 15.3. Time-dependence of the intensity $I(t)$ (left) and its time-correlation function $\langle I(0)I(\tau)\rangle$ (right).

correlation function or strictly speaking the *auto*correlation function (ACF), which is defined by (15.3). Here, it is assumed that the infinite time average ($T \to \infty$) of the intensity is independent of its starting value. Such a property is called a stationary property. In the case of non-periodic fluctuations of a stationary property the correlation function starts from its initial value $\langle I^2\rangle = \langle I(0)I(0)\rangle$ which is a maximum and decays to $\langle I\rangle^2 = \langle I(0)\rangle\langle I(\tau)\rangle$ as $I(t+\tau)$ and $I(t)$ become statistically independent for long times $\tau \to \infty$. The exact form of the correlation function depends on the underlying scattering process and on the experimental conditions which is discussed in more detail later in this chapter. In many applications the correlation function decays like a single exponential. Here the decay time τ_C is the time for which the time-dependent part of the correlation function has decayed to the fraction $1/e$ of its initial value. The decay time τ_C reflects the mean decay behavior or life-time of the fluctuations of a particular property. This is characteristic for the decorrelation of signals.

In a realistic experimental situation, besides the light scattered from the fluctuations in a sample, also contributions from stray light, e.g., from dust on the cell windows or from the cell windows themselves, may occur. Therefore, for a general description, we consider a local oscillator field coherent with the incident electric field. In terms of the total electric field $E(t) = E_S(t)+E_{LO}(t)$, which represents a superposition of the scattered electric field $E_S(t)$ with the local oscillator field $E_{LO}(t)$, the intensity or, more precisely, the radiative flux

$$I(t) = \frac{c\epsilon}{2} E^*(t)E(t), \tag{15.4}$$

measured by a detector, is given by

$$I(t) = \frac{c\epsilon}{2}\left|E_{\mathrm{S}}(t)+E_{\mathrm{LO}}(t)\right|^2 = I_{\mathrm{S}}(t)+I_{\mathrm{LO}}(t)+\frac{c\epsilon}{2}\left[E_{\mathrm{S}}^*(t)E_{\mathrm{LO}}(t)+E_{\mathrm{LO}}^*(t)E_{\mathrm{S}}(t)\right], \tag{15.5}$$

where the asterisk denotes the complex conjugate variable, c the speed of light, and ϵ the permittivity of the medium. In the following the time dependence of the electric field of the incident light at a fixed space point will be considered more precisely by $E_{\mathrm{I}}(t) = E_0 \exp\left[-\mathrm{i}\omega_{\mathrm{I}} t + \mathrm{i}\Psi(t)\right]$, where $\Psi(t)$ is a slowly varying random function representing fluctuations in the phase of the incident light. The characteristic time behavior of the fluctuations in the phase is determined by the inverse linewidth of the incident light. Furthermore, the scattered electric field can be written in the form $E_{\mathrm{S}}(t) = f(t)E_{\mathrm{I}}(t)$, where $f(t)$ is a stochastic complex quantity being proportional to the fluctuations in the electric susceptibility

$$f(t) \propto \Delta\chi_{\mathrm{eq}}(t) = \left(\frac{\partial\chi_{\mathrm{e}}}{\partial H}\right)\Delta H_q(t), \tag{15.6}$$

with $\Delta\chi_{\mathrm{eq}}(t)$ and $\Delta H_q(t)$ being the Fourier amplitudes of $\Delta\chi_{\mathrm{e}}(\boldsymbol{r},t)$ and $\Delta H(\boldsymbol{r},t)$ of a fluctuation with wave vector $\boldsymbol{q}$, respectively [11]. Here, H may be identified with the temperature (or entropy), pressure, and species concentration in fluid mixtures. For a general description also the electric field of a local oscillator will be considered in terms of the incident field by $E_{\mathrm{LO}}(t) = f_{\mathrm{LO}}E_{\mathrm{I}}(t)$ with a constant strength f_{LO}. In calculating (15.3) one obtains from the product $I(t)I(t+\tau)$ sixteen terms, whereby as a result of taking the time average only the six terms

$$\begin{aligned} &I_{\mathrm{S}}(t)I_{\mathrm{S}}(t+\tau) + I_{\mathrm{LO}}(t)I_{\mathrm{LO}}(t+\tau) + I_{\mathrm{S}}(t)I_{\mathrm{LO}}(t+\tau) + I_{\mathrm{LO}}(t)I_{\mathrm{S}}(t+\tau) \\ &\qquad + \frac{c^2\epsilon^2}{4}\left[E_{\mathrm{S}}^*(t)E_{\mathrm{LO}}(t)E_{\mathrm{LO}}^*(t+\tau)E_{\mathrm{S}}(t+\tau) + c.c.\right] \end{aligned} \tag{15.7}$$

show a non-vanishing contribution to the intensity correlation function. The abbreviation *c.c.* stands for complex conjugate. In taking the time average of (15.7) the first term $I_{\mathrm{S}}(t)I_{\mathrm{S}}(t+\tau)$ corresponds to the intensity correlation function of the scattered light,

$$G_{\mathrm{S}}^{(2)}(\tau) = \langle I_{\mathrm{S}}(0)I_{\mathrm{S}}(\tau)\rangle = \frac{c^2\epsilon^2}{4}\langle E_{\mathrm{S}}^*(0)E_{\mathrm{S}}(0)E_{\mathrm{S}}^*(\tau)E_{\mathrm{S}}(\tau)\rangle, \tag{15.8}$$

where a local oscillator is absent. For a Gaussian field, which is characterized in a way that at a point of observation many individual components add to the electric field and that the phase functions of these contributions are equally distributed and mutually independent, the Siegert relation [8]

$$G_{\mathrm{S}}^{(2)}(\tau) = \frac{c^2\epsilon^2}{4}\left[\left|G_{\mathrm{S}}^{(1)}(0)\right|^2 + \left|G_{\mathrm{S}}^{(1)}(\tau)\right|^2\right], \tag{15.9}$$

holds, which connects $G_{\mathrm{S}}^{(2)}(\tau)$ with the field correlation function (first-order correlation function)

$$G_{\mathrm{S}}^{(1)}(\tau) \equiv \langle E_{\mathrm{S}}^{*}(0) E_{\mathrm{S}}(\tau)\rangle = \lim_{T\to\infty} \frac{1}{2T} \int_{-T}^{T} E_{\mathrm{S}}^{*}(t) E_{\mathrm{S}}(t+\tau)\mathrm{d}t\,. \tag{15.10}$$

The optical or first-order power spectrum $S_E(\omega)$ accessible by classical interference spectroscopy is, according to the Wiener-Khintchine theorem, directly connected with $G_{\mathrm{S}}^{(1)}(\tau)$ by a Fourier transform

$$S_E(\omega) = \frac{1}{2\pi} \int_{-\infty}^{+\infty} G_{\mathrm{S}}^{(1)}(\tau) \exp\left(\mathrm{i}\omega\tau\right)\mathrm{d}\tau\,. \tag{15.11}$$

Substituting the above stated expressions for the electric field of the incident and scattered light $E_{\mathrm{I}}(t)$ and $E_{\mathrm{S}}(t)$, respectively, into (15.10) one obtains for the first-order correlation function

$$G_{\mathrm{S}}^{(1)}(\tau) = |E_0|^2 \langle \exp\left[-\mathrm{i}\Psi(0) + i\Psi(\tau)\right]\rangle \langle f^{*}(0) f(\tau)\rangle \exp\left(-\mathrm{i}\omega_{\mathrm{I}}\tau\right), \tag{15.12}$$

where the correlation functions of $f(t)$ and $\exp\left[\mathrm{i}\Psi(\tau)\right]$ are separated since the laser source and the medium can be considered statistically independent of each other. As can be seen from (15.12), the optical power spectrum, which is the Fourier transform of $G_{\mathrm{S}}^{(1)}(\tau)$, see (15.11), is in part determined by the phase fluctuations of the incident light. Thus, a further limiting factor of classical interference spectroscopy is obvious. If the spectral width of the incident light is larger than the width of the spectrum governed by the microscopic fluctuations in the electric susceptibility, the field correlation function of the scattered light and hence the optical power spectrum is dominated by the phase fluctuations of the incident light. In contrast, the phase fluctuations of the incident light cancel out in the second order power spectrum or in the corresponding intensity correlation function of the scattered light

$$G_{\mathrm{S}}^{(2)}(\tau) = I_{\mathrm{S}}^2 + I_{\mathrm{S}}^2 |\langle f^{*}(0) f(\tau)\rangle|^2 \langle f^{*}(0) f(0)\rangle^{-2}, \tag{15.13}$$

which is obtained by substituting (15.12) into the Siegert relation (15.9). In deriving (15.13) it has been assumed that only one individual component dominates the spectrum of the scattered light. This is equivalent to say that only fluctuations in one property H of the medium cause fluctuations in its electric susceptibility. In (15.13) I_{S} denotes the time average of the scattering intensity

$$I_{\mathrm{S}} = \frac{c\epsilon}{2} |E_0|^2 \langle f^{*}(0) f(0)\rangle, \tag{15.14}$$

originated by the fluctuations in the quantity H. With the help of (15.13) and (15.14) and taking into account that there is no interaction between the intensity of the local oscillator and the intensity of the scattered light, one obtains by taking the time average of (15.7) for the intensity correlation function in the presence of a local oscillator field

$$G^{(2)}(\tau) = (I_\mathrm{S} + I_\mathrm{LO})^2 + I_\mathrm{S}^2 |\langle f^*(0) f(\tau)\rangle|^2 \langle f^*(0) f(0)\rangle^{-2} + 2 I_\mathrm{S} I_\mathrm{LO} \langle f^*(0) f(\tau)\rangle \langle f^*(0) f(0)\rangle^{-1}, \tag{15.15}$$

where the time average of the intensity of the local oscillator is given by

$$I_\mathrm{LO} = \frac{c\epsilon}{2} f_\mathrm{LO}^2 |E_0|^2. \tag{15.16}$$

Since the stochastic function $f(t)$ is proportional to the fluctuations $\Delta H_q(t)$, see (15.5), with the help of their normalized time correlation function,

$$g_q(\tau) = \langle \Delta H_q^*(0) \Delta H_q(\tau)\rangle \langle \Delta H_q^*(0) \Delta H_q(0)\rangle^{-1}, \tag{15.17}$$

(15.15) can be rewritten by

$$G^{(2)}(\tau) = (I_\mathrm{S} + I_\mathrm{LO})^2 + I_\mathrm{S}^2 |g_q(\tau)|^2 + 2 I_\mathrm{S} I_\mathrm{LO} g_q(\tau). \tag{15.18}$$

Thus it appears that the intensity correlation function accessible in light scattering experiments gives access to the correlation function of the fluctuations. In the case of a fluid in the hydrodynamic regime where the mean free path length r_0 of the molecules is much smaller than the reciprocal value $1/q$ of the modulus of the scattering vector ($qr_0 \ll 1$) and by this Onsager regression hypothesis holds, the time correlation functions of the fluctuations in the thermophysical properties of state can be derived on the basis of classical hydrodynamics. Because the fluctuations around the equilibrium values of temperature (or entropy), pressure, and in addition of species concentration in fluid mixtures are expected to be very small, the set of the linearized equations of fluid mechanics can be used. For the hydrodynamic modes of a fluid the correlation functions $g_q(\tau)$ can be found ultimately from the linearized hydrodynamic equations by applying a Fourier-Laplace analysis [7]. As for many other non-periodic statistical processes, such as for the diffusion of particles in dispersions, also for the statistical fluctuations of temperature (or entropy) and species concentration in a fluid mixture, the normalized time correlation function decays like a single exponential,

$$g_q(\tau) = \exp\left(-\tau/\tau_\mathrm{C}\right), \tag{15.19}$$

where $\tau_\mathrm{C} = (Dq^2)^{-1}$ is called the "relaxation time" or the correlation time of the property. Here, D may be identified to be the thermal diffusivity a, the mutual diffusion coefficient D_{12} or the particle diffusion coefficient D_P, respectively. For the local pressure fluctuations at constant entropy, which can be represented, to a good approximation, by propagating sound waves, the normalized time correlation function has the form

$$g_q(\tau) = \cos(\omega_\mathrm{S}\tau) \exp\left(-\tau/\tau_\mathrm{C}\right), \tag{15.20}$$

where the correlation time $\tau_\mathrm{C} = (D_\mathrm{S} q^2)^{-1}$ is related to the sound attenuation D_S. In addition, the frequency $\omega_\mathrm{S} = c_\mathrm{S} q$, which is identical with the frequency

of the sound waves observed, gives information about the sound velocity. Actually, even the correlation function $g_q(\tau)$ of a pure fluid does not consist of a simple exponential or damped oscillation, as the fluctuations in pressure and temperature are present simultaneously. The situation complicates, when fluid mixtures or particle dispersions are considered. However, as decay times and/or signal amplitudes are vastly different in many experimental situations, the ACF in a time interval of interest may often be analysed in terms of a simple exponential. This point will be described in more detail in the following sections.

15.2.3 Homodyne and Heterodyne Techniques

As can be seen from (15.18) in the presence of a local oscillator field the correlation function consists of three terms, the constant term $(I_\mathrm{S} + I_\mathrm{LO})^2$, the term $I_\mathrm{S}^2|g_q(\tau)|^2$, which is due to the scattered light alone and is denoted as homodyne term, and the heterodyne term $2I_\mathrm{S}I_\mathrm{LO}g_q(\tau)$. In the case that the correlation function of the hydrodynamic fluctuations $g_q(\tau)$ decays like a single exponential we obtain two exponential functions with decay times being different by a factor of two added to a constant background

$$G^{(2)}(\tau) = (I_\mathrm{S} + I_\mathrm{LO})^2 + I_\mathrm{S}^2 \exp(-2\tau/\tau_\mathrm{C}) + 2I_\mathrm{S}I_\mathrm{LO} \exp(\tau/\tau_\mathrm{C}). \qquad (15.21)$$

As it is very difficult to extract reliable information from a sum of two exponentials with decay times of the same order of magnitude, the aim of the experimenter is to meet a situation where one of the exponentials clearly dominates. Either, one has to design the experiment (see Fig. 15.4) in a way that only light from the sample itself is collected by the detector, $I_\mathrm{LO} \ll I_\mathrm{S}$. In this homodyne case, which may be the easier realized the larger the scattering cross section of the fluctuations is, the normalized intensity correlation function takes the form

$$g^{(2)}(\tau) = 1 + \exp(-2\tau/\tau_\mathrm{C}). \qquad (15.22)$$

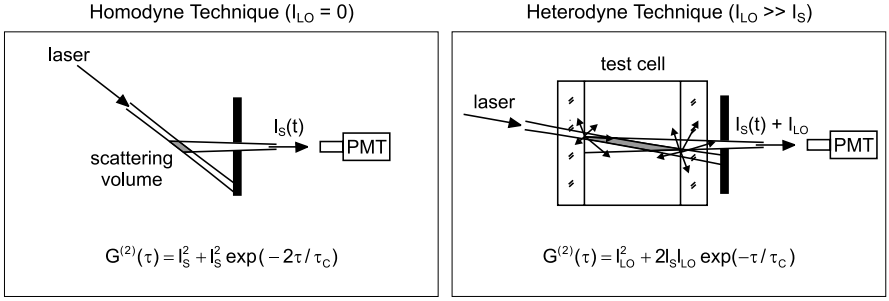

Fig. 15.4. Homodyne and heterodyne detection scheme.

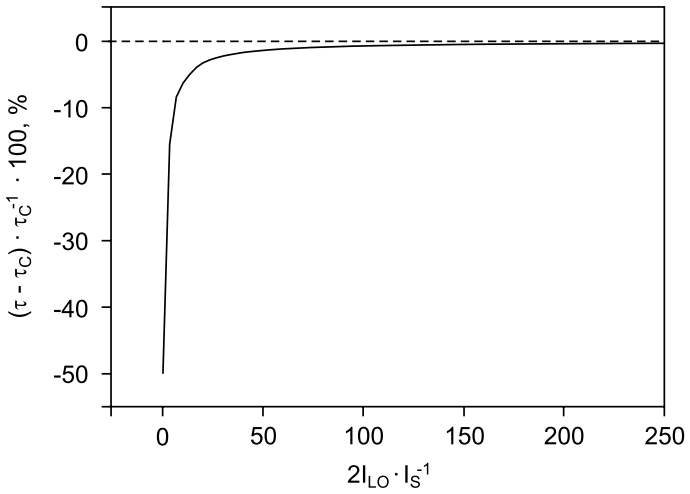

Fig. 15.5. Error in the decay time τ_C for a heterodyne experiment introduced if the ratio $2I_{LO}/I_S$ of local oscillator to scattered light signals is not chosen large enough.

Alternatively, the strict heterodyne case is achieved. This will be done, if the signal is comparatively weak, and may be accomplished by deliberately adding some part of the incident beam to the detected signal in a way that $I_{LO} \gg I_S$. Now the normalized intensity correlation function has the form

$$g^{(2)}(\tau) = 1 + \frac{2I_S}{I_{LO}} \exp(-\tau/\tau_C). \tag{15.23}$$

It is crucial, however, in either case to make sure that one contribution clearly dominates. If not, there may be a considerable error, see Fig. 15.5, as the decay time determined from a fit to a supposed single exponential may be anywhere in between the two cases. As can be seen from Fig. 15.5 it is possible to achieve high accuracy in τ_C by simply adding enough reference light I_{LO} to the signal I_S in the heterodyne technique. A similar solution is not given for the homodyne technique.

The derivation of (15.22) and (15.23), however, makes implicitly use of two idealizing assumptions, which in general do not hold. One simplification is that the scattered light is detected at a point in the far field. In practice, both the scattering volume and the area of detection are finite, which results in a deviation from an ideal coherent detection. Thus, there is an averaging effect with a reduction of the contrast $b = g^{(2)}(0) - 1$ as compared to the value for a perfect registration. The deviation of b from 1 or $2I_S/I_{LO}$ in the case of a homodyne or heterodyne detection scheme, respectively, also takes into account effects of a finite speed of signal processing. Another simplification is the assumption of a constant intensity of the incident light. Slow fluctuations in the light source result in a deviation of the baseline from the

ideal value 1 for the correlation function. Here, another adjustable parameter a is introduced in practice. Thus, a practical ACF takes the form

$$g^{(2)}(\tau) = a + b \exp(-2\tau/\tau_C). \tag{15.24}$$

or

$$g^{(2)}(\tau) = a + b \exp(-\tau/\tau_C). \tag{15.25}$$

assuming homodyne or heterodyne conditions, respectively.

The application of the heterodyne technique is advantageous for achieving high accuracy in the determination of τ_C, see Fig. 15.5, and is especially useful for the evaluation of the periodic pressure fluctuations at constant entropy, which are responsible for the Brillouin components of the spectrum. In the case of a pure fluid a usual homodyne intensity ACF exhibits terms due to both pressure and temperature (or entropy) fluctuations and an additional cross term. To analyze the pressure fluctuations in a heterodyne detection scheme, the frequency of the local oscillator is shifted relative to the frequency ω_I of the laser light by ω_M applying an acousto-optical modulator. The frequency shift ω_M is of the same order of magnitude as the frequency ω_S of the pressure fluctuations observed ($\omega_M \approx \omega_S$). By a proper choice of the intensity of the local oscillator shifted in frequency the signal governed by the periodic pressure fluctuations may be strongly enhanced as compared to that of the temperature (or entropy) fluctuations, and the correlation function takes the form of a damped oscillation

$$g^{(2)}(\tau) = a + b \cos(\Delta\omega\tau) \exp(-\tau/\tau_C). \tag{15.26}$$

Now the speed of sound c_S can be found from the knowledge of the adjusted modulator frequency ω_M and the residual detuning $\Delta\omega = |\omega_S - \omega_M|$ of the correlation function according to $c_S = \omega_S/q = (\omega_M \pm \Delta\omega)/q$. As mentioned above, the sound attenuation D_S can be determined from the correlation time $\tau_C = (D_S q^2)^{-1}$.

15.3 The Dynamic Light Scattering Experiment

15.3.1 Setup

In this section some fundamentals of the design of a light scattering apparatus are discussed. The exact choice of the individual components naturally depends strongly on the exact goal of the experiments, i. e., which property is to be measured. A possible setup is displayed schematically in Fig. 15.6. The main portion of the laser light is irradiated into a thermostated sample cell, beam splitters allow one to add some reference light for a heterodyne detection, the frequency of which may be shifted for measurements on the Brillouin lines. Part of the scattered light is imaged, in the simplest case only by means

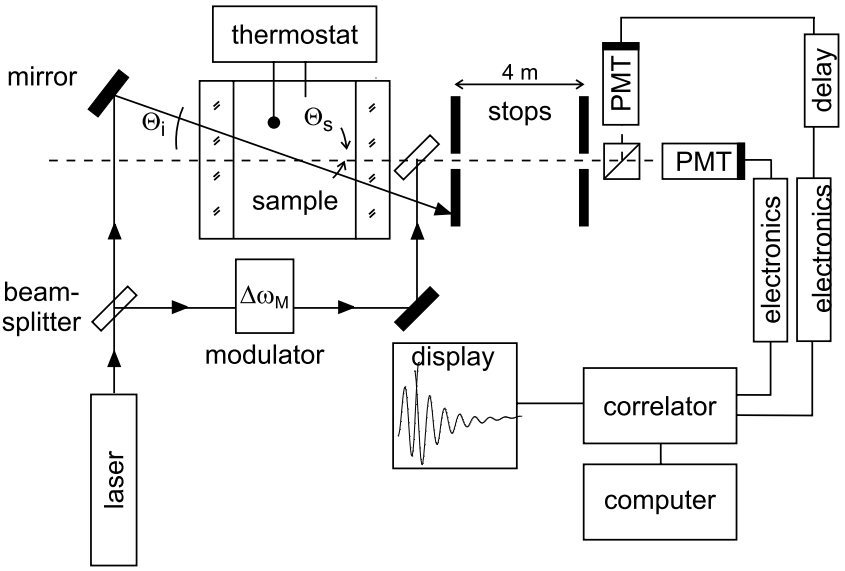

Fig. 15.6. Possible setup for a dynamic light scattering experiment.

of two circular stops, onto a detector, conventionally a photomultiplier tube. The signal is amplified, discriminated and fed into the correlator, a special purpose computer for the computation of the ACF. After this generalized scheme the individual parts shall be given some more discussion.

Laser

The choice of the suitable laser, which should be linearily polarized with orientation of the $\boldsymbol{E}$ vector perpendicular to the scattering plane for usual applications, is mainly determined by the scattering cross section of the fluctuations to be investigated. Low-power He-Ne or semiconductor lasers are in most cases sufficient for measurements of particle diffusion coefficients or phenomena close to critical points. More powerful lasers with an output of typically several hundreds of milliwatts are required for measurements, e.g., of the thermal diffusivity, where conventionally Argon lasers have been used, but where also more recent types of solid-state lasers may be employed.

Which laser may be used also depends on the detection scheme applied. In heterodyne detection the reference beam has to be added coherently on the detector. Thus, the coherence length of the laser must be large enough to ensure that the experiment is not affected by possibly different path lengths of the main and the reference part of the light. The laser should therefore only exhibit a single longitudinal mode, which may be accomplished by inserting an intra-cavity etalon into gas lasers.

Illuminating Optics

Generally, an important feature of the illuminating optical system is that the laser beam should be focused strongly [12, 13], as it can be shown that the signal-to-noise ratio may be improved by reducing the spot size of the laser. Basically, the increased irradiance is balanced by the reduced size of the scattering volume, but as it is possible to reduce the size of stops in the receiving system simultaneously, a net effect results. The major disadvantage or limitation of focusing is the lack of definition in the scattering vector, as now - in a simplified picture - light is incident from various angles, which results in an overlay of several correlation functions. This point is very critical for the measurement of the sound attenuation and will be discussed below.

The scattering vector and thus the scattering angle to be reasonably employed are mainly determined by the process to be investigated. Small scattering angles result in a small linewidth and accordingly in a comparatively long decay time. For a DLS analysis especially of the Brillouin lines it is necessary to realize a small scattering angle in order to obtain reasonable time scales in the computation of the ACF and for signal statistics. Conversely, slow diffusion processes like particle diffusion are favourably analysed with large scattering angles up to a backscattering geometry. For a survey, linewidths and decay times for various scattering angles are given in Table 15.1 for the individual processes and liquid values, which may be regarded as typical in the order of magnitude.

For the determination of the scattering vector the refractive index of the sample must be known which is in general not found tabulated for all samples, thermodynamic states, and wavelengths used. One can solve this problem by actually measuring the refractive index by using the refractions between the external medium and the sample [14, 15]. Another possibility is to make use of the approximation $\sin(\Theta_S/2) \approx (1/2)\sin\Theta_S$ and to replace, according to Snell's law, the resulting term $n \sin\Theta_S$ in the expression for the scattering vector by $\sin\Theta_i$, where Θ_i is the external angle of incidence and the refractive index of the surrounding medium is assumed to be 1 (cf. Fig. 15.7). This

Table 15.1. Typical values for linewidths and decay times in the Rayleigh-Brillouin spectrum. For the Rayleigh lines the subscripts denote thermal diffusivity (t), mutual diffusion (12) and particle diffusion (p).

θ	q/m^{-1}	Γ_B	τ_B	Γ_t	τ_t	Γ_{12}	τ_{12}	Γ_p	τ_p
2°	$5.8{\cdot}10^5$	682 kHz	1.5 μs	14 kHz	73 μs	682 Hz	1.5 ms	1.4 Hz	730 ms
5°	$1.5{\cdot}10^6$	4.3 MHz	235 ns	85 kHz	12 μs	4.3 kHz	235 μs	8.5 Hz	117 ms
20°	$5.8{\cdot}10^6$	68 MHz	15 ns	1.4 MHz	740 ns	68 kHz	15 μs	135 Hz	7.4 ms
90°	$2.4{\cdot}10^7$	1.1 GHz	0.89 ns	22 MHz	45 ns	1.1 MHz	892 ns	2.2 kHz	446 μs
180°	$3.3{\cdot}10^7$	2.2 GHz	0.45 ns	45 MHz	22 ns	2.2 MHz	446 ns	1.1 kHz	223 μs

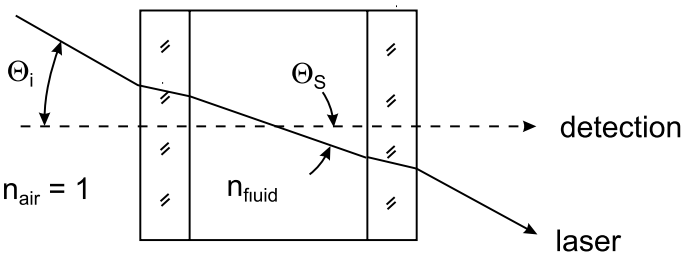

$$q = \frac{4\pi n_{fluid}}{\lambda_0} \sin(\Theta_S / 2) \cong \frac{2\pi n_{fluid}}{\lambda_0} \sin\Theta_S = \frac{2\pi}{\lambda_0} \sin(\Theta_i)$$

Fig. 15.7. Determination of the modulus of the scattering vector in the small-angle approximation.

approximation is very useful for small scattering angles [16], but naturally cannot be used for larger ones.

An exact solution, which may be used for all scattering angles, is a special symmetrical setup of the experiment [13]. Again, the a priori unknown quantities (sample refractive index and scattering angle) may be replaced by the refractive index of the surrounding medium and the angle of incidence.

Sample Cell

The range of possible sample cells is very broad due to the variety of applications, and the actual choice depends on the scattering angle and the path length within the cell to be used. For small scattering angles typically cylindrical cells are employed, where the main body may be made of metal for higher pressure applications, and optical access is provided through cylindrical entrance and exit windows. If larger scattering angles are needed, especially for the measurement of particle diffusion coefficients, glass cuvettes with circular or rectangular cross sections are normally employed, where appropriate modifications with the use of glass rings are done for measurements at higher pressures. An important feature in many DLS systems is the use of an index-matching fluid, i.e. of a liquid with a refractive index very close to that of the glass materials employed, in order to suppress unwanted reflections. A more extensive treatment of sample cell design with some specific examples may be found in [8].

Detection Optics

As DLS probes the temporal evolution of the interference pattern caused by fluctuations in a sample, it is essential to restrict the solid angle of detection in

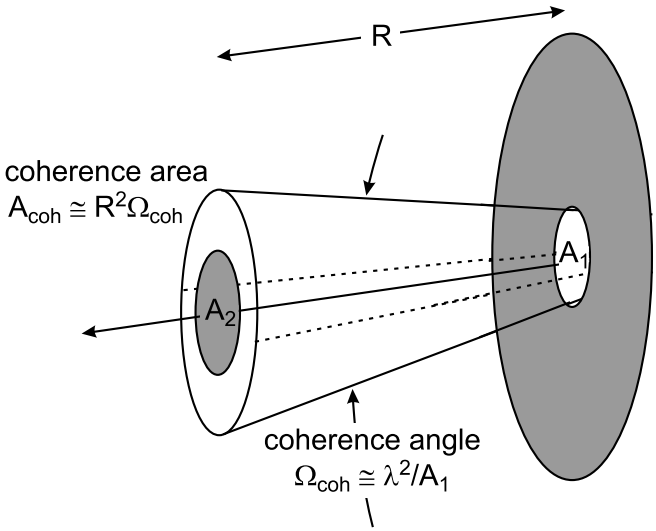

Fig. 15.8. Model for the coherence properties of the detection system; "full" spatial coherence is achieved if the detector area A_2 is smaller than the coherence area A_{coh}.

a way that the pattern of bright and dark speckles is not averaged out. Thus, the receiving system must ensure that the degree of coherence is large enough for a good modulation of the signal. In the simplest way, the choice of the solid angle of detection is realized by two circular stops at a given distance where the complex degree of coherence determining the contrast b in the correlation function (15.24) is a function of stop diameter and distance [12] (cf. Fig. 15.8). Recent approaches employ single-mode optical fibres, which make use of the fact that only one mode of field is propagated and thus enables a perfectly coherent registration [17].

Detector

The standard detector for DLS measurements is a photomultiplier tube, which is operated in a photon-counting mode, i.e. it produces a stream of pulses the frequency of which is proportional to the light flux impinging on it. A fundamental problem encountered in the detection system is that photomultipliers give rise to spurious signals, e.g., there is an afterpulsing effect, meaning that with a certain probability a detected photon may cause another subsequent pulse with no relevance for the process investigated. An elegant solution to get rid of this problem is to use a beam splitter just in front of the detector, to employ two photomultipliers (see Fig. 15.6) instead of a single one and to operate these in a cross-correlation mode [18]. This approach ensures that there is only correlation for events both detectors see simultaneously and spurious uncorrelated pulses in either photomultiplier are

not registered. This cross-correlation scheme turns out to be necessary when fast fluctuations on a time-scale of microseconds and below are investigated, but should not be employed with no actual need for it, as the signal usable is reduced by a factor of two. An alternative to photomultipliers are avalanche photo diodes, which must be operated in a special way and which exhibit a higher quantum efficiency at longer wavelengths [19].

Correlator

Correlators are special-purpose computers which calculate correlation functions in real-time. An important characteristic of correlators is the sample time $\Delta\tau$, which is the time interval used to collect the detector pulses and which determines the resolution of the correlation function. In former times, correlators were bulky stand-alone machines with typically some hundred channels with an identical sample time (single-tau structure). Today, correlators are made in form of plug-in-cards for PCs, and, what is more important, they offer a more sophisticated scheme of sample-time distributions (multiple-tau structure). A possible selection is that after a block of eight or sixteen channels with a constant sample time, $\Delta\tau$ is doubled after each subsequent block. With this quasi-logarithmic channel spacing, sample times span a range from a few nanoseconds up to many seconds so that it is possible to measure processes on a completely different time-scale simultaneously. With the evolution of standard PCs it is also possible to use a fast data-acquisition board and to compute the ACF by a normal software routine; sample-times of nanoseconds, however, are still far away from realization in this way.

15.3.2 Signal Statistics and Data Evaluation

With DLS experiments one should always be well aware that one is probing statistical fluctuations. Therefore it is necessary to average over a large number of independent events in order to be able to extract reliable information from the ACF. It is thus essential to discuss the statistical properties of correlation functions. Let us first consider the variance σ_i^2 of the correlator channel i of a homodyne ACF, where x is the lag-time of the correlator channel in units of the decay time of the intensity ACF, i.e. $x = \tau/\tau_\mathrm{C}$, f is the count rate, i.e. the number of detector pulses per second, and T is the total duration of the experiment. With these abbreviations, the variance may be approximately expressed by [20, 21]

$$\begin{aligned}\sigma_i^2 = \left(b^2/T\right)\Big\{&\tau_\mathrm{C}\left[1+\exp(-2x)(2x+1)+2b\exp(-2x)(-2x-3)\right.\\&+8b\exp(-x)]+2b^{-1}f^{-1}\left[1+\exp(-2x)+2b\exp(-x)\right]\\&\left.+b^{-2}\left[f^2\Delta\tau_i\right]^{-1}\left[1+\exp(-x)\right]\Big\}.\end{aligned}\tag{15.27}$$

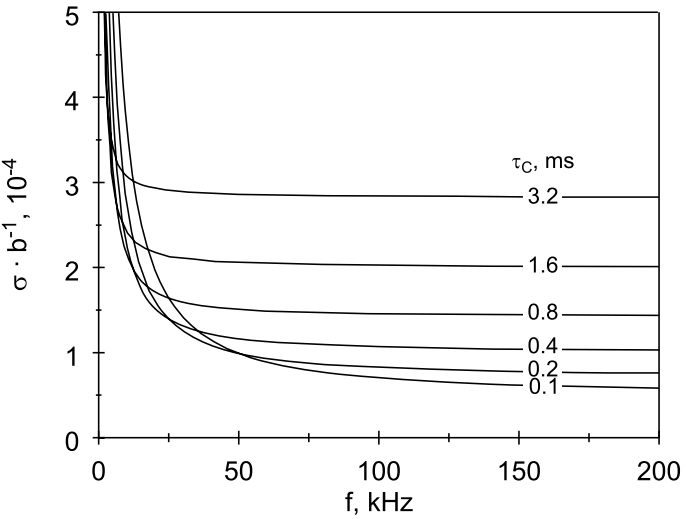

Fig. 15.9. Standard deviation of the ACF at $\tau = \tau_C$ as a function of count rate and decay time; here a correlator with a quasi-logarithmic sample time structure has been assumed.

In this relationship the various sources of noise in correlation functions may be identified. The first line reflects the statistical nature of the experiment itself; this signal noise is proportional to the ratio of decay time and measurement time and thus is reduced when averaging over a larger number of independent events. The second line is a cross term, whereas the third line reflects the imperfect detection, as photons impinging onto the detector only result in a detected pulse with a certain probability given. This detection noise dominates for small values of count rate and sample time; in this case the channel variance is inversely proportional to $\Delta\tau$. This formula has some consequences for the design of an experiment. Firstly, the scattering angle should be chosen in a way that the resulting decay time is not too small in order to ensure that during a sample time of interest there is a large number of detected pulses to keep the detection noise at a low level. On the other hand, if decay times are very large, little can be gained by increasing the count rate of the experiment, e.g., by increasing the laser power, as in this case the statistical nature of the experiment itself dominates. This saturation effect is visualized in Fig. 15.9, where the standard deviation of the channel at a lag time of one τ_C, i.e. $x = 1$, is plotted against the count rate for various values of τ_C.

A central quantity for the evaluation of correlation functions is the decay time τ_C. In order to be able to extract this quantity with high accuracy, it is desirable to ensure experimental conditions where the ACF takes the form of a simple exponential. A curve of form $y = a + b\exp(-\tau/\tau_C)$ is then fitted to the experimental ACF, which may be done using a non-linear algorithm

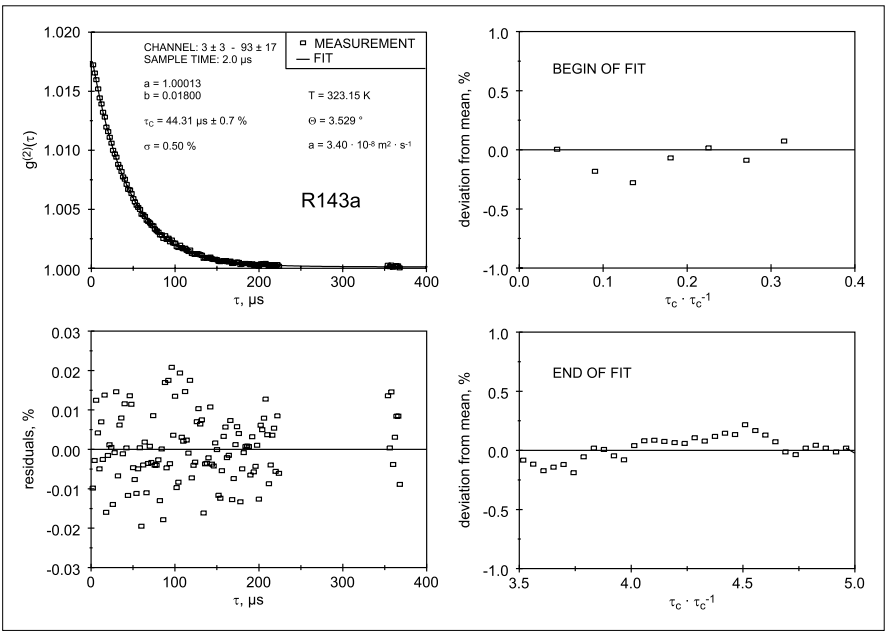

Fig. 15.10. Example for the multi-fit approach for the evaluation of correlation functions taken at the refrigerant R143a in the saturated liquid phase (insert on top left). The insert on bottom left shows the residuals of experimental data and fit, which is free of systematic deviations. The inserts on top and bottom right show the deviation of the decay times determined from the mean value, when the fit is started at different times and is performed up to different lag times, respectively.

according to Marquard and Levenberg [22] and which requires to attribute a correct statistical weight w_i to each data point according to $w_i = (1/\sigma_i)^2$. In this context it is of great importance to make sure that the correlation function actually matches the theoretical model; if this does not hold there is a clear indication that the experiment cannot be relied on. A possible way to perform this check is to transform the experimental correlation function according to $g^{(2)}(\tau) \rightarrow \ln[g^{(2)}(\tau) - 1]$ and to fit a polynom to this expression. In this method of cumulants [23] all orders higher than linear should vanish for a pure exponential and from the quadratic and the linear cofficient a quality factor may be built up to quantify deviations. However, there are two major problems connected with this approach. Firstly, it relies on a value of exactly one for the baseline; even small deviations, which may not affect the measurement in the time interval of interest, may result in erroneously bad values for the quality factor. Secondly, the transformation is basically restricted to positive values of $g^{(2)}(\tau) - 1$; with experimental noise given, the cumulant expansion is restricted to a limited interval of lag times.

A different approach, which overcomes these problems, is to fit an exponential to various lag time intervals [21]. The experimental ACF is only regarded to match the theoretical form if the decay times obtained for these different intervals agree within a certain value given. Moreover, the standard deviation of the single fit may be regarded as a measure of quality, which takes into account both the statistical quality of the experimental data and possible systematic deviations. An example for this procedure is given in Fig. 15.10.

Another important question is that for the time interval that should be employed for the fit. If too many channels at large lag-times are omitted, there will be a significant loss of information; if the fit is extended too much into the background, noisy data without relevance are included. For the multi-fit procedure it has turned out to be advantageous if a span of about $2-6$ decay times is regarded in the evaluation. This ensures that all relevant information is included and that possible deviations from a single exponential can be detected reliably.

15.4 Thermophysical Properties of Fluids Measured by Dynamic Light Scattering

15.4.1 Thermal Diffusivity

The thermal diffusivity a is that transport property for which the development of the DLS technique is probably most advanced and where measurements can be carried out routinely over a wide range of temperature and pressure for the liquid phase and, due to the lower signal levels, in an extended vicinity of the critical point for the vapour phase [24–30]. What makes the measurement of the thermal diffusivity particularly interesting is the fact that it is hardly possible by any other technique than light scattering to measure this property directly with comparable accuracy. Other methods access the thermal conductivity $\lambda = a\rho c_p$, which is related to the thermal diffusivity a by the density ρ and the isobaric heat capacity c_p.

With the exception of measurements in the vicinity of the critical point, normally a heterodyne detection scheme is employed so that the correlation function takes the simple form of (15.25). As the measurement of the thermal diffusivity is performed at low scattering angles of about 2.5° to 5° an accurate measurement of the angle of incidence is of major importance, which may be performed by an autocollimation procedure. The main measuring device is a rotation table, which is placed above the sample cell. With a mirror mounted on this table the laser beam can be reflected into the direction of the source of the laser beam. First the optical axis of observation is defined by aligning the laser beam through the stops, and the angle value is measured by autocollimation. Next the laser beam is adjusted to the angle of incidence desired, and after another autocollimation the angle of incidence

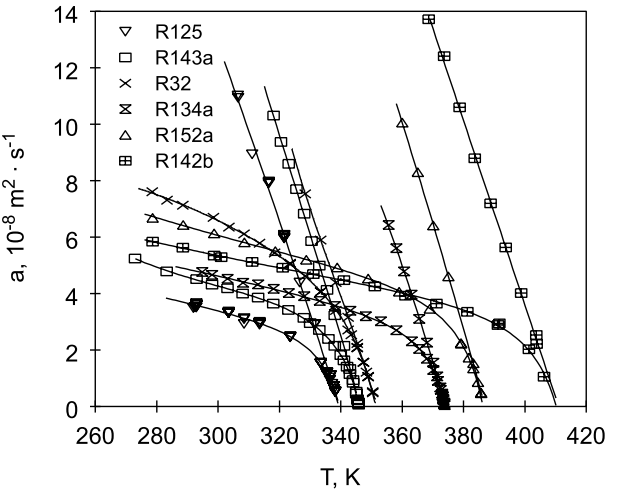

Fig. 15.11. Thermal diffusivity of selected refrigerants on the saturation line [29, 30]; lower trace symbols: liquid; upper trace symbols: vapour.

can be obtained from the difference of the readings on the rotation table. With an uncertainty in the angle measurement of order 0.01° an uncertainty in the thermal diffusivity of about 0.5% to 1% results.

The other major source of error is the determination of the decay time. If the correlation function is free from systematical errors the uncertainty in the determination of τ_C is given by the signal and the experimental duration. Depending on the equipment used, the scattering cross section of the fluctuations investigated and the time available for an experimental run, the uncertainty for a single measurement is of order $1 - 3\%$. If several independent experimental runs are performed, which is superior to running a single experiment over a longer time, this value may of course be improved. Finally, the uncertainty also depends on the definition of the thermodynamic state, especially on the exact measurement of the sample temperature. In conclusion, a total single-measurement uncertainty of 2.5%, as it was derived for measurements on liquid toluene [27], may be regarded as typical.

There have been many applications on the determination of a for a wide range of fluids. DLS has especially contributed to an improvement in the data situation for refrigerants. An example is given in Fig. 15.11, where measurements on new refrigerants with less environmental impact are shown.

Whereas the measurement of a in pure fluids is basically a straightforward task, this is clearly more difficult in fluid mixtures. Even in the simplest case of a binary fluid mixture and neglecting the Brillouin component, the ACF takes the form

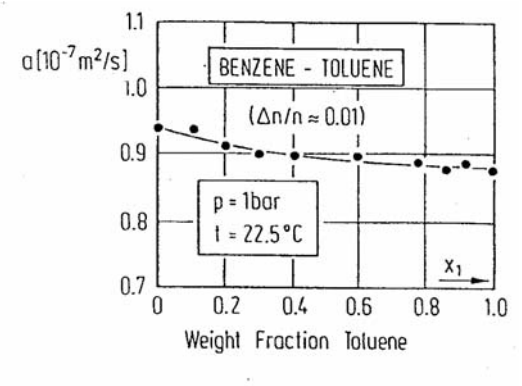

Fig. 15.12. Thermal diffusivity of a mixture of benzene and toluene [31].

$$G^{(2)}(\tau) = \underbrace{(I_{\mathrm{LO}} + I_t + I_c)^2}_{\text{background}} + \underbrace{2I_{\mathrm{LO}} I_t \exp(-\tau/\tau_{C,t}) + 2I_{\mathrm{LO}} I_c \exp(-\tau/\tau_{C,c})}_{\text{heterodyne term}}$$
$$+ \underbrace{I_t^2 \exp(-2\tau/\tau_{C,t}) + I_c^2 \exp(-2\tau/\tau_{C,c})}_{\text{homodyne term}} + \underbrace{2I_t I_c \exp(-\tau/\tau_{C,t} - \tau/\tau_{C,c})}_{\text{cross term}} \tag{15.28}$$

where the subscripts t and c denote the contributions from temperature and concentration fluctuations, respectively. With a large reference light contribution, $I_{\mathrm{LO}} \gg I_t$ and $I_{\mathrm{LO}} \gg I_c$, the ACF simplifies to a sum of two exponentials

$$g^{(2)}(\tau) = a + b_1 \exp(-\tau/\tau_{C,t}) + b_2 \exp(-\tau/\tau_{C,c}). \tag{15.29}$$

It is obvious that even for this simplified function the determination of the decay time $\tau_{C,t}$ is more complicated and associated with a higher degree of uncertainty than in the case of a pure fluid, because a larger number of parameters are to be fitted. The situation becomes easier if the refractive indices of the two components nearly match, as the signal from the concentration fluctuations may then be treated as a low-amplitude perturbation. A possible approach [31] is to expand the exponential decay of the concentration fluctuations in a way that an ACF of form

$$g^{(2)}(\tau) = a + b \exp(-\tau/\tau_{C,t}) + c\tau \tag{15.30}$$

results. The thermal diffusivity of a mixture of benzene and toluene measured in that way is shown in Fig. 15.12.

It is also possible to measure a in mixtures with a larger difference in refractive index. Naturally, this is connected with a loss of accuracy and comes to a limit, when the signal due to temperature fluctuations is much weaker than that by concentration fluctuations.

15.4.2 Mutual Diffusion Coefficient

The problems encountered in measuring the mutual diffusion coefficient D_{12} are of a similar nature as those of measuring the thermal diffusivity of mixtures. In either case there are basically signals from both temperature and concentration fluctuations. As the mutual diffusion coefficient is in general at least one order of magnitude smaller than the thermal diffusivity, larger angles may be chosen for the determination of this property. It is especially interesting, however, to perform the measurements with an identical setup as for a, as both properties may then be measured simultaneously. Whether one succeeds, is again governed by the actual separation of decay times and by the ratio of the signals.

As an example, the thermal diffusivity and the mutual diffusion coefficient of the binary system acetone and carbontetrachloride with a difference in the refractive indices of 7.4% are shown in Fig. 15.13, where the situation is favourable, as the signals are of the same order of magnitude [32].

In most instances, especially when the difference of refractive indices is large, the determination of the mutual diffusion coefficient may be performed by standard experiments. Fig. 15.14 shows the measured temperature dependence of the mutual diffusion coefficient of the separation system n-hexane/nitrobenzene [33]. According to the stability theory of thermodynamics, D_{12} disappears at the critical separation point (temperature T_c), which can be clearly seen from Fig. 15.14. This effect of vanishing diffusivities on approaching the critical point is generally referred to as "critical slowing down". Further details about the theory of mutual diffusion including the phenomenon of the critical slowing down may be found in Chaps. 3 14, and 16 (Fig. 16.29).

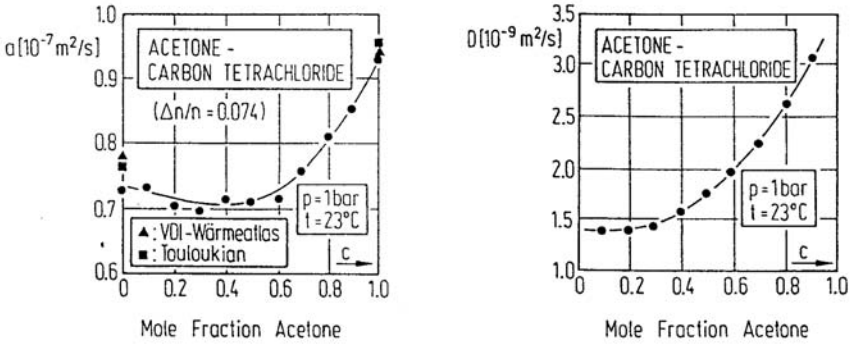

Fig. 15.13. Thermal diffusivity and mutual diffusion coefficient of the mixture acetone/carbon tetrachloride as a function of composition [32].

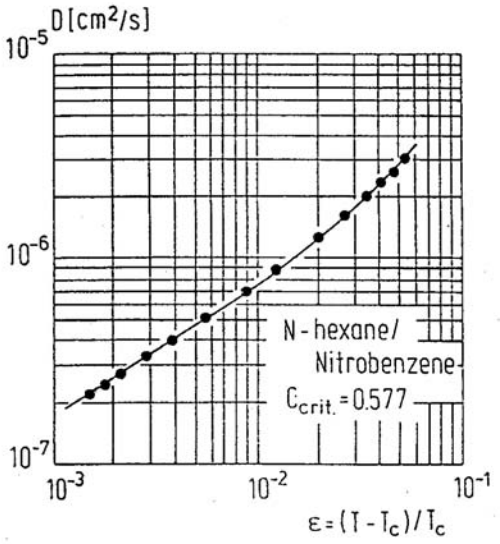

Fig. 15.14. Mutual diffusion coefficient of a separation system as a function of the reduced temperature $\epsilon = (T - T_c)/T_c$ [33].

15.4.3 Dynamic Viscosity

The determination of the dynamic viscosity η of liquids is in some way different from the measurement of the other properties treated so far, as it requires the addition of seed particles. The quantity which is actually measured is the (translational) particle diffusion coefficient D_P of spherical particles, which results in another Rayleigh peak in the spectrum. The particle diffusion coefficient is related via the Stokes-Einstein equation [34, 35]

$$D_P = \frac{k_B T}{3\pi\eta d} \tag{15.31}$$

with viscosity η, particle diameter d, Boltzmann constant k_B and temperature T. In the low-concentration range (i.e. under the assumption that there is no particle-particle interaction as implied in fact for deriving (15.31)) this diffusivity is clearly nothing else than the particle self-diffusivity (cf., e.g., Chaps. 10, 14, and 16). Two possible fields of applications are contained in this relation. One area of research is the determination of particle size distributions and, as macromolecules may be regarded as special particles, the determination of molecular weight [36, 37]. As with a distribution of particle sizes a distribution of particle diffusion coefficients results, the ACF is a superposition of exponentials with various decay times. The major problem in this field is then to recover the size distribution from the experimental ACF, which is a difficult and, with experimental noise given, sometimes impossi-

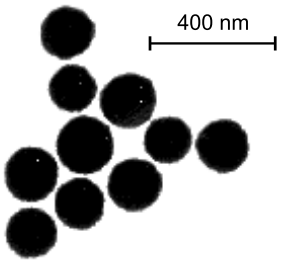

Fig. 15.15. Electron microscope picture of silica particles, courtesy: A.P. Philipse, University of Utrecht.

ble task, as different size distributions may result in very similar correlation functions. Here, the other application related with particle diffusion coefficients shall be given some more consideration, namely the determination of the dynamic viscosity [38–40].

Generally, as D_P is orders of magnitude smaller than the other diffusion coefficients in the Rayleigh-Brillouin spectrum, this quantity is normally probed at large scattering angles. Another difference is that for the determination of the viscosity the usage of low-power lasers such as He-Ne or diode lasers is sufficient in most cases, as the scattering cross section of the particles is usually much larger than that of other fluctuations in the fluid itself. Accordingly, a homodyne detection scheme is normally employed, and the measurements are not affected by other components in the spectrum.

A key to a successful determination of the viscosity is the choice of suitable particles in a size range of some 20 nm to 500 nm. These are to be spherical and monodisperse, or at least are to exhibit a narrow size distribution, in order to ensure a correlation function which matches the model of a pure exponential, which is essential for a reliable data evaluation. Moreover, they must be chemically stable and form stable dispersions. There have been a number of investigations with different seed particles, but it has turned out that silica particles with various surface modifications are most appropriate for a wide range of liquids (see Fig. 15.15). Particle sizes are best calibrated by DLS measurements in liquids with known viscosities. For high-accuracy measurements the governing conditions of the working model must be met what means in this case unhindered particle diffusion and no multiple scattering in the sample. For these reasons it is essential to use low particle volume fractions of typically 10^{-4} and to vary the particle concentration and/or scattering angle. In connection with a careful inspection of the ACF this approach ensures reliable results. An experimental result is shown in Fig. 15.16, where the viscosity of n-heptane was measured to check the technique. This liquid was chosen, because there are reliable reference data [41] both for n-heptane

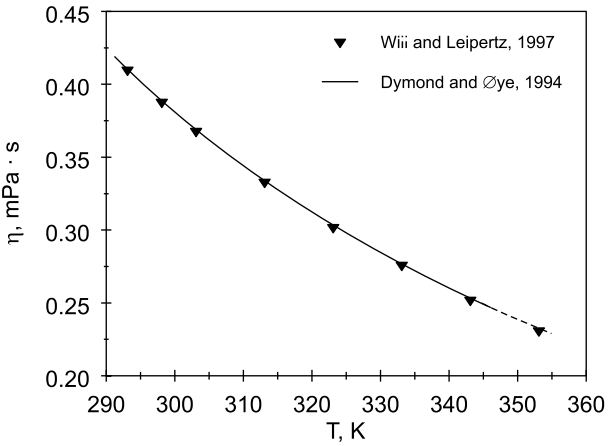

Fig. 15.16. Viscosity of liquid n-heptane [40] in comparison with reference data [41].

itself and for n-hexane and n-octane, which were used for calibrating the particle size at room temperature.

As the numerical value of the mutual diffusion coefficient is in between those of the thermal diffusivity and the particle diffusion coefficient, prospects open of a simultaneous measurement of η and D_{12}. In Fig. 15.17 a correlation function is plotted, which was measured in a paraffin oil, a mixture of many hydrocarbons of chain lengths ranging from about $15-40$ carbon atoms. Per-

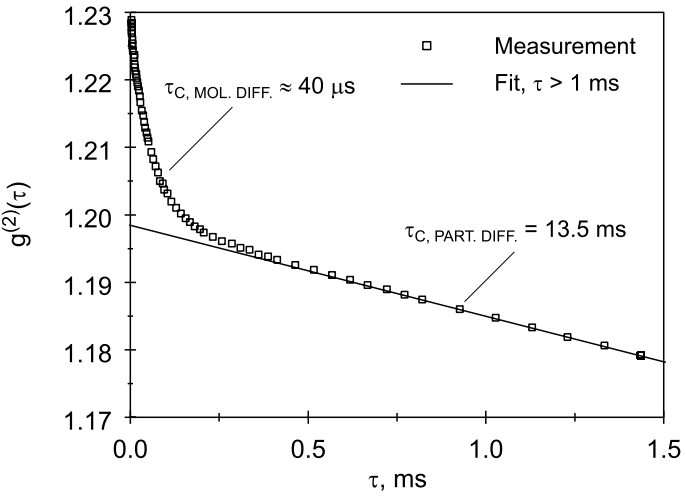

Fig. 15.17. Experimental ACF of a paraffin oil with seed particles added. The signals from particle and molecular diffusion may be clearly separated [42].

forming a fit for times larger than 1 ms the ACF can be very well represented by a single exponential with a decay time of 13.5 ms. Additionally, there is another signal at small decay times, which is due to molecular diffusion and, due to the nature of this multi-component mixture, is built up of several individual diffusion signals.

15.4.4 Sound Velocity and Sound Attenuation

For the measurement of sound velocity c_S and sound attenuation D_S the Brillouin components of the spectrum are investigated. As the Brillouin lines are shifted in frequency, a heterodyne technique with a local oscillator, which is also shifted in frequency by means of an acousto-optic modulator, is used [3]. This results in a correlation function in form of a damped oscillation, (15.26), where the sound attenuation is determined from the decay-time τ_C as usual and the sound velocity is deduced from the known frequency shift by the modulator ω_M and the residual mistuning $\Delta\omega$ of the correlogram. The simplest way of determining $\Delta\omega$ is by applying a Fourier transform to the measured correlation function, where the frequency is found from the maximum of the resulting spectrum [43]. Dynamic light scattering can be used to measure the sound velocity with an uncertainty of about 0.5%. This technique has again been often applied to various refrigerants [29, 44]. An example is depicted in Fig. 15.18.

In determining the sound attenuation one has to face two problems. One is that due to the large width of the Brillouin lines the decay-time of the

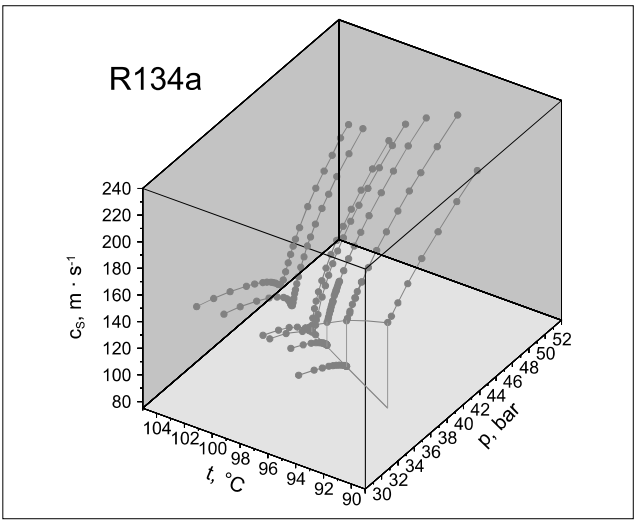

Fig. 15.18. Sound velocity of refrigerant R134a in a wide range around the critical point [46].

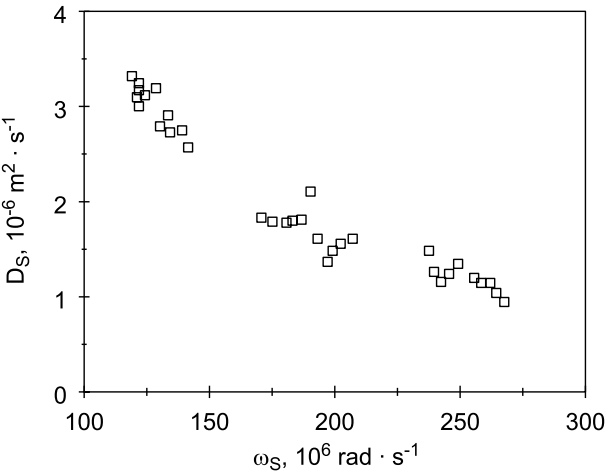

Fig. 15.19. Frequency dispersion with the measurement of sound attenuation; sample: refrigerant R125, saturated liquid at 45°C [44].

correlation function is typically only a few hundreds of nanoseconds, even if small scattering angles are employed, which requires the use of fast correlators. The other problem is of a more fundamental nature and is caused by a lack of definition of the scattering vector [3, 44]. Due to the finite width of stops in the detection optics there is always some angular spread, which is a combination of a simple geometrical and a diffraction effect. This uncertainty does not have a significant effect on probing the Rayleigh line, but causes a spread in the position of the Brillouin line. Thus, the linewidth probed in a spectroscopic experiment is a convolution of the distribution of positions and the actual linewidth. Analyzing the scattered light in the time-domain one obtains in the presence of this effect a decay time being shorter than associated with the sound attenuation. However, one has to realize experimental conditions, where the angular uncertainty is as small as possible. This may be realized by placing the stops in the detection optics as far as $4-6$ m apart from each other.

These difficulties result in a reduced accuracy of measuring D_S of about 10%, which still is better than by direct spectroscopic methods. Finally, it must be pointed out that all measurements of sound velocity and attenuation are basically dependent on the actual frequency used in the experiment. This dispersion effect has turned out to be negligible for many fluids and the frequencies probed by DLS as the sound velocity is considered, but is marked for the sound attenuation, especially of refrigerants, cf. Fig. 15.19.

15.4.5 Landau-Placzek Ratio

The Landau-Placzek ratio S is defined as the ratio of intensities of the Rayleigh to Brillouin lines and is related to the specific heats c_p and c_v by

$$S = \frac{I_\mathrm{R}}{2I_\mathrm{B}} = \frac{(c_p - c_v)}{c_v}. \tag{15.32}$$

The Landau-Placzek ratio may be obtained from the evaluation of the contrasts in various heterodyne experiments, when a local oscillator with defined intensity is added [45]. An example of such measurements is provided by Fig. 15.20.

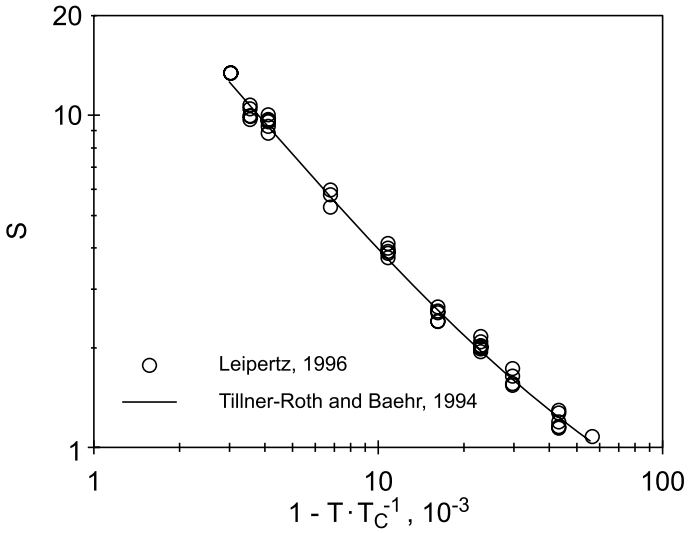

Fig. 15.20. Landau-Placzek ratio for refrigerant R134a obtained by DLS measurements [47] in comparison with reference data from the equation of state [48].

15.4.6 Soret Coefficient

When a binary liquid mixture is brought into a temperature gradient ∇T, mass diffusion occurs resulting in a concentration gradient ∇c. This Soret effect may be described by the relation

$$\nabla c = -S_T \; c(1-c) \; \nabla T, \tag{15.33}$$

where S_T is the Soret coefficient and c is the mass fraction of the heavier component. When DLS experiments are carried out in a steady temperature

gradient, the Soret coefficient may be derived from the amplitude of the concentration mode in the resulting correlation function [49]. As this amplitude is proportional to $(\nabla T)^2/q^4$ very small scattering angles of order 1° must be employed, where the scattering angle can hardly be measured exactly, but may be calibrated by a DLS measurement in a system where the diffusion coefficient is known.

15.4.7 Derivable Properties

Dynamic light scattering is a technique which allows the measurement of a large variety of thermophysical properties, in some instances even within a single experiment. Besides the data, which can be measured directly, more properties may be derived in connection of DLS data with additional information from other techniques. A few examples will be given here.

Whereas the Landau-Placzek ratio relating isobaric and isochoric specific heat capacities, (15.32), may be directly derived from DLS experiments, there is no straightforward access to either of these values. In order to obtain information on c_p, it is therefore necessary to combine data from DLS with other properties from different measurement techniques. As DLS can probe the thermal diffusivity very successfully, the combination with data for the thermal conductivity λ, which can be measured by various techniques directly, and for the fluid density ρ, which can be determined very accurately, yields information on c_p according to $c_p = \lambda/(a\rho)$. An example for this procedure including a comparison with values obtained from an equation of state is given by Fröba et al. [50]. Using c_p and S, the isochoric heat results as $c_v = c_p/(S+1)$ which immediately follows from (15.32).

The isentropic compressibility $\chi_s = 1/(\rho c_\mathrm{S}^2)$ follows directly from density ρ and the sound velocity c_S measured by DLS. Accordingly, the isentropic exponent $\kappa = \rho c_\mathrm{S}^2/p$ may be derived with the knowledge of the equation of state of the fluid. The sound attenuation D_S is related to a number of other thermophysical properties via

$$D_\mathrm{S} = \frac{(4/3)\eta_\mathrm{s} + \eta_v + (1/c_v - 1/c_p)\lambda}{2\rho}. \tag{15.34}$$

In this notation, the usual dynamic viscosity has been given an index s to emphasize that this is the shear viscosity in contrast to the bulk viscosity η_v. With a measurement of D_S and knowledge of the other quantities, which again may mostly be derived from DLS measurements, information on the bulk viscosity may be deduced, which is an important property for the description of structural relaxation and which is not readily obtainable by experiment.

15.5 Related Techniques

15.5.1 Surface Light Scattering

Surface light scattering (SLS) is a technique which is closely related to dynamic light scattering in its classical meaning. The difference is that this technique probes, as the name indicates, fluctuations on the surface of a liquid or, in a more general formulation, at phase boundaries. These fluctuations can be understood as thermally excited capillary waves of small amplitude ($\sim 1 - 100$ nm) and with a characteristic wavelength ($\sim 0.1 - 1000$ μm) and that are quantized in so-called "ripplons" [51].

In general, for the temporal decay of surface fluctuations two cases may be distinguished. In the case of large viscosity and/or small surface tension, the amplitude of surface waves is damped exponentially, while in the case of small viscosity and/or large surface tension the amplitude decays in the form of a damped oscillation. Light interacting with such a fluctuating surface structure is scattered. An exponential decay of surface waves results solely in a spectral broadening of the light spectrum, whereas an oscillatory damping gives rise to a Brillouin doublet [52]. Hence, the spectrum exhibits three characteristic lines, qualitatively similar to that from light scattered in a bulk fluid, where line widths and separation are related to the modulus q of the scattering vector, kinematic viscosity ν, surface tension σ, and density ρ as shown in Fig. 15.21 in a first order approximation. A Lorentzian shape of these lines as well as the relations for line widths and separation as indicated in Fig. 15.21 only hold in the limiting cases $y \gg 0.145$ or $y \ll 0.145$, respectively, with

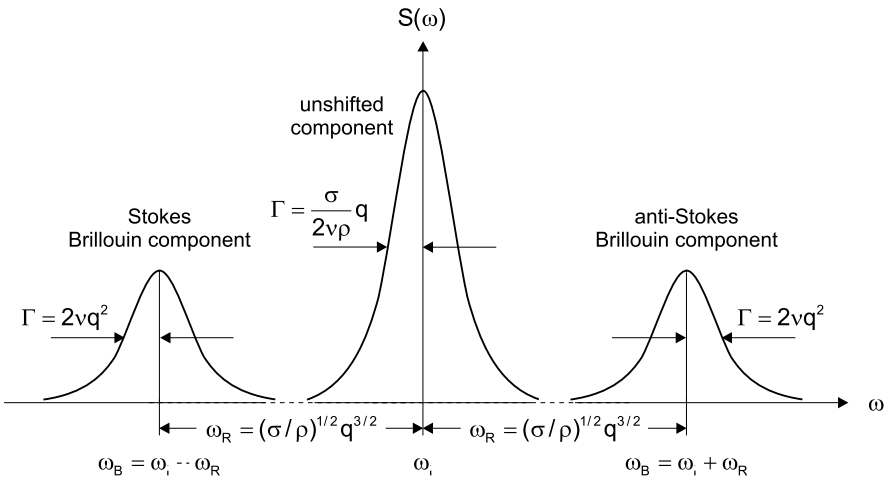

Fig. 15.21. Spectrum of scattered light by surface waves: frequency unshifted line (center) in the case of large viscosity and/or small surface tension; frequency shifted Brillouin lines in the case of small viscosity and/or large surface tension.

$y = \sigma\rho/(4\eta^2 q)$. For y values close to 0.145 the line shapes become more complex [51, 53].

In practice, also the spectrum of light scattered by the fluctuations at a liquid surface can only be resolved in a post-detection filtering scheme using, e.g., photon correlation spectroscopy (PCS). For heterodyne conditions, where the scattered light is superimposed with stronger coherent reference light, the normalized time-dependent intensity correlation function for the analysis of surface fluctuations is described by

$$g^{(2)}(\tau) = a + b\cos(\omega_{\mathrm{R}}\tau)\exp(-\tau/\tau_{\mathrm{C}}). \tag{15.35}$$

or

$$g^{(2)}(\tau) = a + b\exp(-\tau/\tau_{\mathrm{C}}). \tag{15.36}$$

assuming the decay of the amplitude of surface waves is oscillatory ($y \gg 0.145$) or overdamped ($y \ll 0.145$), respectively. Due to the usually small frequency separation of the shifted Brillouin lines commonly no frequency shift of the coherent reference light is necessary. In the propagating case of surface fluctuations the correlation function (15.35) can be used for the simultaneous evaluation of surface tension σ and kinematic viscosity ν. The correlation time τ_{C} and the frequency ω_{R}, which are identical with the mean life time of "ripplons" and the frequency of propagation, respectively, are given in first order approximation by

$$\tau_{\mathrm{C}} = \frac{1}{2\nu q^2} \qquad \omega_{\mathrm{R}} = \left(\frac{\sigma}{\rho}\right)^{1/2} q^{3/2}. \tag{15.37}$$

In the overdamped case, if the fluid viscosity is large and/or the surface tension is very small, the lifetime of "ripplons" in (15.36) is given in a first-order approximation by

$$\tau_{\mathrm{C}} = \frac{2\nu\rho}{\sigma q}. \tag{15.38}$$

For a reliable determination of viscosity and surface tension a more detailed and rigorous consideration of the surface light scattering method than given by (15.35) to (15.38) has to be applied. Here, the reader is referred to literature, see, e.g., [54].

Although it has been shown that SLS may be performed in complete analogy to DLS measurements from bulk fluids using an identical set-up [50, 55], some differing design features are often employed for SLS measurements. One obvious difference is that SLS normally investigates interfaces in horizontal orientation within a sample cell with light impinging from above. Commonly, scattered light is observed near the reflected beam [56], i.e. also in the top direction, which eases the optical access and is of course essential for non-transparent fluids. Alternatively, for transparent fluids scattered light may be observed close to the direction of the refracted beam [57, 58], which is advantageous due to stability considerations and scattering intensities. By

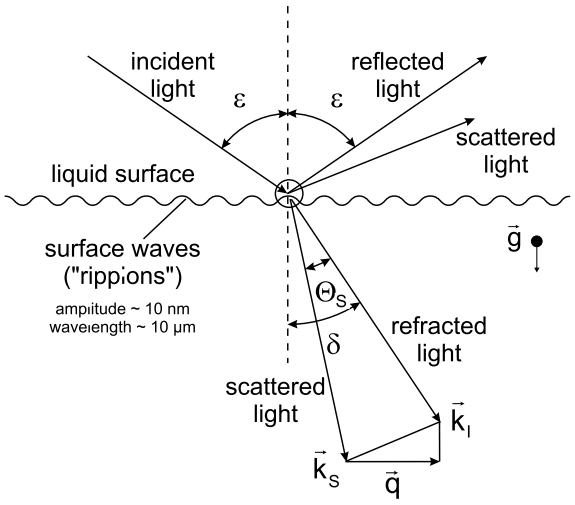

Fig. 15.22. Scattering geometry for the observation of the scattered light in transmission direction.

the choice of the angle of incidence ϵ, resulting in a specific angle δ of the refracted light, and the scattering angle Θ_S the scattering vector $\boldsymbol{q} = \boldsymbol{k}'_\mathrm{I} - \boldsymbol{k}'_\mathrm{S}$ is determined and, by this, the wave vector of the observed surface vibration mode, see Fig. 15.22. Here, $\boldsymbol{k}'_\mathrm{I}$ and $\boldsymbol{k}'_\mathrm{S}$ denote the projections of the wave vectors of the refracted ($\boldsymbol{k}_\mathrm{I}$) and scattered light ($\boldsymbol{k}_\mathrm{S}$) in the surface plane, respectively. For the observation of scattered light within the irradiation plane and assuming elastic scattering (i.e., $k_\mathrm{I} \cong k_\mathrm{S}$), the modulus of the scattering vector is obtained as

$$\begin{aligned} q = \left|\boldsymbol{k}'_\mathrm{I} - \boldsymbol{k}'_\mathrm{S}\right| &\cong 2k_\mathrm{I} \sin(\Theta_\mathrm{S}/2) \cos(\delta - \Theta_\mathrm{S}/2) \\ &= \frac{4\pi n}{\lambda_0} \sin(\Theta_\mathrm{S}/2) \cos(\delta - \Theta_\mathrm{S}/2), \end{aligned} \tag{15.39}$$

where n is the fluid refractive index and λ_0 is the laser wavelength in vacuo. The experimental set-up and the computation of the scattering vector are considerably simplified if the scattered light is observed perpendicularly to the fluid interface, i.e. in a vertical direction with $\Theta_\mathrm{S} = \delta$, where $q = (2\pi/\lambda_0) \sin \Theta_\mathrm{i}$.

SLS experiments typically use small scattering angles of about 0.1° up to a few degrees. The according range of scattering vectors reaches from an order of $10^4\,\mathrm{m}^{-1}$ to about $10^6\,\mathrm{m}^{-1}$, where large q-vectors can be achieved easier with a transmission geometry due to intensity considerations. An advantage of larger scattering vectors is that spectral broadening effects due to an uncertainty Δq in the scattering vector do not play a role in the larger q-range.

As in many applications of DLS also the variant surface light scattering makes it possible to determine two properties simultaneously, in the case of SLS this measurement is performed without any extra effort and yields, with surface tension and viscosity, two quantities whose determination by other means requires two completely different sets of experimental equipment. While commonly the kinematic viscosity ν is regarded as the property directly accessible in SLS experiments, it should be pointed out that this is only true with the simplifying neglect of gas phase properties. With a proper execution of the method and experimental care, however, no measurable differences between the values obtained by SLS and conventional methods, in part relying on bulk properties, could be found. An inaccuracy of 1% for either property can be obtained with SLS [58]. This value is at least comparable with the uncertainty of conventional methods, and, together with the unanimous advantage of a simultaneous determination of surface tension and

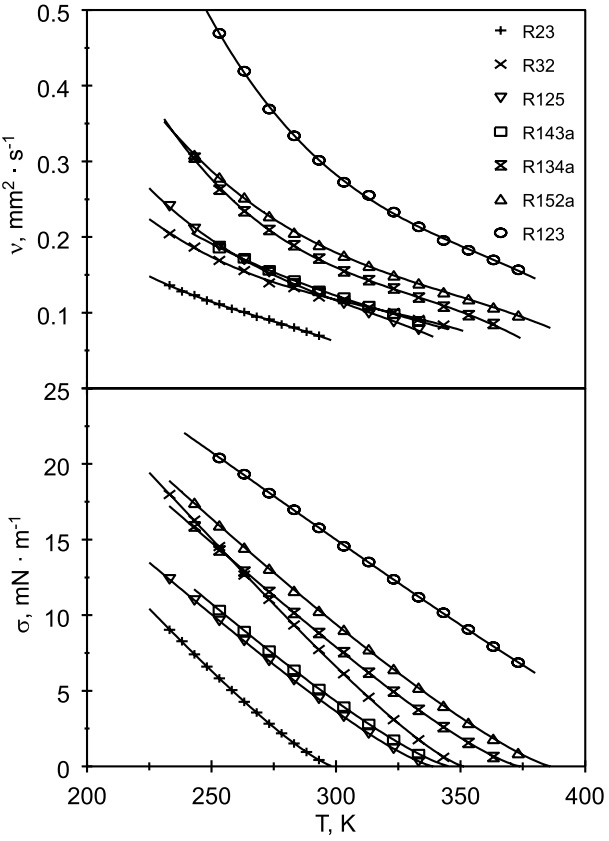

Fig. 15.23. Kinematic viscosity of the liquid phase and surface tension of alternative refrigerants under saturation conditions from SLS [59].

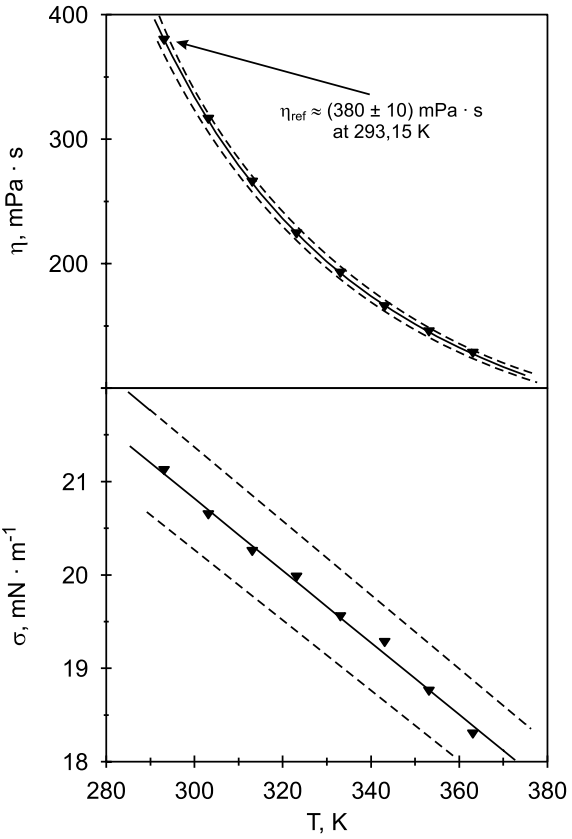

Fig. 15.24. Dynamic viscosity of the liquid phase and surface tension of a silicone oil at ambient pressure from SLS [54].

viscosity, makes the method interesting also for a routine measurement of these properties of simple fluids [59] and mixtures [60, 61]. For both the oscillatory and the overdamped behavior of surface fluctuations, experimental results are shown on various new refrigerants in Fig. 15.23 and on a silicone oil in Fig. 15.24, respectively. For the silicone oil the quantity which has been directly evaluated from the SLS experiment was the ratio of the dynamic viscosity to the surface tension [54]. Assumed that the temperature dependence of the dynamic viscosity and surface tension of the silicone oil can be reflected by a simple Andrade-type and a linear equation, respectively, with the help of a calibration point the dynamic viscosity and surface tension have been derived over the whole temperature range investigated. This procedure is shown in Fig. 15.24, where the dashed curves indicate the uncertainty resulting from the uncertainty of the calibration point. Also, apart from studying specific surface properties, the contactless operation makes SLS ideally suited

for the investigation of high-temperature melts [62], yet presently with clear limitations in accuracy.

15.5.2 Forced Rayleigh Scattering

Forced Rayleigh scattering (FRS) differs from usual dynamic light scattering in the respect that it does not probe statistical fluctuations in a sample but employs a temperature gradient produced by laser irradiation [63,64]. For the realization of a thermal grating the laser light, which is chopped for pulses of a few hundreds of microseconds duration, is split and the two beams are intersected in the sample to produce an interference pattern (see Fig. 15.25). This causes the temperature to rise locally, where in some instances light absorption is increased by doping the sample with an additional dye. The grating is probed by an additional laser beam, where the intensity diffracted into the first order is measured over time. Assuming one-dimensional heat conduction, the grating decays with

$$\delta T(x,\tau) = \Delta T \cos(kx) \exp(-\tau/\tau_{\mathrm{C}}), \tag{15.40}$$

where x is the location in the sample and k is the modulus of the grating vector. The grating relaxes with a characteristic time $\tau_{\mathrm{C}} = 1/(aq^2)$, which is detected by measuring the intensity of the diffracted beam

$$I(\tau) \propto [\Delta T(\tau)]^2 \propto \exp(-2\tau/\tau_{\mathrm{C}}), \tag{15.41}$$

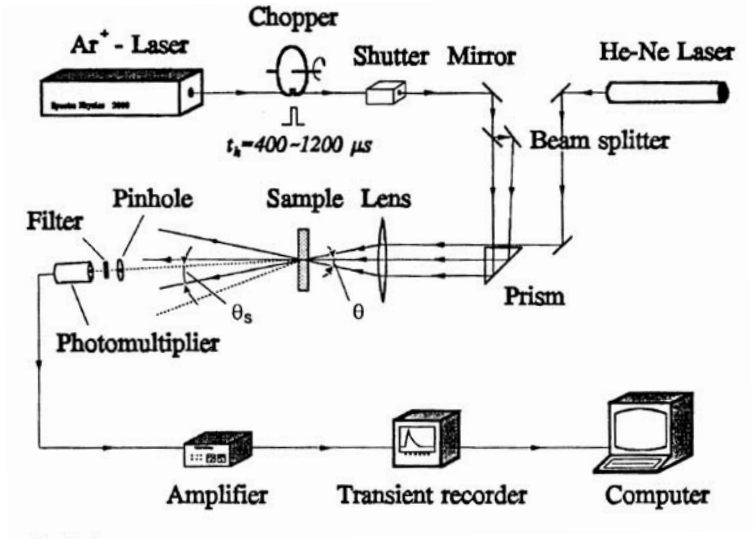

Fig. 15.25. Typical setup for a FRS experiment [63].

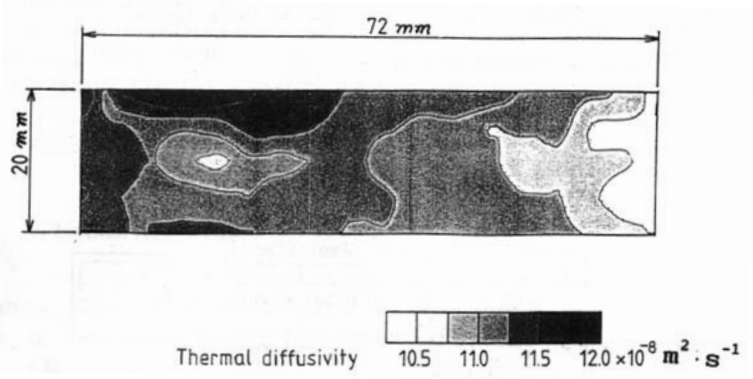

Fig. 15.26. Distribution of thermal diffusivities within a PVC film, obtained by a scanning FRS technique [64].

which is usually done by means of a photomultiplier and a transient recorder. A major advantage of FRS as compared to conventional DLS is that a single measurement may be performed very fast, i.e. in about 1 ms. On the other hand, measurements are not performed in true thermodynamic equilibrium, which makes experiments close to the saturation line or to a critical point difficult, and the technique requires a dye for usual fluids. Additionally, there are deviations from the ideal working model of one-dimensional heat conduction. However, the overall uncertainty of the method is found to be about 1.5% to 3% for usual liquids and is thus similar to that of conventional DLS.

Moreover, there are some fields of application, where FRS is especially attractive. This includes some mixtures, where accurate DLS measurements may be difficult because of a large signal due to concentration fluctuations, water and aqueous mixtures (where DLS cannot be used due to the extreme weakness or lack of the Rayleigh signal), and a number of high temperature melts, e.g., molten salts. Another interesting feature of FRS is illustrated in Fig. 15.26, where the technique has been used to obtain a "map" of thermal diffusivities by scanning the laser beam across a sample. It should be noted that besides the application of FRS to the measurement of thermal diffusivities it is also possible to extend the technique to the determination of some other properties. Similar to DLS, FRS may also be applied to the measurement of the Soret coefficient, as it has been done for polymer solutions [65]. Additionally, FRS has been used to measure the sound velocity in hydrothermal solutions [66], where acoustic waves are generated by using intense pump pulses.

15.6 Conclusion

Light scattering techniques have been widely employed for the investigation of diffusive processes and the determination of transport and other thermophysical properties. The reasons for the success of these methods may be summarized as follows:

- Measurements may be performed in or close to thermodynamic equilibrium, almost without an input of energy.
- Experiments are conducted in a non-contact mode, allowing access to regions of thermodynamic state which can hardly be probed by other techniques.
- The methods allow the determination of a wide range of transport and other thermophysical properties, in some instances even simultaneously.
- The techniques are based on simple and rigid working equations, where the reliability of the measurements can easily be checked.

As the state of development is different for the various properties, major tasks for future work will be both the routine application of light scattering to data acquisition for interesting samples over a wide range of temperature and pressure and the continuous improvement of the experimental techniques themselves. Specific challenges are further applications to samples like high-temperature melts and the simultaneous determination of several properties within a single experiment.

Notation

A	area
a	thermal diffusivity, experimental constant
b	experimental constant
c	concentration, experimental constant
c_p	isobaric specific heat
c_S	speed of sound
c_v	isochoric specific heat
d	particle diameter
D_P	particle diffusion coefficient
D_S	sound attenuation
D_{12}	mutual diffusion coefficient
E	electric field strength
f	stochastic complex quantity, strength, count rate
G	correlation function
g	normalized correlation function
H	state variable
I	intensity

k	modulus of wave vector or grating vector
k_B	Boltzmann constant
n	refractive index
p	pressure
q	modulus of scattering vector
R	distance
S	Landau-Placzek ratio
S_E	power spectral density of the electric field
t	temperature, time
T	temperature, time
Γ	line width
δ	angle of refraction
ϵ	permittivity of the medium, angle of incidence
ϵ_0	permittivity in vacuo
η	dynamic (shear) viscosity
Θ_S	scattering angle
Θ_i	external angle of incidence
κ	isentropic exponent
λ	thermal conductivity
λ_0	laser wavelength in vacuo
ν	kinematic viscosity
ρ	density
σ	surface tension, standard deviation
τ	time
$\Delta\tau$	sample time
χ_e	electric susceptibility
χ_s	isentropic compressibility
Ψ	random function
Ω	solid angle
ω	angular frequency
ACF	autocorrelation function
DLS	dynamic light scattering
FRS	forced rayleigh scattering
PCS	photon correlation spectroscopy
SLS	surface light scattering
$\langle \cdots \rangle$	time average

Sub-/Superscripts

B	Brillouin
C	correlation
c	concentration
c	critical
coh	coherence
I	incident

i	channel number
LO	local oscillator
M	modulator
q	Fourier component
R	Rayleigh, "ripplon"
S	scattered, sound, sample
t	temperature
$'$	projection in the surface plane
$*$	complex conjugate variable

References

1. E. Gulari, R.J. Brown, C.J. Pings: AIChE J. **19**, 1196 (1973)
2. M. Corti, V. Digorgio: J. Phys. C **8**, 953 (1975)
3. G. Simonsohn: Opt. Acta **30**, 875, 1675 (1983)
4. K.J. Czworniak, H.C. Anderson, R. Pecora: Chem. Phys. **11**, 451 (1975)
5. L. Onsager: Phys. Rev. **37**, 405 (1931); **38**, 2265 (1931)
6. S. Will, A. Leipertz. In: *Diffusion in Condensed Matter*, ed by J. Kärger, P. Heitjans, R. Haberlandt (Vieweg, Braunschweig/Wiesbaden 1998) pp 219–244
7. B.J. Berne, R. Pecora: *Dynamic Light Scattering with Applications to Chemistry, Biology, and Physics* (Robert E. Krieger, Malabar 1990)
8. B. Chu: *Laser Light Scattering: Basic Principle and Practice* (Academic, Boston 1991)
9. A.D. May, M. Hubert, V. Ghaem-Maghami: Can. J. Phys. **56**, 1168 (1978)
10. V. Ghaem-Maghami, A.D. May: Phys. Rev. A **22**, 692; **22**, 698 (1980)
11. D.S. Chung, K.Y. Lee, E. Mazur: Appl. Phys. B **64**, 1 (1997)
12. E. Jakeman, C.J. Oliver, E.R. Pike: J. Phys. A **3**, L45 (1970)
13. S. Will, A. Leipertz: Rev. Sci. Instrum. **67**, 3164 (1996)
14. J. Straub. PhD thesis, Technische Universität München (1965)
15. B. Chu, R. Xu, T. Maeda, H.S. Dhadwal: Rev. Sci. Instr. **59**, 716 (1988)
16. G. Simonsohn, F. Wagner: J. Phys. D **22**, 1179 (1989)
17. J. Rička: Appl. Opt. **32**, 2860 (1993)
18. G. Hiller, G. Simonsohn. In: *Photon Correlation Techniques in Fluid Mechanics*, ed by E.O. Schulz-Du Bois (Springer, Berlin Heidelberg New York 1983) pp 377–383
19. R.G.W. Brown, K.D. Ridley, J.G. Rarity: Appl. Opt. **25**, 4122 (1986); **26**, 2383 (1987)
20. K. Schaetzel: Quantum Opt. **2**, 287, 467 (1990)
21. S. Will, A. Leipertz: Appl. Opt. **32**, 3813 (1993)
22. W.H. Press:*Numerical Recipes in C* (Cambridge University, Cambridge 1992)
23. D.E. Koppel: J. Chem. Phys. **57**, 4814 (1974)
24. A. Leipertz: Int. J. Thermophys. **9**, 897 (1988)
25. P. Jany, J. Straub: Int. J. Thermophys. **8**, 165 (1987)
26. M. Hendrix, A. Leipertz, M. Fiebig, G. Simonsohn: Int. J. Heat Mass Transfer **30**, 333 (1987)
27. K. Kraft, M. Matos Lopes, A. Leipertz: Int. J. Thermophys. **16**, 423 (1995)
28. M. Ibreighith, M. Fiebig, A. Leipertz, G. Wu: Fluid Phase Equil. **80**, 323 (1992)

29. K. Kraft, A. Leipertz. In: *Proc. CFCs, The Day After* (Padua Italy 1994) pp 435–442
30. A.P. Fröba, S. Will, A. Leipertz: Int. J. Thermophys. **22**, 1021 (2001)
31. G. Wu, M. Fiebig, A. Leipertz: Int. J. Heat and Mass Transfer **31**, 1471 (1988)
32. G. Wu, M. Fiebig, A. Leipertz: Int. J. Heat and Mass Transfer **31**, 2555 (1988)
33. G. Wu, M. Fiebig, A. Leipertz: Wärme- Stoffübertr. **22**, 365 (1988)
34. L.D. Landau, E.M. Lifschitz: *Lehrbuch der theoretischen Physik, Bd. 6, Hydrodynamik* (Akademie, Berlin 1991)
35. A. Einstein: Z. f. Elektroch. **17**, 235 (1908)
36. *Measurement of Suspended Particles by Quasi-Elastic Light Scattering*, ed by B. Dahneke (Wiley, New York 1984)
37. *Dynamic Light Scattering: The Method and Some Applications*, ed by W. Brown (Oxford Science, London 1993)
38. D.F. Williams, C.H. Byers: J. Chem. Eng. Data **32**, 2534 (1987)
39. S. Will, A. Leipertz: Int. J. Thermophys. **16**, 433 (1995)
40. S. Will, A. Leipertz: Int. J. Thermophys. **18**, 1339 (1997)
41. J.H. Dymond, H.A. Øye: J. Phys. Chem. Ref. Data **23**, 41 (1994)
42. S. Will. Dr.-Ing. thesis, Friedrich-Alexander-Universität Erlangen-Nürnberg (1995)
43. K. Kraft, A. Leipertz: Appl. Opt. **32**, 3886 (1993)
44. K. Kraft, A. Leipertz: Int. J. Thermophys. **16**, 445 (1995)
45. B. Hinz, G. Simonsohn, M. Hendrix, G. Wu, A. Leipertz: J. Mod. Opt. **34**, 1093 (1987)
46. K. Kraft, A. Leipertz: DKV-Tagungsberichte **22**, 199 (1995)
47. A. Leipertz: Fluid Phase Equil. **125**, 219 (1996)
48. R. Tillner-Roth, H.D. Baehr: J. Phys. Chem. Ref. Data **23**, 657 (1994)
49. W.B. Li, J.V. Sengers, R.W. Gammon, P.N. Segrè: Int. J. Thermophys. **16**, 23 (1995)
50. A.P. Fröba, S. Will, A. Leipertz: Fluid Phase Equil. **161**, 337 (1999)
51. D. Langevin: *Light Scattering by Liquid Surfaces and Complementary Techniques* (Marcel Dekker, New York 1992)
52. R.H. Katyl, U. Ingard: Phys. Rev. Letters **19**, 64 (1967)
53. M.A. Bouchiat, J. Meunier: J. de Phys. Paris **32**, 561 (1971)
54. A.P. Fröba. Dr.-Ing. thesis, Friedrich-Alexander-Universität Erlangen-Nürnberg (2001)
55. A.P. Fröba, S. Will, A. Leipertz: Appl. Opt. **36**, 7615 (1997)
56. T. Nishio, Y. Nagasaka: Int. J. Thermophys. **16**, 1087 (1995)
57. T.M. Jørgensen: Meas. Sci. Technol. **3**, 588 (1992)
58. A.P. Fröba, A. Leipertz: Int. J. Thermophys. **24**, 895 (2003)
59. A.P. Fröba, S. Will, A. Leipertz: Int. J. Thermophys. **21**,1225 (2000)
60. A.P. Fröba, S. Will, A. Leipertz: Int. J. Thermophys. **22**, 1349 (2001)
61. A.P. Fröba, A. Leipertz: Int. J. Thermophys. **24**, 1185 (2003)
62. M. Ohnishi, Y. Nagasaka: High Temp.-High Press. **32**, 103 (2000)
63. J. Wang, M. Fiebig: Int. J. Thermophys. **16**, 1353 (1995)
64. A. Nagashima: Int. J. Thermophys. **16**, 1069 (1995)
65. W. Köhler, C. Rosenauer, P. Rossmanith: Int. J. Thermophys. **16**, 11 (1995)
66. T.J. Butenhoff: Int. J. Thermophys. **16**, 1 (1995)

16 Diffusion in Colloidal and Polymeric Systems

Gerhard Nägele, Jan K. G. Dhont, and Gerhard Meier

16.1 Introduction

In this chapter we shall discuss diffusion properties of spherical and rod-like colloids, and of binary polymer melts. In addition, the principles of dynamic light scattering (DLS), fluorescence recovery after photobleaching (FRAP) and fluorescence correlation spectroscopy (FCS), which are methods commonly used to measure various types of diffusion coefficients, are introduced on a basic level. In Sect. 16.2 we discuss light scattering on a heuristic level, and we introduce various kinds of dynamic structure factors. These structure factors describe different types of diffusion processes, like self-, collective-, rotational- and interdiffusion. These diffusion processes, and their connection to the corresponding types of structure factors, are discussed in Sect. 16.3, first for very dilute systems (Sect. 16.3.1) and then for concentrated systems (Sect. 16.3.2). Interdiffusion is especially relevant for the dynamics in binary polymer melts. Since long-time self-diffusion is difficult to measure with light scattering, especially for non-spherical particles, two very direct methods to probe this type of diffusion process are introduced in Sect. 16.4: FRAP (Sect. 16.4.1) and FCS (Sect. 16.4.2). These sections also contain experimental data obtained with these techniques for rod-like macromolecules. Section 16.5 deals with diffusion of spherical colloids, where the various types of diffusion processes that were treated in Sect. 16.3 on a heuristic level, are quantified, and where theoretical short-time and long-time predictions, and computer simulation results, are explored and compared to experimental findings. The systems considered comprise three-dimensional dispersions of neutral and charged colloidal spheres, quasi two-dimensional suspensions of charged particle monolayers between narrow plates, and magnetically interacting particles confined to a liquid-gas interface. Section 16.5 addresses further the diffusion in binary polymer blends, where earlier discussed general relations for interdiffusion are explicitly quantified within the Flory-Huggins approach and the dynamic random phase approximation (RPA).

16.2 Principles of Quasielastic Light Scattering

Light scattering by colloidal suspensions and polymers is a major experimental tool to study the statistical properties of these systems. In this section, light scattering is introduced on a heuristic basis, without considering explicit solutions of the Maxwell equations. The content of this section is much along the lines of [1]. Besides this reference, more about light scattering can be found in [2–5] as well as in Chap. 15.

16.2.1 The Scattered Electric Field Strength

Consider an assembly of points, fixed in space. These points will later be identified as infinitesimally small volume elements that constitute the colloidal particles or polymers. A plane wave of monochromatic light impinges onto this assembly of points. Each of the points is supposed to scatter the incident beam of light in such a way that neither the wavelength nor its phase is changed. Such a scattering process is referred to as quasielastic, since the only energy transfer between the photon and the scatterer is due to exchange of kinetic energy. Due to the extreme difference between the mass of an elementary scatterer and a photon, the change of the wavelength after the collision of the photon with the scatterer is extremely small, and will be neglected. A scattering process of this sort can be thought of as follows. The incident electric field induces a dipole moment which oscillates with the same frequency as the incident field. This oscillating dipole then emits electromagnetic radiation with the same frequency, and hence with the same wavelength.

The scattered intensity is detected in a certain well-defined direction. The total electric field strength that is scattered in that direction is the sum of the scattered electric fields by the individual points. Clearly, the phase difference of the scattered light from two points depends on their relative positions, as well as on the direction in which the electric field strength is measured, as can be seen from the sketch in Fig. 16.1. Let us first calculate the phase difference of electric field strengths scattered by two point scatterers with position coordinates $\boldsymbol{r}$ and $\boldsymbol{r}'$ say, into a direction that is characterized by the scattering angle $\Theta_{\rm s}$, which is the angle between the propagation direction of the incident plane wave and the direction in which the scattered field is detected (see Fig. 16.1).

The incident wavevector $\boldsymbol{q}_0$ is the vector pointing in the propagation direction of the incident field, and its magnitude is $2\pi/\lambda$, where λ is the wavelength of the light. Similarly, $\boldsymbol{q}_{\rm s}$ is the scattered wavevector: its magnitude $q_{\rm s} = |\,\boldsymbol{q}_{\rm s}\,|$ is equal to that of the incident wavevector

$$q_0 \;=\; q_{\rm s} \;=\; 2\pi/\lambda\,. \tag{16.1}$$

The phase difference $\Delta\Phi$ of the electric field strengths scattered by the two points located at $\boldsymbol{r}$ and $\boldsymbol{r}'$ under a scattering angle $\Theta_{\rm s}$ is equal to $2\pi\Delta/\lambda$,

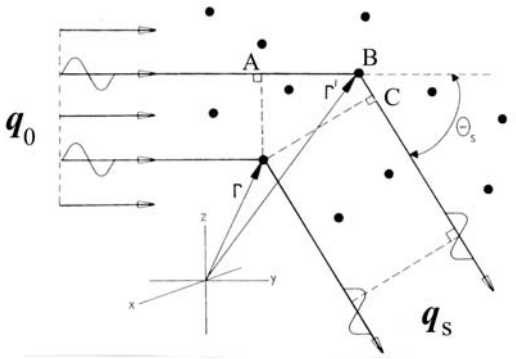

Fig. 16.1. A schematic representation of the scattering of light by an assembly of point scatterers (•). Each macromolecule (a colloidal particle or a polymer molecule) comprises many of such point scatterers. After [1].

where Δ is the difference in distance traversed by the two photons: $\Delta =$ AB+BC (see Fig. 16.1). Now, AB $= (\boldsymbol{r}'-\boldsymbol{r})\cdot\boldsymbol{q}_0/q_0$, and BC $= (\boldsymbol{r}-\boldsymbol{r}')\cdot\boldsymbol{q}_\mathrm{s}/q_\mathrm{s}$. Hence, using (16.1),

$$\Delta\cdot\Phi \;=\; (\boldsymbol{r}'-\boldsymbol{r})\cdot(\boldsymbol{q}_0-\boldsymbol{q}_\mathrm{s})\;. \tag{16.2}$$

One can thus associate to each point $\boldsymbol{r}$ a phase equal to $\boldsymbol{r}\cdot(\boldsymbol{q}_0-\boldsymbol{q}_\mathrm{s})$. The total scattered electric field strength $\boldsymbol{E}_\mathrm{s}$ is then the sum of $\exp\{\mathrm{i}\boldsymbol{r}\cdot(\boldsymbol{q}_0-\boldsymbol{q}_\mathrm{s})\}$ over all volume elements, weighted by the scattering strength of the point scatterers, which is defined as the fraction of the incident field strength that is actually scattered. Now, each point scatterer can be identified as an infinitesimally small volume element with volume $d\boldsymbol{r}$, from which the colloidal particle or polymer molecule is built. The scattering strength of a point scatterer is now written as $d\boldsymbol{r}\,F(\boldsymbol{r})$, where F is referred to here as the scattering strength density. Replacing the sum over point scatterers by integrals yields

$$\boldsymbol{E}_\mathrm{s} \;=\; \int_{V_\mathrm{s}} \mathrm{d}\boldsymbol{r}\,F(\boldsymbol{r})\,\exp\{\mathrm{i}(\boldsymbol{q}_0-\boldsymbol{q}_\mathrm{s})\cdot\boldsymbol{r}\}\,\boldsymbol{E}_0 \tag{16.3}$$

where $\boldsymbol{E}_0$ is the incident field strength, and V_s is the scattering volume, which is the volume from which scattered light is detected. The scattering strength density is proportional to the polarizability $\alpha(\boldsymbol{r})$ of the volume element, relative to a constant background polarizability α_0: the additional scattered field due to the macroscopically large, homogeneous background is zero for scattering angles unequal to 180^0. For a colloidal system, the background polarizability can be taken equal to that of the solvent, while for a binary polymer melt one can take the spatial average of the polarizability

$$F(\boldsymbol{r}) \;\sim\; \alpha(\boldsymbol{r}) \;-\; \alpha_0\;. \tag{16.4}$$

We note that the polarizability is related to the refractive index for frequencies equal to that of light. The integral in (16.3) may be rewritten in order to

make the distinction between interference of light scattered from volume elements within single particles and from distinct particles. Since the scattering strength is only non-zero within the colloidal particles or polymers, (16.3) can be written as a sum of integrals ranging over the volumes $V_j, j = 1, 2, \cdots, N$, occupied by the N particles in the scattering volume,

$$\boldsymbol{E}_{\rm s} \;=\; \sum_{j=1}^{N} \int_{V_j} {\rm d}\boldsymbol{r}\, F(\boldsymbol{r})\, \exp\{{\rm i}(\boldsymbol{q}_0 - \boldsymbol{q}_{\rm s})\cdot \boldsymbol{r}\}\, \boldsymbol{E}_0 \;. \tag{16.5}$$

The integration range V_j is the volume that is occupied by the $j^{\rm th}$ particle. For non-spherical particles this volume depends on the orientation of the particle, and for any kind of particles, also for spherical particles, V_j depends on the location of the $j^{\rm th}$ particle. Let $\boldsymbol{r}_j$ denote a fixed point inside the $j^{\rm th}$ particle, which is referred to as its position coordinate. The position coordinate dependence of V_j can easily be accounted for explicitly, by changing for each j the integration variable to $\boldsymbol{r}' = \boldsymbol{r} - \boldsymbol{r}_j$. The new integration range V_j^0 is the volume occupied by the particle with its position coordinate at the origin. For spherical particles, with their positions chosen at the center of the spheres, V_j^0 is the volume of a sphere with its center at the origin. For non-spherical, possibly flexible particles, V_j^0 depends on the orientation and the internal configuration of particle j. In terms of these new integration variables (16.5) reads

$$\boldsymbol{E}_{\rm s} \;=\; \sum_{j=1}^{N} B_j(\boldsymbol{q})\, \exp\{{\rm i}\,\boldsymbol{q}\cdot \boldsymbol{r}_j\}\, \boldsymbol{E}_0 \;, \tag{16.6}$$

where we abbreviated

$$B_j(\boldsymbol{q}) \;=\; \int_{V_j^0} {\rm d}\boldsymbol{r}'\, F(\boldsymbol{r}') \exp\{{\rm i}\boldsymbol{q}\cdot \boldsymbol{r}'\} \;, \tag{16.7}$$

where B_j is referred to as the scattering amplitude of particle j, and

$$\boldsymbol{q} \;=\; \boldsymbol{q}_0 - \boldsymbol{q}_{\rm s} \tag{16.8}$$

which is referred to as the scattering wavevector. From (16.1) it is easily verified that the magnitude of this scattering wavevector is equal to

$$q \;=\; \frac{4\pi}{\lambda}\, \sin\{\Theta_{\rm s}/2\} \tag{16.9}$$

where $\Theta_{\rm s}$ is the scattering angle that was introduced before as the angle between $\boldsymbol{q}_0$ and $\boldsymbol{q}_{\rm s}$, and λ is the wavelength of the light in the scattering volume. The exponential functions in (16.6) containing the position coordinates $\boldsymbol{r}_j$ describe the interference of light scattered from different colloidal particles, while the scattering amplitudes B_j describe interference of light scattered from different volume elements within single particles.

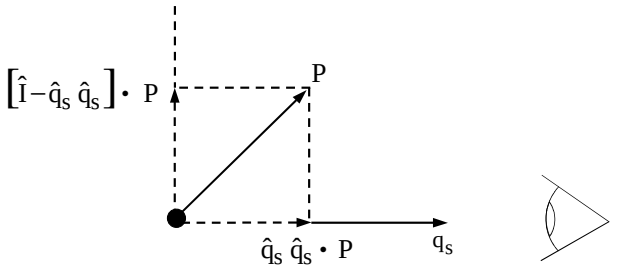

Fig. 16.2. An observer only probes that part of an oscillating dipole $\boldsymbol{P}$ that is perpendicular to the observation direction $\sim \boldsymbol{q}_\mathrm{s}$.

In the above analysis we did not consider polarization effects. Consider the oscillating dipole $\boldsymbol{P}$ that is induced by the incident electric field, from which emitted radiation is detected in the direction $\boldsymbol{q}_\mathrm{s}$. The component of the dipole parallel to $\boldsymbol{q}_\mathrm{s}$ does not contribute to the electric field emitted in that direction: looking "onto the head" of a dipole, one cannot tell whether the dipole oscillates or not, and therefore it cannot radiate in that direction. The part of the dipole that gives rise to emitted radiation in the direction $\boldsymbol{q}_\mathrm{s}$ is the part that is perpendicular to $\boldsymbol{q}_\mathrm{s}$ (see Fig. 16.2). This "effective dipole" is equal to

$$\boldsymbol{P}^{\mathrm{eff}} \;=\; \left[\hat{\boldsymbol{I}} - \hat{\boldsymbol{q}}_\mathrm{s}\hat{\boldsymbol{q}}_\mathrm{s}\right] \cdot \boldsymbol{P} \tag{16.10}$$

where $\hat{\boldsymbol{q}}_\mathrm{s} = \boldsymbol{q}_\mathrm{s}/q_\mathrm{s}$ is the unit vector in the direction of $\boldsymbol{q}_\mathrm{s}$.

Secondly, the polarizability may be anisotropic, that is, the polarizability may depend on the polarization direction of the incident field. For example, for long and thin rods, the polarizability for light with a polarization direction parallel to the rods long axis may be different from the polarizability of light that is polarized in a direction perpendicular to the long axis. Such an anisotropic polarizability is the result of the anisotropic microstructure of the rods material. For such anisotropic polarizabilities, the induced dipole generally has a different orientation than the incident electric field. In such a case, the scattering strength F in (16.4) is a tensor, denoted as $\boldsymbol{F}$, rather than a scalar. Thirdly, in an experiment one usually measures, by means of a polarization filter, the scattered intensity with a prescribed polarization direction, which is characterized by the unit vector $\hat{\boldsymbol{n}}_\mathrm{s}$. The detected electric field strength is simply $\hat{\boldsymbol{n}}_\mathrm{s} \cdot \boldsymbol{E}_\mathrm{s}$. Taking these polarization effects into account, generalizes (16.6) to

$$E_\mathrm{s} \;\equiv\; \hat{\boldsymbol{n}}_\mathrm{s} \cdot \boldsymbol{E}_\mathrm{s} \;=\; \hat{\boldsymbol{n}}_\mathrm{s} \cdot \left[\hat{\boldsymbol{I}} - \hat{\boldsymbol{q}}_\mathrm{s}\hat{\boldsymbol{q}}_\mathrm{s}\right] \cdot \sum_{j=1}^{N} \boldsymbol{B}_j(\boldsymbol{q}) \, \exp\{\mathrm{i}\,\boldsymbol{q}\cdot\boldsymbol{r}_j\} \;\cdot\; \boldsymbol{E}_0 \tag{16.11}$$

where $\boldsymbol{B}_j$ is now defined in (16.7), with the scalar F replaced by the tensor $\boldsymbol{F}$. Note that the polarization direction is always perpendicular to the prop-

agation direction, so that, $\hat{\boldsymbol{n}}_\mathrm{s} \cdot \hat{\boldsymbol{q}}_\mathrm{s} = 0$. Introducing the polarization direction $\hat{\boldsymbol{n}}_0$ of the incident field, where $\boldsymbol{E}_0 = \hat{\boldsymbol{n}}_0 E_0$, with E_0 the magnitude of the incident electric field strength, (16.11) simplifies to

$$E_\mathrm{s} \;=\; \sum_{j=1}^{N} \left[\hat{\boldsymbol{n}}_\mathrm{s} \cdot \boldsymbol{B}_j(\boldsymbol{q}) \cdot \hat{\boldsymbol{n}}_0\right] \exp\{\mathrm{i}\, \boldsymbol{q} \cdot \boldsymbol{r}_j\}\, E_0 \;. \tag{16.12}$$

This equation is at the basis of the analysis of quasielastic light scattering experiments.

Two assumptions, which are implicit in the above analysis, should be mentioned. First of all it is assumed here that the incident field strength is the same at every point in the scattering volume. This is only true if the various scattering elements scatter only a very small fraction of the light. This amounts to what is commonly referred to as "the first Born approximation". Secondly, multiple scattering is neglected. That is, scattered light is assumed not to be scattered by a second and further volume elements. Both these assumptions are satisfied when, according to (16.4), differences in polarizability of the material within the scattering volume are small.

The value of the scattering wavevector q is of special importance. Since the exponential function in (16.12) hardly changes when the position coordinates $\boldsymbol{r}_j$ are changed by an amount less than about $2\pi/q$, the scattered electric field strength changes when particles move over distances of at least $\sim 2\pi/q$. Equivalently, from (16.7) it follows that particle orientations and internal modes can only be probed when the scattering angle is chosen such that the linear dimensions of the scattering particles is at most $\sim 2\pi/q$. We can therefore introduce an effective wavelength

$$\Lambda \;=\; 2\pi/q \tag{16.13}$$

which sets the structural length scale on which dynamics is probed. For example, if the length of a colloidal rod is smaller than Λ, rotation of the rod leaves the scattering amplitude (16.7) virtually unchanged, and does therefore not affect the scattered electric field strength. For such a wavevector, nothing can be learned from a light scattering experiment about the rotational dynamics of these rods. Similarly, if one is interested in the dynamics of internal degrees of freedom of a polymer molecule, the scattering angle should be so large, that Λ is smaller the linear dimension of the polymers. For larger Λ, only translational motion of the polymers is probed. For the same reason, displacements of particles that are smaller than Λ are not seen in a light scattering experiment. According to (16.9), the scattering angle thus sets the length scale on which the dynamics is probed by light scattering.

16.2.2 Dynamic Light Scattering (DLS)

Due to the Brownian motion of the center of mass $\boldsymbol{r}_j$, and of the orientation of particles and their internal fluctuations (which renders the scattering

amplitude $\boldsymbol{B}_j$ time dependent), the scattered intensity fluctuates with time. Clearly, these fluctuations contain information about the dynamics of these degrees of freedom, which are generally affected by interactions between the colloidal particles or polymers. In a dynamic light scattering experiment one measures the so-called intensity autocorrelation function $g_I(\boldsymbol{q}, t)$ (hereafter abbreviated as IACF), which is defined as

$$g_I(\boldsymbol{q}, t) \;\equiv\; \langle i(\boldsymbol{q}, t_0)\, i(\boldsymbol{q}, t + t_0)\rangle \tag{16.14}$$

where the brackets $\langle \cdots \rangle$ denote ensemble averaging. For an equilibrium system, the IACF is independent of the reference time t_0, which we shall therefore set equal to 0 from now on. The IACF contains information about the dynamics of the above mentioned degrees of freedom. The instantaneous intensity is related to the scattered electric field strength as

$$i(\boldsymbol{q}, t) \;\sim\; E_\mathrm{s}(\boldsymbol{q}, t)\, E_\mathrm{s}^\star(\boldsymbol{q}, t) \tag{16.15}$$

where the wavevector and time dependence of the scattered electric field strength is denoted explicitly. The IACF is thus an ensemble average of a product of four electric field strengths

$$g_I(\boldsymbol{q}, t) \;\sim\; \langle E_\mathrm{s}(\boldsymbol{q}, t)\, E_\mathrm{s}^\star(\boldsymbol{q}, t)\, E_\mathrm{s}(\boldsymbol{q}, t = 0)\, E_\mathrm{s}^\star(\boldsymbol{q}, t = 0)\rangle\ . \tag{16.16}$$

The scattered field strength in (16.12) can be written as a sum over many statistically independent terms, where each term itself is a sum over "clusters" of interacting particles. The linear dimension of a cluster is the distance over which interactions between particles extends. These clusters of particles are statistically independent. The central limit theorem implies that the scattered electric field strength is a Gaussian variable (with zero average), provided that the scattering volume contains a large number of such independent clusters of particles. According to Wick's theorem for Gaussian variables, the four-point ensemble average in (16.16) can thus be written as a sum of products of two-point averages (henceforth we simply write $E_\mathrm{s}(0)$ instead of $E_\mathrm{s}(t = 0)$),

$$\begin{aligned} g_I(\boldsymbol{q}, t) \;\sim\; & \langle E_\mathrm{s}(0) E_\mathrm{s}^*(0)\rangle \langle E_\mathrm{s}(t) E_\mathrm{s}^*(t)\rangle \\ & + \langle E_\mathrm{s}(0) E_\mathrm{s}(t)\rangle \langle E_\mathrm{s}^*(0) E_\mathrm{s}^*(t)\rangle \\ & + \langle E_\mathrm{s}(0) E_\mathrm{s}^*(t)\rangle \langle E_\mathrm{s}^*(0) E_\mathrm{s}(t)\rangle\ . \end{aligned} \tag{16.17}$$

For systems in equilibrium, the first of these terms is nothing but I^2, where I is the mean scattered intensity. Defining the electric field autocorrelation function (EACF) g_E as

$$g_E(\boldsymbol{q}, t) \;\equiv\; \langle E_\mathrm{s}(0)\, E_\mathrm{s}^*(t)\rangle \tag{16.18}$$

the third term in (16.17) is equal to $\mid g_E \mid^2$. This will turn out to be the interesting quantity in DLS. The second term in (16.17) is equal to zero for

non-zero wavevectors. This can be seen as follows. The second term consists of ensemble averages of the form

$$\langle \exp\{\mathrm{i}\boldsymbol{q}\cdot(\boldsymbol{r}_i(0)+\boldsymbol{r}_j(t))\}\rangle \,,$$

where i and j are either different or equal. Let $P(\boldsymbol{r}_j,t \mid \boldsymbol{r}_i,0)$ be the conditional pdf (probability density function) for the position $\boldsymbol{r}_j$ of particle j at time t, given that the position of particle i at time $t=0$ is $\boldsymbol{r}_i$. This pdf is only a function of the difference coordinate $\boldsymbol{r}_i-\boldsymbol{r}_j$ for homogeneous systems: $P(\boldsymbol{r}_j,t \mid \boldsymbol{r}_i,t=0)\equiv P(\boldsymbol{r}_i-\boldsymbol{r}_j,t)$. The ensemble average is then equal to (with $\boldsymbol{r}'=\boldsymbol{r}_i(t=0)$ and $\boldsymbol{r}=\boldsymbol{r}_j(t)$)

$$\langle \exp\{\mathrm{i}\boldsymbol{q}\cdot(\boldsymbol{r}_i(t=0)+\boldsymbol{r}_j(t))\}\rangle = \int_{V_\mathrm{s}} \mathrm{d}\boldsymbol{r}' \int_{V_\mathrm{s}} \mathrm{d}\boldsymbol{r}\, P(\boldsymbol{r}'-\boldsymbol{r},t)\, P(\boldsymbol{r}')\, \exp\{\mathrm{i}\boldsymbol{q}\cdot(\boldsymbol{r}'+\boldsymbol{r})\}$$

where $P(\boldsymbol{r}')$ is the equilibrium pdf for the position coordinate. Since $P(\boldsymbol{r}')\equiv 1/V_\mathrm{s}$ for the homogeneous equilibrium system considered here, this can be written, in the thermodynamic limit (where $V_\mathrm{s}\to\infty$ and $\bar{\rho}$ constant), as

$$\frac{1}{8}\left[\lim_{V_\mathrm{s}\to\infty}\frac{1}{V_\mathrm{s}}\int_{V_\mathrm{s}} \mathrm{d}(\boldsymbol{r}'+\boldsymbol{r})\, \exp\{\mathrm{i}\boldsymbol{q}\cdot(\boldsymbol{r}'+\boldsymbol{r})\}\right] \times \int \mathrm{d}(\boldsymbol{r}'-\boldsymbol{r})\, P(\boldsymbol{r}'-\boldsymbol{r},t)$$

where the factor $1/8$ is the Jacobian of the transformation

$$(\boldsymbol{r}',\boldsymbol{r}) \to (\boldsymbol{r}'+\boldsymbol{r},\boldsymbol{r}'-\boldsymbol{r}) \,.$$

The integral with respect to $(\boldsymbol{r}'-\boldsymbol{r})$ is well behaved, since the pdf is a normalized function. The integral between the square brackets is equal to unity for $\boldsymbol{q}=0$, and is zero for $\boldsymbol{q}\neq 0$, since that integral is proportional to the delta distribution of $\boldsymbol{q}$ (for sufficiently large scattering volumes). Hence, the ensemble average is zero for non-zero wavevectors, so that the second term in (16.17) does not contribute. The IACF can thus be written in terms of the mean scattered intensity and the EACF (16.18)

$$g_I(\boldsymbol{q},t) \;=\; I^2 + \mid g_E(\boldsymbol{q},t)\mid^2 \quad . \tag{16.19}$$

This equation is usually referred to as the Siegert relation. The IACF is measured, and interpreted through the more simple EACF via the Siegert relation.

16.2.3 Dynamic Structure Factors

Several types of dynamic structure factors can be defined, each of which describes a different type of diffusion process. The experimental relevance of these structure factors relates to the Siegert relation (16.19). Substitution of (16.12) into the definition (16.18) of the EACF leads to

$$g_E(q,t) \;\sim\; \sum_{l,j=1}^{N} \langle B_l^{\mathrm{p}}(\boldsymbol{q},t)\, B_j^{p\star}(\boldsymbol{q},0) \exp\{\mathrm{i}\,\boldsymbol{q}\cdot(\boldsymbol{r}_i(l)-\boldsymbol{r}_j(0))\}\rangle \tag{16.20}$$

where $\boldsymbol{r}_j(0)$ is the position coordinate at $t=0$, and for brevity we introduced

$$B_j^{\mathrm{p}}(\boldsymbol{q},t) \;=\; \hat{\boldsymbol{n}}_{\mathrm{s}}\cdot\boldsymbol{B}_j(\boldsymbol{q},t)\cdot\hat{\boldsymbol{n}}_0 \tag{16.21}$$

where a superscript "p" is used to indicate that polarization effects are taken into account. Time dependencies are denoted explicitly here. The collective dynamic structure factor is now defined as

$$S_{\mathrm{c}}(q,t) \;=\; \frac{1}{N}\sum_{l,j=1}^{N} \langle \exp\{\mathrm{i}\,\boldsymbol{q}\cdot(\boldsymbol{r}_l(t)-\boldsymbol{r}_j(0))\}\rangle\;. \tag{16.22}$$

This structure factor is proportional to the experimentally obtained EACF, when the scattering amplitudes B_j^{p} can be omitted in (16.20). These scattering amplitudes contribute to the EACF due to rotation and possibly fluctuations of internal degrees of freedom of a particle. Rotation and internal degrees of freedom are not probed when either the wavelength Λ in (16.13) is larger than the linear dimensions of the scattering particles, or when the particles are rigid and spherically symmetric. In the latter case, rotation does not change the scattered intensity and internal degrees of freedom that could contribute to scattering are absent. For such cases, the scattering amplitudes can be omitted in (16.20). It should always be kept in mind, that DLS-data on non-spherical particles at relatively large wavevectors cannot be interpreted directly in terms of the collective dynamic structure factor, whose time dependence is solely determined by the translational dynamics of centers-of-mass.

The collective dynamic structure factor can be related to density fluctuations as follows. The microscopic density is defined as

$$\rho(\boldsymbol{r},t) \;=\; \sum_{j=1}^{N}\delta(\boldsymbol{r}-\boldsymbol{r}_j(t)) \tag{16.23}$$

where δ is the Dirac delta distribution. On ensemble averaging the right-hand side, it is easily shown that the macroscopic density is obtained. The Fourier transform of the microscopic density with respect to $\boldsymbol{r}$ yields

$$\rho(\boldsymbol{q},t) \;=\; \sum_{j=1}^{N}\exp\{\mathrm{i}\boldsymbol{q}\cdot\boldsymbol{r}_j(t)\} \tag{16.24}$$

where $\boldsymbol{q}$ is the Fourier variable conjugate to $\boldsymbol{r}$. The collective dynamic structure factor (16.22) can thus be written as

$$S_{\mathrm{c}}(\boldsymbol{q},t) \;=\; \frac{1}{N}\,\langle \rho(\boldsymbol{q},t)\,\rho^{\star}(\boldsymbol{q},0)\rangle\;. \tag{16.25}$$

The collective dynamic structure factor is thus related to collective motion of many particles. In the next section it will be shown how this structure factor is related to the so-called collective diffusion coefficient, which under certain conditions reduces to Fick's diffusion coefficient.

Consider now an experiment on a binary mixture of particles, where one sort of particles is very dilute and one sort possibly concentrated. Suppose that the possibly concentrated species does not scatter any light, that is, their scattering amplitudes B_j^{p} in (16.20) are 0. These particles are referred to as the host particles. All the scattered intensity originates from the dilute species, the so-called tracer particles. The concentration of tracer particles is chosen so small, that they do not mutually interact. The summations in (16.20) range only over the tracer particles, since the scattering amplitudes are 0 for the host particles. Let us furthermore assume once more, that the wavevector is small enough in order to neglect the contribution of the scattering amplitudes B_j^{p}. Since the tracer particles do not interact, we then have, for $i \neq j$,

$$\langle \exp\{\mathrm{i}\boldsymbol{q}\cdot(\boldsymbol{r}_i-\boldsymbol{r}_j)\}\rangle \;=\; \langle \exp\{\mathrm{i}\boldsymbol{q}\cdot\boldsymbol{r}_i\}\rangle \langle \exp\{-\mathrm{i}\boldsymbol{q}\cdot\boldsymbol{r}_j\}\rangle \,. \tag{16.26}$$

Since the exponential functions are equally often positive and negative (for $\boldsymbol{q} \neq 0$), this ensemble average is 0. For monodisperse tracer particles the EACF is now proportional to the so-called self-dynamic structure factor

$$S_{\mathrm{s}}(q,t) \;=\; \langle \exp\{\mathrm{i}\,\boldsymbol{q}\cdot(\boldsymbol{r}(t)-\boldsymbol{r}(0))\}\rangle \tag{16.27}$$

where $\boldsymbol{r}(t)$ is the position coordinate of a tracer particle. This structure factor contains information about the dynamics of a single particle, possibly interacting with other particles. Its relation to the mean square displacement and the so-called self-diffusion coefficient is discussed in the next section.

A third kind of dynamic structure factor which is of importance is the distinct dynamic structure factor S_{d}, which is defined as

$$S_{\mathrm{d}}(q,t) \;=\; \frac{1}{N}\sum_{l\neq j=1}^{N} \langle \exp\{\mathrm{i}\,\boldsymbol{q}\cdot(\boldsymbol{r}_l(t)-\boldsymbol{r}_j(0))\}\rangle \,. \tag{16.28}$$

The distinct dynamic structure factor is that part of the collective dynamic structure factor which describes time correlations between distinct pairs of particles only.

16.3 Heuristic Considerations on Diffusion Processes

For dispersions of rigid colloidal particles in a solvent and for polymer melts, there are three fundamental types of diffusion processes to be distinguished which are related to translational particle motion: self-diffusion, collective

diffusion, and exchange or interdiffusion between different particle species. In addition to translational diffusion, the particles or polymers undergo further rotational diffusion which is coupled in general to the translational motion. In this section we shall discuss each of these diffusion processes on an intuitive level for a colloidal system of the most simple particle shape: a suspension (i.e. an assembly) of rigid colloidal spheres embedded in a low-molecular-weight fluid (i.e. the solvent) of small molecules as compared to the size of the spheres. The various translational diffusion mechanisms will be further exemplified for binary blends of polymer chains, within time- and length scales accessible to dynamic light scattering.

The basic understanding of diffusion of rigid colloidal spheres is very helpful in improving the understanding of diffusion mechanisms of more complicated non-rigid macromolecules in solution, like polymers and polyelectrolytes, where the fluctuating internal degrees of freedom related to the motion of monomers affect the diffusion properties of the macromelecules. We consider first very dilute colloidal dispersions where the interactions between the colloidal spheres can be disregarded. For this most simple case, only a single diffusion mechanism is present, namely self-diffusion. We then focus on the general case of diffusion in systems of interacting particles.

16.3.1 Very Dilute Colloidal Systems

Translational self-diffusion refers to the random walk of the center of mass of a tagged colloidal sphere (the "tracer particle") in a quiescent and homogeneous suspension caused by thermal collisions with surrounding solvent molecules and other colloidal particles (the so-called "host particles"). For very small sphere concentrations, the dynamics of the colloidal tracer is governed only by the thermal bombardment of the solvent molecules.

The most important quantity that characterizes the translational self-diffusion of the center of mass of a particle is the so-called mean square displacement $W(t)$ (hereafter abbreviated as MSD), which is defined as

$$W(t) \equiv \frac{1}{2d} \langle |\boldsymbol{r}(t) - \boldsymbol{r}(t=0)|^2 \rangle . \tag{16.29}$$

Here, $\boldsymbol{r}(t)$ is the position vector of the center of mass of the tracer sphere at time t, and hence, $\Delta\boldsymbol{r}(t) \equiv \boldsymbol{r}(t) - \boldsymbol{r}(t=0)$ is the sphere displacement during a time interval t. A factor $1/2d$ has been included into the definition of the MSD for later convenience, where d denotes the system dimension. For a homogeneous suspension in thermal equilibrium, the reference time "$t = 0$" is of no significance (stationarity property).

Suppose that at time $t = 0$ a colloidal tracer sphere in an unbound solvent has a translational velocity $\boldsymbol{v}_0$. For very short times, say $t \ll \tau_B$, when the sphere velocity has hardly changed under the impact of solvent molecules, $\boldsymbol{r}(t) - \boldsymbol{r}(0) \approx \boldsymbol{v}_0\, t$, and hence

$$W(t) \sim t^2 \ , \ t \ll \tau_{\rm B} \ . \tag{16.30}$$

For times large as compared to the momentum relaxation time $\tau_{\rm B}$, when the sphere has experienced many collisions with solvent molecules, the MSD has changed into a linear function of time, i.e.

$$W(t) = D_0 \, t \ , \ t \gg \tau_{\rm B} \ , \tag{16.31}$$

where D_0 is referred to as the single particle or Stokes-Einstein diffusion coefficient.

The time scale $\tau_{\rm B}$ can be inferred from the following reasoning originally due to Langevin. A sphere with velocity $\boldsymbol{v}$ experiences through the solvent impacts an average friction force that is equal to $-\gamma \, \boldsymbol{v}$, where γ is referred to as the friction coefficient, and a fluctuating force $\boldsymbol{f}(t)$. For a sphere, the friction coefficient γ is given by the Stokes law $\gamma = 6\pi\eta_0 R$, where η_0 is the shear viscosity of the solvent and R is the radius of the sphere. For times large as compared with the mean collision time, $\tau_{\rm s}$, of solvent molecules (typically, $\tau_{\rm s} \approx 10^{-13} \, s$), the colloidal sphere has experienced many collisions by the solvent molecules. Then the force $\boldsymbol{f}(t)$ can be described as a Gaussian distributed fluctuating quantity completely characterized by its first and second moments

$$\langle \boldsymbol{f}(t) \rangle = 0 \ , \quad \langle \boldsymbol{f}(t) \cdot \boldsymbol{f}(t') \rangle = 2dB \, \delta(t - t') \ . \tag{16.32}$$

Here, $\langle \cdots \rangle$ is an average over the fast solvent collisions, and B is a measure of the strength of the fluctuating force. In thermal equilibrium, $B = k_{\rm B}T\gamma$, i.e. the strength is proportional to the temperature and friction coefficient. The delta function in time indicates that, as seen from a coarse-grained time level $t \gg \tau_{\rm s}$, there is no correlation between solvent impacts at different times.

The Newtonian equation of motion for a Brownian sphere of mass M is thus given, for times $t \gg \tau_{\rm s}$, by

$$M \frac{{\rm d}\boldsymbol{v}}{{\rm d}t} = -\gamma \, \boldsymbol{v}(t) + \boldsymbol{f}(t). \tag{16.33}$$

with the solution

$$\langle \boldsymbol{v}(t) \rangle = \boldsymbol{v}_0 \, \exp\left\{ -\frac{\gamma}{M} \, t \right\} \tag{16.34}$$

for the solvent-collision-averaged velocity. As seen, the velocity remains on average almost equal to the initial velocity $\boldsymbol{v}_0$ for times $t \ll M/\gamma$, which sets the time scale

$$\tau_{\rm B} \equiv \frac{M}{\gamma} = \frac{M}{6\pi\eta_0 R} \tag{16.35}$$

for the average velocity relaxation of a colloidal sphere. For times $t \gg \tau_{\rm B}$, the average velocity of a tagged particle decays towards zero. Using typical values for aqueous colloidal dispersions, one finds that $\tau_{\rm B} \approx 10^{-8} - 10^{-9}$ s, so that $\tau_{\rm B} \gg \tau_{\rm s}$.

So far we have considered the Brownian motion of a sphere with given *fixed* initial velocity $\boldsymbol{v}_0$. In dynamic light scattering experiments, an additional average is performed with respect to a Maxwellian distribution of initial particle velocities since light is scattered from many spheres in thermal equilibrium. Multiplication of (16.33) by $\boldsymbol{v}_0$ and subsequent averaging over solvent collisions *and* initial velocities gives

$$\phi_v(t) \equiv \frac{1}{d}\langle \boldsymbol{v}(t)\cdot\boldsymbol{v}(0)\rangle = \frac{k_\mathrm{B}T}{M}\exp\left\{-\frac{t}{\tau_\mathrm{B}}\right\} \tag{16.36}$$

for the velocity autocorrelation function (VAF), $\phi_v(t)$, of an isolated Brownian sphere. Due to equipartition of energy at equilibrium, $\langle \boldsymbol{v}^2(t)\rangle = dk_\mathrm{B}T/M$. Using that $\boldsymbol{r}(t)-\boldsymbol{r}_0 = \int_0^t \mathrm{d}t'\boldsymbol{v}(t')$ one can easily show for stationary systems that $\phi_v(t)$ is related to the MSD by

$$W(t) = \int_0^t \mathrm{d}u\,(t-u)\,\phi_v(u)\,. \tag{16.37}$$

This relation is valid also for non-dilute system of interacting particles. The MSD of an isolated sphere follows from the substitution of (16.36) into (16.37) as

$$W(t) = D_0 t\left[1-\frac{\tau_\mathrm{B}}{t}\left(1-\mathrm{e}^{-t/\tau_\mathrm{B}}\right)\right] \to \begin{cases} \frac{k_\mathrm{B}T}{2M}\,t^2\,, & \tau_\mathrm{c}\ll t\ll\tau_\mathrm{B} \\ D_0\,t\,, & t\gg\tau_\mathrm{B} \end{cases} \tag{16.38}$$

where D_0 is related to the friction coefficient by the Stokes-Einstein relation

$$D_0 = \frac{k_\mathrm{B}T}{\gamma}\,. \tag{16.39}$$

Equation (16.38) interpolates between random ballistic flight for $t \ll \tau_\mathrm{B}$ and linear diffusive behavior for $t \gg \tau_\mathrm{B}$.

The sphere displacement $\Delta\boldsymbol{r}(t)$ during time t is a Gaussian random variable, since it is linearly related to $\boldsymbol{v}(t)$ and to $\boldsymbol{f}(t)$. The pdf, $P(\Delta\boldsymbol{r},t)$, for such a displacement is thus

$$P(\Delta\boldsymbol{r},t) = \{4\pi\,W(t)\}^{-d/2}\exp\{-\frac{(\Delta\boldsymbol{r})^2}{4W(t)}\} \tag{16.40}$$

with

$$W(t) = \frac{1}{2d}\int \mathrm{d}\boldsymbol{r}^d\,P(\Delta\boldsymbol{r},t)\,(\Delta\boldsymbol{r})^2\,. \tag{16.41}$$

The pdf is the solution of the diffusion-like equation

$$\frac{\partial}{\partial t}P(\Delta\boldsymbol{r},t) = \mathcal{D}(t)\nabla^2 P(\Delta\boldsymbol{r},t)\,, \tag{16.42}$$

where

$$\mathcal{D}(t) \equiv \frac{\mathrm{d}}{\mathrm{d}t} W(t) \;=\; D_0 \left[1 - \mathrm{e}^{-t/\tau_\mathrm{B}}\right] \,, \tag{16.43}$$

subject to the initial condition $P(\Delta\boldsymbol{r}, t=0) = \delta(\Delta\boldsymbol{r})$. The latter follows from (16.40) specialized to $t = 0$. Here, ∇ is the d-dimensional gradient operator. Knowing the pdf we can calculate from (16.40) the self-dynamic structure factor

$$S_\mathrm{s}(q,t) = \int \mathrm{d}(\Delta\boldsymbol{r})\, \mathrm{e}^{\mathrm{i}\boldsymbol{q}\cdot\Delta\boldsymbol{r}}\, P(\Delta\boldsymbol{r}, t) = \exp\{-q^2\, W(t)\} \,, \tag{16.44}$$

which, for uncorrelated spheres, depends on time only through $W(t)$. Note for the dilute dispersions of uncorrelated particles considered here that the collective dynamic structure factor $S_\mathrm{c}(q,t)$ reduces to the self-dynamic one.

In typical dynamic light scattering experiments on colloidal suspensions, times $t > 10^{-6}\, s \gg \tau_\mathrm{B}$ and hence distances large compared to $(D_0\tau_\mathrm{B})^{1/2}$ are resolved. In this so-called diffusive regime, (16.42) reduces to the one-particle diffusion equation

$$\frac{\partial}{\partial t} P(\Delta\boldsymbol{r}, t) \;=\; D_0 \nabla^2 P(\Delta\boldsymbol{r}, t) \,, \tag{16.45}$$

which has (16.40) specialized to $W(t) = D_0\; t$ as its fundamental solution. The diffusion (16.45) is statistically equivalent to the overdamped Langevin equation

$$\boldsymbol{v}(t) \;=\; \frac{1}{\gamma}\, \boldsymbol{f}(t) \,, \tag{16.46}$$

and $\boldsymbol{f}$ according to (16.32), which expresses a force balance, i.e an inertia-free sphere motion for times $t \gg \tau_\mathrm{B}$.

In fact, Brownian motion of a colloidal particle is adequately described by the Langevin equation (16.33) with δ-correlated random force only when solvent inertia is negligible, i.e. for times $t \gg \tau_\mathrm{B}$ only, where it reduces to (16.46). The Langevin equation disregards, for shorter times $t \approx \tau_\mathrm{B}$, the feedback on the particle velocity from the surrounding solvent. The solvent cannot instantaneously follow the changes in the particle velocity. Through the retarded response of the solvent, the sphere velocity is influenced by its values at earlier times. This leads to an enlarged persistence in the velocity autocorrelations. These solvent memory effects on the sphere velocity can be adequately described, for $d = 3$ by the retarded (one-particle) Langevin equation

$$M\, \frac{\mathrm{d}\boldsymbol{v}}{\mathrm{d}t} \;=\; -\int_0^t \mathrm{d}u\, \gamma(t-u)\, \boldsymbol{v}(u) \;+\; \boldsymbol{f}(t) \tag{16.47}$$

which includes a time-dependent friction function $\gamma(t)$ obeying a generalized fluctuation-dissipation relation

$$\langle \boldsymbol{f}(t) \cdot \boldsymbol{f}(t') \rangle \;=\; 3k_\mathrm{B}T\, \gamma(t-t') \,. \tag{16.48}$$

The random force in the retarded Langevin equation is still Gaussian, however it is now correlated for different times, due to cooperative effects of the

fluid motion. The friction function can be calculated, for times $t \gg \tau_s$, using macroscopic equations of motion for the solvent flow. Substitution of the hydrodynamically determined $\gamma(t)$ into the retarded Langevin equation results in closed expressions for the MSD and $\phi_v(t)$. We only quote the asymptotic forms valid for $t \gg \tau_\eta$, viz. [6–8]

$$W(t) \approx D_0 t \left[1 - \frac{2}{\sqrt{\pi}} \left(\frac{\tau_\eta}{t}\right)^{1/2}\right] \tag{16.49}$$

and

$$\phi_v(t) = \frac{\mathrm{d}^2}{\mathrm{d}t^2} W(t) \approx \frac{1}{9\sqrt{\pi}} \frac{k_B T}{m} \left(\frac{t}{\tau_\eta}\right)^{-3/2} \tag{16.50}$$

where $\tau_\eta = a^2 \rho_s / \eta_0 = (9/2)(\rho_s/\rho_M)\tau_B$ is the time needed for a viscous shear wave in the solvent of mass density ρ_s to diffuse across a particle radius. The mass density, ρ_M, of colloidal particles is close to ρ_s, and τ_η and τ_B are thus of the same order of magnitude.

The positive feedback of the solvent flow on the sphere velocity implies an algebraic rather than exponential decay of the VAF. Moreover, the algebraic approach of the single-particle MSD to its long-time-limiting form $W(t) = D_0 t$ is much slower than prediced by (16.38). The occurrence of an algebraic decay in an autocorrelation function is generally referred to as a long-time tail. An algebraic tail proportional to $t^{-1/2}$ in $W(t)$ was indeed observed in dynamic light scattering experiments on very large colloidal spheres (since $\tau_B \propto a^2$) through the measurement of $S_s(q,t)$ and using (16.44) to infer $W(t)$ [9]. While the non-retarded Langevin equation does not describe dilute colloidal dispersions for times $t \approx \tau_B$, it can be applied instead for $t \approx \tau_B$ to aerosols like dust or smoke particles in air, since for these systems one has $\rho_s \ll \rho_M$ and hence $\tau_\eta \ll \tau_B$.

The surrounding solvent molecules exert in addition to a random force a random torque, $\boldsymbol{f}_r(t)$, on the colloidal sphere, which causes a rotational Brownian motion of its angular velocity $\boldsymbol{\omega}(t)$. Neglecting solvent inertia, the erratic sphere rotation can be described in analogy to translational motion by a rotational Langevin equation, given for $d = 3$ and $t \gg \tau_s$ by

$$M_r \frac{\mathrm{d}\boldsymbol{\omega}}{\mathrm{d}t} = -\gamma_r \boldsymbol{\omega}(t) + \boldsymbol{f}_r(t)\,, \tag{16.51}$$

with a stochastic torque of zero mean and δ-correlated covariance

$$\langle \boldsymbol{f}_r(t) \cdot \boldsymbol{f}_r(t') \rangle = 6 k_B T \gamma_r \delta(t - t')\,. \tag{16.52}$$

According to this Langevin equation, the solvent-collisions-averaged angular velocity and the equilibrium angular VAF are, respectively,

$$\langle \boldsymbol{\omega}(t) \rangle = \boldsymbol{\omega}_0 \exp\left\{-\frac{t}{\tau_B^r}\right\} \tag{16.53}$$

and

$$\phi_\omega(t) \equiv \frac{1}{3}\langle \boldsymbol{\omega}(t)\cdot\boldsymbol{\omega}(0)\rangle = \frac{k_{\rm B}T}{M_{\rm r}}\exp\left\{-\frac{t}{\tau_{\rm B}^{\rm r}}\right\} \tag{16.54}$$

with the damping time

$$\tau_{\rm B}^{\rm r} = \frac{M_{\rm r}}{\gamma_{\rm r}}\,. \tag{16.55}$$

Here, $\gamma_{\rm r} = 8\pi\eta_0 a^3$ is the so-called Stokes-Debye friction coefficient of a freely rotating sphere, and $M_{\rm r} = (2/5)Ma^2$ is the moment of inertia of a homogeneous sphere. The damping times for the translational and rotational velocity are of the same order of magnitude, since $\tau_{\rm B}^{\rm r} = (3/10)\tau_{\rm B}$.

When the hydrodynamic solvent-sphere coupling is accounted for through a time-dependent rotational friction function similar to the translational case, the exponential decay of the rotational VAF is changed for times $t \gg \tau_\eta$ into the power-law decay [10, 11]

$$\phi_\omega(t) \approx \frac{1}{60\sqrt{\pi}}\frac{k_{\rm B}T}{M_{\rm r}}\left(\frac{t}{\tau_\eta}\right)^{-5/2} \tag{16.56}$$

which is one power in t slower than the asymptotic decay of the translational VAF. Depolarized dynamic light scattering is a convenient experimental tool to measure rotational Brownian motion of optically anisotropic spheres in the diffusive regime $t \gg \tau_{\rm B}$. As mentioned in Sect. 16.2.1, the polarizability, $\boldsymbol{\alpha}$, of an optically anisotropic uniaxial sphere is a tensor

$$\boldsymbol{\alpha}(\hat{\boldsymbol{u}}) = \alpha_\parallel\,\hat{\boldsymbol{u}}\hat{\boldsymbol{u}} + \alpha_\perp\,(\mathbf{1} - \hat{\boldsymbol{u}}\hat{\boldsymbol{u}}) = \alpha\,\mathbf{1} + \beta\left(\hat{\boldsymbol{u}}\hat{\boldsymbol{u}} - \frac{1}{3}\mathbf{1}\right) \tag{16.57}$$

where $\alpha_\parallel$ and $\alpha_\perp$ are the incremental (relative to the solvent) polarizabilities parallel and perpendicular to the optical axis of the sphere, with $\alpha = (\alpha_\parallel + 2\alpha_\perp)/3$ and $\beta = \alpha_\parallel - \alpha_\perp$, and $\hat{\boldsymbol{u}}(t)$ is the unit orientation vector pointing along the optical axis. The orientation vector is related to the angular velocity of the sphere by $\boldsymbol{\omega}(t) = \hat{\boldsymbol{u}}(t)\times(\mathrm{d}/\mathrm{d}t)\hat{\boldsymbol{u}}(t)$.

In depolarized dynamic light scattering, the polarization of the incident electric light field is chosen perpendicular to the scattering plane spanned by the incident and detected light beam (i.e. $\hat{\boldsymbol{n}}_0 = \hat{\boldsymbol{n}}_{\rm V}$), and one detects the in-plane component (i.e. $\hat{\boldsymbol{n}}_{\rm s} = \hat{\boldsymbol{n}}_{\rm H}$) of the scattered electric field. In this VH-geometry

$$\hat{\boldsymbol{n}}_{\rm s}\cdot\boldsymbol{\alpha}(\hat{\boldsymbol{u}})\cdot\hat{\boldsymbol{n}}_0 = \beta\left(\frac{2\pi}{15}\right)^{1/2}[Y_{2,1}(\hat{\boldsymbol{u}}) + Y_{2,-1}(\hat{\boldsymbol{u}})] \tag{16.58}$$

where $Y_{2,m}$ is a second-order spherical harmonic function. Together with (16.15), this results in the EACF [3]

$$g_E^{\rm VH}(q,t) \propto \beta^2\,S_{\rm s}(q,t)\,S_{\rm r}(t) \tag{16.59}$$

where we have introduced the rotational self-dynamic correlation function

$$S_{\rm r}(r) \;=\; 4\pi\langle Y_{2,-1}(\hat{\boldsymbol{u}}(0))\; Y_{2,1}(\hat{\boldsymbol{u}}(t))\rangle \;=\; \langle P_2(\hat{\boldsymbol{u}}(t)\cdot\hat{\boldsymbol{u}}(0))\rangle\,, \tag{16.60}$$

which includes information on the rotational diffusion. The second equality follows from spatial isotropy, i.e. from the m-independence of $S_{\rm r}(t)$, with P_2 denoting the second-order Legendre polynomial. In deriving (16.60), it has been assumed that the rotational motion of a sphere is decoupled from the translational motion for all $t \gg \tau_{\rm B}$. While this decoupling is strictly valid for dilute dispersions of non-interacting spheres, it is an approximation for non-spherical particles and for concentrated sphere dispersions. Note that $\beta = 0$ for optically isotropic spheres. Then there is no depolarized scattered light as long as multiple light scattering is negligibly small.

The function $S_{\rm s}(q,t)$ of non-interacting spheres can be calculated for $t \gg \tau_{\rm B}$ from the rotational diffusion equation (Debye equation)

$$\frac{\partial}{\partial t}P(\hat{\boldsymbol{u}},t) \;=\; D_0^{\rm r}\;\hat{\boldsymbol{L}}^{\,2}\;P(\hat{\boldsymbol{u}},t) \tag{16.61}$$

which determines the pdf $P(\hat{\boldsymbol{u}},t)$ of finding the sphere with orientation $\hat{\boldsymbol{u}}$ at time t. We have introduced here the diffusion coefficient of a single and freely rotating sphere, related to the rotational friction coefficient by the Einstein-Debye relation

$$D_0^{\rm r} \;=\; \frac{k_{\rm B}T}{\gamma_{\rm r}}\,. \tag{16.62}$$

The Debye equation is the analogue of the translational diffusion equation (16.45), with $\hat{\boldsymbol{L}} = \hat{\boldsymbol{u}} \times \partial/(\partial\hat{\boldsymbol{u}})$ denoting the gradient operator in orientation space. It describes the random walk of the tip of $\hat{\boldsymbol{u}}(t)$ on the unit sphere. Equation (16.61) has the fundamental solution [3]

$$P(\hat{\boldsymbol{u}},t|\hat{\boldsymbol{u}}_0) \;=\; \sum_{l=1}^{\infty}\sum_{m=-l}^{l} Y_{lm}(\hat{\boldsymbol{u}})\; Y_{l,-m}(\hat{\boldsymbol{u}}_0)\;\exp\left\{-l(l+1)\;D_0^{\rm r}t\right\}\,, \tag{16.63}$$

which is the probability density for a sphere to have orientation $\hat{\boldsymbol{u}}$ at time t given that it had orientation $\hat{\boldsymbol{u}}_0$ at initial time $t = 0$. The rotational function $S_{\rm r}(t)$ is then calculated as

$$S_{\rm r}(t) \;=\; \int {\rm d}\hat{\boldsymbol{u}} \int {\rm d}\hat{\boldsymbol{u}}_0\; Y_{2,1}(\hat{\boldsymbol{u}})\; Y_{2,-1}(\hat{\boldsymbol{u}}_0) P(\hat{\boldsymbol{u}},t|\hat{\boldsymbol{u}}_0) \;=\; \exp\left\{-6D_{\rm r}^0 t\right\} \tag{16.64}$$

where we have employed the orthogonality relations of the spherical harmonics. As a consequence, the depolarized EACF of non-interacting sphere dispersions is

$$g_E^{\rm VH}(q,t) \;\propto\; \beta^2\;\exp\left\{-\left(q^2 D_0 + 6D_0^{\rm r}\right)t\right\}\,. \tag{16.65}$$

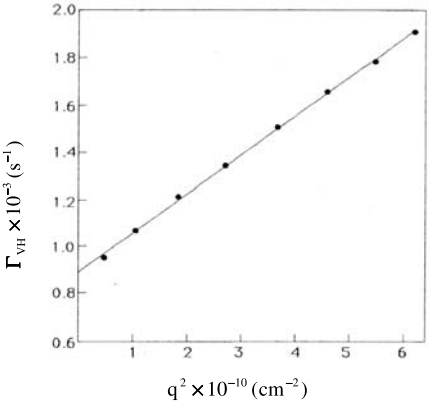

Fig. 16.3. Initial decay rate $\Gamma_{\rm VH} = -\lim_{t\to 0}(\mathrm{d}/\mathrm{d}t)\ln g_E^{\rm VH}(q,t)$ of depolarized EACF versus q^2, for a dilute dispersion of anisotropic teflon spheres ($\Phi = 0.02$). After [12].

One can determine D_0 and $D_0^{\rm r}$ simultaneously from the EACF by plotting the time derivative of $-\ln g_E^{\rm VH}(q,t)$ versus q^2, yielding a straight line of slope D_0 and intercept $D_0^{\rm r}$. Plots of this kind are shown in Fig. 16.3 for depolarized DLS experiments on a dilute dispersion of anisotropic teflon spheres [12]. The particle diameters determined from D_0 and $D_0^{\rm r}$, respectively, are indeed nearly identical.

From employing the fundamental solution, one can further calculate the orientation autocorrelation function

$$\langle \hat{\boldsymbol{u}}(t)\cdot\hat{\boldsymbol{u}}(0)\rangle \;=\; \exp\{-t/\tau_{\rm r}\} \tag{16.66}$$

and the orientation MSD [13]

$$\langle[\hat{\boldsymbol{u}}(t)-\hat{\boldsymbol{u}}(0)]^2\rangle \;=\; 2\left[1-\mathrm{e}^{-t/\tau_{\rm r}}\right] \to \begin{cases} 4D_0^{\rm r}\,t\,, & \tau_{\rm B}^{\rm r} \ll t \ll \tau_{\rm r} \\ 2\,, & t \gg \tau_{\rm r} \end{cases} \tag{16.67}$$

where $\tau_{\rm r} = 1/(2D_0^{\rm r})$ is the orientation relaxation time. The tip of $\hat{\boldsymbol{u}}(t)$ performs, for $t \ll \tau_{\rm r}$, a two-dimensional random walk on the tangential surface touching the unit sphere at $\hat{\boldsymbol{u}}_0$. The MSD saturates to 2 for times $t \gg \tau_{\rm r}$, since $|\hat{\boldsymbol{u}}(t)-\hat{\boldsymbol{u}}(0)| \le 2$ for all t. Typical values of $\tau_{\rm r}$ are $10^{-4}-10^{-3}\,$s which implies the following sequence of time scale separations

$$\tau_{\rm s} \ll \tau_\eta \approx \tau_{\rm B} \approx \tau_{\rm B}^{\rm r} \ll \tau_{\rm r} \tag{16.68}$$

valid for the translational/orientational self-diffusion of non-interacting globular particles.

16.3.2 Diffusion Mechanisms in Concentrated Colloidal Systems

While the diffusion of a non-interacting sphere is completely described by its MSD, which is linear in time in the diffusive time regime $t \gg \tau_{\rm B}$, various

diffusion processes have to be distinguished in non-dilute dispersions of interacting colloidal spheres. These diffusion processes are controlled by different diffusion coefficients which become equal to each other only in the dilute limit when the sphere interactions can be ignored. The spheres influence each other indirectly through the solvent flow field in which they move. These so-called hydrodynamic interactions (HI) propagate on a time scale $\tau_\eta \approx \tau_\mathrm{B}$, so that they act quasi-instantaneously on the diffusive time scale where the fast momentum relaxations of the spheres are not resolved any more. HI affects the sphere dynamics but not the equilibrium microstructure, since as dissipative forces they are not describable in terms of an interaction potential. In addition to the HI, the spheres can have potential interactions with each other through excluded volume, van der Waals and screened electrostatic forces. These direct forces become operative on the interaction time scale τ_I, which is the time after which a particle experiences a substantial change of the potential interactions through a perceptible change in its next neighbor sphere configuration. Very roughly, τ_I can be estimated for a fluid-like suspension as the time needed for a sphere to diffuse across its own radius, viz.

$$\tau_\mathrm{I} \approx \frac{a^2}{D_0}\,, \tag{16.69}$$

with typical values of $10^{-4} - 10^{-3}\,\mathrm{s}$. The short-time regime $\tau_\mathrm{B} \ll t \ll \tau_\mathrm{I}$, for DLS is thus well separated from the long-time regime $t \gg \tau_\mathrm{I}$.

Self-Diffusion

For short times $\tau_\mathrm{B} \ll t \ll \tau_\mathrm{I}$, a sphere diffuses only over a distance small as compared to its own size, and the dynamic "cage" of neighboring spheres has thus hardly changed (as sketched in Fig. 16.4a). The sphere diffuses then, on the average, in a potential minimum of the neighboring particles and is thus influenced only by the instantaneously acting HI. A linear increase

$$W(t) \;=\; D_\mathrm{s}^\mathrm{s}\, t \;\;,\;\; \tau_\mathrm{B} \ll t \ll \tau_I \tag{16.70}$$

of the MSD is thus observed at short times, with a *short-time* self-diffusion coefficient, D_s^s, smaller than the Stokesian diffusion coefficient, D_0, at infinite

Fig. 16.4. Schematic view of a particle cage around a colloidal sphere for (a) short times $\tau_\mathrm{B} \ll t \ll \tau_\mathrm{I}$ and (b) long times $t \gg \tau_\mathrm{I}$.

dilution, owing to the slowing influence of HI. Note that the subscript s in $D_{\rm s}^{\rm s}$ stands for "self" and the superscript for "short". At intermediate times $t \approx \tau_{\rm I}$, the cage becomes distorted from its equilibrium spherical symmetry and the sphere experiences an additional hindrance by potential forces. The cage distortion implies a sub-linear time dependence of $W(t)$. For long times $t \gg \tau_{\rm I}$, a sphere has experienced many independent collisions with neighboring spheres, as sketched in Fig. 16.4b.

This leads again to a linear time-dependence of $W(t)$

$$W(t) \;=\; D_{\rm s}^{\rm l}\, t \;\;,\;\; t \gg \tau_I \;, \tag{16.71}$$

but with a *long-time* self-diffusion coefficient, $D_{\rm s}^{\rm l}$, smaller than the short-time one. Summarizing,

$$0 \leq D_{\rm s}^{\rm l} \leq D_{\rm s}^{\rm s} \leq D_0 \;, \tag{16.72}$$

and one can show that this ordering is valid independent of the type of potential interactions. All three diffusion coefficients are equal to D_0 in the absence of interactions only, whereas $D_{\rm s}^{\rm l}$ is substantially smaller than D_0 for strongly interacting particles. On approach of a glass-transition point, a particle gets eventually trapped in its next-neighbor cage, with a complete blocking of its long-range motion characterized by $D_{\rm s}^{\rm l} \approx 0$ (idealized glass transition scenario). In contrast, $D_{\rm s}^{\rm s} > 0$ since a sphere in a glass can still perform short-time Brownian motion within its cage.

Using (16.37), $D_{\rm s}^{\rm l}$ can be expressed as a Green-Kubo relation

$$D_{\rm s}^{\rm l} \;=\; \int_0^\infty {\rm d}t\; \phi_v(t) \tag{16.73}$$

i.e. in form of a time integral over the VAF. On the coarse-grained level $t \gg \tau_{\rm B}$, the VAF

$$\phi_v(t) \;=\; 2D_{\rm s}^{\rm s}\delta(t) \;-\; \Delta\phi_v(t) \tag{16.74}$$

of interacting spheres consists of a singular part proportional to $D_{\rm s}^{\rm s}$, such that (16.70) is retained from (16.37), and a long-lived negative part, $-\Delta\phi_v(t)$, originating from particle interactions (caging). One can show that $\Delta\phi_v(t) > 0$ and $({\rm d}/{\rm d}t)\Delta\phi_v(t) < 0$, consistent with $D_{\rm s}^{\rm l} < D_{\rm s}^{\rm s}$. The regular part of the VAF is thus negative and increases strictly monotonically towards its final value zero. As one expects intuitively, the collective retarding effect of neighboring spheres leads to anti-correlations in the particle velocity. The positive-valued singular part in the VAF is the residual of the fast initial decay of velocity correlations mediated through the intervening solvent, and manifests itself as a δ-function for $t \gg \tau_{\rm B}$ (see Fig. 16.5).

Substitution of (16.74) in (16.37) gives

$$W(t) \;=\; D_{\rm s}^{\rm l} t + \tau_{\rm m}\left(D_{\rm s}^{\rm s} - D_{\rm s}^{\rm l}\right) - \int_t^\infty {\rm d}u(u-t)\Delta\phi_v(u)\,, \tag{16.75}$$

where

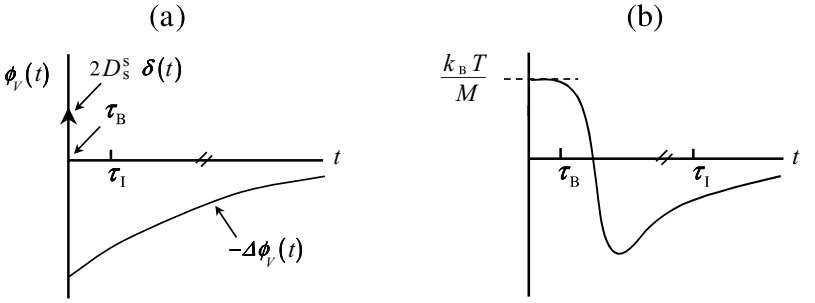

Fig. 16.5. Schematic VAF in (a) the diffusive regime $t \gg \tau_{\rm B}$, and (b) at very short times so that the initial δ-peak is resolved.

$$\tau_{\rm m} \equiv \frac{\int_0^\infty {\rm d}t\ t\ \Delta\phi_v(t)}{\int_0^\infty {\rm d}t\ \Delta\phi_v(t)} \tag{16.76}$$

is the mean relaxation time of $\Delta\phi_v(t)$. It is roughly comparable to $\tau_{\rm I}$. The last term on the right-hand side of (16.75) is the difference between $W(t)$ and its long-time asymptote. The asymptote crosses the vertical axis at the point $\tau_{\rm m}\left(D_{\rm s}^{\rm s} - D_{\rm s}^{\rm l}\right)$. A remarkable feature of $W(t)$ is that the approach towards its long-time form in (16.71) is very slow. In three dimensions, the VAF of a suspension of hard colloidal spheres has a negative long-time tail [14]

$$\phi_v(t) \ = \ -\Delta\phi_v(t) \ \approx -A\left(\frac{t}{\tau_{\rm m}}\right)^{-5/2} \ , \ t \gg \tau_{\rm m} \tag{16.77}$$

with an amplitude $A > 0$ that depends on the sphere concentration. The MSD for large t is consequently

$$W(t) \ \approx \ D_{\rm s}^{\rm l} t + \tau_{\rm m}\left(D_{\rm s}^{\rm s} - D_{\rm s}^{\rm l}\right)\left[1 - \left(\frac{t}{\tau_{\rm l}}\right)^{-1/2}\right] + \mathcal{O}(t^{-1})\,, \tag{16.78}$$

where $\tau_{\rm l}$ is a typical time scale related to $\tau_{\rm m}$. Fig. 16.6 displays a sketch of a three-dimensional MSD.

The relaxation of the VAF becomes extremely slow in two dimensions where $\phi_v(t)$ decays asymptotically as t^{-2} for all concentrations, independent of the nature of the interactions. Therefore, the two-dimensional MSD includes a logarithmic long-time correction [15]

$$W(t) \ \approx \ D_{\rm s}^{\rm l} t + \tau_{\rm m}\left(D_{\rm s}^{\rm s} - D_{\rm s}^{\rm l}\right)\ln\left(\frac{t}{\tau_{\rm l}}\right) + \mathcal{O}(1) \tag{16.79}$$

with diffusion coefficients and decay times different from the three-dimensional case. We emphasize that the negative VAF long-time tails discussed above are due to configurational rearrangements of interacting spheres, and they should not be confused with the positive long-time tail in (16.50). The latter

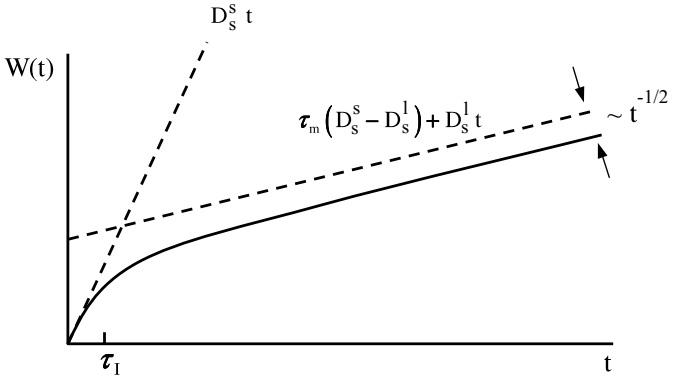

Fig. 16.6. Mean square displacement in three dimensions (for $t \gg \tau_{\rm B}$).

is due to unsteady solvent flow around a sphere in isolation, and appears on a much shorter time scale $t \approx \tau_\eta$.

The long-time decay of the VAF in one dimension is proportional to $-t^{-(d+2)/2}$, with d specialized to one. For particles diffusing along an infinite line which are not allowed to pass each other (single-filing condition) there is, however, a subtle difference to diffusion in higher dimensions. Due to the strong mutual hindrance of particles moving along a line the MSD at long times grows only proportional to $t^{1/2}$. Without HI, the MSD reads thus explicitly [16]

$$W(t) \;\to\; \begin{cases} 2D_0 t\,, & \tau_{\rm B} \ll t \ll \tau_{\rm I} \\ \dfrac{1}{n}\left(\dfrac{4D_0 t}{\pi}\right)^{1/2}, & t \gg \tau_{\rm I} \end{cases} \tag{16.80}$$

with n denoting the line density of particles and interaction time $\tau_{\rm I} = 1/(D_0 n^2)$. It is most likely that only the pre-factor of $t^{1/2}$ will be affected when HI is included. The long-time limiting form of the pdf, $P(x,t)$, for a particle displacement x during time t is given by the Gaussian form in (16.40) for $d = 1$, with $W(t)$ according to (16.80) for $t \gg \tau_{\rm I}$. The absence of a linear long-time term in $W(t)$ implies a vanishing long-time self-diffusion coefficient for an infinite line. Single-file diffusion can be observed, e.g., in superionic conduction, in diffusion of bio-molecules through narrow-sized channels in membranes and in zeolites of one-dimensional channel structure (cf., e.g., Chap. 10, Fig. 10.7, and Chap. 18, (18.107)).

Self-diffusion coefficients can be measured by scattering experiments or by means of specialized techniques that use fluorescently labelled spheres (which will be discussed separately later in this chapter). To measure self-diffusion over an extended time range the system now consists of a possibly concentrated suspension of host spheres, with a few tracer spheres, such that the tracer spheres do not mutually interact with each other. The system

must be prepared such that the scattered intensity from the host particles and the solvent molecules can be neglected against that of the tracer particles. As explained in Sect. 16.2.2, the measured EACF is proportional to the self-dynamic structure factor $S_\mathrm{s}(q,t)$ defined in (16.27), provided tracer and host spheres are different from each other only in terms of their scattering properties.

The self-dynamic structure factor may be expanded in a Taylor series for small wavevectors,

$$S_\mathrm{s}(q,t) \;=\; 1 - \frac{1}{6} q^2 \left\langle |\, \boldsymbol{r}(t=0) - \boldsymbol{r}(t) \,|^2 \right\rangle + \mathcal{O}(q^4) \;, \tag{16.81}$$

meaning that

$$S_\mathrm{s}(q,t) \;=\; \exp\{-q^2 W(t)\} \left[1 + \mathcal{O}(q^2)\right] \;. \tag{16.82}$$

There is a time-dependent non-Gaussian correction of $\mathcal{O}(q^2)$ to $S_\mathrm{s}(q,t)$ originating from particle interactions. This correction is rather small for a fluid-like suspension and becomes zero when the small-q limit is considered. Equation (16.82) allows for measuring the full time-dependence of the MSD. To this end, $-\ln\{S_\mathrm{s}(q,t)\}/q^2$ is plotted for a given time t against q^2, and linearly extrapolated to $q = 0$. The intercept is equal to $W(t)$. Such data obtained from dynamic light scattering experiments on hard-sphere suspensions are given in Fig. 16.7, for various volume fractions [17]. The cross-over from short- to long-time behavior is clearly seen. Further note the diminishing difference between the short- and long-time self-diffusion coefficients when the concentration is decreased.

At infinite dilution, $D_\mathrm{s}^\mathrm{s} = D_0$, $W(t) = D_0 t$ and

$$S_\mathrm{s}(q,t) \;=\; \exp\{-q^2 D_0 t\} \,, \tag{16.83}$$

which is the dynamic structure factor describing the single-particle diffusion of independent particles.

Collective Diffusion

In contrast to self-diffusion, which is the Brownian motion of a tagged particle in a sea of others, collective diffusion refers to the isothermal relaxation of density gradients by the coordinated motion of many colloidal particles. Imagine a colloidal system where the density of colloidal particles, at some instant in time, varies sinusoidally (such a sinusoidal density profile is referred to as a density wave or density mode). That is, at time $t = 0$ say, the number density $\overline{\rho}(\boldsymbol{r}, t=0)$ at position $\boldsymbol{r}$ is equal to

$$\overline{\rho}_q(\boldsymbol{r}, t=0) \;=\; \rho_0 + \overline{\rho}(\boldsymbol{q}, t=0)\, \sin\{\boldsymbol{q}\cdot\boldsymbol{r}\} \tag{16.84}$$

with $\rho_0 = N/V$ the average number density, and $\overline{\rho}(\boldsymbol{q}, t=0)$ the amplitude of the density wave. The bar indicates an ensemble average over a

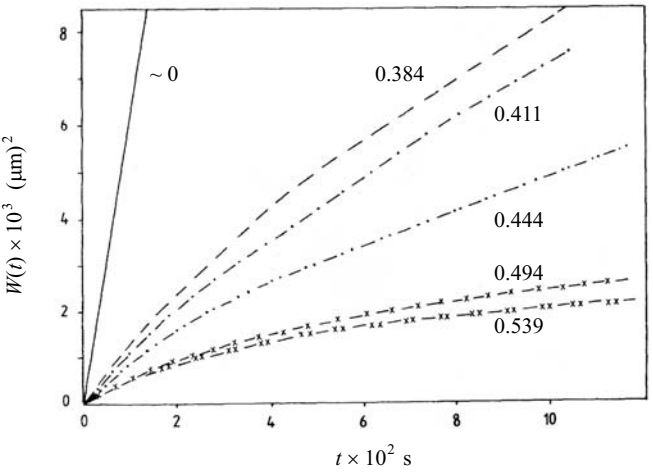

Fig. 16.7. Mean square displacement $W(t)$ of silica tracer spheres in an index-matched host suspension of PMMA spheres (of same size as the silica particles). The curves are labelled by volume fraction Φ. The last two volume fractions represent the co-existing fluid ($\Phi_{\rm freez} = 0.494$) and crystalline ($\phi_{\rm melt} = 0.539$) phases. After [17].

non-equilibrium initial particle distribution. The wavevector $\boldsymbol{q}$ determines both the direction and the wavelength of the sinusoidal density variation. For changes of the position $\boldsymbol{r}$ in the suspension perpendicular to $\boldsymbol{q}$, the phase of the sine function does not change, so that the direction of $\boldsymbol{q}$ is in the "propagation direction" of the sinusoidal variation. A change $\Delta\boldsymbol{r}$ of the position $\boldsymbol{r}$ parallel to $\boldsymbol{q}$ leaves the sine function unchanged when $|\,\Delta\boldsymbol{r}\,| = m \times 2\pi/q$, with m an arbitrary integer. Hence, the wavelength of the density variation is

$$\Lambda \;=\; 2\pi/q\,. \tag{16.85}$$

The density wave will relax away to the homogeneous state due to the collective motion of particles. In the initial stage of relaxation (i.e. for $\tau_{\rm B} \ll t \ll \tau_{\rm I}$), the decay of the density wave is single-exponential in time. At a later stage ($t \approx \tau_{\rm I}$) the decay becomes non-exponentially and slower than initially as a result of interactions between the colloidal particles. In the final long-time regime ($t \gg \tau_{\rm I}$), the density variation may decay once again exponentially in time for selected values of q, however with a decay rate that is usually smaller than the initial one. For a density wave of large amplitude, different wavelengths come into play at a later stage and its shape is then no longer sinusoidal. Long-time collective diffusion describes the final stage of relaxation of a density wave, where the density profile generally strongly deviates from a sinusoidal profile.

A phenomenological description of the relaxation of density waves can be accomplished by using what is known as generalized hydrodynamics. The starting point in a generalized hydrodynamic description is the continuity

equation

$$\frac{\partial}{\partial t}\,\overline{\rho}(\boldsymbol{r},t) \;=\; -\nabla\cdot\overline{\boldsymbol{j}}(\boldsymbol{r},t)\;, \tag{16.86}$$

which relates the particle density to the particle flux density, $\overline{\boldsymbol{j}}(\boldsymbol{r},t)$, and it expresses the conservation of the number of particles. The overbar indicates an average over a non-equilibrium ensemble. The flux density $\overline{\boldsymbol{j}}(\boldsymbol{r},t)$ denotes the number of colloidal particles that cross the point $\boldsymbol{r}$ in the direction in which $\overline{\boldsymbol{j}}$ points, per unit area and unit time.

For small amplitudes in the density variation, and close to thermal equilibrium, the flux is linearly related to gradients in the density, that is (note that at time $t = 0$ relaxation begins)

$$\overline{\boldsymbol{j}}(\boldsymbol{r},t) \;=\; -\int \mathrm{d}\boldsymbol{r}' \int_0^t \mathrm{d}t'\, \boldsymbol{D}_{\mathrm{c}}(\boldsymbol{r}-\boldsymbol{r}',t-t')\cdot\nabla'\overline{\rho}(\boldsymbol{r}',t')\;, \tag{16.87}$$

where the integral kernel tensor $\boldsymbol{D}_{\mathrm{c}}(\boldsymbol{r},t)$ is referred to as the real-space collective diffusion kernel. This phenomenological expression can be interpreted as the leading term in an expansion of the flux $\overline{\boldsymbol{j}}$ with respect to the amplitude of density gradients. The "Taylor coefficient" $\boldsymbol{D}_{\mathrm{c}}$ is independent of the magnitude of gradients whenever these are sufficiently small. Density modes of different wave numbers decay then independently from each other due to linearity in $\overline{\rho}(\boldsymbol{r},t)$. The non-local space and time dependence of $\overline{\boldsymbol{j}}$ on $\nabla\overline{\rho}$ can be understood as follows. The flux at a point $\boldsymbol{r}$ can depend on density gradients at another point $\boldsymbol{r}'$, through interactions between the spheres. Hence, $\boldsymbol{D}_{\mathrm{c}}(\boldsymbol{r}-\boldsymbol{r}',t-t') = 0$ when $|\,\boldsymbol{r}-\boldsymbol{r}'\,| \gg R_I$, where R_I is a measure for the distance over which colloidal particles are correlated. Moreover, the flux at time t can depend on $\nabla\overline{\rho}$ at earlier times, due to the finite time it takes interactions to propagate. Such time-delayed effects are commonly referred to as memory effects. As a consequence, $\boldsymbol{D}_{\mathrm{c}}(\boldsymbol{r}-\boldsymbol{r}',t-t') = 0$ when $t-t' \gg \tau_I$. Note that causality requires that $\boldsymbol{D}_{\mathrm{c}}(\boldsymbol{r},t) = 0$ whenever $t < 0$. The diffusion kernel is a tensor since flux and density gradient may not be collinear. Spatial isotropy requires further that $\boldsymbol{D}_{\mathrm{c}}(\boldsymbol{r},t) = \boldsymbol{D}_{\mathrm{c}}(|\boldsymbol{r}|,t)$. The so-called non-local Fickian law in (16.87) is valid on a mesoscopically coarse-grained level of spatial resolution $\sim (D_0\tau_{\mathrm{I}})^{1/2}$ and time resolution $\sim \tau_{\mathrm{I}}$.

Spatial Fourier transformation of (16.86) with the use of (16.87) leads to

$$\frac{\partial}{\partial t}\,\overline{\rho}(\boldsymbol{q},t) \;=\; -q^2 \int_0^t \mathrm{d}t'\, D_{\mathrm{c}}(q,t-t')\,\overline{\rho}(\boldsymbol{q},t')\;. \tag{16.88}$$

where $D_{\mathrm{c}}(q,t) = \hat{\boldsymbol{q}}\cdot\boldsymbol{D}_{\mathrm{c}}(q,t)\cdot\hat{\boldsymbol{q}}$ is the longitudinal part (parallel to $\boldsymbol{q}$) of the Fourier transform of the diffusion kernel, and $\hat{\boldsymbol{q}} = \boldsymbol{q}/q$. For notational brevity we use the same symbols for the original and Fourier transformed functions, where their argument (either $\boldsymbol{r}$ or $\boldsymbol{q}$) indicates which function is meant. Spatial isotropy requires the Fourier transform of $\boldsymbol{D}_{\mathrm{c}}(\boldsymbol{r},t)$ to depend only on the magnitude q of the wavevector $\boldsymbol{q}$. We learn from (16.88) that

the time rate of change of a density mode becomes increasingly slow with decreasing wavenumber, since particles need to diffuse over an increasingly large distance $\Lambda = 2\pi/q$ to smooth out density variations.

According to the definition of the collective dynamic structure factor, we find from (16.88) (using that the non-equilibrium average density $\overline{\rho}$ satisfies near equilibrium the same linear equation of motion as the equilibrium density autocorrelation function, which is known as an application of Onsager's hypothesis) that

$$\frac{\partial}{\partial t} S_{\rm c}(q,t) \;=\; -\,q^2 \int_0^t {\rm d}t'\, D_{\rm c}(q,t-t') S_{\rm c}(q,t') \;. \tag{16.89}$$

The solution of this equation for $S_{\rm c}$ can be formulated in terms of time-Laplace transforms. The Laplace transform of a function f is defined as

$$f(z) \;\equiv\; \int_0^\infty {\rm d}t\, f(t)\, \exp\{-zt\} \;. \tag{16.90}$$

In terms of such Laplace transforms, the solution of (16.89) reads

$$S_{\rm c}(q,z) \;=\; \frac{S_{\rm c}(q)}{z + q^2\, D_{\rm c}(q,z)} \tag{16.91}$$

with a wavenumber and frequency (i.e. z) dependent collective diffusion kernel $D_{\rm c}(q,z)$. As explained above, the q-dependence of $D_{\rm c}(q,z)$ describes the coupling between the colloidal particle flux at a certain point with density gradients at other points. The z-dependence of $D_{\rm c}$ describes memory effects, that is, the coupling between the flux at a certain time with density gradients that existed at earlier times. For strongly interacting particles memory effects give rise to a complicated time-dependence of $S_{\rm c}(q,t)$, characterized by a whole spectrum of relaxation times. The collective dynamic structure factor (as well as $S_{\rm s}(q,t)$) is a strictly monotonically decaying function in time, for fixed q, with negative slope $({\rm d}/{\rm d}t)S_{\rm c}(q,t) < 0$. This exemplifies an important rule stating that any autocorrelation function is strictly monotonically decaying in time when described within the overdamped colloid dynamics, i. e., for $t \gg \tau_{\rm B}$ [18]. It follows readily that $S_{\rm c}(q,z) > 0$ and $zS_{\rm c}(q,z) < S(q)$. These inequalities in turn imply with (16.91) that $D_{\rm c}(q,z)$ and its associated collective diffusion coefficients are all non-negative, as one expects on physical grounds. For fixed t, $S_{\rm c}(q,t)$ shows damped oscillations in q. A typical q-dependence of $S_{\rm c}(q,t)$ at various t is illustrated in Fig. 16.8, which shows theoretical and computer simulation results of $S_{\rm c}(q,t)$ for a suspension of charge-stabilized colloidal spheres.

There exists a special regime where (16.91) predicts an exponential decay of $S_{\rm c}(q,t)$. In this so-called hydrodynamic regime, only density wave relaxations are resolved with a wavelength much larger than R_I (typically ~ 1 mm), and with a time resolution that is much larger than τ_I (typically $\sim$

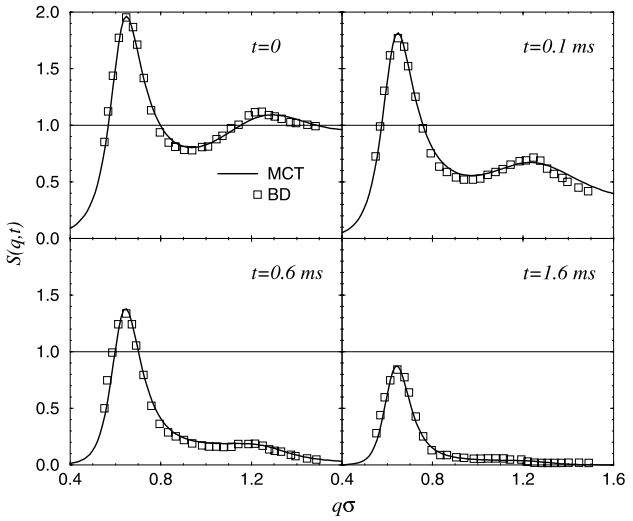

Fig. 16.8. Collective dynamic structure factor of a charge-stabilized colloidal dispersion. Open squares: Brownian dynamics (BD) computer simulations (from [19]); solid line: Mode coupling theory (MCT) result.

1 s). On this strongly coarse-grained level, one can neglect non-local spatial dependencies and memory effects. The collective diffusion kernel is then equal to

$$\boldsymbol{D}_{\mathrm{c}}(\boldsymbol{r}-\boldsymbol{r}',t-t') \;=\; D_{\mathrm{c}}^{\mathrm{l}}\;\mathbf{1}\;\delta(\boldsymbol{r}-\boldsymbol{r}')\;\delta(t-t')\;. \tag{16.92}$$

The coefficient $D_{\mathrm{c}}^{\mathrm{l}}$ is independent of position and time when the amplitude of the density profile is sufficiently small. Hence, from (16.87),

$$\overline{\boldsymbol{j}}(\boldsymbol{r},t) \;=\; -D_{\mathrm{c}}^{\mathrm{l}}\;\nabla\,\overline{\rho}(\boldsymbol{r},t)\;, \tag{16.93}$$

which is Fick's local law of macroscopic gradient diffusion. $S_{\mathrm{c}}(q,t)$ and the associated density wave $\overline{\rho}_q(\boldsymbol{r},t)$ in (16.84) decay thus exponentially, for $q \ll {R_{\mathrm{I}}}^{-1}$ and $t \gg \tau_{\mathrm{I}}$, according to

$$S_{\mathrm{c}}(q,t) = S_{\mathrm{c}}(q)\;\exp\{-q^2 D_{\mathrm{c}}^{\mathrm{l}} t\} \tag{16.94}$$

and

$$\overline{\rho}_q(\boldsymbol{r},t) = \rho_0 + \exp\{-q^2 D_{\mathrm{c}}^{\mathrm{l}} t\}\;\overline{\rho}(\boldsymbol{q},t=0)\sin\{\boldsymbol{q}\cdot\boldsymbol{r}\} \tag{16.95}$$

respectively, where $S_{\mathrm{c}}(q) = S_{\mathrm{c}}(q,t=0)$ is the static structure factor. The correlation length R_{I} can be roughly estimated by $1/q_{\mathrm{m}}$, where q_{m} is the wave number where the static structure factor attains its principal maximum. The average extension of the next-neighbor cage around a sphere is roughly equal to $2\pi/q_{\mathrm{m}}$. The local microstructure around a sphere is not resolved in the hydrodynamic limit. This means that $S_{\mathrm{c}}(q \ll q_{\mathrm{m}})$ in (16.94) is practically equal to the long-wavelength limit

$$S_{\rm c}(0) \equiv \lim_{q\to 0} S_{\rm c}(q) = \rho_0 k_{\rm B}T\chi_T \quad \text{with } \chi_T = \frac{1}{\rho_0}\left(\frac{\partial\rho_0}{\partial p}\right)_T , \qquad (16.96)$$

where, for a one-component suspensions, χ_T is the isothermal *osmotic* compressibility of colloidal spheres.

The transport coefficient $D_{\rm c}^{\rm l}$ is referred to as the long-time collective or gradient diffusion coefficient, since it can be determined, e.g., from macroscopic gradient diffusion experiments near equilibrium. Note here that (16.94) is equivalent to

$$S_{\rm c}(q,z) = \frac{S_{\rm c}(0)}{z + q^2\, D_{\rm c}^{\rm l}} . \qquad (16.97)$$

which shows with (16.91) that $D_{\rm c}^{\rm l}$ is equal to the small-wavenumber and small-frequency (i.e. long-time) limit of the collective diffusion kernel. Explicitly

$$D_{\rm c}^{\rm l} = \lim_{z\to 0}\ \lim_{q\to 0} D_{\rm c}(q,z) , \qquad (16.98)$$

where q^2/z (i.e. $q^2 t$) is kept fixed to a value of order one. The long-time (i.e. zero-frequency) limit $t\to\infty$ (i.e. $z\to 0$) means in physical terms that $t \gg \tau_{\rm I}$ (i.e. $z \ll \tau_{\rm I}^{-1}$). Likewise, the short-time (infinite-frequency) limit $t\to 0$ ($z\to\infty$) should be interpreted as $\tau_{\rm B} \ll t \ll \tau_{\rm I}$ (${\tau_{\rm I}}^{-1} \ll z \ll \tau_{\rm B}^{-1}$).

As a phenomenological approach, generalized hydrodynamics provides no methods to predict the collective diffusion kernel $D_{\rm c}(q,z)$ and its associated long-time diffusion coefficient $D_{\rm c}^{\rm l}$. An actual calculation of $D_{\rm c}(q,z)$ can be accomplished only on the basis of a microscopic theory that relies on a many-sphere extension of the single-particle diffusion equation (16.45) as the appropriate time evolution equation. A microscopic theory of diffusion will be discussed in Sect. 16.5. We will address here only general features of collective diffusion.

At short times, $\tau_{\rm B} \ll t \ll \tau_{\rm I}$, memory effects are not felt yet and

$$S_{\rm c}(q,t) = S_{\rm c}(q)\exp\{-q^2 D_{\rm c}^{\rm s}(q)t\} , \qquad (16.99)$$

i. e. there is an exponential short-time decay of $S_{\rm c}(q,t)$ for all q. We recall that short-time collective diffusion relates to the initial stage of relaxation of a density wave, where it still retains its original form, but just has decreased its amplitude. This process is described by a wavenumber-dependent (i.e. apparent) diffusion coefficient $D_{\rm c}^{\rm s}(q) = D_{\rm c}(q, z\to\infty)$ which quantifies the initial de-correlation of density modes of wavenumber q. Equation (16.99) and the monotonicity of $S_{\rm c}(q,t)$ imply that the longitudinal collective diffusion kernel in (16.89) is decomposable as [18, 20]

$$D_{\rm c}(q,t) = 2D_{\rm c}^{\rm s}(q)\delta(t) - \Delta D_{\rm c}(q,t) , \qquad (16.100)$$

corresponding to

$$\frac{\partial}{\partial t}S_{\rm c}(q,t) = -q^2\, D_{\rm c}^{\rm s}(q)S_{\rm c}(q,t) + q^2 \int_0^t {\rm d}t'\, \Delta D_{\rm c}(q,t-t')S_{\rm c}(q,t') , \qquad (16.101)$$

with a memory function contribution $\Delta D_{\rm c}(q,t) \geq 0$. The non-local memory effect on density relaxations inherent in $\Delta D_{\rm c}(q,t)$ is operative only for times exceeding the short-time regime, and it causes a slower and, in general, non-exponential decay of $S_{\rm c}(q,t)$.

The short-time collective diffusion coefficient is defined as the zero-q limit of the apparent diffusion coefficient

$$D_{\rm c}^{\rm s} \;=\; \lim_{q\to 0} D_{\rm c}^{\rm s}(q)\,, \tag{16.102}$$

and relates to the long-time collective diffusion coefficient through

$$D_{\rm c}^{\rm l} \;=\; D_{\rm c}^{\rm s} - \lim_{q\to 0} \int_0^\infty {\rm d}t\, \Delta D_{\rm c}(q,t)\;. \tag{16.103}$$

The collective diffusion coefficients obey thus the same ordering

$$D_{\rm c}^{\rm l} \;\leq\; D_{\rm c}^{\rm s} \tag{16.104}$$

as the short-time and long-time self-diffusion coefficients. The coefficient $D_{\rm c}^{\rm l}$ quantifies the relaxation of constant density gradients over times $t \gg \tau_{\rm I}$, through cooperative diffusion of spheres opposite to the gradient direction $\hat{\boldsymbol{q}}$. Therefore $D_{\rm c}^{\rm l}$ is intimately related to the average sedimentation velocity, $U^{\rm l}$, as measured in a homogeneous suspension of slowly sedimenting colloidal spheres. To understand this explicitly, consider a homogeneous suspension of equal spheres in a closed vessel which sediment slowly (so that $Pe \equiv U^{\rm l}a/D_0 \ll 0$) under the influence of a constant force of buoyancy $\boldsymbol{F} = F\hat{\boldsymbol{q}}$. This force acting on each sphere drives a sedimentation flux

$$\boldsymbol{j}_{\rm s} \;=\; \rho_0\, U^{\rm l}\, \hat{\boldsymbol{q}}\,. \tag{16.105}$$

At equilibrium, the small concentration gradient, $\nabla\overline{\rho}$, thereby generated will produce an equal, but opposite diffusive flux, $\boldsymbol{j}_{\rm d}$, so that

$$0 \;=\; \boldsymbol{j}_{\rm s} + \boldsymbol{j}_{\rm d} \;=\; \rho_0\, U^{\rm l}\, \hat{\boldsymbol{q}} - D_{\rm c}^{\rm l}\, \nabla\overline{\rho}\,. \tag{16.106}$$

The force on the solvent exerted by the sedimenting particles is balanced through a pressure gradient, $\nabla p = \rho_0 \boldsymbol{F}$, generated by the base of the vessel (which is perpendicular to $\hat{\boldsymbol{q}}$). The pressure gradient drives a back-flow of solvent such that the zero-volume-flux condition is fulfilled: due to incompressibility, the net volume flux of solvent and spheres through any plane perpendicular to $\hat{\boldsymbol{q}}$ is zero. The concentration gradient (at constant temperature and chemical potential) follows next from

$$\nabla\overline{\rho} \;=\; \left(\frac{\partial\rho_0}{\partial p}\right)_{T,\,\mu_{\rm s}} \nabla p \;=\; \beta S_{\rm c}(0)\rho_0 F\, \hat{\boldsymbol{q}}\,. \tag{16.107}$$

Finally, substitution into (16.106) leads to the general relation [21, 22]

$$D_{\rm c}^{\rm l} \;=\; \frac{D_0}{S_{\rm c}(0)}\,\frac{U^{\rm l}}{U_0} \tag{16.108}$$

between $D_{\rm c}^{\rm l}$ and $U^{\rm l}$, where $U_0 = \beta D_0 F$ is the sedimentation velocity at infinite dilution. Equation (16.108) can be derived more rigorously from linear response theory, which provides us further with a microscopic expression for $D_{\rm c}^{\rm l}$.

Very interestingly, the configurational pdf of identical colloidal spheres is not distorted from the equilibrium distribution during sedimentation, as long as HI between spheres can be considered as pairwise additive. This holds true for dilute monodisperse suspensions. The long-time sedimentation velocity $U^{\rm l}$, which is measured in standard sedimentation experiments, becomes then equal to the short-time sedimentation velocity $U^{\rm s}$. The latter is related to the short-time collective diffusion coefficient once again by (16.108), with l replaced by s. Consequently

$$D_{\rm c}^{\rm l} \;=\; D_{\rm c}^{\rm s} \tag{16.109}$$

for pairwise-additive HI. There is thus no distinction between short-time and long-time collective diffusion, which corresponds to a vanishing memory contribution to $D_{\rm c}^{\rm l}$ in (16.103). A density wave retains its sinusoidal shape during the entire process of relaxation whenever the wavelength is much larger than the correlation length R_I. This result is in marked difference to self-diffusion where the long-time self-diffusion coefficient of interacting particles is substantially smaller than the short-time one even when HI is totally disregarded.

Three-body or more-body HI become highly relevant for concentrated dispersions. In these systems, their effect is to distort the suspension microstructure from the initial equilibrium distribution for times $t \sim \tau_{\rm I}$, which causes additional hindrance of particle motion. For $t \gg \tau_{\rm I}$, a new steady-state distribution has been reached, accompanied by a small decrease in the sedimentation velocity such that $U^{\rm l} < U^{\rm s}$ and $D_{\rm c}^{\rm l} < D_{\rm c}^{\rm s}$. Recent calculations for dense hard-sphere suspensions have revealed, however, that the differences between $D_{\rm c}^{\rm l}$ and $D_{\rm c}^{\rm s}$ are quite small (less than 6%), which makes them difficult to detect using DLS [23].

DLS and small-angle quasielastic neutron scattering experiments on colloidal particles which scatter equally strongly, are convenient and widely used tools to determine $S_{\rm c}(q,t)$ over an extended range of times and wave numbers. These methods allow one to study in detail relaxation of density waves for a wavelength set by the experimental scattering angle. The short-time and long-time collective diffusion coefficients can be extracted from linearly extrapolating $-\ln\{S_{\rm c}(q,t)\}/q^2$, measured for fixed $t \ll \tau_{\rm I}$ and $t \gg \tau_{\rm I}$, respectively, to $q = 0$. The sedimentation velocity derives then from (16.108) when in addition $S_{\rm c}(q \ll q_{\rm m})$ is determined by static light scattering.

In dispersions of strongly repelling particles, $D_{\rm c}^{\rm s}$ and $D_{\rm c}^{\rm l}$ can be substantially larger than the Stokesian diffusion coefficient D_0. This feature is mainly

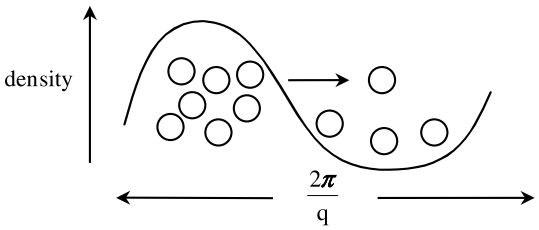

Fig. 16.9. Enhanced relaxation of density fluctuations through low osmotic compressibility.

due to the low osmotic compressibility (i.e. $S_c(0) \ll 0$), which acts as a thermodynamic force driving the relaxation of local density gradients (cf. Fig. 16.9).

A typical concentration dependence of D_c^s for a suspension of moderately charged colloidal spheres and for a suspension of uncharged hard spheres is shown in Fig. 16.10. Note that both $S_c(0)$ and U^s decrease with increasing volume fraction Φ of spheres (cf. (16.108)). At small volume fraction Φ, U^s decreases less strongly than $S_c(0)$ leading to an initial increase in D_c^s. With Φ further increasing, hydrodynamic hindrance starts to overcompensate the electrostatic particle repulsion so that D_c^s goes through a maximum. The maximum in $D_c^s(\phi)$ becomes smaller with increasing amount of added electrolyte, i.e. with enlarged screening of the electrostatic repulsion. While $D_s^s/D_0 \leq 1$ independent of the type of interactions, D_c^s/D_0 is found to be larger than one for repulsive pair interactions. For dispersions with attractive interaction contributions close to a critical point, however, $D_c^s/D_0 \approx 0$ due

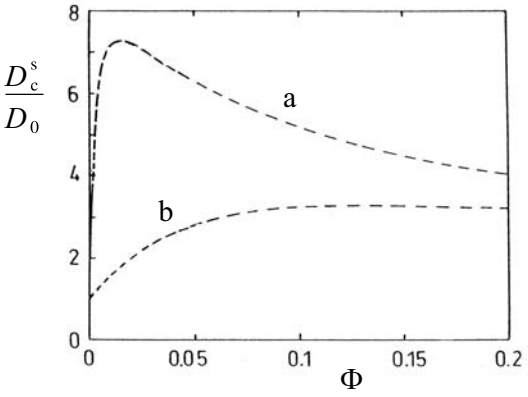

Fig. 16.10. Theoretical prediction for the (reduced) collective diffusion coefficient D_c^s/D_0 versus volume fraction, for typical aqueous solutions of weakly charged spherical micelles. Shown are two curves with (a) low amount and (b) moderately large amount of added electrolyte. After [18].

to the large osmotic compressibility of near-critical systems. The dynamics of such systems is thus very slow (critical slowing down).

On various places we have noted that, aside from small wavenumbers $q \ll q_\mathrm{m}$, $S_\mathrm{c}(q,t)$ decays in general non-exponentially in time. However, recent calculations of $S_\mathrm{c}(q,t)$ for concentrated suspensions with pronounced particle caging have revealed that the dynamic structure factor of these systems does decay exponentially for *long* times, for wavenumbers centered around q_m. The existence of such a collective long-time mode

$$S_\mathrm{c}(q_\mathrm{m},t) \propto \exp\{-q^2 D_\mathrm{c}^\mathrm{l}(q_\mathrm{m})t\}\,,\ t \gg \tau_\mathrm{I} \tag{16.110}$$

characterized by a collective long-time diffusion coefficient, $D_\mathrm{c}^\mathrm{l}(q_\mathrm{m})$, at the finite wave number q_m has been observed indeed in DLS experiments on concentrated suspensions of hard spheres. This peculiar mode describes the decay of concentration fluctuations linked to the average extension of a nearest neighbor cage. According to theory, the long-time mode ceases to exist when the volume fraction of hard spheres is reduced below 0.2. The caging effect is then too small and $S_\mathrm{c}(q_\mathrm{m},t)$ decays non-exponentially at long times.

The long-time coefficient $D_\mathrm{c}^\mathrm{l}(q_\mathrm{m})$ should be distinguished from the q-dependent *mean* collective diffusion coefficient, $\overline{D}_\mathrm{c}(q)$. The latter is defined as

$$\overline{D}_\mathrm{c}(q) \ \equiv\ D_\mathrm{c}(q,z=0) \ =\ D_\mathrm{c}^\mathrm{s}(q) - \int_0^\infty \mathrm{d}t \Delta D_\mathrm{c}(q,t)\,, \tag{16.111}$$

and is related to the mean relaxation time, $\overline{\tau}(q)$, of $S_\mathrm{c}(q,t)$ through

$$\overline{\tau}(q) \ \equiv\ \int_0^\infty \mathrm{d}t\, \frac{S_\mathrm{c}(q,t)}{S_\mathrm{c}(q)} \ =\ \frac{1}{q^2 \overline{D}_\mathrm{c}(q)}\,. \tag{16.112}$$

Contrary to $D_\mathrm{c}^\mathrm{l}(q)$, the coefficient $\overline{D}_\mathrm{c}(q)$ is not a true long-time diffusion coefficient although this has been erroneously claimed. If $D_\mathrm{c}(q,t)$ would decay sufficiently faster than $S_\mathrm{c}(q,t)$, the memory integral in (16.89) could then be de-convoluted for $t \gg \tau_\mathrm{I}$ as

$$\int_0^t \mathrm{d}t' D_\mathrm{c}(q,t-t')\ S_\mathrm{c}(q,t') \approx D_\mathrm{c}(q,z=0)\ S_\mathrm{c}(q,t)\,. \tag{16.113}$$

If this holds true then $\overline{D}_\mathrm{c}(q)$ would be a genuine long-time diffusion coefficient with $S_\mathrm{c}(q,t \gg \tau_\mathrm{I}) \propto \exp\{-q^2 \overline{D}_\mathrm{c}(q)t\}$. However, $D_\mathrm{c}(q,t)$ decays so slowly for finite q that the de-convolution is strictly valid only in the hydrodynamic limit, where $\overline{D}_\mathrm{c}(q)$ reduces to D_c^l. Contrary to $D_\mathrm{c}^\mathrm{l}(q)$ the mean collective diffusion coefficient is defined for any concentration and all values of q, even those where $S_\mathrm{c}(q,t)$ is non-exponential at long times. Note that the ordering relations

$$D_\mathrm{c}^\mathrm{s}(q) > \overline{D}_\mathrm{c}(q) > D_\mathrm{c}^\mathrm{l}(q) \tag{16.114}$$

are valid for the range of q and Φ where $D_\mathrm{c}^\mathrm{l}(q)$ exists. A comparison between the coefficients $D_\mathrm{c}^\mathrm{l}(q_\mathrm{m})$ and $\overline{D}_\mathrm{c}(q_\mathrm{m})$ of hard spheres, as predicted by theory, is

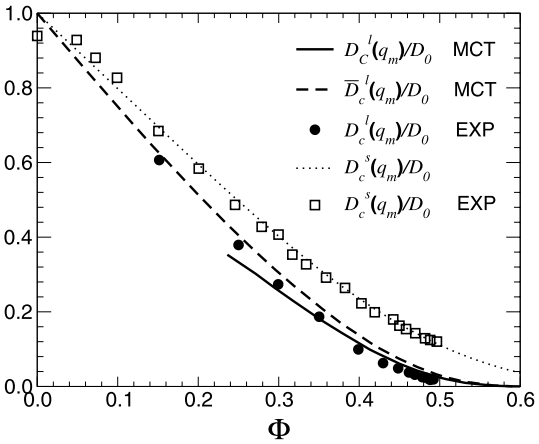

Fig. 16.11. Mode coupling theory (MCT) prediction (from [24]) for the concentration dependence of the collective long-time coefficient $D_{\rm c}^{\rm l}(q_{\rm m})$, and for the mean collective coefficient $\overline{D}_{\rm c}(q_{\rm m})$ of hard-sphere suspensions. The experimental data for $D_{\rm c}^{\rm l}(q_{\rm m})$ are from [25]. For comparison, we include experimental data (from [26]) for the short-time $D_{\rm c}^{\rm s}(q_{\rm m})/D_0$ with corresponding theoretical predictions from (16.213, 16.214).

made in Fig. 16.11. This figure includes also DLS data for $D_{\rm c}^{\rm l}(q_{\rm m})$ which agree well with theory. The difference between both coefficients is rather small over the complete range of volume fractions where $D_{\rm c}^{\rm l}(q_{\rm m})$ exists.

Interdiffusion

So far we have explored diffusion processes in one-component systems of identical particles, as far as the sizes and interaction properties are concerned. In colloidal mixtures, and of course also in atomic and polymer mixtures, an additional interdiffusion mechanism comes into play related to the relaxation of thermal fluctuations in the relative concentration of two components. For simplicity, we will discuss only the most simple case of interdiffusion in binary colloidal dispersions of spherical particles, and in a ternary incompressible melt of two homopolymer species mingled in a matrix of a third homopolymer species. We will address in particular the question whether the interdiffusion coefficient can be expressed alone in terms of the self-diffusion coefficients of both components.

The interdiffusion process mediates the relaxation of thermal fluctuations (under isothermal and isobaric conditions) in the relative particle (monomer) concentration of two components, say component 1 and 2, towards their equilibrium values. There might be additional components present but we focus here on the concentration exchange between components 1 and 2. The Fourier transform of the *incremental* microscopic number density of component $\alpha = 1, 2$, relative to its mean density $\rho_{\alpha 0} = N_\alpha / V_{\rm s}$, reads

$$\rho_\alpha(q,t) \;=\; \sum_{j=1}^{N_\alpha} \exp\{\mathrm{i}\boldsymbol{q}\cdot\boldsymbol{r}_j^\alpha\} - N_\alpha\delta_{\boldsymbol{q},0}\,, \tag{16.115}$$

with $\langle\rho_\alpha(q,t)\rangle = 0$. Here, $\boldsymbol{r}_j^\alpha$ is the center-of-mass position vector of the j-th sphere (monomer) of component α, and N_α is the number of particles of species α in the scattering volume. Small fluctuations in the relative local concentrations of 1-particles with respect to component 2 are quantified by the microscopic concentration variable

$$\rho_{\mathrm{in}}(\boldsymbol{q},t) \equiv \frac{1}{\sqrt{N}}\left[x_2\rho_1(\boldsymbol{q},t) - x_1\rho_2(\boldsymbol{q},t)\right]\,, \tag{16.116}$$

with $N = N_1 + N_2$ and partial molar fraction $x_\alpha = N_\alpha/N$. The interdiffusion process is thus related to the relaxation of $\rho_{\mathrm{in}}(\boldsymbol{q},t)$, whose de-correlation in time is described by the interdiffusion autocorrelation function

$$\begin{aligned} S_{\mathrm{in}}(q,t) &= \langle\rho_{\mathrm{in}}(\boldsymbol{q},t)\;\rho_{\mathrm{in}}(-\boldsymbol{q},0)\rangle \\ &= x_1x_2\left[x_2S_{11}(q,t) + x_1S_{22}(q,t) - 2\,(x_1x_2)^{1/2}\,S_{12}(q,t)\right]\,. \end{aligned} \tag{16.117}$$

The interdiffusion function $S_{\mathrm{in}}(q,t)$ has been further denoted in the literature on X-ray and neutron scattering as the Bhatia-Thornton dynamic concentration-concentration structure factor. It is a special linear combination of three partial collective dynamic structure factors [18]

$$S_{\alpha\beta}(q,t) \;=\; \frac{1}{(N_\alpha N_\beta)^{1/2}}\langle\rho_\alpha(\boldsymbol{q},t)\rho_\beta(-\boldsymbol{q},0)\rangle\,, \tag{16.118}$$

with $\alpha,\beta \in \{1,2\}$ and $S_{12} = S_{21}$. The partial structure factors, $S_{\alpha\beta}(q,t)$, describe time-correlations in the density fluctuations of components α and β, and they form the elements of a symmetric and positive definite 2×2 matrix $\boldsymbol{S}(q,t)$. This matrix is the extension of the collective dynamic structure factor $S_{\mathrm{c}}(q,t)$ of a monodisperse system to binary mixtures. Note that the factors $N^{-1/2}$ and $(N_\alpha N_\beta)^{-1/2}$ in (16.116) and (16.118), respectively, have been introduced to make $S_{\mathrm{in}}(q,t)$ and $\boldsymbol{S}(q,t)$ intensive. The EACF for polarized single scattering from a binary mixture can be expressed in terms of the dynamic structure factor matrix as

$$\begin{aligned} g_E(q,t) \;\propto\; & f_1^2\,S_{11}(q,t) + f_2^2\,S_{22}(q,t) + 2\,f_1\,f_2\,S_{12}(q,t) \\ &= \boldsymbol{f}(q)^{\mathrm{T}}\cdot\boldsymbol{S}(q,t)\cdot\boldsymbol{f}(q)\,, \end{aligned} \tag{16.119}$$

where we have introduced the column vector $\boldsymbol{f} = [f_1,f_2]^{\mathrm{T}}$ of partial scattering strengths $f_\alpha = x_\alpha^{1/2}b_\alpha$. For a binary colloidal suspension, b_α is the *excess* scattering amplitude of a sphere of component $\alpha = 1,2$ relative to the solvent. For a ternary homopolymer blend, b_α is the scattering amplitude of

an α-type monomer relative to the scattering strength of a matrix monomer. In principle, the three partial dynamic structure factors could be measured individually by index matching each of the two interdiffusing components separately to the solvent (matrix). Unfortunately, such an index matching is quite difficult to do from an experimental point of view and has been achieved to date only for a few selected systems. The index matching method is to some extent analogous to the isotope substitution technique used in neutron scattering.

We are interested here in the hydrodynamic regime (i.e. $q \to 0$ and $t \to \infty$ with $q^2 t$ fixed) where the internal structure of the colloidal spheres and homopolymers, and the internal dynamics of the individual homopolymers are not resolved. In this regime, the scattering amplitudes become independent of q. The time evolution of the matrix $\boldsymbol{S}(q,t)$ is shown in the hydrodynamic limit to be governed by

$$\boldsymbol{S}(q,t) \;=\; \exp\{-q^2 \boldsymbol{D}_{\mathrm{c}}^{\mathrm{l}} t\} \;\cdot \boldsymbol{S}(0)\,, \tag{16.120}$$

where $\boldsymbol{D}_{\mathrm{c}}^{\mathrm{l}}$ is the 2×2 long-time collective diffusion matrix, and $\boldsymbol{S}(0) = \boldsymbol{S}(q \to 0, t = 0)$ is the matrix of partial static structure factors in the small-q limit. Equation (16.120) extends (16.94) to (binary) mixtures. It is found that $\boldsymbol{D}_{\mathrm{c}}^{\mathrm{l}}$ is in general not symmetric. However, it can be diagonalized and it possesses real and positive eigenvalues d_+ and d_-, as one expects for an overdamped system. To see this, we introduce the symmetric and positive definite matrix, $\boldsymbol{\mu}^{\mathrm{l}}$, of long-time partial mobilities $\mu_{\alpha\beta}$ through [27, 28]

$$\boldsymbol{D}_{\mathrm{c}}^{\mathrm{l}} \;=\; k_{\mathrm{B}}T\, \boldsymbol{\mu}^{\mathrm{l}} \cdot \boldsymbol{S}(0)^{-1}\,. \tag{16.121}$$

A trivial example is provided for a system of non-interacting particles, where $\mu_{\alpha\beta}^{\mathrm{l}} = \delta_{\alpha\beta} D_{0\alpha}/(k_{\mathrm{B}}T)$. The symmetry and positive definiteness of $\boldsymbol{\mu}^{\mathrm{l}}$ is a consequence of the symmetry of $\boldsymbol{S}(q,t)$, and its monotonic decay in the hydrodynamic limit. That $\boldsymbol{D}_{\mathrm{c}}^{\mathrm{l}}$ is diagonalizable with positive eigenvalues arises then from the possibility to express it as the product of a symmetric and positive definite matrix $\boldsymbol{\mu}^{\mathrm{l}}$ and a symmetric matrix $\boldsymbol{S}^{-1}$. Explicit diagonalization of $\boldsymbol{D}$ leads to the normal-mode expansion [28]

$$\boldsymbol{S}(q,t) \;=\; \boldsymbol{A}_+ \exp\{-q^2 d_+ t\} + \boldsymbol{A}_- \exp\{-q^2 d_- t\} \tag{16.122}$$

of $\boldsymbol{S}(q,t)$ as a sum of two exponentially decaying diffusive modes. The amplitudes $\boldsymbol{A}_+$ and $\boldsymbol{A}_-$ can be expressed in terms of the elements of $\boldsymbol{S}(0)$ and $\boldsymbol{\mu}^{\mathrm{l}}$. The eigenvalues of $\boldsymbol{D}$ are given by

$$d_\pm \;=\; D_{\mathrm{av}} \pm \sqrt{D_{\mathrm{av}}^2 - |\boldsymbol{D}|} \tag{16.123}$$

with $D_{\mathrm{av}} = [D_{11} + D_{22}]/2$ and $|\boldsymbol{D}| = D_{11}D_{22} - D_{12}D_{21}$. In case of a binary colloidal dispersion, the bimodal relaxation described by (16.122) arises from the large differences in the relaxation times of colloidal particles and

solvent molecules. In contrast, the relaxation time of the polymer matrix, which plays the role of the "solvent" in the ternary homopolymer mixture, is comparable to those of the other two components. The bimodal relaxation is here a consequence of the incompressibility constraint

$$\rho_1(\boldsymbol{q}) + \rho_2(\boldsymbol{q}) + \rho_3(\boldsymbol{q}) \;=\; 0\,, \tag{16.124}$$

valid in the diffusive limit, which enables one to express the dynamics of one component, identified as the "matrix", in terms of the other ones. For simplicity, we have assumed here that the segmental volumes of all three homopolymer species are equal to each other. It is clear that $\boldsymbol{S}(q,t)$ in the general case will contain as many exponentially decaying modes as the number of independent components.

It follows from (16.117) and (16.122) that

$$S_{\rm in}(q,t) \;=\; x_1 x_2\, \boldsymbol{e}^{\rm T}\cdot \boldsymbol{S}(q,t)\cdot \boldsymbol{e}\,, \tag{16.125}$$

with $\boldsymbol{e} = \left[\sqrt{x_2}, -\sqrt{x_1}\right]^{\rm T}$, is a superposition of two decaying modes. Nevertheless, the initial decay of $S_{\rm in}(q,t)$ in the hydrodynamic limit can be described for $t \ll 1/d_+$ by the single-exponential form

$$S_{\rm in}(q,t) \;\approx\; \exp\{-q^2 D_{\rm in}^{\rm l} t\}\,, \tag{16.126}$$

which defines the long-time interdiffusion coefficient, $D_{\rm in}^{\rm l}$, as

$$D_{\rm in}^{\rm l} \;=\; \lim_{t\to\infty}\,\lim_{q\to 0}\left[-\frac{1}{q^2}\frac{\partial}{\partial t}\ln S_{\rm in}(q,t)\right]\,. \tag{16.127}$$

By matching the initial relaxation rates in (16.125) and (16.126), we find, using (16.121), that

$$D_{\rm in}^{\rm l} \;=\; \frac{\Lambda_{\rm in}^{\rm l}}{S_{\rm in}(0)}\,, \tag{16.128}$$

with

$$\begin{aligned}\Lambda_{\rm in}^{\rm l} &= k_{\rm B}T\, x_1\, x_2\; \boldsymbol{e}^{\rm T}\cdot\boldsymbol{\mu}^{\rm l}\cdot\boldsymbol{e} \\ &= k_{\rm B}T\, x_1\, x_2\left[x_2\,\mu_{11}^{\rm l} + x_1\,\mu_{22}^{\rm l} - 2\,(x_1\,x_2)^{1/2}\,\mu_{12}^{\rm l}\right]\,.\end{aligned} \tag{16.129}$$

We note that $D_{\rm in}^{\rm l}$ is expressed here as a product of a *kinetic* factor, $\Lambda_{\rm in}^{\rm l} > 0$, and a *thermodynamic* factor equal to $1/S_{\rm in}(q=0)$. For a binary mixture of particles nearly identical in their interactions, $S_{\rm in}(0) \approx x_1 x_2$. For systems with $S_{\rm in}(0) < x_1 x_2$ ($S_{\rm in} > x_1 x_2$) the particles of components 1 and 2 have the tendency to mix (de-mix).

The kinetic factor can be expressed by the Green-Kubo formula

$$\Lambda_{\rm in}^{\rm l} = \lim_{q\to 0}\int_0^\infty {\rm d}t\;\langle j_{\rm in}(\boldsymbol{q},t)\; j_{\rm in}(-\boldsymbol{q},0)\rangle\,, \tag{16.130}$$

where

$$j_{\rm in}(\boldsymbol{q},t) \;=\; \sqrt{N}x_1x_2\left[\frac{1}{N_1}\sum_{j=1}^{N_1} v_j^{(1)}\exp\{{\rm i}\boldsymbol{q}\cdot\boldsymbol{r}_j^{(1)}\}- \right.$$
$$\left. \frac{1}{N_2}\sum_{j=1}^{N_2} v_j^{(2)}\exp\{{\rm i}\boldsymbol{q}\cdot\boldsymbol{r}_j^{(2)}\}\right] \quad (16.131)$$

is the interdiffusion flux related to $\rho_{\rm in}(\boldsymbol{q},t)$. Here, $v_j^{(1)}$ and $v_j^{(2)}$ denote the longitudinal (i.e. parallel to $\boldsymbol{q}$) velocities of component 1 and 2 particles. The interdiffusion flux is seen to be closely related to the relative velocity of the center-of-positions of the two components in the mixture. The derivation of (16.130) can be represented quite generally [28, 29] for any density function $\rho(\boldsymbol{q},t)$ in Fourier space satisfying the continuity equation

$$\dot{\rho}(\boldsymbol{q},t) \;=\; iq\,j(\boldsymbol{q},t)\,. \quad (16.132)$$

Here $j(\boldsymbol{q},t)$ is the longitudinal component of the flux vector $\boldsymbol{j}(\boldsymbol{q},t)$ associated with $\rho(\boldsymbol{q},t)$, and the dot denotes differentiation with respect to time. The long-wavelength limit of the current autocorrelation function follows then as

$$\lim_{q\to 0}\,\langle j(\boldsymbol{q},t)\;j(-\boldsymbol{q},0)\rangle \;=\; \lim_{q\to 0}\;\frac{1}{q^2}\langle\dot{\rho}(\boldsymbol{q},t)\;\dot{\rho}(-\boldsymbol{q},0)\rangle$$
$$=\; -\lim_{q\to 0}\;\frac{1}{q^2}\;\frac{\partial^2 S(q,t)}{\partial t^2} \quad (16.133)$$

where $S(q,t)=\langle\rho(\boldsymbol{q},t)\rho(-\boldsymbol{q},0)\rangle$. For the most right equality we have used the stationarity property which states that equilibrium time-correlation functions are invariant to a shift in the time origin. Next we integrate (16.133) with respect to time to obtain

$$\lim_{q\to 0}\int_0^t {\rm d}t'\;\langle j(\boldsymbol{q},t')\;j(-\boldsymbol{q},0)\rangle \;=\; -\lim_{q\to 0}\frac{1}{q^2}\frac{\partial}{\partial t}S_{\rm in}(q,t) \quad (16.134)$$

where the initial condition

$$\frac{\partial}{\partial t}S(q,t)|_{t=0} \;=\; 0 \quad (16.135)$$

has been used. This initial condition is a consequence of time reversibility, i.e. $\langle A(t)A(0)\rangle=\langle A(-t)A(0)\rangle$ for any dynamic variable A obeying the deterministic Liouville equation. The initial slope of any autocorrelation function is thus zero in Liouville dynamics. Of course, this does not hold for the irreversible dynamical regime described by diffusion equations (e.g., (16.45)), wherein the microscopic short-time regime $t\ll\tau_{\rm B}$ remains unresolved. The

transition to the hydrodynamic regime follows from taking the long-time limit of (16.135). This gives the exact relation

$$\lim_{q\to 0}\int_0^\infty \mathrm{d}t\,\langle j(\boldsymbol{q},t)\,j(-\boldsymbol{q},0)\rangle \;=\; -\lim_{t\to\infty}\lim_{q\to 0}\frac{1}{q^2}\frac{\partial}{\partial t}S(q,t)\,, \qquad (16.136)$$

where the order of the limits is not interchangeable. In specializing this equation to interdiffusion, the Green-Kubo formula for $\Lambda^{\mathrm{l}}_{\mathrm{in}}$ is readily obtained from substituting the hydrodynamic limit form of $S_{\mathrm{in}}(q,t)$ as given in (16.122). When (16.136) is specialized to self-diffusion by choosing $\rho(\boldsymbol{q},t) = \exp\{\mathrm{i}\boldsymbol{q}\cdot\boldsymbol{r}_1(t)\}$ and using that $S_{\mathrm{s}}(q,t) = \exp\{-q^2 D^{\mathrm{l}}_{\mathrm{s}}t\}$ in the hydrodynamic limit, one is led to the Green-Kubo formula for the VAF given in (16.73). For self-diffusion, $\Lambda^{\mathrm{l}}_{\mathrm{s}} = D^{\mathrm{l}}_{\mathrm{s}}$, since the thermodynamic factor $1/S_{\mathrm{s}}(q,t=0)$ is equal to one even for finite q.

For colloidal mixtures, one needs to distinguish between the short-time and long-time interdiffusion coefficient. The definition of $D^{\mathrm{s}}_{\mathrm{in}} = \Lambda^{\mathrm{s}}_{\mathrm{in}}/S_{\mathrm{in}}(0)$ and of its associated short-time kinetic factor $\Lambda^{\mathrm{s}}_{\mathrm{in}}$ follows from considering the time evolution equation

$$\frac{\partial}{\partial t}\boldsymbol{S}(q,t) = -q^2\boldsymbol{D}^{\mathrm{s}}_{\mathrm{c}}(q)\cdot\boldsymbol{S}(q,t) + q^2\int_0^t \mathrm{d}t'\,\boldsymbol{\Delta D}_{\mathrm{c}}(q,t-t')\cdot\boldsymbol{S}(q,t') \quad (16.137)$$

for $\boldsymbol{S}(q,t)$, which constitutes the generalization of (16.101) to colloidal mixtures. Here $\boldsymbol{\Delta D}_{\mathrm{c}}(q,t)$ is a 2×2-matrix of collective memory functions, related to the long-time collective diffusion matrix in (16.121) by (cf. (16.103))

$$\boldsymbol{D}^{\mathrm{l}}_{\mathrm{c}} \;=\; \boldsymbol{D}^{\mathrm{s}}_{\mathrm{c}} - \lim_{q\to 0}\int_0^\infty \mathrm{d}t\,\boldsymbol{\Delta D}_{\mathrm{c}}(q,t)\,, \qquad (16.138)$$

with the short-time collective diffusion matrix $\boldsymbol{D}^{\mathrm{s}}_{\mathrm{c}} = \lim_{q\to 0}\boldsymbol{D}^{\mathrm{s}}_{\mathrm{c}}(q)$. Introducing the short-time mobility matrix through $\boldsymbol{D}^{\mathrm{s}}_{\mathrm{c}} = k_{\mathrm{B}}T\boldsymbol{\mu}^{\mathrm{s}}\cdot\boldsymbol{S}(0)^{-1}$, $\Lambda^{\mathrm{s}}_{\mathrm{in}}$ can be defined in analogy to the long-time kinetic coefficient as

$$\Lambda^{\mathrm{s}}_{\mathrm{in}} \;=\; k_{\mathrm{B}}T\,x_1\,x_2\,\boldsymbol{e}^{\mathrm{T}}\cdot\boldsymbol{\mu}^{\mathrm{s}}\cdot\boldsymbol{e}\,. \qquad (16.139)$$

Contrary to the one-component case, where $D^{\mathrm{s}}_{\mathrm{c}} = D^{\mathrm{l}}_{\mathrm{c}}$ for systems with pairwise additive HI, one finds for mixtures that $\boldsymbol{D}^{\mathrm{s}}_{\mathrm{c}} \neq \boldsymbol{D}^{\mathrm{l}}_{\mathrm{c}}$, and hence $\Lambda^{\mathrm{l}}_{\mathrm{in}} < \Lambda^{\mathrm{s}}_{\mathrm{in}}$ and $D^{\mathrm{l}}_{\mathrm{in}} < D^{\mathrm{s}}_{\mathrm{in}}$, even so when HI is neglected. The reason for the different physical behavior of mixtures is that particles of different components diffuse differently fast under a constant density gradient. Hence, the equilibrium microstructure becomes distorted at longer times. For the memory matrix this implies that $\lim_{q\to 0}\boldsymbol{\Delta D}(q,t) \neq 0$.

The interdiffusion coefficient describes the relaxation of thermally excited fluctuations in the relative composition through the collective motion of particles. Therefore, there is no reason to expect that, except from a few limiting cases, $D^{\mathrm{l}}_{\mathrm{in}}$ can be expressed solely in terms of the self-diffusion coefficients

$$D_{\mathrm{s}\alpha}^{\mathrm{l}} = \int_0^\infty \mathrm{d}t \langle v_i^\alpha(t) v_i^\alpha(0) \rangle \tag{16.140}$$

of both components, with v_i^α denoting the longitudinal velocity of a component α particle. That there are collective contributions to $D_{\mathrm{in}}^{\mathrm{s}}$ which are not contained in the self-diffusion coefficients was explicitly shown for fluid atomic mixtures in [30]. The importance of collective contributions to D_{in} will be exemplified in Sect. 16.5.1 for mixtures of colloidal hard spheres.

An ideal binary mixture is characterized by

$$\Lambda_{\mathrm{in}}^{\mathrm{l}} \propto x_2 D_{\mathrm{s}1}^{\mathrm{l}} + x_1 D_{\mathrm{s}2}^{\mathrm{l}} , \tag{16.141}$$

i.e. the kinetic factor can be expressed solely in terms of a weighted sum of the self-diffusion coefficients. Ideality is implied, in particular, according to (16.130), when velocity cross-correlations $\langle v_i(t) v_j(0) \rangle$ between different particles $i \neq j$ vanish or mutually cancel each other for all t. A trivial example of an ideal system is a binary suspension of non-interacting particles (cf. (14.2) in Chap. 14), where

$$D_{\mathrm{in}}^{\mathrm{l}} = D_{\mathrm{in}}^{\mathrm{s}} = x_2 D_{01} + x_1 D_{02} . \tag{16.142}$$

Here, $D_{0\alpha}$ is the free diffusion coefficient of an α-type particle. Equation (16.141) is the *fast-mode* expression for interdiffusion since for $D_{\mathrm{s}1} \gg D_{\mathrm{s}2}$, D_{in} is dominated by the self-diffusion coefficient of the fast component 1. The fast-mode form of D_{in} is approximately valid for mixtures of Lennard-Jones-type fluids like argon-krypton. However, there are severe deviations from the fast-mode form for mixtures of strongly dissymmetric particles. Perfect ideality is reached only for symmetric bimodal systems, where the particles of both components differ only in their labelling (e.g. in their optical properties). In this limiting case, $S_{\mathrm{in}}(0) = x_1 x_2$, and

$$D_{\mathrm{in}} = D_{\mathrm{s}} \tag{16.143}$$

for arbitrary concentration and particle interactions. Not unexpectedly, this means that the concentration exchange between the two components is only driven by self-diffusion. The interdiffusion coefficient in a symmetric mixture is thus identical with the self-diffusion coefficient. Since all particles are identical regarding their sizes and interactions, there is no gradient in the local chemical potential difference of both species. Each particle experiences a uniform environment as in the case of self-diffusion. An ideal bimodal system in the hydrodynamic limit is further characterized by

$$d_- = D_{\mathrm{in}} , \quad d_+ = D_{\mathrm{c}} \tag{16.144}$$

with $d_- < d_+$. The eigenmode with decay constant d_- (d_+) is thus identified with the interdiffusion (collective diffusion) process, and D_{in} and D_{c} can be extracted, using index matching, from a single measurement of the EACF

of the unmatched (labelled) component α, since then $g_E(q,t) \propto S_{\alpha\alpha}(q,t)$. The two normal modes cannot be identified, in general, as interdiffusion and collective diffusion processes. Moreover, $D_{\rm in}$ cannot be extracted, in general, from the measurement of a single dynamic structure factor, say $S_{11}(t)$, of one component. One needs a second experiment, in which the first component is matched away and $S_{22}(q,t)$ is determined.

Exact microscopic expressions have been derived for the interdiffusion coefficient of colloidal mixtures. These expressions form the basis of its actual calculation (cf. Sect. 16.5). In the case of incompressible polymer melts, an analogous microscopic description is of little use from a computational point of view. Therefore one resorts to approximate schemes like the (dynamic) random phase approximation (RPA), which relates the dynamics of polymer mixtures to the dynamics of single polymer chain in the mixture. In Sect. 16.5.2, we will discuss the application of the RPA to ternary blends of homopolymers. We only mention here that for an incompressible binary blend, the RPA predicts the *slow-mode* expression

$$\frac{1}{\Lambda_{\rm in}} \propto \frac{x_2}{D_{\rm s1}} + \frac{x_1}{D_{\rm s2}} \tag{16.145}$$

for the kinetic factor, with $D_{{\rm s}\alpha}$ the self-diffusion coefficient of an α-type monomer in the melt, and x_α the molar fraction of α-type monomers. The kinetic factor is dominated here by the slow component, as the name "slow mode" implies. The RPA states thus that, due to incompressibility, the dynamics of the fast component is slaved by the slow one. The binary blend is thus an opposite limiting case to ideal solutions of weakly interacting particles and to mixtures of nearly identical components where the fast-mode expression applies.

Rotational Diffusion

We proceed to discuss salient features of rotational diffusion in suspensions of colloidal spheres with spherically symmetric potential interactions, within the time regime accessible by depolarized DLS. As discussed already in Sect. 16.3.1, the decoupling approximation of the depolarized EACF holds then exactly to linear order in t. Consider first the (hypothetical) case of particles which interact by direct potential forces only, and not by HI. Then the rotational self-dynamic correlation function reduces, for all times $t \gg \tau_{\rm B} \approx \tau_{\rm B}^{\rm r}$, to an exponentially decaying function

$$S_{\rm r}(t) \;=\; \exp\{-6D_0^{\rm r}t\}\,. \tag{16.146}$$

This result follows from realizing that the orientational Brownian motion of a sphere with radially symmetric pair interactions is independent of the orientational and translational motion of other spheres, as long as HI is not considered. Recall that, contrary to $S_{\rm r}(t)$, the translational self-dynamic structure

factor $S_\mathrm{s}(q,t)$ is single exponential without HI only at short times. Consequently

$$g_E^{\mathrm{VH}}(q,t) \;\propto\; \beta^2 \exp\{-(q^2 W(t) + 6D_0^\mathrm{r} t)\} \tag{16.147}$$

is valid for all $t \gg \tau_\mathrm{B}$, provided small non-Gaussian corrections to $S_\mathrm{s}(q,t)$ can be discarded. In reality, however, (16.147) is of little use since the HI are very long-ranged. HI decay for long interparticle distances r as r^{-1} regarding collective diffusion, and as r^{-4} and r^{-6}, respectively, in case of translational and rotational self-diffusion. Therefore, HI cannot be neglected in comparison to direct interactions. With HI, $S_\mathrm{r}(t)$ decays exponentially only at short times. The initial decay of $S_\mathrm{r}(t)$ can be quantified by the short-time rotational self-diffusion coefficient D_r^s, defined as

$$D_\mathrm{s}^\mathrm{r} \;=\; -\lim_{t\to 0} \frac{\partial \ln S_\mathrm{r}(t)}{\partial t}\,, \tag{16.148}$$

where $t \to 0$ should be interpreted as $\tau_\mathrm{B} \ll t \ll \tau_\mathrm{I} \approx \tau_\mathrm{r}$. The HI between the spheres cause a hindrance of short-time rotational motion so that $D_\mathrm{s}^\mathrm{r} < D_0^\mathrm{r}$. At infinite dilution, $D_\mathrm{s}^\mathrm{r} \to D_0^\mathrm{r}$. As will be exemplified in Sect. 16.5.1, D_s^r depends crucially on system parameters like the volume fraction, and the particle charge in case of charge-stabilized dispersions.

Memory effects come into play at longer times and lead to deviations of $S_\mathrm{r}(t)$ from the single-exponential decay. For rotational Brownian motion of the tip of the orientation vector $\hat{\boldsymbol{u}}$ on the compact unit sphere, there is no analogue of the hydrodynamic $q \to 0$ limit known from translational self- and collective motion. At long times, $S_\mathrm{r}(t)$ decays in principle non-exponentially, with an average decay rate somewhat smaller than the initial one. Such a non-Debye-like relaxation of $S_\mathrm{r}(t)$ at long times has been observed experimentally and theoretically for various systems. For dilute suspensions of colloidal hard spheres, e.g., it has been shown theoretically that $S_\mathrm{r}(t)$ is non-exponential at intermediate and long times, according to [31]

$$\frac{S_\mathrm{r}(t)}{S_\mathrm{r}^0(t)} \;=\; 1 + \gamma_2(t)\Phi + \mathcal{O}(\Phi^2) \tag{16.149}$$

with a positive-valued function $\gamma_2(t)$. Here, $S_\mathrm{r}^0(t)$ is the rotational self function at infinite dilution, given by (16.146). While a genuine long-time rotational self-diffusion coefficient does not exist, one can always define instead a *mean* orientational self-diffusion coefficient, $\overline{D}_\mathrm{r}$, which depends on the overall time-dependence of $S_\mathrm{r}(t)$ through [31]

$$\frac{1}{6\overline{D}_\mathrm{r}} \;\equiv\; \int_0^\infty \mathrm{d}t\; S_\mathrm{r}(t) \;=\; \frac{1}{6D_0^\mathrm{r}}\left[1 + C_\mathrm{r}\phi + \mathcal{O}(\Phi^2)\right] \tag{16.150}$$

with $C_\mathrm{r} = 0.67$ for hard spheres, resulting in $\overline{D}_\mathrm{r}/D_0^\mathrm{r} = 1 - 0.67\phi + \mathcal{O}(\Phi^2)$. This should be compared with the first-order virial result for the short-time rotational self-diffusion coefficient of hard spheres, given by $D_\mathrm{s}^\mathrm{r}/D_0^\mathrm{r} =$

$1 - 0.63\phi + \mathcal{O}(\Phi^2)$. Thus, memory effects in $S_{\rm r}(t)$ lead to a mean diffusion coefficient only slightly smaller than the short-time one, to first order in Φ.

Whereas a true long-time rotational self-diffusion coefficient, $D_{\rm l}^{\rm r}$ does not exist in monodisperse suspensions, we expect $D_{\rm l}^{\rm r}$ to be a well-defined long-time property when interpreted as the long-time coefficient describing the rotation of a large tracer sphere immersed in a dispersion of small host spheres. Depolarized DLS measurements indicate that a tracer/host size ratio larger than 10 is large enough for $D_{\rm l}^{\rm r}$ to be well-defined. Due to the separation of time scales between the slow motion of the tracer and the fast motion of the host spheres, the tracer experiences the host dispersion as an unstructured effective fluid, characterized by the effective viscosity $\eta_{\rm H}$ of the host dispersion. Thus, one expects that $D_{\rm l}^{\rm r}$ obeys the generalized Stokes-Einstein relation for a perfectly sticking effective fluid, i.e.

$$D_{\rm l}^{\rm r} = \frac{k_{\rm B}T}{6\pi\eta_{\rm H}a_{\rm T}}\,, \tag{16.151}$$

where $a_{\rm T}$ denotes the radius of the tracer. This expectation is supported experimentally, and by calculating the short-time rotational self-diffusion coefficient of the tracer in a dilute host dispersion of hard spheres [32]. For the latter case, $D_{\rm s}^{\rm r}$ is described to good accuracy by [32]

$$D_{\rm s}^{\rm r} = D_0^{\rm r}\left[1 - \frac{2.5}{1+3\lambda^{-1}}\,\Phi + \mathcal{O}(\Phi^2)\right]\,, \tag{16.152}$$

with $\lambda = a_{\rm T}/a_{\rm H}$, and ϕ the volume fraction of host spheres. This equation describes a monotonic decline of the tracer coefficient from $D_{\rm s}^{\rm r} = D_0^{\rm r}$ at $\lambda = 0$ towards $D_{\rm s}^{\rm r} = D_0^{\rm r}\,(1 - 2.5\Phi) = k_{\rm B}T/\left[6\pi\eta_0(1+2.5\Phi)\right] + \mathcal{O}(\Phi^2)$ for $\lambda \to \infty$ (see Fig. 16.12). For very large λ, the tracer sphere experiences thus the host solution as an effective one-component fluid, with an effective shear viscosity given to first order in Φ by the relation $\eta_{\rm H} = \eta_0\,(1 + 2.5\Phi)$. In the opposite limit $\lambda \ll 1$, the point-like (relative to the host) tracer rotates for short times in an essentially stationary environment of host spheres so that its dynamic cage is affected only by the viscosity η_0 of the pure solvent.

16.4 Fluorescence Techniques for Long-Time Self-Diffusion of Non-Spherical Particles

As explained above, in order to measure self-diffusion properties in a concentrated dispersion by means of light scattering, one needs to prepare a system, where only a few particles scatter light (the so-called "tracer particles"), whereas the majority of particles do not contribute to the scattered intensity (the "host particles"). The tracer particles must be so dilute, that they do not mutually interact, but may interact with the host particles. What is then measured is the self-diffusion coefficient at a concentration that is equal

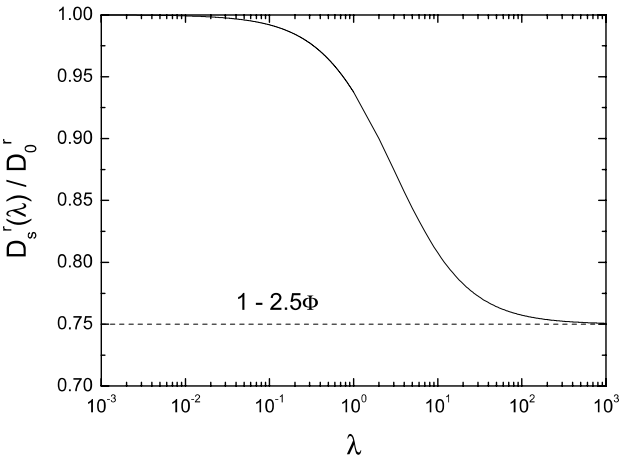

Fig. 16.12. Reduced short-time self-diffusion coefficient D_s^r/D_0^r versus size ratio $\lambda = a_T/a_H$ of a colloidal tracer sphere immersed in a dilute host dispersion of colloidal hard spheres. The volume fraction of host spheres is $\Phi = 0.1$. After [32].

to the overall concentration. Ideally, the pair-interaction potentials between the tracer particles and host particles, and mutually between host particles, are identical. Such a system is difficult to prepare, especially for more complicated colloidal particles such as rods or platelets. In addition, it is not straightforward to obtain true long-time diffusion coefficients by means of light scattering. There exist other experimental techniques which allow for a direct measurement of long-time self-diffusion coefficients, without having to resort to tracer systems. The techniques which will be discussed here are fluorescent recovery after photobleaching (FRAP) and fluorescence correlation spectroscopy (FCS). Both these techniques require the colloidal particles to be labelled with fluorescent dyes.

16.4.1 Fluorescence Recovery After Photobleaching (FRAP)

Consider a monodisperse colloidal system, where each colloidal particle is labelled with a number of fluorescent dye molecules (such as Rhodamine or Fluoresceine Iso Thio Cyanate (FITC)). These dye molecules can be exited by a monochromatic incident light beam, and emit light of a larger wavelength when the exited state of the molecule relaxes to a lower energy state. This process is called fluorescence. When the intensity of the incident beam is very high, the structure of the dye molecules is irreversibly changed, and they loose their fluorescent properties. This process is called bleaching. A bleached dye molecule does not fluoresce anymore. In the early days of FRAP, diffusion of free dye molecules was probed, by first bleaching "a hole" in the sample, by means of a short pulse of high intensity light. Then the intensity of the

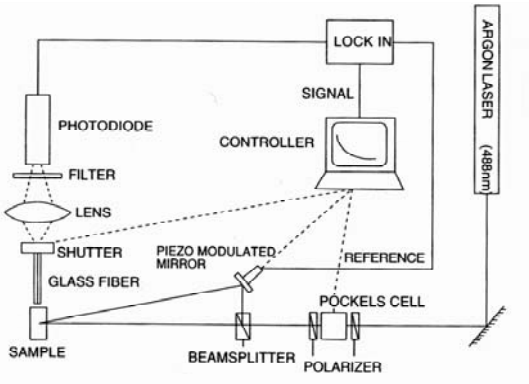

Fig. 16.13. Principle of a FRAP setup. Two beams are crossed under an angle 2Θ. The mirror is mounted on a piezo element, which oscillates with frequency ω during a measurement. A fiber picks up the fluorescent light that originates from the sample. The amplitude of the 2ω-component of the fluorescent intensity is filtered out by means of a lock-in amplifier. From [35].

incident beam was decreased to a level where bleaching is (virtually) absent, and the fluorescent intensity from molecules within the hole is detected as a function of time. Due to diffusion of unbleached molecules from outside the hole into the hole, and of bleached molecules from inside the hole out of the hole, the fluorescent intensity increases ("recovers") with time. Once the geometry of the bleached hole is known, the long-time self-diffusion coefficient can be obtained from the time dependence of the fluorescent intensity. The long-time self-diffusion coefficient is measured here, since (i) the fluorescent intensity from different molecules have no phase relation, so that interference effects on the measured intensity are absent (contrary scattered radiation), and (ii) the size of the hole is much larger than molecular dimensions, so that a significant change in the fluorescent intensity is only measured when the molecules are displaced over distances that are large compared to their own size.

The disadvantage of this older version of FRAP is that the geometry of the bleached volume needs to be known, and that the fluorescent intensity is a very complicated function of time. Furthermore, for macromolecules that are labelled, the time required for the fluorescent intensity to recover would be many hours. The FRAP technique was therefore improved (independently by two groups [33,34]) by employing a diffraction grating or an interference pattern, respectively. The technique described below uses an interference pattern created by two crossing laser beams, as sketched in Fig. 16.13.

Instead of just bleaching a hole, a fringe pattern is bleached. To this end, two laser beams are crossed under an angle 2Θ, say, which gives rise to a standing interference pattern in the sample. For the intensity we have

$$I_0(\boldsymbol{r}) \;\sim\; \cos\{\boldsymbol{q}_0 \cdot \boldsymbol{r}\}\;, \tag{16.153}$$

where the wavevector q_0 is equal to the difference between the wavevectors $\boldsymbol{q}_1$ and $\boldsymbol{q}_2$ of the two crossed beams

$$\boldsymbol{q}_0 \;=\; \boldsymbol{q}_1 - \boldsymbol{q}_2\;. \tag{16.154}$$

Its magnitude is equal to

$$q_0 \;=\; \frac{4\pi}{\lambda}\,\sin\{\Theta\}\;, \tag{16.155}$$

where λ is the wavelength of the laser beam. We note here, that for the almost perpendicular incidence of the two beams onto the sample, the ratio $\sin\{\Theta\}/\lambda$ is independent of whether Θ and λ are both taken equal to their values within the sample, or in air, in the absence of the sample. Typical angles are $\Theta = 1^\circ - 5^\circ$, corresponding to a fringe spacings in the range $10 - 50\,\mu$m. The bleach pulse now creates a sinusoidal concentration pattern of bleached and unbleached particles, as sketched in Fig. 16.14, provided that the amount of bleached dye molecules is proportional to the incident intensity.

The overall concentration (bleached + unbleached colloidal particles) is constant. After this bleach of high intensity, the intensity is lowered to a value where bleaching is virtually absent. Just as in the older version of FRAP, one could now monitor the recovery of fluorescent intensity with time. The measured fluorescent intensity, however, is the sum of a background intensity and a relatively small time dependent contribution. In order to increase the signal-to-noise ratio of the FRAP experiment, instead, the interference pattern is oscillated with a certain frequency ω and amplitude over the bleached pattern. This is accomplished by sinusoidal motion of a mirror in Fig. 16.13 that is mounted on a piezo element, whereby the absolute phase of one of the beams is changed by a phase angle Ψ. This so-called "reading intensity" is then equal to

$$I_0(\boldsymbol{r}, t') \;\sim\; \cos\{\boldsymbol{q}_0 \cdot \boldsymbol{r} + \Psi(t')\}\;, \tag{16.156}$$

where

$$\Psi(t') \;=\; A\,\sin\{\omega\, t'\}\;. \tag{16.157}$$

The optimum value of the amplitude of oscillation A will be discussed later. Since the fluorescent intensity changes when the degree of overlap of the reading fringes with the bleached fringes changes, the measured fluorescent intensity oscillates, generally in a complicated fashion. In addition, due to diffusion the difference in concentration between bleached and unbleached colloidal particles diminishes with time, resulting in a decreasing amplitude of the oscillating fluorescent intensity. The precise time dependence of the fluorescent intensity can be calculated as follows. First of all, the fluorescent intensity I_f is proportional to the local incident intensity $I_0(\boldsymbol{r}, t')$ and the local concentration $c_0(\boldsymbol{r}, t)$ of unbleached dye molecules (which are attached to the colloidal particles), summed over the entire sample volume,

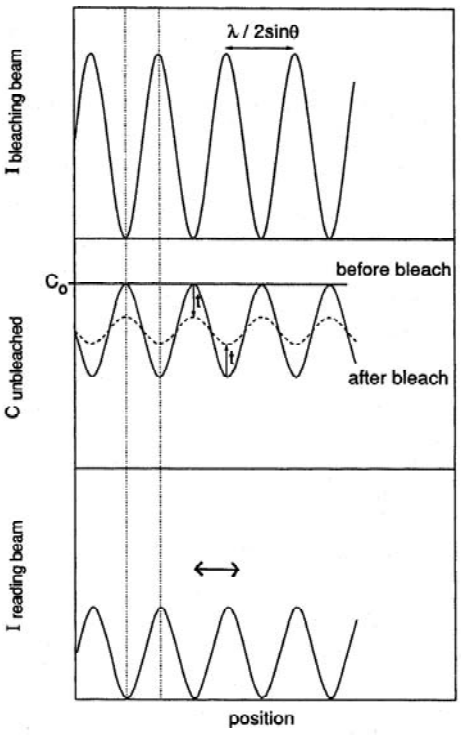

Fig. 16.14. The various stages during a FRAP experiment. The top figure is the intensity of the sinusoidal fringe pattern within the sample. After the bleach pulse, the concentration of unbleached particles is depicted in the middle figure. The amplitude of the concentration profile of unbleached particles diminishes with time due to diffusion. The lower figure depicts the reading intensity with its oscillating position within the sample. From [35].

$$I_f(t',t) \;\sim\; \int \mathrm{d}\boldsymbol{r}\, I_0(\boldsymbol{r},t')\, c_0(\boldsymbol{r},t) \;\sim\; \int \mathrm{d}\boldsymbol{q}\, I_0(\boldsymbol{q},t')\, c_0(\boldsymbol{q},t)\;, \qquad (16.158)$$

where in the second equation, Bessel's theorem is used to express the fluorescent intensity in terms of a wavevector integral over the spatial Fourier transforms of I_0 and c_0. We made here the distinction between the time dependence t resulting from diffusion and the time dependence t' as a result of the oscillating interference pattern. The reason for doing so is that the frequency of oscillation will be assumed large enough, so that over a period of many oscillations the concentration $c_0(\boldsymbol{r},t)$ hardly changes. This will be important in order to be able to filter a certain time-Fourier component by means of a lock-in amplifier from the detected fluorescent intensity. During this filtering, the time dependence due to diffusion must be negligibly small. Since the spatial Fourier transform of I_0 in (16.156) is

$$I_0(\boldsymbol{q},t') \;\sim\; \delta(\boldsymbol{q}-\boldsymbol{q}_0)\,\exp\{\mathrm{i}\Psi(t')\} + \delta(\boldsymbol{q}+\boldsymbol{q}_0)\,\exp\{-\mathrm{i}\Psi(t')\}\;, \qquad (16.159)$$

where the δ's are Dirac delta distributions, (16.158) leads to

$$I_f(t,t') \;\sim\; c_0(\boldsymbol{q}_0,t)\,\cos\{\Psi(t')\}\;, \qquad (16.160)$$

where we used that $c_0(\boldsymbol{q}_0,t) = c_0(-\boldsymbol{q}_0,t)$. A time-Fourier analysis of the fluorescent intensity with respect to its t'-dependence is accomplished by the mathematical identity

$$\cos\{A\,\sin\{\omega\,t'\}\} \;=\; J_0(A) + 2\sum_{n=1}^{\infty} J_{2n}(A)\,\cos\{2n\omega\,t'\}\;, \qquad (16.161)$$

where J_m is an m^{th} order Bessel function. When the lock-in amplifier is set to filter the Fourier component with frequency 2ω, its output, according to (16.160), (16.161), is equal to

$$S(t) \;\sim\; c_0(\boldsymbol{q}_0,t)\;. \qquad (16.162)$$

$S(t)$ is simply referred to as "the FRAP signal". In an experiment, the amplitude A is chosen such that the corresponding prefactor $J_2(A)$ in (16.161) is maximum. Now, since the fringe spacing is much broader than the linear dimensions of the colloidal particles, the fluorescent intensity diminishes only when colloidal particles are displaced over distances much larger than their own size. Hence, long-time diffusion determines the time dependence of the FRAP signal. Furthermore, since fluorescent intensities from different dyes have no phase relation, the FRAP signal is not affected by interference effects, so that self-diffusion in the homogeneous system governs the time dependence. In the long-time limit, the concentration $c_0(\boldsymbol{r},t)$ obeys the diffusion equation

$$\frac{\partial c_0(\boldsymbol{r},t)}{\partial t} \;=\; D_{\mathrm{s}}^{\mathrm{l}}\,\nabla^2 c_0(\boldsymbol{r},t)\;, \qquad (16.163)$$

where $D_{\mathrm{s}}^{\mathrm{l}}$ is the long-time self-diffusion coefficient. The assumption here is that bleaching has no effect on the pair-interaction potential between the colloidal particles. Hence,

$$\frac{\partial c_0(\boldsymbol{q},t)}{\partial t} \;=\; -D_{\mathrm{s}}^{\mathrm{l}}\,q^2\,c_0(\boldsymbol{q},t) \qquad (16.164)$$

and

$$c_0(\boldsymbol{q},t) \;\sim\; \exp\{-D_{\mathrm{s}}^{\mathrm{l}}\,q^2\,t\}\;. \qquad (16.165)$$

From (16.162) one thus obtains the following simple relationship between the FRAP signal and the long-time self-diffusion coefficient:

$$S(t) \;\sim\; \exp\{-D_{\mathrm{s}}^{\mathrm{l}}\,q_0^2\,t\}\;. \qquad (16.166)$$

The nice feature about the improved FRAP technique is that the concentration profile of unbleached colloidal particles remains sinusoidal throughout its relaxation, since the sine-function is an eigenfunction of the operator on the right hand-side in (16.163). This feature leads to the single-exponential behaviour of the FRAP signal in (16.166). This must be contrasted with the concentration profiles during relaxation in the older version of FRAP, where simply a hole is bleached, leading to a Gaussian-like concentration profile after the bleach pulse. Such a Gaussian-like concentration dependence is not an eigenfunction of the operator in (16.163), leading to a much more complicated time dependence of the fluorescent intensity during recovery as compared to the decay of the FRAP signal in (16.166) for the improved FRAP technique.

The above analysis is a simplified version of a much more elaborate analysis as given in [35].

Long-Time Self-Diffusion of Colloidal Rods

The analysis given above holds for colloidal particles of any shape, as long as their linear dimensions are small compared to the fringe spacing. Experimental results on spherical colloids (and mixtures of spheres of various sizes) will be discussed later. In the present subsection we shall discuss FRAP experiments on stiff, colloidal rods, which are taken from [36–38].

Two colloidal systems are discussed here. The first system consists of boehmite rods, where the aluminium core is covered with aluminium chlorohydrate ($Al_2(OH)_5Cl\ 2-3H_2O$, ACH), to partly shield the van der Waals attractions between the cores [38]. The aspect ratio, corrected for the ACH layer thickness and charges of these rods is $L/D = 7.3$ (where $L = 257\,\mathrm{nm}$ is the length of the rods, and D their effective thickness). The solvent is water, with $0.01\,M$ added NaCl. This system will be referred to as "system I". The second system consist of boehmite rods, where the aluminium core is covered with $a \sim 25\,\mathrm{nm}$ thick layer of SiO_2, which virtually completely screens the van der Waals interactions [37]. The aspect ratio, corrected for charge repulsion, is equal to $L/D = 5.4$ (with $L = 323\,\mathrm{nm}$). This system will be referred to as "system II". The solvent here is DMS with $0.01\,M$ LiCl added. The polydispersity in both systems is around 30 % in length and 20 % in thickness. Both systems exhibit an isotropic-nematic (i-n) phase transition.

Typical FRAP data are shown in Fig. 16.15, together with a single-exponential fit (the solid lines) according to (16.166). The two sets of data correspond to a measurement in an isotropic state and the coexisting nematic state, where diffusion along the director is probed.

A reliable value for the long-time diffusion coefficient, accurate to within a few percent, is obtained when 10 to 20 such measurements are averaged. Clearly there is a large difference between the long-time diffusion coefficients in the isotropic phase and the coexisting nematic phase. Within the nematic state, where the orientation of the rods has a preferred direction, which is referred to as the director, two kinds of diffusion coefficients can be probed:

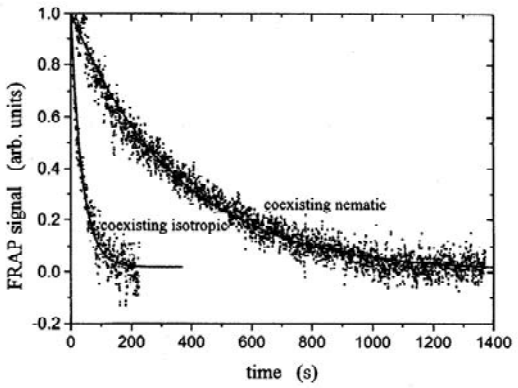

Fig. 16.15. Typical FRAP curves (for system I). The two curves are for the nematic state, where diffusion along the director is probed, and the coexisting isotropic state. After [36, 38].

diffusion along the director and perpendicular to the director. In order to be able to measure these two coefficients, the wavevector $\boldsymbol{q}_0$ in (16.154) must be chosen either along or perpendicular to the director. The corresponding FRAP geometries are sketched in Fig. 16.16, where the z-axis is along the director.

Long-time diffusion coefficients for system I are plotted in Fig. 16.17 as a function of the bare volume fraction (where the thickness is not corrected for the ACH layer thickness and charges). As can be seen, the long-time diffusion coefficients within the nematic phase are an order of magnitude smaller than for the coexisting isotropic phase. Furthermore, the long-time self-diffusion coefficient $D_{\mathrm{nem},\parallel}$ for diffusion along the director is about twice as large as the coefficient $D_{\mathrm{nem},\perp}$ for diffusion in directions perpendicular to the director. Side-wise diffusion is thus two times slower than length-wise diffusion in the nematic phase. This kind of behaviour seems to be very sensitive on flexibility and/or the presence of charge interactions [39].

For low concentrations, in the isotropic state, the long-time diffusion coefficient can be expanded with respect to the (effective) volume fraction Φ as

$$D_{\mathrm{s}}^{\mathrm{l}} \;=\; D_0 \left\{1 - \alpha\, \Phi + \mathcal{O}\left(\Phi^2\right)\right\} \;. \tag{16.167}$$

On the basis of a variational approach for spherically end-capped cylinders with hard-core interactions, the aspect-ratio dependence of the coefficient α is predicted to be equal (to within about 5 %) to [41]

$$\alpha \;=\; 2 + \tfrac{10}{32}\,(p-1) + \tfrac{1}{53}\,(p-1)^2 \;\;,\;\; p \leq 30 \;, \tag{16.168}$$

where $p = L/D$ is the aspect ratio. Here, hydrodynamic interactions have been neglected. For $p = 1$, that is for spherical particles, we have $\alpha = 2$.

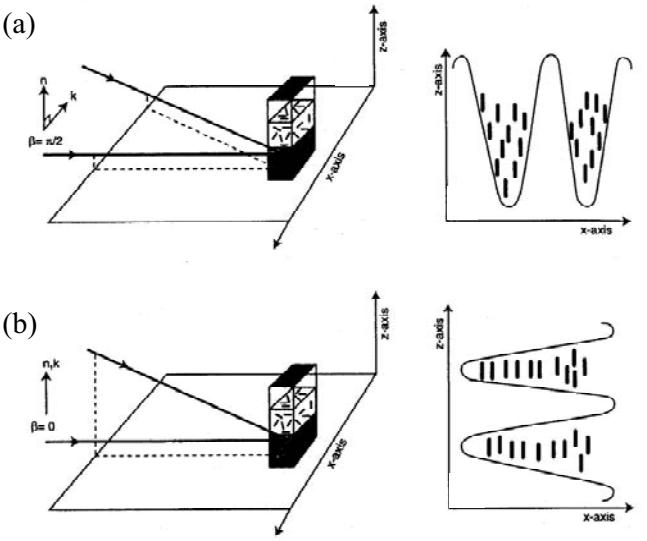

Fig. 16.16. FRAP geometries for the measurement of diffusion coefficients perpendicular to the director (a) and parallel to the director (b). The figures on the right depict the orientation of the fringe patterns relative to the director (which is along the z-axis). After [36, 38].

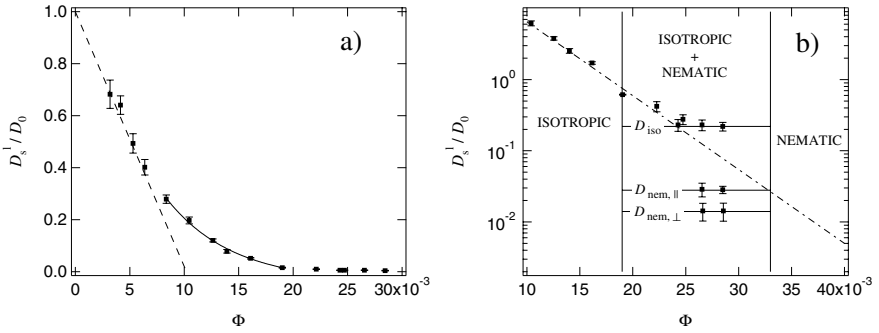

Fig. 16.17. Long-time self-diffusion coefficients for system I, as functions of the bare volume fraction in the isotropic state (a), and up to volume fractions within the i-n coexistence region (b). Diffusion coefficients are normalized to the Stokes-Einstein diffusion coefficient D_0. After [36, 38].

Including hydrodynamic interactions changes this value to 2.10 [1, 42, 43]. Since for rod-like particles the volume fractions of interest are lower than those for spheres, this indicates that hydrodynamic interactions do not very much affect values for long-time self-diffusion coefficients.

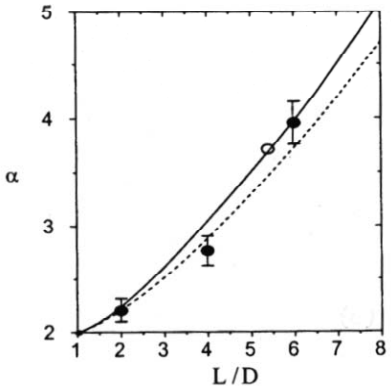

Fig. 16.18. The coefficient α, defined in (16.168), as a function of the aspect ratio $p = L/D$. The two curves are the result of a variational principle where a very simple trial function is used (dotted line) and a more involved trial function (solid line). The solid data points are computer simulation results from [40]. The open circle is the FRAP result for system II. After [36, 37].

Experimental FRAP results for system I are not in accordance with this theoretical prediction. Probably the 2 nm thick ACH layer does not effectively screen van der Waals attractions (a theoretical estimate for the minimum layer thickness to fully screen van der Waals attractions of the aluminium cores in water is about $20 - 30$ nm). For the boehmite rods with the 25 nm thick silica coating, system II, FRAP data are found to be in accordance with the prediction in (16.168). The prediction (16.168), together with the FRAP result for system II (open circle) and computer simulations (solid data points) are plotted in Fig. 16.18. The two curves are the result of the variational principle where a very simple trial function is used (dotted line) and where a more involved trial function is used (solid line) [41]. It remains a theoretical challenge to predict diffusion coefficients at higher concentrations, including the i-n coexistence region.

More FRAP data, for spherical particles, will be discussed later.

16.4.2 Fluorescence Correlation Spectroscopy (FCS)

In fluorescence correlation spectroscopy one measures the fluorescent intensity that originates from a small, relatively strongly illuminated volume. Here, a single laser beam is strongly focussed, and by means of confocal optics, the fluorescent intensity is measured from a region around the focal point, the so-called "confocal volume". The confocal optics is sketched in Fig. 16.19, and explained in the caption.

The intensity distribution within the confocal volume is well represented by a Gaussian profile,

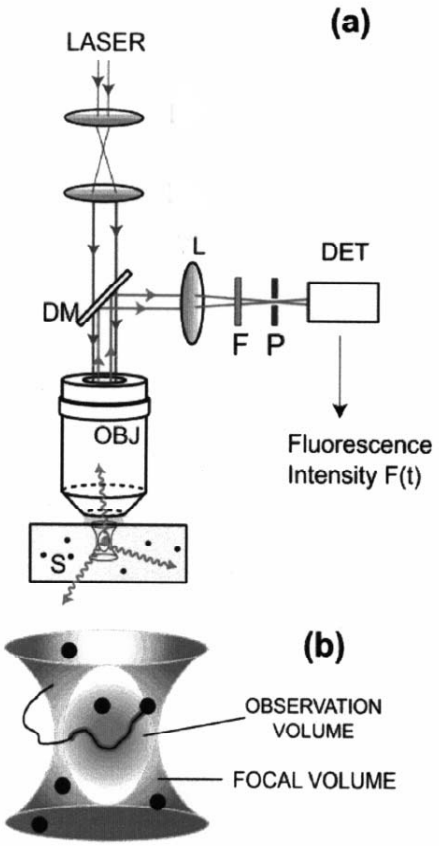

Fig. 16.19. (a) Typical configuration of confocal optics as used in an FCS experiment. A wide laser beam is strongly focussed by means of a high numerical aperture objective (OBJ). The fluorescent light is collected by the same objective, which is reflected by a dichroic mirror (DM), and focussed by a lens (L) onto a pinhole (P). The band filter admits fluorescent light to the detector (DET). The region from which fluorescent light is detected is limited to a small volume (the so-called confocal volume) by means of the pinhole P. (b) A magnification of the confocal volume. Only that part of a macromolecule that is inside the volume contributes to the measured fluorescent intensity. After [44].

$$I_0(\boldsymbol{r}) \;\sim\; \exp\{-(x^2+y^2)/2\sigma_1^2\}\;\exp\{-z^2/2\sigma_2^2\}\;, \tag{16.169}$$

where σ_1 measures the width of the confocal volume in the plane perpendicular to the propagation of the beam, while σ_2 measures the length along the propagation direction. Typically, $\sigma_1 \approx 100-300\,\mathrm{nm}$, and $\sigma_2 \approx 200-600\,\mathrm{nm}$. Similar to (16.158), the fluorescent intensity is equal to

$$I_\mathrm{f}(t) \;\sim\; \int \mathrm{d}\boldsymbol{r}\, I_0(\boldsymbol{r})\, c_\mathrm{d}(\boldsymbol{r},t)\;, \tag{16.170}$$

where c_d is the local concentration of fluorescent dye molecules, which are (at least in part) attached to the colloidal particles. The time dependence is now entirely due to the fact that colloidal particles diffuse in and out of the confocal volume. What is neglected in (16.170) is the dependence of excitation probabilities and fluorescent intensities on the orientation of dye molecules. This is probably a good approximation when there are many dye molecules, with random orientations, attached to the colloidal particles. Contrary to FRAP, the volume from which fluorescent intensities are collected is assumed to contain at most a single colloidal particle. At high concentrations this sometimes requires to mix labelled with unlabelled colloidal particles. In a FCS experiment, the intensity correlation function $C_\mathrm{f}(t) \equiv \langle I_\mathrm{f}(t)\, I_\mathrm{f}(t=0)\rangle$ is measured. From (16.170) we obtain

$$\begin{aligned} C_\mathrm{f}(t) &= \int \mathrm{d}\boldsymbol{r} \int \mathrm{d}\boldsymbol{r}'\, I_0(\boldsymbol{r})\, I_0(\boldsymbol{r}')\, \langle c_\mathrm{d}(\boldsymbol{r},t)\, c_\mathrm{d}(\boldsymbol{r}',t=0)\rangle \\ &\sim \int \mathrm{d}\boldsymbol{q} \int \mathrm{d}\boldsymbol{q}'\, I_0(\boldsymbol{q})\, I_0(\boldsymbol{q}')\, \langle c_\mathrm{d}(\boldsymbol{q},t)\, c_\mathrm{d}(\boldsymbol{q}',t=0)\rangle\;, \end{aligned} \tag{16.171}$$

where in the second equation Bessel's theorem has been applied twice, to convert spatial integrations to wavevector integrations, which will simplify the further mathematical analysis. Here, q- and q'-dependent functions are understood to be spatial Fourier transforms with respect to $\boldsymbol{r}$ and $\boldsymbol{r}'$, respectively. Now suppose that there is at most a single fluorescent colloidal particle inside the confocal volume. The Fourier transform of the dye concentration c_0 can be written as

$$c_0(\boldsymbol{q},t) \;=\; B_\mathrm{f}(\boldsymbol{q},t)\, \exp\{\mathrm{i}\boldsymbol{q}\cdot\boldsymbol{r}_\mathrm{c}(t)\}\;, \tag{16.172}$$

where $\boldsymbol{r}_\mathrm{c}$ is the position coordinate (the position of the center of mass) of the colloidal particle, and the "fluorescence amplitude" B_f is defined as

$$B_\mathrm{f}(\boldsymbol{q},t) \;=\; \int_{V_0(t)} \mathrm{d}\boldsymbol{r}\, \chi_\mathrm{d}(\boldsymbol{r})\, \exp\{\mathrm{i}\boldsymbol{q}\cdot\boldsymbol{r}\}\;, \tag{16.173}$$

where V_0 is the volume occupied by the colloidal particle with its center-of-mass at the origin (as indicated by the subscript "0"), and $\chi_\mathrm{d}(\boldsymbol{r})$ is the characteristic function for the dye on and within the core of the colloidal particle

($\chi_{\rm d}(\boldsymbol{r}) = 1$ when there is a dye molecule at $\boldsymbol{r}$, and $= 0$ otherwise). The exponential with the position coordinate originates from the transformation to the spatial integration with respect to a coordinate system where the center-of-mass is chosen as the origin (similar as has been done in Sect. 16.2, dealing with the principles of light scattering). The integral in (16.173) depends only on the way dye molecules are distributed over its surface and possibly inside its core. The volume V_0 is time dependent for colloidal particles where the dye distribution is non-spherically symmetric, through the orientation of the colloidal particle. Possible rotational contributions to the correlation function $C(t)$ originate from this integral. Such orientational contributions become important when the largest linear dimension of the fluorescent macromolecule are of the order of or larger than the dimensions of the confocal volume. In that case, a mere rotation of the macromolecule can give rise to a change of the fluorescent intensity. Translational contributions originate from the time dependence of the position coordinate $\boldsymbol{r}_{\rm c}$. From (16.171), (16.172) we have

$$\langle c_{\rm d}(\boldsymbol{q},t)\, c_{\rm d}(\boldsymbol{q}',t=0)\rangle \;\sim\; \langle \exp\{{\rm i}\boldsymbol{q}\cdot\boldsymbol{r}_{\rm c}(t)\}\, \exp\{{\rm i}\boldsymbol{q}'\cdot\boldsymbol{r}_{\rm c}(t=0)\}\rangle \;. \quad (16.174)$$

Since, for a homogeneous system, the probability density function P of $\{\boldsymbol{r}_{\rm c}(t), \boldsymbol{r}_{\rm c}(t=0)\}$ depends only on the difference $\boldsymbol{r}_{\rm c}(t) - \boldsymbol{r}_{\rm c}(t=0)$, it follows that (with $\boldsymbol{R} = \boldsymbol{r}_{\rm c} + \boldsymbol{r}'_{\rm c}$ and $\varDelta\boldsymbol{r} = \boldsymbol{r}_{\rm c} - \boldsymbol{r}'_{\rm c}$)

$$\begin{aligned}
&\langle c_{\rm d}(\boldsymbol{q},t)\, c_{\rm d}(\boldsymbol{q}',t=0)\rangle \\
&\qquad \sim \int {\rm d}\boldsymbol{r}_{\rm c} \int {\rm d}\boldsymbol{r}'_{\rm c}\, P(\boldsymbol{r}_{\rm c}-\boldsymbol{r}'_{\rm c},t)\, \exp\{{\rm i}\boldsymbol{q}\cdot\boldsymbol{r}_{\rm c}\}\, \exp\{{\rm i}\boldsymbol{q}'\cdot\boldsymbol{r}'_{\rm c}\} \\
&\qquad\qquad \sim \left\{ \int {\rm d}\boldsymbol{R} \exp\{{\rm i}\tfrac{1}{2}(\boldsymbol{q}+\boldsymbol{q}')\cdot\boldsymbol{R}\} \right\} \\
&\qquad\qquad \times \left\{ \int {\rm d}\varDelta\boldsymbol{r}\, P(\varDelta\boldsymbol{r},t)\, \exp\{{\rm i}\tfrac{1}{2}(\boldsymbol{q}-\boldsymbol{q}')\cdot\varDelta\boldsymbol{r}\} \right\} . \quad (16.175)
\end{aligned}$$

Since

$$\int {\rm d}\boldsymbol{R} \exp\{{\rm i}\tfrac{1}{2}(\boldsymbol{q}+\boldsymbol{q}')\cdot\boldsymbol{R}\} \;\sim\; \delta(\boldsymbol{q}+\boldsymbol{q}') \;, \quad (16.176)$$

where δ is the Dirac delta distribution, it follows from (16.175), that

$$\langle c_{\rm d}(\boldsymbol{q},t)\, c_{\rm d}(\boldsymbol{q}',t=0)\rangle \;\sim\; \langle c_{\rm d}(\boldsymbol{q},t)\, c_{\rm d}(-\boldsymbol{q},t=0)\rangle\, \delta(\boldsymbol{q}+\boldsymbol{q}') \;. \quad (16.177)$$

This equation expresses translational invariance of a homogeneous system. Substitution into (16.171) thus leads to

$$C_{\rm f}(t) \;\sim\; \int {\rm d}\boldsymbol{q}\, I_0^2(\boldsymbol{q})\, \langle B_{\rm f}(\boldsymbol{q},t)\, B_{\rm f}^{\star}(\boldsymbol{q},t=0)\, \exp\{{\rm i}\boldsymbol{q}\cdot(\boldsymbol{r}_{\rm c}(t)-\boldsymbol{r}_{\rm c}(t=0))\}\rangle \;, \quad (16.178)$$

where "$\star$" stands for complex conjugation. Note that, when the core of the colloidal particle is homogeneously labelled, the ensemble average in (16.178)

for the fluorescence autocorrelation function is nothing but the electric field autocorrelation function in (16.20) that one would measure in a dynamic light scattering experiment, provided that the scattering power is homogeneously distributed over the core of the particles. The fluorescence correlation function is a weighted $\boldsymbol{q}$-average of the light scattering correlation function. When the confocal volume is large compared to the linear dimensions of the colloidal particles, the rotational contributions arising from the fluorescence amplitudes B_f in (16.178) do not contribute to the time dependence of the fluorescence correlation function (in fact, numerical calculations for stiff rods show that this is already the case when $\sigma_1 \geq L/2$, with L the length of the rods). Hence, for any practical application we have

$$C_\mathrm{f}(t) \;\sim\; \int \mathrm{d}\boldsymbol{q}\, I_0^2(\boldsymbol{q})\, \langle \exp\{\mathrm{i}\boldsymbol{q}\cdot(\boldsymbol{r}_\mathrm{c}(t)-\boldsymbol{r}_\mathrm{c}(t=0))\}\rangle \;. \tag{16.179}$$

Since the fluorescent intensity only changes when the colloidal particle is displaced over a distance larger or comparable to dimensions of the confocal volume, which is in turn larger than the linear dimensions of the colloidal particles, the correlation function in the above equation is the long-time limiting form as given in (16.165). Using that the Fourier transform of the Gaussian profile in (16.169) is given by

$$I_0(\boldsymbol{q}) \;\sim\; \exp\{-(q_x^2+q_y^2)\sigma_1^2/2\}\; \exp\{-q_z^2\sigma_2^2/2\} \;, \tag{16.180}$$

where q_j is the j-component of $\boldsymbol{q}$, it is thus found that

$$\begin{aligned} C_\mathrm{f}(t) &\sim \int \mathrm{d}q_x\, \exp\{-q_x^2\left[D_\mathrm{s}^\mathrm{l}t+\sigma_1^2\right]\} \times \int \mathrm{d}q_y\, \exp\{-q_y^2\left[D_\mathrm{s}^\mathrm{l}t+\sigma_1^2\right]\} \\ &\times \int \mathrm{d}q_z\, \exp\{-q_z^2\left[D_\mathrm{s}^\mathrm{l}t+\sigma_2^2\right]\} \;\sim\; \left[1+\frac{D_\mathrm{s}^\mathrm{l}\,t}{\sigma_1^2}\right]^{-1} \left[1+\frac{D_\mathrm{s}^\mathrm{l}\,t}{\sigma_2^2}\right]^{-1/2} . \end{aligned} \tag{16.181}$$

The fluorescent intensity autocorrelation function thus decays algebraically with time, with the two time constants $\sigma_{1,2}^2/D_\mathrm{s}^\mathrm{l}$. The geometrical constants $\sigma_{1,2}$ can be determined from a measurement of a dilute system where D_s^l is equal to the Stokes-Einstein diffusion coefficient, that can be obtained independently from dynamic light scattering.

When the size of the particles is not small in comparison with the confocal volume, the q-dependence of the fluorescence amplitudes in (16.178) comes into play. For spherical colloidal particles, in which the fluorescent dye is radially symmetrically distributed, the amplitudes are independent of time, so that (16.178) simplifies to

$$C_\mathrm{f}(t) \;\sim\; \int \mathrm{d}\boldsymbol{q}\; \left[I_0^\mathrm{eff}(\boldsymbol{q})\right]^2\; \langle \exp\{\mathrm{i}\boldsymbol{q}\cdot(\boldsymbol{r}_\mathrm{c}(0)-\boldsymbol{r}_\mathrm{c}(t=0))\}\rangle \;,$$

where

$$I_0^{\rm eff}(\boldsymbol{q}) \;=\; I_0(\boldsymbol{q}) \;|\,B(q)\,|$$

is the Fourier transform of the intensity complying with an "effective confocal volume". For homogeneously labelled spheres, $|\,B(q)\,|$ can be represented quite accurately by a Gaussian $\sim \exp\{-0.11\,q^2a^2\}$, up to wavevectors where $B(q)$ is small enough that it does not contribute anymore to the integral over $\boldsymbol{q}$. Here, a is the radius of the spherical colloidal particle. We thus obtain the "effective size" of the confocal volume as

$$\sigma_{1,2}^{\rm eff} \;=\; \sqrt{\sigma_{1,2}^2 \,+\, 0.22\,a^2}\;.$$

When the particles are large, the fluorescent intensity is non-zero already when the outer part of a particle enters the confocal volume. At that moment the center of the colloid is still outside the confocal volume. This leads to an increase of the apparent confocal volume, as quantified for homogeneously labelled spheres by the present expression for $\sigma_{1,2}^{\rm eff}$.

Experimental correlation functions show some features that we have not discussed above. First of all, in the various steps taken in the above analysis, prefactors are always omitted. It turns out, by including all prefactors, that the proportionality constant in (16.181) is equal to 1/[the average number of fluorescent colloidal particles in the confocal volume]. This reflects the relative decrease of number fluctuations in a given volume with increase of volume. Secondly, there may be free dye molecules, not attached to colloidal particles, in the solvent. When this is the case, there is a second, additive contribution of the form (16.181), except that the time constants are much smaller as compared to those for the colloidal particles. Free dye is therefore seen only at very small times. Thirdly, dye molecules that are excited in long-lived triplet states do not contribute to the fluorescent intensity and therefore temporarily reduce the number of fluorescent dye molecules. Triplet state excitation can thus be regarded as "reversible bleaching" (contrary to the irreversible bleaching in the FRAP experiments described earlier). The relative amplitude of such contributions depends on the sort of dye that is used, as well as the concentration of dye on the surface and/or inside the core of a colloidal particle.

A recent overview of FCS can be found in [44]. An extensive literature list can be found on the FCS website of Zeiss. The above analysis is a simplified version of a more elaborate analysis in [45].

As far as we are aware, there are no systematic FCS investigations published on macromolecular systems. An example of a fluorescence correlation function on fd-virus (a semi-flexible rod of length 880 nm and width of about 6 nm, with a persistence length of 2200 nm), labelled with TARAM , is given in Fig. 16.20 [46]. At very small times a triplet contribution is found, at intermediate times a decay due to free dye and at longer times decay due to diffusion of the fd-virus. The curve is fitted with a sum of three terms: a single exponential function to account for the triplet contribution, and a sum of two contributions of the form as in (16.181) (one for the free dye and one

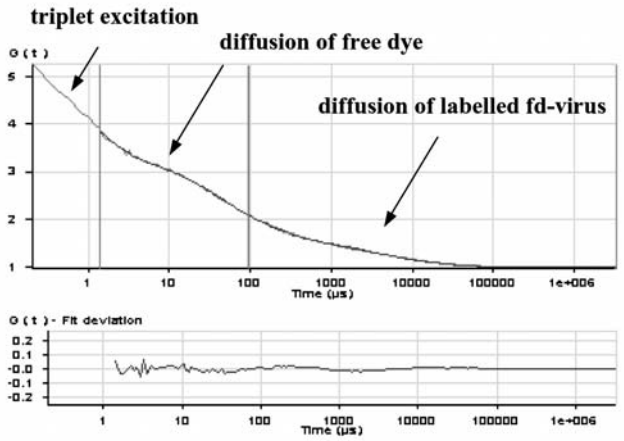

Fig. 16.20. A fluorescence correlation function for fd-virus, labelled with TARAM. At small times a triplet contribution is clearly present, at intermediate times the correlation function decays due to the presence of free dye molecules, and at larger times due to diffusion of fd-virus. The lower part in the figure gives the residues after a least-square fit as described in the main text.

for the fd-virus). Clearly, the conditions should be optimized, in particular to minimize the triple contribution.

16.5 Theoretical and Experimental Results on Diffusion of Colloidal Spheres and Polymers

For times $t \gg \tau_{\mathrm{B}}$, which is the regime of most DLS experiments, the velocities of the colloidal spheres have relaxed to equilibrium, so that only the slow relaxation of the particle positions and orientations is probed. Therefore, the dynamics of interacting spheres is entirely described on this coarse-grained level in terms of a many-particle pdf, $P(\boldsymbol{r}^N, \hat{\boldsymbol{u}}, t)$, in the configuration space of positional and orientational degrees of freedom. The pdf depends thus, in principle, on the center-of-mass position vectors $\boldsymbol{r}^N = (\boldsymbol{r}_1, \cdots, \boldsymbol{r}_N)$ and orientation vectors $\hat{\boldsymbol{u}}^N = (\hat{\boldsymbol{u}}_1, \cdots, \hat{\boldsymbol{u}}_N)$ of all N spheres in the suspension (scattering volume) V_{s}. The equation of motion for $P(\boldsymbol{r}^N, \hat{\boldsymbol{u}}^N, t)$ is a generalization of the one-particle diffusion equation (16.45) to interacting particle systems. This many-particle diffusion equation is known among colloid scientists as the generalized Smoluchowski equation (GSE). In the polymer science community, it is better known as the Kirkwood-Riseman-Zimm equation [13, 47].

The description of the configurational evolution by means of the GSE is founded on the separation of time scales between the fast fluctuating parti-

cle velocities, and the slow configurational changes. Such a description cannot be applied to polymer blends since the relaxation of the matrix, which plays the role of the solvent, is comparable to those of the other components. To explore the polymer dynamics in the diffusion limit (or Markovian limit) of small wavenumbers and long times, we resort therefore to the semiphenomenological dynamic RPA. Using the RPA, we will study the interdiffusion process in a ternary homopolymer mixture.

16.5.1 Colloidal Spheres

Consider N identical colloidal spheres in a quiescent and unbound Newtonian solvent. The evolution for the pdf of the particle positions *alone*

$$P(\boldsymbol{r}^N,t) \;=\; \int \mathrm{d}\boldsymbol{r}^N\; P(\boldsymbol{r}^N,\hat{\boldsymbol{u}}^N,t) \tag{16.182}$$

is described, for $t \gg \tau_{\mathrm{B}}$, by the translational GSE

$$\frac{\partial}{\partial t}P(\boldsymbol{r}^N,t) \;=\; \widehat{O}(\boldsymbol{r}^N)P(\boldsymbol{r}^N,t)\,, \tag{16.183}$$

where

$$\widehat{O}(\boldsymbol{r}^N) \;=\; \sum_{i,j=1}^{N} \nabla_i \cdot \boldsymbol{D}_{ij}(\boldsymbol{r}^N)\cdot[\nabla_j - \beta \boldsymbol{F}_j] \tag{16.184}$$

is the Smoluchowski differential operator. Here, $\boldsymbol{F}_j = -\nabla_j U(\boldsymbol{r}^N)$ denotes the force that all other $N-1$ spheres exert on sphere j, through potential interactions $U(\boldsymbol{r}^N)$. It is assumed here that the potential energy $U(\boldsymbol{r}^N)$ is independent of orientation so that the particles exert no torques on each other. Otherwise, the translational motion would be coupled to the rotational one. The solvent appears in (16.183) only through the time-independent *translational* diffusivity tensors $\boldsymbol{D}_{ij}(\boldsymbol{r}^N)$, which describe the solvent-mediated HI between the spheres. The tensors $\boldsymbol{D}_{ij}(\boldsymbol{r}^N)$ relate the hydrodynamic forces $\{\boldsymbol{F}_j^{\mathrm{H}}\}$, exerted on the surfaces of the spheres by the surrounding fluid to the resulting drift velocity $\boldsymbol{v}_i$ of a sphere i in form of a generalized Stokes' law

$$\boldsymbol{v}_i \;=\; -\frac{1}{k_{\mathrm{B}}T}\sum_{j=1}^{N}\boldsymbol{D}_{ij}(\boldsymbol{r}^N)\cdot\boldsymbol{F}_j^{\mathrm{H}}\,. \tag{16.185}$$

The propagation of hydrodynamic disturbances (via sound and diffusion of shear waves) appears to be infinitely fast for times $t \gg \tau_\eta$. Therefore, the HI between the spheres act quasi instantaneously on these time scales and $\boldsymbol{D}_{ij}(\boldsymbol{r}^N)$ can be determined, in principle, from solving the stationary linearized Navier-Stokes equation describing the creeping flow in an incompressible fluid, augmented by stick boundary conditions on the sphere surfaces. Yet, actual analytical calculations of the $\boldsymbol{D}_{ij}(\boldsymbol{r}^N)$ are very difficult and have

been fully achieved only on the pairwise-additive level, mainly in form of inverse distance expansions. Hereby one disregards the influence of other spheres on the HI between a given pair of spheres, an approximation which is valid only for large interparticle distances. Note for spheres that the $\boldsymbol{D}_{ij}\boldsymbol{r}^N)$ depend only on the positions. For non-spherical particles, HI couple position and orientation variables. If we ignore HI, $\boldsymbol{D}_{ij} = \delta_{ij} D_0 \mathbf{1}$ and (16.185) reduces to the standard Stokes' law for isolated single spheres.

In equilibrium, $(\partial/\partial t)P = 0$, and the GSE is satisfied by the equilibrium pdf

$$P_{\mathrm{eq}}(\boldsymbol{r}^N) \;=\; \exp\{-\beta U(\boldsymbol{r}^N)\} \Big/ \int \mathrm{d}\boldsymbol{r}^N \exp\{-\beta U(\boldsymbol{r}^N)\} \tag{16.186}$$

independent of the $\boldsymbol{D}_{ij}(\boldsymbol{r}^N)$. This shows that the HI are dynamic forces with no effect on static equilibrium properties.

Using the GSE, one can express equilibrium time-correlation functions like $S_{\mathrm{c}}(q,t)$ and $S_{\mathrm{s}}(q,t)$ as

$$S_{\mathrm{A}}(q,t) \;=\; \langle \rho_{\mathrm{A}}(-\boldsymbol{q}) \left(\exp\{\widehat{O}_{\mathrm{B}} t\} \rho_{\mathrm{A}}(\boldsymbol{q}) \right) \rangle \,, \tag{16.187}$$

with $\mathrm{A} = \mathrm{a}, \mathrm{c}$ and microscopic densities $\rho_{\mathrm{c}}(\boldsymbol{q}) = \rho(\boldsymbol{q})$ (see (16.24)) and $\rho_{\mathrm{s}}(\boldsymbol{q}) = \exp\{\mathrm{i}\boldsymbol{q} \cdot \boldsymbol{r}_1\}$. Here

$$\widehat{O}_{\mathrm{B}}(\boldsymbol{r}^N) \;=\; \sum_{i,j=1}^{N} \left[\nabla_i + \frac{1}{k_{\mathrm{B}} T} \boldsymbol{F}_i \right] \cdot \boldsymbol{D}_{ij}(\boldsymbol{r}^N) \cdot \nabla_j \tag{16.188}$$

is the adjoint (or backward) Smoluchowski operator, and

$$\langle \cdots \rangle \;=\; \int \mathrm{d}\boldsymbol{r}^N P_{\mathrm{eq}}(\boldsymbol{r}^N) \, (\cdots) \tag{16.189}$$

is the equilibrium ensemble average. Note that $\widehat{O}_{\mathrm{B}}$ operates only on ρ_{A}, and not on P_{eq}.

In the following subsection, we describe theoretical methods based on the GSE. From a theoretical point of view, it is appropriate to treat short-time diffusion and long-time diffusion separately, since the former is needed as an input to the latter one.

Short-Time Diffusion

In general, $S_{\mathrm{A}}(q,t)$ cannot be calculated exactly from (16.187), owing to the complicated form of the operator $\widehat{O}_{\mathrm{B}}$ for interacting particles. However, for short times $t \ll \tau_{\mathrm{I}}$, $S_{\mathrm{A}}(q,t)$ can be expressed in a series of cumulants, that is

$$S_{\rm A}(q,t) = S_{\rm A}(q)\ \exp\left\{\ \sum_{l=1}^{\infty}(-t)^{\rm l}\,\frac{\Gamma_{\rm A}^{(l)}(q)}{l!}\ \right\} \tag{16.190}$$
$$= S_{\rm A}(q)\ \exp\left\{\ -\Gamma_{\rm A}^{(1)}(q)\,t + \frac{1}{2}\,\Gamma_{\rm A}^{(2)}(q)\,t^2\ +\cdots\ \right\}$$

with $S_{\rm A}(q) = S_{\rm A}(q,t)$. The higher-order cumulants, $\Gamma_{\rm A}^{(l)}$, with $l = 2, 3, \cdots$, measure the deviation of $S_{\rm A}(q,t)$ from a single-exponential decay. Cumulant analysis is a customary tool to analyze DLS data at short times, whereby mainly the first and second cumulants have been determined. One can alternatively expand $S_{\rm A}(q,t)$ in a time Taylor series, resulting in the so-called moment expansion

$$S_{\rm A}(q,t)\ =\ \sum_{n=0}^{\infty}\frac{t^n}{n!}\,S_{\rm A}^{(n)}(q)\ =\ S_{\rm A}(q)+tS_a^{(1)}(q)+\frac{1}{2}t^2\ S_{\rm A}^{(2)}(q)+\ldots\,, \tag{16.191}$$

with moments

$$S_{\rm A}^{(n)}(q)\ =\ \frac{1}{N}\langle\rho_{\rm A}(-\boldsymbol{q})(\widehat{O}_{\rm B})^{n}\rho_{\rm A}(\boldsymbol{q})\rangle\,. \tag{16.192}$$

In deriving (16.192), we have expanded the time evolution operator $\exp\{\widehat{O}_{\rm B}\}$ in (16.187) in powers of t. From a small-t expansion of (16.191), it follows for the two leading cumulants that

$$\Gamma_{\rm A}^{(1)}(q) = -\frac{S_{\rm A}^{(2)}(q)}{S_{\rm A}(q)} \tag{16.193}$$
$$\Gamma_{\rm A}^{(2)}(q) = \frac{S_{\rm A}^{(2)}(q)}{S_{\rm A}(q)} - \left[\frac{S_{\rm A}^{(1)}(q)}{S_{\rm A}(q)}\right]^2\,.$$

In specializing to A = c, the first cumulant of the collective dynamic structure factor follows as

$$\Gamma_{\rm c}^{(1)}(q)\ =\ q^2D_{\rm c}^{\rm s}(q)\ =\ q^2D_0\frac{H(q)}{S_{\rm c}(q)}\,. \tag{16.194}$$

Here, $D_{\rm c}^{\rm s}(q)$ is the apparent short-time collective diffusion coefficient already defined in (16.98), and $H(q)$ is given by

$$H(q)\ =\ \frac{1}{ND_0}\sum_{l,j=1}^{N}\langle\hat{\boldsymbol{q}}\cdot\boldsymbol{D}_{lj}(\boldsymbol{r}^N)\cdot\hat{\boldsymbol{q}}\,\exp\{{\rm i}\boldsymbol{q}\cdot[\boldsymbol{r}_l-\boldsymbol{r}_j]\}\rangle\,. \tag{16.195}$$

The function $H(q) \geq 0$ contains, through the diffusion tensors $\boldsymbol{D}_{lj}$, the influence of HI on the short-time collective diffusion. For this reason, $H(q)$ is known as the hydrodynamic function. Without HI, $H(q) \equiv 1$, so that $D_{\rm c}^{\rm s}(q) = D_0/S_{\rm c}(q)$ in this case. Any q-dependence of $H(q)$ is thus an indicator

for the non-negligible influence of HI. Comparison with the phenomenological (16.108) shows that

$$\lim_{q\to 0} H(q) \;=\; \frac{U^{\mathrm{s}}}{U_0}\,. \tag{16.196}$$

Hence, the long-wavelength limit of the hydrodynamic function is equal to the relative (short-time) sedimentation velocity in a homogeneous suspension. According to (16.195), $H(q)$ is indeed a short-time equilibrium average.

Next, the first cumulant for the self-dynamic structure factor is determined as (see (16.192))

$$\Gamma_{\mathrm{s}}^{(1)}(q) \;=\; q^2 D_{\mathrm{s}}^{\mathrm{s}}\,, \tag{16.197}$$

with the microscopic expression

$$D_{\mathrm{s}}^{\mathrm{s}} \;=\; \langle \hat{\boldsymbol{q}} \cdot \boldsymbol{D}_{11}(\boldsymbol{r}^N) \cdot \hat{\boldsymbol{q}} \rangle \tag{16.198}$$

for the translational short-time self-diffusion coefficient. Without HI, $D_{\mathrm{s}}^{\mathrm{s}} = D_0$ since at short times the Brownian motion of a sphere is not influenced by direct forces.

For large $q \gg q_{\mathrm{m}}$, strong oscillations in the exponential factors in (16.195) cancel each other for $l \neq j$, and $H(q)$ becomes therefore equal to the reduced short-time self-diffusion coefficient, i.e.

$$H(q \gg q_{\mathrm{m}}) \approx \frac{D_{\mathrm{s}}^{\mathrm{s}}}{D_0}\,. \tag{16.199}$$

Likewise, $D_{\mathrm{c}}^{\mathrm{s}}(q \gg q_{\mathrm{m}}) \approx D_{\mathrm{s}}^{\mathrm{s}}$ since $S_{\mathrm{c}}(q \gg q_{\mathrm{m}}) = 1$. Thus, it is in principle possible to determine short-time self-diffusion properties from DLS experiments performed at long wavenumbers without a need for contrast variation. Index matching is needed, however, to determine the MSD at longer times.

Moments up to the third order have been calculated for $S_{\mathrm{A}}(q,t)$. The expression for the second moment of $S_{\mathrm{c}}(q,t)$ reads without HI

$$S_{\mathrm{c}}^{(2)}(q) \;=\; (q^2 D_0)^2 \left\{ 1 + \frac{\beta\rho_0}{q^2} \int \mathrm{d}\boldsymbol{r}\, g(r)\,(1-\cos(\boldsymbol{q}\cdot\boldsymbol{r}))\,(\hat{\boldsymbol{q}}\cdot\nabla)^2 u(r) \right\}. \tag{16.200}$$

It is given in terms of the pair distribution function $g(r)$, and derivatives of the pair potential, $u(r)$, between two spheres. Hereby it is assumed that the total potential energy is pairwise additive, that is $U(\boldsymbol{r}^N) = \sum_{i<j} u(|\boldsymbol{r}_i - \boldsymbol{r}_j|)$. The second cumulant, $S_{\mathrm{s}}^{(2)}(q)$, of $S_{\mathrm{s}}(q,t)$ is given by (16.200) with the $\cos(\boldsymbol{q}\cdot\boldsymbol{r})$ term omitted, since

$$S_{\mathrm{c}}(q \gg q_{\mathrm{m}}, t) \;=\; S_{\mathrm{s}}(q,t) \tag{16.201}$$

due to smallness of the distinct part, $S_{\mathrm{d}}(q,t)$, of $S_{\mathrm{c}}(q,t)$ for $q \gg q_{\mathrm{m}}$ (cf. (16.28)).

Little is known about the higher-order moments. With HI, even the second moment becomes quite complicated, invoking now up to four-particle

static distribution functions. Thus moment expansions are not very helpful in gaining information on $S_{\rm A}(q,t)$ for intermediate and long times. In the following section, we will describe a projection operator method which is far better suited for analyzing the dynamics at long times.

Incidentally, the second moment of $S_{\rm A}(q,t)$ does not exist for systems with singular pair potentials like suspensions of colloidal hard spheres. For the latter case, the non-analytical short-time expansion of $S_{\rm A}(q,t)$ is given by

$$S_{\rm A}(q,\tau) \;=\; S_{\rm A}(q) - \tau + \frac{4\sqrt{\pi}}{3}\, C_{\rm A}(q;\Phi)\, \tau^{3/2} + \cdots \tag{16.202}$$

with $\tau = q^2 D_0 t$. Explicit expressions for the expansion coefficients $C_{\rm s}(q;\Phi)$ and $C_{\rm c}(q;\Phi)$ can be found in [24, 48].

In order to obtain explicit results for the short-time translational property $H(q)$ and its limiting values $U^{\rm s}$ and $D_{\rm s}^{\rm s}$, it is necessary to specify the translational diffusivity tensors $\boldsymbol{D}_{ij}(\boldsymbol{r}^N)$. For this purpose, it is useful to expand $\boldsymbol{D}_{ij}(\boldsymbol{r}^N)$, according to

$$\boldsymbol{D}_{ij}(\boldsymbol{r}^N) \;=\; D_0 \mathbf{1}\delta_{ij} + \boldsymbol{D}_{ij}^{(2)}(\boldsymbol{r}^N) + \boldsymbol{D}_{ij}^{(3)}(\boldsymbol{r}^N) + \cdots\,, \tag{16.203}$$

into contributions, $\boldsymbol{D}_{ij}^{(n)}(\boldsymbol{r}^N)$, originating from increasingly large clusters of n hydrodynamically interacting spheres.

For (very) small volume fractions, it is justified to assume pairwise additivity of the HI. In this case

$$\boldsymbol{D}_{ij}(\boldsymbol{r}^N) \;\approx\; D_0 \mathbf{1}\delta_{ij} + \boldsymbol{D}_{ij}^{(2)}(\boldsymbol{r}^N)\,, \tag{16.204}$$

with

$$\boldsymbol{D}_{ij}^{(2)}(\boldsymbol{r}^N) \;=\; D_0 \left[\delta_{ij} \sum_{l\neq i}^{N} \boldsymbol{\omega}_{11}(\boldsymbol{r}_i - \boldsymbol{r}_l) + (1-\delta_{ij})\, \boldsymbol{\omega}_{12}(\boldsymbol{r}_i - \boldsymbol{r}_j)\right]. \tag{16.205}$$

The first term of (16.205) determines $\boldsymbol{D}_{11}$ in (16.198) so that the tensor $\boldsymbol{\omega}_{11}$ modifies the short-time self-diffusion coefficient as compared to its value, D_0, at infinite dilution. The tensor $\boldsymbol{\omega}_{12}$ determines the distinct part, $i \neq j$, of $H(q)$. For one-component suspensions of spheres, series expansions of $\boldsymbol{\omega}_{11}(\boldsymbol{r})$ and $\boldsymbol{\omega}_{12}(\boldsymbol{r})$ are known, in principle, to arbitrary order. The leading terms in this long-distance expansions are

$$\begin{aligned}
\boldsymbol{\omega}_{11}(\boldsymbol{r}) &= -\frac{15}{4}\left(\frac{a}{r}\right)^4 \hat{\boldsymbol{r}}\hat{\boldsymbol{r}} + \mathcal{O}\left[\left(\frac{a}{r}\right)^6\right] \\
\boldsymbol{\omega}_{12}(\boldsymbol{r}) &= \frac{3}{4}\left(\frac{a}{r}\right)\left[\mathbf{1} + \hat{\boldsymbol{r}}\hat{\boldsymbol{r}}\right] + \frac{1}{2}\left(\frac{a}{r}\right)^3\left[\mathbf{1} - 3\,\hat{\boldsymbol{r}}\hat{\boldsymbol{r}}\right] + \mathcal{O}\left[\left(\frac{a}{r}\right)^7\right],
\end{aligned} \tag{16.206}$$

where $\hat{\boldsymbol{r}} = \boldsymbol{r}/r$. The long-distance (i.e. far-field) expression for $\boldsymbol{\omega}_{12}(\boldsymbol{r})$ up to $\mathcal{O}(r^{-3})$ is the well-known Rotne-Prager (RP) tensor [49].

Substitution of (16.205) into (16.195) and (16.198) leads to the expressions

$$D_{\mathrm{s}}^{\mathrm{s}} = D_0 \left[1 + \rho_0 \int \mathrm{d}\boldsymbol{r}\, g(r)\, \hat{\boldsymbol{q}} \cdot \boldsymbol{\omega}_{11}(\boldsymbol{r}) \cdot \hat{\boldsymbol{q}} \right] \tag{16.207}$$

$$H(q) = \frac{D_{\mathrm{s}}^{\mathrm{s}}}{D_0} + \rho_0 \int \mathrm{d}\boldsymbol{r}\, g(r)\, \hat{\boldsymbol{q}} \cdot \boldsymbol{\omega}_{12}(\boldsymbol{r}) \cdot \hat{\boldsymbol{q}} \cos(\boldsymbol{q} \cdot \boldsymbol{r}) \,, \tag{16.208}$$

valid for pairwise additive HI. The only input needed to calculate $D_{\mathrm{s}}^{\mathrm{s}}$ and $H(q)$ from these expressions is the pair distribution function $g(r)$. The latter gives the conditional probability of finding a second sphere a distance r apart from a given one. For given pair potential $u(r)$, $g(r)$ can be determined using standard integral equation methods or computer simulations [18, 50]. For neutral hard spheres, $g(r)$ has its maximum at contact distance, $r = 2a^+$, whereas it is practically equal to zero for charged spheres up to the nearest-neighbor distance, where it attains a rather pronounced peak. This implies that, contrary to dilute suspensions of charge-stabilized spheres, where only the leading far-field terms in $\boldsymbol{\omega}_{ij}$ are of importance, many more terms need to be summed up for neutral hard spheres.

The most accurate virial expansion result for the $D_{\mathrm{s}}^{\mathrm{s}}$ of monodisperse hard spheres valid to second order in Φ reads [51]

$$\frac{D_{\mathrm{s}}^{\mathrm{s}}}{D_0} = 1 - 1.832\Phi - 0.219\Phi^2 + \mathcal{O}(\Phi^3) \,. \tag{16.209}$$

This result has been obtained from summing up a large number of terms in the inverse-distance expansions of $\boldsymbol{D}_{11}^{(2)}$ and $\boldsymbol{D}_{11}^{(3)}$, and by further accounting for short-range lubrication interactions between nearly touching pairs or triplets of spheres. Three-body terms in $\boldsymbol{D}_{11}$, which contribute to $D_{\mathrm{s}}^{\mathrm{s}}$ to order Φ^2, appear first in order r^{-7}.

Fig. 16.21 depicts $D_{\mathrm{s}}^{\mathrm{s}}$, determined according to (16.209), in comparison with DLS and depolarized DLS data on hard spheres, and with the semi-empirical formula,

$$\frac{D_{\mathrm{s}}^{\mathrm{s}}}{D_0} = (1 - 1.56\Phi)\,(1 - 0.27\Phi) \,, \tag{16.210}$$

proposed by Lionberger and Russel [53]. The latter formula conforms to the (numerically) exact $\mathcal{O}(\Phi)$ limit in (16.209), and it predicts $D_{\mathrm{s}}^{\mathrm{s}}$ to vanish at the volume fraction $\Phi_{\mathrm{rcp}} \approx 0.64$ where random close packing occurs. As seen in Fig. 16.21, the second-order virial form is applicable for $\Phi < 0.3$. The experimental data are overall well described by (16.210) up to $\Phi \approx 0.5$, where the systems begins to freeze into an ordered solid state.

For small Φ, the sedimentation velocity of hard spheres has been determined to linear order by Batchelor [54], and to quadratic order by Cichocki et. al. [55], as

$$\frac{U^{\mathrm{s}}}{U_0} = 1 - 6.546\Phi + 21.918\Phi^2 + \mathcal{O}(\Phi^3) \,. \tag{16.211}$$

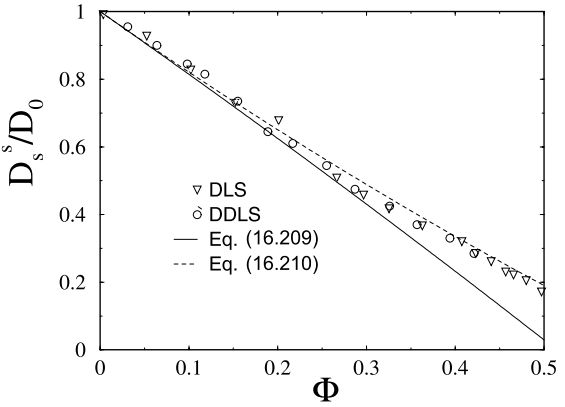

Fig. 16.21. Reduced short-time translational self-diffusion coefficient, $D_{\rm s}^{\rm s}/D_0$, of monodisperse hard-sphere suspensions. We compare experimental DLS [26] and DDLS [31] data with the $\mathcal{O}(\Phi^2)$ expression in (16.209), and the semi-empirical expression in (16.210). After [32,52].

Using that $S_{\rm c}(q=0) = 1 - 8\Phi + 34\Phi^2 + \mathcal{O}(\Phi^3)$, the short-time collective diffusion coefficient of hard spheres at low concentrations is determined as [55]

$$\frac{D_{\rm c}^{\rm s}}{D_0} = 1 + 1.454\Phi - 0.45\Phi^2 + \mathcal{O}(\Phi^3)\,, \tag{16.212}$$

which shows that $D_{\rm c}^{\rm s} > D_0$. The modest initial increase in $D_{\rm c}^{\rm s}$ with Φ described by (16.212) is counter-operated by HI through the factor $H(0)$, which causes $D_{\rm c}^{\rm s}$ to decay towards zero for larger Φ.

For hard spheres up to $\Phi = 0.5$, it has been shown in comparison to exact low-density calculations [56], experimental data [26] and so-called Lattice-Boltzmann computer simulation results for $H(q)$ [26], that [24,56]

$$H(q_{\rm m}) = 1 - 1.35\Phi\,. \tag{16.213}$$

The Lattice-Boltzmann simulation method combines Newtonian dynamics of the solid colloidal particles with a discretized Boltzmann-type equation for the fluid phase (see, e.g., [57]). It is particularly suited to analyze the effect of many-body HI on the colloidal short-time dynamics.

The principal peak height, $S_{\rm c}(q_{\rm m})$, of the hard-sphere static structure factor is well described, within $0 < \Phi < 0.5$, by [24,58]

$$S_{\rm c}(q_{\rm m}) = 1 + 0.644\Phi\, g(r = 2a^+)\,, \tag{16.214}$$

where $g(r = 2a^+) = (1 - 0.5\Phi)/(1 - \Phi)^3$ is the Carnahan-Starling contact value of $g(r)$. Note that $S_{\rm c}(q_{\rm m}) \approx 2.85$ at $\Phi = 0.494$, in accord with the empirical Hansen-Verlet freezing criterion [59]. This criterion states for one-component atomic and colloidal liquids that freezing into an ordered state

sets in when $S_c(q_m)$ exceeds $2.8 - 3.0$. Substitution of (16.213) and (16.214) into $D_c^s(q_m) = D_0 H(q_m)/S_c(q_m)$ gives an analytic expression for the short-time apparent collective diffusion coefficient, $D_c^s(q_m)$, which, according to Fig. 16.11, is in perfect agreement with experimental data.

Calculations of the hard-sphere $H(q)$ in dependence on q have been performed by Beenakker and Mazur [60]. These involved calculations account in an approximate way for many-body HI contributions (through so-called ring diagrams), with results for $H(q)$ which agree, up to $\Phi \approx 0.3$, quite well with experimental data and Lattice-Boltzmann computer simulations [26].

The shape of $H(q)$ is rather similar to that of $S_c(q)$ for the same Φ. The maximim of $H(q)$ is located close to q_m. However, according to (16.213), $H(q_m)$ decreases linearly in Φ, while $S_c(q_m)$ is instead a monotonically increasing function in ϕ (see (16.214)).

Having discussed the short-time properties of colloidal suspensions with short-range, i.e. hard-sphere-like, pair interactions, we proceed to discuss the opposite case of charge-stabilized suspensions with long-range electrostatic repulsions among the particles. We examine in particular systems with small amounts of excess electrolyte (in addition to the neutralizing counterions). The highly charged colloidal particles in these systems are already strongly correlated at volume fractions as low as $\Phi \approx 10^{-4}$. The strong electrostatic repulsion keeps the particles apart from each other such that contact configurations are extremely unlikely. Contrary to hard-sphere dispersions in which near-field hydrodynamic lubrication forces are important, the diffusion of charged colloidal spheres is thus influenced only by the far-field part of the HI. This salient difference in the effect of the HI leads to remarkable qualitative differences in the dynamic behavior of charge-stabilized dispersions and suspensions of hard spheres.

The usual virial expansion in Φ, which is so successful for semi-dilute hard-sphere suspensions, does not apply to charge-stabilized suspensions. Non-linear volume fraction dependencies have been predicted instead by Nägele and co-workers for the short-time transport properties of monodisperse charge-stabilized dispersions [18,61–66]. In particular, D_s^s obeys a fractional Φ-dependence of the form [18]

$$\frac{D_s^s}{D_0} = 1 - a_t \Phi^{4/3}, \tag{16.215}$$

with a parameter $a_t \approx 2.5$ which depends only weakly on the charge of the colloidal particle, provided that the charge remains large enough to mask the physical hard core of the particle. Equation (16.215) is valid typically for $\Phi \leq 0.05$. At larger volume fractions, three- and more-body HI come into play, and (16.215) becomes invalid. The $\Phi^{3/4}$-dependence of D_s^s has been verified in recent DLS measurements on charge-stabilized suspensions with the excess electrolyte (i.e. excess salt ions) removed form the suspension using an ion exchange resin [67]. According to (16.215), the D_s^s of charged spheres is less strongly reduced by HI than for hard spheres at the same volume fraction. In

case of hard spheres, lubrication forces between nearby spheres are operating whereas the dynamics of charged spheres is dominated by far-field HI.

HI have a stronger effect on charged spheres than on neutral ones, when instead of D_s^s the sedimentation velocity in a homogeneous system is considered. In this case, theory predicts for charge-stabilized suspensions with $\Phi < 0.1$ that

$$\frac{U^s}{U_0} = 1 - a_s \Phi^{1/3}, \tag{16.216}$$

with a nearly charge- and particle size-independent coefficient $a_s \approx 1.8$ [18, 62, 63]. The fractional exponent 1/3 has been subsequently confirmed by measurements of the sedimentation velocity in deionized charge-stabilized suspensions [66]. Equation (16.216) predicts, for $\Phi = 10^{-3}$, a reduction in U^s from the zero-density limit U_0 by as much as 15%, whereas the reduction for hard spheres at the same Φ is as small as 0.4% (cf. (16.211)). This is quite remarkable, for in the past the influence of HI on dilute charge-stabilized dispersions had been frequently considered to be negligibly small. The origin for the smaller sedimentation velocity of charged spheres as compared to uncharged ones at the same Φ is that charged particles are more strongly exposed to laminar solvent friction arising from the cumulative backflow of displaced fluid. This backflow friction is more effective for charged particles since, contrary to neutral spheres, nearby particle pairs are very unlikely.

The strong influence of (far-field) HI on charged particles can be observed further in the significant wavenumber dependence of $H(q)$. For charged spheres at $\Phi \leq 10^{-2}$, it is sufficient to substitute in (16.195) the Rotne-Prager limiting form of $\boldsymbol{D}_{ij}$ given in (16.207). This leads to [68]

$$H(y) = 1 - 15\Phi \frac{j_1(y)}{y} + 18\Phi \int_1^\infty \mathrm{d}x\, x\, [g(x) - 1] \{ j_0(xy) - \frac{j_1(xy)}{xy} + \frac{j_2(xy)}{6x^2} \}, \tag{16.217}$$

with $y = 2qa$, $x = r/(2a)$, and j_n the spherical Bessel function of order n. DLS data of Härtl and co-workers [69] for the hydrodynamic function of dilute charge-stabilized suspensions are displayed in Fig. 16.22 for three different concentrations. Notify the pronounced oscillations of $H(q)$ even for the smallest $\Phi \approx 10^{-4}$ considered. The experimental $H(q)$ are overall in very good agreement with the theoretical result in (16.217). The differences at small q can be attributed to the scattering contribution of residual particle aggregates in the experimental probes and to polydispersity effects, which are most influential at small q. The radial distribution function in (16.217) was determined from fitting the peak heights, $S_c(q_m)$, of the experimental $S(q)$ in Fig. 16.22 by static structure factors calculated by means of the rescaled mean spherical integral equation scheme (RMSA).

Contrary to hard spheres, the peak height, $H(q_m)$, of dilute and deionized charged sphere suspensions is larger than one, and it grows with increasing

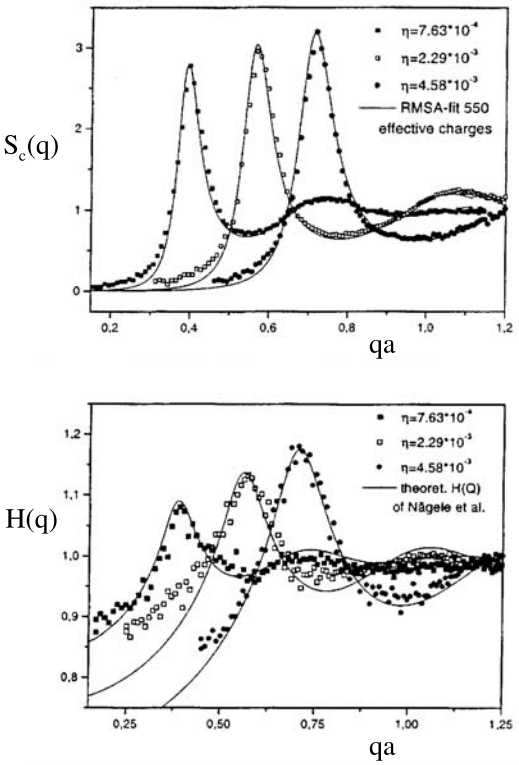

Fig. 16.22. Static structure factor $S_c(q)$(upper figure) and hydrodynamic function $H(q)$ (lower figure) versus qa for aqueous dispersions of strongly charged spheres at $\Phi = 7.63 \times 10^{-4}$, 2.29×10^{-3}, and 4.58×10^{-3} (curves from left to right). Note that without HI, $H(q) \equiv 1$. After [69].

Φ. For $\Phi \leq 10^{-2}$, this peak height is well described by [24, 56]

$$H(q_{\rm m}) = 1 + p\,\Phi^{0.4}\,, \tag{16.218}$$

with a coefficient $p = 1 - 1.5$ moderately dependent on particle size and charge.

We have dealt so far with *translational* short-time properties. The *rotational* short-time self-diffusion coefficient, $D_{\rm s}^{\rm r}$, of interacting colloidal spheres defined in (16.148) can be calculated in analogy with the translational case by accounting also for the orientational degrees of freedom [1, 20, 31, 32, 64]. In this way, one obtains the microscopic expression

$$D_{\rm s}^{\rm r} = \langle \hat{\boldsymbol{q}} \cdot \boldsymbol{D}_{11}^{rr}(\boldsymbol{r}^N) \cdot \hat{\boldsymbol{q}} \rangle \tag{16.219}$$

for $D_{\rm s}^{\rm r}$. The rotational diffusivity tensor, $\boldsymbol{D}_{11}^{rr}$, relates the hydrodynamic torque, $\boldsymbol{T}_1^{\rm H}$, acting on a representative sphere 1 to its angular velocity, $\boldsymbol{\omega}_1$, by

$$\boldsymbol{\omega}_1 = -\frac{1}{k_{\mathrm{B}}T}\, \boldsymbol{D}_{11}^{rr}(\boldsymbol{r}^N) \cdot \boldsymbol{T}_1^{\mathrm{H}}\,, \tag{16.220}$$

on assuming that no hydrodynamic torques and forces are exerted on the remaining $(N-1)$ spheres. To leading order in the a/r expansion, $\boldsymbol{D}_{11}^{rr}(\boldsymbol{r}^N)$ is given by [70]

$$\boldsymbol{D}_{11}^{rr}(\boldsymbol{r}^N) = D_0^{\mathrm{r}} \left[\mathbf{1} + \sum_{l \neq i}^{N} \boldsymbol{\omega}_{11}^{rr}(\boldsymbol{r}_i - \boldsymbol{r}_l) \right]\,, \tag{16.221}$$

with

$$\boldsymbol{\omega}_{11}^{rr}(\boldsymbol{r}) = -\frac{15}{4} \left(\frac{a}{r}\right)^6 [\mathbf{1} - \hat{\boldsymbol{r}}\hat{\boldsymbol{r}}] + \mathcal{O}\left[\left(\frac{a}{r}\right)^8\right]\,. \tag{16.222}$$

The leading-order three-body contribution to $\boldsymbol{D}_{11}^{rr}(\boldsymbol{r}^N)$ is of order r^{-9} [32,51].

On the basis of (16.219), Cichocki et al. [51] have derived for hard spheres the second-order virial expansion result

$$\frac{D_{\mathrm{s}}^{\mathrm{r}}}{D_0^{\mathrm{r}}} = 1 - 0.631\Phi - 0.726\Phi^2\,. \tag{16.223}$$

This expression describes experimental data and Lattice-Boltzmann computer simulation results for $D_{\mathrm{s}}^{\mathrm{r}}$ quite well up to surprisingly large volume fractions $\Phi = 0.4$ [31, 52, 72].

Calculations of $D_{\mathrm{s}}^{\mathrm{r}}$ for charge-stabilized suspensions with leading-order three-body HI included, reveal for small excess electrolyte concentration a purely quadratic Φ-dependence, viz.

$$\frac{D_{\mathrm{s}}^{\mathrm{r}}}{D_0^{\mathrm{r}}} = 1 - a_{\mathrm{r}}\Phi^2\,, \tag{16.224}$$

with a parameter $a_{\mathrm{r}} \approx 1.3$ rather insensitive to particle size and charge. Equation (16.224) has been confirmed by Lattice-Boltzmann computer simulations, which show that it applies quite accurately even up to $\Phi \approx 0.3$ [72].

Figure 16.23 includes the comparison between the theoretical prediction for $D_{\mathrm{s}}^{\mathrm{r}}$ in (16.224), and depolarized DLS measurements of Bitzer et al. [71] on deionized suspensions of highly charged and optically anisotropic fluorinated teflon spheres. For comparison, Fig. 16.23 contains further the hard-sphere $D_{\mathrm{s}}^{\mathrm{r}}$ according to (16.223). The experimental data for $D_{\mathrm{s}}^{\mathrm{r}}$ are seen to be in qualitative accord with the predicted ϕ^2 dependence.

The non-linear volume fraction dependence of the short-time properties of charged spheres arises from the peculiar concentration dependence of the mean diameter, r_{m}, of the average next-neighbor cage around a charged sphere. The length r_{m} coincides with the location of the first maximum, $g(r_{\mathrm{m}})$, of the radial distribution function and is very nearly equal to the mean interparticle distance, $\rho_0^{-1/3}$, which scales in Φ as $\Phi^{-1/3}$. Using this

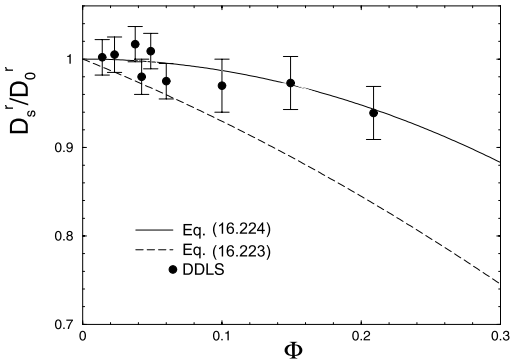

Fig. 16.23. DDLS data (from [71]) and (16.224) for the reduced short-time rotational self-diffusion coefficient, $D_{\rm s}^{\rm r}/D_0^{\rm r}$, versus Φ of charge-stabilized colloidal spheres. The second-order virial expansion result in (16.223) for monodisperse hard spheres is included for comparison.

characteristic property of deionized charge-stabilized suspensions, the exponents in (16.215), (16.216), (16.218) and (16.224) can be derived quite easily on the basis of a simplified model of effective hard spheres of diameter $2r_{\rm m}$. We refer to [18, 63, 65] for more details on the effective hard-sphere model.

Long-Time Diffusion

Theoretical calculations of the intermediate time and long-time behavior of $S_{\rm c}(q,t)$ and $S_{\rm s}(q,t)$, the MSD and the associated translational long-time self-diffusion coefficient are very demanding, since these quantities are affected simultaneously by direct and hydrodynamic interactions. These interactions give rise to time-retarded caging effects. At long times $t \gg \tau_{\rm I}$, the dynamic cage around a sphere is distorted away from its, on the average, spherical symmetry. This implies that, contrary to $D_{\rm s}^{\rm s}$, $D_{\rm s}^{\rm l}$ cannot be expressed in terms of a genuine equilibrium average as the one in (16.198).

A frequently used route to a direct calculation of time dynamic properties at intermediate to long times invokes Brownian dynamics (BD) computer simulations without and, to a certain degree of approximation, with HI included. The BD method allows to generate numerically the trajectories $\{\boldsymbol{r}_i(t)\}$ of colloidal spheres, and it is *statistically* equivalent to solving the GSE (16.183) for the many-sphere pdf. The (translational) displacements of N identical colloidal spheres during a time step Δt, with $\tau_{\rm B} \ll t \ll \tau_{\rm I}$, are generated in this scheme through solving the coupled stochastic finite difference equations [73]

$$\boldsymbol{r}_i(t+\Delta t) - \boldsymbol{r}_i(t) \;=$$
$$\sum_{j=1}^{N}[-\beta \boldsymbol{D}_{ij}(\boldsymbol{r}^N)\cdot\nabla_j U(\boldsymbol{r}^N) + \nabla_j \cdot \boldsymbol{D}_{ij}(\boldsymbol{r}^N)]\Delta t + \Delta\boldsymbol{x}_i + \mathcal{O}(\Delta t^2)\;. \quad (16.225)$$

Here, $\Delta \boldsymbol{x}_i$ is a Gaussian-distributed random displacement vector of zero mean $\langle \Delta \boldsymbol{x}_i \rangle = 0$ due to isotropy, and the covariance matrix

$$\langle \Delta \boldsymbol{x}_i \, \Delta \boldsymbol{x}_j \rangle \; = \; 2 \, \boldsymbol{D}_{ij}(\boldsymbol{r}^N) \Delta t \, . \tag{16.226}$$

For dilute suspensions with long-range repulsive interactions, we have argued before that it is sufficient to account only for the leading asymptotic form of $\boldsymbol{D}_{ij}$, given for an unbound three-dimensional suspension by the Rotne-Prager form in (16.205). Equation (16.225) reduces then to a simpler form, since $\nabla_j \cdot \boldsymbol{D}_{ij} = 0$ within RP approximation. The RP approximation for $\boldsymbol{D}_{ij}$ amounts to neglecting reflections, through other (caging) spheres, of the hydrodynamic flow field created by a moving sphere onto itself. Therefore, $D_{\rm s}^{\rm s} = D_0$ within RP approximation. For dilute charge-stabilized suspensions, DLS experiments show indeed that $D_{\rm s}^{\rm s} \approx D_0$.

In a typical BD simulation, several hundred to several thousand particles confined in a periodically repeated simulation box are equilibrated using, e.g., a canonical ensemble Monte-Carlo method. After equilibration has been reached, several ten thousand production time steps are generated by the algorithm in (16.225) to obtain diffusional (and structural) properties like the particle MSD through

$$W(t) = \frac{1}{2d} \left\langle \frac{1}{N} \sum_{i=1}^{N} [\boldsymbol{r}_i(t) - \boldsymbol{r}_i(0)]^2 \right\rangle \, , \tag{16.227}$$

with t some multiple of Δt. The long-range nature of the HI requires to include an Ewald-type summation technique on the RP level into the BD algorithm, as developed by Beenakker [75]. The influence of HI on dynamic properties can be analyzed through comparison with BD calculations where HI are disregarded, by setting $\boldsymbol{D}_{ij} = D_0 \delta_{ij} \mathbf{1}$. An example for a BD calculation of $S_{\rm c}(q,t)$ without HI has been discussed already in Fig. 16.8, in comparison with a mode coupling theory scheme which will be explained further down. BD simulations with far-field HI included have been performed, e.g., for the in-plane diffusion of planar monolayers of charge-stabilized colloidal spheres [74] and for one-component [58, 76–78] and bidisperse [79] systems of superparamagnetic colloidal spheres confined to a liquid-gas interface, and exposed to an external magnetic field perpendicular to the interface. The induced magnetic moments in the particles lead to long-range dipolar repulsions. A BD study of three-dimensional charge-stabilized suspensions with far-field HI has been discussed in [80].

For an interesting example of a quasi-two-dimensional colloidal suspension, consider a monolayer of electrostatically repelling colloidal spheres diffusing in the midplane between two narrow parallel (charged) walls of separation $h = 2\sigma$, with $\sigma = 2a$ (see Fig. 16.24).

Due to the stronger influence of HI in such confined systems, it is necessary to account for many-body near-field HI (where $\nabla_j \cdot \boldsymbol{D}_{ij} \neq 0$) between

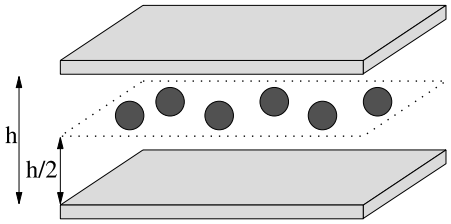

Fig. 16.24. Charged colloidal spheres diffusing in the midplane between two charged plates. The spheres interact by the screened Coulomb potential $u(r) = Q^2 \exp\{-\kappa r\}/r$ for $r > 2a$, with particle charge Q and screening parameter $\kappa = \pi/(h\sqrt{2})$ (see [74] for details).

particles and walls (p-w HI), and among the particles themselves (p-p HI), including also lubrication corrections. Lubrication effects arise when two or more spheres or a sphere and a wall are close to contact: for stick boundary conditions, which we assume here to apply, the mobility for relative motion goes to zero at contact, due to strong lubrication stresses required to expel the solvent from the thin gap between the surface points of closest approach. Moreover, in the present system there is a non-negligible hydrodynamic coupling between the translational and rotational motion of the spheres. To include all these hydrodynamic features of the system one can use the so-called Stokesian dynamics (SD) simulation method. This method is a more sophisticated extension of the BD scheme, pioneered and advanced by Brady and Bossis [81], which accounts to a good approximation for many-body HI contributions and lubrication effects.

Figure 16.25 includes SD simulation results [74] for the self-dynamic and distinct space-time Van Hove functions $G_{\rm s}(r,t)$ and $G_{\rm d}(r,t)$, respectively, defined as [18]

$$G_{\rm s}(r,t) \;=\; \left\langle \frac{1}{N}\sum_{i=1}^{N} \delta(\boldsymbol{r} - \boldsymbol{r}_i(t) + \boldsymbol{r}_i(0)) \right\rangle$$

$$\approx\; [4\pi W(t)]^{-d/2} \exp\{-\frac{r^2}{4W(t)}\} \quad (16.228)$$

and

$$G_{\rm d}(r,t) \;=\; \left\langle \frac{1}{N}\sum_{i\neq j}^{N} \delta(\boldsymbol{r} - \boldsymbol{r}_i(t) + \boldsymbol{r}_j(0)) \right\rangle . \quad (16.229)$$

The second approximate equality in (16.228) applies only when non-Gaussian contributions to $G_{\rm s}(r,t)$ are very small. The function $G_{\rm s}(r,t)$ gives the conditional probability density that a particle undergoes a displacement r during the time interval t. The distinct Van Hove function, with $G_{\rm d}(r,0) = \rho_0 g(r)$, gives the conditional probability density of finding, at time t, a particle a distance r apart from another one at earlier time $t = 0$. Up to the density factor

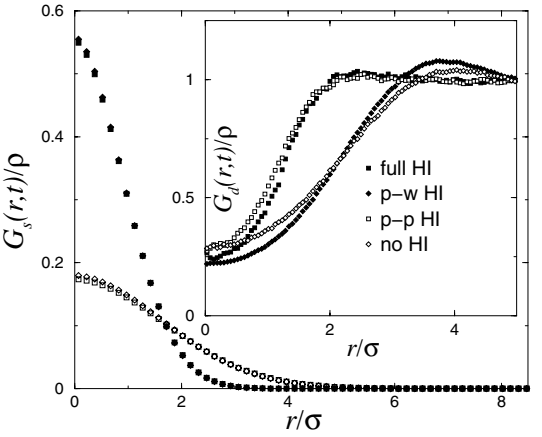

Fig. 16.25. Reduced self-dynamic and distinct Van Hove functions, $G_{\rm s}(r,t)/\rho_0$ and $G_{\rm d}(r,t)\rho_0$ versus $r/(2a)$, for time $t = 3.5\,\tau_{\rm I}$, particle surface fraction $\Phi = 0.062$, and an effective particle charge Q of 10^3 elementary charges. After [74].

ρ_0, $G_{\rm d}(r,t)$ is thus the time-dependent generalization of the radial distribution function. Real-space quantities like $G_{\rm s}(r,t)$, $G_{\rm d}(r,t)$ and $W(t)$ can be *directly* measured in quasi-two-dimensional systems of micron-sized colloidal particles using video microscopy imaging [82,83]. The functions $G_{\rm s}(r,t)$ and $G_{\rm d}(r,t)$ are the Fourier transform pairs, respectively, of $S_{\rm s}(q,t)$ and of the distinct part, $S_{\rm d}(q,t) = S_{\rm c}(q,t) - S_{\rm s}(q,t)$, of $S_{\rm c}(q,t)$, viz.

$$S_{\rm s}(q,t) = \int d\boldsymbol{r}\, \exp\{{\rm i}\boldsymbol{q}\cdot\boldsymbol{r}\}\, G_{\rm s}(r,t) \qquad (16.230)$$

$$S_{\rm d}(q,t) = \int d\boldsymbol{r}\, \exp\{{\rm i}\boldsymbol{q}\cdot\boldsymbol{r}\}\, G_{\rm d}(r,t)\,.$$

The time $t = 3.5\,\tau_{\rm I}$, at which the reduced Van Hove functions $G_{\rm s}(r,t)/\rho_0$ and $G_{\rm d}(r,t)/\rho_0$ are depicted in Fig. 16.25 versus the radial distance r corresponds to the intermediate time regime characterized by a sub-linear increase in $W(t)$. Interestingly enough, the shape of $G_{\rm d}(r,t)$ with full HI (i.e p-p *and* p-w HI) is seen from the figure to be mainly determined by p-p HI. In comparison, the p-w HI has only a minor effect on $G_{\rm d}(r,t)$, giving rise to a somewhat slower decay of interparticle correlations. In sharp contrast to $G_{\rm d}(r,t)$, $G_{\rm s}(r,t)$ is mainly influenced hydrodynamically by the walls (i.e. by p-w HI), which act to slow down the self-diffusion. This is the reason why the $G_{\rm s}(r,t)$ with full HI and with p-w HI alone, which are nearly equal to each other, are much larger for smaller r than the $G_{\rm s}(r,t)$ for the non-confined cases of of p-p HI only and with no HI at all.

Aside from BD and SD computer simulations, various approximate theoretical methods have been developed [27,48,84–91] for calculating long-time

diffusional and rheological properties from the knowledge of $S_c(q)$ or, likewise, $g(r)$. These methods are all based, regarding $S_c(q,t)$, on the microscopic equivalent of the phenomenological memory (16.101), with different approximations involved in each of these methods for the memory function $\Delta D_c(q,t)$. Out of these methods, we discuss here only the mode coupling theory (MCT) for the overdamped dynamics of dense colloidal suspensions [27,68,86,89,91]. The MCT for Brownian systems has been established, through comparison with experiment and computer simulations, as a versatile tool for calculating dynamic transport coefficients and density correlation functions [24,56,92].

In order to derive a microscopic evolution equation for $S_c(q,t)$ it should be realized that the microscopic densities $\rho_A(\boldsymbol{q},t)$, with $A \in \{s,c\}$, are the only slowly relaxing dynamic variables, at least for small q (cf. (16.132)), since momentum and energy of the colloidal spheres are very quickly exchanged with the surrounding fluid. From introducing the projection operator into the subspace of configurational dynamic variables,

$$\hat{P}_c(\cdots) = \frac{\langle(\cdots)\rho_c(-\boldsymbol{q})\rangle}{NS_c(q)}\,\rho_c(\boldsymbol{q})\,, \tag{16.231}$$

Nägele and Baur have derived the following exact evolution equation for $S_c(q,t)$ [68]:

$$\frac{\partial}{\partial t}S_c(q,t) \;=\; -q^2 D_c^s(q) S_c(q,t) - \int_0^t \mathrm{d}u\; M_c^{\mathrm{irr}}(q,t-u)\frac{\partial}{\partial u}\,S_c(q,u)\,. \tag{16.232}$$

This equation relates $S_c(q,t)$ to the so-called irreducible collective memory function $M_c^{\mathrm{irr}}(q,t)$. The function $M_c^{\mathrm{irr}}(q,t)$ is given by an exact but formal equilibrium average invoking $\hat{P}_c$ and the adjoint Smoluchowski operator $\hat{O}_B(\boldsymbol{r}^N)$ (see [27,68] for details).

Time-Laplace transformation of (16.232) leads to

$$S_c(q,z) \;=\; \frac{S_c(q)}{z + \dfrac{q^2 D_c^s(q)}{1 + M_c^{\mathrm{irr}}(q,z)}}\,, \tag{16.233}$$

with $M_c^{\mathrm{irr}}(q,z)$ the Laplace transform of $M_c^{\mathrm{irr}}(q,t)$. It follows from this equation that the collective diffusion kernel, $\boldsymbol{D}_c(q,z)$, in (16.91) can be expressed in terms of $M_c^{\mathrm{irr}}(q,t)$ via

$$D_c(q,z) \;=\; \frac{D_c^s(q)}{1 + M_c^{\mathrm{irr}}(q,z)}\,. \tag{16.234}$$

At this point, it becomes obvious that $M_c^{\mathrm{irr}}(q,z)$ renormalizes the short-time decay rate, $q^2 D_c^s(q)$, of $S_c(q,t)$ due to the presence of memory effects. As a generalization of the single-particle Stokes-Einstein relation $D_0 = k_B T/\gamma$ to interacting particle systems, a wavenumber and frequency-dependent friction

function, $\gamma_c(q,z)$, can be introduced through $D_c(q,z) = k_B T/\gamma_c(q,z)$. Hence, with (16.234), $M_c^{irr}(q,z)$ is identified as being proportional to the frequency-dependent part of the generalized friction function. For given $M_c^{irr}(q,z)$, the long-time collective diffusion coefficient can be calculated from

$$D_c^l \;=\; \frac{D_c^s}{1 + M_c^{irr}(q \to 0, z \to 0)}\,. \tag{16.235}$$

On the basis of the microscopic expression for $M_c^{irr}(q,t)$, it can be shown for vanishing or pairwise additive HI that $M_c^{irr}(q,t)/q^2 \to 0$ for $q \to 0$, which implies that $D_c^l = D_c^s$.

The MCT provides a self-consistent approximation for $M_c^{irr}(q,t)$, which preserves the positive definiteness of the exact $D_c(q,z)$. It is particularly suitable for fluid suspensions of strongly correlated particles. Moreover, as shown in the salient work of Götze and co-workers (see [93–96]), it predicts a consistent dynamic glass transition scenario in good accord with experiment and computer simulation. This scenario is characterized by the appearance of non-ergodicity above a certain concentration threshold, where $S_c(q,t)$ and $S_s(q,t)$ do not relax any more to zero, and where the suspension viscosity diverges.

In the most commonly used version of the MCT, $M_c^{irr}(q,t)$ is approximated without HI by

$$M_c^{irr}(q,t) = \frac{D_0}{2\rho_0(2\pi)^3}\int \mathrm{d}\boldsymbol{k}\,[V_c(\boldsymbol{q},\boldsymbol{k})]^2\; S_c(k,t)\; S_c(|\boldsymbol{q}-\boldsymbol{k}|,t) \tag{16.236}$$

with the vertex amplitude [87, 91, 93, 94],

$$V_c(\boldsymbol{q},\boldsymbol{k}) = \hat{\boldsymbol{q}}\cdot\boldsymbol{k}\;\rho_0\, c(k) + \hat{\boldsymbol{q}}\cdot(\boldsymbol{q}-\boldsymbol{k})\;\rho_0\, c(|\boldsymbol{q}-\boldsymbol{k}|)\,, \tag{16.237}$$

related to collective diffusion. Here, $c(q) = [1 - 1/S_c(q)]/\rho_0$ is the Fourier transform of the two-body direct correlation function $c(r)$ [50]. The vertex amplitude $V_c(\boldsymbol{q},\boldsymbol{k})$ in (16.236) has been derived in the so-called convolution approximation, where the contribution of static three-point direct correlations is neglected. The convolution approximation for the collective vertex amplitude is used in most of the recent applications of the MCT to atomic [95–97] and colloidal dynamics [24, 27, 88, 90, 91].

The MCT has been formulated further for self-diffusional properties related to the self-dynamic structure factor $S_s(q,t)$. The time evolution of $S_s(q,t)$ is described by the exact memory equation [68],

$$\frac{\partial}{\partial t}S_s(q,t) \;=\; -q^2 D_s^s\; S_s(q,t) - \int_0^t \mathrm{d}u\; M_s^{irr}(q,t-u)\frac{\partial}{\partial u}\,S_s(q,u)\,, \tag{16.238}$$

which includes the irreducible memory function, $M_s^{irr}(q,t)$, related to self-diffusion. Without HI, $D_s^s = D_0$, and $M_s^{irr}(q,t)$ is then approximated in MCT by

$$M_{\rm s}^{\rm irr}(q,t) \;=\; \frac{D_0}{(2\pi)^3\rho_0}\int {\rm d}\boldsymbol{k}\;[V_{\rm s}(\boldsymbol{q},\boldsymbol{k})]^2 S_{\rm c}(k,t)\;S_{\rm s}(|\boldsymbol{q}-\boldsymbol{k}|,t)\,, \qquad (16.239)$$

with the vertex function [87]

$$V_{\rm s}(\boldsymbol{q},\boldsymbol{k}) = \hat{\boldsymbol{q}}\cdot\boldsymbol{k}\;(1-\frac{1}{S_{\rm c}(k)})\;. \qquad (16.240)$$

Equations (16.232, (16.236) and (16.237) constitute a self-consistent set of non-linear equations determining $S_{\rm c}(q,t)$ for a given static structure factor $S_{\rm c}(q)$. The latter can be calculated independently for given pair potential using well-established integral equation schemes [18, 50].

Once $S(q,t)$ has been determined, $S_{\rm s}(q,t)$ is obtained from solving (16.238)–(16.240). Knowing $S_{\rm s}(q,t)$, the MSD can be determined from

$$W(t) \;=\; -\lim_{q\to 0}\frac{\log S_{\rm s}(q,t)}{q^2}\;. \qquad (16.241)$$

The long-time self-diffusion coefficient, $D_{\rm s}^{\rm l}$, follows then from

$$D_{\rm s}^{\rm l} \;=\; \lim_{t\to\infty}\frac{W(t)}{t} \;=\; \frac{D_{\rm s}^{\rm s}}{1+M_{\rm s}^{\rm irr}(q\to 0, z\to 0)}\;, \qquad (16.242)$$

where $M_{\rm s}^{\rm irr}(q,z)$ is the Laplace transform of $M_{\rm s}^{\rm irr}(q,t)$.

An approximate incorporation of far-field HI into the MCT equations of monodisperse systems and colloidal mixtures was provided by Nägele and coworkers [27,68,86]. This leads to modifications in the wavenumber dependence of $V_{\rm c}(\boldsymbol{q},\boldsymbol{k})$ and $V_{\rm s}(\boldsymbol{q},\boldsymbol{k})$, and hydrodynamic functions like $H(q)$ are needed as additional external inputs. The MCT with far-field HI aims at describing the dynamics of charge-stabilized suspensions in the fluid regime. So far it has been applied with good success to the self-diffusion of moderately correlated charged particles (see below), and to the electrolyte friction effect experienced by a charged colloidal sphere immersed in an electrolyte solution [98].

Figure 16.8 shows BD results without HI for the $S_{\rm c}(q,t)$ of a charge-stabilized dispersion, in comparison with corresponding MCT prediction without HI. There is no adjustable parameter involved in this comparison. The good agreement between MCT and BD for all times and wavenumbers considered confirms our earlier statement that the MCT is well suited for dense (in the sense of strongly correlated) particle systems. The effect of far-field HI, which is predominant in charge-stabilized suspensions, is to enlarge $D_{\rm s}^{\rm l}$ moderately, and to enhance the decay of $S_{\rm c}(q,t)$. The enhancement of $D_{\rm s}^{\rm l}$ had been originally predicted in [68] from partially self-consistent simplified MCT calculations of $D_{\rm s}^{\rm l}$ with far-field HI included (see Fig. 16.26), and from exact low-density calculations. Meanwhile, hydrodynamic enhancement of long-time self-diffusion has been observed in various colloidal systems characterized by strong and long-range particle repulsions [74,76–78,80]. The

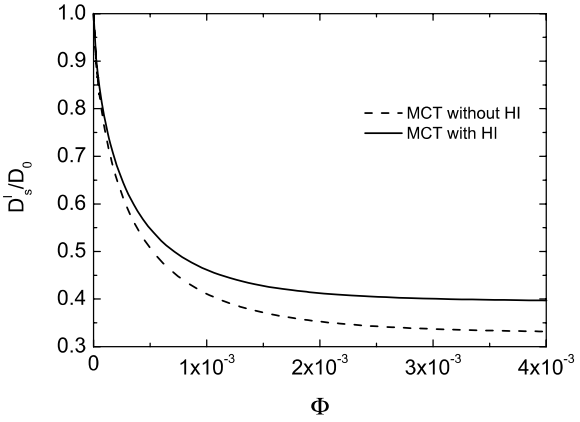

Fig. 16.26. MCT long-time self-diffusion coefficient of a typical deionized charge-stabilized suspension as function of volume fraction. HI leads here to an enhancement of long-time diffusion (see [68, 87]).

far-field HI prevailing in these systems promotes the diffusion of a sphere out of its momentary cage.

A neutral sphere diffusing out of its cage of neighboring hard spheres will, contrary to charged spheres, most probably pass by very closely to one of the caging particles, since the $g(r)$ of hard spheres is maximal at contact. Due to the strongly reduced relative mobility of two spheres near contact, the long-time self-diffusion of a hard sphere is hydrodynamically reduced accordingly. Consider here Fig. 16.27, which shows BD results for the $D_{\rm s}^{\rm l}$ of hard spheres without HI included, versus experimental data obtained from FRAP and DLS measurements. For hard spheres, $D_{\rm s}^{\rm l}/D_0 = 1 - 2.1\Phi$ to leading order in the density. While there are significant differences in $D_{\rm s}^{\rm l}$ for the various sets of experimental data, the hydrodynamically induced de-enhancement of $D_{\rm s}^{\rm l}$ for hard spheres is clearly observable. The diverging experimental results for $D_{\rm s}^{\rm l}$ arise from difficulties in determining the volume fraction unambiguously. Fig. 16.27 includes further the MCT predictions for $D_{\rm s}^{\rm l}$ without and with HI. The MCT locates the glass transition of hard-sphere suspensions at $\Phi = 0.525$ which is lower than the experimental value of approximately 0.58. To correct for this, Φ is rescaled in the MCT results accoding to $\Phi \to \Phi \times \Phi_{\rm g}/0.525$, with a value $\Phi_{\rm g} = 0.62$ selected somewhat larger than the experimental one, so that the MCT-$D_{\rm s}^{\rm l}$ without HI conforms well with the BD data at large concentrations. The influence of many-body HI is accounted for in a semi-heuristic fashion by multiplying (i.e. rescaling) $D_{\rm s}^{\rm l}$ without HI, calculated using the MCT, by the factor $D_{\rm s}^{\rm s}/D_0$ where $D_{\rm s}^{\rm s}$ is determined from (16.210). A rationale for this hydrodynamic rescaling is provided from noting for hard spheres that a particle diffusing out of its cage will move very slowly for a considerable amount of time in the immediate neighborhood of a caging sphere, as adequately described by the short-time self-diffusion coefficient,

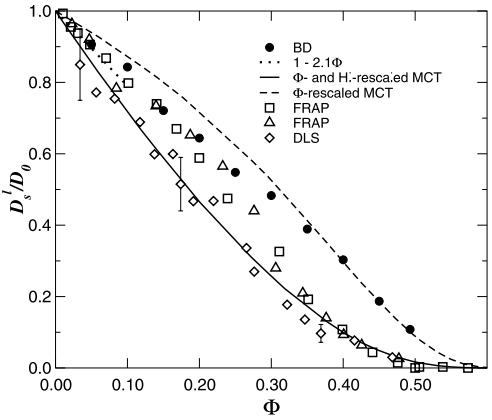

Fig. 16.27. Reduced long-time self-diffusion coefficient for hard spheres as function of volume fraction. Comparison between MCT and experimental data. Filled circles: BD data of Moriguchi et al. [100]. Open diamonds: DLS data of van Megen and Underwood [101]. Open squares and triangles: two sets of FRAP data by Imhof and Dhont [102]. After [24].

before it leaves the cage. According to Fig. 16.27, the D_s^l from the HI-rescaled MCT is overall in good accord with experimental data, in particular for larger concentrations.

An empirical dynamic freezing rule, due to Löwen, Simon and Palberg [99], states that freezing sets in in a three-dimensional monodisperse suspension when the threshold value $D_\mathrm{s}^\mathrm{l}/D_\mathrm{s}^\mathrm{s} \approx 0.1$ has been reached. A value of 0.1 for $D_\mathrm{s}^\mathrm{l}/D_0$ corresponds to $\Phi = 0.949$ within the HI-rescaled MCT. Since $S_\mathrm{c}(q_\mathrm{m}; \Phi = 0.494) = 2.85$, this is also the freezing volume fraction predicted by the static Hansen-Verlet freezing criterion [59]. This observation suggests that both freezing criteria are in fact equivalent, since dynamic properties are derived in MCT from knowledge of the static property $S_\mathrm{c}(q)$. The equivalence of both freezing criteria, and of their two-dimensional analogues, has been further established for systems with long-range repulsive interactions [24,76]. The equivalence of static and dynamic criteria derives from a general dynamic scaling behavior (cf. [58,76] for details on this dynamic scaling), which has led to the formulation of additional dynamic freezing criteria in terms of long-time collective diffusion coefficients [58].

As an example of dynamic scaling, consider Fig. 16.28a. This figure includes the master curve for D_s^l versus $S(q_\mathrm{m})$, calculated using the MCT without HI for a three-dimenisional suspension of highly charged spheres. Note here that a height of 2.85 in the static structure factor peak corresponds to $D_\mathrm{s}^\mathrm{l}/D_0 = 0.1$. Recall further that $D_\mathrm{s}^\mathrm{s} \approx D_0$ for charge-stabilized systems with prevailing far-field HI. BD simulation results of $D_\mathrm{s}^\mathrm{l}/D_0$ versus $S_\mathrm{c}(q_\mathrm{m})$ with and without far-field HI included are shown in Fig. 16.28b for magnetically and electrostatically repelling particles. We observe here that

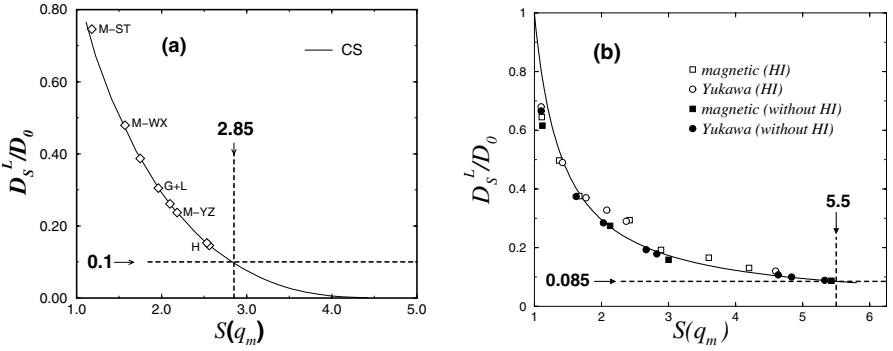

Fig. 16.28. Reduced long-time self-diffusion coefficient, $D_\mathrm{s}^\mathrm{l}/D_0$, versus liquid static structure factor peak height $S_\mathrm{c}(q_\mathrm{m})$. MCT results without HI (from [24]) for deionized three-dimensional suspensions of charge-stabilized spheres are shown in (a). The particle interactions in (a) are described by a Yukawa-like screened Coulomb potential. BD simulation results with and without HI for magnetic and charge-stabilized (Yukawa-like) quasi-two-dimensional systems are depicted in (b) (after [58]).

$D_\mathrm{s}^\mathrm{l}/D_0 \approx 0.085$ for $S_\mathrm{c}(q_\mathrm{m}) \approx 5.5$, in excellent accord with an empirical dynamic criterion for two-dimensional freezing proposed by Löwen [103], which states that $D_\mathrm{s}^\mathrm{l}/D_0 \approx 0.085$ at the freezing line, independent of the pair potential and the nature of the freezing process. Moreover, a value of $S_\mathrm{c}(q_\mathrm{m}) = 5.5$ at freezing is indeed found in computer simulations of two-dimensional systems [104]. As seen from Fig. 16.28b, values of D_s^l close to freezing are only slightly enhanced by HI. This indicates that the dynamic freezing rules remain esentially untouched when far-field HI is included.

As an application of the MCT to colloidal mixtures, we consider long-time interdiffusion in a dilute binary mixture of colloidal hard spheres. To this end, one needs to employ the generalizations of the one-component MCT equations to colloidal mixtures, as provided, e.g., in [27]. The long-time mobility matrix $\boldsymbol{\mu}^\mathrm{l}$, defined in (16.121), can be calculated analytically without HI to yield [27]

$$k_\mathrm{B}T\,\mu_{\alpha\beta}^\mathrm{l} = \delta_{\alpha\beta}\,D_{\mathrm{s}\alpha}^\mathrm{l} + \frac{1}{3}\,D_\alpha^0\,(\Phi_\alpha\,\Phi_\beta)^{1/2}\,\frac{(1+\lambda_{\alpha\beta})^2}{(\lambda_{\alpha\beta})^{3/2}} + \mathcal{O}(\Phi^2) \qquad (16.243)$$

where

$$D_{\mathrm{s}\alpha}^\mathrm{l} = D_{0\alpha}\left[1 - \frac{1}{3}\,\Phi\sum_{\gamma=1}^{2} x_\gamma\,(1+\lambda_{\gamma\alpha})^2\right] + \mathcal{O}(\Phi^2) \qquad (16.244)$$

is the long-time self-diffusion coefficient, without HI, of an α-type hard sphere in the mixture. Here, Φ is the total volume fraction of both components, and $\lambda_{\alpha\beta} = a_\beta/a_\alpha$ is the size ratio of β to α spheres. The MCT result in

(16.243) and (16.244) is not an exact one: the exact expression for $D^{\mathrm{l}}_{\mathrm{s}\alpha}$ is given by (16.244) with the factor 1/3 replaced by 1/2 [18, 42], so that $D^{\mathrm{l}}_{\mathrm{s}}/D_0 = 1 - 2\Phi + \mathcal{O}(\Phi^2)$ in the mondisperse case. The MCT does not describe the dynamics at low densities exactly, since the low-density binary collision part is treated in an approximative way.

Substitution of (16.243) for $\boldsymbol{\mu}^{\mathrm{l}}$ in (16.130) yields the following MCT result for the kinetic factor of a dilute binary hard sphere suspension [27, 105]:

$$\frac{\Lambda^{\mathrm{l}}_{\mathrm{in}}}{x_1\, x_2} = \left(x_2\, D^{\mathrm{l}}_{\mathrm{s}1} + x_1\, D^{\mathrm{l}}_{\mathrm{s}2}\right) + \frac{4}{3}\left(x_1\, \Phi_2\, D_{02} + x_2\, \Phi_1 D_{01}\right) - \frac{2}{3}\,\left(x_1 x_2 \Phi_1 \Phi_2\right)^{1/2} D_{01}\, \frac{\left(1+\lambda_{12}\right)^2}{\left(\lambda_{12}\right)^{3/2}}\,. \quad (16.245)$$

As has been discussed already in the interdiffusion part of Sect. 16.3.2, an ideal binary mixture is characterized by $\Lambda^{\mathrm{l}}_{\mathrm{in}} \propto \left(x_2\, D^{\mathrm{l}}_{\mathrm{s}1} + x_1\, D^{\mathrm{l}}_{\mathrm{s}2}\right)$; i.e., $\Lambda^{\mathrm{l}}_{\mathrm{in}}$ can then be expressed completely in terms of the self-diffusion coefficients. Equation (16.245) implies that a binary mixture of hard spheres is non-ideal already at small concentrations. Ideality is reached only when $a_1 = a_2$, i.e. for labelled but otherwise identical particles.

16.5.2 Polymer Blends and Random Phase Approximation

In this subsection, we analyze the interdiffusion process in binary polymer blends of hompolymers, labelled as A and B. We further consider the interdiffusion of A and B polymers in a matrix of C polymers. Our analysis is restricted to length scales accessible to dynamic light scattering. The lengths $2\pi/q$ resolved in typical DLS experiments on polymer blends are much larger than the average extent of a polymer coil. The average coil size is quantified by the radius of gyration, R_{G}, with $R_{\mathrm{G}} = pa^2/6$ for a Gaussian chain. Here, p is the degree of polymerization, i.e. the number of statistical segments or monomers [13, 47, 106], of a homopolymer chain, and a is the length of a statistical segment. DLS experiments performed in the macroscopic regime, i.e. in the diffusive limit where $qR_{\mathrm{G}} \ll 1$ holds, resolve times which are large as compared to the internal modes of a chain in the melt. Hence, only the center-of-mass diffusion of a chain is resolved.

As discussed earlier in Sect. 16.3.2, the partial static structure factors in a mixture are expressible, in the hydrodynamic limit, as a linear superposition of exponentially decaying hydrodynamic modes (cf. (16.122)). To make contact with the notation commonly used in the polymer field with regard to interdiffusion [28,29], we slightly redefine the partial collective dynamic structure factor, $S_{\alpha\beta}(q,t)$, for the density correlations of α and β-type monomers as $S_{\alpha\beta}(q,t) = \langle \rho_\alpha(\boldsymbol{q},t)\rho_\beta(-\boldsymbol{q},0)\rangle$, which differs from the definition given in (16.118) by a factor of $(N_\alpha N_\beta)^{1/2}$. In the context of polymer blends, N_α denotes the total number of α-type monomers in the melt, with $\alpha \in \{\mathrm{A},\mathrm{B},\mathrm{C}\}$,

and $\rho_\alpha(\boldsymbol{q},t)$ is the incremental number density given in (16.115), with $\boldsymbol{r}_j^\alpha$ pointing to the location of the j-th monomer of type α.

Using this redefinition of the $S_{\alpha\beta}(q,t)$, the EACF for a binary blend is (cf. (16.119))

$$g_E(q,t) \propto b_\mathrm{A}^2\, S_\mathrm{AA}(q,t) + b_\mathrm{B}^2\, S_\mathrm{BB}(q,t) + 2\, b_\mathrm{A}\, b_\mathrm{B}\, S_\mathrm{AB}(q,t)\,, \tag{16.246}$$

where b_α is the scattering amplitude of an α-type monomer (q-independent in the diffusive limit), related to its dielectric polarizability. Equation (16.246) applies also to an *incompressible* ternary blend, with b_A and b_B interpreted now as the excess scattering amplitudes relative to the amplitude, b_C, of matrix monomers. The incremental number density, ρ_C, of matrix molecules is hereby contracted out of the description, by using the local incompressibility constraint (cf. (16.124)),

$$\overline{\rho}_\mathrm{A}(\boldsymbol{q},t) + \overline{\rho}_\mathrm{B}(\boldsymbol{q},t) + \overline{\rho}_C(\boldsymbol{q},t) \;=\; 0\,, \tag{16.247}$$

for the coarse-grained incremental number densities, $\overline{\rho}_\alpha(\boldsymbol{q},t)$. In (16.247), it is assumed that the thermodynamic segmental volumes of the three polymer species are equal.

The interdiffusion of A chains into B chains in the ternary mixture is described by the interdiffusion autocorrelation function,

$$S_\mathrm{in}(q,t) \;=\; \frac{1}{N_\mathrm{A}^2}\, S_\mathrm{AA}(q,t) + \frac{1}{N_\mathrm{B}^2}\, S_\mathrm{BB}(q,t) - \frac{2}{N_\mathrm{A} N_\mathrm{B}}\, S_\mathrm{AB}(q,t)\,, \tag{16.248}$$

which differs from the definition of $S_\mathrm{in}(q,t)$ in (16.117) by a factor $(N x_\mathrm{A} x_\mathrm{B})^{-1}$, with $N = N_\mathrm{A} + N_\mathrm{B}$. Here, $x_\mathrm{A} = N_\mathrm{A}/N$ is the molar fraction, i.e. the volume fraction for equal molar volumes, of A monomers relative to A and B, with $x_\mathrm{B} = 1 - x_\mathrm{A}$. The long-time interdiffusion coefficient has been defined in (16.126) in terms of the initial decay rate of $S_\mathrm{in}(q,t)$ as

$$D_\mathrm{in}^\mathrm{l} \;=\; -\frac{1}{q^2}\frac{\partial}{\partial t} \ln S_\mathrm{in}(q,t)|_{t=0}\;, \tag{16.249}$$

where it is understood that the diffusive limit of $S_\mathrm{in}(q,t)$ is taken before its evaluation at $t = 0$. The 2×2-matrix, $\boldsymbol{\mu}^\mathrm{l}$, of long-time partial mobilities $\mu_{\alpha\beta}$ for the components A and B is introduced, in accordance with (16.121), by

$$k_\mathrm{B}T\mu_{\alpha\beta}^\mathrm{l} \;=\; -\frac{1}{q^2}\frac{\partial}{\partial t} S_{\alpha\beta}(q,t)|_{t=0}\;. \tag{16.250}$$

Then, D_in^l in (16.249) can be re-expressed as [28]

$$D_\mathrm{in}^\mathrm{l} \;=\; \frac{\Lambda_\mathrm{in}^\mathrm{l}}{S_\mathrm{in}} \;=\; k_\mathrm{B}T\, \frac{\frac{\mu_\mathrm{AA}^\mathrm{l}}{N_\mathrm{A}^2} + \frac{\mu_\mathrm{BB}^\mathrm{l}}{N_\mathrm{B}^2} - \frac{2\mu_\mathrm{AB}^\mathrm{l}}{N_\mathrm{A} N_\mathrm{B}}}{\frac{S_\mathrm{AA}}{N_\mathrm{A}^2} + \frac{S_\mathrm{BB}}{N_\mathrm{B}^2} - \frac{2S_\mathrm{AB}}{N_\mathrm{A} N_\mathrm{B}}}\;. \tag{16.251}$$

This equation relates $D_{\rm in}^{\rm l}$ to the long-time and long-wavelength-limiting partial mobilities and partial static structure factors of A and B monomers. The definition of the $\mu_{\alpha\beta}$ in (16.250) differs from the one in (16.121) by the same factor $(N_{\rm A}N_{\rm B})^{1/2}$ as for the partial static structure factors, so that $D_{\rm in}^{\rm l}$ in (16.251) is not affected by these redefinitions.

In the interdiffusion part of Sect. 16.3.2 we have pointed out that, in general, $D_{\rm in}^{\rm l}$ cannot be determined by a single scattering experiment. An important exemption from this rule is an *incompressible* binary blend of A and B polymer chains, void of any vacancies or C polymers. In this case, local incompressibility, $\overline{\rho}_{\rm A} + \overline{\rho}_{\rm B} = 0$, implies that

$$S_{\rm AA}(q,t) \;=\; S_{\rm BB}(q,t) \;=\; -S_{\rm AB}(q,t)\,, \tag{16.252}$$

from which follows with (16.246) and (16.248) that

$$g_E(q,t) \;\propto\; S_{\rm in}(q,t) \;=\; \left(\frac{1}{N_{\rm A}} + \frac{1}{N_{\rm B}}\right)^2 S_{\alpha\alpha}(q)\exp\{-q^2 D_{\rm in}^{\rm l} t\}\,, \tag{16.253}$$

with $\alpha =$ A or B. It can be shown that the amplitude $\boldsymbol{A}_+$ in the normal mode expansion of (16.122) vanishes in case of an incompressible binary blend, so that the (+)-mode with eigenvalue d_+ is not observable. The relaxation coefficient d_+ is identified here with the so-called cooperative diffusion coefficient, which quantifies the long-time relaxation of fluctuations in the total number density $\rho_{\rm A} + \rho_{\rm B}$ [28]. In identifying the normal mode d_- with $D_{\rm in}^{\rm l}$, we can state that in an incompressible binary blend, a measurement of $g_E(q,t)$ yields the interdiffusion coefficient, given here as

$$D_{\rm in}^{\rm l} \;=\; k_{\rm B}T\,\frac{\mu_{\alpha\alpha}^{\rm l}}{S_{\alpha\alpha}}\,, \tag{16.254}$$

since $\mu_{\alpha\alpha}^{\rm l} = \mu_{\beta\beta}^{\rm l} = -\mu_{\alpha\beta}^{\rm l}$ according to (16.250) and (16.252).

To make further progress in determining the interdiffusion coefficient of binary and ternary melts, a method is needed for calculating the $\mu_{\alpha\beta}^{\rm l}$ and $S_{\alpha\beta}$ in (16.251). For an approximate calculation of the $\mu_{\alpha\beta}^{\rm l}$, we employ a dynamic extension of the random phase approximation (RPA) of polymer blends. The dynamic RPA is a self-consistent mean-field-type approach based on linear response theory, which relates the (Laplace-transformed) linear response function , $-\beta({\rm d}/{\rm d}t)S_{\alpha\beta}(q,t)$, of the actual system of interacting chains, to the response function, $-\beta({\rm d}/{\rm d}t)S_{\alpha\beta}^0(q,t)$, of a bare reference system of noninteracting chains. For a derivation of the dynamic RPA, we refer to the work of de Gennes [107], Brochard and de Gennes [108], and for the extension of the RPA to incompressible polymer mixtures with an arbitrary number of components to Akcasu and Tombakoglu [109].

In the dynamic RPA, the static and dynamic properties of the bare system are assumed to be known. The bare system is commonly chosen as one which is identical to the original mixture in all respects except for the absence

of interactions between the monomers and the incompressibility constraint, but with the chain connectivity maintained. As a mean-field-type theory, the (dynamic) RPA should apply only to dense systems (i.e. melts) of sufficiently long polymer chains where density fluctuations are small. Furthermore, its predictions are most reliable for small values of q (as the ones probed in the diffusive limit) since, as the name RPA implies, it involves an averaging over the directions (phase) of $\boldsymbol{q}$.

The mobilities $\{\mu^{\rm l}_{\alpha\beta}\}$, with $\alpha,\beta \in \{\rm A, B\}$, of an incompressible ternary mixture are expressed in the dynamic RPA in terms of the mobilities, $\mu^0_{\alpha\beta}$, of the bare system as [109]

$$\begin{aligned} \frac{1}{\mu^{\rm l}_{\alpha\alpha}} &= \frac{1}{\mu^0_{\alpha\alpha}} + \frac{1}{\mu^0_{\beta\beta}} + \frac{1}{\mu^0_{\beta\beta}+\mu^0_{\rm CC}} \\ \frac{1}{\mu^{\rm l}_{\alpha\beta}} &= -\left[\frac{1}{\mu^0_{\alpha\alpha}} + \frac{1}{\mu^0_{\beta\beta}} + \frac{\mu^0_{\rm CC}}{\mu^0_{\alpha\alpha}\mu^0_{\beta\beta}}\right] \ , \ \alpha \neq \beta \end{aligned} \tag{16.255}$$

where $\mu^0_{\rm CC}$ is the mobility of a C-matrix monomer in the bare system. The mobilities $\mu^0_{\alpha\beta}$ are related to the self-diffusion coefficients in the bare system by

$$\mu^0_{\alpha\beta} \ = \ \delta_{\alpha\beta}\frac{N_\alpha D_{0\alpha}}{k_{\rm B}T} \, , \tag{16.256}$$

with $D_{0\alpha} = k_{\rm B}T/\gamma_\alpha$ the self-diffusion coefficient of an α-type monomer related to the monomer friction coefficient γ_α. This result for $\mu^0_{\alpha\beta}$ is obtained from adopting for the bare system the Rouse model for the dynamics of non-interacting and non-self-avoiding Gaussian chains [13,106] (cf. also Sect. 13.4 of Chap. 13). Here, we use that in a dense system of chains like in a melt, each chain is to a good approximation Gaussian and ideal, with $R_G \propto N^{1/2}$. Within the Rouse model of non-interacting chains,

$$S^0_{\alpha\beta}(q,t) \ = \ \delta_{\alpha\beta}\, N_\alpha\, p_\alpha \, \exp\{-q^2\, D^{\rm p}_{0\alpha}\, t\} \tag{16.257}$$

for $qR_{\rm G} \ll 1$ and for times t large compared to the relaxation times of the internal modes of a Rouse chain. Here, $D^{\rm p}_{0\alpha}$ is the center-of-mass self-diffusion coefficient of a polymer chain, related to the monomer diffusion coefficient by $D^{\rm p}_{0\alpha} = D_{0\alpha}/p_\alpha$, and p_α is the degree of polymerization of an α-chain. Note that $S^0_{\alpha\alpha}(q,t)/N_\alpha$ is the dynamic structure factor of a single Rouse chain. The monomer friction coefficient, γ_α, enters the Rouse dynamics as a parameter that must be specified as an input from elsewhere. Hence, γ_α and $D_{0\alpha}$ are usually interpreted as the friction coefficient and self-diffusion coefficient of an α-monomer in the actual mixture of interacting chains. As such they depend implicitly on the composition and temperature of the mixture. Moreover, it is then necessary to distinguish between systems of unentangled chains, where $D^{\rm p}_\alpha = D_\alpha/p_\alpha$, and systems of very long chains governed by the reptation process, where $D^{\rm p}_\alpha = D_\alpha/p^2_\alpha$ [29,106].

For an application of the RPA, consider first an incompressible binary blend, without any additional matrix molecules or vacancies. Substitution of (16.255) and (16.256), with $\mu^0_{\rm CC}$ set equal to zero, into (16.254) leads for unentangled chains to

$$(N\,x_{\rm A}\,x_{\rm B})\Lambda^{\rm l}_{\rm in} \;=\; \left[\frac{x_{\rm B}}{p_{\rm A}\,D^{\rm p}_{0\rm A}} + \frac{x_{\rm A}}{p_{\rm B}\,D^{\rm p}_{0\rm B}}\right]^{-1}, \qquad (16.258)$$

which is the *slow-mode* form for the long-time kinetic coefficient (cf. (16.145)). Recall here that the definitions of $\Lambda^{\rm l}_{\rm in}$ and $S_{\rm in}$ in (16.130) and (16.117), respectively, differ from the ones used in this subsection by a factor of $N(x_{\rm A}x_{\rm B})^2$. This factor renders them into *intensive*, i. e. N-independent, quantities. According to (16.258), the RPA predicts thus that the interdiffusion process in a binary incompressible blend is dominated, for $D^{\rm p}_{0\rm A} \ll D^{\rm p}_{0\rm B}$, by the slow component A, which enslaves the dynamics of the fast component B in the absence of voids.

To obtain $D^{\rm l}_{\rm in}$, we need to divide $\Lambda^{\rm l}_{\rm in}$ by $S_{\rm in}(q=0)$. The latter is obtained, for consistency, from the static limit of the RPA. For an incompressible ternary blend of A and B chains in a matrix of C chains, the static RPA relates the 2×2 static structure factor matrix, $\boldsymbol{S}(q,t)$, of A and B monomers in the interacting system to the static structure factor matrix, $\boldsymbol{S}^0(q,t)$, of the bare system via (for details see [28, 106, 109])

$$\boldsymbol{S}(q)^{-1} \;=\; \big(\boldsymbol{S}^0(q)\big)^{-1} + \boldsymbol{v}(q)\,. \qquad (16.259)$$

Here, $\boldsymbol{v}(q)$ is a 2×2 excluded volume matrix of elements $v_{\alpha\beta}(q)$, with $\alpha,\beta \in \{\rm A, B\}$, which accounts for the interactions between monomers of type α and β, and for the incompressibility constraint.

The partial static structure factors of the bare system of non-interacting Gaussian chains are explicitly

$$S^0_{\alpha\beta}(q) \;=\; \delta_{\alpha\beta}\,p_\alpha\,f_{\rm D}([qR_{{\rm G}\alpha}]^2)\,, \qquad (16.260)$$

where $f_{\rm D}(x)$ is the Debye function [106], with $f_{\rm D}(x)\approx 1-x/3$ for $x\ll 1$, and $R_{{\rm G}\alpha}$ is the radius of gyration of an α-type chain. Using (16.260) specialized to $qR_{{\rm G}\alpha}\ll 1$, the RPA result in (16.259) simplifies for a binary incompressible melt to

$$\frac{1}{S_{\alpha\alpha}} \;=\; \left(\frac{1}{N_a}+\frac{1}{N_{\rm B}}\right)^2 \frac{1}{S_{\rm in}} \;=\; \frac{1}{N}\left(\frac{1}{x_{\rm A}p_{\rm A}} + \frac{1}{x_{\rm B}p_{\rm B}} - 2\,N\,\chi_{\rm AB}\right)\,. \qquad (16.261)$$

The Flory-Huggins interaction parameter, $\chi_{\rm AB}$, is related to the spatial Fourier transforms, $w_{\alpha\beta}(q)$, of the local interaction potentials, $w_{\alpha\beta}(r)$, of α and β monomers by [28, 106]

$$\chi_{\rm AB} \;=\; \lim_{q\to 0}\frac{1}{k_{\rm B}TV}\left[w_{\rm AB}(q) - \frac{1}{2}\left(w_{\rm AA}(q)+w_{\rm BB}(q)\right)\right], \qquad (16.262)$$

so that $\chi \equiv N\chi_{\rm AB}$ can be interpreted as the Flory-Huggins interaction parameter per segmental volume $v_{\rm s} = V/N$, for equal segmental volumes of both polymer components. Typically, χ exhibits an inverse temperature dependence. Finally, (16.258) and (16.261) yield

$$D_{\rm in}^{\rm l} \;=\; \left(\frac{1}{x_{\rm A}\,p_{\rm A}} + \frac{1}{x_{\rm B}\,p_{\rm B}} - 2\,\chi\right)\left[\frac{1}{x_{\rm A}\,p_{\rm A}\,D_{0{\rm A}}^{\rm p}} + \frac{1}{x_{\rm B}\,p_{\rm B}\,D_{0{\rm B}}^{\rm p}}\right]^{-1} . \quad (16.263)$$

Experiments on binary blends (see the discussion given below) have revealed that the slow-mode result does not satisfactorily describe, in general, the dependence of $\Lambda_{\rm in}^{\rm l}$ on the molecular weight (say $p_{\rm A}$) of its constituents. The observed discrepancy between the slow-mode result for binary incompressible melts and experiment may be due to the presence of vacancies, which add some amount of compressibility to the mixture. When instead of a binary melt, a ternary incompressible blend of A and B chains in a matrix of C-chains is considered, $\Lambda_{\rm in}^{\rm l}$ can be derived within the dynamic RPA from substituting (16.255) and (16.256) into (16.251). This leads to the so-called ANK expression,

$$(N\,x_{\rm A}\,x_{\rm B})\,\Lambda_{\rm in}^{\rm l} \;= \left[x_{\rm B}\,p_{\rm A}\,D_{0{\rm A}}^{\rm p} + x_{\rm A}\,p_{\rm B}\,D_{0{\rm B}}^{\rm p} - \frac{x_{\rm A}\,x_{\rm B}\,(p_{\rm A}\,D_{0{\rm A}}^{\rm p} - p_{\rm B}\,D_{0{\rm B}}^{\rm p})^2}{x_{\rm A}\,p_{\rm A}\,D_{0{\rm A}}^{\rm p} + x_{\rm B}\,p_{\rm B}\,D_{0{\rm B}}^{\rm p} + x_C\,p_C\,D_{0{\rm C}}^{\rm p}}\right] , \quad (16.264)$$

for the kinetic coefficient of unentangled chains, originally derived by Akcasu, Nägele and Klein [28]. Quite remarkably, this expression reduces to the *fast-mode* form (cf. (16.141)),

$$(N\,x_{\rm A}\,x_{\rm B})\,\Lambda_{\rm in}^{\rm l} \;=\; [x_{\rm B}\,p_{\rm A}\,D_{0{\rm A}}^{\rm p} + x_{\rm A}\,p_{\rm B}\,D_{0{\rm B}}^{\rm p}] , \quad (16.265)$$

in the limit of a large self-diffusivity and/or large concentration of matrix molecules, that is for $x_{\rm C}\,p_{\rm C}\,D_{0{\rm C}}^{\rm p} \gg x_\alpha\,p_\alpha\,D_{0\alpha}^{\rm p}$. In this 'solution-like' limit, $g_E(q,t)$ decays in a superposition of two normal modes where, contrary to the incompressible case, d_- and, likewise, d_+ cannot be identified with the interdiffusion process [28]. The slow-mode result is recaptured from the ANK formula when the matrix is removed, i.e. for $x_{\rm C}\,p_{\rm C}\,D_{0{\rm C}}^{\rm p} \to 0$, resulting again in an incompressible mixture of A and B chains. If one is allowed to stretch the validity of the RPA result in (16.264) by allowing the matrix to consist of vacancies instead of homopolymers, the ANK formula predicts a gradual transition from the fast-mode form to the slow-mode form of $\Lambda_{\rm in}^{\rm l}$, when the vacancy concentration, or compressibility, of the mixture is reduced.

Having analyzed the implications of the dynamic RPA and the Flory-Huggins model for the long-time interdiffusion in binary melts, we proceed to scrutinize the RPA predictions against DLS and time-resolved static light scattering experiments on binary homopolymer blends. In DLS experiments on binary blends, an apparent diffusion coefficient,

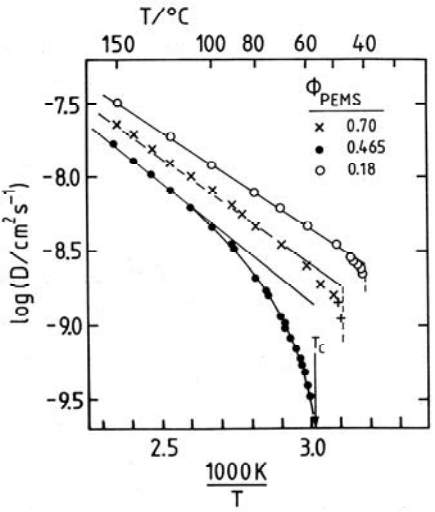

Fig. 16.29. Arrhenius plot of the apparent D for a binary blend of PDMS ($p = 260$) and PEMS ($p = 340$) chains for three different compositions of $\phi_{\rm PEMS}$ as indicated, including the critical one at $\phi_{\rm PEMS} = 0.465$. The critical temperature $T_{\rm c} = 57°{\rm C}$, is indicated by an arrow. The two non-critical data sets for D terminate at the binodal phase-coexistence points. Data from [110].

$$D \equiv -\frac{1}{q^2}\frac{\partial}{\partial t}\ln g_E(q,t)|_{t=0}\,, \tag{16.266}$$

is determined, in the diffusive limit, from a cumulant analysis. Within the RPA, D is identified with $D^{\rm l}_{\rm in} = \Lambda^{\rm l}_{\rm in}/S_{\rm in}$ in case of incompressility, with $\Lambda^{\rm l}_{\rm in}$ given by the slow-mode expression in (16.258). Fig. 16.29 shows DLS results for D in the homogeneous one-phase region, for an almost symmetric mixture of poly(ethylmethylsiloxane) (PEMS) chains of polymerization index $p = 260$ and poly(dimethylsiloxane) (PDMS) chains (with $p = 340$), with both indices below the entanglement threshold. In this so-called Arrhenius plot, the logarithm of D is plotted versus the inverse system temperature for three different volume fractions $\phi_{\rm PEMS} = x_{\rm PEMS}$ of PEMS, including the critical composition $\phi_{\rm PEMS} = 0.465$. This figure nicely illustrates, for $\phi_{\rm PEMS} = 0.465$, the phenomenon of critical slowing down, when T is lowered in the one-phase region to approach the temperature, $T_{\rm c}$, at the critical point of demixing (cf. also Chap. 15, Fig. 15.14). Near the critical point, certain composition fluctuations become anomalously large, and diffusion becomes increasingly slow, with D going to zero for $T \to T_{\rm c}$. Demixing through spinodal decomposition sets in when the temperature is lowered below $T_{\rm c}$. The critical point is the location of a second-order phase transition, characterized by universal scaling laws of its critical exponents (see [110] for details).

In the one-phase region $T > T_c$, with T not too close to T_c, the behavior of S_{in} and D_{in}^l can be described by the mean-field RPA, where the very small values of $D = D_{in}$ near the critical point are ascribed to the divergence of $S_{in} = S_{in}(q = 0)$ at the spinodal line. The (mean-field) spinodal line separates the phase region of mechanical stability from the unstable one. The values of the interaction parameter χ at the spinodal follow from (16.261) as

$$2\,\chi_s(\phi) \;=\; \frac{1}{\phi p_A} + \frac{1}{(1-\phi)p_B}\,, \tag{16.267}$$

with $\phi = x_A$ and $(1-\phi) = x_B$. This allows us to reformulate the (slow-mode) RPA result in (16.263) as

$$D_{in}^l \;=\; \phi(1-\phi)\cdot 2\,[\chi_s(\phi) - \chi]\cdot W^0\,, \tag{16.268}$$

with W^0 defined by

$$W^0 \;=\; \left[\frac{(1-\phi)}{p_A D_{0A}^p} + \frac{\phi}{p_B D_{0B}^p}\right]^{-1}. \tag{16.269}$$

We have factorized D_{in}^l here in a geometric factor, $\phi(1-\phi)$, a thermodynamic factor, $2(\chi_s - \chi)$, and in a kinetic factor, W^0. The kinetic factor depends in the unentangled case on the monomer diffusivities $D_{0\alpha} = p_\alpha D_{0\alpha}^p$ and ϕ only.

For the following discussion, it is convenient to absorb a factor $N[\phi(1-\phi)]^2$ into the definitions of S_{in} and Λ_{in}^l, which renders them intensive. Using this re-definition, S_{in} is given by

$$S_{in} \;=\; \frac{1}{2(\chi_s - \chi)} \;=\; \left[\frac{1}{\phi p_A} + \frac{1}{(1-\phi)p_B} - 2\,\chi(T)\right]^{-1}, \tag{16.270}$$

with zero values of S_{in} at the end-points $\Phi = 0, 1$ of pure components, and a parabolic shape of S_{in} in between. For the kinetic factor then follows

$$W^0 \;=\; \frac{D_{in}^l\, S_{in}}{\phi(1-\phi)} \;=\; \Lambda_{in}^l \phi(1-\phi)\,. \tag{16.271}$$

While (16.271) for W^0 has been derived for the incompressible case only, we will employ it in an operational sense also for the interpretation of scattering data, with the experimental D of (16.266) substituted in place of D_{in}^l, and S_{in} replaced by the experimental static structure factor S. The latter is obtained using static light scattering from the excess Rayleigh ratio (cf. [111]).

When the slow-mode result in (16.269) applies, then $1/W^0 = \phi(1-\phi)/(DS)$ exhibits a linear ϕ-dependence. Measurements of D and of S for a binary mixture of poly(styrene) (PS) and poly(phenylmethylsiloxane) (PPMS) chains [111] are indeed in favor of the RPA slow-mode result, as one can realize from Fig. 16.30. The PS in the PPMS/PS acts as the slower and more

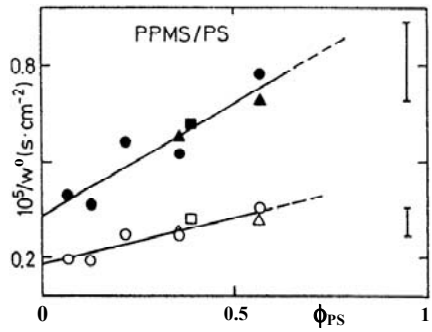

Fig. 16.30. Variation of the inverse of the kinetic factor $W^0 = D\,S/(\phi(1-\phi))$ versus volume fraction of PS, for blends of PS and PPMS ($M = 2600$), with PS molecular weights M of 9000 (circles), 4000 (squares), and 2000 (triangles). Filled symbols refer to $T = 280\,\mathrm{K}$ and open symbols to $T = 330\,\mathrm{K}$. There is a linear ϕ-dependence as predicted by the RPA slow-mode form. Data taken from [111].

'solid-like' component, which reflects its stronger proximity to the glass transition point of pure PS. The blend demixes for larger values of ϕ_{PS}. Therefore, values for W^0 are shown in Fig. 16.30 for the one-phase region only.

According to its definition in (16.271), and according to the fast-mode, slow-mode and ANK results for the $\Lambda^{\mathrm{l}}_{\mathrm{in}}$ of unentangled chains, which depend all on the *segmental* diffusion coefficients $D_{0\alpha}$ only, W^0 should be a local dynamic quantity, independent of the polymerization degree or, likewise, molecular weight of the polymers. The predicted molecular-weight-independence of $W^0 = D\,S/(\phi(1-\phi))$ has been confirmed [112] from static and dynamic light scattering experiments on blends of poly(ethylmethylsiloxane) (PEMS) and poly(dimethylsiloxane) (PDMS) polymers, where the molecular weight of PEMS has been varied (cf. Fig. 16.31).

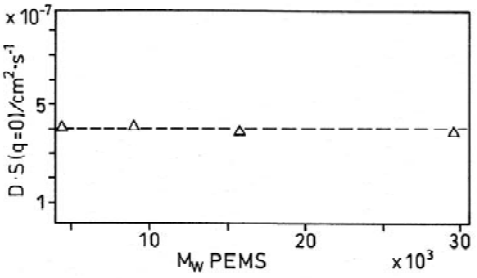

Fig. 16.31. Measured kinetic factor $\Lambda = D\,S(q \to 0)$ for a blend of PDMS ($p = 100$) and PEMS polymers at PEMS volume fraction $\phi_{\mathrm{PEMS}} = 0.67$ and $T = 20^{\circ}C$ versus molecular weight, M_W, of PEMS. The M_W-independence of Λ for Rouse chains is clearly seen. Data from [112].

While the diffusion in certain binary blends, like PS/PPMS, is well described by the RPA slow-mode result of incompressible systems, there is a larger class of blends which conform to the fast-mode form of interdiffusion. One well-characterized example is a nearly symmetric polysiloxane mixture of low-molecular weight PDMS (p=80) and PEMS (p=90) polymers. Due to a very distant glass-transition point, this system appears more as a 'liquid-like' and compressible system. Experimentally determined values for D and S in this blend as function of $\phi_{\rm PEMS}$ are listed in Fig. 16.32a, together with values for the kinetic factor determined from the operational equation (16.271). The linear volume fraction dependence of W^0 is in accord with the fast-mode result in (16.265). We note further that the measured S is well described by (16.270).

There is an interesting relationship between the fast-mode behavior of W^0 in PDMS/PEMS blends and their shear-mechanical properties. From mechanical measurements of the low-shear-rate limiting viscosity, $\eta_{\rm AB}$, in the blend, one can calculate a mean friction coefficient, $\gamma_{\rm AB}$, assuming Rouse dynamics in a mixture [13],

$$\gamma_{\rm AB} \;=\; \frac{36\,\eta_{\rm AB} M_0^2}{\rho\, a^2\, N_{\rm A}\, M}\,, \tag{16.272}$$

where $M_0 = \phi_{\rm A} M_{\rm A} + \phi_{\rm B} M_{\rm B}$ and $\rho = \phi_{\rm A}\rho_{\rm A} + \phi_{\rm B}\rho_{\rm B}$, respectively, are the mean monomeric molecular weight and the mean mass density of the blend; $N_{\rm A}$ is the Avogadro number, and M the mean polymeric molecular weight in the blend. Since mass transport by interdiffusion is related to the viscosity in the medium, it appears likely that a generalized Stokes-Einstein relation $W^0 \propto k_{\rm B}T/\gamma_{\rm AB}$ holds, provided that vitrification effects due to the proximity to a glass point do not play a role. A plot of $1/\gamma_{\rm AB}$ versus ϕ should then result in a linear composition dependence. Fig. (16.32b) proves that this is the case indeed. From the fast-mode-like form of $1/\gamma_{\rm AB}$ one concludes that the inverse of the mean friction coefficient can be expressed solely in terms of the A and B monomer friction coefficients, γ_α in the blend, according to $\gamma_{\rm AB}^{-1} = \phi_{\rm A}\gamma_{\rm A}^{-1} + \phi_{\rm B}\gamma_{\rm B}^{-1}$.

The approximate fast-mode and slow-mode expressions for $\Lambda_{\rm in}^1$ do apply only to selected polymer mixtures, with varying degree of accuracy in each case. The fast-mode or vacancy model appears to be more consistent with lower molecular weight blends, whereas the slow-mode or incompressible model is more consistent in the high molecular weight regime. For an example of this trend, consider Figs. 16.33 and 16.34 which display time-resolved static light scattering data of Feng et. al [114] for the kinetic interdiffusion factor (called mobility M in the notation of [114]) of a poly(styrene)/poly(vinylmethylether) blend (PS/PVME) for varying molecular weight $N_{\rm PS}$ of PS. In the experiments by Feng et al., the interdiffusion coefficient has been determined from temperature quench experiments within the miscible one-phase region. The measured decay of density (composition) fluctuations right after the quench has been interpreted in these experiments

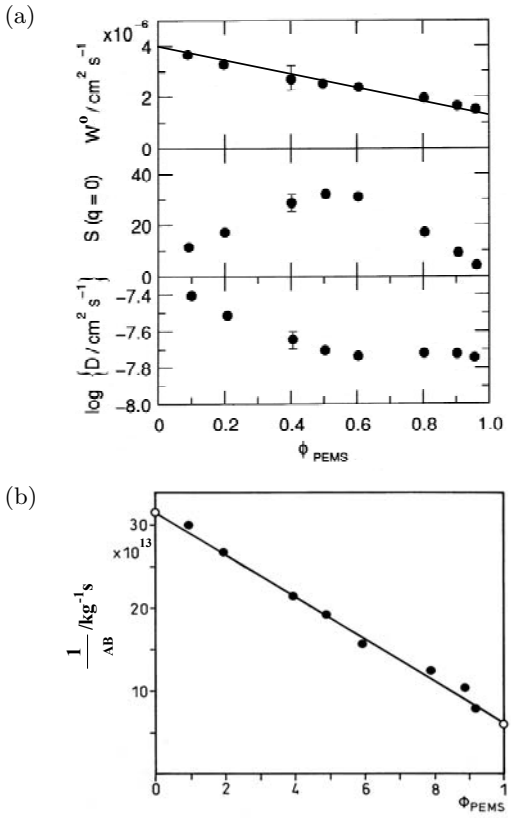

Fig. 16.32. (a) Apparent diffusion coefficient D, measured static structure factor $S(q \to 0)$, and kinetic factor W^0 for a nearly symmetric blend of PDMS (p=80) and PEMS (p=90) versus composition $\phi_{\rm PEMS}$ at $T = 20°$C. The straight solid line is the fast-mode prediction for W^0. Data from [113].
(b) Inverse of the friction coefficient, $\gamma_{\rm AB}$, for the same PDMS/PEMS mixtures as in (a), deduced from rheological measurements of the blend viscosity, $\eta_{\rm AB}$, as explained in the text. The linear composition dependence of $1/\gamma_{\rm AB}$ verifies a generalized Stokes-Einstein relation $W^0 \propto k_{\rm B}T/\gamma_{\rm AB}$ for interdiffusion. Open circles at $\phi_{\rm PEMS} = 0, 1$ refer to the pure components. Data from [112].

in terms of the celebrated Cahn-Hilliard-Cook (CHC) expression for the time-resolved average scattered intensity of binary blends (cf. [29,114]). We remark that the CHC expression is commonly used also to interpret the early stages of spinodal composition of binary mixtures right after a sudden quench into the mechanically unstable two-phase region.

The chains in the PS/PVME blend are in a bulk-entangled state, so that the self-diffusion coefficient of a chain scales, different from Rouse chains, with the inverse *square* of the molecular weight. In the entanglement case, W^0 is not any more a local property independent of molecular weights. Substitution

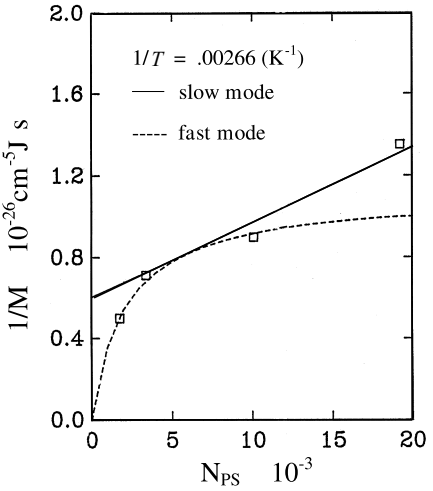

Fig. 16.33. Inverse mobility data, $M^{-1} \propto 1/\Lambda^{\rm l}_{\rm in}$, versus molecular weight, N_{PS}, of PS in PS/PVME blends. The dashed line (solid line) is a fit of the fast-mode (slow-mode) model to the experimental data. Both models show systematic deviations from the data. After [114].

of $D^{\rm p}_{0\alpha} = D_{0\alpha}/p^2_\alpha$ into (16.258), (16.265) and (16.264) leads for the inverse mobility $1/M \propto 1/(x_{\rm A}x_{\rm B}\Lambda^{\rm l}_{\rm in})$, according to the slow-mode expression, to linear dependence on the degree of polymerization p_α. On the other hand, the fast-mode model predicts a concave curve for $1/M$ plotted versus p_α, with an infinite slope at $p_\alpha = 0$ and a horizontal asymptote for large p_α [29]. Fig. 16.33 includes experimental data of $1/M$ for four different molecular weights, $N_{\rm PS}$, of PS. Neither the fast-mode nor the slow-mode expression can adequately fit the data. The fast-mode model applies only to the low-molecular-weight side, and the slow-mode model only for large values of $N_{\rm PS}$ (cf. Fig. 16.33).

Inverse mobility data of PS/PVME versus $N_{\rm PS}$ for two different temperatures are depicted in Fig. 16.34, in comparison with the predictions of the ANK formula. As one can see, the molecular weight dependence of the kinetic factor in PS/PVME is well described by the ANK model, with the (third) matrix component interpreted as 'vacancies'. The solid curves in Fig. 16.34 were plotted using the matrix parameter $x_{\rm C}D_{\rm C0}/p_{\rm C}$ occurring in the entanglement version of the ANK formula as a fitting parameter. However, this matrix parameter can be related to the cooperative diffusion coefficient in a binary mixture, which is a measurable quantity [29]. This deliberates us from needing to assign a meaning to the diffusion coefficient of a vacancy.

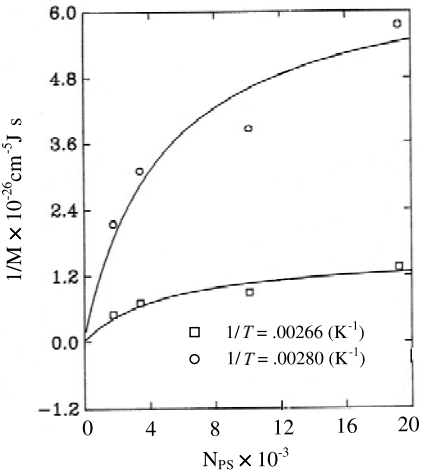

Fig. 16.34. Inverse mobility data, M^{-1}, versus $N_{\rm PS}$, in PS/PVME blends at two different temperatures as indicated. The solid lines are fits of the ANK formula (16.264) to the data, demonstrating the applicability of the ANK-theory over the whole range of PS molecular weights. After [114].

16.6 Conclusion

The aim of this chapter was to analyze the physics of various diffusion processes observed in colloidal fluids of spherical and rod-shaped particles, and in binary polymer melts, to describe dynamic light scattering techniques and other optical methods (FRAP and FCS) used for probing diffusion, and to explain theoretical methods and computer simulation techniques which allow one to calculate diffusional transport properties and scattering functions.

Dynamic light scattering as described in Sect. 16.2 is nowadays a standard technique to measure diffusion properties of colloids and polymers. The new developments in this area are in the direction of scattering geometries, where the dynamics under the influence of external fields (like pressure, shear flow, electric field and temperature gradients), near walls and within interfaces can be probed. In addition, somewhat slower dynamical processes are being studied nowadays by means of optical microscopy, such as confocal laser scanning microscopy (CSLM). Scattering from single colloidal particles can be used to probe local properties in the possibly inhomogeneous system under consideration.

Besides translational dynamics, FRAP can also be used to measure the rotational dynamics, where the polarization dependence of excitation and emission probabilities are exploited. Time-resolved phosphorescence anisotropy (TPA) has recently been used to measure rotational diffusion of colloids as well [115, 116]. FRAP has been applied some time ago to probe long-time diffusion under oscillatory shear flow. A similar method is forced rayleigh

scattering (FRS), where a refractive index grating is created by means of an interference pattern, from which grating scattered intensities are measured (see Sect. 15.5.2 in Chap. 15). FRAP and FRS are specialized to measure long-time translational (and rotational) self-diffusion coefficients of various kinds of macromolecules (also non-spherical molecules). As far as we are aware, FCS has not yet been applied to synthetic macromolecular systems. For very large macromolecules (larger than the dimensions of the confocal volume), FCS probes a combination of translational and rotational motion.

The concentration dependence of translational/rotational diffusion coefficients characterizing the various diffusion mechanisms, of sedimentation coefficients, and the time dependence of mean square displacements, Van Hove functions and dynamic structure factors have been analyzed for colloidal suspensions in Sect. 16.5. The performances of the theoretical methods which have been described in this section (i.e., short-time cluster expansion, MCT, and BD and SD simulations) have been scrutinized through a detailed comparison with experimental results for diffusional properties obtained from DLS, DDLS, FRAP and FCS measurements. Our focus was geared towards qualitative differences in the dynamics of suspensions with short-range particle interactions (i.e., hard spheres), and of systems with long-range repulsion of particles like charge-stabilized dispersions and magnetic particles with dipolar repulsion. In particular, it was shown that charge-stabilized suspensions at low salinity are characterized by peculiar non-linear density dependencies of their (short-time) transport properties. For long times, dynamic scaling is observed, with interesting implications on the equivalence of certain static and dynamic freezing criteria.

For systems of monodisperse colloidal spheres in the fluid phase, meanwhile a quantitative level of understanding has been reached, at least with regard to translational diffusion. As yet, a first-principle inclusion of many-body HI into the theoretical description of concentrated suspensions remains as a major theoretical challenge. For mixtures of colloidal spheres, a semi-quantitative level of accuracy has been reached in existing theoretical methods. Far less is known, however, about diffusion in systems of non-spherical particles like, to mention the most simple case, colloidal hard rods. In these systems, translational particle motion is coupled to the rotational one even at short times. Recent theoretical efforts are devoted to understand diffusion in confined geometries like in colloidal matrices and gels, to electrokinetic effects on charged colloidal macro-ions arising from the dynamics of the neutralizing micro-ion clouds, and to anisotropic diffusion in suspensions under shear.

Our conclusions regarding the dynamics in binary polymer blends in the homogeneous one-phase region are as follows: The derivation of the kinetic interdiffusion coefficient on the basis of the two-component dynamic RPA assumes an incompressible system. This is probably a rather crude assumption since, if it were true, theory would predict a single relaxation process in the time evolution of density autocorrelation function. However, a single

mode is usually not observed in DLS experiments on binary blends, although in some cases the slow-mode result is nevertheless found to be valid. On the other hand, if the fast-mode model of interdiffusion for a compressible system would apply, two modes should be experimentally observable [28]. Yet in the siloxane model system where the fast-mode form holds true, a second mode has never been observed. The ANK formula constitutes certainly a significant progress in our understanding of polymeric interdiffusion, but the conflicting results between experiment and theory regarding the observed scattering modes remain to be understood and resolved in future work.

Notation

a	sphere radius (polymer segment length)
$D_{\mathrm{c}}^{\mathrm{s}}$	short-time collective diffusion coefficient
$D_{\mathrm{c}}^{\mathrm{l}}$	long-time collective diffusion coefficient
$D_{\mathrm{s}}^{\mathrm{s}}$	translational short-time self-diffusion coefficient
$D_{\mathrm{s}}^{\mathrm{l}}$	translational long-time self-diffusion coefficient
$D_{\mathrm{s}}^{\mathrm{r}}$	rotational short-time self-diffusion coefficient
D_{in}	interdiffusion coefficient
$D_{\mathrm{c}}^{\mathrm{l}}(q_{\mathrm{m}})$	collective long-time diffusion coefficient at q_{m}
$\overline{D}_{\mathrm{c}}^{\mathrm{l}}(q_{\mathrm{m}})$	mean collective diffusion coefficient at q_{m}
$D_{0\alpha}^{\mathrm{p}}$	center-of-mass diffusion coefficient of an α-type polymer
D_0	translational free diffusion coefficient
D_0^{r}	rotational free diffusion coefficient
$G_{\mathrm{s}}(t)$	self-dynamic Van Hove function
$G_{\mathrm{d}}(r,t)$	distinct Van Hove function
$g_E(t)$	electric field autocorrelation function
$H(q)$	hydrodynamic function
$j_{\mathrm{in}}(t)$	interdiffusion current
M	mass of a Brownian sphere
$M_{\mathrm{c}}^{\mathrm{irr}}(q,t)$	irreducible collective memory function
$M_{\mathrm{s}}^{\mathrm{irr}}(q,t)$	irreducible self memory function
N_α	number of α-type spheres (monomers)
p_α	polymerization index of α-type homopolymers
$S_{\mathrm{c}}(q,t)$	collective dynamic structure factor
$S_{\mathrm{c}}(q)$	static structure factor
$S_{\mathrm{in}}(q,t)$	interdiffusion autocorrelation function
$S_{\mathrm{r}}(t)$	rotational autocorrelation function
$S_{\mathrm{s}}(q,t)$	self-dynamic structure factor
U	sedimentation velocity
$W(t)$	mean square displacement
W^0	kinetic factor of interdiffusion divided by geometric factor
γ	friction coefficient
Λ_{in}	kinetic factor of interdiffusion

ρ	number density
Φ	volume fraction
$\phi_v(t)$	velocity autocorrelation fuction
$\phi_{\rm A}$	volume fraction of A monomers
$\phi_\omega(t)$	angular velocity autocorrelation function
χ	Flory-Huggins parameter
$\chi_{\rm s}$	Flory-Huggins parameter at the spinodal
BD	Brownian dynamics (simulation)
DDLS	depolarized dynamic light scattering
DLS	dynamic light scattering
EACF	electric field autocorrelation function
FCS	fluorescence correlation spectroscopy
FRAP	fluorescence recovery after photobleaching
GSE	generalized Smoluchowski equation
HI	hydrodynamic interactions
IACF	intensity autocorrelation function
MCT	mode coupling theory
MSD	mean square displacement
RPA	random phase approximation
SD	Stokesian dynamics (simulation)
VAF	velocity autocorrelation function

References

1. J.K.G. Dhont: *An Introduction to Dynamics of Colloids* (Elsevier, Amsterdam 1996)
2. B. Chu: *Laser Light Scattering: Basic Principles and Practice* (Academic Press, London 1991)
3. R. Pecora: *Dynamic Light Scattering; Applications of Photon Correlation Spectroscopy* (Plenum Press, New York 1985)
4. W. Brown: *Dynamic Light Scattering: The Method and some Applications* (Clarendon Press, Oxford 1993)
5. *Light Scattering from Dilute Polymer Solutions*, ed by D. MacIntyre, F. Gornick (Gordon and Breach Science Publishers, New York 1964)
6. R. Zwanzig, M. Bixon: J. Fluid Mech. **69**, 21 (1975)
7. H.J.H. Clercx: Phys. Rev. E **56**, 2950 (1997)
8. E.J. Hinch: J. Fluid Mech. **72**, 499 (1975)
9. G.N. Paul, P.N. Pusey: J. Phys. A **14**, 3301 (1981)
10. N.K. Ailawadi, B.J. Berne: J. Chem. Phys. **54**, 3569 (1971)
11. B. Cichocki, B.U. Felderhof: Physica A **289**, 409 (2001)
12. R. Piazza, V. Degiorgio: Physica A **182**, 576 (1992)
13. M. Doi, S.F. Edwards: *The Theory of Polymer Dynamics* (Clarendon Press, Oxford 1986)
14. B. Cichocki, K. Hinsen: Physica A **166**, 473 (1990)
15. B. Cichockim, B.U. Felderhof: J. Phys. Condens. Matter **6**, 7287 (1994)

16. H. van Beijeren, K.W. Kehr, R. Kutner: Phys. Rev. E **28**, 5711 (1983)
17. W. van Megen, S.M. Underwood, I. Snook: J. Chem. Phys. **85**, 4065 (1986)
18. G. Nägele: Phys. Rep. **272**, 215-372 (1996)
19. K.J. Gaylor, I.K. Snook, W. van Megen, R.O. Watts: J. Phys. A **13**, 2513 (1980)
20. R.B. Jones, P.N. Pusey: Annu Rev Phys Chem **42**, 137 (1991)
21. A.B. Glendinning, W.B. Russel: J. Colloid Interface Sci. **89**, 124 (1982)
22. W.B. Russel, A.B. Glendinning: J. Chem. Phys. **74**, 948 (1981)
23. P. Szymczak, B. Cichocki: Europhys. Lett. **59**, 465 (2002)
24. A.J. Banchio, G. Nägele, J. Bergenholtz: J. Chem. Phys. **113**, 3381 (2000)
25. P.N. Segrè, S.P. Meeker, P.N. Pusey, W.C.K. Poon: Phys. Rev. Lett. **75**, 958 (1995)
26. P.N. Segrè, O.P. Behrend, P.N. Pusey: Phys. Rev. E **52**, 5070 (1995)
27. G. Nägele, J. Bergenholtz, J.K.G. Dhont: J. Chem. Phys. **110**, 7037 (1999)
28. A.Z. Akcasu, G. Nägele, R. Klein: Macromolecules **24**, 4408 (1991)
29. A.Z. Akcasu: Macromol. Theory Simul. **6**, 679 (1997)
30. W. Hess, G. Nägele, A.Z. Akcasu: J. Polym. Sci. B **28**, 2233 (1990)
31. V. Degiorgio, R. Piazza, R.B. Jones: Phys. Rev. E **52**, 2707 (1995)
32. H. Zhang, G. Nägele: J. Phys.: Condens. Matter **15**, S407 (2003)
33. F. Lanni, B.R. Ware: Rev. Sci. Instrum. **53**, 905 (1982)
34. J. Davoust, P.F. Devaux, L. Leger: EMBO Journal **1**, 1233 (1982)
35. A. Imhof: Dynamics of Concentrated Dispersions. PhD thesis, Utrecht University, The Netherlands (1996)
36. M. van Bruggen: Liquid Crystal Formation and Diffusion in Dispersions of Colloidal Rods. PhD thesis, Utrecht University, The Netherlands (1998)
37. M.P.B. van Bruggen, H.N.W. Lekkerkerker, J.K.G. Dhont: Phys. Rev. E **56** 4394 (1997)
38. M.P.B. van Bruggen, H.N.W. Lekkerkerker, G. Maret, J.K.G. Dhont: Phys. Rev. E **58** 7668 (1998)
39. G. Maret, J. Peetermans: private communication on similar, unpublished experiments on fd-virus.
40. H. Löwen: Phys. Rev. E **50**, 1232 (1994)
41. J.K.G. Dhont, M.P.B. van Bruggen, W.J. Briels: Macromolecules **32**, 3809 (1999)
42. G.K. Batchelor: J. Fluid Mech. **131**, 155 (1983)
43. B. Cichocki, B.U. Felderhof: J. Chem. Phys. **89**, 3705 (1988)
44. S.T. Hess, S. Huang, A.A. Heikal, W.W. Webb: Biochemistry **41**, 697 (2002)
45. S.R. Aragón, R. Pecora: J. Chem. Phys. **64**, 1791 (1976); Biopolymers **14**, 119 (1975)
46. A. Patkowski, J. Gapinski: unpublished
47. H. Yamakawa: *Modern Theory of Polymer Solutions* (Harper & Row, New York 1971)
48. B. Cichocki, B.U. Felderhof: Physica A **204**, 152 (1994)
49. J. Rotne, S. Prager: J. Chem. Phys. **50**, 4831 (1969)
50. J.-P. Hansen, I.R. McDonald: *Theory of Simple Liquids*, 2nd edn (Academic Press, London 1986)
51. B. Cichocki, M.L. Ekiel-Jezewska, E. Wajnryb: J. Chem. Phys. **111**, 3265 (1999)
52. G.H. Koenderink, H. Zhang, D.G.A.L. Aarts, M.P. Lettinga, A.P. Philipse, G. Nägele: Faraday Discuss. **123**, 335 (2003)

53. R.A. Lionberger, W.B. Russel: J. Rheology **38**, 1885 (1994)
54. G.K. Batchelor: J. Fluid Mech. **52**, 245 (1972)
55. B. Cichocki, M.L. Ekiel-Jezewska, P. Szymczak, E. Wajnryb: J. Chem. Phys. **117**, 1231 (2002)
56. A.J. Banchio, G. Nägele, J. Bergenholtz: J. Chem. Phys. **111**, 8721 (1999)
57. A.J.C. Ladd: J. Fluid Mech. **271**, 285 (1994); J. Fluid Mech. **271**, 311 (1994)
58. G. Nägele, M. Kollmann, R. Pesché, A.J. Banchio: Mol. Phys. 100, 2921 (2002)
59. J.P. Hansen, L. Verlet: Phys. Rev. **184**, 151 (1969)
60. C.W.J. Beenakker, P. Mazur: Physica A **126**, 349 (1984); A **120**, 388 (1983)
61. G. Nägele, M. Watzlawek, R. Klein: Progr. Colloid. Polym. Sci. **104**, 31 (1997)
62. G. Nägele, B. Steininger, U. Genz, R. Klein: Physica Scripta **T55**, 119 (1994)
63. M. Watzlawek, G. Nägele: J. Colloid Interface Sci. **214**, 170 (1999)
64. M. Watzlawek, G. Nägele: Physica A **235**, 56 (1997)
65. M. Watzlawek, G. Nägele: Phys. Rev. E **56**, 1258 (1997)
66. D.M.E. Thies-Weesie, A.P. Philipse, G. Nägele, B. Mandl, R. Klein: J. Colloid Interface Sci. **176**, 43 (1995)
67. E. Overbeck, Ch. Sinn, M. Watzlawek: Phys. Rev. E **60**, 1936 (1999)
68. G. Nägele, P. Baur: Physica A **245**, 297 (1997)
69. W. Härtl, Ch. Beck, R. Hempelmann: J. Chem. Phys. **110**, 7070 (1999)
70. D.J. Jeffrey, Y. Onishi: J. Fluid Mech. **139**, 261 (1984)
71. F. Bitzer, T. Palberg, P. Leiderer. University of Konstanz, unpublished results
72. M.H.J. Hagen, D. Frenkel, C.P. Lowe: Physica A **272**, 376 (1999)
73. D.L. Ermak, J.A. McCammon: J. Chem. Phys. **69**, 1352 (1978)
74. R. Pesché, G. Nägele: Phys. Rev. E **62**, 5432 (2000)
75. C.W.J. Beenakker: J. Chem. Phys. **85**, 1581 (1983)
76. R. Pesché, M. Kollmann, G. Nägele: J. Chem. Phys. **114**, 8701 (2001)
77. K. Zahn, J.M. Mendez-Alcaraz, G. Maret: Phys. Rev. Lett. **79**, 175 (1997)
78. B. Rinn, K. Zahn, P. Maass, G. Maret: Europhys. Lett. **46**, 537 (1999)
79. M. Kollmann, R. Hund, B. Rinn, G. Nägele, K. Zahn, H. König, G. Maret, R. Klein, J.K.G. Dhont: Europhys. Lett. **58**, 919 (2002)
80. W. Härtl, J. Wagner, CH. Beck, F. Grierschner, R. Hempelmann: J. Phys.: Condens. Matter **12**, A287 (2000)
81. J.F. Brady, G. Bossis: Annu. Rev. Fluid Mech. **20**, 111 (1988)
82. A.E. Larsen, D.G. Grier: Nature **385**, 230 (1997)
83. H. Acuña-Campa, M.D. Carbajal-Tinoco, J.L. Arauz-Lara, M. Medina-Noyola: Phys. Rev. Lett. **80**, 5802 (1998)
84. B. Cichocki, B.U. Felderhof: J. Chem. Phys. **98**, 8186 (1993)
85. M. Medina-Noyola: Faraday Discuss. Chem. Soc. **83**, 21 (1987)
86. G. Nägele, J.K.G. Dhont: J. Chem. Phys. **108**, 9566 (1998)
87. G. Nägele, P. Baur: Europhys. Lett. **38**, 557 (1997)
88. R. Verberg, I.M. de Schepper, E.G.D. Cohen: Europhys. Lett. **48**, 397 (1999)
89. M. Fuchs, W. Götze, I. Hofacker, A. Latz: J. Phys. (France) **3**, 5047 (1991)
90. M. Fuchs, M.R. Mayr: Phys. Rev. E **60**, 5742 (1999)
91. G. Szamel, H. Löwen: Phys. Rev. A **44**, 8215 (1991)
92. A.J. Banchio, J. Bergenholtz, G. Nägele: Phys. Rev. Lett. **82**, 1792 (1999)
93. L. Sjögren: Phys. Rev. A **22**, 2883 (1980)
94. U. Bengtzelius, W. Götze, A. Sjölander: J. Phys. C **17**, 5915 (1984)
95. W. Götze. In: *Liquids, Freezing and Glass Transition*, ed by J.-P. Hansen, D. Levesque, J. Zinn-Justin (North-Holland, Amsterdam, 1991)

96. W. Götze, L. Sjögren: Rep. Prog. Phys. **55**, 241 (1992)
97. M. Fuchs: Transp. Theory Stat. Phys. **24**, 855 (1995)
98. M. Kollmann, G. Nägele: J. Chem. Phys. **113**, 7672 (2000)
99. H. Löwen, T. Palberg, R.G. Simon: Phys. Rev. Lett. **70**, 1557 (1993)
100. I. Moriguchi: J. Chem. Phys. **106**, 8624 (1997)
101. W. van Megen, S.M. Underwood: J. Chem. Phys. **91**, 552 (1989)
102. A. Imhof, J.K.G. Dhont: Phys. Rev. E **52**, 6344 (1995)
103. H. Löwen: Phys. Rev. E **53**, R29 (1996)
104. J.Q. Broughton, G.H. Gilmer, Y.D. Weeks: Phys. Rev. B **25**, 4651 (1982)
105. G. Nägele, H.Y. Zhang: unpublished
106. P.G. de Gennes: *Scaling Concepts in Polymer Physics* (Cornell University, Ithaca 1979)
107. P.G. de Gennes: J. Chem. Phys. **72**, 4756 (1980) 679 (1997)
108. F. Brochard, P.G. de Gennes: Physica A **118**, 289 (1983)
109. A.Z. Akcasu, M. Tombakoglu: Macromolecules **23**, 1511 (1990)
110. G. Meier, B. Momper, E.W. Fischer: J. Chem. Phys. **97**, 5884 (1992)
111. M.G. Brereton, E.W. Fischer, G. Fytas, U. Murschall: J. Chem. Phys. **86**, 5174 (1987)
112. B. Momper, G. Meier, E.W. Fischer: J. Non-Cryst. Solids **131-133**, 624 (1991)
113. G. Meier, G. Fytas, B. Momper, G. Fleischer: Macromolecules **26**, 5310 (1993)
114. Y. Feng, C.C. Han, M. Takenaka, T. Hashimoto: Polymer **33**, 2729 (1992)
115. M.P. Lettinga, M.A.M.J. van Zandvoort, C.M. van Kats, A.P. Philipse: Langmuir **16**, 6156 (2000)
116. G.H. Koenderink, H. Zhang, M.P. Lettinga, G. Nägele, A.P. Philipse: Phys. Rev. E 64, 022401 (2001)

17 Field-Assisted Diffusion Studied by Electrophoretic NMR

Manfred Holz

17.1 Introduction

Nuclear magnetic resonance (NMR), a low-energy radiofrequency (rf) spectroscopic technique, provides a huge number of different experimental methods allowing energy, time and spatially resolved measurements [1,2] (see also Chaps. 9 and 10). In the present chapter an introduction into an NMR method shall be given, which allows the study of transport properties of distinct *electrically charged* species in condensed matter, mainly in the liquid state. Typically, those charged species can be certain simple, monoatomic ions like Li^+, Cs^+, or polyatomic ions as, e.g., alkylammonium ions, or charged macromolecules, like polyelectrolytes as well as charged molecular aggregates, like micelles.

The most interesting transport quantity of charged particles is their mobility $u_\pm$, measured in $m^2s^{-1}V^{-1}$, that is their drift velocity in an electric field of unit field strength. But how is this transport quantity related to diffusion, the main subject of this book? In a liquid, the ions share in the general Brownian motion and have randomly-directed instantaneous velocities of the order of 10^2 ms^{-1}, of course with an extremely short mean free path. In an electric field of say 10^3 Vm^{-1}, the velocity of ions in the field direction is of the order of 10^{-4} to 10^{-6} ms^{-1} resulting in a very small perturbation of the random ionic motions and this represents only a small biasing of the Brownian motion in a given direction. We can speak of a "directed diffusion process" (similar as in the case of mutual or transport diffusion in a concentration gradient) or of "field-assisted diffusion". So, it is understandable that the ionic self-diffusion coefficient $D_\pm$ and the mobility $u_\pm$ must be somehow related and this relation can be expressed at least for the limiting quantities at zero ion concentration $D^*_\pm$ and $u^*_\pm$ by the well-known "Einstein relation"

$$D^*_\pm = RT\frac{u^*_\pm}{zF} \equiv k_\mathrm{B}T\frac{u^*_\pm}{ze}, \tag{17.1}$$

where z is the ion valency, F is the Faraday constant, R is the gas constant and T is the temperature and where the equivalence of the second and third terms results from the fact that $R \equiv k_\mathrm{B}N_\mathrm{A}$ and $F \equiv eN_\mathrm{A}$, with the Avogadro constant N_A and the elementary charge e. However, it should be pointed out

that self-diffusion belongs to the class of incoherent motions, whereas the uniform migration of ions in the field direction is a coherent motion, a fact, which will later be reflected in the NMR experiment. The distinction between coherent and incoherent motion is a topic, which is extensively discussed also in Chaps. 3, 13, and 14.

The most famous classical methods for the measurement of mobilities $u_{\pm}$ and transference numbers $T_{\pm}$ of ions are the "moving boundary" and the "Hittorf" method (see, e. g., [3]). However, these methods fail or are connected with great difficulties in the case of porous media and in the case of mixtures of electrolytes, where the mobility of a distinct kind of ions is the quantity of interest. The simplest electrolyte solution contains three constituents, the anions, the cations and the solvent. Thus, mixed electrolyte solutions consist of a markedly higher number of components and are typical multi-component mixtures. Consequently, a highly selective method of observation is required for obtaining information about a distinct kind of species in the solution.

Such a selective method is NMR, since one can observe selected nuclides as, e.g., ^{1}H, ^{7}Li, ^{13}C, ^{19}F, ^{29}Si, ^{133}Cs etc. or even the resonance lines of the same nucleus, but with different chemical shifts according to different chemical species or groups [1,2]. This frequency (energy) resolved, selective observation technique can be combined with spatially resolving pulsed field gradient (PFG) NMR spin-echo experiments [4, 5], allowing diffusion studies (as outlined in Chap. 10) and flow studies [6, 7]. There are further advantages of NMR, namely (i) the measurement is non-invasive and thus non-destructive, (ii) low-energy electromagnetic fields are applied, which do not disturb the thermal equilibrium of the system and (iii) the systems under investigation can be solid or liquid and there is no need for optical permeability.

Taking all these advantages into consideration it was tempting to use PFG NMR flow measurement techniques to observe the slow drift velocity of distinct charged species in an external electric field E. In 1982, in the present author's group, the first successful experiment of this kind could be performed, namely the measurement of the drift velocity of $(C_2H_5)_4N^+$ ions in water [8]. This new type of experiment thus represented a combination of in-situ electrophoresis with the selectivity of NMR spectroscopy. From 1982 until today a steady methodical and instrumental development in this field of NMR occurred [9]. Johnson and co-workers introduced the name "electrophoretic NMR" (ENMR) [10], where the term "electrophoretic" is used in a general sense for the migration of all kinds of charged particles in an electric field. In general, for all types of NMR experiments, which are performed in presence of an electric direct current (DC) in the sample under investigation, the abbreviation DCNMR [9] is used.

Now, DCNMR experiments are performed in a number of laboratories, but we cannot yet speak of an NMR routine experiment, due to the fact that the field is still under development and that the required accessory units for these experiments are not yet commercially available. On the other hand,

the potential of ENMR has been clearly demonstrated [9,11] and these novel NMR techniques can find many fields of interesting applications, in particular in electrochemistry, biochemistry and in technical sciences.

In the following sections we will briefly discuss the basics of ENMR, the general problems and technical requirements of DCNMR and finally examples as well as applications of actual ENMR experiments will be presented.

17.2 Principles of Electrophoretic NMR

17.2.1 Electrophoresis

The characteristic mobilities of charged solutes in a given solvent can be used to separate the ions on the basis of their different drift velocities in an electric field E. Shortly after the application of the electric field the ions reach a constant drift velocity

$$v_{\pm} = u_{\pm} \cdot E. \tag{17.2}$$

In an electric field E of 10^3–10^4 Vm^{-1}, these drift velocities are typically in the range of 10^{-6} to 10^{-4} ms^{-1} (As we will see, the observation times in ENMR are typically ≤ 1 s and thus the observed spatial displacement of the particles of interest is small compared with the length of the NMR receiver coil, which is typically 1 to 3 cm, and the migrating particles cannot leave the observation volume during the experiment.).

In the case of strong electrolytes, from the single-ion velocity $v_{\pm}$ we can derive another important quantity, namely the transference number $T_{\pm}$, via the relation

$$T_{\pm} = \frac{c v_{\pm} A \cdot F}{I}, \tag{17.3}$$

where c is the ion concentration in moles per liter and A and I denote, respectively, the cross section of the sample cell and the electric current. The knowledge of the mobility of charged species in a given environment is of high interest since $u_{\pm}$ depends upon the properties of the species and of the particular environment and can thus yield information on both of them. The theoretical treatment of $u_{\pm}$ is difficult [12] and one can only derive expressions for $u_{\pm}$ on the basis of approximations. There are two important cases for which we will give the corresponding relations. For ions with a small radius r and at low ionic strength I_{i}, we obtain from (17.1) and from the Stokes-Einstein equation $D = RT/6\pi\eta r$ (see also Sect. 6.3 of Chap. 6), where η is the viscosity, the "small particle limit"

$$u_{\pm} = \frac{z \cdot e}{6\pi\eta r}, \tag{17.4}$$

where $z \cdot e$ is the electric charge of the ion.

Thus (17.2) is applicable in cases where the Stokes-Einstein equation is valid and where the ionic radius r is also small compared to κ^{-1}, the Debye length, that means $\kappa \cdot r \ll 1$. The latter is given by

$$\kappa = \left[\frac{2\rho F^2}{\epsilon_0 \epsilon_\mathrm{r} RT}\right]^{\frac{1}{2}} I_\mathrm{i}^{\frac{1}{2}}\,, \tag{17.5}$$

where ρ is the density and ϵ_0, ϵ_r are the dielectric constant of the vacuum and the relative dielectric constant of the electrolyte solution, respectively.

If $\kappa r \gg 1$, that means large charged particles and a small Debye length, one obtains in this "large-particle limit":

$$u_\pm = \frac{ze}{4\pi r^2} \cdot \frac{1}{\eta \cdot \kappa} = \frac{\sigma}{\eta\kappa}\,. \tag{17.6}$$

$\sigma = ze/4\pi r^2$ is the surface charge density. In the large-particle limit, the mobility $u_\pm$ can also be related to the electrokinetic potential ζ at the surface, the so-called zeta potential, by [13]:

$$u_\pm = \frac{\epsilon_\mathrm{r}\epsilon_0\zeta}{\eta}\,. \tag{17.7}$$

Thus, in this limit the measurement of $u_\pm$ gives valuable information about σ and ζ of large molecules or molecular aggregates.

17.2.2 Pulsed Field Gradient NMR for the Study of Drift Velocities

The basis of NMR diffusion and flow studies is spatially resolved NMR (see also Chap. 10). Since in a homogeneous magnetic field the space points are equivalent, the superimposition of known magnetic field gradients g produces an inequivalence and allows the gain of information from the now spatial dependence of the NMR frequency. If we apply, e.g., a gradient $g = \partial B_z/\partial z$ in z-direction, the NMR signal frequency ω is a function of z:

$$\omega(z) = \gamma B(z) \tag{17.8}$$

with γ = magnetogyric ratio of the nucleus, B = magnetic field strength.

This spatially resolving NMR is also the basis of all NMR imaging techniques, like NMR tomography and microscopy [6]. If a particle, which carries a nucleus under observation, performs a translational motion and consequently changes its position during the observation time, its NMR frequency changes. This frequency change is observed in a "spin-echo experiment" (Fig. 17.1) allowing very elegant NMR diffusion and flow studies, which were developed by Stejskal [14]. Since translational diffusion and flow are different kinds of motion they have different influence on the NMR spin-echo signal. In Fig. 17.2

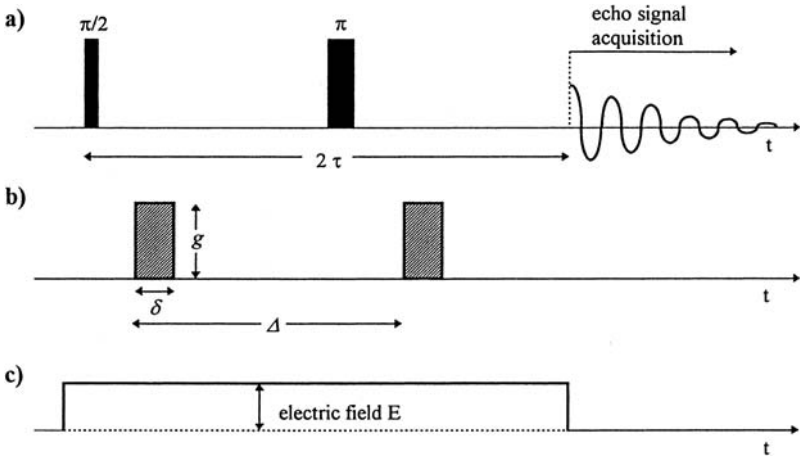

Fig. 17.1. Basic pulsed field gradient (PFG) spin-echo experiment in electrophoretic NMR. The diagram of the pulse program shows the radiofrequency pulses ($\pi/2$- and π-pulse) for the generation of the spin-echo signal at 2τ (a). Pulsed field gradients with a strength g, a duration δ and a distance Δ are applied for flow (and diffusion) measurements (b). In an ENMR experiment the electric field E is switched on in the sample cell during the spin-echo sequence (c). The acquisition of the second half of the spin-echo signal starts at 2τ.

we show the effects of diffusion and flow in a magnetic field gradient g. We see that in the case of diffusion the spins, which were at $t = 0$ in the plane 0, show at times $t > 0$ a frequency distribution, whereas in the case of flow (Fig. 17.2(b)) the frequency of all those species is regularly increasing with t. Diffusion as an incoherent motion produces a damping of the spin-echo signal due to random dephasing of the spin precession about the magnetic field, whereas flow as a coherent motion produces a shift of the spin-echo signal phase.

Since the NMR diffusion experiment is outlined in Chap. 10, we will here deal only with the basics of NMR flow experiments. We consider a flow or drift of particles in z-direction along a stationary gradient $g = \partial B_z/\partial z$. The particles shall have a uniform velocity v and then they have at time t the position $z(t) = v \cdot t$. The nucleus residing in a particle experiences a time-dependent magnetic field

$$B(z(t)) = B_0 + z(t) \cdot g, \tag{17.9}$$

where B_0 represents the constant magnetic main field. The resonance frequency $\omega(t)$ of such a nucleus is then

$$\omega(t) = \gamma B_0 + \gamma g v t. \tag{17.10}$$

This means that at a time t a frequency difference with respect to the reference frequency $\omega_0 = \gamma B_0$ occurs. From (17.10) it follows

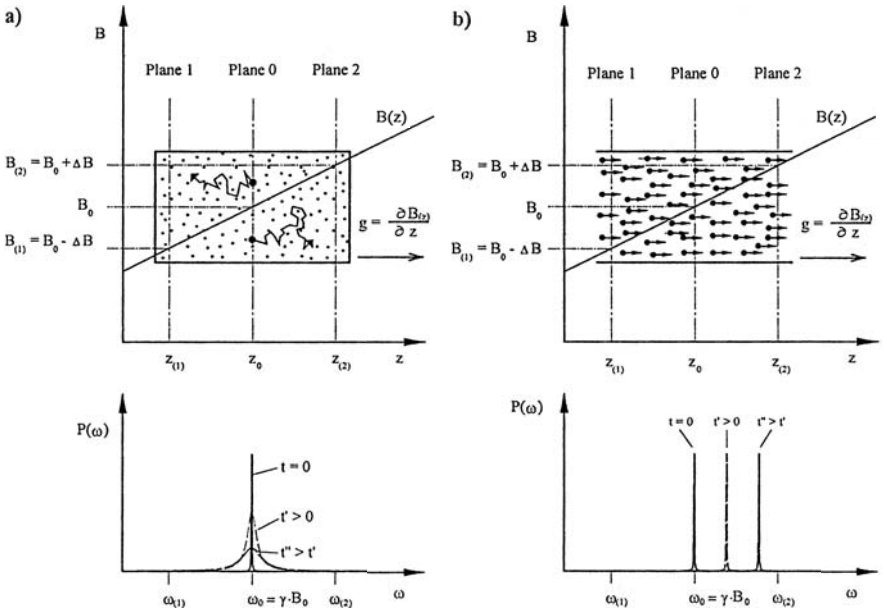

Fig. 17.2. The effect of diffusion (a), and flow (b) in the presence of a magnetic field gradient g in z-direction. The magnetic field $B(z)$ increases from left to right. The nuclear spins in planes 0, 1 and 2 have different NMR resonance frequencies ω_0, $\omega_{(1)}$ and $\omega_{(2)}$, respectively. In the lower diagrams the frequency distribution $P(\omega)$ is given for the nuclear spins, which were at time $t = 0$ in the plane 0. In the case of diffusion (a) the random walk of the spin-carrying particles results in a Gaussian frequency distribution at times $t > 0$, which is the origin of the echo damping. In the case of plug flow (b) the frequency distribution is a δ-function, which is shifted to higher frequencies ω with increasing t, resulting in a phase shift of the spin-echo signal.

$$\Delta\omega(t) = \gamma g v t. \tag{17.11}$$

Since $\Delta\omega = \Delta\phi/t$ is valid, also a phase angle difference increasing with t, with respect to the reference phase, appears. At time $t = \tau$, where the radio frequency π-pulse in the spin-echo pulse sequence is applied (see Fig. 17.1), we have a phase difference

$$\Delta\phi(\tau) = \int_0^\tau \gamma g v t \, \mathrm{d}t = \frac{1}{2}\gamma g v \tau^2. \tag{17.12}$$

The π-pulse has the effect (see also Fig. 13.2 of Chap. 13) that it inverts all nuclear spin precession phases and thus it makes $\Delta\phi(\tau)$ to $-\Delta\phi(\tau)$. At the time 2τ, where the spin echo maximum appears and where the signal is measured, we finally have a phase difference

$$\Delta\phi(2\tau) = -\Delta\phi(\tau) + \int_{\tau}^{2\tau} \gamma g v t \, \mathrm{d}t = \gamma g v \tau^2. \tag{17.13}$$

In an experiment with two pulsed field gradients of length δ and distance Δ (see Fig. 17.1) (pulsed gradients have some important advantages over the application of stationary gradients [4, 5, 7]), the phase shift at 2τ is simply

$$\Delta\phi(2\tau) = \gamma g v \delta \Delta. \tag{17.14}$$

The measurement of $\Delta\phi$ with known g, δ and Δ then allows the determination of the velocity v.

In phase sensitive signal detection, the phase shift $\Delta\phi$ due to the flow leads to a cosine modulation of the signal $S_v(2\tau)$ (the subscript v stands for presence of flow) as a function of g, v, δ or Δ. The total spin-echo signal intensity in presence of diffusion, flow and T_2 relaxation is then [9]:

$$S_v = S_0 \cos(\gamma g v \delta \Delta) \cdot \exp\left[-\frac{2\tau}{T_2} - \gamma^2 D g^2 \delta^2 \left(\Delta - \frac{1}{3}\delta\right)\right]. \tag{17.15}$$

Here we see the three influences on the spin-echo signal, namely the flow (cosine term), T_2 relaxation (first term in the exponent) and diffusion (second term in the exponent). If we measure $S_v(2\tau)$ and then switch off the flow (in electrophoretic NMR one can switch off the electric current) and measure $S_{v=0}(2\tau)$, the simple intensity ratio

$$\frac{S_v(2\tau)}{S_{v=0}(2\tau)} = \cos(\gamma g v \delta \Delta) \tag{17.16}$$

yields the influence of flow alone and represents the first simple method for the actual measurement of v.

How is $\Delta\phi$, the quantity of interest, obtained in practice? In modern NMR spectrometers the resonance signals are first excited and recorded in the time domain and then transformed mathematically into the frequency domain by a Fourier transformation (FT) yielding the NMR spectrum. In principle $\Delta\phi$ can be measured in the time domain [8, 15] or after FT in the frequency domain. The latter is today the method of choice. For the introduction and propagation of this principle, Richard Ernst has been awarded by the 1991 Nobel prize in chemistry [16]. In particular in ENMR there are different possibilities for the practical procedure. $\Delta\phi$ or $\cos(\Delta\phi)$ is measured as a function of one of the variables g, δ, Δ or v, where v can be varied with the applied electric field E and thus by a variation of the electric current I in the sample cell. As shown in Fig. 17.3 it is possible to observe and evaluate the $\cos(\gamma g v \delta \Delta)$ modulation of the NMR line intensity as a function of E (or I). By determination of the electric field E_1, which is required for just one modulation period, one can directly obtain the mobility by means of $u_{\pm} = 2\pi/\gamma g \delta \Delta E_1$.

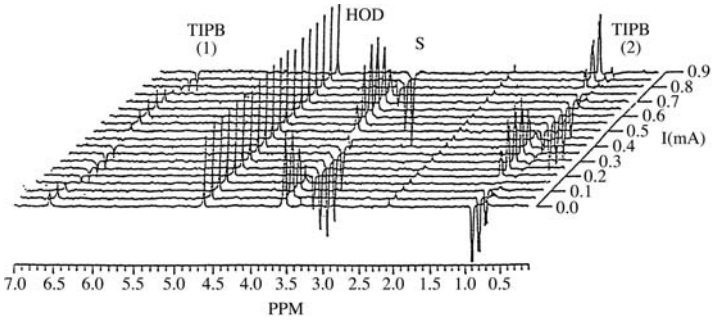

Fig. 17.3. ^{1}H ENMR spectra of an "oil-in water" microemulsion as a function of the electric current I [10], showing the $\cos(\Delta\phi)$ modulation of the lines of electrically charged species, whereas the line of the solvent water (HOD) is unaffected. (S = ionic surfactant, TIPB = triisopropylbenzene).

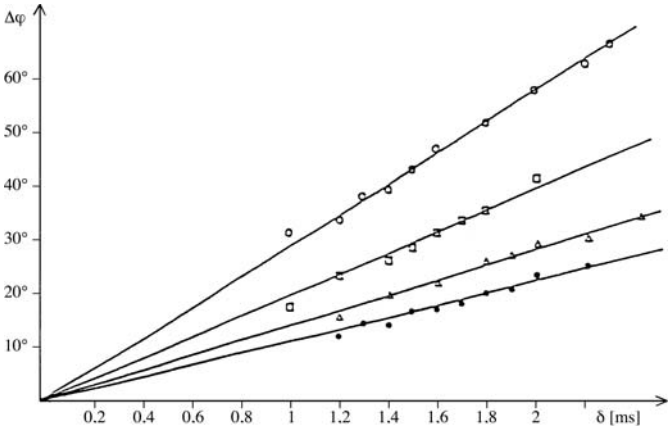

Fig. 17.4. $^7Li^+$ spin-echo phase shifts $\Delta\phi$ as a function of the PFG duration δ. The different slopes correspond to different Li^+ mobilities in various aqueous LiCl solutions [15].

With modern NMR instruments a signal phase shift of a line in the spectrum can be directly observed and printed out. Thus one can, e.g., vary δ, resulting in the linear dependence $\Delta\phi(\delta) = K\delta$ with $K = \gamma g v \Delta$. From the slope of this straight line the velocity v is derived (see Fig. 17.4). Since the really acting magnetic field gradient g is the variable, which is less accurately known compared with the quartz controlled times δ and Δ, often, similar as in NMR self-diffusion studies [5], measurements are performed relative to a reference system, here with known v. This procedure then allows velocity measurements by a simple comparison of slopes, without the need of knowing the actual g values.

17.3 NMR in Presence of an Electric Direct Current. Technical Requirements, Problems and Solutions

The DCNMR experiments are performed in common NMR spectrometers, normally equipped with a superconducting magnet. For the PFG experiments a probe head with gradient coils (actively shielded coils are recommended) is required together with the corresponding gateable high-current power supply. Such units are commercially available. Special accessories for DCNMR are the probe cells with two electrodes, where the electric field E can be applied (see Fig. 17.5) and a gateable constant DC power supply (typically 0–250 mA, 0–1 000 V) for the electrophoretic cell. The electric field is applied as a pulsed field (see Fig. 17.1) where the gate pulses are usually derived from the computer system of the spectrometer and are thus synchronized with the rf excitation pulses and the magnetic field gradient pulses. The electrodes used are Pt or Ag/AgX (X=Cl,Br,J) electrodes. More technical details can be found elsewhere [8–11].

The electric current flowing during the NMR experiment in the sample cell is the origin of a number of experimental problems, which shall be briefly discussed together with the solutions found so far:

Magnetic Fields Induced by the Electric Current

The electric current produces a magnetic field in the plane perpendicular to its direction of flow. This field can interfere with the Zeeman field B_0 and results in undesired B_0 field inhomogeneities and instabilities. However, there is a relatively easy way to overcome this problem by choosing as the current direction that of the magnetic field B_0 (z-direction) (see Fig. 17.5). The additional magnetic fields then lie in the x, y-plane and have no components in the z-direction, which is the relevant direction in the NMR experiment and thus no signal disturbances are produced. This z-direction for the electric current is the "natural" direction in superconducting magnets since it is also the axis of the magnet bore, and cylindrical sample cells are commonly mounted parallel to this axis.

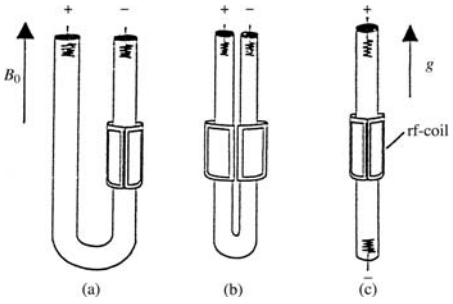

Fig. 17.5. Three basic DCNMR cell geometries (a), (b), (c), with the corresponding electrode arrangements. The radio frequency (rf) transmitter/receiver coil is a saddle coil. The direction of the Zeeman field B_0 and of the imposed field gradient $g = \partial B_z/\partial z$ is also shown.

Resistive Heating by the Current in the Sample Cell

More serious problems in ENMR can arise from resistive heating. The undesired heat production by the current in the electrolyte solution can result in a temperature increase, unstable temperature conditions and finally in a macroscopic convection in a liquid sample. Any macroscopic motion in a liquid system like convection, vibrations or shock waves can be the source of dramatic measuring errors in NMR mobility or diffusion measurements since we have to measure small displacements in the micrometer or sub-micrometer region.

The first step to solve the problem of resistive heating is the application of *pulsed* electric fields, so that a current flows only during the relatively short time of the spin-echo sequence, and the use of effective cooling systems. As a second step there is the possibility of using stabilizers against convection as agar-agar [17] or some other gelling agents. In particular agar-agar proved to be a suitable stabilizer for aqueous solutions without affecting markedly the diffusion and mobility of ions and the diffusivity of the solvent water. However, the experience shows that with low electric currents of $\lesssim 10$ mA also measurement in the free solution is possible. A third possibility to overcome heat-induced convection is the application of special pulse sequences, including rf, magnetic gradient and electric field pulses, which remove spectral artifacts arising from convection. This novel method is called "Convection compensated ENMR" [18].

Electro-Osmotic Flow

When ions migrate in the electric field there are always collisions with the neutral solvent molecules which are connected with a transfer of momentum in the direction of the ion flow. However, this effect is cancelled by the counter-ions, which move in the opposite direction, but the cancellation acts only under the condition that there is a homogeneous charge distribution, which means local charge neutrality [19]. On the other hand, an inhomogeneous contribution of mobile charges occurs on charged surfaces, since only the screening counter-ions are mobile. This fact results in a solvent flow at the surface in the direction of the electrophoretic migration, and in a vertical sample tube a counterflow appears in the centre. In this way electro-osmosis produces macroscopic flow in the sample, which disturbs the ENMR experiment, resulting in an undesired damping of the NMR signal intensity [10,20]. The solution of this problem is not so easy, however also here a gelling agent proved to be successful. Johnson and coworkers [10] proposed a coating of the surface by methylcellulose to reduce electro-osmosis.

Mechanical Disturbances

Due to the fact that in DCNMR experiments electric direct currents are switched in a strong external magnetic field B_0, strong forces are acting on all electrical connections (gradient coils, wires, electrodes etc.) in which the

current does not flow parallel to B_0. In this case during switching shock waves may be generated, which can lead to displacements in the electrolyte solution. This problem must be solved by a very careful rigid fixing of all electrical connections and electrodes within the probe head.

17.4 ENMR Sample Cells

We will give two examples of electrolytic cells in use in our laboratory. They are both cylindrical cells oriented in z-direction (B_0 direction). The first one [9, 21] is simply cylindric with an upper and a lower electrode (see Fig. 17.6 (a). The advantage of this cell is a good filling factor, giving a good signal-to-noise ratio, which is important for nuclei other than ^{1}H, the so-called heteronuclei. The disadvantage comes from a possible gassing of the lower electrode, which is not vented to the atmosphere. The second one (see Fig. 17.6 (b) is a concentric cylindric chamber, where in the inner cylinder the sample of interest is located. The outer cylinder is filled with an electrolyte solution as a conductor. In order to be able to use as conductor in

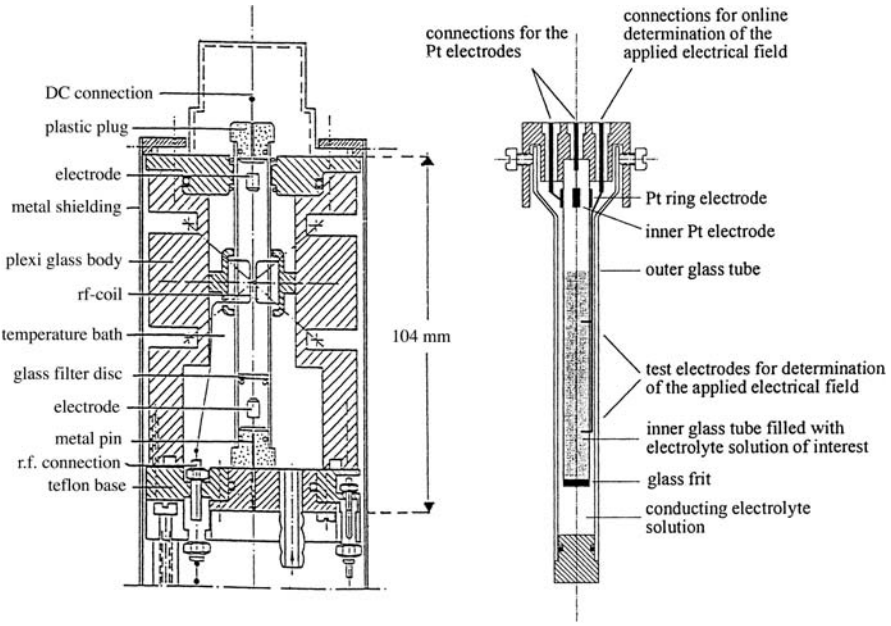

Fig. 17.6. Two examples of ENMR cells. (a) probe head insert consisting of a plexi glass body on which the gradient coils are mounted. The electrophoresis cell in the centre is surrounded by a temperature bath liquid [21]. (b) Concentric cylindrical ENMR cell, where the two electrodes are located in the upper part of the cell.

the outer cell always the same kind of electrolyte solution as it is observed in the inner cylinder, in the author's laboratory a very successful procedure has been developed, which eliminates the undesired NMR signal contributions from the ions in the outer cylinder. For this purpose in the outer cylinder suited small beads are added, which due to magnetic susceptibility and/or surface relaxation effects extremely broaden NMR signals coming from the outer cylinder. Thus the undesired signals are suppressed by a "T_2-filter". The advantage of this cell is that both electrodes are vented to the atmosphere, the disadvantage is the lower filling factor.

17.5 ENMR Experiments (1D, 2D and 3D) and Application Examples

First we ask the question: which nuclei can be used in ENMR? Whereas in ordinary NMR more than 100 nuclides are accessible to the experiment, the number of nuclides, which are suited for ENMR and NMR diffusion experiments, is in the range of 10 to 30. The reason for that lies in the PFG spin-echo experiment, which is applied and where the particles move during a defined time (Δ) and after that time the displacement is measured via the spin-echo signal at 2τ. Thus, in particular for slowly moving particles, Δ cannot be chosen too short, since a measurable displacement $\langle \Delta z \rangle$ has to be achieved. On the other hand, as can be seen from (17.15), the spin-echo signal decreases with the nuclear magnetic relaxation (time constant T_2) and therefore the maximum "observation time" Δ is limited by the relaxation influence. There are so-called "stimulated-echo" experiments [9–11], which can be used in those cases where the transverse relaxation time T_2 is much smaller than the longitudinal relaxation time T_1 and then commonly T_1 is the limiting factor (see also Sect. 10.3.4 of Chap. 10). There is a large amount of nuclides with nuclear spin $I > 1/2$, which relax by the so-called quadrupole mechanism and have often very short T_1 and T_2 values in the μs range in liquid solutions so that they are not suited for ENMR measurements. Generally, one can say that all spin-1/2 nuclides with a not too low NMR receptivity should be usable, as, e.g., ^{1}H, ^{13}C, ^{19}F, ^{29}Si, ^{31}P, ^{113}Cd, ^{119}Sn and ^{205}Tl. There are several quadrupolar nuclei, which are candidates for ENMR, namely for example ^{2}H, ^{7}Li, ^{23}Na, ^{27}Al, ^{35}Cl, ^{51}V and ^{133}Cs, since they have under normal circumstances relaxation times, which are long enough for the spin-echo experiment.

So far, in the comparatively young field of applied ENMR, the nuclei ^{1}H, ^{7}Li, ^{13}C, ^{19}F and ^{133}Cs have actually been used in experiments, where of course ^{1}H ENMR plays an outstanding role, owing to the high sensitivity of ^{1}H NMR and also as a consequence of the huge number of hydrogen containing compounds of interest in pure and applied chemistry and in life sciences.

In NMR, in the last two decades a number of highly sophisticated techniques have been developed allowing the representation of the spectra in a multi-dimensional form [16]. Thus, we distinguish one- (1D), two- (2D) and three-dimensional (3D) NMR experiments, corresponding to the representation of the line intensities as a function of one, two or three axes. In describing typical ENMR experiments in the following, we will demonstrate their possible applications. We shall begin with common 1D ENMR.

17.5.1 1D ENMR Applications

The first ENMR experiments were performed on simple aqueous solutions of tetraalkylammonium salts, where e.g. the concentration dependence of the mobility of the hydrogen containing cations has been measured for the purpose of demonstrating the agreement with results from classical methods [8, 17]. However, as pointed out above, the main advantage of ENMR lies in the possibility of studying distinct species in multi-component mixtures.

Mobility Studies in Mixtures

Owing to difficulties with classical methods, there exist in the literature only a few reliable mobility data of simple ions in electrolyte mixtures. Also for such a simple system like LiX/CsX (X=Cl,Br,J) in aqueous solution there were no data available. $^{7}Li^{+}$ and $^{133}Cs^{+}$ are excellently suited for ENMR and these two cations differ appreciably in their ionic radii. In Fig. 17.7 we see, as an example for aqueous LiBr/CsBr mixtures at constant ionic strength, the mobilities $u_{\pm}$ for both ions [21]. As a by-product one always obtains (with electric current $I = 0$) the ionic self-diffusion coefficients $D_{\pm}$, which are also given in Fig. 17.7. It can be recognized that the mobilities show a curved composition dependence, with opposite curvature for Li^{+} and Cs^{+}, which means that the "fast" cation accelerates the migration of the "slow" cation in the mixture. An opposite result represents the linear dependence of the ionic diffusion coefficients. However, this is not surprising since, in contrast to u_{+}, D_{+} is an equilibrium quantity. Having measured the mobilities of the two cations, the transference numbers T_{+} could be calculated. Since the sum of all transference numbers must be equal to one, T_{-} for the common anion could also be determined (see Fig. 17.7).

Another example is shown in Fig. 17.8 where by high-resolution ^{1}H ENMR the electrophoretic mobilities of the amine and the amino acid in an aqueous mixture could be measured simultaneously [10].

More recently, mixed anionic-nonionic surfactant micelles have been studied by the same experimental technique with the aim of characterizing the surfaces of ionic micelles. New insight in counterion binding could be derived, which cannot be easily gained by other methods. [23]

In the study and application of polyelectrolytes the quantitative determination of the effective charge density is an important but difficult task. Applying the combination of ENMR and PFG diffusion measurements, Wong

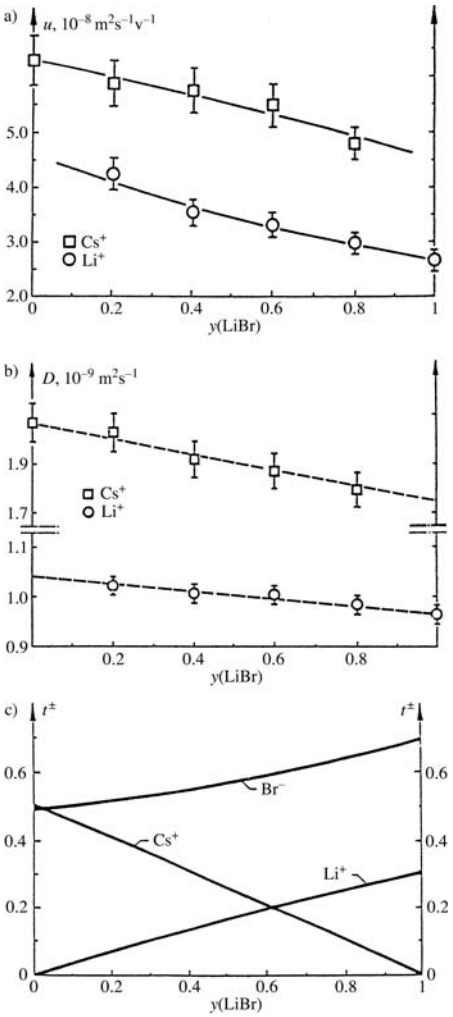

Fig. 17.7. Results of ENMR measurements on a ternary aqueous mixture of simple ions at constant ionic strength [21]. System $y \times 0.5$ m LiBr + $(1 - y) \times 0.5$ m CsBr in H_2O.
(a) The mobilities u_+ of Li^+ and Cs^+ as a function of mixture composition.
(b) The ionic self-diffusion coefficients D_+ of Li^+ and Cs^+.
(c) The transference numbers $T_\pm$ of the three ionic constituents Li^+, Cs^+ and Br^- in the mixed electrolyte solution.

and Scheler [24, 25], for the first time succeeded in measuring in this way the electrophoretic mobility of polyelectrolytes in solution and they could determine the effective charge density. The effect of addition of common salts could also be analysed.

Diffusion and Field-Assisted Diffusion of Ions in Porous Media

In the literature it is often assumed, that the ionic mobility within a pore can be approximated by its mobility in the bulk fluid and that therefore the electric conduction of a porous system, filled with a liquid electrolyte, is only restricted by geometrical factors [16]. The validity of this assumption could not be experimentally checked by classical methods. ENMR, as a non-invasive

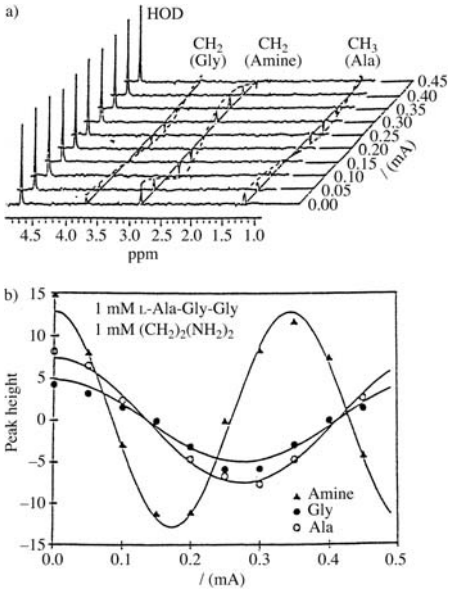

Fig. 17.8. (a) ^{1}H ENMR (250 MHz) spectra of a mixture of 1 mM ethylene diamine with an amino acid (1 mM L-Ala-Gly-Gly) in D_2O [10].
(b) The intensity of the ^{1}H NMR lines in Fig. 17.8a versus current I. From the different cosine modulations of the amine line and the amino acid lines, the different mobilities can be derived [10].

technique, which is also independent of optical properties, is a unique tool for the investigation of the transport of ionic charge carriers in disordered media. Thus, it is not surprising that this field of ENMR application developed comparatively fast in the last years. The first successful measurements of ionic mobilities in porous systems, namely in gels, have been performed in the author's laboratory [26, 27]. It could be demonstrated that in the fluid-filled pore space both the observed ionic self-diffusion coefficient $D_{\pm}$ and the ionic mobility $u_{\pm}$ in an external electric field show a dependence on the observation time Δ (see Fig. 17.9). As previously observed for *liquid molecules* confined in porous media the phenomenon of "anomalous diffusion" occurs (see Chaps. 10, 19 and 22). Now, this phenomenon has been also observed for self-diffusion of *charged species* and for the first time it has been shown that also the analogous phenomenon of "anomalous field-assisted diffusion" or "anomalous electric mobility" exists [26], which means that there is a time regime, where the average displacement $\langle z(\Delta) \rangle$ of an ion by migration along the electric field is a non-linear function of time. At long observation times Δ the quantities D_+ and u_+ become independent of Δ and reach their effective values D_+^{eff} and u_+^{eff} in the porous system, the quantities D_+/D_+^0 and u_+/u_+^0 in Fig. 17.9 thus reach plateau values. (The index "0" refers to quantities in the non-confined state.) The inverse plateau value $\mathcal{T}(D_+) = D_+^0/D_+^{eff}$ delivers an important characteristic value of the porous medium, namely its tortuosity $\mathcal{T}$ (see, e. g., [28]; cf also Fig. 10.13 in Chap. 10). $\mathcal{T}$ of a porous medium is usually defined as the squared ratio of the true migration path length of a fluid particle and the straight-line distance between the

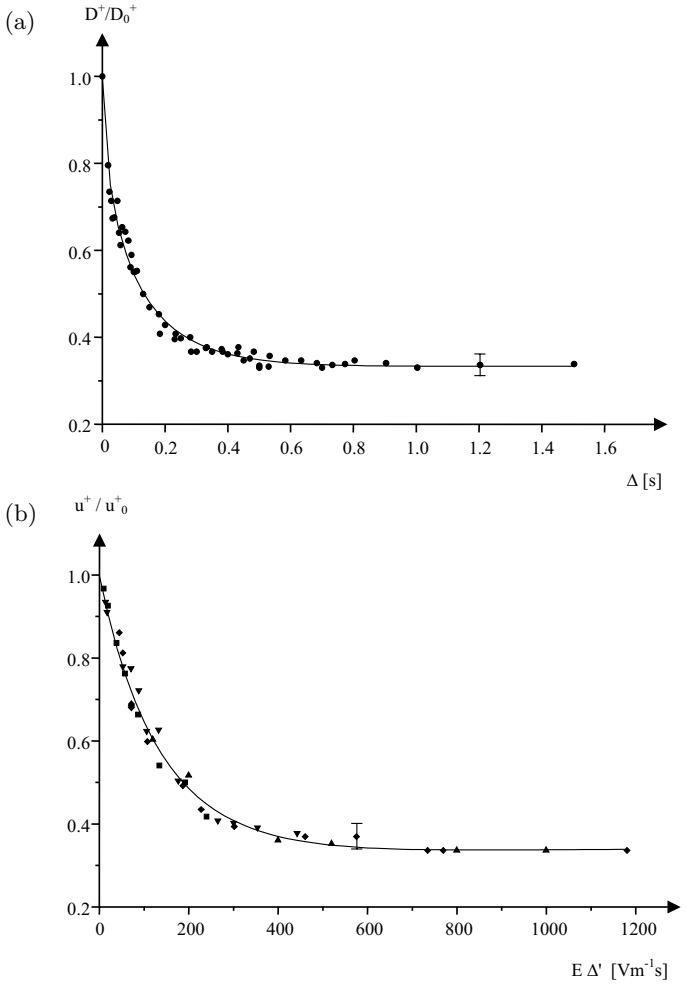

Fig. 17.9. (a) The relative ionic self-diffusion coefficient D_+/D_+^0 of the $(C_4H_9)_4^+$ cation in aqueous solution confined in the gel Sephadex LH-20 as a function of the observation time Δ. $D_+^0 = 0.49 \times 10^{-9}\,\mathrm{m^2 s^{-1}}$ is the ionic self-diffusion coefficient in the non-confined bulk solution [26].
(b) The relative ionic mobility u_+/u_+^0 as a function of the product of observation time Δ' and the externally applied electric field E. $u_+^0 = 1.22 \times 10^{-8}\,\mathrm{m^2 s^{-1} V^{-1}}$. All other details as in (a).

starting and finishing point of the particle's motion in this medium. Since, in general, the translational motion can have its origin in different processes as flow, diffusion or electric field-assisted diffusion, one sometimes speaks of "hydraulic", "diffusional" or "electric" tortuosity, respectively [29]. From the plateau value $\mathcal{T}(u_+) = u_+^0/u_+^{\mathrm{eff}}$ again the tortuosity of the system is

available, now measured via the electric mobility. The comparison of the behaviour of the ionic self-diffusion coefficient and the electric mobility of the same ion in the medium with internal boundaries allows a first direct experimental check of the validity of a very important relation in porous media, namely the Einstein relation ($D_{\pm} \propto u_{\pm}$, see (17.1)). Fig. 17.9 reveals that $\mathcal{T}(u_+) = \mathcal{T}(D_+)$ is found, which means that indeed in the porous gel system under investigation the Einstein relation remains valid [26,27]. In the paper by Holz et al. [27], also a first attempt has been undertaken to derive the specific surface S/V_{p} of the porous medium from the time-dependence of the field-assisted diffusion, similarly, as it has been performed, e. g., by means of the observation time-dependence of the self-diffusion coefficient in Sect. 10.5.3 of Chap. 10 [30–32]. The present author and his co-workers also discussed basic advantages of time-dependent electric mobility measurements for morphology studies of porous media [27].

Very important special porous media in life science and in technical applications are membranes, and it has been pointed out that ENMR might be a powerful technique for the study of ion transport in those media [9]. Polymer electrolyte membranes are of outstanding interest in connection with fuel cells. Ise et al. [33] succeeded in measuring by ENMR the electro-osmotic drag coefficient K_{drag} in polymer membranes. This drag coefficient is defined as the number of water molecules transferred through the membrane per H^+ ion, and the authors could determine K_{drag} as a function of water content and temperature for different membrane materials as Nafion and sulfonated polyetherketones.

Anion and cation (Li^+) transference numbers have been studied in composite polymer electrolytes with fumed silica as an inorganic filler by ^{19}F and ^{7}Li ENMR, respectively, [34,35]. In this way the ionic transport properties could be investigated as a function of filler content and Li salt concentration without the usual need of assumptions. The power and validity of ENMR could be demonstrated by the independent measurement of the anion and cation transference numbers for different salts, where within the experimental error these transference numbers sum to unity. Also in lithium polymer gel electrolytes, used in lithium secondary batteries, the individual ionic mobilities of cations and anions could be measured by ^{7}Li and ^{19}F ENMR experiments [36]. The authors also observed by ^{1}H ENMR a solvent drift in the gel electrolyte when the strength of the applied electric field exceeds a distinct value, where also an anomalous change of the Li^+ mobility occurs. They discuss as a possible reason a flow of lithium, compensating lithium deposition at the electrode surface, possibly causing a counter flow of solvent.

Detection and Identification of Charged Species by ENMR Phase Difference Spectroscopy

We saw that for resonance lines of coherently moving particles a typical phase shift $\Delta\phi$ occurs in the spectrum (Sect. 17.2.2). If a mixture contains both charged and uncharged species, in an ENMR experiment only the lines of

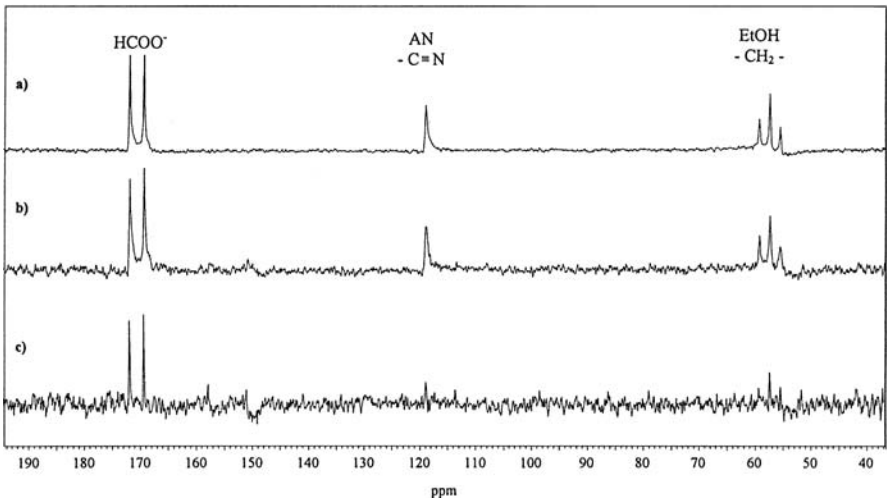

Fig. 17.10. "Mobility filter" ENMR experiment: ^{13}C NMR spectra of an aqueous mixture of ethanol (EtOH), acetonitrile (AN) and sodium formate [40]. (a) Normal (undecoupled) ^{13}C NMR spectrum ($I = 0$); (b) ^{13}C ENMR spectrum ($I \neq 0$); (c) Difference spectrum of (a) and (b), where only the lines of charged species ($HCOO^-$) remain.

charged species are phase-shifted while the lines of uncharged particles are not affected. This fact can be utilized for the detection and identification of charged species in multi-component mixtures, provided that these species contain the nucleus under observation. As an example of such a procedure, we show first in Fig. 17.10 (a) the normal ^{13}C spectrum ($I = 0$) of an aqueous mixture of ethanol (EtOH), acetonitrile (AN) and sodium formate [40]. When the same spectrum is then taken in presence of an electric field ($I \neq 0$) (Fig. 17.10 (b)) only the formate ion lines are phase-shifted and in the difference spectrum of the spectra with $I = 0$ and $I \neq 0$ the lines without a phase shift disappear and only the lines of the ion remain (see Fig. 17.10 (c)).

In this way, in a simple 1D ENMR experiment a "mobility filter" can be generated, which is able to filter from a complex spectrum only the lines of migrating species, which in this way can be detected and simultaneously identified via their NMR lines [40].

17.5.2 2D and 3D Experiments

In 2D NMR a two-dimensional data set is generated and the signal intensities $S(F_1, F_2)$ are given as a function of two variables F_1 and F_2. One advantage of 2D NMR is the fact that the spectrum is stretched in two dimensions and much more lines can be resolved. However, the main advantage is that in the 2D spectrum "correlations" between certain values of F_1 and F_2 can be detected and assigned.

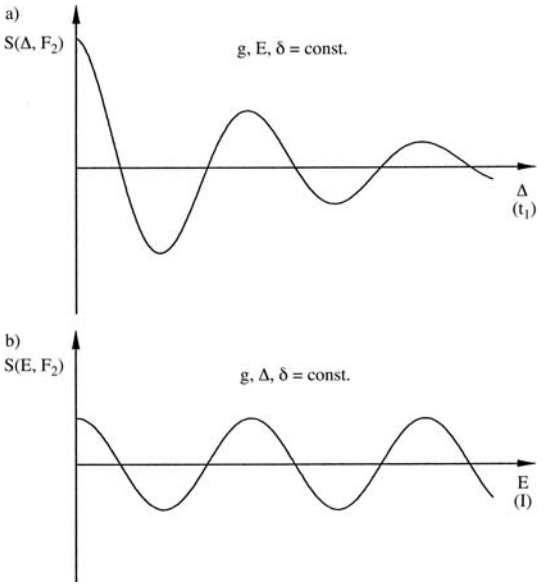

Fig. 17.11. ENMR signal intensity S at a given frequency F_2, (a) when $\Delta = t_1$ is (stepwise) varied, (b) when the electric field E (current I) is varied.

The 2D spectrum is obtained by recording the NMR signals in the time domain as a function of the acquisition time t_2, as in normal 1D NMR, however, this is performed k times, whereby another time t_1 (or another variable) is stepwise increased in k increments resulting in k signals with $2N$ data points:

$$S_1(t_1^{(1)}, t_2),\ S_2(t_1^{(2)}, t_2),\ \cdots\ ,\ S_k(t_1^{(k)}, t_2).$$

Thereafter, a first Fourier transformation with respect to t_2 is performed, followed by a second Fourier transformation with respect to t_1, yielding the 2D spectrum $S(F_1, F_2)$ with $k \times N$ data points [2, 16].

In 2D ENMR, F_2 is the chemical shift axis, which allows the identification of the chemical species and F_1 is the mobility axis. In this way the observed species are "correlated" with their mobility in the electric field. This kind of experiments, developed by Johnson and co-workers [10, 11], is called "mobility-ordered spectroscopy" (MOSY) and it should be mentioned that also very interesting analogous 2D "diffusion-ordered spectroscopy" (DOSY) experiments have been developed, where the second axis is the diffusion axis [11, 41].

In practical 2D ENMR two quantities can be incremented, namely Δ in the PFG experiment (Fig. 17.11) or the velocity v, via a stepwise increase of the electric field E and thus of the current I. If we choose $t_1 = \Delta$ and stepwise increase Δ, the influence of normal diffusion on the decay of the transverse magnetization S also increases (see (17.15) and Fig. 17.11 (a)), leading to a

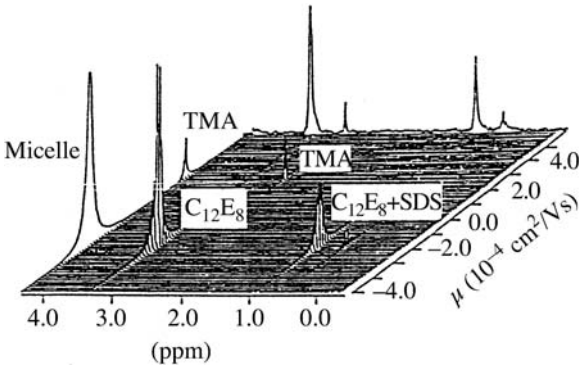

Fig. 17.12. Mobility-ordered (MOSY) 2D ENMR spectrum (stacked plot) of $(CH_3)_4^+$ (TMA) in the presence of mixed micelles [11]. [Sodium dodecyl sulfate (SDS) and octaethylene glycol dodecyl ether ($C_{12}E_8$)]. Note the different sign for the mobilities of TMA and $C_{12}E_8$.

line broadening in the 2D spectrum. Thus, it proved to be more favourable to hold constant all the timing parameters and to increment the field E since in this case the intensity oscillations are not damped (Fig. 17.11 (b)) [10, 11]. 2D ENMR experiments require the observation (and Fourier transformation) of several intensity oscillations as a function of Δ or E, that means in these experiments high $\Delta\phi$-values must be achieved. Since $\Delta\phi$ is proportional to the magnetogyric ratio γ of the nucleus, 2D ENMR is much easier performed with high-γ nuclides as ^{1}H, ^{19}F than with nuclides having a lower γ as ^{7}Li or ^{13}C [40]. So far, 2D experiments have only been performed with ^{1}H ENMR.

In Figs. 17.12 and 17.13 two examples of MOSY experiments are given, where in Fig. 17.12 the 2D spectrum is shown as a stacked plot and in Fig. 17.13 as a contour map, which is the mostly used representation of spectra in 2D NMR. The two examples show the most interesting field of application of 2D ENMR, namely mobility measurement of molecular aggregates, as micelles and vesicles. In Fig. 17.12 the ^{1}H MOSY spectrum of a mixture of $(CH_3)_4N^+$ ions and micelles is shown. This spectrum also demonstrates the important fact that in ENMR not only the amplitude but also the sign of the mobility is obtained, allowing the determination of the sign of charge of the species of interest. In the second example (Fig. 17.13) glucose, as a good NMR active label, has been entrapped inside vesicles, for which in this way the vesicle mobilty in water is found to be $u = 2 \times 10^{-8}$ m^{2}V^{-1}s^{-1}.

A very interesting extension of ENMR, namely 3D ENMR for the study of protein mixtures, has been demonstrated by He and co-workers [37, 38]. With two frequency axes a 2D spectrum of the protein mixture is generated. However, in protein mixtures severe signal overlapping occurs and conventional NMR methods have difficulties in characterising structures or structural changes of multiple protein components in biochemical reactions. Now

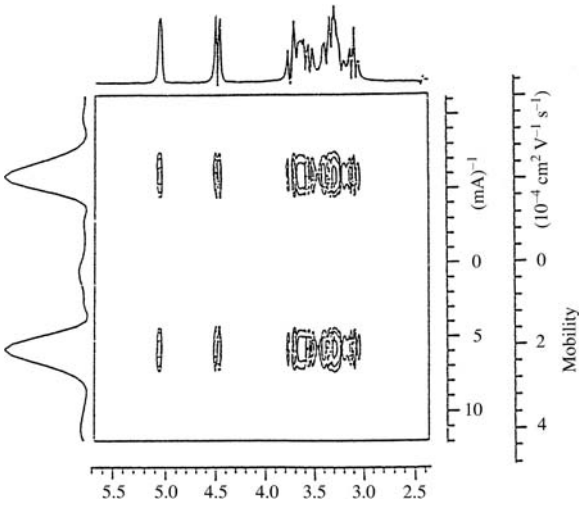

Fig. 17.13. Example of a MOSY contour map. 2D ^{1}H ENMR spectrum of glucose entrapped inside vesicles [11]. The 1D NMR spectrum of glucose is shown as a projection at the top. At the left the 1D mobility spectrum is given.

the overlapping signals can be separated in a 3D experiment, where the third axis is the electrophoretic mobility, allowing the simultaneous measurement of the different proteins due to their differing mobility. The otherwise needed physical separation is no more necessary. "Capillary array ENMR", developed by the same group [39], allows the study of protein mixtures at high ionic strength in buffer solutions.

17.5.3 Mobility and Velocity Distributions. Polydispersity and Electro-Osmotic Flow

In Fig. 17.11 (b) we saw that in an ENMR experiment the intensity oscillations are not damped if we vary the electric field E. However, there it was supposed that all observed particles have the same velocity. In polydisperse samples, on the other hand, we have a distribution of mobilities $g(u)$ of particles with the same chemical shift (of the same chemical kind) but of different size and mass. In such a case, in (17.14), (17.15) we have to replace $\cos(\gamma g v \delta \Delta) = \cos(\gamma g u E \delta \Delta)$ by $\int_{-\infty}^{+\infty} g(u) \cos(\gamma g u E \delta \Delta) \mathrm{d}u$ and this results in a damping of the intensity oscillations as a function of E (or I) (see Fig. 17.14 (a). However, from an inverse FT of $S(E, F_2)$ with respect to E (or I) the mobility distribution $g(u)$ can be derived (Fig. 17.14 (b) [10,42].

Even for monodisperse solutions the presence of electro-osmotic flow leads to mobility (velocity) distributions. Such a mobility distribution was studied in the just described manner in an oil-in-water microemulsion [43]. The aim was the study of the development of the electro-osmosis profile in a vertical

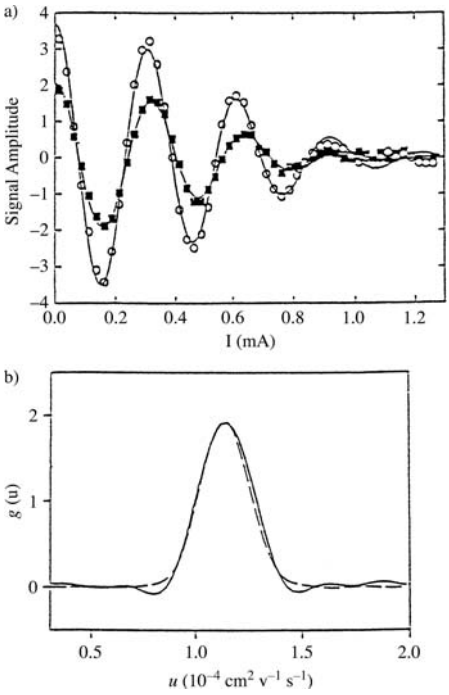

Fig. 17.14. (a) ^{1}H ENMR signal intensity of sucrose entrapped in charged phospholipid vesicles versus current I in a polydisperse system, showing the damping of $S(E, F_2)$ due to a mobility distribution [42]. (b) The mobility distribution $g(u)$ obtained by a Fourier transformation of the data in (a) (solid line). The dashed line represents a fit curve [42].

cylindrical tube as a function of Δ and as a function of t_{el}, i. e. of the time during which the current flowed before the PFG experiment was started. The result (Fig. 17.15) shows the development of the mobility distribution $g(u)$ with time, when both electrophoretic and electro-osmotic mobilities are present. The electrophoretic migration velocity is then superimposed by an opposite flow at the wall and a counterflow in the centre of the tube. After a time of ca 400 ms in this example the system reached equilibrium and, as theoretically expected, the flow profile, that is the mobility as a function of the tube radius r_{t}, becomes purely parabolic [42].

For the study of the electro-osmotic flow profile in capillaries also highly sophisticated NMR micro-imaging techniques have been applied, which as well deliver the velocity distributions and their time dependence [44].

The DCNMR studies described in this section might be a very interesting tool for future developments in capillary electrophoresis (CE), where the electro-osmotic flow is the driving force in these extremely important separation techniques in biochemistry.

17.6 Conclusion

The possibility of performing NMR experiments in presence of an electric current in the sample under investigation opens a novel way of using NMR

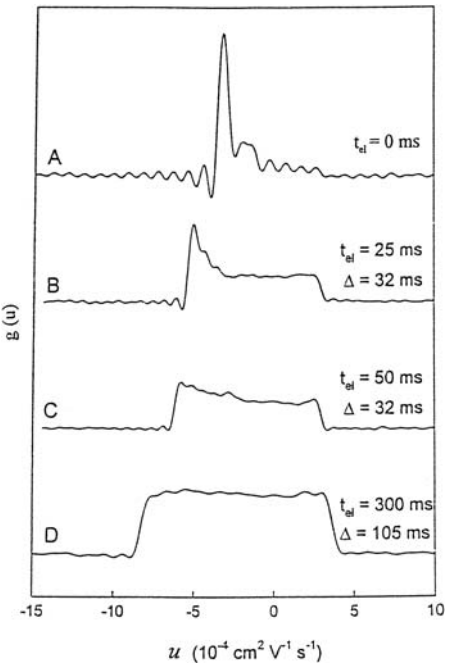

Fig. 17.15. Mobility (velocity) distributions $g(u)$ in presence of electro-osmotic flow for various electric field durations t_{el} and flow times Δ, showing the development of the electro-osmotic flow profile in an "oil-in-water" microemulsion [43].

techniques in the wide field of electrochemistry and its applications. The electric charge or the electric current is thus introduced as a new parameter in the NMR experiment. Electrophoretic NMR combines in-situ electrophoresis with the selectivity of NMR, a fact, which is of particular importance for the study of transport properties in complex multi-component fluid systems with charge-carrying species, such as simple ions, charged macromolecules, and charged supramolecular systems. In mixtures of organic compounds the single components can be simultaneously observed, however, separated by ^{1}H or ^{13}C NMR.

The pulsed field gradient NMR methods allow the non-invasive measurement of electrophoretic mobilities $u_{\pm}$ and one always obtains the self-diffusion coefficient $D_{\pm}$ of the distinct charged particles as a by-product. This offers the possibility of a systematic qualitative comparison of transport diffusion (here field-assisted diffusion) with self-diffusion, that means transport in the non-equilibrium state with transport in the equilibrium state. Furthermore, being independent of the optical properties of the sample, the ENMR methods may also be applied to porous systems. This field of application is just in its beginning, but seems to be very promising for basic electrophoretic mobility studies in systems with confined geometry.

Apart from mobility and diffusion studies, DCNMR also offers a new entrance to the investigation of electro-osmotic flow and phenomena related with it. In particular in capillaries and porous systems those electro-osmotic

flow studies, also combined with NMR imaging techniques, represent a powerful new tool.

On the other hand, ENMR has certain limitations owing to the comparatively low sensivity of radiofrequency spectroscopy and owing to problems with nuclides or systems with short nuclear magnetic relaxation times T_1 and T_2. However, it should be pointed out that the low energies connected with electromagnetic radiofrequency waves have the advantage that investigations can be performed without any disturbance of thermal equilibrium.

ENMR is a comparatively young and novel technique and the required accessory units are partly not yet commercially available and therefore so far we cannot speak of an NMR "routine technique". On the other hand, the power of ENMR and DCNMR methods has been impressively demonstrated [9–11] and it is clear that a further development of special techniques and a further extension of applications will take place in the coming years.

Notation

A	cross section of the electrophoretic cell
B	magnetic field
B_0	magnetic field, corresponding to the NMR reference frequency ω_0
c	concentration of an electrolyte in the solution
D	self-diffusion coefficient
$D_{\pm}^{*}$	ionic self-diffusion coefficient at $c \to 0$
$D_{\pm}^{0}$	ionic self-diffusion coefficient in the non-confined state
DCNMR	direct current NMR
DOSY	diffusion ordered spectroscopy
E	electric field
ENMR	electrophoretic NMR
F	Faraday constant
g	magnetic field gradient
$g(u)$	mobility distribution
I	electric current
I_{i}	ionic strength
K_{drag}	electroosmotic drag coefficient
MOSY	mobility ordered spectroscopy
PFG	pulsed field gradient
$P(\omega)$	NMR frequency distribution
r	radius of a particle
rf	radio frequency
S	NMR signal intensity
S_k	NMR signal intensity at the kth step in a 2D experiment
S_v	NMR signal intensity in presence of flow
S_0	initial NMR signal intensity
S/V_{p}	surface to pore volume ratio, also called "specific surface"

$\mathcal{T}$	tortuosity
$T_{\pm}$	transference number of an ion
T_1	spin-lattice (longitudinal) relaxation time
T_2	spin-spin (transverse) relaxation time
$u_{\pm}$	electrophoretic mobility of an ion
$u_{\pm}^{*}$	electrophoretic mobility of an ion at $c \rightarrow 0$
$u_{\pm}^{0}$	electrophoretic mobility of an ion in the non-confined state
v	velocity
$v_{\pm}$	ionic drift velocity
$z \cdot e$	electric charge of a particle
1D	one-dimensional
2D	two-dimensional
3D	tree-dimensional
γ	magnetogyric ratio of a nuclide
δ	duration of a pulsed magnetic field gradient
Δ	distance between two pulsed magnetic field gradients
$\Delta\phi$	phase shift difference of NMR signals
ϵ_0	dielectric constant of the vacuum
ϵ_{r}	relative dielectric constant of the medium
ζ	electro kinetic potential (zeta potential)
η	viscosity
κ	inverse Debye length
ρ	density
σ	surface charge density of a particle
τ	radio frequency pulse distance in a spin-echo experiment
ϕ	phase angle of the NMR signal
ω	NMR frequency

References

1. H. Günther: *NMR Spectroscopy* (Wiley, Chichester 1995)
2. R. Kimmich: *NMR Tomography, Diffusometry, Relaxometry* (Springer, Berlin Heidelberg New York 1997)
3. M. Spiro. In: *Physical Methods of Chemistry, Vol. 2 Electrochemical Methods* (Wiley, New York 1986) p 663
4. E.O. Stejskal, J.E. Tanner: J. Chem. Phys. **42**, 288 (1964)
5. P. Stilbs: Prog. Nucl. Magn. Reson. Spectrosc. **19**, 1 (1987)
6. P.T. Callaghan: *Principles of Nuclear Magnetic Resonance Microscopy* (Clarendon Press, Oxford 1991)
7. K.J. Packer: *Encyclopedia of Nuclear Magnetic Resonance*, vol 3 (Wiley, New York 1997) p 1615
8. M. Holz, C. Müller: Ber. Bunsenges. Phys. Chem. **86**, 141 (1982)
9. M. Holz: Chem. Soc. Rev. **23**, 165 (1994)
10. C.S. Johnson Jr., Q. He: Adv. Magn. Reson. **13**, 131 (1989)

11. C.S. Johnson Jr. In: *Nuclear Magnetic Resonance Probes of Molecular Dynamics*, ed by R. Tycko (Kluwer, Dordrecht 1994) p 455
12. P. Turq, J. Barthel, M. Chemla: *Transport, Relaxation and Kinetic Processes in Electrolyte Solutions* (Springer, Berlin Heidelberg New York 1992)
13. P.H. Rieger: *Electrochemistry* (Chapman and Hall, New York 1994)
14. E.O. Stejskal: J. Chem. Phys. **43**, 3597 (1965)
15. M. Holz, C. Müller, A.M. Wachter: J. Magn. Reson. **69**, 108 (1986)
16. R.R. Ernst (Nobel Lecture): Angew. Chem. Int. Ed. **31**, 805 (1992)
17. M. Holz, O. Lucas, C. Müller: J. Magn. Reson. **58**, 294 (1984)
18. Q. He, Z. Wei: J. Magn. Reson. **150**, 126 (2001)
19. K.P. Tikhomolova: *Electro-Osmosis* (Ellis Horwood, New York 1993)
20. F.M. Coveney, J.H. Strange, E.G. Smith: Mol. Phys. **75**, 127 (1992)
21. M. Holz, D. Seiferling, X.A. Mao: J. Magn. Reson. A **105**, 90 (1993)
22. F.A.L. Dullien: *Porous Media* (Acad. Press, San Diego 1992)
23. P.C. Griffiths, E. Pettersson, P. Stilbs, A.Y.F. Cheung, A.M. Howe, A.R. Pitt: Langmuir **17**, 7178 (2001)
24. S. Wong, U. Scheler: Colloids and Surfaces A **195**, 253 (2001)
25. U. Scheler. In: *Handbook of Polyelectrolytes and their Application*, vol 2, ed by S.K. Tripathy, J. Kumar, H.S. Nalwa (American Scientific Publishers, 2002) p 173
26. S.R. Heil, M. Holz: J. Magn. Reson. **135**, 17 (1998)
27. M. Holz, S.R. Heil, I. A. Schwab: Magn. Reson. Imaging **19**, 457 (2001)
28. L.L. Latour, R.C. Kleinberg, P.P. Mitra, C.H. Sotak: J. Magn. Reson. A **112**, 83 (1995)
29. H. Pape, J.E. Tillich, M. Holz (2003), submitted
30. A.I. Maklakov, N.F. Fatkullin, N.K. Dvoyashkin: Zh. Eksp. Teor. Fiz. **101**, 901 (1992)
31. P.P. Mitra, P.B. Sen, L.M. Schwartz: Phys. Rev. B **47**, 8565 (1993)
32. F. Stallmach, C. Vogt, J. Kärger, K. Helbig, F. Jacobs: Phys. Rev. Lett. **88**, 105505 (2002)
33. M. Ise, K.D. Kreuer, J. Maier: Solid State Ionics **125**, 213 (1999)
34. H.J. Walls, T.A. Zawodzinski: Electrochem. Solid State Lett. **3**, 321 (2000)
35. H.J. Walls, P.S. Fedkiw, S.A. Khan, T.A. Zawodzinski: Proc. Electrochem. Soc. **99**, 524 (2000)
36. H. Kataoka, Y. Saito, S. Deki, T. Ikeda: J. Phys. Chem. B **105**, 2546 (2001)
37. Q. He, Y. Liu, T. Nixon: J. Am. Chem. Soc. **120**, 1341 (1998)
38. Q. He, W. Lin, Y. Liu, E. Li: J. Magn. Reson. **147**, 361 (2000)
39. Q. He, Y. Liu, H. Sun, E. Li: J. Magn. Reson. **141**, 355 (1999)
40. S.R. Heil, M. Holz: Angew. Chem. Int. Ed. Engl. **35**, 1717 (1996)
41. K.F. Morris, C.S. Johnson Jr: J. Am. Chem Soc. **115**, 4291 (1993)
42. D.P. Hinton, C.S. Johnson Jr: J. Colloid Interface Sci. **173**, 364 (1995)
43. D. Wu, A. Chen, C.S. Johnson Jr: J. Magn. Reson. A **115**, 123 (1995)
44. B. Manz, P. Stilbs, B. Jönsson, O. Södermann, P.T. Callaghan: J. Phys. Chem. **99**, 11297 (1995)

Part IV

Theoretical Concepts and Models

18 Diffusion of Particles on Lattices

Klaus W. Kehr†, Kiaresch Mussawisade, Gunter M. Schütz, and Thomas Wichmann

18.1 Introduction

Diffusion processes take place almost everywhere in the material world; they are ubiquitous in condensed matter. Diffusion occurs in the different forms of condensed matter: in fluids, complex fluids, and solids. This chapter is concerned with the description of diffusion of particles in *lattices*. The theoretical description refers to diffusion in crystalline but also amorphous solids. Experimental facts on diffusion processes in solids are given in Chaps. 1-6, in particular. Empirical information gives the motivation and the basis for the theoretical description. Two important special cases of diffusion processes in crystalline solids are the tracer diffusion, where the displacement of marked atoms (radioactive isotopes) is determined, and interstitial diffusion, where atoms move on interstitial sites within the solid (see Chap. 1).

Diffusion processes appear in two distinct forms, namely

- Relaxation of density disturbances, or particle currents induced by density gradients or external forces. These phenomena are usually described by Fick's laws.
- Displacements of individual entities (particles, aggregates of particles) within condensed matter systems. The first description of these phenomena was provided by Einstein [1].

The treatment of diffusion of particles on lattices is theoretically advantageous for the following reasons: Lattice problems are generally easier to treat than continuum problems. The most important point, however, is the *separation of time scales* that exists between the elementary transition processes of the particles between lattice sites, and the succession of steps that lead to the observed diffusion phenomena. The elementary step of diffusion of a particle on a lattice, for instance exchange of a vacancy with a tracer atom, or motion of an interstitial atom, is generally rapid compared to the time between two elementary steps. Hence the problem of a theory of diffusion in lattices can be separated into two different tasks:

† Klaus W. Kehr died in 2000. He was the leading author of the corresponding chapter of the first edition on which the present chapter is based.

– *Theory for rate of the individual step*
This topic is usually not treated in detail in books on diffusion in solids. An exception is the monograph of Flynn [2]. A more general review on activated processes is given in [3]. Diffusion processes in solids are promoted by thermal activation. Usually an Arrhenius law is assumed for the transition rate Γ

$$\Gamma = \Gamma_0 \exp(-\Delta E/k_{\mathrm{B}}T)\,. \tag{18.1}$$

The prefactor Γ_0 is sometimes interpreted as an attempt frequency. ΔE is the activation energy; it is actually a free energy, or a free enthalpy. Further details may be found in Chap. 1, where different factorizations of Γ into prefactor and exponential factor are made. The theory of the transition rate Γ is especially interesting for light particles (hydrogen, muons), where possible quantum effects are discussed.

– *Combination of several/many individual steps to diffusion in lattices*
This is the topic addressed in this chapter.

Let us begin with a few general remarks on the correlation between theoretical models and experimental systems. Experimental systems of current interest are very complicated. Examples are polycrystalline systems, amorphous metals, glasses, etc. Theoretical modeling of particle diffusion in such systems has evolved in different ways and one may distinguish between several classes of models:

– *Models that are extensions of models for regular lattices with uniform transition rates*
Examples are two-state models for diffusion and trapping, and lattice models with correlated walks. These models are often useful for the interpretation of experiments. One may also subsume the effective-medium approximation under this class, for it relates a disordered system to an ordered, effective medium [4].

– *Models with disordered transition rates*
There are various idealized models, for instance random barriers or random traps, and realistic models that try to incorporate as much as possible the complexities of real substances. The idealized models are treated by exact or approximate analytical methods, supported by numerical simulations. The realistic models are typically investigated by numerical simulations (e.g. [5]).

– *Models that realize new paradigms for disordered systems*
Examples are percolation models, fractal structures, and Sinai models. These models are rarely realized in ideal form in nature, however, they capture essential properties of disordered systems; for instance, the appearance of scaling laws with different exponents.

In this chapter lattice models with uniform and disordered transition rates will be considered ("idealized models" in the above sense). Models that contain the new paradigms of fractality and percolation are treated in Chaps. 10, 19 and 22. Realistic models for particle transport in ionic conductors are described in Chaps. 20 and 21.

This chapter consists of four sections:

- *One particle on uniform lattices*
  Diffusion of one particle is well understood for regular lattices with uniform transition rates. The treatment is basic for many extensions, as exemplified in Chaps. 1, 3, 9 and 10.
- *One particle on disordered lattices*
  The problem of diffusion of one particle on a regular lattice with disordered transition rates is now relatively well understood. It will be one major focus of this chapter.
- *Many particles on uniform lattices*
  The problem of diffusion of many identical particles on regular lattices with uniform transition rates is also quite well understood, provided that exclusion of double occupancy is taken into account. Here the distinction between collective or Fickian and tracer diffusion is essential. A particularly interesting topic is tracer diffusion in one dimension.
- *Many particles on disordered lattices*
  The theory of diffusion of many particles on disordered lattices is a difficult problem, except for collective diffusion on lattices with symmetric barriers. In this chapter collective diffusion of particles on lattices with site-energy disorder will be included.

Finally, some remarks on the general literature will be made. Monographs on the topics of random walks have been represented by Barber and Ninham [6], and Weiss [7]. Somewhat more mathematical are the books of van Kampen [8], Spitzer [9], Spohn [10], and Liggett [11]. Monographs that are more focused on diffusion in metals are cited in Chap. 1. A survey on the fields of fractals, percolation, and other disordered systems is given in the book of Bunde and Havlin [12]. Several reviews on the topics addressed in this chapter have appeared, with quite different emphasis, namely Alexander et al. [13], Weiss and Rubin [14], Haus and Kehr [15], Havlin and ben-Avraham [16], Bouchaud and Georges [17] and Schütz [18].

18.2 One Particle on Uniform Lattices

18.2.1 The Master Equation

In this section the diffusion of one particle, or of an ensemble of independent particles on regular lattices with uniform transition rates, is considered. Examples are

- One, or few independent interstitial particle(s) (muon, low concentration of hydrogen). The particles diffuse on the lattice of interstitial sites that is schematically represented in Fig. 18.1 (a). Actual lattices of interstitial sites may have a more complicated structure.
- One vacancy, or small concentration of vacancies. This diffusion process is important for diffusion in metals. Figure 18.1 (b) gives a schematic representation of this process.

These two processes are the simplest ones for a theoretical description. There are other important diffusion processes in metals that are described in the monographs, for instance by Manning [19] and Philibert [20]. These mechanisms are also addressed in Chaps. 1 and 2.

The theoretical description of the lattice diffusion process is provided by the *master equation*. It is an equation for $P(\boldsymbol{l}t|\mathbf{0}0)$, the conditional probability of finding a particle at site $\boldsymbol{l}$ at time t when it was at site $\mathbf{0}$ at time 0. The quantity P is generally referred to as the propagator (see Chaps. 10, 19, 23). The sites are designated by d-dimensional integer vectors $\boldsymbol{l}$. The master equation reads

$$\frac{d}{dt}P(\boldsymbol{l}t|\mathbf{0}0) = \Gamma \sum_{\langle \boldsymbol{l}',\boldsymbol{l}\rangle} [P(\boldsymbol{l}'t|\mathbf{0}0) - P(\boldsymbol{l}t|\mathbf{0}0)] \,. \tag{18.2}$$

The sum in (18.2) runs over the nearest-neighbour sites $\boldsymbol{l}'$ of $\boldsymbol{l}$. This equation is essentially a balance equation for the increase/decrease of $P(\boldsymbol{l}t|\mathbf{0}0)$. It consists of a gain term, describing the jumps from nearest neighbours $\boldsymbol{l}'$ to $\boldsymbol{l}$, and a loss term describing the jumps off site $\boldsymbol{l}$ to nearest neighbour sites. Γ is the

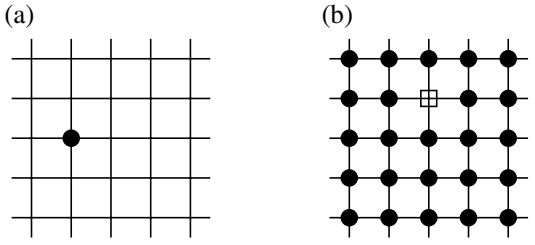

Fig. 18.1. (a) Single particle on uniform lattice; (b) single vacancy in occupied lattice.

transition rate between two nearest-neighbour sites. The last term can also be written as $-z\Gamma P(\boldsymbol{l}t|\mathbf{0}0)$, where z is the number of nearest neighbours. The master equation is intuitively obvious.

Theoretically, the master equation follows from the assumption of a Markovian process for the lattice diffusion problem. In a Markovian process, the present state is determined by the past state at one time, rather than by a more complicated history such as states at two different times, etc. More details about these types of processes including the derivations of the most essential relations may be found in van Kampen's monograph [8].

18.2.2 Solution of the Master Equation

The solution of the master equation is obtained by Fourier transformation. This is a general method for lattice-translation invariant problems (connected with the validity of Bloch's theorem). The spatial Fourier transform is defined by

$$P(\boldsymbol{k},t) = \sum_{\boldsymbol{l}} e^{-\mathrm{i}\boldsymbol{k}\cdot\boldsymbol{R}_l} P_{\boldsymbol{l}}(t)\,. \tag{18.3}$$

It is in fact this spatial Fourier transform of the propagator which is directly experimentally accessible by quasielastic neutron scattering (in particular by the neutron spin echo method - see Chaps. 3 and 13) and by pulsed field gradient NMR (Chap. 10).

The initial condition will not be written explicitly henceforth.

For simplicity, a restriction to the hypercubic lattices (chain, square lattice, simple-cubic lattice, etc.) will be made. A cube with $N = L^d$ sites will be introduced, and periodic boundary conditions are assumed. The sum over $\boldsymbol{l}$ in (18.3) then runs over N sites, whose position vectors are given by

$$\boldsymbol{R}_l = (al_1, \ldots, al_d) \tag{18.4}$$

with the lattice constant a. The periodic boundary conditions imply for the wavevector $\boldsymbol{k}$

$$\boldsymbol{k} = \frac{2\pi}{La}\nu, \tag{18.5}$$

where ν is an integer vector, restricted to values between $-L/2$ and $L/2$ (first Brillouin zone).

The master equation (18.2) can be written in a more compact form as

$$\frac{\mathrm{d}}{\mathrm{d}t}P(\boldsymbol{l}t|\mathbf{0}0) = -\sum_{\boldsymbol{l}'} \Lambda_{\boldsymbol{l},\boldsymbol{l}'} P(\boldsymbol{l}'t|\mathbf{0}0) \tag{18.6}$$

$$\Lambda_{\boldsymbol{l},\boldsymbol{l}'} \sim \begin{cases} z\Gamma & \boldsymbol{l} = \boldsymbol{l}' \\ -\Gamma & \boldsymbol{l},\boldsymbol{l}' \text{ nearest neighbours} \\ 0 & \text{otherwise}\,. \end{cases} \tag{18.7}$$

Note that for uniform lattices, the matrix $\Lambda_{\boldsymbol{l},\boldsymbol{l}'}$ only depends on $|\boldsymbol{l} - \boldsymbol{l}'|$.

The above equation has a convolution form. It is well-known that convolution in direct space becomes a product in Fourier space,

$$\frac{\mathrm{d}}{\mathrm{d}t}P(\boldsymbol{k},t) = -\Lambda(\boldsymbol{k})P(\boldsymbol{k},t)\,, \tag{18.8}$$

with the Fourier transform of the transition rate matrix

$$\Lambda(\boldsymbol{k}) = \Gamma \sum_{\boldsymbol{l}-\boldsymbol{l}'} e^{-\mathrm{i}\boldsymbol{k}\cdot(\boldsymbol{R}_l - \boldsymbol{R}_{l'})}\,. \tag{18.9}$$

(One can derive (18.8) directly by multiplying (18.6) for fixed $\boldsymbol{l}$ with $\exp(-i\boldsymbol{k}\cdot\boldsymbol{R}_l)$ and summing over $\boldsymbol{l}$). For hypercubic lattices is

$$\Lambda(\boldsymbol{k}) = \Gamma\left[z - 2\sum_{j=1}^{d}\cos(k_j a)\right]\,. \tag{18.10}$$

The main point is that a diagonalization of the master equation (18.6) has been accomplished through Fourier transformation. Now the solution of the master equation is possible

$$P(\boldsymbol{k},t) = P(\boldsymbol{k},0)\exp[-\Lambda(\boldsymbol{k})t] \qquad t \geq 0\,. \tag{18.11}$$

The initial condition is

$$P(\boldsymbol{k},0) = \sum_{\boldsymbol{l}} e^{-\mathrm{i}\boldsymbol{k}\cdot\boldsymbol{R}_l} P(\boldsymbol{l}0|\boldsymbol{0}0) = 1\,. \tag{18.12}$$

There are experimental methods that also allow a determination of the Fourier transforms of the conditional probability $P(\boldsymbol{l}t|\boldsymbol{0}0)$ from time to the frequency domain. It is defined by

$$P(\boldsymbol{k},\omega) = \int_{-\infty}^{\infty} \mathrm{d}t\, e^{\mathrm{i}\omega t} P(\boldsymbol{k},t)\,. \tag{18.13}$$

The quantity $P(\boldsymbol{k},t)$ is also required for negative times. It can be obtained by symmetric continuation,

$$P(\boldsymbol{k},-t) = P(\boldsymbol{k},t)\,. \tag{18.14}$$

Performing the Fourier integral (18.13) one obtains

$$P(\boldsymbol{k},\omega) = \frac{2\Lambda(\boldsymbol{k})}{\omega^2 + \Lambda^2(\boldsymbol{k})}\,. \tag{18.15}$$

This is a Lorentzian, whose width $\Lambda(\boldsymbol{k})$ can be measured, e. g. by quasielastic Mößbauer spectroscopy and quasielastic incoherent neutron scattering. Details may be found in Chaps. 2 and 3. Also the NMR relaxation times are determined by Fourier transforms of (different) correlation functions. This topic is considered in Sects. 9.2 and 9.9 of Chap. 9.

18.2.3 Diffusion Coefficient

In this section the diffusion coefficient of a particle that performs random walk on a regular lattice with uniform transition rate will be calculated. For this purpose, the mean square displacement of the particle is derived from the solution of the master equation. Consider the definition of the Fourier transform which was given in (18.3), and differentiate it with respect to a component of the wavevector $\boldsymbol{k}$,

$$\frac{\partial}{\partial k_j} P(\boldsymbol{k}, t) = \sum_{\boldsymbol{l}} (-\mathrm{i} R_{\boldsymbol{l}j}) e^{-\mathrm{i}\boldsymbol{k}\cdot\boldsymbol{R}_{\boldsymbol{l}}} P(\boldsymbol{l}t|\boldsymbol{0}0) \,. \tag{18.16}$$

Differentiate the expression again and sum over all components,

$$\sum_{j=1}^{d} \frac{\partial^2}{\partial k_j \partial k_j} P(\boldsymbol{k}, t) = -\sum_{\boldsymbol{l}} (\sum_{j=1}^{d} R_{\boldsymbol{l}j}^2) e^{-\mathrm{i}\boldsymbol{k}\cdot\boldsymbol{R}_{\boldsymbol{l}}} P(\boldsymbol{l}t|\boldsymbol{0}0) \,. \tag{18.17}$$

The expression on the right-hand side, evaluated at $\boldsymbol{k} = 0$, is the mean square displacement of the particle at time t, when it started at site $\boldsymbol{0}$ at time 0,

$$\langle \boldsymbol{R}^2 \rangle(t) = -\sum_{j=1}^{d} \frac{\partial^2}{\partial k_j \partial k_j} P(\boldsymbol{k}, t) \mid_{\boldsymbol{k}=0} \,. \tag{18.18}$$

From the explicit solution of the master equation (18.11) one obtains

$$\langle \boldsymbol{R}^2 \rangle(t) = \sum_{j=1}^{d} \frac{\partial^2 \Lambda(\boldsymbol{k})}{\partial k_j \partial k_j} \mid_{\boldsymbol{k}=0} \; t \,. \tag{18.19}$$

For hypercubic lattices one finds from (18.10)

$$\sum_{j=1}^{d} \left. \frac{\partial^2 \Lambda(\boldsymbol{k})}{\partial k_j \partial k_j} \right|_{\boldsymbol{k}=0} = 2d\Gamma a^2 \,. \tag{18.20}$$

Hence one has

$$\langle \boldsymbol{R}^2 \rangle(t) = 2dDt, \tag{18.21}$$

with the diffusion coefficient

$$D = \Gamma a^2 \,. \tag{18.22}$$

In this derivation, the diffusion coefficient has been derived from the mean squared spreading of the conditional probability with time. This is Einstein's description of particle diffusion [1].

It is possible to derive the diffusion equation (see Chandrasekhar [21]) from the master equation in the long-wavelength limit $\boldsymbol{k} \to 0$. For this purpose one has to replace the discrete conditional probability by a continuous probability density,

$$P(\boldsymbol{l},t) \longrightarrow p(\boldsymbol{r},t)\,, \tag{18.23}$$

where $p(\boldsymbol{r},t)\mathrm{d}^d r$ is the probability density of finding the particle in the volume element $\mathrm{d}^d r$ at location $\boldsymbol{r}$ and time t (initial conditions omitted). The probability density obeys the diffusion equation (Fick's 2$^{\mathrm{nd}}$ law)

$$\frac{\partial}{\partial t}p(\boldsymbol{r},t) = D\nabla\cdot\nabla p(\boldsymbol{r},t), \tag{18.24}$$

where $\nabla\cdot\nabla$ is the Laplace operator in d dimensions.

18.2.4 Extensions

There are important extensions of the master-equation description of diffusion of a single particle on a regular lattice with uniform transition rates.

- *More complicated lattices*
  Examples are lattices with a basis, e.g. the lattice of tetrahedral sites of hydrogen in bcc metals. This extension is trivial from the theoretical point of view, however, the derivation of $P(\boldsymbol{k},t)$ may require considerable labour. References are given in [15].

- *Lattices with inequivalent sites*
  Inequivalent sites can occur in lattices with a basis, when some sites in the unit cell are energetically lower than the others. This leads to a larger thermal occupation of these sites. The problem of taking the different thermal occupation factors into account was solved in principle in [22] and [23], for a review, see [15]. Applications were made by Anderson et al. [24].

- *Two-state models for diffusion and trapping*
  These models provide a very simple description of trapping processes. The basis is the decomposition of the conditional probability into a part corresponding to a free state and a part corresponding to a trapped state,

$$P_{\boldsymbol{l}}(t) = P_{\boldsymbol{l}}^{\mathrm{free}}(t) + P_{\boldsymbol{l}}^{\mathrm{trapped}}(t)\,. \tag{18.25}$$

  A particle may be alternatively in a free or a trapped state, with mean times of stay τ_1, or τ_0, respectively. The two-state model can be treated by differential equations (Schroeder [25]), or by integral equations (Richter and Springer [26]), with equivalent results. The differential equations are somewhat more compact and they read

$$\begin{aligned}\frac{\mathrm{d}}{\mathrm{d}t}P_{\boldsymbol{l}}^{f}(t) &= \Gamma\sum_{\langle\boldsymbol{l}',\boldsymbol{l}\rangle}[P_{\boldsymbol{l}'}^{f}(t) - P_{\boldsymbol{l}}^{f}(t)] \\ &\quad - \Gamma_{\mathrm{t}}P_{\boldsymbol{l}}^{f}(t) + \Gamma_{\mathrm{r}}P_{\boldsymbol{l}}^{t}(t) \\ \frac{\mathrm{d}}{\mathrm{d}t}P_{\boldsymbol{l}}^{t}(t) &= -\Gamma_{\mathrm{r}}P_{\boldsymbol{l}}^{t}(t) + \Gamma_{\mathrm{t}}P_{\boldsymbol{l}}^{f}(t),\end{aligned} \tag{18.26}$$

with the trapping rate $\Gamma_t = 1/\tau_1$ and the release rate $\Gamma_r = 1/\tau_0$. The first equation in (18.26) is the usual master equation, augmented by a loss and gain term, corresponding to transitions into and out of the trapped state. The second equation describes the temporal development of the trap state. An application of the two-state model has been given in Sect. 3.6 of Chap. 3.

All models mentioned above, and some additional models, for instance correlated-walk models, have in common that they are lattice-translation invariant. Hence they are solved by similar techniques as described above. Spatial Fourier transformation leads to a partial diagonalization, the rest is the solution of coupled ordinary first-order differential equations. As already said, this may require considerable effort in complicated cases, but in principle the solution of these models is understood.

18.3 One Particle on Disordered Lattices

18.3.1 Models of Disorder

In this section the random walk of a single particle, or of independent particles, on lattices with disordered transition rates will be considered. The main emphasis of this chapter will be on the derivation of asymptotic diffusion coefficients, but also the time dependence of the mean square displacement, or the frequency dependence of the conductivity will be considered. The models of disorder will be defined on regular lattices, and topological disorder will not be included. This is a popular approach for modeling diffusion in disordered materials, even if many materials of interest do not have crystalline structure. It means that the disorder is put completely into the transition rates,

$$\Gamma \longrightarrow \Gamma_{\mathrm{fi}} \,, \tag{18.27}$$

which depend on the initial (i) and final (f) sites. The rates are assumed to be fixed, i.e. the case of quenched disorder is treated. In principle, one could include transitions between arbitrary sites, in practice only nearest-neighbour transitions are taken into account, as is appropriate for diffusion of atoms.

Various models of disorder have been introduced in different contexts. Here some idealized models of disorder will be considered:

– *Random barriers (RB)*
  In this model the transition rates between neighbour sites have the symmetry

$$\Gamma_{ji} = \Gamma_{ij} \,. \tag{18.28}$$

  It is usually assumed that the rates are given by an Arrhenius law,

$$\Gamma_{ji} = \Gamma_0 \exp\left(-\frac{E_{ji}}{k_B T}\right) \qquad E_{ji} \geq 0 \,. \tag{18.29}$$

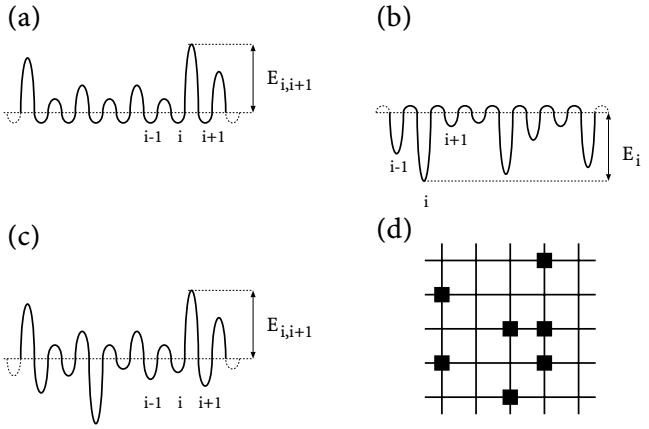

Fig. 18.2. Models of disorder.

The disorder then originates from random barrier energies E_{ji}, which are taken from a distribution $\nu_{\mathrm{B}}(E)$. A pictorial representation of the RB model is given in Fig. 18.2(a).

– *Random site energies (RT)*
Another important model is the random site-energy model, which is also called random-trap model. One should keep in mind that the traps do not capture the particles permanently. The model is defined by transition rates that depend on the initial sites, but not on the final sites,

$$\Gamma_{ji} = \Gamma_0 \exp\left(\frac{E_i}{k_{\mathrm{B}}T}\right) \qquad E_i \leq 0\,. \tag{18.30}$$

The site energies E_i are counted negative and they are taken from a distribution $\nu_{\mathrm{T}}(E)$. A pictorial representation of the RT model is given in Fig. 18.2(b).

– *Combination of RB and RT*
In this chapter also a combination of random barriers and random site energies will be studied. The rates of the combined RB and RT model shall be given by

$$\Gamma_{ji} = \Gamma_0 \exp\left(-\frac{E_{ji} - E_i}{k_{\mathrm{B}}T}\right)\,. \tag{18.31}$$

The random-barrier energies E_{ji} and the random-site energies E_i are taken independently from the distributions $\nu_{\mathrm{B}}(E)$ and $\nu_{\mathrm{T}}(E)$. A pictorial representation of the model is given in Fig. 18.2(c). Note that all energies refer to a common origin $E = 0$.

– *Randomly blocked sites (RBS)*
Finally, the model of randomly blocked sites will be included in this list of models of disorder. Sites of a lattice are randomly blocked with probability $1-p$ and not accessible to the particle that performs random walk. The transition rates of this model are defined by

$$\Gamma_{ji} = \begin{cases} \Gamma & \text{if } j \text{ is "open"} \\ 0 & \text{if } j \text{ is blocked.} \end{cases} \tag{18.32}$$

The pictorial representation of the model is included in Fig. 18.2(d). Of course, this model is nothing else than the site percolation model, which is exclusively treated in Chap. 22. In the present chapter, however, the RBS model will only be considered for concentrations p of open sites above the percolation threshold, where long-range diffusion of a particle is possible.

There are other models with disordered transition rates which are not included in the list above. One example is the Miller-Abrahams model, where transitions that lead to sites with lower energies have rates that do not depend on the energy difference, while the transitions to sites with higher energies require thermal activation. For a treatment of this model with similar methods as applied here the reader is referred to [29].

18.3.2 Exact Expression for the Diffusion Coefficient in $d = 1$

It is possible to give an exact expression for the diffusion coefficient of a particle in a linear chain for rather general disordered rates. Some restrictions on the disorder have to be made, which will be explained below. Linear chains with sites at a distance a will be considered and one may view Fig. 18.2(c) as a graphical representation of such a model. The task is to derive the asymptotic, long-time diffusion coefficient of a particle, averaged over the disorder.

The expression to be given below was derived independently by Dieterich [27] and Kutner [28], and by Wichmann [29]. Dieterich and Kutner calculated the mobility of a particle from the linear response to a force while Wichmann used a mean first-passage time method. Here a derivation will be given which utilizes Fick's first law. Of course, there are relations between the different derivations.

Consider a finite chain of length Na, as schematically displayed in Fig. 18.3. A particle current I (precisely: probability current) into site 0 is assumed such that P_0 is fixed. The same particle (probability) current is then taken out at site N and a stationary situation is maintained.

The derivation for general disorder is somewhat tedious and hence put into the appendix. A much simpler derivation can be made for the random-barrier model with $\Gamma_{i+1,i} = \Gamma_{i,i+1}$ and it should convey the idea of the derivation.

Consider Kirchhoff's node equation for site 0 which expresses the fact that the sum of all currents into the site must be zero:

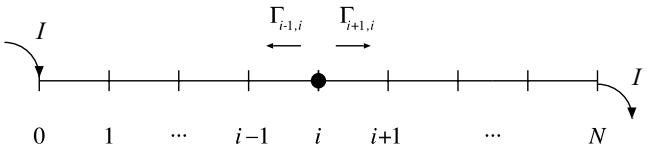

Fig. 18.3. Linear chain with constant current I.

$$I + \Gamma_{10}(P_1 - P_0) = 0\,. \tag{18.33}$$

The master equation at site 1 reads

$$\frac{\mathrm{d}}{\mathrm{d}t}P_1 = \Gamma_{10}(P_0 - P_1) + \Gamma_{21}(P_2 - P_1)\,. \tag{18.34}$$

One finds in the stationary situation

$$\Gamma_{21}(P_1 - P_2) = \Gamma_{10}(P_0 - P_1) = I\,, \tag{18.35}$$

where also (18.33) was used. The same consideration yields for all sites $0 \le i < N$

$$\Gamma_{i+1,i}(P_i - P_{i+1}) = I\,. \tag{18.36}$$

One can now play the following trick: Write

$$\begin{aligned} P_0 - P_N = {} & P_0 - P_1 + P_1 - P_2 + P_2 \mp \ldots \\ & -P_{N-1} + P_{N-1} - P_N\,. \end{aligned} \tag{18.37}$$

Introduce the current I into the differences by using (18.36),

$$P_0 - P_N = I\left(\sum_{i=0}^{N-1}\frac{1}{\Gamma_{i+1,i}}\right)\,. \tag{18.38}$$

This expression is already Fick's first law. To recognize this, rewrite (18.38) as

$$\frac{P_0 - P_N}{N} = I\left\{\frac{1}{\Gamma}\right\}, \tag{18.39}$$

where the sum has been replaced by the disorder average (valid for large N)

$$\left\{\frac{1}{\Gamma}\right\} = \frac{1}{N}\sum_{i=0}^{N-1}\frac{1}{\Gamma_{i+1,i}}\,. \tag{18.40}$$

The length of the chain is Na and the probability density at site i is P_i/a. Hence one can identify the gradient of the probability density,

$$\frac{P_0 - P_N}{Na^2} = -\nabla n\,. \tag{18.41}$$

Fick's first law reads $I = -D\nabla n$. Comparison with the above expressions yields

$$D = \left\{ \frac{1}{\Gamma} \right\}^{-1} a^2. \tag{18.42}$$

The expression (18.42) is the exact result for the diffusion coefficient of the RB model in $d = 1$, which is known since a long time [13].

The physical significance of the result is that the highest barriers dominate diffusion in $d = 1$. This is evident: particles have to overcome all barriers in the course of long-range diffusion, and it takes long times to overcome the high barriers.

The generalization of the result to arbitrarily disordered transition rates is

$$D = \left\{ \frac{1}{\Gamma_{i+1,i}\rho_i} \right\}^{-1} a^2, \tag{18.43}$$

with the thermal occupation factors

$$\rho_i = \frac{\exp(-\beta E_i)}{\frac{1}{N}\sum_{j=0}^{N-1} \exp(-\beta E_j)}\,, \tag{18.44}$$

where $\beta = 1/(k_{\mathrm{B}}T)$. The existence of the thermal occupation factors ρ_i is required in the proof, which is given in the appendix. The ρ_i exist when one can introduce a reference energy E_0 and the sum in the denominator of (18.44) remains finite for arbitrary N. A counterexample, where the ρ_i do not exist in the limit $N \to \infty$ will be given in Sect. 18.3.7.

The expression (18.43) for the diffusion coefficient of a particle on a linear chain with general disorder means that one has to use transition rates that are weighted by the mean thermal occupation of the sites. This is an exact result in $d = 1$ (see [27–29]).

18.3.3 Applications of the Exact Result

The expression (18.43) for the diffusion coefficient in $d = 1$ will now be examined for the models that have been introduced in Sect. 18.3.1. Henceforth the lattice constant will be set $a = 1$.

For the random barrier model, where $\Gamma_{i,i+1} = \Gamma_{i+1,i}$ one has $\rho_i = 1$. The result (18.42) is then immediately obtained from (18.43) and it is the correct result in $d = 1$.

In the random site-energy model, where $\Gamma_{ji} = \Gamma_0 \exp(\beta E_i)$, the product is

$$\Gamma_{ji}\rho_i = \Gamma_0 \left[\frac{1}{N} \sum_j \exp(-\beta E_j) \right]^{-1}. \tag{18.45}$$

Hence the diffusion coefficient is given by

$$D = \frac{\Gamma_0}{\frac{1}{N}\sum_j \exp(-\beta E_j)} \,. \tag{18.46}$$

This is the exact result in $d = 1$; it is also valid in *all* dimensions [15, 30]. Normally it is written in the form $D = \{\frac{1}{\Gamma}\}^{-1}$ which is equivalent to (18.46). Equation (18.46) signifies that the diffusion coefficient of the RT model is solely determined by the inverse of a partition function, which becomes large for strong site-energy disorder and/or low temperatures.

An immediate consequence of the exact expression (18.46) for the diffusion coefficient of the RT model is its downward curvature in an Arrhenius plot, where $\ln D$ is displayed as a function of $\beta = 1/k_{\mathrm{B}}T$. Differentiating $\ln D$ according to (18.46) with respect to β one obtains

$$\frac{\partial \ln D}{\partial \beta} = \frac{\sum_j E_j \exp(-\beta E_j)}{\sum_j \exp(-\beta E_j)} = \langle E \rangle \,. \tag{18.47}$$

Thus the slope of the Arrhenius plot of D is the mean thermal energy of a particle in the RT model. The mean thermal energy decreases with increasing β in the case of energetic disorder, hence one has convex (downward) curvature of $D(\beta)$ in the Arrhenius plot. This is the generic cause for downward curvature of $D(\beta)$ in the Arrhenius plot.

Finally the combined RB and RT model will be considered. The rates of this model were given in (18.31). The weighted rates are then

$$\Gamma_{ji}\rho_i = \Gamma_0 \left[\frac{1}{N}\sum_j \exp(-\beta E_j)\right]^{-1} \exp(-\beta E_{ji}) \,. \tag{18.48}$$

One obtains for independent distributions of barrier and site energies [31]

$$D_{\mathrm{comb}} = \frac{1}{\Gamma_0} D_{\mathrm{RB}} D_{\mathrm{RT}} \,. \tag{18.49}$$

Thus the diffusion coefficient of this model factorizes into two independent contributions in $d = 1$. A numerical verification of the result is given in Fig. 18.4.

18.3.4 Frequency Dependence in $d = 1$: Effective-Medium Approximation

Not only the asymptotic behaviour of the mean square displacement is of interest, but also the behaviour at finite times. It corresponds to the frequency dependence of the mobility. Asymptotic expansions of the time-dependent mean square displacement were made for the RB and RT models; they yield exact results in $d = 1$ for the RB model and all d for the RT model [32, 33]. Here an approximate treatment will be introduced for several reasons:

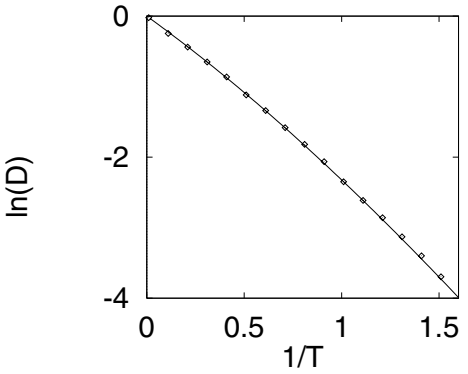

Fig. 18.4. Diffusion coefficient in combined RB and RT model. Uniform distributions of barriers and site energies of width $E_c = 2$. Line: Equation (18.48); symbols: Monte Carlo (MC) simulations.

i) The technique is rather simple and intuitive.

ii) The approximation yields an overall description of the frequency-dependent mobility.

iii) It is easily generalized to higher dimensions.

To formulate the effective-medium approximation (EMA), the random barrier model will be considered in $d = 1$. The master equation reads

$$\frac{\mathrm{d}}{\mathrm{d}t}P_i(t) = \Gamma_{i,i+1}[P_{i+1}(t) - P_i(t)] + \Gamma_{i,i-1}[P_{i-1}(t) - P_i(t)] \,. \tag{18.50}$$

The rates $\Gamma_{i,i\pm1}$ are taken from a common distribution $\rho(\Gamma)$ (or, equivalently, are determined from the distribution of barrier energies).

The frequency-dependent formulation of the EMA was developed by several authors around 1980 (Alexander and Orbach [34], Summerfield [35], Odagaki and Lax [36], Webman [37]). Here a derivation by an embedding procedure will be given, following Haus et al. [38]. One systematic, random transition rate Γ_{01} is embedded in a linear chain, which consists of time-dependent, effective transition rates. A graphical representation is given by Fig. 18.5 (bottom).

The systematic rate is taken from the distribution $\rho(\Gamma)$ and, once selected, considered as fixed.

The master equations for the conditional probabilities $P_i(t)$ for sites that do not involve sites 0 and 1 are

$$\frac{\mathrm{d}}{\mathrm{d}t}P_i(t) = \int_0^t \mathrm{d}t' \Gamma_{\mathrm{eff}}(t-t')[P_{i+1}(t') + P_{i-1}(t') - 2P_i(t')] \,. \tag{18.51}$$

The master equation for the conditional probabilities P_0 and P_1 is then

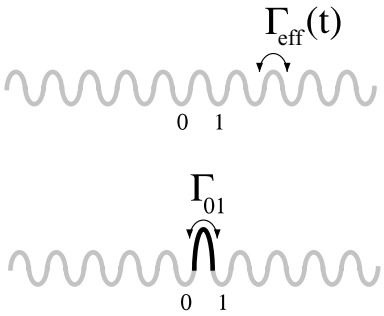

Fig. 18.5. Embedding procedure for effective-medium approximation.

$$\begin{aligned}\frac{\mathrm{d}}{\mathrm{d}t}P_0 &= \int_0^t \mathrm{d}t' \Gamma_{\mathrm{eff}}(t-t')[P_{-1}(t') - P_0(t')] \\ &\quad + \Gamma_{01}[P_1(t) - P_0(t)]\,, \\ \frac{\mathrm{d}}{\mathrm{d}t}P_1 &= \Gamma_{01}[P_0(t) - P_1(t)] \\ &\quad + \int_0^t \mathrm{d}t' \Gamma_{\mathrm{eff}}(t-t')[P_2(t') - P_1(t')]\,. \end{aligned} \tag{18.52}$$

This set of master equations will be compared with the master equation for the effective medium only, where the conditional probability will be called $E_i(t)$ (see also Fig. 18.5 (top))

$$\frac{\mathrm{d}}{\mathrm{d}t}E_i(t) = \int_0^t \mathrm{d}t' \Gamma_{\mathrm{eff}}(t-t')[E_{i+1}(t') + E_{i-1}(t') - 2E_i(t')]\,. \tag{18.53}$$

Now a Fourier and Laplace transformation of both equations will be made. The Laplace transform of a function $f(t)$ is defined by

$$\tilde{f}(s) = \int_0^\infty \mathrm{d}t E^{-st} f(t)\,. \tag{18.54}$$

The advantage of the Laplace transformation is that the initial condition of the master equations appears explicitly, because

$$\begin{aligned}\int_0^\infty \mathrm{d}t\, e^{-st}\frac{\mathrm{d}f(t)}{\mathrm{d}t} &= e^{-st}f(t)\,|_0^\infty + s\int_0^\infty \mathrm{d}t e^{-st} f(t) \\ &= s\tilde{f}(s) - f(t=0)\,. \end{aligned} \tag{18.55}$$

The master equation for the effective medium reads after the transformations

$$[s + 2\Gamma_{\mathrm{eff}}(s)(1-\cos ka)]\tilde{E}(k,s) = 1\,. \tag{18.56}$$

The 1 on the right-hand side of the equation comes from the initial condition $E_i(t=0) = \delta_{i,0}$.

It is possible to solve the equations for $\tilde{P}_0(s)$ and $\tilde{P}_1(s)$, as explicitly shown in the appendix. The requirement will be made that the average over the different realizations of the embedded bond will reproduce the effective medium. Hence the requirement is

$$\{\tilde{P}_0(s)\}_{\rho(\Gamma)} = \tilde{E}_0(s)\,. \tag{18.57}$$

Equation (18.57) is a self-consistency condition for $\tilde{\Gamma}_{\text{eff}}(s)$. In the appendix the following explicit form of the self-consistency condition is derived,

$$\left\{ \frac{\tilde{\Gamma}_{\text{eff}}(s) - \Gamma_{10}}{\Gamma_{1,0} + s\tilde{E}_0(s)[\tilde{\Gamma}_{\text{eff}}(s) - \Gamma_{10}]} \right\}_{\rho(\Gamma_{10})} = 0\,. \tag{18.58}$$

The conditional probability of the effective medium at site 0 can be given explicitly in $d = 1$,

$$\tilde{E}_0(s) = [s(s + 4\tilde{\Gamma}_{\text{eff}}(s))]^{-1/2}\,. \tag{18.59}$$

The self-consistency condition (18.58) corresponds to a fourth-order equation whose general solution is of no practical use. Hence an ansatz is made to determine $\Gamma_{\text{eff}}(s)$ for small s, corresponding to long times,

$$\Gamma_{\text{eff}}(s) = \Gamma_{\text{eff}}(1 + \vartheta_1(s/\Gamma_{\text{eff}})^{1/2} + \cdots) \qquad s \longrightarrow 0\,. \tag{18.60}$$

The self-consistency condition yields

$$\Gamma_{\text{eff}} = \left\{ \frac{1}{\Gamma} \right\}^{-1} \tag{18.61}$$

and

$$\vartheta_1 = \frac{1}{2}\Gamma_{\text{eff}}^2 \left\{ \left(\frac{1}{\Gamma} - \frac{1}{\Gamma_{\text{eff}}} \right)^2 \right\}\,. \tag{18.62}$$

The results for Γ_{eff} and ϑ_1 are exact [32]; note that ϑ_1 is specific for the presence of disorder.

Having obtained the effective transition rate for small s, one can deduce the asymptotic mean square displacement of a particle by an extension of the procedure of Sect. 18.2.3. The result for the disorder-averaged mean square displacement is

$$\{\langle \delta x^2 \rangle\}(t) = 2\Gamma_{\text{eff}} a^2 \left(t + 2\vartheta_1 (t/\pi\Gamma_{\text{eff}})^{1/2} + \cdots \right)\,. \tag{18.63}$$

There appears a "long-time tail" correction to the asymptotic mean square displacement. Note that (18.63) together with (18.61) reproduces the exact result (18.42) of the RB model, which was derived earlier.

The result for the s-dependence of the effective transition rate gives also information on the frequency dependence of the mobility. The frequency-dependent mobility of a particle is obtained from the linear response to a

periodic force. Equivalently, one may define a frequency-dependent diffusion coefficient as the Fourier transform of the velocity autocorrelation function of the particle. The connection with the s-dependent effective rate is ($a = 1$)

$$D(\omega) = \mathrm{Re}[\tilde{\Gamma}_{\mathrm{eff}}(s = \mathrm{i}\omega)] \tag{18.64}$$

and comparison with (18.60) shows that

$$D(\omega) = \Gamma_{\mathrm{eff}}(1 + \vartheta_1(\omega/\Gamma_{\mathrm{eff}})^{1/2} + \cdots) \qquad \omega \longrightarrow 0\,. \tag{18.65}$$

Hence one finds a strong increase of the diffusion coefficient and the mobility with frequency, for small frequencies.

18.3.5 Higher-Dimensional Lattices: Approximations

Approximations are generally necessary when one treats diffusion of single particles on higher-dimensional lattices. An exception is the random site-energy model, where the diffusion coefficient is known exactly in all dimensions [15, 30]. First the effective-medium approximation (EMA) will be discussed; this is an approximation that includes frequency dependence. As already said in the introduction, the EMA replaces the disordered medium by an effective ordered medium. A candid criticism of the philosophy of the EMA from the point of view of a theorist has been given by Anderson [4]. Nonetheless, EMA provides an adequate overall description of various disordered systems.

Effective-Medium Approximation

The embedding procedure for one random bond described in the previous section can be extended to higher dimensions. The result is the self-consistency condition [37]

$$\left\{ \frac{\tilde{\Gamma}_{\mathrm{eff}}(s) - \Gamma}{\frac{z-2}{2}\tilde{\Gamma}_{\mathrm{eff}}(s) + \Gamma + s\tilde{E}_0(s)[\tilde{\Gamma}_{\mathrm{eff}}(s) - \Gamma]} \right\}_{\rho(\Gamma)} = 0\,. \tag{18.66}$$

The relevant parameter is z, the coordination number; $z = 2d$ for hypercubic lattices. The conditional probability for the effective medium $\tilde{E}_0(s)$ is more complicated for $d > 1$ than in $d = 1$. To obtain the static, long-time diffusion coefficient one has to set $s = 0$. The product $s\tilde{E}_0(s)$ vanishes for $s = 0$ in all d and the self-consistency condition reduces to

$$\left\{ \frac{\Gamma_{\mathrm{eff}} - \Gamma}{\frac{z-2}{2}\Gamma_{\mathrm{eff}} + \Gamma} \right\}_{\rho(\Gamma)} = 0\,. \tag{18.67}$$

This self-consistency condition was already established by Kirkpatrick [39] who considered the equivalent problem of random resistor networks. If the

effective transition rate has been determined, the diffusion coefficient is given by $D = \Gamma_{\text{eff}} a^2$ in hypercubic lattices.

The average in (18.67) can be evaluated explicitly for a uniform distribution of activation energies [40],

$$\nu_{\text{B}}(E) \;=\; \begin{cases} \frac{1}{E_{\text{c}}} & 0 \le E \le E_{\text{c}} \\ 0 & \text{otherwise}\,. \end{cases} \tag{18.68}$$

One finds for $E_{\text{c}} \gg k_{\text{B}}T$ and $z > 2$

$$\Gamma_{\text{eff}} \longrightarrow \frac{2\Gamma_0}{z-2} \exp\left(-\frac{2E_{\text{c}}}{z k_{\text{B}} T}\right)\,. \tag{18.69}$$

The EMA result for the simple-square lattice is then

$$\Gamma_{\text{eff}} \longrightarrow \Gamma_0 \exp\left(-\frac{E_{\text{c}}}{2k_{\text{B}}T}\right)\,, \tag{18.70}$$

and the one for the simple-cubic lattice

$$\Gamma_{\text{eff}} \longrightarrow \frac{\Gamma_0}{2} \exp\left(-\frac{E_{\text{c}}}{3k_{\text{B}}T}\right)\,. \tag{18.71}$$

Good agreement with numerical simulations has been found [41, 42]. Figure 18.6 shows simulation results [42] for the mean square displacement of particles on a simple-square lattice with random barriers. One observes pronounced transient behaviour for stronger disorder at intermediate times, until the asymptotic behaviour is reached. Good agreement with the predicted asymptotic behaviour (18.70) is recognized.

Critical-Path Approach

For very large disorder or very low temperatures, the diffusion coefficient of the RB model can be estimated by the critical-path approach. This intuitive method was proposed by Shklovskii and Efros [43] and by Ambegaokar, Halperin, and Langer [44]. Consider a large but finite d-dimensional lattice and decorate the bonds with random hopping rates. Identify the largest hopping rate on the lattice, then the second largest rate, etc. (see Fig. 18.7).

Continue until a connection between two opposite sides of the (large) lattice is obtained. In the limit $N \longrightarrow \infty$ the possibility of connection defines the bond percolation threshold [45], see also Chap. 22. The smallest rate in the set of all selected rates represents an estimate for the diffusion coefficient.

The activation energy for the smallest rate will be determined for the uniform distribution of activation energies. Evidently (cf. Fig. 18.8)

$$\int_0^{E^*} \mathrm{d}E\; \nu_{\text{B}}(E) = p_{\text{c}}\,. \tag{18.72}$$

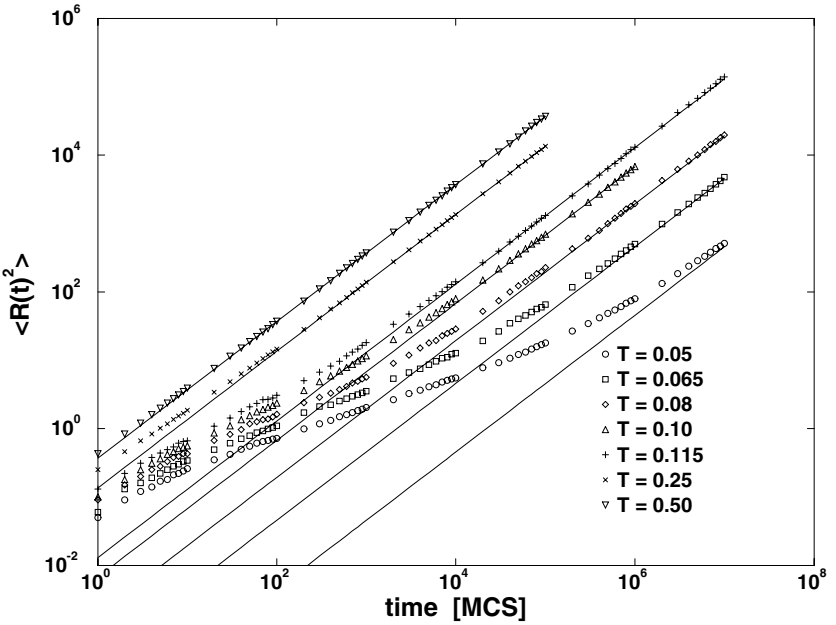

Fig. 18.6. Mean square displacement of particles in the RB model in $d = 2$ as a function of time. Lines: (18.70); symbols: MC simulations. Uniform distributions of activation energies; T is given in units of $E_c/2$. From [42].

For the uniform distribution one obtains

$$E^* = p_c E_c \,. \tag{18.73}$$

Hence the estimate for the diffusion coefficient is

$$D \cong \Gamma_0 \exp\left(-\frac{p_c E_c}{k_B T}\right) \,. \tag{18.74}$$

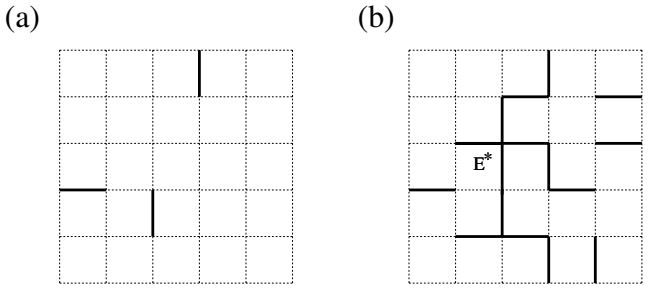

Fig. 18.7. Construction of the critical path: (a) the three largest transition rates are identified; a percolating path has been closed by bond with barrier E^*.

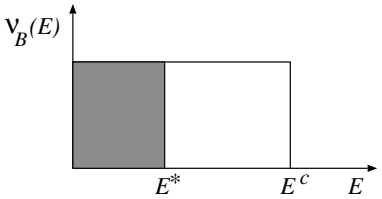

Fig. 18.8. Determination of the barrier E^* from density of states.

In $d = 2$ the bond percolation threshold is $p_c = 0.5$ and one has

$$D \cong \Gamma_0 \exp\left(-\frac{E_c}{2k_B T}\right) . \tag{18.75}$$

This result is identical to the EMA result (18.70). In fact, it is an exact result, as was shown by Bernasconi et al. using the self-duality of the square lattice [46]. In $d = 3$, where $p_c \approx 0.244$ one obtains

$$D \cong \Gamma_0 \exp\left(-\frac{0.244 E_c}{k_B T}\right) , \tag{18.76}$$

i. e. a result that is different from the EMA result. As said above it gives the dominant behaviour for very low temperatures or very strong disorder, but there are important corrections to it [47, 48].

Single Particles in the RBS Model

The diffusion of single particles in lattices with randomly blocked sites belongs to the same category of problems as other diffusion models on disordered lattices. However, the methods of treatment are somewhat different. As already said, only low concentrations p of blocked sites will be considered, such that long-range diffusion of test particles is always possible. An approximate derivation of the diffusion coefficient was made by Tahir-Kheli [49] and his result is ($a = 1$)

$$D = \Gamma_0 \left(1 - \frac{1-p}{f} + \cdots\right) . \tag{18.77}$$

In the formula the correlation factor f for tracer diffusion in lattice gases appears, which will be discussed in Sect. 18.4.3. Ernst et al. [50] could establish (18.77) by performing a perturbation expansion with respect to $1 - p$.

The validity of (18.77) was investigated by numerical simulations in simple-cubic lattices [51] and it was found that it is a good approximation for small and moderate concentrations of blocked sites, see Fig. 18.9.

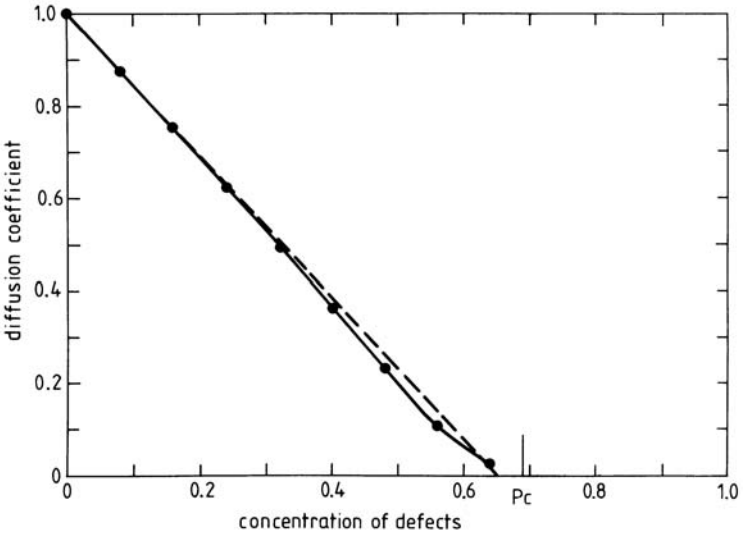

Fig. 18.9. Diffusion coefficient of single particles in the RBS model, as a function of the concentration of blocked sites. Symbols: MC simulations; continuous line: spline fit to the MC results; dashed line: (18.77). From [51].

18.3.6 Higher-Dimensional Lattices: Applications

Vanishing of D for Exponentially Distributed Site Energies

An interesting application of the exact result (18.46) for the RT model in arbitrary dimensions can be made for the exponential energy distribution. This distribution is given by

$$\nu_{\mathrm{T}}(E) = \frac{1}{E_{\mathrm{c}}} \exp\left(\frac{E}{E_{\mathrm{c}}}\right) \qquad E \leq 0\,. \tag{18.78}$$

Combining this expression with the Arrhenius law (18.30) for the transition rates of the RT model, one can calculate the distribution of transition rates $\rho(\Gamma)$ (this is equivalent to a change of the integration variable from E to Γ),

$$\rho(\Gamma) = \frac{\alpha}{\Gamma_0}\left(\frac{\Gamma}{\Gamma_0}\right)^{\alpha-1} \quad , \quad \Gamma \leq \Gamma_0\,, \tag{18.79}$$

where $\alpha = k_{\mathrm{B}}T/E_{\mathrm{c}}$. The inverse of the diffusion coefficient is then given by ($a = 1$)

$$D^{-1} = \int_0^{\Gamma_0} \mathrm{d}\Gamma \rho(\Gamma) \frac{1}{\Gamma}\,. \tag{18.80}$$

D^{-1} diverges for $\alpha < 1$, and consequently

$$D \equiv 0 \qquad \text{for} \quad \alpha < 1\,. \tag{18.81}$$

Hence the diffusion coefficient vanishes for random site energies with an exponential distribution, for temperatures $k_{\mathrm{B}}T \leq E_{\mathrm{c}}$, in arbitrary dimensions.

The mean square displacement of particles does no longer exhibit linear behaviour at long times for $\alpha < 1$. Instead one finds subdiffusive behaviour, as was derived by Havlin, Trus, and Weiss [52]:

$$\langle \boldsymbol{R}^2 \rangle(t) \;\sim\; \begin{cases} t^{\frac{2\alpha}{\alpha+1}} & d = 1 \\ t^{\alpha} & d \geq 2\,. \end{cases} \tag{18.82}$$

Combined RB and RT Model for $d > 1$

How can one treat more general models with disorder by approximations in higher dimensions? The EMA as formulated above with one systematic bond requires symmetric rates. A hint can be obtained from the exact result (18.43) for generally disordered rates in $d = 1$. The message of this result is: Use thermally weighted transition rates $\Gamma_{ji}\rho_i$ for the general models. Invoking the relation of detailed balance,

$$\Gamma_{ji}\rho_i = \Gamma_{ij}\rho_j\,, \tag{18.83}$$

one observes that the thermally weighted rates are symmetric, hence they can be employed in the EMA as formulated above.

The utilization of thermally weighted transition rates will be illustrated for the combined RB and RT model. Its rates were given in (18.31) and the weighted rates were already given in (18.48). From the self-consistency condition (18.67) follows for independent barriers and site-energies in arbitrary dimensions [31]

$$D^{\mathrm{EMT}}_{\mathrm{comb}} = \frac{1}{\Gamma_0} D^{\mathrm{EMT}}_{\mathrm{RB}} D_{\mathrm{RT}}. \tag{18.84}$$

Since D_{RT} is known exactly, cf. (18.46), only the application of the EMA for the random barriers is necessary [31].

The interest in the combined RB and RT model originates from experiments on diffusion in amorphous metallic alloys. The diffusion coefficient in these substances exhibits typically linear behaviour in an Arrhenius plot of $\ln D$ vs. $\ln 1/T$. This is not expected from the simple models for diffusion in disordered lattices.

As was discussed in Sect. 18.3.3, the RT model exhibits downward curvature in an Arrhenius plot of $\ln D$ versus $\ln 1/T$ (i. e. the deepest trap sites dominate at low temperatures). In contrast, the RB model exhibits upward curvature in an Arrhenius plot of $\ln D$ vs. $\ln 1/T$ for $z > 4$. One can give the following argument for the origin of this upward curvature: The critical path dominates the behaviour of the diffusion coefficient at the lowest temperature; additional paths contribute at higher temperatures and they comprise higher activation energies.

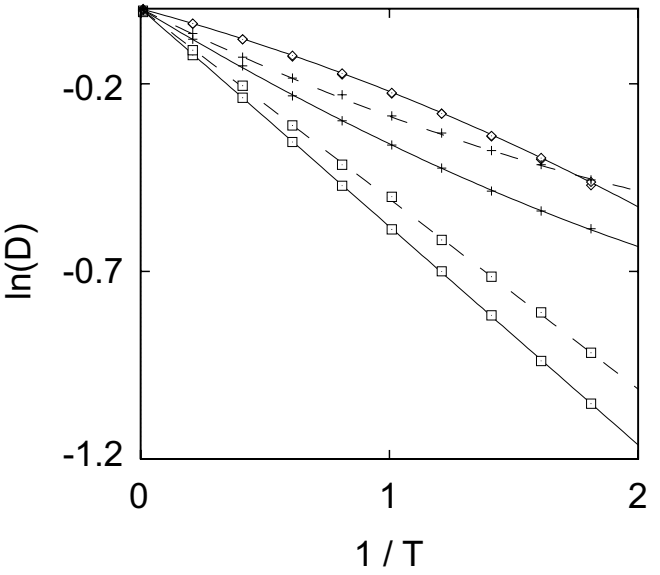

Fig. 18.10. Arrhenius plot of the diffusion coefficient for two-level models. Continuous lines: EMA, $d = 3$; dashed lines: EMA, $d = 5$. Symbols: MC results (+: RB model, ⋄: RT model, □: combined model).

Limoge and Bocquet suggested a possible compensation of the effects of random barriers and of random traps [53]. The original derivations given in [53] were only partially satisfactory. We investigated the problem by the analytic approach outlined above and by numerical simulations [54]. This reference also contains a more detailed discussion of the previous work. It was found that compensation is possible in finite temperature intervals if the relative strengths of RB and RT are properly adjusted. Fig. 18.10 shows this compensation for uniform distributions of barrier and trap energies in $d = 3$ when $|E_c^T| \approx 3/5\ E_c^B$. Complete compensation of the curvature is only possible for $d \longrightarrow \infty$, as was shown by Wichmann [29].

Frequency Dependence

Only some remarks on the frequency dependence of the mobility or the diffusion coefficient will be made. There are many observations of frequency-dependent conductivities in disordered substances with typically

$$\sigma(\omega) \sim \omega^{\beta} \qquad 0 < \beta < 1\,. \tag{18.85}$$

The question is whether this behaviour can be understood in the framework of single-particle theories, for instance by EMA. So far, asymptotic results were derived for the frequency-dependent conductivity in the limit $\omega \to 0$ [33], for

a review, see [15]. They seem to be not really useful in the frequency ranges of interest. Numerical evaluations of the self-consistency condition for finite ω were made by Wagener and Schirmacher [55] and Hoerner et al. [56]. The authors found a frequency dependence in qualitative accord with (18.85). In the opinion of the authors, no simple physical picture of the origin of anomalous frequency dependence has been established so far (see however Chap. 21).

It should also be pointed out that the problem of the frequency-dependent mobility is truly a many-particle problem, in addition, the particles can have interactions. Work has been done on this problem mainly by numerical simulations [57–59], see also Chap. 20.

18.3.7 Remarks on Other Models

In this section some comments will be made concerning several models that are not treated in this chapter. The first three are addressed in other chapters of this textbook, hence some cursory remarks will suffice.

Fractals

These objects are considered in Chaps. 10 and 19. If they are regularly constructed objects, often an explicit solution of recursion relations is possible, and the mean square displacement of diffusing particles can be calculated.

Percolation lattice

This model is treated in Chap. 22, together with experimental realizations. It can be viewed as the RBS model, where the concentration of blocked sites is adjusted at the threshold value where the diffusion coefficient vanishes. Diffusion of particles on fractals and on percolation lattices exhibits an interesting behaviour including scaling laws that are different from ordinary diffusion.

Extended defects

Also extended defects are not included in this chapter. An example are grain boundaries, which are of great practical importance. They are treated in Chap. 8.

Sinai model

Also here no detailed treatment will be given, only some introductory considerations concerning the one-dimensional model will be presented.

In the Sinai model (see the references in [60]) the transition rates to the right, $\Gamma_{i+1,i}$, and to the left, $\Gamma_{i-1,i}$, are independent random variables with the restriction

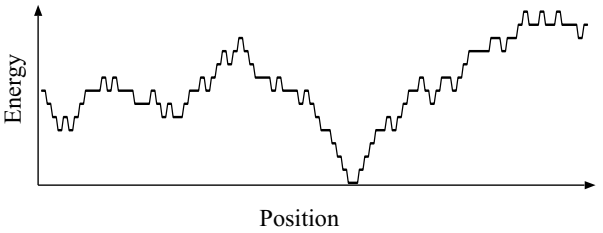

Fig. 18.11. Pictorial representation of the Sinai model on a larger scale.

$$\left\{ \ln \frac{\Gamma_{i+1,i}}{\Gamma_{i-1,i}} \right\} = 0 \,. \tag{18.86}$$

The potential that would yield such transition rates from the Arrhenius law can be imagined as representing a random walk by itself, cf. Fig. 18.11. The Sinai condition can be interpreted as the requirement that the potential does not contain additional systematic forces that would induce drift of the particle in either direction.

An estimate of the behaviour of the mean square displacement can be given in the following way [60]: Since the potential displayed in Fig. 18.11 represents a random walk, the typical height difference over a length L is described by

$$V \sim \sqrt{L} \,. \tag{18.87}$$

The motion of the particle requires thermal activation, hence the typical time for a particle to move the length L is

$$t \sim \exp(V/k_{\mathrm{B}}T) \,. \tag{18.88}$$

Using (18.87) one finds $\sqrt{L} \sim \ln t$. Hence the typical mean square displacement in this model is given by

$$\langle \delta x^2 \rangle \sim (\ln t)^4 \,. \tag{18.89}$$

Diffusion of a particle in the Sinai model cannot be treated by the methods of Sect. 18.3.2, because the condition of existence of the ρ_i is violated. If one increases the length of the chain, deeper and deeper valleys appear, in which the ρ_i are concentrated. Thus the limit $L \to \infty$ does not exist for the ρ_i. In summary, the Sinai model is theoretically extremely interesting. Its practical relevance, however, is limited: unbounded variations of the potential are not physical for real substances.

18.4 Many Particles on Uniform Lattices

18.4.1 Lattice Gas (Site Exclusion) Model

In the lattice-gas model, sites of a lattice are occupied by particles. Each site can be occupied by at most one particle. A pictorial representation is given in Fig. 18.12.

There are many applications of lattice-gas models. Two prominent examples are hydrogen in metals (see Sect. 3.5 in Chap. 3), where the atoms occupy interstitial sites of the metal lattice, and impurity atoms on surfaces of crystals.

The concentration of the lattice gas is defined as

$$c = \frac{\text{number of particles } N_\mathrm{p}}{\text{number of available sites } N} \,. \tag{18.90}$$

The simplest lattice-gas model is the site-exclusion model, where multiple occupancy of the sites is excluded, and no further interactions of the particles are taken into account. Of course, real particles have interactions, but many important properties of lattice gases can already be studied in this model. In this section uniform lattices will be considered, where the transition rate of a particle to an *empty* site is Γ everywhere.
Two different diffusion coefficients have to be defined for lattice gases:

- *Coefficient of collective diffusion,* D_coll
  This diffusion coefficient is defined through Fick's law (1^st or 2^nd law), and it describes the decay of density disturbances. Alternative expressions are chemical or transport diffusivity.
- *Coefficient of tagged-particle diffusion,* D_t
  This coefficient is defined through the mean square displacement of tagged particles. It is commonly called tracer diffusion coefficient or self-diffusion coefficient.

The single-particle diffusion coefficient, which was discussed in the preceding sections, is obtained either from the collective diffusion coefficient, or from the tagged-particle diffusion coefficient, in the limit of small particle concentrations, $c \to 0$. Both definitions lead to the single-particle diffusion coefficient in this limit.

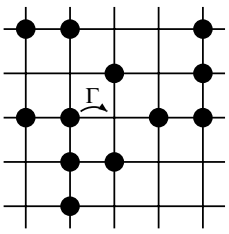

Fig. 18.12. Site-exclusion lattice gas.

In all lattice-gas models the physical properties depend crucially on whether a net bias in the hopping rates leads to a mean drift in the motion of the particles (and hence to a finite density-dependent current) or not. The intrinsic non-equilibrium behavior of driven diffusive systems is reviewed in detail in [18,61]. Besides the existence of novel and unusual non-equilibrium phase transitions, the most remarkable features are the occurrence of shocks [62–64] and the importance of the physical boundaries of the system [65–69]. In this section we consider only symmetric hopping models where the rate of hopping does not depend on the direction of hopping across the bond between the two sites.

18.4.2 Collective Diffusion

Consider the most basic site exclusion model where particles hop between nearest neighbor sites with a constant rate Γ. This model is known as the simple symmetric exclusion process, introduced by Spitzer [70]. Many exact results are known, see [18,71].

The basic quantity for the description of collective diffusion is $P(\boldsymbol{l},t)$, the probability that site $\boldsymbol{l}$ is occupied by a particle at time t. The important point is that the identity of the particles is disregarded in its definition. The quantity $P(\boldsymbol{l},t)$ has a different meaning than the conditional quantity $P_{\boldsymbol{l}}(t)$ in the single-particle case. It is a member of a set of probabilities, defined on the lattice sites $\boldsymbol{l}$ which gives the mean occupation number and hence the mean density on site $\boldsymbol{l}$ at time t . Let $P(\bar{\boldsymbol{l}},t)$ be the probability that site $\boldsymbol{l}$ is empty. Obviously the following normalization condition holds:

$$P(\boldsymbol{l},t) + P(\bar{\boldsymbol{l}},t) = 1\,. \tag{18.91}$$

The master equation for $P(\boldsymbol{l},t)$ in the site-exclusion model is:

$$\frac{\mathrm{d}}{\mathrm{d}t}P(\boldsymbol{l},t) = \Gamma \sum_{\langle \boldsymbol{l}',\boldsymbol{l}\rangle} [P(\boldsymbol{l}',\bar{\boldsymbol{l}},t) - P(\boldsymbol{l},\bar{\boldsymbol{l}}',t)]\,. \tag{18.92}$$

Here $P(\boldsymbol{l}',\bar{\boldsymbol{l}},t)$ is the joint probability that site $\boldsymbol{l}'$ is occupied *and* site $\boldsymbol{l}$ is empty at time t. The joint probabilities fulfil the relations

$$\begin{aligned} P(\boldsymbol{l}',\bar{\boldsymbol{l}},t) + P(\boldsymbol{l}',\boldsymbol{l},t) &= P(\boldsymbol{l}',t) \\ P(\boldsymbol{l},\bar{\boldsymbol{l}}',t) + P(\boldsymbol{l},\boldsymbol{l}',t) &= P(\boldsymbol{l},t)\,. \end{aligned} \tag{18.93}$$

Since $P(\boldsymbol{l},\boldsymbol{l}',t) = P(\boldsymbol{l}',\boldsymbol{l},t)$, insertion of (18.93) into (18.92) yields

$$\frac{\mathrm{d}}{\mathrm{d}t}P(\boldsymbol{l},t) = \Gamma \sum_{\langle \boldsymbol{l}',\boldsymbol{l}\rangle} [P(\boldsymbol{l}',t) - P(\boldsymbol{l},t)]\,. \tag{18.94}$$

This equation is identical to the master equation for the single-particle case. The initial conditions, however, are different. The derivation presented above

including that of the coherent dynamical structure function has been proposed by Kutner [72].

As a consequence of the master equation (18.94), the coefficient of collective diffusion results to be

$$D_{\mathrm{coll}} = \Gamma a^2 \,, \tag{18.95}$$

which is identical to the diffusion coefficient of a single particle on a uniform lattice (The numerical factor applies to hypercubic lattices in *all* dimensions). The important feature of (18.95) is that the collective diffusion coefficient does not depend on the concentration of the site-exclusion lattice gas.

The mathematical reason for the absence of the concentration dependence in the symmetric exclusion process is an underlying SU(2) symmetry of the generator of this Markov process. In the quantum Hamiltonian formalism for the master equation the Markov generator turns out to be the SU(2)-symmetric quantum Hamiltonian of the Heisenberg ferromagnet [73, 74]. In this correspondence the (many-particle) dynamics of the local density $P(\boldsymbol{l}, t)$ is related in a simple fashion to the (single-particle) spin-wave dynamics of the ferromagnet. This accounts for the identity of the dynamical equation (18.94) for the local density with the single-particle diffusion equation.

18.4.3 Tracer Diffusion for $d > 1$

The diffusion coefficient of a tagged particle, D_{t}, is defined from the asymptotic behaviour of its mean square displacement for $t \to \infty$

$$\langle \boldsymbol{R}^2 \rangle(t) \to 2dD_{\mathrm{t}}t \,. \tag{18.96}$$

In this chapter only a cursory treatment of tagged-particle diffusion in the site-exclusion model for $d > 1$ will be given.

Consider a tagged particle. Its mean transition rate is $(1 - c)\Gamma$, where $1 - c$ is the blocking factor, i. e. the probability of finding an unoccupied site in the site-exclusion model. A mean field estimate of the tagged-particle diffusion coefficient is

$$D_{\mathrm{t}}^{\mathrm{MF}} = (1 - c)\Gamma a^2 \,, \tag{18.97}$$

hence D_{t} is smaller than D_{coll}. Bardeen and Herring [75] pointed out that (in the limit $c \to 1$) there exists a backward correlation in the random walk of a tagged atom. To understand its origin, regard Fig. 18.13, where a tagged particle has made an exchange with an empty site.

Immediately after the transition there is an increased probability for a backward transition of the tagged particle, due to the presence of a vacancy, with certainty, at the initial particle position. This can be accounted for by introducing a correlation factor $f(c)$, with generally $f(c) \leq 1$,

$$D_{\mathrm{t}} = (1 - c)\Gamma a^2 f(c) \,. \tag{18.98}$$

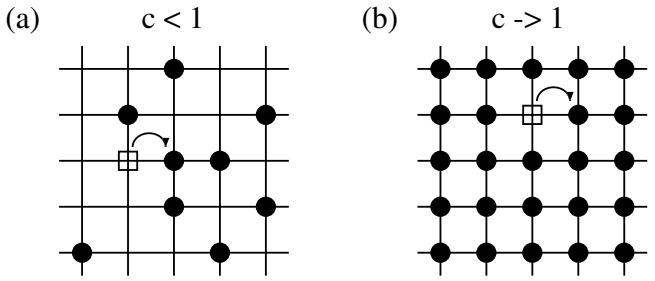

Fig. 18.13. Illustration of origin of backward correlation; (a) lattice gas of arbitrary concentration; (b) limit relevant to metal physics.

In metal physics the factor $1-c$ is the concentration c_V of thermally activated vacancies and $c_V \ll 1$. The correlation factor $f = f(c \to 1)$ can be calculated from the random walk of a single vacancy. Its walk is uncorrelated and can be described by the methods of Sect. 18.2.1. The tagged atom, however, performs correlated random walk. In the limit $c \to 1$ only consecutive jumps of the tagged particle are correlated. Then [76]

$$f = \frac{1 + \langle \cos \vartheta \rangle}{1 - \langle \cos \vartheta \rangle}, \tag{18.99}$$

where $\langle \cos \vartheta \rangle$ is the average angle between two consecutive transitions of the tagged particle. This quantity can be calculated exactly from the random walk of a single vacancy [77]. Values of $\langle \cos \vartheta \rangle$ and f for various lattices are given in [78]. An example is the value $f = 0.727\ldots$ for the bcc lattice.

Extensions to arbitrary concentrations of the lattice gas were made by Nakazato and Kitahara [79] and Tahir-Kheli and Elliott [80]. They derived

$$f = \frac{1 + \langle \cos \vartheta \rangle}{1 + [(2-3c)/(2-c)] \langle \cos \vartheta \rangle}, \tag{18.100}$$

where $\langle \cos \vartheta \rangle$ has the same meaning as above. Equation (18.100) is an approximate expression, but simulations show that the deviations are less than 1-2 % of the correct value (see Fig. 18.14). Of course, $f(c = 0) = 1$, and $f(c \to 1)$ reproduces (18.99). More details about the correlation factor, in particular about its relevance for experimental studies, have been presented in Chap. 1.

18.4.4 Tagged-Particle Diffusion on a Linear Chain

Tagged-particle diffusion on a linear chain is completely different from tagged-particle diffusion in higher dimensions ($d \geq 2$). The reason is that the tagged particle cannot pass the other particles, as schematically illustrated by Fig. 18.15.

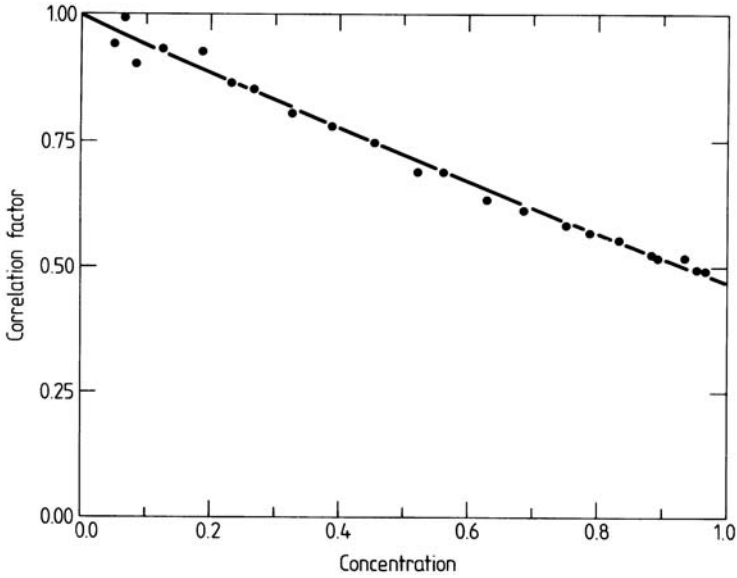

Fig. 18.14. Correlation factor for site-exclusion lattice gas on a square lattice as a function of concentration. Line: (18.100); symbols: MC simulations. From [81].

As a consequence, the mean square displacement of the tagged particle, $\langle \delta x^2 \rangle(t)$, is no longer proportional to t. It turns out that the mean square displacement of a tracer particle under the single-file constraint is asymptotically proportional to $\sqrt{t}$. This phenomenon is called single-file diffusion and it was first described in the physical literature by Richards [82]. There exist formal derivations of this behaviour (see [83] and references therein). However, the analytical derivations are rather difficult. Therefore, a derivation of the asymptotic behaviour from a physical consideration will be presented that is due to Alexander and Pincus [84]. The main idea is that the relative displacements of two tagged particles are caused by density fluctuations of the other particles. These density fluctuations are governed by collective diffusion.

For the derivation a continuum description will be adopted. In Fig. 18.16 the equilibrium positions and the displacements of two tagged particles are indicated.

A relation between the displacement difference and the change of density $\delta n(x,t)$ in between the two particles is required. This relation is derived in

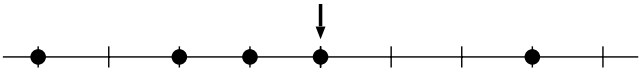

Fig. 18.15. Tagged-particle diffusion on a linear chain.

Fig. 18.16. Coordinates for the derivation of the mean square displacement in single-file diffusion, following [84].

the appendix (Sect. 18.7.3) and it reads in Fourier space

$$\frac{1}{n}\delta n(k,t) = \mathrm{i}ku(k,t)\,, \tag{18.101}$$

where u(k,t) is the Fourier transform of the displacement $u(x,t)$ of the tagged particle. It follows

$$u(x,t) - u(x,0) = \frac{1}{n}\int \frac{\mathrm{d}k}{2\pi} e^{\mathrm{i}kx}\frac{1}{\mathrm{i}k}[\delta n(k,t) - \delta n(k,0)]\,. \tag{18.102}$$

The square of this expression will be taken. One is interested in the random-walk average of the square. Instead of performing this average, one can take the ensemble average over many tagged particles, with the result

$$\begin{aligned}\langle [u(x,t) - u(x,0)]^2\rangle &= \frac{1}{N}\int \mathrm{d}x[u(x,t) - u(x,0)]^2 \\ &= \frac{1}{Nn^2}\int \frac{\mathrm{d}k}{2\pi}\frac{2}{k^2}[\langle \delta n(k,0)\delta n(-k,0)\rangle \\ &\quad -\langle \delta n(k,t)\delta n(-k,0)\rangle]\,. \end{aligned}\tag{18.103}$$

Here the density fluctuations are averaged over the stochastic dynamics of the lattice gas. The decay of density fluctuations is governed by collective diffusion; in the limit of long wavelengths $k \to 0$, i.e., for long times, one has

$$\langle \delta n(k,t)\delta n(-k,0)\rangle \longrightarrow Nc(1-c)\exp(-D_{\mathrm{coll}}k^2 t)\,. \tag{18.104}$$

Insertion of this relation into (18.103) and transcription of the right-hand side into a lattice formulation gives ($a = 1$)

$$\langle [u(t) - u(0)]^2\rangle = \frac{2(1-c)}{c}\int_{-\infty}^{\infty}\frac{\mathrm{d}k}{2\pi}\frac{1-\exp(-Dk^2 t)}{k^2}\,. \tag{18.105}$$

The integral is

$$\int_0^{\infty}\mathrm{d}x\frac{1-e^{-\lambda^2 x^2}}{x^2} = \lambda\sqrt{\pi}\,. \tag{18.106}$$

Hence one obtains using the result (18.95) for D_{coll}

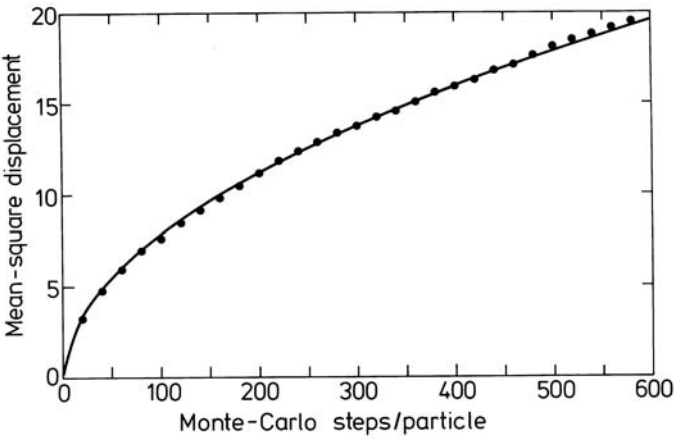

Fig. 18.17. Mean square displacement of tagged particles on a linear chain at concentration $c \approx 0.5$ as a function of time. Lines: theory; symbols: MC simulations. From [83].

$$\langle [u(t) - u(0)]^2 \rangle = \frac{2(1-c)}{c} \sqrt{\frac{\Gamma t}{\pi}}. \tag{18.107}$$

This is the characteristic behaviour of the mean square displacement of tagged particles under the single-file constraint. Experimental evidence for single-file diffusion is reported in Chap. 10.

Expression (18.107) is valid for long times. For short times $(1-c)\Gamma t \ll 1$ one has

$$\langle \delta x^2 \rangle(t) = 2(1-c)\Gamma a^2 t \,. \tag{18.108}$$

In this time regime one recovers the mean-field result (18.97) for the tracer diffusion coefficient. In [83], an approximate expression was derived that covers the complete time region. Figure 18.17 shows numerical simulation results for the mean square displacement of tagged particles, together with the theoretical curve of [83]. One recognizes the proportionality of $\langle \delta x^2 \rangle(t)$ with $\sqrt{t}$ for longer times.

It is instructive to consider two coupled lines between which the particles can make transitions with rate $\Gamma_\perp$, under the condition that the target sites on the other chain are not occupied, cf. Fig. 18.18. The single-file constraint is now relieved and one expects that a tagged particle makes asymptotically normal diffusion,

$$\langle \delta x^2 \rangle(t) = 2D_\mathrm{t} t \,. \tag{18.109}$$

A heuristic derivation of the diffusion coefficient D_t in this situation can be given by putting together single-file mean square displacements of the particle according to (18.107) at time intervals $1/\Gamma_\perp(1-c)$, see Fig. 18.19.

This is the mean time, where a tagged particle makes a transition to the other chain and starts a new displacement. The slope of the dashed line

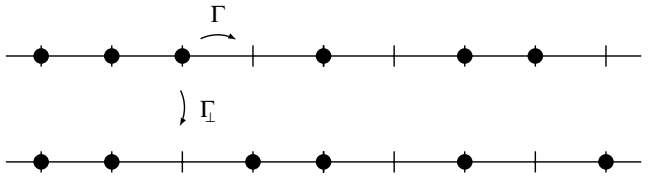

Fig. 18.18. Particle diffusion on two coupled lines.

in Fig. 18.19 can be determined in the following way: Take $\langle \delta x^2 \rangle$ at time $t = 1/\Gamma_\perp(1-c)$ and divide by this time. This gives as an estimate for the diffusion coefficient

$$D_{\mathrm{t}} \cong \frac{(1-c)^{3/2}}{c} \Gamma \sqrt{\frac{\Gamma_\perp}{\Gamma}} \,. \tag{18.110}$$

An approximate theory which is valid at all times, was given in [85]. Figure 18.20 presents the results of numerical simulations together with the theoretical results of this paper. One recognizes how the asymptotic behaviour $\sim t$ is reached for $\Gamma_\perp/\Gamma \neq 0$ after a crossover region.

18.5 Many Particles on Disordered Lattices

18.5.1 Models with Symmetric Rates

In this final section of this chapter, diffusion of many particles on regular lattices with disordered transition rates will be treated. The disordered rates are assumed to be fixed, i. e. quenched disorder is assumed. The considerations will be restricted to the site exclusion model, where double occupancy of the sites is forbidden, and no further interactions of the particles are present. Only the coefficient of collective diffusion will be studied. Even with all

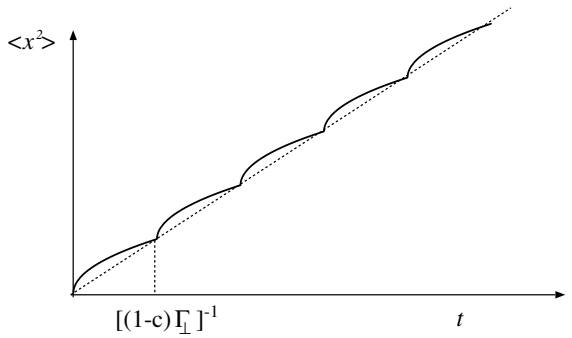

Fig. 18.19. Heuristic derivation of the diffusion coefficient of a tagged particle on two coupled lines.

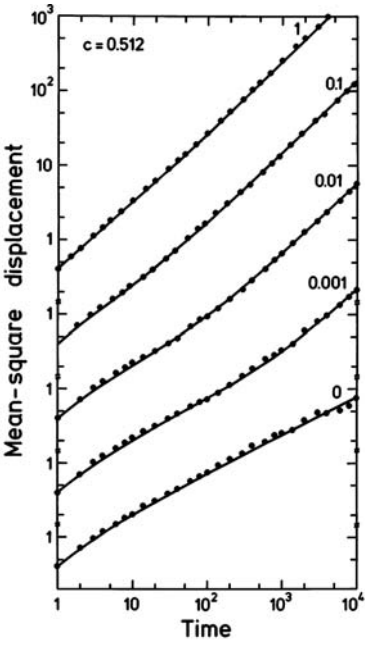

Fig. 18.20. Mean square displacement of tagged particles on two coupled lines as a function of time. Lines: theory; symbols: MC simulations. The ratio $\Gamma_\perp/\Gamma$ is indicated on the curves. From [85].

these restrictions, the problem is very difficult, with one important exception. Namely, for symmetric transition rates, the problem can be reduced to the independent-particle problem. This case will be treated in this section.

The cancelation of the joint probabilities in the master equation for $P(\boldsymbol{l}, t)$ that has been shown in Sect. 18.4.2 for lattices with uniform transition rates is also valid for disordered lattices as long as $\Gamma_{ij} = \Gamma_{ji}$. In this case the hierarchy of many-particle equations reduces to the single-particle equation with disordered, symmetric rates. Consequently [86]

$$\text{if} \quad \Gamma_{ij} = \Gamma_{ji} \quad \text{then} \quad D_{\text{coll}} = D_{\text{s.p.}} \,. \tag{18.111}$$

The index s.p. means single, independent particles. The origin of this cancellation is the symmetry under the Lie algebra for the special unitary group SU(2) of the generator of the process which holds on any type of lattice with arbitrary bond-symmetric disorder [74]. Also symmetric processes with partial exclusion of up to M_i particles on lattice site i have this property [18]. A result equivalent to (18.111) was obtained for the conductivity by Harder et al. [87].

The models of interest are the random barrier model and the model with randomly blocked sites.

18.5.2 Selected Results for the Coefficient of Collective Diffusion in the Random Site-Energy Model

The nontrivial case for collective diffusion of site-exclusion lattice gases in disordered lattices is the case of site-energy disorder. No cancelation of the joint probabilities $P(\boldsymbol{l}, \boldsymbol{l}', t)$ occurs in the master equation and one has to resort to approximations, with two exceptions. The first exception is the site-exclusion lattice gas on a linear chain with random site energies (RT model) in the limit of very small vacancy concentrations, $c_V \to 0$. The diffusion problem of single vacancies can then be solved, for instance by the methods of Sect. 18.3.2, and the exact result for the corresponding diffusion coefficient $D_{\text{s.v.}}$ was given in [88]. In the limit $c \to 1$ $D_{\text{s.v.}}$ agrees with D_{coll}. Second, an *exact* expression for the collective diffusion coefficient can be given for the RT model in the limit of infinite dimensions. Apart from these two cases, no further exact results for the collective diffusion coefficient are known. Hence approximate treatments are necessary.

An effective medium approximation for collective diffusion of site-exclusion lattice gases can be formulated in the following way. First the problem has to be reduced to an effective one-particle problem. This can be achieved by an obvious extension of the results for the single-particle case, where weighted transition rates were used. The following effective or mean field single-particle transition rates will be introduced

$$\Gamma_{ji}^{\text{Sym}} = \frac{P_i(1-P_j)\Gamma_{ji}}{\{P_i(1-P_i)\}} \,. \tag{18.112}$$

The quantity P_i is the thermal equilibrium occupation of site i. It is normalized differently from ρ_i, hence a normalization factor in the denominator of Γ_{Sym} is required. The symmetry of the rates Γ_{Sym} follows from detailed balance. The rate equations (18.112) were already introduced in [89] in the context of lattice-gas diffusion on linear chains.

The second step is the use of Γ_{Sym} in an effective-medium approximation. Since the rate equations (18.112) are symmetric, the formulation of the EMA of Sect. 18.3.5 can be used. From the EMA the limit of infinite dimensions (infinite coordination number) is easily obtained [90]. The result is

$$D_{\text{coll}}^{\text{phen}} = \{\Gamma_{ji}^{\text{Sym}}\} = \frac{P_i(1-P_j)\Gamma_{ji}}{\{P_i(1-P_i)\}} \tag{18.113}$$

and it represents a phenomenological expression for the collective diffusion coefficient that was derived in the context of metal physics [91] and surface physics [92]. It is not surprising that a phenomenological theory is obtained in the limit of infinite coordination number. The main problem in treating collective diffusion of lattice gases in disordered lattices are the correlations that are caused by particles which occupy sites with low energies and act as blocking sites. The effects of these correlations become irrelevant in the limit of infinite coordination number.

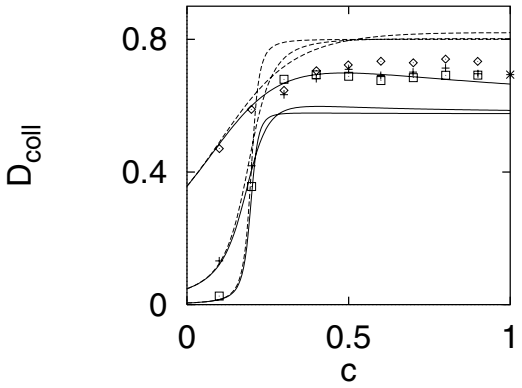

Fig. 18.21. Collective diffusion coefficient of site-exclusion lattice gas in a two-level RT model in $d = 3$, as a function of concentration. 20 % of the sites are trap sites. Continuous lines: EMA; dashed lines: phenomenological theory; symbols: MC results for $\Gamma^{<}/\Gamma = 0.1$ ($\diamond$), 0.01 ($+$) and 0.001 ($\square$). Limiting value $c \to 1$: $*$.

Fig. 18.21 shows results for a two-level RT model in $d = 3$ which consists of free sites with concentration $1 - c_t$ and transition rates Γ, and trap sites with concentration c_t and rates $\Gamma^{<}$. The results of numerical simulations are compared with the EMA and the phenomenological expression (18.113).

The main feature of the results is that D_{coll} is determined by the saturation of deep trap sites by particles. This was first pointed out by Kirchheim who modelled hydrogen diffusion in metglasses [93]. The saturation effect is a rather general feature of collective diffusion in systems with site-energy disorder and is not restricted to a particular realization of the disorder.

The figure also shows that the single-particle result is approached for $c \to 0$. Also the limit $c \to 1$ and $\Gamma^{<}/\Gamma \ll 1$ can be understood for the two-level RT model. In this limit D_{coll} is given by the single-particle result for the RBS model. Namely, the deep trap sites are saturated by particles and act as blocking sites. It was discussed in Sect. 18.5.1 that for the RBS model $D_{coll} \equiv D_{s.p.}$. Additional EMA and numerical results are given in [90].

It has been shown in Sect. 18.3.6 that the diffusion coefficient of single, independent particles vanishes in the RT model for an exponential distribution of site energies, at low temperatures. The relevant parameter is $\alpha = k_B T/E_c$, where E_c characterizes the width of the distribution. The result was $D_{s.p.} \equiv 0$ for $\alpha < 1$ (cf. (18.81)).

What happens when a finite concentration of particles is filled into the lattice? The particles tend to occupy the sites with low site-energies, saturating thereby the low-lying levels. If now a density disturbance is set up in the lattice gas, the disturbance should decay by collective diffusion. This was indeed observed in the numerical simulations of [94], and D_{coll} was obtained by monitoring the decay of cosine density profiles.

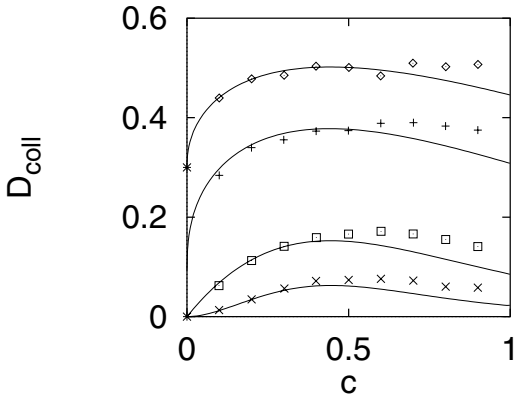

Fig. 18.22. Collective diffusion coefficient in the RT model in $d = 3$ with exponential distribution of site energies. Continuous lines: EMA; symbols: MC results for $\alpha = 1.43$ ($\diamond$), 1.0 ($+$), 0.5 ($\Box$), and 0.333 ($\times$). Limit $c \to 1$ (*).

Fig. 18.22 shows numerical results for the RT model in $d = 3$ together with EMA results. It is evident that $D_{\rm coll}(c \to 0) \longrightarrow D_{\rm s.p.}$, also for $\alpha < 1$, where $D_{\rm s.p.} = 0$. There is qualitative agreement between the simulations and the EMA, particularly at lower particle concentrations.

The behaviour of $D_{\rm coll}$ for $c \ll 1$ can be understood from the following qualitative consideration: Since only one particle can occupy a given site, the equilibrium occupancy of a site is given by the Fermi-Dirac distribution. In the limit of low temperatures, all levels are occupied up to a pseudo Fermi level E^* (see Fig. 18.23). For the exponential distribution

$$\int_{-\infty}^{E^*} {\rm d}E \frac{1}{E_{\rm c}} \exp\left(\frac{E}{E_{\rm c}}\right) = c\,, \tag{18.114}$$

from which follows

$$E^* = E_{\rm c} \ln(c)\,. \tag{18.115}$$

At small concentrations and low T, diffusion is mainly carried by particles at or above the Fermi level, and the coefficient of collective diffusion is approximately given by the single-particle diffusion expression,

$$D_{\rm coll}^{-1} \approx \int_{E^*}^{0} {\rm d}E \nu_{\rm T}(E) \frac{1}{\Gamma(E)}\,. \tag{18.116}$$

The result for small c is (note that $\alpha < 1$)

$$D_{\rm coll} \approx \Gamma_0 \left(\frac{1}{\alpha} - 1\right) c^{(\frac{1}{\alpha}-1)}\,. \tag{18.117}$$

That is, $D_{\rm coll}$ exhibits a power-law dependence on the concentration.

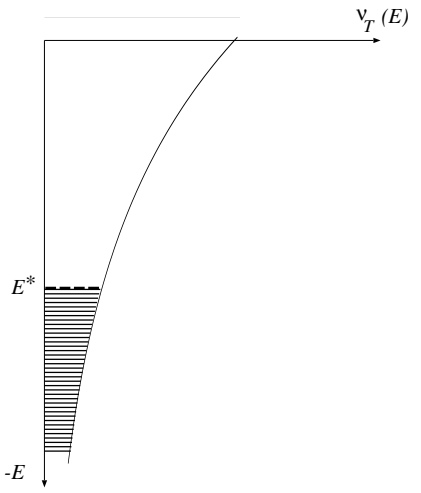

Fig. 18.23. Exponential density of site energies; the levels are filled up to the "Fermi" level E^*.

Power-law dependence of the conductivity on the concentration has been observed in ionic conductors, see, e. g., [95]. Of course, the actual systems are much more complex than described by the site-exclusion lattice gas in the RT model. Indeed, power-law dependence of the mobility was obtained in numerical simulations of models that were designed to describe superionic conductors [96, 97]. Nonetheless, it is interesting to note that already rather simple models exhibit these effects.

18.6 Conclusion

This chapter was concerned with the theoretical description of diffusion of particles on lattices. Two different dimensions of difficulties were encountered: Diffusion of single versus many particles and diffusion in ordered versus disordered lattices. The diffusion of a single particle on a uniform lattice is a well-understood textbook problem. Of practical interest are extensions of this problem, for example two-state models for diffusion and trapping of single particles. The problem of diffusion of a single particle in disordered lattices is now well understood with respect to the asymptotic properties, if local (site and/or bond) disorder is present. One remaining topic for future work is diffusion in the presence of extended defects. Also the frequency dependence seems to be not completely understood.

Various aspects of the diffusion of many particles on uniform lattices have been clarified in the past, in particular the differences between collective and tracer diffusion, the inherent correlation effects in tracer diffusion, and the anomalous diffusion of tagged particles on linear chains (single-file diffusion). Open problems can be found in the consideration of various forms of the interactions of the particles.

Least well understood is, of course, the problem of diffusion of many particles in lattices with quenched, disordered transition rates. Since this is a problem of current interest, the corresponding remarks will be more detailed than those concerning the previous sections. In the preceding section diffusion of site-exclusion lattice gases in disordered lattices was considered. There exist now reasonable appoximate descriptions for the coefficient of collective diffusion in form of the phenomenological theory and the EMA. The approximations are rather accurate for two-level models of site energies if the lattice-gas concentration c is smaller than the trap concentration c_t. However, one should be aware of the limitations of the approximations. Simulation results in $d = 3$ show that there are large discrepancies between the approximations and the numerical results when $c \approx c_t$. Hence an exact theory for collective diffusion for the site-exclusion model in disordered linear chains is desired.

The following important aspects of diffusion of lattice gases in disordered lattices were omitted in this chapter:

- *Tracer diffusion*
  The theory of tracer diffusion is more complicated than that of collective diffusion, in view of the inherent backward correlations for tracer diffusion. The inclusion of backward correlations in the presence of quenched disorder appears to be very difficult.
- *Effects of interactions*
  Even for lattices with uniform transition rates, interactions can only be treated by approximations like mean field. If disorder is present, and the particles have interactions, one has to resort to numerical simulations, see [57–59, 96, 97] and Chap. 20.
- *Frequency dependence*
  Although frequency dependence was investigated in numerical works (see the references given in the preceeding item), many of the observed features are not yet understood in a qualitative way (see however Chap. 21).

One could easily add more points to this list of partially understood problems. The main message perhaps should be that the field of diffusion of particles in condensed matter systems is still an open field with many unsolved problems.

18.7 Appendix

18.7.1 Derivation of the Result for the Diffusion Coefficient for Arbitrarily Disordered Transition Rates

Consider a segment of a linear chain with general (nonsymmetric) transition rates, as indicated in Fig. 18.3 of Sect. 18.3.2. A constant current I is fed into site 0 and extracted at site N. Kirchhoff's node equation for site 0 is

$$\Gamma_{10} P_0 - \Gamma_{01} P_1 = I \,. \tag{18.118}$$

It expresses the fact that the sum of all currents into site 0 is zero. The master equation for site 1 is

$$\frac{\mathrm{d}}{\mathrm{d}t}P_1(t) = \Gamma_{10}P_0(t) + \Gamma_{12}P_2(t) - (\Gamma_{01} + \Gamma_{21})P_1(t)\,. \tag{18.119}$$

One has in the stationary situation

$$-\Gamma_{10}P_0 + (\Gamma_{01} + \Gamma_{21})P_1 - \Gamma_{12}P_2 = 0. \tag{18.120}$$

Add this equation to the node equation (18.118) to obtain

$$\Gamma_{21}P_1 - \Gamma_{12}P_2 = I\,. \tag{18.121}$$

This procedure is continued and the equation for site i is

$$\Gamma_{i+1,i}P_i - \Gamma_{i,i+1}P_{i+1} = I\,. \tag{18.122}$$

The last equation is Kirchhoff's node equation at site N,

$$\Gamma_{N,N-1}P_{N-1} - \Gamma_{N-1,N}P_N = I\,. \tag{18.123}$$

The aim is to relate I to the difference $P_0 - P_N$. This can be achieved by first expressing P_{N-1} through P_N, I, using (18.123),

$$P_{N-1} = \frac{\Gamma_{N-1,N}}{\Gamma_{N,N-1}}P_N + \frac{I}{\Gamma_{N,N-1}}\,. \tag{18.124}$$

The quantity P_{N-2} can be expressed through P_{N-1} and I,

$$P_{N-2} = \frac{\Gamma_{N-2,N-1}}{\Gamma_{N-1,N-2}}P_{N-1} + \frac{I}{\Gamma_{N-1,N-2}}\,. \tag{18.125}$$

Insert P_{N-1} to obtain a relation between P_{N-2}, P_N, and I,

$$\begin{aligned} P_{N-2} = {} & \frac{\Gamma_{N-2,N-1}}{\Gamma_{N-1,N-2}}\frac{\Gamma_{N-1,N}}{\Gamma_{N,N-1}}P_N \\ & + \left(\frac{\Gamma_{N-2,N-1}}{\Gamma_{N-1,N-2}}\frac{1}{\Gamma_{N,N-1}} + \frac{1}{\Gamma_{N-1,N-2}}\right)I. \end{aligned} \tag{18.126}$$

Continue this procedure with P_{N-3}, etc. The final result is

$$\begin{aligned} P_0 = {} & \frac{\Gamma_{01}\Gamma_{12}\times\cdots\times\Gamma_{N-1,N}}{\Gamma_{10}\Gamma_{21}\times\cdots\times\Gamma_{N,N-1}}P_N \\ & + \Big(\frac{\Gamma_{01}\times\cdots\times\Gamma_{N-2,N-1}}{\Gamma_{10}\times\cdots\times\Gamma_{N-1,N-2}}\frac{1}{\Gamma_{N,N-1}} \\ & + \frac{\Gamma_{01}\times\cdots\times\Gamma_{N-3,N-2}}{\Gamma_{10}\times\cdots\times\Gamma_{N-2,N-3}}\frac{1}{\Gamma_{N-1,N-2}} \\ & + \cdots \\ & + \frac{\Gamma_{01}}{\Gamma_{10}}\frac{1}{\Gamma_{21}} + \frac{1}{\Gamma_{10}}\Big)I\,. \end{aligned} \tag{18.127}$$

The expression (18.127) can be further simplified by introducing the relation of detailed balance which holds in thermal equilibrium. It is clear that a non-equilibrium situation is maintained in the segment of the chain. The relation of detailed balance will be used to express the ratio of two rates by equilibrium occupation factors. An implicit assumption is the validity of the Arrhenius law. The equilibrium occupation probabilities are proportional to

$$\rho_i \sim \exp(-\beta E_i)\,; \tag{18.128}$$

note that $E_i \leq 0$. The condition of detailed balance is

$$\Gamma_{01}\rho_1 = \Gamma_{10}\rho_0 \tag{18.129}$$

or

$$\frac{\Gamma_{01}}{\Gamma_{10}} = \frac{\rho_0}{\rho_1} = \exp[-\beta(E_0 - E_1)]\,. \tag{18.130}$$

The product of two factors is

$$\frac{\Gamma_{12}\Gamma_{01}}{\Gamma_{21}\Gamma_{10}} = \exp[-\beta(E_1 - E_2)]\exp[-\beta(E_0 - E_1)] = \exp[-\beta(E_0 - E_2)] \tag{18.131}$$

and the product

$$\prod_{i=0}^{N-1} \frac{\Gamma_{i,i+1}}{\Gamma_{i+1,i}} = \exp[-\beta(E_0 - E_N)]\,. \tag{18.132}$$

Equation (18.127) can then be written as

$$\begin{aligned} P_0 - \exp[-\beta(E_0 - E_N)]P_N &= \\ = \Big(&\frac{1}{\exp[-\beta(E_{N-1} - E_0)]\Gamma_{N,N-1}} + \frac{1}{\exp[-\beta(E_{N-2} - E_0)]\Gamma_{N-1,N-2}} \\ &+ \cdots + \frac{1}{\exp[-\beta(E_1 - E_0)]\Gamma_{21}} + \frac{1}{\Gamma_{10}}\Big) I\,. \end{aligned} \tag{18.133}$$

It will be required that $P_0 = P_N$ if $I = 0$, and $P_0 \neq P_N$ only through maintaining a current through the chain. This requirement will be satisfied if $E_0 = E_N$, i. e., if the initial and final site energies are equal. It is henceforth assumed that always $E_0 = E_N$, which is a reasonable assumption.

The disorder average of (18.133) will now be taken. Each term on the right-hand side of this equation can be averaged independently and the pertinent quantities are taken from common distributions. The result is then

$$P_0 - P_N = N\left\{\frac{1}{\Gamma_{i+1,i}\exp[-\beta(E_i - E_0)]}\right\} I, \tag{18.134}$$

where the dummy indices have been kept to indicate the direction of the transition rate. The curly brackets represent the average over the different realizations of the disorder.

The further requirement will be made that the initial site is a typical site with respect to the disorder average. Hence it is assumed that

$$\{\exp(-\beta E)\} = \exp(-\beta E_0)\,. \tag{18.135}$$

This means that the thermal occupation of the initial (and final) site is equal to the average occupation. Large segments will be considered, where the disorder average is approximated by the sum over all sites,

$$\{\exp(-\beta E)\} = \frac{1}{N}\sum_{j=0}^{N}\exp(-\beta E_j)\,. \tag{18.136}$$

Thermal occupation factors will be defined by

$$\rho_i = \frac{\exp(-\beta E_i)}{\{\exp(-\beta E)\}} = \frac{\exp(-\beta E_i)}{\frac{1}{N}\sum_{j=0}^{N-1}\exp(-\beta E_j)}\,. \tag{18.137}$$

Relation (18.134) between $P_0 - P_N$ and the current I can then be written as

$$P_0 - P_N = IN\left\{\frac{1}{\Gamma_{i+1,i}\rho_i}\right\}\,. \tag{18.138}$$

This relation represents Fick's first law. The following identification can be made (lattice constant $a = 1$)

$$\frac{P_0 - P_N}{N} \cong -\nabla n \qquad\qquad d = 1\,. \tag{18.139}$$

Fick's first law reads

$$I = -D\nabla n\,. \tag{18.140}$$

Hence one finds

$$D = \left\{\frac{1}{\Gamma_{i+1,i}\rho_i}\right\}^{-1}\,. \tag{18.141}$$

18.7.2 Derivation of the Self-Consistency Condition for the Effective-Medium Approximation

The Fourier-Laplace transformation of the conditional probability $P_l(t)$ is defined by

$$\tilde{P}(k,s) = \int_0^\infty \mathrm{d}t\exp(-st)\sum_l \exp(-\mathrm{i}ka)P_l(t)\,. \tag{18.142}$$

The equation for $\tilde{P}(k,s)$ is obtained by multiplying (18.51) and (18.52) with $\exp(-\mathrm{i}kal)$, summing over l, and integrating:

$$[\ s\ +2\tilde{\Gamma}_{\rm eff}(s)(1-\cos ka)]\tilde{P}(ks,) = 1+(e^{-{\rm i}ka}-1)[\tilde{\Gamma}_{\rm eff}(s)-\Gamma_{10}]\,[\tilde{P}_1(s)-\tilde{P}_0(s)]\,. \tag{18.143}$$

Combining this equation with the master equation (18.56) for the effective medium one finds

$$\tilde{P}(k,s) = \tilde{E}(k,s)+\tilde{E}(k,s)(e^{-{\rm i}ka}-1) \times[\tilde{\Gamma}_{\rm eff}(s)-\Gamma_{10}][\tilde{P}_1(s)-\tilde{P}_0(s)]\,. \tag{18.144}$$

The inverse Fourier transform of $\tilde{E}(k,s)$ is

$$\tilde{E}_l(s) = \int_{-\pi}^{\pi}\frac{dk}{2\pi}\frac{\exp({\rm i}kal)}{s+2\tilde{\Gamma}_{\rm eff}(s)(1-\cos ka)}\,. \tag{18.145}$$

Note that $\tilde{E}_l(s)=\tilde{E}_{-l}(s)$. Multiplying (18.144) with $1/2\pi$ and integrating over k one obtains

$$\tilde{P}_0(s) = \tilde{E}_0(s)+[\tilde{E}_1(s)-\tilde{E}_0(s)][\tilde{\Gamma}_{\rm eff}(s)-\Gamma_{10}]\,[\tilde{P}_1(s)-\tilde{P}_0(s)]\,. \tag{18.146}$$

Multiplying (18.144) with $\exp({\rm i}ka)/2\pi$ and integrating one obtains

$$\tilde{P}_1(s) = \tilde{E}_1(s)+[\tilde{E}_1(s)-\tilde{E}_0(s)][\tilde{\Gamma}_{\rm eff}(s)-\Gamma_{10}]\,[\tilde{P}_1(s)-\tilde{P}_0(s)]\,. \tag{18.147}$$

The difference of the two equations is

$$\tilde{P}_1(s)-\tilde{P}_0(s) = \frac{\tilde{E}_1(s)-\tilde{E}_0(s)}{1+2[\tilde{E}_1(s)-\tilde{E}_0(s)][\tilde{\Gamma}_{\rm eff}(s)-\Gamma_{10}]} \tag{18.148}$$

and thus

$$\tilde{P}_0(s) = \tilde{E}_0(s)+\frac{[\tilde{E}_1(s)-\tilde{E}_0(s)]^2[\tilde{\Gamma}_{\rm eff}(s)-\Gamma_{10}]}{1+2[\tilde{E}_1(s)-\tilde{E}_0(s)][\tilde{\Gamma}_{\rm eff}(s)-\Gamma_{10}]}\,. \tag{18.149}$$

The self-consistency requirement $\{\tilde{P}_0(s)\}=\tilde{E}_0(s)$ (cf. (18.57)) leads to

$$\left\{\frac{[\tilde{E}_1(s)-\tilde{E}_0(s)]^2[\tilde{\Gamma}_{\rm eff}(s)-\Gamma_{10}]}{1+2[\tilde{E}_1(s)-\tilde{E}_0(s)][\tilde{\Gamma}_{\rm eff}(s)-\Gamma_{10}]}\right\}=0\,. \tag{18.150}$$

The difference squared in the numerator is systematic and can be factored out. From the master equation for the effective medium in $d=1$ follows

$$\tilde{E}_1(s)-\tilde{E}_0(s) = \frac{s\tilde{E}_0(s)-1}{2\Gamma_{\rm eff}(s)}\,. \tag{18.151}$$

The self-consistency condition can now be brought into the form that has been given in the main text.

18.7.3 Relation Between the Relative Displacement and the Density Change

The displacements of two tagged particles from their equilibrium positions x and $x+\delta x$ are considered. The notation is explained in Fig. 18.16. The initial distance changes into the actual distance

$$\delta x \longrightarrow \delta x + u(x+\delta x) - u(x)\,. \tag{18.152}$$

Because the number of particles in the interval between the two tagged particles is conserved, the local density change induced by the difference in the displacements of the two particles is

$$\delta n = \frac{n\delta x}{\delta x + u(x+\delta x) - u(x)} - n\,. \tag{18.153}$$

Here n is the (spatially constant) equilibrium particle density. A Taylor expansion for small δx is made, together with the assumption of small gradients, $\partial u/\partial x \ll 1$. From (18.153) follows in linear approximation

$$\frac{1}{n}\delta n = -\frac{\partial u}{\partial x}\,. \tag{18.154}$$

The inverse Fourier transformation is defined by

$$f(x,t) = \int \frac{\mathrm{d}k}{2\pi} e^{\mathrm{i}kx} f(k,t)\,. \tag{18.155}$$

The relation between density change and displacement gradient reads in Fourier space

$$\frac{1}{n}\delta n(k,t) = \mathrm{i}ku(k,t)\,. \tag{18.156}$$

This is the relation used in the main text.

Notation

$D = D_{\mathrm{s.p.}}$	Diffusion coefficient of single, independent particles
D_{coll}	Collective (Fick's) diffusion coefficient
D_{t}	Tagged particle (tracer) diffusion coefficient
E_i	Energy level of site i
E_{ij}	Activation energy of barrier between sites i and j
$f(c)$	Correlation factor for tagged-particle diffusion in lattice gas
$f = f(c \to 1)$	Correlation factor for metal physics
$P(\boldsymbol{l}t\|\mathbf{0}0)$	Conditional probability of finding a particle on site $\boldsymbol{l}$ at time t when it was at site $\mathbf{0}$ at $t = 0$.
$P_{\boldsymbol{l}}(t)$	Abbreviated form of $P(\boldsymbol{l}t\|\mathbf{0}0)$

$P(\boldsymbol{l},t)$	Probability of finding a particle at site $\boldsymbol{l}$ at time t (applies to lattice gases)
$P(\boldsymbol{k},t)$	Fourier transform of $P_{\boldsymbol{l}}(t)$
$\tilde{P}(\boldsymbol{l},s)$	Fourier-Laplace transform of $P_{\boldsymbol{l}}(t)$
Γ	Transition rate between two neighbour sites in uniform lattice
Γ_{ji}	Transition rate from site i to neighbour site j in disordered lattice
$\Gamma_{\rm eff}(t)$	Time-dependent transition rate in effective medium
$\Lambda_{\boldsymbol{l},\boldsymbol{l}'}$	Transition-rate matrix between two neighbour sites
$\Lambda(\boldsymbol{k})$	Fourier transform of transition rate matrix
$\nu_{\rm B}(E)$	Density of activation energies of random barriers
$\nu_{\rm T}(E)$	Density of random site energies
$\rho(\Gamma)$	Probability density of random transition rates
$\langle \quad \rangle$	Random walk and/or thermal average
$\{ \quad \}$	Average over (quenched) disordered rates.

References

1. A. Einstein: Ann. Phys. (Leipzig) **17**, 549 (1905)
2. C.P. Flynn: *Point Defects and Diffusion* (Clarendon, Oxford 1972)
3. P. Hänggi, P. Talkner, M. Borkovec: Rev. Mod. Phys. **62**, 251 (1990)
4. P.W. Anderson. In: *Ill-Condensed Matter*, Les Houches, Session XXXI, ed by R. Balian, R. Maynard, G. Toulouse (North Holland, Amsterdam 1979) p 159
5. K. Mussawisade. PhD thesis, Univ. Köln (2000)
6. N.M. Barber, B.W. Ninham: *Random and Restricted Walks* (Gordon and Breach, New York 1970)
7. G.H. Weiss: *Aspects and Applications of the Random Walk* (Clarendon Press, Oxford 1996)
8. N.G. van Kampen: *Stochastic Processes in Physics and Chemistry* (North Holland, Amsterdam 1987)
9. F. Spitzer: *Principles of Random Walks* (Van Nostrand, Princeton NJ 1964)
10. H. Spohn: *Large Scale Dynamics of Interacting Particles* (Springer, Berlin Heidelberg New York 1991)
11. T.M. Liggett: *Stochastic Interacting Systems: Contact, Voter and Exclusion Processes* (Springer, Berlin Heidelberg New York 1999)
12. *Fractals and Disordered Systems*, ed by A. Bunde, S. Havlin (Springer, Berlin Heidelberg New York 1996)
13. S. Alexander, J. Bernasconi, W.R. Schneider, R. Orbach: Rev. Mod. Phys. **53**, 175 (1981)
14. G.H. Weiss, R.J. Rubin: Adv. Chem. Phys. **52** 363 (1983)
15. J.W. Haus, K.W. Kehr: Phys. Rep. **150**, 263 (1987)
16. S. Havlin, D. ben-Avraham: Adv.Phys. **36**, 695 (1987)
17. J.-P. Bouchaud, A. Georges: Phys. Rep. **195**, 127 (1990)
18. G.M. Schütz. In: *Phase Transitions and Critical Phenomena*, vol 19, ed by C. Domb, J. Lebowitz (Academic, London 2000)

19. J.R. Manning: *Diffusion Kinetics for Atoms in Crystals* (Van Nostrand, Princeton 1968)
20. J. Philibert: *Atom Movements. Diffusion and Mass Transport in Solids* (Les Editions de Physique, Les Ulis 1991)
21. S. Chandrasekhar: Rev. Mod. Phys. **15**, 1 (1943)
22. R. Kutner, I. Sosnowska: J.Phys.Chem. Solids **38**, 741 (1977)
23. K.W. Kehr, D. Richter, R.H. Swendsen: J. Phys. F. **8**, 433 (1978)
24. I.S. Anderson, A. Heidemann, J.E. Bonnet, D.K. Ross, S.K.P. Wilson, M.W. McKergow: J. Less Common Met.**101**, 405 (1984)
25. K.W. Schroeder: Z. Physik **B25**, 91 (1976)
26. D. Richter, T. Springer: Phys. Rev. B **18**, 126 (1978)
27. W. Dieterich (unpublished)
28. R. Kutner: Physica A **224**, 558 (1996)
29. T. Wichmann. PhD thesis, Univ. Köln (1996)
30. J.W. Haus, K.W. Kehr, J.W. Lyklema: Phys.Rev.B **25**, 2905 (1982)
31. K. Mussawisade Diploma thesis, Univ. Köln (1996)
32. R. Zwanzig: J. Stat. Phys. **28**,127 (1982)
33. P.J.H. Denteneer, M.H. Ernst: J. Phys.C **16**, L961 (1983); Phys.Rev.B **29**, 1755 (1984)
34. S. Alexander, R. Orbach: Physica **107B**, 675 (1981)
35. S. Summerfield: Solid State Commun. **39**, 401 (1981)
36. T. Odagaki, M. Lax: Phys. Rev. B **24** 5284 (1981)
37. I. Webman: Phys. Rev. Lett. **47**, 1496 (1981)
38. J.W. Haus, K.W. Kehr, K. Kitahara: Phys. Rev. B **25**, 4918 (1982); Z.Physik B **50**, 161 (1983)
39. S. Kirkpatrick: Rev. Mod. Phys. **45**, 574 (1973)
40. J. Bernasconi: Phys. Rev. B **7**, 2252 (1973)
41. H. Ambaye, K.W. Kehr: Phys. Rev. E **51**, 5101 (1995)
42. P. Argyrakis, A. Milchev, V. Pereyra, K.W. Kehr: Phys. Rev. E **52**, 3623 (1995)
43. B.I. Shklovskii, A.L. Efros: Soviet Physics JETP **33**, 468 (1971)
44. V. Ambegaokar, B.I. Halperin, J.S. Langer: Phys. Rev. B **4**, 2612 (1971)
45. D. Stauffer, A. Aharony: *Introduction to Percolation Theory*, 2nd edn (Taylor & Francis, London, 1994)
46. J. Bernasconi, W.R. Schneider, H.J. Wiesmann: Phys. Rev. B **16**, 5250 (1977)
47. S. Tyc, B.I. Halperin: Phys. Rev. B **39**, 877 (1989)
48. P. Le Doussal: Phys. Rev. B **39**, 881 (1989)
49. R.A. Tahir-Kheli: Phys. Rev. B **28**, 3049 (1983)
50. M.H. Ernst, T.M. Nieuwenhuizen, P.F.J. van Velthoven, J. Phys. A **20**, 5335 (1987)
51. M. Braun, K.W. Kehr: Phil.Mag.A **61**, 855 (1990)
52. S. Havlin, B.L. Trus, G.H. Weiss: J. Phys. A **19**, L817 (1986)
53. Y. Limoge, J.L. Bocquet: Phys. Rev. Lett. **65**, 60 (1990)
54. K. Mussawisade, T. Wichmann, K.W. Kehr: J. Phys.: Condens. Matter **9**, 1181 (1997)
55. M. Wagener, W. Schirmacher: Ber. Bunsenges. Phys. Chem. **95**, 983 (1991)
56. A. Hoerner, A. Milchev, P. Argyrakis: Phys. Rev. E **52**, 3570 (1995)
57. W. Dieterich, D. Knoedler, P. Pendzig: J. Non-Cryst. Solids **172-174** 1237 (1994)
58. P. Maass, M. Meyer, A. Bunde: Phys. Rev. B **51**, 8164 (1995)

59. D. Knoedler, P. Pendzig, W. Dieterich: Solid State Ionics **86-88**, 29 (1996)
60. E. Marinari, P. Parisi, D. Ruelle, P. Windey: Phys. Rev. Lett. **50**, 1223 (1983)
61. B. Schmittmann, R.K.P. Zia. In: *Phase Transitions and Critical Phenomena*, vol 15, ed by C. Domb, J. Lebowitz (Academic, London 1995)
62. P. Ferrari, L.R.G. Fontes, E. Saada: Ann. Prob. **19**, 226 (1991)
63. B. Derrida, J.L. Lebowitz, E. Speer: J. Stat. Phys. **89**, 135 (1997)
64. C. Pigorsch, G.M. Schütz: J. Phys. A **33**, 7919 (2000)
65. J. Krug: Phys. Rev. Lett. **67**, 1882 (1991)
66. G. Schütz, E. Domany: J. Stat. Phys. **72**, 277 (1993)
67. M.R. Evans, D.P. Foster, C. Godrèche, D. Mukamel: J. Stat. Phys. **80**, 69 (1995)
68. A.B. Kolomeisky, G.M. Schütz, E.B. Kolomeisky, J.P. Straley: J. Phys. A **31**, 6911 (1998)
69. J. Hager, J. Krug, V. Popkov, G.M. Schütz: Phys. Rev. E **63** 056110 (2001)
70. F. Spitzer: Adv. Math. **5**, 246 (1970)
71. T.M. Liggett: *Stochastic Interacting Systems: Contact, Voter and Exclusion Processes* (Springer, Berlin Heidelberg New York 1999)
72. R. Kutner: Phys. Lett. **81A**, 239 (1981)
73. S. Alexander, T. Holstein: Phys. Rev. B **18**, 301 (1978)
74. G. Schütz, S. Sandow: Phys. Rev. E **49**, 2726 (1994)
75. J. Bardeen, C. Herring. In: *Imperfections in Nearly Perfect Crystals*, ed by W. Shockley (Wiley, New York 1952) p 261
76. A.D. Le Claire. In: *Physical Chemistry* vol 10, ed by H. Eyring, D. Henderson, W. Jost (Academic, New York 1970) p 261
77. G.L. Montet: Phys. Rev. B **7**, 650 (1973)
78. S. Ishioka, M. Koiwa: J. Stat. Phys. **30**, 477 (1983)
79. K. Nakazato, K. Kitahara: Progr. Theor. Phys. **64**, 2261 (1980)
80. R.A. Tahir-Kheli, R.J. Elliott: Phys.Rev.B **27**, 844 (1983)
81. K.W. Kehr, K. Binder. In: *Applications of the Monte Carlo Method in Statistical Physics*, Topics in Current Physics, vol 36, 2nd edn, ed by K. Binder (Springer, Berlin Heidelberg New York 1987) p 181
82. P.M. Richards: Phys. Rev. B **16**, 1363 (1977)
83. H. van Beijeren, K.W. Kehr, R. Kutner: Phys. Rev. B **28**, 5711 (1983)
84. S. Alexander, P. Pincus: Phys. Rev. B **18**, 2011 (1978)
85. R. Kutner, H. van Beijeren, K.W. Kehr: Phys. Rev. B **30** 4382 (1984)
86. R. Kutner, K.W. Kehr: Phil. Mag. A **48**, 199 (1983)
87. H. Harder, A. Bunde, W. Dieterich, J. Chem. Phys. **85**, 4123 (1986)
88. K.W. Kehr, O. Paetzold, T. Wichmann: Phys. Lett. A **182**, 135 (1993)
89. P. Gartner, R. Pitis: Phys. Rev. B **45**, 7739 (1992)
90. T. Wichmann, K.W. Kehr: J. Phys.: Condens. Matter **7**, 717 (1995)
91. R.C. Brower, E. Salomons, R. Griessen: Phys. Rev. B **38**, 10217 (1988); E. Salomons: J. Phys. C **21**, 5935 (1988)
92. V.P. Zhdanov: Surface Science **149**, L13 (1985); V. Pereyra, G. Zgrablich, V.P. Zhdanov: Langmuir **6**, 691 (1990)
93. R. Kirchheim, U. Stolz: Acta metall. **35**, 281 (1987)
94. T. Wichmann, K.G. Wang, K.W. Kehr: J. Phys. A **27**, L263 (1994)
95. M.D. Ingram: Phys. Chem. Glasses **28**, 215 (1987)
96. P. Maass, A. Bunde, M.D Ingram: Phys. Rev. Lett. **68**, 3064 (1992)
97. D. Knoedler, P. Pendzig, W. Dieterich: Solid State Ionics **70-71**, 356 (1994)

19 Diffusion on Fractals

Uwe Renner, Gunter M. Schütz, and Günter Vojta

19.1 Introduction: What a Fractal is

In recent years, there has been a growing interest in the physics and physical chemistry of fractals. Fractal systems show new physical properties and anomalous behaviour. This is particularly interesting in the field of transport processes. The name fractal was coined in 1975 by Benoit B. Mandelbrot, the founder of modern fractal science. It is derived from the Latin verb frangere: to break (fractum: broken), cf. words like fraction, fracture, fragment ...

A fractal is defined as a mathematical point set or a physical (chemical, biological ...) system with a fractional geometrical (spatial) dimension (more exactly: dimensionality). This dimension is called the fractal dimension or Mandelbrot dimension $\bar{d}$. Its rigorous and general mathematical foundation is given by the Hausdorff dimension d_{H}, see [1]. There also exist typical fractals which (by chance) carry integer dimensions, e.g., certain Viscek fractals or the Wiener trajectory of a Brownian particle during normal diffusion ($\bar{d} = 2$), see Sect. 19.4. This fact indicates difficulties to give a suitable definition of the fundamental concept "fractal" which is not too narrow and not too wide – these difficulties being shared by definitions of many other basic notions.

Objects embedded in our common (Euclidean) space are characterized by (topological) dimensions $d = 1$, 2, or 3. In order to understand the notion of a fractional dimension attributed to a physical system let us consider some specific fractal structures. A good introductory example is a solid surface with defects like steps, dislocations, cavities, with regard to its capacity to adsorb say atoms (Fig. 19.1). With increasing number of defects, the adsorptive capacity becomes larger and larger and approaches that of a sponge, to which can be assigned a dimension $d = 3$. Therefore, it makes sense to introduce an effective dimension $\bar{d}$ regarding adsorption, where $2 < \bar{d} < 3$. The topological dimension of the surface is now $d = 2$ as before: One indeed deals with a surface, even if curvature and many twists are present. The embedding dimension (or Euclidean dimension) of the system is $d_{\mathrm{E}} = 3$.

The surface of a real solid is a typical stochastic fractal. In principle, one has to distinguish two types of fractals:

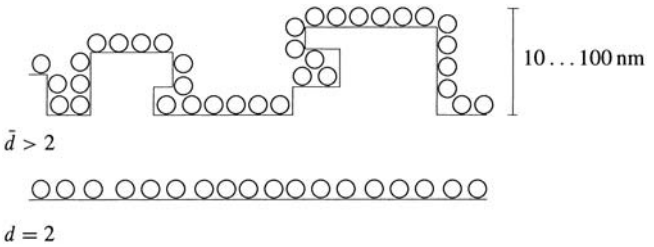

Fig. 19.1. A real solid surface shows a larger capacity to adsorb atoms than an ideal flat surface.

- regular, deterministic or ideal fractals, model fractals; these fractals are constructed as mathematical objects according to a well-defined (unique) prescription or algorithm;
- irregular, random or stochastic (or statistical) or real fractals, they are objects of nature or in the laboratory, yet they can be constructed theoretically as well.

The fractal systems of interest in physical science can be divided into three classes, typical representatives of which are:

1. Natural objects (systems with mass) like
   solid surfaces, enzyme surfaces, irregular porous solids, e. g. catalysts, polymer systems (see Chap. 10), percolation networks (see Chap. 22), irregular particle aggregates, and many others.
2. Particle trajectories of classical Brownian motion (Wiener process), particle trajectories of anomalous diffusion e. g. on fractal systems (the so-called fractional Brownian motion [2]) or due to time-correlations in non-Markovian stochastic processes, quantum mechanical state vectors (wave function) of disordered electronic systems.
3. Sets in state diagrams, in particular boundaries of attractors and attractor basins of chaotic systems, i. e. classical dissipative dynamical systems with deterministic chaos, sets of complex zeros of partition functions in the frame of statistical thermodynamics (Lee-Yang theorem).

In order to define and investigate the basic properties of these systems, it is convenient to consider ideal deterministic fractals. A typical example is the elementary Sierpiński fractal (Sierpiński network, lattice, triangle or gasket); its construction is indicated in Fig. 19.2.

With growing number n of construction steps the structure becomes finer and finer, nevertheless one has nothing else than a surface with holes, i. e. an object with the geometrical (topological) dimension $d = 2$. Only in the limit $n \to \infty$ is a fractal generated; its dimension (see below) is $\bar{d} = \ln 3 / \ln 2 = 1.5849 \ldots < 2$. The Sierpiński fractal is a prototype of a

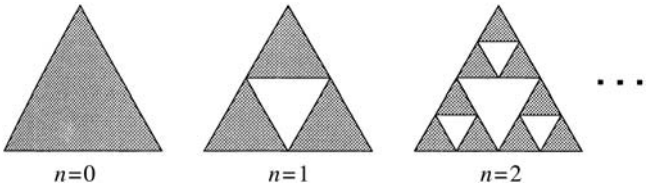

Fig. 19.2. Construction of a Sierpiński gasket; n: number of construction steps. Sketched are prefractals; the proper fractal is created in the limit $n \to \infty$.

model for the physics of fractals and renders good services in the exploration of the new and sometimes strange phenomena occurring in fractal systems. Ideal fractals are characterized by two basic, closely related properties:

- Self-similarity at all length scales, dilatation invariance (structural invariance against the dilatation group), i.e., existence of a hierarchical structure.
- The lack of any characteristic length (including such important characteristic lengths of real physical systems as atomic diameter, lattice constant, mean free paths, and correlation lengths).

Stochastic fractals are said to possess "stochastic self-similarity", defined below. The best-known representative is the percolation cluster (see Chap. 22), generated by randomly breaking either bonds or sites from, say, a square lattice. For small break-off probability just some bonds are missing, but there are still many connected paths that lead through the lattice. On the other hand, for large break-off probability the lattice breaks into disjointed, irregular sublattices. At the critical break-off probability where connected paths through the lattice cease to exist the system becomes a stochastic fractal, i.e., average properties attain fractal dimensions.

By definition, ideal fractals have an infinitely fine structure and a spatially infinite extension. When such a fractal is used to model a real physical system, it is necessary to introduce two cut-off lengths: a lower cut-off given e. g. by the lattice constant or atomic diameters, and an upper cut-off due to the finite size of the system considered. At length scales between these two cut-off lengths, the fractal is a good model for a disordered system, e. g. a percolation labyrinth or a porous solid with stochastic distributions of pore locations and pore diameters. In Sect. 10.5.3 of Chap. 10 even grains of sand are identified as particles exhibiting surface fractality between certain cut-off lengths. The essential property of (stochastic) self-similarity remains still valid over some length scales.

With this in mind we can now define the notion of a fractal dimension. The non-integer dimension of a fractal system is caused by the imperfect filling of space; there are typically holes at all orders of magnitude (see Fig. 19.2). For a rigorous and quantitative definition of the fractal dimension, it is useful to assign a mass to the fractal (say, with mass density 1). The total mass M of

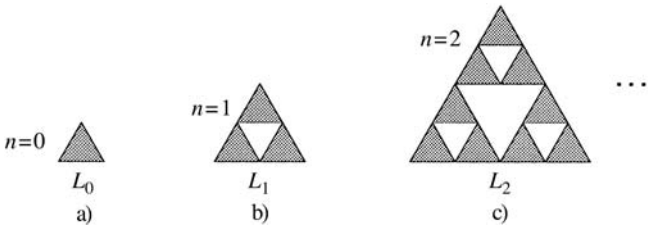

Fig. 19.3. Another construction of the Sierpiński gasket a) The initiator: $L = L_0$, $M = M_0$. b) The generator: $L_1 = 2L_0$, $M_1 = 3M_0$. c) $n = 2$: $L_2 = 2^2 L_0$, $M_2 = 3^2 M_0$.

a common object in an Euclidean space of dimension $d = 1$, 2, or 3 (say, a given straight line, a square, or a cube) scales with the length (edge length) L according to

$$M \sim L^d. \tag{19.1}$$

The factor of proportionality plays no role; important is only the algebraic functional law between M and L which is determined by the dimensionality of the system. Generally one defines

$$\text{extensive property} \sim \text{length}^{\text{dimension}}. \tag{19.2}$$

For an ideal fractal, the dimension $\bar{d}$ is defined by

$$M \sim L^{\bar{d}}. \tag{19.3}$$

However, it is now important to take the limit $n \to \infty$ in the definition of the fractal.

As an example, let us again consider the Sierpiński gasket, now constructed with another algorithm, as shown in Fig. 19.3. After step n one has a prefractal with

$$L_n = 2^n L_0, \qquad M_n = 3^n M_0.$$

Equation (19.3) yields

$$\begin{aligned} \bar{d} &= \lim_{n\to\infty} \frac{\ln M_n}{\ln L_n} = \lim_{n\to\infty} \frac{\ln(3^n M_0)}{\ln(2^n L_0)} \\ &= \lim_{n\to\infty} \frac{\ln 3^n + \ln M_0}{\ln 2^n + \ln L_0} = \lim_{n\to\infty} \frac{n \ln 3}{n \ln 2} = \frac{\ln 3}{\ln 2} < 2. \end{aligned} \tag{19.4}$$

The quantities L_0, M_0, and the factor of proportionality no longer play any role.

For (nearly) all ideal fractals constructed in this manner one can easily find the fractal dimension $\bar{d}$ by the rule

$$\bar{d} = \frac{\ln(\text{scaling factor of mass})}{\ln(\text{scaling factor of length})}. \tag{19.5}$$

A stochastic fractal is given a dimension $\bar{d}$ by the relation

$$\langle M \rangle \sim L^{\bar{d}}; \tag{19.6}$$

the averaging $\langle \cdots \rangle$ is to be performed over many samples of the fractal considered. Often, of course, one is confronted with the task of determining the fractal dimension of a natural structure where no generating algorithm is known. Methods of measuring the fractal dimension of a given object are reviewed in [3]. The basic idea behind these methods is the assignment of a mass function $M(L)$ to a definite volume $V \sim L^d$ in the embedding space and then to measure this mass for a suitably chosen sequence of test volumes. This yields a sequence of data $M(L_i)$ from which one obtains the fractal dimension via (19.5).

Clearly, a fractal defined in this manner is not only invariant with regard to dilatations of space. It is also irrelevant *where* in space the structure is studied: All triangles in the Sierpińsky gasket are treated in the same way in all consecutive iteration steps. However, fractal systems may be more complicated. A multifractal is, crudely spoken, a fractal system with a space-dependent fractal dimension. Typical multifractals are aggregates of (colloidal) particles. Such structures are not covered in this brief introduction to diffusion on fractals. More important for our purposes is another variant of fractals, viz. self-affine fractals. Isotropic fractals as, e.g., the Sierpińsky gasket remain invariant under rescaling all the directions of the embedding space by the same factor. Another important generalization is the introduction of anisotropic scaling where each direction of the embedding space is scaled by a different amount. Structures that are invariant under such rescaling are self-affine fractals. A common example (in this case, of a stochastic fractal) is the trajectory of a random walk where the time direction is scaled differently, as discussed below. More about the fundamentals and applications of fractal science can be found in excellent books [1, 3–5]; a short review of selected applications is given in [6].

19.2 Anomalous Diffusion: Phenomenology

Diffusion is the fundamental process of mass transport in a tremendous variety of systems. Since also fractal structures are not uncommon (of course, with the limiting upper and lower cut-offs, resp., in real systems) it is rather important to investigate diffusion processes on fractal systems. Our topic is the overall behaviour of diffusing particles, i.e., the statistics of the many steps of one, several, or many particles, not the elementary process of one step.

Let us first recall the basic facts of normal diffusion in common (i. e. Euclidean) systems (see also Chaps. 1, 10, 18, 23 and [7, 8]). Our starting point is the linear diffusion equation of Fick for the particle number density $n(x, y, z, t) = n(\boldsymbol{r}, t)$ in a one-component system

$$\frac{\partial}{\partial t} n = D \Delta n, \tag{19.7}$$

where D is the diffusion coefficient and $\Delta = \partial^2/\partial x^2 + \partial^2/\partial y^2 + \partial^2/\partial z^2$ the Laplacian. This equation results from the existence of a diffusive current

$$\boldsymbol{j} = -D \nabla n \tag{19.8}$$

due to the random motion of particles (Fick's law) and the continuity equation

$$\frac{\partial}{\partial t} n = -\nabla \boldsymbol{j}, \tag{19.9}$$

resulting from the conservation of the number of particles.

Let N be the total number of particles in the system, then

$$P(\boldsymbol{r}, t) = \frac{n(\boldsymbol{r}, t)}{N} \tag{19.10}$$

appears as the spatial probability density to find one particle at the place $\boldsymbol{r}$ at time t.

The diffusion equation

$$\frac{\partial}{\partial t} P = D \Delta P \tag{19.11}$$

with the initial condition $P(\boldsymbol{r}, t_0) = \delta(\boldsymbol{r} - \boldsymbol{r}_0)$ (corresponding to particles localized at the point $\boldsymbol{r}_0$ at time t_0) has as solution the Gaussian distribution

$$P(\boldsymbol{r}, t | \boldsymbol{r}_0, t_0) = \frac{1}{(4\pi D\,(t - t_0))^{d/2}} \exp\left(-\frac{(\boldsymbol{r} - \boldsymbol{r}_0)^2}{4D\,(t - t_0)} \right). \tag{19.12}$$

This is the Green's function (or propagator) of the diffusion equation. (R. P. Feynman has first coined the name propagator, but for the quantum mechanical transition probability *amplitude*.) The evaluation for the case of normal diffusion of, e.g., guest molecules in zeolites is given in Chap. 23.

The basic quantity $P(\boldsymbol{r}, t | \boldsymbol{r}_0, t_0)$ is the conditional spatial probability density to find one particle at $\boldsymbol{r}, t$, given the initial position $\boldsymbol{r}_0, t_0$. In physical terms it is simply the spatial transition probability density from $\boldsymbol{r}_0, t_0$ to $\boldsymbol{r}, t$ for one particle. We remark that the propagator is *not* a self-correlation function in the proper sense, though it may be represented in terms of the self-correlation function of $\delta(r - r(t))$ where $r(t)$ denotes the position of a given particle at time t. Hence in Mößbauer and neutron scattering spectroscopy (see Chaps. 2 and 3) both terms are often used simultaneously.

With the variables $\boldsymbol{r}_0 = 0$, $t_0 = 0$ the propagator

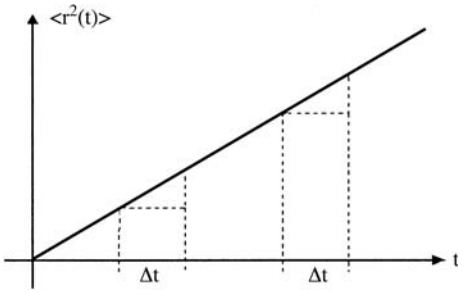

Fig. 19.4. Normal diffusion. In equal time intervals Δt the mean square displacement increases by equal amounts.

$$P(\mathbf{0}, t|\mathbf{0}, 0) \sim t^{-d/2} \tag{19.13}$$

represents the probability density to find a particle at the (arbitrary) origin at time t, if it was at the origin at time 0.

The mean square displacement, with (19.12) and $r_0 = t_0 = 0$, becomes

$$\begin{aligned} \left\langle \boldsymbol{r}^{\,2}(t) \right\rangle &= \int \boldsymbol{r}^{\,2} P(\boldsymbol{r}, t|\mathbf{0}, 0) \mathrm{d}^d r \\ &= 2d\, D\, t \qquad (d = 1, 2, 3, 4, \ldots). \end{aligned} \tag{19.14}$$

The proportionality between $\left\langle \boldsymbol{r}^{\,2}(t) \right\rangle$ and t for all integer dimensions d reflects the universality of normal diffusion (see Fig. 19.4).

The diffusion equation (19.11) allows for the factorization of the solution P:

$$P(x, y, z, t) = P(x, t) P(y, t) P(z, t). \tag{19.15}$$

This means that there is no correlation between the particle motions in x-, y-, and z-direction, respectively. Likewise, for the normal diffusive motion of one particle, there is no correlation of the individual particle displacements in time, which is reflected in the Gaussian distribution of the probability density and therefore also in a linear relation between $\langle r^2 \rangle$ and t as shown in Fig. 19.4. Rigorously speaking, the universality of normal diffusion results from the central limit theorem which asserts that independent, identically distributed increments of a random variable (here the particle position) with finite mean and variance always lead to a Gaussian distribution.

The anomalous diffusion on fractal systems, e. g. on the network of a Sierpiński gasket, is caused by the self-similarity at all length scales [5]. A diffusing particle has to circumvent all holes resulting in an increasing effect of hindrance. Experiments show, however, that it is not only the diffusion coefficient D which is diminished; even the functional law (19.14) is changed, leading to the relation

$$\left\langle \boldsymbol{r}^2(t) \right\rangle \sim t^{\kappa}, \quad \kappa < 1. \tag{19.16}$$

The time exponent κ shows no universality:

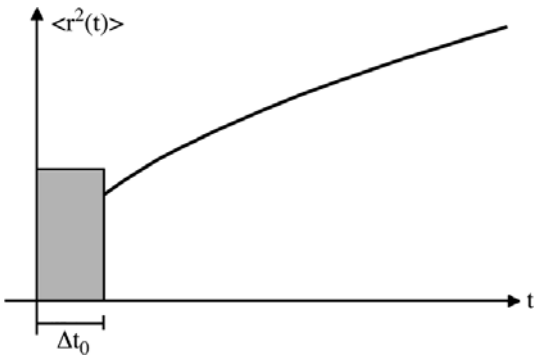

Fig. 19.5. Mean square displacement for anomalous diffusion; $\kappa = 1/2$; cf. Fig. 19.4. The diffusion law (19.16) acts as an asymptotic law; therefore, the curve is not valid during a time interval Δt_0 immediately after the starting time t_0 of the process. This time interval covers say $3 \ldots 10$ elementary steps of the walking particle.

1. κ is a specific quantity for every fractal type, κ depends on the fractal dimension $\bar{d}$.
2. The anomalous diffusion becomes a stochastic process with correlation in time, its increments are no longer independent; see below and [9].
3. It follows from the time hindrance as schematically shown in Fig. 19.5 that the initial time t_0 and hence the time interval Δt is no longer arbitrary, contrary to the situation in normal diffusion (Fig. 19.4). This is important for the correct theoretical description of experiments on anomalous diffusion, e. g. by use of the pulsed-field-gradient NMR technique (cf. Fig. 19.5, Chap. 10 and [10,11]).

It can easily be understood by means of the following simple calculation that independent time increments are incompatible with anomalous diffusion.

Following the representation of Fig. 19.6 we decompose the transition from, say, the origin, to a position $\boldsymbol{r}$ into two consecutive transitions first to a point $\boldsymbol{r}_1$ at some time t_1 and by another displacement $\boldsymbol{r}_2 = \boldsymbol{r} - \boldsymbol{r}_1$. Therefore

$$\boldsymbol{r}(t) = \boldsymbol{r}_1 + \boldsymbol{r}_2, \qquad \boldsymbol{r}_1 = \boldsymbol{r}_1(t_1), \qquad \boldsymbol{r}_2 = \boldsymbol{r}_2(t_2)$$
$$\text{with} \qquad t = t_1 + t_2, \qquad t, t_1, t_2 \text{ are fixed times.}$$

Then the mean square displacement is given by

$$\left\langle \boldsymbol{r}^2(t) \right\rangle = \left\langle (\boldsymbol{r}_1 + \boldsymbol{r}_2)^2 \right\rangle = \left\langle \boldsymbol{r}_1^2 \right\rangle + \left\langle \boldsymbol{r}_2^2 \right\rangle + 2 \left\langle \boldsymbol{r}_1 \cdot \boldsymbol{r}_2 \right\rangle . \tag{19.17}$$

With (19.14) for normal diffusion, (19.17) yields

$$\left\langle \boldsymbol{r}^2(t) \right\rangle = 2dD(t_1 + t_2) + 2 \left\langle \boldsymbol{r}_1 \cdot \boldsymbol{r}_2 \right\rangle .$$

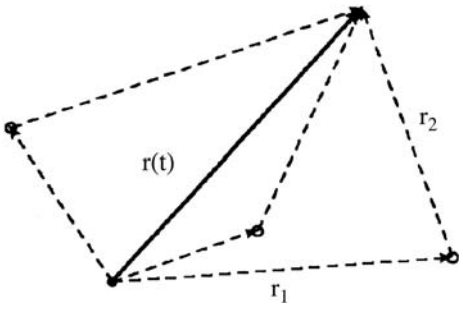

Fig. 19.6. Displacements for the explanation of anticorrelation during anomalous diffusion.

On the other hand, $\langle \boldsymbol{r}^2(t) \rangle = 2dDt$ which – since $t = t_1 + t_2$ – is in agreement with the absence of correlations (i.e., $K(t_1, t_2) \equiv \langle \boldsymbol{r}_1 \cdot \boldsymbol{r}_2 \rangle = 0$) between the increments $\boldsymbol{r}_1$ and $\boldsymbol{r}_2$, respectively.

In contrast, for anomalous diffusion with (19.16) one obtains

$$t^{\kappa} = t_1^{\kappa} + t_2^{\kappa} + 2K(t_1, t_2), \tag{19.18}$$

which proves that the correlation function $K(t_1, t_2)$ is non-zero and, for $\kappa < 1$, negative:

$$K(t_1, t_2) < 0 \quad \text{for} \quad \kappa < 1. \tag{19.19}$$

Equation (19.19) quantifies the phenomenon of "anticorrelation" and also provides a physical interpretation (Fig. 19.6): The diffusing particle is walking preferentially in the "backward" direction with an (averaged) angle larger than $\pi/2$ between the last two steps. Thus the diffusion is slowed down and one speaks of subdiffusive behaviour. The quantity

$$d_{\mathrm{w}} = 2/\kappa \tag{19.20}$$

is called the walk dimension as it describes the distribution of trajectories the random walker may take. One has

$$\kappa = \frac{2}{d_{\mathrm{w}}} \leq 1, \quad 2 \leq d_{\mathrm{w}} \leq 6. \tag{19.21}$$

The limiting case $d_{\mathrm{w}} = 2$ corresponds to normal diffusion: $\kappa = 1$.

Closely related to the anomalous walk dimension in a fractal is the observation of an anomalous decay

$$P(\mathbf{0}, t|\mathbf{0}, 0) \sim t^{-\tilde{d}/2}. \tag{19.22}$$

of the return probability (19.13). It is remarkable that $\tilde{d} \neq \bar{d}$. In fact, (19.22) *defines* a new dynamical dimension, the so-called spectral dimension $\tilde{d}$, governing the dynamics of fractal systems to a large extent (though one should be aware of exceptions [20]). Often one has $\tilde{d} \approx 4/3$ [21–23].

19.3 Stochastic Theory of Diffusion on Fractals

The aim of a more detailed stochastic theory of dynamic processes in fractal systems is twofold,

- to furnish methods for the analytical or numerical calculation of dynamical dimensions, mean square displacements, reaction velocities and other quantities,
- to provide a deeper understanding of dynamic processes in fractals.

Given the scale invariance both of the fractal and of the trajectory of the diffusing particle (see below) the natural choice of approach is the use of scaling relations, and, for more detailed study, the renormalization group formalism. The central idea behind all scaling approaches and renormalization schemes is the study of quantities of interest under a repeated rescaling of space and time. Renormalization can be implemented in many different ways which we cannot review here in this brief survey in any detail. We only point out some of the relevant literature for further reading.

A main problem is the evaluation of the propagator $P(\boldsymbol{r}, t|\boldsymbol{r}_0, t_0)$ which no longer satisfies the simple equation (19.11), and of quantities derived from it, in particular, the mean square displacement (19.16) and the return probability (19.22). There exist several analytical methods [5,7,9] (see also Chap. 18) which make use of either

- the simple random walk (RW) of one diffusing particle. This particle jumps in fixed time steps to neighbouring lattice sites and thus accomplishes a Markovian process,
- or the continuous time random walk (CTRW), the diffusing particle jumps at arbitrary times to neighbouring sites and generally performs a non-Markovian process (technically a semi-Markovian process) which shows some type of memory.

For simulation purposes the most transparent way to study the properties of diffusion in fractals is the simple (discrete-time) random walk. This is a legitimate approach to obtaining more general results because usually power law relations such as those discussed above are universal reflecting the properties of large classes of systems rather than the properties of only the specific model under investigation. In the basic relations (19.16), (19.22) the parameter t is then understood as a large integer number, representing the number of steps a random walker has taken.

There are two related formalisms for the analytical investigation of CTRW, namely the master equation method [5, 7] and the propagator formalism [7, 9].

The basic quantity of the propagator formalism is the waiting time distribution (probability density) $w(t)$ (another widely used symbol is $\psi(t)$). The

waiting time is defined as the time which a particle spends at a definite site until the next jump. For the special case of an exponential distribution

$$w(t) = \alpha \mathrm{e}^{-\alpha\, t}, \tag{19.23}$$

where $1/\alpha = \langle t \rangle$ is the mean waiting time, the total process (in time) becomes a Poisson process which is Markovian.

Generally, the propagator $P(\boldsymbol{r}, t|\boldsymbol{r}_0, t_0)$ is given by the summation of waiting time distributions up to the finite time t, more precisely by the convolution product (power)

$$P(t) = w(t)^{*k}, \quad k = 1, 2, \ldots . \tag{19.24}$$

After Laplace transformation in time a convenient formalism emerges [9]. A dynamic real-space renormalization procedure then yields the walk dimension d_w (19.20) as well as $P(\boldsymbol{r}, t|\boldsymbol{r}_0, t_0)$ [9, 18, 21]. The walk dimension, e. g. of the Sierpiński gasket, is $d_\mathrm{w} = \ln 5/\ln 2 > 2$; its spectral dimension is $\tilde{d} = \ln 9/\ln 5 < 2$. These quantities may also be derived using renormalization within the master equation approach [22]. Using renormalization techniques the spectral dimensions for a variety of lattices have been calculated [23].

The CTRW formalism can be generalized by including a probability distribution of random flying times of the diffusing particle considered; this supplies a generalized non-Markovian master equation and the equivalent general propagator formalism [19]. Other theoretical possibilities are furnished by the fractional calculus (with the application of differential quotients and integrals of fractional order) [9, 24]. The differential equations of diffusion, i .e . the extensions of the Fick equation (19.7) or (19.11), are more complicated and no longer universal; their analytical form depends on the fractal type.

19.4 Anomalous Diffusion: Dynamical Dimensions

Anomalous diffusion can be conveniently described by use of dynamical dimensions which only in part imply a geometrical meaning. Simple scaling laws already give valuable insights into their significance and interrelations, without the necessity of employing the full renormalization group machinery.

The return probability for normal diffusion is connected with the propagator formula (19.13). Generalizing (19.13) we have introduced the spectral dimension $\tilde{d}$ (19.22) (another common symbol: d_s) of anomalous diffusion. Another definition of the spectral dimension is possible on the basis of the Debye theory of atomic vibrations in a crystalline monatomic solid. The vibrational spectrum (hence the name "spectral dimension") is determined by the vibrational density of states

$$\begin{aligned} &\varrho(\omega) \sim \omega^{d-1} && \text{for normal solids } (d = 2, 3, 4, \ldots) \\ &\varrho(\omega) \sim \omega^{\tilde{d}-1} && \text{for fractals,} \end{aligned} \tag{19.25}$$

i. e. for prefractals whose vertices (lattice sites) are occupied by vibrating atoms. Both definitions (19.22) and (19.25) yield the same spectral dimension [5].

A second important dynamical dimension is the walk dimension d_{w} (19.20) for the mean square displacement. Since the walk dimension describes the typical region explored by the random walker after some time t one defines a diffusion length $l \equiv l(t)$ by means of

$$\left\langle \boldsymbol{r}^2(t) \right\rangle = l^2. \tag{19.26}$$

Then (19.20) can be given the form

$$t \sim l^{d_{\mathrm{w}}}. \tag{19.27}$$

The time t is proportional to the contour length of the trajectory of the diffusing particle. In lattice language this corresponds to the number of steps the random walker has taken. Considering the trajectory itself as a stochastic fractal, the contour length is also proportional to the mass of the fractal and (19.27) becomes a special case of the general formula (19.2).

Therefore, in most cases the walk dimension d_{w} is identical to the geometrical fractal dimension $\bar{d}$ which can be assigned to the single-particle trajectory of the diffusion process considered as Wiener process or generalized Wiener process. The Wiener theory of normal diffusion describes the usual Brownian motion discovered nearly 200 years ago. The corresponding trajectory is schematically represented in Fig. 19.7. It is the simplest possible rigorous mathematical theory of a (continuous) Markovian process (i. e. a process without memory) governing normal diffusion. Nevertheless, the particle trajectory is a very complicated curve, filling a (twisted) plane essentially densely and being characterized by a dimension $\bar{d} = 2 = d_{\mathrm{w}}$. This curve is everywhere continuous, but nowhere differentiable. These are typical features of a fractal which in this case is a self-affine structure. This can be seen from (19.27): The particle trajectory remains (on average) invariant under the anisotropic scaling $\boldsymbol{r} \to b\boldsymbol{r}$, $t \to b^{d_{\mathrm{w}}} t$ in the embedding $(\boldsymbol{r}, t)$ space. This dynamical scale invariance with $d_{\mathrm{w}} = 2$ shows up also in the propagator (19.13). For hindered diffusion one gets $\bar{d} = d_{\mathrm{w}} > 2$, that means that the particle trajectory is even more densely packed. There are, however, also exceptions of the rule $d_{\mathrm{w}} = \bar{d}$ [12].

Since the trajectory of a Brownian particle itself defines a fractal the theory of diffusion on fractals has to deal with understanding the impact of an underlying fractal space on the statistical properties of curves which are already (self-affine, dynamical) fractals in normal (Euclidean) space. As a general relation between the three dimensions $\bar{d}, \tilde{d}, d_{\mathrm{w}}$ one has

$$\kappa = \frac{2}{d_{\mathrm{w}}} = \frac{\tilde{d}}{\bar{d}}. \tag{19.28}$$

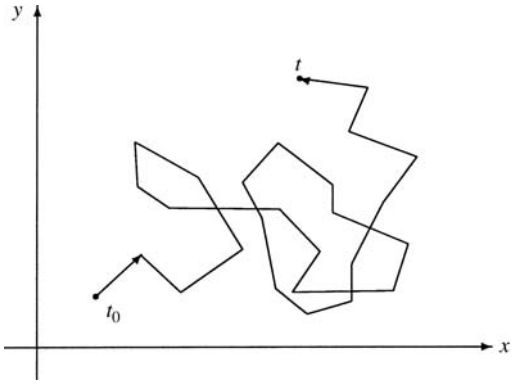

Fig. 19.7. Wiener trajectory of normal diffusion, coarse grained.

Here $\bar{d}$ denotes the fractal dimension of the system considered (not of the particle trajectory). For a common (Euclidean) system one has $\tilde{d} = \bar{d} = d$, $d_{\mathrm{w}} = 2$. A fractal system is characterized by $\kappa < 1$, i. e. $\tilde{d} < \bar{d}$.

A proof of the basic relation (19.28) can be given by the following scaling argument. It is a typical example of the methodology of fractal science. With the definition (19.26) of the diffusion length l one has

$$l = l(t) \sim t^{1/d_{\mathrm{w}}}. \tag{19.29}$$

The volume visited by a particle on the average up to the time t is given by

$$V(t) \sim l^{\bar{d}} \sim t^{\bar{d}/d_{\mathrm{w}}}. \tag{19.30}$$

The probability (density) to find the particle at time t at any definite place within the fractal, e. g. at the origin, hence follows as

$$P(0,t) \sim \frac{1}{V(t)} \sim t^{-\bar{d}/d_{\mathrm{w}}}\,. \tag{19.31}$$

On the other hand, according to (19.22) one has

$$P(0,t) \sim t^{-\tilde{d}/2}. \tag{19.32}$$

The comparison of (19.31) and (19.32) yields (19.28). This proof is essentially rigorous. Similar scaling arguments may also be employed for other transport processes, e.g., electronic transport [5, 13].

An important quantity intimately connected with the return probability is the number $S(t)$ of *different* locations in space that the diffusing particle has visited after time t. Here a "location" means some small volume element of the order of the particle size. One may therefore think of the (continuous) space as being divided in a lattice with a lattice constant equal to the particle diameter and view the random motion as a hopping process between these sites as explained in detail in Chap. 18. In d-dimensional Euclidean space

(19.30) reads $V(t) \sim t^{d/2}$. On the other hand, the number of jumps $N(t)$ made after time t is proportional to t. Therefore the mean time spent on each site is given by the ratio

$$V(t)/N(t) \sim t^{1-d/2}.$$

In more than two dimensions this mean time decreases with increasing time. This implies that the probability that a random walker ever returns to a given site tends to zero as t becomes large and one speaks of a non-recurrent random walk. Hence the number $S(t)$ of different visited sites is just proportional to $N(t)$ and therefore increases linearly in time. On the other hand, for $d < 2$ the mean time spent at each site diverges and the return probability approaches 1; the random walk is recurrent. In this case $S(t) \sim t^{d/2}$ is proportional to the explored volume $V(t)$. In the borderline case of two dimensions there is a logarithmic correction to the asymptotic law $S \sim t$. For recurrent walks on fractal objects these considerations apply accordingly. Using (19.30) one finds

$$S(t) \sim t^{\bar{d}/d_{\mathrm{w}}} \tag{19.33}$$

which may be written in terms of the spectral dimension as $S(t) \sim t^{\tilde{d}/2}$. For $\tilde{d} > 2$ the random walk on the fractal is non-recurrent. In this case $S(t) \sim t$.

19.5 Anomalous Diffusion and Chemical Kinetics

An important field of application of diffusion on fractals are diffusion-limited reactions, e.g., on the fractal surface of catalysts. Usually chemical reactions are studied in terms of parameters which concern the electronic structure of the molecules or atoms involved in that reaction, the environment in which the reactions take place seems irrelevant. This treatment then leads to rate equations with reaction constants that depend on those microscopic molecular parameters. Probably the simplest example is the bimolecular reaction

$$\mathrm{A} + \mathrm{A} \xrightarrow{k} \mathrm{C}$$

where A are the reactants and C is an inert reaction product. This is a reaction where two A particles are "annihilated" when they meet inside some effective reaction volume, with a reaction constant k. In the absence of a back reaction $\mathrm{C} \to 2\mathrm{A}$ all A-particles will eventually disappear. We point out that such a reaction mechanism need not necessarily be of chemical nature where new chemical bonds are formed between reactants. Also physical processes such as laser-induced exciton hopping can be described in terms of such processes [31]. In this case the "particles" are excitons moving e.g. along a polymer chain. The reaction corresponds to the decay upon encounter under the emission of light (playing the part of the inert reaction product).

Since two A-particles are necessary for an annihilation to take place the rate equation describing the temporal change of the concentration C of A-particle simply reads

$$\dot{c} = -kc^2. \tag{19.34}$$

This is the well-known law of mass action. Equation (19.34) is easy to integrate, with the result

$$c(t) = \frac{c_0}{1 + c_0 kt}$$

for an initial concentration c_0 of A-particles. At long times the concentration decays algebraically

$$c = 1/(kt) \tag{19.35}$$

and is quite remarkably independent of the initial concentration. The same reasoning may be applied to a reaction of the type $\mathrm{A} + \mathrm{A} \rightarrow \mathrm{A} + \mathrm{C}$ or even to mixed reactions where either both particles disappear or only one, with some probability. Various models for these systems can be shown to be exactly equivalent by a mathematical transformation of the observables [26, 29, 32].

The assumptions regarding the spatial distribution of A-particles which lead to (19.34) are two-fold: Firstly, one assumes the reaction to take place in a homogeneous environment so that for a homogeneous initial distribution of A-particles the particle concentration would remain space-independent for all times. Secondly – and this is more subtle – one assumes that at each instant of time the probability of finding a second A-particle inside the reaction volume of the first is proportional to the overall probability of finding particles, i.e., to the concentration. This is a mean-field assumption which would be valid if *correlations* between particle positions could be ignored.

Of course, the validity of such an assumption is somewhat questionable, particularly if one thinks of reacting particles diffusing e.g. on the surface of a catalyst. If a reaction has just taken place the reaction volume is empty rather than filled with a probability proportional to c. Only after surrounding particles have had sufficient time to diffuse and thus restore an uncorrelated filling of space, the mean-field assumption will again be valid and further annihilations can take place according to (19.34). Hence the mean-field treatment of an intrinsically diffusion-limited reaction is justified only if the reacting particles are stirred sufficiently quickly (so that the reaction is not diffusion-limited anymore) or if diffusion is sufficiently efficient to maintain an essentially uncorrelated state of the system at all times.

It was already realized by Smoluchowski [25] that in low-dimensional reaction media the mean field law (19.34) is actually not valid. Here diffusive mixing is ineffective and large correlations persist for all times. Instead of assuming that there is a second reacting particle with a probability proportional to c one has to consider the flux of particles from the environment into the reaction volume of the first particle. This approach leads to an effective reaction "constant" $k(t)$ determined not only by microscopic molecular parameters but also by the process of diffusion as described by Fick's law

(19.8). In one space dimension calculating the flux leads to a decaying reaction parameter $k(t) \sim 1/\sqrt{t}$. Inserting this into (19.34) leads to an anomalous decay

$$c \sim 1/\sqrt{t} \tag{19.36}$$

of the particle density. This demonstrates that the effect of correlations is particularly pronounced in low dimensions which has been verified experimentally in the last two decades (for a review see [31]). Exact results derived from lattice models (reviewed in [28]) show that the time-dependent concentration becomes independent of the initial concentration, as in mean field theory. Exactly solvable lattice models allow not only for the explicit calculation of the concentration. Also density profiles for spatially inhomogeneous initial distributions and correlations can be calculated. Thus one has a very detailed knowledge of the properties of the reaction $\mathrm{A} + \mathrm{A} \to \mathrm{C}$ and some other simple reactions which goes far beyond the fluctuation-corrected mean-field theory of Smoluchowski.

According to Smoluchowski's theory the validity of the asymptotic mean field law depends on the dimensionality of the reaction medium because of the properties of the particle flux. In two dimensions one has a logarithmic correction to (19.35), whereas in dimensions higher than two mean field theory remains valid. For other reactions, e.g., the bimolecular Langmuir-Hinshelwood reaction $\mathrm{A} + \mathrm{B} \to \mathrm{C}$, the critical dimension above which mean-field theory is valid is equal to four for initially equal concentrations of randomly distributed A and B particles. Below four dimensions one has $c \sim t^{-d/4}$. Hence already in ordinary three-dimensional reaction environments mean-field theory fails, in this case due to concentration fluctuations inside pure A and B domains which build up as the reaction goes on. This is confirmed by renormalization group studies [30].

The anomalous behaviour of diffusion-limited reactions in low-dimensional systems naturally leads to the question what happens in a fractal where the dimension is not integer and, moreover, the environment is not homogeneous anymore so that the flux cannot be calculated simply using Fick's law. It comes as no surprise that as a result of anomalous diffusion, chemical reactions in fractal media (heterogeneous reactions, heterogeneous catalysis) show strange behaviour [2, 14–17]. Also in the presence of disorder, diffusion can become anomalous (Chap. 18 and 22) and the decay law (19.36) changes [26, 27].

Rather than calculating the flux it is convenient to consider $S(t)$, the number of different sites visited, since the change of this quantity in time is proportional to the effective reaction constant,

$$k \sim \frac{\mathrm{d}S(t)}{\mathrm{d}t}. \tag{19.37}$$

The quantity $S(t)$ has been discussed in Sect. 19.4 in some detail. Its connection to the flux can be understood qualitatively by noting that the particle

flux entering the Smoluchowski approach is proportional to the probability flux of finding a particle. This probability flux, however, is proportional to the change in the number of sites visited because of the recurrence properties of the underlying random walk. For a fractal one may then use (19.33) together with (19.34) to obtain an effective rate equation for the diffusion-limited annihilation process on a fractal. One then finds for long times

$$c \sim t^{-\bar{d}/d_{\mathrm{w}}} \tag{19.38}$$

for spectral dimensions below 2. The mechanism for this fractal correction to mean field behaviour is the same as in a low-dimensional Euclidean medium. As time passes particles tend to be more isolated than they would be in an uncorrelated random ensemble, i. e. particle positions become increasingly anticorrelated. Diffusion under recurrence conditions is too inefficient to wash out those anticorrelations since particles are not sufficiently likely to explore a large volume in between reactions.

The decrease of the reaction rate has a striking effect when comparing to originally identical reaction vessels, one of which is stirred very quickly (thus destroying anticorrelations) after some time. From this point on the reaction in the undisturbed vessel will proceed more slowly. In a rate-controlled reaction such stirring would have no effect on the reaction velocity. Similar considerations may be adapted to the heteronuclear Langmuir-Hinshelwood reaction $\mathrm{A} + \mathrm{B} \rightarrow \mathrm{C}$.

19.6 Conclusion

The importance and usefulness of the fractal concept can be summarized as follows:

1. Fractals possess mathematically strange properties and imply very interesting novel physical phenomena.
2. Fractals are suitable to model complicated real systems.
3. Fractals can characterize disordered systems by only a few structural quantities, viz. geometric fractal dimension and dynamical dimensions (dynamical exponents).
4. Fractals allow for the application of rigorous scaling and renormalization methods without approximations.

For the study of random walks (which are stochastic fractals by themselves, even without underlying fractal medium) not only the fractal dimension $\bar{d}$ of the medium is relevant. The distribution of possible pathways gives rise to an independent exponent, the walk exponent d_{w}, describing the statistical properties of trajectories of diffusing particles. In the presence of interactions, e.g. chemical reactions, correlations between particle positions

are a new determining factor for the behaviour of diffusion-limited chemical reactions. However, for some simple paradigmatic processes the origin of these correlations (in fact, anticorrelations) can be traced back to the statistical properties of single random walks. Anomalous decay laws result from inefficient diffusive mixing in recurrent random walks and hence can be found in fractals as well as in low-dimensional Euclidean media. An entirely unexplored field are nonequilibrium interacting particle systems undergoing biased diffusion on a fractal under the action of a driving force. One-dimensional (Euclidean) lattice models for such systems are reasonably well-understood [28, 33]. However, even basic questions such as the behaviour of the stationary particle current as a function of particle density are unanswered for fractals.

Notation

c	particle concentration
d	integer (Euclidean) dimension
d_{E}	(Euclidean) embedding dimension
$\bar{d}$	geometric fractal dimension, Mandelbrot dimension (also Hausdorff dimension)
$\tilde{d}$	spectral dimension
d_{w}	walk dimension
D	diffusion coefficient
h	heterogeneity exponent
k	chemical rate constant
l	diffusion length
$n = n(\boldsymbol{r}, t)$	particle number density
N	total number of particles in a system
$P(\boldsymbol{r}, t) = P(\boldsymbol{r}, t\|\boldsymbol{r}_0, t_0)$	propagator
r	reaction order
$\boldsymbol{r} = (x, y, z)$	coordinate vector
$S(t)$	number of different sites visited by a diffusing particle on average up to time t
$V(t)$	volume visited by a diffusing particle on average up to time t
$w(t)$	waiting time distribution
ε	reaction efficiency
κ	diffusion exponent
$\varrho(\omega)$	vibrational density of states

References

1. B.B. Mandelbrot: *The Fractal Geometry of Nature* (Freeman, New York 1983)
2. I.M. Sokolov, J. Klafter, A. Blumen: Phys. Today **55**, 48 (2002)

3. *Fractals in Science*, ed by A. Bunde, S. Havlin (Springer, Berlin Heidelberg New York 1995)
4. M. Schroeder: *Fractals, Chaos, Power Laws* (Freeman, New York 1991)
5. *Fractals and Disordered Systems*, 2nd edn, ed by A. Bunde, S. Havlin (Springer, Berlin Heidelberg New York 1996)
6. H. Spindler, G. Vojta: Z. Chem. **28**, 421 (1988)
7. J.W. Haus, K.W. Kehr: Phys. Rep. **150**, 263 (1987)
8. J. Kärger, D.M. Ruthven: *Diffusion in Zeolites and other Microporous Solids* (Wiley, New York 1992)
9. U. Renner: Stochastische Theorie von Transportprozessen in ungeordneten und fraktalen Systemen. PhD thesis, Universität Leipzig (1993)
10. J. Kärger, G. Vojta: Chem. Phys. Lett. **141**, 411 (1987)
11. J. Kärger, H. Pfeifer, G. Vojta, Phys. Rev. A **37**, 4514 (1988)
12. Ph. de Forcrand, J. Pasche, D. Petritis: J. Phys. A: Math. Gen. **21**, 3771 (1988)
13. U. Renner, G. Vojta. In: *Synergie, Syntropie, Nichtlineare Systeme*, vol 1 (Wissenschaftszentrum Leipzig, 1995) p 35
14. P. Pfeifer: Chimia **39**, 120 (1985)
15. A. Blumen, G.H. Köhler: Proc. R. Soc. London, Ser. A **423**, 189 (1989)
16. R. Kopelman: Science **241**, 1620 (1988)
17. G. Vojta: Materials Science Forum **62**, 743 (1990)
18. C. Van den Broeck: Phys. Rev. Lett. **62**, 1421 (1989)
19. S. Richter, G. Vojta: Physica A **188**, 631 (1992)
20. A. Vojta, G. Vojta, M. Vojta, T. Vojta: J. Phys.: Condens. Matter **7**, L67 (1995)
21. S. Alexander, R. Orbach: J. Phys. (Paris) Lett. **43**, L625 (1982)
22. R. Rammal, G. Toulouse: J. Phys. (Paris) Lett. **44**, L13 (1983)
23. R.A. Guyer: Phys. Rev. A **29**, 2751 (1984); **30**, 1112 (1984)
24. H.E. Roman, P.H. Alemany: J. Phys. A: Gen. Math. **27**, 3407 (1994)
25. M. von Smoluchowski: Z. Phys. Chem. **92**, 129 (1917)
26. G.M. Schütz: Z. Phys. B **104**, 583 (1997)
27. G.M. Schütz, K. Mussawisade: Phys. Rev. E **57**, 2563 (1998)
28. G.M. Schütz. In: *Phase Transitions and Critical Phenomena*, vol 19, ed by C. Domb, J. Lebowitz (Academic Press, London 2000) pp 1–251
29. M. Henkel, E. Orlandini, G.M. Schütz: J. Phys. A **28**, 6335 (1995)
30. B.P. Lee: J. Phys. A **27**, 2633 (1994)
31. *Nonequilibrium Statistical Mechanics in One Dimension*, ed by V. Privman (Cambridge University Press, Cambridge U.K. 1997)
32. H. Simon: J. Phys. A **28**, 6585 (1995)
33. T.M. Liggett: *Stochastic Interacting Systems: Contact, Voter and Exclusion Processes* (Springer, Berlin Heidelberg New York 2000)

20 Ionic Transport in Disordered Materials

Armin Bunde, Wolfgang Dieterich, Philipp Maass, and Martin Meyer

20.1 Introduction

The low-frequency dynamic response of many non-metallic materials is governed by the transport of mobile ions or other charged mobile defects. The classes of such materials include traditional ionic glasses, polymeric and glassy superionic conductors, highly defective crystals or even highly viscous liquids such as glassforming melts. To get an understanding of the microscopic transport mechanism in these materials, a large number of experimental techniques has been applied, among them are tracer experiments (Chap. 1 and [1]), conductivity measurements including impedance spectroscopy (Chap. 21, [2–5]), nuclear magnetic resonance (NMR) relaxation (Chap. 9, [6–10]), quasielastic neutron scattering (Chaps. 2, 3 and 13, [11, 12]), internal friction and ultrasonic absorption measurements (Brillouin scattering) (Chap. 11, [13, 14]). In all these experiments the measured quantities show characteristic deviations from the standard behavior that one would expect for a purely random motion of the mobile ions.

For example, the dynamic conductivity $\hat{\sigma}(\omega)$ in disordered crystalline and glassy ionic conductors exhibits, for fixed temperature T, a dc-plateau at low frequencies (below some crossover frequency $1/\tau_\sigma$), and follows an approximate power law behavior at larger frequencies [15],

$$\hat{\sigma}(\omega) \sim \begin{cases} \sigma_{\rm dc}\,, & \omega\tau_\sigma \ll 1, \\ ({\rm i}\omega)^{n_\sigma}\,, & \omega\tau_\sigma \gg 1. \end{cases} \tag{20.1}$$

The dc conductivity $\sigma_{\rm dc}$ usually shows an Arrhenius behavior below the glass transition temperature,

$$\sigma_{\rm dc}T = A_\sigma \exp(-E_\sigma/k_{\rm B}T)\,, \tag{20.2}$$

and also the crossover frequency τ_σ^{-1} is thermally activated with the same activation energy E_σ. The exponent $n_\sigma > 0$ tends to increase, if the temperature is lowered or if the frequency is increased by several orders of magnitude. From standard random walk theory on a lattice with equivalent sites one would expect no dispersion to occur, i.e. $n_\sigma = 0$ (see Sect. 20.2.2). The overall behaviour (20.1) is not restricted to ionically conducting solids but

occurs also in disordered electronic conductors such as amorphous semiconductors, electronic conducting polymers and disordered polaronic conductors. The widespread occurrence of such similar low-frequency dielectric behavior in all disordered solids was first pointed out by Jonscher [16] and is known as the "universal dielectric response".

A second, "universal" type of response in disordered ionic systems occurs at even higher frequencies, $\omega > \omega_{\rm NCL} \gg \tau_\sigma^{-1}$. Going at ambient temperatures to the Gigahertz regime, the real part of the conductivity increases nearly linearly with frequency,

$$\mathrm{Re}\,\hat{\sigma}(\omega) \sim \omega; \quad \omega > \omega_{\rm NCL}. \tag{20.3}$$

This is equivalent with a frequency-independent dielectric loss, $\chi''(\omega) \simeq$ const, and is thus known as "nearly constant loss" (NCL) response [17–19]. Its temperature dependence is much weaker than implied by (20.2) and (20.1) with the consequence that at low temperatures the NCL response dominates the spectrum in the experimentally accessible frequency-range.

In some glassy fast ion conductors it was found that the dc-conductivity shows strong deviations from a simple Arrhenius law even below the glass transition temperature [20, 21]: The values of $\sigma_{\rm dc}$ at ambient temperatures are significantly smaller than expected when extrapolating the Arrhenius law valid at low temperatures T. We note that a non-Arrhenius behaviour was found earlier in ion conducting glasses but disappeared after annealing [22].

Strongly non-Arrhenius diffusion of a different type occurs in yet another class of amorphous materials, namely ion conducting polymers above their glass transition temperature [23]. Certain chain polymers carry polar groups in their repeat unit and are therefore capable of dissolving salts. When temperature is lowered, the polymer chains tend to freeze. In contrast to (20.2), the strong coupling of ions to the network degrees of freedom generally leads to Vogel-Fulcher-Tammann (VFT)-type behavior [24] of the conductivity,

$$\sigma_{\rm dc} T \propto \exp(-E/k_{\rm B}(T - T_{\rm VFT})) \tag{20.4}$$

Here E is an energy parameter and $T_{\rm VFT}$ the VFT-temperature, commonly referred to as "ideal glass transition temperature". Much effort is being spent to explore transport mechanisms in these complex materials, and to optimize their electrical conduction properties with respect to their use in electrochemical devices.

Apart from conduction and dielectric measurements, the perhaps most common experimental technique to probe ionic motion in disordered media is nuclear magnetic resonance (see Chap. 9). The behavior of the diffusion-induced spin-lattice relaxation (SLR) rate $1/T_1(\omega_{\rm L}, T)$, as a function of temperature T and Larmor frequency $\omega_{\rm L}$, can be summarized as follows:

$$\frac{1}{T_1}(\omega_{\rm L}, T) \sim \begin{cases} \exp(E_1^{\rm SLR}/k_{\rm B}T)\,, & T \gg T_{\max}(\omega_{\rm L}), \\ \omega_{\rm L}^{n_{\rm SLR}-2} \exp(-E_2^{\rm SLR}/k_{\rm B}T)\,, & T \ll T_{\max}(\omega_{\rm L}), \end{cases} \tag{20.5}$$

with an exponent $n_{\mathrm{SLR}} \geq 0$. In an Arrhenius plot, $1/T_1$ shows a maximum at $1/T_{\max}(\omega_{\mathrm{L}})$, where the temperature $T_{\max}(\omega_{\mathrm{L}})$ decreases with decreasing frequency. Since generally $E_1^{\mathrm{SLR}} > E_2^{\mathrm{SLR}}$, the curve is asymmetric in shape. In contrast to this overall behavior, the standard Bloembergen-Purcell-Pound (BPP) theory [25] predicts a symmetric maximum of $1/T_1$ in the Arrhenius plot with $n_{\mathrm{SLR}} = 0$ (see Sect. 20.2.4).

Dynamic scattering of neutrons is another technique to investigate the ionic transport. In many structurally disordered ionic conductors broad quasielastic components in the scattering spectra are observed. The line shapes of these components often deviate from simple Lorentzians, which are expected in the simple random walk case (see Sect. 20.2.3). A similar behavior has been found in mechanical loss spectroscopy [13, 14]. The spectra are usually much broader than simple Debye spectra, reflecting an inherent non-exponential nature of the ionic relaxation processes.

From a theoretical point of view, the ionic transport in solids is a very complex phenomenon (for a recent review, see [26]) and rigorous solutions are not available. For an ordered host lattice a mode-coupling theory has been developed to study the effect of Coulomb interactions between the mobile ions [27]. One fundamental consequence of the long-range nature of Coulomb forces is the non-analytic dependence of the tracer diffusion coefficient on the ion concentration c in dilute systems, $c \to 0$. To describe the experimental situation for arbitrary c and arbitrary frequencies, however, it has turned out that also the structural disorder plays an essential role [28–30]. Various phenomenological and semi-microscopic approaches have been successfully applied. Prominent examples are the coupling scheme proposed by Ngai [31], the jump relaxation model pioneered by Funke [11] that recently was extended by means of the concept of mismatch and relaxation, see Chap. 21, and the diffusion-controlled relaxation model elaborated by Elliott and Owens [32]. Attempts have been made to map the dynamics of the many body problem onto the dynamics of a single particle moving in a complex energy landscape (see Chap. 18, [33–35]).

For a more microscopic description of the ionic transport one is dependent upon numerical investigations. Important microscopic insight emerged from recent molecular dynamics studies [36–38]. In this chapter we are mainly concerned with the results of semi-microscopic Monte Carlo studies [28–30, 39–41], where the effects of long-range Coulomb interactions between the mobile ions and structural disorder in the host lattice are investigated in a systematic way. The chapter is organized as follows. In Sect. 20.2 the basic dynamic quantities under study are defined and discussed with respect to their standard behaviour, obtained from simple random walk theory. In Sects. 20.3 and 20.4 we introduce different versions of the Coulomb lattice gas model pertaining to glasses, and represent computed relaxation spectra. In Sect. 20.5 the origin of the non-Arrhenius behavior seen in fast conducting glasses is investigated. Interacting Coulombic traps are considered in Sect.

20.6 as a mechanism that can explain the NCL response. Peculiarities in the transport properties associated with compositional changes in ion conducting glasses are discussed in Sect. 20.7. In Sect. 20.8 we turn to polymer electrolytes and present calculations of their typical transport properties as a function of temperature, pressure and salt content. Sect. 20.9 finally concludes the paper with a brief summary and discussion. For ionic transport in systems with disorder on macroscopic length scales we refer to Chap. 22.

20.2 Basic Quantities

In this section we discuss the standard behavior of the basic quantities of interest. We assume that the mobile particles perform simple random walks on a d-dimensional (cubic) lattice with lattice constant a. The lattice has length L and the particle density is $\rho = N/L^d$, where N is the number of particles. We assume that the mean residence time τ_0 between two jumps of a particle is $\tau_0 = \tau_\infty \exp(V_0/k_\mathrm{B}T)$, where τ_∞ is a rattling time and V_0 is the structural energy barrier between two nearest neighboring lattice sites.

20.2.1 Tracer Diffusion

The tracer diffusion coefficient D is related to the long time limit of the mean square displacement $\langle r^2(t)\rangle$ of a tracer particle, $D = \lim_{t\to\infty}\langle r^2(t)\rangle/2dt$. Experimentally, D can be obtained from the concentration profile of radioactive tracers introduced into the material under investigation (see Chap. 1).

It is convenient to define (in d dimensions) a generalized frequency-dependent tracer diffusion coefficient $\hat{D}(\omega)$ by

$$\hat{D}(\omega) = -\frac{\omega^2}{2d}\lim_{\epsilon\to+0}\int_0^\infty \langle r^2(t)\rangle \mathrm{e}^{\mathrm{i}\omega t-\epsilon t}\mathrm{d}t, \tag{20.6}$$

which for $\omega \to 0$ approaches D.

If the particles perform simple random walks, subsequent jumps of a tracer particle are uncorrelated and the mean square displacement increases linearly with time according to $\langle r^2(t)\rangle = a^2t/\tau_0$, yielding $\hat{D}(\omega) = D = a^2/2d\tau_0$, independent of frequency. If the particle hops are correlated, $\langle r^2(t)\rangle$ only increases linearly for very small and very large times, and one can define a tracer correlation factor f_tr as the ratio of the long-time diffusion coefficient D and the short-time diffusion coefficient D_st by $f_\mathrm{tr} \equiv D/D_\mathrm{st}$. The deviation of f_tr from unity can be regarded as a measure of the strength of the correlations. If a particle prefers to jump back to the site where it came from (backward correlations) $f_\mathrm{tr} < 1$; if it prefers to jump forward (forward correlations), we have $f_\mathrm{tr} > 1$.

20.2.2 Dynamic Conductivity

The dynamic conductivity $\hat{\sigma}(\omega)$ can be expressed by the auto-correlation function $\langle \boldsymbol{j}(t) \cdot \boldsymbol{j}(0) \rangle$ of the current density in the absence of the electric field (Kubo formula, [42]):

$$\hat{\sigma}(\omega) = \frac{L^d}{dk_\mathrm{B}T} \lim_{\epsilon \to +0} \int_0^\infty \langle \boldsymbol{j}(t) \cdot \boldsymbol{j}(0) \rangle \mathrm{e}^{\mathrm{i}\omega t - \epsilon t} \mathrm{d}t. \tag{20.7}$$

The brackets $\langle\rangle$ denote a thermal average and the current density is given by the sum over the particle velocities, $\boldsymbol{j}(t) = (e\rho/N) \sum_{i=1}^{N} \boldsymbol{v}_i(t)$, where e is the charge of the particles. (For non-interacting particles the charge e means only a formal coupling to the external electric field.) Separating the velocity autocorrelation function $\langle \boldsymbol{v}_i(t) \cdot \boldsymbol{v}_i(0) \rangle \equiv \langle \boldsymbol{v}(t) \cdot \boldsymbol{v}(0) \rangle$ from the cross-correlation part, we can write

$$\langle \boldsymbol{j}(t) \cdot \boldsymbol{j}(0) \rangle = \frac{\rho e^2}{L^d} \left[\langle \boldsymbol{v}(t) \cdot \boldsymbol{v}(0) \rangle + \frac{1}{N} \sum_{i \neq j}^{N} \langle \boldsymbol{v}_i(t) \cdot \boldsymbol{v}_j(0) \rangle \right]. \tag{20.8}$$

In the absence of interactions between the mobile particles, the cross terms in (20.8) vanish, $\langle \boldsymbol{v}_i(t) \cdot \boldsymbol{v}_j(0) \rangle = 0$ for $i \neq j$. Using that together with (20.6), (20.7) and the relation $2\langle \boldsymbol{v}(t) \cdot \boldsymbol{v}(0) \rangle = \mathrm{d}^2 \langle r^2(t) \rangle / \mathrm{d}t^2$ one obtains the Nernst-Einstein relation for non-interacting particles,

$$\hat{\sigma}(\omega) = \frac{\rho e^2}{k_\mathrm{B}T} \hat{D}(\omega). \tag{20.9}$$

For the simple random walk case, this yields $\hat{\sigma}(\omega) = \rho e^2 a^2 / 2dk_\mathrm{B}T\tau_0$ independent of ω. In interacting systems, on the other hand, cross-correlations are non-negligible. Equation (20.9) is then generalized to

$$\hat{\sigma}(\omega) = \frac{\rho e^2}{k_\mathrm{B}T \hat{H}_\mathrm{R}(\omega)} \hat{D}(\omega) \tag{20.10}$$

where $\hat{H}_\mathrm{R}(\omega)$ is the complex Haven ratio. For frequencies ω much larger than the hopping rate the cross-correlations vanish even if the particles interact and $\hat{H}_\mathrm{R}(\omega)$ approaches one. In the limit $\omega \to 0$, $\hat{H}_\mathrm{R}(\omega)$ approaches the ordinary Haven ratio $H_\mathrm{R} = \rho e^2 D / k_\mathrm{B}T\sigma_\mathrm{dc}$.

20.2.3 Probability Distribution and Incoherent Neutron Scattering

For a more detailed description of the diffusion process, one considers the distribution function $P(\boldsymbol{r}, t)$, also called the "propagator" (see e.g. Chaps. 10, 19 and 23), which denotes the probability for an ion to be on a (lattice) site

$\boldsymbol{r}$ at time t, if it started at $t = 0$ from site $\mathbf{0}$. The Fourier transform of $P(\boldsymbol{r}, t)$ is the incoherent structure factor $S_{\mathrm{inc}}(\boldsymbol{k}, \omega)$ (see Chaps. 3, 13 and 23),

$$S_{\mathrm{inc}}(\boldsymbol{k}, \omega) = \frac{1}{2\pi} \int \mathrm{d}^3 r \int \mathrm{d}t\, P(\boldsymbol{r}, t) \mathrm{e}^{-\mathrm{i}(\boldsymbol{k}\cdot\boldsymbol{r} - \omega t)} \equiv \frac{1}{2\pi} \int \mathrm{d}t\, S_{\mathrm{inc}}(\boldsymbol{k}, t) \mathrm{e}^{\mathrm{i}\omega t}, \tag{20.11}$$

which contributes to the differential cross section obtained in scattering experiments.

For simple random walks on a Bravais lattice, the intermediate scattering function $S_{\mathrm{inc}}(\boldsymbol{k}, t)$ decays exponentially

$$S_{\mathrm{inc}}(\boldsymbol{k}, t) = \exp\left(-\Lambda(\boldsymbol{k}) \frac{|t|}{\tau_0}\right), \tag{20.12}$$

with $\Lambda(\boldsymbol{k}) = \sum_{\boldsymbol{d}} (1 - \cos(\boldsymbol{d}\,\boldsymbol{k}))/\nu$, where the sum runs over all nearest-neigbor vectors $\boldsymbol{d}$ and ν is the number of nearest neigbors. Accordingly, $S_{\mathrm{inc}}(\boldsymbol{k}, \omega)$ is a simple Lorentzian with width $\Lambda(\boldsymbol{k})/\tau_0$.

20.2.4 Spin-Lattice Relaxation

In an external static magnetic field $\boldsymbol{B}$, the alignment of the nuclear magnetic moments of the mobile ions gives rise to a total magnetization in the direction of the applied field (see Chap. 9). By a radiofrequency pulse perpendicular to the static field this magnetization can be rotated into the opposite direction. Fluctuating local magnetic and electric fields cause the magnetization to relax into the original direction parallel to the static field $\boldsymbol{B}$ in a characteristic time T_1. The spin-lattice relaxation rate $1/T_1$ depends on both the magnitude of the field $\boldsymbol{B}$ and the temperature T. In the case of ionic conductors mainly two mechanisms give rise to the fluctuating local fields:

(i) The magnetic dipole-dipole interaction between the mobile particles.

(ii) The interaction of the nuclear quadrupole moment of one particle with the electric field gradient of another particle (as far as the ions have nuclear spin larger than 1/2 and the quadrupole moment of the nucleus does not vanish).

According to standard theory (Sects. 9.2 and 9.9 in Chap. 9, [43, 44]), $1/T_1$ is determined by the spectral densities $J^{(1)}(\omega)$ and $J^{(2)}(\omega)$ at $\omega = \omega_{\mathrm{L}}$ and $\omega = 2\omega_{\mathrm{L}}$, respectively,

$$\frac{1}{T_1} = C(J^{(1)}(\omega_{\mathrm{L}}) + J^{(2)}(2\omega_{\mathrm{L}}))\,, \tag{20.13}$$

where $\omega_{\mathrm{L}} = \gamma B$ is the Larmor frequency. The spectral densities are the Fourier transforms of the SLR correlation functions $G^{(q)}(t)$,

$$J^{(q)}(\omega) = \int_{-\infty}^{\infty} G^{(q)}(t) \mathrm{e}^{\mathrm{i}\omega t}\, \mathrm{d}t, \quad q = 1, 2. \tag{20.14}$$

In both cases (i) and (ii) the correlation functions $G^{(q)}(t)$ can be written as [44]

$$G^{(q)}(t) = \frac{1}{N} \sum_{i \neq j}^{N} \langle F_{ij}^{(q)*}(t) F_{ij}^{(q)}(0) \rangle, \tag{20.15}$$

where $F_{ij}^{(q)}(t) = q(8\pi/15)^{1/2} Y_2^q(\Omega_{ij}(t))/r_{ij}^3(t)$ is the local field between the particles i and j. Y_2^q are the spherical harmonics, and Ω_{ij} and r_{ij} are the spherical coordinates of the vector $\boldsymbol{r}_{ij}$ pointing from particle i to particle j, with respect to the magnetic field. The constant C in (20.13) depends on the nuclear properties of the mobile particles, $C = (3/2)\gamma^4 \hbar^2 I(I+1)$ in case (i) and $C = (3/2)(\mathrm{e}^2 Q/\hbar)^2\, I(I+1)/(I(2I-1))^2$ in case (ii). Here γ is the magnetogyric ratio, I the spin and Q the quadrupole moment of the nucleus.

The ansatz $G^{(q)}(t) = G^{(q)}(0)\mathrm{e}^{-t/\tau_0}$, commonly referred to as the BPP ansatz [25], leads to

$$\frac{1}{T_1} = C G^{(1)}(0) \left[\frac{\tau_0}{1 + (\omega_\mathrm{L}\tau_0)^2} + \frac{4\tau_0}{1 + (2\omega_\mathrm{L}\tau_0)^2} \right] \tag{20.16}$$

where we have used $G^{(2)}(0) = 4G^{(1)}(0)$ valid for an isotropic distribution of the ions [43]. In an Arrhenius plot of $\ln 1/T_1$ versus inverse temperature, the curve is symmetric in shape with slopes equal to V_0 and $-V_0$ on the high and low temperature side of the $1/T_1$ maximum, which occurs at $\omega_\mathrm{L}\tau_0 \approx 1$. V_0 is the activation energy. At the low temperature side, $\omega_\mathrm{L}\tau_0 \gg 1$, $1/T_1$ decreases as $\omega_\mathrm{L}^{-2} = (\gamma B)^{-2}$ with increasing field B.

It may be shown [30] that for simple random walks the *asymptotic* decay of $G^{(q)}(t)$ is algebraic rather than exponential. However, for (20.16) to be approximately valid it is sufficient that the correlation functions decay linearly with t for small times and faster than $1/t$ for large times. Since both conditions are satisfied in the simple random walk case (for $d = 3$), the deviations from the exponential decay do not lead to pronounced changes of the standard behavior of $1/T_1$, according to (20.16).

20.3 Ion-Conducting Glasses: Models and Numerical Technique

As discussed in the introduction (Sect 20.1), in most cases strong deviations from the standard behavior are experimentally observed. We will show below that for a more realistic description of the ionic transport that goes beyond the simple random walk case, one has to take into account at least (a) the Coulomb interaction between the mobile charge carriers and (b) the structural disorder of the host system.

In glassy systems the ions cannot enter all regions of the substrate but are confined to diffusion paths with high mobility. Starting from a lattice

gas model allowing nearest-neighbor hops, we thus make only a fraction p of lattice sites accessible for the mobile ions, totally blocking the rest of them. This construction is known as the site percolation model (Chap. 22, [45]). For p well above the percolation threshold p_c ($p_c \cong 0.312$ for the sc lattice), most of the accessible sites belong to the "infinite percolation cluster" (IPC), which connects opposite sides of the lattice. We disregard the small finite clusters of accessible sites in the system and consider as our model for structural disorder only the IPC where all mobile ions exhibit long-range mobility (see Chap. 22 for a sketch of the IPC). This disordered structure of accessible sites is reminiscent to a "connective tissue" or a "crumbled handkerchief", which has been suggested to model diffusion paths in ionic glasses [46]. In the detailed numerical procedure we choose a simple cubic lattice of length L with lattice constant a and use periodic boundary conditions. A fraction $1-p$ ($p > p_c$) of the lattice sites is randomly blocked and the IPC is determined with the help of the Hoshen-Kopelmann algorithm [47].

The simple percolation model is sufficient to explain anomalous features found in the relaxation spectra. However, it cannot explain the non-Arrhenius behaviour observed in some fast ion conductors. In order to take into account the energy scale associated with the disorder present in the diffusion paths itself, we will also study a modified model, where instead of simply blocking sites for the ions, an energy ϵ_i is assigned to each lattice site i drawn from a Gaussian distribution $P(\epsilon)$ with zero mean and variance σ_ϵ^2 (see Chap. 18). The percolative disorder can be regarded as a limiting case, where only two site energies are allowed, one being zero (with probability p) and one being infinite (with probability $1-p$).

In network glasses modified by alkali-oxides or -sulfides the diffusing alkali ions will experience the Coulomb fields arising from immobile counterions. At low doping level, this leads to the picture of well-separated, negatively charged Coulomb traps, fixed at random positions $\boldsymbol{R}$, which temporarily can bind the diffusing cations and thus will have a strong influence on the conduction process. To implement such a mechanism, we assume that cations diffuse on a simple cubic lattice where a fraction $c \ll 1$ of randomly selected unit cubes carry a counterion at their midpoint $\boldsymbol{R}$. The eight corner sites of each such cube will then constitute the binding sites for the mobile ions.

In the framework of Coulomb lattice gases, those three models of disorder in the site energies can be summarized as follows:

I) Percolative disorder

$$\epsilon_i = \begin{cases} 0 & \text{probability } p \\ \infty & \text{probability } 1-p \end{cases} \tag{20.17}$$

II) Gaussian disorder

$$P(\epsilon) = (2\pi\sigma_\epsilon^2)^{-1/2} \exp(-\epsilon/2\sigma_\epsilon^2) \tag{20.18}$$

III) Randomly placed counterions

$$\epsilon_i = -\sum_{\boldsymbol{R}} \frac{n_{\boldsymbol{R}} e^2}{|\boldsymbol{r}_i - \boldsymbol{R}|} \quad . \tag{20.19}$$

If c is the number of mobile ions per lattice site, then with probability c, $n_{\boldsymbol{R}} = 1$, otherwise $n_{\boldsymbol{R}} = 0$. In this way charge neutrality is maintained.

In all these models, we assume that sites cannot be occupied by more than one ion. The strength of the Coulomb interaction relative to the thermal energy $k_{\mathrm{B}}T$ is characterized by $\Gamma \equiv V_{\mathrm{c}}/(k_{\mathrm{B}}T)$, where $V_{\mathrm{c}} \equiv e^2/r_{\mathrm{s}}$ is the typical interaction energy and $r_{\mathrm{s}} \equiv (3/4\pi\rho)^{1/3}$ the half mean distance between the mobile ions. Here $\rho = c/a^3$ denotes the ionic number density.

To model the diffusion process we use a standard Monte Carlo algorithm: In each elementary step of the simulation, an ion is chosen randomly, and a nearest neighbor site is also chosen, to which the ion attempts to jump. If the neighboring site is blocked or occupied by another ion, the jump is rejected. If the neighboring site is vacant, the ion jumps to it with probability $w = \min\{1, \exp(-\Delta E/k_{\mathrm{B}}T)\}$, where ΔE is the change of the total energy caused by the jump and is given by $\Delta E = \Delta E_{\mathrm{s}} + \Delta E_{\mathrm{c}}$. Here $\Delta E_{\mathrm{s}} = \epsilon_j - \epsilon_i$ is the site energy difference ($\Delta E_{\mathrm{s}} \equiv 0$ for the percolation model) and ΔE_{c} is the energy difference due to the Coulomb interaction of the jumping particle with all other particles. For the calculation of ΔE_{c} one has to take care of the image charges caused by the periodic boundary conditions, which is done by using Ewald's method ([48], see also Chap. 16). After each elementary step, the time t is incremented by τ_0/N, where $\tau_0 = \tau_\infty \exp(V_0/k_{\mathrm{B}}T)$ is the mean residence time between two jumps of an ion in the absence of Coulomb interactions and structural disorder (see Sect. 20.2).

Initially the particles are randomly distributed over the system. In order to reach a thermalized state at the final simulation temperature, the system is cooled down from a high temperature, $k_{\mathrm{B}}T = 10\max\{\sigma_\epsilon, V_{\mathrm{c}}\}$, to the simulation temperature by a linear increase of $1/T$. After the cooling process, the temperature is held constant for a time equal to the cooling time; then the quantities of interest are determined. The time for the thermalization process is chosen such that the mean total energy of the ion system does not change significantly during the constant temperature phase, and is typically 3 to 5 times larger than the simulation time itself.

To obtain the mean square displacement $\langle r^2(t)\rangle$, all particle positions $\boldsymbol{r}_i(0)$ are stored at time $t = 0$ after thermalization. At time t, the particles are at positions $\boldsymbol{r}_i(t)$, and the mean square displacement is calculated from $\langle r^2(t)\rangle = (1/N)\sum_{i=1}^{N}[\boldsymbol{r}_i(t) - \boldsymbol{r}_i(0)]^2$. To obtain the SLR correlation functions $G^{(q)}(t)$, the magnetic field $\boldsymbol{B}$ is aligned along the z-direction and all pair vectors $\boldsymbol{r}_{ij}(0)$ are stored at time $t = 0$ using the minimum image convention [48]. At time t these pair vectors are $\boldsymbol{r}_{ij}(t)$, and the $G^{(q)}(t)$ are calculated according to (20.15).

The frequency dependent conductivity is determined by the current response to a (small) external sinusoidal electric field $E(t) = E_0 \sin(\omega t)$ aligned in the x-direction. The effect of the field is taken into account by the way the neighboring site is chosen to which an ion attempts to jump (see above). In the absence of the electric field, the 6 nearest neighbor sites are equivalent and are chosen with equal probability 1/6. In the presence of the field, the sites in the $\pm x$-direction are chosen with probability $(1 \pm \epsilon(t))/6$, where $\epsilon(t) \equiv eE(t)a/2k_{\mathrm{B}}T \ll 1$. The resulting current density $j_x(t)$ in the x-direction is determined by counting the number $N_+(t)$ and $N_-(t)$ of jumps in the $+x$- and $-x$-direction in a small time interval $t - \Delta t/2 \leq t < t + \Delta t/2$, where $\Delta t \ll 2\pi/\omega$. The mean values of $N_+(t)$ and $N_-(t)$, averaged over several samples, determine the mean current density $j_x(t) = ea(\langle N_+(t)\rangle - \langle N_-(t)\rangle)/L^3$ and, since $j_x(t)$ can be written as $j_x(t) = \sigma'(\omega)E_0 \sin(\omega t) - \sigma''(\omega)E_0 \cos(\omega t)$, the real and imaginary part $\sigma'(\omega)$ and $\sigma''(\omega)$ of the frequency dependent conductivity. In order to improve the statistics, the results are finally averaged over typically 100 thermalized configurations.

20.4 Dispersive Transport

For model I, most of our numerical simulations have been performed on a simple cubic lattice of length $L = 39a$, fixed ion density $c = 10^{-2}$ and fixed $\eta = e^2/(r_{\mathrm{s}}V_0) = 5$, which defines our set of standard parameters. V_0 denotes the structural potential barrier. To investigate the effect of percolative disorder, we compare results for the ordered lattice ($p = 1$) with those for the disordered substrate ($p = 0.4$). The strength of the Coulomb interactions, represented by the plasma parameter Γ, is varied by changing the temperature.

Figures 20.1 (a) and (b) show the time dependent diffusion coefficient $D(t) \equiv \langle r^2(t)\rangle/2dt$ in units of $D_0 \equiv a^2/2d\tau_0$ as a function of t/τ_0 for $\Gamma = 0$, 40, and 80 in (a) the ordered lattice ($p = 1$) and (b) the disordered system ($p = 0.4$). For $t/\tau_0 \ll 1$, $\langle r^2(t)\rangle$ is proportional to the total number of successful hops, which increases linearly with time and therefore $D(t)$ is constant, $D(t) = D_{\mathrm{st}}$. For $t/\tau_0 > 1$, $D(t)$ decreases with time t and finally approaches D_{tr}. In the ordered system, the decrease of $D(t)$ is comparatively weak, even at large plasma parameters Γ (low temperatures), while in the disordered system, $D(t)$ decreases over several orders of magnitude for large Γ. This behavior is reflected in the temperature dependence of the tracer correlation factor $f_{\mathrm{tr}}(\Gamma) = D_\infty/D_{\mathrm{st}}$ shown in Fig. 20.1 (c). In both the ordered and the disordered system, f_{tr} is thermally activated, $f_{\mathrm{tr}}(\Gamma) = f_{\mathrm{tr}}(0)\exp(-\Delta E_{\mathrm{f}}/k_{\mathrm{B}}T)$, but the activation energy ΔE_{f} being the difference between the activation energies for the long and short time diffusion coefficients, is much larger in the disordered system ($\Delta E_{\mathrm{f}} = 0.05e^2/r_{\mathrm{s}} = 0.27V_0$) than in the ordered one ($\Delta E_{\mathrm{f}} = 0.01e^2/r_{\mathrm{s}} = 0.06V_0$). We conclude that in order to obtain strong

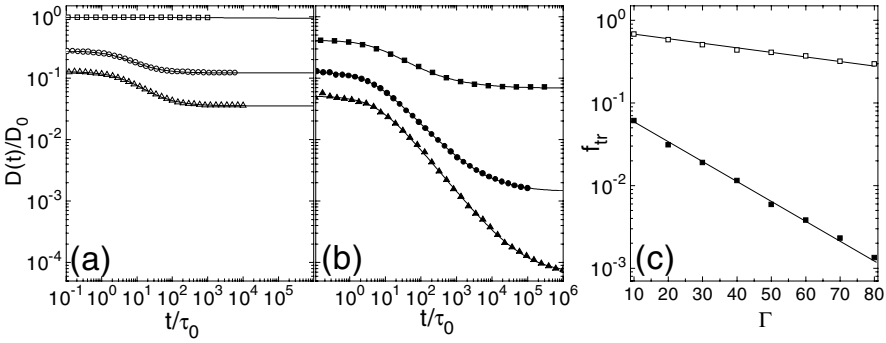

Fig. 20.1. Plot of (a) $D(t)$ in the ordered lattice for $\Gamma = 0$ (□), 40 (○), and 80 (△), (b) $D(t)$ in the disordered system (model I) for $\Gamma = 0$ (■), 40 (●), and 80 (▲), and (c) the tracer correlation factor as a function of the plasma parameter Γ in the ordered lattice (□) and in the disordered system (■). The full lines in (a) and (b) are least-square fits according to (20.21).

dispersion in the diffusive transport, we need both Coulomb interactions *and* structural disorder. In the following we will concentrate on this relevant case only and consider the curves shown in Fig. 20.1 (b) in more detail.

For $\Gamma \geq 20$, an intermediate time regime $t_1 < t < \tau_{\rm D}$ occurs, where $D(t)$ shows approximate power law behavior,

$$D(t) \sim t^{-n_{\rm D}}, \quad t_1 < t < \tau_{\rm D}. \tag{20.20}$$

The upper crossover time $\tau_{\rm D}$ and the exponent $n_{\rm D}$ increase with increasing Γ (decreasing temperature), while the lower crossover time t_1 is approximately independent of Γ and of the order of the inverse hopping rate $a^2/6D_{\rm st}$. The whole time dependence of $D(t)$ can be well described by the formula

$$D(t) = D_\infty + (D_{\rm st} - D_\infty)\left(1 + \frac{t}{t_1}\right)^{-n_{\rm D}}, \tag{20.21}$$

which has been suggested earlier by Funke on the basis of his jump relaxation model [11].

From the Nernst-Einstein relation (20.9) we expect that the power law behavior of $D(t)$ at intermediate time scales is reflected in a power law behavior of $\hat{\sigma}(\omega)$ at intermediate frequency scales, $1/\tau_{\rm D} < \omega < 1/t_1$. To determine $\hat{\sigma}(\omega)$ we have studied the current response to an external electric field $E(t) = E_0 \sin(\omega t)$ as described in Sect. 20.3. Figure 20.2 shows the real and imaginary parts $\sigma'(\omega)$ and $\sigma''(\omega)$ of the conductivity $\hat{\sigma}(\omega)$ in units of $\sigma_0 \equiv e^2/2k_{\rm B}Ta\tau_0$ as a function of $\omega\tau_0$ for (a) $\Gamma = 0$, (b) $\Gamma = 40$ and (c) $\Gamma = 80$.

For comparison we show also the real and imaginary parts of $\hat{\sigma}_{\rm D}(\omega) \equiv \rho e^2 \hat{D}(\omega)/k_{\rm B}T$ (full lines in the figure), which one obtains for the complex

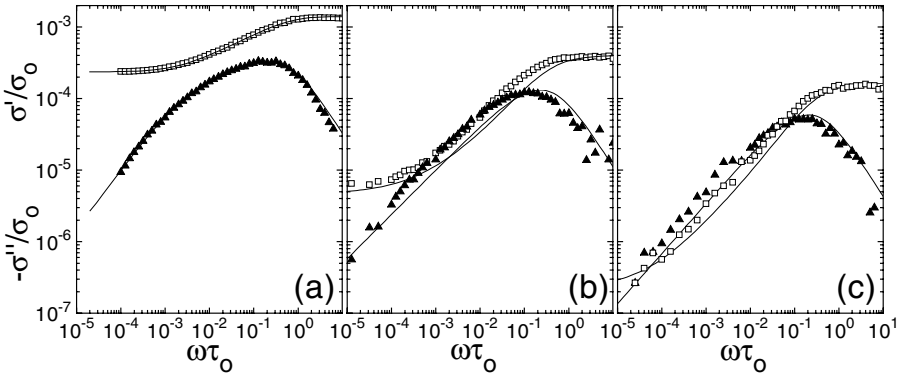

Fig. 20.2. Real (□) and imaginary part (▲) of the conductivity in model I for (a) $\Gamma = 0$, (b) $\Gamma = 40$, and (c) $\Gamma = 80$. The full lines are explained in the text.

conductivity when neglecting the cross-correlations in the autocorrelation function of the current density in (20.8). The frequency dependent tracer diffusion coefficient $\hat{D}(\omega)$ is obtained numerically by a Laplace transform of $\langle r^2(t)\rangle$ (see (20.6)). Since $\sigma''(\omega) \leq 0$, we have plotted $-\sigma''(\omega)$ in the figure. For $\Gamma = 0$, $\hat{\sigma}(\omega)$ and $\hat{\sigma}_{\rm D}(\omega)$ coincide, since in this case the cross-correlations practically vanish (the effect of the hard-core interaction between the mobile ions can be neglected since $c = 0.01$ is very small). For $\Gamma = 40$ and 80, $\hat{\sigma}(\omega)$ and $\hat{\sigma}_{\rm D}(\omega)$ are equal at high frequencies, but deviate at lower frequencies. Despite this, the overall behavior is quite similar. Both $\sigma'(\omega)$ and $\sigma'_{\rm D}(\omega)$ exhibit a dc plateau at low frequencies $\omega \ll 1/t_2$ and approach $\sigma_\infty = \rho e^2 D_{\rm st}/k_{\rm B}T$ at high frequencies $\omega \gg 1/t_1$. In between they can be approximately described by

$$\sigma'(\omega) \sim (\omega\tau_0)^{n_\sigma}, \quad \tau_0/\tau_\sigma \ll \omega\tau_0 \ll \tau_0/t_1, \tag{20.22}$$

where $n_\sigma = n_{\rm D}$ and $\tau_\sigma \approx \tau_{\rm D}$. At very high frequencies the conductivity becomes constant again. This high frequencies plateau is difficult to detect experimentally, especially in glasses, because dynamical processes not included in the lattice gas model, e.g. vibrations of the glassy matrix, become dominant (see however [49]). In some crystalline ion conductors as e.g. $RbAg_4I_5$ or Na-β''-Alumina, however, a high frequency plateau was found ([3], Chap. 23).

Since the cross-correlations do not affect strongly the overall behavior of $\sigma(\omega)$ one can hope to understand the origin of the conductivity dispersion from the behavior of the time dependent tracer diffusion coefficient. Indeed, to map the complex dynamics of the many-particle system to an effective dynamics of a one-particle system, it has been suggested that the mutual interactions between the ions can be described by an effective distribution $\psi(\tau_{\rm w})$ of waiting times $\tau_{\rm w}$ between successive jumps of a tracer particle. This continuous time random walk model (CTRW) (see e.g. [50]) was proposed by

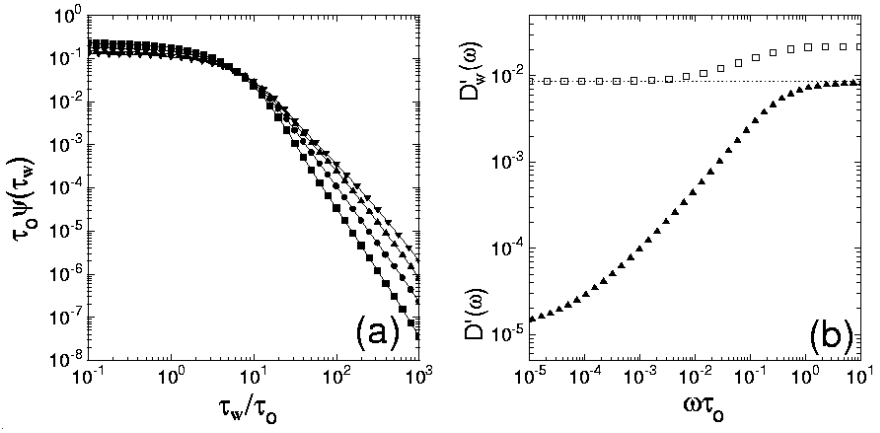

Fig. 20.3. Plot for model I of (a) the distribution function of the waiting time τ_w between successive jumps as a function of τ_w/τ_0 for different plasma parameters, $\Gamma = 20$ (■), 40 (●), 60 (▲) and 80 (▼), and (b) the real part of the diffusion coefficient $D'_{\rm w}(\omega)/D_0$ (obtained from the approximation (20.23)) (□) and the correct $D'(\omega)/D_0$ (obtained from (20.6)) (▲) for $\Gamma = 80$.

Scher and Lax [51] to describe the dielectric response of amorphous semiconductors.

To test if the CTRW model applies here, we have determined the number $N(\tau_{\rm w})$ of waiting times $\tau'_{\rm w}$ between two successive jumps of a tracer particle, which lie in the interval $\tau_{\rm w} - \Delta\tau_{\rm w} \le \tau'_{\rm w} < \tau_{\rm w} + \Delta\tau_{\rm w}$. The waiting time distribution $\psi(\tau_{\rm w})$ is related to $N(\tau_w)$ by $\psi(\tau_{\rm w}) = AN(\tau_{\rm w})/2\Delta\tau_{\rm w}$, where the prefactor A follows from the normalization condition, $\int_0^\infty d\tau_{\rm w}\psi(\tau_{\rm w}) = 1$. Figure 20.3 (a) shows $\psi(\tau_{\rm w})$ times τ_0 as a function of $\tau_{\rm w}/\tau_0$ for various plasma parameters Γ. For all values of Γ, $\tau_0\psi(\tau_{\rm w}) \simeq 10^{-1}$ is approximately constant for $\tau_{\rm w}/\tau_0 < 1$ and decreases rapidly for $\tau_{\rm w}/\tau_0 > 10$. As one would expect, the decrease is weaker for larger Γ, but no significant change of $\psi(\tau_{\rm w})$ occurs if Γ is increased.

The one-sided Fourier transform of the waiting time distribution $\psi(\tau_{\rm w})$ is (within the CTRW model) related to the frequency dependent diffusion coefficient $\hat{D}_{\rm w}(\omega)$ by [51]

$$\hat{D}_{\rm w}(\omega) = \frac{a^2}{6}\frac{{\rm i}\omega\hat{\psi}(\omega)}{1-\hat{\psi}(\omega)}. \tag{20.23}$$

In Fig. 20.3 (b) we compare $D'_{\rm w}(\omega)/D_0$ (obtained from (20.23)) with the correct $D'(\omega)/D_0$ (obtained from (20.6)) for $\Gamma = 80$. The two curves are completely different: In contrast to $D'(\omega)$, $D'_{\rm w}(\omega)$ shows only a very weak dispersion. The *low*-frequency limit of $D'_{\rm w}(\omega)$ is the same as the *high*-frequency limit of $D'(\omega)$.

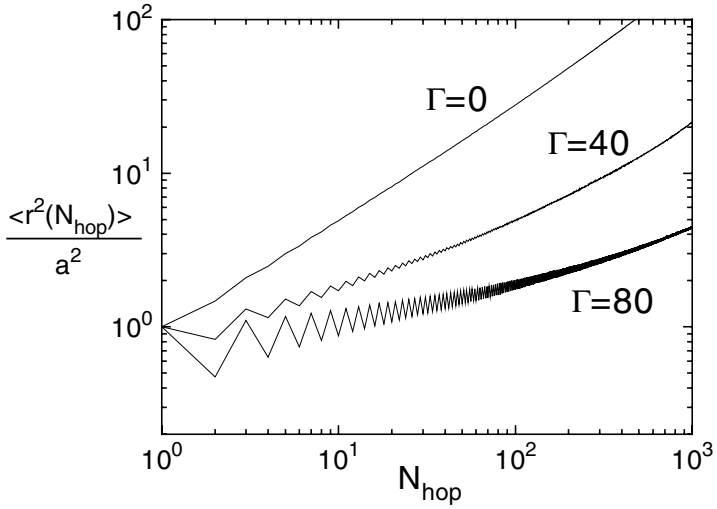

Fig. 20.4. Mean square displacement $\langle r^2(N_{\rm hop})\rangle$ as a function of the number of performed hops $N_{\rm hop}$ for different plasma parameters Γ.

These deviations show clearly the principle difficulties of the CTRW-model (see also [52]). If the initial waiting time $\tau_{\rm w}^0$, the tracer particle needs for the first jump, is chosen according to the proper stationary distribution, $\psi_0(\tau_{\rm w}^0) = \int_0^\infty d\tau_{\rm w}\psi(\tau_{\rm w}^0+\tau_{\rm w})/\int_0^\infty d\tau_{\rm w}^0\int_0^\infty d\tau_{\rm w}\psi(\tau_{\rm w}^0+\tau_{\rm w})$, then $D(\omega)$ shows no dispersion at all, $D(\omega) = D_{st}$ just as in the simple random walk case. The larger value of $D_{\rm w}$ at high frequencies is an artifact of the CTRW-model and results from the fact that the initial time $\tau_{\rm w}^0$ is assumed to be distributed according to ψ rather than to the stationary distribution.

Since the time inhomogeneities in the tracer motion can not be responsible for the dispersion, we now study spatial correlations in the tracer trajectory. We consider the mean square displacement $\langle r^2(N_{\rm hop})\rangle$ as a function of the number of performed hops $N_{\rm hop}$, which is shown in Fig. 20.4 for various plasma parameters Γ. At $N_{\rm hop} = 1$, $\langle r^2(N_{\rm hop})\rangle/a^2 = 1$ for all Γ since a tracer particle has moved the distance a after the first jump. At small plasma parameters, $\langle r^2(N_{\rm hop})\rangle$ increases monotonously with $N_{\rm hop}$. At larger values of Γ ($\Gamma \geq 20$), a striking alternation of $\langle r^2(N_{\rm hop})\rangle$ for even and odd $N_{\rm hop}$ begins to emerge for $1 < N_{\rm hop} < N_{\rm hop}^{(2)}$, which becomes more pronounced at larger Γ. The upper crossover number $N_{\rm hop}^{(2)}$ increases with increasing Γ and is of the order of the product of the jump rate $6D_{\rm st}/a^2$ and the crossover time $t_2 \approx \tau_\sigma$, $N_{\rm hop}^{(2)} \simeq 6D_{\rm st}t_2/a^2$. For even values of $N_{\rm hop}$, $\langle r^2(N_{\rm hop})\rangle$ shows approximate power law behavior

$$\langle r^2(2N_{\rm hop})\rangle \sim (2N_{\rm hop})^k, \quad 1 < N_{\rm hop} < N_{\rm hop}^{(2)}, \tag{20.24}$$

where $k = 1 - n_{\mathrm{D}} = 1 - n_\sigma$ is the exponent expected from the behavior of $\langle r^2(t)\rangle$, if t is simply replaced by the average time $2N_{\mathrm{hop}}/6D_{\mathrm{st}}$ after $2N_{\mathrm{hop}}$ jumps of the tracer particle, $\langle r^2(2N_{\mathrm{hop}})\rangle \simeq \langle r^2(t = 2N_{\mathrm{hop}}/6D_{\mathrm{st}})\rangle$.

The striking alternation of $\langle r^2(N_{\mathrm{hop}})\rangle$ is caused by strong forward-backward correlations in the tracer motion, which occurs on length scales of the order of the lattice constant a. Before its first jump the tracer ion finds itself in a deep energy minimum, which is created by the surrounding ions. After its first jump the ion is in an energetically unfavourable situation and has a large tendency to jump back to the original site. Thus $\langle r^2(N_{\mathrm{hop}} = 2)\rangle < \langle r^2(N_{\mathrm{hop}} = 1)\rangle = a^2$. Repetition of these forward-backward jumps leads to the alternating behavior of $\langle r^2(N_{\mathrm{hop}})\rangle$. Sometimes it happens that an energetically unfavourable position is stabilized by jump relaxation processes of the surrounding ions. This causes $\langle r^2(N_{\mathrm{hop}})\rangle$ to increase slightly, but the increase is much weaker than in the absence of the forward-backward correlations. The presence of disorder is important for the forward backward correlations to arise because the surrounding ions cannot follow the tracer ion without making detours, which delays the local relaxation process considerably. A similar suppression of the mobility of the surrounding ion cloud can be expected to occur in ordered lattices by a complex lattice structure with several sites per unit cell, as, for example, in the crystalline superionic conductor $RbAg_4I_5$. In ordered Bravais lattices, the surrounding ions can easily stabilize the position of the tracer ion and the forward-backward correlations are very small. The forward-backward correlations dominate the overall behavior on a length scale of the lattice constant. When $\langle r^2(N_{\mathrm{hop}})\rangle^{1/2}$ has reached a few lattice constants at $N_{\mathrm{hop}} \gg N_{\mathrm{hop}}^{(2)}$, the effect ceases to be dominant and the dispersion becomes considerably weaker.

In order to understand why the even values of N_{hop} between 1 and $N_{\mathrm{hop}}^{(2)}$ determine the behavior of $\langle r^2(t)\rangle$ between $t_1 \simeq 1/6D_{\mathrm{st}}$ and $t_2 \simeq N_{\mathrm{hop}}^{(2)}/6D_{\mathrm{st}}$, one must be aware that for a fixed time t the probability that the tracer ion has performed an even number of jumps is much larger than the probability that it has performed an odd number of jumps. After an odd number of jumps the tracer ion mostly finds itself in an energetically unfavourable position and stays there only for a short time (compared to the time spent on a site after an even number of jumps). Hence the probability that a particle has performed an odd number of jumps at a given time t is small, and does not contribute to the mean square displacement at t.

The forward-backward correlations also cause characteristic changes of the distribution function $P(\boldsymbol{r}, t)$ and its Fourier transforms. Fig. 20.5 (a) shows $\log(P(\boldsymbol{r}, t)/P(0, t))$ as a function of the scaled distance $r/R(t)$, where $R(t) = \langle r^2(t)\rangle^{1/2}$ is the root mean square displacement, in the disordered system for $\Gamma = 40$ and 80, and several times t in the dispersive regime. It is remarkable that although $R(t)$ is small in this regime, the curves collapse, showing that the simple scaling relation $P(\boldsymbol{r}, t)/P(0, t) = f(r/R(t))$ holds as in the simple random walk case. For $\Gamma = 40$ and 80, the scaling function $f(x)$ is no longer

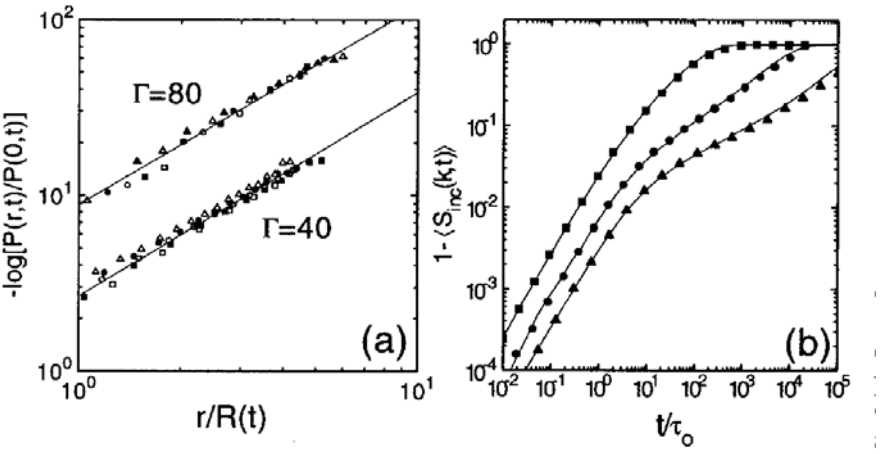

Fig. 20.5. Plot of (a) the distribution function $\log(P(\boldsymbol{r},t)/P(0,t))$ versus $r/R(t)$ in the disordered system I ($p = 0.4$) for $\Gamma = 40$ and 80, and (b) of $1 - \tilde{S}_{\rm inc}(k,t)$ for $k = 2\pi/10a$ as a function of t/τ_0. In (a) different symbols refer to different times: For $\Gamma = 40$: $t/\tau_0 = 546$ (□), 1130 (■), 2340 (○), 4830 (●), and 10000 (△) and for $\Gamma = 80$: $t/\tau_0 = 113$ (□), 264 (■), 616 (○), 1440 (●), 3360 (△), and 7850 (▲). The data points for $\Gamma = 80$ have been multiplied by a factor of 4. In (b) different symbols refer to different plasma parameters $\Gamma = 0$ (■), 40 (●), and 80 (▲), and the full lines are the approximation (20.26).

a Gaussian, but a stretched Gaussian, $f(x) = \exp(-cx^u)$, with $u \simeq 1.2$. For $\Gamma = 0$ in contrast, $P(\boldsymbol{r},t)$ shows the expected scaling behavior with a Gaussian scaling function only at larger times (Fig. 20.5 (b)). It is interesting to note that the exponent u satisfies the relation

$$u = \frac{2}{1+n_{\rm D}} \quad , \tag{20.25}$$

which has been originally derived to describe the distribution function of random walks on random fractal structures [53].

In order to discuss the Fourier transform of $P(\boldsymbol{r},t)$, the intermediate scattering function, we first remove any artificial effects of the lattice anisotropy by averaging $S_{\rm inc}(\boldsymbol{k},t)$ over the $\boldsymbol{k}$-vector orientation $\tilde{S}_{\rm inc}(k,t) \equiv (4\pi)^{-1} \int {\rm d}\Omega$ $S_{\rm inc}(\boldsymbol{k},t)$. For $kR(t) \ll 1$ and $R(t) \ll 1$ it is easy to verify that $\tilde{S}_{\rm inc}(k,t)$ can be approximated by

$$\tilde{S}_{\rm inc}(k,t) \simeq \exp(-\frac{k^2 R^2(t)}{6}). \tag{20.26}$$

Fig. 20.5 (b) shows $1 - \tilde{S}_{\rm inc}(k,t)$ for $k = 2\pi/10a$ and $\Gamma = 0$, 40, and 80. Quite surprisingly, the simple approximation (20.26) holds in the whole decay regime, showing that the decay changes from a simple to a stretched exponential when Γ becomes larger (see also [11]).

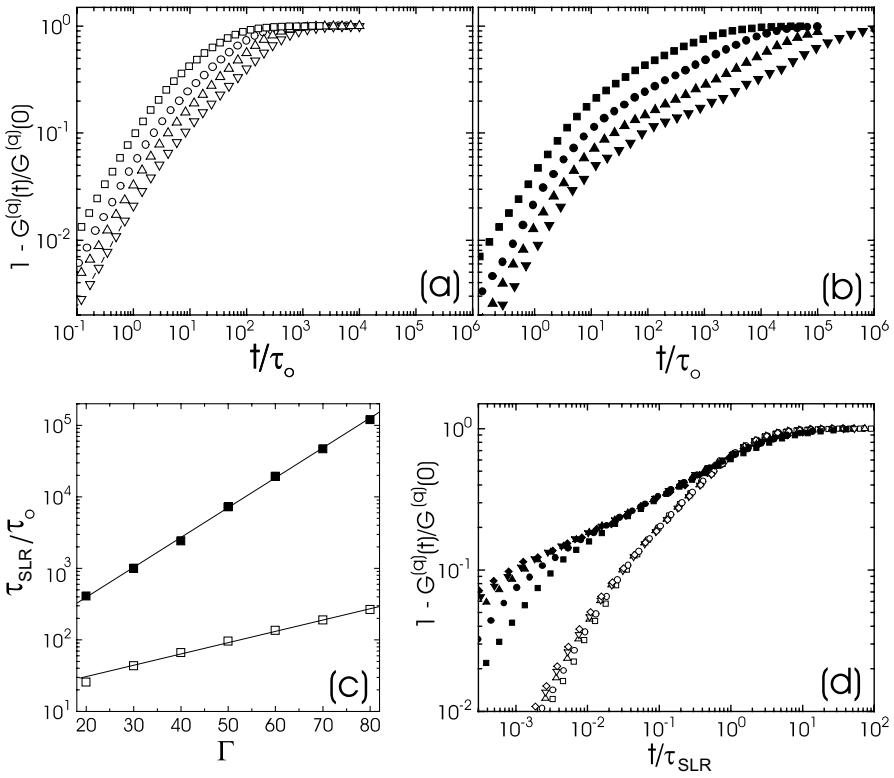

Fig. 20.6. Plot of $1 - G^{(2)}(t)/G^{(2)}(0)$ in model I (a) as a function of t/τ_0 for $p = 1$ and $\Gamma = 20$ (□), 40 (○), 60 (△) and 80 (▽), (b) as a function of t/τ_0 for $p = 0.4$ and $\Gamma = 20$ (■), 40 (●), 60 (▲) and 80 (▼). Part (c) shows the correlation time $\tau_{\rm SLR}$ for $p = 1$ (□) and $p = 0.4$ (■) as a function of Γ, and part (d) $1 - G^{(2)}(t)/G^{(2)}(0)$ as a function of the scaling parameter $t/\tau_{\rm SLR}$ for $p = 1$ (open symbols), $p = 0.4$ (full symbols) and $\Gamma = 40$ (□,■), 50 (○, ●), 60 (△, ▲), 70 (▽, ▼) and 80 (◇, ◆).

Next we discuss the SLR correlation functions $G^{(q)}(t)$, $q = 1, 2$. We again compare our results for the ordered lattice ($p = 1$) and the disordered substrate ($p = 0.4$). For sufficiently large values of Γ ($\Gamma > 1$) the distribution of the mobile ions is isotropic and therefore $G^{(2)}(0) = 4G^{(1)}(0)$ [43]. Numerically we find that for $\Gamma > 10$, $G^{(2)}(t) \cong 4G^{(1)}(t)$ is valid for all times t, and thus $G^{(2)}(t)/G^{(2)}(0) \equiv G^{(1)}(t)/G^{(1)}(0)$. Since the $G^{(q)}(t)$ decay faster than $1/t$ for very long times, the asymptotics is irrelevant for $1/T_1$ (see the discussion above, Sect. 20.2.4), and the relevant decay regime is most conveniently discussed in terms of the functions $1 - G^{(q)}(t)/G^{(q)}(0)$, which are shown in Fig. 20.6. Both in the ordered lattice (Fig. 20.6 (a)) and the disordered system (Fig. 20.6 (b)), $1 - G^{(q)}(t)/G^{(q)}(0)$ are proportional to t/τ_0 for small t/τ_0 values. Similar as in the diffusion coefficient, an intermediate time regime can be well identified in the disordered system for $\Gamma > 20$, where

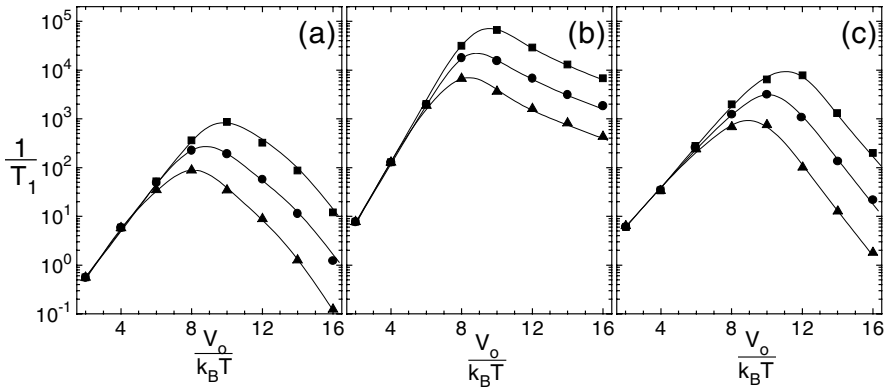

Fig. 20.7. Spin-lattice relaxation rate $1/T_1$ in units of $C\tau_\infty$ as a function of $V_0/k_\mathrm{B}T$ for (a) $p = 1$ and $\eta = 5$ (ordered system with Coulomb interaction), (b) $p = 0.4$ and $\eta = 5$ (disordered system with Coulomb interaction), and (c) $p = 0.4$ and $\eta = 0$ (disordered system without Coulomb interaction). Different symbols denote different frequencies. In (a) $\omega_\mathrm{L}\tau_\infty = 3\cdot 10^{-7}$ (■), $9.5\cdot 10^{-7}$ (●) und $3\cdot 10^{-6}$ (▲), in (b) $\omega_\mathrm{L}\tau_\infty = 3\cdot 10^{-9}$ (■), $9.5\cdot 10^{-9}$ (●) und $3\cdot 10^{-8}$ (▲), and in (c) $\omega_\mathrm{L}\tau_\infty = 3\cdot 10^{-6}$ (■), $9.5\cdot 10^{-6}$ (●) und $3\cdot 10^{-5}$ (▲).

$1 - G^{(q)}(t)/G^{(q)}(0) \sim (t/\tau_0)^{1-n_\mathrm{SLR}}$. The exponent n_SLR is independent of temperature, $n_\mathrm{SLR} \cong 0.73$. In the ordered lattice, the decay of the $G^{(q)}(t)$ is much faster and a corresponding intermediate time interval is hardly seen.

Figure 20.6 (c) shows the SLR correlation time τ_SLR, which we define as the time, where $G^{(q)}(t)$ has decreased to $1/e$ of its initial value, i. e. $G^{(q)}(\tau_\mathrm{SLR})/G^{(q)}(0) = 1/e$. Due to strong correlations in the ionic motion, τ_SLR is stronger activated than τ_0, $\tau_\mathrm{SLR}/\tau_0 = \exp(\Delta E_\mathrm{SLR}/k_\mathrm{B}T)$, $\Delta E_\mathrm{SLR} \equiv E_\mathrm{SLR} - V_0 > 0$. The activation energy ΔE_SLR is smaller in the ordered lattice ($\Delta E_\mathrm{SLR} \cong 0.04e^2/r_\mathrm{s} = (0.04\eta V_0)$) than in the disordered system ($\Delta E_\mathrm{SLR} \cong 0.09e^2/r_\mathrm{s} = (0.09\eta V_0)$), where τ_SLR exceeds τ_0 by more than 5 orders of magnitude for $\Gamma = 80$.

Fig. 20.6 (d) shows $1 - G^{(q)}(t)/G^{(q)}(0)$ as a function of t/τ_SLR. The data collapse shows that on time scales larger than τ_0, $G^{(q)}(t)/G^{(q)}(0)$ is only a function of t/τ_SLR (independent of Γ), in particular $1 - G^{(q)}(t)/G^{(q)}(0) \sim (t/\tau_\mathrm{SLR})^{1-n_\mathrm{SLR}}$ for $\tau_0/\tau_\mathrm{SLR} \ll t/\tau_\mathrm{SLR} < 1$. Accordingly in the relevant decay regime, the correlation functions can be approximately written in KWW form, $G^{(q)}(t) = G^{(q)}(0)\exp(-(t/\tau_\mathrm{SLR})^{1-n_\mathrm{SLR}})$, in the relevant regime.

With (20.13) we obtain $1/T_1(\omega_\mathrm{L}, T)$ by Fourier transformation. Figure 20.7 shows $1/T_1(\omega, T)$ as a function of $V_0/k_\mathrm{B}T$ for $\eta = 5$ and various Larmor frequencies ω_L in (a) the ordered lattice, and (b) the disordered system. For comparison, we show in (c) also the behavior of $1/T_1$ for uncharged particles ($\eta = 0$, $\Gamma \equiv 0$) diffusing in the disordered system. Since in all cases (a)–(c), the $G^{(q)}(t)$ decay faster than $1/t$ for large times, $1/T_1$ is independent of ω_L at the high temperature side of the maximum. For the uncharged par-

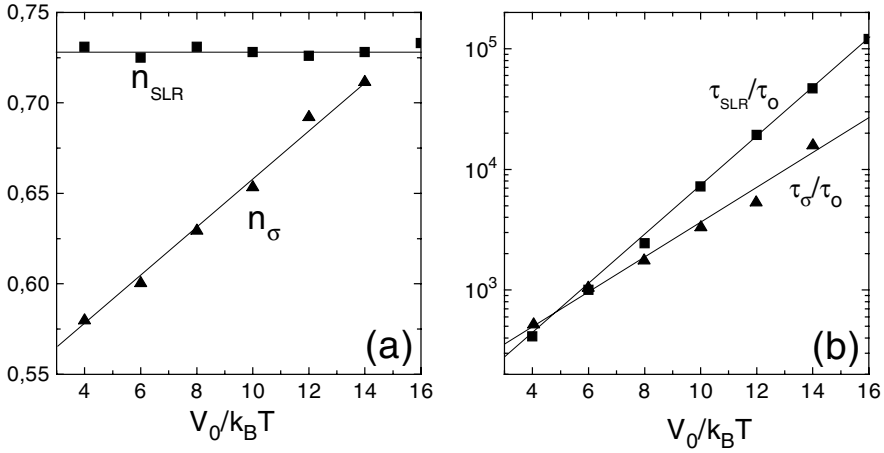

Fig. 20.8. Plot of (a) the exponents n_σ and $n_{\rm SLR}$ and (b) the correlation times τ_σ/τ_0 and $\tau_{\rm SLR}/\tau_0$ as a function of $V_0/k_{\rm B}T$ for $p = 0.4$ and $\eta = 5$.

ticles (Fig. 20.7 (c)), $1/T_1$ shows no significant deviation from the standard BPP behavior. For charged particles slight deviations occur in the ordered lattice (Fig. 20.7 (a)), but the typical non-BPP behavior according to (20.5) does not occur. The deviations predominantly show up in a weak asymmetry of $1/T_1$ near the maximum. In case (b), when both disorder and Coulomb interactions are present, we obtain the typical non-BPP behavior: The curves are asymmetric in shape, the maximum occurs at $\omega_{\rm L}\tau_{\rm SLR} \approx 1 \gg \omega_{\rm L}\tau_0$ (note that this relation is the only way to experimentally determine $\tau_{\rm SLR}$ as a function of T), and $1/T_1$ decreases as $1/T_1 \sim \tau_0(\omega_{\rm L}\tau_0)^{n_{\rm SLR}-2}$ at low temperatures ($\omega_{\rm L} \gg 1/\tau_{\rm SLR}$). The activation energies are $E_1^{\rm SLR} \cong 1.5V_0$ and $E_2^{\rm SLR} \cong 0.4V_0$. Since $E_{\rm SLR} \cong 1.45V_0$ for $\eta = 5$ (see above) also $E_{\rm SLR} \simeq E_1^{\rm SLR}$ is fulfilled. We conclude that, similar to our result for the conductivity $\sigma(\omega)$, both structural disorder and Coulomb interactions are needed to obtain qualitative agreement with the experimental findings. Again, we concentrate on this relevant case only.

As a consequence of the scaling behavior of $G^{(q)}(t)$, $1/T_1(\omega_{\rm L}, T)$ obeys the simple scaling relation

$$\frac{1}{T_1}(\omega_{\rm L}, T) = \tau_{\rm SLR} g(\omega_{\rm L}\tau_{\rm SLR}), \tag{20.27}$$

with $g(x) = $ const. for $x \ll 1$ and $g(x) \propto x^{n_{\rm SLR}-2}$ for $x \gg 1$. Equation (20.27) implies $E_1^{\rm SLR} = E_{\rm SLR}$ and the relation $E_2^{\rm SLR} = (1 - n_{\rm SLR})E_1^{\rm SLR}$ first proposed by Ngai [31].

Next we compare the exponent $n_{\rm SLR}$ and the correlation time $\tau_{\rm SLR}$ with the corresponding quantities in the conductivity spectra. Figure 20.8 (a) shows that n_σ is smaller than $n_{\rm SLR}$ for $V_0/k_{\rm B}T < 16$ and seems to approach

n_{SLR} at lower temperatures. Only at these very low temperatures we expect mean field approaches [11] yielding $n_\sigma = n_{\mathrm{SLR}}$ to be applicable. From Fig. 20.8 (b) we find that the conductivity relaxation time τ_σ is less activated than the correlation time τ_{SLR} in spin-lattice relaxation, and therefore $\tau_{\mathrm{SLR}}/\tau_\sigma \gg 1$ at lower temperatures. This is in accordance with experimental results for, e.g., $(\mathrm{LiCl})_{0.6}(\mathrm{Li_2O})_{0.7}(\mathrm{B_2O_3})_{1.0}$ [54], glassy $\mathrm{LiAlSi_2O_6}$ [55] and $\mathrm{LiAlSi_4O_{10}}$ [56], and flourozirconate glasses [7]. The reason for these differences is that although the phenomena observed in both experiments originate from the same ion transport mechanism, they are governed by *different* correlation functions: In spin-lattice relaxation, the correlation functions are determined by diffusion of ion pairs, while in conductivity the current correlation function is mainly determined by the diffusion of single ions.

20.5 Non-Arrhenius Behavior

In the preceding section, we have shown that simple percolative disorder and the Coulomb interaction between the ions can account for the typical anomalies found in several transport quantities. Another interesting effect is the non-Arrhenius behaviour of fast ion conducting glasses [20]. Clearly it would be desirable to confirm this effect also in tracer diffusion measurements [57].

In order to explain non-Arrhenius behaviour, one has to include the energy fluctuations associated with the disorder present in the material. To begin our discussion of energy fluctuations, we first assume non-interacting particles moving between lattice sites with energies drawn form a Gaussian distribution, as in model II, cf. (20.18). For that problem, the dc activation energy at low T can be calculated analytically [33, 34]. Since double occupancy of sites is forbidden, the ions in equilibrium are distributed according to a Fermi distribution. At temperatures $T \ll \sigma_\epsilon/k_{\mathrm{B}}$, the activation energy follows from a critical percolation path argument [58, 59], $E_\sigma = \epsilon_{\mathrm{c}} - \epsilon_{\mathrm{f}}(c)$. Here $\epsilon_{\mathrm{f}}(c)$ is the Fermi energy, defined by $\int_{-\infty}^{\epsilon_{\mathrm{f}}} P(\epsilon)d\epsilon = c$, and ϵ_{c} is the critical energy given by $\int_{-\infty}^{\epsilon_{\mathrm{c}}} P(\epsilon) = p_{\mathrm{c}}$, where p_{c} is the percolation threshold [45] in the sc-lattice, $p_{\mathrm{c}} \simeq 0.3117$. For $c = 0.01$ we obtain $E_\sigma = 1.84\sigma_\epsilon$. Because of the weak dependence of ϵ_{f} on c (see Sect. 20.7), E_σ assumes similar values for other reasonable concentrations $c \ll 1$.

At high temperatures $T \gg \sigma_\epsilon/k_{\mathrm{B}}$, the conductivity is well approximated by $\sigma_{\mathrm{dc}} \simeq \sigma_{\mathrm{hf}} = \rho q^2 a^2 W_0/6k_{\mathrm{B}}T$. As can be shown by a high-temperature expansion, W_0 is given by $W_0 \simeq (1-c)\mathrm{erfc}(\sigma_\epsilon/(2k_{\mathrm{B}}T)) \simeq (1-c)\exp(-\sigma_\epsilon/\sqrt{\pi}k_{\mathrm{B}}T)$, in leading order of $\sigma_\epsilon/k_{\mathrm{B}}T$. Hence we obtain a high-temperature activation energy $E_0 = \sigma_\epsilon/\sqrt{\pi} \cong 0.56\sigma_\epsilon$ that is smaller than E_σ. Accordingly, the apparent activation energy $E(T)$ changes from E_σ for low temperatures to E_0 at a crossover temperature $T_x \simeq \sigma_\epsilon/k_{\mathrm{B}}$. Figure 20.9 (a) shows the simulation results for σ_{dc} (data points) in comparison

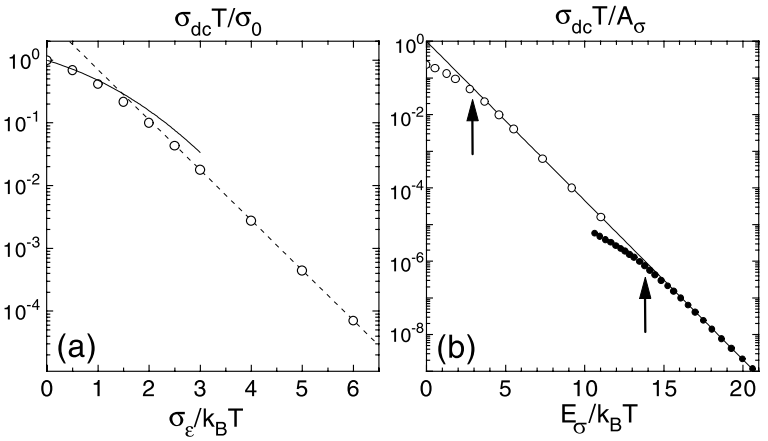

Fig. 20.9. Arrhenius plot of $\sigma_{\rm dc}T$ for $V_{\rm c} = 0$ and $c = 0.01$ (open circles) (a) in units of σ_0 as a function of $\sigma_\epsilon/k_{\rm B}T$ and (b) in units of the preexponential factor A_σ of the low-temperature Arrhenius law as a function of $E_\sigma/k_{\rm B}T$. In (a) the full line shows the high temperature approximation (see text), the dashed line corresponds to $A_\sigma \exp(-E_\sigma/k_{\rm B}T)$, where $E_\sigma = 1.84\sigma_\epsilon$ and A_σ was taken to get the best fit to the data. For comparison, the experimental data for $0.4{\rm AgI}+(0.6)[0.525{\rm Ag_2S}+0.475({\rm B_2S_3}{:}{\rm SiS_2})$ are shown in (b) (filled symbols, redrawn from [20]). The solid line is drawn as guide for the eye.

with the analytical results (lines). Except for the crossover regime $T \approx T_x$, the calculated activation energy agrees perfectly with the simulation data.

At first glance, the crossover at high temperatures seems to be very similar to recent experimental results for fast ion glasses [20]. Notice however, that both E_σ and $k_{\rm B}T_x$ are of the same order of magnitude, determined by σ_ϵ. This is a serious disagreement to the experiments, where the non-Arrhenius behavior sets in at temperatures more than one order of magnitude smaller than $E_\sigma/k_{\rm B}$. The disagreement can be seen clearly in Fig. 20.9 (b), where we have plotted both the simulation results in the absence of Coulomb interactions (open circles) and the experimental data (filled circles) [20] as a function of $E_\sigma/k_{\rm B}T$. The arrows indicate the crossover temperatures and show that both disagree by about an order of magnitude.

Next we include the Coulomb interaction i. e. consider the complete model II, cf. (20.18). That model now is characterized by the typical interaction energy $V_{\rm c} \equiv e^2/r_{\rm s}$ and the disorder energy σ_ϵ. Since we have found in Sect. 20.4 that the cross correlations give only a minor contribution to the conductivity, we have calculated the dc conductivity from the long-time limit of $D(t)$ by using (20.9) and neglecting the cross correlations. Figure 20.10 (a) shows $\sigma_{\rm dc}T$ in units of σ_0 as a function of $V_{\rm c}/k_{\rm B}T$ for $c = 0.01$ and $\sigma_\epsilon/V_{\rm c} = 0.0115$, 0.018, 0.036, and 0.072. At low temperatures, each curve follows a straight line corresponding to an Arrhenius law with constant activation energy E_σ,

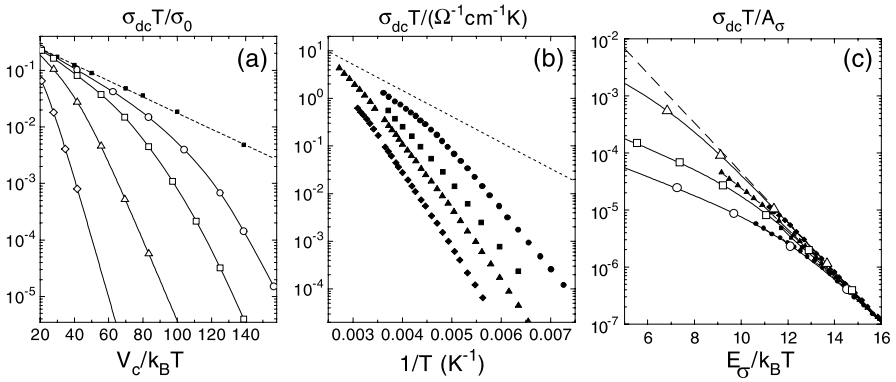

Fig. 20.10. Arrhenius plots of the dc conductivity $\sigma_{\rm dc}T$ (a) in model II, cf. (20.18) in units of σ_0 for $\sigma_\epsilon/V_{\rm c} = 0$ (■), 0.0115 (○), 0.018 (□), 0.036 (△), and 0.072 (◊), and (b) for zAgI+$(1-z)$[0.525Ag_2S+0.475(B_2S_3:SiS_2)] in units of $\Omega^{-1}{\rm cm}^{-1}{\rm K}$ for $z = 0$ (⧫), 0.2 (▲), 0.3 (■), and 0.4 (●) (redrawn from [20]). The dashed lines indicate the upper mobility limit predicted by the model. In (c) the data from (a) and (b) are shown together as functions of $E_\sigma/k_{\rm B}T$ and are normalized with respect to the preexponential factors A_σ in the corresponding Arrhenius laws. The solid lines in (a) and (c) are drawn as guide for the eye.

and E_σ decreases with decreasing σ_ϵ. The Arrhenius law is valid up to a crossover temperature T_x, where the curves bend toward lower diffusivities. In all cases, the crossover temperature T_x is of the order of $\sigma_\epsilon/k_{\rm B}$. For comparison we have redrawn in Fig. 20.10 (b) the experimental conductivity data [20] for zAgI+$(1-z)$[0.525Ag_2S+0.475(B_2S_3:SiS_2)] with mole fractions z between zero and 0.4. Evidently, when increasing z, the experimental behavior is analogous to the model behavior when decreasing σ_ϵ: E_σ becomes smaller and the non-Arrhenius behavior starts to occur at lower T.

The similarity between the results found in the model and in the experiment becomes even more evident in Fig. 20.10 (c), where the data from Fig. 20.10 (a) and Fig. 20.10 (b) are plotted in the same way as in Fig. 20.9 (b). The experimental curve for $z = 0.4$ is almost perfectly reproduced by the model when $\sigma_\epsilon = 0.0115V_{\rm c}$ (see the filled and open circles in Fig. 20.10 (c)). The experimental curves for $z = 0$, 0.2 and 0.3 correspond to disorder strengths within a range $0.015V_{\rm c} < \sigma_\epsilon < 0.036V_{\rm c}$. It is remarkable that the model not only gives a good fit to the overall shape of the conductivity curves but also reproduces the small values of $k_{\rm B}T_x/E_\sigma$. Within the framework of the model, the non-Arrhenius behaviour thus may be explained as a cross-over from a high activation energy at low temperatures, where the ionic motion is dominated by disorder and interaction effects, to a low activation energy at high temperatures, where only the interaction is relevant.

20.6 Counterion Model and the "Nearly Constant Dielectric Loss" Response

Models with smooth distribution of uncorrelated site energies, as implied by (20.18), have been studied also with respect to ac transport properties [39], in addition to dc transport considered in the foregoing section. Generally speaking, the outcome for time-dependent mean square displacements and frequency-dependent conductivities in Coulomb lattice gases with Gaussian and percolative disorder (Sect. 20.4) is similar, provided $\Gamma \gg 1$. Qualitative features of conductivity spectra are therefore robust with respect to the particular type of disorder, an issue which is important for understanding their "universal" nature [26].

Let us turn now to yet another disorder model, the counterion model (20.19), which will allow us to discuss both composition-dependent dc-transport properties and dispersive effects, including "nearly constant loss" (NCL)-type high-frequency phenomena [40].

Clearly, in that model with $c \ll 1$ two nearby counterions are separated by a Coulomb barrier whose height is a sensitive function of their distance $2r_s$. Consequently, we observe Arrhenius behavior for both σ_{dc} and τ_σ with an activation energy $E_\sigma(c)$ determined by that Coulomb barrier, which grows with decreasing concentration c. From simulations one can extract $E_\sigma(c) \simeq \mathrm{const} - 0.11(e^2/a)\ln c$ in the relevant concentration range, a variation with c on an energy scale of order 1 electronvolt, which favourably compares with some experiments, see also Sect. 20.7. Regarding dc transport, other notable features of the counterion model are preexponential factors in the Arrhenius law for σ_{dc} satisfying the Meyer-Neldel compensation rule [60] and Haven ratios (see Sect. 20.2) which decrease sharply with increasing c for dilute systems, in qualitative accord with the measurements [61].

The dynamic conductivity in the counterion model with $c \ll 1$ displays four distinct frequency regimes and reflects the experimental behavior of dilute samples in a wide frequency range. Those regimes can directly be connected with specific kinds of ionic motions in space and time [62]. Figure 20.11 shows a typical set of data for $\sigma'(\omega)$, normalized by the high-frequency conductivity $\sigma(\infty)$. Below the usual high-frequency plateau (regime I, defined by $\omega > \tau_{\mathrm{MC}}^{-1}$, where τ_{MC} is one Monte Carlo time step) a second regime II appears where $\sigma'(\omega)$ raises with ω approximately in a linear fashion. This effect will be discussed below in greater detail. A simultaneous analysis of the mean square displacement shows that regime II has limits $\tau_1^{-1} < \omega < \tau_{\mathrm{MC}}^{-1}$, where τ_1 is defined by $\langle r^2(\tau_1)\rangle = a^2$. Therefore, in II, the ions essentially remain bound to a counterion and are able to perform only local motions of the character of dipolar reorientation steps. Regime III, related to the Jonscher regime, corresponds to escape processes out of the Coulomb trap. This interpretation is confirmed by noting that the conductivity relaxation time τ_σ in this model satisfies $\langle r^2(\tau_\sigma)\rangle = r_s^2$, where $r_s = a(3/4\pi c)^{1/2}$ amounts to half the distance between two counterions. Finally, for even lower frequencies

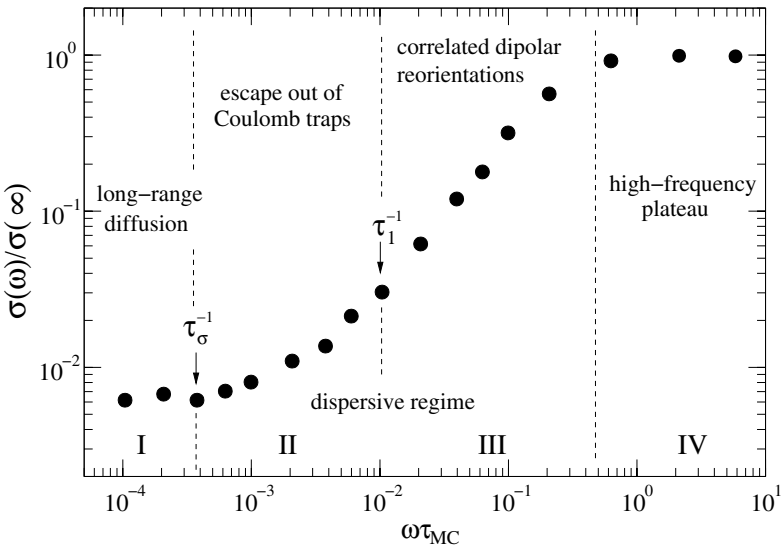

Fig. 20.11. Frequency dependence of the conductivity (in a double-logarithmic plot) in the counterion model for $c = 0.03$ and $e^2/ak_BT = 20$. τ_{MC} corresponds to one Monte Carlo time step (after [40]).

(regime IV, $\omega < \tau_\sigma^{-1}$) the ions can complete effective hops to the next or to further distant counterions, and $\sigma(\omega)$ approaches the dc-plateau.

Now we return to the regime II, where $\sigma'(\omega) \propto \omega$. As mentioned in the introduction (Sect. 20.1), such a behavior in fact is widely observed in glassy materials and defective crystals. The "universal dielectric response" represented by (20.1) therefore has to be supplemented by a high-frequency contribution, see (20.3)

$$\sigma_{NCL}(\omega) \simeq A(T)\omega; \quad \omega > \omega_{NCL}(T) \gg \tau_\sigma^{-1} \tag{20.28}$$

In view of the relationship $\hat{\chi}(\omega) = -4\pi i\hat{\sigma}(\omega)/\omega$ between $\hat{\sigma}(\omega)$ and the dielectric susceptibility $\hat{\chi}(\omega)$, this amounts to a frequency-independent dielectric loss, $\chi''(\omega) \propto A(T)$, known as NCL response. In distinction to the parameters in (20.2), both $A(T)$ and $\omega_{NCL}(T)$ are not thermally activated, but only weakly decrease with temperature [17,63]. Therefore, cooling to helium temperatures, $\sigma_{dc} \propto \tau_\sigma^{-1}$ becomes unmeasurably small while the NCL response (20.28) dominates and typically extends over several orders of magnitude in frequency.

Up to now, the physical origin of the NCL response is unclear. A common picture adheres to the "asymmetric double well potential (ADWP)" model, which rests on the assumption of thermally activated local relaxational steps of charged defects subject to a broad distribution of activation barriers [64].

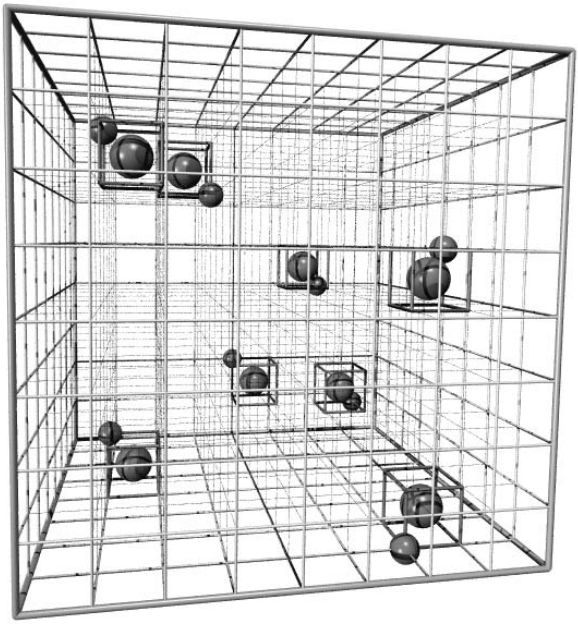

Fig. 20.12. Section of the dipolar lattice gas model (after [66]).

Recently, the idea has been advanced that long-range interactions among dipolar centres can give rise to long-time tails in dielectric relaxation, consistent with NCL-type spectra [65, 66]. Evidence for the relevance of this mechanism arose from dynamic Monte Carlo simulations of a "dipolar lattice gas". This model consists of a spatially random assembly of dipolar centres, where charged particles (ions) perform reorientational steps next to their associated immobile counterion. Contrary to the ADWP-model, this model requires no extrinsic local disorder within the individual centres, but emphasises the importance of dipole-dipole interactions.

Clearly, that dipolar lattice gas directly emerges from the counterion model (see Sect. 20.3, (20.19)) and Fig. 20.11, simply by cutting the bonds which leave the first shell surrounding a counterion. Moreover, it is required that each such shell contains exactly one mobile charge carrier. For an illustration see Fig. 20.12. The reduced number of configurations in comparison with the full counterion model clearly facilitates numerical simulations and also allows us to set up analytic approaches, namely exact diagonalization of the underlying master equation for small systems and a dynamic pair approx-

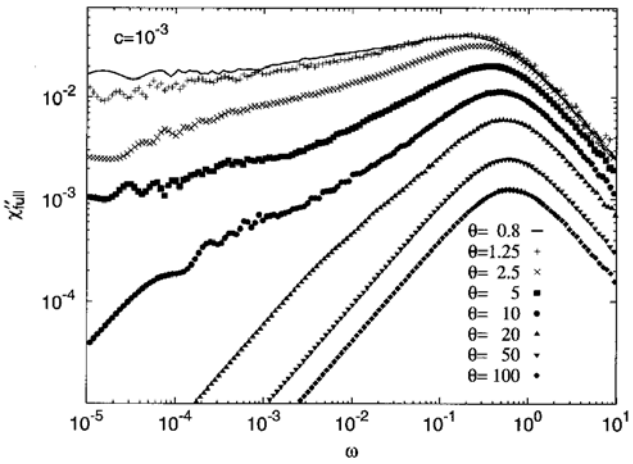

Fig. 20.13. Dielectric loss spectrum $\chi''(\omega)$ of a dipolar lattice gas with $c = 10^{-3}$ at different reduced temperatures $\theta = k_{\mathrm{B}}T/V_{\mathrm{dip-dip}}$, showing the gradual transition between Debye and NCL behavior (for a specification of parameters see [66]).

imation [67, 68]. For details we refer to the original works. In Fig. 20.13 we present a set of simulated loss spectra for a fairly dilute system with a fraction $c = 10^{-3}$ of dipolar centers relative to the total number of unit lattice cells. Temperature enters via the ratio $\theta = k_{\mathrm{B}}T/V_{\mathrm{dip-dip}}$, where $V_{\mathrm{dip-dip}}$ denotes the typical interaction strength between centers. Rather than simulating the current correlation function, it is more convenient in this case to obtain the correlation function of the total polarisation $\boldsymbol{P}(t) = \sum \boldsymbol{p}_i(t)$, which is a sum over the dipole moments of all centers, and to use

$$\chi''(\omega) = \frac{\beta\omega}{3}\mathrm{Re}\int_0^\infty \langle \boldsymbol{P}(t)\cdot\boldsymbol{P}(0)\rangle \mathrm{e}^{\mathrm{i}\omega t}\,\mathrm{d}t \tag{20.29}$$

Similar to Sect. 20.4 it turns out that the qualitative behavior of $\chi''(\omega)$ is already contained in the "self-part" $\chi''_{\mathrm{self}}(\omega)$ being determined by the self-correlation function $\langle \boldsymbol{p}_i(t)\boldsymbol{p}_i(0)\rangle$. This quantity can be decomposed into a short-time contribution, which corresponds to relaxation of a selected dipole in a static energy landscape due to the other dipoles and a long-time contribution due to temporal renewals in the minimum energy position of that individual dipole. The latter process turns out to be responsible for the slow decay at long times and for NCL behavior, in contrast to the Debye-like behavior of the initial decay [26].

Further notable features of this model are a significant enhancement of the overall NCL response $\chi''(\omega)$ relative to the "self-part" $\chi''_{\mathrm{self}}(\omega)$, the appearance of different concentration-dependent scenarios in approaching a constant loss under decreasing temperature and a robustness of the results against changes in the character of positional disorder [66].

20.7 Compositional Anomalies

In ion-conducting glasses long-range transport properties depend in an unexpected anomalous way on the composition of mobile ions. One anomaly refers to the dependence of the conductivity on the ionic concentration. Experiments show that the dc conductivity $\sigma_{\rm dc}$ raises very steeply with the ion content [69]. Taking Na_2O-B_2O_3 glasses at 300°C as an example, the conductivity increases approximately by a factor 10^6 as the mole fraction of Na_2O is increased from 0.15 to 0.5. As mentioned in Sect. 20.6, the variation of the conductivity can in general be described by an activation energy that decreases logarithmically with the ionic concentration c, $E_\sigma \simeq A - B\ln(c)$. This behavior corresponds to a power law dependence $\sigma_{\rm dc} \sim c^{B/k_{\rm B}T}$, where the exponent $B/k_{\rm B}T$ becomes much larger than one at low T.

Another anomaly pertains to the variation of the conductivity if one type of mobile ion A is successively replaced by a another type of mobile ion B. As a function of the mixing ratio $x = c_{\rm B}/(c_{\rm A} + c_{\rm B})$, where $c_{\rm A} = (1-x)c$ and $c_{\rm B} = xc$ are the partial concentrations ($c = c_{\rm A} + c_{\rm B}$), $\sigma_{\rm dc}(x)$ runs through a minimum that becomes more pronounced with decreasing temperature. Well below the calorimetric glass transition temperature T_g, the conductivity at the minimum is several orders of magnitude lower than the conductivities of the corresponding single ionic glasses ($x = 0, 1$). For example, in $x{\rm K_2O}(1-x){\rm Li_2O}{\cdot}2{\rm SiO_2}$ glasses at 150°C, the minimum conductivity is about 10^4 times smaller than that of either single cation glass. In fact, all properties of glasses that are strongly affected by long-range motions of mobile ions (tracer diffusion coefficients, conductivity, internal friction, viscosity, etc.), show strong deviations from a simple additive behavior upon mixing of two different types of mobile ions. This phenomenon is known as the mixed alkali effect [70] and occurs in all ionically conducting glasses, regardless of the types of ions that are mixed and the type of network constituents forming the disordered host matrix for the ionic motion. Of fundamental importance for the effect are the behaviors of the tracer diffusion coefficients $D_{\rm A}$ and $D_{\rm B}$ of ion species A and B. When A ions are replaced by B ions, $D_{\rm A}$ always decreases and $D_{\rm B}$ always increases (and vice versa). These changes in the diffusivities are caused by changes in the respective activation energies $E_{\rm A,B}$, such that $D_{\rm A}$ and $D_{\rm B}$ vary by several orders of magnitude at low temperatures T.

Like the dispersive transport properties, these compositional anomalies can be understood from lattice gas models with fluctuating site energies. As discussed in Sect. 20.5, the activation energy E_σ can, in the presence of a continuous distribution of site energies, be calculated from a critical percolation path argument. Accordingly, $E_\sigma(c) = \epsilon_{\rm c} - \epsilon_{\rm f}(c)$ is the difference between the critical energy $\epsilon_{\rm c}$ determined by the percolation threshold $p_{\rm c}$ and the Fermi energy $\epsilon_{\rm f}(c)$ that, due to the filling up of low-energy sites, increases with c. A calculation of this c-dependence [33, 71] for the Gaussian site energy model (20.18) yields, at intermediate concentrations c, a behavior very similar to a logarithmic increase of $\epsilon_{\rm f}(c)$ with c. Accordingly, an approximate logarith-

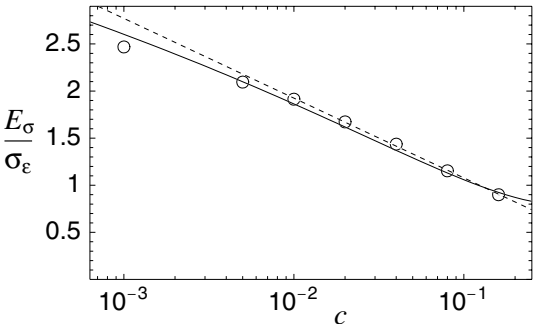

Fig. 20.14. Plot of the activation energy $E_\sigma/\sigma_\varepsilon$ as a function of the ionic concentration c in a lattice gas with Gaussian distributed site energies (20.18). The open circles represent the values obtained from Monte Carlo simulations, while the solid line marks the result from the critical path analysis. The dashed lined is a fit with respect to a logarithmic dependence of E_σ on c, $E_\sigma = A - B\ln(c)$ with $A \cong 0.23$ and $B \cong 0.37$ (redrawn from [71]).

mic decrease of $E_\sigma(c)$ is found, in qualitative agreement with experiment, see Fig. 20.14. For an exponential distribution of site energies, the logarithmic decrease $E_\sigma(c) = A - B\ln c$ comes out exactly [72,73]. It is important to note that the logarithmic behavior can prevail when the Coulomb interactions between the mobile ions are taken into account also [72]. As first shown in [30], the activation energy $E_\sigma(c)$ for the Coulomb lattice gas with uncorrelated site energy disorder can be expressed as a sum of the "structural contribution" $E_\sigma^{(0)}(c) = A - B\ln c$ coming from the critical percolation path analysis and a Coulomb contribution $E_\sigma^{\rm coul} \propto q^2/r_{\rm s} \propto q^2 c^{1/3}$. For low concentrations c, the behavior is dominated by the structural contribution. Moreover, the logarithmic behavior can be supported by the Coulomb trapping effect of the counterions discussed in Sect. 20.6.

In order to understand the mixed alkali effect one has to realize that different types of ions exhibit distinct local environments in the glassy network. This has been shown by EXAFS measurements [74] and been verified also by means of neutron and X-ray diffraction measurements on mixed alkali phosphate glasses in combination with reverse Monte-Carlo simulations [75]. Accordingly, the energy landscapes $\epsilon_i^{\rm A}$ and $\epsilon_i^{\rm B}$ encountered by A and B ions, respectively, must be different; a preferable low-energy site for an A ion is not a preferable low-energy site for a B ion and vice versa. These experimental findings are the starting point of the "dynamic structure model" [76,77]. The central idea of the dynamic structure model is that sites are created in response to the needs of the cations. Thus, in single and in mixed Na^+/K^+ ion glass, Na sites are created for Na^+ ions and K sites for K^+ ions. Structure building in the molten or solid glass depends on the dynamic responses of the network to the moving ions. The preferred sites are created mostly during the cooling process (and possibly, although it is the subject of debate, in

the glass) by an accommodation of the network in the local environment of each mobile ion. Thereby preferred diffusion paths for each type of ion are formed. The dependence of the connectivity of these diffusion paths on the ionic composition was shown to provide an explanation for both the mixed alkali effect and the steep increase of the conductivity with ionic concentration in single modified glasses. For a further discussion of the mixed alkali effect and further developments of the dynamic structure model, which take into account cation size effects and interactions between interchange and network structure, we refer to [78–80]. Signatures of the mixed alkali effect were also found in molecular dynamics studies [37, 81].

Within our description of ionic transport in terms of lattice gases with fluctuating site energies, the simplest approach is to assume that the two ion species move independently of each other and that the sets of low-energy sites for A and B ions are disjoint. Under these assumptions the activation energies $E_{\mathrm{A}}(x)$ and $E_{\mathrm{B}}(x)$ for the tracer diffusion coefficients can be calculated from the activation energies $E_{\mathrm{A}}^{(0)}(c_{\mathrm{A}})$ and $E_{\mathrm{B}}^{(0)}(c_{\mathrm{B}})$ of the corresponding single ionic glasses by taking $E_{\mathrm{A}}(x) = E_{\mathrm{A}}^{(0)}((1-x)c)$ and $E_{\mathrm{B}}(x) = E_{\mathrm{A}}^{(0)}(xc)$ [72,73]. Hence, with increasing replacement of A ions by B ions, i.e. increasing x, $E_{\mathrm{A}}(x)$ becomes larger while $E_{\mathrm{B}}(x)$ is lowered. As a consequence, D_{A} decreases and D_{B} increases very strongly with x at low temperatures.

Comparison with experimental data, however, reveals that this picture of independent ion species is not sufficient. While the *direction* of changes in the activation energies is in qualitative agreement with the experimental data, the dependence of $\mathrm{d}E_{\mathrm{A}}(x)/\mathrm{d}x$ and $\mathrm{d}E_{\mathrm{B}}(x)/\mathrm{d}x$ on x is not correctly reproduced. In linear-log plots of the mixing ratio versus the tracer diffusion coefficients, this leads to "curvatures" $\partial^2 \ln D_{\mathrm{A}}/\partial x^2$ and $\partial^2 \ln D_{\mathrm{B}}/\partial x^2$ having wrong signs in comparison with those found in measurements. As shown in Fig. 20.15, however, this problem may be resolved by taking into account the Coulomb interaction between the mobile ions. The Coulomb interaction seems to be of particular importance in the "dilute foreign alkali regimes" $x \to 0$ or $x \to 1$. Since the minority ions in these regimes are immobile on the diffusive time scale of the majority ions, they can, due to the Coulomb repulsion, create "blocking regions" for the majority ions on length scale large compared to the typical jump distance. Immobile minority ions replacing the majority ions in these dilute regimes are thus very effective in interfering the preferred diffusion paths of the majority species and lead to a very strong reduction of their mobility. The model of ions moving in energy landscapes being different for different types of ions allows one to address further important issues [72]: (i) the degree of validity of the empirical Meyer-Neldel rule (cf. Sect. 20.6), (ii) the mixed alkali internal friction peaks occurring in mechanical relaxation spectra, (iii) the behavior of a third tracer impurity ion in a binary mixed alkali glass as measured in [82], and (iv) the question if a clustering of like ions should be expected.

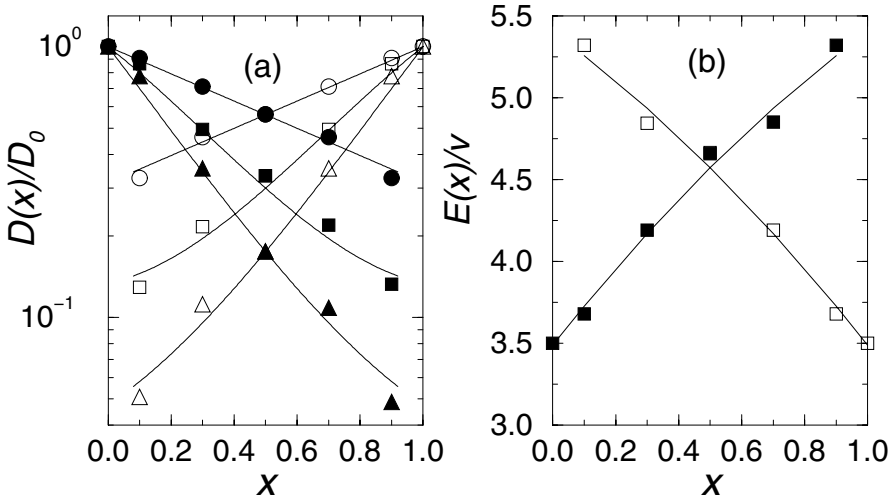

Fig. 20.15. (a) Monte-Carlo results for normalised tracer diffusion coefficients $D_{\mathrm{A,B}}(x)$ of two ion types A and B as a function of their mixing ratio $x = c_B/(c_A + c_B)$ in a lattice gas with exponentially distributed and uncorrelated site energies ϵ_i^{A} and ϵ_i^{B} (redrawn from [72]). Long-range Coulomb interactions between the mobile ions were taken into account in the simulations. Full symbols refer to ion type A, open symbols to ion type B, and different symbol types refer to different temperatures. The activation energies $E_{A,B}(x)$ are shown in (b). For a specification of the parameters, see [72].

Before closing this section, we note that a mixed alkali effect also occurs in certain crystals with structure of β- and β''-alumina type, where the ionic motion is confined to two-dimensional conduction planes [83–87]. For this effect a quantitative theoretical description is possible [88, 89] due to a wealth of structural information (see e.g. [85, 90, 91]). This theory is based on the fact that A and B ions have a different preference to become part of mobile defects, and this preference is caused by a different interaction of the ions with the local environment. Hence, the very origin of the mixed alkali effect in crystals and glasses might be similar. On the other hand, since the concentration of mobile ions in the crystals is large and since there is no strong structural disorder in the conduction planes, Fermi- and critical energies are not relevant. Instead, blocking and redistribution effects of ions in the conduction planes are important to understand the mixed alkali effect in the crystalline systems (see [88, 89] for a detailed discussion of these points).

20.8 Ion-Conducting Polymers

In the preceding sections we discussed charge transport in lattice gases that exhibit frozen disorder either by introducing at random a certain fraction of inaccessible sites (percolative disorder) or through some randomness in the site energies. The assumption of ion diffusion in a rigid matrix showing structural randomness on interatomic length scales turned out to constitute a general frame for the description of ionic transport in inorganic glasses and highly defective crystals.

As indicated already in the introduction (Sect. 20.1), a significantly more complex situation occurs in ion-conducting polymers [23,92]. Prototype materials are polymer-salt solutions based on polyethylene-oxide (PEO). The electronegative oxygen atom in the repeat unit of the PEO-chain tends to bind cations and hence favors salt dissociation. Above their glass transition temperature such systems can exhibit significant ionic conductivities. Distinctive features in comparison with inorganic glasses are the simultaneous diffusion of cations and anions and, most important, matrix fluctuations through the polymer segmental motions, which stochastically provide pathways for ion migration. This last issue is important also in problems of gas permeation through polymer membranes [93], but coupling of the diffusing particles with network degrees of freedom is much stronger in the polymer electrolytes discussed here.

Detailed insight into the coordination of cations by polymer chain segments and the resulting migration mechanisms emerged during recent years from classical molecular dynamics simulations, mostly on alkali-halide/PEO-systems [94–97]. Moreover, for understanding general trends in the ion and chain diffusion properties under varying temperature, pressure and salt-content, a coarse-grained description in terms of stochastic lattice models has proved useful [98–100]. Below we briefly outline this kind of approach. Subsequently we turn to a simplified, athermal model for particle diffusion in a fluctuating network of chain molecules. A mapping of that model onto dynamic percolation theory is proposed [101, 102]. Favorable tests against Monte Carlo simulations suggest that dynamic percolation could become a useful concept for studies of diffusion in fluctuating realistic structures. Finally, we adopt a more macroscopic viewpoint and summarize some ideas, based on differential effective-medium theory [103], how to interpret the recently discovered enhancement of ionic conductivities in stretched polymer systems [104].

20.8.1 Lattice Model of Polymer Electrolytes

For PEO-type electrolytes we adopt a simple model of lattice chains, where beads occupy a sequence of nearest-neighbour points on a simple cubic lattice of spacing a. We distinguish between C-beads and X-beads in sequences $C(XCC)_n$, where X corresponds to an oxygen atom and C to a hydrocarbon

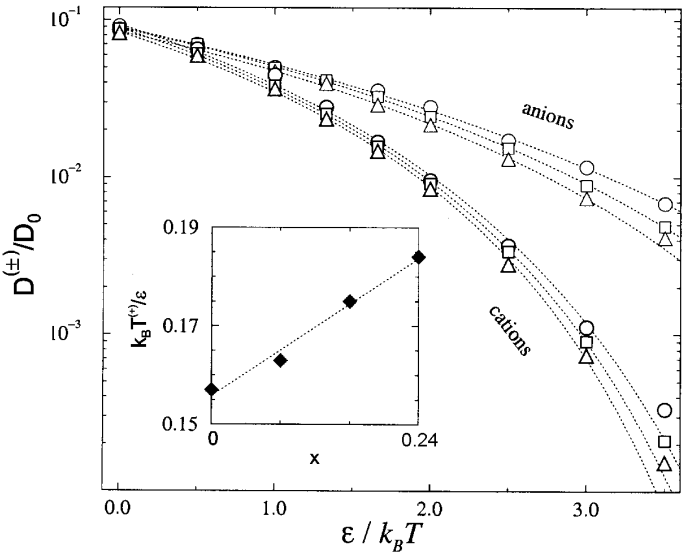

Fig. 20.16. Temperature-dependent cation and anion diffusion coefficients $D^{(\pm)}$ (normalized by the diffusion coefficient D_0 of non-interacting point particle) versus inverse temperature (data points) and VFT-fits (dotted lines) for different ion concentrations $x = 0.08$ (circles), $x = 0.16$ (squares) and $x = 0.24$ (triangles). The inset shows the variation of the VFT-temperature $T^{(+)}(x)$ with x (after [100]).

group. The total length of the chain is $r = 3n + 1$. Beads on nearest neighbor positions interact with a common repulsion $\epsilon_0 > 0$, which drives the system from the fluid to a glassy state upon lowering the temperature. Ions are represented as point particles carrying charges $\pm q$, and experience their mutual Coulomb forces. The asymmetry in the cation-chain and anion-chain interactions is introduced by assuming that X-beads attract cations with strength $-\epsilon < 0$. In order to reduce the number of free parameters in our model, we assume that $\epsilon_0 = \epsilon$. Elementary moves of the chains follow the generalized Verdier-Stockmayer algorithm [105,106], including kink jump, end jump and crankshaft moves. Such moves are known to conform with Rouse-dynamics in the case of sufficiently long chains (see Chap. 13). Ions simply perform nearest-neighbor hops. Transition probabilities in our Monte Carlo simulations are given by the Metropolis algorithm. For further details we refer to the original literature [100]. Considering techniques of lattice Monte Carlo simulations for polymers, we should remark at this point that the dynamics of dense polymer melts, especially their associated scaling properties, are most efficiently investigated by using the bond-fluctuation model [107]. However, in view of the chemical heterogeneity within a repeat unit in PEO-chains and the specific interactions of ions with chain beads it seems more natural in the present context to employ the lattice chain model described above.

Now we turn to some representative results. Figure 20.16 shows Arrhenius plots of the diffusion coefficients $D^{(\pm)}$ and $D^{(P)}$ for cations, anions and the polymer center of mass, respectively. The downward curvature of the data allows fits in terms of the empirical Vogel-Fulcher-Tammann (VFT) equation, well-known from relaxation studies in supercooled fluids [24],

$$D^{(\alpha)}(T,x) = D_\infty(x) \exp\left(-\frac{E^\alpha(x)}{k_{\mathrm{B}}(T - T^{(\alpha)}(x))}\right) \tag{20.30}$$

where $\alpha = \pm, P$. The ion concentration enters through the parameter x which measures the number of cations relative to the number of X-beads in the sample. $E^\alpha(x)$ is a characteristic energy and $T^{(\alpha)}(x)$ the VFT-temperature. For low ion content, $x \ll 1$, one finds that $T^+(x) \simeq T^{(P)}(x)$, which confirms the strong coupling of cations to the chain beads and suggests that freezing of the network simultaneously suppresses cation diffusion. By contrast, anion diffusion shows a much weaker temperature dependence, with $T^{(-)}(x) < T^{(P)}(x)$. VFT-temperatures generally increase with x, as indicated in the inset of the figure. These findings agree qualitatively with diffusion measurements on PEO-based electrolytes by the NMR pulsed-field gradient method [108], cf. Chap. 10, and with the general experimental observation of an increase in the glass transition temperature T_g with x [109].

The VFT-expressions (20.30) together with the equality $T^{(+)}(x) \simeq T^{(P)}(x)$ for $x \ll 1$ immediately imply, for fixed x, that

$$D^{(+)}(T,x) \propto (D^{(P)}(T,x))^{n_+(x)} \tag{20.31}$$

where the exponent

$$n_+(x) = E^{(+)}(x)/E^{(P)}(x) \quad < 1 \tag{20.32}$$

decreases with increasing x. Thus, when temperature is varied, the cation diffusion coefficient depends in a power-law fashion on the diffusion coefficient for the chain center-of-mass motion. As shown in Fig. 20.17, such a relationship holds over at least three decades in $D^{(+)}$. Qualitatively, we expect that diffusion coefficients of non-entangled chains reflect the behavior of the viscosity η of the system, $D^{(P)} \sim \eta^{-1}$. Equation (20.31) would then imply $D^{(+)} \sim \eta^{-n_+}$. Such a relationship appears interesting in connection with recent experimental observations of a "fractional Stokes-Einstein" law in ionic melts [110]. Figure 20.17 also shows that under variation of both T and x the anion diffusion coefficients can be represented by a unique function of $D^{(P)}$. This suggests that, for given T and x, anion diffusion depends only on a single time scale that characterizes the chain motion, a result which perfectly agrees with the idea of dynamic percolation. There one considers a random walk in an environment with percolative disorder. As time proceeds, the disorder configurations are continually renewed at a certain rate. In Sect. 20.8.2 we shall come back to this model in greater detail.

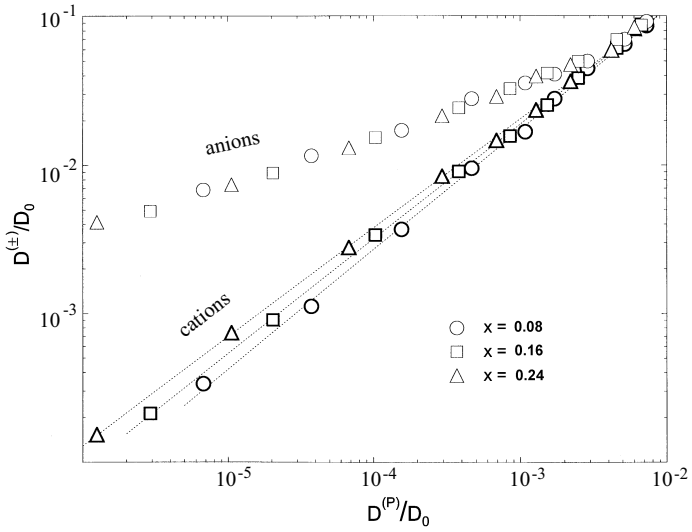

Fig. 20.17. Self-diffusion coefficients $D^{(\pm)}$ of cations and anions (normalized by the diffusion coefficient D_0 of non-interacting point particle) against chain diffusion coefficients $D^{(P)}$, for different ion concentrations (after [100]).

Several further studies have been carried out in a reduced polymer electrolyte model with only one species of mobile point-like particles. The latter assumption may directly apply to the so-called ionenes, where the anions are chemically grafted to the chains [111]. By combining the quasi-chemical approximation for the equation of state with standard simulations at constant volume, information on the isobaric-isothermal ensemble can be gained [112]. Ion diffusion coefficients in dense systems were found to decrease exponentially with pressure, in accord with experiments [111]. Further studies considered the variation of VFT-temperatures with salt concentration, keeping the pressure fixed. As x becomes of the order of unity, the VFT-temperatures $T^{+}(x)$ and $T^{(P)}(x)$ tend to saturate in this model and get decoupled, $T^{+}(x) < T^{(P)}(x)$, such that ions keep some mobility when the network freezes.

20.8.2 Diffusion through a Polymer Network: Dynamic Percolation Approach

With the aim to investigate generic aspects of random walks in a dynamically disordered environment, several authors have developed models of dynamic percolation (DP) [113–116]. The most common starting point is a bond percolation model with global, instantaneous renewals of the disorder configurations. These renewal events occur in time according to some waiting time distribution $\psi(t)$. Denoting by $\langle r^2(t)\rangle_0$ the mean square displacement of the

walker in the absence of renewals (frozen disorder), one can show [117] that the long-time (zero-frequency) diffusion coefficient in $d = 3$ dimensions is given by

$$D = \frac{1}{6} \frac{\int_0^\infty \mathrm{d}t\, \psi(t) \langle r^2(t) \rangle_0}{\int_0^\infty \mathrm{d}t\, \psi(t) t} \tag{20.33}$$

In the special case of a Poisson renewal process with mean waiting time λ^{-1}, we have $\psi(t) = \lambda^{-1} \mathrm{e}^{-\lambda t}$, so that $D = D_0(\lambda)$, where $D_0(\lambda)$ is determined by the Laplace transform of $\langle r^2(t) \rangle_0$. More generally, the frequency-dependent diffusivity $D(-\mathrm{i}\omega)$ in the case of Poisson renewals satisfies the analytic continuation rule [113]

$$D(-\mathrm{i}\omega) = D_0(-\mathrm{i}\omega + \lambda) \tag{20.34}$$

In an attempt to map a random walk through a system of fluctuating polymer chains onto that model, the primary task is to extract an appropriate waiting time distribution $\psi(t)$, to be used in (20.33), from the actual polymer dynamics. For that purpose the following scheme has been advanced recently [102,118]. The function $\psi(t)$ is related to the stochastic process $n_i(t)$, representing the occupation of a site i by a polymer bead. That site i is chosen to be a nearest neighbor of a fixed position of the walker. By this, the correlation function $\langle n_i(t) n_i(0) \rangle$ reflects the closing or opening statistics of a bond connected to the walker. Renewal events in an associated DP model are now identified with occupational changes at site i. This will allow us to express $\psi(t)$ in terms of $\langle n_i(t) n_i(0) \rangle$.

To put this idea on a quantitative basis, we introduce the probability $\Phi(t)$ with $t > 0$ that no renewal takes place in the interval $[0, t]$, after a previous renewal at an arbitrary time $t_0 < 0$. Hence, with probability $\Phi(t)$ the occupation of site i does not change, so that $n_i(t) = n_i(0)$, with possible values 0 and 1, and $n_i(t) n_i(0) = (n_i(0))^2 = n_i(0)$. Conversely, with probability $1 - \Phi(t)$, one or more renewals occur within $[0, t]$. Then, since configurations are randomly reassigned, $n_i(t)$ can be replaced by its average c, and $n_i(t) n_i(0) = c\, n_i(0)$. Averaging in addition over the initial occupation $n_i(0)$, we obtain

$$\langle n_i(t) n_i(0) \rangle = c\, \Phi(t) + c^2 (1 - \Phi(t)) \tag{20.35}$$

or

$$\Phi(t) = \frac{\langle n_i(t) n_i(0) \rangle - c^2}{c(1 - c)} \tag{20.36}$$

The final step is to utilize the result from renewal theory [117], that

$$\psi(t) = \bar{\lambda}^{-1} \Phi''(t) \tag{20.37}$$

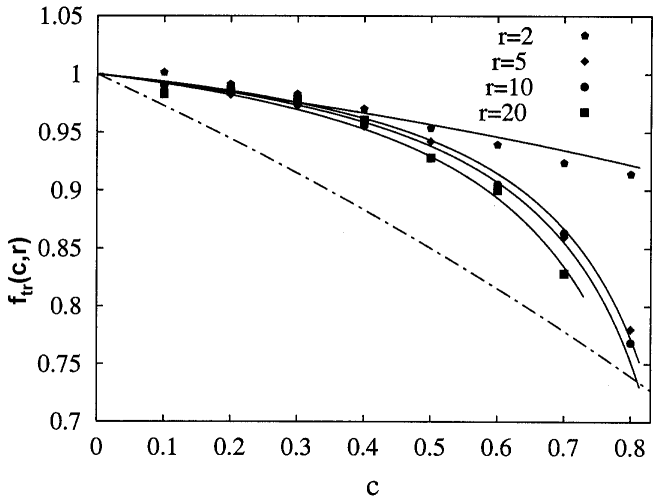

Fig. 20.18. Comparison of tracer correlation factors from dynamic percolation theory for chains of different lengths r (data points) with results from simulations (full lines, representing fit functions of simulation data). The dashed-dotted line shows the tracer correlation factor of a hard core lattice gas that corresponds to $r = 1$.

where $\bar{\lambda}^{-1} = \int_0^\infty \mathrm{d}t\, \psi(t) t$ is the mean renewal time. These arguments generalize earlier ideas of constructing effective-medium theories for many-particle systems with the help of DP theory [119].

When applying this concept, based on (20.33), (20.36) and (20.37), to tracer diffusion within a polymer host, one has to find the two input quantities $\langle r^2(t)\rangle_0$ and $\langle n_i(t) n_i(0)\rangle$ from simulations of the two separate problems: random walk of a tracer particle through a frozen polymer host and local occupational correlation function due to polymer segmental motions next to a frozen tracer. Both of these problems are expected to be computationally much less demanding than the simulation of the full system dynamics.

Recently that DP scheme has been tested against Monte Carlo simulations for the case of an athermal model, where multiple occupation of lattice sites by either chain beads or (point-like) tracer particles is excluded [102]. As usual, we define the tracer correlation factor $f_{\mathrm{tr}}(c, r)$ in terms of the tracer diffusion coefficient D by

$$D = (1 - c) f_{\mathrm{tr}}(c, r) D_0 \tag{20.38}$$

which now depends both on the overall concentration c of occupied sites and on the chain length r. Data points in Fig. 20.18 show DP results for $f_{\mathrm{tr}}(c, r)$ up to a chain length $r = 20$, while the full lines represent fits to Monte Carlo simulations of the complete system dynamics. Obviously the agreement

between both methods is excellent, suggesting that the DP description may become a useful tool also in studies of more realistic systems. It is important to note that in order to achieve this degree of accuracy in DP theory, the non-Poisson character of the waiting-time distribution has to be taken into account. In particular, the function $\Phi(t)$ reflecting the polymer dynamics shows slow relaxation which for longer chains becomes even more pronounced.

Figure 20.18 includes data for the well-known case of a hard core lattice gas, which emerges here as the limit $r = 1$. Since for $c < 0.8$ one finds $f_{\mathrm{tr}}(c,1) < f_{\mathrm{tr}}(c,r)$ with $r \neq 1$, we conclude that in this concentration range chain connectivity enhances tracer diffusion. This conforms with the additional observation that a random walker in a $3-d$ system of frozen chains ceases to percolate at a threshold concentration $c_{\mathrm{crit}}(r)$ which increases with r.

20.8.3 Diffusion in Stretched Polymers

Recent experiments on stretched PEO-based polymer electrolyte films have revealed an enhancement of ionic diffusion and conductivity in the stretch direction, while these transport coefficients in the normal direction decrease [104]. A preferential migration of cations along the helical structure of the PEO-chain, detected in molecular dynamics simulations [94], can in principle lead to that kind of macroscopic anisotropy when chains get oriented through stretch. This situation has been described qualitatively by an effective two-phase model, where a highly conducting phase is associated with those oriented molecular structures, but is surrounded by poorly conducting boundary regions [103]. The effective conductivity was evaluated by using differential effective-medium theory (DEMT), which accounts for the fact that the highly conducting phase with conductivity σ_2 never percolates; rather, the conduction paths always have to pass the boundary phase with conductivity $\sigma_1 \ll \sigma_2$. Under stretch, the shape of one-phase regions changes from spherical to prolate-ellipsoidal. As a stretch parameter one uses the ratio λ between the long and the short axis of these ellipsoids. A version of DEMT capable of taking into account these non-spherical shapes is due to Mendelson et al. [120].

Conductivities perpendicular and parallel to the stretch direction are plotted in Fig. 20.19 as a function of λ for different volume fractions f_2 of the highly conducting phase. While the directions of change in $\sigma_{\parallel}$ and $\sigma_{\perp}$ with λ agree with experiments, the model calculations show further details which remain to be tested against more refined measurements. For example, as f_2 increases, $\sigma_{\parallel}(\lambda)$ becomes more sensitive to changes in λ, whereas $\sigma_{\perp}$ becomes less sensitive. Clearly, in the interpretation of these and other features of that model, care has to be taken in relating the degree of macroscopic stretch to anisotropies on the molecular level.

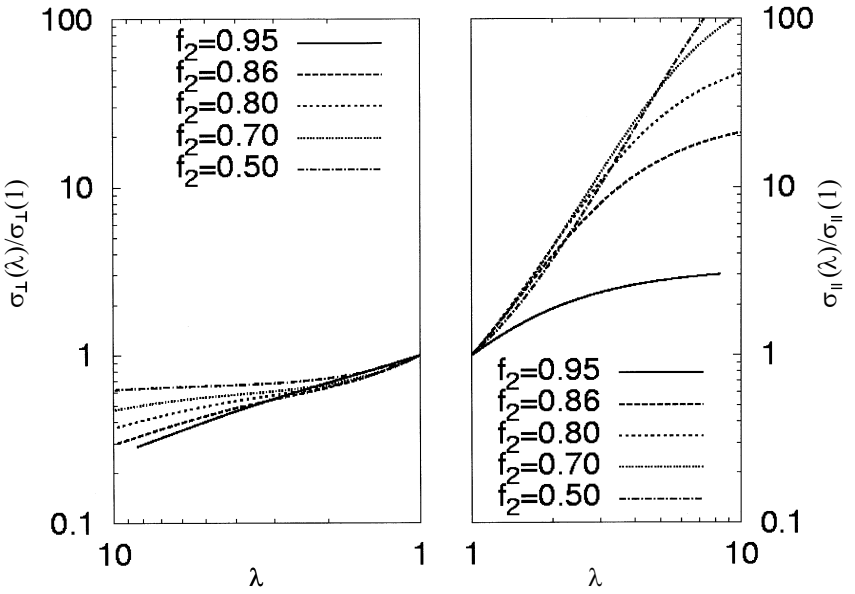

Fig. 20.19. Ratio between conductivities of the stretched film in the stretch direction (right) and perpendicular to it (left) and the conductivity in the isotropic unstretched film ($\sigma_\perp(1) = \sigma_\parallel(1)$) as a function of the stretch parameter λ for several values of the volume fraction f_2 of the low-conductivity phase with $\sigma_1/\sigma_2 = 10^{-4}$ (after [103]).

20.9 Conclusion

In Sects. 20.3–20.6, models for ionic transport in complex systems have been presented which keep the essential physics: Coulombic interaction between the ions and structural disorder in the substrate. These models are simple enough to be treated numerically by Monte-Carlo simulation techniques. Several ionic transport quantities, such as the mean square displacement, the frequency dependent conductivity and the spin-lattice relaxation rate, have been discussed and it was found that *both* ingredients (structural disorder *and* Coulomb interactions) are needed to find the typical dispersion behavior widely observed in experiments. It is remarkable that inclusion of the simple percolative type of disorder allows one to account for the delicate differences between conductivity relaxation and spin-lattice relaxation found in experiments. However, for the theoretical understanding of the non-Arrhenius behaviour observed in fast ion conductors the consideration of the different energies associated with the different environments encountered by the mobile ions becomes important.

In Sects. 20.4 and 20.5 it has been assumed that the charges of the mobile cations are balanced by a homogeneous background charge, and that the en-

ergetic disorder is spatially uncorrelated. On the other hand, the assumption of randomly placed immobile counterions leads to a spatially correlated one-particle energy landscape. Local motions of ions on binding sites next to an associated counterion can give rise to a "nearly constant loss"-type response. This was shown by additional simulations of a dipolar lattice gas discussed in Sect. 20.6. Other effects caused by spatial correlations in the disorder are considered in [121]. By taking into account that the energetic disorder is different for different types of mobile ions, a natural explanation for the mixed alkali effect in glasses was discussed in Sect. 20.7. Coulomb interaction effects are important to understand why the long-range mobility of a particular ion type behaves quite differently if its concentration is changed via dilution or if its (partial) concentration is changed via replacement by another type of mobile ion.

Furthermore we have shown in Sect. 20.8 that a stochastic model of lattice polymers and point-like particles (ions) with specific interactions can account for characteristic conductance and network relaxational properties of polymer electrolytes. On a coarse-grained level, dynamic percolation theory appears as a promising tool to study ionic diffusion through a fluctuating polymer matrix.

Notation

a, L	lattice constant, system size
d	space dimension
D, D_{st}	long-time, short-time diffusion coefficient
$D(t)$	time dependent diffusion coefficient
$\hat{D}(\omega)$	complex frequency dependent diffusion coefficient
ΔE_{SLR}	activation energy of the correlation time in spin-lattice relaxation
E_1^{SLR}, E_2^{SLR}	activation energy of spin-lattice relaxation rate at high- and low-temperature side of maximum
E_σ, ΔE_f	activation energy of conductivity and tracer correlation factor
f_{tr}	tracer correlation factor
$G^{(q)}(t)$	correlation function for spin-lattice relaxation
$\hat{H}_{\mathrm{R}}(\omega)$	complex Haven ratio
I, Q	spin and quadrupole moment of nucleus
$\boldsymbol{j}(t)$	current density
$\langle \boldsymbol{j}(t) \cdot \boldsymbol{j}(0) \rangle$	current auto-correlation function
n_σ, n_{D}	conductivity and diffusion exponent
p	fraction of lattice sites accessible for mobile ions
p_{c}	percolation threshold
$P(\boldsymbol{r}, t)$	diffusion propagator
$\boldsymbol{P}(t)$	electric polarization
r	length of polymer chains
$\langle r^2(t) \rangle$	mean square displacement

$\langle r^2(N_{\rm hop})\rangle$	mean square displacement as a function of performed hops
$S_{\rm inc}(\boldsymbol{k},\omega)$	incoherent structure factor
$1/T_1(\omega,T)$	spin-lattice relaxation rate
$T_{\rm max}$	temperature of maximum in spin-lattice relaxation rate
$T^{(\alpha)}$	Vogel-Fulcher-Tammann temperature for polymer chains ($\alpha = P$), cations ($\alpha = +$) and anions ($\alpha = -$)
V_0	structural energy barrier for hops
$V_{\rm dip-dip}$	dipole-dipole interaction energy
γ	magnetogyric ratio
Γ	plasma parameter
$\overline{\lambda}$	mean renewal rate
ν	number of nearest neighbours
ρ	number density
$\sigma_{\|\|}$, $\sigma_\perp$	parallel, perpendicular conductivity in stretched polymer films
$\hat{\sigma}(\omega)$, $\sigma_{\rm dc}$	complex dynamic conductivity, dc-conductivity
τ_∞	rattling time or inverse attempt frequency for hops
$\tau_{\rm SLR}$	correlation time in spin-lattice relaxation
τ_σ, $\tau_{\rm D}$	conductivity and diffusion relaxation time
$\hat{\chi}(\omega)$	complex dielectric susceptibility
$\psi(t)$	waiting time distribution for renewals
$\psi(\tau_{\rm w})$	effective distribution of waiting times τ_w
$\omega_{\rm NCL}$	cross-over frequency to "nearly constant loss" regime

References

1. H. Jain, N.L. Peterson, H.L. Downing: J. Non-Cryst. Solids **55**, 283 (1983)
2. *Impedance Spectroscopy*, ed by J.R. Macdonald (John Wiley & Sons, New York 1987)
3. K. Funke: Prog. Solid St. Chem. **22**, 111 (1993)
4. C.T. Moynihan, L.P. Boesch, N.L. Laberge: Phys. Chem. Glasses **14**, 122 (1973)
5. M.D. Ingram: Phys. Chem. Glasses **28**, 215 (1987)
6. O. Kanert, J. Steinert, H. Jain, K.L. Ngai: J. Non-Cryst. Solids **131-133**, 1001 (1991); O. Kanert, R. Küchler, K.L. Ngai, H. Jain: Phys. Rev. B **49**, 76 (1994)
7. O. Kanert, R. Küchler, J. Diekhöfer, X. Lu, H. Jain: Phys. Rev. B **49**, 629 (1994)
8. P. Heitjans, W. Faber, A. Schirmer: J. Non-Cryst. Solids **131-133**, 1053 (1991); P. Heitjans: Solid State Ionics **18/19**, 50 (1986)
9. W. Franke, P. Heitjans: Ber. Bunsenges. Phys. Chem. **96**, 1674 (1992)
10. P. Heitjans, S. Indris: J. Phys.: Condens. Matter **15** R1257 (2003)
11. K. Funke, I. Riess: Z. Phys. Chem. Neue Folge **140**, 217 (1984); K. Funke: Z. Phys. Chem. Neue Folge **154**, 251 (1987)
12. T. Suemoto, M. Ishigame: Phys. Rev. B **33**, 2757 (1986)
13. L. Börjesson, L.M. Torrel, W.S. Howells: Phil. Mag. B **59**, 105 (1989); L. Börjesson Phys. Rev. B **36**, 4600 (1987)

14. G. Carini, M. Federico, G. Tripodo: Phil. Mag. B **65**, 153 (1992)
15. D.P. Almond, G.K. Duncan, A.R. West: Solid State Ionics **8**, 159 (1983)
16. A.K. Jonscher: Nature **267**, 673 (1977)
17. A.S. Nowick, B.S. Lim, A.V. Vaysleyb: J. Non-Cryst. Solids **172**–**174**, 1243 (1994)
18. K.L. Ngai: J. Chem. Phys. **110**, 10576 (1999)
19. H. Jain, S. Krishnaswami, O. Kanert: J. Non-Cryst. Solids **307**–**310**, 1017 (2002)
20. J. Kincs, S.W. Martin: Phys. Rev. Lett. **76**, 70 (1996)
21. K.L. Ngai, A.K. Rizos: Phys. Rev. Lett. **76**, 1296 (1996)
22. M.D. Ingram, C. Vincent, A. Wandless: J. Non-Cryst. Solids **53**, 73 (1982)
23. F.M. Gray: *Solid Polymer Electrolytes* (VCH Publishers, New York 1991)
24. H. Vogel: Physik. Zeitschrift **22**, 645 (1921); G.S. Fulcher: J. Am. Ceram. Soc. **8**, 339 (1925); G. Tammann, W. Hesse: Z. anorg. u. allg. Chem. **156**, 245 (1926)
25. N. Bloembergen, E.M. Purcell, R.V. Pound: Phys. Rev. **73**, 679 (1948)
26. W. Dieterich, P. Maass: Chem. Phys. **284**, 439 (2002)
27. A. Bunde, D.K. Chaturvedi, W. Dieterich: Z. Physik B **47**, 209 (1982); A. Bunde, W. Dieterich: Phys. Rev. B **31**, 6012 (1985)
28. P. Maass, J. Petersen, A. Bunde, W. Dieterich, H.E. Roman: Phys. Rev. Lett. **66**, 52 (1991)
29. M. Meyer, P. Maass, A. Bunde: Phys. Rev. Lett. **71**, 573 (1993)
30. P. Maass, M. Meyer, A. Bunde: Phys. Rev. B **51**, 8164 (1995)
31. K.L. Ngai: Comments Solid State Phys. **9**, 127, 141 (1979); K.L. Ngai. In: *Fast Ion Transport in Solids*, ed by P. Vashishta, J.N. Mundy, G.K. Shenoy (North Holland, New York 1979); K.L. Ngai, O. Kanert: Solid State Ionics **53-56**, 936 (1992)
32. S.R. Elliott, A.P. Owens: Phys. Rev. B **44**, 47 (1991)
33. W. Schirmacher, M. Prem, J.-B. Suck, A. Heidemann: Europhys. Lett. **13**, 523 (1990)
34. J.C. Dyre: Phys. Rev. B **48**, 12511 (1993)
35. A. Hunt: J. Phys. C **3**, 7831 (1991); **4**, 5371 (1992); J. Non-Cryst. Solids **160**, 183 (1993)
36. H. Lammert, M. Kunow, A. Heuer: Phys. Rev. Lett. **90**, 215901 (2003)
37. J. Habasaki, Y. Hiwatari: Phys. Rev. B **69**, 144207 (2004)
38. M. Vogel: Phys. Rev. B **70**, 094302 (2004)
39. J. Petersen, W. Dieterich: Phil. Mag. B **65**, 231 (1992)
40. D. Knödler, P. Pendzig, W. Dieterich: Solid State Ionics **86**–**88**, 29 (1996)
41. P. Maass, M. Meyer, A. Bunde, W. Dieterich: Phys. Rev. Lett. **77**, 1528 (1996)
42. R. Kubo, M. Toda, N. Hashitsume: *Statistical Physics II* (Springer-Verlag, Berlin Heidelberg New York 1985)
43. A. Abragam: *The Principles of Nuclear Magnetism* (Clarendon Press, Oxford 1962)
44. D. Wolf: *Spin-Temperature and Nuclear-Spin Relaxation in Matter* (Clarendon Press, Oxford 1979)
45. A. Bunde, S. Havlin. In: *Fractals and Disordered Systems*, 2nd edn, ed by A. Bunde, S. Havlin (Springer, Berlin Heidelberg New York 1996)
46. M.D. Ingram: J. Non-Cryst. Solids **131-133**, 955 (1991)
47. J. Hoshen, R. Kopelman: Phys. Rev. B **14**, 3438 (1976)

48. M.P. Allen, D.J. Tildesley: *Computer Simulation of Liquids* (Clarendon Press, Oxford 1987)
49. C. Cramer, K. Funke, T. Saatkamp: Phil. Mag. B **71**, 701 (1995)
50. G.H. Weiss. In: *Fractals in Science*, ed by A. Bunde, S. Havlin (Springer, Berlin Heidelberg New York 1994)
51. H. Scher, M. Lax: Phys. Rev. B **7**, 4491 (1973)
52. J.W. Haus, K.W. Kehr: Phys. Rep. **150**, 263 (1987)
53. A. Bunde, S. Havlin, H.E. Roman: Phys. Rev. A **42**, 6274 (1990)
54. M. Tatsumisago, C.A. Angell, S.W. Martin: J. Chem. Phys. **97**, 6968 (1992)
55. B. Munro, M. Schrader, P. Heitjans: Ber. Bunsenges. Phys. Chem. **96**, 1718 (1992); W. Franke, P. Heitjans, B. Munro, M. Schrader. In: *Defects in Insulating Materials*, ed by O. Kanert, J.M. Spaeth (World Scientific, Singapore 1993) p 1009
56. R. Winter, K. Siegmund, P. Heitjans: J. Non-Cryst. Solids **212**, 215 (1997)
57. E. Bychkov: Solid State Ionics **136 - 137**, 1111 (2000)
58. V. Ambegoakar, B.I. Halperin, J.S. Langer: Phys. Rev. B **4**, 2612 (1971); B.I. Shklovskii A.L. Efros: Zh. Eksp. Teor. Fiz. **60**, 867 (1971) [Sov. Phys. JETP **33**, 468 (1971)]
59. H. Bässler: Phys. Rev. Lett.**58**, 767 (1987)
60. W. Meyer, H. Neldel: Z. Tech. Phys. **12**, 588 (1937)
61. J.E. Kelly III, J.F. Cordaro, M. Tomozawa: J. Non-Cryst. Solids **41**, 47 (1980)
62. P. Pendzig, W. Dieterich: Solid State Ionics **105**, 209 (1998)
63. C.A. Angell, K.L. Ngai, G.B. McKenna, P.F. McMillan, S.W. Martin: J. Appl. Phys. **88**, 3113 (2000)
64. M. Pollak, G.E. Pike: Phys. Rev. Lett. **28**, 1449 (1972)
65. D. Knödler, P. Pendzig, W. Dieterich: Mat. Res. Soc. Symp. Proc. **369**, 225 (1995)
66. T. Höhr, P. Pendzig, W. Dieterich, P. Maass: Phys. Chem. Chem. Phys. **4**, 3168 (2002)
67. P. Pendzig. PhD thesis, University of Konstanz (1998)
68. P. Pendzig, W. Dieterich: Solid State Ionics **105**, 209 (1998)
69. M.D. Ingram. In: *Materials Science and Technology*, vol 9, ed by J. Zarzycki (VCH Verlagsgesellschaft, Weinheim 1991) p 715
70. D.E. Day: J. Non-Cryst. Solids **21**, 343 (1976)
71. M. Porto, P. Maass, M. Meyer, A. Bunde, W. Dieterich: Phys. Rev. B **61**, 6057 (2000)
72. P. Maass: J. Non-Cryst. Solids **255**, 35 (1999)
73. A. Hunt: J. Non-Cryst. Solids **175**, 129 (1994)
74. G.N. Greaves, S.J. Gurman, C.R.A. Catlow, A.V. Chadwick, S. Houde-Walter, C.M.B. Henderson, B.R. Dobson: Phil. Mag. A **64**, 1059 (1991); S.N. Houde-Walter, J.M. Inman, A.J. Dent, G.N. Greaves: J. Phys. Chem. **97**, 9330 (1993)
75. J. Swenson, A. Matic, C. Karlsson, L. Börjesson, C. Meneghini, W.S. Howells: Phys. Rev. B **63**, 132202 (2001)
76. P. Maass, A. Bunde, M.D. Ingram: Phys. Rev. Lett. **68**, 3064 (1992)
77. A. Bunde, M.D. Ingram, P. Maass: J. Non-Cryst. Solids **172**–**174**, 1222 (1994)
78. M.D. Ingram, J.E. Davidson, A.M. Coats, E.I. Kamitsos, J.A. Kapoutsis: Glass Science and Technology **73**, 89 (2000)
79. P.W.S.K. Bandaranayake, C.T. Imrie, M.D. Ingram: Phys. Chem. Chem. Phys. **4**, 3209 (2002); M.D. Ingram, B. Roling: J. Phys.: Condens. Matter **15**, 1595 (2003)

80. A. Bunde, M.D. Ingram, S. Russ: Phys. Chem. Chem. Phys. **6**, 3663 (2004)
81. J. Habasaki, I. Okada, Y. Hiwatari: J. Non-Cryst. Solids **208**, 181 (1996)
82. H. Jain, N.L. Peterson: J. Am. Ceram. Soc. **66**, 174 (1983)
83. G.V. Chandrashekhar, L.M. Foster: Solid State Commun. **27**, 269 (1978)
84. L.M. Foster, M.P. Anderson, G.V. Chandrashekhar, G. Burns, R.B. Bradford: J. Chem. Phys **75** (1981)
85. J.A. Bruce, M.D. Ingram: Solid State Ionics **9&10**, 717 (1983)
86. T. Tsurumi, G. Singh, P.S. Nicholson: Solid State Ionics **22**, 225 (1987)
87. S. Nariki, S. Ito, K. Uchinokura, T. Uchida, N. Yoneda: Solid State Ionics **36**, 193 (1989)
88. M. Meyer, V. Jaenisch, P. Maass, A. Bunde: Phys. Rev. Lett. **76**, 2338 (1996)
89. M. Meyer, P. Maass, A. Bunde: J. Chem. Phys. **109**, 2316 (1998)
90. J.P. Boilot, G. Collin, Ph. Colomban, R. Comes: Phys. Rev. B **22**, 5912 (1980)
91. J.C. Wang, M. Gaffari, Sang-il Choi: J. Chem. Phys **63**, 772 (1975); J.C. Wang, J.B. Bates, T. Kenda, H. Engstrom, D.F. Pickett, Sang-il-Choi. In: *Fast Ion Transport in Solids*, ed by P. Vashista, J.N. Mundy, G.K. Shenoy (Elsevier, Amsterdam 1979)
92. A. Nitzan, M. Ratner: J. Phys. Chem. **98**, 1765 (1994)
93. A.A. Gusev, S. Arizzi, U.W. Suter: J. Chem. Phys. **99**, 2221 (1993)
94. F. Müller-Plathe, W.F. von Gunsteren: J. Chem. Phys. **103**, 4745 (1995)
95. B. Mos, P. Verkerk, S. Pouget, A. van Zon, G.-J. Bel, S.W. de Leeuw, C.D. Eisenbach: J. Chem. Phys. **113**, 4 (2000)
96. J.J. de Jonge, A. van Zon, S.W. de Leeuw: Solid State Ionics **147**, 349 (2002)
97. O. Borodin, G.D. Smith: J. Phys. Chem. B. **107**, 6801 (2003)
98. R. Olender, A. Nitzan: J. Chem. Phys. **100**, 705 (1994); **101**, 2338 (1994)
99. R. Olender, A. Nitzan, D. Knödler, W. Dieterich: J. Chem. Phys. **103**, 6275 (1995)
100. P. Pendzig, W. Dieterich, A. Nitzan: J. Non-Cryst. Solids **235**–**237**, 748 (1998)
101. O. Dürr, W. Dieterich, A. Nitzan: Solid State Ionics **149**, 125 (2002)
102. O. Dürr, T. Volz, W. Dieterich, A. Nitzan: J. Chem. Phys. **117**, 441 (2002)
103. O. Dürr, W. Dieterich, P. Maass, A. Nitzan: J. Phys. Chem. B **106**, 6149 (2002)
104. D. Golodnitsky, E. Peled: Electrochimica Acta **45**, 1431 (2000)
105. P.H. Verdier, W.H. Stockmayer: J. Chem. Phys. **36**, 227 (1962)
106. P.H. Verdier: J. Comput. Phys. **4**, 227 (1969)
107. For a review, see K. Binder. In: *Monte Carlo and Molecular Dynamics Simulations in Polymer Science*, ed by K. Binder (Oxford University Press, New York Oxford 1995) p 3
108. C.A. Vincent: Electrochimica Acta **40**, 2035 (1995)
109. M.G. McLin, C.A. Angell: Solid State Ionics **53**–**56**, 1072 (1992)
110. A. Voronel, E. Veliyulin, V.S. Machavariani, A. Kislink, D. Quitmann: Phys. Rev. Lett. **80**, 2630 (1998)
111. M. Duclot, F. Alloin, O. Brylev, J.Y. Sanchez, J.L. Souquet: Solid State Ionics **136**–**137**, 1153 (2000)
112. O. Dürr, W. Dieterich, A. Nitzan: J. Chem. Phys. **121**, 12732 (2004)
113. S.F. Druger, A. Nitzan, M.A. Ratner: J. Chem. Phys. **79**, 3133 (1983)
114. S.F. Druger, M.A. Ratner, A. Nitzan: Phys. Rev. B **31**, 3939 (1985)
115. A.K. Harrison, R. Zwanzig: Phys. Rev. A **32**, 1072 (1985)

116. R. Hilfer, R. Orbach. In: *Dynamical Processes in Condensed Molecular Systems*, ed by J. Klafter, J. Jortner, A. Blumen (World Scientific, Singapore 1989) p 175
117. S.F. Druger, M.A. Ratner: Phys. Rev. B **38**, 12589 (1988)
118. O. Dürr, W. Dieterich, A. Nitzan. In: *Multiscale Computational Methods in Chemistry and Physics*, NATO Science Series III, vol 177, ed by A. Brandt, J. Bernholc, K. Binder (IOS Press, Amsterdam 2001) p 288
119. R. Granek, A. Nitzan: J. Chem. Phys. **92**, 1329 (1990); **93**, 5918 (1990); M. Silverberg, M.A. Ratner, R. Granek, A. Nitzan: J. Chem. Phys. **93**, 3420 (1990)
120. K.S. Mendelson, M.H. Cohen: Geophysics **47**,257 (1982)
121. P. Maass, M. Meyer: J. Chem. Phys. **103**, 5776 (1995)

21 Concept of Mismatch and Relaxation for Self-Diffusion and Conduction in Ionic Materials with Disordered Structures

Klaus Funke, Cornelia Cramer, and Dirk Wilmer

21.1 Introduction

In the ion conducting materials to be discussed in this chapter, structural and dynamic disorder is the key property. A simple scheme may serve to highlight the remarkable implications of this property with regard to the movements of the ions. In this scheme, perfectly ordered crystals are placed at *level one*. At this level, there is no possibility for the ions to leave their sites; thus no ionic transport can occur. Historically, the decisive step forward was made when site disorder was discovered and point-defect thermodynamics were developed. At this stage, which we call *level two*, ionic transport is accomplished by point defects moving randomly from site to site. In fact, modern materials science and engineering build on the concept of level two.

Dramatic changes are encountered as we move on to materials with disordered structures, i.e., from level two to *level three*. Now, point defects are no longer isolated structural elements. It is even no longer sensible to *speak* of defects, since the entire structure is disordered. Therefore, ionic transport cannot be described in terms of individual defects performing random walks in a static energy landscape. Instead, we are facing a challengingly complicated many-particle problem, with the mobile ions interacting with each other and with their surrounding matrix.

In materials with disordered structures, the number of available sites by far exceeds the number of mobile ions, and it turns out to be impossible to arrange the ions unambiguously in an optimised manner. These materials may be crystalline or glassy. They are fast ion conductors, if the barrier to be surmounted in a hop is of the order of the thermal energy.

The transition from level two to level three, i.e., from a random hopping of individual defects to a non-random correlated motion of interacting ions, is found to be accompanied by prominent changes in the shapes of functions which are experimentally accessible. For instance, the ionic conductivity assumes a characteristic frequency dependence, and spin-lattice relaxation rates are no longer properly described by the model of Bloembergen, Purcell and Pound [1] (cf. Chaps. 9 and 20). Surprisingly, the experimental phenomena are very much the same in structurally disordered crystals such as $RbAg_4I_5$, in glasses, and even in supercooled melts.

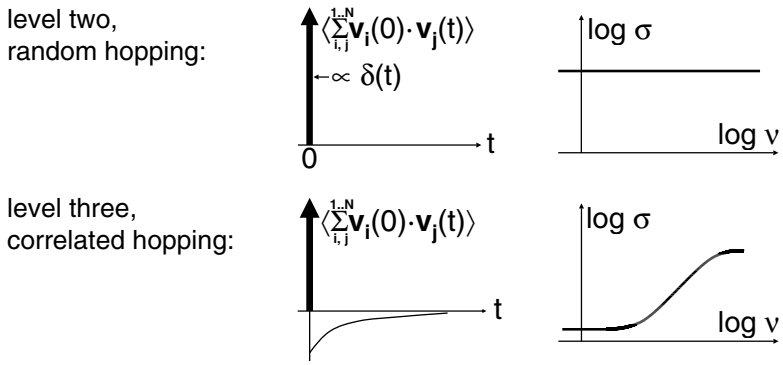

Fig. 21.1. Random versus correlated jump diffusion.

In this chapter, the diffusive motion of mobile ions in disordered materials will be analysed on the basis of the frequency-dependent electrical (ionic) conductivity, $\sigma(\nu)$. Figure 21.1 illustrates the change observed in the shape of this function as random hopping is replaced by correlated hopping. In Fig. 21.1, we have used a relationship from linear response theory which states that $\widehat{\sigma}(\nu)$ is proportional to the Fourier transform of the autocorrelation function of the current density [2]. If all mobile ions have the same charge, the current density will be proportional to the sum of their velocities. Therefore, $\sigma(\nu)$ is proportional to the Fourier transform of the velocity correlation function, $\langle \sum_{i,j}^{1..N} \boldsymbol{v}_i(0) \cdot \boldsymbol{v}_j(t) \rangle$.

If the ions (or mobile defects) are random walkers, as in level two, they do not know of each other, and all the cross terms vanish. Also, random walkers have no memory. Hence each hop is only correlated to itself. On a time scale that does not resolve a few picoseconds, the velocity correlation function is, therefore, proportional to a delta function at time zero, $\delta(t)$. The Fourier transform of a delta function being a constant, $\sigma(\nu)$ will be constant at least up to microwave frequencies. Such a behaviour is indeed observed in the case of level-two materials such as AgBr. By contrast, ionic materials with disordered structures display frequency-dependent conductivities, $\sigma(\nu)$, as in Fig. 21.2. In this case, the conductivity caused by the hopping motion of the ions is well described by a constant minus a bell-shaped contribution centred at $\nu = 0$. The corresponding velocity correlation function is, therefore, characterised by a sharp peak at $t = 0$, plus a decaying negative contribution at $t > 0$, see Fig. 21.1. While the sharp peak once again reflects the self-correlation of the velocity during hops, the decaying negative contribution results from a decaying probability for an ensuing *backward* hop, if the hop performed at time $t = 0$ defines the *forward* direction. If the dc conductivity, $\sigma_{\mathrm{dc}} = \sigma(0)$, is much smaller than the conductivity measured at microwave frequencies, correlated forward-backward hops have to be considered the rule rather than the exception.

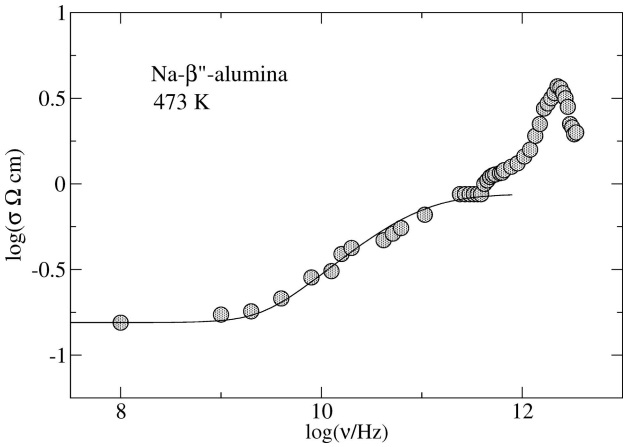

Fig. 21.2. Frequency-dependent conductivity, $\sigma(\nu)$, of crystalline Na-β''-alumina at 473 K [3]. Below 100 GHz, $\sigma(\nu)$ is essentially caused by the hopping motion of the sodium ions, while above 1 THz it is essentially due to the excitation of transverse optical phonons.

There is a direct analogy between this effect and the Debye-Hückel-Onsager-Falkenhagen effect, cf. Fig. 21.3. In Fig. 21.3 (a), consider a dilute strong liquid electrolyte. Suppose an ion is virtually displaced at time zero. As a consequence, it is no longer at the centre of its ion cloud. Two competing relaxation processes tend to restore equilibrium. The ion may move backward or the cloud may move forward. This results in a flow of charge in the direction opposite to the initial displacement, and Fourier transformation of the current density autocorrelation function yields a small increase of the conductivity as a function of frequency.

In a structurally disordered solid electrolyte, see Fig. 21.3 (b), the translational motion is achieved by hops, and the neighbouring mobile ions play the role of the ion cloud. Again, there is a competition between two relaxation processes. After each hop of a mobile ion, the ion may either hop backwards or its neighbours may rearrange. However, there is a striking difference between Fig. 21.3 (a) and Fig. 21.3 (b) concerning the respective magnitude of the effect. The amount of backward flow of charge and hence the resulting dispersion of $\sigma(\nu)$ are dramatically larger in the solid than in the dilute liquid electrolyte.

In this chapter, the correlated ionic motion in materials with disordered structures is studied on the basis of experimental conductivity spectra, $\sigma(\nu)$. In particular, a simple set of rules is derived that grasp the essential aspects of the ion dynamics and outline their development with time. Indeed, experimental conductivity spectra have led us to derive two coupled rate equations which describe the ion dynamics in a very general fashion and provide a means not only for reproducing the frequency-dependent conductivities, but

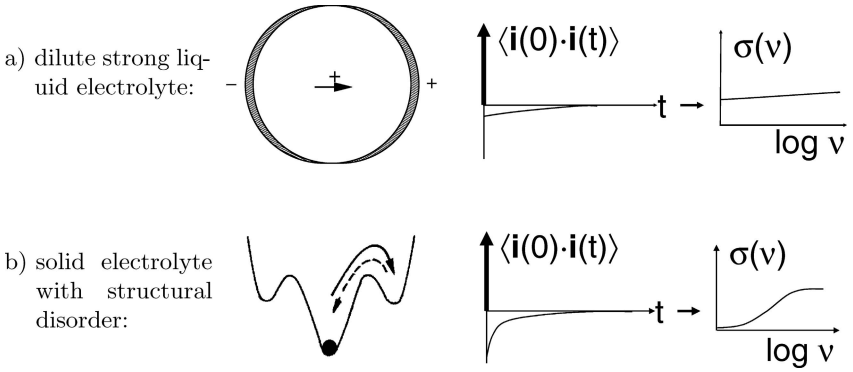

Fig. 21.3. Schematic comparison of the current density autocorrelation function and the conductivity dispersion in a) a dilute strong liquid electrolyte and b) a structurally disordered solid electrolyte.

also for tracing the specific traits of the spectra back to their dynamic origins. These rate equations make up the concept of mismatch and relaxation (CMR), to be presented and discussed in this chapter.

This chapter is organised as follows. In Sect. 21.2, the experimental techniques used in conductivity spectroscopy are briefly introduced, and the characteristic features of frequency- and temperature-dependent conductivities, $\sigma(\nu, T)$, are summarised. In Sect. 21.3, we give a brief outline of the formal relationships between conductivities, $\sigma(\nu)$, and time-dependent correlation functions. We also give interpretations of the experimental features and present models for the ion dynamics on a microscopic scale. In Sect. 21.4, we introduce the two rate equations of the CMR and show how time-dependent functions and realistic model conductivity spectra are obtained from them. Section 21.5 is devoted to a brief discussion of the scaling properties of the model spectra. It also provides relationships between model parameters and characteristic frequencies of the conductivity spectra, thus facilitating their interpretation. The physical concept leading to the two rate equations of the CMR is then outlined in Sect. 21.6. Examples of sets of complete conductivity spectra (extending at least up to millimetre-wave frequencies) taken at different temperatures are presented and discussed in Sects. 21.7 and 21.8, for solid electrolytes and for a fragile supercooled ionic melt, respectively. Section 21.9 deals with the shape of frequency-dependent conductivities of many glassy and crystalline materials as measured in the so-called impedance frequency regime, below some 10 MHz. In Sect. 21.10 we discuss localised movements of interacting charged particles and their manifestation in $\sigma(\nu, T)$.

21.2 Conductivity Spectra of Ion Conducting Materials

Conductivity spectroscopy spans more than 17 decades on the frequency scale, ranging from less than 10^{-3} Hz to more than 10^{14} Hz. The width of the time scale thus covered is unsurpassed by any other technique. Besides offering a broad variety of applications in the characterisation of materials, the technique also provides a unique possibility to study the motion of charged particles (ions or polarons) on rather different time scales, even resolving their elementary hopping processes. Therefore, it plays the role of an extremely powerful 'microscope in time'. A schematic survey of the requisite spectroscopies is given in Fig. 21.4. Experimentally, four frequency regimes may be discerned:

(i) the impedance regime, below some 10 MHz,
(ii) the radio regime, from some 10 MHz to a few GHz,
(iii) the microwave regime, from a few GHz to about 150 GHz, and
(iv) the (far-) infrared regime, above 150 GHz.

Electrodes are used only in (i). Guided electromagnetic waves are employed in (ii) and (iii), and free ones in (iv). Coaxial waveguides are practicable up to 18 GHz. At higher microwave frequencies, they are replaced by rectangular waveguide systems. Fourier transform spectroscopy is the method of choice in the (far) infrared. Although a number of different experimental setups are required to cover the entire frequency range, the general procedure towards the electrical characterisation of materials is essentially the same in any part of the spectrum. The complex electrical conductivity, $\widehat{\sigma}(\nu)$, is always determined by measurement of amplitudes and phases of quantities related to the field-induced current in the sample. These are voltages and currents, if electrodes are employed [4–6]. If the experimental technique is electrode-free, the relevant quantities are, instead, complex field amplitudes of electromagnetic waves transmitted or reflected by the sample [7]. In the latter case, the complex conductivity, $\widehat{\sigma}(\nu)$, is obtained from the measured data by means

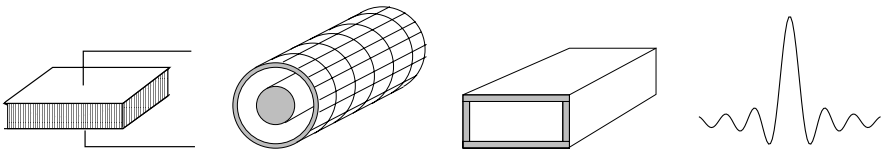

Fig. 21.4. Schematic overview of different techniques for the measurement of frequency-dependent conductivities.

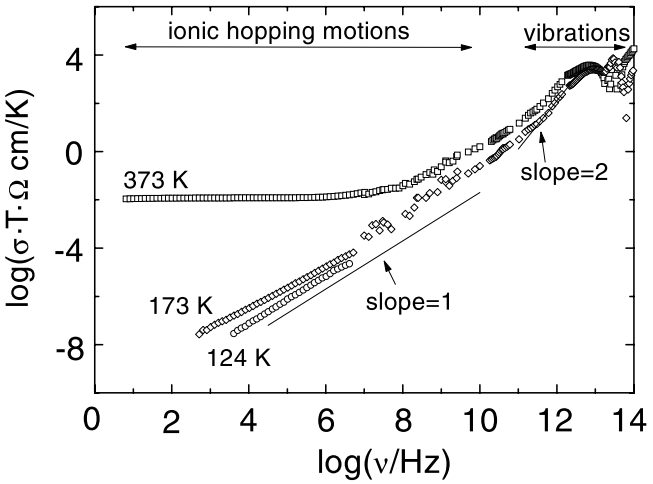

Fig. 21.5. Typical conductivity spectra of an ion conducting material, viz., glassy $B_2O_3 \cdot 0.56\,Li_2O \cdot 0.45\,LiBr$.

of Maxwell's equations and the boundary conditions at the interfaces, which guarantee the continuity of the electric and magnetic field components.

In spite of their potential for unravelling microscopic mechanisms of ionic motion, complete conductivity spectra of ion conducting materials, like the one presented in Fig. 21.2, are still very rare. In Fig. 21.5, we present another example, viz., conductivity spectra of glassy $B_2O_3 \cdot 0.56\,Li_2O \cdot 0.45\,LiBr$, extending up to 100 THz. Above 100 GHz, the conductivity is governed by vibrational contributions featuring a ν^2 frequency dependence on the low-frequency flank. In amorphous materials without lattice periodicity there are no selection rules for far-infrared absorption; hence the vibrational peaks are much broader than in crystals, cf. Fig. 21.2.

Conductivity spectra of different ion conducting materials with disordered structures show many common features. Phenomenologically, the following characteristics have been identified:

(i) A dc conductivity plateau, $\sigma_{\rm dc} = \sigma(0)$, is attained at sufficiently low frequencies. In ionic solids and strong ionic melts, $\sigma_{\rm dc} \cdot T$ is usually Arrhenius activated, viz., $\sigma_{\rm dc} \cdot T = A \cdot \exp(-E_{\rm dc}/(k_{\rm B}T))$, while fragile melts show a pronounced deviation from the Arrhenius law [8].

(ii) The ac conductivity, $\sigma(\nu)$, increases monotonically with frequency [9], at least up to millimetre-wave frequencies. In the very far infrared, displacive and vibrational contributions to $\sigma(\nu)$ are usually hard to distinguish.

(iii) In some cases, however, this distinction has been possible, and the so-called high-frequency plateau, $\sigma_{\rm hf} = \sigma(\infty)$, has been identified. An

example has been given in Fig. 21.2. Wherever detected, high-frequency plateau conductivities are found to obey the Arrhenius law with an activation energy lower than E_{dc} [3, 7, 10–12].

(iv) Typically, the shape of $\sigma(\nu)$, as observed in a log-log plot below the microwave regime, does not depend on temperature. Therefore, a master curve is obtained when these sections of the conductivity spectra are shifted and superimposed. This is the time-temperature superposition principle [13–17].

(v) In a log-log plot of $\sigma \cdot T$ versus frequency, the onset of the dispersion is often found to occur along a straight line with a slope of one, implying that the onset frequency and $\sigma_{\mathrm{dc}} \cdot T$ are both activated with E_{dc}. This is the so-called Summerfield scaling [18], exemplified in Fig. 21.6 where conductivity spectra of glassy $0.3\,\mathrm{Na_2O} \cdot 0.7\,\mathrm{B_2O_3}$ taken at different temperatures have been scaled to fall on a single master curve.

(vi) Master curves constructed from spectra $\sigma(\nu)$ of a large number of different ionic materials with disordered structures are surprisingly similar in shape [15, 17, 19].

(vii) At any temperature, the initial part of $\sigma(\nu)$ *roughly* follows the Jonscher power law, i.e., $\sigma(\nu) - \sigma(0) \propto \nu^p$ with an exponent p between 0.6 and 0.7 in most cases. This behaviour, found in a broad variety of materials, is often called universal dynamic response (UDR) [20].

(viii) Two-dimensional ion conductors such as the beta aluminas [21], crystals and glasses with low number densities of mobile ions, see Sect. 21.9 and [17], and mixed cation glasses [22, 23] exhibit a particularly gradual onset of the dispersion of $\sigma(\nu)$.

(ix) As temperature is decreased, the slope of $\sigma(\nu)$ in the log-log plot approaches the value of one at any given audio or radio frequency, while the conductivity becomes decreasingly temperature-dependent, cf. Fig. 21.5. As $\sigma(\nu) \propto \nu$ corresponds to a frequency-independent dielectric loss, this feature has come to be known as nearly constant loss (NCL) behaviour [24–26].

(x) As a consequence of (vii) and (ix), the typical shape of empirically constructed master curves of ionically conducting materials is characterised by an apparent exponent which increases with increasing reduced frequency, gradually approaching the value of one.

(xi) Remarkably, the NCL feature has also been found in ionic crystals and glasses at cryogenic temperatures, where it is certainly not related to ionic transport [27].

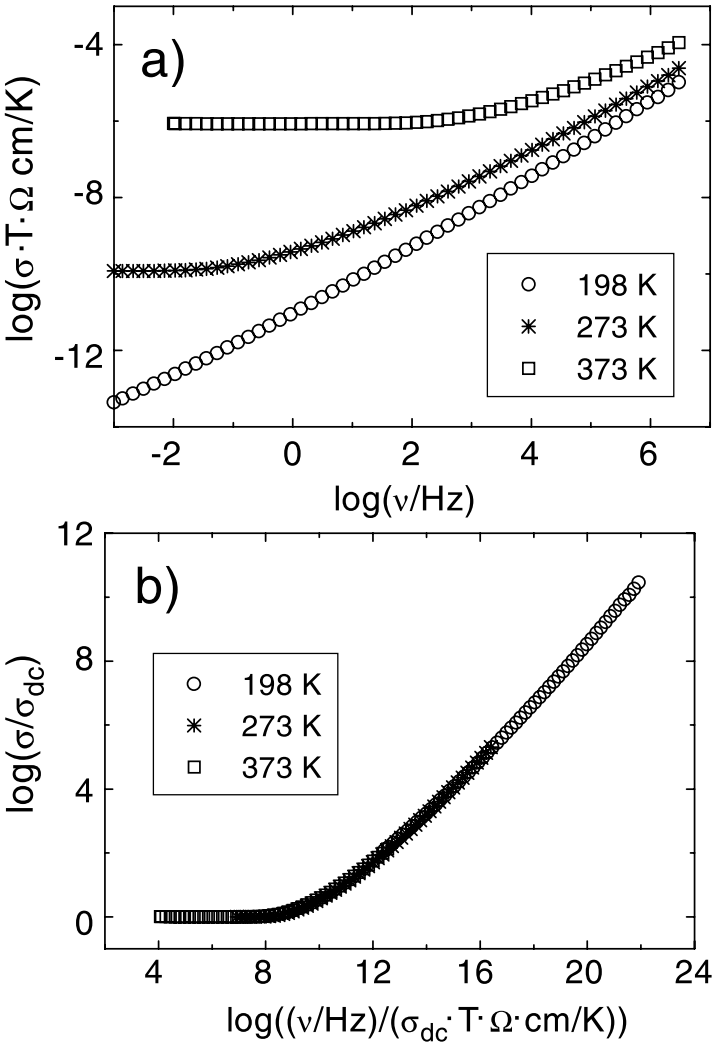

Fig. 21.6. a) Experimental conductivity spectra of glassy $0.3\,Na_2O \cdot 0.7\,B_2O_3$. b) Scaled representation of the data presented in a).

21.3 Relevant Functions and Some Model Concepts for Ion Transport in Disordered Systems

Conductivity spectra convey information on the microscopic dynamics of the mobile charge carriers, since according to linear response theory [2], $\widehat{\sigma}(\omega)$, with $\omega = 2\pi\nu$, is the Fourier transform of the autocorrelation function of the current density:

$$\widehat{\sigma}(\omega) = \frac{V}{3k_{\mathrm{B}}T} \cdot \int_0^\infty \langle \boldsymbol{i}(0) \cdot \boldsymbol{i}(t) \rangle \exp(-\mathrm{i}\omega t) \mathrm{d}t \ . \tag{21.1}$$

In (21.1), the current density,

$$\boldsymbol{i}(t) = \frac{1}{V} \sum_{i=1}^{N} q_i \boldsymbol{v}_i(t) \ , \tag{21.2}$$

and its autocorrelation function are real functions of time. V is the volume of the sample, and the summation is over all N charge carriers. Their charges and velocities are denoted by q_i and $\boldsymbol{v}_i$, respectively. In systems with only one type of mobile charge carrier, the complex conductivity, $\widehat{\sigma}(\omega)$, is connected with the complex coefficient of self diffusion of this carrier, $\widehat{D}(\omega)$, via

$$\widehat{\sigma}(\omega) = \frac{Nq^2}{Vk_{\mathrm{B}}T} \cdot \frac{1}{\widehat{H}_{\mathrm{R}}(\omega)} \cdot \widehat{D}(\omega) \ . \tag{21.3}$$

In (21.3), $\widehat{H}_{\mathrm{R}}(\omega)$ denotes the frequency-dependent complex Haven ratio,

$$\widehat{H}_{\mathrm{R}}(\omega) = \frac{N \int_0^\infty \langle \boldsymbol{v}(0) \cdot \boldsymbol{v}(t) \rangle \ \exp(-\mathrm{i}\omega t) \, \mathrm{d}t}{\int_0^\infty \langle \sum_{i,j}^{1..N} \boldsymbol{v}_i(0) \cdot \boldsymbol{v}_j(t) \rangle \ \exp(-\mathrm{i}\omega t) \, \mathrm{d}t} \ , \tag{21.4}$$

which becomes a real number in its low-frequency limit: $H_{\mathrm{R}} = \widehat{H}_{\mathrm{R}}(\omega = 0)$. If cross correlations between movements of different ions i, j may be neglected, the Haven ratio becomes unity. Within this approximation we then obtain the Nernst-Einstein relation,

$$\widehat{\sigma}(\omega) = \frac{Nq^2}{Vk_{\mathrm{B}}T} \cdot \widehat{D}(\omega) \ . \tag{21.5}$$

Monte-Carlo simulations by Maass et al. [28] have shown that the overall shape of conductivity spectra is indeed well described, if only correlations between hops of a single ion are taken into account. Within this "single particle approximation", the dynamic conductivity can be expressed by the Fourier transform of the velocity autocorrelation function,

$$\begin{aligned} \widehat{\sigma}(\omega) &= \frac{Nq^2}{3Vk_{\mathrm{B}}T} \cdot \int_0^\infty \langle \boldsymbol{v}(0) \cdot \boldsymbol{v}(t) \rangle \exp(-\mathrm{i}\omega t) \, \mathrm{d}t \\ &= -\omega^2 \frac{Nq^2}{6Vk_{\mathrm{B}}T} \cdot \lim_{\epsilon \to 0} \int_0^\infty \langle r^2(t) \rangle \exp(-\epsilon t - \mathrm{i}\omega t) \, \mathrm{d}t \ . \end{aligned} \tag{21.6}$$

Here, $\langle r^2(t) \rangle$ is the time-dependent mean square displacement of the mobile ions. Equation (21.6) implies that the dynamic conductivity can be derived from a model-based velocity autocorrelation function, $\langle \boldsymbol{v}(0) \cdot \boldsymbol{v}(t) \rangle$.

In the most simple approach, the ions are assumed to be random walkers, cf. Fig. 21.1, and the velocity autocorrelation function reads:

$$\langle \boldsymbol{v}(0) \cdot \boldsymbol{v}(t) \rangle_{\mathrm{RW}} = \frac{\Gamma x_0^2}{2} \cdot \delta(t) \; . \tag{21.7}$$

Here Γ and x_0 are the hopping rate and the elementary jump distance of the ions, respectively. Combination of (21.6) and (21.7) yields a hopping conductivity which is real and constant up to about 100 GHz:

$$\widehat{\sigma}_{\mathrm{RW}} = \sigma_{\mathrm{RW}} = \frac{N q^2 x_0^2 \Gamma}{6 V k_{\mathrm{B}} T} \; , \tag{21.8}$$

see also Fig. 21.1.

However, (21.8) is in marked contrast to experimental conductivity spectra like those presented in Figs. 21.2 and 21.5. As outlined in Sect. 21.1, correlated hopping processes of the ions have to be taken into account. In the latter case, both the current density autocorrelation function, $\langle \boldsymbol{i}(0) \cdot \boldsymbol{i}(t) \rangle$, and the velocity autocorrelation function, $\langle \boldsymbol{v}(0) \cdot \boldsymbol{v}(t) \rangle$, strongly deviate from those of a random walker, cf. Fig. 21.1.

Over the years, various concepts, models and computer simulations have been published, all of them aiming at a realistic description of the nonrandom ion transport in disordered systems. The most important ones are briefly summarised in the following.

(i) In his coupling concept, Ngai described the time-dependent decay of an electric field in an electrolyte by joining together an exponential and a stretched-exponential (Kohlrausch-Williams-Watts) decay function. The model yields $\sigma_{\mathrm{dc}} = \sigma(0)$, $\sigma_{\mathrm{hf}} = \sigma(\infty)$, and a dispersive conductivity in between [29–31].

(ii) The physical picture of mismatch and mismatch relaxation was first introduced in the jump relaxation model. Being based on interactions between the ions, the model was able to reproduce essential features of the spectra in a closed expression [32, 33].

(iii) Introducing disorder on a square lattice, Bunde and co-workers obtained time-correlation functions and spectra $\sigma(\nu)$ from Monte-Carlo simulations [34] (see Chap. 20).

(iv) In their counter-ion model, Dieterich and co-workers considered both disorder and interactions and were thus able to derive realistic spectra from numerical simulations [35, 36] (see Chap. 20).

(v) It has been realised that the combined validity of the time-temperature superposition principle and the Summerfield scaling implies that the only effect of temperature is to change the hopping rates of the ions while their hopping mechanism is preserved.

(vi) The asymmetric double well potential (ADWP) model [37] has been used by Nowick, Jain, and their co-workers to explain the NCL behaviour. Jain coined the phrase "jellyfish" behaviour [38]. Both Nowick and Jain have always regarded UDR and NCL as different features [26].

(vii) On the other hand, concepts have also been developed which self-consistently explain a continuous transition from UDR to NCL. One of these is the random barrier model as treated mathematically by Dyre and Schrøder [39, 40]. However, the comparatively large rms value of the distance at which an ion loses memory of its previous position is an unsolved problem of this approach.

(viii) The concept of mismatch and relaxation (CMR) also provides realistic spectra including the UDR-NCL transition. It has the further advantage of reproducing spectra with different shapes in a one-parameter treatment, see the following section.

(ix) On the basis of the CMR, the non-Arrhenius dc conductivity encountered in fragile supercooled ionic melts has been shown to be a direct consequence of a short-time behaviour characterised by Arrhenius-activated elementary displacements normally followed by roll-back processes [12].

(x) According to recent computer simulations [41], the NCL behaviour observed at cryogenic temperatures can be explained by strictly localised movements of interacting ions (cf. Chap. 20). The same result is obtained from a suitably modified version of the CMR [42].

21.4 CMR Equations and Model Conductivity Spectra

Before embarking on the construction of the CMR, it is useful to consider the shapes of some relevant functions. This is done with the help of Fig. 21.7, where the approximation of (21.6) has been adopted, i. e., it is assumed that no essential error is introduced by putting $H_\mathrm{R} = 1$, cf. [43]. For convenience, one further function is introduced, viz., the time-dependent correlation factor, $W(t)$ [32]. This function is a normalised integral of $\langle \boldsymbol{v}(0) \cdot \boldsymbol{v}(t) \rangle$ and, at the same time, a normalised derivative of the mean square displacement, $\langle r^2(t) \rangle$:

$$\frac{2}{\Gamma_0 x_0^2} \int_0^t \langle \boldsymbol{v}(0) \cdot \boldsymbol{v}(t') \rangle \mathrm{d}t' = W(t) = \frac{1}{\Gamma_0 x_0^2} \frac{\mathrm{d}}{\mathrm{d}t} \langle r^2(t) \rangle \; . \tag{21.9}$$

Here, Γ_0 denotes the elementary hopping rate of the ions.

At very short times, when each ion performs at most one hop, correlations are not yet visible. Therefore, we have $W(0) = 1$, and $\langle r^2(t) \rangle$ increases linearly with time, see Fig. 21.7 (b) and Fig. 21.7 (d). Note that the ballistic short-time behaviour, with $\langle r^2(t) \rangle \propto t^2$, is not included as jump processes are considered only. At longer times, when negative values of $\langle \boldsymbol{v}(0) \cdot \boldsymbol{v}(t) \rangle$ contribute significantly to the expression in (21.9), $W(t)$ is found to decay with time, and $\langle r^2(t) \rangle$ increases in a sublinear fashion. This time regime is sometimes called "subdiffusive" or "anomalous" (cf. Chaps. 10, 18, 19, 22).

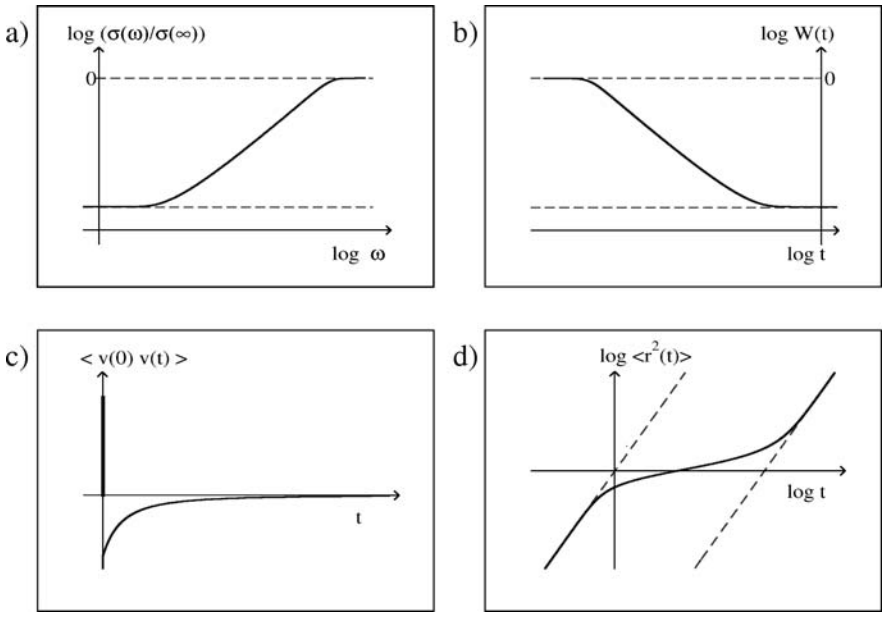

Fig. 21.7. Schematic plot of relevant functions. (a) Normalised frequency-dependent conductivity caused by the hopping motion of the ions, versus angular frequency in a log-log representation. (b) Time-dependent correlation factor versus time in a log-log representation. (c) Velocity autocorrelation function of the mobile ions versus time. (d) Mean square displacement of the mobile ions versus time in a log-log representation.

Only at much longer times, when $\langle \boldsymbol{v}(0)\boldsymbol{v}(t)\rangle$ becomes very small and, consequently, $W(t)$ tends to its long-time limit, $W(\infty)$, does $\langle r^2(t)\rangle$ change from its subdiffusive behaviour into its diffusive long-time behaviour, which is linear in time, with $\langle r^2(t)\rangle = 6Dt$, where D is the coefficient of self-diffusion. Note that $\sigma(\nu)/\sigma(\infty)$ and $W(t)$, in log-log representations, are almost perfect mirror images of each other, see Fig. 21.7 (a) and Fig. 21.7 (b) as well as Fig. 21.8. Although this approximate symmetry is useful for practical purposes, we will not use it for deriving model spectra, $\sigma(\nu)/\sigma(\infty)$. Rather, exploiting the relationships between $\sigma(\nu)$ and $\langle \boldsymbol{v}(0)\boldsymbol{v}(t)\rangle$, and between $\langle \boldsymbol{v}(0)\boldsymbol{v}(t)\rangle$ and $W(t)$, we write

$$\frac{\sigma(\nu)}{\sigma(\infty)} = 1 + \int_0^\infty \dot{W}(t)\cos(2\pi\nu t)\mathrm{d}t \; . \tag{21.10}$$

From (21.10) it is evident that $\sigma(\nu)/\sigma(\infty)$ will be known as soon as $W(t)$ is known. The basic idea of the CMR is now to find $W(t)$ from simple rate equations that describe the development of the ion dynamics with time.

In the following, we present the equations that allow us to determine functions $W(t)$ and $\sigma(\nu)/\sigma(\infty)$. We also present and discuss general features of

the conductivity spectra thus obtained, while the explanation of the physical concept of the model is postponed to Sect. 21.6.

The rate equations used in the CMR are

$$-\dot{g}(t) = A\, g^K(t)\, W(t) \tag{21.11}$$

and

$$-\dot{W}(t) = -B\, W(t)\, \dot{g}(t)\ . \tag{21.12}$$

These equations contain two time-dependent functions, $W(t)$ and $g(t)$. Here $W(t)$ is the time-dependent correlation factor, while $g(t)$ is a normalised mismatch function, see Sect. 21.6. They also contain three parameters, viz., A, B and K. The first parameter, A, is an internal frequency which turns out to be proportional to the high-frequency conductivity, $\sigma(\infty)$. The second parameter, B, determines the ratio $\sigma(0)/\sigma(\infty) = W(\infty)$ via $W(\infty) = \exp(-B)$. In many cases, $W(\infty)$ is found to be Arrhenius activated which implies that B should be proportional to the inverse temperature, $1/T$. In the following section, see (21.25), we will show that the ratio A/B is not only proportional to $\sigma(\infty)\cdot T$, and hence to the elementary hopping rate of the mobile ions, Γ_0, but that A/B and Γ_0 may even be assumed to be identical (at least for the example studied, within the limits of experimental error). The value of the third parameter, K, influences the shape of the resulting conductivity spectra in the vicinity of the onset of the dispersion, see the end of this section as well as the discussion at the end of Sect. 21.6. In glassy and crystalline electrolytes with high concentrations of mobile ions, K is typically found to be 2 or close to 2.

Functions $W(t)$ and $g(t)$ satisfying the rate equations are shown in Fig. 21.8 (a). The particular parameter values used are $W(\infty) = 0.001$ and $K = 2$. The time axis has been normalised by multiplication with the internal frequency A. In a second step, application of (21.10) yields the normalised conductivity spectrum, $\sigma(\nu)/\sigma(\infty)$, represented in Fig. 21.8 (b) by the solid line. Note that the broken line in Fig. 21.8 (b), obtained from $W(t)$ by forming the mirror image, provides a good approximation to the exact solution, i.e.,

$$\frac{\sigma(\omega)}{\sigma(\infty)} \approx W\left(\frac{2}{\pi\omega}\right)\ . \tag{21.13}$$

Here, the factor $2/\pi$ arises as (21.13) is an approximation for an expression obtained by Fourier transformation. Figure 21.9 shows the shape of the frequency-dependent conductivity for a fixed value of B ($B = 25$), and also demonstrates the effect of varying the parameter K. In the first place, it is important to note that, irrespective of the value of K, the model conductivity spectra do not obey a power law. Rather, as in Fig. 21.6, the apparent slope in the log-log representation increases continuously, approaching the value of one before the high-frequency plateau is attained. This is the UDR–NCL transition. Of course, this transition can only be observed, if

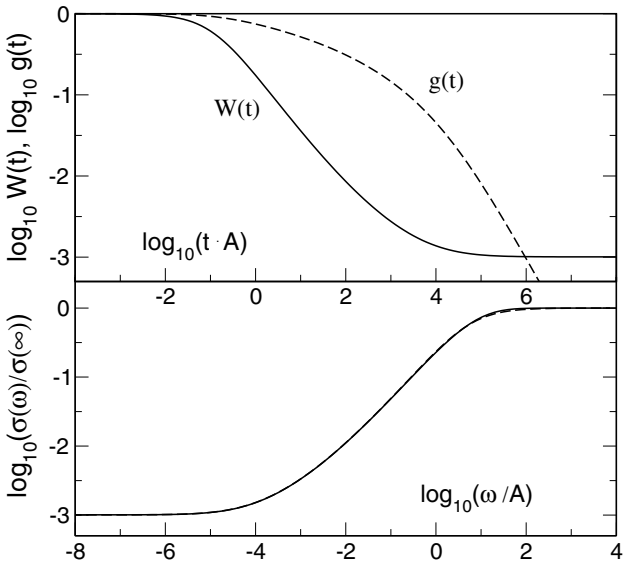

Fig. 21.8. (a) Functions $W(t)$ and $g(t)$ satisfying (21.11) and (21.12) for $W(\infty) = \exp(-B) = 0.001$ and $K = 2$. (b) Solid line: normalised conductivity caused by hopping motion versus normalised angular frequency as obtained by inserting $W(t)$ from panel (a) into (21.10). Broken line: mirror-image approximation for the normalised conductivity.

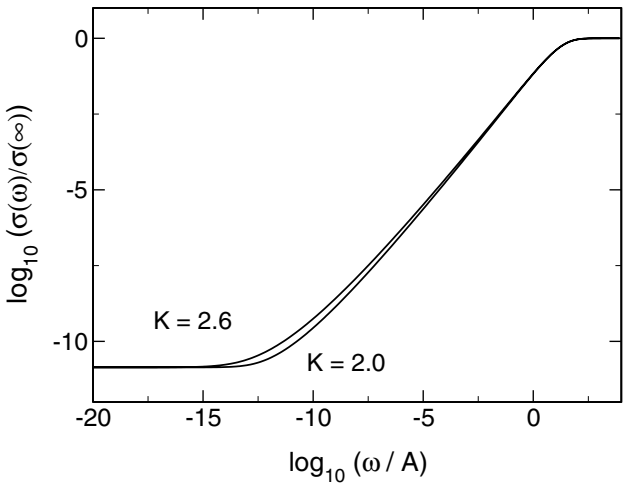

Fig. 21.9. Shape of frequency-dependent conductivity as obtained from the CMR for fixed B, with $B = 25$, including the effect of different values of K.

$W(\infty) = \sigma(0)/\sigma(\infty) = \exp(-B)$ is sufficiently small, i.e., at sufficiently low temperatures. Otherwise, the high-frequency plateau will be attained before the transition becomes visible.

Figure 21.9 also shows how the numerical value of K influences the shape of the spectrum. As K is increased, the transition from $\sigma_{\mathrm{dc}} = \sigma(0)$ into the dispersive regime becomes more and more gradual. Indeed, such a variation has been observed experimentally, e.g., upon reducing the number density of mobile ions in a solid electrolyte [17] or when moving from a binary alkali-ion conducting glass into the mixed-alkali regime [22,23]. Examples will be given in Sect. 21.9.

21.5 Scaling Properties of Model Conductivity Spectra

On the basis of (21.11) and (21.12) specific predictions can be made with regard to the behaviour of $W(t)$ and $\sigma(\omega)/\sigma(\infty)$ in the vicinity of those times and angular frequencies that mark the transitions from σ_{dc} into the dispersive regime and from the dispersive regime into σ_{hf}. We will in particular show that model conductivity spectra possess the property of scaling in both limiting cases. This means that the shapes of frequency-dependent model conductivities are preserved in either frequency regime as the temperature is varied. Of course, this requires sufficiently large ratios of $\sigma(\infty)/\sigma(0)$ as well as a fixed value of the parameter K.

For the purpose of scaling, temperature-dependent angular frequencies ω_{O} and ω_{E} will be introduced which mark the onset and the end of the dispersion, respectively.

The situation is particularly simple at short times, when $g(t)$ is still close to one, cf. Fig. 21.8 (a). In this case, (21.11) and (21.12) may be combined and approximated by

$$-\dot{W}(t) = ABW^2(t) \; . \tag{21.14}$$

Equation (21.14) has the solution

$$W(t) = \frac{1}{1 + ABt} \; . \tag{21.15}$$

This implies that, according to the mirror image approach, the high-frequency solution for the conductivity should be close to

$$\frac{\sigma(\omega)}{\sigma(\infty)} = \frac{1}{1 + 2AB/(\pi\omega)} \; . \tag{21.16}$$

We may, therefore, somewhat arbitrarily, define an "end angular frequency" as

$$\omega_{\mathrm{E}} = AB \; . \tag{21.17}$$

Equation (21.16) is remarkable as it describes the nearly-constant-loss behaviour encountered at angular frequencies ω below ω_{E}, provided $g(1/\omega)$ is

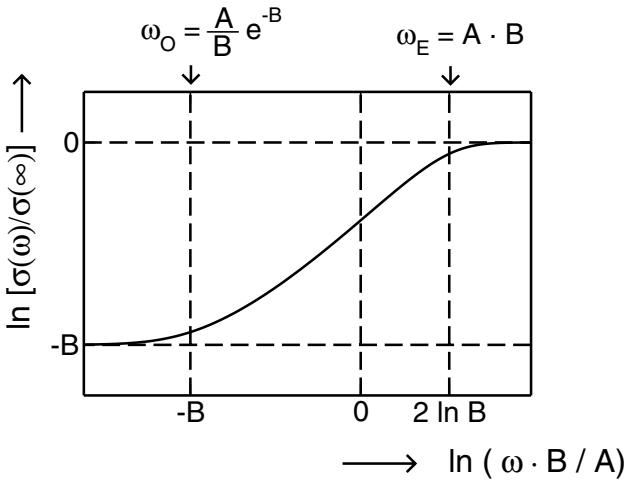

Fig. 21.10. A CMR model conductivity spectrum, with $B = 8$ and $K = 2$. The angular frequencies ω_{O} and ω_{E} mark the onset and the end of the dispersion.

still close to one. At sufficiently low temperatures, this requirement is indeed satisfied in a wide range of angular frequencies that are still well below ω_{E}. In Fig. 21.10, the position of ω_{E} has been marked in a plot of $\ln(\sigma(\omega)/\sigma(\infty))$ versus $\ln(\omega B/A)$. The plot also contains a mark for the corresponding "onset angular frequency", ω_{O}. An expression for ω_{O} is obtained by considering low frequencies, corresponding to long times, where $W_{\mathrm{scaled}} = W(t)/W(\infty)$ tends to unity. In this case we combine (21.11) and (21.12) to form

$$-\frac{\mathrm{d}}{\mathrm{d}t}\ln W_{\mathrm{scaled}}(t) = AB\exp(-B)W_{\mathrm{scaled}}(t)\left[\frac{\ln W_{\mathrm{scaled}}(t)}{B}\right]^{K} \tag{21.18}$$

or, with

$$\omega_{\mathrm{O}} = AB^{1-K}\exp(-B) \tag{21.19}$$

and

$$t_{\mathrm{scaled}} = t\omega_{\mathrm{O}}\ , \tag{21.20}$$

$$-\frac{\mathrm{d}}{\mathrm{d}t_{\mathrm{scaled}}}\ln W_{\mathrm{scaled}} = W_{\mathrm{scaled}}\cdot(\ln W_{\mathrm{scaled}})^{K}\ . \tag{21.21}$$

Integration of (21.21) yields

$$t_{\mathrm{scaled}} = \int_{\ln W_{\mathrm{scaled}}}^{-\ln W(\infty)} x^{-K}e^{-x}\,\mathrm{d}x \approx \int_{\ln W_{\mathrm{scaled}}}^{\infty} x^{-K}e^{-x}\,\mathrm{d}x\ . \tag{21.22}$$

The approximation made on the right-hand side of (21.22) is always valid at times that are much longer than $1/\omega_{\mathrm{E}}$. In particular, it is always valid in

the "long-time regime" that corresponds to the impedance frequency range, below 10 MHz. This is important, because experimental conductivities used for scaling purposes have almost exclusively been measured below 10 MHz.

From (21.22) it is evident that in the long-time regime W_{scaled} is a unique decaying function of t_{scaled}. Correspondingly, $\sigma(\omega)/\sigma(\infty)$ also exhibits scaling, and the "onset angular frequency" may be chosen to be ω_{O} from (21.19). In the frequent case of $K = 2$, we have

$$\omega_{\mathrm{O}} = \frac{A}{B}\exp(-B) \quad \text{for } K = 2\,. \tag{21.23}$$

This "onset angular frequency" ω_{O} has been marked in Fig. 21.10.

The inverse onset angular frequency, $1/\omega_{\mathrm{O}}$, plays the role of a crossover time at which macroscopic random diffusion is attained. Likewise, a crossover distance, ℓ_{O}, may be defined by $\ell_{\mathrm{O}} = (6D/\omega_{\mathrm{O}})^{1/2}$. The example of $RbAg_4I_5$ is particularly clear-cut. In this solid electrolyte, the density of mobile ions is high, the value of K is found to be 2 as in Fig. 21.10, and the elementary hopping distance, x_0, is known. From the conductivity spectra of $RbAg_4I_5$, to be discussed in Sect. 21.7, we find that within experimental error there is no difference between x_0 and the distance ℓ_{O}, after which random diffusion prevails. This means that an ion, after a hop from one site to another, loses its memory of the previous site as soon as it succeeds in stabilising its position at the new one. Therefore, within experimental error, ω_{O} can be identified with the "random hopping rate" or "rate of successful hops" of the ions, Γ:

$$\omega_{\mathrm{O}} \approx \Gamma = 6D/x_0^2\,. \tag{21.24}$$

Equation (21.24) is expected to hold not only in the particular case of $RbAg_4I_5$ but in many other ionic materials as well.

As only a fraction $\Gamma/\Gamma_0 = W(\infty) = \exp(-B)$ of all hops are successful, we find that the elementary hopping rate should be

$$\Gamma_0 = \Gamma \cdot \exp(B) \approx \omega_{\mathrm{O}} \exp(B) = \frac{A}{B} \quad \text{for } K = 2\,. \tag{21.25}$$

As illustrated in Fig. 21.10, the position of $A/B \approx \Gamma_0$ is situated between $\omega_{\mathrm{O}} \approx \Gamma$ and $\omega_{\mathrm{E}} = AB$ on the frequency scale.

In most crystalline and glassy electrolytes, the dc conductivity, $\sigma_{\mathrm{dc}} = \sigma(\infty)\exp(-B)$ is found to obey the Arrhenius law. This means that $\sigma_{\mathrm{dc}} \cdot T$ is proportional to $\exp(-E_{\mathrm{dc}}/k_{\mathrm{B}}T)$, where E_{dc} is the activation energy. In those cases, where high-frequency conductivities, $\sigma(\infty)$, have also been determined, they turn out to be Arrhenius activated as well, cf. Sect. 21.2. Conductivity spectra of this kind are easily reproduced by the CMR, with A and B depending on temperature in a known and simple fashion, and a complete set of isothermal conductivity spectra at different temperatures is readily constructed, as shown in Fig. 21.11. According to (21.24), the onset

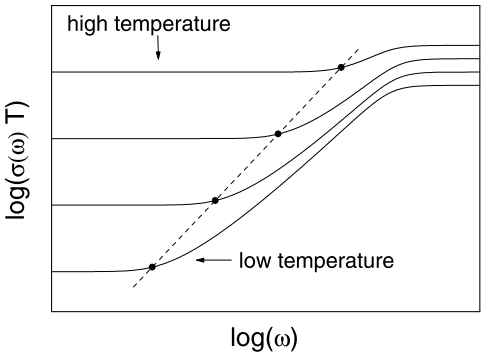

Fig. 21.11. Sketch of a set of frequency-dependent conductivity isotherms as obtained from the CMR for the case where dc conductivity and high-frequency conductivity both follow the Arrhenius law. The value of the parameter K is again 2.

angular frequency is expected to be proportional to the coefficient of self-diffusion and, because of the Nernst-Einstein relation, also proportional to the product of dc conductivity and temperature. In Fig. 21.11, the onset of the dispersion at different temperatures is, therefore, marked by a straight line with a slope of one. This kind of scaling, with $\omega_{\mathrm{O}} \propto \sigma(0) \cdot T$, is sometimes called "Summerfield scaling" [18] and has already been mentioned in Sect. 21.2.

Figure 21.11 also shows that shifting individual conductivity spectra along the line with slope one will result in a superposition of their low-frequency sections. This procedure was applied in Fig. 21.6, producing one experimental master curve and, likewise, one model master curve. The same procedure has proved successful for many glassy and crystalline electrolytes. Further examples are glassy $\mathrm{B_2O_3} \cdot 0.56\,\mathrm{Li_2O} \cdot 0.45\,\mathrm{LiBr}$, cf. Fig. 21.12, and glassy $0.3\,\mathrm{Li_2O} \cdot 0.7\,\mathrm{B_2O_3}$, cf. Fig. 21.18 in Sect. 21.9.

Experimentally, materials usually do not display noticeable variations in the shapes of their low-frequency conductivities as the temperature is changed. In the CMR, this corresponds to a fixed value of the parameter K. Recently, changes in shape have, however, been observed in the temperature-dependent conductivity spectra of the mixed alkali glass $0.3\,[x\mathrm{Li_2O} \cdot (1 - x)\,\mathrm{Na_2O}] \cdot 0.7\,\mathrm{B_2O_3}$ [23].

21.6 Physical Concept of the CMR

The concept of mismatch and relaxation builds on the jump relaxation model [32,33], the central idea being unchanged. Each mobile ion is assumed to have vacant sites in its immediate neighbourhood, while other mobile ions are present in its further surroundings, very much like the ion cloud in Debye-Hückel theory. Due to their mutual repulsive interaction, the ions tend to stay at some distance from each other. Each ion experiences a time-dependent effective potential which consists in part of the static potential provided by the immobile crystalline or glassy network and in part of a time-dependent

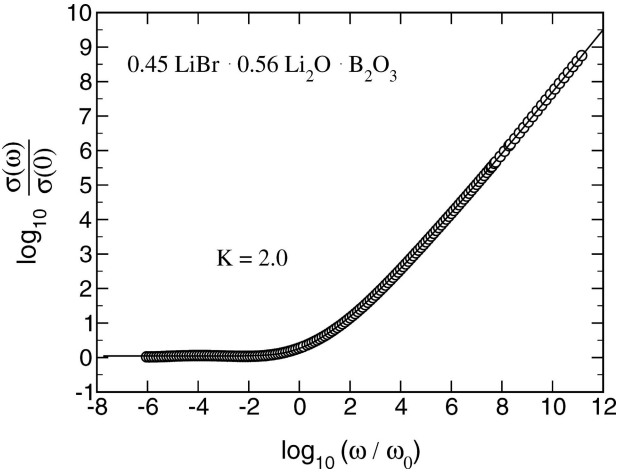

Fig. 21.12. Scaled representation of experimental and model conductivities (circles and solid line, respectively) for $B_2O_3 \cdot 0.56\,Li_2O \cdot 0.45\,LiBr$ glass. The value of K is again 2. For more details on this particular system, see [23].

cage-effect potential provided by its mobile neighbours. Suppose the ion performs a hop to a neighbouring site. As a consequence, mismatch will usually be created between its own position and the momentary arrangement of its mobile neighbours. There are two possible ways for the system to reduce the mismatch. Either the neighbours rearrange or the "central" ion hops back into its previous site. This explains the existence of forward-backward correlations of successive hops. Consequently, the mean square displacement exhibits a "subdiffusive" behaviour, cf. Fig. 21.7 (d), and dispersion is observed in frequency-dependent ionic conductivities.

Suppose mismatch is created by a hop of a mobile ion at time $t = 0$. Then the mismatch function $g(t)$, for $t > 0$, has the meaning of a normalised distance between the actual position of the ion and the position at which it would be optimally relaxed with respect to the momentary arrangement of its mobile neighbours. The function $g(t)$ varies with time from $g(0) = 1$ to $g(\infty) = 0$, describing the way mismatch decays because the neighbouring ions rearrange, while the "central" ion is supposed to stay at its position. The negative time derivative, $-\dot{g}(t)$, is thus the rate of mismatch relaxation on the "many-particle route". On the other hand, $-\dot{W}(t)/W(t)$ is interpreted as the rate of mismatch relaxation on the "single-particle route", with the ion hopping backwards. Here, the factor $1/W(t)$ is required, since we focus on those cases where the ion has not yet moved backwards at time t. The central assumption of the CMR is then expressed by (21.12), i.e., the rates of relaxation on the single- and many-particle routes are assumed to be proportional to each other at all times. In other words, the tendency for the central

ion to hop backwards is assumed to be proportional to the tendency of its neighbours to rearrange.

Up to this point, the CMR and its predecessor, the jump relaxation model, are identical. The CMR differs from the jump relaxation model by inclusion of (21.11). In this equation, we consider the rate of decay of $g(t)$, $-\dot{g}(t)$. Here it is important to realise that $g(t)$ plays the role of a normalised dipole moment. Its dipole field is the driving force felt by the neighbouring mobile ions, inducing their rearrangement and, as a consequence, the concomitant decay of $g(t)$ itself. As the rearrangement of the surrounding "ion cloud" proceeds, the central dipole will become increasingly shielded. This means that two effects occur simultaneously. One is the decay of $g(t)$ with time. The other is the shrinking of the effective volume of the dipole field. In other words, the effective number of mobile neighbours available for the relaxation becomes time-dependent. It is evident that this is an extremely complicated dynamic process, much more complicated than Debye-Hückel theory. Any attempt to grasp its essence in a simple equation must contain approximations. For deriving a suitable equation we start from the relation,

$$-\dot{g}(t) \propto g(t) * \langle \boldsymbol{v}(0)\boldsymbol{v}(t)\rangle \cdot \#(t) \; . \tag{21.26}$$

Here, the rate of decay of $g(t)$ at time t is expected to be proportional to the convolution, denoted by "$*$", of the driving force and the velocity autocorrelation function of the neighbouring mobile ions. No distinction is made between the velocity autocorrelation function of the central ion and that of its mobile neighbours. Furthermore, the rate of decay of $g(t)$ is expected to be also proportional to a function $\#(t)$ denoting the time-dependent effective number of mobile neighbours available for the relaxation.

It is now easy to show numerically that $g(t)$ varies with time much more slowly than $\langle \boldsymbol{v}(0)\boldsymbol{v}(t)\rangle$ does. As a consequence, the convolution is well approximated by the product of $g(t)$ and the time integral of $\langle \boldsymbol{v}(0)\boldsymbol{v}(t)\rangle$, which is proportional to $W(t)$. Indeed, functions $g(t)$ and $W(t)$ obtained by use of the approximation are found to satisfy the exact equation (with the convolution) perfectly [12]. Equation (21.26) thus becomes

$$-\dot{g}(t) \propto g(t)\, W(t) \cdot \#(t) \; . \tag{21.27}$$

While $\#(t)$ is certainly a decaying function of time, its shape is not easily determined from simple model considerations. Therefore, in a more empirical approach, we have tried to determine its shape by comparing experimental spectra, $\sigma(\nu)$, and model spectra obtained from (21.10), (21.12), and (21.27) using functions $\#(t)$ with different shapes. As a result, good agreement between model spectra and experimental spectra is obtained, if $\#(t)$ is assumed to decay as $g(t)$ or slightly faster. This results in (21.11) with $K = 2$ or $K > 2$.

Interestingly, the value of K appears to be related to the overall number density of mobile ions. If the number density is high, then $K \approx 2$ gives

excellent results in most cases, implying that $\#(t)$ should be roughly proportional to $g(t)$. Smaller number densities are reflected by a more gradual increase of $\sigma(\nu)$ in the vicinity of the onset angular frequency, ω_{O}. According to Fig. 21.9, this corresponds to a larger value of K implying a more rapid decay of $\#(t)$, cf. (21.27). A tentative simple explanation of this effect may be as follows. Let us assume the unshielded effective volume of the dipole field and the number of mobile ions contained in it do, indeed, decay with time in the same fashion as $g(t)$ does. Then, if the overall number density of mobile ions is large, the difference between the number of mobile ions contained in that volume and the number $\#(t)$ will not be significant, since it is only one (the "central" ion). However, if the number density becomes smaller, then this difference becomes increasingly significant. The function $\#(t)$ will then decay faster than $g(t)$, and the effect will be the more pronounced, the smaller the number density is.

At this point, we should like to compare the model concept of the CMR with approaches that focus on the effects of static disordered energy landscapes on the ion dynamics, see e.g. [39, 44]. In either treatment, each mobile ion encounters varying potentials in the course of time. In a static energy landscape, this happens as the ion explores larger and larger parts of its neighbourhood. In the CMR, however, this happens locally, as the potential is considered time-dependent itself. Therefore, the characteristic length ℓ_{O} after which a mobile ion loses memory of a previous site and starts to diffuse at random will necessarily be larger in models with static energy landscapes than it is in the CMR. Here it is important to note that, in agreement with the CMR approach, we find $\ell_{\mathrm{O}} = x_0$ from the data available for rubidium silver iodide, see Sects. 21.5 and 21.7.

21.7 Complete Conductivity Spectra of Solid Ion Conductors

The vast majority of measurements of frequency-dependent conductivities of solid ion conductors have been performed in the impedance frequency regime, below 10 MHz. There are only few examples where measurements have been extended into the radio, microwave and far-infrared frequency ranges. Of course, measurement of such "complete" conductivity spectra is a prerequisite for detecting the high-frequency plateau. Nevertheless, the detection of the high-frequency plateau often poses severe experimental problems, in particular in the case of glassy electrolytes, where it is usually swamped by the vibrational contributions to the conductivity, cf. Sect. 21.2 and [45]. In a few cases, however, the variation of the vibrational far-infrared conductivity with frequency is so clear-cut that attempts to remove it appear justified. An example is the glassy electrolyte silver thio germanate, of composition $0.5\,Ag_2S \cdot 0.5\,GeS_2$, where conductivity spectra have been taken continuously up to infrared frequencies [46]. In this case it has been possible to prove that,

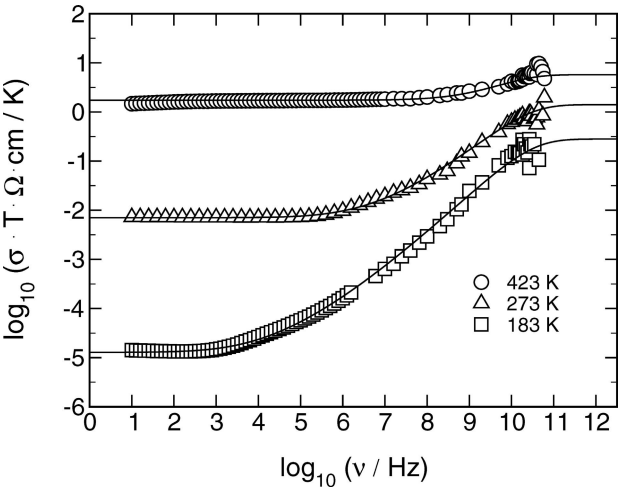

Fig. 21.13. Conductivity spectra of $0.5\,Ag_2S \cdot 0.5\,GeS_2$ glass, after removal of vibrational contributions. The solid lines result from the CMR. As in Fig. 21.11, the values of $A(T)$ and $B(T)$ have been chosen such that both dc and hf conductivity are Arrhenius activated. The value of K is 2.3.

within the limits of error, the low-frequency flank of the vibrational conductivity is exactly proportional to frequency squared [23]. In Fig. 21.13 we show a set of non-vibrational conductivity spectra of glassy $0.5\,Ag_2S \cdot 0.5\,GeS_2$ which have been obtained from the original ones by removing the vibrational component. Although the uncertainty introduced by this procedure is considerable at microwave frequencies above 10 GHz, it is evident that the spectra of Fig. 21.13 closely resemble the model spectra of Fig. 21.11. The solid lines included in Fig. 21.13 are CMR model spectra. Both A/B and $\exp(-B)$ are thermally activated, the activation energies of A/B and $\sigma(\infty) \cdot T$ being identical. The best choice for the value of K is 2.3.

While the spectra of Fig. 21.13 suffer from the scatter of the data in the microwave regime, the separation of the vibrational and non-vibrational contributions to $\sigma(\nu)$ is less problematic in the case of crystalline rubidium silver iodide, $RbAg_4I_5$, see Fig. 21.14.

$RbAg_4I_5$ is a prominent member of the class of optimised silver ion conductors with structurally disordered silver sublattices [47–49]. High-frequency conductivity spectra of $RbAg_4I_5$ extending up to infrared frequencies have been published in [7,10,50]. In the microwave regime and below, the conductivity is dominated by the translational motion of the silver ions via tetrahedral sites. Slow vibrations of the silver ions within their flat potentials have been shown to be responsible for a maximum in $\sigma(\nu)$ observed in the far infrared, at about 0.5 THz [50]. Conductivity maxima beyond 1 THz are due

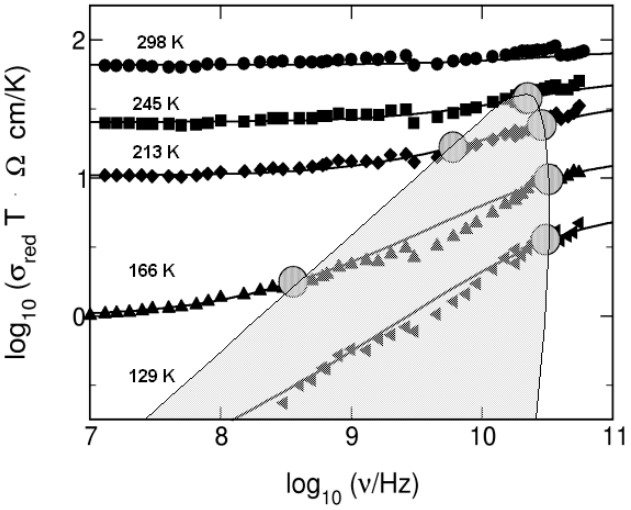

Fig. 21.14. Radio and microwave conductivities of the crystalline fast ion conductor $RbAg_4I_5$ at different temperatures. The notation σ_{red} indicates that vibrational contributions to the conductivity have been removed. The solid lines result from the CMR, with $K = 2$, the shaded area marks the dispersive regime. For details, see text.

to the excitation of transverse optical phonons (cf. Fig. 21.2 for the case of Na-β''-alumina).

The non-vibrational radio and microwave conductivity isotherms of Fig. 21.14 have been obtained from the experimental spectra by removing the low-frequency flank of the slow vibrational contribution. At millimetre-wave frequencies, they gradually approach their high-frequency plateaux. Again, the product $\sigma(\infty) \cdot T$ is thermally activated, the activation energy now being $E_{\mathrm{hf}} = 0.053\,\mathrm{eV} \pm 0.005\,\mathrm{eV}$. As noted earlier, this value is identical with the potential barrier between adjacent tetrahedral sites in $RbAg_4I_5$ as derived from a probability density contour map for the silver ions [50]. This identity is not surprising, since elementary hops are registered individually in the high-frequency limit.

In Fig. 21.14, CMR model spectra are presented along with the experimental ones. The values of the parameter A are found to be exactly proportional to $\sigma(\infty)$, while the best choice for K is 2.0. For each dispersive spectrum, the onset of the frequency dependence is marked in the figure at $\nu_{\mathrm{O}} = \omega_{\mathrm{O}}/(2\pi)$, while its end is marked at $\nu_{\mathrm{E}} = \omega_{\mathrm{E}}/(2\pi)$. In Fig. 21.14, the onset frequencies ν_{O} lie on a straight line with a slope of one, signifying the validity of the Summerfield scaling on the low-frequency side of the dispersion. As noted earlier, the values of $\omega_{\mathrm{O}}(T) = (A(T)/B(T)) \exp(-B(T))$ and those of the random hopping rate, $\Gamma(T)$, of the mobile silver ions are found to be identical within the experimental limits of error:

$$\omega_{\mathrm{O}}(T) \approx \Gamma(T) \; . \tag{21.28}$$

To determine $\Gamma(T)$, we have used the Nernst-Einstein relation,

$$\Gamma(T) \approx \frac{6\sigma(0)k_{\mathrm{B}}T}{N_V e^2 x_0^2} \; , \tag{21.29}$$

where N_V and e denote the number density of the silver ions and the elementary charge, respectively. The Haven ratio has not been included in (21.29) as it is close to one [43]. As a consequence of (21.28), the ratio $A(T)/B(T)$ has to be interpreted as the elementary hopping rate, $\Gamma_0(T)$, cf. Sect. 21.5. Equation (21.28) also implies that the time when random diffusion is attained corresponds to a root mean square displacement of about one elementary hopping distance.

In Fig. 21.14, the marks for ν_{O} and ν_{E} are on the edge of a shaded area. Within this area the spectra display dispersion, while they become flat outside. On the frequency scale, the width of the shaded area is found to shrink as the temperature is increased, until a particular point is attained at its top, resembling a critical point and signifying the end of the dispersive regime. We thus observe, for the first time in a solid ion conductor, a smooth transition from a non-random hopping at lower temperatures to a random hopping at higher temperatures. In fact, at 298 K the "ion cloud" appears to relax almost instantaneously after each hop of the "central ion", leaving no energetic advantage for a correlated backward hop and no memory of the previously occupied site.

For $W(\infty) = \exp(-B)$ we observe a gradual transition from a thermally activated low-temperature behaviour to its high-temperature value of one. Because of the relation $\sigma(0) = \exp(-B) \cdot \sigma(\infty)$, this has the following implication. In an Arrhenius plot of the dc conductivity, there is a slight, gradual change of slope as $\sigma(0)$ approaches $\sigma(\infty)$ with increasing temperature. In fact, this kind of non-Arrhenius behaviour appears to be characteristic of a number of fast ion conductors, both crystalline and glassy. Examples include Na-β''-alumina [51,52], argyrodite (Ag_7GeSe_5I) [53], and glasses of the system $AgI - Ag_2S - B_2S_3 - SiS_2$ [54].

21.8 Ion Dynamics in a Fragile Supercooled Melt

Comparing the dynamics of the mobile ions in glassy and crystalline electrolytes on the one hand and in fragile supercooled ionic melts such as $0.6\,KNO_3 \cdot 0.4\,Ca(NO_3)_2$ [11] and $LiCl \cdot 7\,H_2O$ [12] on the other, one finds surprising similarities as well as characteristic differences. Both are outlined in this section. Considering the fragile melt $LiCl \cdot 7\,H_2O$, we show that the CMR is, indeed, applicable to this system [42].

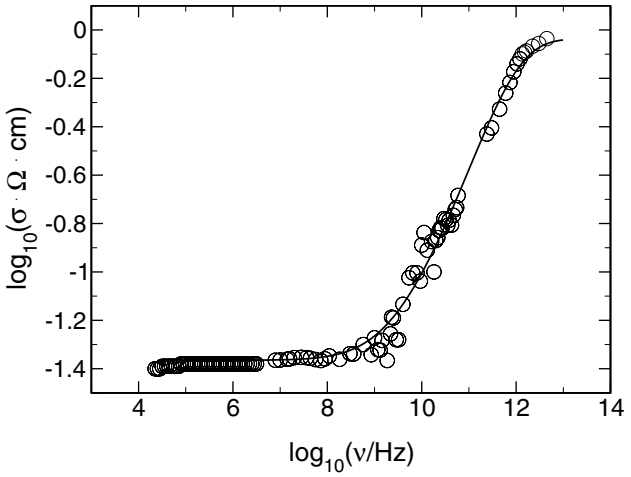

Fig. 21.15. Non-vibrational conductivity spectrum of the fragile supercooled ionic melt $LiCl \cdot 7\,H_2O$ at 253 K. The solid line is a CMR model spectrum, with $K = 2$.

In the case of supercooled $LiCl \cdot 7\,H_2O$, careful removal of the low-frequency part of the vibrational contribution to the conductivity results in non-vibrational conductivity spectra as the one presented in Fig. 21.15. At frequencies around 1 THz, the spectrum of Fig. 21.15 is seen to level off and to approach its high-frequency plateau. In the figure, a CMR model spectrum is included for comparison. Here, the numerical value of K used for modelling has again been chosen to be 2.0 [42]. The same value of K has also been used for fitting four other $\sigma(\nu)$ isotherms, and the entire set of CMR model spectra thus obtained is presented in Fig. 21.16. Interestingly, the high-frequency conductivities of Fig. 21.16 turn out to follow the Arrhenius law, with a thermal activation energy of $0.08\,\mathrm{eV} \pm 0.005\,\mathrm{eV}$ for $\sigma(\infty) \cdot T$ [12].

The observation of a thermally activated high-frequency conductivity in a melt impacts strongly on the assessment of model approaches for the ion dynamics. Evidently, the melt behaves solid-like, if the time window is not larger than a fraction of a picosecond. In this short-time regime, one may visualise individual activated displacements of individual ions. At longer times, however, the structure does not remain rigid. Structural relaxation sets in, and the concept of fixed sites has to be abandoned. Nevertheless, the CMR equations, (21.11) and (21.12), still seem to apply. Conceptually, it is now important to separate the two routes of relaxation expressed by the two equations. In particular, it is important to note that by definition $-\dot{g}(t)$ is the rate of mismatch relaxation due to the rearrangement of the neighbours under the virtual condition $W(t) \equiv 1$, i.e., without considering the backward motion of the central ion itself. Therefore, the factor $W(t)$ is once again included in (21.12). Also, the meaning of $W(t)$ itself is different from what it

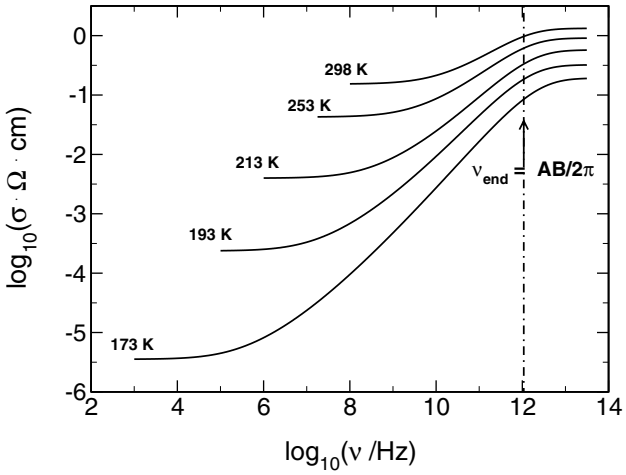

Fig. 21.16. Set of CMR model isotherms for the fragile supercooled ionic melt $LiCl \cdot 7\,H_2O$ obtained on the basis of experimental conductivity spectra as in Fig. 21.15, with $K = 2$.

is in a solid. The function now denotes the average fraction of an original displacement that is still encountered at time t.

It is most interesting to compare the conductivity isotherms of Fig. 21.16 with those of Fig. 21.11. The spectra shown in the two figures have many properties in common. Firstly, they display the same shape, even the value of K being identical. Secondly, the high-frequency conductivities are Arrhenius activated in both cases. Thirdly, the time-temperature superposition principle appears to be satisfied not only in the solid electrolyte, but also in the supercooled melt. Nevertheless, the two systems differ strongly with regard to the temperature dependence of their dc conductivities. In contrast to the example of Fig. 21.11, the dc conductivity is clearly non-Arrhenius in the case of the fragile supercooled melt. Most remarkably, this property turns out to be a direct consequence of the short-time dynamics of the mobile ions.

The key feature causing the non-Arrhenius behaviour of the dc conductivity is, in fact, the constancy of the crossover angular frequency at the end of the dispersive regime, $\omega_E = AB$, as a function of temperature, which is evident from Fig. 21.16. As a consequence of $\omega_E(T) = A(T)B(T) = const.$ and $A(T) \propto \sigma_{hf}(T)$, $B(T)$ is proportional to $1/\sigma_{hf}(T)$. As the dc conductivity varies with temperature as $\sigma_{dc}(T) = \sigma_{hf}(T)\exp(-B)$, we find

$$\sigma_{dc}(T) = \sigma_{hf}(T) \cdot \exp\left(-\frac{\sigma^*}{\sigma_{hf}(T)}\right) , \tag{21.30}$$

where σ^* is a constant. Equation (21.30) replaces the empirical Vogel-Fulcher-Tammann [55–57] relation. Apart from resulting from the short-time dynam-

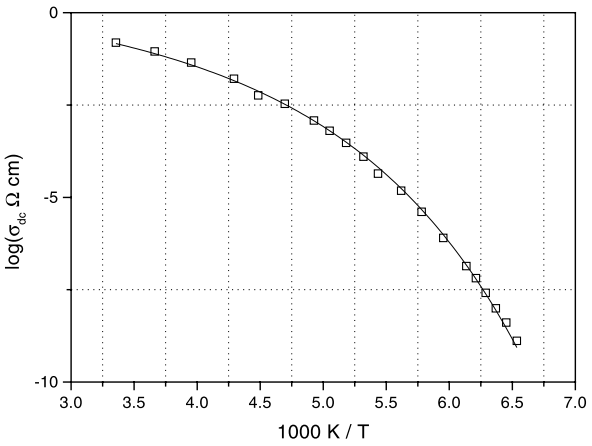

Fig. 21.17. Dc conductivity data of $LiCl \cdot 7\,H_2O$. The solid line is from (21.30), see main text.

ics, it has the further advantage of not predicting a singularity of the temperature derivative of the dc conductivity.

The temperature-dependent dc conductivity of $LiCl \cdot 7\,H_2O$ is plotted in Fig. 21.17. Here, the squares mark our data points [12], while the solid line is obtained from (21.30) with Arrhenius-activated high-frequency conductivities taken from Fig. 21.16. The meaning of the constant σ^* becomes obvious by extrapolating (21.30) to a higher temperature T^*, where B is only one. For that particular temperature, σ^* and σ_{hf} are identical.

Finally, it is worth emphasising that the distinguishing mark of a fragile melt, resulting in (21.30), is the absence of any temperature dependence of the crossover angular frequency ω_{E}. This feature corresponds to a non-activated roll-back process occurring in most cases after a thermally activated displacement. Such a view of the short-time dynamics is well in line with the conception of a fragile melt as an ionic system whose structure does not easily provide preexisting neighbouring sites for its mobile ions. The situation would be different in a strong glass-forming melt, where (21.30) would not apply, the reason being the existence of available neighbouring sites in the network. The backward hop from such a site would require some activation energy, and hence ω_{E} would become temperature-dependent.

21.9 Conductivities of Glassy and Crystalline Electrolytes Below 10 MHz

Below 10 MHz, where waveguide techniques are not required, conductivities of materials are measured not only much more easily, but also with much higher precision than at higher frequencies. Therefore, characteristic variations in

the shapes of conductivity spectra of solid electrolytes are best detected in the low-frequency range. In this section, low-frequency conductivities of various glassy and crystalline ion conductors are presented and compared with CMR model spectra. The result of the comparison turns out to be twofold. In the first place, we find that the model conductivities always agree very well with the experimental ones. However, to achieve good agreement, different values of the parameter K have to be adopted, and the remaining question is how to relate those values to the structures and dynamics of the materials studied.

In Fig. 21.18, we present frequency-dependent conductivities of a lithium borate glass of composition $0.3\,Li_2O \cdot 0.7\,B_2O_3$ as measured at four different temperatures. The dc values of the conductivities follow the Arrhenius law. The solid lines included in the figure are CMR model spectra calculated with $K = 2.0$. Both the experimental and the model conductivities satisfy the time-temperature superposition principle, and the Summerfield scaling is found to apply. Utilising the Summerfield scaling, the four experimental spectra can be collapsed in one master curve which is, indeed, indistinguishable from those already shown for other glasses in Fig. 21.6 and Fig. 21.12. Likewise, the model spectra are automatically collapsed in one curve, if the angular frequency is scaled in units of $\omega_O = (A/B)\exp(-B)$, as described in Sect. 21.5. The master spectrum thus obtained and the one of Figs. 21.6 and 21.12 are identical, since the value of K is 2.0 in all cases.

More examples of low-frequency conductivity spectra of glassy electrolytes are given in Figs. 21.19 and 21.20. The data have been taken from a silver sulphate silver metaphosphate glass of composition $0.3\,Ag_2SO_4 \cdot 0.7\,AgPO_3$ [42] and from a mixed alkali-alkaline-earth silicate glass of composition $K_2O \cdot$

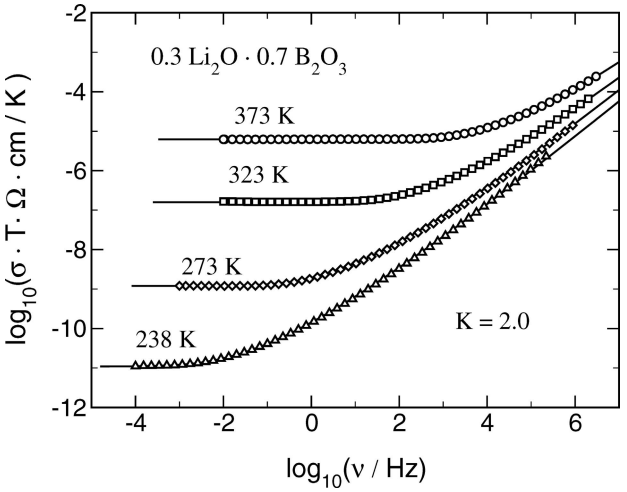

Fig. 21.18. Comparison of CMR model conductivities (solid lines, $K = 2$) and experimental ones (symbols) for $0.3\,Li_2O \cdot 0.7\,B_2O_3$ glass at different temperatures.

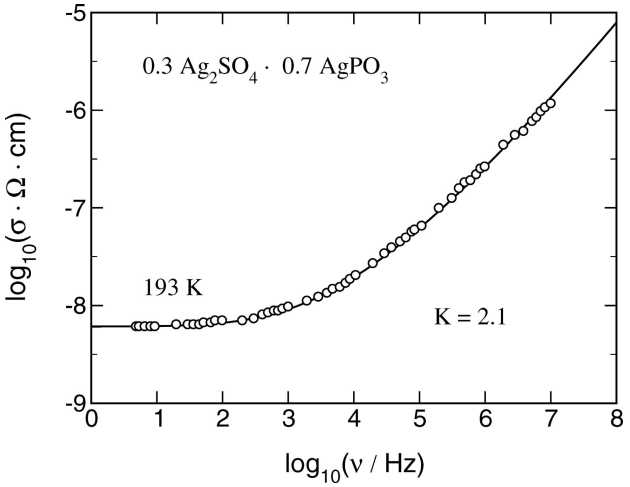

Fig. 21.19. Experimental conductivity isotherm of glassy $0.3\,Ag_2SO_4 \cdot 0.7\,AgPO_3$ at 193 K (circles) and CMR model spectrum with $K = 2.1$ (solid line).

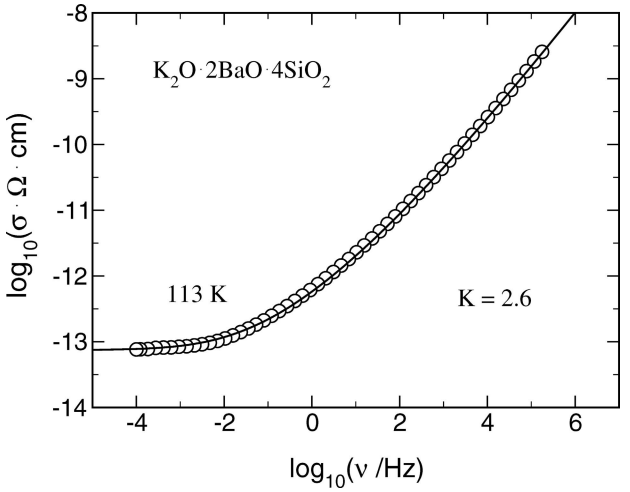

Fig. 21.20. Experimental conductivity isotherm of glassy $K_2O \cdot 2\,BaO \cdot 4\,SiO_2$ at 113 K (circles) and CMR model spectrum with $K = 2.6$ (solid line).

$2\,BaO \cdot 4\,SiO_2$ [42], respectively. The data of Fig. 21.19 are best reproduced with $K = 2.1$, while a considerably larger value of K, viz., 2.6, is required to describe the frequency-dependent conductivity of the mixed cation glass of Fig. 21.20. The rather gradual onset of the dispersion observed in Fig. 21.20 is reminiscent of many mixed alkali glasses, where the same feature

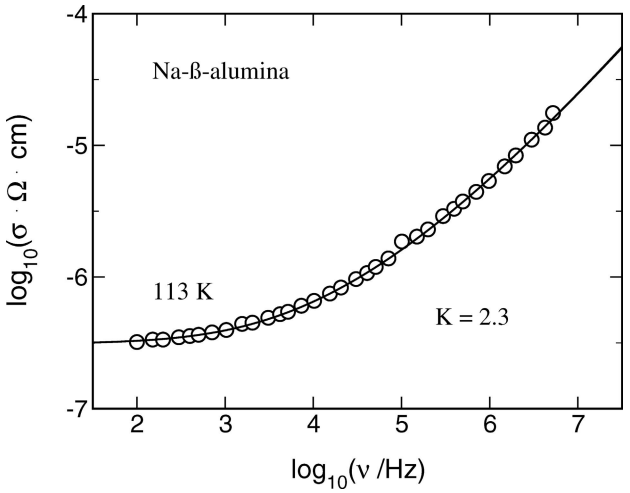

Fig. 21.21. Experimental conductivity isotherm of Na-β-alumina at 113 K (circles) [58] and CMR model spectrum with $K = 2.3$.

has been identified as a characteristic property of their frequency-dependent conductivities [22].

Values of K larger than 2 are not only found for mixed-cation glasses, but also for crystalline ion conductors with a reduced dimensionality of the sublattice of the mobile ions. The effect of dimensionality on the shape of conductivity spectra has recently been pointed out by Sidebottom [21]. (For the influence of reduced dimensionality on neutron scattering and NMR spin-lattice relaxation results see Chap. 3 and 9, respectively.) The most famous two dimensional fast ion conductor is probably Na-β-alumina. In Fig. 21.21, we reproduce conductivity data of this material published by Almond, West and Grant [58]. To reproduce the data in terms of the CMR, the best choice of K is 2.3.

Crystalline electrolytes in which the number of mobile ions is limited by the particular defect structure constitute another interesting class of materials. Examples are the low-temperature γ-phase of $RbAg_4I_5$, stable below the first-order β-γ-transition at 122 K [59] and β-AgI where the defect structure is frozen-in at reduced temperatures. In both cases, the conductivity spectra are well reproduced by the CMR, if K is chosen to be as high as 2.6 [42, 60]. A spectrum of β-AgI is shown in Fig. 21.22, while the case of γ-$RbAg_4I_5$ will be discussed in Sect. 21.10.

The impression that K may be causally related to the number density of translationally mobile ionic charge cariers is thus corroborated. The view that enhanced values of K correspond to a reduced number density of potentially mobile ions in the neighbourhood of the "central" ion also seems to agree with the observation that large values of K are found in mixed cation glasses

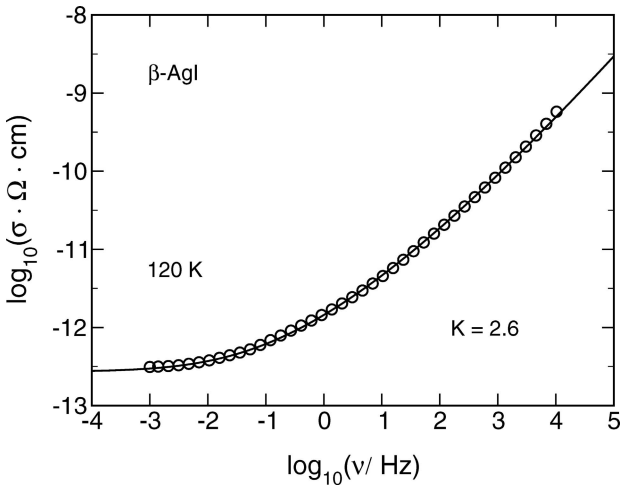

Fig. 21.22. Experimental conductivity isotherm of β-AgI at 120 K (circles) [58] and CMR model spectrum with $K = 2.6$.

as well. In such glasses, only a fraction of the neighbouring ions may be considered mobile, since most of them are unable to find suitable sites in their immediate neighbourhood. In spite of the above pieces of evidence, it is felt that the tentative interpretation towards an understanding of the meaning of K given at the end of Sect. 21.6 is not yet sufficiently conclusive. Rather, further investigations are required to get a better insight into this problem.

21.10 Localised Motion at Low Temperatures

The short-time solution for $W(t)$ as given in (21.15) applies as long as $g(t)$ is close to one. This is the case in a broad interval on the logarithmic time scale, if B is sufficiently large. Equation (21.15) then corresponds to a conductivity that increases almost linearly with frequency, before the high-frequency plateau is attained. Approaching this regime from low frequencies, the CMR predicts a continuous increase of the apparent power-law exponent, with one as a limiting value. Experimentally, such a behaviour has been observed in many ion-conducting solid materials, both crystalline and glassy, cf. Fig. 21.5. Another agreement between experimental and model conductivities concerns the very small temperature dependence in the NCL regime. As outlined in Sect. 21.5, the low-frequency parts of spectra like those in Fig. 21.11 can be superimposed by shifting them along a line with a slope of one. This implies that at frequencies where $\sigma(\omega) \propto \omega$ is roughly satisfied, the temperature dependence of the conductivity should, indeed, become very small.

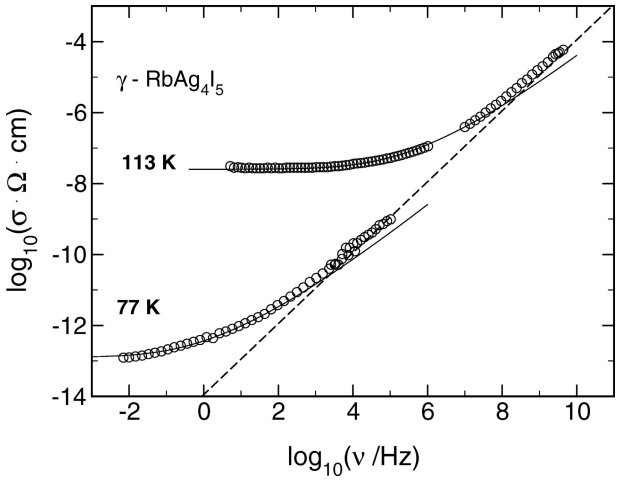

Fig. 21.23. Two conductivity isotherms of $RbAg_4I_5$ taken in the low-temperature γ-phase (circles). The solid lines are CMR model spectra, with $K = 2.6$.

Interestingly, an approximately linear dependence $\sigma(\omega) \propto \omega$ has been found in the impedance frequency regime not only in materials featuring non-zero dc conductivities, but also in cases where, at a few Kelvin, ionic hopping transport can be safely excluded as the cause of the effect [26, 27, 61, 62]. To explain such data, one has to envisage small localised displacements over low potential barriers. It appears obvious that in this process interactions between locally mobile ionic charge carriers will play an important role.

The purpose of this section is twofold. In the first place, we show that the CMR equations, when slightly modified, are able to describe completely localised movements of interacting ions, reproducing the low-temperature NCL behaviour. Secondly, we present experimental conductivity spectra featuring the CMR behaviour as outlined in Sects. 21.4 to 21.6 *plus* the low-temperature NCL effect. In fact, in the γ-phase of rubidium silver iodide, cf. Fig. 21.23, both types of ionic motion appear to contribute simultaneously to the frequency-dependent conductivity. This will be discussed at the end of this section.

In the literature, the low-temperature NCL behaviour is usually described in terms of the asymmetric double well potential (ADWP) model [37]. In that model, the potentials considered are static and exhibit particular distributions of their barrier energies and asymmetries. The resulting conductivity spectra have the same features as the one presented in Fig. 21.24. As the frequency is increased, the slope in the log-log plot of $\sigma(\omega)$ changes first from two to one and later from one to zero. The two crossover angular frequencies correspond to a longest and a shortest relaxation time. However, there are two aspects to the ADWP model that appear unsatisfactory. One is the ne-

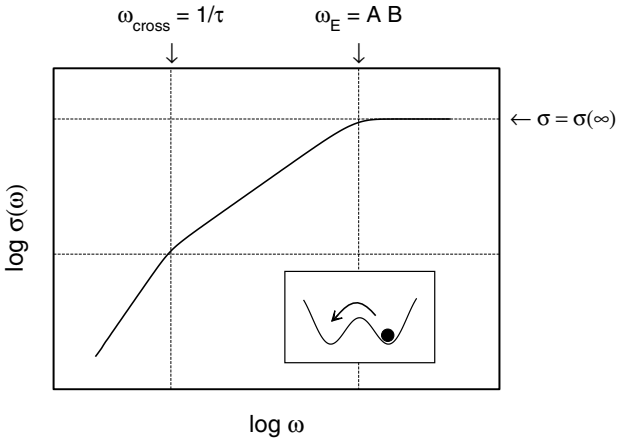

Fig. 21.24. CMR model conductivity spectrum for an assembly of interacting localised ions in flat double-well potentials ($B = 100$, $A\tau = 10^6$).

cessity to assume particular distributions. The other is the lack of any time dependence in the shape of the potentials. Of course, such a time dependence has to be expected, reflecting the interactions with other ions which are also locally mobile. Indeed, if the dynamics of local electric dipoles are simulated on a computer, and if interactions between them are taken into account, particular distributions turn out to be unnecessary, and the spectra obtained again display the features of the one shown in Fig. 21.24 [41] (cf. Chap. 20).

The derivation of the conductivity spectrum of Fig. 21.24 has not required any particular distribution, nor a computer simulation. Instead, the CMR has been used to introduce the interaction. The rationale is as follows. Without any interaction, the dynamics of an individual ion in a flat double-well potential would be properly described by an exponentially decaying function $W(t)$. This would imply $-(\mathrm{d}W(t)/\mathrm{d}t)/W(t) = 1/\tau$, where τ is the relaxation time. Taking interactions with other dipoles into account, we replace the right-hand side with $-B \cdot \mathrm{d}g(t)/\mathrm{d}t + 1/\tau$ and again describe the decay of the normalised mismatch function, $g(t)$, by the short-time version of (21.11):

$$-\frac{\mathrm{d}}{\mathrm{d}t}g(t) = A \cdot g^K\,(t) \cdot W\,(t) \simeq A \cdot W(t) \tag{21.31}$$

$$-\left(\frac{\mathrm{d}}{\mathrm{d}t}W\,(t)\right) \cdot \frac{1}{W\,(t)} = -B \cdot \frac{\mathrm{d}}{\mathrm{d}t}g\,(t) + \frac{1}{\tau}\,. \tag{21.32}$$

At low temperatures, $1/\tau$ is only a small additive constant on the right-hand side of (21.32). At short times, when $1/\tau$ is still much smaller than $-B \cdot \mathrm{d}g(t)/\mathrm{d}t$, the functions $W(t)$ and $\sigma\,(\omega)\,/\sigma\,(\infty)$ obtained from (21.31) and (21.32) are almost identical with those obtained without inclusion of $1/\tau$. If the dc conductivity is extremely low, corresponding to a large value

of B, and if $1/\tau$ is small, we thus find a nearly-constant-loss behaviour in a wide range of frequencies. At very long times, however, when $-B \cdot \mathrm{d}g(t)/\mathrm{d}t$ becomes even smaller than $1/\tau$, $W(t)$ will decay exponentially. This results in a $\sigma(\omega) \propto \omega^2$ behaviour at low frequencies. Both features are clearly seen in Fig. 21.24.

The crossover from the $\sigma(\omega) \propto \omega^2$ regime into the NCL regime occurs at an angular frequency $\omega_{\mathrm{cross}} = 1/t_{\mathrm{cross}}$. At the particular time t_{cross}, the two terms on the right-hand side of (21.32) become identical. As $g(t)$ is still close to unity, we find from (21.31) and (21.32) that $W(t_{\mathrm{cross}})$ should be $1/(AB\tau)$. On either axis of a $\sigma(\omega)$ plot, the corresponding crossover point and the high-frequency crossover point (at angular frequency $\omega_{\mathrm{E}} = AB$) should, therefore, be apart from each other by a factor of $AB\tau$. This implies

$$\omega_{\mathrm{cross}} = 1/\tau \tag{21.33}$$

as indicated in Fig. 21.24.

In Fig. 21.23, the CMR model curves provide fits to the experimental conductivities of γ-$RbAg_4I_5$ only at sufficiently low frequencies, while increasing discrepancies are observed at higher frequencies. Forming the difference between the measured conductivity isotherms and the model curves we obtain the same straight line with a slope of one at both temperatures. This extra contribution to the conductivity of γ-$RbAg_4I_5$ is thus – within the limits of experimental error – both linear in ω and temperature-independent. It is, therefore, interpreted as resulting from a strictly localised ionic motion as described by (21.31) and (21.32). In the α- and β-phases of $RbAg_4I_5$ where all the silver ions are translationally mobile, this contribution to $\sigma(\omega)$ has not been detected, as it is evidently swamped by the regular CMR spectrum. For a complete and satisfactory description of the ion dynamics in γ-$RbAg_4I_5$ it will, of course, be important to elucidate the detailed structural properties of this phase, which are still unknown.

The conductivity isotherms of Fig. 21.23 are especially valuable, as they put an end to a long-standing discussion. Until now, there have been two seemingly contradictory points of view. Authors who have been measuring ionic conductivities over wide ranges of frequency and temperature have been convinced that the NCL behaviour is observed in any structurally disordered solid electrolyte, if $\sigma(\nu)/\sigma(0)$ is sufficiently large, but σ_{hf} is not yet attained, the effect being caused by the short-time hopping dynamics of the mobile ions [63, 64]. On the other hand, those who have been measuring nearly constant losses at low temperatures, have been convinced that this effect is certainly not related with ionic hopping and ionic transport [27, 62]. The two views are now reconciled, since Fig. 21.23 provides an example where the strictly localised kind of ionic motion is found to coexist with the translational one.

21.11 Conclusion

Conductivity spectra of ionic materials with disordered structures contain valuable information on the diffusion dynamics of the mobile ions. Phenomenologically, they display a number of common features. For any *given* ion conducting material, these include the time-temperature superposition principle and the UDR – NCL transition. With regard to *different* ion conducting materials, they include surprisingly close similarities in the shapes of the spectra of crystalline, glassy, and even molten systems. On the other hand, specific differences are also observed concerning, e.g., the temperature dependence of the dc conductivity and the way $\sigma(\nu)$ increases in the vicinity of the onset frequency of the dispersion.

In this chapter, we have presented a set of simple rules, expressed in the form of rate equations, which describe the development of the ion dynamics with time. The rules reproduce the observed phenomena and explain them in terms of microscopic processes. Our CMR model bears analogy to Debye-Hückel-Falkenhagen theory in considering the coupling between mobile ions and their surrounding ion clouds. It is able to reproduce and explain the time-temperature superposition principle as well as the UDR – NCL transition and the low-temperature NCL behaviour. The specific differences in shape encountered in conductivity spectra of different ion conducting materials are reproduced with the help of only one parameter, K. Although it is clear that there is a connection between K and the number density of the mobile ions, more work is required in order to quantify this relationship.

Notation

A	parameter of the CMR model; internal frequency
B	parameter of the CMR model: $B = \ln(\sigma(\infty)/\sigma(0))$
D	coefficient of self diffusion
e	elementary charge
E_{dc}	activation energy of the dc conductivity
$g(t)$	normalised mismatch function, normalised dipole field
H_{R}	Haven ratio
$\boldsymbol{i}$	current density
$\langle \boldsymbol{i}(0) \cdot \boldsymbol{i}(t) \rangle$	current density autocorrelation function
i	imaginary unit, $\mathrm{i} = \sqrt{-1}$
k_{B}	Boltzmann constant
ℓ_{O}	characteristic length for loss of memory
N	number of mobile carriers
N_V	particle density
q	electrical charge
$\langle r^2(t) \rangle$	mean square displacement
t	time
T	temperature

$\boldsymbol{v}$	velocity
$\langle \boldsymbol{v}(0) \cdot \boldsymbol{v}(t) \rangle$	velocity autocorrelation function
V	volume
$W(t)$	time dependent correlation factor
x_0	jump distance
Γ	rate of "successful" hops, random hopping rate
Γ_0	elementary hopping rate
ν	frequency
σ	electrical conductivity
ω	angular frequency
ω_{O}	angular frequency marking the onset of dispersion
ω_{E}	angular frequency marking the end of dispersion
$\#(t)$	effective number of mobile ions available for relaxation

Complex quantities are marked by a circumflex ("$\hat{}$").

References

1. N. Bloembergen, E.M. Purcell, R.V. Pound: Phys. Rev. **73**, 679 (1948)
2. R. Kubo: J. Phys. Soc. Japan **12**, 570 (1957)
3. C. Cramer, R. Graeber, M.D. Ingram, T. Saatkamp, D. Wilmer, K. Funke: Mat. Res. Soc. Symp. Proc. **369**, 233 (1995)
4. B. A. Boukamp: Solid State Ionics **18/19**, 136 (1986)
5. *Impedance Spectroscopy: Emphasizing Solid State Materials and Systems*, ed by J.R. MacDonald (Wiley, New York 1987)
6. I. Riess: Solid State Ionics **91**, 221 (1996)
7. R. Hoppe, T. Kloidt, K. Funke: Ber. Bunsenges. Phys. Chem. **95**, 1025 (1991)
8. C.A. Angell: J. Non-Cryst. Solids **131-133**, 13 (1991)
9. J.C. Kimball, L.W. Adams Jr: Phys. Rev. B **18**, 5851 (1978)
10. K. Funke, T. Kloidt, D. Wilmer, C.J. Carlile: Solid State Ionics **53-56**, 947 (1992)
11. K. Funke: Z. Phys. Chem. **206**, 101 (1998)
12. K. Funke, B. Heimann, M. Vering, D. Wilmer: J. Electrochem. Soc. **A148**, 395 (2001)
13. H. E. Taylor: Trans. Faraday Soc. **52**, 873 (1956)
14. J.O. Isard: J. Non-Cryst. Solids **4**, 357 (1970)
15. H. Kahnt: Ber. Bunsenges. Phys. Chem. **95**, 1021 (1991)
16. B. Roling, A. Happe, K. Funke, M. Ingram: Phys. Rev. Lett. **78**, 2160 (1997)
17. B. Roling: Solid State Ionics **105**, 185 (1998)
18. S. Summerfield: Phil. Mag. B **52**, 9 (1985)
19. J. C. Dyre: J. Appl. Phys. **64**, 2456 (1988)
20. A. K. Jonscher: Nature **267**, 673 (1977)
21. D. L. Sidebottom: Phys. Rev. Lett. **83**, 983 (1999)
22. B. Roling, C. Martiny: Phys. Rev. Lett. **85**, 1274 (2000)
23. C. Cramer, S. Brückner, Y. Gao, K. Funke: Phys. Chem. Chem. Phys. **4**, 3214 (2002)
24. W.-K. Lee, J.F. Liu, A.S. Nowick: Phys. Rev. Lett. **67**, 1559 (1991)

25. A.S. Nowick, B.S. Lim, A.V. Vaysleyb: J. Non-Cryst. Solids **172-174**, 1243 (1994)
26. H. Jain, S. Krishnaswami: Solid State Ionics **105**, 129 (1998)
27. X. Lu, H. Jain: J. Phys. Chem. Solids **55**, 1433 (1994)
28. P. Maass, J. Petersen, A. Bunde, W. Dieterich, H.E. Roman: Phys. Rev. Lett. **66**, 52 (1991)
29. K. L. Ngai: Comments Solid State Phys. **9**, 127 (1979)
30. K. L. Ngai: Comments Solid State Phys. **9**, 141 (1980)
31. K. L. Ngai: Solid State Ionics **5**, 27 (1981)
32. K. Funke: Prog. Solid St. Chem. **22**, 111 (1993)
33. K. Funke: Solid State Ionics **94**, 27 (1997)
34. P. Maass, M. Meyer, A. Bunde: Phys. Rev. B **51**, 8164 (1995)
35. D. Knödler, P. Pendzig, W. Dieterich: Solid State Ionics **70-71**, 356 (1994)
36. D. Knödler, P. Pendzig, W. Dieterich: Solid State Ionics **86-88**, 29 (1996)
37. M. Pollak, G.E. Pike: Phys. Rev. Lett. **28**, 1449 (1972)
38. H. Jain: Met. Mater. Process. **11**, 317 (1999)
39. J.C. Dyre, T.B. Schrøder: Rev. Mod. Phys. **72**, 873 (2000)
40. J.C. Dyre, T.B. Schrøder: Phys. Rev. Lett. **84**, 310 (2000)
41. B. Rinn, W. Dieterich, P. Maass: Phil. Mag. B **77**, 1283 (1998)
42. K. Funke, R.D. Banhatti, S. Brückner, C. Cramer, C. Krieger, A. Mandanici, C. Martiny, I. Ross: Phys. Chem. Chem. Phys. **4**, 3155 (2002)
43. K. Funke: Prog. Solid St. Chem. **11**, 345 (1976)
44. J.C. Dyre: Phys. Rev. B **49**, 11709 (1994)
45. K. Funke, C. Cramer, B. Roling: Glastechnol. Ber. Glass Sci. Technol. **73**, 244 (2000)
46. R. Belin, G. Taillades, A. Pradel, M. Ribes: Solid State Ionics **136-137**, 1025 (2000)
47. B.B. Owens, G.R. Argue: Science **157**, 308 (1967)
48. S. Geller: Science **157**, 310 (1967)
49. J.N. Bradley, P.D. Greene: Trans. Farad. Soc. **63**, 424 (1967)
50. K. Funke, H.J. Schneider: Solid State Ionics **13**, 335 (1984)
51. W.L. Roth, R.L. Beneson, W.K. Tikku, J.L. Briant, B. Dunn: Solid State Ionics **5**, 163 (1981)
52. J.C. Bates, H. Engstrom, J.C. Wang, B.C. Larson, N.J. Dudney, W.E. Brundage: Solid State Ionics **5**, 159 (1981)
53. A. Zerouale, B. Deroide, B. Cros, M. Ribes: Solid State Ionics **28-30**, 1317 (1988)
54. J. Kincs, S.W. Martin: Phys. Rev. Lett. **76**, 70 (1996)
55. H. Vogel: Phys. Z. **22**, 645 (1921)
56. G.S. Fulcher: J. Am. Ceram. Soc. **8**, 339 (1925)
57. V.G. Tammann, H. Hesse: Z. Anorg. Chem. **156**, 245 (1926)
58. D. Almond, A. West, R. Grant: Solid State Commun. **44**, 1277 (1982)
59. W.V. Johnston, H. Wiedersich, G.W. Lindberg: J. Chem. Phys. **51**, 3739 (1969)
60. K. Funke, R.D. Banhatti, I. Ross, D. Wilmer: Z. Phys. Chem. **217**, 1245 (2003)
61. A.S. Nowick, A.V. Vayleyb, W. Liu: Solid State Ionics **105**, 121 (1998)
62. A.S. Nowick: Solid State Ionics **136-137**, 1307 (2000)
63. B. Roling, C. Martiny, S. Murugavel: Phys. Rev. Lett. **87**, 85901 (2001)
64. K. Funke, B. Roling, M. Lange: Solid State Ionics **105**, 195 (1998)

22 Diffusion and Conduction in Percolation Systems

Armin Bunde and Jan W. Kantelhardt

22.1 Introduction

Percolation is a standard model for disordered systems. Its applications range from transport in amorphous and porous media and composites to the properties of branched polymers, gels and complex ionic conductors. Because of universality the results do not depend on the specific model, and general scaling laws can be deduced. In this chapter we give a short introduction to percolation theory and describe one application to composites. We start with the structural properties of site percolation clusters and their substructures and report on other percolation systems after that. Then we turn to the dynamical properties of percolation clusters and discuss the way the laws of diffusion and conduction are modified on random fractal structures. Finally, we review a particular application of the percolation concept, transport in heterogeneous ionic conductors.

22.2 The (Site-)Percolation Model

Percolation represents the basic model for a structurally disordered system (for recent reviews see [1–3], for applications see [4, 5]). Let us consider a square lattice, where each site is occupied randomly with probability p or is empty with probability $1 - p$ (see Fig. 22.1). Occupied and empty sites may stand for very different physical properties. For illustration, let us assume that the occupied sites are electrical conductors, the empty sites represent insulators, and that electrical current can only flow between nearest-neighbour conductor sites.

At low concentration p, the conductor sites are either isolated or form small clusters of nearest-neighbour sites. Two conductor sites belong to the same cluster if they are connected by a path of nearest-neighbour conductor sites, and a current can flow between them. At low p values, the mixture is an insulator, since no conducting path connecting opposite edges of our lattice exists. At large p values, on the other hand, many conducting paths between opposite edges exist, where electrical current can flow, and the mixture is a conductor. At some concentration in between, therefore, a threshold concentration p_c must exist where for the first time electrical current can percolate

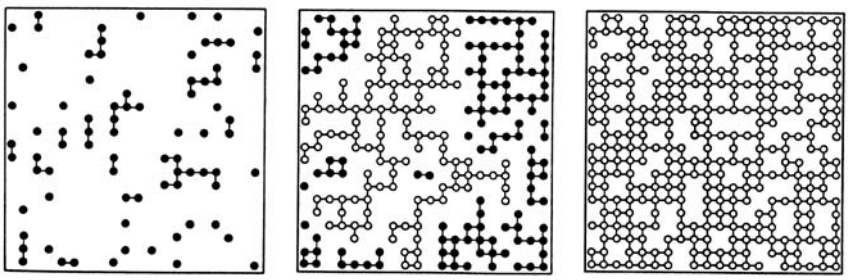

Fig. 22.1. Site percolation on the square lattice: The small circles represent the occupied sites for three different concentrations: $p = 0.2$, 0.59, and 0.80. Nearest-neighbour cluster sites are connected by lines representing the bonds. Filled circles are used for finite clusters, while open circles mark the large *infinite* cluster.

from one edge to the other. Below p_c we have an insulator, above p_c we have a conductor. The threshold concentration is called the percolation threshold, or, since it separates two different phases, the critical concentration.

If the occupied sites are superconductors and the empty sites are conductors, p_c separates a normal-conducting phase below p_c from a superconducting phase above p_c. Another example is a mixture of ferromagnets and paramagnets, where the system changes at p_c from a paramagnet to a ferromagnet.

In contrast to the more common thermal phase transitions, where the transition between two phases occurs at a critical temperature, the percolation transition described here is a geometrical phase transition, which is characterized by the geometric features of large clusters in the neighbourhood of p_c. At low values of p only small clusters of occupied sites exist. When the concentration p is increased the average size of the clusters increases. At the critical concentration p_c a large cluster appears which connects opposite edges of the lattice. We call this cluster the *infinite* cluster, since its size diverges in the thermodynamic limit. When p is increased further the density of the infinite cluster increases, since more and more sites become part of the infinite cluster, and the average size of the *finite* clusters, which do not belong to the infinite cluster, decreases. At $p = 1$, trivially, all sites belong to the infinite cluster.

The critical concentration depends on the details of the lattice and increases, for fixed dimension d of the lattice, with decreasing coordination number z of the lattice: For the triangular lattice, $z = 6$ and $p_c = 1/2$, for the square lattice, $z = 4$ and $p_c \cong 0.592746$, and for the honeycomb lattice, $z = 3$ and $p_c \cong 0.6962$. For fixed z, p_c decreases if the dimension d is enhanced. In both the triangular lattice and the simple cubic lattice we have $z = 6$, but p_c for the simple cubic lattice is considerably smaller, $p_c \cong 0.3116$.

Table 22.1. Critical exponents and fractal dimensions for percolation in two and three dimensions. The numerical values are taken from [1, 6, 7].

Quantity		Exp.	$d = 2$	$d = 3$
Order parameter	$P_\infty(p) \sim (p - p_c)^\beta$	β	5/36	0.417 ± 0.003
Correlation length	$\xi(p) \sim \lvert p - p_c\rvert^{-\nu}$	ν	4/3	0.875 ± 0.008
Cluster mass	$M(r) \sim r^{d_f}$	d_f	91/48	2.524 ± 0.008
Backbone mass	$M_B(r) \sim r^{d_B}$	d_B	1.6432 ± 0.0008	1.855 ± 0.015
Chemical Path	$\ell(r) \sim r^{d_{min}}$	d_{min}	1.1307 ± 0.0004	1.374 ± 0.004
Random Walk	$\langle r^2(t)\rangle \sim t^{2/d_w}$	d_w	2.871 ± 0.001	3.80 ± 0.02
Conductivity	$\sigma_{dc}(p) \sim (p_c - p)^\mu$	μ	1.310 ± 0.001	1.99 ± 0.01
Superconductivity	$\sigma_S(p) \sim (p - p_c)^{-s}$	s	1.310 ± 0.001	0.74 ± 0.03

The percolation transition is characterized by the geometrical properties of the clusters near p_c [1, 2]. The probability P_∞ that a site belongs to the infinite cluster is zero below p_c and increases above p_c as

$$P_\infty \sim (p - p_c)^\beta. \tag{22.1}$$

This behaviour is illustrated in Fig. 22.2. The linear size of the *finite* clusters, below and above p_c, is characterized by the correlation length ξ. The correlation length is defined as the mean distance between two sites on the same finite cluster and represents the characteristic length scale in percolation. When p approaches p_c, ξ increases as

$$\xi \sim |p - p_c|^{-\nu}, \tag{22.2}$$

with the same exponent ν below and above the threshold (see also Fig. 22.2). While p_c depends explicitly on the type of the lattice, the critical exponents β and ν are universal and depend only on the dimension d of the lattice, but not on the type of the lattice. The values of the critical exponents are given in Tab. 22.1 for two and three dimensions.

22.3 The Fractal Structure of Percolation Clusters near p_c

Near p_c on length scales smaller than ξ both the infinite cluster and the finite clusters are self-similar, i.e., if we cut a small part out of a large cluster, magnify it to the original cluster size and compare it with the original, we cannot tell the difference: Both look the same. This feature is illustrated in Fig. 22.3, where a large cluster at p_c is shown in four different magnifications.

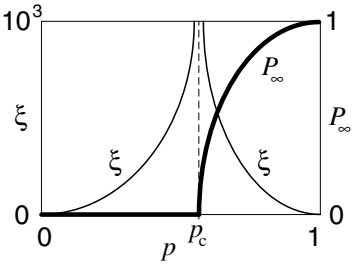

Fig. 22.2. Schematic diagram of the probability P_∞ (cf. (22.1), bold line) and the correlation length ξ (cf. (22.2), thin line) versus the concentration p of occupied sites.

We leave it to the reader to find out what is the original and what are the magnifications.

We have learnt in Chap. 19 that – as a consequence of the (non-trivial) self-similarity – the cluster is characterized by a "fractal" dimension, which is smaller than the dimension d of the embedding lattice. The mean mass of the cluster within a circle of radius r increases with r as

$$M(r) \sim r^{d_\mathrm{f}}, \quad r \ll \xi, \tag{22.3}$$

with the fractal dimension d_f. The numerical values of d_f can be found in Table 22.1. Above p_c on length scales *larger* than ξ the infinite cluster can be regarded as an homogeneous system which is composed of many cells of size ξ. Mathematically, this can be summarized as

$$M(r) \sim \begin{cases} r^{d_\mathrm{f}}, \text{ if } r \ll \xi, \\ r^{d}, \text{ if } r \gg \xi. \end{cases} \tag{22.4}$$

Fig. 22.4 shows a part of the infinite cluster above p_c ($p = 1.003\,p_\mathrm{c}$) on different length scales. At large length scales ($r \gg \xi$, upper left) the cluster appears homogeneous, while on lower length scales ($r \ll \xi$, lower pictures) the cluster is self-similar.

The fractal dimension d_f can be related to β and ν in the following way: Above p_c, the mass M_∞ of the infinite cluster in a large lattice of size L^d is proportional to $L^d P_\infty$. On the other hand, this mass is also proportional to the number of unit cells of size ξ, $(L/\xi)^d$, multiplied by the mass of each cell which is proportional to ξ^{d_f}. This yields (with (22.1) and (22.2))

$$M_\infty \sim L^d P_\infty \sim L^d (p - p_\mathrm{c})^\beta \sim (L/\xi)^d \xi^{d_\mathrm{f}} \sim L^d (p - p_\mathrm{c})^{\nu d - \nu d_\mathrm{f}}, \tag{22.5}$$

and hence, comparing the exponents of $(p - p_\mathrm{c})$,

$$d_\mathrm{f} = d - \frac{\beta}{\nu}. \tag{22.6}$$

Since β and ν are universal exponents, d_f is also universal.

A fractal percolation cluster is composed of several fractal substructures, which are described by other exponents [1, 2]. Imagine applying a voltage

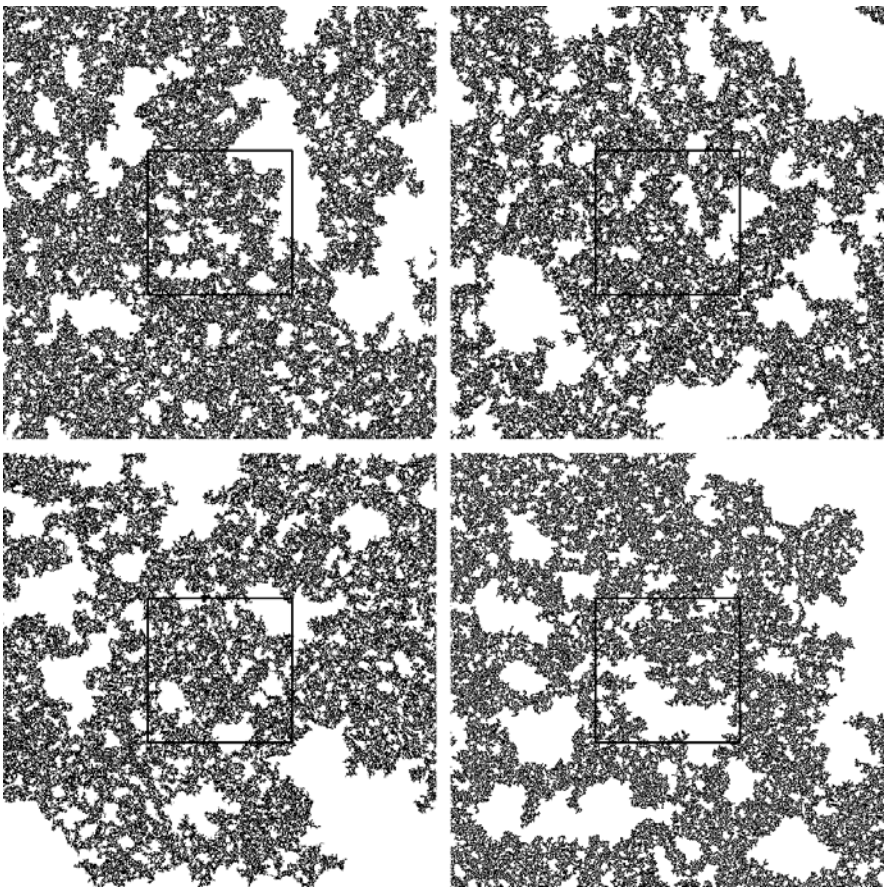

Fig. 22.3. Four successive magnifications of the incipient infinite cluster that forms at the percolation threshold on the square lattice. Three of the panels are magnifications of the center squares marked by black lines. In the figure that you see, however, the labels of the four panels have been removed and the panels have been scrambled. Attempt to put them back into sequence by eye – it is extremely difficult if the system is at the percolation threshold ($p = p_c$). An educational game is to time how long it takes each player to detect by eye which of the 24 possible orderings is the correct one that arranges the four panels in increasing order of magnification.

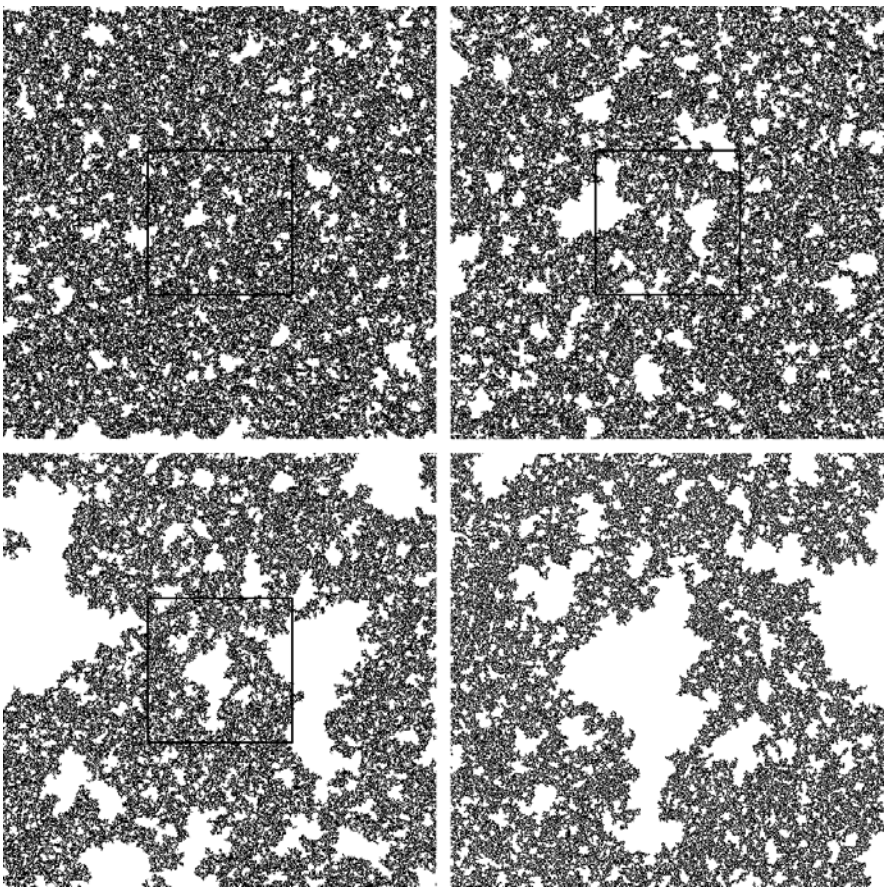

Fig. 22.4. The same as Fig. 22.3 except that now the system is slightly (0.3 %) above the percolation threshold and the panels are not scrambled. The upper left picture shows the original and the other pictures are magnifications of the center squares marked by black lines. The correlation length ξ is approximately equal to the linear size of the third (lower left) picture. When comparing the two lower pictures, the self-similarity at small length scales below ξ is easy to recognize.

between two sites at opposite edges of a metallic percolation cluster: The backbone of the cluster consists of those sites (or bonds) which carry the electric current. The topological distance between both points (also called chemical distance) is the length of the shortest path on the cluster connecting them. The dangling ends are those parts of the cluster which carry no current and are connected to the backbone by a single site only. The red bonds (or singly connected bonds), finally, are those bonds that carry the total current; when they are cut the current flow stops.

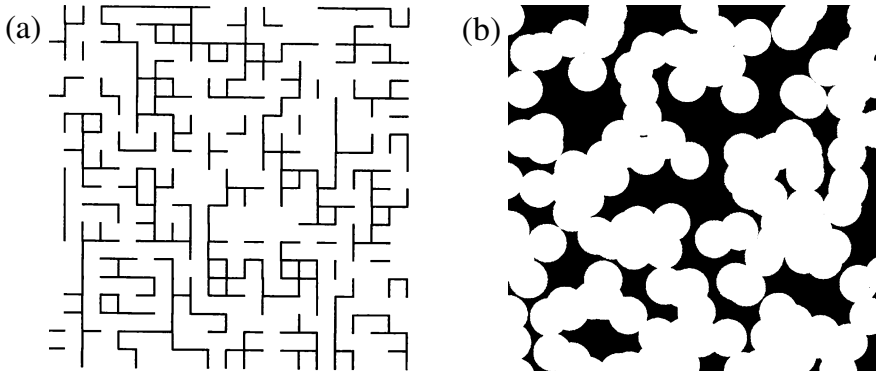

Fig. 22.5. Further percolation systems: (a) Bond percolation cluster on a square lattice and (b) continuum percolation of conductive material with circular holes of fixed radius at the percolation threshold.

The fractal dimension d_{B} of the backbone is smaller than the fractal dimension d_{f} of the cluster, reflecting the fact that most of the mass of the cluster is concentrated in the dangling ends. On the average, the topological length ℓ of the path between two points on the cluster increases with the Euclidean distance r between them as $\ell \sim r^{d_{\min}}$. The values of the fractal dimensions d_{B} and $d_{\min}$ are given in Table 22.1 for two and three dimensions. The fractal dimensions of the red bonds d_{red} are known from exact analytical arguments. The mean number of red bonds varies with p as $n_{\mathrm{red}} \sim (p - p_{\mathrm{c}})^{-1} \sim \xi^{1/\nu} \sim r^{1/\nu}$, and the fractal dimension of the red bonds is therefore $d_{\mathrm{red}} = 1/\nu$ [1].

A further important substructure of the cluster is the external perimeter (which is also called the hull). The hull consists of those sites of the cluster which are adjacent to empty sites and are connected with infinity via empty sites. It is an important model for random fractal interfaces. In two dimensions, the hull has the fractal dimension $d_{\mathrm{h}} = 7/4$, while its mass seems to be proportional to the mass of the cluster in $d = 3$, i.e. $d_{\mathrm{h}} = d_{\mathrm{f}}$. In contrast to the hull, the total perimeter also includes the holes in the cluster.

22.4 Further Percolation Systems

So far we have considered site percolation, where the sites of a lattice have been occupied randomly. When the sites are all occupied, but the bonds between the sites are randomly occupied with probability q, we speak of bond percolation (see Fig. 22.5 (a)). Two occupied bonds belong to the same cluster if they are connected by a path of occupied bonds, and the critical concentration q_{c} of bonds ($q_{\mathrm{c}} = 1/2$ in the square lattice and $q_{\mathrm{c}} \simeq 0.2488$ in

the simple cubic lattice) separates a phase of finite clusters of bonds from a phase with an infinite cluster [1, 2].

If sites are occupied with probability p *and* bonds are occupied with probability q, we speak of site–bond percolation. Two occupied sites belong to the same cluster if they are connected by a path of nearest-neighbour occupied sites with occupied bonds in between. For $q = 1$, site–bond percolation reduces to site percolation, for $p = 1$ it reduces to bond percolation. In general, both parameters characterize the state of the system. Accordingly, a critical line in p-q space separates both phases, which for $p = 1$ and $q = 1$ takes the values of the critical bond and site concentrations, respectively.

Perhaps the most common example of bond percolation in physics is a random resistor network, where the metallic wires in a regular network are cut randomly with probability $1-q$. Here q_c separates a conductive phase at large q from an insulating phase at low q. A possible application of bond percolation in chemistry is the polymerization process, where small branching molecules can form large molecules by activating more and more bonds between them. If the activation probability q is above the critical concentration, a network of chemical bonds spanning the whole system can be formed, while below q_c only macromolecules of finite size can be generated. This process is called a sol-gel transition. An example of this gelation process is the boiling of an egg, which at room temperature is liquid and upon heating becomes a more solid-like gel. Site–bond percolation can be relevant for gelation in dilute media.

The most natural example of percolation is continuum percolation, where the positions of the two components of a random mixture are not restricted to the discrete sites of a regular lattice. As a simple example, consider a sheet of conductive material, with circular holes punched randomly in it (see Fig. 22.5 (b)). The relevant quantity now is the fraction p of remaining conductive material. Compared with site and bond percolation, the critical concentration is further decreased: $p_c \cong 0.312$ for $d = 2$, when all circles have the same radius. This picture can easily be generalized to three dimensions, where spherical voids are generated randomly in a cube, and $p_c \cong 0.034$. Due to its similarity to Swiss cheese, this model of continuous percolation is called the Swiss cheese model. Similar models, where also the size of the spheres can vary, are used to describe sandstone and other porous materials. Often also the inverse model is considered, where the circular discs or spheres represent the conductive material [8].

It is important that close to the percolation threshold all these different percolation systems are characterized by the same critical exponents β, ν, and d_f given in Table 22.1. The exponents are universal and depend neither on the structural details of the lattice (e.g., square or triangular) nor on the type of percolation (site, bond, or continuum), but only on the dimension d of the system.

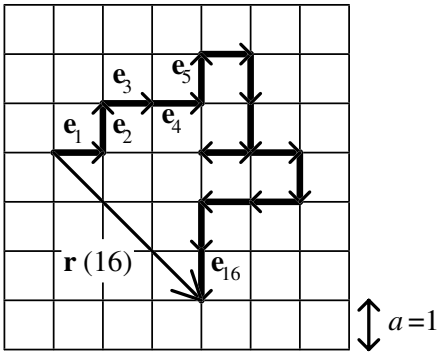

Fig. 22.6. Random walk on a square lattice. The lattice constant $a = 1$ is equal to the jump length of the random walker. Sixteen steps of the walk are shown.

22.5 Diffusion on Regular Lattices

After we have discussed the structural properties of percolation systems close to the percolation threshold, we will now focus on the *dynamical* properties of percolation systems, where to each site or bond a physical property such as conductivity is assigned. We show that due to the fractal nature of the percolation clusters near p_c, the physical laws of dynamics are changed essentially and become *anomalous*.

At first, we consider regular lattices. The diffusion process is commonly modelled by a simple random walk (see e. g., Chaps. 18 and 19), which advances one step of length a in one time unit. Each step brings the random walker to a randomly chosen nearest-neighbour site on a given d-dimensional lattice. Assume that the walker starts at time $t = 0$ at the origin of the lattice. After t time steps, the actual position is described by the vector (see Fig. 22.6)

$$\mathbf{r}(t) = a \sum_{\tau=1}^{t} \mathbf{e}_\tau, \tag{22.7}$$

where $\mathbf{e}_\tau$ denotes the unit vector pointing in the direction of the jump at the τ th time step.

The mean distance the random walker has travelled after t time steps is described by the root mean square displacement $R(t) \equiv \langle r^2(t)\rangle^{1/2}$, where the average $\langle \cdots \rangle$ is over all random-walk configurations on the lattice. From (22.7) we obtain

$$\langle r^2(t)\rangle = a^2 \sum_{\tau,\tau'=1}^{t} \langle \mathbf{e}_\tau \cdot \mathbf{e}_{\tau'}\rangle = a^2 t + \sum_{\tau \neq \tau'} \langle \mathbf{e}_\tau \cdot \mathbf{e}_{\tau'}\rangle. \tag{22.8}$$

Since jumps at different steps τ and τ' are uncorrelated, we have $\langle \mathbf{e}_\tau \cdot \mathbf{e}_{\tau'}\rangle = \delta_{\tau\tau'}$, and we obtain the Einstein relation

$$\langle r^2(t)\rangle = a^2 t, \tag{22.9}$$

which is equivalent to Fick's first law (see Chap. 10). Note that (22.9) is independent of the dimension d of the lattice.

In the general case, when the lengths of the steps of the random walker may vary, (22.9) is modified into

$$\langle r^2(t)\rangle = 2dDt, \tag{22.10}$$

where D is the diffusion coefficient. The diffusion coefficient is (approximately) related to the dc conductivity $\sigma_{\rm dc}$ by the Nernst-Einstein equation,

$$\sigma_{\rm dc} = n(e^2/k_{\rm B}T)D, \tag{22.11}$$

where n is the density and e the charge of the diffusing particles.

A more complete description of the diffusion process is possible with the probability density $P(r,t)$, which is the probability of finding the walker after t time steps at a site within distance r from its starting point. The mean square displacement can be obtained from $P(r,t)$ via $\langle r^2(t)\rangle = \int {\rm d}\boldsymbol{r}\, r^2 P(r,t)$. For $t \gg r$, $P(r,t)$ is described by a Gaussian: $P(r,t) \cong \frac{1}{\sqrt{2\pi t}} e^{-r^2/2t}$. This "normal" probability density – commonly referred to as the propagator (see Chaps. 10, 18, and 23) – characterizes the diffusion on regular lattices. Next we consider disordered structures.

22.6 Diffusion on Percolation Clusters

We start with the infinite percolation cluster at the critical concentration $p_{\rm c}$. The cluster has loops and dangling ends, and both substructures slow down the motion of a random walker. Due to self-similarity, loops and dangling ends occur on all length scales, and therefore the motion of the random walker is slowed down on *all* length scales. The time t the walker needs to travel a distance R is no longer, as in regular systems, proportional to R^2, but scales as $t \sim R^{d_{\rm w}}$, where $d_{\rm w} > 2$ is the fractal dimension of the random walk [1,2,9]. For the mean square displacement this yields immediately

$$\langle r^2(t)\rangle \sim t^{2/d_{\rm w}}. \tag{22.12}$$

The fractal dimension $d_{\rm w}$ is approximately equal to $3d_{\rm f}/2$ [10]; the results of numerical simulations can be found in Table 22.1. For continuum percolation (Swiss cheese model) in $d = 3$, $d_{\rm w}$ is enhanced: $d_{\rm w} \cong 4.2$ [11]. Diffusion processes described by (22.12) are generally referred to as anomalous diffusion (cf. Chap. 10).

The probability density $\langle P(r,t)\rangle_N$, averaged over N percolation clusters, is not so easy to calculate. Analytical expressions for $\langle P(r,t)\rangle_N$ that fully describe the data obtained from numerical simulations can be derived. The derivation is beyond the scope of this book and we refer the interested reader to [1, 12].

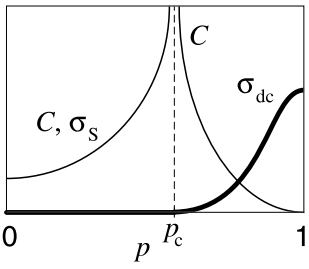

Fig. 22.7. Schematic diagram of the (usual) dc conductivity $\sigma_{\rm dc}$ (cf. (22.15), bold line) and the conductivity $\sigma_{\rm S}$ for a conductor-superconductor percolation network (cf. (22.20), thin line for $p < p_{\rm c}$) versus the concentration p of occupied sites. The cluster capacitance C is proportional to $\sigma_{\rm S}$ for $p < p_{\rm c}$ and diverges with the same exponent for $p > p_{\rm c}$ (see (22.25)).

Comparatively simple, however, is the scaling behaviour of $\langle P(0,t)\rangle$, that denotes the probability of being, after t time steps, at the site where the random walker started. Since for very large times each site has the same probability of being visited, the probability of being at the origin is proportional to the inverse of the number of distinct sites $S(t)$ the random walker visited. Since $S(t)$ increases with $R(t) \equiv \langle r^2(t)\rangle^{1/2}$ as $S(t) \sim R(t)^{d_{\rm f}}$, we have

$$\langle P(0,t)\rangle \sim R(t)^{-d_{\rm f}} \sim t^{-d_{\rm f}/d_{\rm w}} \tag{22.13}$$

(see also Chap. 19). Above $p_{\rm c}$, fractal structures occur only within the correlation length $\xi(p)$ from (22.2). Thus the anomalous diffusion law, (22.12), occurs only below the corresponding crossover time $t_\xi \sim R(t_\xi)^{d_{\rm w}} \sim \xi^{d_{\rm w}}$, which decreases proportional to $(p-p_{\rm c})^{-\nu d_{\rm w}}$, if p is further increased. Above t_ξ, on large time scales, the random walker explores large length scales where the cluster is homogeneous, and $\langle r^2(t)\rangle$ follows Fick's law (cf. (22.9) or (22.10)) increasing linearly with time t. Thus,

$$\langle r^2(t)\rangle \sim \begin{cases} t^{2/d_{\rm w}}, & \text{if } t \ll t_\xi, \\ t, & \text{if } t \gg t_\xi. \end{cases} \tag{22.14}$$

22.7 Conductivity of Percolation Clusters

The diffusion coefficient is related to the dc conductivity $\sigma_{\rm dc}$ by the Nernst-Einstein equation, (22.11). Below $p_{\rm c}$, there is no current between opposite edges of the system, and $\sigma_{\rm dc} = 0$. Above $p_{\rm c}$, $\sigma_{\rm dc}$ increases by a power law (see Fig. 22.7 for illustration),

$$\sigma_{\rm dc} \sim (p - p_{\rm c})^{\mu}, \tag{22.15}$$

where the critical exponent μ is (semi)-universal. For percolation on a lattice, μ depends only on d; the numerical results are contained in Table 22.1. For continuum percolation (Swiss cheese model) in $d = 3$, however, μ is enhanced: $\mu \cong 2.38$.

Combining (22.11) and (22.15), we can obtain the behaviour of the diffusion coefficient D as a function of $p - p_{\rm c}$. Since only the particles on

the infinite cluster contribute to the dc conductivity, we have (from (22.1)) $n \sim P_\infty \sim (p - p_c)^\beta$ in (22.11). This yields

$$D \sim (p - p_c)^{\mu-\beta}. \tag{22.16}$$

Next we use scaling arguments to relate the exponent μ to d_w. Equations (22.16) and (22.10) imply that above t_ξ the mean square displacement $\langle r^2(t)\rangle$ behaves as

$$\langle r^2(t)\rangle \sim (p - p_c)^{\mu-\beta} t, \quad t > t_\xi. \tag{22.17}$$

On the other hand we know that for times below t_ξ on distances $r < t_\xi^{1/d_w}$,

$$\langle r^2(t)\rangle \sim t^{2/d_w}, \quad t < t_\xi. \tag{22.18}$$

By definition, for $t = t_\xi$, we have $\langle r^2(t)\rangle \sim \xi^2$. Substituting this into (22.17) and (22.18) and equating both relations we obtain immediately $(p - p_c)^{\mu-\beta} t_\xi \sim t_\xi^{2/d_w}$. Using $t_\xi \sim \xi^{d_w} \sim (p - p_c)^{-\nu d_w}$ (from (22.2)) we get the relation between μ and d_w,

$$d_w = 2 + (\mu - \beta)/\nu. \tag{22.19}$$

22.8 Further Electrical Properties

In the last section we have already seen that the dc conductivity in the conductor-insulator system is zero below p_c and increases with a power law above p_c. If we consider, instead, the corresponding superconductor-conductor system, the conductivity is infinite above p_c and diverges with a power law when approaching p_c from below (see Fig. 22.7),

$$\sigma_S \sim (p_c - p)^{-s}. \tag{22.20}$$

The numerical results for s can be found in Tab. 22.1.

Next, for generalizing this result and for obtaining further electric properties, let us assume that each bond in the network represents (with probability p) a circuit consisting of a resistor with resistivity $1/\sigma_A^0$ and a capacitor with capacitance C_A, or (with probability $1 - p$) a circuit consisting of a resistor with resistivity $1/\sigma_B^0$ and a capacitor with capacitance C_B. The (complex) conductivity of each bond is therefore either $\sigma_A = \sigma_A^0 - i\omega C_A$ or $\sigma_B = \sigma_B^0 - i\omega C_B$. This model is called equivalent circuit model. At the percolation threshold the total conductivity follows a power law [1, 13, 14],

$$\sigma(\omega) = \sigma_A (\sigma_A/\sigma_B)^{-u}, \tag{22.21}$$

where the exponent

$$u = \mu/(\mu + s) \tag{22.22}$$

is related to the exponents μ and s from above, $u = 0.5$ in $d = 2$ and $u \cong 0.71$ in $d = 3$ (see Tab. 22.1).

For extending this result to the critical regime below and above p_c, we multiply (22.21) by a complex scaling function $S(z)$ that depends on $z = |p - p_c|(\sigma_A/\sigma_B)^{\Phi}$ and can be different above and below p_c [15, 16],

$$\sigma(\omega) = \sigma_A(\sigma_A/\sigma_B)^{-u} \cdot S[|p - p_c|(\sigma_A/\sigma_B)^{\Phi}]. \tag{22.23}$$

The exponent Φ as well as the asymptotic behaviour of the scaling function is determined by the asymptotic behaviour of $\sigma(\omega)$ in the limit $\omega \to 0$ and $(\sigma_A/\sigma_B) \to \infty$.

In the following, let us concentrate on the conductor-capacitor limit, where $\sigma_A = \sigma_A^0$ and $\sigma_B = -i\omega C_B$. Then the complex scaling variable z is proportional to $|p-p_c|[\sigma_A^0/(-i\omega C_B)]^{\Phi} \sim (\tau\omega)^{-\Phi}$, and $\tau = |p-p_c|^{-1/\Phi} C_B/\sigma_A^0$ defines the characteristic time scale in this short-circuit model. Splitting the complex function $(-i)^u S(z)$ into its real part S_1 and imaginary part S_2, we obtain for the complex conductivity

$$\sigma(\omega) = \sigma_A^0(C_B/\sigma_A^0)^u \cdot \omega^u \cdot [S_1(\tau\omega)] + iS_2(\tau\omega)], \tag{22.24}$$

where S_1 and S_2 are real functions.

According to standard electrodynamics, in the limit of $\omega \to 0$ the real part of the complex conductivity tends to σ_{dc}, while the imaginary part becomes $-\omega C$, with C the capacitance of the whole system:

$$\sigma(\omega) \to \begin{cases} \sigma_{dc} - i\omega C, & \text{if } p > p_c, \\ -i\omega C, & \text{if } p < p_c \end{cases} \quad (\omega \to 0). \tag{22.25}$$

For satisfying these conditions, we must require that $S_1(\tau\omega) \sim (\tau\omega)^{-u}$ above p_c and $S_2(\tau\omega) \sim (\tau\omega)^{1-u}$ below and above p_c. The first condition determines, together with (22.15) and (22.22), the scaling exponent Φ, $\Phi = 1/(\mu + s)$. The second condition yields the new relation for the capacitance [1, 15, 16],

$$C \sim S_2(\tau\omega) \sim |p - p_c|^{(u-1)/\Phi} = |p - p_c|^{-s}, \tag{22.26}$$

with the same exponent s below and above p_c (see Fig. 22.7). The divergency of C at p_c has a simple physical interpretation: each pair of neighboured clusters forms a capacitor. The effective surface increases when p_c is approached and tends to infinity at p_c. Accordingly, the effective capacitance C of the system also diverges. Next, we discuss a (non-trivial) application of the percolation concept, the ionic transport in heterogeneous ionic conductors. For a recent application of the percolation concept in gas sensors, see [17].

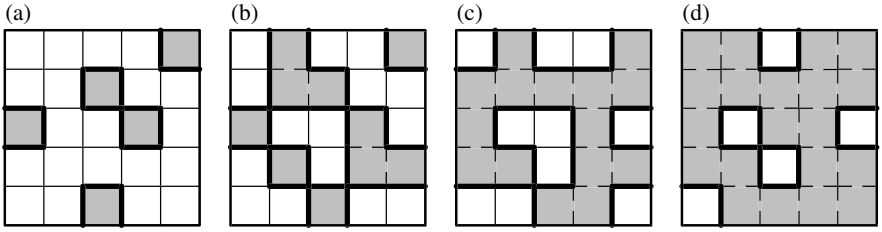

Fig. 22.8. Illustration of the three-component percolation model for dispersed ionic conductors, for different concentrations p of the insulating material. The insulator is represented by the grey area, the ionic conductor by the white area. The bonds can be highly conducting bonds (A bonds, bold lines), normal conducting bonds (B bonds, thin lines), or insulating (C bonds, dashed lines). (a) $p < p'_c$, (b) $p = p'_c$, (c) $p = p''_c$, and (d) $p > p''_c$ (redrawn after [22]).

22.9 Application of the Percolation Concept: Heterogeneous Ionic Conductors

22.9.1 Interfacial Percolation and the Liang Effect

Let us now turn to percolation models that describe electrical transport in specific composite materials. A substantial amount of research has concentrated on "dispersed ionic conductors" after the discovery by Liang [18] that insulating fine particles with sizes of the order of 1 μm, dispersed in a conductive medium (e. g. Al_2O_3 in LiI), can lead to a conductivity enhancement [19]. This effect has been found to arise from the formation of a defective, highly conducting layer following the boundaries between the conducting and the insulating phase [20]. Effectively, the system thus contains three phases. Theoretical studies therefore have focused on suitable three-component impedance network models.

Figure 22.8 shows a two-dimensional illustration of such composites in a discretized model [21, 22]. In its simplest version this model is constructed by randomly selecting a fraction p of elementary squares on a square lattice, which represent the insulating phase, while the remaining squares are the conducting phase. The distribution of both phases leads to a correlated bond percolation model with three types of bonds and associated bond conductances σ_α; $\alpha = \mathrm{A}, \mathrm{B}, \mathrm{C}$; as defined in Fig. 22.8. For example, bonds in the boundary between conducting and insulating phases correspond to the highly conducting component (A bonds). The analogous construction for three dimensions is obvious. Finite-frequency effects are readily included, when we allow bond conductances to be complex [23]. For simplicity, we may assume the ideal behaviour $\sigma_\alpha = \sigma^0_\alpha - i\omega C_\alpha$, as in the previous section, but more general forms can be chosen when necessary. Clearly, the experimental situation described above requires that $\sigma^0_\mathrm{A}/\sigma^0_\mathrm{B} = \tau \gg 1$; $\sigma^0_\mathrm{C} = 0$. Thereby it is

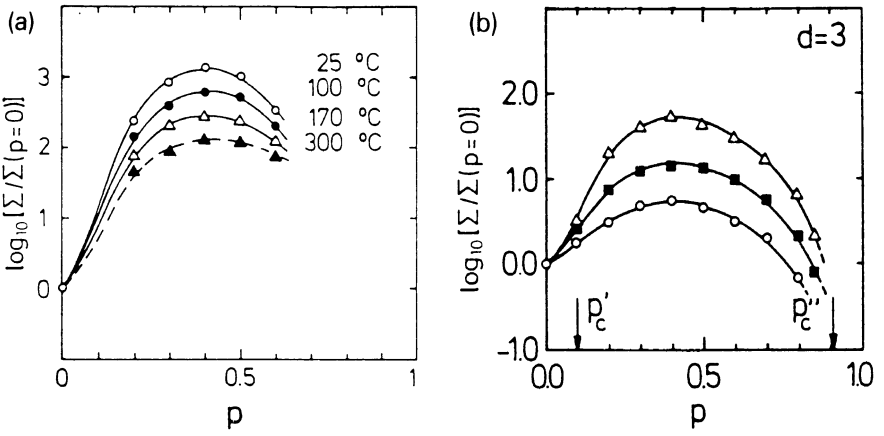

Fig. 22.9. (a) Normalized conductivity of the LiI-Al_2O_3 system as a function of the mole fraction p of Al_2O_3 at different temperatures (after [24]). (b) Normalized conductivity resulting from Monte Carlo simulations of the three-component percolation model, as a function of p, for $\sigma_A^0/\sigma_B^0 = 10$ (circles), 30 (full squares), and 100 (triangles) (after [22]).

natural to assume that σ_A^0 and σ_B^0 are thermally activated, such that their ratio $\tau \propto \exp(-\Delta E/k_B T)$ increases with decreasing temperature.

A remarkable feature of this model is the existence of two threshold concentrations. At $p = p_c'$, interface percolation (i.e., percolation of A bonds) sets in, whereas at $p = p_c'' = 1 - p_c'$ (normally not accessible by experiment) the system undergoes a conductor-insulator transition. In two dimensions we have $p_c' = 0.41$, while in $d = 3$, $p_c' = 0.097$, corresponding to the threshold for second-neighbour ($d = 2$) and third-neighbour ($d = 3$) site percolation on a d-dimensional lattice, respectively. At zero frequency, the total conductivity can be obtained from Monte Carlo simulation [21, 22].

Figure 22.9 shows experimental results for LiI-Al_2O_3 at four different temperatures [24] and simulation results for $d = 3$ at three different temperatures (corresponding to $\tau = 10$, 30 and 100) [22]. Good agreement is achieved, since both plots show a broad maximum. Changing τ (by varying the temperature) offers the possibility to interpret the measured activation energies as a function of p [25] and, in principle, also to detect the critical transport behaviour associated with interface percolation. In the vicinity of p_c' it seems interesting in addition to study critical ac effects. For examples, at p_c' the effective capacitance develops a peak, whose height should scale with τ as $C_{\text{eff}} \sim \tau^{1-u}$, where $u = \mu/(\mu + s)$, see (22.21) and (22.22). Ac properties in the whole range of p-values have been calculated by renormalization group techniques [23].

Several extensions of this model are conceivable. In the case of dc transport ($\omega = 0$), the variation of the total conductivity with the size of dis-

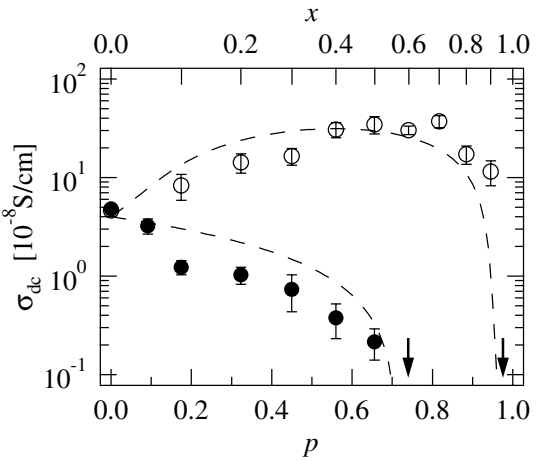

Fig. 22.10. Plot of the dc conductivity of micro- and nanocrystalline $(1-x)Li_2O{:}xB_2O_3$ composites vs volume fraction p (bottom scale) and mole fraction x (top scale) of insulating B_2O_3, at $T = 433\,K$. The experimental conductivity of the nanocrystalline samples (open circles) shows an enhancement up to a maximum at $p \approx 0.7$ ($x \approx 0.5$), while the conductivity of the microcrystalline composites (full circles) decreases monotonically. The arrows indicate the compositions where the dc conductivities fall below the detection limit. The dashed lines show the dc conductivities obtained from the continuum percolation model discussed in the text (after [37, 39]).

persed particles has been calculated and successfully compared with experiments [26–29]. In particular, it was found that as the particle size decreases while the thickness of the highly conducting interfacial layer is fixed, the maximum in the total conductivity as a function of the insulator concentration p shifts to smaller values of p. The observation of conductivity maxima at very low volume fractions ($\simeq 10\%$) in certain composite electrolytes, however, was interpreted by a grain boundary mechanism within the bulk of the electrolyte phase [30].

Related work also emphasized aspects of continuum percolation in dispersed ionic conductors [27, 29], which, depending on the geometrical conditions, can lead to dynamical critical properties differing from lattice percolation (see e.g. Sect. 22.7).

22.9.2 Composite Micro- and Nanocrystalline Conductors

In the foregoing subsection, we have discussed dispersed ionic conductors that were prepared by melting the ionic conductor and adding the insulator (mainly Al_2O_3) to it. Next we consider diphase micro- and nanocrystalline materials, which were prepared by mixing the two different powders and

pressing them together to a pellet. This way, in contrast to the classic dispersed ionic conductors discussed above, the grain size of both ionic conductor and insulator can be varied over several orders of magnitude. For reviews on nanocrystalline materials, see e. g. [31–36] (cf. also Chap. 9).

Recently, the ionic conductivity of micro- and nanocrystalline $(1-x)Li_2O$: xB_2O_3 composites, for different contents x of insulator B_2O_3, has been studied [37–39]. In the nanocrystalline samples, with an average grain size of about 20 nm, the dc conductivity increases with increasing content of B_2O_3 up to a maximum at $x \approx 0.5$. Above 0.92, the dc conductivity vanishes.

In contrast, in the microcrystalline samples (grain size about 10 μm), the dc conductivity decreases monotonically when x is increased and seems to vanish above $x \approx 0.55$ (see Fig. 22.10). The activation energy remains almost constant in both cases, $E_{\mathrm{act}} \cong 1$ eV, for all x values.

To explain these surprising experimental observations, Indris et al. [37] assumed that (as for the classical dispersed ionic conductors) (i) B_2O_3 acts as an insulator for the lithium ions, (ii) the mobility of the Li ions along the diphase boundaries between ionic conductor and B_2O_3 is larger than in the bulk lithium oxide, and (iii) that the thickness λ of this highly conducting interface is independent of the grain size.

For a quantitative treatment one has to note that the insulator content x is related to the volume fraction p (considered in percolation theory) by $p = \alpha x/(\alpha x - x + 1)$, where $\alpha = V_{\mathrm{mol}}(B_2O_3)/V_{\mathrm{mol}}(Li_2O) \approx 1.9065$ is the ratio between the mole volumes. Accordingly, the experimental results suggest the existence of two different percolation thresholds for the conduction paths, $p_{\mathrm{c}} \approx 0.7$ for the microcrystalline samples and $p_{\mathrm{c}} \approx 0.96$ for nanocrystalline ones, above which the dc conductivity of the composite vanishes.

These different thresholds can be understood by simple geometrical arguments. In the case of micro-crystalline samples, the highly conducting region at the interface between B_2O_3 and Li_2O grains does not play a role since its width is negligible compared to the grain sizes, and conducting paths can open up only when two Li_2O grains get in direct contact to each other. Qualitatively, we can expect a percolating conducting path when the Li_2O concentration gets larger than 0.3 (i.e., $p = 0.7$), which is between the percolation threshold of spheres in a three-dimensional continuum percolation model and the percolation threshold of sites in the simple cubic lattice.

In the case of nanocrystalline samples, however, the width of the highly conducting interface becomes comparable to the grain sizes. In this case, the highly conducting region can act as a bridge between two Li_2O grains not in direct contact to each other, opening up additional paths for Li ions. A percolating conducting path can be disrupted only at much higher concentrations of B_2O_3 than for micrometer sized grains. Again, the value suggested by the experiment is in the expected regime.

To describe the actual dependence of the dc conductivity of Li_2O:B_2O_3 composites, $\sigma_{\mathrm{dc}}(p)$, on the insulator concentration p, Indris et al. [37] em-

ployed a continuum percolation model similar to that studied earlier for dispersed ionic conductors [27]. In this model, the size of dispersed particles is considered explicitly and the conductivity is estimated by means of the effective-medium approximation (EMA), yielding an analytical expression for $\sigma_{\rm dc}(p)$. Denoting by $P_0(p)$, $P_{\rm A}(p)$, and $P_{\rm B}(p)$ the concentrations of the insulator, the highly conducting diphase boundaries and the ionic conductor, respectively, $\sigma_{\rm dc}(p)$ is given within EMA by

$$\sigma_{\rm dc}(p) = \sigma_{\rm B}^0 \frac{1}{z-2} \left\{ -A + [A^2 + 2\tau(z-2-zP_0)]^{1/2} \right\}, \tag{22.27}$$

where $A = \tau(1 - zP_{\rm A}/2) + (1 - zP_{\rm B}/2)$, z is a parameter determining the percolation threshold $p_{\rm c}$ at which $\sigma_{\rm dc} = 0$, and $\tau = \sigma_{\rm A}^0/\sigma_{\rm B}^0$ is (as before) the enhancement factor, defined as the ratio between the conductivities of the highly conducting interface and of pure Li_2O, respectively. For details of the treatment, we refer to [27, 37]. The concentrations of the three components are given by $P_0(p) = p$, $P_{\rm B}(p) = (1-p)^{\eta}$ and $P_{\rm A}(p) = 1 - p - P_{\rm B}(p)$, with

$$\eta = \frac{R+\lambda}{R}, \tag{22.28}$$

where R is the radius of the particles ($R \cong 10$ nm for the nanoparticles and $R \cong 5\,\mu$m for the microparticles) and λ between 1 and 2 nm.

According to (22.27), the percolation threshold for the disruption of conducting paths, $p_{\rm c}$, is given by $p_{\rm c} = (z-2)/z$. Thus, from our previous discussion, we expect that for nanocrystalline samples, $p_{\rm c} \approx 0.96$, obtaining $z_{\rm nano} = 59$, while in the microcrystalline case $p_{\rm c} \approx 0.7$ and $z_{\rm poly} = 7$. The remaining parameters, except the interface conductivity $\sigma_{\rm A}^0$ can be easily estimated from the measurements. The theoretical results, obtained for a reasonable fit of $\sigma_{\rm A}^0$, are displayed in Fig. 22.10 as dashed lines. The agreement is quantitatively good in view of the simplicity of the model employed.

Both nanocrystalline and microcrystalline materials have been described within the same model. The striking difference between both is the parameter η; $\eta - 1$ describes the thickness of the interface in relation to the grain size. For η close to one, the blocking effect of the large insulating grains dominates, and the dc conductivity decreases monotonically, while for smaller grain sizes a similar behaviour as in the classic dispersed ionic conductors occurs.

The results summarized here are consistent with results of nuclear magnetic resonance studies on the same composites, presented in Sect. 9.6.4 of Chap. 9.

22.10 Conclusion

In this chapter we gave a short introduction to the standard model for disordered systems, the percolation model. Percolation clusters at the critical

concentration are self-similar on all length scales and their structure as well as several substructures can be described with the concept of fractal dimensions. Because the clusters have loops and dangling ends on all length scales diffusion processes on these structures are slowed down and become anomalous. Diffusion is related to electrical conductivity via the Nernst-Einstein relation, and thus the scaling behaviour of the dc conductivity can be deduced from it. Other scaling arguments give the dependence of the capacity on the concentration of conducting sites, and show that the capacity diverges at the percolation threshold. In the last section, we reviewed experimental results and numerical simulations for ionic conduction in heterogeneous ionic conductors.

Notation

C	capacitance
D	diffusion coefficient
M	cluster mass
p, q	concentration of occupied sites, resp. bonds
p_c, q_c	critical concentrations (percolation thresholds)
P_∞	concentration of sites from infinite cluster
$P(r,t)$	probability density of random walk
r, ℓ	Euclidean and topological (chemical) distance
$R(t) \equiv \langle r^2(t)\rangle^{1/2}$	root mean square displacement of random walk
ξ	correlation length
σ_{dc}	dc conductivity
σ_S	conductivity in conductor-superconductor system

References

1. *Fractals and Disordered Systems*, 2nd edn, ed by A. Bunde, S. Havlin (Springer, Berlin Heidelberg New York 1996)
2. D. Stauffer, A. Aharony: *Introduction to Percolation Theory* (Taylor & Francis, London 1992)
3. G.R. von Grimmett: *Percolation*, 2nd edn (Springer, Berlin Heidelberg New York 1999)
4. M. Sahimi: *Application of Percolation Theory* (Taylor & Francis, London 1994)
5. A. von Hunt: *Percolation Theory for Flow in Porous Media*, Lecture Notes in Physics, vol 674 (Springer, Berlin Heidelberg New York 2005)
6. P. Grassberger: J. Phys. A **25**, 5475 (1992)
7. P. Grassberger: Physica A **262**, 251 (1999)
8. C.D. Lorenz, R.M. Ziff: J. Chem. Phys. **114**, 3659 (2001)
9. D. BenAvraham, S. Havlin: *Diffusion and Reactions in Fractals and Disordered Systems* (Cambridge University Press, Cambridge 2005)
10. S. Alexander, R.L. Orbach: J. Phys. Lett. (Paris) **43**, L625 (1982)
11. S. Feng, B.I. Halperin, P. Sen: Phys. Rev. B **35**, 197 (1987)

12. A. Bunde, J. Dräger: Phys. Rev. E **52**, 53 (1995)
13. A.M. Dykne: Zh. Eksp. Theor. Fiz. **59**, 110 (1970); Sov. Phys. JETP **32**, 63 (1971)
14. J.P. Straley: J. Phys. C **9**, 783 (1976); Phys. Rev. B **15**, 5733 (1977)
15. A.L. Efros, B.I. Shklovskii: Phys. Stat. Sol. B **76**, 475 (1976)
16. D. Stroud, D.J. Bergman: Phys. Rev. B **25**, 2061 (1982)
17. M. Ulrich, A. Bunde, C.-D. Kohl: Appl. Phys. Lett. **85**, 242 (2004)
18. C.C. Liang: J. Electrochem. Soc. **120**, 1289 (1973)
19. For a review see: A.K. Shukla, V. Sharma. In: *Solid State Ionics: Materials Applications*, ed by B.V.R. Chowdari, S. Chandra, S. Singh, P.C. Srivastava (World Scientific, Singapore 1992) p 91
20. J. Maier. In: *Superionic Solids and Electrolytes*, ed by A.L. Laskar, S. Chandra (Academic Press, New York 1989) p 137
21. A. Bunde, W. Dieterich, H.E. Roman: Phys. Rev. Lett. **55**, 5 (1985)
22. H.E. Roman, A. Bunde, W. Dieterich: Phys. Rev. B **34**, 3439 (1986)
23. R. Blender, W. Dieterich: J. Phys. C **20**, 6113 (1987)
24. F.W. Poulsen, N.H. Andersen, B. Kindl, J. Schoonman: Solid State Ionics **9/10**, 119 (1983)
25. C. Li-Quan, Z. Zong-Yuan, W. Chao-Ying, L. Zi-Rong: Acta Phys. Sin. **34**, 1027 (1984)
26. H.E. Roman, M. Yussouff: Phys. Rev. B **36**, 7285 (1987)
27. H.E. Roman: J. Phys.: Condens. Matter **2**, 3909 (1990)
28. G.M. Zhang: Phys. Rev. B **53**, 6256 (1996)
29. B. Roling, S. Murugavel: Z. Phys. Chem. **219**, 23 (2005)
30. A.J. Bhattacharya, T. Dutta, S. Roy, S. Tarafdar, T.R. Middya. In: *Materials Science Forum 223–224*, ed by D.K. Chaturvedi, G.E. Murch (Trans Tech Publications, Switzerland 1996) p 279
31. H. Gleiter: Progress in Materials Science **33**, 223 (1989)
32. J. Maier: Prog. Solid State Chem. **23**, 171 (1995)
33. *Amorphous and Nanocrystalline Materials*, Advances in Materials Research, vol 3, ed by A. Inoue, K. Hashimoto (Springer, Berlin Heidelberg New York 2001)
34. J. Jamnik, J. Maier: Phys. Chem. Chem. Phys. **5**, 5215 (2003)
35. P. Heitjans, S. Indris: J. Phys.: Condens. Matter **15**, R1257 (2003)
36. V.V. Kharton, F.M.B. Marques, A. Atkinson: Solid State Ionics **174**, 135 (2004)
37. S. Indris, P. Heitjans, H.E. Roman, A. Bunde: Phys. Rev. Lett. **84**, 2889 (2000)
38. M. Ulrich, A. Bunde, S. Indris, P. Heitjans: Phys. Chem. Chem. Phys. **6**, 3680 (2004)
39. S. Indris, P. Heitjans, M. Ulrich, A. Bunde: Z. Phys. Chem. **219**, 89 (2005)

23 Statistical Theory and Molecular Dynamics of Diffusion in Zeolites

Reinhold Haberlandt

23.1 Introduction

That part of theoretical physics where the macroscopic behaviour of systems is derived from their microscopic structure and from the properties of the particles is called Statistical Physics.

In order to evaluate the structural, thermodynamic or transport behaviour of macroscopic systems, statistical physics gives the starting quantities – radial distribution functions, partition functions or correlation functions – and the interrelations between them. The foundations will be sketched in the next section. One finds more detailed descriptions in the literature [1–3].

The motion of systems with different numbers of particles can be discussed within three levels

- *mechanical*: for small particle numbers ($N < 3$), allowing an analytical solution of the equation of motions,
- *statistical theory*: for large numbers of particles ($N \approx 10^{23}$), by applying methods of statistical physics on the basis of theoretical mechanics and probability theory,
- *computer simulations*: in a wide range up to some thousand particle systems, which are already representative of macroscopic systems in many properties ($N < 10^5$). This last level completes the treatment of systems by use of computers and concepts of mechanics, statistics and probability theory.

In general, however, there is some lack of knowledge in the statistical theory itself (especially for irreversible processes) as well as in structural details, such as, e. g., inter- and intramolecular potentials. Computer simulation can help to overcome these difficulties in evaluating the properties one is interested in.

Figure 23.1 (left) shows the double role of such simulations in understanding the behaviour of macroscopic objects following the detailed microscopic motion of the particles belonging to the macroscopic system. For instance, Fig. 23.1 (right) shows a snapshot of the diffusion of CH_4 molecules through different cavities of Linde type A (LTA) zeolites using special models for structures and potentials, respectively (more details will be given in Sect. 23.4).

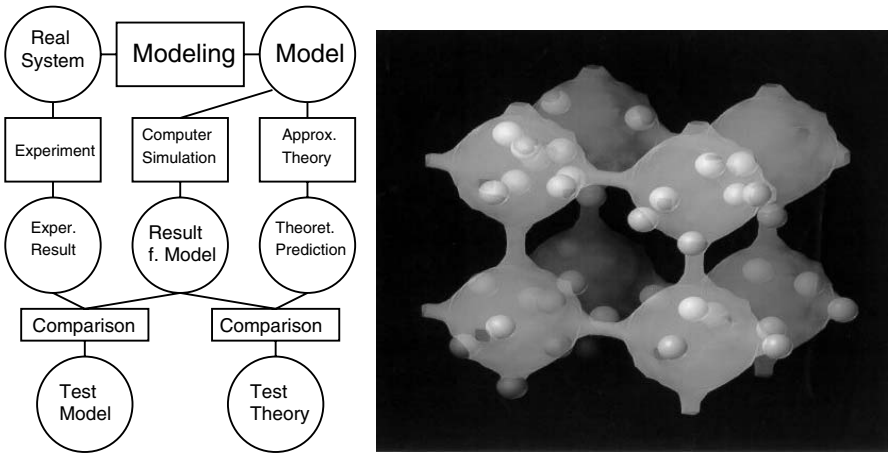

Fig. 23.1. Left: Role of computer simulations. Right: Snap shot of methane molecules (small light grey spheres) in LTA zeolites. Large cavities are represented by grey isopotential surfaces. The occupation number is $I = 5$ molecules. The initial state is represented by small dark grey spheres in the lower left cavity.

The validity of the models used is checked by comparing the experimental results with the simulations.

On the other hand, one can test the approximation of the theory by comparing its results with the simulations. Thus, computer simulations can give a more detailed understanding of complex processes. This will be demonstrated by the case of zeolitic diffusion in Sect. 23.4. Some features of computer simulations [4–13], especially molecular dynamics (MD), are given in Sect. 23.3.

23.2 Some Notions and Relations of Statistical Physics

In this section, the radial distribution function $g(r)$ and the correlation function $K(r, t)$, as two fundamental quantities of statistical thermodynamics and non-equilibrium theory, are introduced and correlated with the observables and system properties that can be evaluated.

23.2.1 Statistical Thermodynamics

General Mechanical Background

The mechanical state of a system of f degrees of freedom can be illustrated *geometrically* in a so-called gas configuration space (Γ-space) using the generalized coordinates q_i and the generalized velocities $\dot{q}_i$

$$q_1, q_2, q_3, \ldots, q_f, \quad \text{for short: } q, \qquad \dot{q}_1, \dot{q}_2, \dot{q}_3, \ldots, \dot{q}_f, \quad \text{for short: } \dot{q}\,, \tag{23.1a}$$

where the $\dot{q}_i$ are related to the generalized momenta p_i

$$p_i = \frac{\partial L}{\partial \dot{q}_i} \qquad i = 1, 2, \ldots, f, \tag{23.1b}$$

$L = L(q_i, \dot{q}_i, t)$ is the Lagrangian function, connected with a Legendre-Transformation to the Hamiltonian function

$$H(q_i, p_i, t) = \sum_i p_i \dot{q}_i - L(q_i, \dot{q}_i, t). \tag{23.2}$$

The mechanical motion of the systems is governed by equations of motion, e. g. Lagrange's equations of motion or Hamilton's (canonical) equations of motion, respectively

$$\frac{\mathrm{d}}{\mathrm{d}t}\frac{\partial L}{\partial \dot{q}_i} - \frac{\partial L}{\partial q_i} = 0; \qquad \dot{q}_i = \frac{\partial H}{\partial p_i}, \qquad \dot{p}_i = -\frac{\partial H}{\partial q_i} \tag{23.3a}$$

and – as an important starting point for molecular dynamics – Newton's equations of motion (Newton's second law) for the radius vector $\boldsymbol{r}_i$ of the ith particle (in Cartesian coordinates)

$$m_i \ddot{\boldsymbol{r}}_i = \boldsymbol{F}_i, \quad \text{with} \qquad F_i = -\frac{\partial U}{\partial r_i}, \tag{23.3b}$$

with m_i : particle masses, F_i : force components, $U(r_i)$: potential energy.

The whole system is considered as a single super-molecule with f generalized coordinates and f generalized momenta. Following Gibbs, a large number of physically equivalent systems – the Gibbs ensemble – is considered. This ensemble can be visualized in the gas configuration space by a cloud of phase points distributed with the particle density $\rho(q, p, t)$. Its motion will characterize the mechanical state of the system. With respect to different physical situations there exist different ensembles, e. g. the microcanonical ensemble of isolated systems (energy E, volume V, particle number N) and the canonical ensemble of closed systems in contact with a heat bath for thermalization (temperature T, volume V, particle number N). Initially, molecular dynamics (MD) was conducted in the microcanonical ensemble and Monte Carlo (MC) in the canonical ensemble. Today both MD and MC can use several ensembles [5–8]. For macroscopic systems – in the thermodynamic limit with $N \to \infty$ and $N/V = \text{const}$ – all ensembles yield equivalent results, differing in fluctuations only, which are not important for our current purposes.

Distribution Functions

Considering an ensemble of ν systems with f degrees of freedom each (total number of degrees of freedom $F = \nu \times f$ in Γ-space) then $\rho_\nu^{(N)}(q, p, t)\mathrm{d}q\mathrm{d}p$ is

the number of systems in the range $q \ldots q + \mathrm{d}q, p \ldots p + \mathrm{d}p$ of Γ-space. Introducing the (normalized) phase space density or the N-particle distribution function, respectively, $\rho^{(N)}(q,p,t)$ by

$$\rho^{(N)}(q,p,t) = \frac{1}{\nu}\rho_{\nu}^{(N)}(q,p,t), \tag{23.4}$$

$\rho^{(N)}(q,p,t)\mathrm{d}q\mathrm{d}p$ is the probability to find the system – consisting of N particles – in $q \ldots q + \mathrm{d}q, p \ldots p + \mathrm{d}p$ of the Γ-space. More often it is sufficient to use so-called reduced distribution functions for finding k particles ($k \leq N$) only, defined by a k-particle distribution function

$$\rho^{(k)}(q,p,t) = \int \rho^{(N)}(q,p,t)\,\mathrm{d}q^{(N-k)}\mathrm{d}p^{(N-k)}. \tag{23.5a}$$

Particularly important are the two-particle distribution function ($k = 2$) and the one-particle distribution function ($k = 1$). Integration over the momentum space gives

$$n^{(2)}(q) = \int \rho^{(2)}(q,p,t)\,\mathrm{d}p, \qquad n^{(1)}(q) = \int \rho^{(1)}(q,p,t)\,\mathrm{d}p. \tag{23.5b}$$

$n^{(2)}(q_i,q_j)\mathrm{d}q_i\mathrm{d}q_j$ is the probability to find a particle i in $q_i \ldots q_i + \mathrm{d}q_i$ and another particle j in $q_j \ldots q_j + \mathrm{d}q_j$. $n^{(1)}(q_i)\mathrm{d}q_i$ is the probability to find a single particle i in $q_i \ldots q_i + \mathrm{d}q_i$. For $N \gg 1$, one can introduce a distribution function $g(q_i, q_{ji})$ by

$$n^{(2)}(q_i,q_j) = n^{(1)}(q_i)n^{(1)}(q_j)g(q_i,q_{ji}). \tag{23.6}$$

$g(q_i, q_{ji})$ tends towards one for $q_{ji} = |\boldsymbol{q}_i - \boldsymbol{q}_j| \to \infty$. The deviation from one is a measure for the correlation of the pairs of molecules (pair distribution function). The total potential energy U_N is assumed to be pair-wise additive:

$$U_N(q_i,q_j) = \sum_{i<j} u(q_{ij}).$$

In isotropic systems $u(q_{ij})$, $g(q_i, q_{ji})$ are functions of the distance $q_{ji} = r$ only. The thus defined radial distribution function $g(r)$ is very important to evaluate structural and thermodynamic data and to compare them with experimental data as well. As examples, some relations are given for the internal energy U, the pressure p, the chemical potential μ and the static structure factor $S(k)$ – particularly important to compare theoretical data with experiments (see, e. g. , Chaps. 3, 18, 20 and [14]):

$$U = \frac{3}{2}Nk_{\mathrm{B}}T + \frac{1}{2}Nn\int_0^{\infty} u(r)g(r,n,T)4\pi r^2\,\mathrm{d}r, \tag{23.7a}$$

$$p = k_{\mathrm{B}}Tn - \frac{n^2}{6}\int\limits_0^\infty ru'(r)g(r,n,T)4\pi r^2\,\mathrm{d}r, \qquad u'(r) = \partial u/\partial r, \tag{23.7b}$$

$$\frac{\mu}{k_{\mathrm{B}}T} = \ln(n\lambda^3) + \frac{n}{k_{\mathrm{B}}T}\int\limits_0^1\int\limits_0^\infty u(r)g(r,\xi)4\pi r^2\,\mathrm{d}r\mathrm{d}\xi\,, \quad \lambda = \left(\frac{h^2}{2\pi m k_{\mathrm{B}}T}\right)^{1/2} \tag{23.7c}$$

with ξ as insertion parameter ($0 \le \xi \le 1$), the Boltzmann constant k_{B}, and the de Broglie wavelength λ [6]. The structure factor

$$S(k) = 1 + n\int\{g(r) - 1\}\exp\left(i\boldsymbol{k}\cdot\boldsymbol{r}\right)\mathrm{d}\boldsymbol{r} = 1 + nh(k) \tag{23.7d}$$

plays an important role in the comparison between theoretical and experimental data (scattering data: neutron, X-ray; see, e. g., Chaps. 3, 13, 15 and [15]). There are: n – density; $h(k)$ – Fourier transform of $\{g(r) - 1\}$. The limit for $k \to 0$ gives

$$\lim_{k\to 0} S(k) = 1 + n\int\{g(r) - 1\}\,\mathrm{d}\boldsymbol{r}. \tag{23.7e}$$

23.2.2 Statistical Theory of Irreversible Processes

Irreversible processes are driven by generalized forces X and characterized by transport coefficients L [2,15,16]. It is very important to determine transport coefficients – e. g. using the famous linear response theory (Kubo [17]) – via correlation functions [18, 19]. The correlation functions are as powerful in non-equilibrium as partition functions or radial distribution functions are in equilibrium (see, e. g., (23.7)).

Transport Coefficients and Correlation Functions

In the linear approximation, the transport coefficients L_{ik} are defined by relations between the flux densities J_i and their corresponding generalized forces X_k

$$J = L\cdot X + (\text{higher terms}) \qquad J_i = \sum_k L_{ik}X_{ik}, \tag{23.8}$$

with the Onsager-Casimir reciprocity relations $L_{ik} = L_{ki}$ – valid near equilibrium. For instance, in the case of diffusion the particle transport is caused by concentration gradients:

$$J_z = -D\cdot\frac{\partial n_1}{\partial z} + (\text{higher terms}). \tag{23.9}$$

Using the ensemble average in the Γ-space

$$\langle A \rangle_\Gamma = \int\int A(q(t), p(t)) \rho(q(t), p(t)) \, \mathrm{d}q\mathrm{d}p \tag{23.10}$$

with the equilibrium phase space density (cf. (23.4)), classical time correlation functions

$$K_{AB}(t) = \langle A(t)B(0) \rangle_\Gamma = \int \cdots \int A(q, p, t) B(q, p, 0) \rho(q, p) \, \mathrm{d}q\mathrm{d}p, \tag{23.11}$$

for the phase space functions $A\{q(t), p(t)\} = A(t)$ and $B\{q(t), p(t)\} = B(t)$ are defined by (23.11). With $A = B$, $K_{AA}(t)$ is called autocorrelation function, and for $A = B = \boldsymbol{v}$ (velocity): velocity autocorrelation function $K_{vv}(t)$. The spectral density $f(\omega)$, which is important for comparisons with experimental data, is a Fourier transform of the velocity autocorrelation function

$$f(\omega) = \int_0^\infty \frac{\langle \boldsymbol{v}(0) \cdot \boldsymbol{v}(t) \rangle}{\langle \boldsymbol{v}(0)^2 \rangle} \cos(\omega t) \, \mathrm{d}t. \tag{23.12}$$

Linear Response Theory – Green-Kubo and Einstein Relations

The linear response theory [17] is a bridge between microscopic theory and experiment. It can be outlined as follows

- The linear response theory assumes near-equilibrium situations so that linear relations are sufficient (e. g. also to describe relaxations back to equilibrium).
- This linear response is determined by fluctuations from equilibrium.

The linear response theory yields relations between the irreversible behaviour of the systems and the observables to measure, but no instruction to determine the transport properties. Here methods of statistical physics – including molecular dynamics – and measurements come into play. Generalized susceptibilities (transport coefficients) are Fourier transforms of correlation functions

$$\sigma(\omega) = \int_0^\infty \exp(-i\omega t) \langle \dot{A}(t) \dot{B}(0) \rangle_\Gamma \, \mathrm{d}t. \tag{23.13a}$$

In the limit of long waves ($\omega \to 0, k \to 0$) – sufficient for transport coefficients – it is

$$\sigma = \int_0^\infty \langle \dot{A}(t) \dot{B}(0) \rangle_\Gamma \, \mathrm{d}t \qquad L_{ij} = \int_0^\infty \langle \dot{J}_i(t) \dot{J}_j(0) \rangle_\Gamma \, \mathrm{d}t. \tag{23.13b}$$

In the long-time limit ($t \to \infty$) for autocorrelation functions, (23.13b) can be substituted by Einstein relations of the kind

$$2t\sigma = \langle (A(t) - A(0))^2 \rangle. \tag{23.13c}$$

A further important quantity in comparing theoretical and experimental data is the dynamic structure factor (see Chaps. 3, 13, 16, 20, and [14])

$$S(\boldsymbol{k}, \omega) = \frac{1}{2\pi} \int_{-\infty}^{\infty} F(\boldsymbol{k}, t) \exp i\omega t \, \mathrm{d}t. \tag{23.14a}$$

Here $F(\boldsymbol{k}, t)$ is the – numerically as well evaluable – scattering function (Chaps. 2, 13 (cf. (13.1)))

$$F(\boldsymbol{k}, t) = \frac{1}{N} \langle \rho(\boldsymbol{k}, t) \rho(-\boldsymbol{k}, 0) \rangle, \tag{23.14b}$$

which is related to the so-called Van Hove correlation function $G(\boldsymbol{k}, t)$ by

$$F(\boldsymbol{k}, t) = \int G(\boldsymbol{r}, t) \exp(-i\boldsymbol{k} \cdot \boldsymbol{r}_j) \, \mathrm{d}\boldsymbol{r} \tag{23.14c}$$

(cf Chap. 3, (3.10)) and can be determined by ensemble averaging $\langle \cdots \rangle$ over the Fourier transform $\rho(\boldsymbol{k}, t)$ of the local one-particle density as well:

$$\rho(\boldsymbol{k}, t) = \sum_j \exp(i\boldsymbol{k} \cdot \boldsymbol{r}_j(t)) = \int \rho(\boldsymbol{r}, t) \exp(i\boldsymbol{k} \cdot \boldsymbol{r}_j) \, \mathrm{d}\boldsymbol{r}. \tag{23.14d}$$

In the limit $\omega \to 0$, $k \to 0$ one has the usual static structure factor (see (23.7d)).

As an example of the discussed general theory of irreversible processes (see Table 23.1) here only relations for the (self-) diffusion coefficient are given:

$$D = \frac{1}{3} \int_0^{\infty} \langle \boldsymbol{v}(t) \cdot \boldsymbol{v}(0) \rangle \, \mathrm{d}t; \qquad 2tD = \frac{1}{3} \langle (\boldsymbol{r}(t) - \boldsymbol{r}(0))^2 \rangle. \tag{23.15}$$

Table 23.1. Correlation functions – theoretical and experimental quantities

Observable	Correlation Function	Equation
spectral density	$\langle \boldsymbol{v}(0) \cdot \boldsymbol{v}(t) \rangle$	(23.12)
structure factor	$\langle \rho(\boldsymbol{k}, t) \rho(-\boldsymbol{k}, 0) \rangle$	(23.14a)
transport coefficient	$\langle \dot{J}_i(t) \dot{J}_j(0) \rangle_\Gamma$	(23.15)

23.3 Molecular Dynamics

Due to the lack of *analytical* solutions, the motion of guest molecules in zeolites must be evaluated *numerically* by computer simulations (molecular dynamics (MD), Monte Carlo (MC)). Computer simulations are reviewed in many text books [4–9], thus here only a few principles of MD simulations are sketched.

23.3.1 General Remarks

The procedure of MD simulations may be subdivided into several steps:

- Analysis of the physical situation
- Derivation of the equations of motion (e. g. (23.3b))

$$m_i \ddot{r}_i = -\frac{\partial U}{\partial r_i} \tag{23.16}$$

- Selection of the interaction potential $U(r)$.
  From the great variety of (empirical) potential functions (e. g. [1]), Figs. 23.2 and 23.3 display only two examples:
  a) *Square well potential*

$$\begin{aligned} U(r) &= \infty \qquad r < \sigma_1 \\ U(r) &= -\epsilon \qquad \sigma_1 < r < \sigma_2 \\ U(r) &= 0 \qquad r > \sigma_2 \,, \end{aligned} \tag{23.17}$$

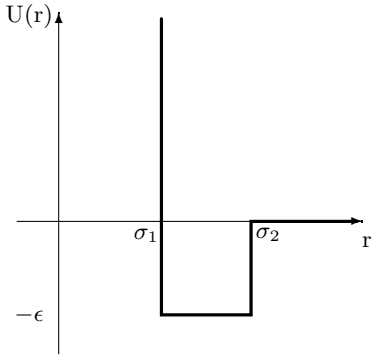

Fig. 23.2. The square well potential.

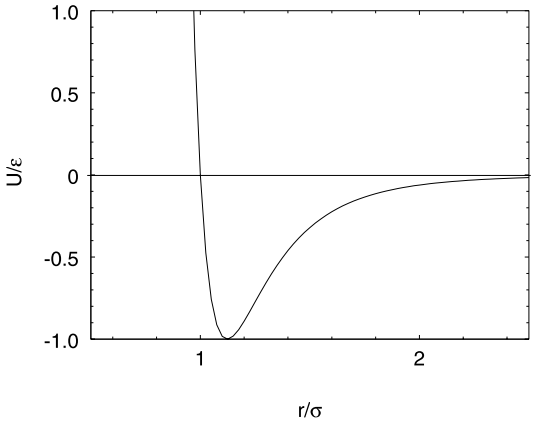

Fig. 23.3. Typical representative of the potentials used in MD simulations (Lennard-Jones-potential U(r)).

b) *Lennard-Jones potential*

$$U = 4\epsilon \left\{ \left(\frac{\sigma}{r}\right)^{12} - \left(\frac{\sigma}{r}\right)^{6} \right\} \tag{23.18}$$

with ϵ denoting the minimum value of the potential energy and σ defined by $U(\sigma) = 0$.

These and other potential functions [1] are often used, while quantum chemical calculations of potential surfaces are restricted to systems being not too complex.

- Selection of the computational model (algorithms, time steps (l), duration ($l \times \tau$))
- Solution of the equations of motion (trajectories, propagators)
- Evaluation of the desired dynamical data via time averages of a single system

$$\langle A \rangle_\tau = \frac{1}{\tau} \sum_{n=1}^{n=l} A(n\Delta t) \tag{23.19}$$

or ensemble averages $\langle A \rangle_\Gamma$ (cf. (23.10)) and correlation functions $K_{AB}(t)$, (cf. (23.11)), respectively

- Discussion of the results.

23.3.2 Procedure of an MD Simulation

Starting with the first MD papers for hard sphere systems in 1957 [10] many investigations and applications have been published using several different

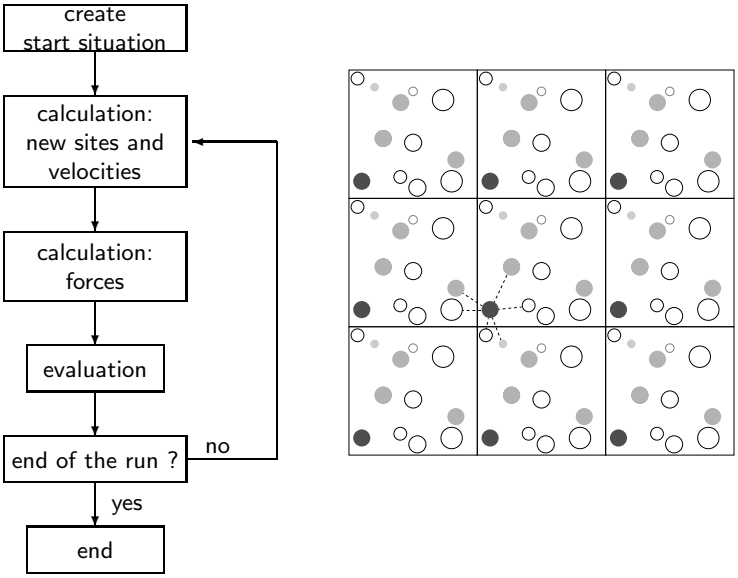

Fig. 23.4. Schematic representation of the procedure of MD simulations (left) and of the periodic boundary conditions. (right)

algorithms to solve the equations of motion (e. g. [4–7,10–13]). Fig. 23.4 (left) shows the principal organization of an MD program (Verlet algorithm).

To calculate the velocities in each step by the often used velocity-Verlet-Algorithm one needs the knowledge of the already calculated forces and also of those corresponding to the *new* sites. Therefore it is suitable to calculate the new velocities in two steps: considering first that part, which needs only the former forces and second the final new velocities using the new calculated forces.

Here – as an example only – this often used Verlet algorithm (cf. (23.20b)) and its velocity version (cf. (23.20c,23.20d)) are outlined. Adding to the Taylor series

$$\boldsymbol{r}_i(t+h) = \boldsymbol{r}_i(t) + \boldsymbol{v}_i h + \frac{h^2}{2}\ddot{\boldsymbol{r}}_i(t) + ... \tag{23.20a}$$

its analogue for $\boldsymbol{r}_i(t-h)$, all terms with odd powers of the time increment h will be cancelled and one gets up to terms of the fourth order

$$\boldsymbol{r}_i(t+h) = 2\boldsymbol{r}_i(t) - \boldsymbol{r}_i(t-h) + h^2\ddot{\boldsymbol{r}}_i(t). \tag{23.20b}$$

As the velocity version of the Verlet algorithm one obtains in a similar way

$$\boldsymbol{r}_i(t+h) = \boldsymbol{r}_i(t) + h\boldsymbol{v}_i(t) + \frac{h^2}{2m_i}\boldsymbol{F}_i(t), \tag{23.20c}$$

$$\boldsymbol{v}_i(t+h) = \boldsymbol{v}_i(t) + \frac{h}{2m_i}[\boldsymbol{F}_i(t) + \boldsymbol{F}_i(t+h)]. \tag{23.20d}$$

23.3.3 Methodical Hints

For the complete wealth of tricks in handling MD simulations one clearly has to consult the relevant literature (see, e. g., [5, 6]). However, the following methodical hints aim to summarize a few of the most basic procedures:

- Periodic boundary conditions – replication of the MD box by periodic continuation (see Fig. 23.4 (right)) – can help to overcome artificial surface effects due to spatially restricted systems.
- To avoid unnecessary calculations the interaction is taken into account only in appropriate short distances (potential cutoff and shifted forces). To take into account long-range interactions, special techniques (e. g. the Ewald summation) must be used.
- To save computer time, the time steps should be as large as possible (but the energy must be maintained) and as short as necessary (fast processes). In some cases multiple step lengths are recommended (multiple time step method).
- In order to avoid further time consuming calculations the number of pair separations explicitly considered is reduced (Verlet neighbour list, updated from time to time).

23.4 Simulation of Diffusion in Zeolites

23.4.1 Introduction

Diffusion processes in gases, liquids, solids and at interfaces have been studied with different theoretical and experimental methods for a long time. The present textbook provides a broad survey of this subject.

Bulk measurements of (self-) diffusion coefficients D_s over wide ranges of temperature T are often described generally by the Arrhenius relation (cf Chap. 1)

$$D_\mathrm{s} = D_0 \exp\left(-\frac{E_\mathrm{A}}{k_\mathrm{B}T}\right) \tag{23.21}$$

with the pre-exponential factor D_0, an activation energy E_A (in a certain sense). This relation can be explained using the transition theory of Eyring, but its range of validity is not quite clear.

In this section, MD simulations will be applied in helping to understand the features of molecular diffusion in more microscopic detail, namely under the influence of the confined geometries in microporous materials. These microporous materials – especially zeolites – have attained a steadily increasing

role for both applications and fundamental research [14,20]. The study of diffusion processes in zeolites is of great interest because these crystals contain very regular internal surfaces and they have been used for many industrial purposes [14].

Since the paper of Yashonath et al. [21], MD simulations (see Sect. 23.3, [5, 6]) are applied to diffusion in zeolites to discuss the dynamics of kinetic processes in zeolites in more detail. In the recent literature one finds some reviews (e. g. [22–30]) and papers of several groups [39–81]).

MD simulations can use different models for guest molecules, lattices and their interaction and allow, especially, variations in the system parameters that are not possible in experiments. So, interrelations and dependences can be examined.

In this section it will be discussed how MD simulations can answer questions like, e. g.:

1. Does there exist a macroscopic behaviour (i. e. thermalization, Maxwell-Boltzmann distribution) of the few particles diffusing in the narrow holes of zeolites?
2. What is the range of validity of the Arrhenius relation (23.21)?
3. How are the evaluated diffusion data influenced, e. g., by
   a) small changes of parameter sets (structural, potential)?
   b) idealization of the models used (neglecting of cations, fixed lattice)?
   c) taking into account concentration gradients?
   d) technical points with respect to the MD simulation?
4. How one can use additional theoretical tools – e. g. propagators – to improve the understanding of diffusion processes in zeolites?
5. Can MD simulations at all describe experimental NMR data and/or QENS data of diffusion?
6. What is the result for mixtures?

23.4.2 Simulations

To answer the above mentioned questions the calculations should at first be restricted to simple model systems. Thus, in the beginning of this section, the diffusion of (simple spherosymmetric) methane guest molecules through idealized zeolites of LTA-type neglecting the exchangeable cations (for short: ZK4) is examined. Then we will proceed with more complex guest molecules, mixtures and take into account the cations of the zeolite lattice additionally. Possible improvements of the model and application to mixtures of guest molecules will be discussed later on.

Fig. 23.5 (left) shows the general structure of zeolites of type LTA used for the calculations. The sodalite units form a cubic lattice with large cavities connected by so-called windows consisting of eight oxygen atoms.

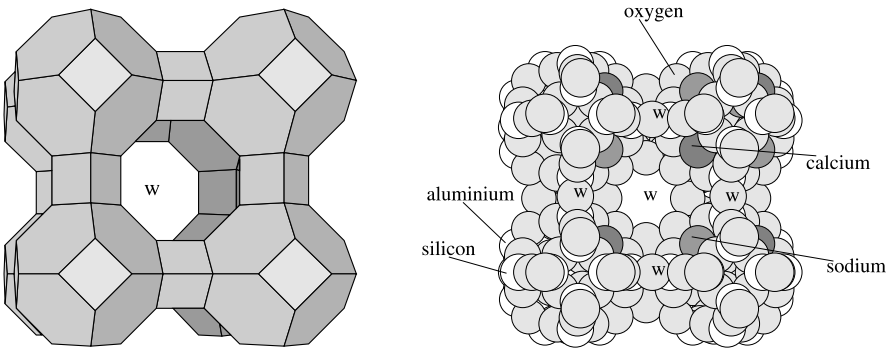

Fig. 23.5. Structure of zeolites of type LTA (left: general view; right: interior view), see text.

In Fig. 23.5 (right) the distribution of the lattice atoms around a large cavity in the NaCaA zeolite is to be seen. Lattice atoms in front have been removed in order to open the view into the interior of the cavity (windows are marked by w).

One of the crucial points in determining diffusion coefficients in zeolites is the knowledge of the inter- and intramolecular potentials. The forces acting between the guest molecules and the zeolite lattice as well as among the guest molecules must be known as good as possible in order to solve Newton's equations for the guest molecules in zeolites.

These forces can be derived from interaction potentials (for more details see, e. g., [1, 22–24] and references therein). Potentials can be obtained from quantum chemical calculations [24] and/or from fit procedures using experimental results (for an illustrative example see [31] and [32–34]).

Alternatively – at least in the future –, the forces and potential energies can be obtained by including quantum mechanical density functional calculations into an otherwise classical MD run [35–38]. However, such methods are extremely computer-time consuming and can yield the trajectories only for short times and/or small systems until now. So, they cannot be used for long-time diffusion processes in large systems.

Here, for the interaction between the guest molecules CH_4 and the lattice atoms of a cation-free analogue of LTA zeolites ('ZK4'), we again use (23.18), the well-known Lennard-Jones (LJ) (12,6) potential.

For NaCaA zeolites, additional polarization energy terms due to the cations have been included. Using the conventional microcanonical MD ensemble the self-diffusivity is calculated, while a generalized non-equilibrium (NEMD) ensemble is used to determine the transport-diffusivities [48].

In order to get appropriate diffusion coefficients, long-run simulations were carried out with up to 6 000 000 time steps with short step lengths of 5 and 10 fs, respectively. The basic MD box contains between 8 and 343 large cavities

with occupation numbers varying between 1 and 11 per cavity, respectively. The velocity-Verlet-algorithm (see (23.20c), (23.20d)) is used [5, 6].

23.4.3 Results

Computer simulations not only yield the diffusion coefficients as the final results, but, additionally, residence times, velocity autocorrelation functions (vacf), potential surfaces, density distributions, and – last but not least – propagators and Van Hove correlation functions. Thus a better understanding of the diffusion processes is possible.

To demonstrate the influence of the potential the results of two sets of potential parameters A and B (see Table 23.2, p. 932) are compared.

Applicability of the Diffusion Equation

First of all one must answer the non-trivial question whether or not systems of a few particles in narrow-sized pores obey the diffusion equation. In the kinetic theory of fluids this equation has been proven rigorously only in the case of dilute gases. But, it is possible to check it here in the considered case by computer experiments [42]. The validity of the diffusion equation (see, e. g., Chaps. 1, 10, 18-20, and [2]) for an infinite system can be examined by the propagator

$$P(\boldsymbol{r}, \boldsymbol{r}_0, t, 0) = (4\pi Dt)^{-3/2} \exp\left\{\frac{-(\boldsymbol{r} - \boldsymbol{r}_0)^2}{4Dt}\right\}. \tag{23.22}$$

$P(\boldsymbol{r}, \boldsymbol{r}_0, t, 0)$ is the (conditional) probability density to find a particle at a site $\boldsymbol{r}$ at time t, which started at $t = 0$ at the site $\boldsymbol{r}_0$. It is the solution of the diffusion equation

$$\partial P/\partial t = D\Delta P \qquad \Delta : \text{Laplacian} \tag{23.23}$$

with the initial condition $P(\boldsymbol{r}, \boldsymbol{r}_0, t = 0) = \delta(\boldsymbol{r} - \boldsymbol{r}_0)$.

To examine the form of the solution of the diffusion equation, it is necessary and sufficient that all moments $\langle f(\boldsymbol{r})^\nu \rangle$ of $f(\boldsymbol{r}) = (\boldsymbol{r} - \boldsymbol{r}_0)$ (cf. (23.22, 23.24a)) will give the same diffusion coefficient. Applying the definition

$$\langle f(\boldsymbol{r})^\nu \rangle = \int P(\boldsymbol{r}, \boldsymbol{r}_0, t) f(\boldsymbol{r})^\nu d\boldsymbol{r} \tag{23.24a}$$

we find for the first four moments $\nu = 1, 2, 3, 4$ of this distribution

$$\left\langle \mid \boldsymbol{r} - \boldsymbol{r}_0 \mid \right\rangle = 4\sqrt{\frac{Dt}{\pi}}\,, \tag{23.24b}$$

$$\left\langle (\boldsymbol{r} - \boldsymbol{r}_0)^2 \right\rangle = 6Dt\,, \tag{23.24c}$$

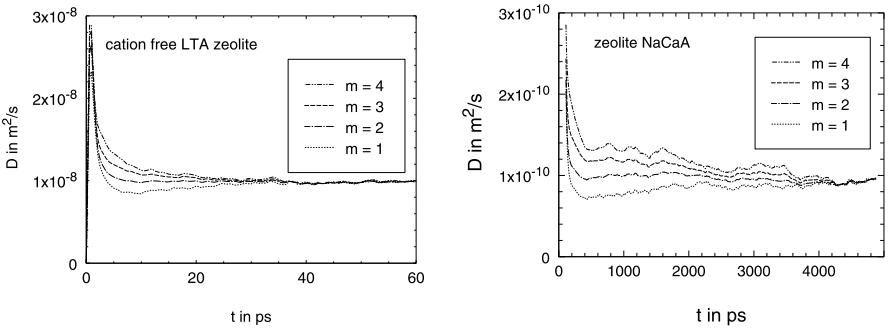

Fig. 23.6. D_s from the first four moments of the displacement; left hand side: methane in a cation-free LTA zeolite $T = 300\,\mathrm{K}$, parameter set A (see Table 23.2), 3 methane per cavity, right hand side: methane in a NaCaA zeolite, set B, $T = 173\,\mathrm{K}$, 7 methane per cavity.

$$\left\langle \mid (\boldsymbol{r} - \boldsymbol{r}_0)^3 \mid \right\rangle = \frac{32(Dt)^{3/2}}{\sqrt{\pi}}\,, \tag{23.24d}$$

$$\left\langle (\boldsymbol{r} - \boldsymbol{r}_0)^4 \right\rangle = 60(Dt)^2\,. \tag{23.24e}$$

From each one of these equations an expression for Dt can be obtained, e. g. for the first moment

$$Dt = \pi \left\langle \mid \boldsymbol{r} - \boldsymbol{r}_0 \mid \right\rangle^2 / 16 \tag{23.24f}$$

or

$$D = \frac{\pi}{16}\frac{\mathrm{d}}{\mathrm{d}t} \left\langle \mid \boldsymbol{r} - \boldsymbol{r}_0 \mid \right\rangle^2\,. \tag{23.24g}$$

The differentiation (cf. (23.24g)) was used instead of simple division by t (cf. (23.24f)) because one gets a faster convergence of the results. Correspondingly one gets for the second moment – the mean square displacement (MSD) –

$$D = \frac{1}{6}\frac{\mathrm{d}}{\mathrm{d}t} \left\langle (\boldsymbol{r} - \boldsymbol{r}_0)^2 \right\rangle\,. \tag{23.24h}$$

This equation is usually used to obtain the diffusion coefficient from MD simulations. If the diffusion equation is valid then the D values derived from the different moments should agree [42]. In Fig. 23.6 (left) an example of the diffusivities in the cation-free analogue of NaCaA ('ZK4') is given. It can be seen that there is good agreement for times larger than about 50 ps. That means that in this case the hydrodynamical state is reached and we conclude that (23.22) is then valid. The diffusion equation can be simply obtained by comparing space and time derivatives of (23.22) and, hence, it must be valid, too. In [42] this was also checked for other occupation numbers.

If the diffusion coefficients are smaller – as in the case of NaCaA (see Fig. 23.6 (right)) – the hydrodynamical state is reached later (for NaCaA in about 6 000 ps) [44]. This is probably also due to the additional cations.

Residence Times and Velocity Autocorrelation Functions

In trying to understand the diffusion behaviour in more detail we define the residence time for a given guest molecule as the time difference between successive passages of limiting planes situated in the centre of each window perpendicular to the window axis.

Fig. 23.7 shows the probability density of the thus defined residence times within the individual cavities for three different sorbate concentrations, i. e. loadings I (given in molecules per supercage), and temperatures, respectively (parameter set A, see Table 23.2). The first maximum at ~ 0.3 ps corresponds to times which are too short to allow a passage through the cavity to one of the five other windows [43]. Therefore, this maximum must be attributed to trajectories, which are reversed immediately after the molecule has passed the window.

It is interesting to note that the intensity of this first maximum increases with increasing sorbate concentration. It may be concluded, therefore, that the reversal in the trajectory is mainly caused by the influence of the other adsorbate molecules. The second maximum corresponds to the passage through the adjacent windows and is therefore responsible for diffusion.

These conclusions are confirmed by minima in the velocity autocorrelation function (vacf) (see [43]) where the dependence of these minima on temperature and loading are in agreement with the above reasoning (see Fig. 23.8).

Fig. 23.1 shows a typical situation in a system where methane molecules are enclosed in cavities of the cation-free LTA zeolite. The large cavities and the windows connecting them are indicated by grey isopotential surfaces. To illustrate the time development all methane molecules that were initially situated in the left hand lower cavity are marked by dark spheres while the other ones are fair. So the exchange can be observed.

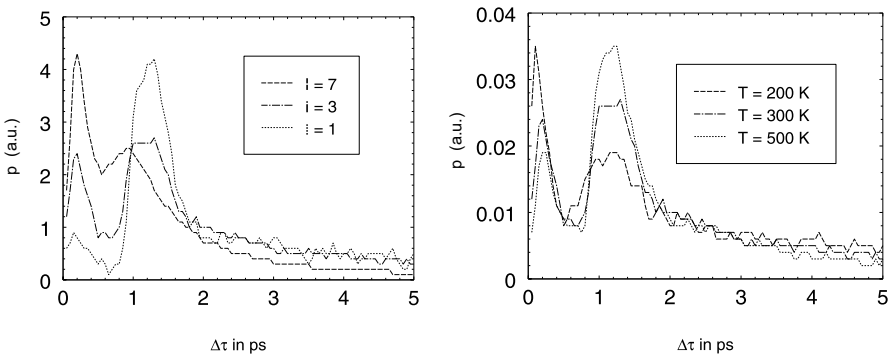

Fig. 23.7. Probability density of residence times of particles as function of time for different loadings I (left) and different temperatures T (right).

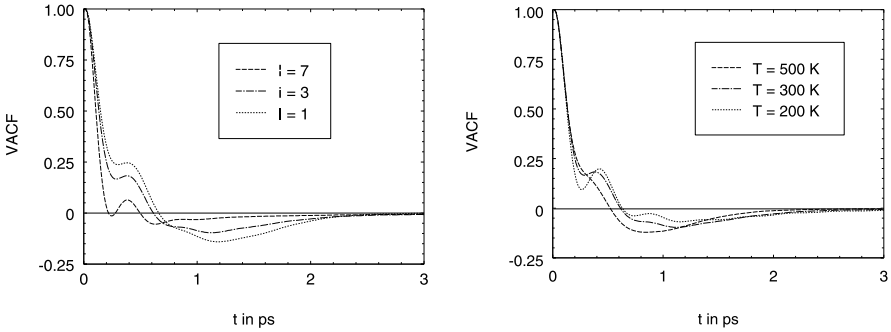

Fig. 23.8. Velocity autocorrelation function (vacf) for different loadings (left) and temperatures (right).

Density Distributions

The density distribution in cation-free LTA zeolites shown in Fig. 23.9 may well be understood by isopotential lines (Fig. 23.10 and [43]) for the zeolites. The density distributions – demonstrated in a plane through the centre of the large cavity – show a remarkable structure. Corresponding to the potential surface these distributions are different from zero practically only near the cavity wall and have maxima in the window (set A, cf Table 23.2) and *in front of* them (set B), respectively.

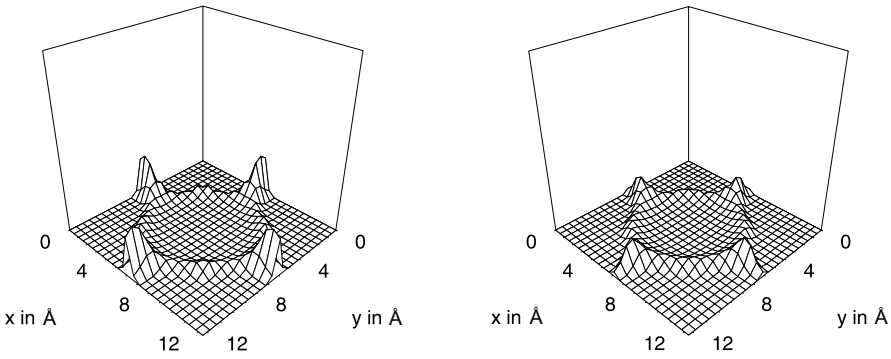

Fig. 23.9. Density distribution of CH_4 in a cation-free LTA with a loading of $I = 3$ at $T = 300\ K$ monitored in a plane through the cavity centres (left: set A; right: set B, cf Table 23.2) [51].

Influence of the Potential Parameters on D

The influence of potential parameters on the diffusion coefficients is remarkable. Even small parameter changes may cause significant changes in the

Table 23.2. Parameter sets used for the LJ potential (cf. (23.18)).

zeolite		σ in Å	ϵ in kJ/mol
LTA	$CH_4 - CH_4$	3.817	1.232
LTA	$CH_4 - Si$	2.14	0.29
LTA	$CH_4 - O$ (set A)	3.14	1.5
LTA	$CH_4 - O$ (set B)	3.46	0.81
LTA	$C_2H_6 - O$	3.775	1.536
silicalite	$CH_4 - CH_4$	3.730	1.230
silicalite	$CH_4 - O$	3.214	1.108
silicalite	$Xe - Xe$	4.064	1.870
silicalite	$Xe - O$	3.296	1.679

diffusion processes (see Fig. 23.11). It has been shown that the choice of the σ parameter of the Lennard-Jones potential, (23.18), for the methane–oxygen interaction has a dramatic influence not only on the value of the diffusion coefficient but on its concentration dependence. In [43], two different Lennard-Jones potentials – based on the sets A,B of potential parameters shown in Table 23.2 – have been compared.

Analogously to the density distribution (Fig. 23.9), Fig. 23.10 shows the shape of the potential surface and visualizes the different behaviour in the vicinity of the window, resulting from the parameter set A (left) and set B (right), respectively. It can be seen that the potential values are high in the centre of the large cavity and, of course, at the repulsive walls. The potential

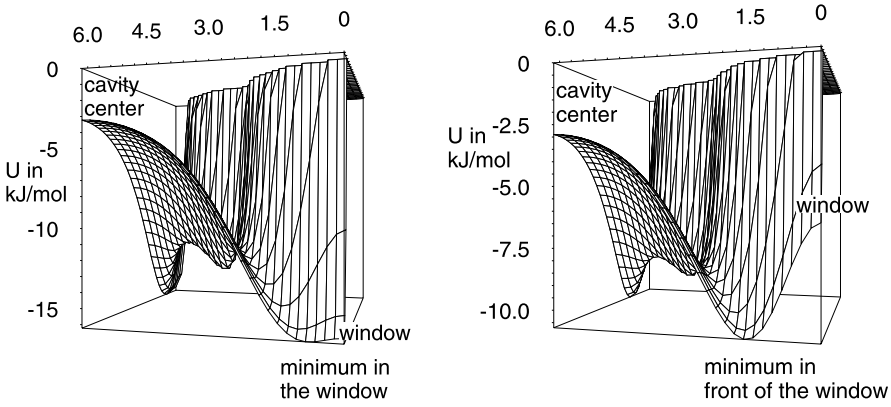

Fig. 23.10. Potential surface plotted through one quarter of the planes considered in Fig. 23.9 (left: set A; right: set B, cf Table 23.2).

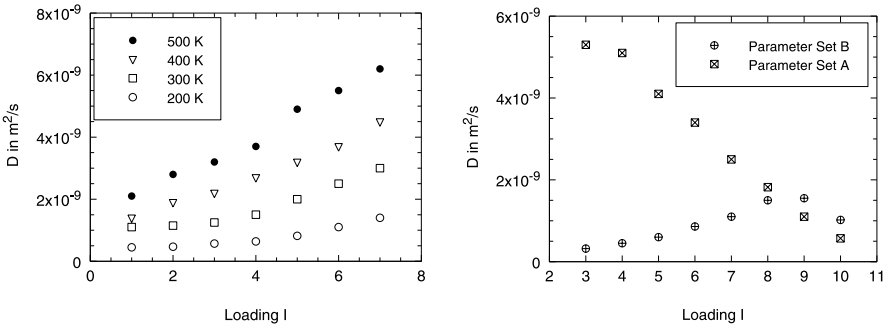

Fig. 23.11. Diffusion coefficient D for different loadings of methane in the cation-free LTA zeolite (left: different temperatures, set B; right: $T = 173$ K, set A,B)

has a minimum in the window in set A, while for set B the maximum is in front of the window and a saddle point in the centre of the window. This threshold reduces the diffusivity in set B. From the larger value of σ in set B, for the dominating oxygen–guest interaction in the zeolite there results a narrower window between adjacent cavities. Especially for methane, which has a similar size as the window, this causes dramatic changes. This effect seems to be the consequence of the interrelation of two effects (reflection at the inlet of the window, coming back after passing the window) with different density dependence [43, 51].

Fig. 23.11 (left) shows that the diffusion coefficient D increases with increasing mean number of guest molecules per cavity and temperature for set B while this dependence for set A – demonstrated for $T = 173$ K – is reversed (right). Both cases show an Arrhenius-like behaviour (cf. (23.21)) (for non-Arrhenius behaviour see, e. g., [67, 68]).

For higher loadings this figure shows an interesting cross-over of the two curves. Increasing diffusivities with increasing concentration is in fact the behaviour found for paraffin in A type zeolites experimentally by PFG NMR (see Chap. 10).

Influence of Lattice Vibrations on the Diffusion Coefficients

The influence of lattice vibrations on the diffusion coefficient in the cation-free LTA zeolite is not very large for both of the parameter sets under consideration as can be seen in Fig. 23.12 (left) [22, 58, 60, 66, 67]. Thus, the result, initially given by Suffritti and Demontis [47] was corrected, who found a much stronger effect using a parameter set beyond the region of A and B. (Since their parameters lead to a practically closed window, it is most likely that an occasional opening of the windows by vibrations may drastically increase D in such cases.) Moreover, Fig. 23.12 again shows how the potential parameter σ may affect the influence of another feature of the system (viz. the lattice flexibility) on the diffusion coefficients.

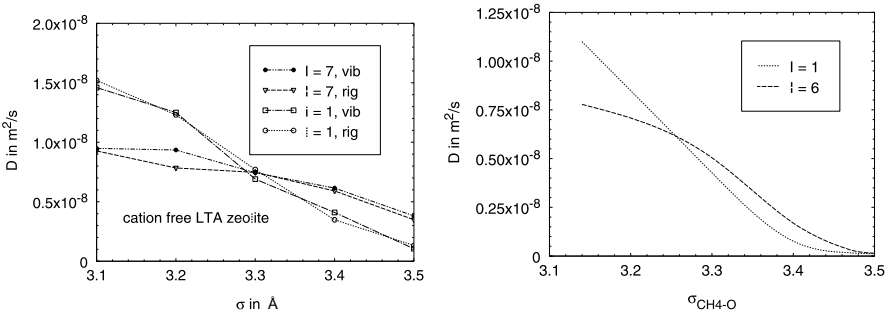

Fig. 23.12. Comparison of D with rigid and vibrating lattice (left: set A; right: set B)

Influence of Cations on D

The dynamics of even small neutral molecules with saturated bindings is strongly influenced by the presence of exchangeable cations [44, 46]. This is investigated for the NaCaA zeolite with 4 Na^+ and 4 Ca^{++} ions. In this case the windows – marked by w in Fig. 23.5 (right) – are (as in the case of the cation-free LTA) free from cations. The unexpected (see [20]) strong effect can clearly be seen in Fig. 23.13 (left) and has been confirmed experimentally, meanwhile ([105], see Chap. 10). In comparison with the cation-free LTA, the self-diffusivity decreases by up to two orders of magnitude. It should be noted that the computational effort is much larger in this case than in the simulations for the cation-free form since much longer trajectories (up to 5-10 ns) are necessary to evaluate such small diffusivities. Additionally, the calculation of the forces resulting from the polarization energy is very

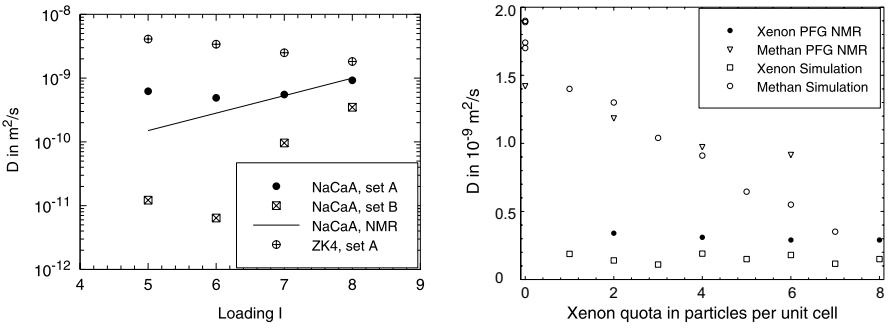

Fig. 23.13. Calculated diffusion coefficients compared with NMR data (left: D of methane in NaCaA and cation-free LTA; right: mixture of CH_4/Xe in silicalite at a total loading of 8 guest molecules per unit cell. The ratio of Xe/CH_4 content is varied keeping the sum of concentrations constant.)

time-consuming although the full Ewald sum can be replaced by a corrected r space part of this sum.

Comparison between MD Simulations and Experimental NMR Data

Fig. 23.13 (left) shows MD results for different situations. Comparison with experimental results from NMR measurements [106] yields satisfactory agreement in the case of set A.
Fig. 23.13 (right) shows that the agreement between numerical MD values and measured NMR data is sufficient also in the case of methane and xenon mixtures (for more details, see [107, 108]).

Propagators and Related Functions

So-called propagators $P(\boldsymbol{r},\, t\,|\boldsymbol{r}_0,\, 0)$ (see p. 928 and (23.22)) represent another way to describe diffusion processes.

Experimentally accessible is the averaged propagator

$$P(\boldsymbol{r},\, t) = \int p(\boldsymbol{r}_0)\, P(\boldsymbol{r}_0 + \boldsymbol{r},\, t\,|\boldsymbol{r}_0,\, 0)\, \mathrm{d}\,\boldsymbol{r}_0\,, \tag{23.25}$$

where $p(\boldsymbol{r}_0)$ denotes the probability density of finding a molecule at position $\boldsymbol{r}_0$. The averaged propagator represents the probability distribution of molecular displacements $\boldsymbol{r}$ during the time interval t for an arbitrarily selected molecule within the sample under study. The pulsed field gradient (PFG NMR) technique [82] allows the determination of the averaged propagator [83, 84] over time and space scales of typically milliseconds and micrometers. As an example, Fig. 10.1 of Chap. 10 displays the propagation patterns of ethane in beds of zeolite NaCaA with two different crystallite sizes for different temperatures [83].

In statistical physics and quasielastic neutron scattering (QENS) – with the relevant time and space scales of 1...100 ps and nanometers –, the averaged propagator $P(\boldsymbol{r},\, t)$ is generally referred to as the self-part $G_\mathrm{s}(\boldsymbol{r}, t)$ of the Van Hove autocorrelation function $G(\boldsymbol{r}, t)$ [40, 54–58]

$$G(\boldsymbol{r}, t) = \frac{1}{N} \left\langle \sum_{j=1}^{N} \sum_{\ell=1}^{N} \delta[\boldsymbol{r} + \boldsymbol{r}_\ell(0) - \boldsymbol{r}_j(t)] \right\rangle, \tag{23.26}$$

with N denoting the particle number. This is seen to be the probability density of finding some particle at time t at distance $\boldsymbol{r}$ from the position of a particle at time $t_0 = 0$. For distinguishable particles one can split $G(\boldsymbol{r}, t)$ into the *self*-part G_s and the *distinct*-part G_d

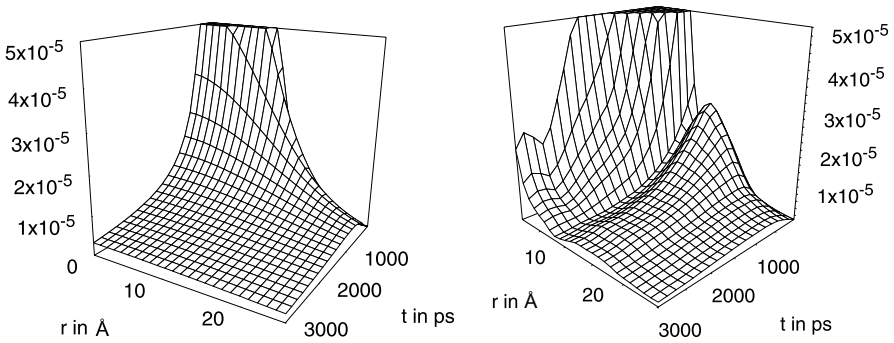

Fig. 23.14. Propagator $P(\boldsymbol{r}, t)$ as function of $\boldsymbol{r}$ and t; left: in ideal bulk systems; right: in 'ZK4' (set B, $I = 3$, $T = 300$ K).

$$G(\boldsymbol{r}, t) = G_{\mathrm{s}}(\boldsymbol{r}, t) + G_{\mathrm{d}}(\boldsymbol{r}, t), \tag{23.27}$$

$$G_{\mathrm{s}}(\boldsymbol{r}, t) = \frac{1}{N} \left\langle \sum_{j=1}^{N} \delta[\boldsymbol{r} + \boldsymbol{r}_j(0) - \boldsymbol{r}_j(t)] \right\rangle , \tag{23.28}$$

$$G_{\mathrm{d}}(\boldsymbol{r}, t) = \frac{1}{N} \left\langle \sum_{j=1}^{N} \sum_{\ell=1(\neq j)}^{N} \delta[\boldsymbol{r} + \boldsymbol{r}_\ell(0) - \boldsymbol{r}_j(t)] \right\rangle . \tag{23.29}$$

The *self*-part G_{s} correlates positions of the *same* particle ($j = \ell$) at different times while G_{d} correlates positions of *different ones* ($j \neq \ell$). $G_{\mathrm{s}}(\boldsymbol{r}, t)$ gives the probability density that within time t a particle moves by $\boldsymbol{r}$, while $G_{\mathrm{d}}(\boldsymbol{r}, t)$ gives the probability density of finding a particle at time t at a distance $\boldsymbol{r}$ from the position of another particle at time 0.

In a homogeneous system, the propagator $P(\boldsymbol{r}, t)$ (cf. (23.25)) is easily found to have a Gaussian form

$$P\left(\boldsymbol{r},\, t\right) = (4\pi D t)^{-\frac{3}{2}} \, \exp\left(-r^2 / \left(4Dt\right)\right), \tag{23.30}$$

with D denoting the self-diffusivity.

The evolution of the probability of particle displacements as contained in the spatial-temporal dependence of the propagator, corresponding to (23.30), is shown in Fig. 23.14 (left). Fig. 23.14 (right) illustrates that the heterogeneity of the host system leads to a fine-structure of the propagator – with spacings given by the separation between adjacent pore centres. The propagator in Fig. 23.14 (right) has been determined by MD simulations for methane in a cation-free A-type zeolite (ZK4) for potential set B (see Table 23.2), loading $I = 3$ and temperature $T = 300\,\mathrm{K}$ [54, 55].

Fig. 23.15 shows – in another representation – the same behaviour for the Van Hove function $G_s(x, t)$, Gaussian in the free space (above) and structured for methane in ZK4 at $I = 3$ and $T = 300\,\mathrm{K}$ (below). The specific structurization of the propagators (see Figs. 23.14 (right) and 23.19) is caused by the

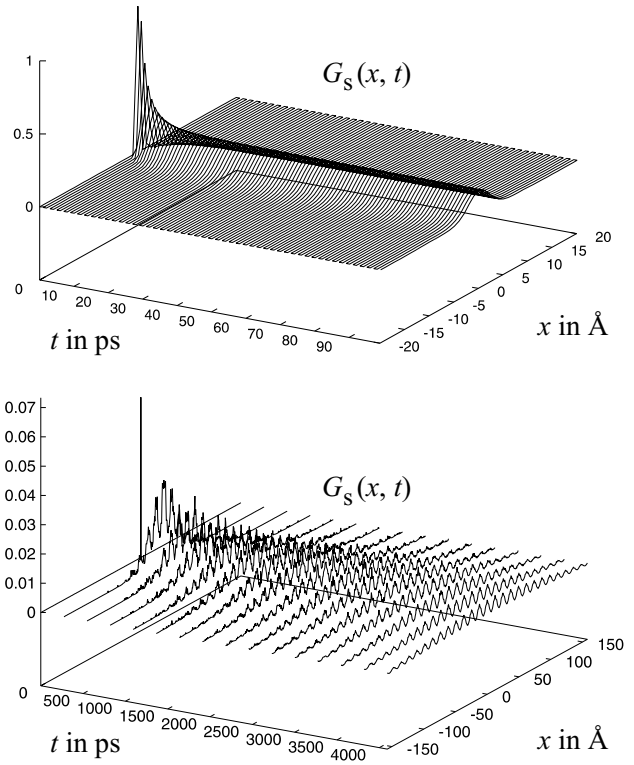

Fig. 23.15. Self-part $G_s(x,t)$ of the Van Hove correlation function in the bulk (above) and the diffusion of methane in ZK4 at $I = 3$ and $T = 300\,\mathrm{K}$ (below).

reflections of the guest molecules at the walls of the cavities in the zeolites which yield peaks in the correlation functions. For an ideal zeolite lattice, the periodicity of the propagator is conserved over arbitrarily large space and time scales. This is demonstrated by Fig. 23.15.

Figure 23.16 shows the dynamic structure factor $S(\boldsymbol{k},\omega)$ ($\boldsymbol{k}$ – wave vector, ω – frequency), i. e. the double Fourier transform of the propagator (self-part of the Van Hove function)

$$S(\boldsymbol{k},\omega) = \frac{1}{2\pi}\int_{-\infty}^{\infty}\int P(\boldsymbol{r},t)e^{-i(\boldsymbol{k}\cdot\boldsymbol{r}-\omega t)}\mathrm{d}\boldsymbol{r}\,\mathrm{d}t \tag{23.31}$$

as the quantity directly accessible by QENS [52, 53] (see Chaps. 2 and 3). $S(\boldsymbol{k},\omega)$ is a generalization of the static case in which the differential cross section is expressed in terms of the pair distribution function (see (23.7d)).

Fig. 23.17 shows the intermediate scattering function $F(\boldsymbol{k},t)$ of QENS, which is defined by

$$F(\boldsymbol{k},t) = \int P(\boldsymbol{r},t)\; e^{-i\,\boldsymbol{k}\,\boldsymbol{r}}\,d\,\boldsymbol{r}\,, \qquad G_s(\boldsymbol{r},t) \equiv P(\boldsymbol{r},t) \tag{23.32}$$

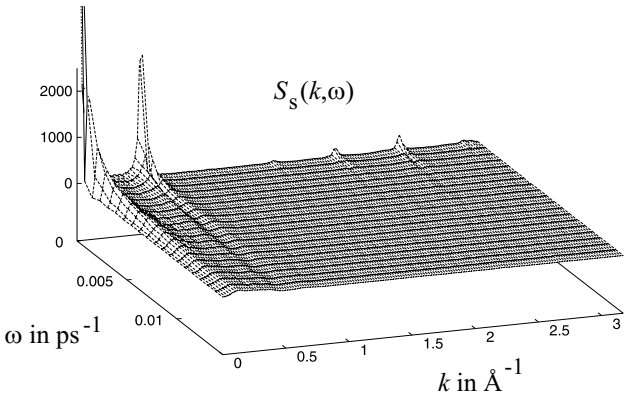

Fig. 23.16. Self-part $S_s(k, \omega)$ of the dynamic structure factor for methane in ZK4 at $I = 3$ and $T = 300\,\mathrm{K}$.

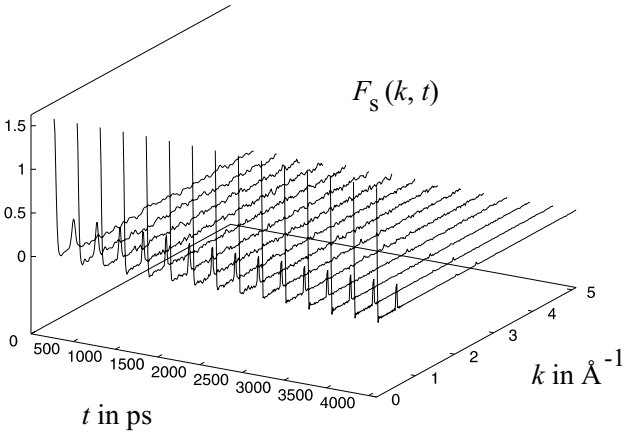

Fig. 23.17. Self-part $F_s(k, t)$ of the scattering function for methane in ZK4 at $I = 3$ and $T = 300\,\mathrm{K}$.

using the propagator of methane in cation-free zeolite LTA [54,55]. The scattering vector $\boldsymbol{k}$ has been chosen to be parallel to one of the crystallographic axes.

For zeolites of non-cubic structure, the propagator exhibits the differences of molecular propagation in different directions. This is exemplified by Fig. 23.18 showing the propagator with respect to the x-, y- and z-axes for methane in silicalite.

The over-all self-diffusion coefficient D evaluated from the corresponding scattering factor $S(\boldsymbol{k}, \omega)$ is $8.6 \cdot 10^{-9}\,\mathrm{m^2 s^{-1}}$, which is in good agreement with the experimental value of $9.3 \cdot 10^{-9}\,\mathrm{m^2 s^{-1}}$ extrapolated from QENS data measured by Jobic et al. [52]. Analytical approximations for $G_s(\boldsymbol{r}, t)$ and the related quantities are given in [54,55]. The experimental observation of such

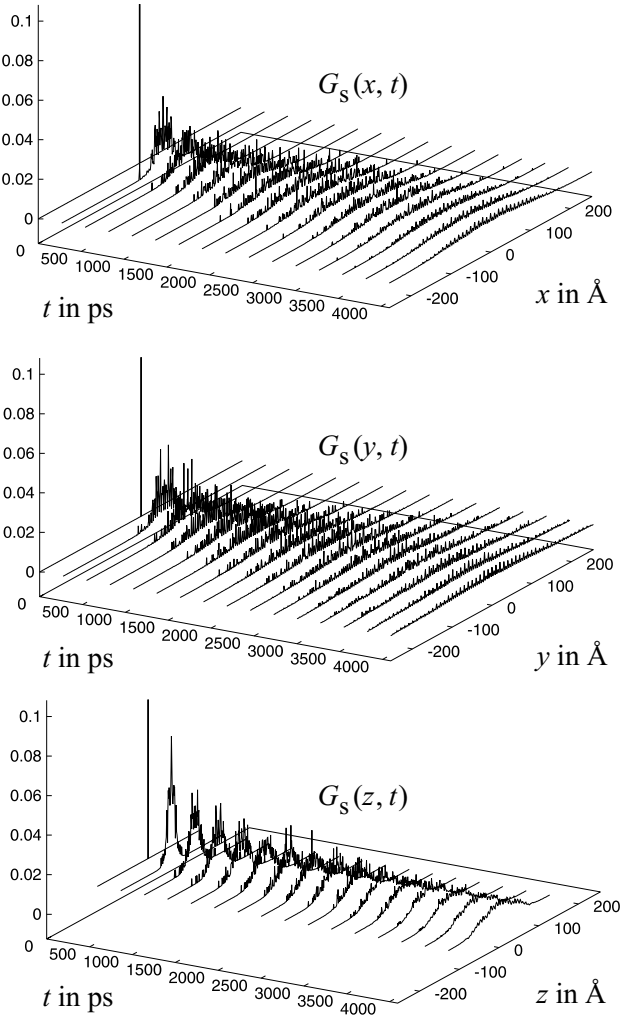

Fig. 23.18. Self-part G_s of the Van Hove correlation function for the diffusion of methane in silicalite in x-, y-, and z-direction at $I = 3$ and $T = 300\,\mathrm{K}$.

structured propagators is a challenging task for QENS. In the light of the theory, such a behaviour should quite generally be expected.

Fig. 23.19 uses an alternative representation of the propagator for visualizing the diffusion behaviour of C_2H_6 in ZK4 in a time interval of $t = 1....1000$ ps [57, 61]. In this case, the propagator was calculated with respect to two coordinates x, y. It can be seen that the propagator shows a more complicated structure than in the case of CH_4, most likely as a consequence of the more intricate intermolecular interaction.

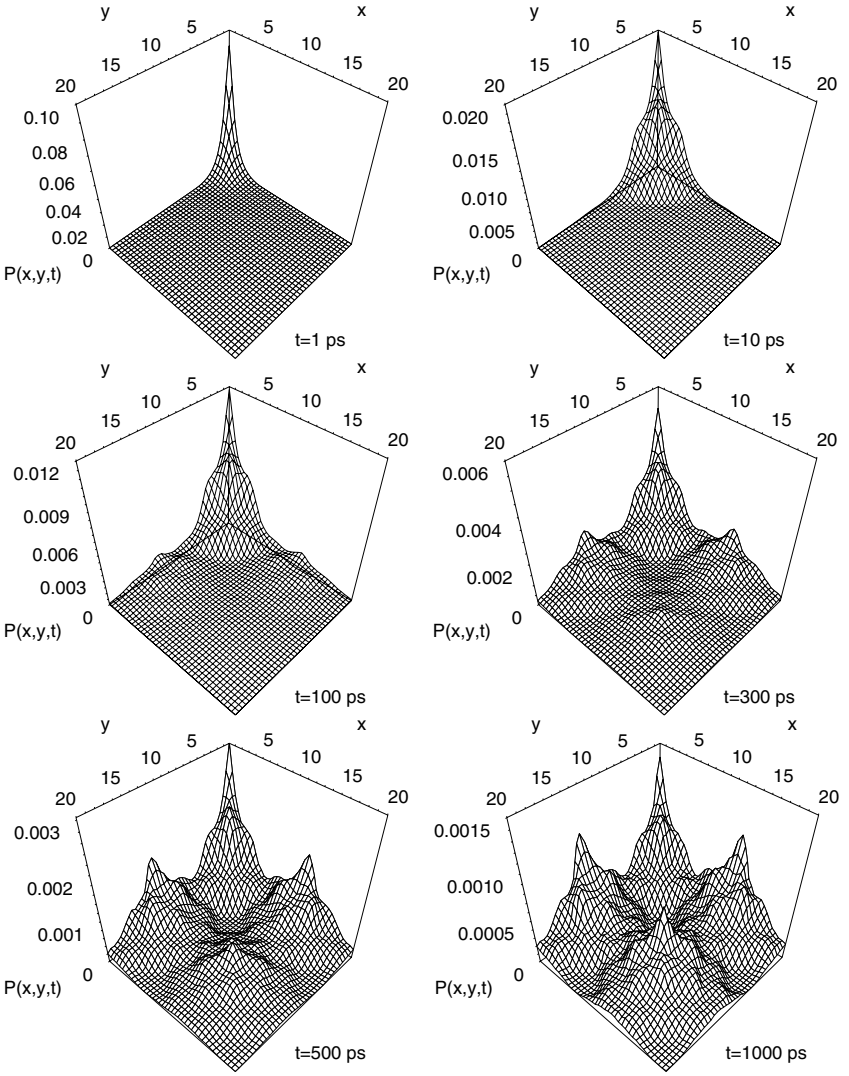

Fig. 23.19. Two-dimensional graph of the time development of the propagator $P(x, y, t)$ (x, y in Å; t in ps) calculated from a trajectory (potential set A, see Table 23.2, $I = 3$, $T = 300\,\mathrm{K}$, $D = 2 \cdot 10^{-9}\mathrm{m}^2\mathrm{s}^{-1}$) [61].

Transport-Diffusivity, Corrected Diffusivity and Self-Diffusivity

While the self-diffusion coefficient D according to the Kubo theory may be obtained from [2, 6, 17, 27, 48]

$$D = \frac{1}{3N} \sum_{j=1}^{N} \int_0^\infty \mathrm{d}t \langle \boldsymbol{v}_j(0) \boldsymbol{v}_j(t) \rangle \,, \tag{23.33a}$$

the so-called corrected diffusion coefficient D_c includes the cross-correlations between velocities of different particles

$$D_\mathrm{c} = \frac{1}{3N} \sum_{j=1}^{N} \sum_{k=1}^{N} \int_0^\infty \mathrm{d}t \langle \boldsymbol{v}_j(0) \boldsymbol{v}_k(t) \rangle \,. \tag{23.33b}$$

The diffusion coefficient that appears in Fick's law is often called transport diffusion coefficient D_T [14]

$$J = -D_\mathrm{T} \frac{\mathrm{d}\, n}{\mathrm{d}x} \,, \tag{23.33c}$$

J is the flux and n is the density. If the force F in the well-known relation

$$v = BF \,, \tag{23.33d}$$

is substituted by the chemical potential μ one has

$$J = -nB \frac{\mathrm{d}\, \mu}{\mathrm{d}x}, \tag{23.33e}$$

where B is the mobility. According to Kubo's theory B is connected with the corrected diffusivity by the relation

$$D_\mathrm{c} = B k_\mathrm{B} T. \tag{23.33f}$$

Comparison of (23.33c) and (23.33e) together with (23.33f) leads to

$$D_\mathrm{T} = D_\mathrm{c} \frac{n}{k_\mathrm{B} T} \frac{\mathrm{d}\mu}{\mathrm{d}n} \,, \tag{23.33g}$$

which is a somewhat unusual form of the well-known Darken equation and has been used already in Sect. 4.4 of Chap. 10 (cf. (10.23)) [14]. These different diffusivities obtained from equilibrium and non-equilibrium MD simulations are compared with each other (Fig. 23.20 (right)). The self-diffusion coefficients have been obtained from the mean square displacement. D_T results from non-equilibrium simulations in which a density gradient (see Fig. 23.20 (left)) in six layers of cavities is created by randomly inserting particles that leave the last layer and enter into the first layer. The flux has been evaluated in the intermediate region only [48]. D_s^{xy} is obtained from the mean square

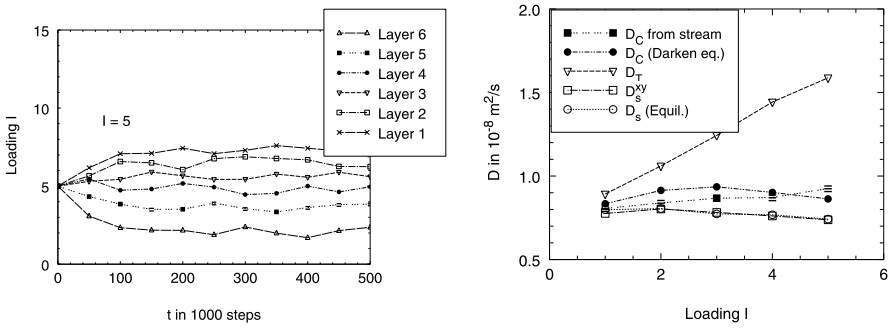

Fig. 23.20. Transport diffusion coefficients (left: Concentration gradient versus time; right: Transport diffusion coefficient D_{T} from non-equilibrium MD) in comparison to self-diffusion coefficient D and corrected diffusion coefficient D_{c}.

displacement perpendicular to the density gradient. It turns out that the flux has practically no influence on the self-diffusion in the direction perpendicular to the flux. D_{c} is somewhat larger than D, which might be attributed to the collective effects expressed by the cross-correlation terms in (23.33b). D_{c} is obtained from D_{T} by the Darken equation and compared with results from another non-equilibrium MD experiment. In this experiment, a flux is produced by an external field. Measuring this flux, D_{c} may be obtained from (23.33f).

23.5 Conclusion

Diffusion coefficients of guest molecules in zeolites have been calculated under different conditions:

1. Statistical physics and molecular dynamics provide the basis for the evaluation of diffusion coefficients of guest molecules in zeolites and for the comparison to experimental data.
2. Summarizing this chapter one can state:
   a) Even single particles diffusing through narrow cavities in zeolites show a macroscopic behaviour, which obeys the diffusion equation for not too small times and distances.
   b) Temperature dependencies of diffusion coefficients of guest molecules show very often an Arrhenius behaviour.
   c) Small changes in lattice parameters can cause dramatic changes in the diffusion coefficient, even in the dependence on concentration.
   d) The presence of cations Na^{+}, Ca^{++} strongly influences the diffusion of even neutral molecules [46], while the assumption of a fixed lattice seems to significantly affect the diffusion coefficients only in exceptional cases. Thus, as a rule, a fixed lattice can be used.

e) MD calculations for single- and two-component adsorbates are in fair agreement with measured NMR and QENS data [22, 53, 108].
f) Non-equilibrium simulations show that transport-diffusion includes additional contributions in comparison with self-diffusion.
g) In order to get reliable data in evaluating the diffusion coefficients one needs good statistics, i. e. long runs with short time steps (up to millions of steps of 5-10 fs each) and a large number of MD boxes (here used up to 343).
h) Hierarchical simulations lead to an extension of the possible time scale of the examined processes by orders of magnitude.

3. More information, especially about the analytical treatment of the diffusion of guest molecules in zeolites (using for instance the Maxwell–Stefan formulation (MS method) [26, 85, 86]), transition state theory (TST), dynamically corrected transition state theory (DCTST), lattice gas theories and dynamical Monte Carlo simulations, respectively), can be found in the literature [22, 90–104].
4. More and more the potentials used will be determined by different methods such as fitting procedures (i. e. comparison with experimental data) and more sophisticated methods in determining intermolecular potentials (i. e. quantum mechanical calculations and, later on, density functional methods) [27, 28, 67].
5. For the future, one can look forward to solving more complex and realistic problems including diffusion and/or reaction – up to catalysis – of non-reactive [107, 108] and reactive mixtures of guest molecules. An overview of a lot of recent examinations in the field of diffusion and also some simple models of chemical reactions and catalysis can be found in [22, 23, 67, 109–123].

Notation

$\langle A\rangle_\Gamma$, $\langle A\rangle_\tau$	ensemble, time average
D, D_s	(self-) diffusion coefficient
D_c, D_T	corrected, transport diffusivity
F_i	force components
$F(\boldsymbol{k}, t)$	scattering function
$f(\omega)$	Fourier transform of $\langle \boldsymbol{v}(0) \cdot \boldsymbol{v}(t)\rangle$
$G(r, t)$	Van Hove auto correlation function
$g(r)$	radial distribution function
$H(q_i, p_i, t)$	Hamiltonian function
$\langle \dot{J}_i(t)\dot{J}_j(0)\rangle_\Gamma$	transport coefficient
J_i, X_z	flux densities, generalized forces
$K_{AB}(t)$	time correlation function $\langle A(t)B(0)\rangle_\Gamma$
k_B	Boltzmann constant

$L(q_i, \dot{q}_i, t)$	Lagrangian function
L_{ik}	Onsager coefficients
N	particle number
$n = \frac{N}{V}$	particle number density
$n^{(1)},\ n^{(2)}$	single-, two-particle density in the q-space
$P(\boldsymbol{r}, t\|\boldsymbol{r}_0, t_0),\ P(\boldsymbol{r}, t)$	propagator
$q, p;\ q_i, p_i$	generalized coordinates and momenta
p	pressure
r	distance between particles
$S(k),\ S(k, \omega)$	(static, dynamic) structure factor
U	internal energy
$U(r),\ U_N(q_i, p_i)$	intermolecular potential
$u(r),\ u(q_{ij})$	potential energy between two particles
$\langle \boldsymbol{v}(0) \cdot \boldsymbol{v}(t) \rangle$	spectral density
μ	chemical potential
ν	number of systems in ensembles of Γ-space
$\rho^{(k)}(q_i, p_i, t)$	k-particle distribution function in Γ-space ($k \leq N$)
$\langle \rho(\boldsymbol{k}, t) \rho(-\boldsymbol{k}, 0) \rangle$	structure factor
$\sigma(\omega)$	(generalized) susceptibility

References

1. J.O. Hirschfelder, C.F. Curtiss, R.B. Bird: *Molecular Theory of Gases and Liquids* (Wiley, New York, 1954)
2. D.A. McQuarrie: *Statistical Mechanics* (Harper & Row, New York London 1976)
3. J.P. Hansen, I.R. McDonald: *Theory of Simple Fluids* (Academic Press, London 1986)
4. *Simulation of Liquids and Solids - Molecular Dynamics and Monte Carlo Methods in Statistical Mechanics*, ed by G. Cicotti, D. Frenkel, I.R. McDonald (North-Holland, Amsterdam 1990)
5. M.P. Allen, D.J. Tildesley: *Computer Simulation of Liquids* (Clarendon Press, Oxford 1990)
6. R. Haberlandt, S. Fritzsche, G. Peinel, K. Heinzinger: *Molekulardynamik. Grundlagen und Anwendungen* (with a chapter *MC-Methods* by H.L. Vörtler), (Vieweg, Wiesbaden 1995)
7. F.F. Abraham: Adv. Phys. **35**, 1 (1985)
8. K. Binder, D.W. Heermann: *Monte Carlo Simulations in Statistical Physics* (Springer, Berlin Heidelberg New York 1988)
9. D. Frenkel, B. Smit: *Understanding Molecular Simulation* (Academic Press, San Diego 1996)
10. B.J. Alder, T.E. Wainwright: J. Chem. Phys. **27**, 1208 (1957); **31**, 459 (1959)
11. A. Rahman: Phys. Rev. **136A**, 405 (1964)
12. L. Verlet: Phys. Rev. **159**, 98 (1967); **165** 201 (1968)
13. A. Rahman, F.H. Stillinger: J. Chem. Phys. **55**, 3336 (1971)

14. J. Kärger, D.M. Ruthven: *Diffusion in Zeolites and other Microporous Solids* (Wiley, New York 1992)
15. J.P. Boon, S. Yip: *Molecular Hydrodynamics* (McGraw-Hill, New York 1980)
16. H.J. Kreuzer: *Nonequilibrium Thermodynamics and its Statistical Foundations* (Clarendon Press, Oxford 1981)
17. R. Kubo, M. Toda, N. Hashitsume: *Statistical Physics II Nonequilibrium Statistical Mechanics* (Springer, Berlin Heidelberg New York 1991)
18. G.D. Harp, B.J. Berne: Phys. Rev. A **2**, 975 (1970)
19. R. Zwanzig: J. Chem. Phys. **33**, 1338 (1960); Annu. Rev. Phys. Chem. **12**, 67 (1961)
20. General Discussion during the Faraday Symposium 26 on 'Molecular Transport in Confined Regions and Membranes', J. Chem. Soc. Faraday Trans. **87**, 1797 (1991)
21. S. Yashonath, P. Demontis, M.L. Klein: Chem. Phys. Lett. **153**, 551 (1988)
22. R. Haberlandt, S. Fritzsche, H.-L. Vörtler: Simulation of microporous systems: confined fluids in equilibrium and diffusion in zeolites. In: *Handbook of Surfaces and Interfaces of Materials*, vol 5, ed by H.S. Nalwa (Academic Press, New York 2001) pp 357–443
23. F. Keil: *Diffusion und Chemische Reaktionen in der Gas/Feststoff–Katalyse* (Springer, Berlin Heidelberg New York 1999)
24. J. Sauer: Zeolites – Applications of computational methods. In: *Encyclopaedia of Computational Chemistry*, ed by R. Schleyer et al (Wiley, Chicester 1998) pp 3248–3264
25. S. Bates, R. van Santen: Adv. Catal. **42**, 1 (1998)
26. F. Keil, R. Krishna, M.-O. Coppens: Chem. Eng. J. **16**, 71 (2000)
27. D.N. Theodorou, R.Q. Snurr, A.T. Bell: Molecular Dynamics and Diffusion in Microporous Materials. In: *Comprehensive Supramolecular Chemistry*, vol 7, ed by G. Alberti, T. Bein (Pergamon, Oxford 1996) pp 507–548
28. P. Demontis, G. B. Suffritti: Chem. Rev. **97**, 2845 (1997)
29. S. Fritzsche: Phase Transitions **52**, 169 (1994)
30. N. Chen, J.T.F. Degnan, C. Smith: *Molecular Transport und Reaction in Zeolites* (VCH, New York 1994)
31. B. Smit: J. Chem. Phys. **99**, 5597 (1995)
32. C. Bussai, S. Hannongbua, R. Haberlandt: J. Phys. Chem. B **105**, 3409 (2001)
33. C. Bussai, S. Hannongbua, S. Fritzsche, R. Haberlandt: Chem. Phys. Lett. **354**, 310 (2002)
34. C. Bussai, H. Liu, S. Vasenkov, W. Böhlmann, S. Hannongbua, S. Fritzsche, R. Haberlandt, J. Kärger: Appl. Catal., A **232**, 59 (2002)
35. R. Car, M. Parrinello: Phys. Rev. Lett. **55**, 2471 (1985)
36. E. Nusterer, P. Blöchl, K. Schwarz: Angew. Chem. **35**, 175 (1996)
37. E. Nusterer, P. Blöchl, K. Schwarz: Chem. Phys. Lett. **253**, 448 (1996)
38. F. Haase, J. Sauer: Microporous and Mesoporous Materials **35-36**, 379 (2000)
39. S. Fritzsche, R. Haberlandt, J. Kärger, H. Pfeifer, M. Wolfsberg: Chem. Phys. Lett. **171**, 109 (1990)
40. S. Fritzsche, M. Gaub, R. Haberlandt, G. Hofmann: J. Mol. Model. **2**, 286 (1996)
41. C.R.A. Catlow, C.M. Freeman, B. Vessal, S.M. Tomlinson, M. Leslie: J. Chem. Faraday Trans. **87**, 1947 (1991)
42. S. Fritzsche, R. Haberlandt, J. Kärger, H. Pfeifer, K. Heinzinger: Chem. Phys. Letters **198**, 283 (1992)

43. S. Fritzsche, R. Haberlandt, J. Kärger, H. Pfeifer, K. Heinzinger: Chem. Phys. **174**, 229 (1993)
44. S. Fritzsche, R. Haberlandt, J. Kärger, H. Pfeifer, M. Waldherr-Teschner. In: *Studies in Surface Science and Catalysis*, vol 84 (Elsevier, Amsterdam 1994) p 2139
45. S. Fritzsche, M. Gaub, R. Haberlandt, G. Hofmann, J. Kärger. In: *Studies in Surface Science and Catalysis*, vol 105 (Elsevier, Amsterdam 1997) p 1859
46. S. Fritzsche, R. Haberlandt, J. Kärger, H. Pfeifer, K. Heinzinger, M. Wolfsberg: Chem. Phys. Lett. **242**, 361 (1995)
47. P. Demontis, G.B. Suffritti: Chem. Phys. Lett. **223**, 355 (1994)
48. S. Fritzsche, R. Haberlandt, J. Kärger: Z. Phys. Chem. **189**, 211 (1995)
49. P. Demontis, E.S. Fois, G.B. Suffritti, S. Quartieri: J. Phys. Chem. **94**, 4329 (1990)
50. E.J. Maginn, A.T. Bell, D.N. Theodorou: J. Phys. Chem. **97**, 4173 (1993)
51. S. Fritzsche, R. Haberlandt, G. Hofmann, J. Kärger, K. Heinzinger, M. Wolfsberg: Chem. Phys. Letters **265**, 253 (1997)
52. H. Jobic, H. Bée, G. Kearly: Zeolites **9**, 312 (1989)
53. H. Jobic: Physical techniques for solid materials. In: *Catalyst Characterization*, ed by B. Imelik, J. Vedrine (Plenum Press, New York 1994) p 347
54. M. Gaub: Molekulardynamische Untersuchungen zur Diffusion von Methan in Zeolithen. PhD thesis, University of Leipzig (1998)
55. M. Gaub, S. Fritzsche, R. Haberlandt, D.N. Theodorou: J. Phys. Chem. **103**, 4721 (1999)
56. J. Kärger, D. Ruthven: Self–diffusion and diffusive transport in zeolite crystals. In: *Progress in Zeolite and Microporous Materials*, ed by Y.U.H. Chon, S.-K. Ihm (Elsevier, Amsterdam 1997) pp 1843–1858; Stud. Surf. Sci. Catal. **105**, 1843 (1997)
57. R. Haberlandt, J. Kärger: Chem. Eng. J. **74**, 15 (1999)
58. R. Haberlandt: Thin Solid Films **330**, 34 (1998)
59. G. Schrimpf, M. Schlenkrich, J. Brickmann, Ph. Bopp: J. Phys. Chem. **96**, 7404 (1992)
60. S. Fritzsche, M. Wolfsberg, R. Haberlandt, P. Demontis, G.B. Suffritti, A. Tillocca: Chem. Phys. Lett. **296**, 253 (1998)
61. A. Schüring: Molekulardynamik–Simulation zum Diffusionsverhalten von Ethan im kationenfreien A–Zeolithen. Diploma thesis, University of Leipzig (1997)
62. C. Catlow, C. Freeman, B. Vessal, S. Tomlinson, M. Leslie: J. Chem. Soc. Faraday Trans. **87**, 1947 (1991)
63. G. Sastre, C. Catlow, A. Corma: J. Phys. Chem. B **103**, 5187 (1999)
64. N. Raj, G. Sastre, C. Catlow: J. Phys. Chem. B **103**, 11007 (1999)
65. G. Sastre, C. Catlow, A. Chica, A. Corma: J. Phys. Chem. B **104**, 516 (2000)
66. S. Fritzsche, M. Wolfsberg, R. Haberlandt: Chem. Phys. **253**, 283 (2000)
67. S. Fritzsche: Untersuchung ausgewählter Nichtgleichgewichtsvorgänge in Vielteilchensystemen mittels statistischer Physik und Computersimulationen. Habilitation Thesis, University of Leipzig (1998)
68. A. Schüring, S.M. Auerbach, S. Fritzsche, R. Haberlandt: J. Chem. Phys. **116**, 10890 (2002)
69. C. Bussai, S. Fritzsche, R. Haberlandt, S. Hannongbua: Langmuir **21**, 5847 (2005)

70. O. Saengsawang, T. Remsungnen, S. Fritzsche, R. Haberlandt, S. Hannongbua: J. Phys. Chem. B **109**, 5684 (2005)
71. C. Bussai, S. Fritzsche, R. Haberlandt, S. Hannongbua: J. Phys. Chem. B **108**, 13347 (2004)
72. A. Schüring, S. M. Auerbach, S. Fritzsche, R. Haberlandt: Stud. Surf. Sci. Catal. **154**, 2110 (2004)
73. A. Loisruangsin, S. Fritzsche, S. Hannongbua: Chem. Phys. Lett. **390**, 485 (2004)
74. R. Haberlandt, S. Fritzsche, H.-L. Vörtler: Modeling and Simulation of Structure, Thermodynamics, and Transport of Fluids in Molecular Confinements. In: *Molecules in Interaction With Surfaces*, ed by R. Haberlandt, D. Michel, A. Pppl, R. Stannarius (Springer, Berlin Heidelberg New York 2004) pp 1–88
75. A. Schüring, S. Fritzsche, R. Haberlandt, S. Vasenkov, J. Kärger: Phys. Chem. Chem. Phys. **6**, 3676 (2004)
76. C. Bussai, S. Fritzsche, R. Haberlandt, S. Hannongbua: Stud. Surf. Sci. Catal. **154**, 2104 (2004)
77. C. Bussai, S. Fritzsche, S. Hannongbua, R. Haberlandt: J. Phys. Chem. B **107**, 12444 (2003)
78. S. Fritzsche, R. Haberlandt, M. Wolfsberg: Chem. Phys. **289**, 321 (2003)
79. C. Bussai, S. Vasenkov, H. Liu, W. Böhlmann, S. Fritzsche, S. Hannongbua, R. Haberlandt, J. Kärger: Appl. Catal. A **232**, 59 (2002)
80. S. Fritzsche, J. Kärger: Stud. Surf. Sci. Catal. **142**, 1955 (2002)
81. C. Bussai, S. Hannongbua, S. Fritzsche, R. Haberlandt: Stud. Surf. Sci. Catal. **142**, 1979 (2002)
82. H. Pfeifer: Phys. Rep. **26**, 293 (1976)
83. J. Kärger, W. Heink: J. Magn. Reson. **51**, 1 (1983)
84. P. Callaghan: *Principles of Nuclear Magnetic Resonance Microscopy* (Clarendon Press, Oxford 1991)
85. R. Krishna: Chem. Phys. Lett. **326**, 447 (2000)
86. F. Kapteijn, J. Moulijn, R. Krishna: Chem. Engn. Sci. **55**, 2923 (2000)
87. R. Krishna, B. Smit, T. Vlugt: J. Phys. Chem. A **102**, 7727 (1998)
88. R. Krishna, D. Paschek: Ind. Eng. Chem. Res. **39**, 2618 (2000)
89. T. Vlugt, R. Krishna, B. Smit: J. Phys. Chem. B **103**, 1102 (1999)
90. J. Kärger, H. Pfeifer, R. Haberlandt: J. C. S. Faraday I **76**, 1569 (1980)
91. R. June, A. Bell, D. Theodorou: J. Phys. Chem. **95**, 8866 (1991)
92. R.Q. Snurr, A.T. Bell, D.N. Theodorou: J. Phys. Chem. **98**, 11948 (1994)
93. T. Mosell, G. Schrimpf, J. Brickmann: J. Phys. Chem. **100**, 4571 (1996)
94. T. Mosell, G. Schrimpf, J. Brickmann: J. Phys. Chem. **100**, 4582 (1996)
95. B. Smit, L. Loyens, G. Verbist: Faraday Discuss. **106**, 93 (1997)
96. F. Jousse, S. Auerbach: J. Chem. Phys. **107**, 9629 (1997)
97. C. Tunca, D. Ford: J. Chem. Phys. **111**, 2751 (1999)
98. A. Voter: J. Chem. Phys. **106**, 4665 (1997)
99. A. Voter: Phys. Rev. Lett. **78**, 3908 (1997)
100. S. Pal, K. Fichthorn: Chem. Eng. J. **74**, 77 (1999)
101. S. Sarkar, A. A. Kumar, S. Yashonath: J. Chem. Phys. **112**, 965 (2000)
102. J. Ray, H. Graben: Phys. Rev. A **44**, 6905 (1991)
103. A. Voter, J. Doll: J. Chem. Phys. **82**, 80 (1985)
104. D. Chandler: J. Chem. Phys. **68**, 2959 (1978)
105. W. Heink, J. Kärger, S. Ernst, J. Weitkamp: Zeolites **14**, 320 (1994)

106. W. Heink, J. Kärger, H. Pfeifer, P. Salverda, K.P. Datema, A. Nowak: J. Chem. Soc. Faraday Trans. **88**, 515 (1992)
107. S. Jost, S. Fritzsche, R. Haberlandt: Chem. Phys. Lett. **279**, 385 (1997)
108. S. Jost, N.-K. Bär, S. Fritzsche, R. Haberlandt, J. Kärger: J. Phys. Chem. B **102**, 6375 (1998)
109. R. June, A. Bell, D. Theodorou: J. Phys. Chem. **96**, 1051 (1992)
110. M. Allen, P. Schofield: Mol. Phys. **39**, 207 (1980)
111. D. Zichi, G. Ciccotti, J. Hynes, M. Ferrario: J. Phys. Chem. **93**, 6261 (1989)
112. F. Delogu, P. Demontis, G. Suffritti, A. Tilocca: J. Chem. Phys. **109**, 2865 (1998)
113. P. Demontis, G. Suffritti, A. Tilocca: J. Phys. Chem. B **103**, 8141 (1999)
114. P. Demontis, G. B. Suffritti, A. Tilocca: J. Chem. Phys. **111**, 5529 (1999)
115. F.J. Keil, M. Coppens: Monte Carlo Simulation of Reaction Rates by Zeolites. In: *Computer Modelling of Microporous and Mesoporous Materials*, ed by C. Catlow, R. van Santen, B. Smit (Academic Press, Amsterdam 2004)
116. F. Keil, J. Hinderer, A. Garayhi: Catal. Today **50**, 637 (1999)
117. J. Schlitter, M. Engels, P. Krüger, E. Jacoby, A. Wollmer: Molec. Simul. **10**, 291 (1993)
118. P. Ferrara, J. Apostolakis, A. Caflisch: Proteins: Structure, Function and Genetics **39**, 252 (2000)
119. S.C. Turaga, Sc.M. Auerbach: J. Chem. Phys. **118**, 6512 (2003)
120. T.C. Bowen, R.D. Noble and J.L. Falconer: J. Membr. Sci. **245**, 1 (2004)
121. X.Q. Bing-Jian Zhang, H, Zhanga, W. Hub: Fluid Phase Equilib. **219**, 123 (2004)
122. K. S. Smirnov, D. Bougeard: Chem. Phys **292**, 53 (2003)
123. J. Pieper, G. Charalambopoulou, Th. Steriotis, S. Vasenkov, A. Desmedt, R.E. Lechner: Chem. Phys. **292**, 465 (2003)

List of Contributors

Dipl.-Phys. Roger Biel
CIBA Vision GmbH
Postfach 74
63702 Aschaffenburg
Germany

Prof. Armin Bunde
Justus-Liebig-Universität Gießen
Institut für Theoretische Physik III
Heinrich-Buff-Ring 16
35392 Gießen
Germany
bunde@physik.uni-giessen.de

Dr. Cornelia Cramer
Westfälische Wilhelms-Universität Münster
Institut für Physikalische Chemie
Corrensstraße 30/36
48149 Münster
Germany
cramerc@uni-muenster.de

Prof. Jan K. G. Dhont
Forschungszentrum Jülich GmbH
Institut für Festkörperforschung
52425 Jülich
Germany
J.K.G.Dhont@fz-juelich.de

Prof. Wolfgang Dieterich
Universität Konstanz
Fachbereich Physik
78457 Konstanz
Germany
wolfgang.dieterich
@uni-konstanz.de

Prof. Franz Faupel
Universität Kiel
Lehrstuhl für Materialverbunde
Kaiserstr. 2
24143 Kiel
Germany
ff@tf.uni-kiel.de

Dr.-Ing. Andreas P. Fröba
Universität Erlangen
Lehrstuhl für Techn. Thermodynamik
Am Weichselgarten 8
91058 Erlangen
Germany
apf@ltt.uni-erlangen.de

Prof. Klaus Funke
Westfälische Wilhelms-Universität Münster
Institut für Physikalische Chemie
Corrensstraße 30/36
48149 Münster
Germany
K.Funke@uni-muenster.de

Prof. Ulrich Gösele
Max-Planck-Institut für Mikrostrukturphysik
Weinberg 2
06120 Halle
Germany
goesele@mpi-halle.de

Prof. Wolfgang Grill
Universität Leipzig
Institut für Experimentelle Physik II
Linnéstr. 5
04103 Leipzig
Germany
grill@uni-leipzig.de

Prof. Reinhold Haberlandt
Universität Leipzig
Institut für Theoretische Physik
Augustusplatz 10/11
04109 Leipzig
Germany
Reinhold.Haberlandt
@physik.uni-leipzig.de

Prof. Paul Heitjans
Universität Hannover
Institut für Physikalische Chemie
und Elektrochemie
Callinstr. 3-3a
30167 Hannover
Germany
heitjans@pci.uni-hannover.de

Prof. Christian Herzig
Westfälische Wilhelms-Universität
Münster
Institut für Materialphysik
Wilhelm-Klemm-Straße 10
48149 Münster
Germany
herzig@uni-muenster.de

Dr. Manfred Holz
Universität Karlsruhe
Institut für Physikalische Chemie
Kaiserstr. 12
76128 Karlsruhe
Germany
Manfred.Holz
@chemie.uni-karlsruhe.de

Dr. Myron Hupalo
Iowa State University
Dept. of Physics and Astronomy
Ames, Iowa 50011
U.S.A.
hupalo@ameslab.gov

Dr. Sylvio Indris
Universität Hannover
Institut für Physikalische Chemie
und Elektrochemie
Callinstr. 3-3a
30167 Hannover
Germany
indris@pci.uni-hannover.de

Prof. Jan W. Kantelhardt
Martin-Luther-Universität Halle-
Wittenberg
FG Theoretische Physik
von Senckendorff-Platz 1
06099 Halle
Germany
kantelhardt@physik.uni-halle.de

Prof. Jörg Kärger
Universität Leipzig
Institut für Experimentelle Physik I
Linnéstr. 5
04103 Leipzig
Germany
kaerger@physik.uni-leipzig.de

Dr. Ruep E. Lechner
Hahn-Meitner-Institut
Glienicker Straße 100
14109 Berlin
Germany
lechner@hmi.de

Prof. Alfred Leipertz
Universität Erlangen
Lehrstuhl für Technische Thermody-
namik
Am Weichselgarten 8
91058 Erlangen
Germany
sek@ltt.uni-erlangen.de

Prof. Philipp Maass
Technische Universität Ilmenau
Fachgebiet Theoretische Physik II
Weimarer Straße 25
98684 Ilmenau
Germany
philipp.maass@tu-ilmenau.de

Prof. Manfred Martin
RWTH Aachen
Institut für Physikalische Chemie I
Landoltweg 2
52074 Aachen
Germany
martin@rwth-aachen.de

Prof. Helmut Mehrer
Westfälische Wilhelms-Universität Münster
Institut für Materialphysik
Wilhelm-Klemm-Straße 10
48149 Münster
Germany
mehrer@nwz.uni-muenster.de

Dr. Gerhard Meier
Forschungszentrum Jülich GmbH
Institut für Festkörperforschung
52425 Jülich
Germany
G.Meier@fz-juelich.de

Dr. Martin Meyer
Justus-Liebig-Universität Gießen
Institut für Theoretische Physik III
Heinrich-Buff-Ring 16
D-35392 Gießen
Germany

Prof. Yuri Mishin
George Mason University
School of Computational Sciences
4400 University Drive, MSN 5C3
Fairfax, VA 22030-4444
U.S.A.
ymishin@gmu.edu

Prof. Ole G. Mouritsen
University of Southern Denmark
Physics Department
Campusvej 55
5230 Odense M
Denmark
ogm@memphys.sdu.dk

Dr. Kiaresch Mussawisade
Forschungszentrum Jülich GmbH
Institut für Festkörperforschung
52425 Jülich
Germany
k.mussawisade@fz-juelich.de

Prof. Gerhard Nägele
Forschungszentrum Jülich GmbH
Institut für Festkörperforschung
52425 Jülich
Germany
G.Naegele@fz-juelich.de

Dr. Klaus Rätzke
Universität Kiel
Lehrstuhl für Materialverbunde
Kaiserstr. 2
24143 Kiel
Germany
kr@tf.uni-kiel.de

Dr. Uwe Renner
Wissenschaftszentrum Leipzig-Förderverein
Goldschmidtstr. 26
04103 Leipzig
Germany

Prof. Dieter Richter
Forschungszentrum Jülich GmbH
Institut für Festkörperforschung
52425 Jülich
Germany
D.Richter@fz-juelich.de

Dr. Andreas Schirmer
Strahlenmessstelle der Bundeswehr
Humboldtstraße
29633 Munster
Germany

Dr. Martin Schubert
Universität Leipzig
Institut für Experimentelle Physik II
Linnéstr. 5
04103 Leipzig
Germany

Prof. Gunter M. Schütz
Forschungszentrum Jülich GmbH
Institut für Festkörperforschung
52425 Jülich
Germany
G.Schuetz@fz-juelich.de

Prof. Bogdan Sepiol
Universität Wien
Institut für Materialphysik
Strudlhofgasse 4
1090 Wien
Austria
bogdan.sepiol@ap.univie.ac.at

Prof. Tasso Springer
Geigerstr. 7
82166 Gräfeling
Germany

Dr. Frank Stallmach
Universität Leipzig
Institut für Experimentelle Physik I
Linnéstr. 5
04103 Leipzig
Germany
stallmac@physik.uni-leipzig.de

Prof. Teh Yu Tan
Duke University
Department of Mechanical Engineering & Materials Science
Box 90300 Hudson Hall
Durham, NC 27708-0300
U.S.A.
ttan@acpub.duke.edu

Prof. Michael C. Tringides
Iowa State University
Dept. of Physics and Astronomy
Ames, Iowa 50011
U.S.A.
tringides@ameslab.gov

Prof. Ilpo Vattulainen
Helsinki University of Technology
Laboratory of Physics
P.O. Box 1100
02015 HUT Helsinki
Finland
ilp@fyslab.hut.fi

Prof. Gero Vogl
Universität Wien
Institut für Materialphysik
Strudlhofgasse 4
1090 Wien
Austria
gero.vogl@ap.univie.ac.at

Prof. Günter Vojta
Donndorfstr. 20
01217 Dresden
Germany

Prof. Hermann Weingärtner
Ruhr-Universität Bochum
Lehrstuhl für Phys. Chemie II
Universitätsstr. 150
44780 Bochum
Germany
Hermann.Weingaertner
@ruhr-uni-bochum.de

Dr. Thomas Wichmann
Weilerswisterstr. 6
50968 Köln
Germany

Dr. Dirk Wilmer
Westfälische Wilhelms-Universität
Münster
Institut für Physikalische Chemie
Corrensstraße 30/36
48149 Münster
Germany
wilmer@uni-muenster.de

Dr. Karl Ullrich Würz
PBS Softwareberatung
Schwanheimer Str. 144a
64625 Bensheim
Germany

Index